



DEVELOPMENT OF A NEW DESIGN METHOD FOR THE CROSS-SECTION CAPACITY OF STEEL HOLLOW SECTIONS

A thesis

Submitted in fulfillment of the requirements for the degree

Of

Doctor in Applied Sciences

By

JOANNA NSEIR

19 June 2015

MEMBERS OF THE JURY

M. Philippe Rigo (President of the jury)
University of Liège, Department Argenco
Chemin des Chevreuils, 1 B52
B – 4000 LIEGE – Belgium

M. Jean-Pierre Jaspart (Supervisor)
University of Liège, Department Argenco
Chemin des Chevreuils, 1 B52
B – 4000 LIEGE – Belgium

M. Fadi Geara (Supervisor)
Saint-Joseph University USJ, Engineering Faculty ESIB
Technologies and Sciences Campus, Mar Roukoz, Mkalles
Riad El Solh, Beyrouth, 11 07 2050 – Lebanon

M. Nicolas Boissonnade (Supervisor)
University of Applied Sciences of Western Switzerland – Fribourg
Bd de Perolles 80 – CP 32
CH-1705 Fribourg – Switzerland

M. Leroy Gardner
Imperial College London
Department of Civil and Environmental Engineering
South Kensington Campus, London, SW7 AZ, UK

M. Alfred Seyr
Voestalpine Krems GmbH
Schmidhüttenstrasse 5, Krems Austria

M. Jean-Francois Demonceau
University of Liège, Department Argenco
Chemin des Chevreuils, 1 B52
B – 4000 LIEGE – Belgium

‘Il faut avoir beaucoup étudié pour savoir peu’

‘Montesquieu’

ACKNOWLEDGEMENTS

I would like to thank all the people who contributed in some way to the work described in this thesis. First and foremost, I would like to express my special appreciation and thanks to my supervisor M. Nicolas Boissonnade, who has been a tremendous mentor for me. I would like to thank you for encouraging my research and for allowing me to grow as a research scientist. Your advice on both research as well as on my career have been priceless. I would also like to express my sincere gratitude to my directors, M. Jean-Pierre Jaspard and M. Fadi Geara who have both become role models for me. Thank you for your encouragements, constructive moments and advices necessary for my progress through my doctoral program.

I also want to thank the jury, M. Philippe Rigo, M. Leroy Gardner, M. Alfred Seyer and M. Jean-francois Demonceau, for dedicating their time and lending me their expertise in order to accomplish this work, for that i am very honored.

I would like to thank the universities who accompanied and supported me during my thesis. I owe my gratitudes to the University of Applied Sciences of Western Switzerland, Fribourg (HEIA-FR), Liege University, Belgium (Ulg) and Saint-Joseph University, Lebanon (USJ).

This project was financed by CIDECT and AUF. I could not have completed my work without their financial support. I owe also gratitude to Voestalpine Krems for supplying the necessary specimens for my experiments.

A big thank you to all my colleagues and friends Raja, Laurent, Julien, Vincent, Yongzhen, Raphael, Delphine, Ana, Jonathan and the Lab technicians Jean-Paul and Dominique. I had an enormous pleasure to work and interact with all of you in a very good atmosphere.

Many thanks for Yanis Schaller. Thank you for helping me and bearing with me during my experimental tests. Although I was always leaving a huge mess behind me in the lab, you supported me and helped me through my campaign.

Many Thanks to Elsy and Marielle, my two steel PhD colleagues for the lovely moments we spent together and the long working days we had in our messy office. We shared lot of great funny moments during our stay in Switzerland and in many congresses.

Thanks to Lionel Moreillon who helped me in the test set-up drawings of my thesis and who gave me and taught me a great experience in research during my masters, which was an encouragement for me to start my PhD.

I would particularly like to thank Joao Tomas Silva for his continuous support during my thesis. Thank you Joao for being my little brother (sorry big) and thank you for helping me during my hardest moments of my PhD. I would never forget you standing by my side and helping me in the Lab until 4am in the morning.

I am most grateful for all the support I received from my family. Special thanks to mom and dad, for being always beside me and supporting me in every task i was involved in. Thanks mom for your continuous prayers for me and sorry for making you worry about me during my hardest times in my PhD. Dad, thank you for always making me feel that you are proud of me no matter what, and always supporting me.

Finally, and last but certainly not least in any way, my deep gratitudes to my dear fiancé Simon Yared for his massive support and infinite patience all along my PhD period. I am lucky to have met Simon and i thank him for his love, friendship and unyielding support.

Joanna Nseir, June 2015

ABSTRACT

The cross-sectional behaviour of steel sections can be shown to be influenced by two extreme behaviors: the resistance and the instability. These boundaries are accounted for in current standards through a classification system consisting on rules depending on the cross-section dimensions. For example, in EN 1993-1-1, classes are defined spanning from stocky sections (class 1) able to develop their full plastic capacity, to slender sections (class 4) for which the effective properties are used with the use of the effective width method (EWM). However, for cold-formed steel sections, characterized by a non-linear material law, the cross-section resistance can go beyond its plastic capacity due to strain hardening effects. Moreover, with the emergence of high strength steel (i.e. cross-sections falling into class 4) and more complex cross-section shapes, the effective width method is becoming too complicated. Many other reasons and discrepancies are making the cross-section classification too complex and inconsistent.

The Overall Interaction Concept (OIC) stands as a new design approach that aims at a straightforward design check of the stability and resistance of steel cross-sections. Based on the use of a generalized relative slenderness and so-called interaction curves, it can be applied to any type of cross-section, further includes potential non-linear material behaviour and covers combined loading cases. The main aim of this thesis is to develop and propose OIC interaction curves dedicated to steel hollow sections subjected to various load cases.

A test program was carried out as a part of a European project named ‘HOLLOPOC’ to investigate the cross-sectional behavior of cold-formed hot-finished and hot-rolled square, rectangular and circular sections. 57 cross-sections tests including simple and combined load cases were performed. Besides, a finite element model was developed and calibrated on the basis of the tests, and its accuracy was seen to be sufficient to subsequently undergo an extensive numerical parametric study for hot-rolled and cold-formed cross-sections, leading to over than 40 000 numerical results. Based on these computations, design proposals were made within the context of the Overall Interaction Concept, using an extension of the Ayrton-Perry approach. Finally, a validation of the proposed formulae was made through a comparison with existing approach and worked examples were presented, in order to illustrate (i) the application of the method and (ii) its benefits in comparison to application of current EC3 rules.

TABLE OF CONTENTS

ACKNOWLEDGEMENTS.....	III
ABSTRACT	V
NOTATIONS.....	XIV
1. INTRODUCTION.....	22
1.1. Context	22
1.2. Scope and objectives of the thesis	25
1.3. Outline of the thesis.....	28
2. STATE OF THE ART	30
2.1. Literature review on local buckling.....	30
2.1.1. Brief historical review	30
2.1.2. Elastic behavior of plates under edge compression	31
2.1.2.1. Elastic buckling stress of plates.....	33
2.1.2.2. Elastic local buckling coefficient of plates and sections	38
2.1.2.2.1. Plate buckling coefficient.....	38
2.1.2.2.2. Cross-sectional buckling	42
2.1.3. Post-buckling behavior and effective width methods.....	47
2.1.4. Influence of residual stresses and initial imperfections on plate buckling	54
2.2. Brief review of plastic theory	56
2.3. Available methods for the determination of buckling loads	58
2.3.1. Finite element method	58
2.3.2. Plastic mechanisms.....	59
2.3.3. Ultimate buckling curves.....	61
2.4. Actual design specifications.....	62

2.4.1. Cross-section classification concept.....	62
2.4.2. Shortcomings of the classification system.....	75
2.4.2.1. Classification system background and emergence of non-linear materials.....	75
2.4.2.2. Emergence of high strength steel	75
2.4.2.3. Boundary conditions and post-buckling reserves.....	76
2.4.2.4. Slenderness definition	77
2.4.2.5. Gap of resistance between class 2 and class 3.....	81
2.4.2.6. Errors and contradictions in table 5.2 of EN 1993-1-1	83
2.4.2.7. Unconformity in the determination of the class 4 plate slenderness limit	89
2.4.2.8. Other inconsistencies.....	91
2.5. Design alternatives in development – Use of modern tools	92
2.5.1. Direct strength method – DSM.....	93
2.5.1.1. Introduction	93
2.5.1.2. Cross-section slenderness definition	93
2.5.1.3. Base curves.....	94
2.5.1.3.1. Sections in compression	94
2.5.1.3.2. Beams	96
2.5.1.3.3. Beam-columns.....	97
2.5.1.4. Practical and theoretical advantages and limitations of DSM.....	99
2.5.2. The continuous strength method – CSM	101
2.5.2.1. Introduction	101
2.5.2.2. Cross-section slenderness definition	102
2.5.2.3. Strain ratio and material model	102
2.5.2.4. Base curve	105
2.5.2.5. Cross-section bending and compression resistance.....	107
2.5.2.6. Cross-section beam-column resistance.....	108
2.5.2.7. Simplified CSM for beam-column	109
2.5.2.8. Practical and theoretical advantages and limitations.....	109
2.6. Summary	110
3. EXPERIMENTAL INVESTIGATIONS	112
3.1. Introduction and objectives.....	112

3.2. Test program	112
3.3. Preliminary measurements.....	116
3.3.1. Cross-sectional dimensions	116
3.3.2. Geometrical imperfections.....	118
3.3.3. Residual stresses	120
3.3.3.1. Fabrication process and type of residual stresses	120
3.3.3.2. Experimental techniques	125
3.3.3.3. Residual stresses measurements	126
3.3.4. Material properties.....	143
3.3.4.1. Tensile tests	143
3.3.4.2. Stub column tests.....	146
3.4. Cross-section tests	152
3.4.1. Testing procedure and results	152
3.4.2. Comparison with EC3 predictions and discussion	161
3.5. Collection of existing results.....	167
3.6. Summary	171
4. NUMERICAL INVESTIGATIONS.....	172
4.1. General	172
4.2. Validation against test results	172
4.2.1. UAS Western Switzerland Fribourg campaign	172
4.2.1.1. Numerical model – Features and characteristics	172
4.2.1.1.1. Elements and meshing.....	172
4.2.1.1.2. Loading and support conditions	176
4.2.1.1.3. Material modeling and residual stresses.....	178
4.2.1.2. Validation: FE results vs. test results	180
4.2.2. TU Graz campaign.....	186
4.2.2.1. General scope of the study	186
4.2.2.2. Numerical model – Features and characteristics	187
4.2.2.2.1. Meshing, geometrical dimensions and imperfections	187

4.2.2.2.2. Loading and support conditions	188
4.2.2.2.3. Material modelling and residual stresses.....	188
4.2.2.3. Validation: FE results vs. test results	190
4.3. Numerical parametric study	192
4.3.1. Meshing, loading and support conditions.....	192
4.3.2. Initial geometrical imperfections.....	193
4.3.2.1. Introduction	193
4.3.2.2. Initial imperfection sensitivity study.....	196
4.3.2.2.1. Local imperfect shape for tested cross-sections	196
4.3.2.2.2. Local imperfect shape study on other cross-sections	205
4.3.2.2.3. Imperfection amplitude study.....	209
4.3.2.2.4. Final selection of geometrical imperfections and recommendations for FE modelling.....	211
4.3.3. Load-path sensitivity	213
4.3.4. Numerical study of hot-rolled sections.....	222
4.3.4.1. Material law and residual stresses	222
4.3.4.2. Parameters considered.....	224
4.3.5. Numerical study of cold-formed sections.....	227
4.3.5.1. Material law and residual stresses	227
4.3.5.2. Cross-sections and parameters considered	229
4.4. Determination of R-factors involved in the OIC approach.....	230
4.4.1. Determination of R_{RESIST}	230
4.4.2. Determination of R_{STAB}	240
4.5. Gathered experimental data vs. FE results.....	243
4.6. Summary	245
5. DESIGN PROPOSAL – OVERALL CROSS-SECTION DESIGN.....	246
5.1. Identification of key parameters.....	246
5.1.1. Influence of yield stress, geometrical imperfections and residual stresses	246
5.1.2. Influence of material law	247
5.1.3. Influence of cross-section shape and load case	250

1.1.1. Influence of warping and second-order effects	252
5.2. Towards a design proposal: Mechanical background	253
5.2.1. Empirical formulations	254
5.2.2. Merchant-Rankine formulation	255
5.2.3. Ayrton-Perry format	257
5.2.4. Adopted formulation.....	259
5.3. Determination of interaction curves.....	261
5.3.1. Simple load cases.....	262
5.3.1.1. Axial compression.....	262
5.3.1.1.1. Hot-rolled sections.....	262
5.3.1.1.2. Cold-formed sections.....	268
5.3.1.2. Major-axis bending.....	277
5.3.1.2.1. Hot-rolled sections.....	277
5.3.1.2.2. Cold-formed sections.....	281
5.3.1.3. Minor-axis bending	287
5.3.1.3.1. Hot-rolled sections.....	287
5.3.1.3.2. Cold-formed sections.....	290
5.3.2. Combined load cases	292
5.3.2.1.1. Hot-rolled sections.....	292
5.3.2.1.2. Cold-formed sections.....	306
6. ACCURACY OF PROPOSED MODELS – COMPARISON WITH ACTUAL RULES.....	324
7. SUMMARY AND RECOMMENDATIONS	344
8. WORKED EXAMPLES	349
8.1. Introduction	349
8.2. Square hollow section: SHS 250x5.....	349
8.2.1. Cross-section and member properties.....	349
8.2.2. Cross-section resistance.....	350

8.2.2.1. Eurocode 3 approach	350
8.2.2.2. OIC approach.....	355
8.3. Rectangular hollow section: RHS 200x100x5	356
8.3.1. Cross-section properties.....	356
1.1.2. Cross-section resistance.....	357
1.1.2.1. Eurocode 3 approach	357
8.3.1.1. OIC approach.....	360
8.4. Summary of results and conclusions	361
9. CONCLUSIONS.....	362
9.1. General	362
9.2. Personal contributions	363
9.3. Suggestions for further studies.....	365
10. REFERENCES	368
11. ANNEXES.....	377
11.1. Annex 1 – Geometrical dimensions.....	377
11.2. Annex 2 – Detailed results of tensile tests	379
11.3. Annex 3 – Detailed results of residual stresses determination	384
11.4. Annex 4 – Detailed results of geometrical imperfection measurements	394
11.5. Annex 5 – Detailed results of stub column tests	396
11.6. Annex 6 – Detailed cross-section test results and comparison with FE results	433
LISTE OF FIGURES.....	608
LISTE OF TABLES.....	627

NOTATIONS

Abbreviations:

AISC	American Institute of Steel Construction
CF	Cold-Formed
CHS	Circular Hollow Section
CSM	Continuous Strength Method
DSM	Direct Strength Method
EC3	Eurocode 3
EN	European Standard
EWM	Effective Width Method
FE	Finite Element
GMNIA	Geometrically, materially nonlinear analysis with imperfections
HF	Hot-Finished
HR	Hot-Rolled
LBA	Linear buckling analysis
LC	Load Case
LVDT	Linear Variable Displacement Transducer
MNA	Materially nonlinear analysis
OIC	Overall Interaction Concept
PNA	Plastic Neutral Axis
RHS	Rectangular Hollow Section
SHS	Square Hollow Section
1S	Upper LVDT at position 1

2S	Upper LVDT at position 2
3S	Upper LVDT at position 3
4S	Upper LVDT at position 4
1B	Bottom LVDT at position 1
2B	Bottom LVDT at position 2
3B	Bottom LVDT at position 3
4B	Bottom LVDT at position 4

Latin letters:

a	Length of local panel
a	Measured deflection of the strip (only used in section 3.3.3)
a	Initial imperfection amplitude (only in section 4.3.2)
B	Section width
b	Width of local panel
b_e	Effective width
b_f	width of the flange
d_z, d_y	Distance between LVDTs along z -axis and y -axis respectively
d_{y1}, d_{y2}	Distance between LVDTs and the centerpoint of the application load along y -axis
d_{z1}, d_{z2}	Distance between LVDTs and the centerpoint of the application load along z -axis
e_y	Excentricity in y -axis direction
e_z	Excentricity in z -axis direction
E	Young's modulus of elasticity
E_m	Young's modulus of elasticity, mean
E_{LVDT}	Young's modulus from LVDTs

E_{SG}	Young's modulus from strain gauges
f	Stress
f_{u_flat}	Material ultimate stress of the flat region
f_{u_corner}	Material ultimate stress of the corner region
$f_{u,m}$	Ultimate stress, mean
f_{csm}	Limiting CSM stress
f_y	Material yield stress
f_{ym}	Material yield stress, mean of yield plateau
f_u	Material ultimate stress
f_{max}	Ultimate tensile stress
F_{exp}	Applied force at ultimate load for experimental tests
F_{FE}	Applied force at ultimate load for Finite Element simulations
F_{pl_actual}	Plastic load based on actual properties
F_{pl_nom}	Plastic load based on nominal properties
h_w	Height of the web
H	Section depth
I_y	Moment of inertia about the strong axis
I_z	Moment of inertia about the weak axis
k	Correction factor (only used in section 3.3.4.2)
k, k_σ	Plate buckling coefficient
l_{final}	Final length measured by the extensometer
$l_{initial}$	Initial length measured by the extensometer
L	Length
L_{arc_i}	Arc length at the inner surface
L_{arc_f}	Arc length at the outer surface
$L_{arc_i_or_f}$	Arc length at the inner or the outer surface

L_{arc_m}	Arc length at the neutral axis
L_{arc_final}	final arc length
m	Number of sine waves of a panel in the x direction
m_y	Normalized major-axis bending moment
m_z	Normalized minor-axis bending moment
M_{Ed}	Design value of the acting bending moment
M_{el}	Elastic cross-section resistance for pure bending moment
M_{pl}	Plastic cross-section resistance for pure bending moment
M_y	Bending moment about the strong axis (y-y)
M_z	Bending moment about the weak axis (z-z)
n	Number of sine waves of a panel in the y direction (used only in section 2.1)
n	Normalized axial force, equal to N / N_{pl}
N	Axial force
N_{pl}	Plastic cross-section resistance for pure axial force
N_{Ed}	Design value of the acting axial force
N_u	Ultimate compression load
N_x	Compression load
P	Compression force
P_{crl}	Elastic local buckling load
P_{crd}	Elastic distortional buckling load
P_{cre}	Elastic global buckling load
P_{nd}	Maximum distortional buckling strength
P_{ne}	Maximum global buckling strength
P_{nl}	Maximum local buckling strength

P_{test}	Test load
P_y	Squash load
r	Corner radius
R_e	External curvature radius
R_i	Internal curvature radius
R_m	curvature radius at the neutral axis
R_{m_final}	Final mid-thickness radius of curvature
R_{ULT}	Ultimate load multiplier
R_{RESIST}	Resistance load multiplier
R_{STAB}	Critical load multiplier
t	Thickness
t_f	Thickness of the flange
t_w	Thickness of the web
w	Deflection of local panel
W_{pl}	Plastic section modulus
W_{el}	Elastic section modulus

Greek letters:

α	Angle of curvature
α	Degree of bi-axiality
α_{CS}	Cross-section imperfection factor
β	Factor relative to the instability limit
β_{crl}	Critical elastic local buckling magnitude under combined P-M-M resultant;
β_y	First yield under combined P-M-M resultant

γ	Exponent factor to the level of axial forces n
γ, β, α	Constants determined based on the manufacturing process (only in section 4.3.2)
Δ_b	Bottom displacement
δ_c	Corrected stub column end-shortening
δ_{LVDT}	End-shortening recorded by LVDTs
Δ_{TOT}	Total displacement
Δ_u	Upper displacement
ε	Strain of $\sqrt{\frac{235}{f_y}}$
ε_{CSM}	CSM strain
ε_{fb}	Failure strain
ε_{fb}	Critical strain
ε_u	Material ultimate strain
ε_x	Strain at position x
ε_y	Material yield strain
η	Generalized imperfection factor
θ_{yb}	Bottom rotation around y -axis
θ_{yu}	Upper rotation around y -axis
θ_{zb}	Bottom rotation around z -axis
θ_{zu}	Upper rotation around z -axis
λ	Relative slenderness
λ_0	End of plateau slenderness
λ_{cs}	Cross-section slenderness
$\lambda_{CS,M}$	Cross-section slenderness relative to a bending load case

$\lambda_{CS,N}$	Cross-section slenderness relative to a compression load case
λ_p	plate slenderness
ξ_f	Clamping coefficient for flange
ξ_w	Clamping coefficient for web
σ	Stress
$\sigma_{0.2}$	0.2% proof stress
σ_{cr}	Critical stress
σ_{ext}	External stress
σ_{max}	Maximum edge stress
σ_{rc}	Stress due to residual stresses
σ_{ult}	Ultimate stress
σ_y	Yield stress
ν	Poisson's ratio
ϕ	Variable accounted for in the Ayrton-Perry formula
χ	Buckling reduction factor
χ_{cs}	Cross-section reduction factor
χ_N	Buckling reduction factor in case of compression
ψ	Fraction of yield stress in tension

1. Introduction

1.1. Context

The use of hollow structural steel has been increasing in the past few years. Although the price per ton of hollow sections is much higher than that of open profiles, their aesthetic appeal and their enhanced static values allow lighter construction and economic structures. Long-span roof structures and industrial buildings are increasingly designed with structural hollow sections. Modern architecture is dominated by tubular cold-formed structure, while industrial structures are dominated by hot-rolled tubular sections. Figure 1 shows some astonishing tubular structures made around the world.



Figure 1– Australia stadium (Australia), the kelpies (Scotland), Liege Guillemins railway station (Belgium), Madrid Barajas international airport (Spain), London eye (Britain).

The increase use of tubular sections is not only due to their excellent architectural aspect but also to their economic advantages in comparison with open sections. Square, rectangular or round cross-sections have outstanding static properties which can be presented as follows:

- (i) Their excellent behavior towards global buckling, lateral torsional buckling and torsion is due to their closed shape and the favourable distribution of material around the longitudinal axis of the section;
- (ii) The use of the internal volume to increase the load bearing capacity of the column by filling it with concrete;
- (iii) The corrosion protection can be applied economically compared to open sections considering that hollow sections have smaller and smoother surfaces without any sharp edges.

However, the use of hollow sections present an inconvenient for the case of elements for which bending is the primary action since the uniform distribution of material around the longitudinal axis of the section would constitute a handicap compared to open sections (H or I). Indeed, for bending, hollow profiles have generally a high sufficient thickness (due to both webs) to absorb shear stresses, but the flange thicknesses are not economically sufficient to absorb the normal stresses due to bending. Therefore, the hollow profiles are undeniably the ideal profiles for columns while open profiles are more suitable for the beams. However, the occurrence of lateral torsional buckling in open sections may change this last conclusion and make the hollow profiles best suited to be used for both columns and beams.

The buckling behavior of hollow profiles becomes even better when the material is distributed as far as possible from the longitudinal axis of the section. For an identical area, one comes to consider that economy will lead to hollow profiles of greater widths and smaller thicknesses. The resulting thinness of the plates may however lead to another phenomenon of instability named '**local buckling**' which is the main issue studied in this thesis. Moreover, the increase in yield stress plays a similar role as the decrease in plates' thicknesses and will also trigger local buckling.

The modern trend is to produce thin-walled hollow sections and high yield strength with significant interaction between local buckling and global buckling. This thesis is only concerned with the study of the behavior of hollow cross-section capacities which will endure either **material yielding or local buckling**.

For what concerns local buckling, most of the actual codes rely on the effective width concept, and the classification system which propose so-called b/t limit ratios that each of the section's wall should fulfill to be considered as non-affected by early local buckling. Besides, recently developed alternatives based on the use of more sophisticated tools [1] or on a continuous relationship between strains and plate slenderness [2] have been suggested.

From a practical point of view, these codes and methods however suffer from a series of issues and inadequacies. Amongst them, the handling of local buckling may appear as the one causing most problems; it is indeed usual to adopt a design resistance formula in accordance with the proneness of the cross-sections to suffer from early local buckling: the earlier the occurrence of local buckling is expected to occur, the more restricted the design rules. In Eurocode 3, this is accounted for through an additional step prior to the verification process that consists in the classification of the cross-section. According to the class of the section¹, different sets of formulae are to be used for the design checks of both sections and members, i.e. plastic or elastic equations. It has been shown [3] that several values of the b/t limit ratios of Eurocode 3 are often misleading, further to suffering from a lack of mechanical background. Moreover, the concept of classes, as it is defined – discrete and artificial – generates a gap of resistance at the class 2-3 border, which is mechanically meaningless and unacceptable.

Recently, improvements have been brought to the European standards, in terms of corrected b/t tables and of additional rules allowing for a linear transition along the class 3 ranges. Although reflecting the actual best knowledge in this field, these design rules still deserve improvements for situations where instability effects are important [4]. Also, in the particular case of plastic and compact sections, several research works suggest that a rational exploitation of strain hardening results in a better prediction of observed behavior and potentially leads to material savings, especially for cold-formed or stainless steel profiles but also for hot-rolled members [5].

Therefore, the aim of the research works presented herein is to contribute in improving this situation and proposing a new design approach replacing the actual classification system, leading to a more mechanical and rigorous approach. This approach would treat accurately

¹ The class of a section is governed and defined by the class of its worst (i.e. weakest) element: in Eurocode 3, class 1 stands for “plastic”, 2 for “compact”, 3 for “semi-compact” and 4 for “slender”.

the occurrence of local buckling and material yielding in short hollow members - in which only local buckling instability might develop - and would allow for a proper interaction between stability (buckling) and resistance (material yielding). This approach is named the **Overall Interaction Concept (OIC)** and will be presented in the following section.

1.2. Scope and objectives of the thesis

The basis of the Overall Interaction Concept depicted herein lies in the well-known interaction between the two main phenomena influencing the carrying capacity of structural members: resistance and instability. The behavior of a real cross-section is therefore influenced by both aspects, acting as upper bounds of the real behavior, as well as by initial imperfections (e.g. out-of-straightness, residual stresses, non-homogenous material...).

In this context, the accurate treatment of the interaction is a key point for a realistic prediction of the section's resistance. No recognized general theoretical background has been established to organize and unify the handling of this crucial interaction in a global way. However, recent developments ([4] & [6]) have offered a glimpse that such an ambitious general approach can fill this fundamental gap of knowledge: the "Overall Interaction Concept". Despite its formal simplicity, the potential of the OIC is such that all structural sections and members, whatever the material, could be treated with an identical general, global, accurate yet simple and sound-based background.

The proposed approach relies on the generalization of the relative slenderness concept, and on establishing this parameter as the key to rule the interaction. This concept of relative slenderness is familiar to structural engineers, and is widely used nowadays to deal with flexural buckling behavior for example. It is suggested within the OIC to drastically enlarge the field of application of this slenderness-related approach through the generalization of the idea of relative slenderness as follows:

$$\lambda_{rel} = \sqrt{\frac{R_{RESIST}}{R_{STAB}}} \quad (1)$$

where R_{RESIST} represents the factor by which the initial loading has to be multiplied to reach the pure resistance limit, while R_{STAB} is the factor used to reach the buckling load of the ideal member (stability limit).

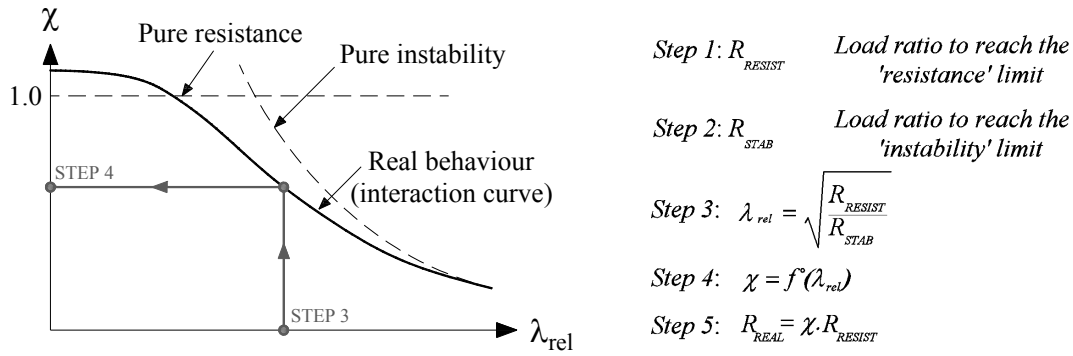


Figure 2 – Principles and application steps of proposed “Overall Interaction Concept”.

Doing so allows the generalized relative slenderness to take a non-dimensional balance between the relative influences of instability and resistance, and makes it capable of dealing with combined loading situations or cross-sectional (local) instability effects as well. Once determined, this λ_{rel} value is further used in the design procedure to get into a so-called “interaction curve” (also sometimes referred to as “buckling curve”) and leads to the determination of a “ χ ” value (see Figure 2). This χ value (analogous to the one used in Eurocode 3), which may also be called “reduction factor”, represents the penalty due to instability effects on the pure resistant behavior, and χ can obviously only be lower than 1.0. Then, the final resistance is evaluated as $\chi \cdot R_{RESIST}$; Figure 2 further illustrates the proposed approach and its application steps.

This rather simple procedure can be applied to many situations within structural engineering – e.g. member buckling, **cross-sectional resistance**... – regardless of the material behavior, and acts as a general approach to each design situation where instability affects the resistance.

Therefore, **the prime aim of this thesis is to investigate the behavior of steel hollow sections and propose a suitable new design curves for the prediction of their cross-section capacities, through a new concept termed the Overall Interaction Concept, OIC.**

The main goals can be subdivided into further sub-sections consisting in:

- (i) A comprehensive literature survey on the local buckling, plastic design history, actual treatment of the cross-section resistance and existing alternatives;
- (ii) An experimental study of the behavior of cold-formed, hot-rolled and hot-finished square, rectangular and circular sections under simple and combined loading. The

identification of a plastic collapse mechanism relative to short members with stocky sections, from a local buckling instability collapse relative to short members with slender sections is required;

- (iii) A simulation of the behavior of tested elements by means of finite element calculations, with the aim of validating the numerical model;
- (iv) An extension and use of the validated finite element model to conduct two numerical parametric studies relative to cold-formed and hot-rolled section that account for the effect of imperfections, varying material properties, specimen dimensions, residual stresses distributions and various load cases going from simple ones to combined ones;
- (v) An Analysis of the governing parameters affecting the cross-section resistance of hollow cross-sections;
- (vi) A proposal of new design curves relative to the cross-section resistance of hollow sections going from stocky to slender ones, subjected to simple and combined load cases, different fabrication processes and different yield limits;
- (vii) A comparison of the proposed design approach with existing design recommendations.

The OIC approach is actually at the core of the STSS project (“Simple Tools Sell Steel”, STSS 2012), whose main objective is to develop and assess new design concepts to predict accurately the response of members made of standard and high-strength steel up to collapse. The objectives are to remove the cumbersome complexity of nowadays calculation methods and to provide efficient design method and tools.

This thesis is concerned with only the cross-sectional resistance of hollow sections and is a part of European project named ‘HOLLOPOC’ with a financed support being provided by the ‘Comité International pour le Developpement et l’Etude de la Construction Tubulaire’ (CIDECT).

1.3. Outline of the thesis

In order to pursue the objectives described in the previous section, this thesis has been organized in the following separate chapters:

Chapter two presents the state of the art concerning this PhD topic; a detailed historical review of local buckling and plastic design is presented. Methods for ultimate buckling load calculations are listed and described. Then, the current design specifications are presented with its shortcomings and finally a discussion is made concerning the existing alternatives.

Chapter three reports on a series of 57 cross-section tests subjected to compression and combined compression and bending. Preliminary measurements were also performed and described in this chapter. They consist in the measurements of the geometrical dimensions and imperfections, the material laws, the residual stresses and the testing of stub columns. The cross-section tests were analyzed and constituted an experimental reference to assess numerical FE models in chapter four. They were then compared with the existing design formulae of EN 1993-1-1.

Chapter four describes finite element models and the simulation of the 57 cross-section tests with the measured imperfections, material law and residual stresses. The numerical model was compared and validated against the 57 experimental cross-section tests. In a subsequent step, the validation was also performed using experimental data from [7]. The validated finite element model was then used to generate an extensive set of numerical cross-section tests (more than 40 000 results were computed) with the aim of investigating the physical behavior of square and rectangular hollow sections.

Chapter five suggests a design model and proposed curves after targeting and analyzing the governing parameters affecting the cross-section resistance of square and rectangular hollow sections.

Chapter six illustrates the accuracy of the proposed design formulae and statistical results of the comparison between FEM, EC3 and proposal calculations are presented.

Chapter seven gives a summary of the proposed design formulae and recommendations for practical design.

Chapter eight provides some worked examples of the newly developed design curves.

Chapter nine summarizes the research, presents the original contributions of this work and gives aspects and suggestions for further investigations.

2. State of the art

2.1. Literature review on local buckling

2.1.1. Brief historical review

Steel structures are usually composed of flat plate elements and are either fabricated through rolling into standard shapes or assembled from individual plates by welding, riveting, bolting, etc.

The buckling of a component plate element can influence the strength of a structural member in two different ways; from one hand, the buckling may occur before the overall failure, thus, making the buckled plate ineffective; from the other hand, the buckling may induce a redistribution of stresses that influences the cross-section and member carrying capacities.

The maximum stress which can be applied to a plate element depends on the width-thickness ratio of the plate, on the boundary conditions and on the stress distribution. The maximum reached stress can be smaller or larger than the theoretical elastic buckling stress, depending on the post-buckling capacity of the constitutive plate element. Cold-formed sections, usually having high b/t ratios, cannot reach their yield strength due to the high slenderness of plate components, but they can however reach strengths higher than their elastic buckling strength, entering thus the post-buckling stage. Rolled sections or built-up sections from thick plates can usually attain the yield stress of the material, due to their small width-to-thickness ratios. In practical design, the width-to-thickness ratio is selected in a way of avoiding the buckling of the plate element below the yield level. The width-to-thickness ratio is not the only factor affecting the maximum average stress reached; the stress distribution and the plate boundary conditions also play a crucial role in the occurrence of local buckling.

In 1823, Navier was the first to formulate the correct differential equation of a buckled plate. His equation is applicable to rectangular plates subjected to equal edge pressure in two directions. Consecutively, he formulated an equation adapted to the current interest in plate vibration (sound produced by a vibrating plate) which was forgotten until Bryan in 1888 was able to solve the plate buckling problem by deriving the following differential equation for a simply supported rectangular plate subjected to a one direction edge compression:

$$\frac{Et^3}{12(1-\nu^2)} \left(\frac{\partial^4 w}{\partial x^4} + 2 \frac{\partial^4 w}{\partial x^2 \partial y^2} + \frac{\partial^4 w}{\partial y^4} \right) = -N_x \frac{\partial^2 w}{\partial x^2} \quad (2)$$

where E is the modulus of elasticity, ν is poisson's ratio, t is the plate thickness, w is the lateral deflection of the plate, and N_x is the edge compression load. Later, Timoshenko (1907) and H. Reissner (1909) analyzed plates with various boundary conditions and Timoshenko investigated the influence of plate buckling on the column strength.

Bleich in 1924 gave the first treatment of inelastic plate buckling and Ros and Eichinger followed him with important contributions in 1932. Later on, the requirements of the aircraft and shipbuilding industries urged and stimulated further developments on plate buckling theories.

It was not until 1930 that the post-buckling strength of plates was noticed. Consequently, empirical approaches were developed for this purpose but were unsuitable for any practical use. Then, in 1932, Von Karman introduced the concept of the effective width to handle this problem, and an approximate formula was derived for simply supported plates. In 1947, Winter made an important contribution for structural engineering in proposing effective width formulae based on extensive test series. These formulae are still used nowadays in many design standards.

The buckling of structural steel plates in the strain-hardening range has been studied since 1956. Members with low slenderness can undergo considerable plastic deformation without local buckling occurrence, thus reaching the strain-hardening range which is subsequently essential to avoid underestimation of plastic capacities in plastic design. The effect of residual stresses on the buckling of plates in the elastic and plastic ranges has been intensively studied since 1962.

2.1.2. Elastic behavior of plates under edge compression

In order to better visualize the plate behavior under edge compression, Figure 3 illustrates the behavior of a perfectly flat rectangular plate made of an ideal material and subjected to edge compression in one direction. The loading is applied through rigid end blocks and the edges are considered to remain straight during loading. A diagram of plate behavior is obtained by plotting the average compressive stress P/bt versus the average strain ε , where b is the plate width and t its thickness.

The line $OABC$ in Figure 3 is a typical load-path for a plate with a large width-thickness ratio b/t .

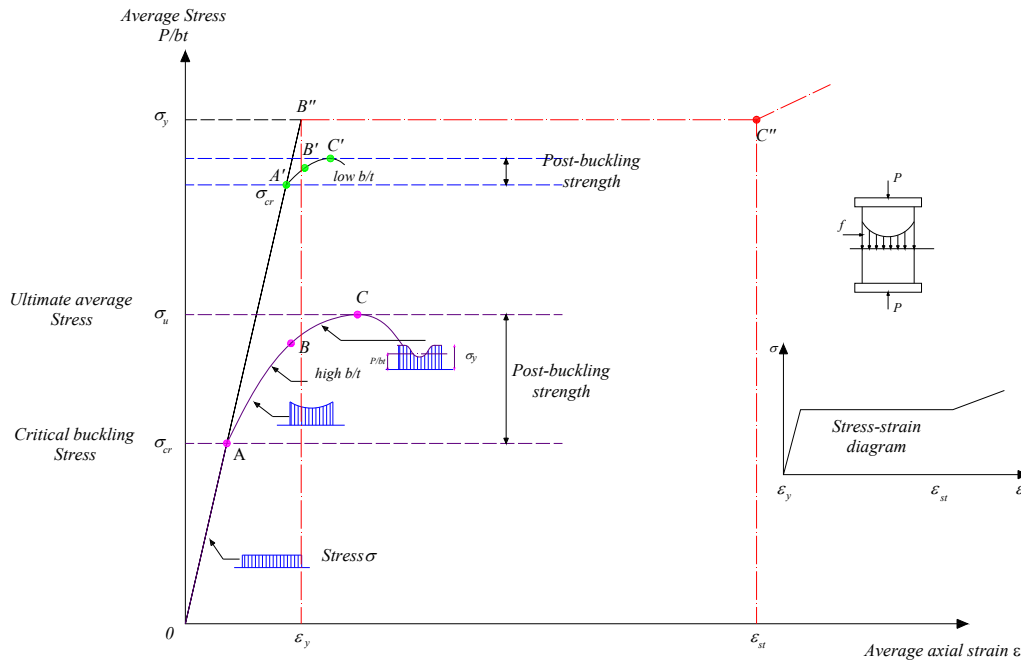


Figure 3 – Behavior of plates under edge compression.

Several stages can be observed; at first, the strain increases with the increasing average stress P/bt . At this stage, the stress σ is distributed uniformly across the width with no out of plane deflection of the plate. Afterwards, the plate starts deflecting and buckles once the average stress P/bt reaches a certain magnitude σ_{cr} (point A). For plates, the load carrying capacity continues in a stable manner even after buckling (due to the redistribution of axial compressive stresses and tensile membrane action that come with the out-of-plane bending of the plate in both the longitudinal and transverse directions [8]). Subsequently, their post-buckling strengths can be greater than their buckling strengths, especially for slender plates. The increase in average stress beyond buckling may be quite substantial for high b/t ratios.

This property is of great interest to structural engineering as it can be utilized to their advantage. The post-buckling strength takes place thanks to the restraint of the buckles provided by the plate spanning in the transverse direction, enabling thus the plate to carry additional loads beyond buckling.

After buckling occurs, the uniform stress distribution becomes a non-uniform pattern as shown for portion AB. This non-uniform distribution is accentuated with an increasing loading leading to greater and gradually stresses redistributions in the stiffer edge directions

until yielding occurs at these edges (point B). Yielding then spreads quickly until the ultimate stress σ_u is reached.

For plates with lower width-to-thickness ratios, the critical stress is close to σ_y and yielding develops almost immediately after buckling. The ultimate stress is then only insignificantly above the critical stress, as shown by the line OA'B'C' in Figure 3.

For cases in which the width-to-thickness b/t ratio reach really small values, the average P/bt will be able to reach the yield point σ_y without buckling and even undergo further strain at the same stress level as shown by the dash-dot line OB''C'' in Figure 3 (Point C'' reflects the beginning of the strain-hardening). The plate will eventually fail at a certain strain before or after C'', depending on the b/t ratio.

Plates with different edge support conditions and stress distribution behave in similar qualitative manner and the main differences lie in the magnitude of the critical buckling stress, and the amount of post-buckling strength.

2.1.2.1. Elastic buckling stress of plates

The buckling load is defined as the load at which a structure becomes in a state of indifferent equilibrium and the corresponding structure may assume more than one deflected position without disturbing equilibrium [9]. Figure 6 illustrates the behavior of a perfectly-flat rectangular plate with simply supported edges and subjected to a uniformly distributed edge compression in one direction. Once the buckling stress is reached, it will remain constant and the plate will be able to deflect in either direction as shown by point A in Figure 6.

Considering a simply supported square plate subjected to a uniform compression stress in one direction, it will buckle in a single curvature in both directions. However, for individual elements of a section, the length of the element is usually much larger than the width so that many waves length shall be developed as seen in Figure 4 and Figure 5 .

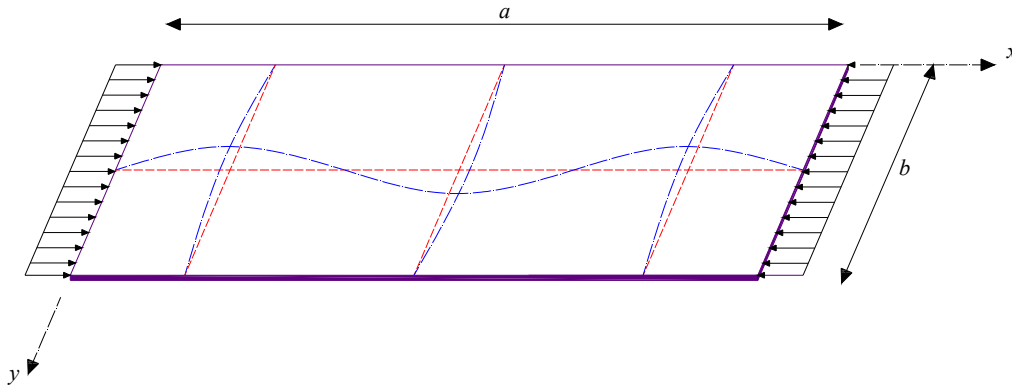


Figure 4 – Behavior of rectangular plates under edge compression.

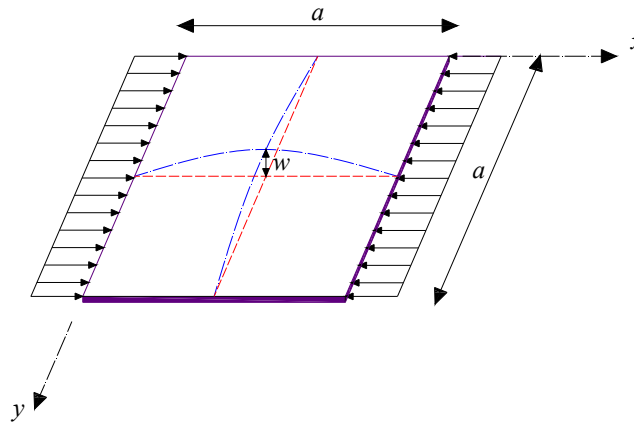


Figure 5 – Behavior of square plates under edge compression.

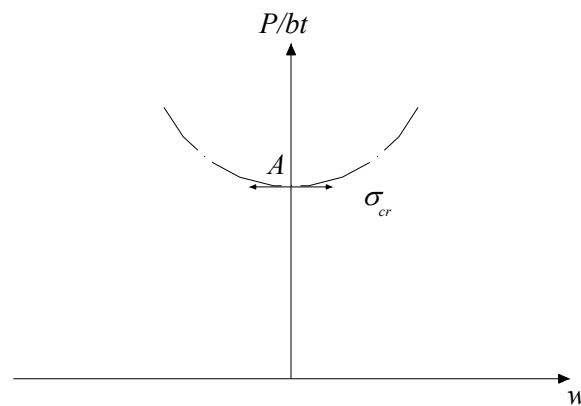


Figure 6 – Lateral deflection of a buckled plate.

The buckling phenomenon for a plate under compression in one direction is described by Equation (2). The solution is obtained with an approach assuming the deflection w to be

represented by a series, satisfying the boundary conditions. For a simply supported plate, the following series is assumed:

$$w = \sum_{m=1,2,3,\dots} \sum_{n=1,2,3,\dots} w_{mn} \sin \frac{m\pi x}{a} \sin \frac{n\pi y}{b} \quad (3)$$

m and n in Equation (3) indicate the number of half sine waves, respectively in the x and y directions of the buckling mode. This shape automatically satisfies the boundary conditions for the plate, that are, $w = 0$ at $x = 0$, $x = a$, $y = 0$ and $y = b$.

Substitution of Equation (3) into Equation (2) gives:

$$\left(\frac{m^4 \pi^4}{a^4} + 2 \frac{m^2 n^2 \pi^4}{a^2 b^2} + \frac{n^4 \pi^4}{b^4} \right) = \frac{12(1-\nu^2)}{Et^3} (N_x)_{cr} \frac{m^2 \pi^2}{a^2} \quad (4)$$

Therefore

$$(N_x)_{cr} = \frac{\pi^2 Et^3}{12(1-\nu^2)} \frac{(m^2/a^2 + n^2/b^2)^2}{m^2/a^2} = \frac{\pi^2 Et^3}{12(1-\nu^2)} \left(\frac{m}{a} + \frac{n^2 a}{mb^2} \right)^2 \quad (5)$$

Equation (5) can be written as follows:

$$(N_x)_{cr} = \left[m \frac{b}{a} + \frac{a}{b} \frac{n^2}{m} \right]^2 \frac{\pi^2 Et}{12(1-\nu^2)} \left(\frac{t}{b} \right)^2 \quad (6)$$

The braked expression is defined as the plate buckling coefficient k :

$$k = \left[m \frac{b}{a} + \frac{a}{b} \frac{n^2}{m} \right]^2 \quad (7)$$

Noting that the buckling load N_{cr} is the product of the buckling stress σ_{cr} and the thickness t , the critical buckling stress is thus defined as the following equation:

$$\sigma_{cr} = \frac{k \pi^2 E}{12(1-\nu^2)(b/t)^2} \quad (8)$$

In Equation (7), the minimum value in square brackets corresponds to $n = 1$, i.e. only one half sine wave occurs in the y direction. Therefore, to find the minimum value of m , Equation (7) is derived in function of m , leading to the following expression:

$$\frac{\partial}{\partial m} \left[m \frac{b}{a} + \frac{a}{bm} \right]^2 = 2 \left(\frac{mb}{a} + \frac{a}{bm} \right) \left(\frac{b}{a} - \frac{a}{bm^2} \right) = 0 \quad (9)$$

Therefore $b/a - a/bm^2 = 0$ and, thus $m = a/b$. The solutions of $n=1$ and $m = a/b$ in Equation (9) leads to:

$$k_{\min} = 4 \quad (10)$$

The value of k is shown in Figure 7 for different a/b ratios. For a/b values comprised between 0 and 1, considering a value of k equal to 4 would be too conservative, whereas this will not be the case for a/b values bigger than 1.0.

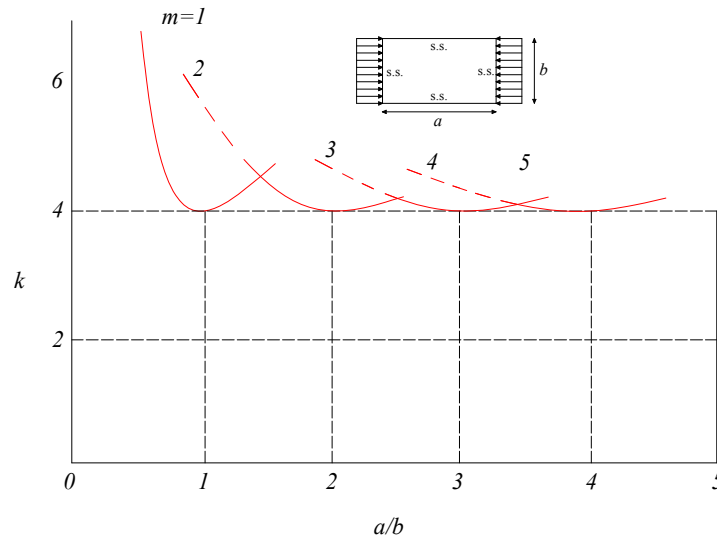


Figure 7 – Buckling coefficient for rectangular plate.

The value of k equals 4.0 when the ratio a/b is an integer. This would be correct for an individual plate but no longer fits with group of connected plates.

From Figure 7 and Equation (7), the transition from m to $m+1$ half sine-waves occurs when the two corresponding curves have equal ordinates, that is,

$$m \left(\frac{b}{a} \right) + \frac{1}{m} \left(\frac{a}{b} \right) = (m+1) \left(\frac{b}{a} \right) + \frac{1}{m+1} \left(\frac{a}{b} \right) \quad (11)$$

Thus,

$$\frac{a}{b} = \sqrt{m(m+1)} \quad (12)$$

For a long plate:

$$\frac{a}{b} \cong m \quad (13)$$

Equation (13) indicates that the number of half sine waves increases with the increase of a/b ratios. For a long plate in which a is much greater than the width b , multiple buckles in alternate directions develops with a square possible shape, i.e. the length of the half waves equals approximately the width of the plate. This happens when the buckling of a longitudinal strip in the plate finds itself resisted by a transverse strip whose curvature is much less than the longitudinal strips. The resistance is thus much greater than the tendency to buckle and the strength of the mode with $m = 1$ is found to be very high. Consequently, the plate will buckle in a way that the longitudinal and transverse strips are as equal as possible, i.e. square.

Although the buckling formulae of a plate and a column are identical², their behavior is quite different. In the case of an ideal column, as the axial load is increased, the lateral displacement remains zero until the attainment of the critical buckling load. This is called the fundamental path. However, when the axial load reaches Euler buckling load, the lateral displacement increases considerably while the load stays constant. This is called the secondary path, or also the bifurcation path at the buckling load and represents a neutral equilibrium. For practical columns having initial imperfections, a smooth transition from the first to the secondary path occurs (see Figure 8).

A perfectly flat plate behaves similarly to an ideal column only at the fundamental path stage. The secondary path reached at the critical buckling load reflects the ability of the plate to carry loads higher than the elastic critical load, and is not considered as a collapse path but rather as a post-buckling path. In other terms, a slender element plate element does not fail by elastic buckling, but exhibits significant post-buckling behavior. The axial stiffness in such

² For a very wide plate, that is, when b/a is very large, a/b tends to zero, and by taking $k_{min}=1$ with the introduction of the the radius of gyration, equation (6) becomes identical with the Euler column buckling formula, except for the fact that it is a function of $(1-\nu^2)$, which reflects the effect of plate action due to Poisson's ratio.

plates drops suddenly to a smaller value after buckling but remains relatively constant afterwards. However for practical plates having initial imperfections, a smooth transition, just like the practical columns, occurs with a gradual loss of stiffness (see Figure 8).

The unloading occurs after the actual failure load is reached once the yielding spreads from the supported edges, triggering thus the collapse in both columns and plates.

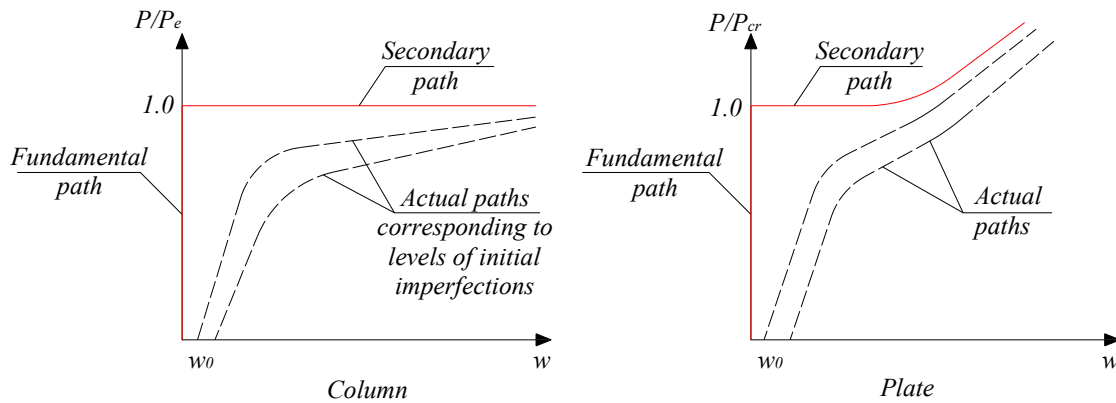


Figure 8 – Load versus out-of-plane displacement curves.

2.1.2.2. Elastic local buckling coefficient of plates and sections

2.1.2.2.1. Plate buckling coefficient

In general, the plate buckling stress is conveniently given by

$$\sigma_{cr} = k \frac{\pi^2 E}{12(1-\nu^2)} \left(\frac{t}{b}\right)^2 \quad (14)$$

k , the plate buckling coefficient, should be determined for each particular case of plate geometry, boundary conditions, material, and edge loading. So far, it has been assumed that the plate is free to rotate about the longitudinal edges.

Hill, [10] presented a chart for the determination of k values in which he gathered different cases employing various methods – mentioned in Table 1 – using as a background the energy method of Timoshenko. A chart is presented for the k -coefficient in the formula for the critical compressive stress relative to flat rectangular plates uniformly compressed in one direction. The chart presents various combinations of fixed, simply supported and free edges. Since it would be complicated to include all the possible variations or combinations of edge

conditions, only the mentioned edge conditions were considered. The curves of Figure 9 represent various approximations to the theoretical value, and it can be seen that for the case 3 (relative to a stiffened element), the minimum reached value is lower than 4, when Timoshenko's theory of elasticity is used. However, in the case of an unstiffened element, the minimum reached value in Figure 9 is higher than the value of 0.425 in Figure 10.

Table 1 – Source of k values plotted in Figure 9.

Case	Source
<i>1</i>	Solution from Timoshenko's 'Theory of Elastic Stability'[9]
<i>1a</i>	Approximate solution using the energy method and the deflection method
<i>2</i>	Solution from Timoshenko's 'Theory of Elastic Stability'[9]
<i>2a</i>	Approximate solution using the energy method and the deflection method
<i>3</i>	Solution from Timoshenko's 'Theory of Elastic Stability'[9]
<i>3a</i>	Solution from Timoshenko's 'Theory of Elastic Stability'[9]
<i>4</i>	Solution following the method employed in 'Theory of Elastic Stability'
<i>4a</i>	The rotation of this curve to that for case 4 is estimated from the rotations between the curves for cases 3 and 3a and cases 5 and 5a
<i>5</i>	Solution from Timoshenko's 'Theory of Elastic Stability'[9]
<i>5a</i>	Solution from 'Buckling of compressed rectangular plates with Built-in Edges'

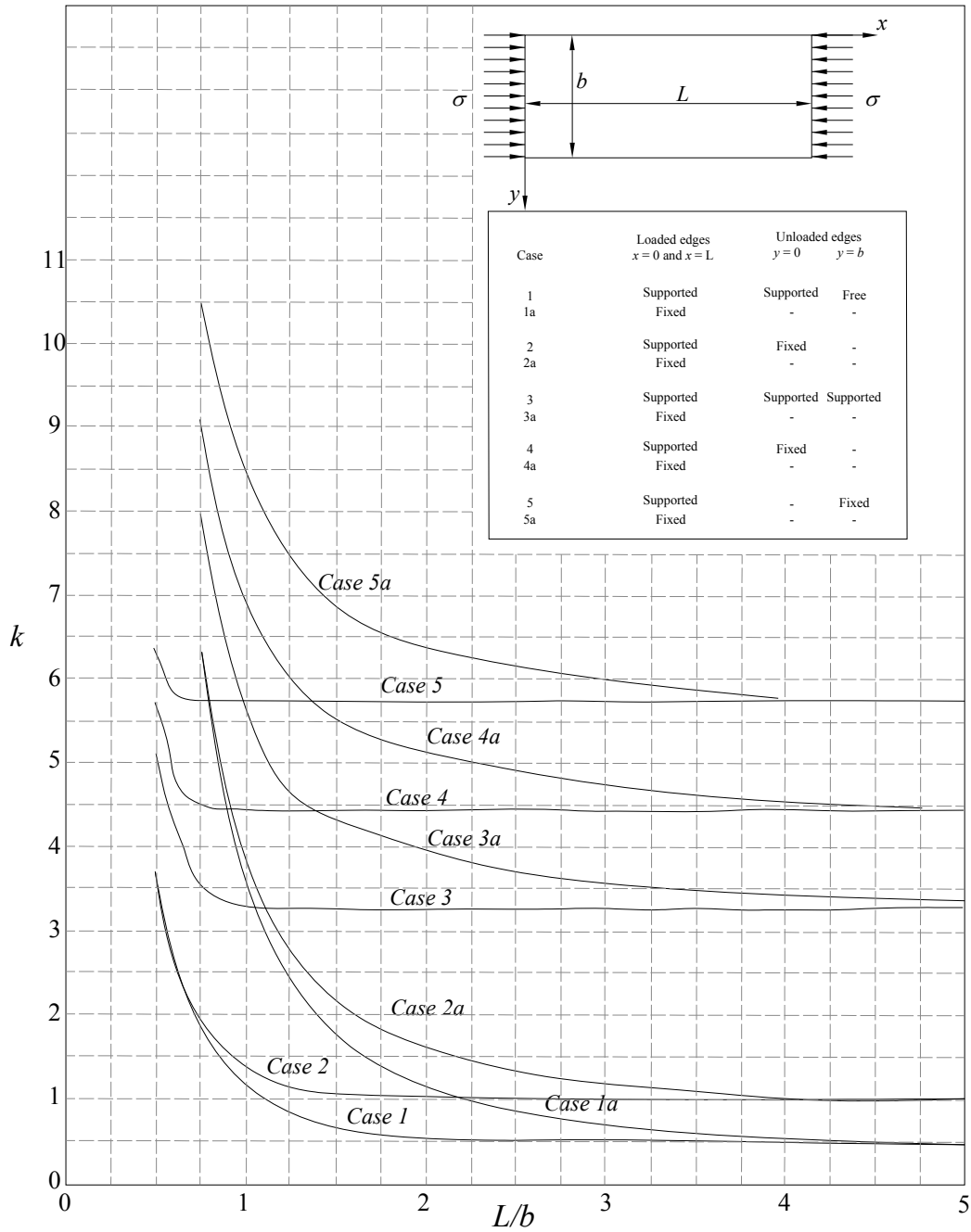


Figure 9 – k-curves.

The local buckling capacity of cross-sections is nowadays analyzed approximately by assuming that the plate elements are hinged along their common boundaries, so that each plate acts as if simply supported along its connected boundary and free along any unconnected boundary. The buckling stress of each plate element can then be determined

with the appropriate use of k -value, and the lowest obtained stress can be considered as the buckling load of the entire member.

Figure 10 gives the values of the buckling coefficient k for long rectangular plates with various common support conditions and loading cases adopted in actual standards. The buckling coefficient k , and thus the critical stress, are seen to vary considerably.

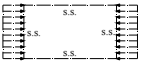
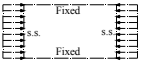
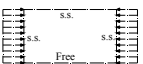
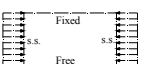
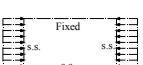
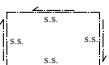

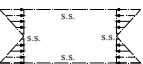

Case	Boundary Condition	Type of stress	Value of k
(a)	 Both edges simply supported	Compression	4.0
(b)	 Both edges fixed	Compression	6.97
(c)	 One edge simple supported, the other free	Compression	0.425
(d)	 One edge fixed, the other free	Compression	1.277
(e)	 One edge fixed, the other simply supported	Compression	1.277
(f)		Shear	5.34
(g)		Shear	8.98
(h)		Bending	23.9
(i)		Bending	41.8

Figure 10 – Values of k for various boundary conditions.

2.1.2.2.2. Cross-sectional buckling

Usually, today’s standards assume cross-section elements (e.g. web, flange) to be hinged along their boundaries. However, the edge conditions could differ from one section to another and is deeply questionable. For example, a rectangular section, made up of four plates with stiff flanges, would not have a k -value equal to that of a section with simply supported plates. Actually, stiff flanges would prevent the rotation of the corners and the web plates will behave as their longitudinal edges were fixed. Therefore, the resistance offered by the transverse strips in the webs will be considerably higher than a plate with simply supported edges and the buckling stress will be subsequently higher. However, if the flanges are less stiff and prone to local buckling just like the webs, then the corners will not be fixed anymore and will rotate. Hence, in that case, the buckling stress will be the same as that for a plate with simply supported longitudinal edges.

Therefore, the determination of k -values mentioned in the previous section could however lead to conservative or unconservative results, since all plates are connected with rigid joints and buckle simultaneously at an intermediate stress between the lowest and the highest calculated buckling stresses of each element separately. A number of analyses have been made concerning the stress at which simultaneous buckling takes place. Figure 11 presents examples for the determination of the elastic buckling coefficient k for an I-section under uniform compression and for a box section under uniform compression, respectively. Such stresses with these k values lead to economic thin-walled compression members.

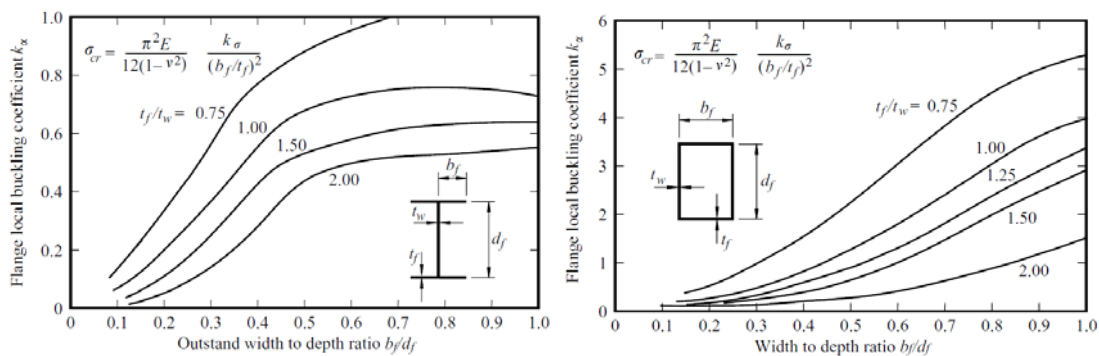


Figure 11 – Local buckling coefficients for I-section (left) and box section (right) compression members.

In particular, Stowell and Lundquist [11] provided charts for the coefficients k for I, Z and RHS, based on the principles of moment distribution to the stability of thin plates. The critical compressive stress for the calculation of a rectangular-tube section is given by:

$$\frac{\sigma_{cr}}{\eta} = \frac{k\pi^2 E t_h^2}{12(1-\mu^2)h^2} \quad (15)$$

in which η represents a non-dimensional coefficient that takes into account a reduction of the modulus of elasticity for stresses above the elastic range (i.e., within the elastic range, $\eta=1$). When the stresses are above the elastic range, σ_{cr}/η is first evaluated and σ_{cr} is determined in a 2nd step by means of a curve given in [11]. As for the k -value, charts were developed to represent the interaction between elements (see Figure 12).

In general, when an element fails by local instability, one of the constitutive elements of the cross-section is mainly responsible for the instability, i.e. when the critical value is reached, this element will need support and restraint from the adjacent elements since it will no longer be capable of supporting the imposed loads. This restraint will provide additional delay before buckling occurs, until the cross-section as a whole becomes unstable. Figure 12 represents a chart which provide the k -value for a rectangular section, and in which a dashed line is drawn connecting the points for which the two elements are equally responsible for the instability of the section, dividing the chart in two regions (see red line in Figure 12): in one region, the ‘side wall’ or web is primarily responsible for instability and in the other region the ‘end wall’ or flange is primarily responsible for instability. Therefore the response of a cross-section will be governed by one of these two regions depending on the values of the various cross-sectional ratios.

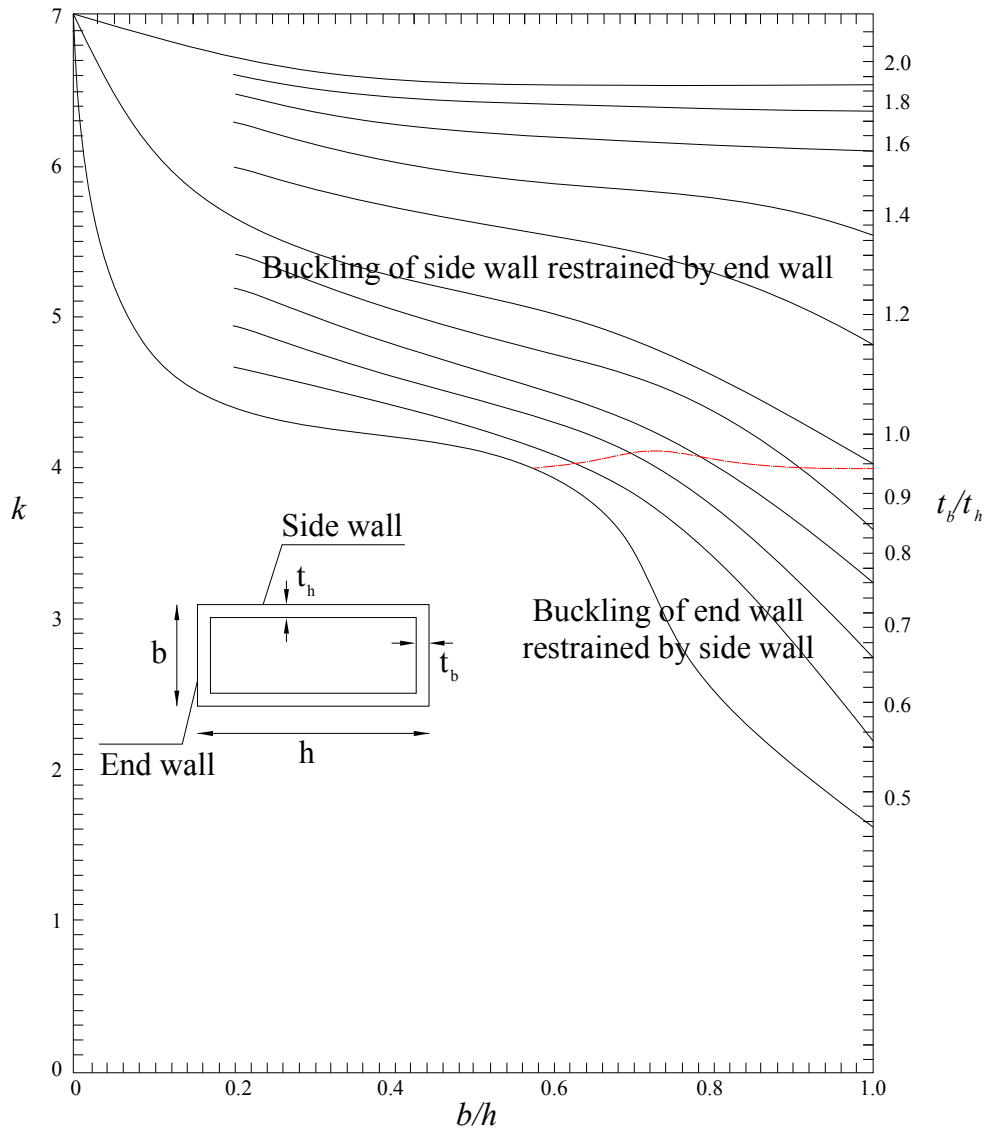


Figure 12 – Values of k for centrally loaded columns of rectangular tube section from [11].

Bleich [12] presented an approximation in order to take into account the interaction between flange and web and for the calculation of the plate buckling coefficients. Equation (16) represents the limiting geometrical value for which the web and flange buckles simultaneously:

$$\frac{b_f t_w}{h_w t_f} = \sqrt{\frac{0.425}{4}} = 0.326 \quad (16)$$

Bleich introduced a clamping coefficient to represent the web-flange interaction. Thus for values of $b_f t_w / h_w t_f$ lower than 0.326, the web is supported by the flanges and the buckling stress of the whole cross-section can be calculated as the following:

$$\sigma_{cr} = \frac{k_w \pi^2 E}{12(1-\nu^2)} \left(\frac{t_w}{h_w} \right)^2 \quad (17)$$

$$\text{with } k_w = \left(2 + \frac{2}{10\xi_w + 3} \right)^2 \quad \text{and } \xi_w = \frac{t_w^3}{t_f^3} \frac{0.16 + 0.0056 \left(\frac{h_w}{b_f} \right)}{1 - \frac{4}{0.425} \left(\frac{b_f t_w}{h_w t_f} \right)^2}$$

For values higher than 0.326, the flanges are supported by the web and the buckling stress of the whole cross-section can be calculated as followed,

$$\sigma_{cr} = \frac{k_f \pi^2 E}{12(1-\nu^2)} \left(\frac{t_f}{h_f} \right)^2 \quad (18)$$

$$\text{with } k_f = \left(0.65 + \frac{2}{3\xi_w + 4} \right)^2 \quad \text{and } \xi_f = 2 \frac{t_w^3}{t_f^3} \frac{h_w}{b_f} \frac{1}{1 - \frac{0.425}{4} \left(\frac{h_w t_f}{b_f t_w} \right)^2}$$

Recently, Seif and Schafer ([13] & [14]) presented equations in which the variation in k may be expressed as a function of the member geometry and loading conditions while including the web-flange interaction through simple equations as shown below.

The buckling coefficient k factors suggested for box sections are as follow:

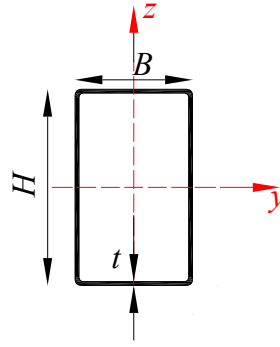


Figure 13 – Cross-section geometry for use in Equations (19) (20) and (21).

Axial compression:

$$k_b = \frac{4.0}{\left(\frac{h}{b}\right)^{1.7}} \quad f_{cr} = \frac{k_b \pi^2 E}{12(1-\nu^2)} \left(\frac{t}{b}\right)^2 \quad (19)$$

Major-axis bending:

$$\frac{1}{k_h} = \frac{0.19}{\left(\frac{h}{b}\right)^3} + 0.03 \quad f_{cr} = \frac{k_h \pi^2 E}{12(1-\nu^2)} \left(\frac{t}{h}\right)^2 \quad (20)$$

Minor-axis bending:

$$k_b = \frac{5.5}{\left(\frac{h}{b}\right)^2} \quad f_{cr} = \frac{k_b \pi^2 E}{12(1-\nu^2)} \left(\frac{t}{b}\right)^2 \quad (21)$$

with $b = B - t$ and $h = H - t$ considered as the centerline web and flange elements.

The primary means of consideration of local buckling in Eurocodes, AISC specifications and many other codes lies in the use of assumed plate buckling coefficient k for each element of the section showed in Figure 10.

In [13], it turned out that for both the web and flange results:

- (i) There is a big difference between the assumed k -values in standards and those calculated with finite strips;
- (ii) The calculated values can be outside expected bounds, such as the example of cross-sections in which web local buckling is driving the flange local buckling, i.e. the flange

support conditions become worse than simply supported (which constitutes a lower bound of the plate buckling coefficients) because a rotational restraint must be provided to the web. Therefore, wider ranges of k values must be accounted for, if the cross-section is considered as a whole.

Nowadays, numerical software dedicated to elastic buckling calculations taking the elements' interaction into account in a quite accurate way are now available. Thus, the local buckling stress of a cross-section can be calculated with the use of numerical softwares such as CUFSM [15] and GBTUL [16] with a very good accuracy.

The edge conditions are also of prime importance for the post-buckling behavior and not only for the critical buckling stress. As already explained before, if the flanges are stiff enough to prevent corner rotations, the transverse strips in the webs will be tensile and the lateral deflections will be retained because of the stiffness brought to the web from the flanges. However, if the edges are free to rotate, the transverse strips in the webs will not behave in a similar manner as previously and the plate will be prone to larger deflections at the post-buckling stage.

2.1.3. Post-buckling behavior and effective width methods

Post-buckling behavior of plates can be analyzed in an exact way by using the large-deflection theory of plates. Von Karman [17] derived the corresponding differential equations from this theory in 1910, but were too complicated to find practical applications:

$$\frac{\partial^4 w}{\partial x^4} + 2 \frac{\partial^4 w}{\partial x^2 \partial y^2} + \frac{\partial^4 w}{\partial y^4} = \frac{t}{D} \left(\frac{\partial^2 \sigma}{\partial y^2} \frac{\partial^2 w}{\partial x^2} - 2 \frac{\partial^2 \sigma}{\partial x \partial y} \frac{\partial^2 w}{\partial x \partial y} + \frac{\partial^2 \sigma}{\partial x^2} \frac{\partial^2 w}{\partial y^2} \right) \quad (22)$$

where σ is a stress function defining the mid-thickness fiber stress of the plate, and

$$\sigma_x = \frac{\partial^2 \sigma}{\partial y^2} \quad \sigma_y = \frac{\partial^2 \sigma}{\partial x^2} \quad \tau_{xy} = - \frac{\partial^2 \sigma}{\partial x \partial y}$$

Consequently, Von Karman introduced the 'effective width' concept as an engineering simplification of the developed theory.

The physical nature of the post-buckling plate behavior can be explained best by means of a model. The plate can be imagined as being replaced by a system of straight bars in both the horizontal and vertical directions, as shown in Figure 14. As soon as the plate starts to buckle,

the horizontal bars in the grid of the model will act as tie rods to forbid and prevent the increasing deflection of the longitudinal bars, enabling these longitudinal bars to carry additional loads because of the additional support provided. The central part – being the farthest from the edges – of the plate will be the first to endure deflections and buckles.

With the loaded horizontal edges remaining straight, the load on the vertical bars closer to the side edges will be greater than on the bars in the middle, for these bars deflect less. Thus, the stress distribution on the plate becomes non-uniform, the maximum stress being at the edges and the lowest stress in the middle. However the longitudinal strips close to the edges will continue to carry additional load because the extremities of the transverse strips next to the edges will not be affected by any instability yet, thus enabling the horizontal bars in these regions to carry additional stress. Consequently, the stress distribution across the width will become non-uniform with outer bars carrying more stress than the inner bars, as long as the transverse bars continue to stretch and support the longitudinal ones. The stability of the plate in the post-buckling range is thus ensured. Eventually, with an increasing axial load, the redistributions with the corresponding deflections and buckles will be more pronounced and the stress at the edges will reach the yield point. At this stage, the plate deflection would increase very rapidly and the plate will be considered to have failed. The yielded edges zones will try to widen with a reduction of the stress in the middle portion until the plate will no longer be able to carry additional load. Actually, any increase after the edges yielding is relatively small, that is why this first yielding is usually considered as the ultimate load. The redistribution phenomenon is illustrated in Figure 15. This post-buckling phenomenon will be the most pronounced for wide elements with large b/t ratios.

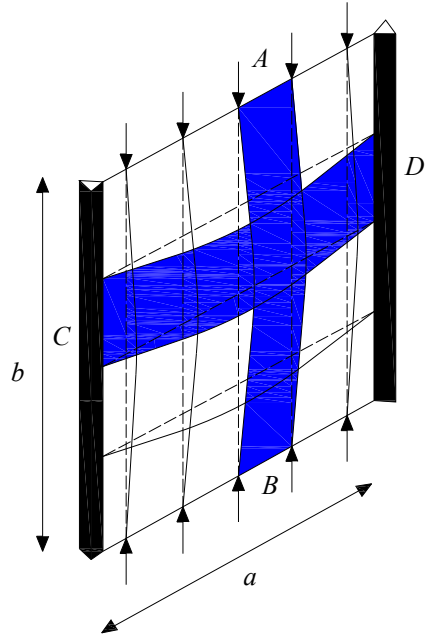


Figure 14 – Buckling of a plate under uni-axial compression.

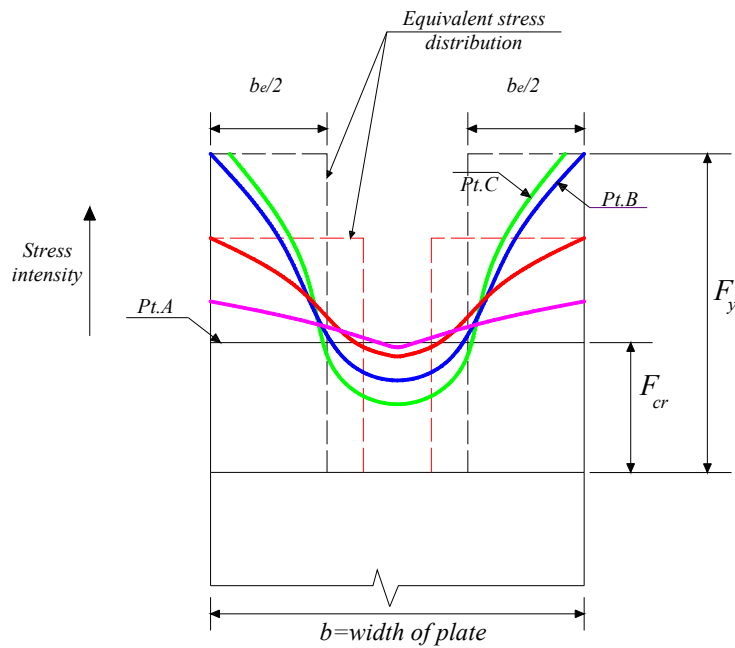


Figure 15 – Stress distribution and effective widths b_e (points A, B and C are to be referred to in Figure 3).

The concept of the effective width, proposed by Von Karman was used to calculate the load carrying capacity of the plate in the post-buckling range. Actually, the non-uniform stress

distribution across the buckled plate, was replaced by a uniform stress bloc (see dashed lines in Figure 15) equal to edge stress – which is the controlling stress of the plate – over a width of $b_e / 2$ on either side where b_e is called the effective width of the plate. This effective width can be calculated by equating the non-uniform stress bloc and the uniform one.

This effective width b_e may be considered to represent a particular width of the plate which may be determined as follows:

$$\sigma_{cr} = \sigma_y = \frac{\pi^2 E}{3(1-\nu^2)(b_e / t)^2} \quad (23)$$

Von karman formula for the design of stiffened elements may be also determined as follows:

$$b_e = Ct \sqrt{\frac{E}{\sigma_y}} = 1.9t \sqrt{\frac{E}{\sigma_y}} \quad (24)$$

where

$$C = \frac{\pi}{\sqrt{3(1-\nu^2)}} = 1.9 \quad (25)$$

However if $b > b_e$, then b_e can be replaced by b and σ_y by σ_{cr}

$$\sigma_{cr} = \frac{\pi^2 E}{3(1-\nu^2)(b/t)^2} \quad (26)$$

Or also

$$b = Ct \sqrt{\frac{E}{\sigma_{cr}}} \quad (27)$$

From Equations (24) and (27), the following relationship can be obtained:

$$\frac{b_e}{b} = \sqrt{\frac{\sigma_{cr}}{\sigma_y}} \quad (28)$$

However, Winter [18], conducted extensive investigation on light gage cold-formed steel sections, and indicated that Equation (24) can be applicable to an element in which the stress is below the yield stress. Thus, Equation (24) can be written as the following:

$$b_e = Ct \sqrt{\frac{E}{\sigma_{\max}}} \quad (29)$$

where σ_{\max} is the maximum edge stress of the plate which may be less than the yield stress of steel. Moreover, with tests previously conducted by Sechler and Winter, a straight line relationship could be found between the non-dimensional parameter $\sqrt{E/\sigma_{\max}} (t/b)$ and the term C (see Figure 16).

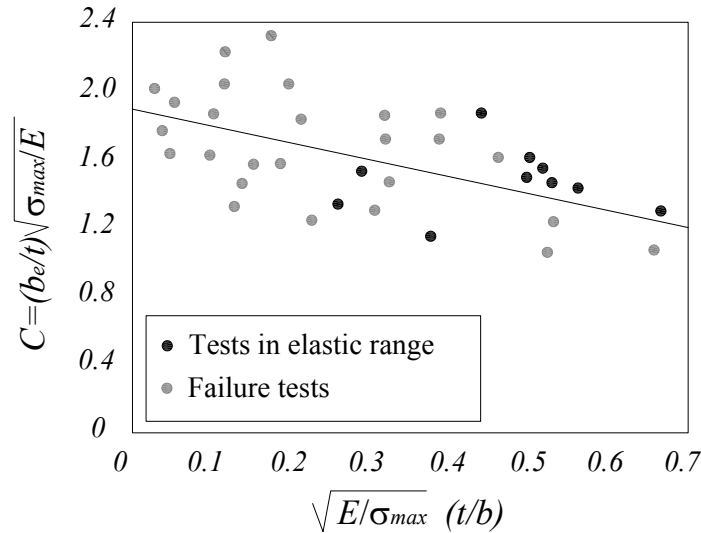


Figure 16 – Experimental determination of effective width [18].

Winter, based on his experimental investigations, developed the following equation for the term C:

$$C = 1.9 \left[1 - 0.475 \left(\frac{t}{b} \right) \sqrt{\frac{E}{\sigma_{\max}}} \right] \quad (30)$$

The straight line in Figure 16 starts at a value of 1.9 for $\sqrt{E/\sigma_{\max}} (t/b) = 0$, which means that it is the case of an extremely large b/t ratio with relatively high stress. For this particular case, the experimental determinations agrees well with Von Karman’s original formula (see Equation (27)).

Then, Winter in 1947 presented the following Von Karman modified formula for computing the effective width b_e for plates simply supported along both longitudinal edges:

$$b_e = 1.9t \sqrt{\frac{E}{\sigma_{\max}}} \left[1 - 0.475 \left(\frac{t}{b} \right) \sqrt{\frac{E}{\sigma_{\max}}} \right] \quad (31)$$

The effective width in Equation (31) depends not only on the edge stress σ_{\max} but also on the b/t ratio. Equation (31) may be written in terms of the ratio of $\sigma_{cr} / \sigma_{\max}$ with the use of the σ_{cr} expression derived from Equation (27):

$$\frac{b_e}{b} = \frac{1.9t}{b} \sqrt{\frac{E}{\sigma_{\max}}} \left(1 - 0.25 \times 1.9 \frac{t}{b} \sqrt{\frac{E}{\sigma_{\max}}} \right) \quad (32)$$

Leading to the following expression:

$$\frac{b_e}{b} = \sqrt{\frac{\sigma_{cr}}{\sigma_{\max}}} \left(1 - 0.25 \sqrt{\frac{\sigma_{cr}}{\sigma_{\max}}} \right) \quad (33)$$

To sum up, Equations (31) and (33) may be considered as generalizations of Equations (24) and (28) in two aspects:

- (i) By introducing σ_{\max} for σ_y , the equations can be applied to service limit states as well as to ultimate limit states;
- (ii) Empirical correction factors have been introduced and account for the cumulative effect of the residual stresses, deviations from planeness.

Later on and after a longtime experience, a more realistic equation was proposed for the determination of the effective width b :

$$b_e = 1.9t \sqrt{\frac{E}{\sigma_{\max}}} \left[1 - 0.415 \left(\frac{t}{b} \right) \sqrt{\frac{E}{\sigma_{\max}}} \right] \quad (34)$$

The correlation between Equation (34) and the results of tests conducted by Sechler and Winter is illustrated in Figure 17.

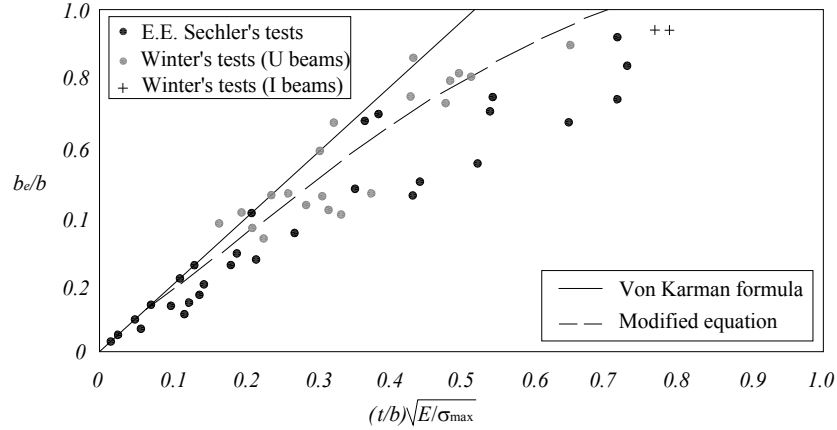


Figure 17 – Correlation between test data on stiffened compression and design criteria [19].

It should be noted that Equation (34) may be rewritten in terms of the $\sigma_{cr} / \sigma_{max}$ ratio as follows:

$$\frac{b_e}{b} = \sqrt{\frac{\sigma_{cr}}{\sigma_{max}}} \left(1 - 0.22 \sqrt{\frac{\sigma_{cr}}{\sigma_{max}}} \right) \quad (35)$$

Therefore, the effective width b_e can be determined as $b_e = \rho b$, where the reduction factor ρ is given as follows:

$$\rho = \frac{1 - 0.22 / \sqrt{\sigma_{max} / \sigma_{cr}}}{\sqrt{\sigma_{max} / \sigma_{cr}}} = \frac{1 - 0.22 / \lambda}{\lambda} \leq 1 \quad (36)$$

In which $\rho = 1$ when $\lambda \leq 0.673$ (with λ being the plate slenderness).

In Equation (36), λ is a slenderness factor determined as

$$\lambda = \sqrt{\frac{\sigma_{max}}{\sigma_{cr}}} = \sqrt{\frac{\sigma_{max} [12(1-\nu^2)(b/t)^2]}{k\pi^2 E}} = \left(\frac{1.052}{\sqrt{k}} \right) \left(\frac{b}{t} \right) \sqrt{\frac{\sigma_{max}}{E}} \quad (37)$$

In which k , b/t , σ_{max} , and E were previously defined. The value of ν was taken as 0.3.

The derived formula for steel plates supported along one edge was as follows:

$$\frac{b_e}{b} = 1.19 \sqrt{\frac{\sigma_{cr}}{\sigma_{max}}} \left(1 - 0.3 \sqrt{\frac{\sigma_{cr}}{\sigma_{max}}} \right) \quad (38)$$

Thus the reduction factor ρ would be given through the following equation,

$$\rho = \frac{1.19(1 - 0.3/\lambda)}{\lambda} \quad (39)$$

which is the same as the formula used nowadays in EN 1993-1-1 [20] :

$$\rho = \frac{1}{\lambda} \left(1 - \frac{0.188}{\lambda} \right) \quad (40)$$

2.1.4. Influence of residual stresses and initial imperfections on plate buckling

The influence of residual stresses on the axial loading required to initiate plate buckling was first recognized in tests on welded crane girders in 1941. Residual stresses are induced during the different fabrication processes. Residual compressive stresses in the central region of a simply supported thin plate can cause a premature buckling and a reduction in its ultimate strength (see Figure 18).

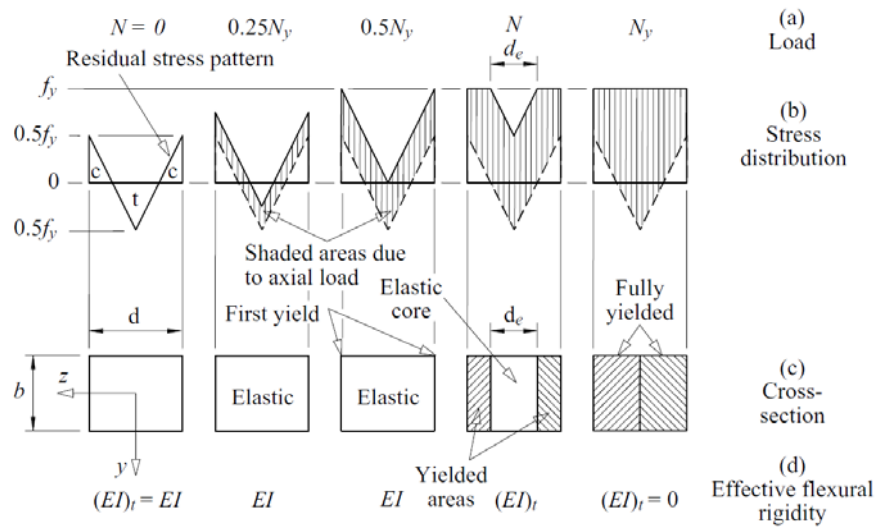


Figure 18 – Effective section of a member with residual stresses [21].

Residual stresses cause premature yielding in plates of intermediate slenderness, but have a negligible effect on the strain-hardening buckling of stocky plates (see Figure 19).

When the compressive residual stress $\sigma_{comp-res}$ is nearly uniformly distributed over the width of the plate (such as in welded plates), it can be added to the external applied stress, i.e. the

required stress σ_{ext} to produce buckling would approximately be equal to the buckling stress less the residual stresses.

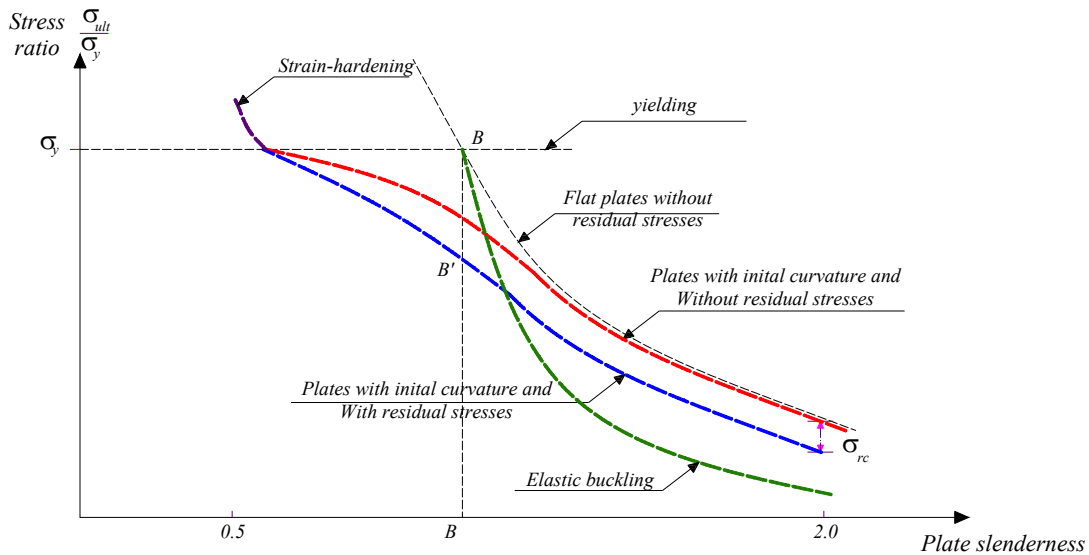


Figure 19 – Effect of residual stresses and initial imperfections on plate buckling.

The red and blue curves of Figure 19 show, respectively, the buckling stress of a plate without residual stresses and of a plate with residual stresses ([22], [23] & [24]). It is interesting to note that for slendernesses larger than indicated by the dashed line BB', the blue curve lies below the red curve almost exactly by the magnitude of the residual compressive stress (noted σ_{rc} in Figure 19). Actually the plate buckling problem becomes more involved when compressive residual stresses cause local yielding before the buckling stress is reached.

As for the initial imperfections, the initial curvature of a plate will cause a transverse deflection as soon as it is loaded. The corresponding deflections will increase rapidly as the elastic buckling is approached, but slow down beyond the buckling stress. In a thin plate with initial curvature, the failure and the first yield will occur slightly before they do in a plate without imperfections, whereas this effect will disappear in thick plates since they are not affected by initial curvatures. It is only in a plate of intermediate slenderness that the initial curvature and the residual stresses cause a significant reduction in the resistance.

Now that local buckling, which is one of the two ‘extremes’ behavior characterizing cross-sections, has been well discussed and detailed, a brief review of plastic theory would be

presented in the next section since it constitutes the other ‘extreme’ behavior affecting cross-sections.

2.2. Brief review of plastic theory

Although plasticity has been sometimes briefly mentioned in the previous section, a small summary on its history will be presented herein, in order to achieve and complete the necessary knowledge related to it.

The theory of elasticity, with Hooke’s Law (1635-1703), was the initial basis of the design of steel structures in the nineteenth century. The initial tests in steel beams were conducted to confirm the elastic behavior of beams. The first yielding was regarded as the limit load. Lyse and Godfrey [25] considered this fact and wrote:

‘Since the usefulness of beams is determined by the maximum load it can contain without excessive deflection, the determination of its yield point becomes the most important factor in testing... the ultimate load has little significance beyond the fact that it is a measure of the toughness of the beam after it has lost its usefulness... The yield point strength of the beam was used as the criterion for its load-carrying capacity’

Ewing [26] was the first to mention the plastic behavior of steel structural members and identified the full plastic moment of a rectangular cross-section to be equal to $bh^2 / 4f_y$. He wrote:

‘the outer layers of the beam are taking permanent set [yielding] while the inner layers are still following Hooke’s law... And any small addition to the stress produces a relatively very large amount of strain’.

It was not known if Ewing carried out any experiments on steel beams but the earliest recorded experiments on beams were reported by Meyer [27]. Meyer conducted tests on simply supported beams of rectangular cross-sections and identified a dramatic increase in the deflection once M_p was reached.

Kazinczy [28] was the first to discover the plastic hinge development. He conducted experimental investigations on beams fixed at both ends loaded by a uniformly distributed load. Kazinczy proposed a ‘plastic solution’ since he concluded from his tests that the formation of three plastic hinges defined the ultimate load of the systems considered.

Kist [29] was the one who proposed the elastic-perfectly plastic material law to use in order to calculate the ultimate load.

Maier-Leibnitz [30] & [31] observed the ductile behavior of simple and continuous beams and was the best known of the early researchers on plastic behavior. In 1930, Fritsche was the first to devise equations for the bending moment M_{pl} of fully plastic rectangular and H-shaped cross-sections in the case of pure bending. He also concluded that no strain hardening is to be expected at low levels of strains, but a strain of 4-5% would be sufficient to activate 99% of M_{pl} . Fritsche later came to the conclusion that the yield stress of mild steel represents the most critical parameter for the calculation of the ultimate load and was based on the experimental tests of Meyer [27], Leibnitz [31] & [30] and Schaim [32].

In 1931 and 1932, Girkman [33], based on his own tests, suggested a plastic design method for indeterminate frameworks and wrote:

'Apart from the savings in weight that can be achieved, the use of this method makes it possible to reduce the maximum moments, to even out the differences in the thicknesses of the cross-sections required and hence to simplify the construction details and reduce their costs'.

Baker and Roderick [34] & [35] conducted further investigations of the plastic behavior of complete structures. They reported series of experiments at the civil engineering department of the University of Bristol, England between 1936 and 1939 concerning very small scale rectangular portal frames of I-sections. The first book on plastic theory of structural steel work was then published in 1956 and Baker, Horne and Heyman [36] stated:

'...portals subjected to vertical loads had a great reserve of strength beyond the point at which yield was first developed, and that collapse, the growth of large uncontrolled deflections, did not occur until a mechanism had formed by the development of three plastic hinges... the agreement is good... between the observed and calculated collapse loads of the portals...it was realised, of course, that it was a far cry from calculating the vertical loads which would cause collapse of a rectangular portal frame to deriving an acceptable method of designing redundant structures based on collapse, but...incomplete though [the results] were, they formed the basis of much wartime [World War 2] design'.

Research into plastic design continued in Cambridge after World War 2 and by the 1950s, the plastic design method was being accepted by the engineering community and a large number of published papers written by the Cambridge research was provided [36].

Although the plastic design method was accepted by the 1960s, some critics still remained. An excerpt from a publication of Stussi in 1962 stated:

'A statically indeterminate structure remains statically indeterminate also if the limit of proportionality or the yield strength of the material is exceeded in particular cross-sections. This means that besides the equilibrium conditions, the deformation conditions also remain valid even in the post-elastic loading range. The inadequacy of the ultimate load method is based on the fact that it treats this fundamental fact wrongly and upon closer inspection its 'simplicity' is revealed as unacceptable primitiveness.'

Even with such critics, the plastic theory was solid enough and it was mainly in the 1970s that Massonnet [37] promoted the European recommendations for the plastic design of structural steel structures.

Now that the two limits consisting in local buckling and plasticity have been well discussed, methods for determining ultimate buckling loads of cross-sections, known to be affected by these two extreme limits, will be discussed in the following section.

2.3. Available methods for the determination of buckling loads

Three principal methods for determining the ultimate buckling loads are briefly presented and discussed in this section. They consist in (i) the finite element method, (ii) plastic mechanism and (iii) ultimate buckling curves. The most adequate one or also the most adequate combination of a couple of methods is chosen and justified.

2.3.1. Finite element method

Using the nonlinear theory, the finite element method allows the study of the behavior of an element, till the failure along with the post-peak stage.

Computational modeling requires sophisticated mechanics to provide accurate solutions. It would be of great significance to understand the capacities and limitations of the theoretical model employed. Sensitivities and model inputs such as, solvers, element choice and discretization, boundary conditions, material models, initial imperfections, initial residual

stresses and strains all affect the solution in different influences and should be chosen carefully. However despite the known shortcomings, computational modeling has a really important role in the future of steel research and design and is used through this study as a basis for resorting numerical results served for the derivation of design curve.

2.3.2. Plastic mechanisms

A different method for calculating the buckling load of a short column can be obtained by applying to each side of the profile the method of plastic mechanisms and consider that the failure load of the short column is given by the sum of the failure loads of the four sides of the tube. In this method, the ultimate load of a monoaxially compressed plate is given by the intersection of a curve showing the elastic behavior of the sheet in the post-critical phase (taking, optionally, into account the geometric imperfection in the establishment of the equation of the curve) and a curve representing a kinematically admissible plastic mechanism. As shown in Figure 20, this method leads to an approximate value of the failure load of the plate.

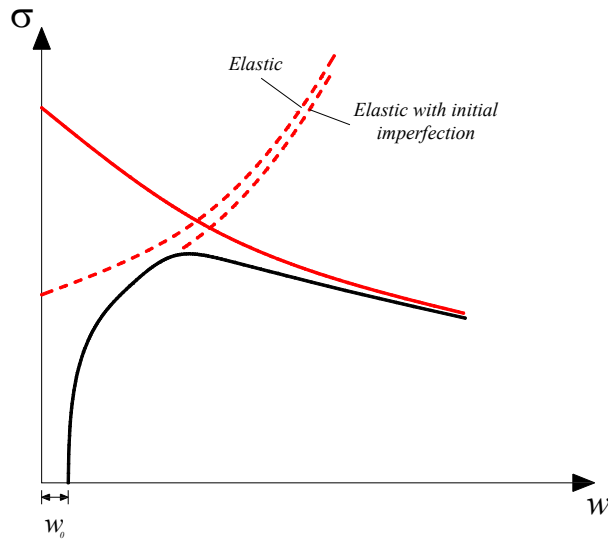


Figure 20 – Stress-deflection curve for a plate subjected to mono-axial compression.

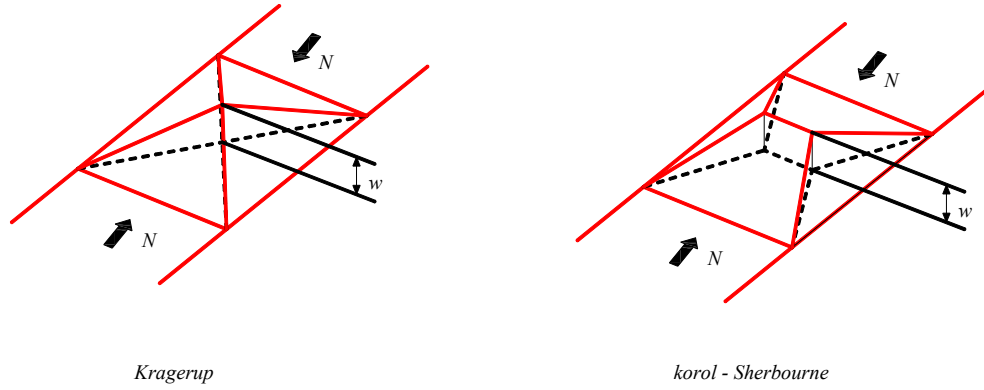


Figure 21 – Plastic mechanism.

Figure 21 represents two simple mechanisms proposed respectively by Kragerup [38] and Korol and Sherbourne [39] [40]. Other mechanisms may be found in the literature.

Introducing the buckling reduction factor (case of a pure compression), defined by:

$$\chi_N = \frac{N}{b.t.f_y} \quad (41)$$

The failure mechanisms of Figure 21 have the following equations:

Kragerup mechanism:

$$\chi_N = \frac{1}{2} \left(1 - \frac{2w}{t} + \sqrt{1 + 4 \left(\frac{w}{t} \right)^2} \right) \quad (42)$$

Korol and Sherbourne mechanism:

$$\chi_N = 1 - 0.355 \frac{w}{t} + 0.056 \left(\frac{w}{t} \right)^2 - 0.003 \left(\frac{w}{t} \right)^3 \quad (43)$$

The Korol and Sherbourne mechanism was seen however to provide more accurate results compared to the Kragerup mechanism.

One must recognize that the method of plastic mechanism is simple to provide reliable quantitative assessment of the failure load. However, various criticisms can indeed be made to this method, including:

- (i) The brutal passage from the elastic behavior to the plastic one;

(ii) The membrane effect that appears when the plate deflection becomes large is neglected.

2.3.3. Ultimate buckling curves

Among the three proposed approaches for the calculation of the buckling failure load of a structural element, only that based on buckling curves allows simple, fast and accurate calculation. Its analytical formulation has the advantage of being able to be incorporated into the study of complex problems.

For instance, many important, theoretical and experimental works were performed in Cambridge in the field of plate local buckling. Also, extensive developments have been conducted to derive buckling curves for different loading conditions and types of sections taking into account the cross-section as a whole and not plates separately. Figure 22 shows the resulting curves from Cambridge research with symbols O, P, Q referring to different types of welding. More details can be found in [41], [42], [39] & [43].

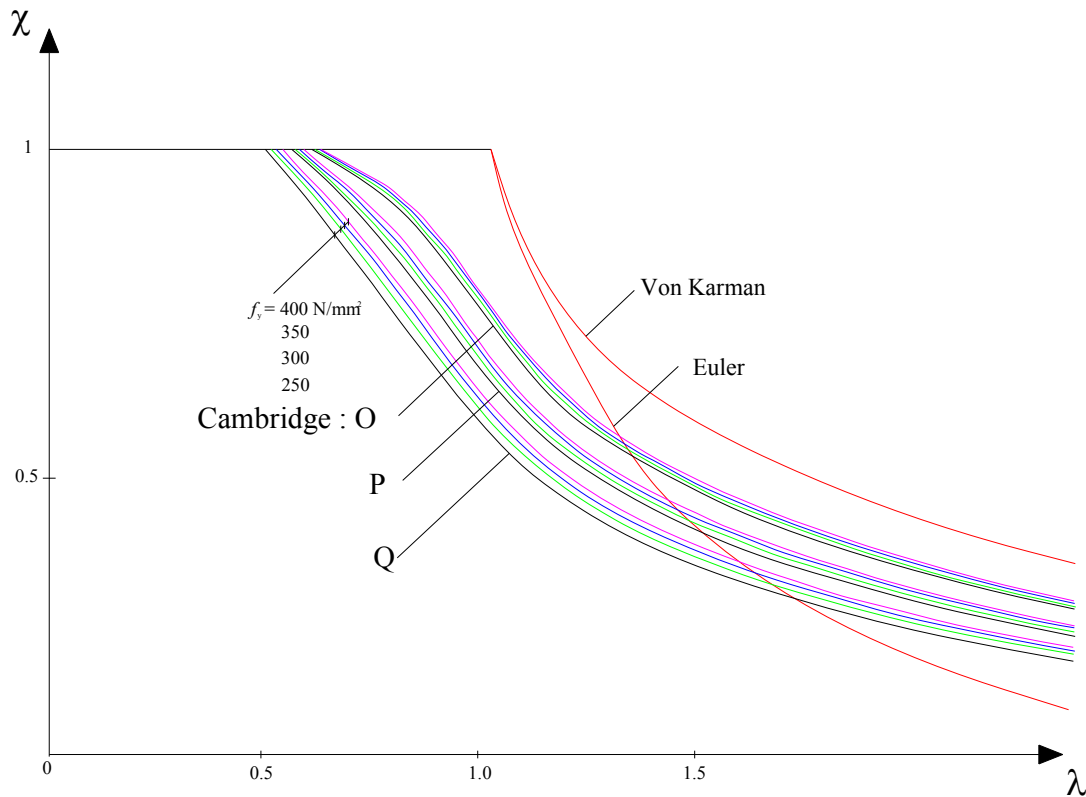


Figure 22 – Plate local buckling curves.

Accordingly, it would be convenient to adopt the buckling curve method for the calculation of local buckling failure loads of structural elements, while using non-linear numerical

software with a validated numerical model as a basis for the derivation of accurate design curves, with adequate model numerical inputs.

2.4. Actual design specifications

2.4.1. Cross-section classification concept

Rules concerning local buckling are required for the design of structural steel members. Therefore, in any specification, the combination of cross-sectional dimensions and yield strength are taken into account in order to determine limits at which local buckling can be expected to occur for a designer. In other words, to prevent premature local buckling, slenderness limits for the plate elements in members have been established. The intention is to have a capacity controlled by the overall strength of the particular element and not by local buckling. Therefore, the local buckling rules play an important part in the design of structural steel members.

In this section, the main local buckling rules and issues concerning cross-section slenderness and cross-section resistance are analyzed and pointed out from a selected list of specifications. The intention here is to show the various local buckling rules and point out the diversity among several specifications. The list includes major codes in the world (the notation in parentheses indicates the adopted abbreviation used for each design standard):

- (i) Eurocode 3, (EC3), 1993, Common Unified code of practice for steel structures;
- (ii) AISC-LRFD, (AISC LRFD), 1994, Specification for structural steel buildings;
- (iii) BS 5950 Part 1, (BS 5950), 2000, Structural use of steelwork in building;
- (iv) DIN 18800 Teil 1, (DIN 18 800), 1990, Steel structures, Design and construction;
- (v) AS 4100, (AS 4100), 1998, SAA Steel structures Code.

The comparison will only be focused on I-shapes and rectangular sections as shown in Table 2. A wider study can be found in [44] & [45].

Table 2 – Studied elements and load conditions.

Section	Element	Case no.
I-shape	Flange in compression	1
	Web in axial compression	2
	Web in bending	3
	Web in combined axial compression and bending	4
Hollow section	Flange in compression	5

Before starting the comparison of the actual limits of each specification, the formats adopted along with the plate definition width deserves clarifications.

As already mentioned, the solution for the elastic local buckling stress σ_{cr} is given by:

$$\sigma_{cr} = \frac{k\pi^2 E}{12(1-\nu^2)(b/t)^2} = \frac{A^2}{(b/t)^2} \quad (44)$$

The equation is simplified by substituting $A^2 = k\pi^2 E / (12(1-\nu^2))$. To prevent a plate from buckling before it reaches its yield stress, σ_y should be smaller than σ_{cr} , therefore,

$$\sigma_y \leq \frac{A^2}{(b/t)^2} \quad (45)$$

with A^2 being the constant $A^2 = k\pi^2 E / (12(1-\nu^2))$ found in Equation (44). Equation (45) can be rearranged in terms of the geometrical slenderness limit b/t , with H a constant to be determined:

$$\frac{b}{t} \leq \frac{H}{\sqrt{\sigma_y}} \quad \text{or} \quad \frac{b}{t} \sqrt{\sigma_y} \leq H \quad (46)$$

Hence, there are different formats in which a slenderness limit can be expressed. Table 3 gives the format used by the various specifications. Five formats are presented:

- (i) The β -format gives actual b/t ratios for steel of 235 MPa yield strength used within the Eurocode 3;

- (ii) The δ -format defines b/t depending upon the yield strength in US customary units (ksi), used within AISC-LRFD;
- (iii) The γ -format gives actual b/t ratios for steel of 275 MPa yield strength used within BS 5950;
- (iv) The μ -format gives actual b/t ratios for steel of 240 MPa yield strength used within the DIN 18800;
- (v) The α -format gives actual b/t ratios for steel of 250 MPa yield strength used within AS 4100.

In addition conversion factors are presented in Table 4, which enable ‘movement’ from one specification’s format to another.

Table 3 – Format of local buckling rules.

Format #	Maximum b/t	Dimensions	Used in specifications
1	$\beta \sqrt{\frac{235}{f_y}}$	f_y [MPa]	EC3
2	$\delta \frac{1}{\sqrt{f_y}}$	f_y [ksi]	AISC ¹
3	$\gamma \sqrt{\frac{275}{f_y}}$	f_y [MPa]	BS 5950
4	$\mu \sqrt{\frac{240}{\gamma_M \cdot \sigma_x}} = \mu \sqrt{\frac{240}{1.1 \sigma_x}}$	f_y [MPa]	DIN 18800
5	$\alpha \sqrt{\frac{250}{f_y}}$	f_y [MPa]	AS 4100

¹This format is AISC-LRFD 1994 format. However, AISC 2005 specification is characterized by ‘ $\delta \sqrt{\frac{E}{f_y}}$ ’, which is similar to the 1994 version but with replacing E by 29 000 ksi (=200 000MPa).

Table 4 – Conversion factors.

<i>Conversion factors</i>					
	β	δ	γ	μ	α
$\beta=$	1.00	0.17	1.08	0.96	1.03
$\delta=$	5.83	1.00	6.31	5.62	6.02
$\gamma=$	0.92	0.15	1.00	0.89	0.95
$\mu=$	1.03	0.17	1.12	1.00	1.07
$\alpha=$	0.96	0.16	1.04	0.93	1.00

As for the plate width definitions, Figure 23 shows the definition of an element width as used in the various specifications. Most specifications use a variety of letters to identify the plate width, but within this study b is the adopted terminology used to define the plate's width.

Table 5, presents a brief general overview (only for hot-finished sections) of the adopted width definition of plate elements in all the selected design specifications.

Table 5 – Definition of width of plate elements in selected design specifications.

	EC3	AISC LRFD	BS 5950	DIN 18800	AS 4100
I-H section flange	Flat width	Mid-thickness width	Mid-thickness width	Flat width	Clear width
I-H section web	Flat width	Flat width	Flat width	Flat width	Clear width
RHS flange or web	Flat width	Flat width	Flat width	Flat width	Clear width

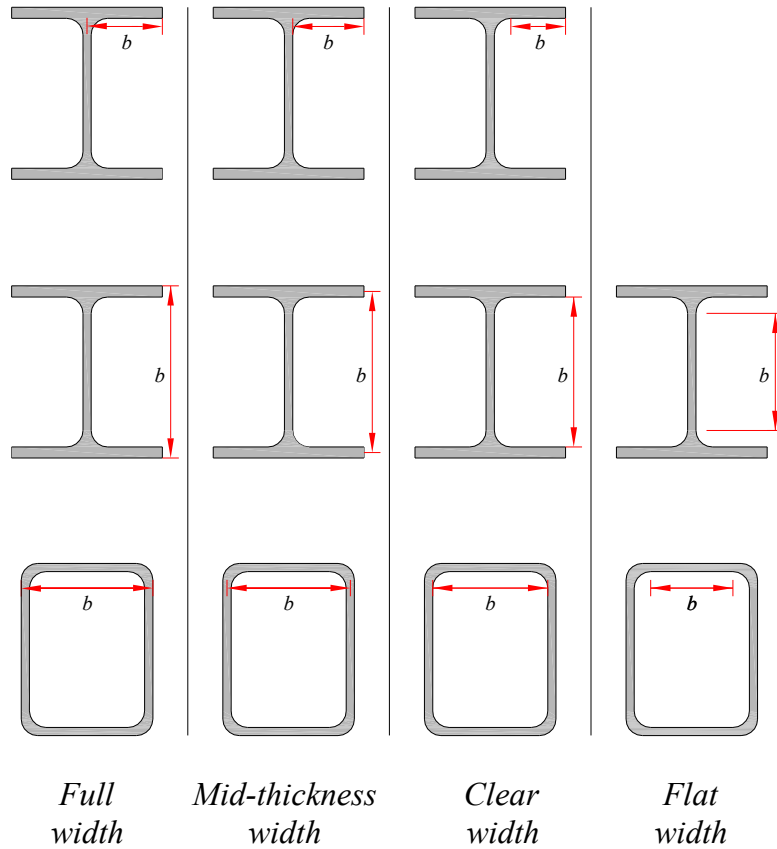


Figure 23 – Definition of plate widths.

Kettler [7] performed a comparison study between the different definitions of plate-widths in order to analyse the relation between these width-definitions, based on hot-rolled I-sections and hot-finished or cold-formed RHS. The following values have been chosen based on the investigation shown in Figure 24 and Figure 25, i.e.:

$$\frac{c_{flat}}{c_{mid-thickness}} = 0.8 \text{ and } \frac{c_{flat}}{c_{clear}} = 0.8 \quad (47)$$

It should be noted that a value of 1 of the investigated ratios would indicate that the slenderness limits of the different design codes can be compared to each other directly.

As for the hot-finished sections and cold-formed RHS (when the web is decisive), the following value has been adopted:

$$\frac{c_{flat}}{c_{clear}} = 0.9 \text{ when the web is decisive} \quad (48)$$

For cold-formed RHS sections, when the flange is decisive, the following value has been adopted:

$$\frac{c_{flat}}{c_{clear}} = 0.8 \text{ when the flange is decisive} \quad (49)$$

The definitions of flat or clear width were not significantly different for hot-finished sections (flat width given by $h - 3t$, external radius $1.5t$), but would however result in rather large differences for cold-formed RHS (since the flat width is given by $h - 5t$, with an external radius of $2t$ for a thickness comprised between 6mm and 10mm), (see Figure 26). The ratios defined in Kettler [7] will be adopted also herein, for the following comparison study. A similar study can also be found in [46].

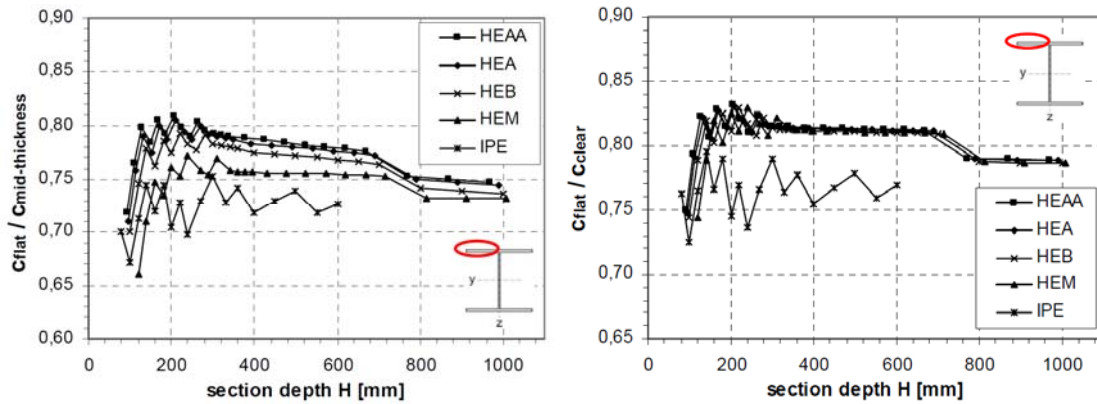


Figure 24 – Ratio of flange widths definitions-flat width (EN,DIN) over mid-thickness width(BS)-I-sections,b-ratio of flange width definitions; flat width (EN,DIN)over clear-width (AS 4100),I-section [7].

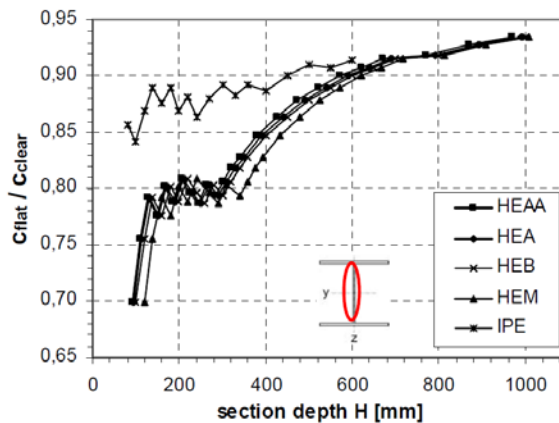


Figure 25 – Ratio of the web widths definitions; flat width over clear-width ; I-sections [7].

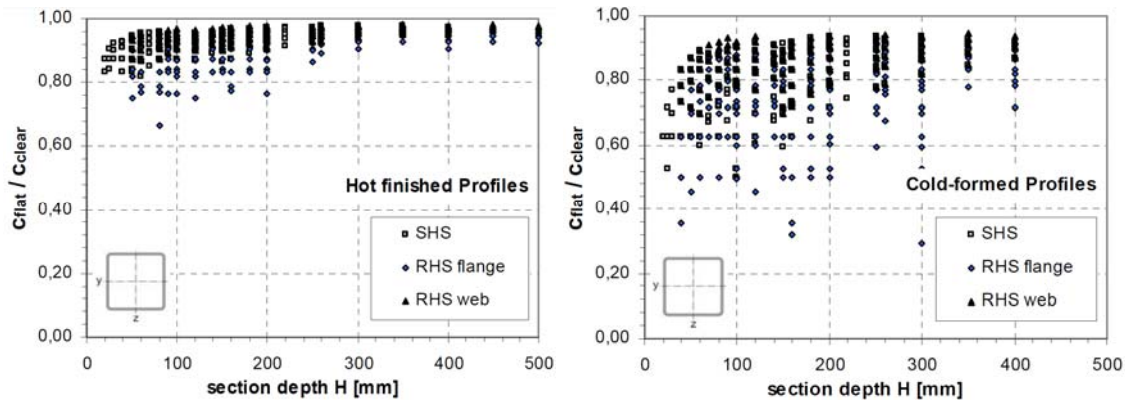


Figure 26 – a) Ratio of widths definitions; flat-width over clear-width,hot-finished RHS, b) Ratio of widths definitions; flat width over clear-width; cold-formed RHS [7].

Table 6 summarizes the terminology adopted in each design standard in order to refer to cross-sections. They consist of 4 classes, sometimes grouped in 3 in some specifications. Class 1, also called a plastic design cross-section, is one which can both reach its plastic moment capacity and has enough rotation capacity to permit redistribution of moments. A class 2 section, also called a compact section, is one which can just reach its plastic moment capacity but has a rapid drop-off in capacity at that point. A class 3 section, also called a non-compact section, is one which is able to reach only the yield-moment capacity. In these definitions it is understood that any moment capacity includes the effect of axial force present.

Table 6 – Denomination of cross-section classes in each specification.

Specification	Types of classes			
Eurocode 3	Class 1	Class 2	Class 3	Class 4
AISC-LRFD	Compact	Non-compact		Slender
DIN 18800	P-P	E-P		E-E
BS 5950	Plastic	Compact	Semi-compact	Slender
AS 4100	Compact	Non-Compact		Slender

The rules for local buckling provided by each specification can be found in [47], [48], [49], [50], [20] & [46]. There is a difference in the capacity specifications between the international design codes. The common thing between them all is that the cross-section

capacity is defined based on the slenderness ratios of the single elements constituting a section. Some specifications make a distinction between hot-rolled and welded sections. BS 5950 includes however a wider variety of fabrication processes for which different slenderness limits are defined. The British Standard BS 5950 [49], Australian Standard AS 4100 [48] and the American code AISC-LRFD [47] allow for a linear interpolation (slightly under linear one for BS 5950 only) for the transition of the mono-axial bending moment resistances from plastic to elastic. The European standard EC3 [20] and the German DIN 18800 [50] define two classes with either full plastic capacity or only elastic capacity. Concerning slender sections, all codes have similar design specifications for the calculation of effective widths, based on the Winter-formula presented previously.

Table 7 presents the information relative to each of the five specifications in a comparative numerical form for cases 1, 2, 3 and 5 with each format specified in Table 3 (only for hot-rolled cases). However, the case of a web in bending and compression is treated separately in a graphical comparative form in function of the degree of axial forces $n = N / N_y$ (i.e. $n = 0$ corresponds to a load case of pure bending and $n = 1$ to a case of pure compression) in each of the 4 following formats: β , δ , γ , μ . The slenderness limits were thus defined in a similar way to the AISC-LRFD, through the definition of the slenderness limit for webs as a function of the level of axial compression. Thus, the following relations were assumed:

$$\alpha = \frac{(n+1)}{2} \quad (50)$$

and

$$\psi = 2n - 1 \quad (51)$$

with α defined as the fraction of web in compression and ψ the fraction of yield stress in tension.

In Figure 27 and Figure 28, results are presented for all 4 four classes together, whereas Figure 29 to Figure 32 present each group of class separately for each of the four formats, for sake of a better visualization.

In all the comparative figures, the conversion factors in Table 4 are used along with the correction width definition ratios according to [7].

For the case 4 of a web in bending and compression, EC3 and DIN 18800 seemed to be grouped together against BS 5950 and AISC-LRFD which show more generous web slenderness limits for classes 1 and 2. As for the class 3, the AISC-LRFD is shown to differ considerably from the three other standards with a generous linear relationship between the web slenderness and the degree of axial load. However, AS4100, EC3 and DIN 18800 curves are showing a ‘crossing’ for high degrees of axial loads and the DIN 18800 who had the most generous web slenderness limit, becomes the one with the most strict slenderness limit.

In Table 7, the differences became smaller once the conversion factor and the width correction ratios were used. However, AS 4100 seemed to provide almost for all studied cases the strictest slenderness limits, whereas AISC-LRFD provides the most generous limits, except for the case 1. In case 2, the limit slenderness values are very close to each other according to investigated specifications. In case 3, i.e. the comparison for stiffened elements under flexural compression, the limit specified in LRFD is considerably more generous than the other specifications’ limits.

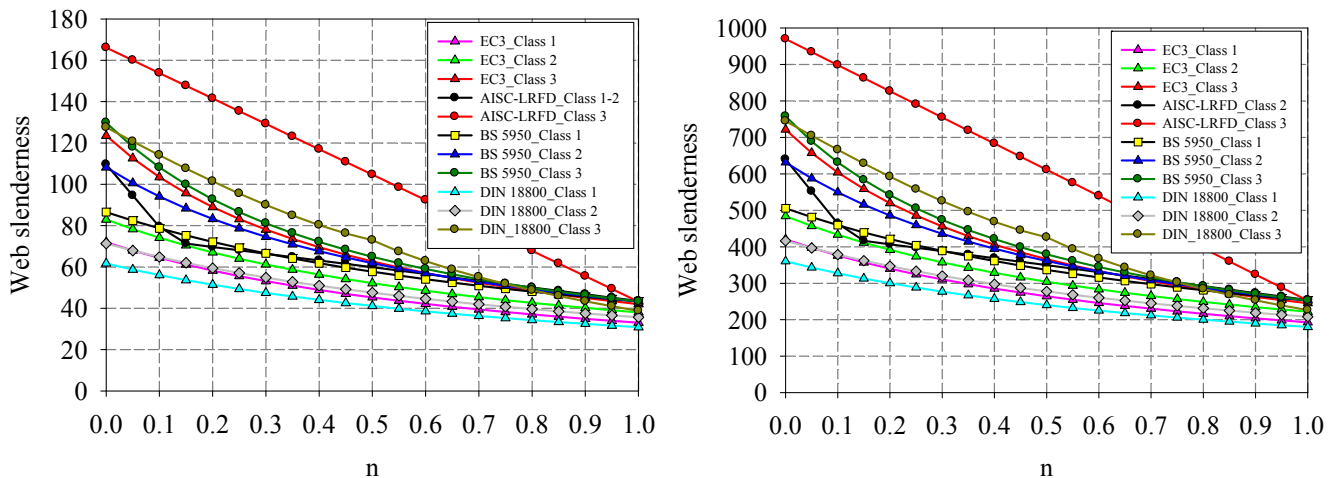


Figure 27 – Numerical comparison of local buckling rules, a) case 4_β-format_all classes, b) case 4_δ-format_all classes.

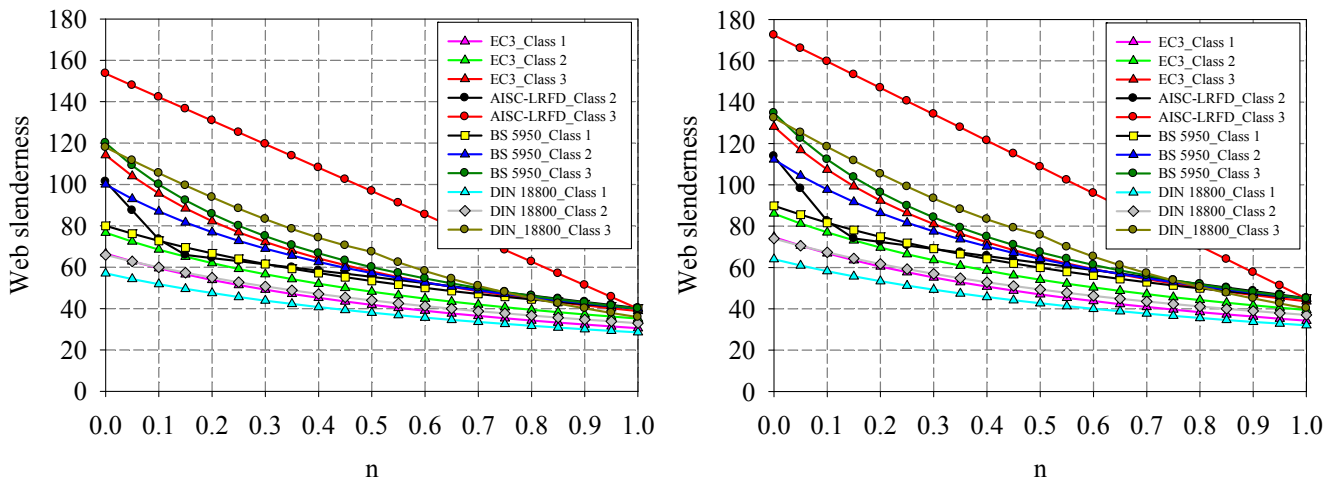


Figure 28 – Numerical comparison of local buckling rules, a) case 4_γ-format_all classes, b) case 4_μ-format_all classes.

Through this section, it can be clearly seen that there are non-negligible differences between various standards adopting the cross-section classification system. This is mainly due to the absence of a solid background behind the cross-section classification system. The following section will list and explain additional shortcomings of this system in order to better understand the need for a new uniform consistent design approach.

Table 7 – Numerical comparison of local buckling rules (case 1, 2, 3, and 5).

Case	Specification	β			δ			γ			μ			α		
		Class 1	Class 2	Class 3	Class 1	Class 2	Class 3	Class 1	Class 2	Class 3	Class 1	Class 2	Class 3	Class 1	Class 2	Class 3
1	EC3	9	10	11	52.5	58.4	64.2	10.4	11.6	12.7	9.3	10.4	11.4	10.9	12.1	13.3
	AISC LRFD	-	-	10.4	-	-	95	-	-	12	-	-	10.8	-	-	12.6
	BS 5950	9.7	10.8	13	56.8	63.2	94.7	9	10	15	8.1	9	13.5	9.4	10.5	15.7
	DIN 18800	8.7	9.6	12.4	63.3	70.3	90.7	10	11.1	14.4	9	10	12.9	10.5	11.7	15.1
	AS 4100	9.3	-	13.2	54.2	-	96.3	8.6	-	15.3	7.7	-	13.7	9	-	16
2	EC3	33	38	42	192.7	221.8	245.2	30.5	35.1	38.8	34.2	39.4	43.6	40	46.1	50.9
	AISC LRFD	-	-	43.3	-	-	253	-	-	40.1	-	-	45	-	-	52.5
	BS 5950	-	-	43.3	-	-	252.6	-	-	40	-	-	44.9	-	-	52.4
	DIN 18800	30.8	35.7	36.4	180	208.1	212.6	28.5	33	33.7	32	37	37.8	37.4	43.2	44.1
	AS 4100	24	-	36	144.5	-	216.8	22.9	-	34.3	25.7	-	38.5	30	-	45
3	EC3	72	83	124	420.3	484.6	723.9	66.6	76.7	114.6	74.7	86.1	128.7	87.3	100.6	150.3
	AISC LRFD	109.6	-	166.1	640	-	970	101.3	-	153.6	113.8	-	172.4	132.9	-	201.4
	BS 5950	86.5	108.2	129.8	505.2	631.5	757.9	80	100	120	89.8	112.3	134.7	104.9	131.1	157.3
	DIN 18800	61.7	71.3	128.2	360	416.3	748.2	57	65.9	118.5	64	74	133	74.7	86.4	155.3
	AS 4100	65.6	-	92	395	-	554	62.5	-	87.7	70.2	-	98.4	82	-	115
5	EC3	33	38	42	192.7	221.8	245.2	30.5	35.1	38.8	34.2	39.4	43.6	40	46.1	50.9
	AISC LRFD	32.5	-	40.8	190	-	238	30.1	-	37.7	33.8	-	42.3	39.4	-	49.4
	BS 5950	-	-	43.3	-	-	252.6	-	-	40	-	-	44.9	-	-	52.4
	DIN 18800	30.8	35.7	36.4	180	208.1	212.6	28.5	33	33.7	32	37	37.8	37.4	43.2	44.1
	AS 4100	24	-	36	144.5	-	216.8	22.9	-	34.3	25.7	-	38.5	30	-	45

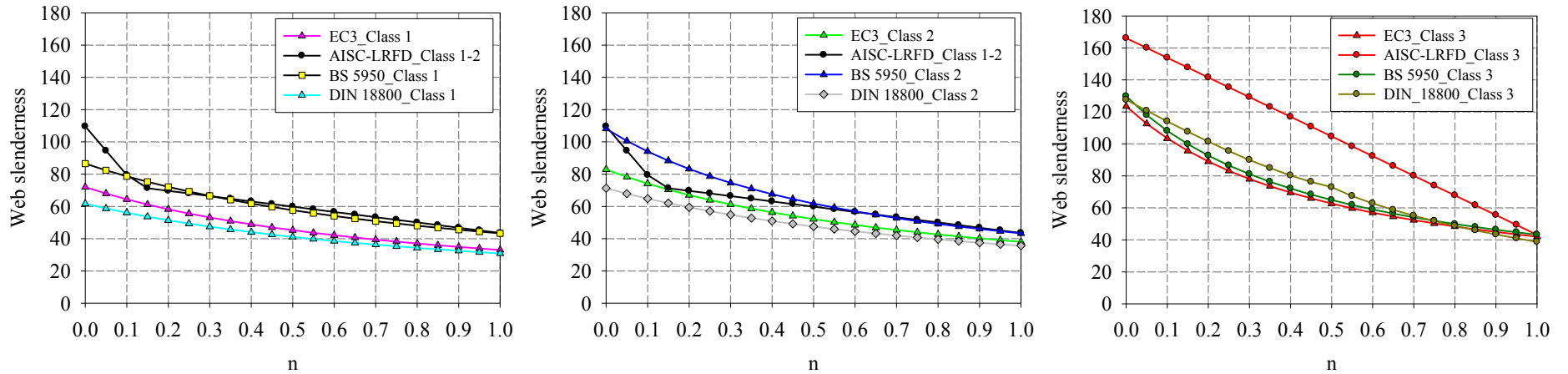


Figure 29 – Numerical comparison of local buckling rules_case 4 β -format_class 1(left), class 2 (middle), class 3 (right).

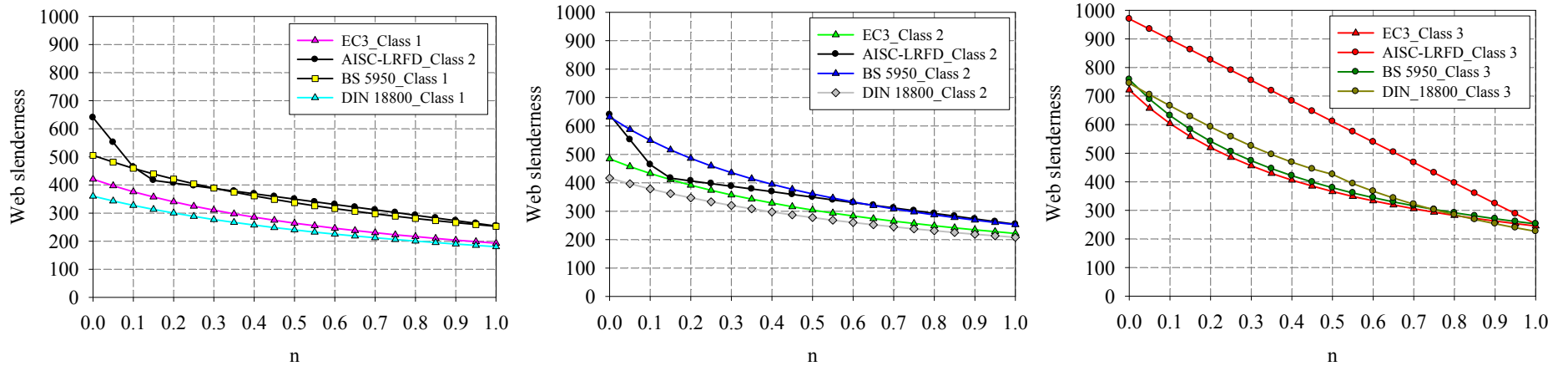


Figure 30 – Comparison of local buckling rules_case 4 δ -format_class 1(left), class 2 (middle), class 3 (right).

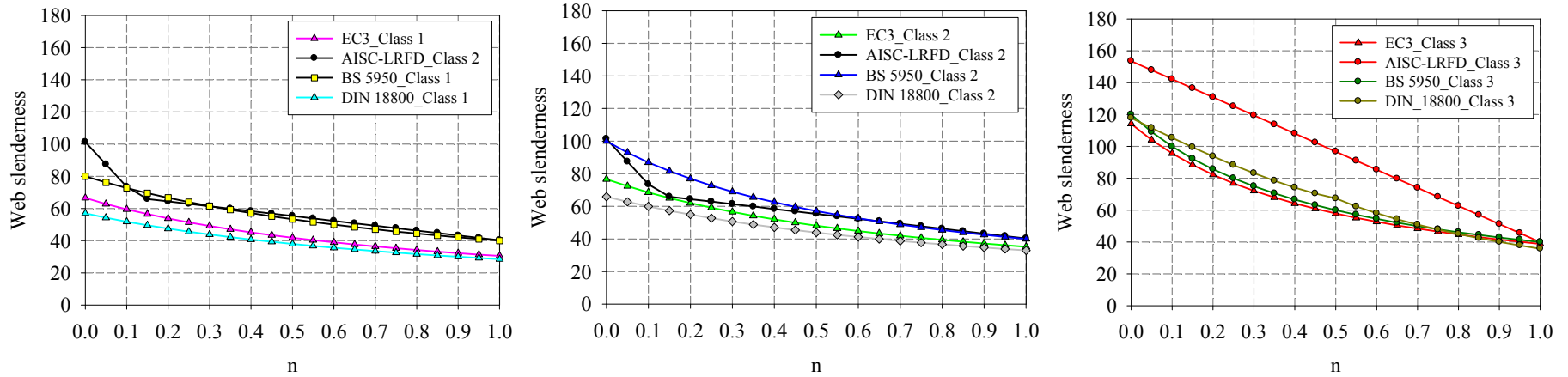


Figure 31 – Numerical comparison of local buckling rules_case 4_γ-format_class 1(left), class 2 (middle), class 3 (right).

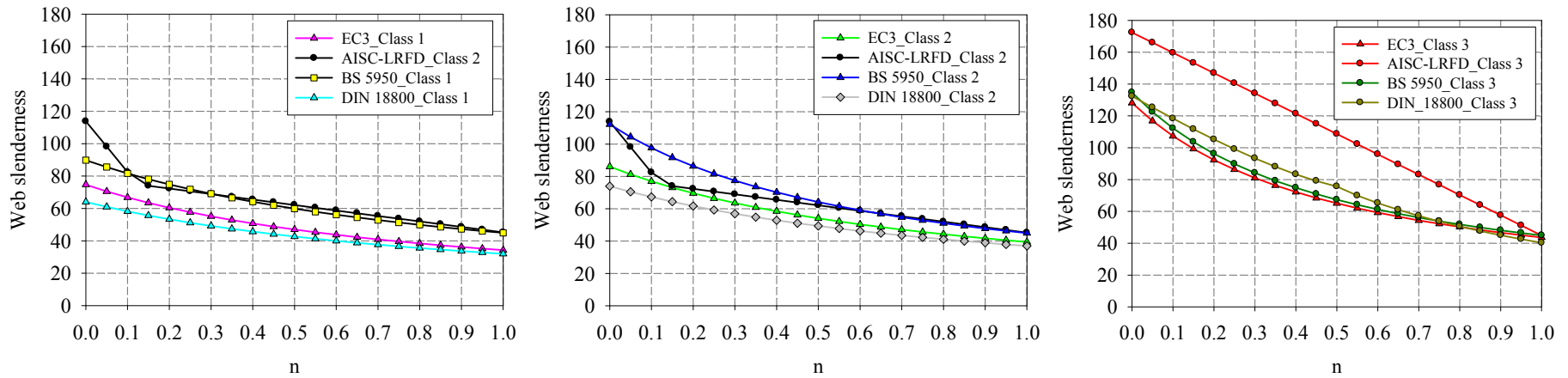


Figure 32 – Numerical comparison of local buckling rules_case 4_μ-format_class 1(left), class 2 (middle), class 3 (right).

2.4.2. Shortcomings of the classification system

The classification systems of various standards have been discussed in the previous section. A comparison between information relative to each specification was presented and commented. However, this section classification system is known to be a useful but artificial way with no scientific justified background and has a lot of shortcomings. This section discusses the most important ones in order to justify the need for a new design proposal which is the target of this work.

2.4.2.1. Classification system background and emergence of non-linear materials

The resistance of structural cross-sections obviously remains a continuous function of the slenderness of the constituent plate elements. However, the cross-section classification system relies on the assignment of cross-sections to artificial discrete classes, which is contradictory to the idea of a continuous function of the plates' slenderness, since it would lead to a simplified too conservative approach (see Figure 33).

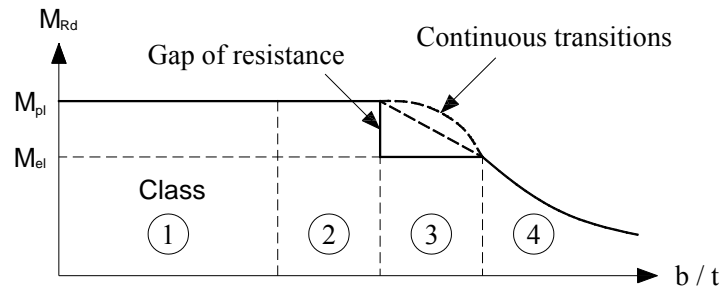


Figure 33 – Eurocode 3 cross-section classes.

Moreover, the basic philosophy of the classification system relies on bilinear (elastic, perfectly-plastic) material behavior. With the emergence of non-linear materials such as aluminium, stainless steel and high strength steel, the framework of the cross-section classification will not fit anymore with their response. Thus, a most continuous way would bring even greater consistency for such non-linear materials for which the cross-section classification will not be able to accurately predict their corresponding behavior.

2.4.2.2. Emergence of high strength steel

Over time, steel has not stagnated with a particular change occurring in the yield stress increasing in such a way that high strength steel emerged and will be futurely followed by ultra-high strength steel. Since metallurgists have not been able to increase the modulus of elasticity at reasonable costs, such materials will become from one hand class 4 cross-

sections and from another hand non-linear materials will not fit with the cross-section classification system anymore. Firstly, class 4 cross-sections will require endless tedious calculations with iterations and secondly, the stability will control the strength. If one wants to take full advantage of such changes in the steel performance, new methods for predicting the cross-section resistance and stability should be developed and employed to improve and create new structural steel shapes and increase the power of the analytical tools. Many other problems will arise from such a radical change in performance such as the weldability fatigue and fracture problems, as well as the impact of ductility losses on the design assumptions.

2.4.2.3. Boundary conditions and post-buckling reserves

The classification system in Eurocode 3 and the Winter approach for class 4 cross-sections are based on plate's theory. In other words, the cross-section depends on the most slender constitutive plate, treated separately with pinned end conditions. This approximation does not represent accurately the real behavior of the entire cross-section, since it may lead to conservative results and even unconservative results. In EN 1993-1-1, the boundary conditions were represented through a plate buckling coefficient k which is discussed in details in section 2.1. As a complement to what have been discussed, Seif and Schafer [13] determined the plate buckling coefficients through a conversion of buckling stresses determined by a finite strip analysis of various types of sections. They compared the assumed finite strip k -values with the k -values defined in the AISC and it turned out that the finite strip k values fall in a wide range and the use of a single value k -value, as defined in most of the standards, is found to be quite approximate. Some cases may fall close to the k -value defined in standards, but in other cases, it may be significantly higher or lower than the assumed k in the standards. Figure 34 shows an example of the computed plate buckling coefficient of k_h (plate buckling coefficient of the web) of rectangular hollow sections subjected to a strong bending moment with the computed k -value corresponding to the AISC and the mean value resorted from the finite strip analysis. This case shows clearly that the plate buckling coefficient is overestimated in the AISC and most importantly the calculated k -value with the finite strip analysis are scattered through a considerable range. The actual impact of the k -value should be taken in the context of each specification and the lack of a consistent rational basis for the assumed k -values employed in any specification would lead to inaccurate prediction of local buckling phenomenon and most importantly to unsafe cases sometimes. The k -value impact would however be minimized if GMNIA calculations were made since

many effects will be added, such as cross-section plasticity, geometrical imperfections, residual stresses etc...

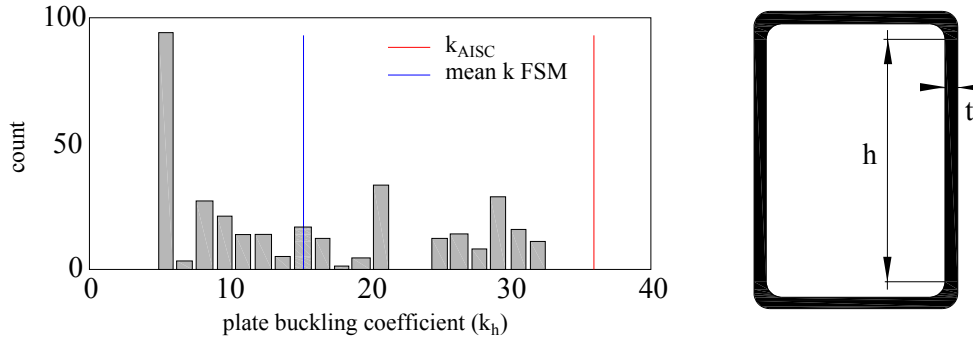


Figure 34 – Plate buckling coefficient (of the web) from the AISC and from the finite strip analysis for the rectangular hollow sections subjected to a strong bending moment [13].

Moreover, and since the classification system has a target of avoiding the occurrence of local buckling, the beneficial post-buckling reserves would be totally ignored, leading to considerable non optimal use of material.

2.4.2.4. Slenderness definition

The plate relative slenderness λ_p used in the Eurocode 3 to determine the class limit is defined as follows:

$$\lambda_p = \sqrt{\frac{f_y}{\sigma_{cr}}} = \sqrt{\frac{f_y}{k \cdot \frac{\pi^2 E}{12(1-\nu^2)} \cdot \left(\frac{t}{b}\right)^2}} \cong \frac{b/t}{28.4 \varepsilon \sqrt{k}} \quad (52)$$

with $\sigma_{cr} = k \frac{\pi^2 E}{12(1-\nu^2)} \left(\frac{t}{b}\right)^2$ being the elastic local buckling stress of a plate of width b .

The k -factor is given in the standards, and is considered as the parameter which takes into account the boundary conditions of the corresponding plate with its stress distribution. These k -factors are derived through a superposition of the various buckling curves of a plate and the corresponding minimum value of this superposition is considered as the relative k -value (see Table 8 and Figure 35).

Table 8 – Determination of the plate buckling coefficient for particular cases.

		Boundary conditions				
		ψ				
$-\sigma$	$-\sigma$	1	4.00	6.97	0.426	1.28
$-\sigma$	$+\sigma$	-1	23.9	39.52	-	-

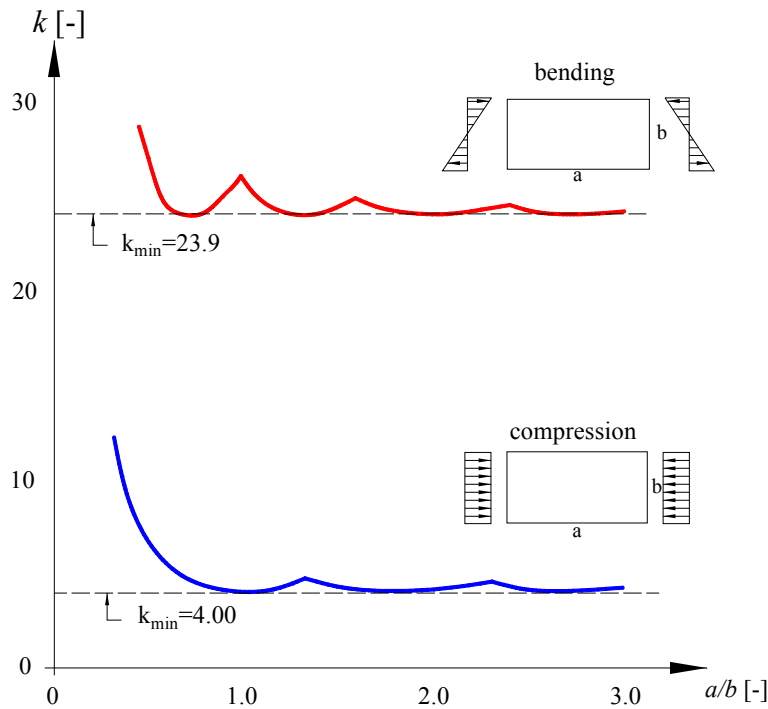


Figure 35 – k_{min} values for two types of stress distributions on a simply supported plate.

By setting limits on the plate slenderness, it would be possible to calculate and determine the corresponding b/t ratios for each section class. That way, the classification of a cross-section would be based on the slenderness, the steel grade, the stress distribution and the boundary conditions.

The λ_p value corresponding to the border between class 3 and 4 has been based on the Winter formula, while the λ_p values corresponding to the border of class 1-2 ($\lambda_p = 0.5$) and

2-3 ($\lambda_p = 0.6$) look like they were determined arbitrarily, seemingly with little physical background.

Concerning the determination of λ_p relative to the class 3-4 border, two Winter formulae were defined as the following for the case of a plate simply supported (see Table 9).




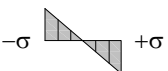
The original Winter formula:

$$\rho = \frac{\lambda_p - 0.05(3 + \psi)}{\lambda_p^2} \quad (53)$$

and the Modified Winter formula:

$$\rho = \frac{\lambda_p - 0.055(3 + \psi)}{\lambda_p^2} \quad (54)$$

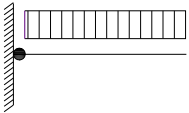
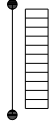
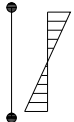
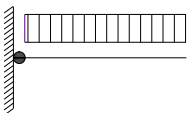
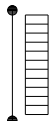
Table 9 – λ_p values relative to the class 3-4 border.

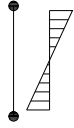
		Plate boundary conditions		
				
		Winter	Modified Winter	Winter
Stress distribution	ψ	$1 = \frac{\lambda_p - 0.05(3 + \psi)}{\lambda_p^2}$	$1 = \frac{\lambda_p - 0.055(3 + \psi)}{\lambda_p^2}$	$1 = \frac{\lambda_p - 0.188}{\lambda_p^2}$
	1	0.724	0.673	0.749
	-1	0.887	0.874	-

Back-calculated border limits based on the b/t ratios from one hand and on the λ_p values from another hand have been performed to show the inconsistency in the plate slenderness definitions. The results are shown in Table 10, which is divided in two parts (delimited by grey rows) and consist in:

- (i) First part: assuming the existing b/t ratios in the EN 1993-1-1, and calculating the corresponding plate slenderness relative to each b/t value. It can be clearly seen that none of the back-calculated values correspond to the $\lambda_p = 0.5$ for the border class 1-2, neither $\lambda_p = 0.6$ for the border class 2-3 and nor the λ_p values corresponding to Winter equations;
- (ii) Part two: assuming the plate slenderness values λ_p and calculating the corresponding b/t ratios for each λ_p . Again, none of the back-calculated values correspond to the b/t ratios defined in the En 1993-1-1, table 5-2.

Table 10 – Comparison of b/t ratios with relative plate slenderness values λ_p .

	border class 1-2 => $\lambda_p=?$	border class 2-3 => $\lambda_p=?$	border class 3-4 => $\lambda_p=?$
	$9\varepsilon \Rightarrow \lambda_p = 0.486$ $\neq 0.5$	$10\varepsilon \Rightarrow \lambda_p = 0.539$ $\neq 0.6$	$14\varepsilon \Rightarrow \lambda_p = 0.755$ $\neq 0.749$
	$33\varepsilon \Rightarrow \lambda_p = 0.581$ $\neq 0.5$	$38\varepsilon \Rightarrow \lambda_p = 0.669$ $\neq 0.6$	$42\varepsilon \Rightarrow \lambda_p = 0.739$ $\neq 0.673^{**}$
	$72\varepsilon \Rightarrow \lambda_p = 0.519$ $\neq 0.5$	$83\varepsilon \Rightarrow \lambda_p = 0.598$ $\neq 0.6$	$124\varepsilon \Rightarrow \lambda_p = 0.893$ $\neq 0.673^{**}$
	$\lambda_{p \text{ class I}}=0.5 \Rightarrow$ border class 1-2?	$\lambda_{p \text{ class I}}=0.6 \Rightarrow$ border class 2-3?	$\lambda_{p \text{ class I}}=\text{var}^* \Rightarrow$ border class 3-4?
	9.268ε $\neq 9\varepsilon$	11.12ε $\neq 10\varepsilon$	13.88ε ($\lambda_p = 0.749$) $\neq 14\varepsilon$
	28.4ε $\neq 33\varepsilon$	34.08ε $\neq 38\varepsilon$	41.04ε ($\lambda_p = 0.724$) 38.21ε ($\lambda_p = 0.673$) Both $\neq 42\varepsilon$

	69.42ε $\neq 72\varepsilon$	83.301ε $\neq 83\varepsilon$	123.14ε $(\lambda_p = 0.887)$ 121.36ε $(\lambda_p = 0.874)$ Both $\neq 124\varepsilon$
---	--	---	--

*var is relative to the winter equation. In cases where two values are calculated, the first one is relative to the original Winter formula and the second value to the modified Winter formula

**the comparison is based on the modified Winter formula

2.4.2.5. Gap of resistance between class 2 and class 3

Another problem of the classification system is the presence of a discontinuity between two classes (in some standards). The European design code for structural steel EN 1993-1-1 defines 3 situations of stress distributions: steel sections classified as ‘plastic’ (class 1 and 2), ‘elastic’ (class 3) and effective (class 4). ‘Plastic’ cross-sections are equivalent to ‘compact’ cross-sections of other standards, capable of reaching their full plastic section capacity and ‘elastic’ cross-sections are equivalent to semi-compact cross-sections capable of reaching only the elastic capacity. This condition will result in a significant discontinuity at the border between class 2 and class 3 cross-sections (see Figure 36); such discontinuity has no physical meaning and could lead to conservative and uneconomical cross-section capacities for class 3 cross-sections. However, British standard BS 5950-1, Australian standard AS 4100 and American code AISC-LRFD overcame this shortcoming by allowing for linear interpolations (slightly under linear with BS 5950-1) for the transition of the mono-axial bending moment resistances from plastic to elastic. This is shown in Figure 37 and Figure 38 for the case of stiffened element of an RHS subjected to a minor-axis bending. As for the European standards, Lechner and Kettler ([46] & [7]) proposed a linear transition between class 2 and class 3. The interaction criterion for hollow sections is shown in Figure 39.

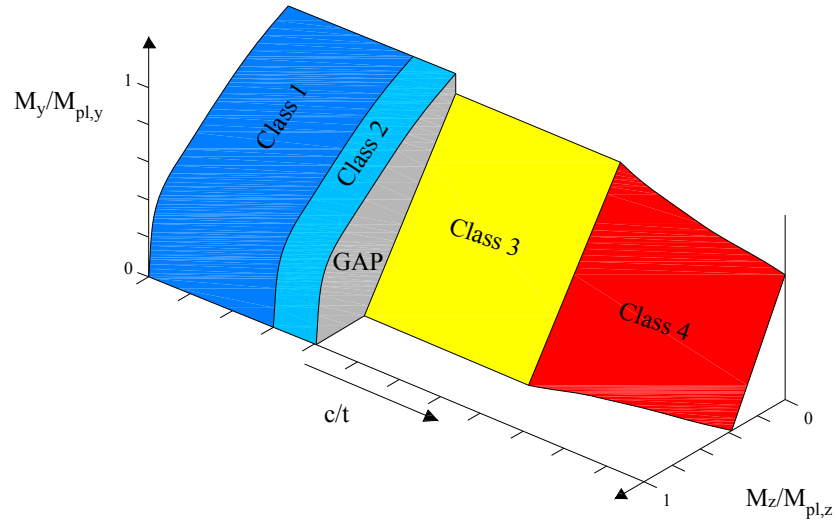


Figure 36 – Comparison of class 3 cross-section resistances according to various standards for a hot finished RHS under major-axis bending – a) flange decisive – b) web decisive [7].

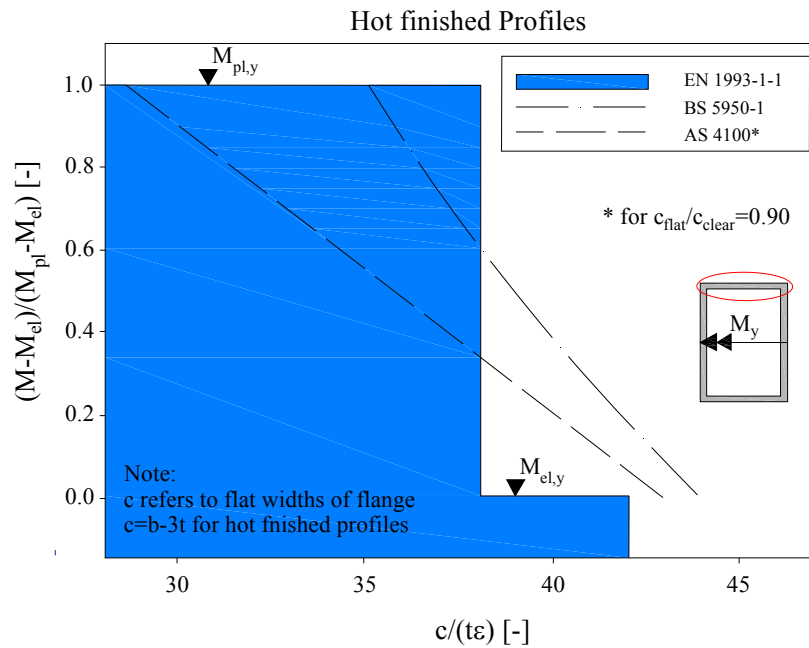


Figure 37 – Comparison of class 3 cross-section resistances according to various standards for a hot finished RHS under major-axis bending – Flange decisive [7].

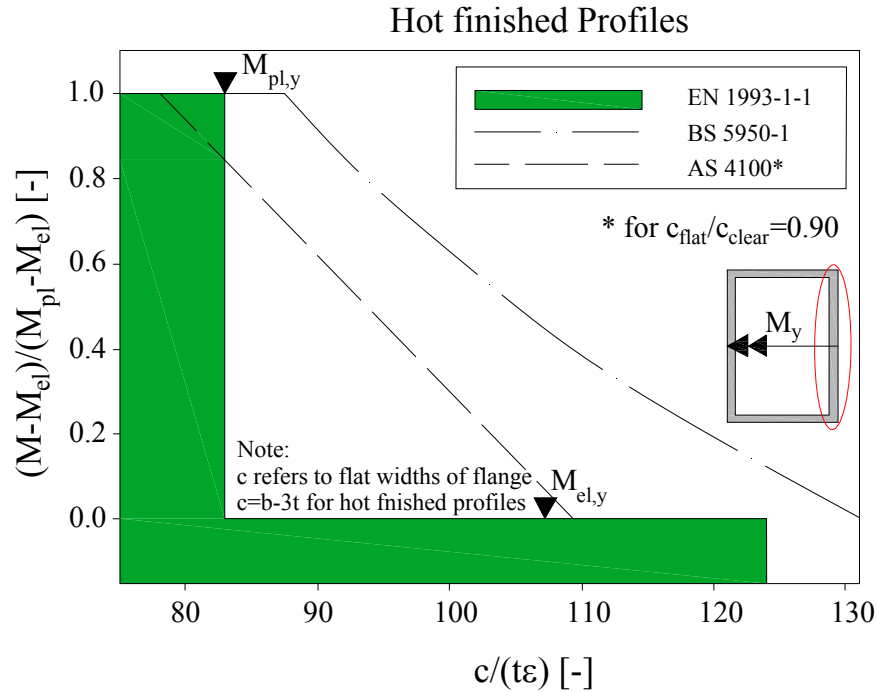


Figure 38 – Comparison of class 3 cross-section resistances according to various standards for a hot finished RHS under major-axis bending – Web decisive [7].

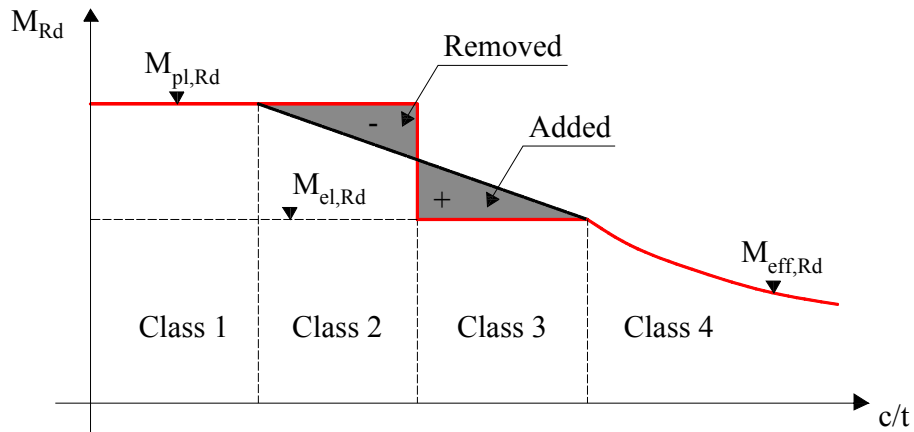


Figure 39 – Design proposal for cross-section resistance of tubular sections [7].

2.4.2.6. Errors and contradictions in table 5.2 of EN 1993-1-1







Villette [51] presented a deep analysis concerning the cross-section classification system and the slenderness limits presented in table 5.2 of EN 1993-1-1 and showed many serious errors and paradoxes concerning the way the cross-sections are being classified. Three paradoxes will be presented in this sub-section and more details can be found in Villette [51].

Villette considered a monosymmetric I section subjected to a major-axis bending. All calculations presented herein were made by considering the yield limit to be 235 MPa. The first paradox consisted in the following:

- (i) *The plastic analysis may be authorized through the simple reduction of the web thickness of an I section subjected to a major-axis bending.*

This paradox is clearly shown and demonstrated through Table 11 and Figure 40. Once the web thickness is increased by 25% the section surprisingly do not verify the class 1 criteria, although it was verified with the same section having a smaller web thickness. Figure 40 illustrates the shift in the plastic neutral axis between both considered sections with the relative class 1 criteria verified for the section having the smaller web thickness but not for the other, making it classified as a cross-section of class 2.

Table 11 – Application of table 5.2 of EN 1933-1-1 for two dissymmetric sections subjected to a major-axis bending with different web thicknesses (highlighted in red).

		Class 1	Class2	Class 3	Section class
Upper flange	430x25				1
Web	1000x6	Verified	Verified	Verified	
Bottom flange	367x20	Verified	Verified	Verified	
Upper flange	430x25				2
Web	1000x7.5	Not Verified	Verified	Verified	
Bottom flange	367x20	Not Verified	Verified	Verified	

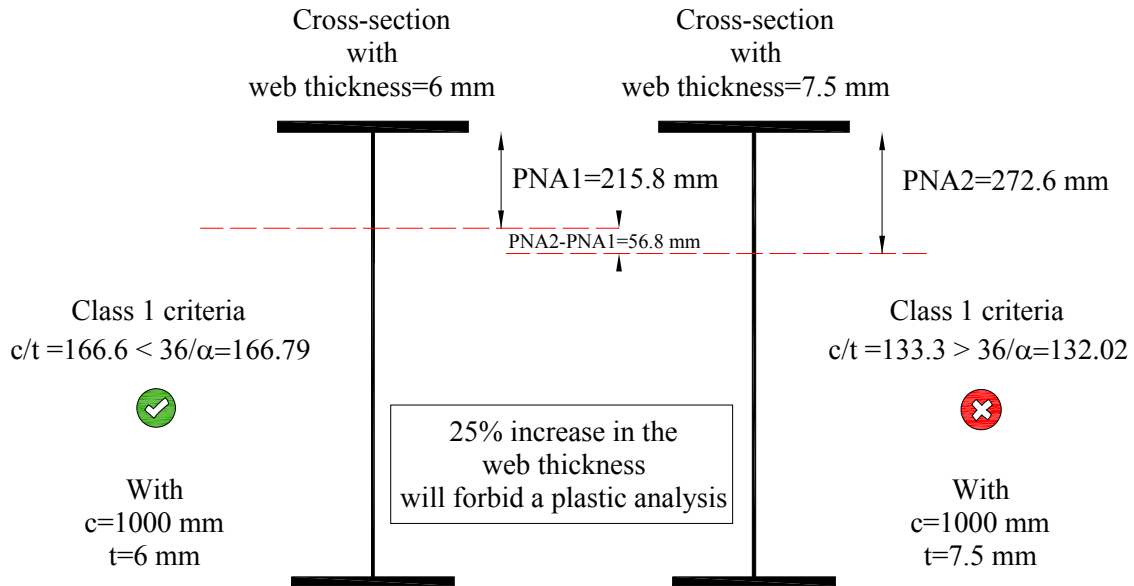


Figure 40 – Verification of class 1 criteria for two dissymmetric cross-sections differing in their web thicknesses, and subjected to a major-axis bending moment.

The second paradox consists in the following:

- (ii) *Two I sections subjected to a major-axis bending moment M_y with the web thickness being the only difference, will lead in some cases to a higher cross-section capacity for the section having the thinner web thickness.*

This case is presented and illustrated in both Table 12 and Figure 41. Three cross-sections have been considered in which the web thickness was increased (highlighted in red in Table 12). The first cross-section with a web thickness of $t = 6$ mm, belonged to class 2. When considering a higher web thickness equal to 7 mm for the second section, the cross-section was thrown into the class 3, while a further increment of the web thickness (this time 7.5 mm) threw back the cross-section into the class 2.

Table 12 – Application of table 5.2 of EN 1933-1-1 for three dissymmetric sections subjected to a major-axis bending.

		Class 1	Class2	Class 3	Section class
Upper flange	340x25				2
Web	1115x6				
Bottom flange	319x15	Verified	Verified	Verified	
Upper flange	340x25				3
Web	1115x7				
Bottom flange	319x15	Not Verified	Not Verified	Verified	
Upper flange	340x25				2
Web	1115x7.5				
Bottom flange	319x15	Not Verified	Verified	Verified	

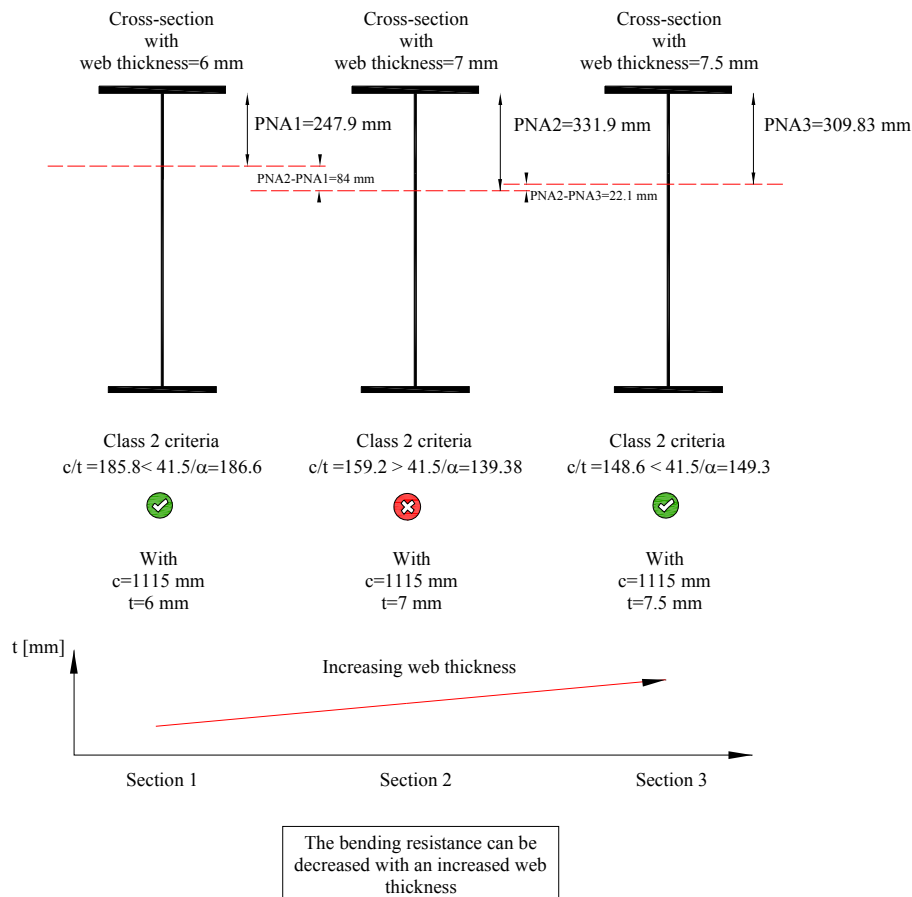
















Figure 41 – Verification of class 2 criteria for three dissymmetric cross-sections differing in their web thicknesses, and subjected to a pure major-axis bending moment.

And finally the third paradox consists in the following:

(iii) Every I section sufficiently dissymmetric and subjected to a major-axis bending moment is supposed to be a class 1 cross-section, but the thinness of its web can throw it into the class 4

In current practice, if a cross-section fulfils a certain criterion relative to a specific class, the criteria corresponding to the higher classes are supposed to be also fulfilled. Table 13 shows a number of examples showing that this is not the case and a contradiction is clearly highlighted. The computations corresponding to each class criterion are also represented in Table 13. The inaccuracy of the class 1 definition is particularly illustrated in the first example of a cross-section for which any practitioner with common sense will not accept a plastic analysis for such section and would even refuse to use such section. But according to the EN 1993-1-1, the class 1 and 2 criteria are well verified and the class 3 criterion based on an elastic distribution is not. So the cross-section would be considered as having two classes which is completely absurd and wrong. The same contradiction is seen in the following 3 cross-section examples with more reasonable dimensions, and for which any practitioner would make the mistake of considering them as class 1 cross-sections. The web thickness is unsatisfying to benefit from the full elastic capacity, but is completely adequate for the allowance of a plastic analysis. The fifth example shows a similar contradiction, but this time between the class 2 and class 4 criteria.

Table 13 – Application of table 5.2 of EN 1933-1-1 for 5 dissymmetric sections subjected to a major-axis bending.

		Class 1	Class2	Class 3	Section class
Upper flange	500x28	$c/t = 440 < 36/\alpha = 535$  Verified	$c/t = 440 < 41.5\alpha = 617$  Verified	$c/t = 440 > \frac{42}{0.67 + 33\psi} = 85$  Not Verified	1 or 4?
Web	2200x5				
Bottom flange	320x14				
Upper flange	360x20	$c/t = 200 < 36/\alpha = 205$  Verified	$c/t = 200 < 41.5\alpha = 236$  Verified	$c/t = 200 > \frac{42}{0.67 + 33\psi} = 96$  Not Verified	1 or 4?
Web	1000x5				
Bottom flange	330x12				
Upper flange	360x22	$c/t = 180 < 36\alpha = 200$  Verified	$c/t = 180 < 41.5/\alpha = 231$  Verified	$c/t = 180 > \frac{42}{0.67 + 33\psi} = 102$  Not Verified	1 or 4?
Web	900x5				
Bottom flange	360x14				
Upper flange	460x26	$c/t = 167 < 36/\alpha = 170$  Verified	$c/t = 167 < 41.5/\alpha = 196$  Verified	$c/t = 167 > \frac{42}{0.67 + 33\psi} = 107$  Not Verified	1 or 4?
Web	1000x6				
Bottom flange	425x20				
Upper flange	480x25	$c/t = 153 > 36/\alpha = 136$  Not Verified	$c/t = 153 < 41.5/\alpha = 157$  Verified	$c/t = 167 > \frac{42}{0.67 + 33\psi} = 113$  Not Verified	2 or 4?
Web	920x6				
Bottom flange	470x20				

In summary, the main conclusion resorting from such analysis is that the two criteria relative to the class 1 and 2 based on a plastic stress distribution are incompatible with the criteria relative to the class 3 and 4 based on an elastic stress distribution. All criteria should ideally be based on a same type of stress distributions with different class limits, since these three presented paradoxes showed that:

- (i) The plastic analysis can be allowed through a simple reduction of the web thickness of an I section subjected to a major-axis bending moment;

- (ii) The bending capacity of an I section can be seen to decrease with an increase of its corresponding web thickness;
- (iii) An I section, subjected to a major-axis bending, can be found to belong at the same time to the class 1 and 4 and also with a possibility of belonging at the same time to the class 2 and 4.

Accordingly, the cross-section classification system needs to be improved or even removed to allow for a suggestion of a more accurate and consistent design proposal.

2.4.2.7. Unconformity in the determination of the class 4 plate slenderness limit

Computations relative to class 4 cross-sections are presented based on two approaches; the first approach rely on the application of the EN 1993-1-1 and the second is relative the EN 1993-1-5. The corresponding limits based on the two defined approaches have been calculated for stress distributions ratios ψ going from 1 to -2 [52].

With the application of EN 1993-1-1, the following values could be found:

- (i) For $\psi = 1$, i.e. pure compression, the limit class 3-4 will be equal to 42ε ;
- (ii) For $\psi = -1$ i.e. pure bending, the limit class 3-4 will be equal to 124ε ;
- (iii) For $-1 < \psi < 1$, i.e for a combined load case with compression, the limit class 3-4 will be equal to $\frac{42\varepsilon}{0.67 + 0.33\psi}$;
- (iv) For $\psi < -1$, i.e. for a combined load case with tension, the limit class 3-4 will be equal to $62\varepsilon(1-\psi)\sqrt{-\psi}$.

With the application of EN 1993-1-5, the following values could be found:

A cross-section is considered fully effective when $\rho = 1$ with relative plate slenderness being equal to

$$\lambda_p = \sqrt{\frac{f_y}{\sigma_{cr}}} = \frac{b/t}{28.4\varepsilon\sqrt{k_\sigma}} = 0.673 \quad (55)$$

The ratio b/t can be calculated with the use of Equation (55):

$$\frac{b}{t} = 0.673 \times 28.4 \times \varepsilon \sqrt{k_\sigma} \quad (56)$$

where k_σ depends on the stress distribution of the plate

Therefore,

(i) For $\psi = 1$, i.e. for a pure compression, k_σ will be equal to 4 and the limit class 3-4 will be equal to 38ε ;

(ii) For $\psi = -1$, i.e. for a pure bending, k_σ will be equal to 23.9 and the limit class 3-4 will be equal to 94ε ;

(iii) For $0 < \psi < 1$, i.e. for a combined load case without tension, k_σ will be equal to $\frac{8.2}{1.05 + \psi}$ and the limit class 3-4 will be equal to $\frac{55\varepsilon}{\sqrt{1.05 + \psi}}$;

(iv) For $-1 < \psi < 0$, i.e. for a combined load case with compression, k_σ will be equal to $7.81 - 6.29\psi + 9.78\psi^2$ and the limit class 3-4 will be equal to $19\varepsilon\sqrt{7.81 - 6.29\psi + 9.78\psi^2}$;

(v) For $\psi < -1$, i.e. for a combined load case with tension, k_σ will be equal to $5.98(1 - \psi)^2$ with the limit class 3-4 being equal to $43\varepsilon(1 - \psi)$.

The following curves shown in Figure 42 represent the comparison between the two approaches. It is clearly seen that the approach relative to EN 1993-1-5 would provide ineffective portions in the cross-section plates deemed to be considered fully effective according to EN 1993-1-1. There is thus a discontinuity in the transition between class 3 and class 4.

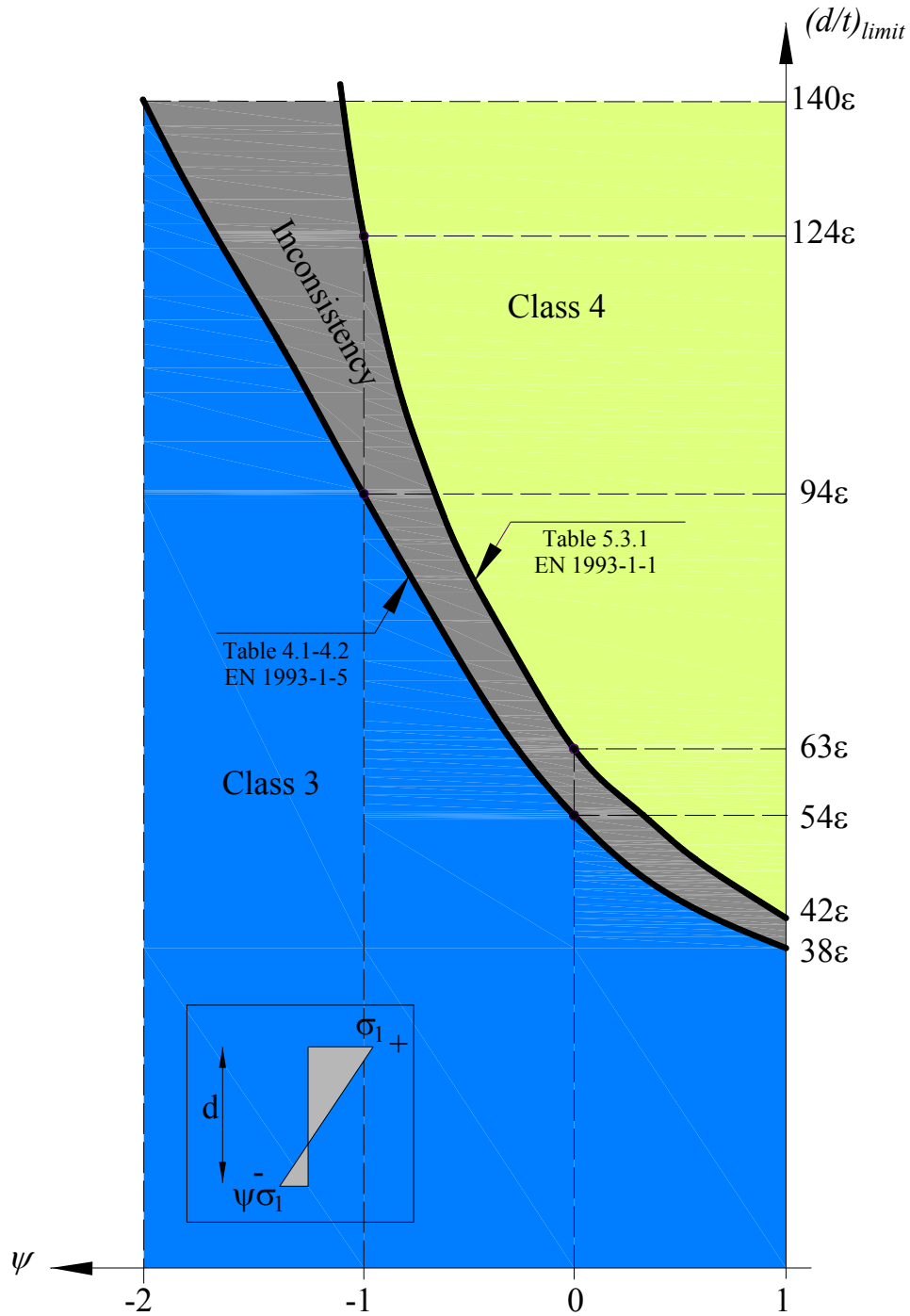


Figure 42 – Plate slenderness limits for class 4 categories, based on the EN 1993-1-5, Table 4.1-4.2 and the EN 1993-1-1, table 5.3.1.

2.4.2.8. Other inconsistencies

Many other inconsistencies and shortcomings are attached to the cross-section classification system and should be evaluated and studied from scratch since no mechanical or physical

background exists behind them. Some shortcomings can be cited here and explained briefly herein. They consist in:

- (i) No difference is made between fabrication processes. Only the definition of the plate width differs with the adoption of a $b - 3t$ value for the hot-rolled and $b - 5t$ for the cold formed sections;
- (ii) The determination of the effective section for class 4 cross-sections, require tedious long calculations with iterations;
- (iii) In a same element, a section can have different classes depending on the load case combination;
- (iv) No method is defined for the determination of effective section properties of the class 4 circular sections;
- (v) For cross-sections submitted to combined loading, the EC3 plastic interaction equations presents some approximations discussed in section 4.3.3;
- (vi) The inclusion of element interaction is absent.

All the shortcomings listed in this section emphasize the necessity of alternative design approaches for the classification system. Accordingly, the next section will present the most important existing alternatives in development with their relative aspects.

2.5. Design alternatives in development – Use of modern tools

In this section, the two main alternatives will be presented and discussed. They consist in (i) the DSM: Direct Strength Method [1] & [53] and (ii) the CSM: Continuous Strength Method [2]. The DSM is based on the assumption that the strength can be predicted from the ratio of the yield strength to the elastic critical load in conjunction with a strength curve for the entire cross-section. As for the CSM, it is a deformation-based approach based on a continuous relationship between cross-sectional slenderness and cross-section deformation capacity and a rational exploitation of strain hardening. These two approaches are considered to be the actual leading approaches in steel design and the inspiration of nowadays research developments. Therefore, a detailed presentation is essential for a better understanding of these existing two approaches.

2.5.1. Direct strength method – DSM

2.5.1.1. Introduction

The Direct Strength method is basically designed for cold-formed steel and does not rely on effective widths method but is rather based on an accurate member elastic stability. It was formally adopted in 2004 as Appendix 1 to the North American Specification for the design of cold-formed steel structural members [54]. Therefore, the elastic buckling load in local P_{crit} , distortional P_{crd} , and global buckling load P_{cre} (derived using computational tools, such as CUFSM [15] or GBTUL [16]) along with the load that causes first yield is used in a series of simple equations providing the corresponding section or member strength.

The DSM is essentially an extension of the use of column curves for global buckling but with consideration of other instabilities such as local and distortional modes with an appropriate consideration of post-buckling reserves and interaction in these modes.

A brief explanation of the cross-section slenderness with base curves for beams, columns and beam-columns is presented in the following section along with the corresponding advantage and limitations of the DSM.

2.5.1.2. Cross-section slenderness definition

As opposed to the effective width method, the direct strength method does not use a strength curve for each element of the section but for the entire cross-section. However, it is based on an empirical study, just like the effective width method. The Winter curve is again adopted as the relevant type curve. Nevertheless, the determination of the non-dimensional plate slenderness λ_p presents a small difference; while the effective width approach describes λ_p as a function of stresses, the direct strength method calculates this value on the basis of internal forces.

Therefore, in the case of cross-sections subjected to compression, the cross-section slenderness would be as the following:

$$\lambda_l = \lambda_{CS,N} = \sqrt{\frac{N_y}{N_{cr}}} \quad (57)$$

where N_y is the squash load and N_{cr} the critical elastic local column buckling load.

For the case of cross-sections subjected to bending, the cross-section slenderness would be as the following:

$$\lambda_l = \lambda_{CS,M} = \sqrt{\frac{M_y}{M_{cr}}} \quad (58)$$

where M_y is the yield moment and M_{cr} the critical elastic local buckling moment.

2.5.1.3. Base curves

Generally, the DSM is unable to distinguish between the support conditions of individual elements of the cross-section neither between different types of sections. As a result, only one conservative strength curve shall be used for all cross-section element types and for all cross-section types. Concerning the local buckling strength, the direct strength expressions are used to provide such type of strength including interaction with global buckling strength. However in this study, only local buckling is considered, thus short elements are assumed to be fully laterally braced and the global buckling strength is simply the strength at first yield ($P_{ne} = P_y$ and $M_{ne} = M_y$). Therefore, in the following sub-sections, only the strength curves relative to local buckling will be presented.

2.5.1.3.1. Sections in compression

For columns, the beginning of the DSM was traced to research when Hancock et al. [55] collected research and demonstrated that for a large variety of cross-sections the measured compressive strength in a distortional failure correlated well with elastic distortional mode slenderness. Hancock attributed his findings to Trahair's work on the strength prediction of columns undergoing flexural-torsional buckling. Therefore and as already said, the DSM is an extension of existing methods to new instability limit states with adequate consideration of instability interactions and post-buckling reserves. A much wider set of cold-formed steel cross-section and tests (267 columns [56], [57], [58] & [53]) which included failures in local, distortional and global flexural or flexural-torsional modes were gathered and used for the development of the direct strength method beyond the previous findings concerning distortional buckling. Figure 43 presents the gathered data in the direct strength format. For the local failures the normalization of P_{test} is to P_{ne} , the maximum strength due to global buckling (i.e. local-global interaction), while for distortional buckling the normalization of P_{test} is to P_y , the squash load of the column.

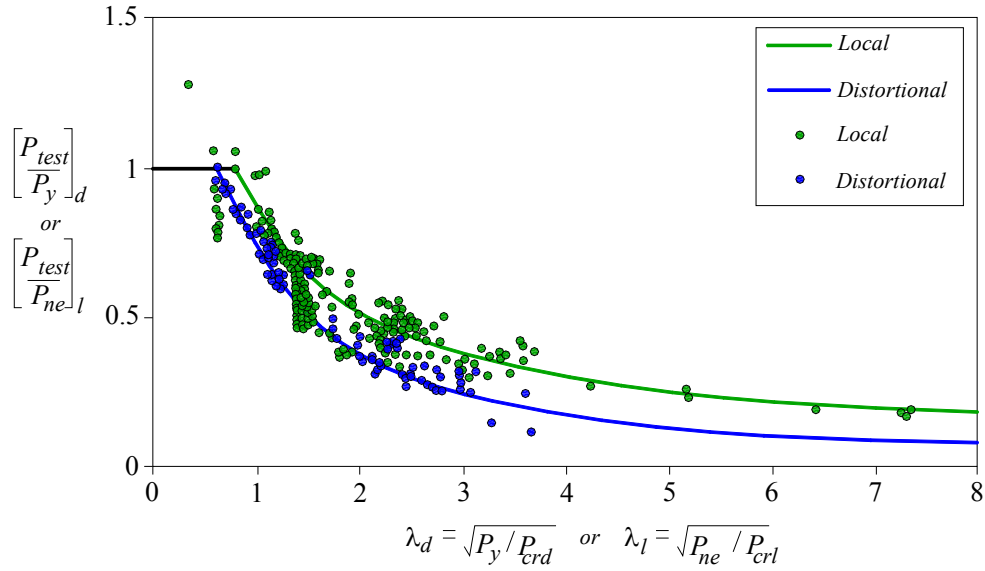


Figure 43 – Comparison of the Direct Strength Method predictor curves with test data for columns.

The nominal axial strength P_{nl} , for local buckling is:

$$P_{nl} = \begin{cases} P_{ne} & \text{for } \lambda_l \leq 0.776 \\ \frac{\left(1 - 0.15 \left(\frac{P_{crl}}{P_{ne}}\right)^{0.4}\right)}{\left(\frac{P_{crl}}{P_{ne}}\right)^{0.4}} P_{ne} & \text{for } \lambda_l > 0.776 \end{cases} \quad (59)$$

However if the following cross-sectional slenderness is introduced (as discussed in the previous section):

$$\lambda_l = \lambda_{CS,N} = \sqrt{\frac{N_y}{N_{cr}}} \quad (60)$$

where N_{cr} is the critical elastic local column buckling load and N_y the yield load.

Equation (59) becomes:

$$N_{dsm} = \begin{cases} N_y & \text{for } \lambda_{CS,N} \leq 0.776 \\ \left(1 - \frac{0.15}{\lambda_{CS,N}^{0.8}}\right) N_y & \text{for } \lambda_{CS,N} > 0.776 \end{cases} \quad (61)$$

2.5.1.3.2. Beams

The first mention of the direct strength method was relative to the development of the method for beams. Schafer [58] & [53] collected a large database of sections to explore distortional buckling in C and Z section beams and local and distortional buckling in deck sections with multiple longitudinal intermediate stiffeners in the compression flange. Meanwhile, Hancock and related researchers at the University of Sydney demonstrated that distortional buckling failures for a wide variety of failures were well correlated with the elastic distortional slenderness ([59] & [55]). The performance of the DSM against experimental data (569 beam tests) is graphically provided in Figure 44.

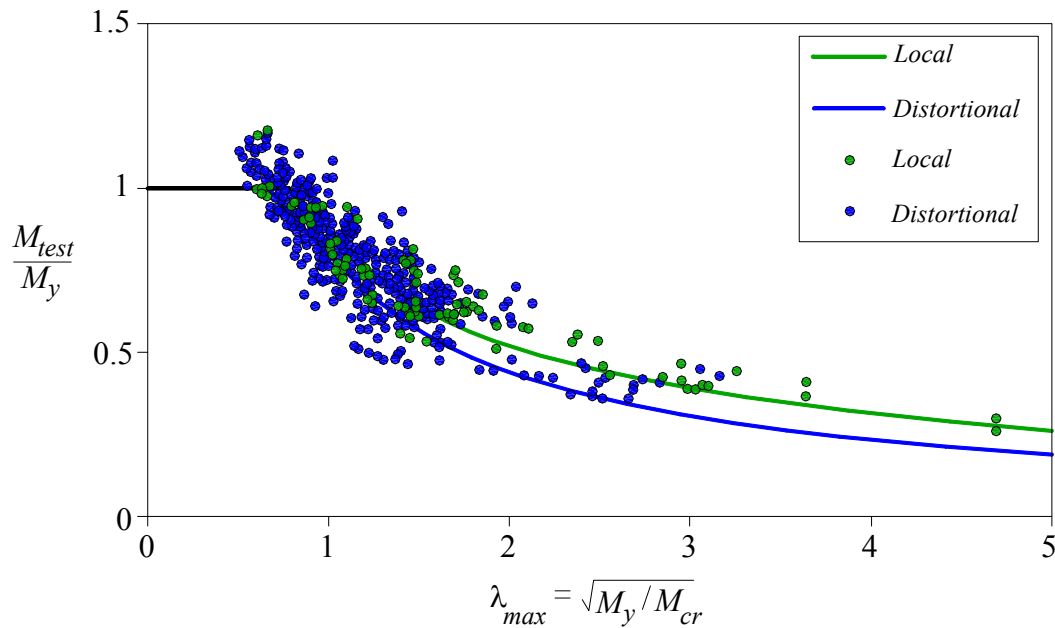


Figure 44 – Comparison of the DSM predictor curves with test data for beams.

Note for the beams of Figure 44, all of the M_{test} values are normalized against the moment at first yield, M_y , because all the employed test data were for laterally braced members.

The nominal flexural strength M_{nl} , for local buckling is:

$$M_{nl} = \begin{cases} M_{ne} & \text{for } \lambda_l \leq 0.776 \\ \left(1 - 0.15 \left(\frac{M_{crl}}{M_{ne}} \right)^{0.4} \right) \frac{M_{ne}}{\left(\frac{M_{crl}}{M_{ne}} \right)^{0.4}} & \text{for } \lambda_l > 0.776 \end{cases} \quad (62)$$

However if the following cross-sectional slenderness is used (as discussed in the previous section):

$$\lambda_l = \lambda_{CS,M} = \sqrt{\frac{M_y}{M_{cr}}} \quad (63)$$

where M_{cr} is the critical elastic local buckling moment and M_y the yield moment.

Equation (62) becomes:

$$M_{dsm} = \begin{cases} M_y & \text{for } \lambda_{CS,M} \leq 0.776 \\ \left(1 - \frac{0.15}{\lambda_{CS,M}^{0.8}} \right) \frac{M_y}{\lambda_{CS,M}^{0.8}} & \text{for } \lambda_{CS,M} > 0.776 \end{cases} \quad (64)$$

2.5.1.3.3. Beam-columns

The DSM proposed beam-columns equations are the same as for simple load cases, but replacing P_{cr} and P_y with β_{cr} and β_y to obtain the nominal capacity β_n :

$$\beta_n = f(\beta_{cr}, \beta_y) \quad (65)$$

In other terms, if we consider the P - M - M space defined in z - x - y and in Cartesian or spherical coordinates (see Figure 45), then:

$$x = \frac{M_1}{M_{y1}}; y = \frac{M_2}{M_{y2}}; z = \frac{P}{P_y} \quad (66)$$

and the nominal capacity λ_n would be equal to:

$$\beta_n = \sqrt{x^2 + y^2 + z^2} \quad (67)$$

with

$$\theta_{MM} = \tan^{-1}(y/x) \text{ and } \phi_{PM} = \cos^{-1}(z/\beta) \quad (68)$$

Thus the nominal local strength β_{nl} would be:

For $\lambda_l \leq 0.776$

$$\beta_{nl} = \beta_{ne} \quad (69)$$

For $\lambda_l > 0.776$

$$\beta_{nl} = \left(1 - 0.15 \left(\frac{\beta_{crl}}{\beta_y} \right)^{0.4} \right) \left(\frac{\beta_{crl}}{\beta_y} \right)^{0.4} \beta_y \quad (70)$$

where $\lambda_l = \sqrt{\frac{\beta_y}{\beta_{crl}}}$;

β_{crl} = Critical elastic local buckling magnitude under combined P-M-M resultant;

β_y = First yield under combined P-M-M resultant.

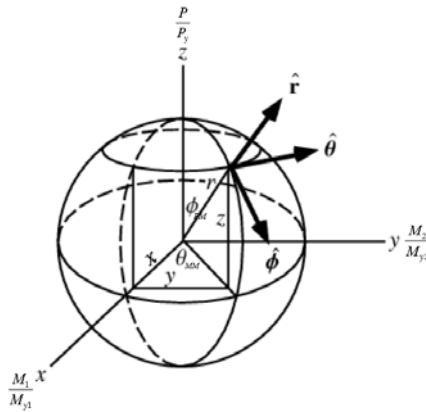


Figure 45 – P-M-M space.

That way, the radial distance β_n will be able to capture the combined loading and buckling collapse with only minor changes in the DSM equations. Some improvements need to be applied to these equations, mainly the introduction of inelastic bending reserve capacity into

the β_n prediction. More details on the Direct Strength Method for beam-columns can be found in ([58], [53] & [60]).

Now that main DSM aspects relative to local buckling have been presented, advantages and limitations will be listed in this section for a clear overview on DSM characteristics.

2.5.1.4. Practical and theoretical advantages and limitations of DSM

Advantages:

A good number of practical advantages exist with the use of the DSM, mainly:

- (i) No effective width calculations with long iterative procedures as DSM uses gross cross-section properties;
- (ii) Elastic buckling analysis can be achieved by means of computer softwares with the use of freely available tools like CUFSM and the calculations are directly integrated into DSM in a simple way;
- (iii) DSM provides a general method for the design of cold-formed steel members with much broader extensions than traditional limited specification methods. The main focus is on correct determination of elastic buckling behavior rather than effective widths determinations;
- (iv) DSM includes the interaction of elements within a cross-section. A simple example for columns, included in Figure 46, shows the importance of the consideration of the interaction of elements. To better visualize this effects, the strength prediction of the EWM and the DSM are compared as a function of the web slenderness of a C section column. Both methods seemed to provide similar overall reliability levels, but a closer look into Figure 46 demonstrates some errors in the strength predictions with the EWM. As web slenderness increases, the EWM solution becomes conservative. This behavior is due to the fact that for such C-sections, the flange keeps almost the same width when the web depth increases, i.e. the local web/flange interaction is essential and the detrimental behavior expressed with the EWM is mainly due to the fact that the EWM uses the element approach, so that the web and flange are considered totally independent. However, DSM, which include element interaction, has a good reliability over the full range of web slenderness, thus accurate strength prediction should include element interaction [53];

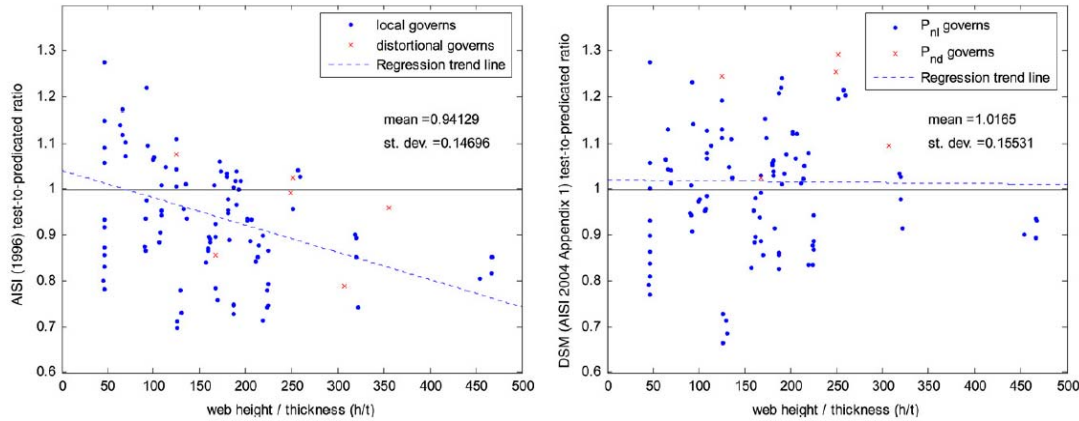


Figure 46 – Test-to-predicted ratio for the Effective Width Method (left) and the Direct Strength Method (right) for all lipped columns [1].

- (v) Design for distortional buckling of beams and columns is derived, thus DSM includes all stability limit states;
- (vi) DSM encourages cross-section optimization and provides a good simple basis for rational analysis extensions.

Limitations:

Many limitations of DSM exist as well, such as:

- (i) There is a limited number and geometry of pre-qualified members;
- (ii) DSM can be overly conservative if very slender elements are used, because the neutral axis shift is ignored and the DSM performs an analysis conducted on the entire-section as a whole, not for the elements in isolation, i.e. DSM will predict a low strength for the entire member if there is a very slender element in the cross-section which could drive the elastic buckling stress of the cross-section to approach zero. However the EWM will only consider a low strength for the slender element, i.e. that only the element itself will have no strength, allowing thus the rest of the elements to carry additional load. However, one should keep in mind that such cross-sections will have serviceability problems, and the addition of appropriate stiffeners in the slender element will improve the DSM predicted strength;
- (iii) The DSM strengths equations are empirical, just like the effective width equation and the columns curves but with a quite bigger range of cross-sections investigated;

- (iv) The derived DSM curves do not account for strength increase due to cold-work of forming;
- (v) No definitive provisions for inelastic reserve: however, a first proposal for inclusion of inelastic reserve is presented in [61].
- (vi) No web crippling provisions and no provisions for members with holes;
- (vii) Significant research remains to extend DSM to structural hot-rolled steel. A proposal for hot-rolled and welded cross-section in compression and bending is made in [62]. Structural steel is characterized with thickness variations inexistent in thin cold-formed section thus creating unique cross-section stability modes. Moreover, inelastic buckling is more pronounced in structural steel and the influence of residual stresses and strain hardening must be taken into account in a proper way.

2.5.2. The continuous strength method – CSM

2.5.2.1. Introduction

The continuous strength method was designed as an alternative to the concept of cross-section classification mainly for materials exhibiting a non-linear behavior. A more accurate material modeling and continuous non-dimensional numerical measure of the deformation capacity is proposed, instead of the currently classification technique suitable for materials with a stress-strain response resembling the idealized elastic-perfectly plastic material model. The strength is limited by either material yielding of the gross section, with a plastic or elastic-plastic distribution of stresses, or yielding of an effective section, neglecting thus the strain hardening effect of non-linear materials. A replacement of the behavioral classes has been proposed by Gardner ([2] & [63]) and consists of a continuous measure of the deformation capacity of the cross-section. A relationship between the cross-section slenderness and the cross-section deformation capacity has been proposed on the basis of stub column tests, so that the strength of the corresponding cross-section may be then determined using this deformation capacity and a material model reflecting the non-linear nature of materials.

So, two key features represent the basis of the continuous strength CSM:

- (i) A base curve defining the strain level of a cross-section in function of its slenderness;

(ii) A material model, reflecting the strain-hardening capacities of the studied material.

A brief explanation of the cross-section slenderness, the key role of strain ratio and the material model of the CSM is followed, to then present the CSM base curve of I sections and box sections and the way to derive the compression and bending resistance of a cross-section.

2.5.2.2. Cross-section slenderness definition

The cross-section slenderness is defined in a non-dimensional form as the square root of the ratio of the yield stress f_y to the elastic buckling stress of the section. However, for cross-section with interactive connected plates, the elastic buckling stress of the entire cross-section $\sigma_{cr,cs}$ can be used to allow for the plates' interaction. Therefore, the elastic buckling stress can be determined by either the approach adopted in the direct strength method ([14] & [13]) (to account for the plates' interaction) or also as recommended in the Eurocodes [64].

The Eurocode approach is proved to be conservative according to [65] and the DSM approach from Seif and Schafer ([13] & [14]) accounting for the total cross-section element interaction for local buckling will result in a stockier cross-section and favorable results. However, the Seif and Schafer ([13] & [14]) method is not yet presently recognized in Eurocodes and not adapted for combined load cases. Therefore, the Eurocodes method may be adopted to avoid these instances and stay on the safe side with the consideration of a most slender element as the leading element in the cross-section capacity determination [65].

2.5.2.3. Strain ratio and material model

The strain ratio $\varepsilon_{csm} / \varepsilon_y$ representing the cross-section deformation capacity is defined in a normalized way and taken as the ratio of the strain at the ultimate load and the yield strain. The strain ratio can be determined from collected stub column and beam test results. The following graphs represent the gathered data for both stub and beam test results.

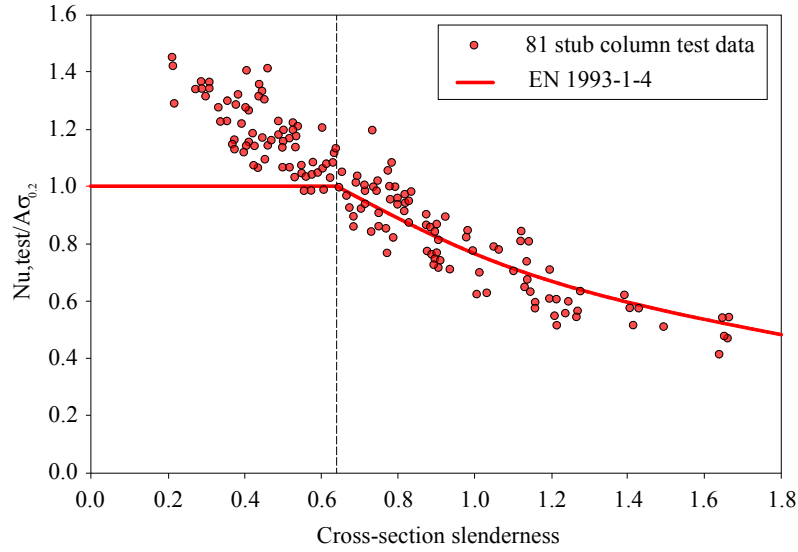


Figure 47 – Comparison of stub columns test with Eurocodes [2] & [63].

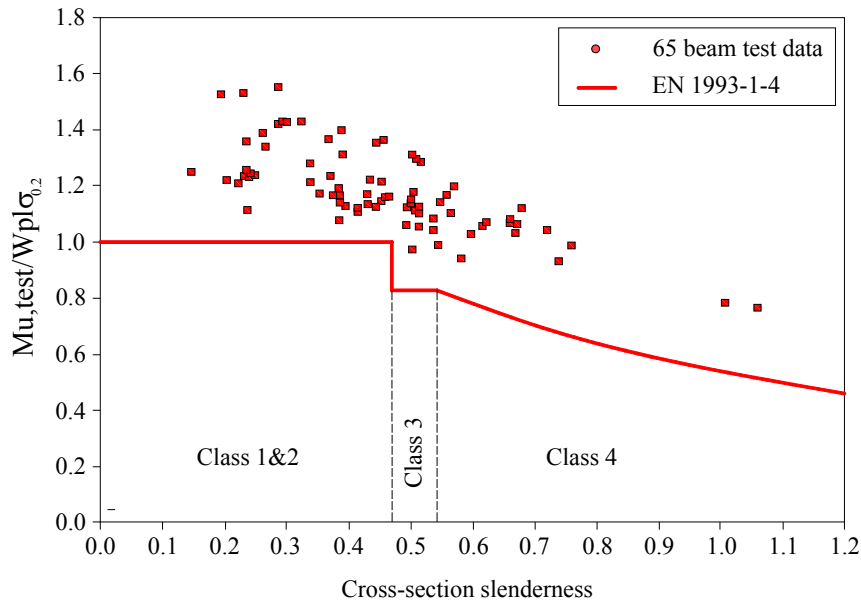


Figure 48 – Comparison of beam test results with Eurocodes [2] & [63].

To make the transition between slender and non-slender sections, a linear regression based on the test data indicated a value of $\lambda_p = 0.678$, for which $N_{u,test} / A\sigma_{0.2}$ equals unity. Therefore, this slenderness value marks the interest of applicability of the CSM, since no strain hardening can be developed beyond this limit.

Earlier versions of the CSM employed the Ramberg-Osgood material model, which led to complex resistance equations incorporating many factors. This is the reason why CSM employed a material law which was a compromise between hot-rolled and cold-formed material laws since bi-linear, elastic-perfectly plastic material laws were out of the question due to their conservatism and no strain hardening consideration. This law was composed of an elastic portion followed by a linear hardening material stage as shown in Figure 49.

The adopted model consists of an initial linear region with its corresponding Young's modulus E , ending up to a stress point defined as (f_y, ε_y) where f_y is taken as the material 0.2% proof stress and ε_y is the corresponding elastic strain $\varepsilon_y = E / f_y$. A strain-hardening region follows defined by its corresponding slope E_{sh} , determined from the line passing from the 0.2% proof stress to a maximum point $(\varepsilon_{max}, f_{max})$ with ε_{max} taken as $0.16\varepsilon_u$ where ε_u is the ultimate tensile strain, and f_{max} is taken as the ultimate tensile stress. A value of $E_{sh} = E / 100$ combined with the condition $f_u / f_y > 1.1$ (based on EN 1993-1-5 and EN 1993-1-1) leads to the proposed combined criteria of E_{sh} :

$$\frac{E_{sh}}{E} = \frac{f_u / f_y - 1}{10} \quad (71)$$

$$\text{With } \frac{E_{sh}}{E} \leq 0.01$$

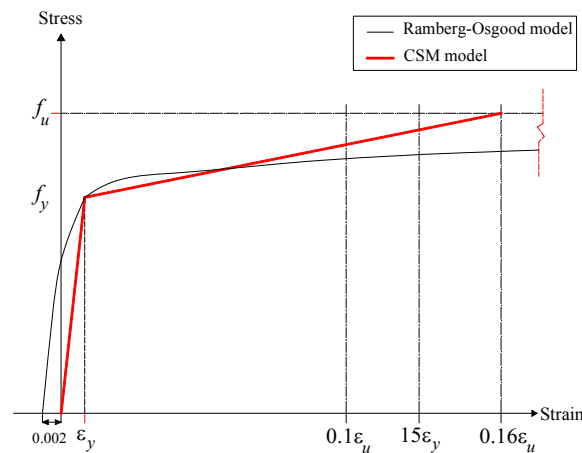


Figure 49 – CSM elastic, linear hardening material model.

The end shortening at the ultimate load δ_u divided by the stub column length L is used to define the failure strain of the cross-section ε_{lb} for stub columns where the ultimate test load N_u exceeds the section yield load N_y . The deformation capacity ε_{csm} is then defined as $\varepsilon_{lb} - 0.002$ for sake of compatibility with the adopted material law avoiding thus over-predictions of capacity (see Figure 50).

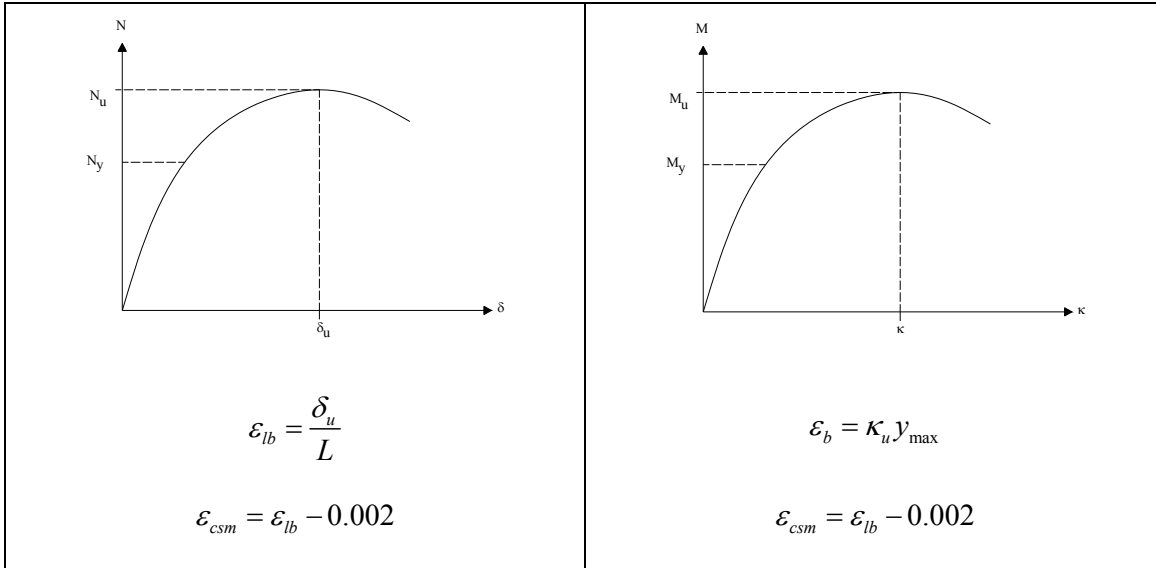


Figure 50 – Stub column load end-shortening response ($N_u > N_y$) (left), beam moment-curvature response ($M_u > M_{el}$) (right).

In cases of slender sections where failure occurs before reaching the yield limit, elastic local buckling will be followed by a stable post-buckling stage, resulting in a high deformation capacity but a peak load below the yield load leading thus to over-predictions when using the former CSM strain ratio definition. Therefore the deformation capacity is thus defined for slender cross-sections with the following equation:

$$\frac{\varepsilon_{csm}}{\varepsilon_y} = \frac{N_u}{N_y} \quad (72)$$

2.5.2.4. Base curve

Test data on stainless steel and carbon steel stub and 4 point bending tests were gathered from a wide variety of experimental programs and plotted in Figure 51, in the CSM format, i.e. as a function of the normalized deformation capacity $\varepsilon_{csm} / \varepsilon_y$ versus cross-section slenderness λ_p .

A similar function form to the one given by Equation (74) was suggested (see Equation (73)) and the relationship between normalized critical elastic buckling strain $\varepsilon_{cr} / \varepsilon_y$ and plate slenderness was adopted for the definition of the CSM curve which was then fitted to the test data and the values A and B were determined and accounted for the effects of inelastic buckling, imperfections, residual stresses and post-buckling response. Equation (75) was thus proposed and passed through the identified limit point (0.68, 1) between slender and non-slender sections.

$$\frac{\varepsilon_{csm}}{\varepsilon_y} = \frac{A}{\lambda_p^B} \quad (73)$$

$$\frac{\varepsilon_{cr}}{\varepsilon_y} = \frac{1}{\lambda_p^2} \quad (74)$$

$$\frac{\varepsilon_{csm}}{\varepsilon_y} = \frac{0.25}{\lambda_p^{3.6}} \quad (75)$$

$$\text{With } \frac{\varepsilon_{csm}}{\varepsilon_y} \leq \min\left(15, \frac{0.1\varepsilon_u}{\varepsilon_y}\right)$$

Two upper bounds were attached to the proposed CSM equation; the first one limits the cross-section deformation capacity to a value of 15 which is in accordance to the material ductility recommended in EN 1993-1-1 and also to prevent excessive strains. The second upper bound for the cross-section deformation capacity was set to $0.1\varepsilon_u / \varepsilon_y$, related to the proposed stress-strain material model and ensures that the material strength is not over-predicted.

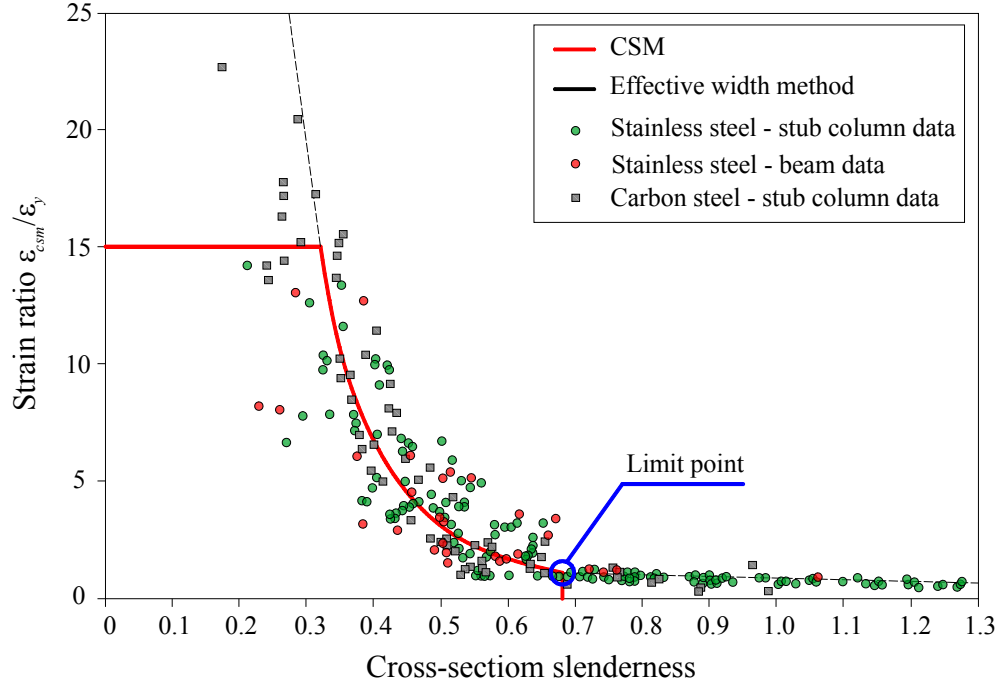


Figure 51 – Base curve-relationship between strain ratio and slenderness.

2.5.2.5. Cross-section bending and compression resistance

Once the normalized deformation capacity of the cross-section $\varepsilon_{csm} / \varepsilon_y$ is established through on the design base curve, the CSM proposed material model can now be used to determine both compression and bending resistances.

Compression resistance

The cross-section compression resistance is given by Equation (76) where A is the gross cross-section area f_{csm} is the limiting stress determined from the strain hardening material (see Equation (77)):

$$N_{csm,Rd} = \frac{Af_{csm}}{\gamma_{M0}} \quad (76)$$

$$f_{csm} = f_y + E_{sh} \varepsilon_y \left(\frac{\varepsilon_{csm}}{\varepsilon_y} - 1 \right) \quad (77)$$

Bending resistance

M_{csm} can be calculated with conjunction of the material material through Equation (78) – assuming that plane sections remain plane and normal to the neutral axis in bending – where f is the stress in the section with a maximum outer fibre value of f_{csm} , y being the distance from the neutral axis and dA is the incremental cross-sectional area:

$$M_{csm} = \int_A fy dA \quad (78)$$

Detailed derived CSM equations for minor and major-axis bending can be found in [63].

2.5.2.6. Cross-section beam-column resistance

The proposed CSM interaction formulae for hollow sections under major or minor-axis bending with compression is given by the following two equations:

$$M_{Ed,y} \leq M_{R,csm1,y} = M_{csm,y} \left[1 - \left(\frac{N_{Ed}}{N_{csm}} \right)^{\alpha_y} \right]^{1/b_y} \quad (79)$$

$$M_{Ed,z} \leq M_{R,csm1,z} = M_{csm,z} \left[1 - \left(\frac{N_{Ed}}{N_{csm}} \right)^{\alpha_z} \right]^{1/b_z} \quad (80)$$

while the expression for biaxial bending with compression is given by the following equation:

$$\left(\frac{M_{Ed,y}}{M_{R,csm,y}} \right)^{\alpha_{csm}} + \left(\frac{M_{Ed,z}}{M_{R,csm,z}} \right)^{\beta_{csm}} \leq 1 \quad (81)$$

where N_{csm} , $M_{csm,y}$ and $M_{csm,z}$ are the CSM compression and bending (major and minor axes) resistances, which act as the end points of the interaction curves and are calculated as mentioned in the previous section. $M_{R,csm,y}$ and $M_{R,csm,z}$ are the reduced CSM bending resistances about the major and minor axes due to the existence of the axial load N_{Ed} .

Note that the ‘1’ in the subscript signifies resistances determined on the basis of the proposals of Liew and Gardner [66].

2.5.2.7. Simplified CSM for beam-column

A simplified CSM approach is proposed, in which for hollow sections under uniaxial bending plus compression, the bi-linear form of the Eurocode interaction curves is maintained, but with N_{csm} , $M_{csm,y}$ and $M_{csm,z}$ replacing $A\sigma_{0.2}$, $M_{pl,y}$ and $M_{pl,z}$ as shown in Equation (82) and Equation (83), where $M_{R,csm,y}$ and $M_{R,csm,z}$ are respectively the reduced CSM bending resistances about major and minor axes due to N_{Ed} .

$$M_{Ed,y} \leq M_{R,csm,y} = M_{csm,y} \frac{(1-n_{csm})}{(1-0.5a_w)} \leq M_{csm,y} \quad (82)$$

$$M_{Ed,z} \leq M_{R,csm,z} = M_{csm,z} \frac{(1-n_{csm})}{(1-0.5a_f)} \leq M_{csm,z} \quad (83)$$

The interaction formula for hollow sections under biaxial bending plus compression is shown in Equation (84) in which α_{csm} and β_{csm} are taken from EN 1993-1-1, but based on the CSM end points, i.e. $\alpha_{csm} = \beta_{csm} = 1.66 / (1 - 1.13n_{csm}^2)$ in which $n_{csm} = N_{Ed} / N_{csm}$. It is proposed that Equations (82) and (84) apply when the cross-section slenderness λ_p is less than or equal to 0.6. For λ_p greater than 0.6, the linear interaction given by Equation (85) is proposed to ensure compatibility with increasingly elastic end points as the cross-section slenderness approaches $\lambda_p = 0.678$, where the CSM axial and bending resistance are equal to $A\sigma_{0.2}$, $M_{el,y}$ and $M_{el,z}$ [67].

$$\left[\frac{M_{Ed,y}}{M_{R,csm,y}} \right]^{\alpha_{csm}} + \left[\frac{M_{Ed,z}}{M_{R,csm,z}} \right]^{\beta_{csm}} \leq 1 \quad (84)$$

$$\frac{N_{Ed}}{N_{csm}} + \frac{M_{Ed,y}}{M_{csm,y}} + \frac{M_{Ed,z}}{M_{csm,z}} \leq 1 \quad (85)$$

The approach of using the CSM compression and bending resistances as the end points for the Eurocode interaction curves was shown to provide accurate predictions of the resistance of stainless steel cross-sections under combined loading [67].

2.5.2.8. Practical and theoretical advantages and limitations

Advantages

A good number of practical advantages exist with the use of the CSM, mainly:

- (i) The strain hardening effects are taken into account in design unlike all other design approaches limiting the cross-section resistance to the yield load. The main focus is on the correct determination of the strain reached to be able to calculate the corresponding stress;
- (ii) Being based on the strain capacities, the CSM allow for an accurate determination of the relative stress, since a stress could be constant in a material law (i.e. elastic plastic material law), i.e. a stress value could have many strain deformation values, but a strain can never be constant in a material law, and leading the design through deformations at first would be way more accurate than leading it starting with stresses;
- (iii) CSM encourages cross-section optimization with the provision of a good simple basis.

Limitations

- (i) The CSM strengths equations are empirical based on a curve fitting of the strain curve with gathered results;
- (ii) No shear provisions, no web crippling provisions and no provisions for members with holes are available.

2.6. Summary

Literature review has been conducted in this chapter. The plate buckling background has been deeply reviewed, along with the possible methods to get and an adequate buckling curve. An overview of the history of plasticity was also presented. Besides, many current design methods were introduced, compared and commented and in particular the shortcomings of the classification system were listed and detailed. Then, existing alternatives were also introduced and discussed.

All of these sections and sub-sections would be of a great importance for the derivation of the OIC design curves, since an adequate method has been selected, after getting a strong basis and overview on the local buckling and plasticity background. Most importantly, the described existing alternatives would constitute a strong inspiration for the OIC since the new design approach will include many of the offered features of the DSM and the CSM.

In summary, this state of the art would serve the author through the following listed aspects:

- (i) A deep understanding of local buckling background is of a prime importance since it is one of the aspects which should be treated in this work. Therefore, derived Von Karman and Winter formulae would be used and extended since they constitute a basis of the existing first developments regarding local buckling;
- (ii) Since the main target of this work is to propose interaction buckling curves, the methods of treating and getting the ultimate buckling loads were presented and the most practical simple, yet accurate method was seen to be the method of the interaction buckling curves which will be developed and derived using numerical results in next chapters;
- (iii) It would be also important for the author to get an overview of the actual treatment of local buckling in various standards. It turned out that there are non-negligible differences amongst the classification systems of these specifications and a better solid and accurate basis was needed for a better uniformity among various codes;
- (iv) A better understanding of the need to remove the actual classification system in itself was presented through listing its various shortcomings. It was clearly seen that there are lots of discrepancies, inconsistencies and inaccuracy through the use and application of the cross-section classification system;
- (v) This chapter could not be completed without presenting the actual alternatives of the classification system. The most important two research advances were presented: the DSM and CSM. Many aspects included in both alternatives would be very useful for the author to derive the OIC interaction design curves relative to hollow steel sections.

3. Experimental investigations

3.1. Introduction and objectives

This chapter mainly summarizes experimental activities led towards the cross-sectional resistance of tubular profiles and the development and validation of associated finite element models. A series of tests on short tubular profiles is first described, as well as complementary measurements relative to:

- (i) Material properties;
- (ii) Residual stresses;
- (iii) Geometrical imperfections.

Then, a total of 12 stub columns and 45 cross-sectional tests with various loading conditions are presented with the test set-up and the testing procedure. The tests have been conducted on square, rectangular and circular sections, and cover several fabrication modes. The complete set of results is provided in Annex 5 and Annex 6. At the end of this chapter, comparisons are made with EC3 predictions and a collection and analysis of experimental data in literature are presented.

3.2. Test program

The experimental program was carried out on a wide variety of cross-sectional shapes (RHS, SHS, CHS) with various dimensions and local plate slenderness in order to investigate the influence of local buckling on the plastic, elastic-plastic or slender cross-section capacity of the tubular sections. The main aim of this test series was to examine the cross-sectional behavior of structural hollow sections and to provide an experimental reference to the assessment of numerical models.

The test program comprised 57 tests involving 12 different section shapes with various fabrication modes (cold-formed, hot-finished and hot-rolled), selected so that their cross-sectional behavior span from plastic to slender:

- (i) RHS 200x100x4, S355, cold-formed;
- (ii) RHS 220x120x6, S355, cold-formed;
- (iii) RHS 250x150x5, S355, hot-finished;

- (iv) RHS 200x100x5, S355, hot- finished;
- (v) SHS 200x200x5, S355, hot- finished;
- (vi) SHS 200x200x5, S355, cold-formed;
- (vii) SHS 200x200x6, S355, cold-formed;
- (viii) SHS 200x200x6.3, S355, hot- finished;
- (ix) CHS 156x6.3, S355, hot-rolled;
- (x) CHS 159x6.3, S355, cold-formed;
- (xi) CHS 159x5, S355, hot-rolled;
- (xii) CHS 159x7.1, S355, hot-rolled.

Nine 3.5 m and 6 m beams (for a total of twelve elements) were delivered at the Structural Engineering Laboratory of the University Of Applied Sciences Of Western Switzerland – Fribourg. Each beam was divided into 700 mm length short specimens and pieces of each parent beam were kept for the residual stresses measurements, tensile tests coupons and stub column testing (see Figure 52). The test program is summarized in Table 14.

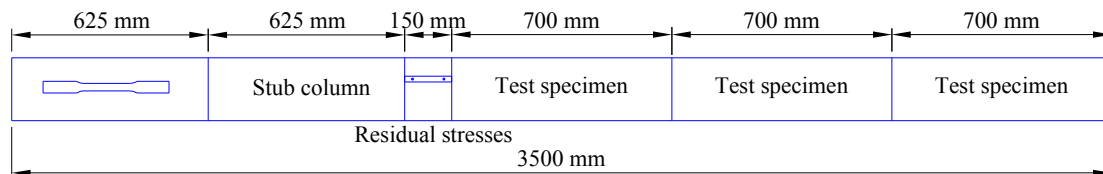


Figure 52 – Partition of a 3500 m beam.

Measurements of cross-sectional dimensions and of geometrical imperfections were made, and tensile tests were carried out to determine the material stress-strain behavior. Stub column tests were also performed for all cross-section types. As for the main cross-sectional tests, six load cases (LCs) were differentiated. Mono-axial and bi-axial bending with axial compression load cases were considered through the application of eccentrically-applied compression forces. Different M/N ratios have been adopted, in order to vary the distribution of stresses on the flanges and webs – thus the failure modes – and the following load cases were adopted:

- (i) LC1: pure compression N ;
- (ii) LC2: major-axis bending $M_y(50\%)$ + axial compression $N(50\%)^3$;
- (iii) LC3: bi-axial bending $M_y(33\%)+M_z(33\%)+$ axial compression $N(33\%)$;
- (iv) LC4: minor-axis bending $M_z(50\%)+$ axial compression $N(50\%)$;
- (v) LC5: bi-axial bending $M_y(25\%)+M_z(25\%)+$ axial compression $N(50\%)$;
- (vi) LC6: bi-axial bending $M_y(10\%)+M_z(10\%)+$ axial compression $N(80\%)$.

³ The percentages reported here are relative to the (expected) amount of cross-sectional resistance respectively mobilized by each internal force.

Table 14 – Test program for cross-sectional tests.

Test #	Specimen	Fabrication process	Length [mm]	Load case
1	RHS_LC1_S355CF_200x100x4	Cold-formed	700	N
2	RHS_LC1_S355CF_220x120x6	Cold-formed	700	N
3	RHS_LC1_S355HF_250x150x5	Hot- finished	700	N
4	RHS_LC1_S355HF_200x100x5	Hot- finished	700	N
5	SHS_LC1_S355CF_200x200x5	Cold-formed	700	N
6	SHS_LC1_S355CF_200x200x6	Cold-formed	700	N
7	SHS_LC1_S355HF_200x200x5	Hot- finished	700	N
8	SHS_LC1_S355HF_200x200x6.3	Hot- finished	700	N
9	CHS_LC1_S355CF_159x6.3	Cold-formed	700	N
10	CHS_LC1_S355HF_159x6.3	Hot-Rolled	700	N
11	CHS_LC1_S355HF_159x5	Hot-Rolled	700	N
12	CHS_LC1_S355HF_159x7.1	Hot-Rolled	700	N
13	RHS_LC2_S355CF_200x100x4	Cold-formed	700	$N + M_y$
14	RHS_LC2_S355CF_220x120x6	Cold-formed	700	$N + M_y$
15	RHS_LC2_S355HF_250x150x5	Hot- finished	700	$N + M_y$
16	RHS_LC2_S355HF_200x100x5**	Hot- finished	700	$N + M_y$
17	SHS_LC2_S355CF_200x200x5	Cold-formed	700	$N + M_y$
18	SHS_LC2_S355CF_200x200x6	Cold-formed	700	$N + M_y$
19	SHS_LC2_S355HF_200x200x5	Hot- finished	700	$N + M_y$
20	SHS_LC2_S355HF_200x200x6.3	Hot- finished	700	$N + M_y$
21	CHS_LC2_S355CF_159x6.3	Cold-formed	700	$N + M_y$
22	CHS_LC2_S355HF_159x6.3	Hot-Rolled	700	$N + M_y$
23	CHS_LC2_S355HF_159x5	Hot-Rolled	700	$N + M_y$
24	CHS_LC2_S355HF_159x7.1**	Hot-Rolled	700	$N + M_y$
25	RHS_LC3_S355CF_200x100x4	Cold-formed	700	$N + M_y + M_z$
26	RHS_LC3_S355CF_220x120x6	Cold-formed	700	$N + M_y + M_z$
27	RHS_LC3_S355HF_250x150x5	Hot- finished	700	$N + M_y + M_z$
28	RHS_LC3_S355HF_200x100x5	Hot- finished	700	$N + M_y + M_z$
29	SHS_LC3_S355CF_200x200x5	Cold-formed	700	$N + M_y + M_z$
30	SHS_LC3_S355CF_200x200x6	Cold-formed	700	$N + M_y + M_z$
31	SHS_LC3_S355HF_200x200x5	Hot- finished	700	$N + M_y + M_z$
32	SHS_LC3_S355HF_200x200x6.3	Hot- finished	700	$N + M_y + M_z$
33	CHS_LC3_S355CF_159x6.3	Cold-formed	700	$N + M_y + M_z$
34	CHS_LC3_S355HF_159x6.3	Hot-Rolled	700	$N + M_y + M_z$
35	CHS_LC3_S355HF_159x5	Hot-Rolled	700	$N + M_y + M_z$
36	CHS_LC3_S355HF_159x7.1	Hot-Rolled	700	$N + M_y + M_z$
37	2_SHS_LC1_S355CF_200x200x6*	Cold-formed	700	N
38	2_SHS_LC2_S355CF_200x200x6*	Cold-formed	700	$N + M_y$
39	2_SHS_LC3_S355CF_200x200x6*	Cold-formed	700	$N + M_y + M_z$
40	RHS_LC4_S355CF_220x120x6	Cold-formed	700	$N + M_y + M_z$
41	RHS_LC5_S355CF_220x120x6	Cold-formed	700	$N + M_y + M_z$

42	RHS_LC6_S355CF_220x120x6	Cold-formed	700	$N + M_y + M_z$
43	RHS_LC4_S355CF_200x100x4	Cold-formed	700	$N + M_y + M_z$
44	RHS_LC5_S355CF_200x100x4	Cold-formed	700	$N + M_y + M_z$
45	RHS_LC6_S355CF_200x100x4	Cold-formed	700	$N + M_y + M_z$
46	RHS_Stub_S355CF_200x100x4	Cold-formed	600	Stub
47	RHS_Stub_S355CF_220x120x6	Cold-formed	680	Stub
48	RHS_Stub_S355HF_250x150x5	Hot- finished	750	Stub
49	RHS_Stub_S355HF_200x100x5	Hot- finished	600	Stub
50	SHS_Stub_S355CF_200x200x5	Cold-formed	600	Stub
51	SHS_Stub_S355CF_200x200x6	Cold-formed	600	Stub
52	SHS_Stub_S355HF_200x200x5	Hot- finished	600	Stub
53	SHS_Stub_S355HF_200x200x6.3	Hot- finished	600	Stub
54	CHS_Stub_S355CF_159x6.3	Cold-formed	480	Stub
55	CHS_Stub_S355HF_159x6.3	Hot-rolled	480	Stub
56	CHS_Stub_S355HF_159x5	Hot-rolled	480	Stub
57	CHS_Stub_S355HF_159x7.1	Hot-rolled	480	Stub

* The rectangular cross-section 200x200x6 has two test specimens for the first three load cases.

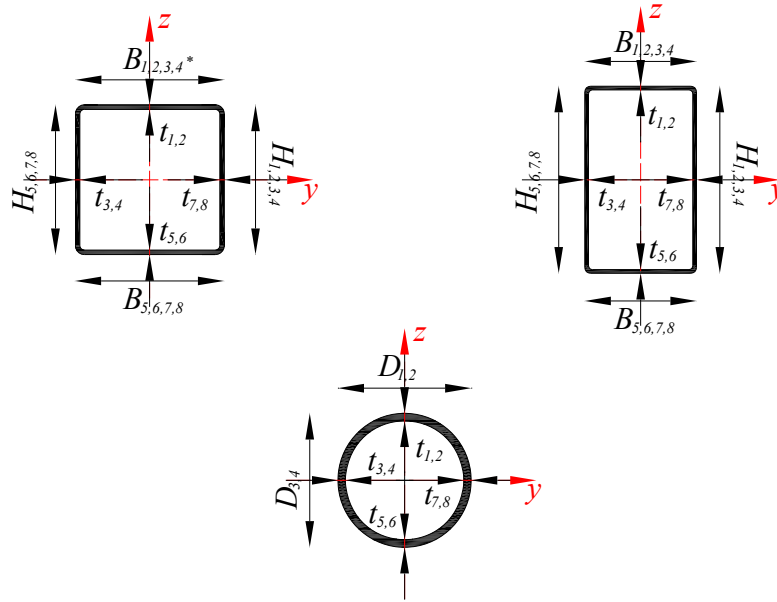
** No available results recorded.

It should be noted that recorded data from two experimental tests (RHS_LC2_S355HF_200x100x5 and CHS_LC2_S355HF_159x7.1) could not be retrieved due to unexpected technical and electrical difficulties with the recording software, which explains that no results corresponding to these two tests will be presented.

3.3. Preliminary measurements

3.3.1. Cross-sectional dimensions

The cross-section dimensions such as the depth H , the width B , the thickness t and the diameter D were measured before welding end plates at the specimens' ends (see Figure 53). It is indeed of a prime importance to have the actual cross-sectional dimensions for sake of an accurate test vs. FE modeling comparison. The measurements were performed using tools such as calipers, micrometers and measuring tapes. The depth H , the width B and the diameter D were measured several times along the specimen length (see Figure 53). As for the specimens' thicknesses, they were measured at both ends of each element. The tabulated values as well as a comparison with the tolerances of the relevant codes (EN 10210-2 [68] for hot formed sections and EN 10219-2 [69] for cold formed sections) can be found in Annex 1, Annex 5 and Annex 6. An illustrative example of the measured cross-sectional dimensions for the profile RHS_200x100x5_HF is presented in Figure 54.



* Number of measurements along the element length

Figure 53 – Measured dimensions.

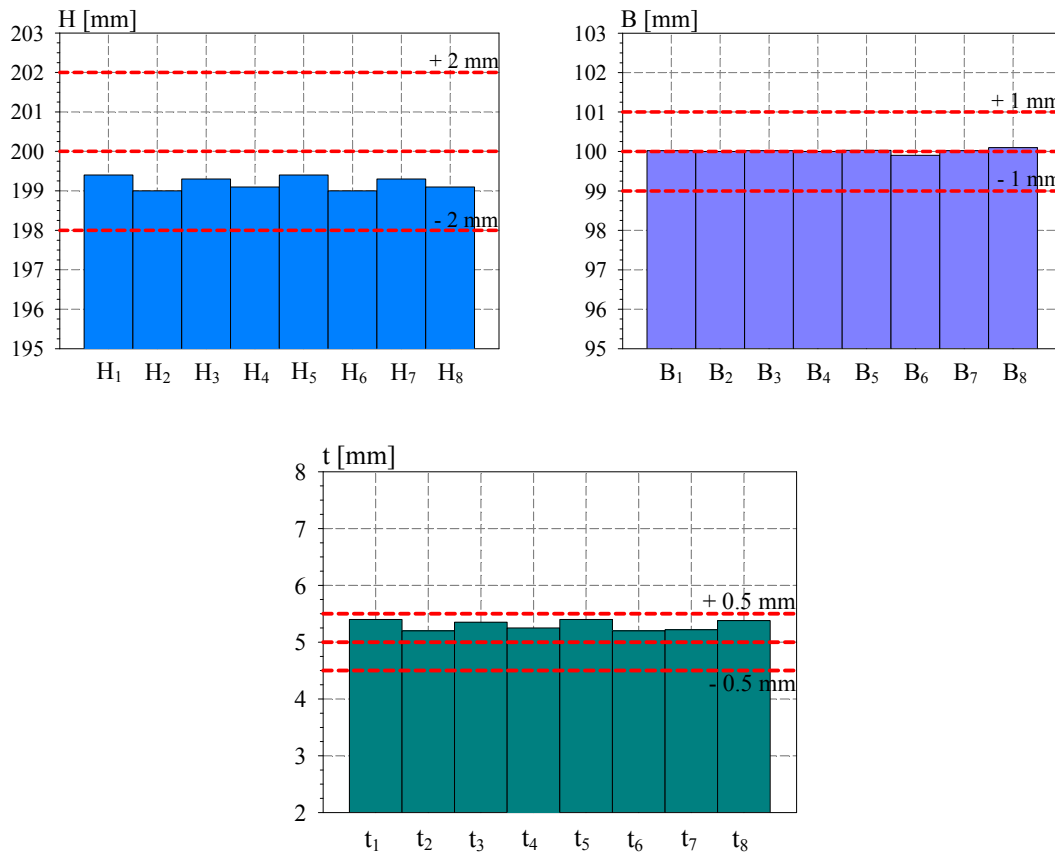


Figure 54 – Measured cross-sectional dimensions and tolerances – RHS_200x100x5_HF.

3.3.2. Geometrical imperfections

Measurement of geometrical imperfections was achieved by means of an aluminium perforated bar containing 9 equally-spaced variable displacement transducers (LVDTs), the bar being displaced sideways on each specimen's plate in order to get 3D geometrical plate representations (see Figure 55) ([3] & [7]); after having measured all 4 faces of a specimen, all information have been gathered in a recomposed specimen that contains the measured local geometrical imperfections (see Figure 56). The measured grid was introduced in a code specially developed for adapting the measured grid to the FE desired mesh, through a double interpolation in both directions of the constitutive plates of each profile. The objective was to provide accurate data for the FE models in a later stage of the investigations. The aluminium bar supporting the LVDTs was designed so as to be able to move the LVDTs themselves within the bar, and to let the possibility to adjust the position according to the desired height corresponding to the end plate dimensions. An example of the measurement procedure of local imperfections is shown below, along with a general imperfect shape of the specimen SHS_LC2_200x200x6_CF with the contour plots of its imperfect plates separately. All measured data with general imperfect shapes can be found in Annex 5 and Annex 6 along with a set of illustrative figures of the measuring procedure for the three types of sections (square, rectangular and circular).



Figure 55 – Geometrical imperfections measurement – LVDTs detail.

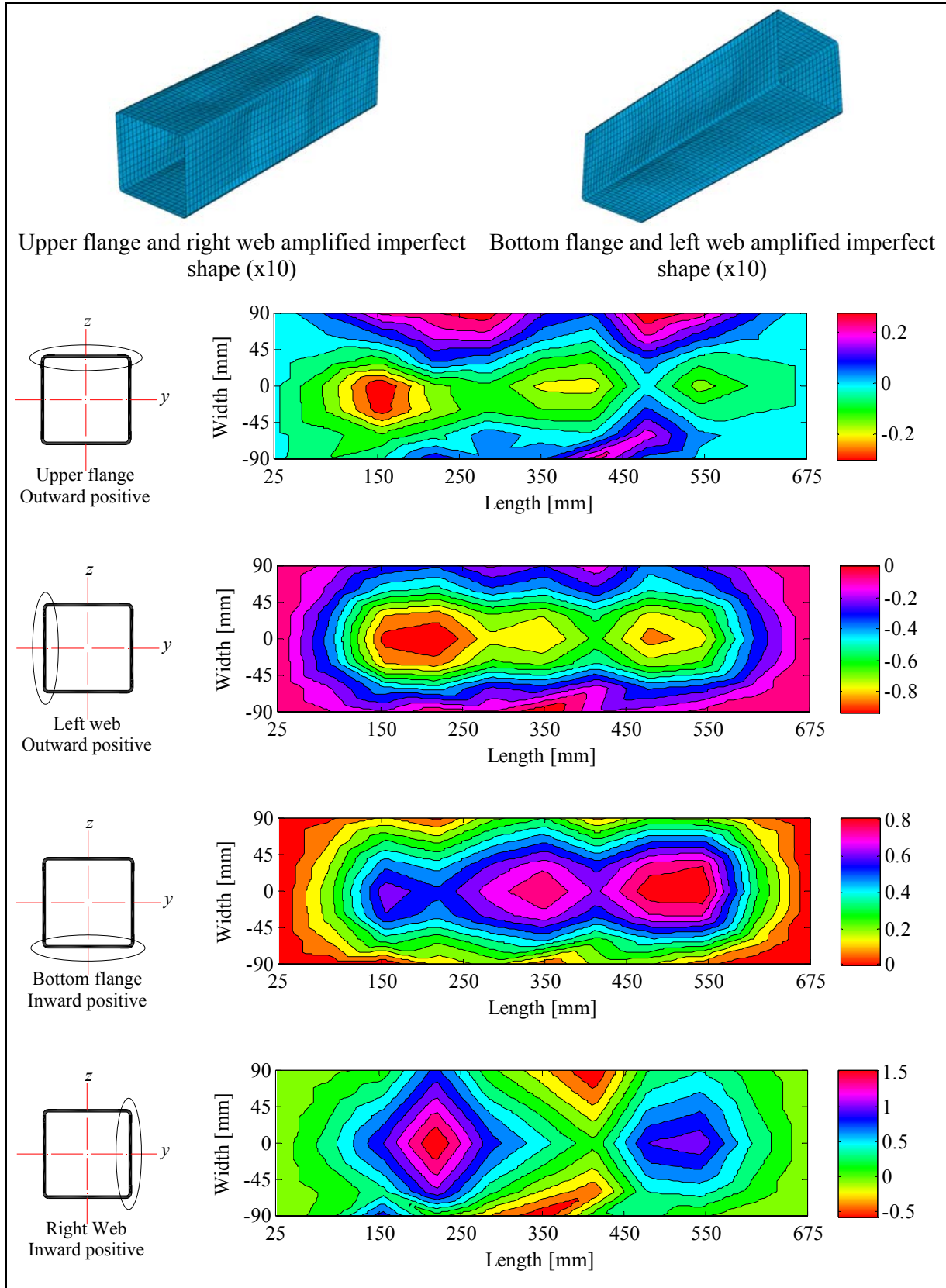


Figure 56 – Measured local flange and web geometrical imperfections of specimen

SHS_LC2_200x200x6_CF.

3.3.3. Residual stresses

3.3.3.1. Fabrication process and type of residual stresses

Residual stresses are defined as self-equilibrated stresses present in materials under uniform temperature conditions without external loading. Their origin is related to the section production process and is associated with differential cooling and/or non-uniform plastic deformation, i.e. such stresses will always be produced if regions of a material are inhomogeneously deformed in such a permanent manner that strain incompatibilities occur. The premature yielding is therefore considered as the cause of the general influence of residual stresses on structural members, leading to a loss of stiffness and a reduction in load-carrying capacity since the stress state will be composed of loading stresses in addition to residual stresses.

The resultant force and the resultant moment produced by the residual stresses must be zero since they are self-equilibrated stresses. There are three recognized types of residual stresses that equilibrate over different scales:

- (i) Type I macroscopic residual stresses act and equilibrate over the macro-scale. They are nearly constant in magnitude and direction across large areas (i.e. across several grains) of a material. The type I stresses have the greatest effect on the structural behavior;
- (ii) Type II is nearly constant in magnitude and direction across microscopic areas (i.e. one grain or part of a grain) of a material and are equilibrated across small parts of a grain;
- (iii) Types III micro-residual stresses act over the micro-scale and are related to more local stress disturbances caused between and within the metal grain structure. Neither their magnitude nor their direction are constant across submicroscopic areas of material (i.e. several atomic distances within a grain) and are equilibrated across small parts of a grain.

Further details on these distinctions and on the origin of residual stresses are given in [70] & [71].

Several factors such as manufacturing process, cross-section shape and thickness may cause different residual stress distribution. In roll-forming of closed-form sections, the residual stresses are mainly created during the fabrication process and are associated with plastic deformations and differential cooling. The main stages causing the formation of residual stresses include:

- (i) First stage: the sheet coil is flattened; the sheet material used for cold forming can be either hot-rolled or cold-reduced; sheet material is then rolled onto a coil for storage and transportation. Subsequently, the material is uncoiled and leveled for further processing. The process of coiling and uncoiling the sheet material induces additional plastic deformation altering the through thickness residual stresses distribution;
- (ii) Second stage: roll forming, i.e. the sheet is bent progressively along the width direction;
- (iii) Third stage: welding of the bent strips to form a circle or a square section;
- (iv) Fourth and last stage: sizing to finalize the exact shape.

Usually, the roll-formed hollow sections do not receive post-forming stress-relieving heat treatment, resulting in locked-in residual stresses approaching the yield stress of the material. Their distribution is known to be complex both around the section and through the section thickness. The cold-formed non stress-relieved sections and the common structural sections are distinguished by flexural through thickness stresses.

Aforementioned in the third stage above, a cold-formed square or rectangular hollow section can be formed by rolling an annealed flat strip directly into a square hollow section, which is then welded at the edges (press bending). Also, bending an annealed flat strip into a circular hollow section first can create a cold-formed hollow section, which is then welded at the edges. This process is completed by further rolling into a square hollow section (roll bending). Differing levels of plastic deformation resulting in different residual stress patterns will result from the two cold-forming techniques. The cold-rolling process is actually preferable due to its more effective production. More details concerning the differences in residual stresses with these two fabrication process are discussed in [72].

The residual stresses formed in hot-rolled sections are normally due to differential cooling rates due to variation in material thickness. The faster cooling regions of the section, such as the corners, are left in residual compression and the slower cooling regions such as the webs and flanges are left in residual tension (see Figure 57).

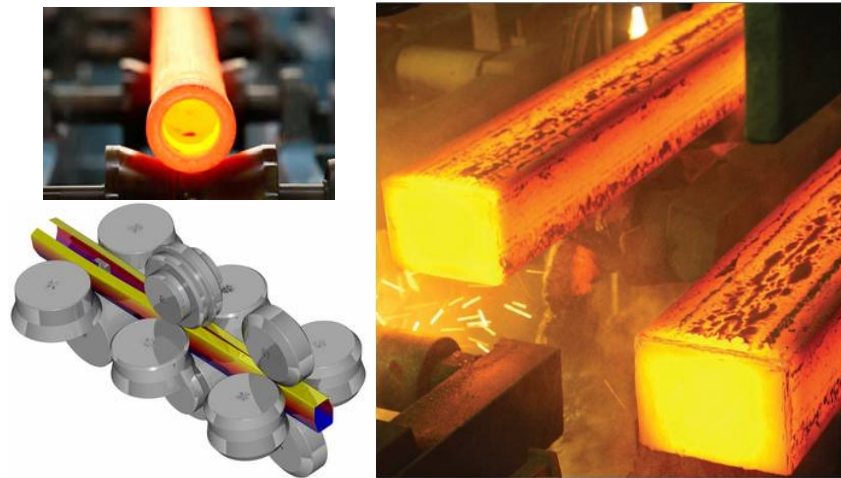


Figure 57 – Cold-rolled (left bottom) and hot rolled fabrication process.

Regarding the particular cases of circular sections, and in hot-rolled fabricated sections, the residual stresses will mainly be flexural (thermal) stresses caused by uneven cooling between the inner and outer surface. As for the cold-formed circular sections, they will also be exhibiting flexural stresses, due however to plastic deformation and not thermal conditions. The longitudinal stresses present in both fabrication processes will mainly be flexural and not membrane due to the section polar shape enabling a ‘theoretical’ even cooling in each inner or outer surface alone, leading subsequently to the elimination or neglect of the membrane residual stresses.

A summary of the main sources and sub-sources of Type I residual stresses are presented in the following table [71]:

Table 15 – Main and sub-sources of Type I residual stresses.

Main source of 1 st kind residual stresses	Sub sources of 1 st kind residual stresses
Elastic-plastic loading	Bending, torsion, tension, compression
Machining	Grinding, turning, milling, planning, drilling
Joining	Welding, soldering, brazing, adhering
Forming	Rolling, pressing, forging, spinning
Heat-treating	Quenching, transformation, hardening, case hardening
Coating	Spraying, plating, galvanizing

Key and Hancock [73] studied the influence of residual stresses components on the axial compression behavior of thick carbon steel hollow sections. Their measurements were able to show the complex through-thickness residual stress distribution. The measured residual stresses components in both the longitudinal and transverse directions were included progressively in the finite strip analysis of stub column behavior. Key and Hancock [73] proposed models for the through-thickness variation as shown in Figure 58.

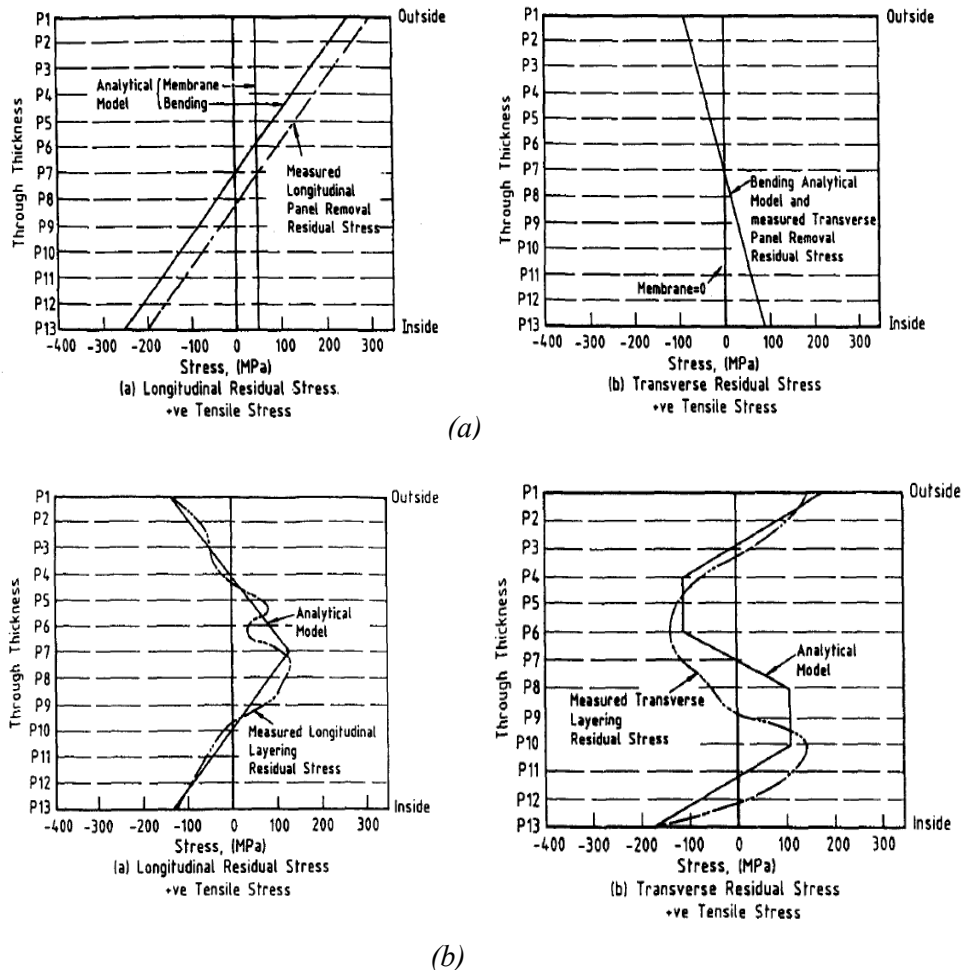


Figure 58 – Analytical models for through-thickness residual stresses; (a) analytical model for panel removal residual stress, (b) analytical model for layering residual stresses.

Key and Hancock [73] concluded that the longitudinal membrane residual stresses component had a negligible influence on the section behavior, whereas flexural residual stresses which varied linearly through the plate thickness affected the results and the ultimate load as well as the axial stiffness. The addition of the layering residual stresses induced a small influence on the ultimate load, but the axial stiffness was reduced at an early stage.

Finally the addition of the measured transverse residual stresses resulted in a small decrease in ultimate load, but around a 9% decrease in the axial stiffness. Therefore, the two kind of residual stresses affecting the most, the ultimate load capacity and the axial stiffness of stub columns are the bending and transverse residual stresses [74].

Cruise and Gardner [75] investigated residual stress distributions on hot-rolled pressed braked and cold-formed stainless steel sections, where the highest magnitude was found in the cold-rolled box sections. Jandera et al. ([76] & [77]) studied the influence of bending and membrane residual stresses on global and local buckling through GMNIA calculations. Jandera et al. ([76] & [77]) found that the inclusion of residual stresses can lead to an increase in load-carrying capacity of non-linear material, mainly due to the tangent modulus which was increased in some regions of the stress-strain curve. This was applied to the cases where column failure strains coincided with these increased tangent modulus regions. Tong et al. [72] performed an experimental investigation on longitudinal residual stresses for cold-formed thick-walled square hollow sections in which they [72] concluded that non-linear stress distributions were present along the thickness, and two patterns have been proposed based on the test results obtained from his study for the cold-formed thick-walled square hollow sections with two different forming processes (rolling a flat strip directly into a square or rectangular shape and rolling a flat strip into a circular profile first than continuing with a square or rectangular section). Schafer and Pekoz [78] collected and studied available experimental data on press-braked and roll-formed specimens for which residual stresses were idealized as a summation of flexural and membrane types, with a pragmatic choice [78]. They presented statistical results for both membrane and flexural stresses. An approximation of the magnitude of residual stresses was done through the use of a Cumulative Distribution Function (CDF). They also showed the significant qualitative effect of the flexural residual stresses on the structural response of an element and concluded that the primary importance of residual stresses is in how load is carried, not in final magnitude since residual stresses are self-equilibrated. It's rather the early yielding on the face of the plates which has a strong influence on stress distributions and on analysis of the way the load is carried in the plate. Schafer and Pekoz [78] finally proposed a direct probabilistic simulation considering both distribution and magnitude of residual stresses as random quantities. However, this approach requires a large amount of analyses.

The residual stresses distributions are rather complex due to the interference of a multitude of factors affecting their distribution. It is therefore difficult to obtain the distribution of residual

stresses using analytical methods. Consequently, experimental approaches are the most reliable method to get the closer to real distribution information.

3.3.3.2. Experimental techniques

Although various techniques have been developed, cheap, simple and reliable methods for the quantitative determination of residual stresses states do not however exist. Principally, techniques may be classified as either destructive or non-destructive (see Table 16).

Table 16 – Residual stresses measuring techniques.

Method	Residual stresses determined	Character
Mechanical	1 st kind	Destructive
Electrical	1 st kind	Destructive
X-ray diffraction	1 st , 2 nd kind	Non-destructive
Neutron diffraction	1 st , 2 nd kind	Non-destructive
Ultrasonic	1 st , 2 nd , 3 rd kind	Non-destructive
Magnetic	1 st , 2 nd , 3 rd kind	Non-destructive

Non-destructive methods include X-ray, neutron or electron diffraction, ultrasonic methods and magnetic methods. The first two methods are based on the measurements of lattice strains of specific atomic planes. The X-ray measures residual stresses on the surface, but is available until 1 mm penetration whereas the neutron diffraction method measures the residual strain within a volume of sample; therefore it is valid for larger penetrations up to 50 mm. Ultrasonic techniques rely on variations of velocity of ultrasonic waves, which can be related to the residual stresses state. Magnetic measuring methods are based on the interaction between magnetization and elastic strain in ferromagnetic materials.

Destructive methods rely on the measurement of deformations due to the release of residual stresses upon removal of material from the specimen. The principal destructive technique used to measure residual stresses in structural members is sectioning. This method has been extensively used to analyze residual stresses in structural carbon steel, aluminium and stainless steel sections and is adopted in this study. Hole drilling and layer removal are other well-known destructive techniques as well as some others in development which include the contour and deep hole methods. The hole drilling method provides depth measurements, and

the contour method provides area maps of residual stresses. More details concerning the destructive and non-destructive techniques are described in [70], [79], [77], [76] & [80].

The equipment available within the structural laboratory of civil engineering in Fribourg is suitable to the sectioning technique which is further discussed in the following section.

3.3.3.3. Residual stresses measurements

An experimental program to examine the residual stresses in carbon steel sections from different production routes has been carried out. Comprehensive residual stresses distributions have been obtained for 12 sections (5 cold-formed, 4 hot-finished and 3 hot-rolled), with a total of 4 000 readings taken. The sectioning technique was used to quantify the longitudinal residual stresses distributions.

The strip-cutting method has been adopted to measure both flexural stresses and membrane residual stresses. It consists in a destructive technique relying on the measurement of strains linked with the release of residual stresses after the cutting of small strips within the cross-section; material relaxation generates either elongation or shortening of the strips due to membrane stresses and a curvature due to flexural (through thickness) stresses, which are linked to the initial residual stresses. Membrane residual stresses generally dominate in hot-rolled and fabricated sections whereas flexural residual stresses lead in cold-formed sections

Residual stresses which occur along the length of the member are known to be the most influential on structural behavior. However, significant residual stresses can also exist in the transverse or circumferential direction. This technique is suitable for elements in which the longitudinal stresses are dominant, but can also be used to measure the transverse stresses through the cutting of transverse strips. Several experiences already performed proved that the sectioning method is suitable, economical and accurate enough for this type of measurements, provided that a rigorous and methodic technique is adopted to obtain reliable results.

Specimen preparation

Residual stresses from all twelve parent members were measured; in this respect, a segment of the parent beam was specifically kept to measure residual stresses, and was cut into small strips along the cross-section. Sufficient material on either side of the segment was kept to ensure a representative stress distribution and prevent any relaxing of stresses due to the

neighborhood of the specimen edges, i.e. Saint-Venant's assumption was respected. Prior to cutting, the strips were marked on the cross-section by two 100 mm⁴ spaced circular marks (see Figure 59) and measurements of length variation were achieved, with an accuracy of +/- 3 mm. An 'invar' bar with a 100 mm basis served as a reference for each measure. The extensometer was calibrated on this bar before each measurement. The length and the curvature were measured respectively before and after cutting.

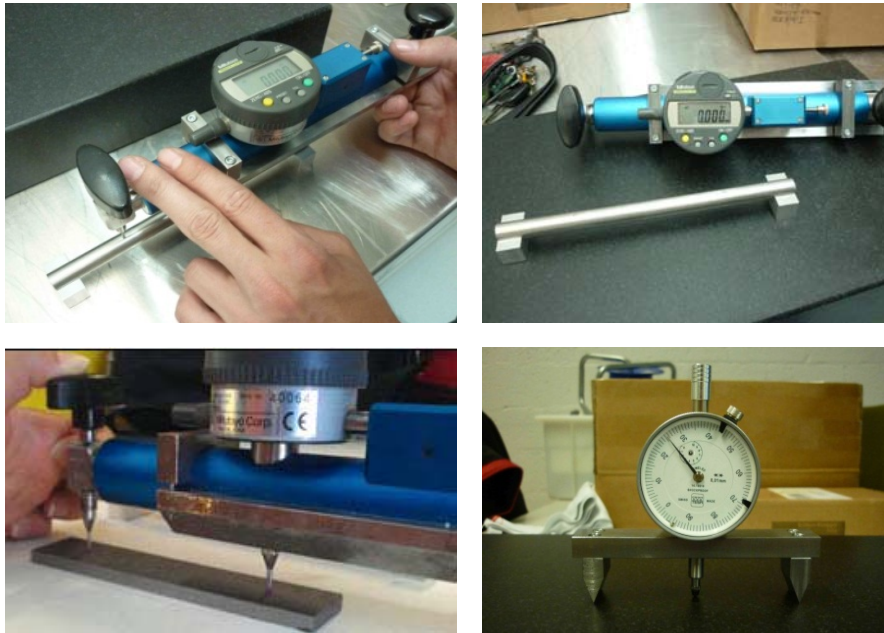


Figure 59 – Strip length and curvature measurements.

Sectioning was performed on an automated milling machine as shown in Figure 60. Hooke's law, along with geometrical equations for the curvature determination was used to get both flexural and membrane residual stresses distributions. A set of released strips from cold-formed section is shown in Figure 61.

All the hot-finished sections had a welding on their edges, i.e. the sections were formed at room temperature with subsequent heat treatment. Hot-finished sections are treated the same as the hot-formed sections, provided that the hollow sections formed 'cold' are fully annealed in a subsequent heat treatment. However, the different manufacturing processes result in several key differences from physical to mechanical properties. Unfortunately, the difference between hot-rolled and hot-finished sections could not be investigated in this study, because

⁴ Strips were short enough to ensure a better curvature measurement.

all the corresponding square and rectangular sections were hot-finished, and all the corresponding circular sections were hot-rolled. However, a comparative study on cold-formed, hot-formed and hot-finished structural hollow sections is presented in [81]. It is found that the cold-formed sections had the highest longitudinal stresses, exceeding the corresponding nominal yield stress. The hot-formed ones had the smallest residual stresses. The distributions of residual stresses in the hot-finished sections were extremely similar to those in the cold-formed sections, but the values were much smaller. Therefore, the hot-formed sections had the least locked-in residual stresses, followed by the hot-finished then cold-formed sections.

Two European product standards for the manufacturing of tubes are available; EN10219-1 [69] which covers cold-formed sections and EN10210-2 [68] which covers hot-finished sections. EN10210 include more than one fabrication process. However, Wardenier states that “the standard EN10210-1 applies to hot-finished hollow sections formed hot with or without subsequent heat treatment or formed cold with subsequent heat treatment to obtain equivalent metallurgical conditions to those obtained in the hot-formed product”. So, these three fabrication processes are covered by the same product norm ([69] & [68]).

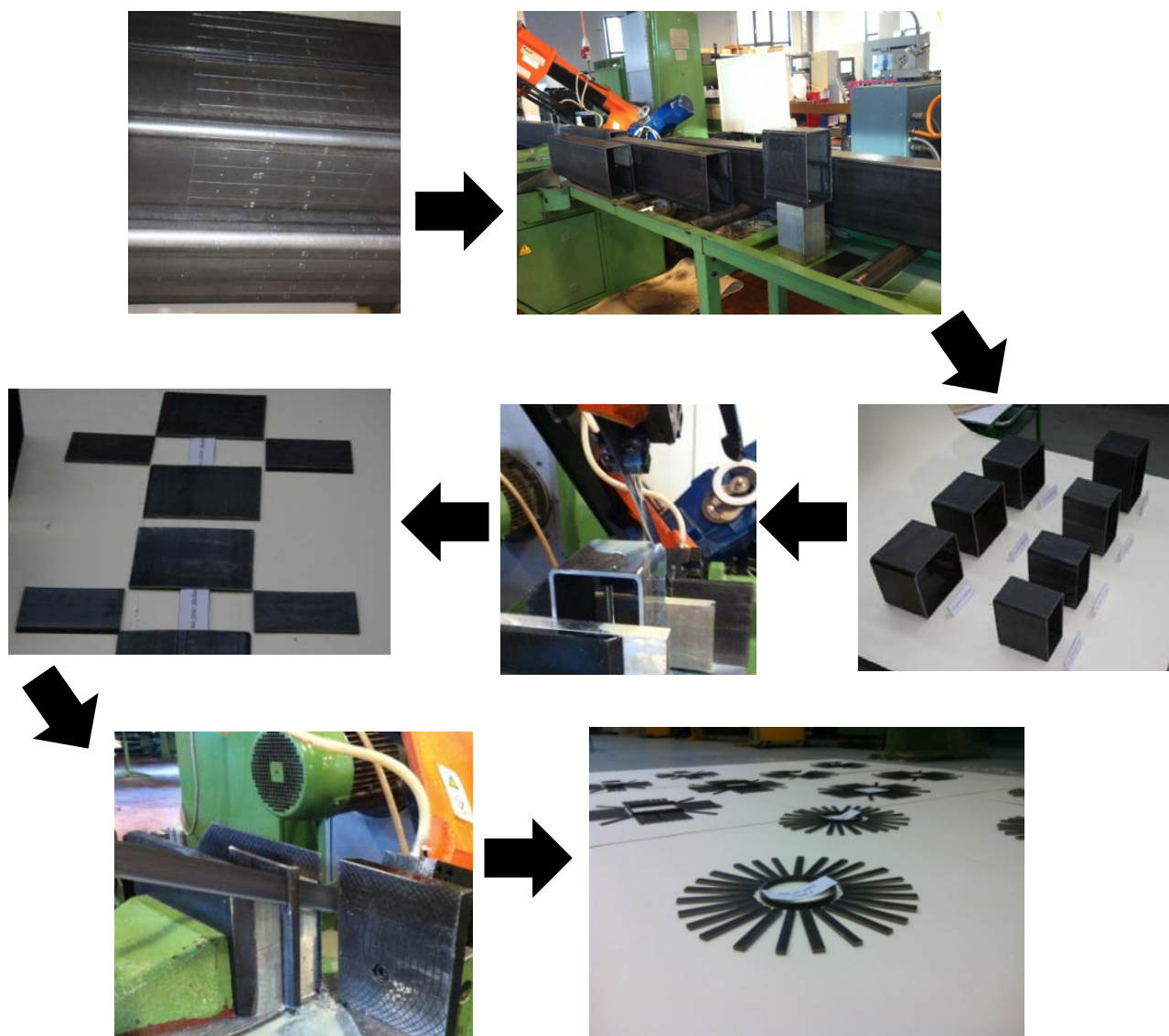


Figure 60 – Strip-cutting process.

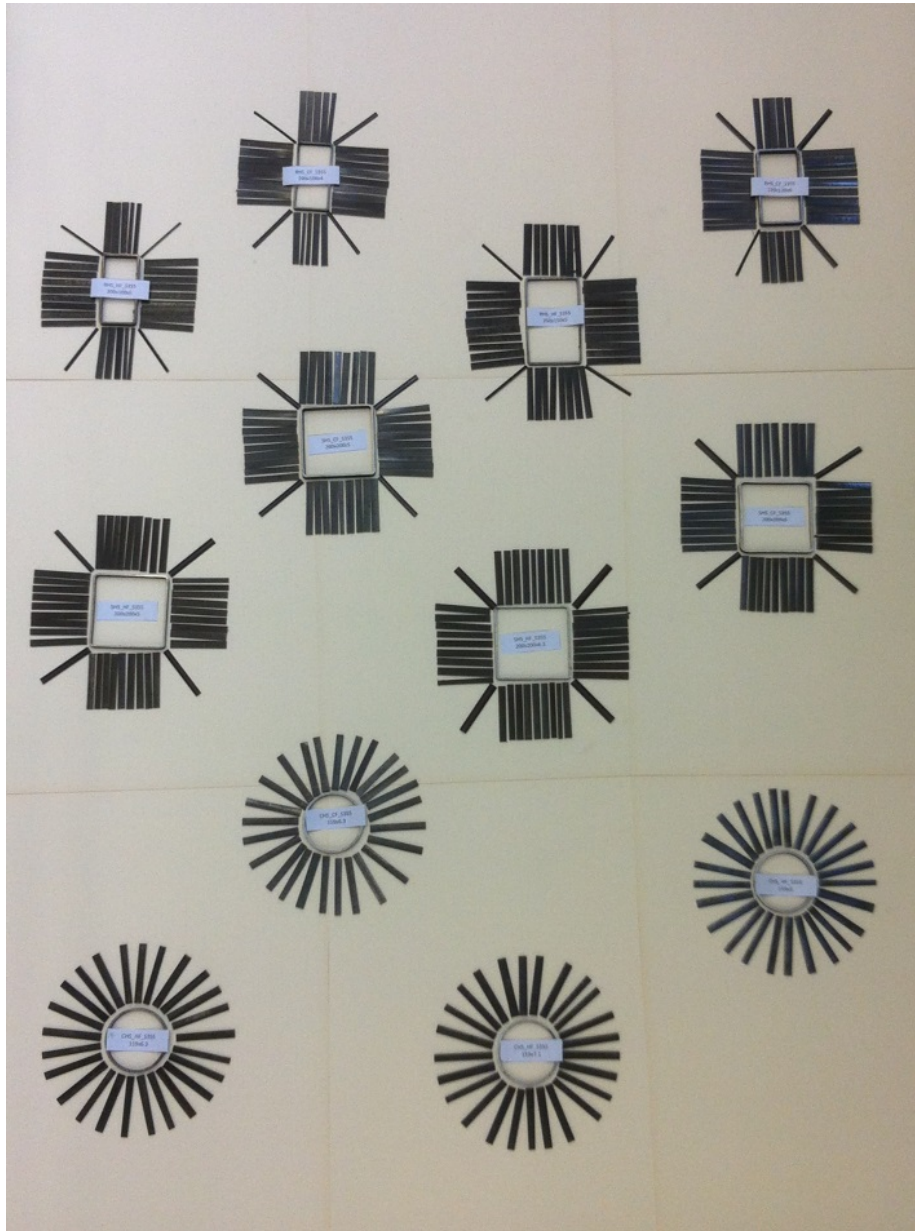


Figure 61 – Cross-section released strips after cutting.

Several assumptions and corrections are included in the determination of the residual stresses with the sectioning method. Firstly, the analysis and calculations are simplified by ignoring the transversal stresses effect, which are known to affect the results ([82] & [77]). Obviously, the lower the transverse stresses are, the more accurate the results will be. The second assumption concerns the process and the way the strips were cut; during the cutting, additional residual stresses are created due to the heating generated by the saw. The strip width should be large enough in order to consider this effect negligible, but small enough to

have sufficient measurement points. Regardless of the adopted strip width, the speed of sawing and the thickness of the plate will also affect the additional stress creation. Measurements considering this sawing effect were performed in [83] at the saw cut edge and stresses of the order of 3-10 MPa were observed. However these results can be lowered through an effective liquid cooling system during the sawing, enabling the neglect of the sawing effects. This was done in this study.

Views of the strip-cutting technique are shown in Figure 60 while Figure 62 to Figure 66 represent all the measured residual stresses corresponding to the twelve sections. On the left, membrane residual stresses are represented with positive values corresponding to compressive stresses and negative values to tension stresses. On the right, the flexural residual stresses are represented with positive values corresponding to tension stresses on the outer faces and negative values to compressive stresses.

For the cold-formed sections, the flexural residual stresses are seen to be much higher than their membrane counterparts, due to cold-forming effects; significant residual curvatures of all strips (after cutting) were clearly visible, except for the corner strips. This was later confirmed through the measurement of high flexural residual stresses (>350 MPa). Similar results were also reported in [3]. As for the hot-finished sections, the flexural stresses were seen to be negligible compared to the membrane residual stresses due to their subsequent heat-treatment.

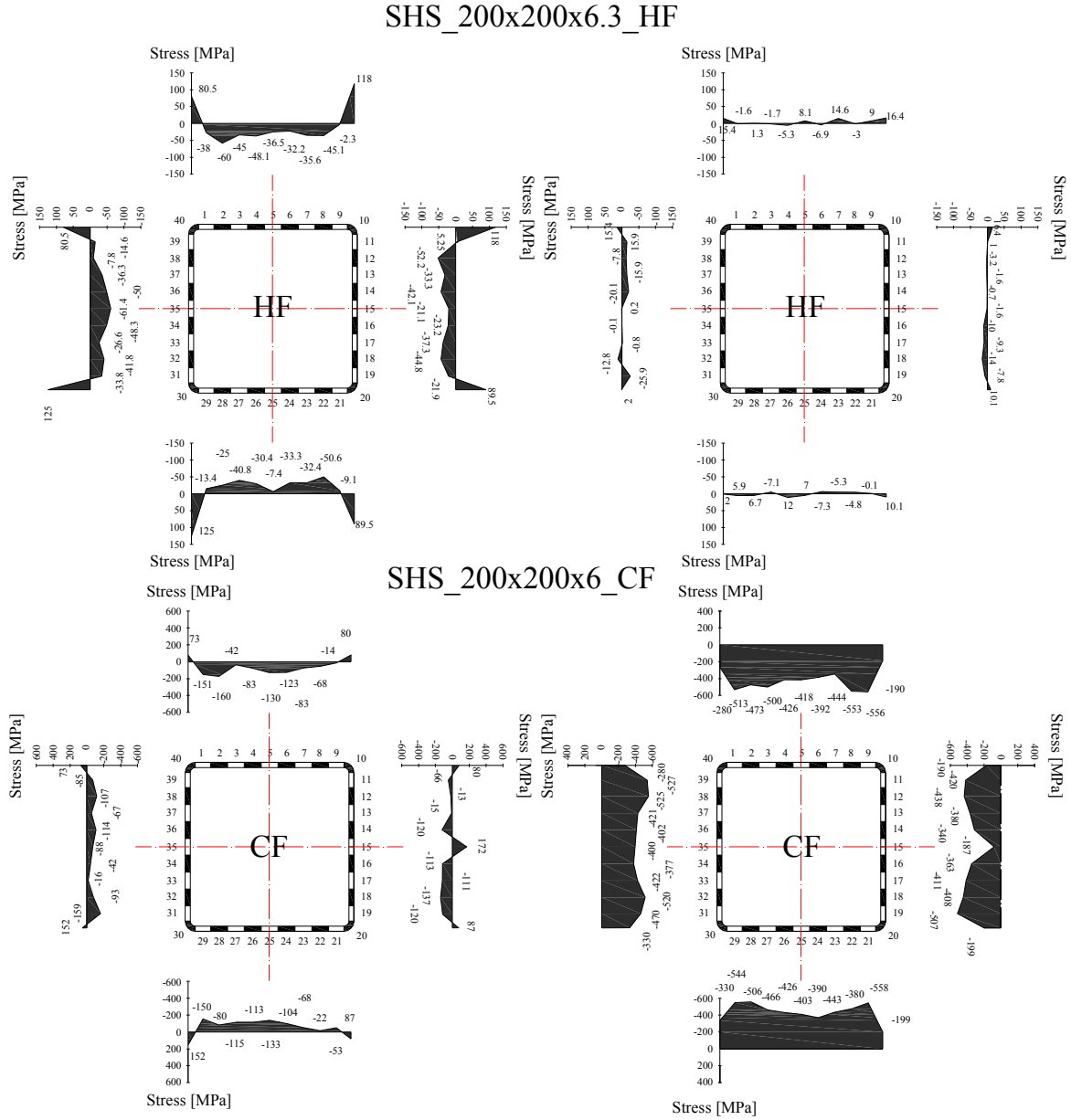


Figure 62 – Measured membrane (right column) and flexural (left column) stresses of square sections (part 1).

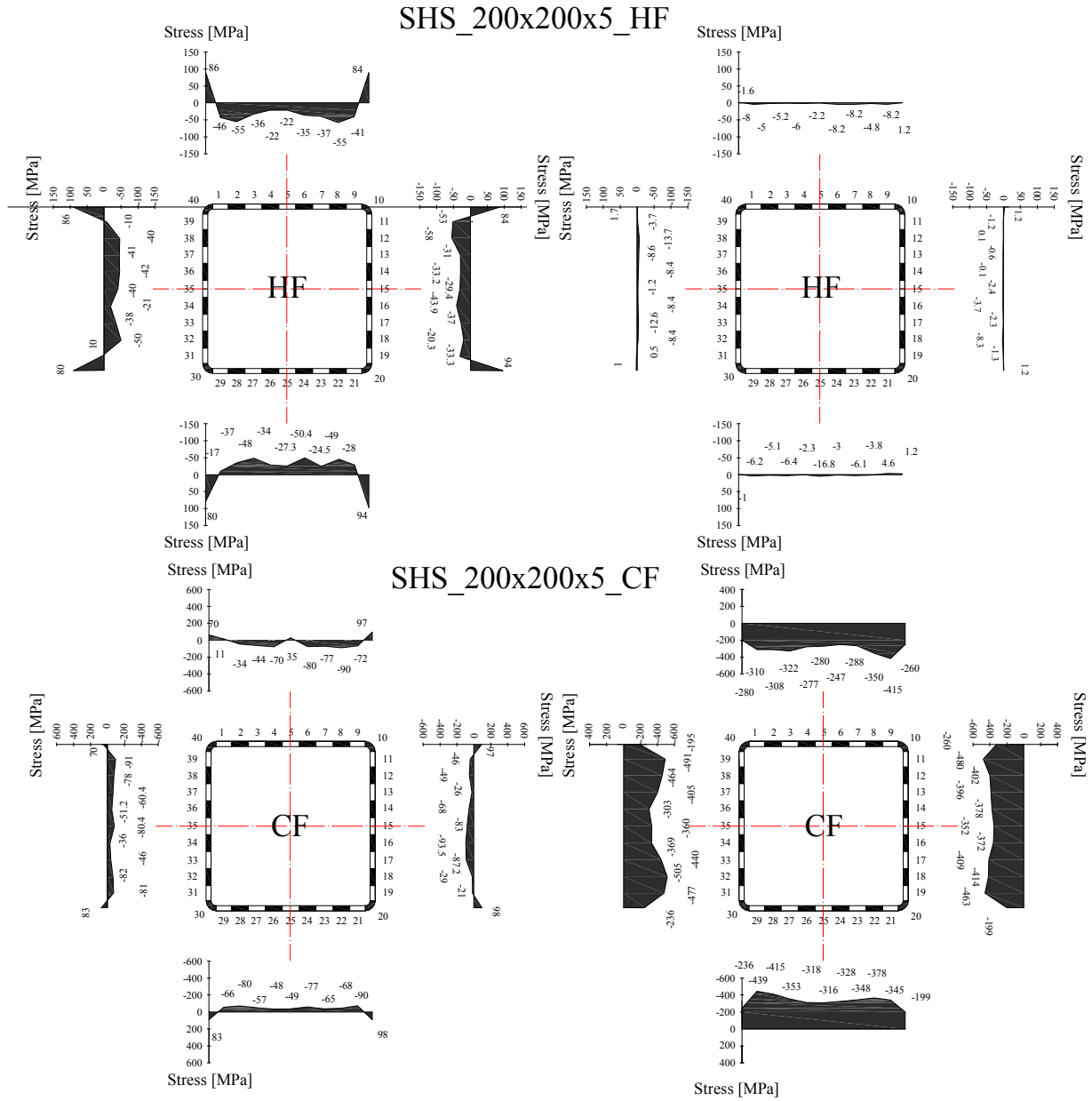


Figure 63 – Measured membrane (right column) and flexural (left column) stresses of square sections (part 2).

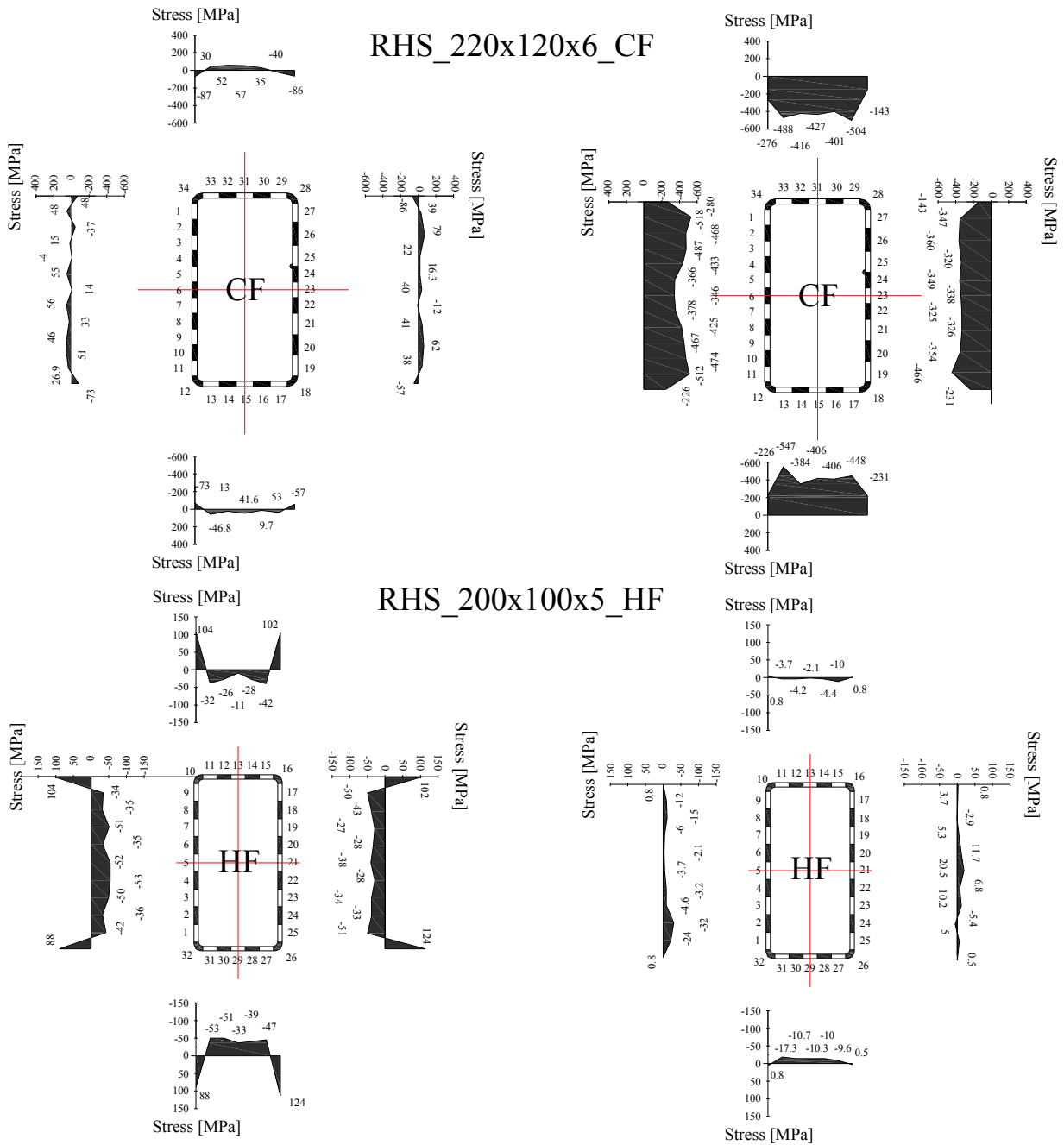


Figure 64 – Measured membrane (right column) and flexural (left column) stresses of rectangular sections (part 1).

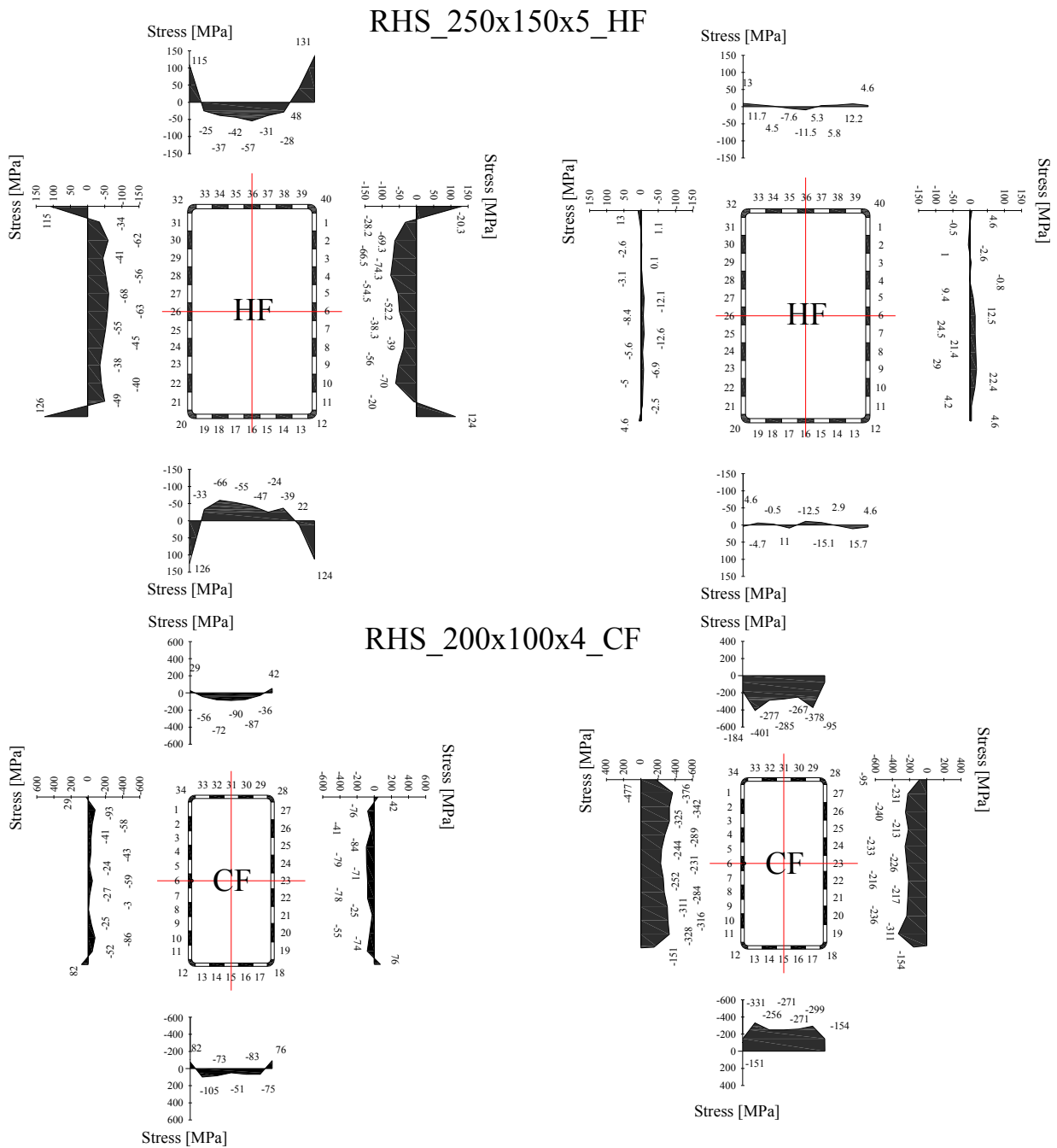


Figure 65 – Measured membrane (right column) and flexural (left column) stresses of rectangular sections (part 2).

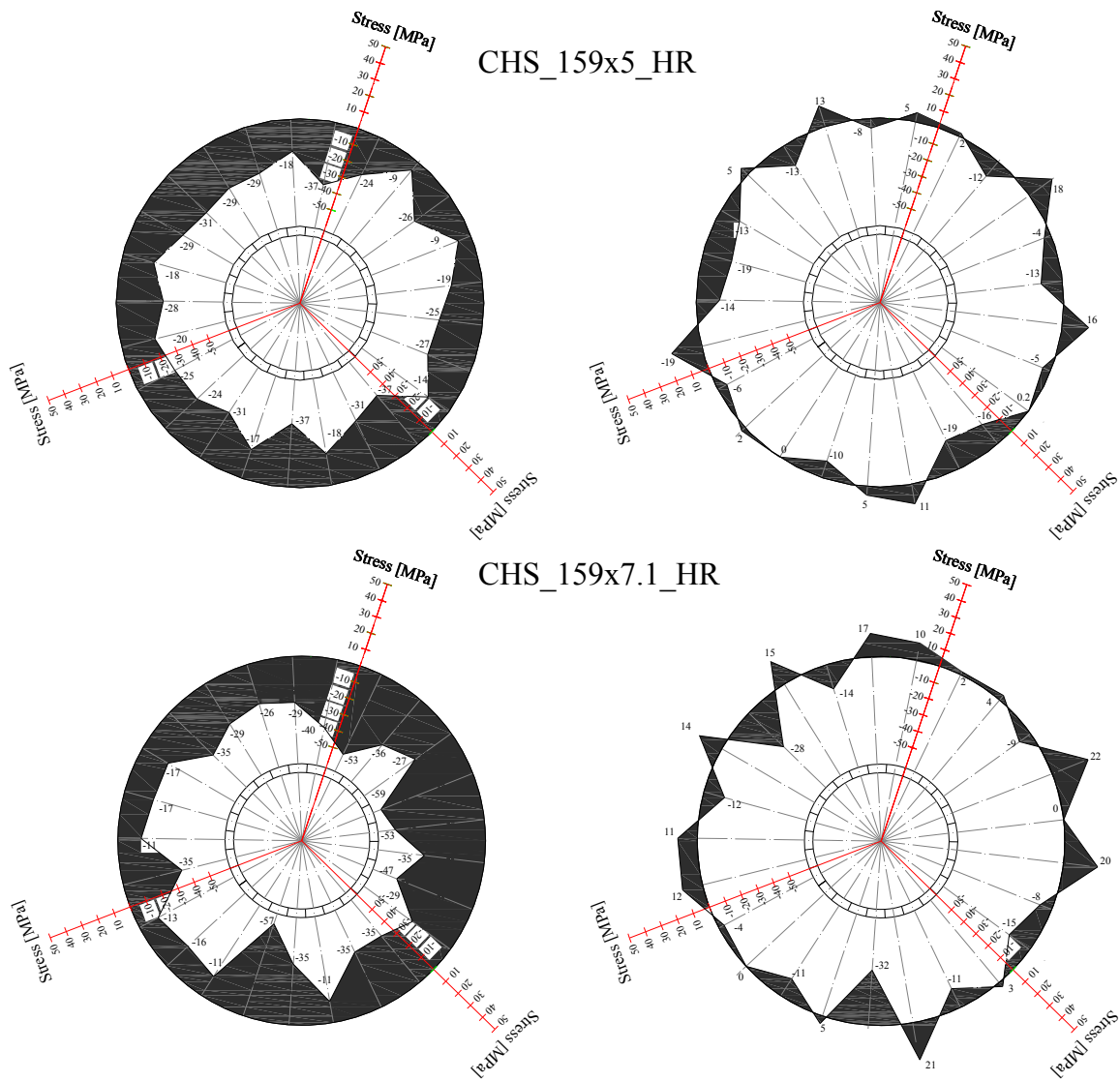


Figure 66 – Measured membrane (right column) and flexural (left column) stresses of circular sections (part 1).

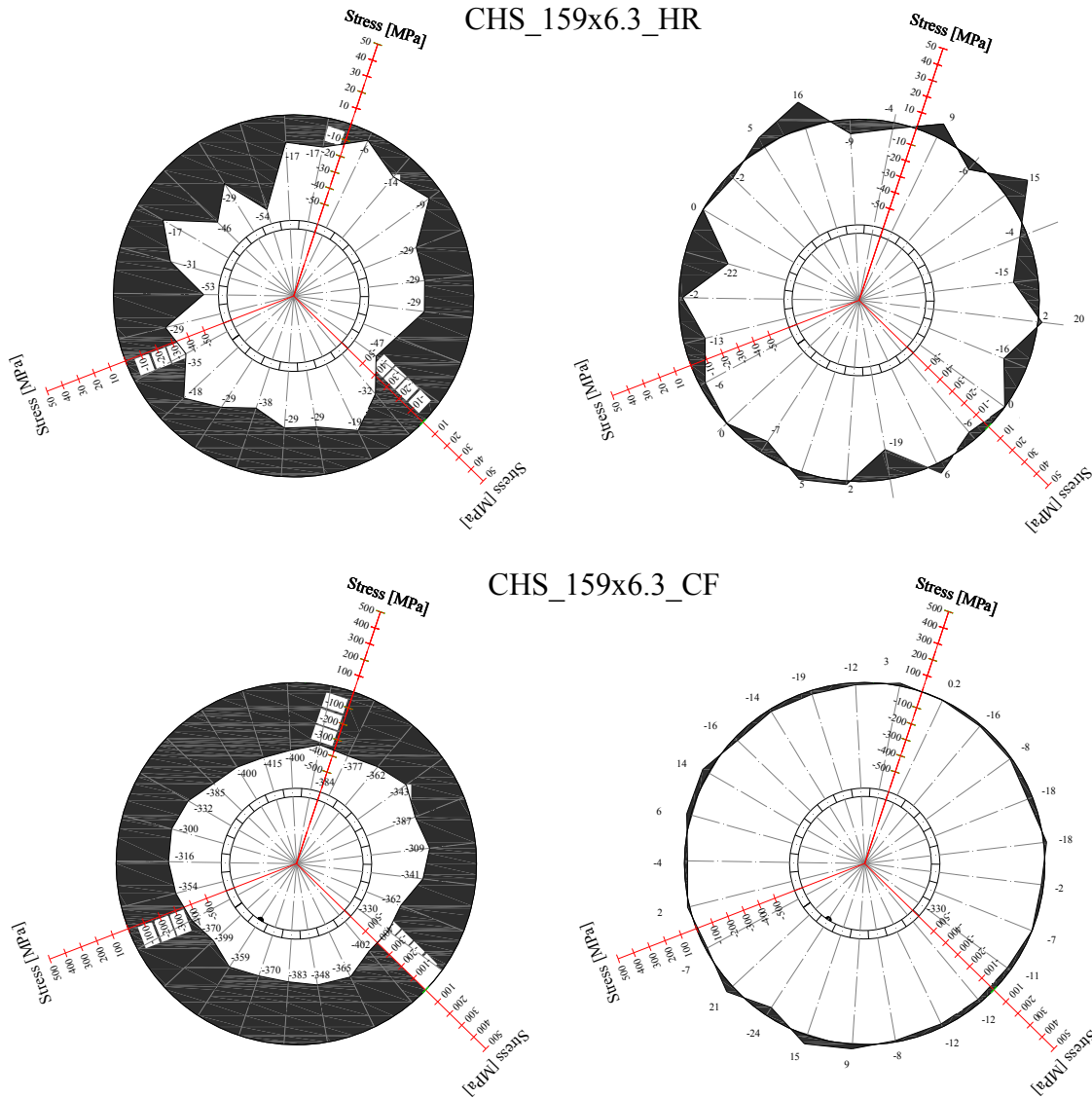


Figure 67 – Measured membrane (right column) and flexural (left column) stresses of circular sections (part 2).

Flexural residual stresses:

Flexural residual stresses were initially determined by assuming a linearly varying through thickness stress distribution. Even though a non-linear distribution can be shown to develop through the thickness of the sections, the linear distribution is adopted in this study for sake of simplicity and more importantly due to the small thicknesses of the tested sections. The flexural residual stresses were thus calculated by means of the following equation:

$$\sigma_{flexural} = E \frac{L_{arc_e_or_i} - L_{arc_m}}{L_{arc_e_or_i}} \quad (86)$$

Where $L_{arc_e_or_i}$ stands for the arc length at the inner or outer surface of the strip and L_{arc_m} stands for the neutral axis arc length. Equation (86) can actually be rewritten in the following way:

$$\sigma_{flexural} = E \frac{\alpha R_{i_or_e} - \alpha R_m}{\alpha R_{i_or_e}} = E \frac{\nu}{R_{i_or_e}} \quad (87)$$

where α being the angle of curvature calculated as follows (see Figure 68):

$$\alpha = \arcsin \left(\frac{l_{final} - l_{initial}}{2R_{i_or_e}} \right) \quad (88)$$

with l_{final} and $l_{initial}$ being the lengths measured by the extensometer before and after strip cutting.

R_m (curvature radius at the neutral axis and R_i and R_e stands for external or internal radius curvature) is calculated by means of the following relationship through the addition or subtraction of ν where ν is the half strip thickness $t / 2$.

$$R_m = R_{i_or_e} \pm \nu \quad (89)$$

The change in radius of curvature R_m (or R_e and R_i) of the strips was calculated with the following equations⁵:

⁵ It was assumed that the curvature was constant along the length of the strips

$$(R - \Delta a)^2 + \left(\frac{L_0}{2}\right)^2 = R^2 \quad (90)$$

$$R = \frac{L_0^2}{8\Delta a} + \frac{\Delta a}{2} \quad (91)$$

where L_0 is the length over which the deflection is measured (here 100 mm corresponding to the curvature measuring device), Δa is the difference between the initial deflection $a_{initial}$ of the strip and the final deflection of the strip a_{final} (see Figure 68).

$$\Delta a = a_{final} - a_{initial} \quad (92)$$

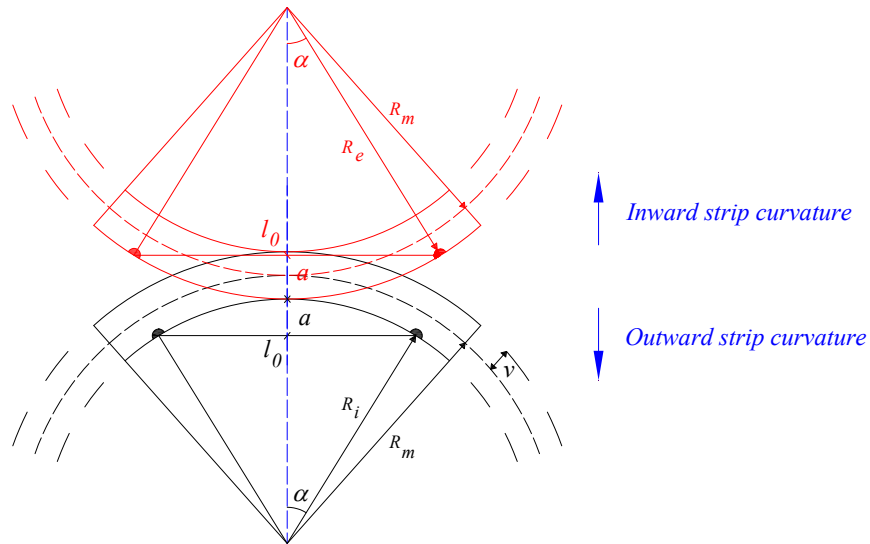


Figure 68 – Geometrical deformation due to residual stresses.

Membrane residual stresses:

The calculation of the membrane residual stress is more complex, since the measurements made by the extensometer must be corrected in order to remove the effects of strip curvature caused by the existence of flexural residual stresses. Therefore, the stress measured through the extensometer is considered as a cumulate of flexural and membrane stresses influences, in which a part is reserved to the shortening due to the membrane stresses and the other part is reserved to the curvature implied by the flexural stresses.

Galambos and Sherman have proposed expressions to calculate membrane residual stresses from an extensometer and curvature dial measurements ([84] & [85]). Both approximate the

curvature of the released strips as parabolic, though this is found in [74] to be inappropriate in the presence of large flexural residual stresses. An alternative circular approximation is therefore adopted [74], whereby the released strip is assumed to be a circular arc and the extensometer length is assumed to be a chord of length l_0 .

The corrections proposed by Galambos and Sherman ([84] & [85]) were developed principally to remove the influence of strip curvature (due to flexural residual stresses) during the calculation of membrane residual stresses in hot rolled sections. In such sections, the approximation of a parabolic curvature would induce minimal errors since the flexural stresses are low. However, this is not the case for cold-formed sections in which flexural residual stresses are far more significant, and the adoption of Galambos or Sherman approximations will thus lead to larger discrepancies between calculated membrane residual stresses with parabolic curvature from those determined using the circular approximation.

By comparison of residual stresses determined by mechanical means with those determined by electrical strain gauges, it was later demonstrated that the circular approximation remains accurate, even in the presence of high curvatures associated with cold-forming effects [74].

Measuring the residual stresses by means of electrical strain gauges presents physical constraints in the case of hollow sections, because it is not possible to place inner gauges on the inner surface of the sections; Cruise and Gardner [74] adopted a procedure in which the second set of strain gauges was attached to the inner surface of the strips after cutting, and the strips were bent back to their initial flat configuration. Jandera et al. [86] adopted a different procedure in which an opening was cut out in the web facing the measured face of the section and strain gauges were attached to the inner surface of the measured web. This method obviously implies that the measurements could be done only on one plate of the section.

The arc length L_{arc} had to be calculated using the chord length and through the calculation of the curvature angle α . Using the radius of curvature of the strips measured to the mid-thickness R_m and the angle of curvature α , the length along the arc can be calculated by means of the following equation:

$$L_{arc} = R_m \times 2\alpha \quad (93)$$

Therefore the membrane residual stresses can be calculated by means of the following equation:

$$\sigma_{membrane} = E \frac{L_{arc_f} - L_{arc_i}}{L_{arc_i}} \quad (94)$$

where L_{arc_i} and L_{arc_f} are the initial and final arc length calculated as mentioned above.

An attempt to quantify the non-equilibrated stresses in the measured residual stresses of the sections above has been made through the calculation of the ratio representing the percentage of non-equilibrated stresses over the total stresses:

$$Ratio = \frac{\sum (b_i \sigma_{tension_i} + b_i \sigma_{compression_i})}{\sum (|b_i \sigma_{tension_i}| + |b_i \sigma_{compression_i}|)} \quad (95)$$

where b_i represents the strip width and $\sigma_{tension_i}$, $\sigma_{compression_i}$ the tension and compressive stresses measured on each strip (see Figure 69).

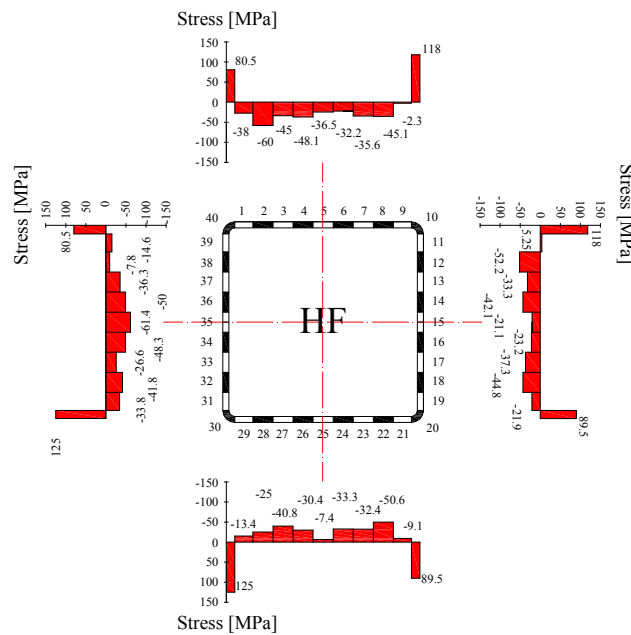


Figure 69 – Adopted block representation for the calculation of the non-equilibrated stresses (Profile SHS_HF_200x200x6.3).

This ratio was calculated through the consideration of a constant measured stress value over the strip width (see Figure 69). Obviously, the measured stress on the strip will not be constant but the corresponding distribution is unknown because ‘one single point’ was

measured on the whole strip width and most importantly this ratio calculated herein represents only a quantitative way to evaluate and assess the reliability of the results.

The main reasons behind these somewhat high ratios are the laboratory effects, the way of holding the extensometer, the variation of the inclination of the extensometer before and after cutting, the presence of impurities in the holes, etc... The extensometer has also an accuracy of $\pm 5 \mu\text{m}$. This precision value will not affect the residual stresses in the corners as much as those found in the flat faces, because of the small magnitudes measured in the flat faces.

Therefore, if we consider for instance, the highest percentage (57%) reached with the profile RHS_200x100x4 and its corresponding measured values decreased or increased depending on the precision factor⁶, then, the obtained percentage will drop from 57% to 30%. Therefore, the residual stresses distributions are considered to be accurate enough. However, the measured magnitudes are affected by many laboratory inconsistencies, the reason why, the adopted residual stresses pattern for the numerical validation have been taken as an approximation of the measured residual stresses with respect to an auto-equilibrated pattern.

Table 17 – Percentage of non-equilibrated stresses.

Profile (hot-rolled and hot-finished)	% of non-equilibrated stresses	Profile (cold-formed)	% of non- equilibrated stresses
RHS_S355_200x100x4	57%	RHS_S355_200x100x5	44%
RHS_S355_220x120x6	45%	RHS_S355_250x150x5	48%
SHS_S355_200x200x5	56%	SHS_S355_200x200x6	41%
SHS_S355_200x200x6.3	47%	SHS_S355_200x200x5	49%
CHS_S355_159x6.3	37%	CHS_S355_159x6.3	43%
CHS_S355_159x7.1	4%		
CHS_S355_159x5	2%		

⁶ It is improbable that all the values reach a positive precision correction, but this is being done just to show the influence of the precision factor on the results.

3.3.4. Material properties

3.3.4.1. Tensile tests

The stress-strain behavior of the materials was determined through 55 tensile tests. Four necked coupons were cut from the middle of each flat face of the eight SHS and RHS parent elements. Two straight corner coupons were also manufactured and tested for each of these eight sections in order to investigate the increase in strength of the cold-formed corners and to confirm uniform properties in the hot-rolled corners (see Figure 70). As for the CHS specimens, two coupons were extracted from each section. Figure 70 shows the location of the coupons in the hollow sections, together with the adopted labeling system. Obviously, the coupon location was shifted in faces containing a weld. All the coupons were 270 mm long with nominal cross-section dimensions of $t \times 10$, where t represents the profile thickness. The corners' coupons and the CHS coupons were 150 mm long with cross-sections dimensions of $3 \text{ mm} \times 3 \text{ mm}$ cut inside the cross-section thicknesses in order to avoid creating eccentric loads while testing (see Figure 71). Once the coupons were cut and edges cleaned, the cross-section dimensions were recorded at various locations along the middle portion of the coupons. However, for the corner coupons and CHS coupons, the area was also determined by dividing its weight by its initial length and density. The necked coupons were tested in a 100 kN testing machine with hydraulic grips for the load application. The corner and CHS were tested in a 10 kN testing machine due to their smaller size and cross-section. The coupons were gripped in place in the testing rig and a 20 mm clip gauge was attached at the middle of the coupon segment. A constant rate of strain (0.045%/s) was applied until fracture (see Figure 72).

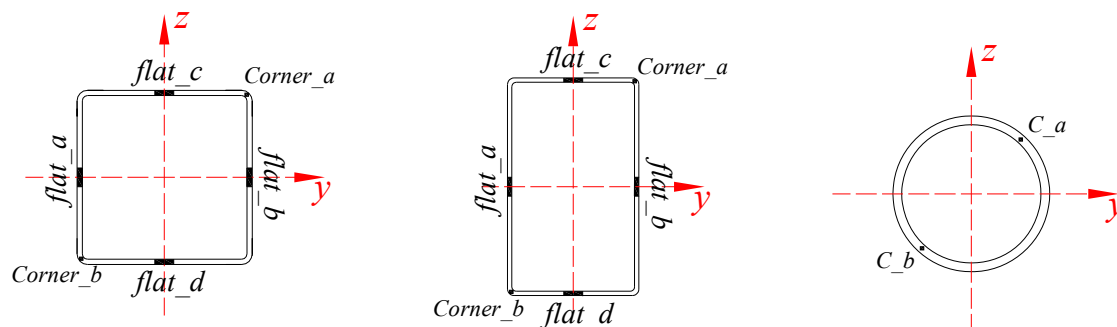


Figure 70 – Locations of the tensile coupons were cut from different faces.



Figure 71 – Necked and straight tensile coupons.

The stresses were calculated on the basis of the applied force and the measured initial cross-section of each coupon (i.e. engineering stresses).

Typical stress-strain curves measured from hot-rolled and cold-formed material are shown in Figure 73 and Figure 74. The hot-finished material law is clearly displaying the sharply defined yield point with the yield plateau followed by a subsequent strain-hardening, whilst the cold-formed material law is showing a more rounded response.

Tabulated data, measured stress-strain curves and details can be found in Annex 2, Annex 5 and Annex 6. The yield strength used in the finite element calculations for materials showing a distinctive yield plateau, i.e. hot-finished or hot-rolled profiles, is the value f_{ym} representing the mean between onset of yielding, which was the upper yield strength, and the onset of strain hardening for each coupon. This value was graphically determined from the stress-strain curves. For cold-formed cases, the 0.2% proof stress was determined for both flat and corner material curves. The young's modulus E was taken as the gradient between 20% and 80% of f_y . For all tested coupons (hot-rolled, hot-finished and cold-formed), the highest reached stress f_u was reported after the yielding, along with the ultimate and fracture strain ϵ_u and ϵ_t .

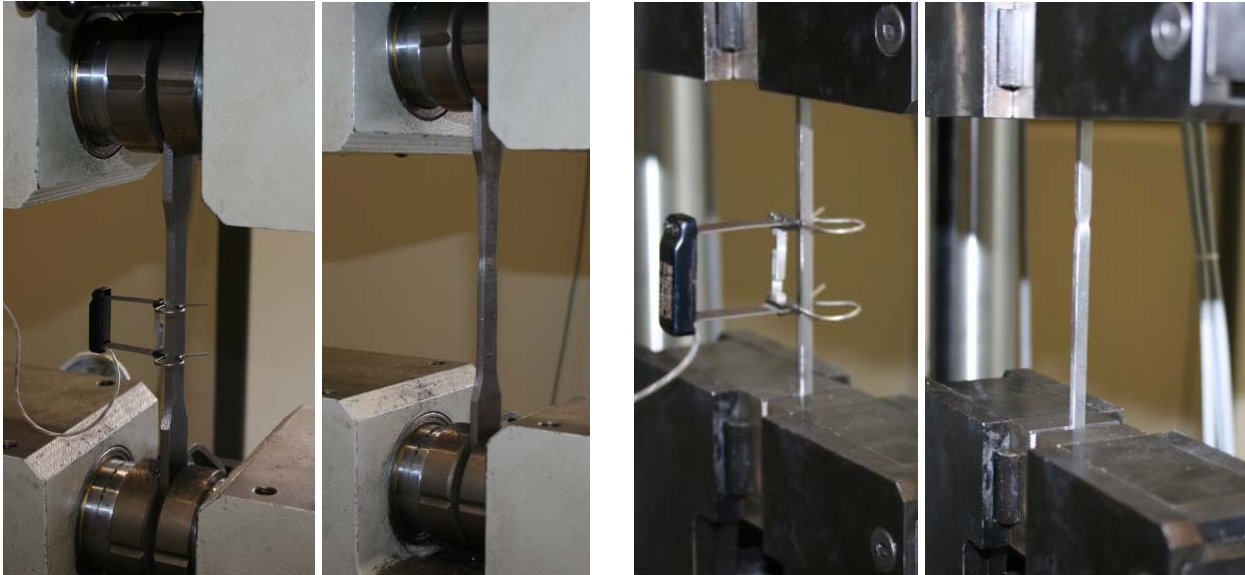


Figure 72 – Tensile coupons testing.

It shall be mentioned that the corner coupons where the measured ultimate strength is smaller than the corresponding ultimate strength in the flat coupons is mainly due to the uniform geometry of the prismatic manufactured coupon. In some tests, the stresses were localized in the grips zone and premature failure occurred in this region, leading to an overly reduced ductility (1% ultimate strain) as well as to a smaller ultimate strength.

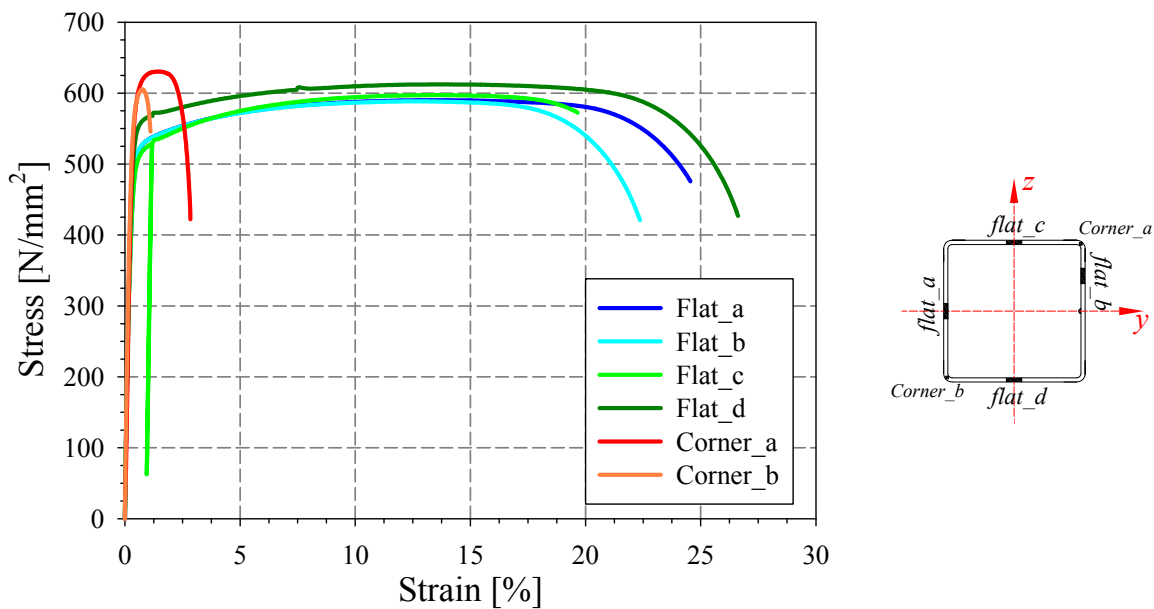


Figure 73 – Stress-strain curves from flat and corner regions of a cold formed profile
– SHS_200x200x6_CF.

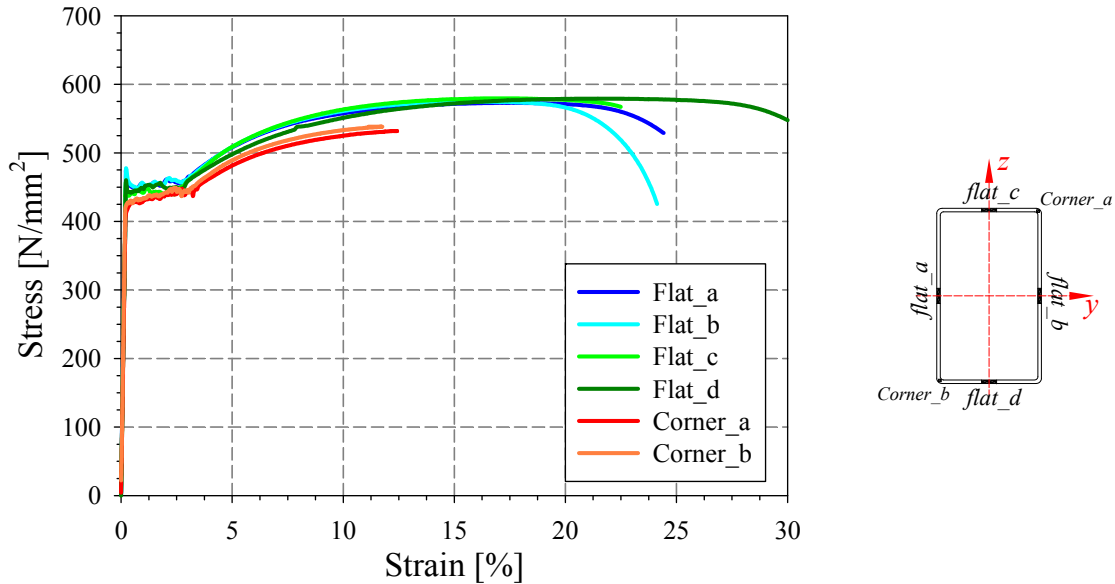


Figure 74 – Stress-strain curves from flat and corner regions of a hot-finished profile
– RHS_250x150x5_HF.

3.3.4.2. Stub column tests

12 stub column tests were performed for each cross-section type. Their main purpose was to (i) determine the average stress-strain relationship over the complete cross-section, (ii) examine the influence of the residual stresses on the cross-sectional response and (iii) characterize the early/late occurrence of local buckling. The length of each stub column was chosen as three times the height of the cross-section, in an attempt to limit member buckling, but sufficiently long to bear the same initial residual stresses pattern as a much longer member. For cold-formed sections, the stub column test was not only aimed at determining the effect of local buckling, but also the effect of cold-forming on the column performance.

The cross-section dimensions were measured at both ends repeatedly using a digital micrometer. Moreover, the length and weight of each specimen were measured prior to testing, and used later on for the calculation of the measured area assuming a density of 7850 kg/m^3 . The ends of the columns were milled plane and perpendicular to the longitudinal axis of the column. Two strain gauges have been attached at mid-height of all the elements after polishing and cleaning the surface. The specimens were set in a 5000 kN hydraulic machine between flat bearing plates thick enough to ensure a uniform distribution of load through the specimen, and also to protect the testing machine surface. Four LVDTs were used in order to record the average end-shortening behavior.

During the test, strains were monitored live to ensure that not only compression was kept concentrically-applied but also to check the load displacement behavior of the specimen in the elastic range in order to assess the corresponding Young's modulus. All sections exhibited locally deformed shapes with inward and outward buckles of half sine waves. For stocky sections, typical failure occurred with a whole cross-section yield with local buckling near the ends of the specimens, whilst for slender sections, local buckling was located at the middle of the specimen. As for the circular sections, the maximum load was reached as a result of bulging near the ends for three specimens and a circumferentially symmetric outward buckle for one specimen. The measured ultimate loads F_{exp} of the tested specimens are listed in Table 18. The failure shapes of all stub columns along the experimental test setup are shown in Figure 75.



Figure 75 – General test setup and failure shapes of the stub columns.

The end-shortening measurements from the displacement transducers were different from the strains registered from the strain gauges. A correction method described by the Centre for Advanced Structural Engineering ([87], [88] & [89]) was used, which combined both sets of measurements since the strain gauges provide the correct initial Young's modulus slope as

they were directly in contact with the column faces however providing less useful information when influenced by local buckling. In contrast, the LVDTs provide good post-yield information but pick up the stiffness of the end plates leading to an incorrect initial stiffness. The method consists of a correction factor k representing the undesired displacement, which is then deduced from the end displacement. Figure 76 shows an example of two load displacement curves, before and after the correction of the corresponding slopes.

$$k = \frac{L}{2} \left(\frac{1}{E_{LVDT}} - \frac{1}{E_{SG}} \right) \quad (96)$$

$$\delta_c = \delta_{LVDT} - 2kf \quad (97)$$

In Equation (96) E_{LVDT} represents the initial Young's modulus calculated from the LVDT readings and E_{SG} represents the initial Young's modulus calculated from the strain gauges. In Equation (97), f represents the applied stress, δ_{LVDT} the displacement due to LVDTs and δ_c the corrected displacement.

Table 18 – Measured properties and ultimate loads of stub columns.

Test #	Specimen	H [mm]	B [mm]	t [mm]	D [mm]	Area [mm ²]	Calculated area* [mm ²]
46	RHS_Stub_S355CF_200x100x4	200.5	100.28	4.01	-	2295	2186.8
47	RHS_Stub_S355CF_220x120x6	220.6	121.02	5.85	-	3840	3675.75
48	RHS_Stub_S355HF_250x150x5	250	150	5.30	-	3873	4167.42
49	RHS_Stub_S355HF_200x100x5	199.2	100.01	5.12	-	2873	2855.63
50	SHS_Stub_S355CF_200x200x5	200.44	200.94	5.19	-	3836	3676.1
51	SHS_Stub_S355CF_200x200x6	200	199.77	5.97	-	4563	4356.07
52	SHS_Stub_S355HF_200x200x5	200.2	199	5.19	-	3873	3619.96
53	SHS_Stub_S355HF_200x200x6.3	199.9	199.9	6.42	-	4839	4575.37
54	CHS_Stub_S355CF_159x6.3	-	-	6.1	159.1	3020	2870.54
55	CHS_Stub_S355HF_159x6.3	-	-	6.49	159	3020	3131.63
56	CHS_Stub_S355HF_159x5	-	-	5.29	158.9	2420	2454.88
57	CHS_Stub_S355HF_159x7.1	-	-	7.18	159	3390	3290.87

* The calculated areas were also presented for sake of a comparison with measured areas which didn't account for the welding presence in some specimens. The calculated areas were determined by dividing the weight of the specimens by their measured lengths and density ($G=7.85\text{g/cm}^3$).

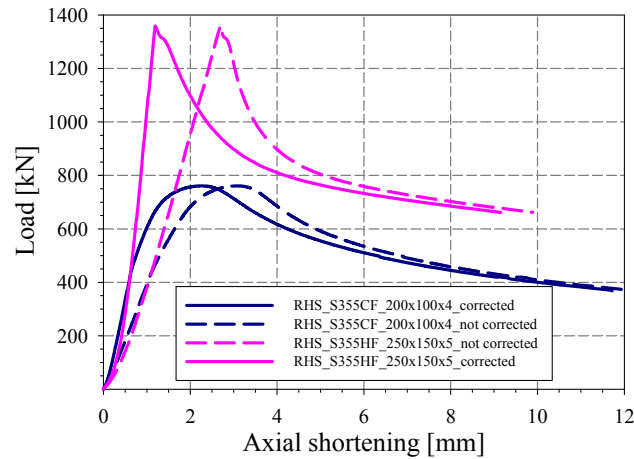


Figure 76 – Load-displacement corrected curves.

The essence of a stub column test lies in its usefulness at determining the tangent modulus at any load level, which further can be used to express column strength in function of it. Actually, the difference between Young's modulus and the tangent modulus determined from a compression test on the complete cross-section essentially reflects the effect of residual stresses. The presence of residual stresses in the cross-section implies that some fibres are in a state of residual compression reaching the first the yield limit under load. The residual stresses are thus a major factor affecting the strength of axially loaded columns, and a conservative value for this strength may be specified in terms of the tangent modulus determined from the results of a stub-column test. It would be interesting to mention that residual stresses can have a positive influence on column strength depending on the failure strain occurring in a region with an increased tangent modulus [90].

All stub columns failed by local buckling either prior to or subsequent to the onset of yielding. For the non-slender cases, deviation from the material $\sigma - \varepsilon$ curve occurred approximately at ultimate load where there is the onset of local buckling. For the slender cases, local buckling occurred in the elastic range, and deviation from the stress-strain curve may be followed by considerable post-buckling deformation. Deviations for the material stress-strain are obviously also due to other several effects including geometric imperfections, inelastic material behavior and post-buckling response. Some examples of material stress-strain and stub strain responses are shown Figure 77 to Figure 79, and more details can be found in Annex 5.

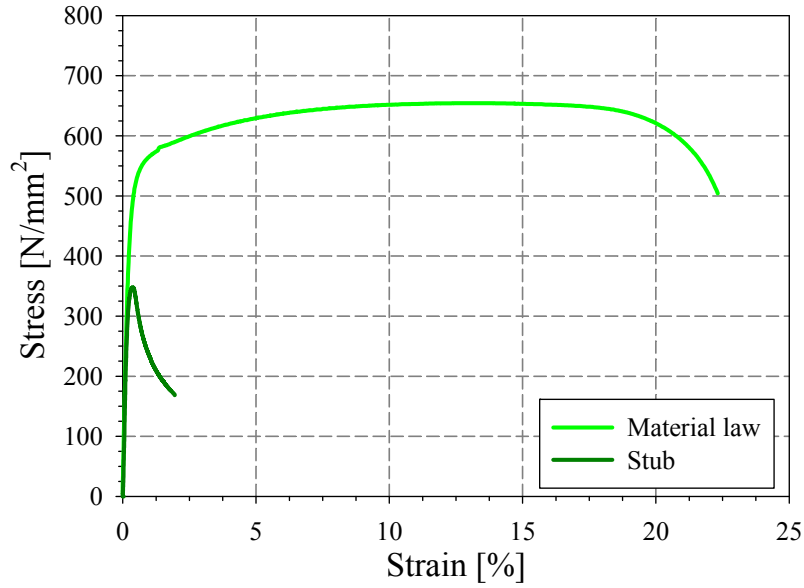


Figure 77 – Material vs. stub stress-strain curves - RHS_200x100x4_CF.

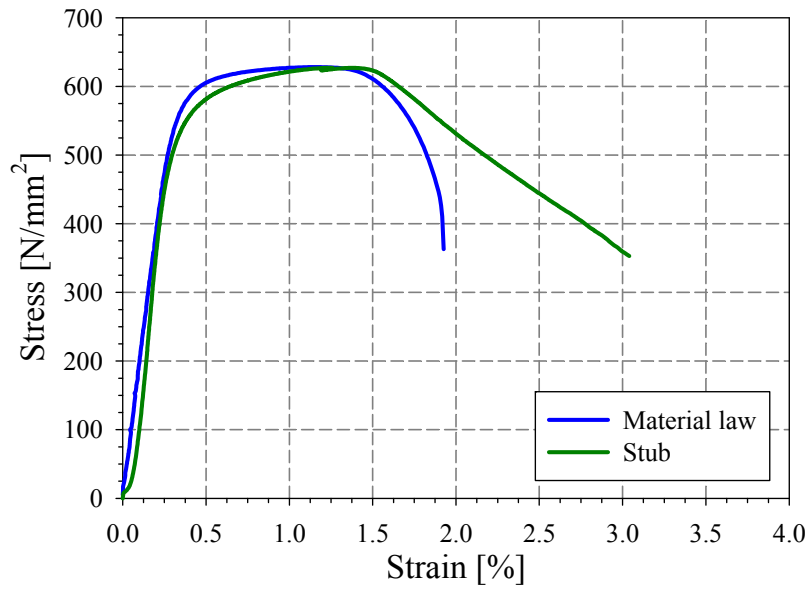


Figure 78 – Material vs. stub stress-strain curves – CHS_159_6.3_CF.

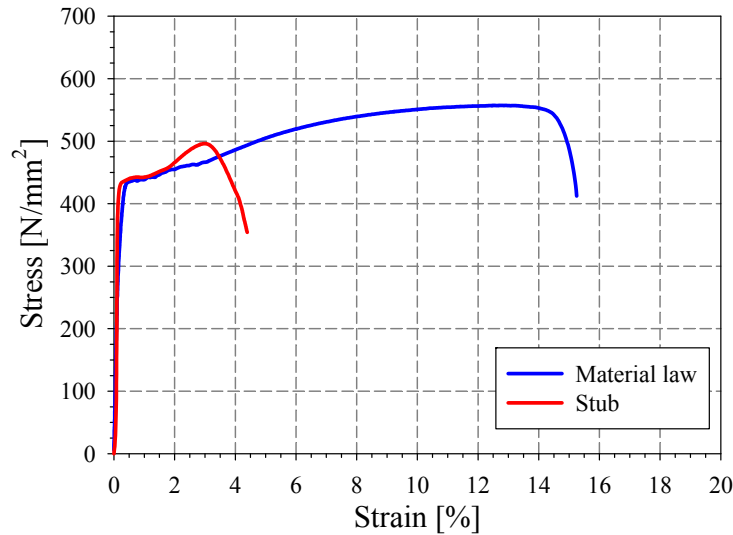


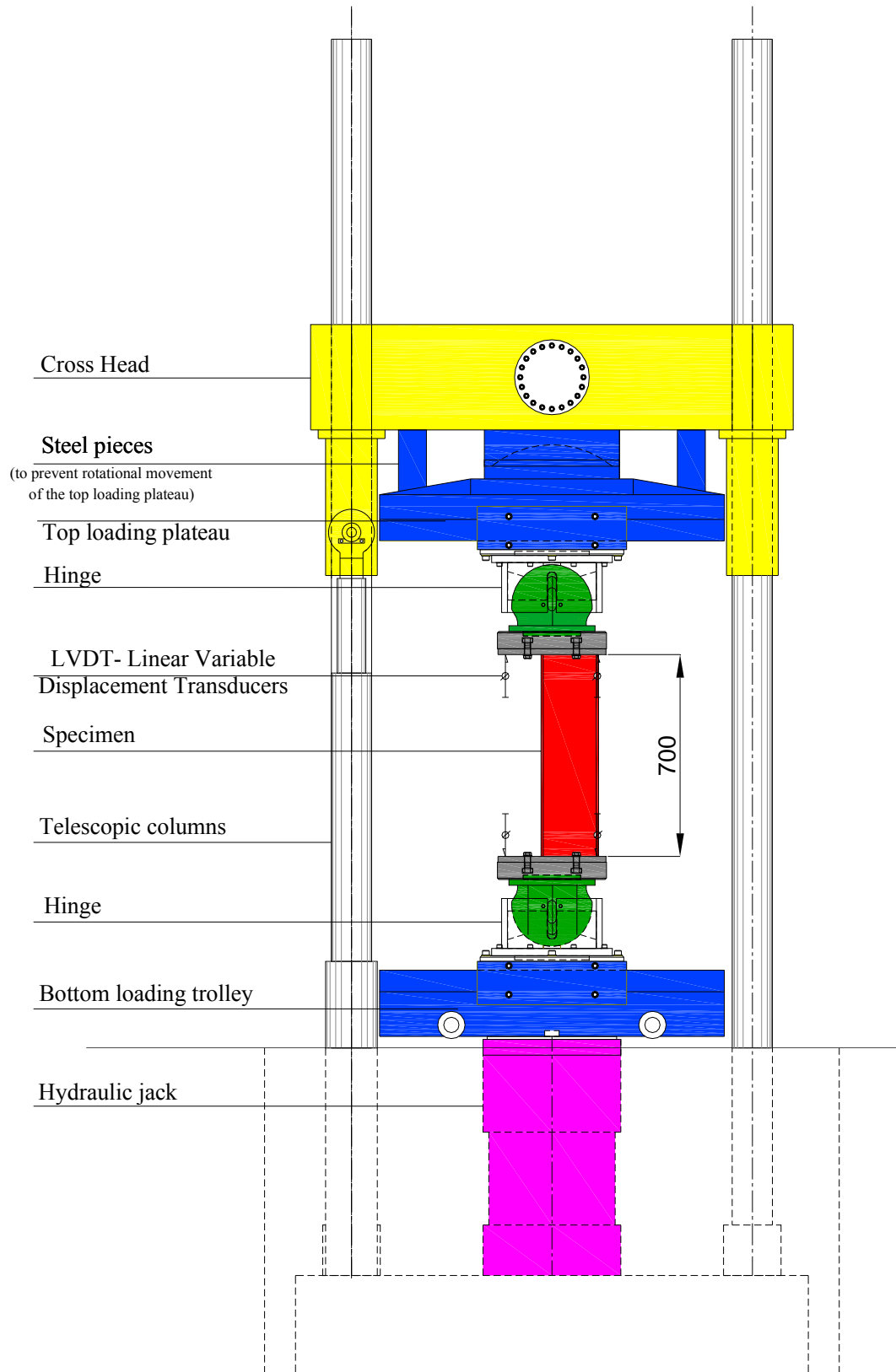
Figure 79 – Material vs. stub stress-strain curves – CHS_159_7.1_HF.

3.4. Cross-section tests

3.4.1. Testing procedure and results

The mono-axial and the bi-axial-bending with axial compression load cases were obtained through applying compression eccentrically. This procedure of load application was the simplest and most practical way of obtaining both constant axial compression and constant bending moment along the specimens.

As shown in Figure 80, the loading rig consisted of a hydraulic jack at the bottom, designed for applying the compressive force, and a top plateau fixed at a prescribed height. Two spherical supports were specially designed to provide pin-pin end restraints for the specimens (see Figure 81). End-plates were welded to the profiles with different eccentricities, according to the desired load case. A connecting plate was placed at the bottom of the hinges with two rails meant for bolts retaining the specimen endplates to slide and to be adjusted at the expected location (see Figure 82).



Front View

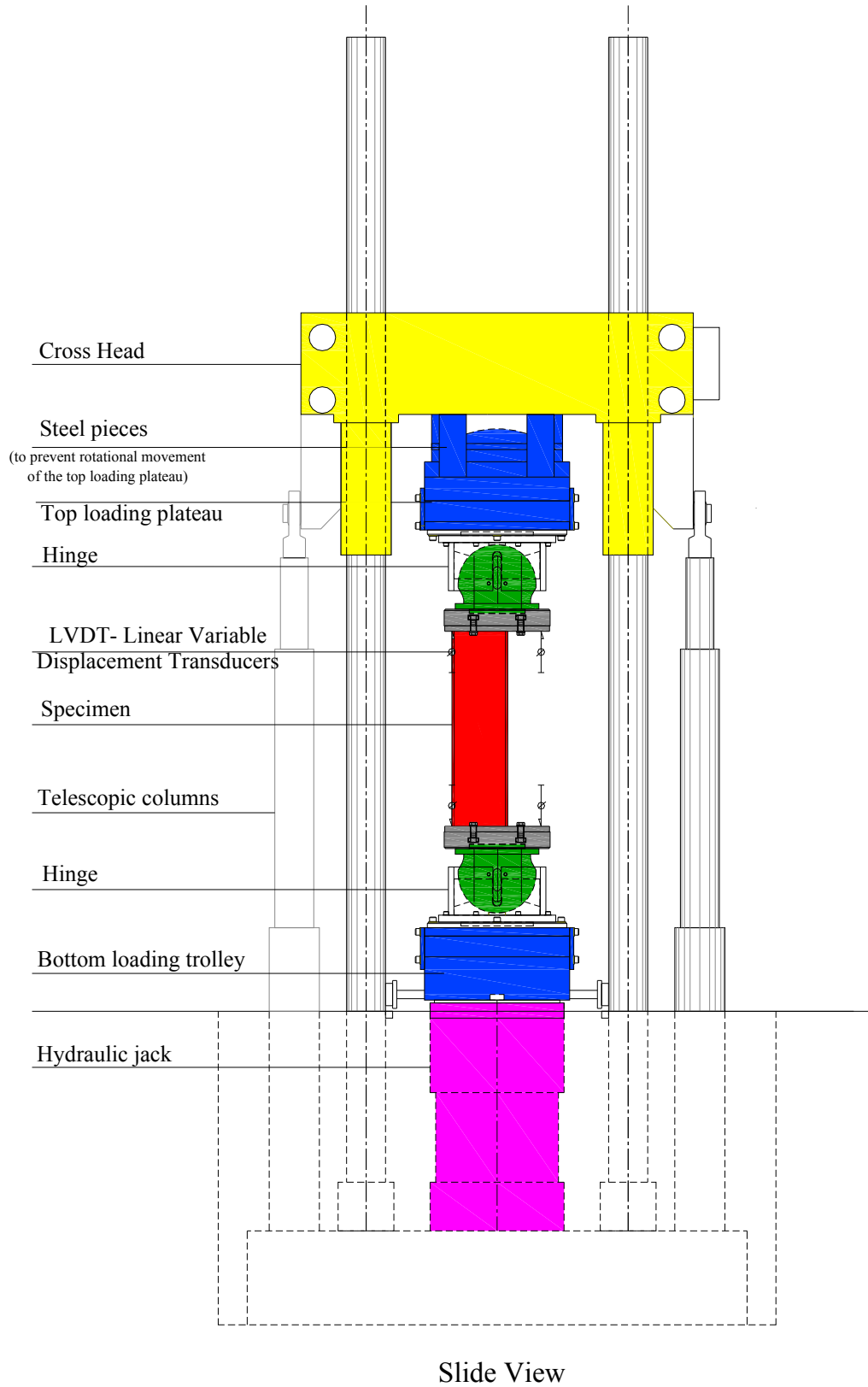


Figure 80 – General test configuration – Front and side views.

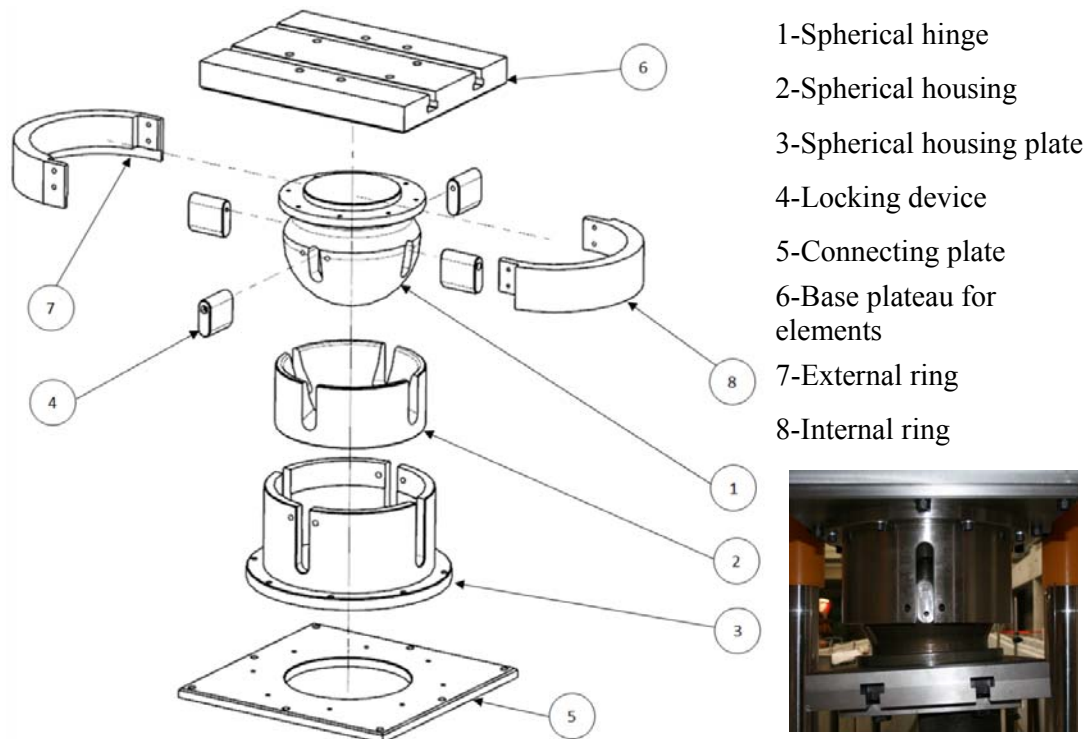


Figure 81 – Hinge detail.

Locking wrenches could be inserted inside the spherical hinge in order to provide torsional rotational restraint for the tested elements. This was done for all specimens, except for the loading cases of compression and biaxial bending, where this was not possible. The bolts were adequately pre-stressed in order to prevent uplift or detachment of the specimens' endplates. This procedure enabled the test setup to be used several times for all columns in the most practical effective way.



Figure 82 – Endplate fixed to bottom hinge plate with bolts.

The setup configuration including the hydraulic jack and the hinges with a short set specimen is shown in Figure 80 and Figure 84.

The test setup was equipped with a series of linear variable transducers (LVDTs) to record rotations and displacements of the specimens during testing. Moreover, strain gauges were attached at the middle of the specimen in order to recorder deformations during testing. All LVDTs and strain gauges were routed to spiders recording at 2 Hz. A controller machine linked to the monitoring computer drove the jack displacement and the compression load, through respectively an internal LVDT installed near the hydraulic jack and a load cell connected to it.

All positions of recording devices are illustrated in Figure 80 and Figure 83. Four upper LVDTs and four Bottom LVDTs were set to record respectively the upper plate rotations and displacements and the bottom plate rotations and displacements.

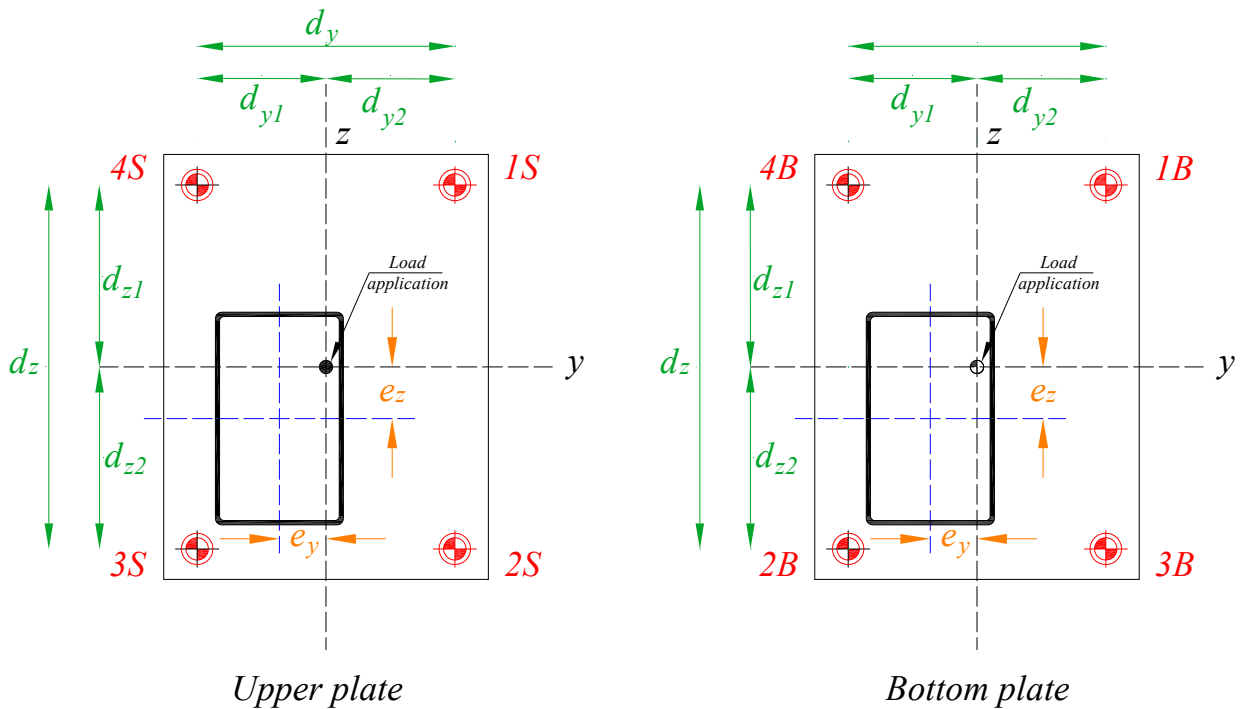


Figure 83 – LVDTs and specimen positions on upper and bottom endplates.

The upper and bottom displacements Δ_u and Δ_b were calculated as follows:

$$\Delta_u d_z = \frac{2S + 3S}{2} d_{z1} + \frac{1S + 4S}{2} d_{z2} \quad (98)$$

$$\Delta_b d_z = \frac{2B + 3B}{2} d_{z1} + \frac{1B + 4B}{2} d_{z2} \quad (99)$$

Leading to:

$$\Delta_u = \frac{2S + 3S + 1S + 4S}{4} \text{ And } \Delta_b = \frac{2B + 3B + 1B + 4B}{4} \quad (1)$$

$$\text{If } d_{z1} = d_{z2}$$

The total displacement will thus be calculated as the following:

$$\Delta_{TOT} = |\Delta_b| - |\Delta_u| \quad (2)$$

The rotations were calculated as follows, at the upper plate:

$$\theta_{zu} = \frac{1}{d_y} \left[\frac{3S + 4S}{2} - \frac{1S + 2S}{2} \right] \text{ And } \theta_{yu} = \frac{1}{d_z} \left[\frac{2S + 3S}{2} - \frac{1S + 4S}{2} \right] \quad (3)$$

$$\theta_{zb} = \frac{1}{d_y} \left[\frac{3B + 4B}{2} - \frac{1B + 2B}{2} \right] \text{ And } \theta_{yb} = \frac{1}{d_z} \left[\frac{2B + 3B}{2} - \frac{1B + 4B}{2} \right] \quad (4)$$

where 1S, 2S, 3S and 4S are the longitudinal displacements of the upper LVDTs, 1B, 2B, 3B and 4B are the displacement of the bottom LVDTs, and $d_z, d_y, d_{y1}, d_{y2}, d_{z1}$ and d_{z2} are the distances respectively between the LVDTs themselves and between the LVDTs and the centreline of the application of the load. $\theta_{zu}, \theta_{yu}, \theta_{zb}, \theta_{yb}$ are the upper and bottom rotations around y and z axes.

The values recorded with the LVDTs had to be geometrically corrected, with respect to the level of rotation reached. The corrections were quite negligible for almost all specimens where no important rotations developed, and affected most importantly the post-peak curve, where higher rotations capacities occurred.

All tests were performed in the Structural Engineering Laboratory of the University of Applied Sciences, Fribourg. The end plates and the loading plates had respectively a thickness of 20 mm and 40 mm in order to apply the loading evenly on the ends of the specimen.

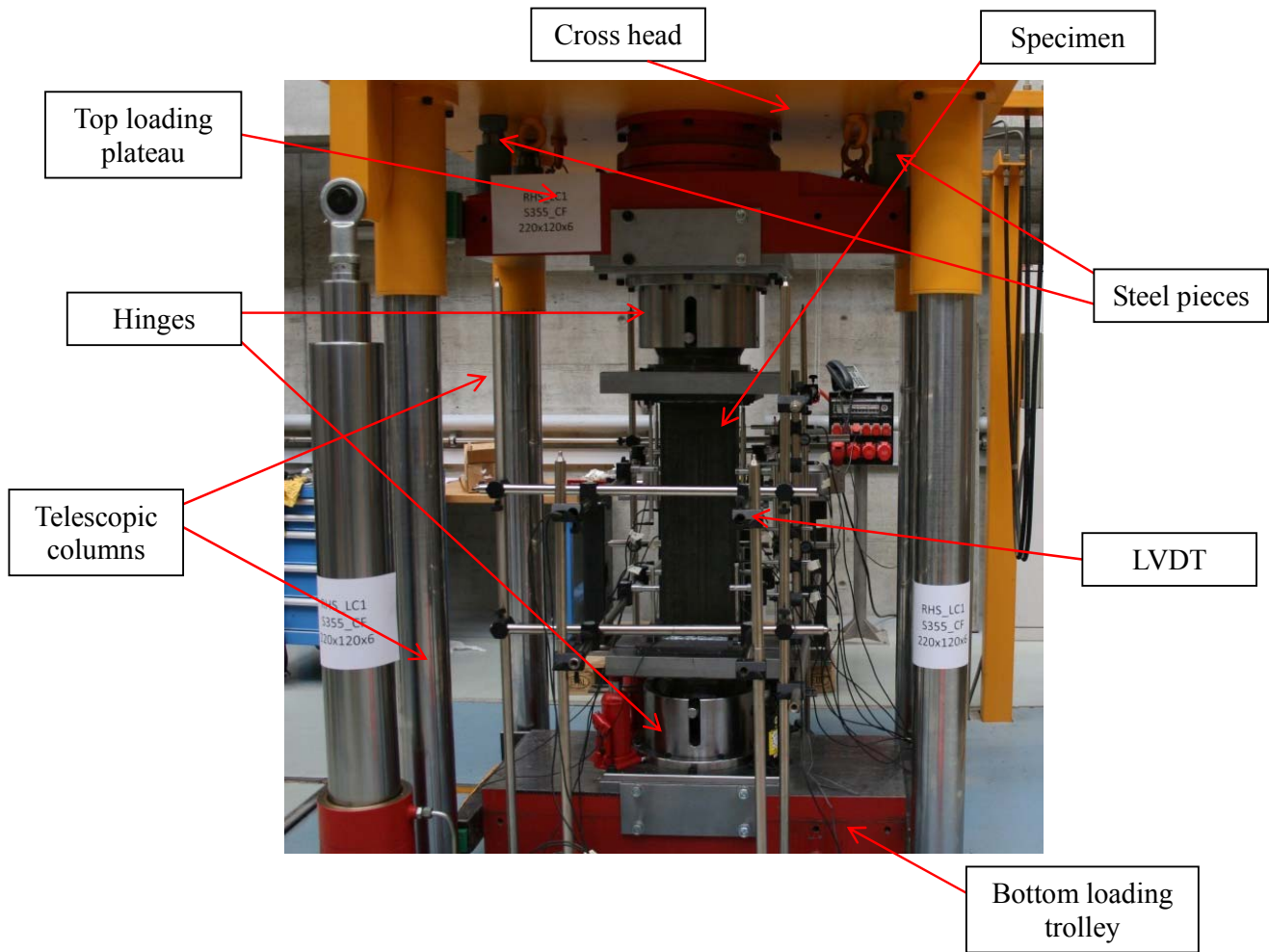


Figure 84 – General test setup of cross-section tests.

All failure modes are pictured in Figure 85. The measured maximum forces of all tested specimens are listed in Table 19.

LC1



LC2



LC3



LC4



LC5



LC6



Figure 85 – Failure shapes of all cross-section tests.

Table 19 – Comparison of numerical and experimental ultimate loads.

Test #	Specimen	Load case	e_z, e_y^* [mm]-[mm]	F_{exp} [kN]
1	RHS_LC1_S355CF_200x100x4	$N (100\%)$	0_0	773
2	RHS_LC1_S355CF_220x120x6	$N (100\%)$	0_0	1594
3	RHS_LC1_S355HF_250x150x5	$N (100\%)$	0_0	1477
4	RHS_LC1_S355HF_200x100x5	$N (100\%)$	0_0	1159
5	SHS_LC1_S355CF_200x200x5	$N (100\%)$	0_0	1300
6	SHS_LC1_S355CF_200x200x6	$N (100\%)$	0_0	1936
7	SHS_LC1_S355HF_200x200x5	$N (100\%)$	0_0	1604
8	SHS_LC1_S355HF_200x200x6.3	$N (100\%)$	0_0	2168
9	CHS_LC1_S355CF_159x6.3	$N (100\%)$	0_0	1788
10	CHS_LC1_S355HF_159x6.3	$N (100\%)$	0_0	1531
11	CHS_LC1_S355HF_159x5	$N (100\%)$	0_0	1284
12	CHS_LC1_S355HF_159x7.1	$N (100\%)$	0_0	1637
13	RHS_LC2_S355CF_200x100x4	$N (50\%) + M_y(50\%)$	60_0	597
14	RHS_LC2_S355CF_220x120x6	$N (50\%) + M_y(50\%)$	67_0	1160
15	RHS_LC2_S355HF_250x150x5	$N (50\%) + M_y(50\%)$	47_0	1063
16	RHS_LC2_S355HF_200x100x5**	$N (50\%) + M_y(50\%)$	65_0	-
17	SHS_LC2_S355CF_200x200x5	$N (50\%) + M_y(50\%)$	77_0	816
18	SHS_LC2_S355CF_200x200x6	$N (50\%) + M_y(50\%)$	72_0	1179
19	SHS_LC2_S355HF_200x200x5	$N (50\%) + M_y(50\%)$	62_0	942
20	SHS_LC2_S355HF_200x200x6.3	$N (50\%) + M_y(50\%)$	60_0	1302
21	CHS_LC2_S355CF_159x6.3	$N (50\%) + M_y(50\%)$	45_0	1060
22	CHS_LC2_S355HF_159x6.3	$N (50\%) + M_y(50\%)$	50_0	747
23	CHS_LC2_S355HF_159x5	$N (50\%) + M_y(50\%)$	41_0	725
24	CHS_LC2_S355HF_159x7.1**	$N (50\%) + M_y(50\%)$	50_0	-
25	RHS_LC3_S355CF_200x100x4	$N (33\%) + M_y (33\%) + M_z (33\%)$	63_39	420
26	RHS_LC3_S355CF_220x120x6	$N (33\%) + M_y (33\%) + M_z (33\%)$	72_40	851
27	RHS_LC3_S355HF_250x150x5	$N (33\%) + M_y (33\%) + M_z (33\%)$	82_50	623
28	RHS_LC3_S355HF_200x100x5	$N (33\%) + M_y (33\%) + M_z (33\%)$	48_25	589
29	SHS_LC3_S355CF_200x200x5	$N (33\%) + M_y (33\%) + M_z (33\%)$	62_60	771
30	SHS_LC3_S355CF_200x200x6	$N (33\%) + M_y (33\%) + M_z (33\%)$	65_65	1069
31	SHS_LC3_S355HF_200x200x5	$N (33\%) + M_y (33\%) + M_z (33\%)$	60_60	829
32	SHS_LC3_S355HF_200x200x6.3	$N (33\%) + M_y (33\%) + M_z (33\%)$	50_50	1069
33	CHS_LC3_S355CF_159x6.3	$N (33\%) + M_y (33\%) + M_z (33\%)$	50_45	893
34	CHS_LC3_S355HF_159x6.3	$N (33\%) + M_y (33\%) + M_z (33\%)$	50_50	623
35	CHS_LC3_S355HF_159x5	$N (33\%) + M_y (33\%) + M_z (33\%)$	40_40	619
36	CHS_LC3_S355HF_159x7.1	$N (33\%) + M_y (33\%) + M_z (33\%)$	50_50	705
37	2_SHS_LC1_S355CF_200x200x6	$N (100\%)$	0_0	1954
38	2_SHS_LC2_S355CF_200x200x6	$N (50\%) + M_y(50\%)$	71_0	1194
39	2_SHS_LC3_S355CF_200x200x6	$N (33\%) + M_y (33\%) + M_z (33\%)$	62_62	1076
40	RHS_LC4_S355CF_220x120x6	$N (50\%) + M_z(50\%)$	0_40	972
41	RHS_LC5_S355CF_220x120x6	$N (50\%) + M_y (25\%) + M_z(25\%)$	33_20	1182

42	RHS_LC6_S355CF_220x120x6	$N (80\%) + M_y (10\%) + M_z (10\%)$	10_6	1606
43	RHS_LC4_S355CF_200x100x4	$N (50\%) + M_z (50\%)$	0_35	471
44	RHS_LC5_S355CF_200x100x4	$N (50\%) + M_y (25\%) + M_z (25\%)$	31_19	625
45	RHS_LC6_S355CF_200x100x4	$N (80\%) + M_y (10\%) + M_z (10\%)$	6_5	763
46	RHS_Stub_S355CF_200x100x4	Stub - $N (100\%)$	0_0	761
47	RHS_Stub_S355CF_220x120x6	Stub - $N (100\%)$	0_0	1648
48	RHS_Stub_S355HF_250x150x5	Stub - $N (100\%)$	0_0	1358
49	RHS_Stub_S355HF_200x100x5	Stub - $N (100\%)$	0_0	1163
50	SHS_Stub_S355CF_200x200x5	Stub - $N (100\%)$	0_0	1296
51	SHS_Stub_S355CF_200x200x6	Stub - $N (100\%)$	0_0	1957
52	SHS_Stub_S355HF_200x200x5	Stub - $N (100\%)$	0_0	1607
53	SHS_Stub_S355HF_200x200x6.3	Stub - $N (100\%)$	0_0	2227
54	CHS_Stub_S355CF_159x6.3	Stub - $N (100\%)$	0_0	1800
55	CHS_Stub_S355HF_159x6.3	Stub - $N (100\%)$	0_0	1560
56	CHS_Stub_S355HF_159x5	Stub - $N (100\%)$	0_0	1255
57	CHS_Stub_S355HF_159x7.1	Stub - $N (100\%)$	0_0	1632

* e_z : excentricity along the z-axis, e_y : excentricity along the y-axis

** No available results recorded

3.4.2. Comparison with EC3 predictions and discussion

The experimental cross-section capacity for RHS, SHS and CHS specimens are presented in Figure 86 to Figure 93 and compared in a non-dimensional way, to EN 1993-1-1 [20] classification rules with respect to the elastic cross-section capacity. The target of such representation is avoiding a representation of each experimental test separately in different diagrams. On both axes, two limits were considered:

- (i) On the x-axis, the lower limit is the class 2-3 border (i.e. $c / t\varepsilon = 0$) and the upper limit is related to the class 3-4 border (i.e. $c / t\varepsilon = 1$)⁷;
- (ii) On the y-axis, the lower limit is related to the elastic capacity (i.e. 0) and the upper limit is related to the plastic capacity (i.e. 1.0).

Therefore, all test results can be represented within a unified single diagram. All test results are presented within four pages (SHS and RHS separated from CHS results), with upper diagrams representing the results with the nominal value of f_y (i.e. 355 MPa) and the lower

⁷ ε has been taken equal to $\sqrt{\frac{235}{f_y}}$ according to Eurocode 3 specifications [20]

diagrams with the actual measured value of f_y . Through these comparisons, the following conclusions can be drawn:

- (i) The class 2-3 border (for RHS and SHS) is hardly met and unconservative (see Figure 86 and Figure 87). The plastic capacity is not reached in many combined load cases (especially for square hollow sections). However, the presence of partly plastic capacities for sections classified as class 3 is evidenced. New boundaries and continuous transitions between elastic and plastic capacities have been already proposed in [3].
- (ii) Results with nominal f_y values are not really useful for numerical validation, but they are however showing unsafe cases (see Figure 86).
- (iii) For simple load cases (of RHS and SHS sections), the plastic capacity is barely met for two results when the actual f_y - which is much higher than the nominal f_y - value is used (see Figure 88 and Figure 89).
- (iv) As far as the results for CHS cross-section are concerned (Figure 90 to Figure 93), it can be stated that the combined load cases results with both nominal and actual values represent an unconservatism at the class 1 border, whereas the simple load cases results can be considered to fulfill the Eurocode 3 [20] requirements. This is mainly due to the unified Eurocode 3 specifications for circular sections with different load distributions. Not to mention the absence of provisions for class 4 circular sections, the cross-section specifications relative to such sections should be reviewed and modified in EN 1993-1-1 [20].

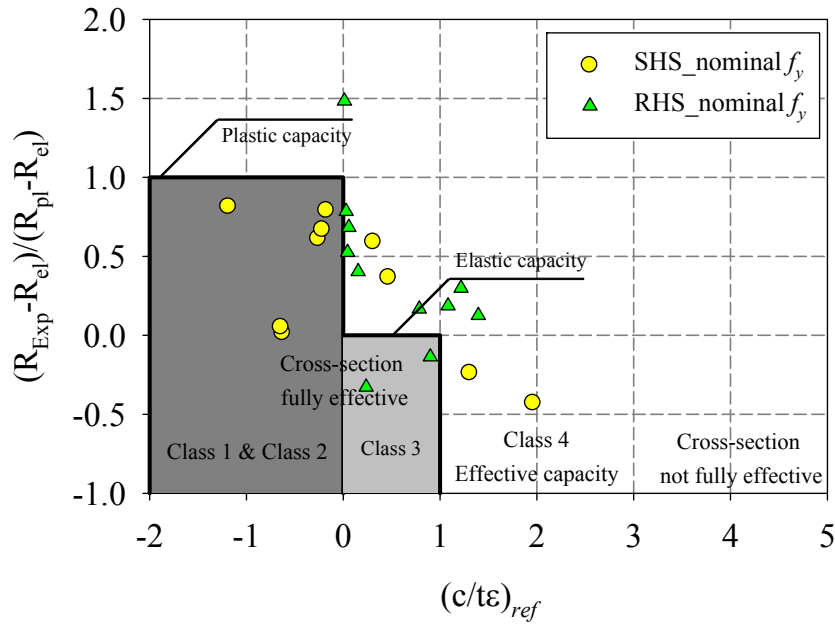


Figure 86 – Comparison of cross-section capacity of RHS and SHS experimental results with EC3- resistances – nominal f_y value – combined load cases.

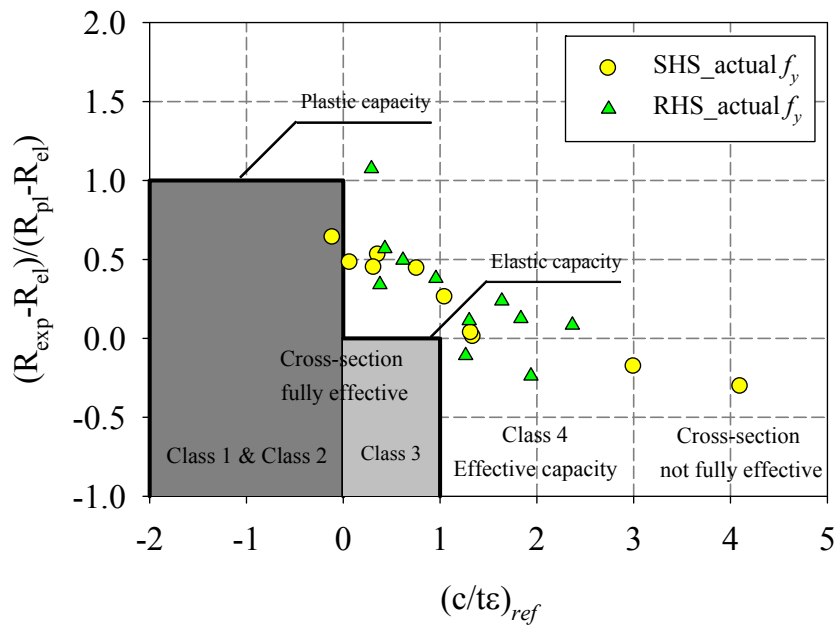


Figure 87 – Comparison of cross-section capacity of RHS and SHS experimental results with EC3- resistances – actual f_y value – combined load cases.

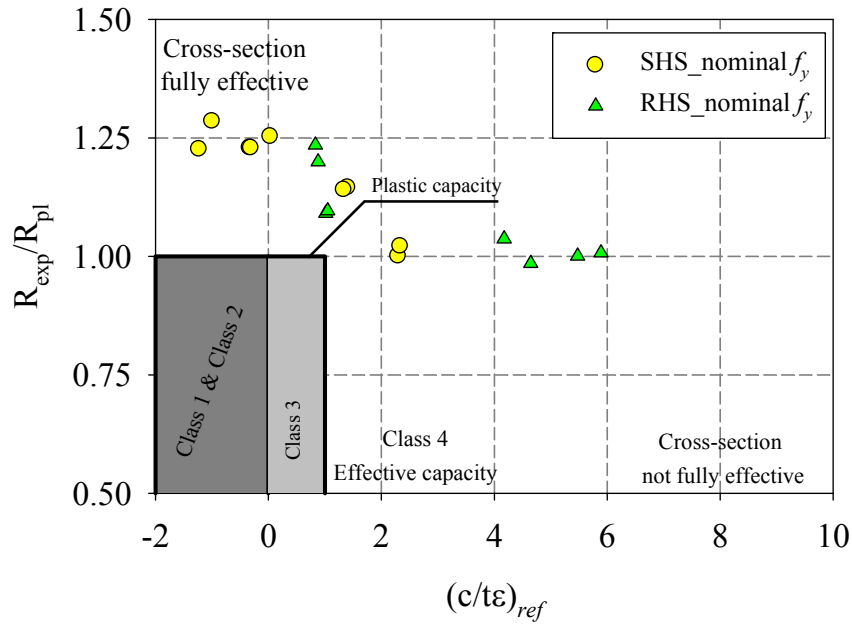


Figure 88 – Comparison of cross-section capacity of RHS and SHS experimental results with EC3- resistances – nominal f_y value – simple load cases.

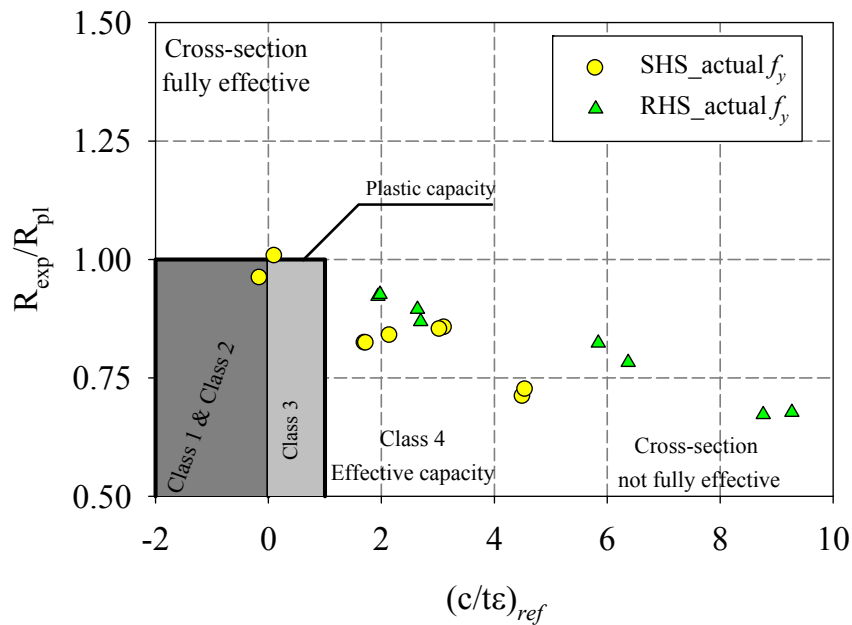


Figure 89 – Comparison of cross-section capacity of RHS and SHS experimental results with EC3- resistances – actual f_y value – simple load cases.

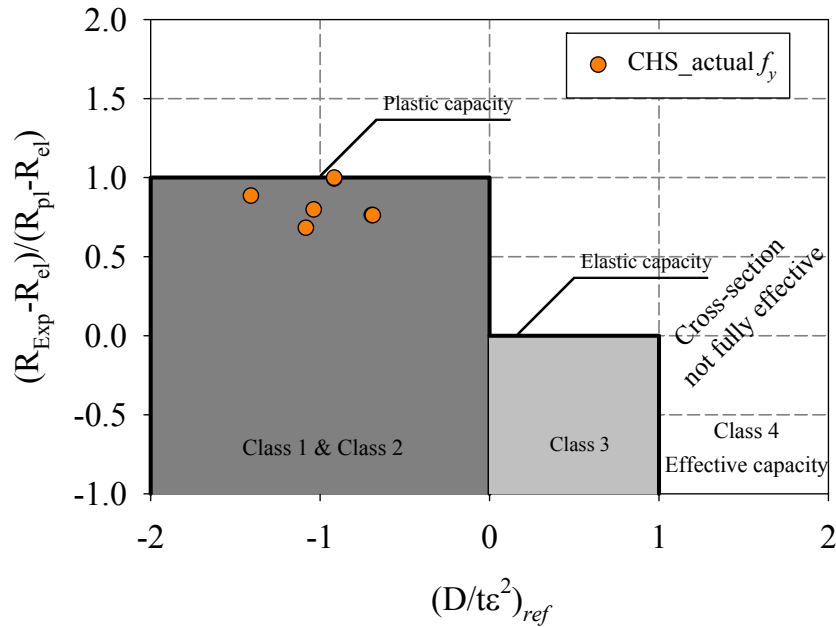


Figure 90 – Comparison of cross-section capacity of CHS experimental results with EC3-resistances – nominal f_y value – combined load cases.

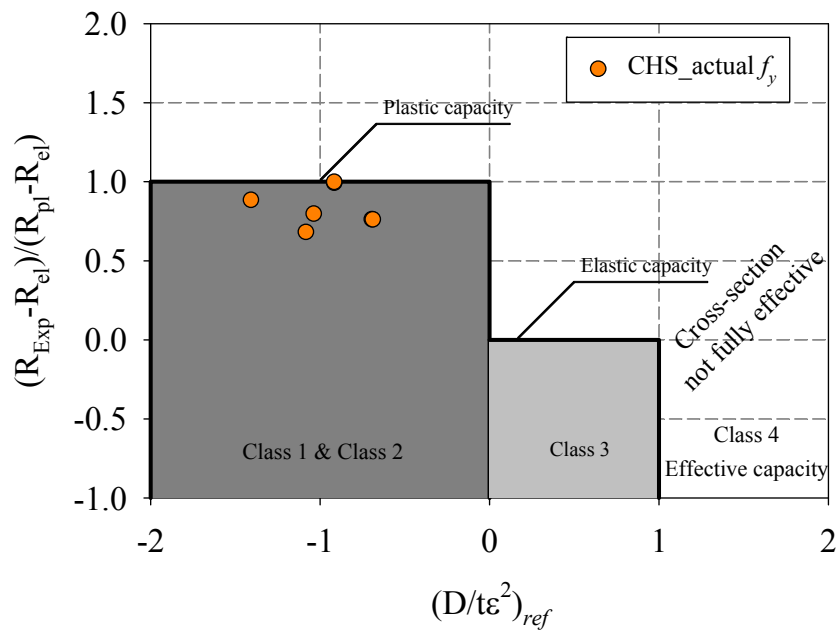


Figure 91 – Comparison of cross-section capacity of CHS experimental results with EC3-resistances – actual f_y value – combined load cases.

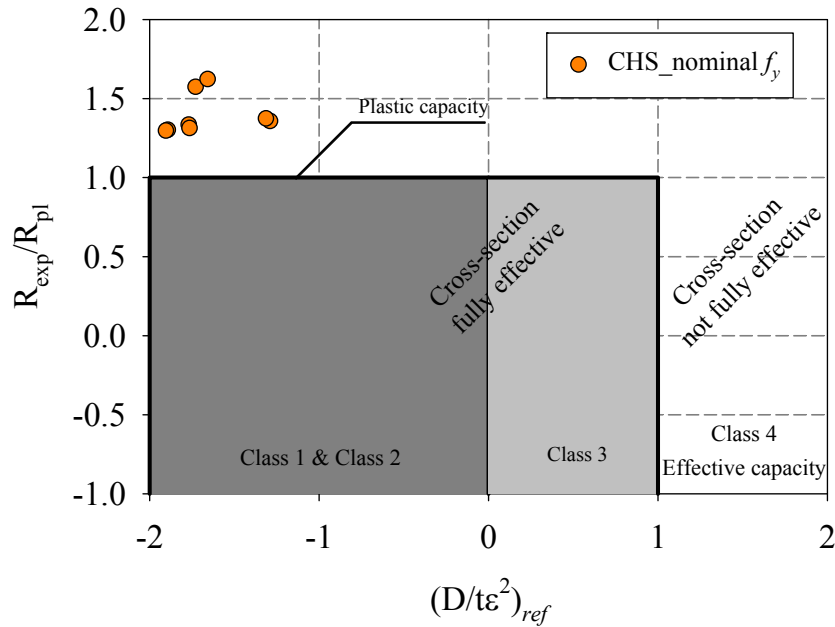


Figure 92 – Comparison of cross-section capacity of CHS experimental results with EC3-resistances – nominal f_y value – simple load cases.

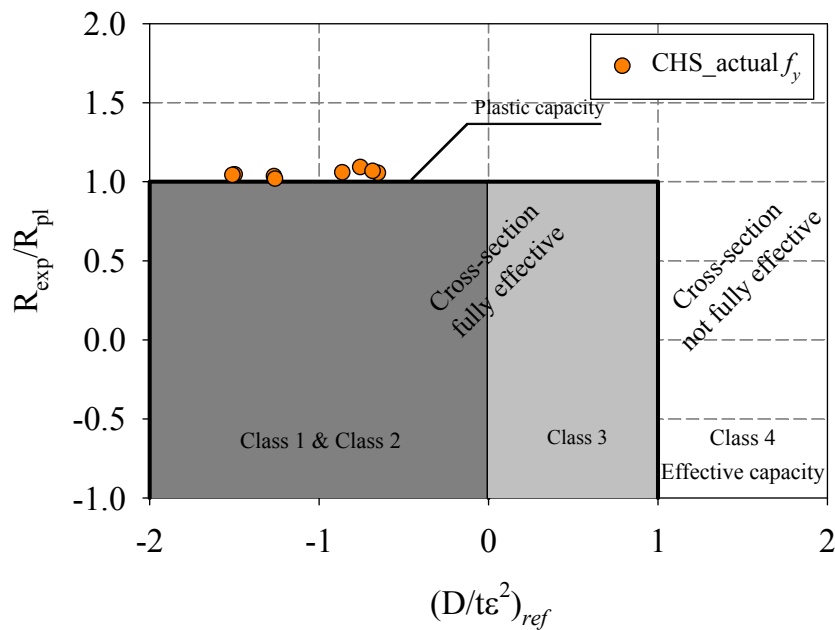


Figure 93 – Comparison of cross-section capacity of CHS experimental results with EC3-resistances – actual f_y value – simple load cases.

3.5. Collection of existing results

An extensive experimental database was collected and used in section 4.2 to compare them with the computed numerical results. The database was based upon published experimental results and the interest was in profiles with cross-sections covering the 4 classes in order to investigate all kind of capacities going from stocky to slender sections with various load combinations including simple and combined ones. The total number of gathered results reached 290. The collected test data is summarized in Table 20 along with the corresponding references. The shape, fabrication process, number of tests, load cases and measured yield strengths were provided. A dash was put for cases where no available information was provided in literature.

The results presented herein were taken from Kettler [7], Lechner [46], Stranghoner [91], Sedlacek and Rondal [92], Chiew, Lee and Shanmugan [93], Clarin [94], Salvarinas, Barber and Birkemoe [95], Usami and Fukumoto ([96] & [97]), Grimault, Plumier and Rondal [98], Kloppel, Schmied and Schubert [99], Gardner, Saari and Wang [100], Wilkinson [45], Kotelko, Lim and Rhodes [101], Key, Hasan and Hancock [102] and Zhao and Hancock [103]. The experimental results conducted in this work were also presented.

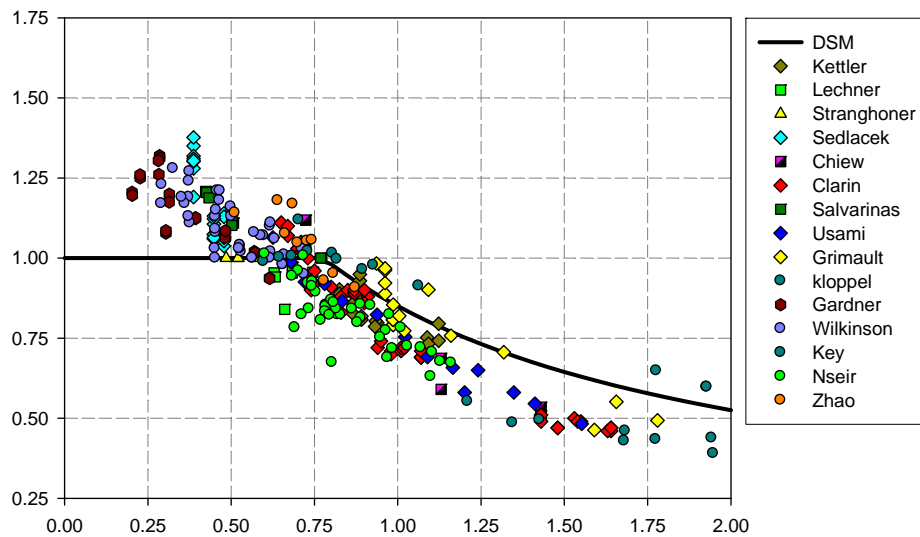


Figure 94 – Gathered results and comparison with DSM curve.

The results in Figure 94 to Figure 97 are presented in the OIC format, i.e. the horizontal axis relates to the generalized slenderness λ_{CS} while the vertical axis reports on the cross-section

reduction factor χ_{CS} . The DSM curve is also plotted for comparison and reference purposes with experimental results. Figure 94 shows results relative to all load cases while Figure 95, Figure 96 and Figure 97 show results respectively relative to pure compression load cases, major-axis bending load cases and combined load cases. For each load case, cold-formed test results were separated from hot-rolled hot-formed and hot-finished test results. This was seen as the most appropriate way of representing the gathered data in a categorized way.

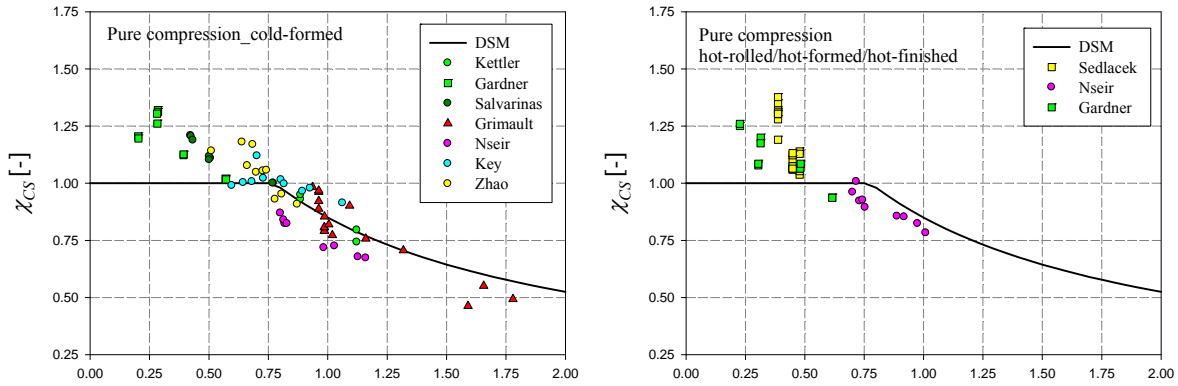


Figure 95 – Experimental results relative to pure compression load cases, a) cold-formed cross-sections, b) hot-rolled and hot-formed cross-sections.

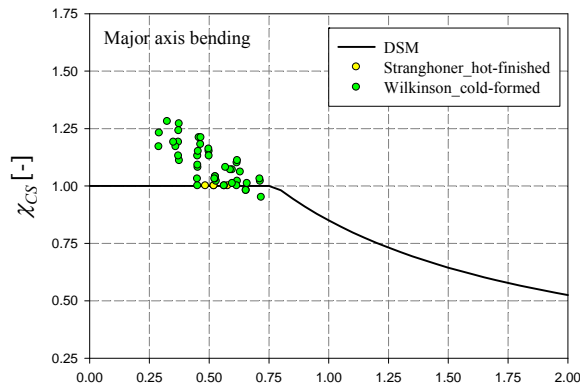


Figure 96 – Experimental results relative to major-axis bending load cases.

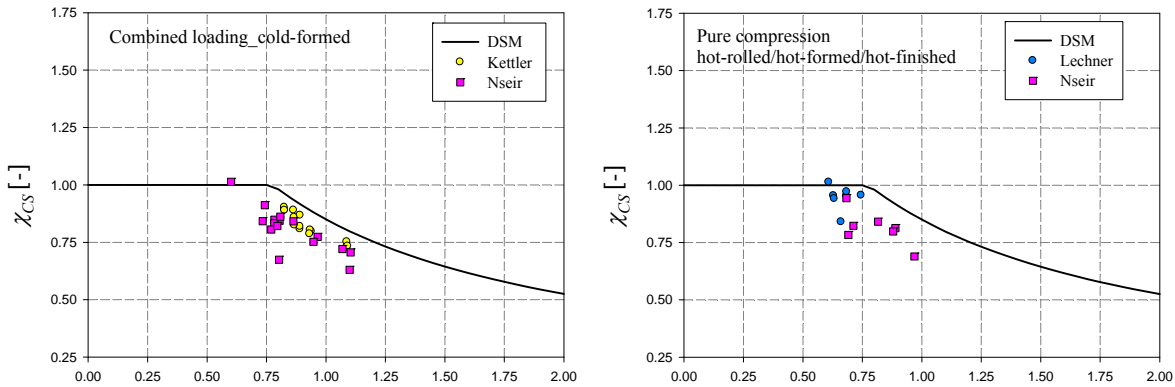


Figure 97 – Experimental results relative to combined load cases, a) cold-formed cross-sections, b) hot-rolled and hot-formed cross-sections.

All types of results presented with the various load cases can clearly show a general tendency and design curves can surely be derived for hollow sections. The following conclusions can be drawn from the upper figures:

- (i) The DSM curve utilized mainly for cold-formed thin-walled open sections is seen to be unconservative and cannot be applied for hollow sections. This is clearly seen in all figures in which results lie below the DSM curve.
- (ii) Strain hardening tendencies are seen with almost all types of load cases and should be accounted for in the new proposed design curves.
- (iii) An appropriate end of plateau value is required since the DSM proposed value for thin-walled – mostly open – cold-formed cross-sections is seen to be unconservative.
- (iv) A design approach taking into account appropriate post-buckling capacities should be derived for the various types of load cases;

Table 20 – Summary of the gathered test data.

Source	Shape	Fabrication process*	Number of tests	Load case	f_y [MPa] (measured)*
Kettler [7]	SHS	Cold-Formed	3	$N + M_y$	400
		Cold-Formed	6	$N + M_y + M_z$	400
		Cold-Formed	2	N	400
	RHS	Cold-Formed	6	$N + M_y + M_z$	398

		Cold-Formed	2	N	398
Lechner [46]	SHS	Hot-Finished	1	$N + M_y$	540
		Hot-Finished	6	$N + M_y + M_z$	359, 540
Stranghoner [91]	SHS	Hot-Finished	4	M_y	-
Sedlacek and Rondal [92]	RHS	Hot-formed	15	N	465 to 693
	SHS	Hot-formed	8	N	538
Chiew, Lee and Shanmugan [93]	Box-sections	-	6	N	-
Clarín [94]	Box-sections	-	48	N	Unknown
Salvarinas, Barber and Birkemoe [95]	CF	Cold-formed	8	N	411 to 444
Usami and Fukumoto [96]&[97]	Box-sections	-	14	N	High strength
Grimault, Plumier and Rondal [98]	RHS	Cold-formed	16	N	270 to 481
	SHS	Cold-formed	2	N	436, 480
Kloppel, Schmied and Schubert [99]	SHS,RHS	-	27	$N, N + M_y$	-
Gardner, Saari and Wang [100]	RHS,SHS	Cold-formed	10	N	361 to 482
		Hot-rolled	10	N	449 to 504
Wilkinson [45]	RHS,SHS	Cold-formed	44	M_y	349 to 457
Kotelko, Lim and Rhodes [101]	RHS	Cold-formed	6	M_y	-
Key, Hasan and Hancock [102]	RHS	Cold-formed	6	N	-
	SHS	Cold-formed	4	N	-
Zhao and Hancock [103]	RHS	Cold-formed	7	N	448 to 452
	SHS	Cold-formed	3	N	435 to 490
Nseir	RHS	Hot-finished	4	N	420, 447
	RHS	Hot-finished	1	$N + M_y$	447
	RHS	Hot-finished	2	$N + M_y + M_z$	420, 447
	RHS	Cold-formed	4	N	455, 495
	RHS	Cold-formed	2	$N + M_y$	455, 495

	RHS	Cold-formed	2	$N + M_z$	455, 495
	RHS	Cold-formed	6	$N + M_y + M_z$	455, 495
	SHS	Hot-finished	4	N	453, 475
	SHS	Hot-finished	2	$N + M_y$	453, 475
	SHS	Hot-finished	2	$N + M_y + M_z$	453, 475
	SHS	Cold-formed	5	N	480, 501
	SHS	Cold-formed	3	$N + M_y$	480, 501
	SHS	Cold-formed	3	$N + M_y + M_z$	480, 501

*a dash was put for cases where no available information was provided in literature.

3.6. Summary

In this section, a wide experimental campaign was presented. It consisted of 57 cross-section tests subjected to various load cases. A series of preliminary measurements was described and presented in this section. They consisted in the measurements of the geometrical dimensions and imperfections, the material law determination, the measurements of the residual stresses and the testing of stub columns. Then, the cross-section test results were investigated and compared to the existing design formulae of EN 1993-1-1. It turned out that Eurocodes plate slenderness limits were in some cases inappropriate leading to unconservative results. Finally, an experimental collected database was presented and consisted in various cross-section test results with various load cases, fabrication processes and yield strengths. Observations could be deduced from the collected database which would be used in the next chapter for a comparison with numerical parametric results.

In the next section finite element validation will be presented to continue with the conducted numerical parametrical studies on hot-rolled and cold-formed sections, used subsequently as a database for the derivation of adequate OIC interaction curves.

4. Numerical investigations

4.1. General

This chapter describes the development and validation of finite elements models. It provides detailed information on the boundary conditions, loading procedure, modeling of the measured material laws, residual stresses, geometrical dimensions and imperfections. The results of the FE computations and the experimental results are compared and the validation procedure is provided for the 55 tests of this thesis as well as for the 22 hollow cross-section tests done in Graz Technical University [7].

This finite element model is further used to generate an extensive set of numerical results to investigate deeply the structural behavior of cross-sections belonging to all classes defined according to the Eurocode 3 classification system, i.e. from plastic to slender sections [20]. The numerical study concerns hot-rolled and cold-formed sections having nominal geometrical dimensions and various parameters with the target of capturing their physical behavior. In view of further mechanical analyses, the parameters were chosen in order to cover all four classes' ranges with different load cases going from simple to combined ones. These numerical computations, carried by means of the finite element software FINELg, provided a basis for the generation of several design curves.

4.2. Validation against test results

4.2.1. UAS Western Switzerland Fribourg campaign

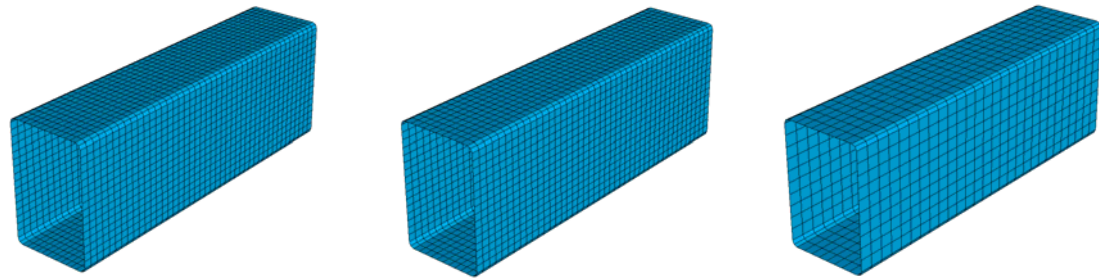
4.2.1.1. Numerical model – Features and characteristics

4.2.1.1.1. Elements and meshing

To select proper FE meshes that provide accurate results with minimum computational effort, five different mesh configurations were considered as shown in Figure 98. The main aim of this study is to choose an adequate mesh capable of providing a good approximation of local buckling. The cross-sections were modeled with the use of quadrangular 4-nodes plate-shell finite elements with typical features (corotational total Lagrangian formulation, Kirchhoff's theory for bending). The corners of square and rectangular profiles were modeled with 2 linear shell elements per corner.

The selected mesh densities span from fine to coarse. While elastic buckling analysis is usually used to test the mesh adequacy, both GMNIA and LBA analysis were performed in this study.

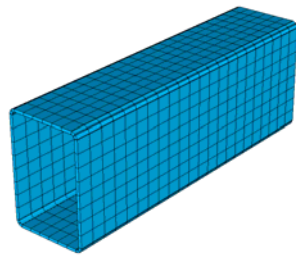
Several rectangular and square cross-sections were analyzed, each type consisting of different dimensions and thickness. Two different load cases were considered: compression and major-axis bending. In Figure 99, LBA results are presented on the left column and GMNIA results on the right column. R_{STAB} corresponds to the critical buckling load amplification factor and R_{ULT} represents the ultimate load amplification factor. It can be seen that the difference between all the corresponding meshes is not pronounced. The main concern is here to accurately simulate the collapse mechanism, which is known to be quite sensitive to the mesh refinement. In other words, the post-peak branches provided by the different meshing types will differ depending on how fine the mesh is. The plastic mechanisms occurring in relatively short lengths require a fine mesh capable of accurately representing the development of yield lines, thus providing a more accurate result. In a coarse mesh, the elements are not small enough to accurately represent the development of plastic strains, resulting in an overly-stiff failure mechanism. For some cases, type VI and type V mesh were seen to lead to the highest differences compared to other meshes. Type III mesh generally indicated a similar numerical result compared to the more refined types I and II, and was seen to provide accurate representations in terms of peak load and yield development; hence, no further mesh refinement was deemed necessary. Even though all types I, II, and III could provide a good prediction of the ultimate load, type III meshing was selected as it provides sufficient compromise between satisfactory accuracy and minimum computational time.



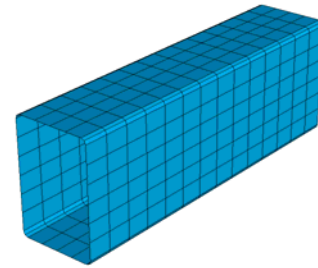
Type I

Type II

Type III

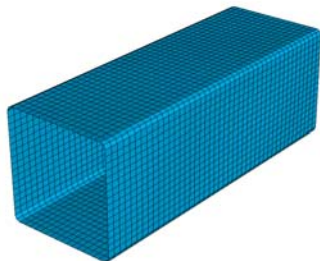


Type IV

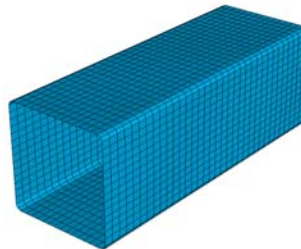


Type V

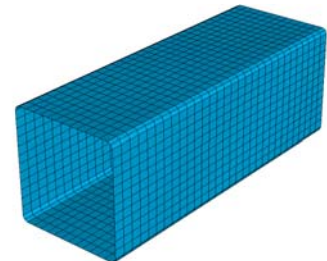
Rectangular sections



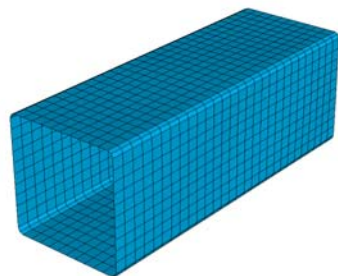
Type I



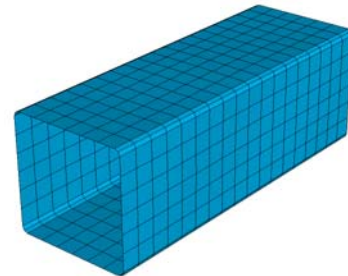
Type II



Type III



Type IV



Type V

Square sections

Figure 98– Mesh configurations.

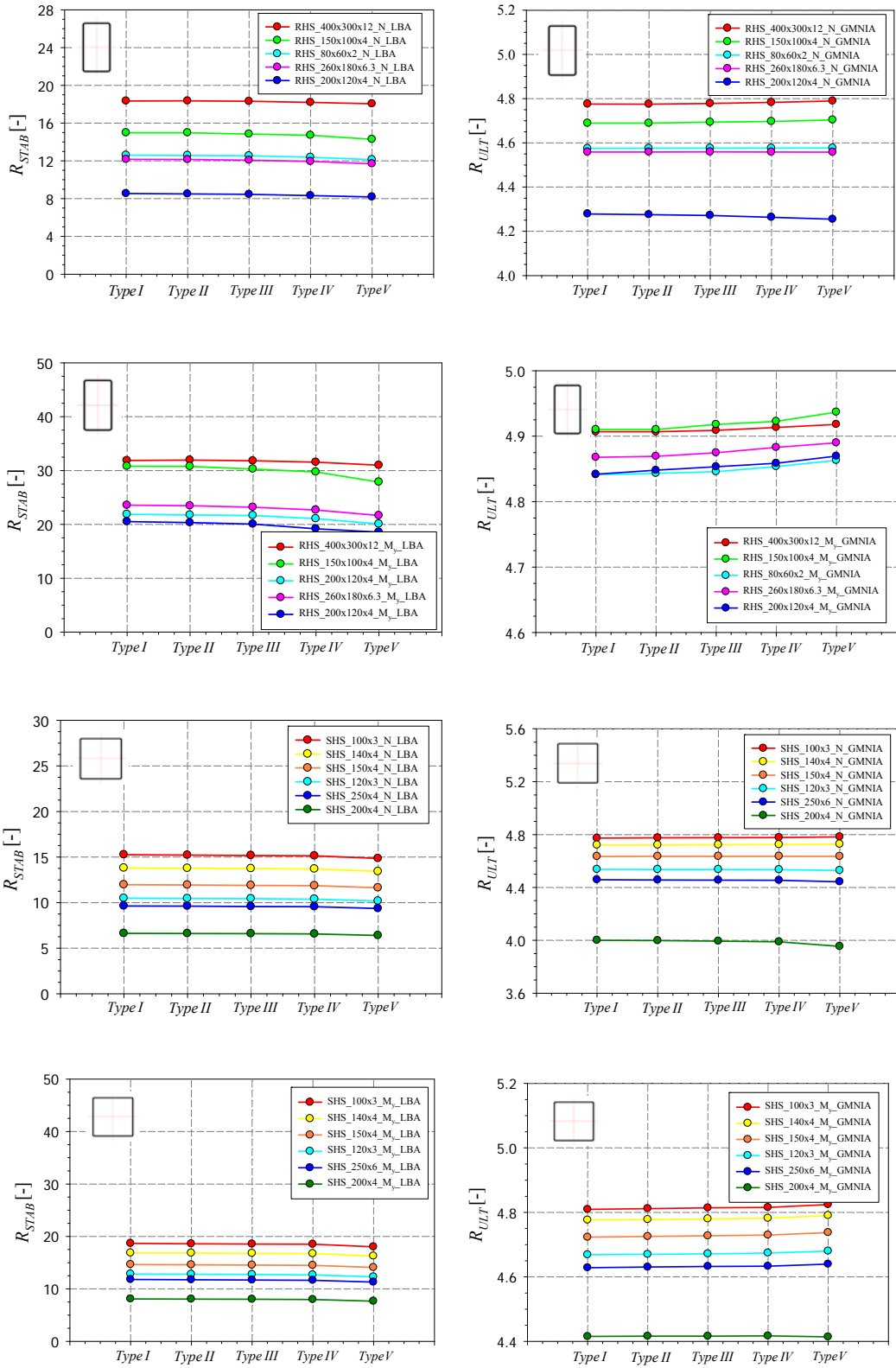


Figure 99 – LBA (left) and GMNIA (right) results for SHS and RHS sections.

4.2.1.1.2. Loading and support conditions

In order to represent accurately the experimental behavior of the specimens, a suitable corresponding FE model had to be developed. The endplates were represented through rigid plates having an equivalent thickness of 80 mm and modeled with shell elements that remain elastic during loading. The plates' stiffness allowed an even distribution of the applied load at the ends of the sections and prevented any cross-sectional deformation at both ends while allowing free rotations. As for the behavior of the hinges, truss elements were used to simulate the assumed-rigid spherical hinges at both ends. All trusses were connected to the rigid end plates nodes and to the centroid of the hinge (see Figure 100). The load was applied at the center of rotation of the hinge, and the cases of combined loads with compression were represented through an axial load applied at the centroid of the hinge with the corresponding measured eccentricities of the cross-section tests (see Figure 101).

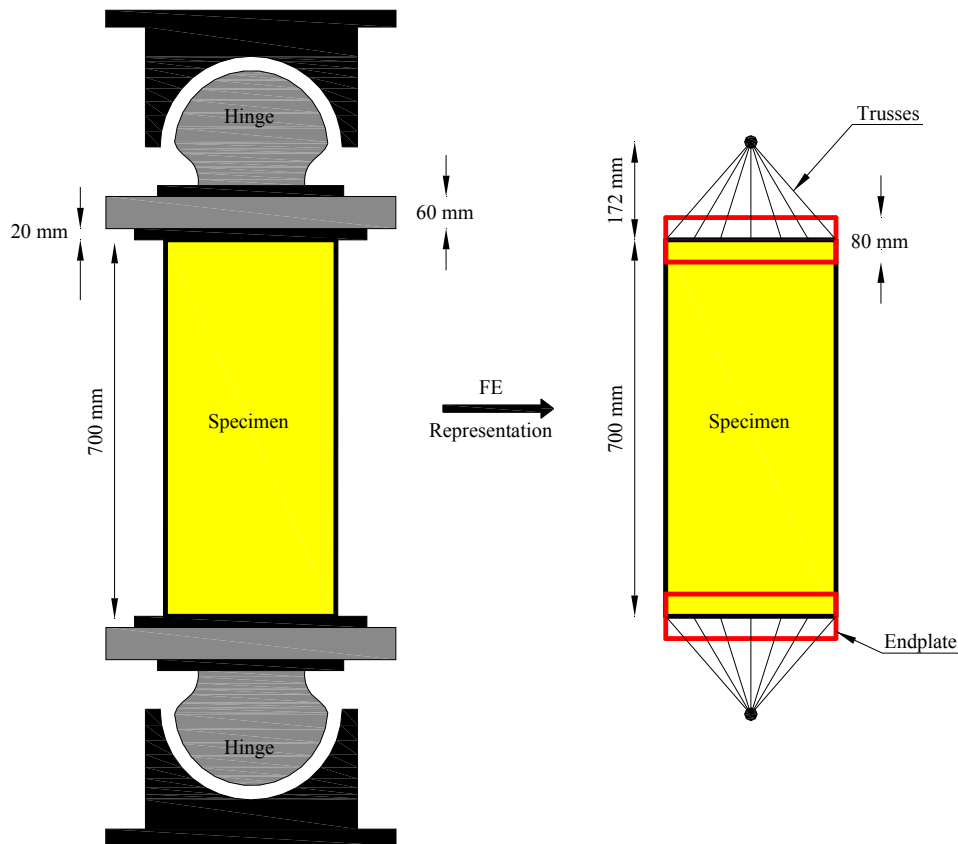


Figure 100 – Finite element model assumptions.

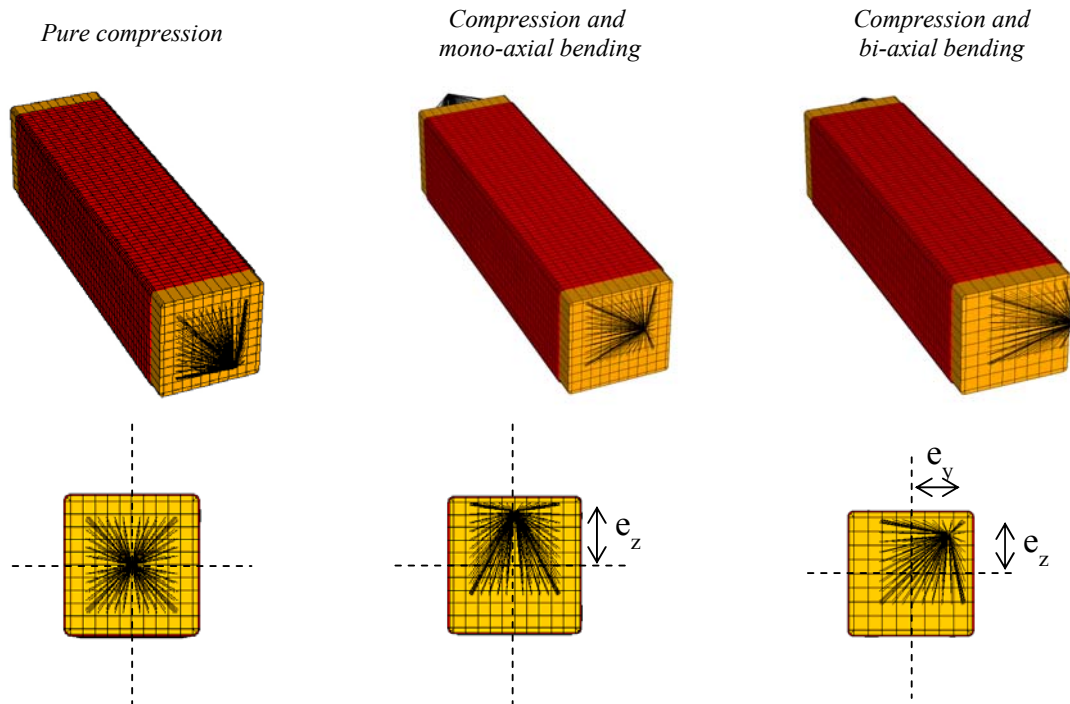


Figure 101 – Applied load with shifted truss center corresponding to different load cases.

Series of numerical computations have been performed with the use of non-linear finite element software FINELg, continuously developed at the University of Liège and Greisch Engineering Office since 1970 [104]. This software offers almost all types of FEM types of analyses, and present investigations have mainly been resorting to so-called MNA (Materially Non-linear Analysis), LBA (Local Buckling Analysis) and GMNIA (Geometrically and Materially Nonlinear Analysis with Imperfections) analyses. The cross-sections were modelled with the use of the QSCRA element, a quadrangular 4-nodes plate-shell finite element with typical features (corotational total Lagrangian formulation, Kirchhoff's theory for bending). The corners of square and rectangular profiles were modeled with 4 linear shell elements per corner (see Figure 102).

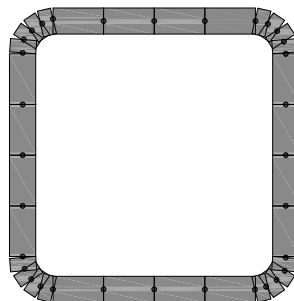


Figure 102 – Detail view of the corner modeling.

4.2.1.1.3. Material modeling and residual stresses

Averaged measured geometrical dimensions were used in the numerical calculations together with measured local imperfections for each specimen (see Annex 5 and Annex 6). Measured membrane stresses were introduced for the hot-finished profiles, whereas both measured flexural and membrane residual stresses were introduced for cold-formed profiles. As for the circular hot-rolled profiles, only flexural residual stresses were introduced. Figure 103 displays an example of the adopted measured membrane stresses for specimen SHS_HF_200x200x6.3.

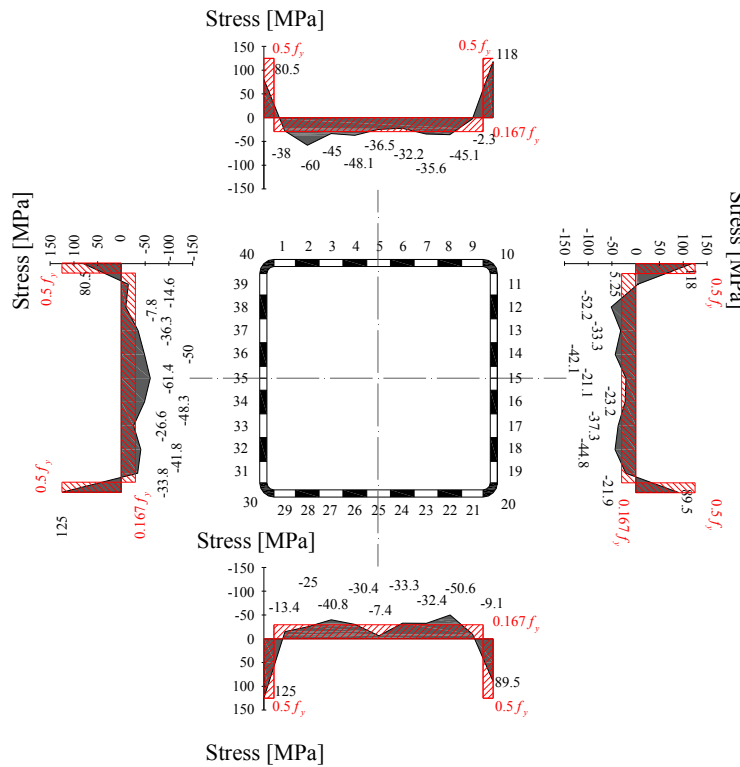


Figure 103 – Adopted measured membrane stresses for section SHS_HF_200_200_6.3.

Measured material stress-strain behavior including strain-hardening effects was also included. For the cold-formed tubular profiles, two material laws have been defined; one for the base material and one for the corner regions. Ramberg-Osgood material law was used for the flat regions while a multi-linear law was adopted for the corners region, since a simple Ramberg-Osgood was not suitable (see Figure 104).

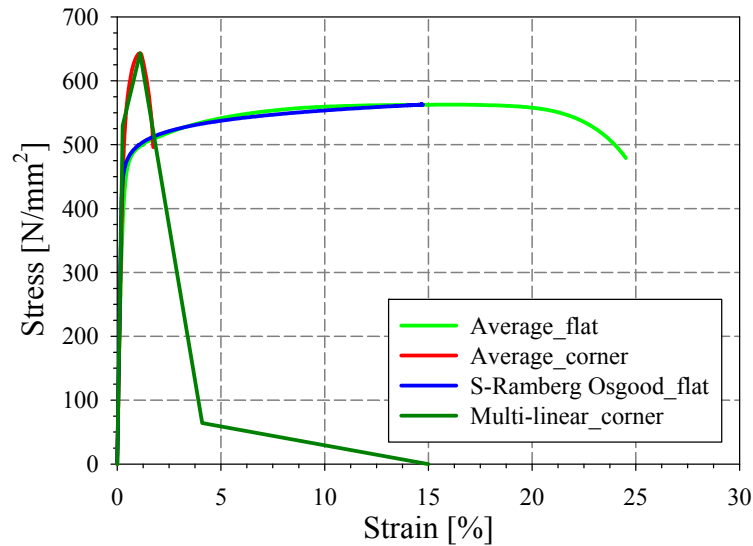


Figure 104 – Material stress strain laws adopted in FE calculations for specimens
RHS_220x120x6_CF.

For cases in which the corner coupon test results were inconsistent with an ultimate stress smaller than the one of the flat face, a multi-linear law was set for such cases using the following equations (see Figure 105):

$$f_{y_corner} = 1.15 f_{y_flat} \quad (5)$$

$$f_{u_corner} = 1.15 f_{u_flat} \quad (6)$$

The factor 1.15 was adopted on the basis of statistical studies on material laws from literature, and shown to be convenient. Accordingly, higher yield strength in the cold-formed corner regions was taken into account.

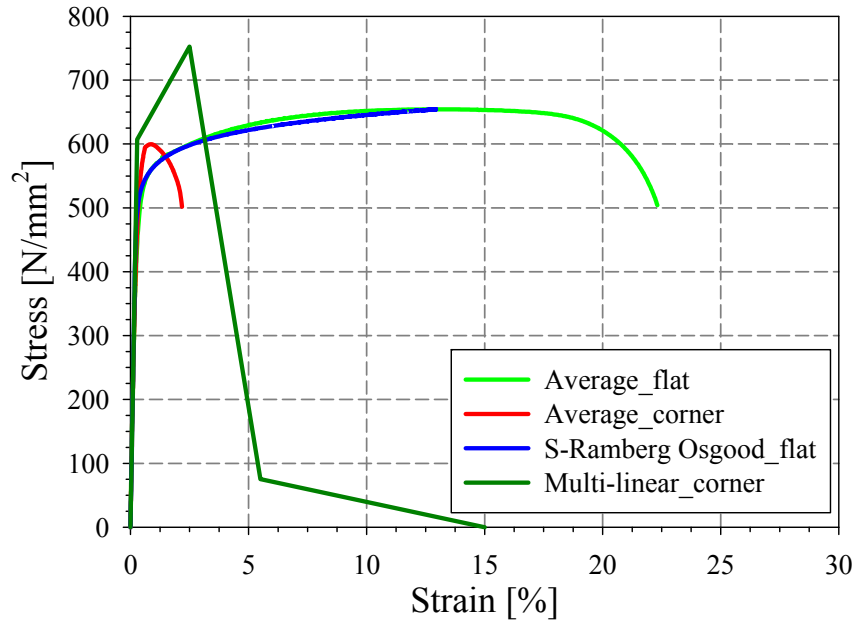


Figure 105 – Material stress strain laws adopted in FE calculations for specimens
RHS_200x100x4_CF.

4.2.1.2. Validation: FE results vs. test results

The experimental cross-section capacities reached by the tested specimens were compared to the numerically-predicted ones. The ultimate loads and the ratio of the experimental ultimate loads to their numerical counterparts are given for the tested cross-sections in Table 19 (stubs, LC1, LC2, LC3, LC4, LC5 and LC6). As previously mentioned, all numerical simulations of the specimens were based on actual cross-sectional dimensions and on actual material properties.

Numerical simulations represented the real behavior quite accurately (see Table 21). A graphical comparison of the ultimate loads of the FE simulations and of the experiments is shown in Figure 106 in which the red lines indicate a deviation of +/- 10%.

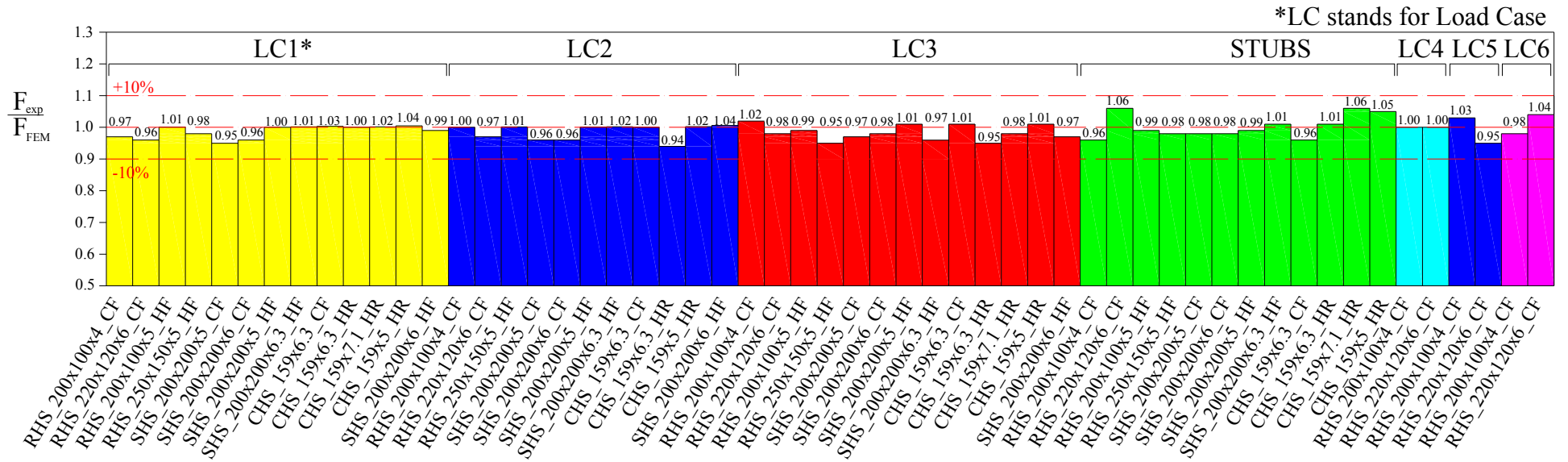


Figure 106 – FE peak loads vs. experimental loads.

It can be seen that all numerical simulations provide ultimate loads in excellent accordance with the test results. All values oscillate very closely to the $F_{exp} / F_{FEM} = 1.0$ ideal line, which indicates a very good accordance between test and numerical results.

Figure 107 and Figure 108 provide representative examples of experimental and numerical load-displacement curves. The differences in initial stiffness, ultimate load and post-peak behavior between numerical and experimental results are mainly caused by non-explicitly modeled sources, such as a little friction in the hinges (i.e. the boundary conditions are never as clean as in the computational model and are far more complicated than assumed in the numerical model⁸), inconsistencies in the imperfections measurements and unexpected eccentricities. The complete test setup stiffness was also not modeled. Since a maximum deviation of 6% among all F_{exp} / F_{FEM} values is reported, the ability of the numerical model to accurately predict the failure load is obvious. However, the initial stiffness and post-peak behavior showed larger discrepancies between numerical and experimental results, which can be attributed to previously mentioned numerical modeling issues.

⁸ The numerical model is assumed to be free from any friction in the hinges – preliminary measurements showed that friction could be neglected.

Table 21 – Comparison of numerical and experimental ultimate loads.

Test #	Specimen	Load case	e_z, e_y^* [mm]- [mm]	F_{exp} [kN]	F_{FEM} [kN]	F_{exp}/F_{FEM} [-]
1	RHS_LC1_S355CF_200x100x4	$N (100\%)$	0_0	773	796	0.97
2	RHS_LC1_S355CF_220x120x6	$N (100\%)$	0_0	1594	1651	0.96
3	RHS_LC1_S355HF_250x150x5	$N (100\%)$	0_0	1477	1499	0.98
4	RHS_LC1_S355HF_200x100x5	$N (100\%)$	0_0	1159	1143	1.01
5	SHS_LC1_S355CF_200x200x5	$N (100\%)$	0_0	1300	1307	0.99
6	SHS_LC1_S355CF_200x200x6	$N (100\%)$	0_0	1936	1967	0.98
7	SHS_LC1_S355HF_200x200x5	$N (100\%)$	0_0	1604	1603	1.00
8	SHS_LC1_S355HF_200x200x6.3	$N (100\%)$	0_0	2168	2141	1.01
9	CHS_LC1_S355CF_159x6.3	$N (100\%)$	0_0	1788	1727	1.03
10	CHS_LC1_S355HF_159x6.3	$N (100\%)$	0_0	1531	1519	1.00
11	CHS_LC1_S355HF_159x5	$N (100\%)$	0_0	1284	1228	1.04
12	CHS_LC1_S355HF_159x7.1	$N (100\%)$	0_0	1637	1597	1.02
13	RHS_LC2_S355CF_200x100x4	$N (50\%) + M_y (50\%)$	60_0	597	595	1.00
14	RHS_LC2_S355CF_220x120x6	$N (50\%) + M_y (50\%)$	67_0	1160	1141	1.01
15	RHS_LC2_S355HF_250x150x5	$N (50\%) + M_y (50\%)$	47_0	1063	1052	1.01
16	RHS_LC2_S355HF_200x100x5**	$N (50\%) + M_y (50\%)$	65_0	-	-	-
17	SHS_LC2_S355CF_200x200x5	$N (50\%) + M_y (50\%)$	77_0	816	848	0.96
18	SHS_LC2_S355CF_200x200x6	$N (50\%) + M_y (50\%)$	72_0	1179	1218	0.96
19	SHS_LC2_S355HF_200x200x5	$N (50\%) + M_y (50\%)$	62_0	942	932	1.01
20	SHS_LC2_S355HF_200x200x6.3	$N (50\%) + M_y (50\%)$	60_0	1302	1272	1.02
21	CHS_LC2_S355CF_159x6.3	$N (50\%) + M_y (50\%)$	45_0	1060	1056	1.00
22	CHS_LC2_S355HF_159x6.3	$N (50\%) + M_y (50\%)$	50_0	747	787	0.94
23	CHS_LC2_S355HF_159x5	$N (50\%) + M_y (50\%)$	41_0	725	705	1.02
24	CHS_LC2_S355HF_159x7.1**	$N (50\%) + M_y (50\%)$	50_0	-	-	-
25	RHS_LC3_S355CF_200x100x4	$N (33\%) + M_y (33\%) + M_z (33\%)$	63_39	420	408	1.02
26	RHS_LC3_S355CF_220x120x6	$N (33\%) + M_y (33\%) + M_z (33\%)$	72_40	851	861	0.98
27	RHS_LC3_S355HF_250x150x5	$N (33\%) + M_y (33\%) + M_z (33\%)$	82_50	623	630	0.98
28	RHS_LC3_S355HF_200x100x5	$N (33\%) + M_y (33\%) + M_z (33\%)$	48_25	589	606	0.97
29	SHS_LC3_S355CF_200x200x5	$N (33\%) + M_y (33\%) + M_z (33\%)$	62_60	771	792	0.97
30	SHS_LC3_S355CF_200x200x6	$N (33\%) + M_y (33\%) + M_z (33\%)$	65_65	1069	1082	0.98
31	SHS_LC3_S355HF_200x200x5	$N (33\%) + M_y (33\%) + M_z (33\%)$	60_60	829	812	1.01
32	SHS_LC3_S355HF_200x200x6.3	$N (33\%) + M_y (33\%) + M_z (33\%)$	50_50	1069	1078	0.98
33	CHS_LC3_S355CF_159x6.3	$N (33\%) + M_y (33\%) + M_z (33\%)$	50_45	893	881	1.01
34	CHS_LC3_S355HF_159x6.3	$N (33\%) + M_y (33\%) + M_z (33\%)$	50_50	623	653	0.95
35	CHS_LC3_S355HF_159x5	$N (33\%) + M_y (33\%) + M_z (33\%)$	40_40	619	610	1.01
36	CHS_LC3_S355HF_159x7.1	$N (33\%) + M_y (33\%) + M_z (33\%)$	50_50	705	717	0.98
37	2_SHS_LC1_S355CF_200x200x6	$N (100\%)$	0_0	1954	1974	0.99
38	2_SHS_LC2_S355CF_200x200x6	$N (50\%) + M_y (50\%)$	71_0	1194	1143	1.04
39	2_SHS_LC3_S355CF_200x200x6	$N (33\%) + M_y (33\%) + M_z (33\%)$	62_62	1076	1102	0.97
40	RHS_LC4_S355CF_220x120x6	$N (50\%) + M_z (50\%)$	0_40	972	970	1.00

41	RHS_LC5_S355CF_220x120x6	$N (50\%) + M_y (25\%) + M_z (25\%)$	33_20	1182	1231	0.96
42	RHS_LC6_S355CF_220x120x6	$N (80\%) + M_y (10\%) + M_z (10\%)$	10_6	1606	1581	1.01
43	RHS_LC4_S355CF_200x100x4	$N (50\%) + M_z (50\%)$	0_35	471	470	1.00
44	RHS_LC5_S355CF_200x100x4	$N (50\%) + M_y (25\%) + M_z (25\%)$	31_19	625	605	1.03
45	RHS_LC6_S355CF_200x100x4	$N (80\%) + M_y (10\%) + M_z (10\%)$	6_5	763	769	0.99
46	RHS_Stub_S355CF_200x100x4	Stub - $N (100\%)$	0_0	761	788	0.96
47	RHS_Stub_S355CF_220x120x6	Stub - $N (100\%)$	0_0	1648	1546	1.06
48	RHS_Stub_S355HF_250x150x5	Stub - $N (100\%)$	0_0	1358	1380	0.98
49	RHS_Stub_S355HF_200x100x5	Stub - $N (100\%)$	0_0	1163	1164	0.99
50	SHS_Stub_S355CF_200x200x5	Stub - $N (100\%)$	0_0	1296	1350	0.96
51	SHS_Stub_S355CF_200x200x6	Stub - $N (100\%)$	0_0	1957	2002	0.97
52	SHS_Stub_S355HF_200x200x5	Stub - $N (100\%)$	0_0	1607	1615	0.99
53	SHS_Stub_S355HF_200x200x6.3	Stub - $N (100\%)$	0_0	2227	2194	1.01
54	CHS_Stub_S355CF_159x6.3	Stub - $N (100\%)$	0_0	1800	1872	0.96
55	CHS_Stub_S355HF_159x6.3	Stub - $N (100\%)$	0_0	1560	1543	1.01
56	CHS_Stub_S355HF_159x5	Stub - $N (100\%)$	0_0	1255	1187	1.05
57	CHS_Stub_S355HF_159x7.1	Stub - $N (100\%)$	0_0	1632	1538	1.06

* e_y represents the adopted eccentricity along y-y axis, e_z is the adopted eccentricity along z-z axis

** No available results recorded

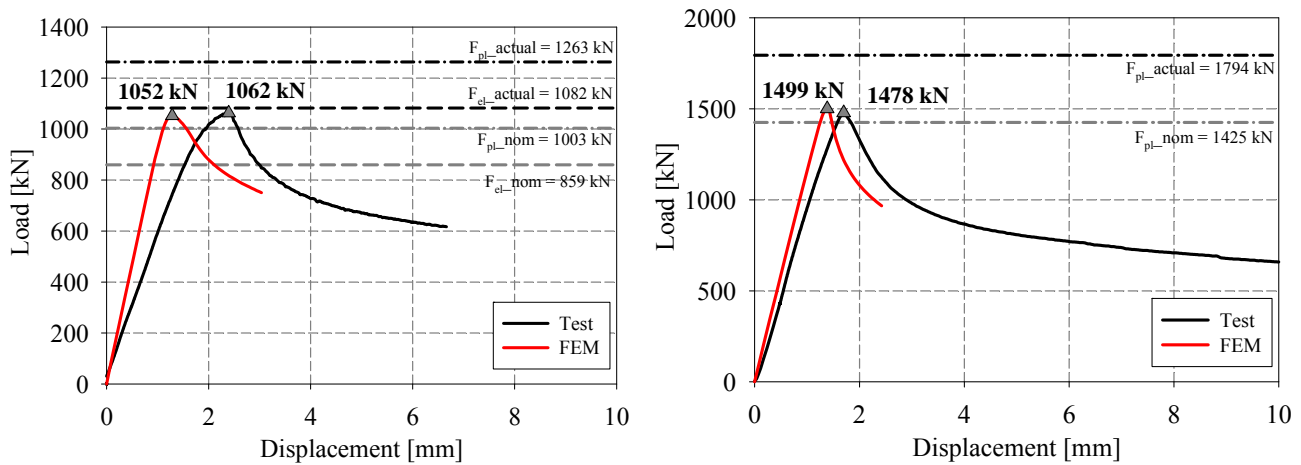


Figure 107 – Numerical vs. experimental load displacement curves of specimens,
a) LC2_RHS_250x150x5_HF, b) LC1_RHS_250x150x5_HF.

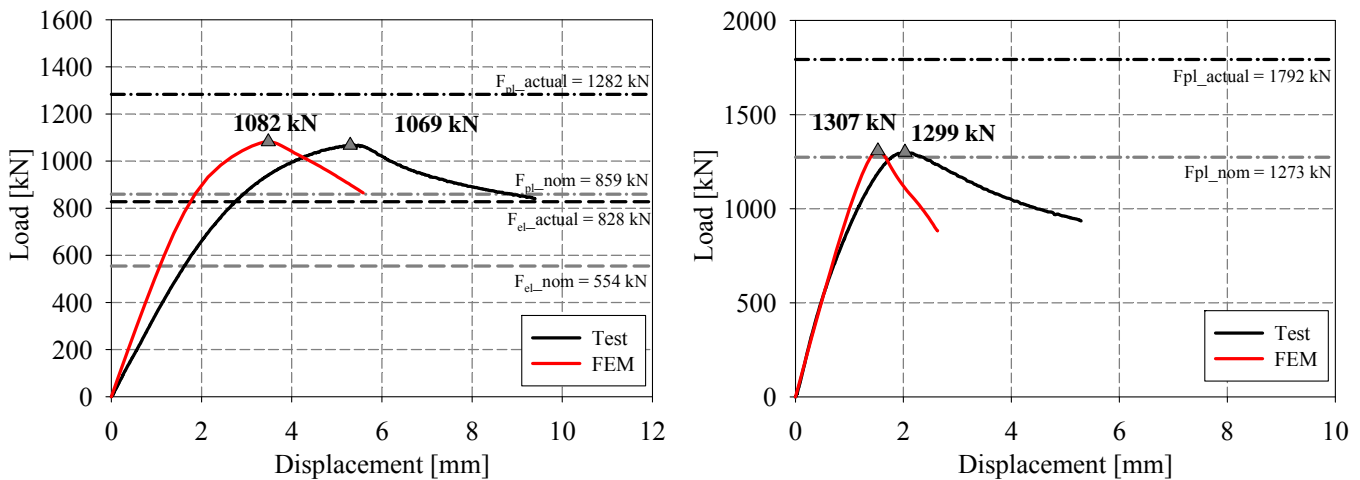


Figure 108 – Numerical vs. experimental load displacement curves of specimens,
a) LC3_SHS_200x200x6_CF, b) LC1_SHS_200x200x5_CF.

Based on these comparisons, which comprise many representative load cases and different cross-section slenderness, dimensions and production routes, the finite element models developed can be asserted to accurately represent the real behavior of such members and may safely be substituted to physical testing. Even if a slightly different finite element model – adapted from the one referred to herein – will be used in consecutive parametric studies, the models were shown to be fully suitable and satisfactory, and able to provide accurate and reliable numerical reference results.

4.2.2. TU Graz campaign

4.2.2.1. General scope of the study

Kettler [7] conducted a test program to investigate the cross-section response of semi-compact class 3 sections. The testing program was part of a European project [3] and comprised hot-rolled and welded open sections, cold-formed square and rectangular hollow sections. Kettler [7] validated his finite element model with the use of the non-linear software ABAQUS [105]. In this chapter, an attempt is made to validate as well a numerical model developed in FINELg against the hollow cross-section tests made in [7]. The numerical investigation concerning the open sections with FINELg, can be found in [62].

Kettler tested cross-sections submitted to simple load cases and combined ones. The combined load cases were obtained in a similar way to the tested cross-section in the present work, i.e. through an eccentric load applied at the ends of the specimens through thick endplates. The bottom plate of the testing machine was restrained against translation and rotation whereas the top endplate was allowed for all rotational degrees of freedom. The lengths of the specimens were selected small enough to prevent global failure and long enough to limit the influence of the boundary conditions. Figure 109 provides a general view of the test setup. The testing program comprised the following cross-sections:

Table 22 – Test program for cross-section tests [7].

Specimen	Section	Length [mm]	Nominal parameters		Actual parameters**		Loading system
			Eccentricity e[mm]	Angle* α [degrees]	Eccentricity e[mm]	Angle* α [degrees]	
Sc_A13_1			300	0	300.2	0.3	
Sc-A13-2			300	0	299.2	-0.2	$N + M_y$
Sc_A13-3			300	0	300.2	-0.2	
Sc_A14-1			300	20	300.7	20.1	
Sc_A14-2	SHS	700	300	20	297.5	19.3	$N + M_y + M_z$
Sc_A14-3	180/180/5		300	20	299.9	19.1	
	S355						
Sc_A15-1			300	45	298.6	43.9	
Sc_A15-2			300	45	302.1	45.3	$N + M_y + M_z$
Sc_A15-3			300	45	299.6	45.7	
Sc_A16-1			0	0	-	-	Stub Column

Sc_A16-2			0	0	-	-	
Sc_A18-1			300	20	300.5	20.8	
Sc_A18-2			300	20	298.1	20.2	$N + M_y + M_z$
Sc_A18-3			300	20	298.5	20	
Sc_A19-1	RHS		300	45	298.5	44	
Sc_A19-2	200/120/4	700	300	45	302.8	44.6	$N + M_y + M_z$
	S275						
Sc_A19-3			300	45	299.3	45.4	
Sc_A20-1			0	0	-	-	
Sc_A20-2			0	0	-	-	Stub Column

* α being the specimen rotation angle on the endplates.

**for stub columns actual areas were measured, see [7].



Figure 109 – Testing rig and torsional restraints of loading points of the specimen [7].

4.2.2.2. Numerical model – Features and characteristics

4.2.2.2.1. Meshing, geometrical dimensions and imperfections

Since type III mesh was seen to provide accurate results in terms of peak load and yield development (see section 4.3.1), it has been again used in the present investigation. The

following cross-sectional dimensions measured in [7] were taken into account in the numerical model (Table 23).

Table 23 – Measured cross-sectional dimensions [7].

	H [mm]	B [mm]	t [mm]
SHS_180/180/5 S355	180.2	180.2	4.7
RHS_200/120/4 S275	200.1	120.4	3.6

Kettler [7] measured the imperfections with regularly-spaced linear variable displacement transducers inserted in a perforated bar that was moved sideways in order to obtain a grid of measured imperfections at the locations of the linear variable transducers. The measured grid was adapted to the desired FE mesh, with the use of a double interpolation in both directions of the plates of each profile. This was done to represent as closely as possible the experimental conditions.

4.2.2.2.2. Loading and support conditions

In the model, pinned-end conditions were applied and a rigid plate of 120 mm thickness, modelled with an elastic material law, was linked to the specimen on both sides. The load was applied at the middle of the endplates in case of simple compression cross-section tests, and with an axial load and a bending moment in case of tests with combined load cases (i.e. having eccentricities). The thick plates allowed an even distribution of the applied load with no out-of-plane deformations. The bending moment applied in case of combined load cases was obtained by multiplying the axial compression and the eccentricity.

4.2.2.2.3. Material modelling and residual stresses

Averaged material stress-strain behavior including strain hardening effects was used. Since all hollow sections were cold-formed, two material laws have been defined – one for the flat regions and one for the corner regions⁹. Figure 110 shows an example of stress-strain curve for specimen sc- A17-1 and measured properties are summarized in Table 24.

⁹ In the corners of the tubular profiles, coupons were cut from the section and attachments were welded on both ends. These attachments could be fixed easily with the hydraulic grips of the testing machine [7].

Table 24 – Measured material properties [7].

Coupon	Specimen	Coupon location	E_m [N/mm ²]	$f_{y,m}$ [N/mm ²]	$f_{u,m}$ [N/mm ²]	$\varepsilon_y=f_{y,m}/E_m$ [-]	$(f_u/f_y)_m$ [-]
sc 17-1	SHS_180/180/5	Flat	187800	400	533.2	0.00213	1.33
sc 17-2	S355	Flat					
sc 17-1	SHS_180/180/5	Corner	198400	600.4	649.7	0.00303	1.08
sc 17-2	S355	Corner					
sc 21-1	SHS_200/120/4	Flat	196800	397.8	499.6	0.00202	1.26
sc 21-2	S275	Flat					
sc 21-1	SHS_200/120/4	Corner	200600	561.3	627	0.00280	1.12
sc 21-2	S275	Corner					

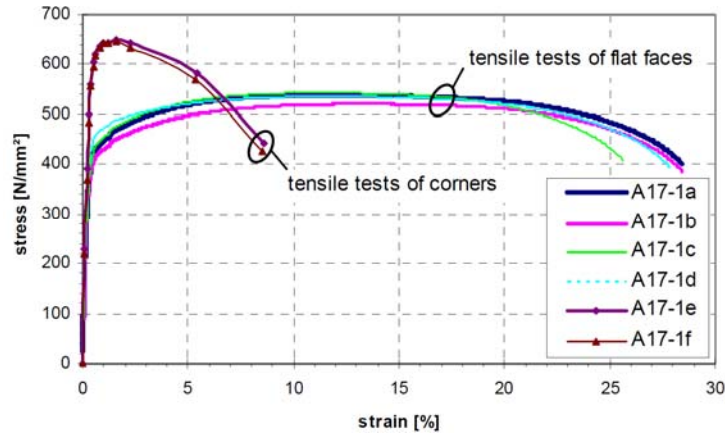


Figure 110 – Stress-strain curve for specimen sc_A17-1-SHS 180/5 – S355.

Residual stresses based on DIN recommendations [50] were adopted in [7] and also introduced in the numerical model of this investigation (see Figure 111).

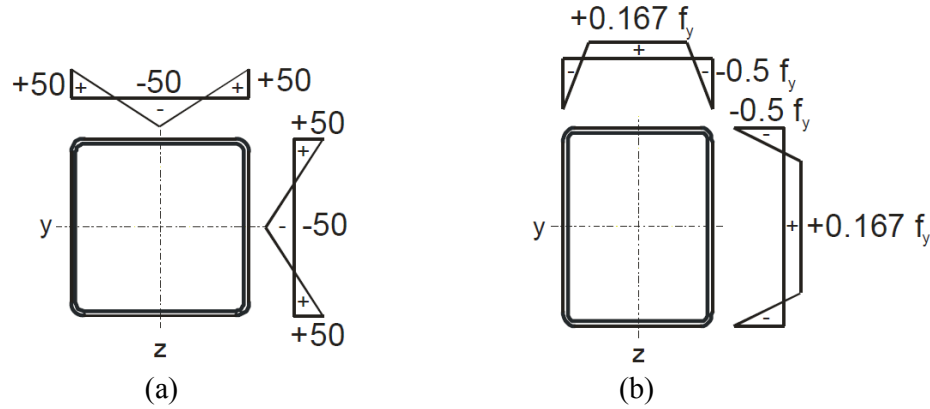


Figure 111 – Residual stress patterns for a) square hollow sections, b) rectangular hollow sections [50].

4.2.2.3. Validation: FE results vs. test results

All numerical simulations based on actual cross-section dimensions, measured initial imperfections and actual material properties are shown in Table 25 and compared to the experimental capacities achieved by the specimens tested in TU Graz [7]. The equivalent study performed with TU Graz has been also reported in Table 25. Therefore, the performance of both finite element models was compared.

Table 25 – Comparison of experimental and numerical ultimate loads.

Specimen	Section	F_{Exp} [kN]	F_{FINELg} [kN]	F_{ABAQUS} [kN]	F_{FINELg}/F_{Exp} [kN]	F_{ABAQUS}/F_{Exp} [kN]
Sc-A13-1		227.9	228.1	241	1.00	1.06
Sc-A13-2		245.6	232.2	240	0.94	0.98
Sc-A13-3		230.8	229.2	240	0.99	1.04
Sc-A14-1	SHS_180/180/5	240	223.1	237	0.92	0.99
Sc-A14-2	S355	226.1	226.2	243	1.00	1.07
Sc-A14-3		233.4	236.7	241	1.01	1.03
Sc-A15-1		237.6	225.6	244	0.95	1.03
Sc-A15-2		237.3	222	243	0.94	1.02
Sc-A15-3		235.6	219	241	0.93	1.02
Sc-A18-1		139.5	141	142	1.01	1.02
Sc-A18-2	RHS_200/120/4	142.2	138	144	0.97	1.01
Sc-A18-3	S275	139.5	144	144	1.03	1.03

Sc-A19-1	110.7	113.1	112	1.02	1.01
Sc-A19-2	112.5	115	110	1.02	0.98
Sc-A19-3	110.8	115.7	110	1.04	0.99

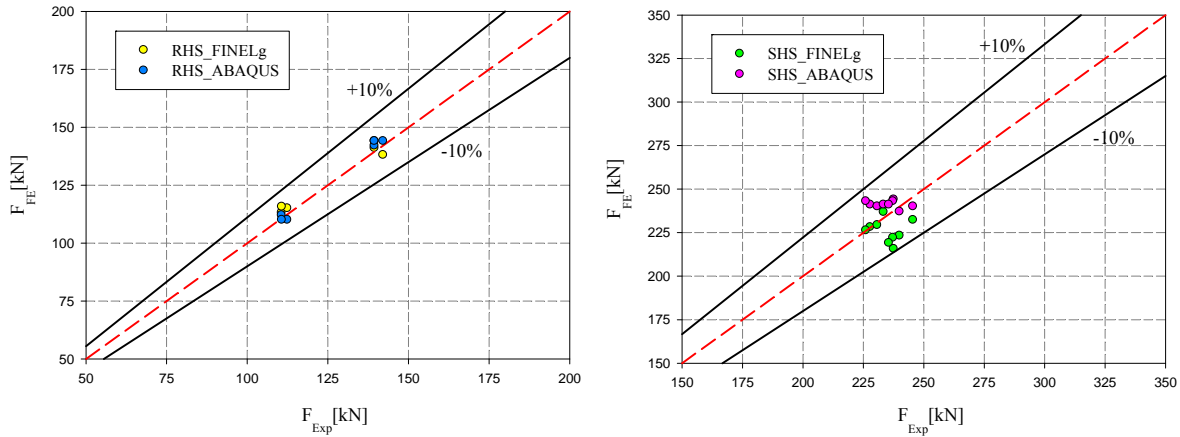


Figure 112 – FE results vs experimental results.

Figure 112 shows a graphical comparison of the ultimate loads of the FE simulations (with both FINELg and ABAQUS softwares) with the experiments; a deviation of 10% is marked with black lines. All values oscillate very closely around the dashed red line indicating a good accordance between both sources of results. The finite element model is validated and can be well adopted for further parametric studies. The agreement between both finite element programs is very good for all considered cases. However, it is remarkable that the results obtained with FINELg and with the particular case of square sections, are always slightly smaller than the results obtained with ABAQUS. Most of ABAQUS computed results are unconservative compared to experimental results, whereas FINELg computed results are shown to be conservative. However, such a comparison is not 100% valid; even if the input data were chosen equal (i.e. residual stresses, geometrical imperfections, material laws, support conditions), the way the load was introduced in ABAQUS (i.e. generation of the entire test setup or part of it) is unknown and it is difficult to assert problems relative to the load introduction. This could be the reason behind the small differences between both sources of results. Even with such dissimilarities, the agreement between both finite element programs is still considered to be very good.

4.3. Numerical parametric study

4.3.1. Meshing, loading and support conditions

With the developed FE models being shown to be adequate, a derived one has been implemented on the basis of the validated one. Again, QSCRA shell element, a quadrangular four node shell element with corotational total Lagrangian formulation has been adopted in all simulations. Special attention has been paid to a correct representation of the corner zones through two shell elements, possessing a parabolic curvature in order to characterize the real curvature of the corner.

A numerical modeling resorting to linear constraints has been developed. The end cross-section only exhibits a maximum of three degrees of freedom: axial global displacement, rotation about the major-axis and rotation about the minor-axis. Only three different nodes are then necessary to describe the displacement of any point in the cross-section once the linear relationships for axial displacements are established. In other words, a maximum of three nodes may experience a “free” longitudinal displacement, while all other nodes’ x-displacements linearly depend on the longitudinal displacements of the “x-free” nodes to respect a global cross-sectional displaced configuration. The three “x-free” nodes were chosen at the plate edges (at the beginning of different corners) of the cross-section, and all the nodes in between were constrained to the three main nodes with respected linear relationships.

Additional fictitious nodes have been defined at the centroids of the end-cross-sections for the definition of the support conditions, and transverse supports preventing from local buckling have also been implemented. This modeling technique was validated and adopted successfully in many FE studies [3].

The application of an external loading at the member’s ends (i.e. major and minor-axis bending moments and/or axial forces) is straightforward, and has been implemented by means of suitable distributions of concentrated forces at the flanges plates’ tips. This particular way of introducing end forces could be shown to avoid any unintended stress concentration (see Figure 113).

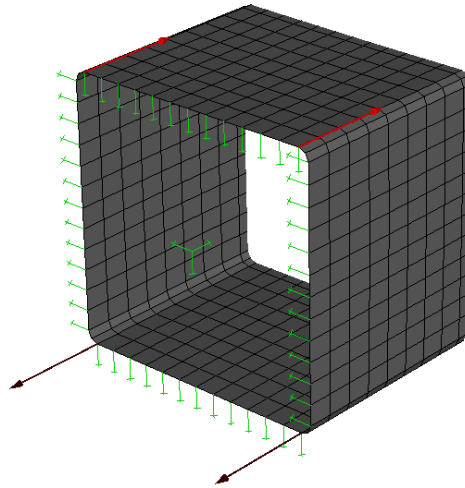


Figure 113 – Support conditions and external load application.

As for the mesh density, case studies detailed in section 4.3.1 showed that a “Type III” mesh can provide accurate results in terms of peak load and extent of yielding, and was thus adopted in all simulations as it provides adequate accuracy and reliable results with minimum computational effort in representing the structural behavior of cross-sections.

4.3.2. Initial geometrical imperfections

4.3.2.1. Introduction

Since real initial geometric imperfections are in general unknown, the most unfavorable shape of the imperfections should be taken into account with the amplitudes given by fabrication tolerances. Scarce guidelines for modeling initial imperfections of plates are given in the new European standard for plated structural elements [64], which allows to model geometric imperfections together with structural imperfections due to welding and cutting process, as equivalent geometric imperfections with amplitudes given at the allowable fabrication tolerances (see Figure 114). It is necessary to consider relevant imperfection shapes presented and to determine the most unfavorable combination in terms of leading structural or geometrical imperfection with full amplitude and accompanying imperfection with 70% of the amplitude given in Figure 114. In other words if the residual stresses pattern are introduced in the model, the accompanying geometrical imperfection amplitude can be considered as 70% of the amplitude mentioned in Figure 114. Also, the Eurocode 3 part 1-5 [64] allows to model imperfections with 80% of the geometric fabrication tolerances

combined with residual stresses represented by a stress pattern from the fabrication process with amplitudes equivalent of the mean expected values.

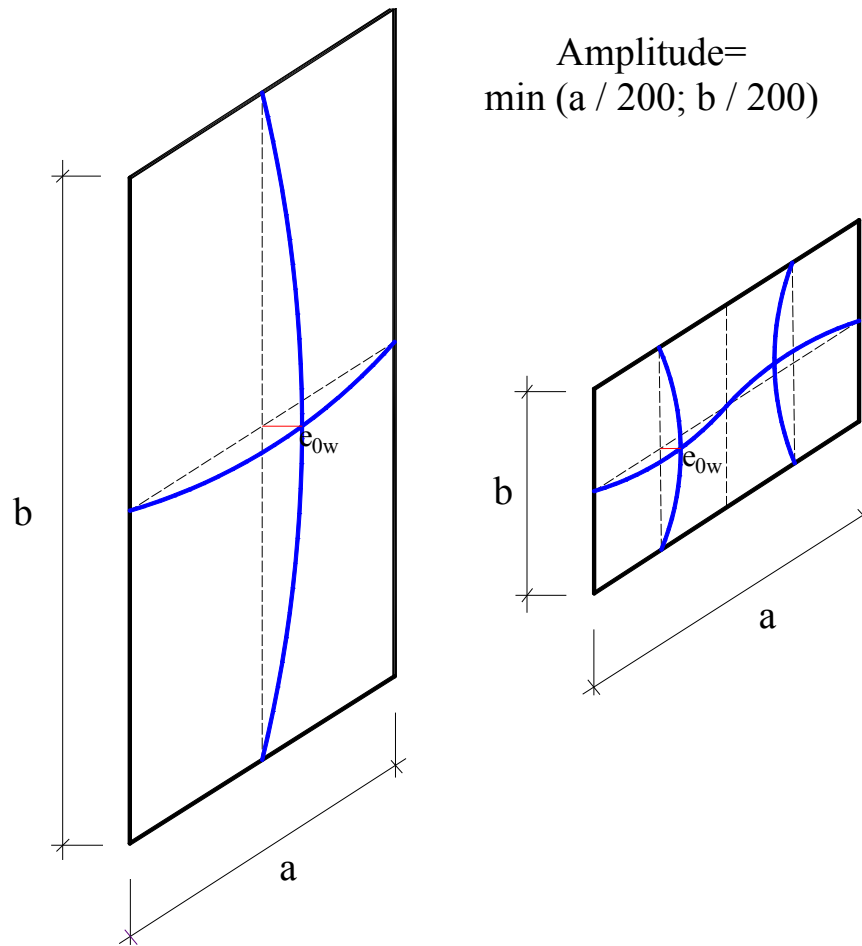


Figure 114 – Local imperfection according to Eurocode 1993 part 1-5.

Kettler [7] introduced local geometrical imperfections through an appropriate modification of node coordinates, obtained from the first buckling eigenmode shape of the corresponding element subjected to axial compression.

Greiner et al. [3] adopted a predicted shape of the local instability mode with the use of a sine function shape of initial deformation and an appropriate amplitude for each plate separately.

Besides, Dawson and Walker [106] generated an expression to predict the initial imperfection amplitudes in simply supported plates and in the plate elements of square hollow sections. Different generalized geometric imperfection parameters were studied and the effects were compared to established test data obtained from cold-formed steel sections subjected to either bending or compression. A suitable and completely general parameter

describing the imperfection's amplitude, of a plate with thickness t , was derived by means of the following three equations:

$$a = \alpha t \quad (100)$$

$$a = \beta \left(\frac{\sigma_y}{\sigma_{cr}} \right)^{0.5} t \quad (101)$$

$$a = \gamma \left(\frac{\sigma_y}{\sigma_{cr}} \right) t \quad (102)$$

where a is the initial imperfection amplitude, t is the plate thickness, σ_y is the yield proof stress of the material, σ_{cr} is the plate critical buckling stress and γ , α and β are constants to be determined for each type of material and are assumed as influenced by the manufacturing process; Walker [106] recommended a value γ of 0.2 for cold-formed steel sections.

To take due account of the variation of edge restraints for various cross-sectional geometries of cold-formed steel members, Walker [106] recommended the use of Equation (101) with a value of $\beta = 0.3$. Cruise and Gardner [107] adopted Dawson and Walker expression and proposed a value of $\beta = 0.023$ for cold-rolled stainless steel rectangular hollow sections and replaced the yield stress σ_y with the 0.2% proof stress $\sigma_{0.2}$, whereas Jandera et al.[77] obtained a value of 0.045 which lies between the upper (0.111) and lower (0.012) bounds proposed by Cruise and Gardner [107].

Unlike almost all studies focusing on the sole imperfections' amplitude, Schafer and Pekoz [78] studied both amplitude and distributions and proposed simple rules of thumb assorted with a probabilistic treatment of the maximum imperfection magnitude as a random variable. Numerically estimated cumulative function CDF values were proposed and served as a basis for connecting a probability of occurrence with a particular imperfection magnitude. Schafer [78] also performed an experimental program to examine the actual imperfection distributions; he used the imperfection spectrum of this experimental program to determine the imperfection magnitude in a particular eigenmode. Five artificial imperfection signals were generated and the conclusions resorted from this type of imperfection were seen to be more complicated than those from modal imperfections. In these latter type of imperfections, failure mechanisms were either local or distortional

depending on the imperfection magnitude (local and distortional modes were studied), whereas analysis through the generalized imperfections showed that failure was dependent on magnitude and on distribution of imperfections. Moreover, with generalized imperfections, yielding and final failure mechanism occurred at a variety of locations (but eventually at large deflections an eigenmode shape was formed) whereas a regular failure mechanism was developed with modal imperfections (e.g. distortional failures with distortional modal imperfection).

4.3.2.2. Initial imperfection sensitivity study

4.3.2.2.1. Local imperfect shape for tested cross-sections

The treatment of geometric imperfections is of significant importance in structural steel, since both ultimate strength and post-buckling capacities are imperfection sensitive.

In a first attempt to examine the imperfection sensitivity, a study of the influence of different shapes and amplitudes of initial local geometric imperfections on the cross-section capacity of the tested square and rectangular sections was undertaken. The global initial imperfections were obviously not introduced since the cross-section capacity is only being studied herein. The main aim of this first attempt was to compare the different initial adopted shapes with the real imperfections of the experimental tests. Subsequently, the imperfection sensitivity to the expected magnitude can be accurately assessed.

Therefore, a series of FE calculations were carried out on all the 45 plated sections¹⁰ with the imperfections and amplitudes mentioned in Figure 115 and the ultimate loads were compared with the experimental results. All FE calculations comprised measured geometrical dimensions, material laws and residual stresses. The only changed parameter was the initial geometrical imperfection as shown in Figure 115.

Two main types of imperfections were considered:

- (i) Type I: imperfections introduced through an appropriate modification of node coordinates with adequate sine waves equations in both direction of the considered plate. The adopted amplitudes are illustrated in Figure 115 for each plate element individually;

¹⁰ 45 cross-section tests were only considered in this sub-study, i.e. stubs and the couple of tests where no recorded data were available, were not accounted for (see section 3.4).

- (ii) Type II: modal imperfections based on the first eigenmode of a linear buckling analysis with scaled amplitude taken as the average of the values $h/200$ and $b/200$ where h and b are the web width and the flange width of the section, respectively.

Type I consisted in three variables in which the sine period was modified (case (a), case (b), case (c)). Case (a) consisted of a sine wave imperfection with the periodicity being equal to the bigger plate width of the section, case (b) with the smaller plate width of the section and case (c) with an average period of both constitutive plates of the section. Case (d) is relative to the type II imperfections.

It is to be noted that the adopted amplitudes corresponded to the prescribed amplitude in EN 1993-1-5 [64] without a reduction of 30%, although the residual stress patterns were introduced in the calculations. The amplitudes are therefore considered as conservative values.

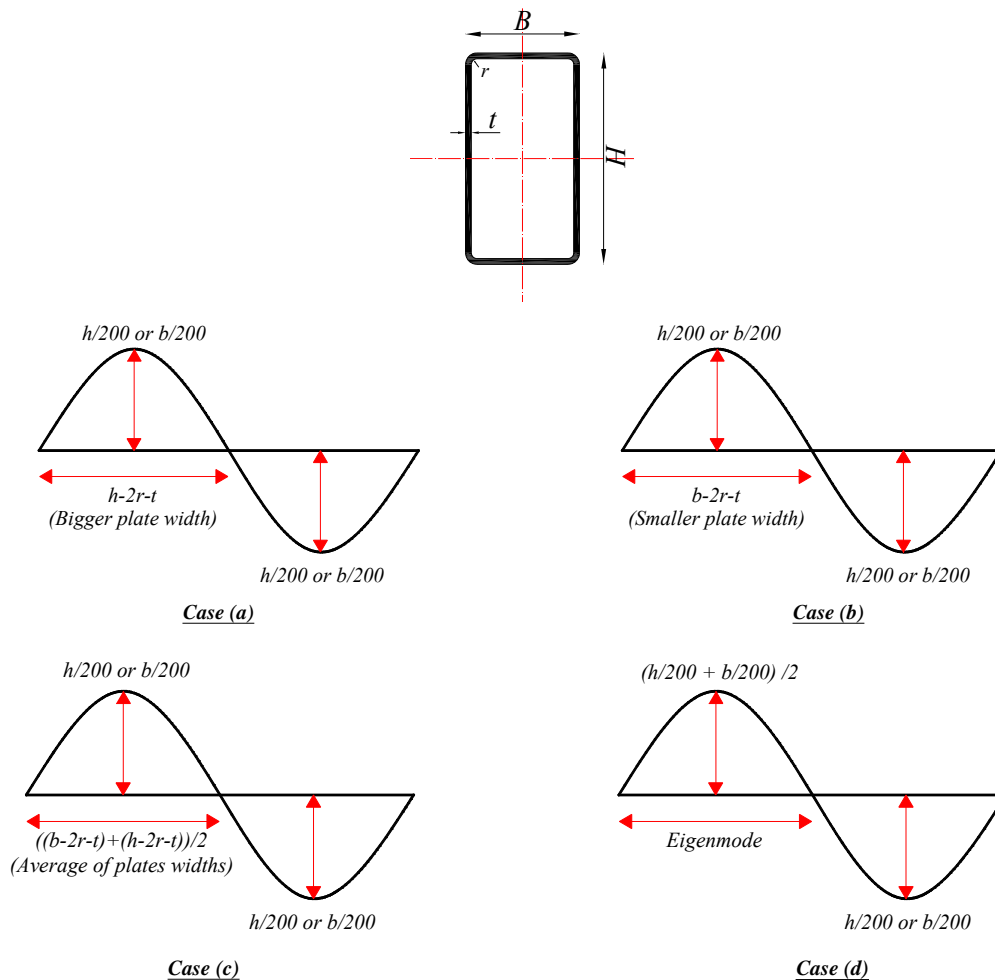


Figure 115 – Adopted imperfections for the 45 plated tests.

Figure 116 and Figure 117 show examples of the different initial geometrical imperfections for the rectangular cross-section RHS 200x100x4, introduced through adequate sine curve in both directions with respect to the periods and amplitudes represented in Figure 115.

Figure 117 represents the different eigenmode shapes corresponding to the different load cases considered in the experimental campaign for the RHS 200x100x4.

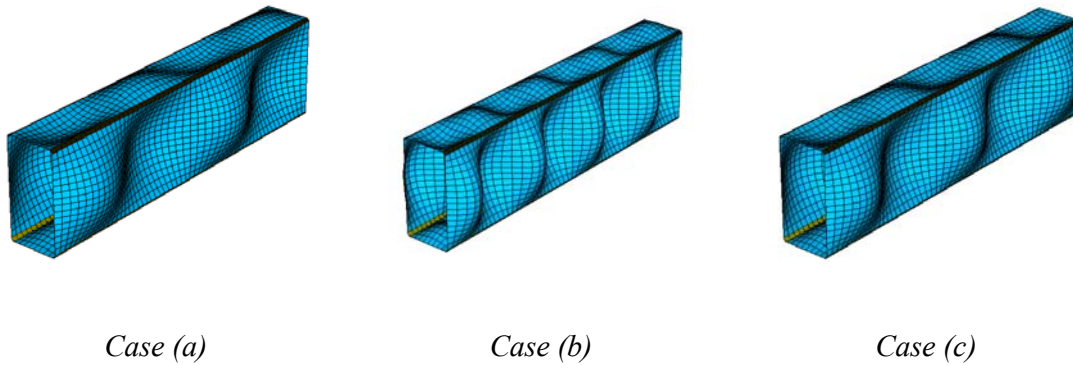


Figure 116 – Initial imperfections introduced by hand for the RHS 200x100x4 specimen.

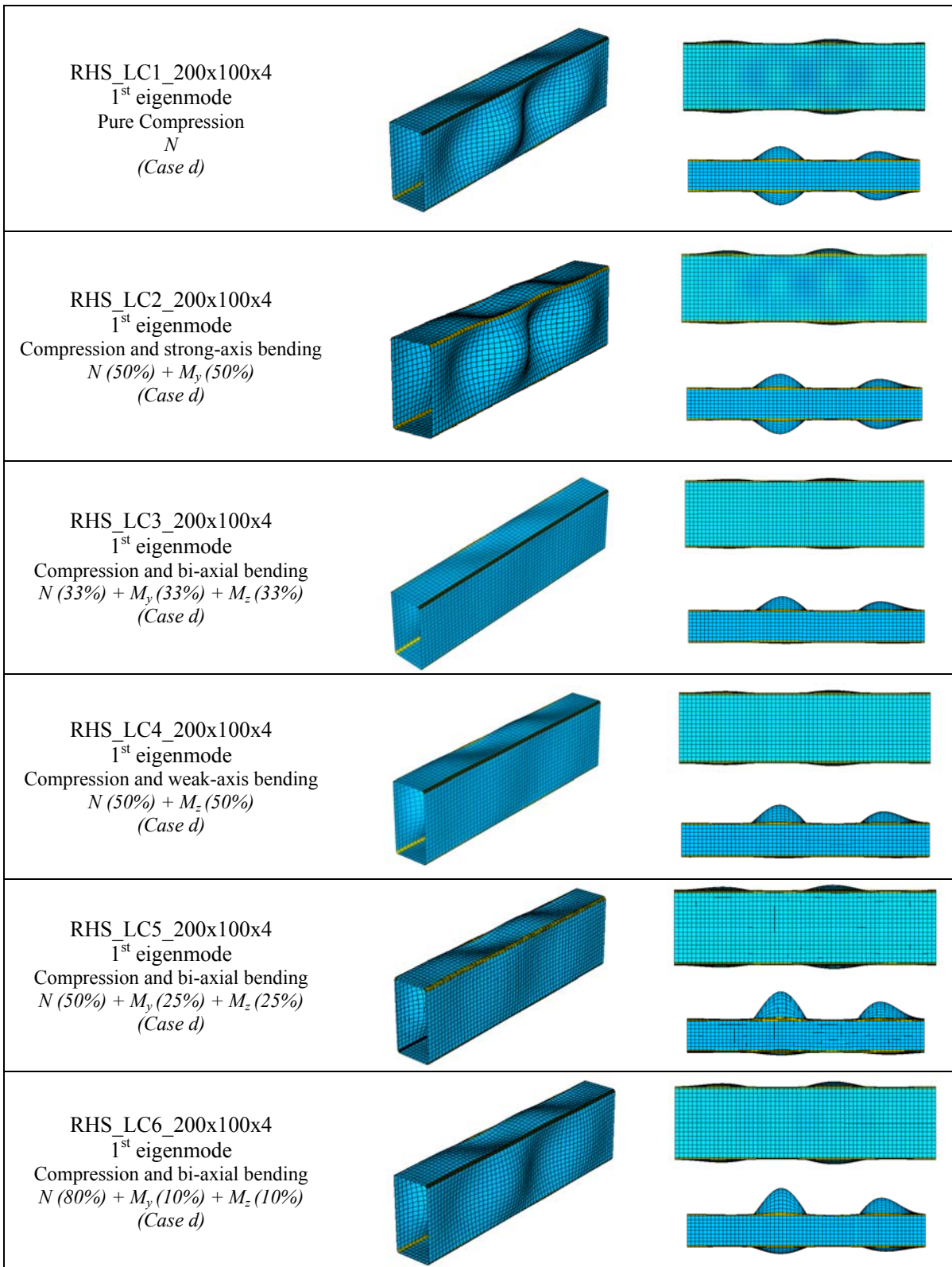


Figure 117 – Different imperfections of specimen RHS 200x100x4 introduced through the first buckling mode.

Figure 118 to Figure 121 show a comparison of the cross-section capacities having different imperfection patterns with respect to their experimental results. The cross-section capacities with measured imperfections are also included in the comparisons. Figure 118 represents the results corresponding to the cold-formed cross-sections, Figure 119 represents the hot-finished cross-section tests, Figure 120 the cold formed stub columns and Figure 121 the hot-finished stubs columns. Each figure is accompanied by a corresponding table (see Table 26 to Table 29) in which results are presented in the form of comparative ratios with the experimental results.

The following conclusions can be drawn from these figures:

- (i) The results showed a minor difference between all the adopted initial imperfections and the experimental results. Nevertheless, this difference is expected to decrease due to the conservative amplitudes in which the reduction of 30% due to the introduction of the residual stresses was not accounted for.
- (ii) Cross-section capacities with measured imperfections were obviously the closest to the experimental results. Then, amongst the rest of the considered imperfection pattern, Type II led to the closest results to the experimental counterparts in almost all cases, whereas the case (*b*) was the farthest from the experimental results. This was expected since the wave lengths in that case are numerous due to the adopted period of the smallest plate width, leading to a drop in the cross-section capacity compared to the cases (*a*) and (*c*) in which the periods were deemed more reasonable.
- (iii) The results showed that case (*a*) in which the period of the sine wave corresponds to the bigger plate width is closer to the ‘eigenmode imperfection’ result.

Table 26 – Comparison of experimental ultimate load factor with ultimate load factors of cold-formed sections according to the different imperfections adopted.

	$R_{ULT_bigger\ plate} / R_{ULT_exp}$	$R_{ULT_smaller\ plate} / R_{ULT_exp}$	$R_{ULT_average} / R_{ULT_exp}$	$R_{ULT_eigenmode} / R_{ULT_exp}$	$R_{ULT_measured} / R_{ULT_exp}$
SHS_LC1_200x200x6	0.99	0.99	0.99	1.01	1.02
RHS_LC1_200x100x4	1.05	1.03	1.03	1.05	1.03
RHS_LC1_220x120x6	0.97	0.95	0.95	0.99	1.03
RHS_LC1_200x200x5	0.92	0.92	0.92	0.94	1.05
RHS_LC1_200x200x6	0.91	0.91	0.91	0.94	1.01
RHS_LC2_200x200x6_2	0.91	0.91	0.91	0.93	1.05
RHS_LC2_200x100x4	0.95	0.89	0.91	0.95	1.00
SHS_LC2_200x200x6	0.96	0.96	0.96	0.98	1.03
RHS_LC2_220x120x6	0.91	0.87	0.88	0.92	1.02
RHS_LC2_200x200x5	0.90	0.90	0.90	0.94	1.03
RHS_LC3_200x200x6_2	0.96	0.96	0.96	0.95	1.01
RHS_LC3_200x100x4	0.98	0.94	0.97	0.97	0.97
RHS_LC3_220x120x6	0.95	0.91	0.92	0.95	1.01
RHS_LC3_200x200x5	0.89	0.89	0.89	0.90	1.03
SHS_LC3_200x200x6	0.92	0.92	0.92	0.91	1.03
RHS_LC4_200x100x4	0.96	1.01	1.01	0.94	1.00
RHS_LC4_220x120x6	0.94	0.90	0.91	0.96	1.00
RHS_LC5_200x100x4	0.92	0.89	0.90	0.92	0.97
RHS_LC5_220x120x6	0.93	0.89	0.90	0.94	1.04
RHS_LC6_200x100x4	0.98	0.95	0.95	0.98	1.01
RHS_LC6_220x120x6	0.91	0.88	0.89	0.93	0.96

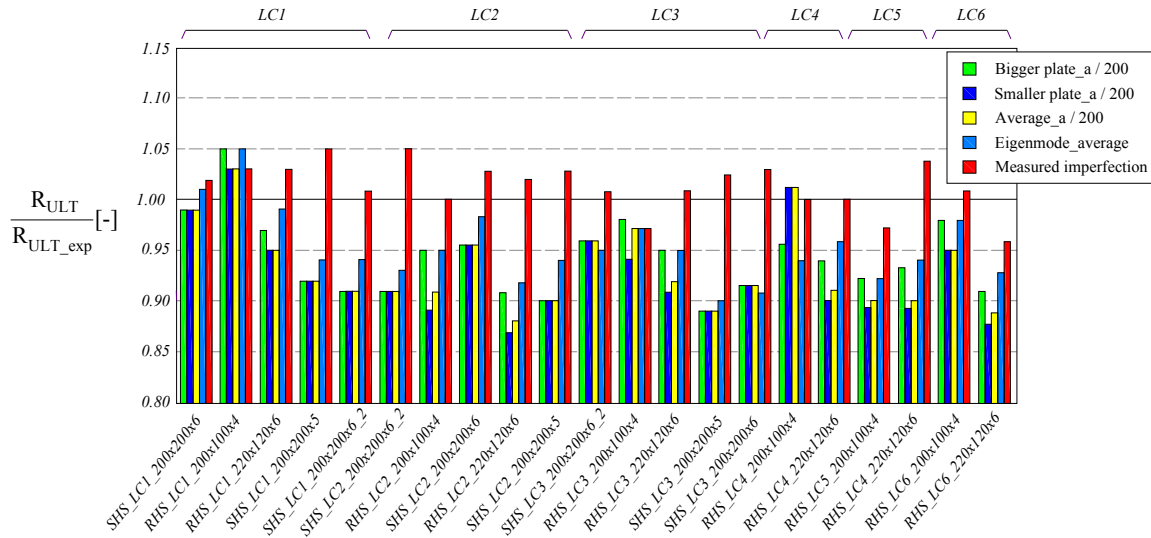


Figure 118 – Ultimate results of cold-formed sections according to the different adopted imperfections.

Table 27 – Comparison of experimental ultimate load factor with ultimate load factors of hot-finished sections according to the different imperfections adopted.

	$R_{ULT_bigger\ plate} / R_{ULT_exp}$	$R_{ULT_smaller\ plate} / R_{ULT_exp}$	$R_{ULT_average} / R_{ULT_exp}$	$R_{ULT_eigenmode} / R_{ULT_exp}$	$R_{ULT_measured} / R_{ULT_exp}$
RHS_LC1_200x100x5	1.00	0.93	0.96	1.01	0.99
RHS_LC1_250x150x5	1.00	0.92	0.95	1.00	1.01
RHS_LC1_200x200x5	0.92	0.92	0.92	0.96	1.00
RHS_LC1_200x200x6.3	0.95	0.95	0.95	0.97	0.99
RHS_LC2_250x150x5	1.02	0.94	0.97	1.01	0.99
RHS_LC2_200x200x5	0.95	0.95	0.95	0.98	0.99
RHS_LC2_200x200x6.3	0.92	0.92	0.92	0.93	0.98
RHS_LC3_200x100x5	1.02	0.96	1.01	1.02	1.00
RHS_LC3_250x150x5	0.94	0.88	0.90	0.92	1.05
RHS_LC3_200x200x5	0.87	0.87	0.87	0.86	0.98
RHS_LC3_200x200x6.3	0.94	0.97	0.97	0.96	1.01

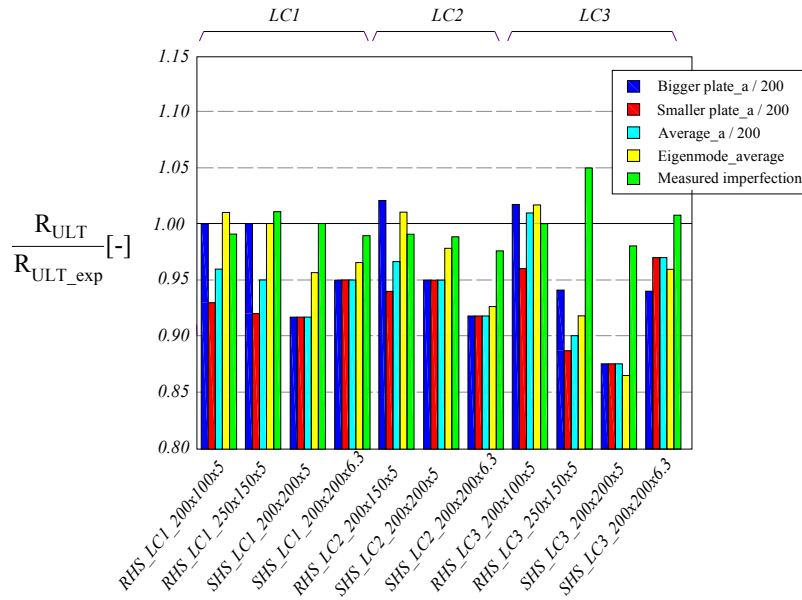


Figure 119 – Ultimate results of hot-finished sections according to the different imperfections adopted.

Table 28 – Comparison of experimental ultimate load factor with ultimate load factors of cold-formed stub columns according to the different imperfections adopted.

	$R_{ULT}^{bigger\ plate} / R_{ULT\ exp}$	$R_{ULT}^{smaller\ plate} / R_{ULT\ exp}$	$R_{ULT}^{average} / R_{ULT\ exp}$	$R_{ULT}^{eigenmode} / R_{ULT\ exp}$	$R_{ULT}^{measured} / R_{ULT\ exp}$
RHS_Stub_200x100x4	1.06	1.02	1.03	1.05	1.04
RHS_Stub_220x120x6	0.98	0.92	0.92	0.96	0.93
RHS_Stub_200x200x5	0.93	0.93	0.93	0.92	1.01
RHS_Stub_200x200x6	1.01	1.01	1.01	1.00	1.02

Table 29 – Comparison of experimental ultimate load factor with ultimate load factors of hot-finished stub columns according to the different imperfections adopted.

	$R_{ULT}^{bigger\ plate} / R_{ULT\ exp}$	$R_{ULT}^{smaller\ plate} / R_{ULT\ exp}$	$R_{ULT}^{average} / R_{ULT\ exp}$	$R_{ULT}^{eigenmode} / R_{ULT\ exp}$	$R_{ULT}^{measured} / R_{ULT\ exp}$
RHS_Stub_250x150x5	1.04	0.95	0.98	1.03	1.02
RHS_Stub_200x100x5	1.02	0.93	0.95	1.00	1.00
RHS_Stub_200x200x5	0.94	0.94	0.94	0.93	1.00
RHS_Stub_200x200x6.3	0.91	0.91	0.91	0.90	0.98

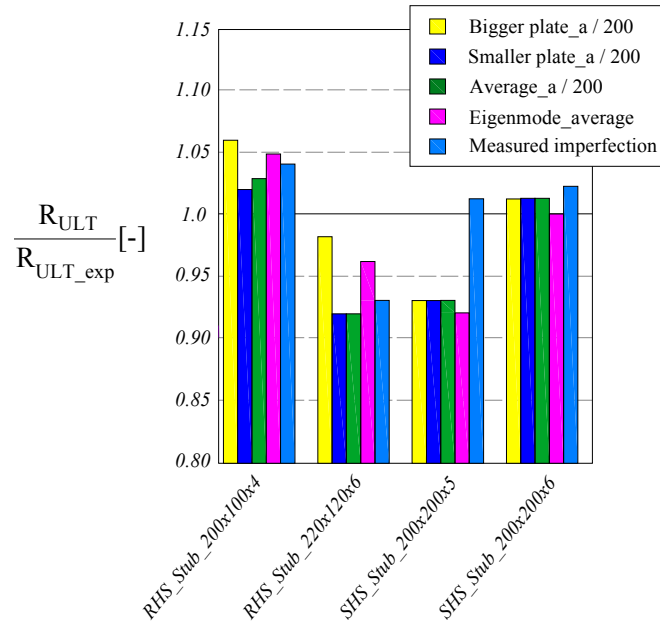


Figure 120 – Ultimate results of hot-finished stub columns according to the different imperfections adopted.

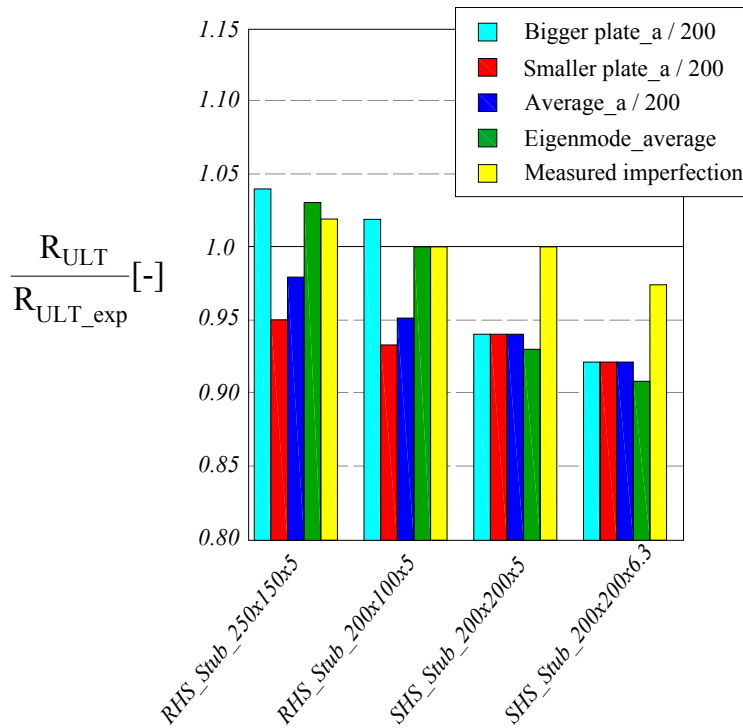


Figure 121 – Ultimate results of hot-finished stub columns according to the different imperfections adopted.

4.3.2.2.2. Local imperfect shape study on other cross-sections

A wider study has been conducted on hot-rolled cross-sections from various classes with two different simple load cases: axial compression and major-axis bending. Sections from all classes were selected along with a wider variety of initial imperfections cases, as shown in Figure 122.

Five types of periods were adopted:

- (i) *Average* refers to average sine period of $(h - 2r - t)$ and $(b - 2r - t)$;
- (ii) *Per plate* refers to sine period of each plate alone $(h - 2r - t)$ or $(b - 2r - t)$;
- (iii) *Smaller* refers to a sine period of the smallest plate (i.e. $b - 2r - t$) for all the plates of the section;
- (iv) *Bigger* refers to a sine period of the smallest plate (i.e. $h - 2r - t$) for both all the plates of the section;
- (v) *Eigenmode* refers to the first eigenmode shape of the linear buckling calculation.

Besides, four types of amplitude $a / 200$ were adopted:

- (i) *Average* refers to an 'a' equal to $[(h - 2r - t) + (b - 2r - t)] / 2$;
- (ii) *Per plate* refers to an 'a' equal to $(h - 2r - t)$ or $(b - 2r - t)$;
- (iii) *Bigger* refers to an 'a' equal to $(h - 2r - t)$;
- (iv) *Smaller* refers to an 'a' equal to $(b - 2r - t)$.

The case name was divided into two parts; the first part indicates the period of the sine wave and the second part the amplitude adopted. For example, in 'smaller/per plate', 'smaller' refers to a period based on the smaller plate width, and 'per plate' refers to an amplitude $a / 200$ in which a stands for the corresponded plate width, as explained in the previous paragraph.

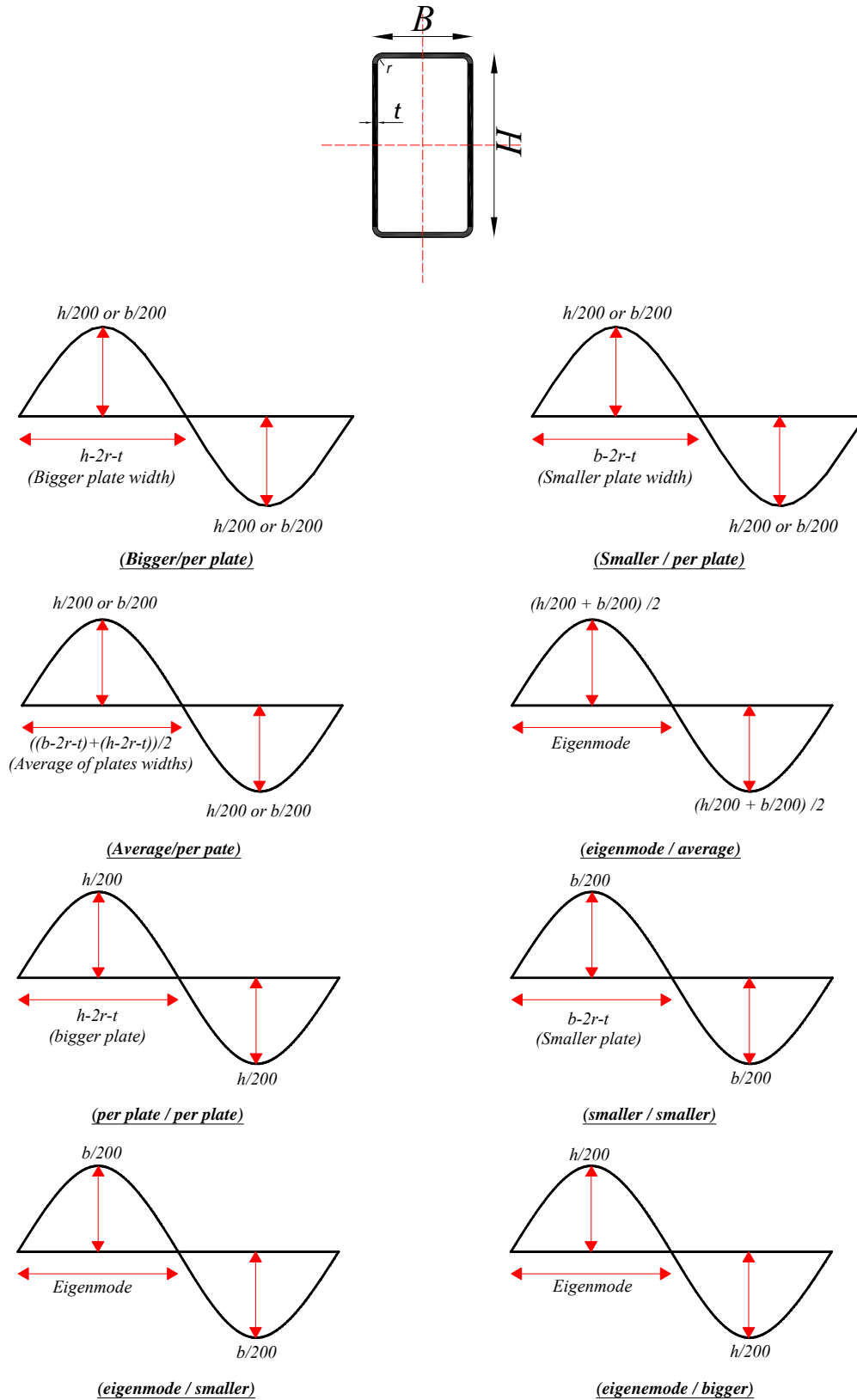


Figure 122 – Ultimate results of hot-formed stub columns according to the different imperfections adopted.

In the vertical axis of Figure 123 and Figure 124, the ultimate compression load and the ultimate bending load were normalized to their respective plastic counterparts (i.e. N_u / N_{pl} and M_u / M_{pl}). The cross-section class of the chosen profiles is also reported in the horizontal axis.

The imperfection study revealed that:

- (i) The cross-sections subjected to a major-axis bending are less sensitive to the adopted type of imperfection than the cross-sections subjected to compression. The highest difference between the most favorable imperfect shape and the least favorable one in the case of pure compression is about 11%, and is reached for the class 3 sections which are known to be the most sensitive type of cross-section class to imperfections. However, with the major-axis bending load case, this percentage reaches a value of only 2%;
- (ii) The eigenmode cases gave the highest results for the pure compression case and the lowest for the major-axis bending case. This is mainly due to the unfavorable shape of the eigenmode in the bending load cases in which the compressed flange is subjected to many buckles with no buckles occurring in the tension flange, whereas the imperfection shapes introduced through sine curves in all the plates, including the tension flange, are found to be favorable to this particular load case, given that the sine waves introduced in the tension flange will delay the process in which the plate will become tense. The eigenmode imperfect shape for compression is found to be the least unfavorable one, because the sine periods have the highest periodicities in comparison to the other imperfect shapes introduced by means of sine curves;
- (iii) Class 1 cross-sections are the least affected by the geometrical imperfections themselves and the different types adopted in this study;
- (iv) In the case of compression load cases, the most unfavorable imperfect shape is revealed to be the case of smaller/per plate because of the multitude generated buckles in the bigger and smaller plate of the section, in comparison to other imperfect shapes. This phenomenon is accentuated for cross-sections with higher h/b ratios;
- (v) Moreover, different groups of imperfect shapes are seen to have an almost similar effect on the cross-section capacity. Therefore, the imperfect shapes of *bigger/per plate*, and *bigger/bigger* are seen to have almost equivalent effect on the cross-section capacity as

well as for the imperfect shapes of *average/per plate* and *average/average*. The leading parameter in the imperfection shape adoption would thus be the period of the sine wave and not its amplitude, as long as this amplitude is taken as a factor of 1/200, with the factor being the average or exact widths of the plates constituting the section.

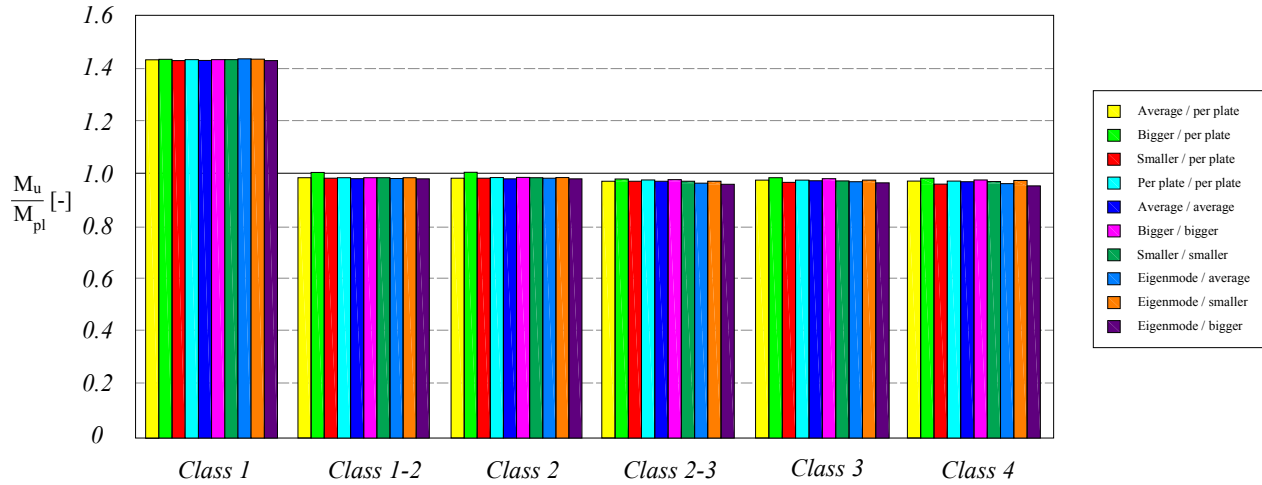


Figure 123 – Ultimate results of hot-rolled stub columns according to the different imperfections adopted¹¹.

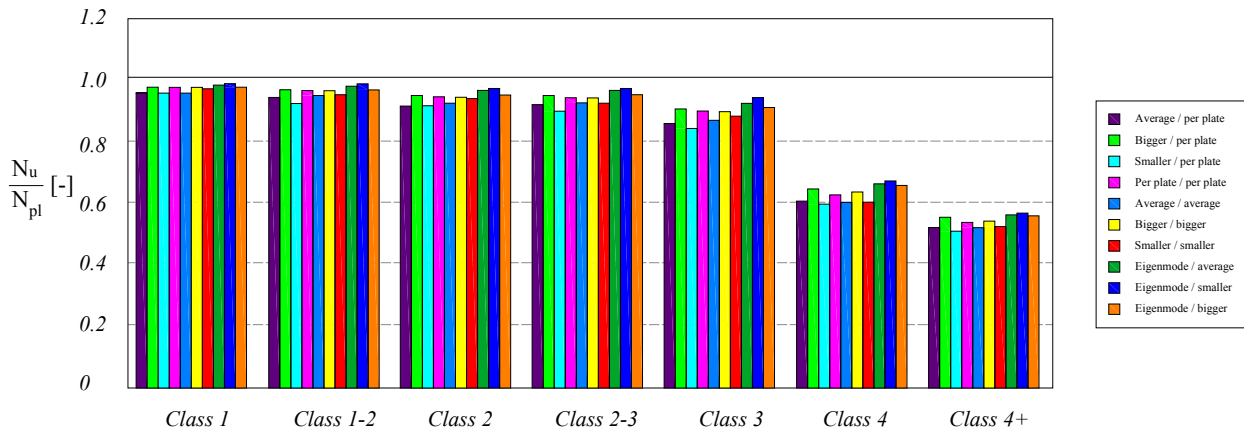


Figure 124 – Ultimate results of hot-rolled stub columns according to the different imperfections adopted.

¹¹ Cross-sections belongs to the various classes (Class i) were considered, as well as cross-sections belonging to the border between two classes (Class i-j)

4.3.2.2.3. Imperfection amplitude study

Another study was conducted to investigate the effect of the imperfection amplitude. The main target was to vary the denominator value (i.e. the value 200 in the $a/200$ amplitude) while maintaining the nominator equivalent to each plate width (i.e. the factor a).

Four different amplitudes were adopted: $a/100, a/200, a/300$ and $a/400$. 600 FE parametric results were obtained for rectangular sections with a ratio of h/b equal to 1.5. Again, two simple load cases were adopted: compression and major-axis bending. The results are shown in the Figure 125 and Figure 126, in which the horizontal axis provides the χ_{CS} factor, i.e. the ultimate capacity normalized to the plastic capacity, while the horizontal axis represents the cross-section slenderness value λ_{CS} .

It was shown that:

- (i) The stocky and slender cross-sections are less sensitive to the imperfection amplitude;
- (ii) The amplitude of $a/100$ is the most unfavorable amplitude but is considered too severe to be adopted in FE calculations;
- (iii) The difference between the different amplitudes tends to hardly increase with decreasing adopted amplitudes. Therefore the difference between the curves with $a/200, a/300$ and $a/400$ becomes less pronounced once the amplitude decreases.

Through this study, the effect of the imperfection amplitude is seen to have a non-negligible impact on a structural response as much as the sinewaves' periodicities were shown to have.

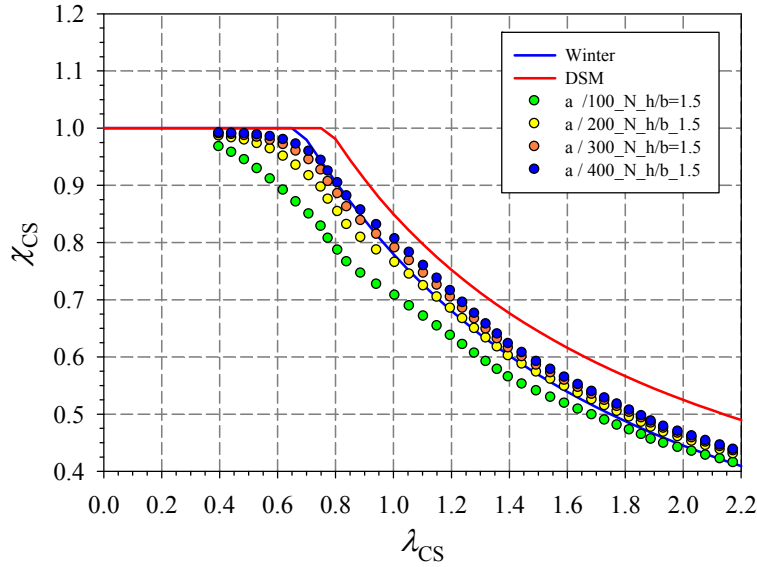


Figure 125 – RHS cross-section capacities subjected to pure compression under different imperfections' amplitude.

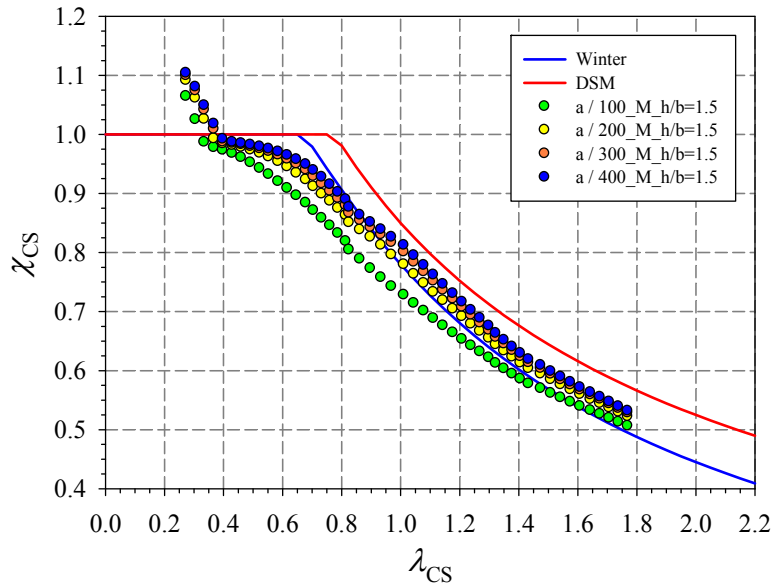


Figure 126 – RHS cross-section capacities subjected to major-axis bending under different imperfections' amplitude.

4.3.2.2.4. Final selection of geometrical imperfections and recommendations for FE modelling

Following previous studies, the most realistic chosen type and magnitude of imperfections were chosen as follows:

- (i) Periodicity: average of plate widths;
- (ii) Magnitude: $h / 200$ with h being the depth of the corresponding plate.

The approach consisting in introducing imperfection patterns by means of to the first buckling mode was seen to be less realistic, mainly for load cases other than the pure compression, and does not guaranty safer conservative results. Therefore, initial geometrical imperfections have been basically introduced through adequate modifications of node coordinates. Only local geometrical imperfections have been adopted and were defined as half-wave patterns in both directions of the flanges and webs (see Figure 127).

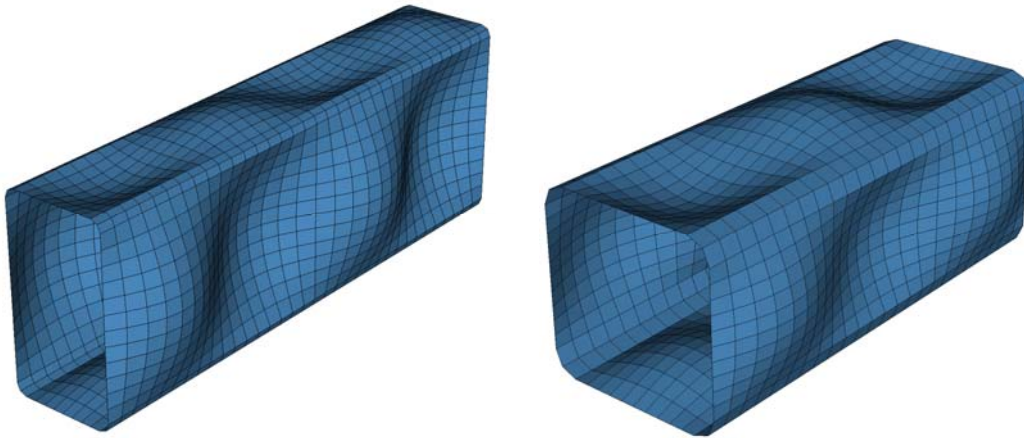


Figure 127 – Local geometrical imperfections adopted for both square and rectangular hollow sections.

It is to be noted that the definition of the sine waves periods must be dependent of both the web and flanges widths, so that rectangular sections can possess the same number of half-waves in both webs and flanges. The following equation has been used accordingly:

$$period = \frac{(h-t-2r) + (b-t-2r)}{2} \quad (103)$$

Thus, the local imperfections in the flanges and webs will be continuous and coherent, with the corner remaining unaffected, i.e. if the web buckles in an outward direction, the flanges' buckles should be inward and vice versa, as shown in Figure 128.

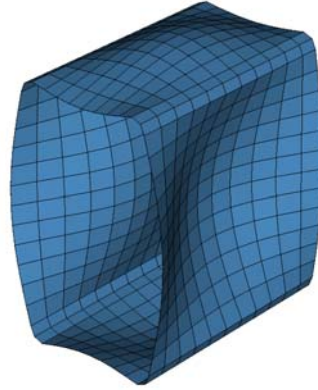


Figure 128 – Half sine wave in a rectangular cross-section.

4.3.3. Load-path sensitivity

A sub-study has been undertaken in an attempt to characterize the differences that arise in the structural response of sections if the load is applied in different sequences for a given load combination. Figure 129 illustrates the ‘load-paths’ considered in this study. Four cases have been investigated in which 3 cases are divided into two-stages loading. They consisted in:

- (i) Case 1: applying N and M_y and M_z simultaneously (*cyan* load-path in Figure 129);
- (ii) Case 2: applying N in a first stage, then continue with $M_y + M_z$ simultaneously in the second stage (*red* load-path in Figure 129);
- (iii) Case 3: applying M_y in a first stage then continue with $N + M_z$ simultaneously in the second stage (*blue* load-path in Figure 129);
- (iv) Case 4: applying M_z in a first stage, then continue with $N + M_y$ simultaneously in the second stage (*green* load-path in Figure 129).

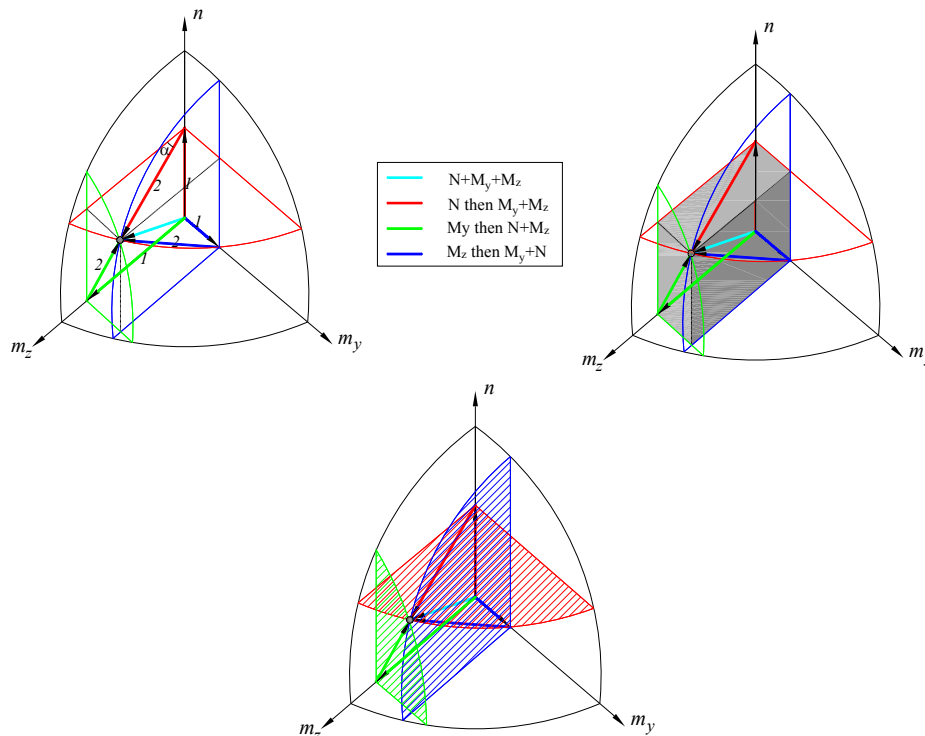


Figure 129 – Load-path representation¹².

¹² Figure 129 is only an illustrative drawing of the adopted load paths, in which n refers to the applied level of axial forces, m_y and m_z are respectively respectively to the applied levels of major and minor-axis bending.

Cases 2, 3 and 4 load sequences are generally adopted with a target of amplifying the initial geometrical imperfections. Fictitious interactive curves have been drawn in Figure 129 for illustrative purposes of showing a target grey dot that all load-paths should lead to if they would give identical responses.

For this parametric study, 600 GMNIA calculations were carried out:

- (i) 25 square cross-sections and 25 rectangular cross-sections going from compact to slender sections;
- (ii) 1 steel grade: S355;
- (iii) 4 different load sequences, as previously explained;
- (iv) 3 load cases consisting in the following:
 - (iv1) Load case 1: n30_50 i.e. $N / N_{pl} = 30\%$ with a 50 degrees angle representing the level of bi-axiality in a m_y - m_z ¹³ plot;
 - (iv2) Load case 2: n30_70 i.e. $N / N_{pl} = 30\%$ with a 70 degrees angle representing the level of bi-axiality in a m_y - m_z plot;
 - (iv3) Load case 3: n70_50 i.e. $N / N_{pl} = 70\%$ with a 50 degrees angle representing the level of bi-axiality in a m_y - m_z plot.

Load case 1 was adopted as a ‘reference’ case for which the degree of bi-axiality was only increased leading to load case2 in a first step, and in a second step, the degree of axial forces was only increased leading to load case 3. Subsequently, the influence of axial forces and of bi-axiality can be evaluated separately.

In Figure 130 to Figure 135, results corresponding to square sections are presented in two-dimensional interaction diagrams of $M / M_{el,y}$ vs. $M / M_{el,z}$ in the left column and N / N_{pl} vs. $M / M_{el,y}$ in the right column with the intention of visualizing the degree of reached axial forces for each load-path on one hand and the interaction $M_y - M_z$ in each load-path on

¹³ A degree of bi-axiality equal to 0 indicates that only major-axis bending is present, while a degree of bi-axiality equal to 90 indicates that only minor-axis bending is present (more explanation can be found in section 4.3.4)

another hand. Identical diagram types are presented in Figure 136 to Figure 141 for rectangular sections.

The following conclusions can be drawn from these figures:

- (i) For load-paths in which the axial level was not defined in the first load sequence, the cross-sections could reach higher levels of axial forces at the expense of smaller degrees of strong and minor-axis bending;
- (ii) All load sequences showed relatively scattered results for compact and slender sections, and closer ones were seen for semi-compact cross-sections;
- (iii) The load sequence 1, i.e. $N + M_y + M_z$, exhibited the most conservative responses compared to other load-paths, and for all cross-section types;
- (iv) Cross-sections computed with the load-path 3, were seen to reach the highest level of axial forces for all load cases, in comparison with load-path 2 and 4;
- (v) For stocky cross-sections, the load-path 2, i.e. N first followed by concomitant $M_y + M_z$, reaches the farthest degree of bi-axiality at failure with respect to the ‘restrained’ defined degree of axial forces, which was attained for all cross-sections, except for slender ones having a high degree of axial forces to reach (i.e. for N / N_{pl} , slender cross-sections failed before the end of stage 1). Conclusions (i) and (v) would also be similar for other types of load-paths in which M_y or M_z are applied in the first stage.

All results were represented in Figure 142 to Figure 144 in an OIC format, where the horizontal axis relates to the generalized slenderness λ_{CS} while the vertical axis reports on the cross-section reduction factor χ_{CS} . Three major conclusions can be drawn from these figures:

- (i) Cross-sections computed with the load-path 1 are showing the most conservative results for all load cases;
- (ii) For moderate axial load and degree of bi-axiality, cross-sections computed with load-path 2, 3 and 4 are showing almost similar responses (see Figure 142). This was expected because the way R_{STAB} and R_{RESIST} for such cases were not calculated with two stages like the corresponding GMNIA computations. An initial loading – based on the

GMNIA results – was increased proportionally in order to get the plastic load multiplier R_{RESIST} and the critical load multiplier R_{STAB} ;

- (iii) For a high degree of axial forces (i.e. $N / N_{pl} = 70$) or for a high degree major/minor-axis bending moment, i.e. here, for a high degree of minor-axis bending moment with $\alpha = 70$, cross-sections computed with load-paths starting in the first stage of loading with the corresponding high degree of axial forces, or minor or major bending moment, were no more showing similar results to cross-sections computed with the other load-paths defined with two stages, but were rather exhibiting more conservative results for only compact and semi-compact cross-sections, since the slender ones failed before the end of the stage 1 of loading.

Case 1 load-path has been adopted in this study since it represents the most commonly adopted and accepted way of load application. However, a minor inconvenient arises, with the fact that all ultimate points will have different levels of axial load, different levels of major-axis bending moment and different levels of minor-axis bending moments, leading to a somewhat ‘skewed’ representation such as in a 3D graph. Unlike case 1, case 2, 3 and 4, distinct levels are reached for all numerical results (i.e. a specified axial level in case 2, a specified major-axis bending moment level in case 3 and a specified minor-axis bending moment level in case 3) which can be represented in a 2D surface plot in a clearer way. However, in these latter cases, and for the particular cases of semi-compact to slender sections, an element may fail before reaching the second stage of loading, making thus the achievement of such load-paths impossible for such cross-section slenderness.

In summary, the results computed with the different load-paths showed considerable differences. Each one bears different advantages and inconvenients. Moreover, the plotting of the various sequence combinations of results in the OIC format is not strictly 100% valid and accurate since the way R_{STAB} and R_{RESIST} for cases 2, 3 and 4, were not calculated similarly to R_{ULT} (i.e. with two stages), because of the lack of adapted tools for such types of calculations. Therefore, the ultimate obtained results were taken as a basis for generating initial loading used for R_{STAB} and R_{RESIST} with N , M_y and M_z being applied simultaneously. Additional studies need to be done in order to quantify more precisely the differences between load-paths. For this study, no more developments have been undertaken because of a lack of time, and the load-path 1 was seen to be the most appropriate and safe case to adopt.

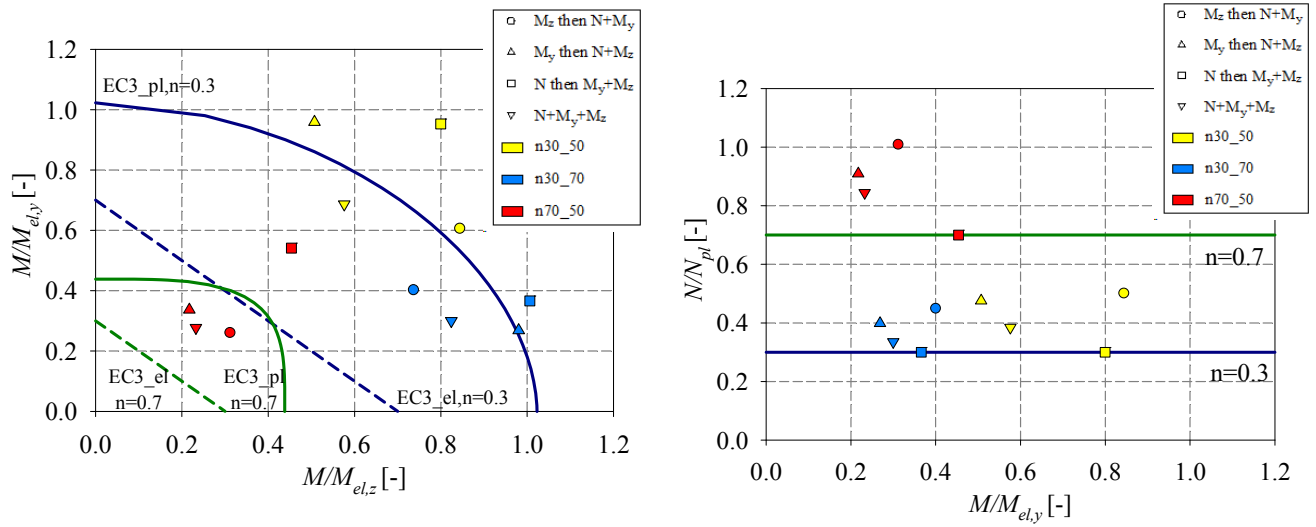


Figure 130 – Comparison of GMNIA results for the SHS 60x60x2.6 – a) $M/M_{el,y}$ vs. $M/M_{el,z}$ diagram – b) N/N_{pl} vs. $M/M_{el,y}$ diagram.

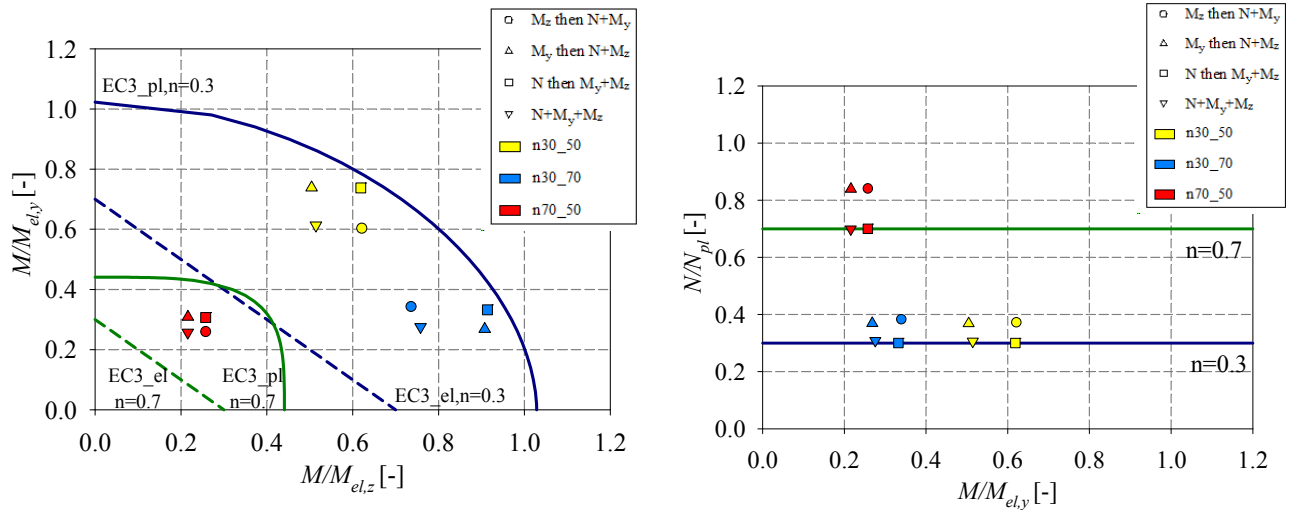


Figure 131 – Comparison of GMNIA results for the SHS 80x80x2.58 – a) $M/M_{el,y}$ vs. $M/M_{el,z}$ diagram – b) N/N_{pl} vs. $M/M_{el,y}$ diagram.

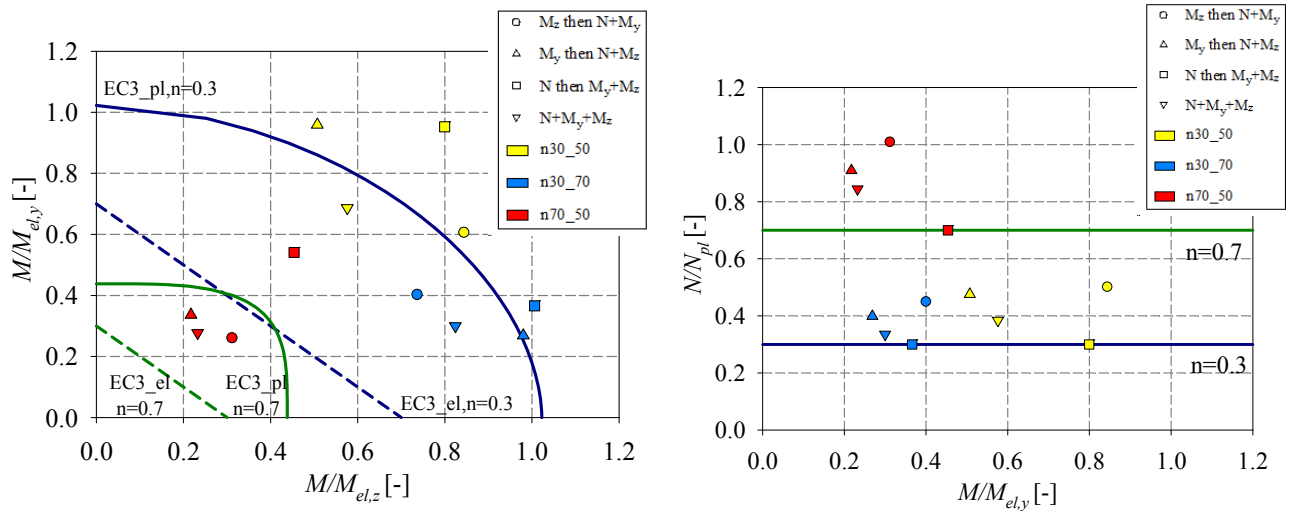


Figure 132 – Comparison of GMNIA results for the SHS 100x100x2.56 – a) $M/M_{el,y}$ vs. $M/M_{el,z}$ diagram – b) N/N_{pl} vs. $M/M_{el,y}$ diagram.

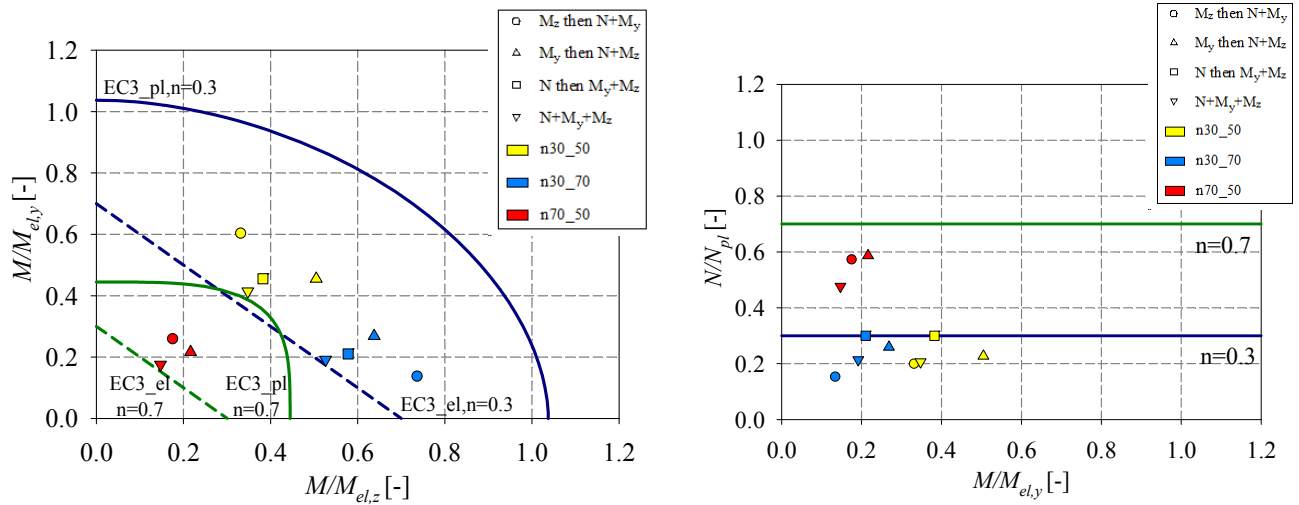


Figure 133 – Comparison of GMNIA results for the SHS 150x150x2.54 – a) $M/M_{el,y}$ vs. $M/M_{el,z}$ diagram – b) N/N_{pl} vs. $M/M_{el,y}$ diagram.

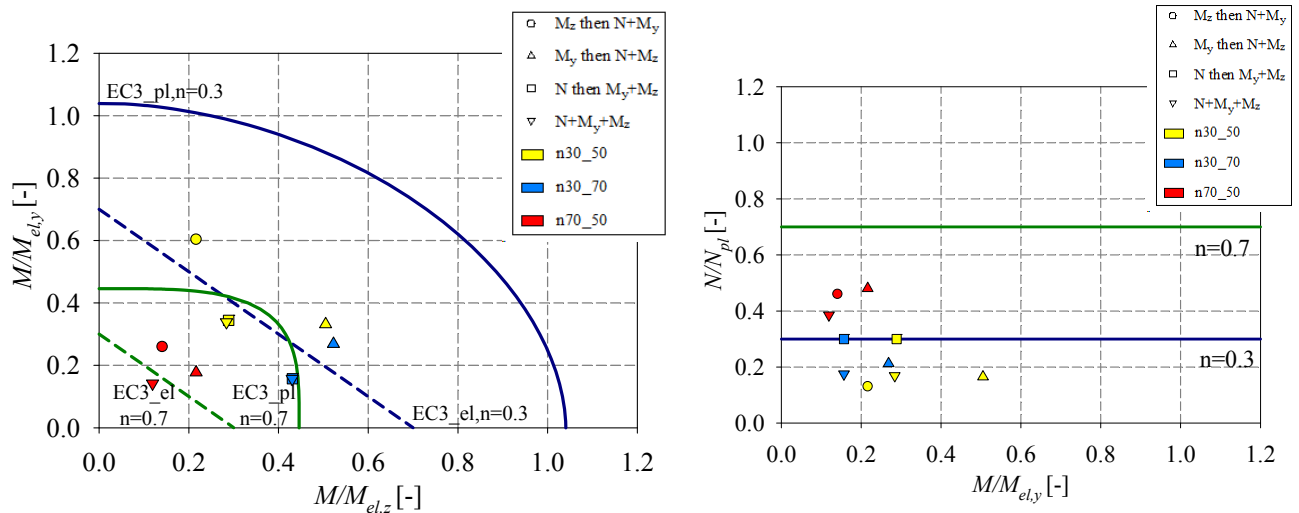


Figure 134 – Comparison of GMNIA results for the SHS 200x200x2.53 – a) $M/M_{el,y}$ vs. $M/M_{el,z}$ diagram – b) N/N_{pl} vs. $M/M_{el,y}$ diagram.

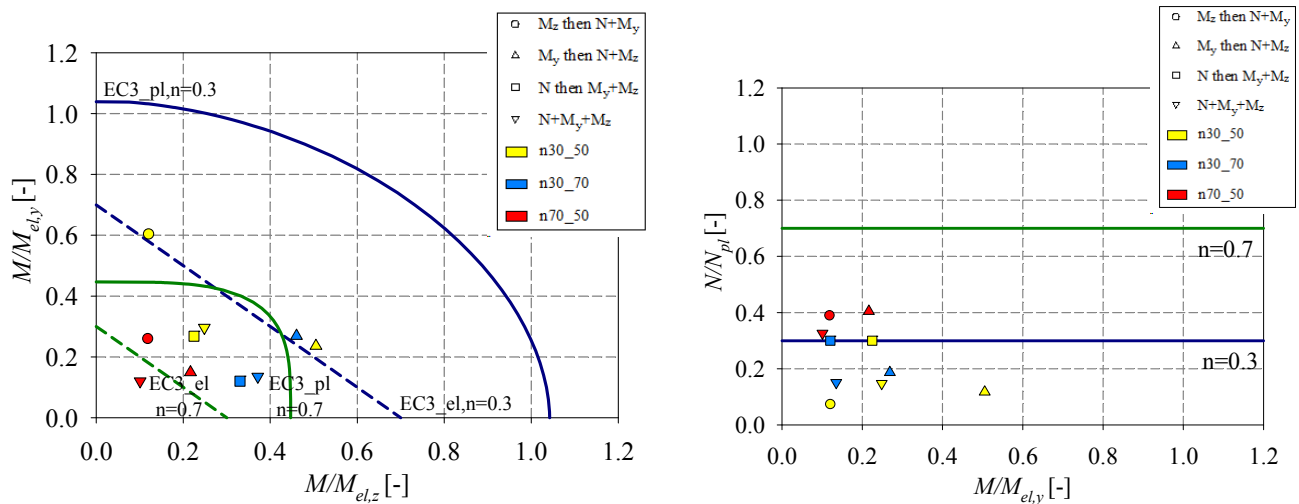


Figure 135 – Comparison of GMNIA results for the SHS 250x250x2.52 – a) $M/M_{el,y}$ vs. $M/M_{el,z}$ diagram – b) N/N_{pl} vs. $M/M_{el,y}$ diagram.

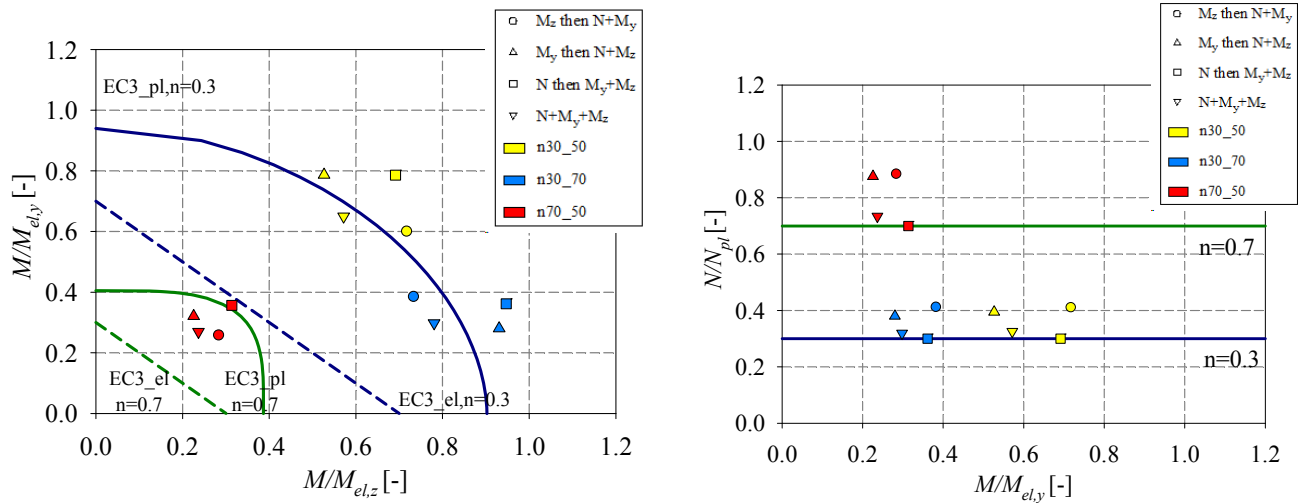


Figure 136 – Comparison of GMNIA results for the RHS 60x30x2.6 – a) $M/M_{el,y}$ vs. $M/M_{el,z}$ diagram – b) N/N_{pl} vs. $M/M_{el,y}$ diagram.

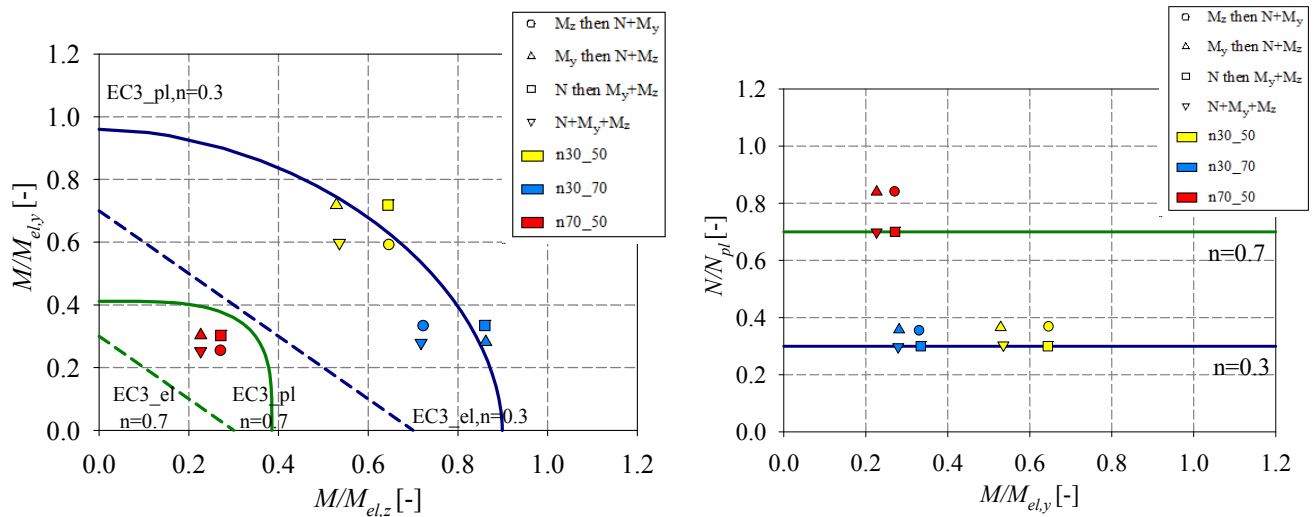


Figure 137 – Comparison of GMNIA results for the RHS 80x40x2.58 – a) $M/M_{el,y}$ vs. $M/M_{el,z}$ diagram – b) N/N_{pl} vs. $M/M_{el,y}$ diagram.

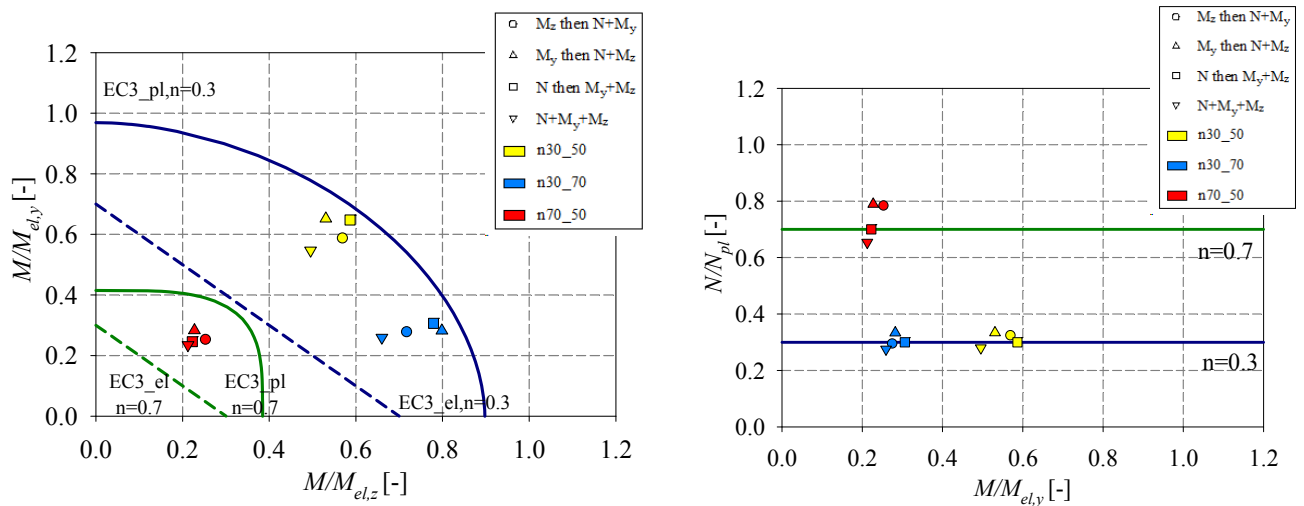


Figure 138 – Comparison of GMNIA results for the RHS 100x50x2.56 – a) $M/M_{el,y}$ vs. $M/M_{el,z}$ diagram – b) N/N_{pl} vs. $M/M_{el,y}$ diagram.

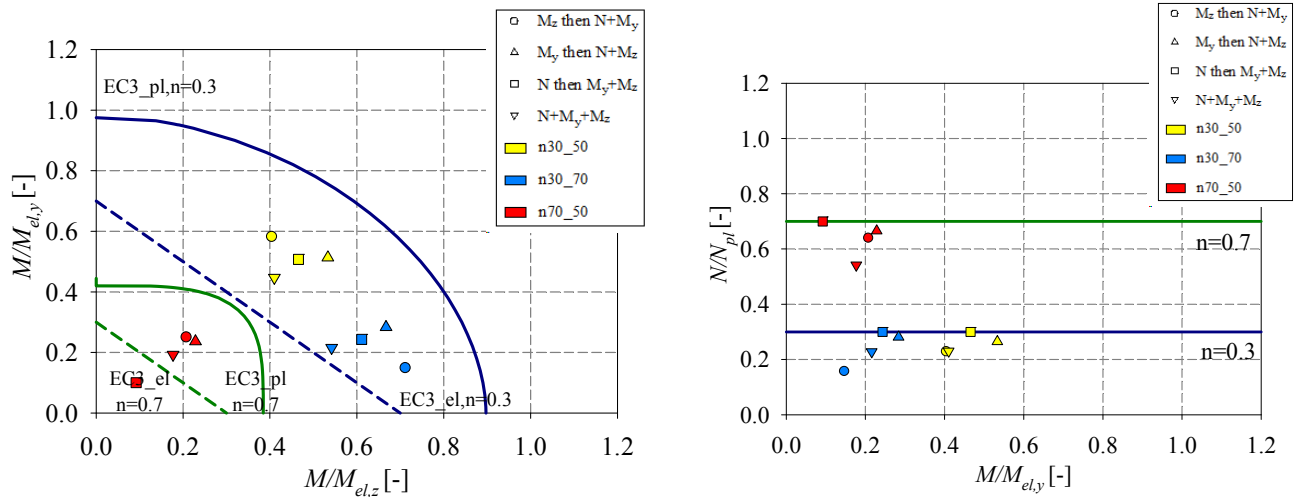


Figure 139 – Comparison of GMNIA results for the RHS 150x75x2.54 – a) $M/M_{el,y}$ vs. $M/M_{el,z}$ diagram – b) N/N_{pl} vs. $M/M_{el,y}$ diagram.

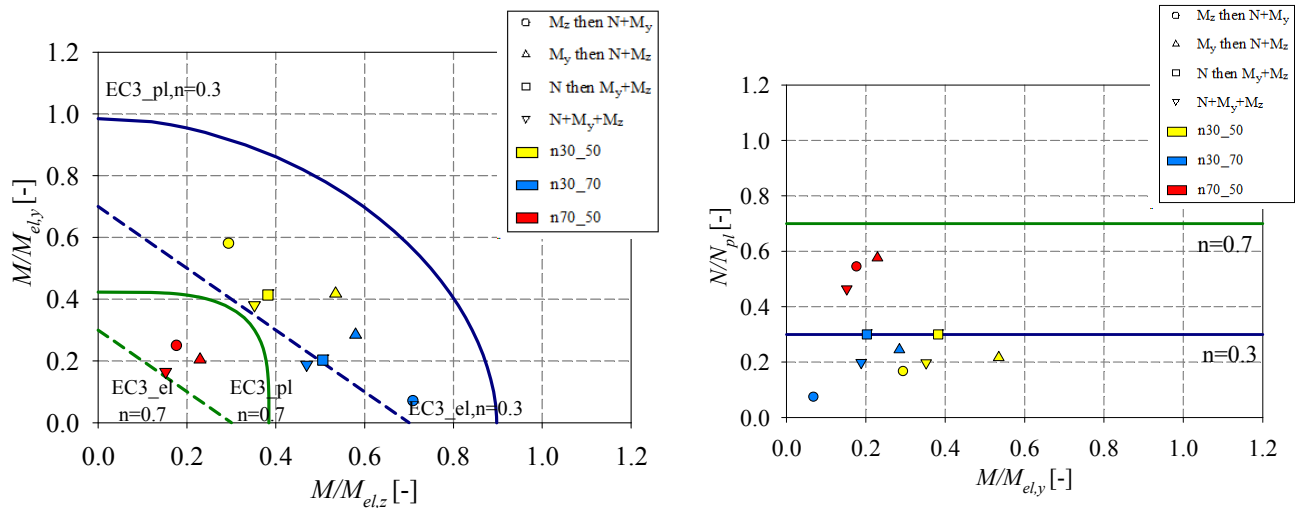


Figure 140 – Comparison of GMNIA results for the RHS 200x100x2.53 – a) $M/M_{el,y}$ vs. $M/M_{el,z}$ diagram – b) N/N_{pl} vs. $M/M_{el,y}$ diagram.

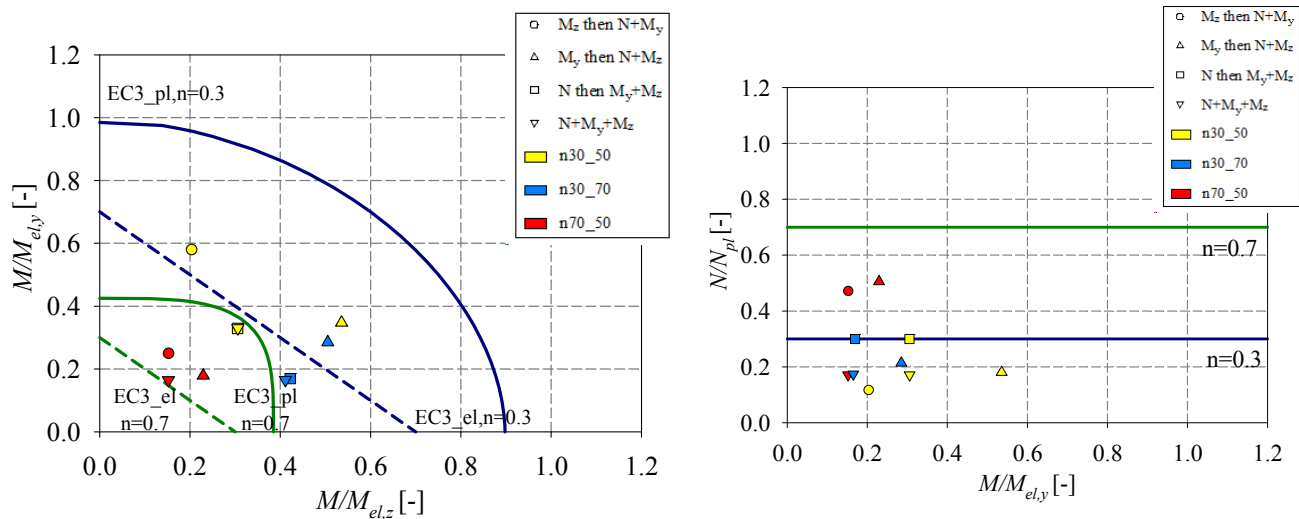


Figure 141 – Comparison of GMNIA results for the RHS 250x125x2.52 – a) $M/M_{el,y}$ vs. $M/M_{el,z}$ diagram – b) N/N_{pl} vs. $M/M_{el,y}$ diagram.

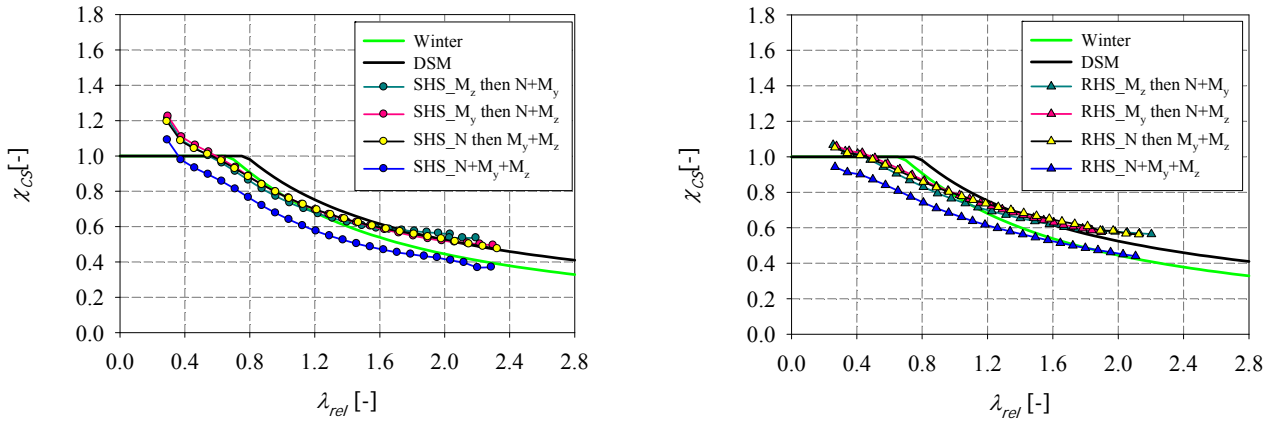


Figure 142 – GMNIA results for the load case n30_50 – a) Square hollow sections – b) Rectangular hollow sections.

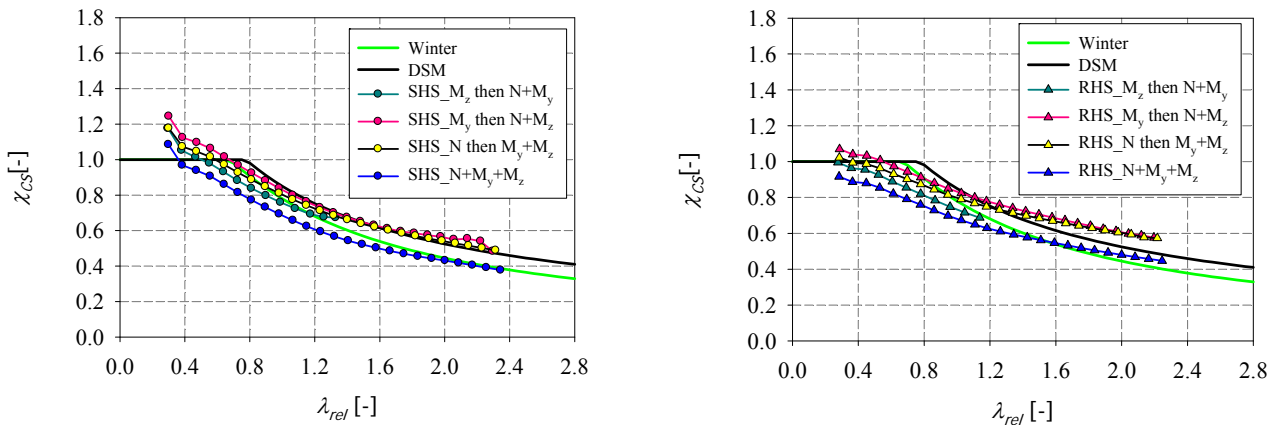


Figure 143 – GMNIA results for the load case n30_70 – a) Square hollow sections – b) Rectangular hollow sections.

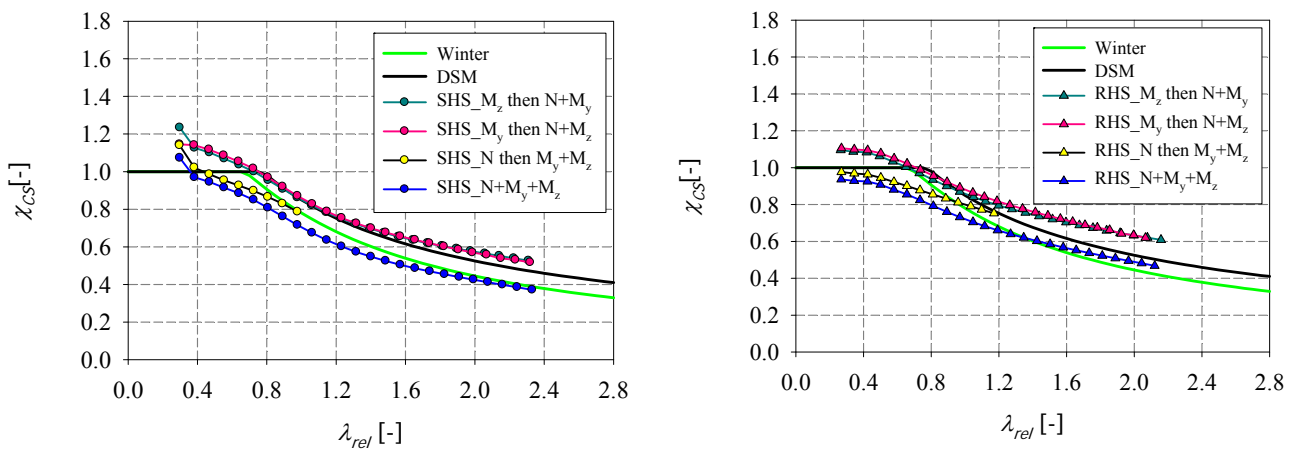


Figure 144 – GMNIA results for the load case n70_50 – a) Square hollow sections – b) Rectangular hollow sections.

4.3.4. Numerical study of hot-rolled sections

4.3.4.1. Material law and residual stresses

Typical elastic-perfectly plastic constitutive laws with strain-hardening have been adopted, on the basis of nominal values of the yield stress. The commonly used model is the elastic-plastic law without strain-hardening. However, according to DIN 18800 part 2 [108], strain hardening effects shall be considered if it develops over locally limited areas. The adopted material law thus includes a 2% strain hardening region (see Figure 145).

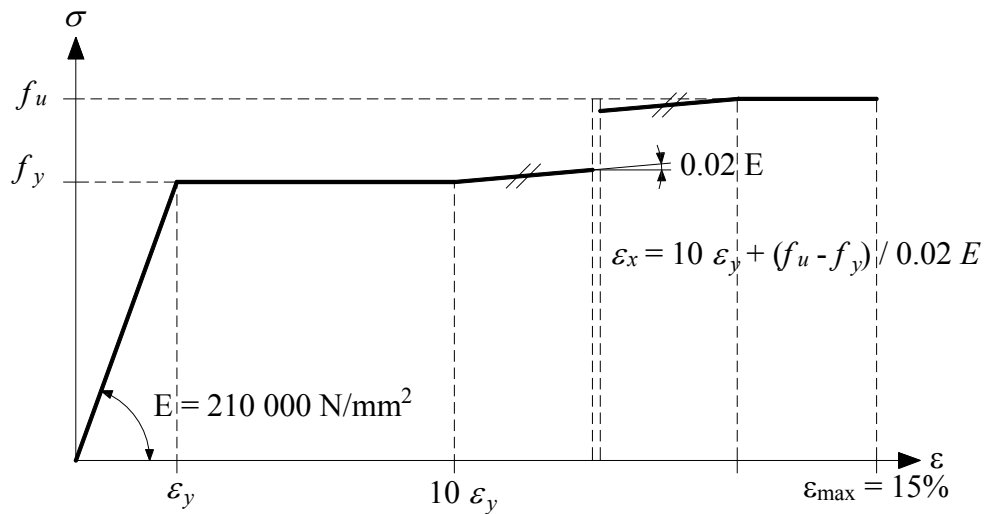


Figure 145 – Elastic-perfectly plastic with 2% strain hardening adopted material law.

Accordingly, due to a young's Modulus $E = 0$ along the plastic plateau, yielded fibres shall no longer exhibit any stiffness once they reach this stage, and numerical problems may occur. This problem is dealt with the assumption of a nearly-zero slope plateau, as illustrated in Figure 146, where the very small E_p value equal to $0.001f_y / (9\epsilon_y)$ along the plastic plateau enables a more stable numerical calculation. The material behavior with strain hardening shown in Figure 145 goes back to the ECCS publication n°33 [109] and has been supplemented with the horizontal line $\sigma = f_u$ and a consideration of an ultimate deformation capacity of 15%, which is guaranteed by steel producers for normal strength steel.

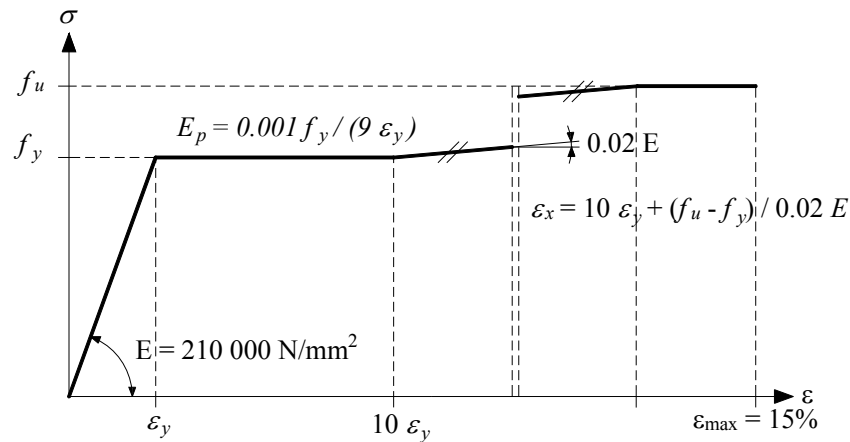


Figure 146 – Assumptions for material behavior.

Besides, residual stresses have been introduced in the models. A typical approximation of residual stress patterns frequently used in advanced structural analysis consists in the trapezoidal shape shown in Figure 147. However, for sake of a simpler numerical implementation, constant residual stresses patterns have been adopted and were seen to be sufficiently accurate. Based on these recommendations and on the actual measured residual stresses, a proposal with $0.5f_y$ ¹⁴ at the corners was assumed and the corresponding values needed to reach equilibrium in flanges and webs were calculated by means of usual structural mechanics equations. The residual stresses pattern adopted in the subsequent numerical parametric studies is represented in Figure 148.

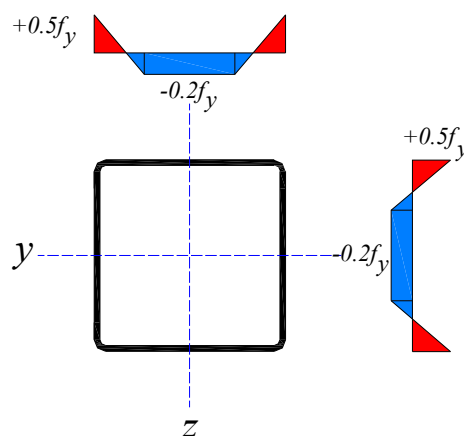


Figure 147 – DIN recommendations for residual stresses.

¹⁴ f_y refers to a conventional yield stress of 235 N/mm².

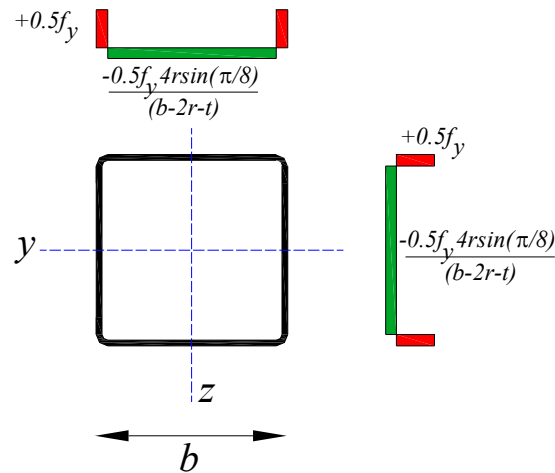


Figure 148 – Numerical residual stress assumptions (with 2 elements at the corners).

4.3.4.2. Parameters considered

Numerical parametric calculations have been carried out for the cross-section resistance of various section shapes, dimensions and steel grades. The sections covered all of the class ranges according to EN 1993-1-1 [20]. Firstly, 296 tubular geometries selected from the European catalogue were considered along with 156 rectangular cross-sections and 140 square cross-sections.

Secondly, an additional set of invented sections was analyzed. This was done in order to better visualize more distributed results along higher slenderness, since the European sections would be covering only a limited range of cross-section slenderness. Thus, the proposed sections have been derived with respect to the h/b and b/t ratios; 4 values of h/b ranging from square sections to highly rectangular ones, have been considered: $h/b = 1, 1.5, 2, 2.5$. For each h/b proposed value, b/t values spanning from 15 to 115 with a step of 2 have been considered for the load cases of pure compression and major-axis bending, and values going from 15 to 115 with a step of 4 for the load cases of minor-axis bending and combined compression with mono or bi-axial bending.

The following set of parameters has been considered for these sections:

- (i) 3 different steel grades: S235, S355, S460;
- (ii) Different load combinations:

- (ii1) Compression;
- (ii2) Major-axis bending;
- (ii3) Minor-axis bending;
- (ii4) Combined compression and biaxial bending.

For the combined load cases, a difference has been made between the different loading situations, namely with respect to the degree of bi-axiality, i.e. the M_y / M_z ratio; this ratio was varied on the basis of α angles of 0, 30, 50, 70 and 90 degrees between plastic capacities $M_{pl,y}$ and $M_{pl,z}$ as shown in Figure 149. As for the non-dimensional influence of axial force n , 6 values were adopted going from 0 (i.e. $N / N_{pl} = 0$, the load case becoming thus a biaxial bending $M_y + M_z$) to 90 (i.e. $N / N_{pl} = 90\%$, the load case becoming thus a compression of $90\%N_{pl}$ with biaxial bending $M_y + M_z$). The adopted intermediate values are shown in Table 30 and Table 31. The following denomination will be adopted for the distinction of the various combined load cases:

$$nx_ \alpha$$

where x represents the non-dimensional axial force in percentage, and α is the angle representing the degree of bi-axiality (in degrees), as shown in Figure 149 and Figure 150. For example $n50_30$, refers to a combined load case of $50\%N_{pl}$ with a degree of bi-axiality characterized by an angle of 30 degrees. These values are then divided by factor 5 to provide the initial loading to be taken into account in the corresponding finite element computations.

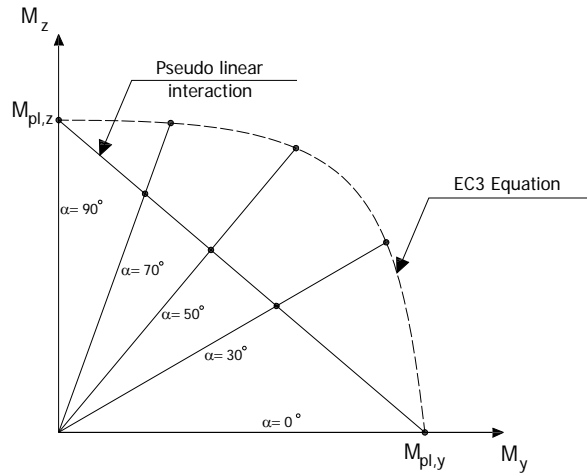


Figure 149 – Selection of load cases for $N + M_y + M_z$ combined situations.

It is reminded that the loading was applied proportionally for both N , M_y and M_z , for all combined load cases. Table 30 represents the adopted cases for the European sections, and Table 31 for the invented sections. In total, some 22 000 non-linear shell calculations have been performed for hot-rolled cross-sections.

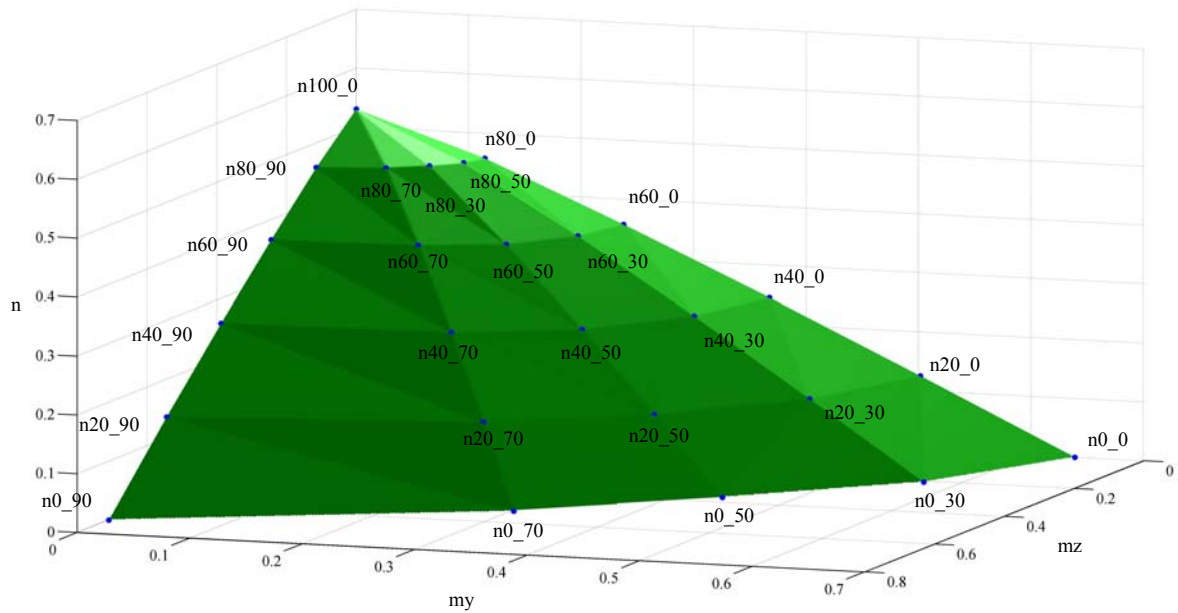


Figure 150 – Strength surface of a rectangular hollow section.

Table 30 – Adopted combined load cases for European sections.

		α				
		0	30	50	70	90
<i>n</i>	0					
	20	x	x	x	x	x
	40					
	60	x	x	x	x	x
	80					
	90					

Table 31 – Adopted combined load cases for inverted sections.

		α				
		0	30	50	70	90
<i>n</i>	0	x	x	x	x	x
	20	x	x	x	x	x
	40	x	x	x	x	x
	60	x	x	x	x	x
	80	x	x	x	x	x
	90	x	x	x	x	x

4.3.5. Numerical study of cold-formed sections

4.3.5.1. Material law and residual stresses

Averaged measured material stress-strain behavior including strain-hardening effects was accounted for in cold-formed sections. Accordingly, two material laws have been defined: one for the base material and one for the corner regions.

A Ramberg-Osgood material law was used for the flat regions, since it was seen to be in a good accordance with experimental strain-stress curves. The following simple Ramberg-Osgood material (see Equation(104)) was included in FE parametric studies of cold-formed sections:

$$\varepsilon = \frac{\sigma}{E} + 0.002 \left(\frac{\sigma}{\sigma_{0.2}} \right)^n \quad (104)$$

with the n parameter chosen equal to 22 (see Figure 151). This value has been chosen based on obtained tensile test results in section 3.3.4 and gathered data from literature [110].

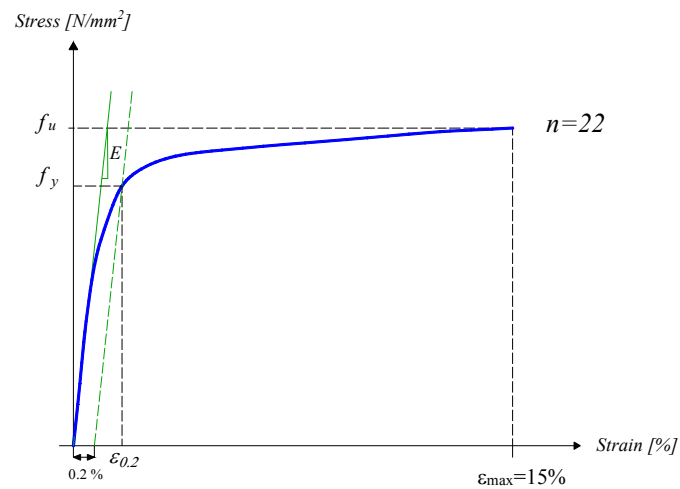


Figure 151– Adopted simple Ramberg-Osgood material law for flat regions.

As for the corner regions, a multi-linear law was considered with the following parameters, and shown in Figure 152:

$$f_{y_corner} = 1.15 f_{y_flat} \quad (105)$$

$$f_{u_corner} = 1.15 f_{u_flat} \quad (106)$$

The factor 1.15 was adopted on the basis of statistical study on material laws from literature, and shown to be convenient; further studies are however under way to confirm the adequacy of this factor. Accordingly, a higher yield strength in the cold-formed corner regions was taken into account.

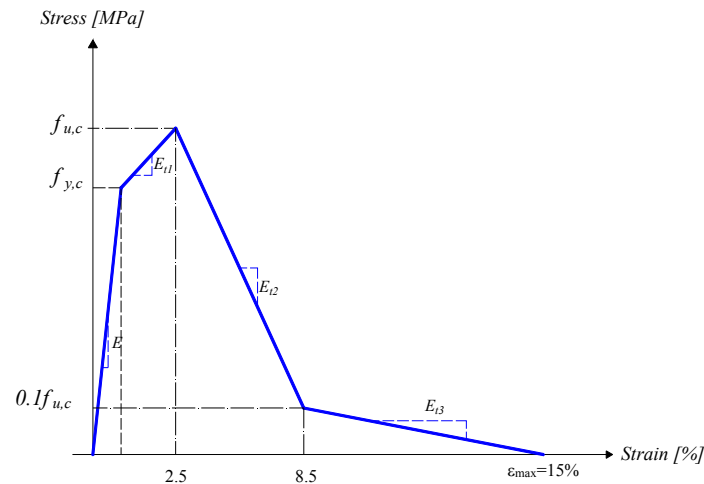


Figure 152– Adopted multi-linear material law for corner regions.

Residual stresses and cold-work of forming cannot be separated and should be modelled together since they are invented from the same process. In other words, increasing the yield stress in the corner regions of an FE model will provide inaccurate higher strength predictions unless the residual stresses developed in the bending process are also included. Ignoring both effects will implicitly have the same effect, since they roughly offset one another. Since the membrane residual stresses are insignificant in the cold-formed section, flexural stresses were only considered. Flexural stresses at the flat regions were taken equal to $1.2f_y$ with f_y being taken as the reference yield stress equal to 235 MPa. As for the corner regions in which the longitudinal stresses are less important than the flat regions, a value of 235 MPa was adopted. These choices were based on residual stresses measurements done in the experimental campaign.

4.3.5.2. Cross-sections and parameters considered

Similarly to hot-rolled sections, parametric calculations have been carried out for the cross-section resistance of the cold-formed section shapes, dimensions and steel grades. The sections covered all of the class ranges according to EN 1993-1-1 [20]. Firstly, 305 tubular geometries gathered from the European catalogue were considered with 163 rectangular cross-sections and 142 square cross-sections. The second set of invented cross-sections was similar to the hot-formed invented sections with the difference of adjusting the corner radius (taken as $1.5t$ for hot-formed sections and $2t$ for cold-formed section). The adopted set of parameters and load cases can be seen in section 4.3.4.

4.4. Determination of R-factors involved in the OIC approach

As explained previously in the section 1, the proposed OIC approach relies on the generalization of the relative slenderness concept, establishing this parameter as the key to rule the interaction between resistance and instability. It is suggested within the OIC to enlarge the field of application of this slenderness-related approach through the following generalization of the relative slenderness:

$$\lambda_{CS} = \sqrt{\frac{R_{RESIST}}{R_{STAB}}} \quad (107)$$

The proposed generalized slenderness is based on the calculation of “R-factors” (“load ratios”). Although their calculations do not raise particular difficulties for simple cases, it may appear much more delicate under biaxial bending and compression for example. In the following paragraphs, the way the ‘R-factors’ are determined is explained in details.

4.4.1. Determination of R_{RESIST}

A study has been undertaken to investigate the most appropriate way to calculate R_{RESIST} ¹⁵, and also to evaluate the Eurocode 3 interaction plastic equations. A specially designed Matlab tool [111] has been developed for this purpose, and is capable of calculating the ‘exact’ load multiplier of a hollow section experiencing all kind of load cases, from simple to combined ones. The Matlab tool was kept as a reference in the following calculations.

The effect of corners is properly taken into account in the Matlab software, whereas the EC3 equations assume that the hollow cross-sections have no corners, and their effect is taken into account only through the area A introduced in the interaction formula.

The plastic capacity of 25 cold-formed cross-sections has been calculated with the following three ways:

- (i) MNA calculations using the non-linear software FINELg;
- (ii) EC3 plastic interaction equations;

¹⁵ R_{RESIST} is a reference to the plastic resistance and could be denoted as R_{pl} . However, a denomination of R_{RESIST} (i.e. the resistance limit) was seen to be more appropriate and general since R_{pl} refers to a plastic resistance calculated on the basis of linear material law, and should be reviewed if no more plastic plateau is accounted for. Therefore a reference to the resistance limit is better than the plastic limit.

(iii) Matlab calculations with the discretization of the cross-section into n elements and getting the exact plastic load multiplier through iterative computations.

3 load cases were considered for each of the 25 chosen cross-section with the following characteristics:

- (i) n40_70: 40% of N_{pl} with an angle of 70 degrees representing the degree of bi-axiality;
- (ii) n60_70: 60% of N_{pl} with an angle of 70 degrees representing the degree of bi-axiality;
- (iii) n80_70: 80% of N_{pl} with an angle of 70 degrees representing the degree of bi-axiality.

Figure 153 to Figure 155 represent the obtained results, shown separately and grouped on a load case basis, for sake of clarity. The results are also presented in an OIC format. All results are also summarized in Table 32, in order to compare MNA and EC3 relative computations with the Matlab counterparts, considered as the reference tool for the calculation of an accurate value of R_{RESIST} .

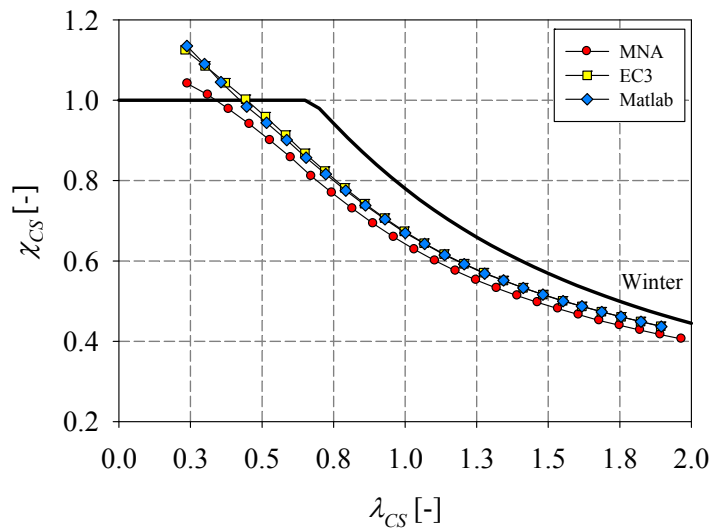


Figure 153 – Comparison of R_{RESIST} calculations with MNA, EC3 and Matlab tool for the combined load case: n40_70.

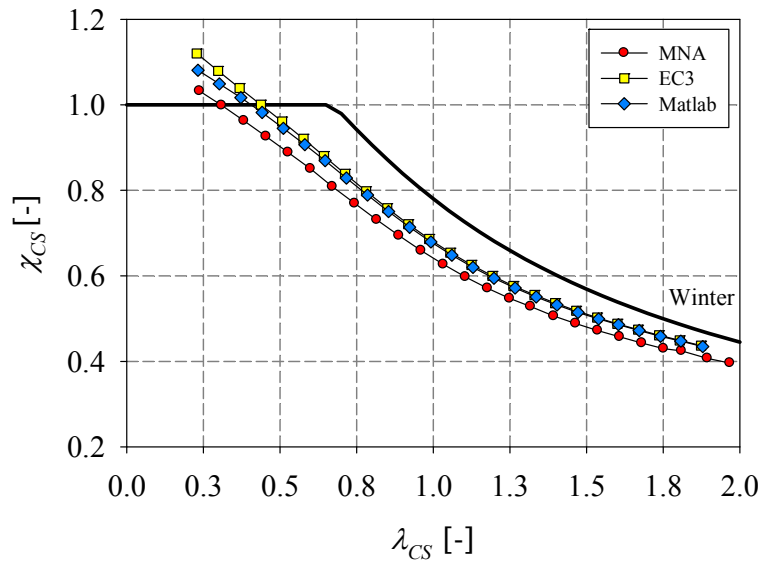


Figure 154 – Comparison of R_{RESIST} calculations with MNA, EC3 and Matlab software for the combined load case: n60_70.

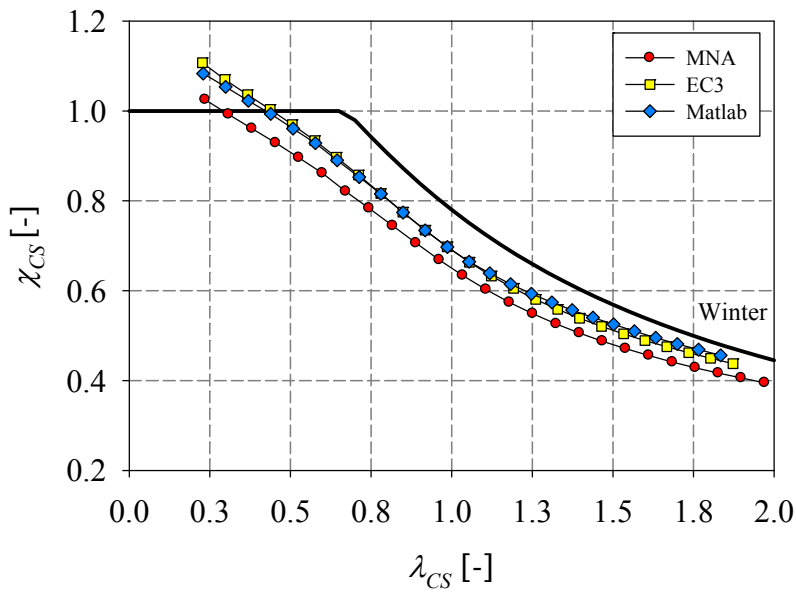


Figure 155 – Comparison of R_{RESIST} calculations with MNA, EC3 and Matlab software for the combined load case: n80_70.

Table 32 – Comparisons of R_{RESIST_EC3} and R_{RESIST_MNA} with R_{RESIST_Matlab} , load cases: n40_70, n60_70, n80_70.

Load case	n40_70		n60_70		n80_70	
Cross-section	$R_{RESIST_EC3} / R_{RESIST_Matlab}$	$R_{RESIST_MNA} / R_{RESIST_Matlab}$	$R_{RESIST_EC3} / R_{RESIST_Matlab}$	$R_{RESIST_MNA} / R_{RESIST_Matlab}$	$R_{RESIST_EC3} / R_{RESIST_Matlab}$	$R_{RESIST_MNA} / R_{RESIST_Matlab}$
SHS_40x40x2.66	0.94	1.02	0.96	1.04	0.97	1.05
SHS_50x50_2.63	1.03	1.08	0.97	1.05	0.98	1.06
SHS_60x60x2.60	1.08	1.16	0.97	1.05	0.98	1.06
SHS_70x70x2.59	0.98	1.04	0.98	1.06	0.98	1.06
SHS_80x80x2.58	0.98	1.05	0.98	1.06	0.99	1.07
SHS_90x90x2.57	0.98	1.05	0.98	1.06	0.99	1.07
SHS_100x100x2.56	0.98	1.06	0.98	1.07	0.99	1.08
SHS_110x110x2.55	0.99	1.06	0.98	1.07	0.99	1.08
SHS_120x120x2.55	0.99	1.06	0.98	1.07	0.99	1.09
SHS_130x130x2.55	0.99	1.06	0.98	1.08	0.99	1.09
SHS_140x140x2.54	0.99	1.06	0.98	1.08	0.99	1.09
SHS_150x150x2.54	0.99	1.06	0.99	1.08	0.99	1.09
SHS_160x160x2.54	0.99	1.06	0.99	1.08	1.00	1.10
SHS_170x170x2.53	0.99	1.07	0.99	1.08	1.00	1.11
SHS_180x180x5.53	0.99	1.06	0.99	1.08	1.01	1.12
SHS_190x190x2.53	0.99	1.07	0.99	1.08	1.02	1.12
SHS_200x200x2.53	1.00	1.07	0.99	1.08	1.02	1.13
SHS_210x210x2.53	0.99	1.07	0.99	1.08	1.03	1.14
SHS_220x220x2.53	0.99	1.07	0.99	1.08	1.03	1.14
SHS_230x230x2.52	0.99	1.07	0.99	1.09	1.04	1.15
SHS_240x240x2.52	0.99	1.07	0.99	1.09	1.04	1.15
SHS_250x250x2.52	0.99	1.07	0.99	1.08	1.04	1.15
SHS_260x260x2.52	1.00	1.07	0.99	1.08	1.04	1.15
SHS_270x270x2.52	0.99	1.07	0.99	1.09	1.04	1.15
SHS_280x280x2.52	0.99	1.07	0.99	1.09	1.04	1.15
MEAN	0.99	1.06	0.98	1.07	1.01	1.11
Standard deviation	0.07	0.02	0.008	0.012	0.02	0.03

It is clearly noticeable that MNA results with FINELg are showing too conservative results compared to EC3 plastic equations. To simulate an MNA calculation in FINELg, a really short element was considered for each section (not longer than 10 mm), with the main reason of excluding the non-linearities occurring due to geometrical imperfections (obviously no mechanical imperfections were included). But unfortunately, this small length induced a strengthening effect due to boundary conditions resulting in a higher R_{RESIST} , which in turn led to conservative reduction factors χ_{CS} . Consequently, the MNA way of getting the plastic load multiplier R_{RESIST} was eliminated and not adopted in calculations.

The biggest disparity between EC3 plastic equations and the Matlab tool occurred for stocky sections. This was expected since the relative corner area for such sections is bigger than for slender sections.

A simple example can explain this disparity; if we consider two sections having two different classes:

- (i) Section 1: a stocky cross-section: $100 \times 40 \times 4$;
- (ii) Section 2: same as section 1 but with double web height: $100 \times 80 \times 4$.

Their corresponding true and EC3 areas will be as the following table:

Table 33 – Illustrated errors with area consideration in the Eurocode 3.

Cross-section	True Area [mm ²]	EC3_Area [mm ²]	Error [%]
Section 1	1015	1056	3.9
Section 2	1815	1856	2.2

The error of section 1 is thus almost twice the error of section 2 and shall increase if going to even more slender sections. EC3 considers an area without corners, whereas the Matlab tool takes them into account in an accurate way. Consequently, within a slender section, the influence of corners on the cross-section response tends to be negligible compared to the whole section area and the results corresponding to both ways of calculating R_{RESIST} will be almost similar. As for stocky sections, the corner effect will be significant and the difference between EC3 plastic interaction equations and the Matlab tool will become bigger. This is

shown in almost all results at the range of relatively small slenderness values. However, this difference does not exceed a value of 4%, which remain acceptable.

The highest disparities can occur between EC3 plastic equations and Matlab tool, for combined loading situations in which axial levels of compression can reach values between 0% and 50% of N_{pl} in the presence of a major-axis bending, and between 0% and 20% of N_{pl} when paired with a minor-axis bending. These ranges correspond to the approximations made in the EC3 plastic equations, which can lead to both unsafe and safe results, depending on the EC3 and Matlab curves dispositions and on the cross-section slenderness. This is clearly illustrated in Figure 156 for the case of a rectangular hollow section RHS 200x100x4.

The highest differences between EC3 plastic equations and Matlab software reached a maximum 'mean' value of 2%. This was confirmed by another additional study conducted on 25 cross-sections going from stocky to slender ones, which comprised the following load cases:

- (i) n0_45: 0% of N_{pl} with a an angle of 45 degrees representing the degree of bi-axiality;
- (ii) n40_45: 40% of N_{pl} with a an angle of 45 degrees representing the degree of bi-axiality;
- (iii) n80_45: 80% of N_{pl} with an angle of 45 degrees representing the degree of bi-axiality.

Figure 157 and Figure 158 provide the corresponding results along with the tabulated data in Table 34. This study was performed only to focus on the differences between EC3 plastic equations and Matlab software, which were seen again to be negligle. No consideration of MNA calculations was done since it led to inaccurate results in the previous study.

However, and since the biggest disparities would occur for relatively low axial levels as mentioned above, an additional sub-study was deemed necessary to quantify and assess this probable difference. Thus, another 25 additional calculations, with the same sections and same degree of biaxiality (i.e. 45 degrees), but with 20% of N_{pl} , have been computed and the corresponding results reported in Figure 159 and Table 35. The highest ratio between both sources reached a value of 6%, with the results corresponding to EC3 plastic equations being on the safe side when represented in the OIC format. This value has been considered as

acceptable and R_{RESIST} was therefore determined by means of Eurocode 3 [20] plastic interaction formulae in the following parametric studies.

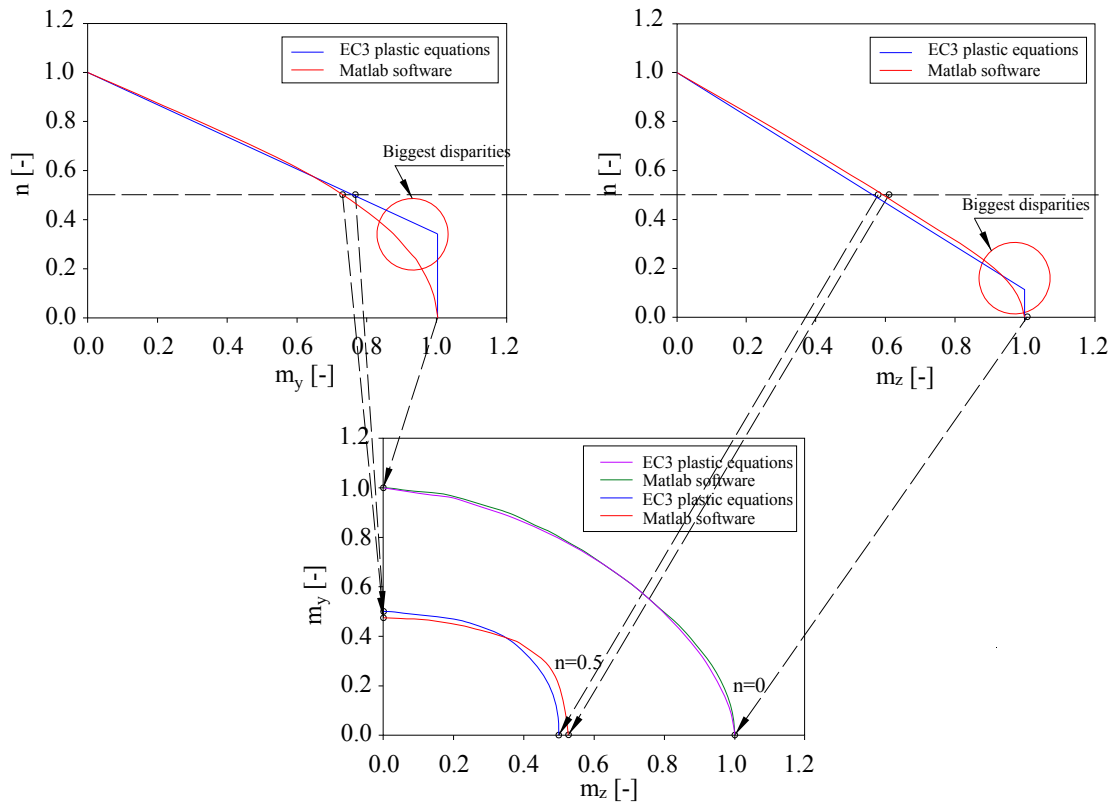


Figure 156 – Highest disparities likely to occur between the EC3 plastic equations and Matlab software – Example for RHS 200x100x4 section.

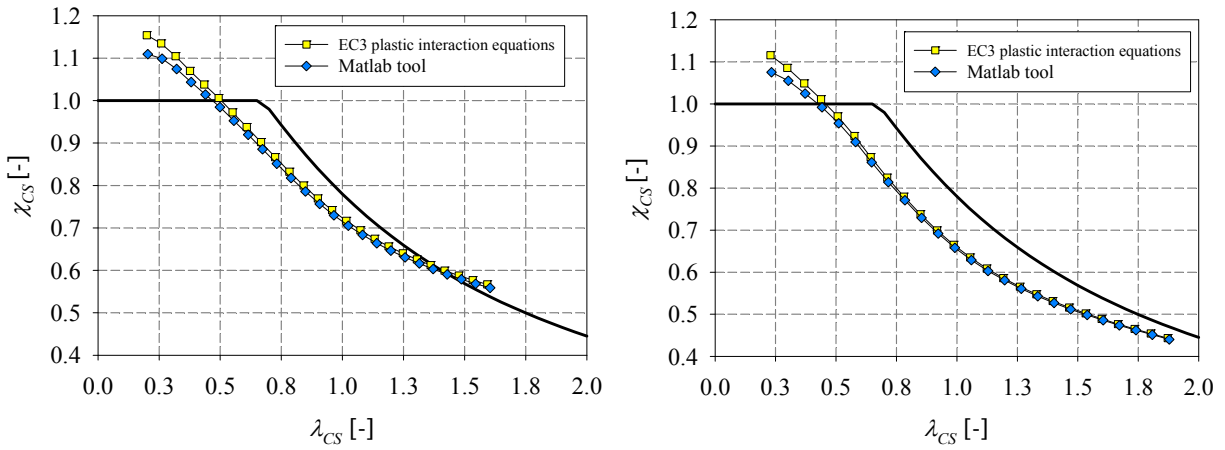


Figure 157 – Comparison of R_{RESIST} calculations with EC3 and Matlab tool for the combined load case: a) n0_45, b) n40_45.

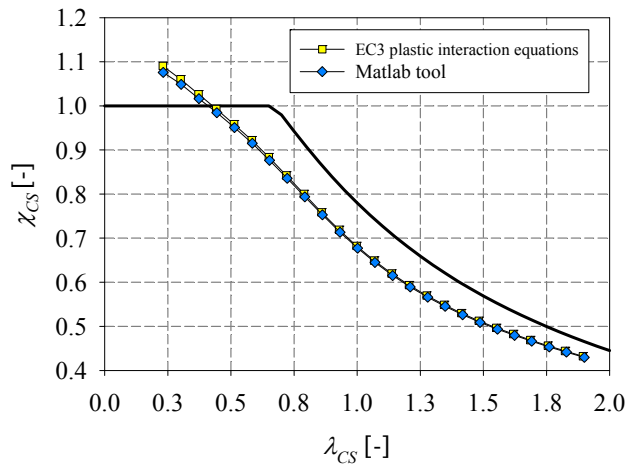


Figure 158 – Comparison of R_{RESIST} calculations with EC3 and Matlab software for the combined load case: n80_45.

Table 34 – Comparisons of R_{RESIST_EC3} with R_{RESIST_Matlab} , load cases: n0_45, n40_45 and n80_45.

	n0_45	n40_45	n80_45
Cross-section	$\frac{R_{RESIST_EC3}}{R_{RESIST_Matlab}}$	$\frac{R_{RESIST_EC3}}{R_{RESIST_Matlab}}$	$\frac{R_{RESIST_EC3}}{R_{RESIST_Matlab}}$
SHS_40x40x2.66	0.96	0.96	0.99
SHS_50x50_2.63	0.97	0.97	0.99
SHS_60x60x2.60	0.97	0.98	0.99
SHS_70x70x2.59	0.98	0.98	0.99
SHS_80x80x2.58	0.98	0.98	0.99
SHS_90x90x2.57	0.98	0.98	0.99
SHS_100x100x2.56	0.98	0.99	0.99
SHS_110x110x2.55	0.98	0.99	0.99
SHS_120x120x2.55	0.98	0.99	0.99
SHS_130x130x2.55	0.98	0.99	0.99
SHS_140x140x2.54	0.98	0.99	0.99
SHS_150x150x2.54	0.98	0.99	0.99
SHS_160x160x2.54	0.98	0.99	0.99
SHS_170x170x2.53	0.98	0.99	0.99
SHS_180x180x5.53	0.98	0.99	0.99
SHS_190x190x2.53	0.98	0.99	0.99
SHS_200x200x2.53	0.98	0.99	0.99
SHS_210x210x2.53	0.98	0.99	0.99
SHS_220x220x2.53	0.98	0.99	0.99
SHS_230x230x2.52	0.98	0.99	0.99
SHS_240x240x2.52	0.98	0.99	0.99
SHS_250x250x2.52	0.99	0.99	0.99
SHS_260x260x2.52	0.99	0.99	0.99
SHS_270x270x2.52	0.99	0.99	0.99
SHS_280x280x2.52	0.99	0.99	0.99
Mean	0.98	0.99	0.99
Standard deviation	0.006	0.007	0.002

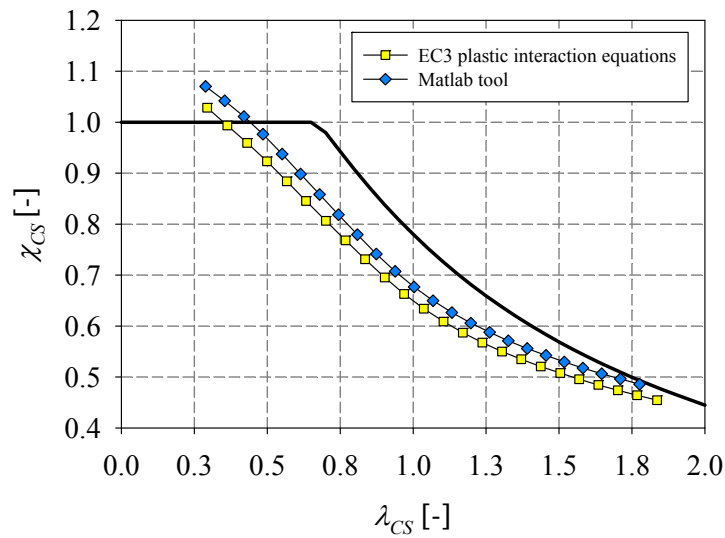


Figure 159 – Comparison of R_{RESIST} calculations with, EC3 and Matlab software for the combined load case: n20_45.

Table 35 – Comparisons of R_{RESIST_EC3} with R_{RESIST_Matlab} , load case: n20_45.

Load case	n20_45
Cross-section	$\frac{R_{RESIST_EC3}}{R_{RESIST_Matlab}}$
SHS_40x40x2.66	1.02
SHS_50x50_2.63	1.04
SHS_60x60x2.60	1.04
SHS_70x70x2.59	1.05
SHS_80x80x2.58	1.05
SHS_90x90x2.57	1.06
SHS_100x100x2.56	1.06
SHS_110x110x2.55	1.06
SHS_120x120x2.55	1.06
SHS_130x130x2.55	1.06
SHS_140x140x2.54	1.06
SHS_150x150x2.54	1.06
SHS_160x160x2.54	1.06
SHS_170x170x2.53	1.06

SHS_180x180x5.53	1.06
SHS_190x190x2.53	1.06
SHS_200x200x2.53	1.06
SHS_210x210x2.53	1.06
SHS_220x220x2.53	1.06
SHS_230x230x2.52	1.06
SHS 240x240x2.52	1.06
SHS_250x250x2.52	1.06
SHS_260x260x2.52	1.06
SHS_270x270x2.52	1.06
SHS_280x280x2.52	1.06
Mean	1.06
Standard deviation	0.01

4.4.2. Determination of R_{STAB}

R_{STAB} was calculated through LBA simulations, using FINELg [104] as well. However, R_{STAB} can nowadays also quite efficiently be computed with softwares such as CUFSM [15] or GBTUL [16]. In order to evaluate in which extent this may cause differences, a limited study conducted on 125 sections with various aspect ratios covering all kind of cross-section classes is reported here – a load case with a $20\%N_{pl}$ and biaxial bending ($\alpha = 30^\circ$) was selected. The results are represented in Table 36 in terms of $R_{STAB_FINELg} / R_{STAB_CUFSM}$ ratios. It can be seen that although the differences seem to be negligible, CUFSM always leads to higher results compared to FINELg. For a better visualization, the same results are represented in Figure 160, in function of the section class, going from stocky sections at the left hand side to slender sections at the right hand side. As already said, the ratio is always seen to remain below unity, indicating higher results calculated with CUFSM. However, in the “class 3 range” (see red circle in Figure 160), the difference reaches its higher values for square and rectangular sections.

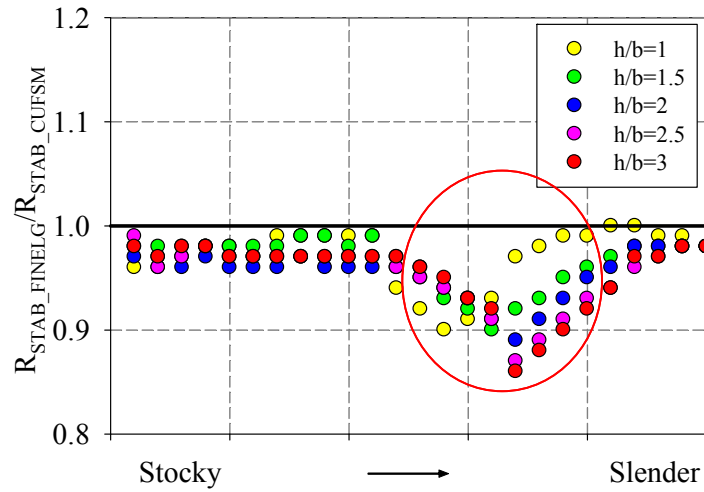


Figure 160 – $R_{STAB_FINELg} / R_{STAB_CUFISM}$ graphical representation as a function of sections' slenderness (class).

Table 36 – R_{STAB_FINELg} vs. R_{STAB_CUFISM} tabulated values for calculated sections under combined load case.

$R_{STAB_FINELg} / R_{STAB_CUFISM}$				
$h/b=1$	$h/b=1.5$	$h/b=2$	$h/b=2.5$	$h/b=3$
0.96	0.98	0.97	0.99	0.98
0.97	0.98	0.96	0.96	0.97
0.97	0.98	0.96	0.97	0.98
0.98	0.98	0.97	0.98	0.98
0.98	0.98	0.96	0.97	0.97
0.87	0.98	0.96	0.97	0.97
0.99	0.98	0.96	0.97	0.97
0.99	0.99	0.97	0.97	0.97
0.99	0.99	0.96	0.97	0.97
0.99	0.98	0.96	0.97	0.97
0.99	0.99	0.96	0.97	0.97
0.94	0.96	0.97	0.96	0.97
0.92	0.95	0.96	0.95	0.96
0.90	0.93	0.94	0.94	0.95
0.91	0.92	0.93	0.93	0.93
0.93	0.90	0.91	0.91	0.92
0.97	0.92	0.89	0.87	0.86
0.98	0.93	0.91	0.89	0.88
0.99	0.95	0.93	0.91	0.90

0.99	0.96	0.95	0.93	0.92
1.00	0.97	0.96	0.94	0.94
1.00	0.98	0.98	0.96	0.97
0.99	0.98	0.98	0.97	0.97
0.99	0.98	0.98	0.98	0.98
0.98	0.98	0.98	0.98	0.98

CUFSM [15] which provides an implementation of the semi-analytical finite strip method (FSM) is the most common tool used for the determination of the elastic buckling loads. FINELg is based on the finite element method. So basically, finite elements are replaced by strips with CUFSM, reducing thus the number of elements and the computational required time. Moreover, the main difference between these two softwares is the ability of CUFSM (through cFSM) – and also GBT [16] – to allow for discrete separation of local distortional and global deformations. FSM provides a complete set of different buckling modes occurring within a section for different wavelengths (i.e. signature curve). In finite elements models, the common approach is to vary the length of a member in order to mimic the finite strip method. However, if the FEM model has the same boundary conditions as the FSM model, agreement is generally excellent. The comparison for one unique member length between both softwares will give similar accurate results. However, some differences may occur; finite element models may combine and superpose different modes with one unique mode. Such a result won't be possible with finite strip model.

In this study, the Finite Element Method will be adopted for the calculation of R_{STAB} , since its accuracy against the finite strip method has been confirmed and most importantly to keep a consistency in terms of the numerical model and use unique software for the calculation of both of the R_{ULT} and R_{STAB} factors.

4.5. Gathered experimental data vs. FE results

The collected experimental results from section 3.5 were used herein and presented with numerical computed results. Figure 161 shows the experimental and numerical results of cold-formed, hot-rolled and hot-formed cross-sections subjected to compression. Figure 162 presents the numerical and experimental tests of only cold-formed cross-sections subjected to major-axis bending since the number of hot-rolled cross-sections was seen to be insufficient to be represented in Figure 162. Finally, Figure 163 represents the cold-formed, hot-rolled and hot-formed results relative to experimental and numerical cross-section tests subjected to combined load cases.

Based on these figures, it can be stated that:

- (i) In all figures, a reasonably correct tendency of the experimental results with the numerical ones is observed;
- (ii) Numerical results are showing conservative tendencies especially for cold-formed cross-sections subjected to compression (see Figure 161). In other words, numerical computed results are showing a quite safe-sided lower bound approximation of experimental results, especially for the mentioned case. Even though, general imperfections introduced in numerical computations were conservative, many experimental results would fall within the studied numerical test range, indicating that reasonably appropriate adopted imperfections were made;
- (iii) The end of plateau limit adopted within the DSM is seen to be unconservative and cannot be applicable for hollow rectangular and square sections. However, computed numerical results are seen to provide a reasonably accurate end of plateau limit especially for hot-rolled and hot-formed cross-sections subjected to compression (see Figure 161b) and cold-formed cross-sections subjected to major-axis bending (Wilkinson tests in Figure 162);
- (iv) For combined load cases, results were represented in a general way, i.e. no distinction between combined ‘compression + major or minor-axis bending’ and ‘compression + major-axis bending + minor-axis bending’ was made. A more detailed analysis will be made in the following sections to separate the various combined load cases. However, the one thing that could be stated based on Figure 163 is that experimental results are lying within the numerical computed range and are following the same tendencies.

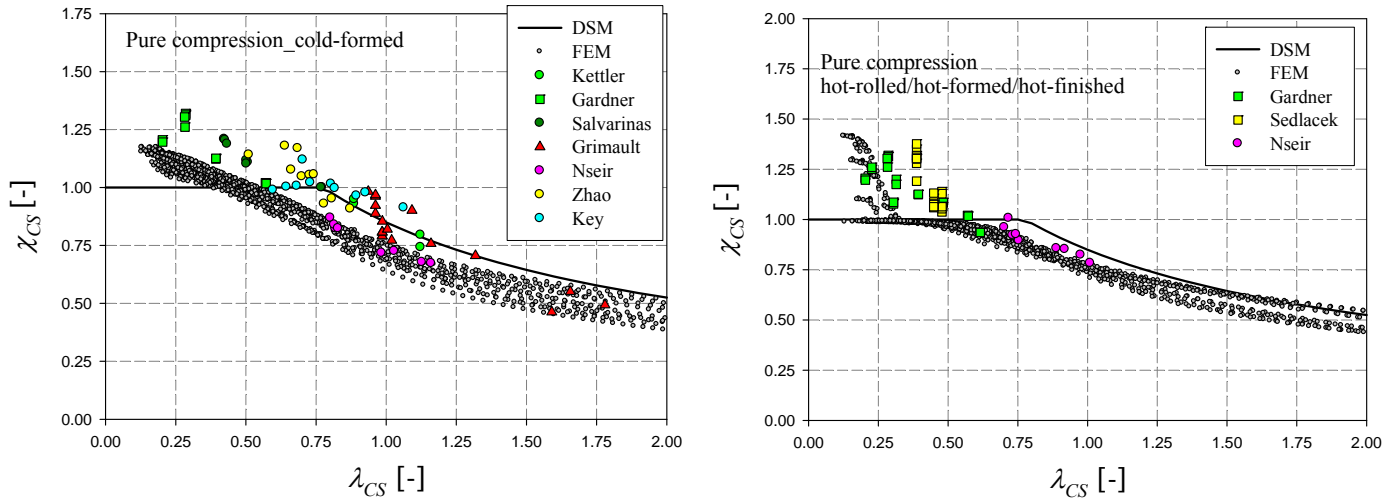


Figure 161 – Experimental and numerical test results relative to pure compression load cases,
a) cold-formed cross-sections, b) hot-rolled and hot-formed cross-sections.

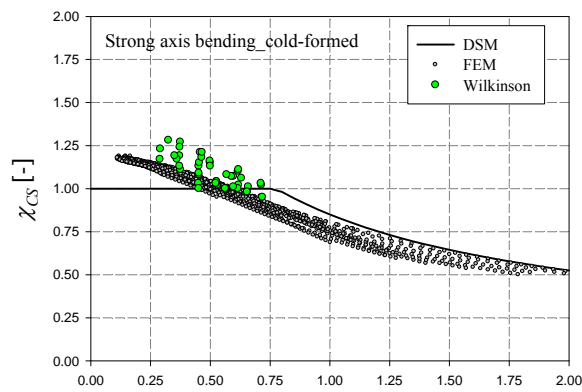


Figure 162 – Experimental and numerical test results relative to major-axis bending load cases.

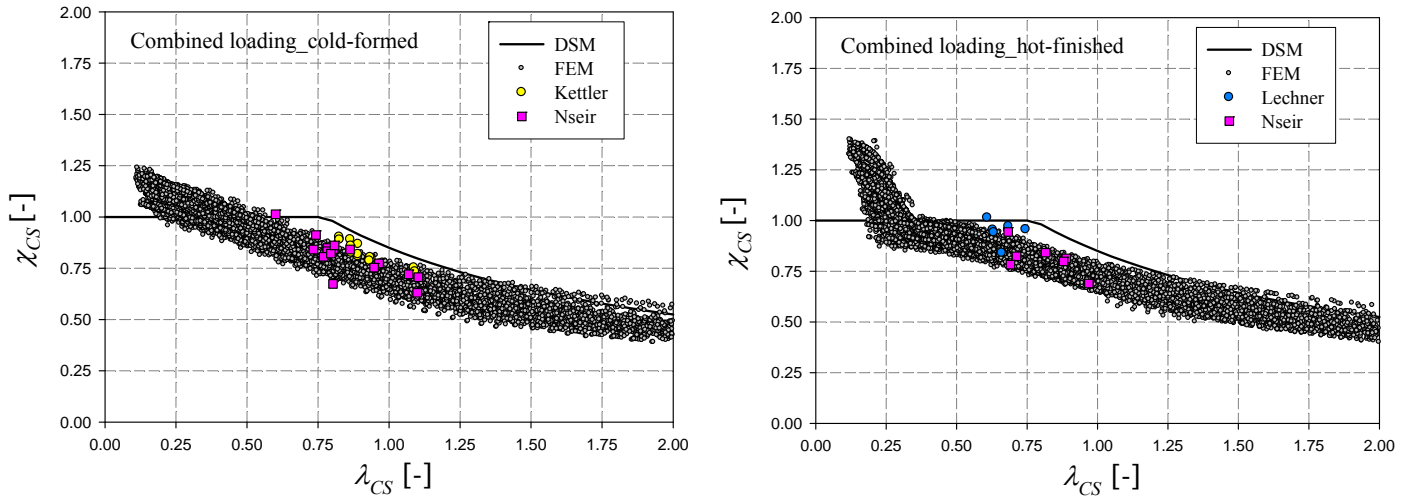


Figure 163 – Experimental and numerical test results relative to combined load cases,
a) cold-formed cross-sections, b) hot-rolled and hot-formed cross-sections.

4.6. Summary

This chapter described finite element modelling of the conducted 57 cross-section tests with the measured imperfections, material law and residual stresses. Also, a numerical model was compared and validated against experimental data from Kettler [7]. The numerical model was seen to be fully appropriate compared to the experimental results and was subsequently used and extended to generate two set of numerical cross-sections tests resorting to almost 40 000 computed cold-formed and hot-rolled cross-section results. The principal aim of the numerical campaign was to investigate the physical behaviour of square and rectangular hollow sections, so that appropriate interaction curves could be derived. At the end of this section, collected experimental database in section 3.5 was plotted with the computed numerical results. It turned out that numerical results are showing in general, safe-sided lower approximations of the experimental results. However, many experimental results fell inside the numerical studied range and some load cases were seen to have sufficiently accurate predictions of the end-of plateau value.

Now that both experimental and numerical investigations were covered, the following chapter will present the adopted design model with its corresponding design curves relative to hot-rolled and cold-formed cross-sections subjected to simple and combined load cases.

5. Design proposal – Overall cross-section design

5.1. Identification of key parameters

5.1.1. Influence of yield stress, geometrical imperfections and residual stresses

Various cold-formed and hot-rolled material laws were adopted as represented in Figure 164. The membrane residual stresses included in the hot-rolled sections were introduced with a reference yield stress of 235 MPa. Therefore, and based on the obtained numerical results, the main influence of the yield stress was reflected in the ‘imperfections-governed’ zone, since the residual stresses – which are based on a reference yield of 235MPa – will have a less important influence on the cross-sections having higher yield stresses than 235 MPa. Similarly, for cold-formed sections, the flexural residual stresses were introduced based on a reference yield stress of 235 MPa and cases with high yield strength will thus have a higher value of the penalty factor χ_{CS} .

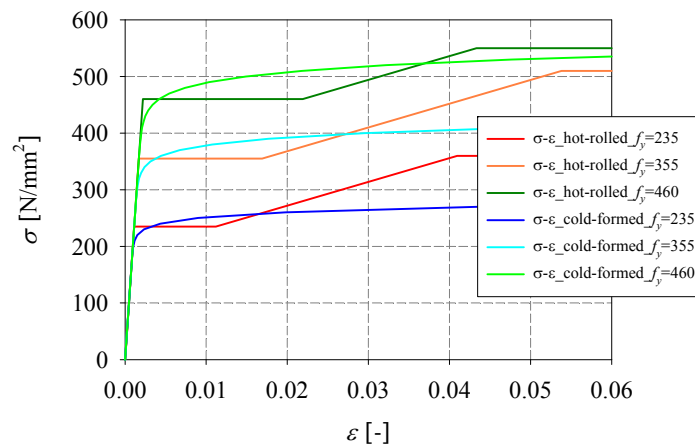


Figure 164 – Hot-rolled and cold-formed material laws adopted in numerical computations.

Another difference between results concerning cold-formed sections with various yield stresses is highlighted and discussed in more details in section 5.3.1.1. This difference, which is mainly due to the choice of the non-linear material laws, was seen to affect the resistance of cross-sections on the complete range of slendernesses without being localised within the ‘imperfection-governed’ zone.

However, the differences relative to the influence of yield stresses were seen to be negligible in all cases and this parameter was thus not considered as one of the leading parameters for

the derivation of the interaction curves. The interaction curves were thus based on the numerical results relative to the S235 yield stress.

The mechanical and geometrical imperfections influences were considered to be in the series of the leading parameters since their effect is non-negligible. Therefore, a factor accounting for mechanical and geometrical imperfections was included in all the derived interaction curves.

5.1.2. Influence of material law

The material law choice will obviously affect the numerical results, especially in terms of the adopted type of the material law. For hot-rolled cross-sections, a linear elastic plastic material law with strain hardening was adopted while a non-linear Ramberg Osgood law was adopted for cold-formed sections. The resulting material laws are presented in Figure 164.

For certain ranges of the strains, the cold-formed material law lies below the hot-rolled material laws, and the opposite is seen for other strain ranges. This would be reflected in results which will depend on the ultimate strain reached at failure. A comparison between results relative to hot-rolled and cold-formed cross-sections subjected to compression is presented in Figure 165 and clearly reflects the effect of the material law on the cross-section resistance. Therefore, for cross-section penalty factors smaller than 1.0 ($\chi_{CS} < 1.0$), i.e. $\varepsilon < \varepsilon_y$, the cold-formed results lie below the hot-rolled results in a consistent way with both material laws. For $\varepsilon > \varepsilon_y$, the opposite is observed, since the cold-formed material law is lying above the hot-rolled material law.

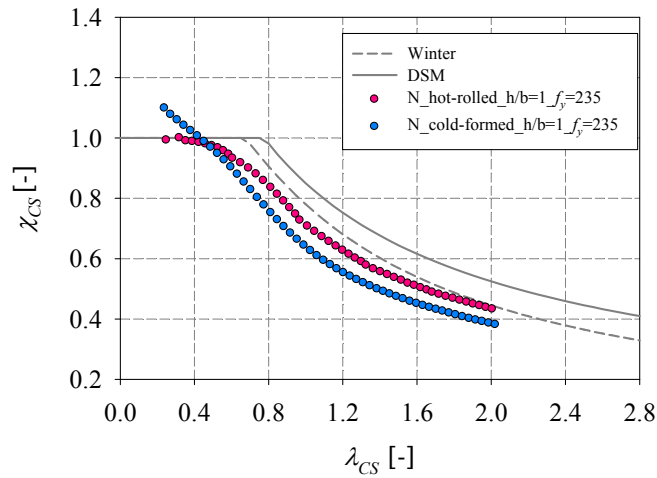


Figure 165 – Numerical results relative to hot-rolled and cold-formed cross-sections subjected to compression.

Consequently, the effect of the material law was not introduced in the proposed curve: separate curves were derived for both types of material laws, i.e. for both types of fabrication processes. The choice of a material response is however accompanied by important other assumptions such as the residual stresses patterns and the consideration of different structural behavior in the corners of cold-formed sections etc...

It would be interesting in this section to open small brackets concerning the structural behavior of cross-sections at failure. The stress-strain results at failure of cross-sections subjected to a pure compression were reported in Figure 166, along with the corresponding stress-strain material law. The numerical results relative to cold-formed and hot-rolled cross-sections with various yield stresses were reported on the six relative material laws. It can be seen for hot-rolled sections that almost none of the results could reach an ultimate strain within the plateau range. This was due to the material law shape having a plastic plateau with almost a negligible slope introduced in the numerical model; the sections could not undergo further deformation unless the stress increased with it as well. This was not seen in cold-formed sections since the material laws were non-linear. However, what was remarkable in cold-formed sections is that the results would seem grouped at relatively large strains and no additional strains could be achieved. This is mainly due to the adopted material law in the corners of cold-formed sections which were characterized by a small ductility and a maximum strain of 2.5%. Therefore, once the cross-sections reached that level of strain, the

corners would find themselves ineffective leading to the failure of the entire cross-section, and no more strains could be achieved beyond this value of 2.5% strain.

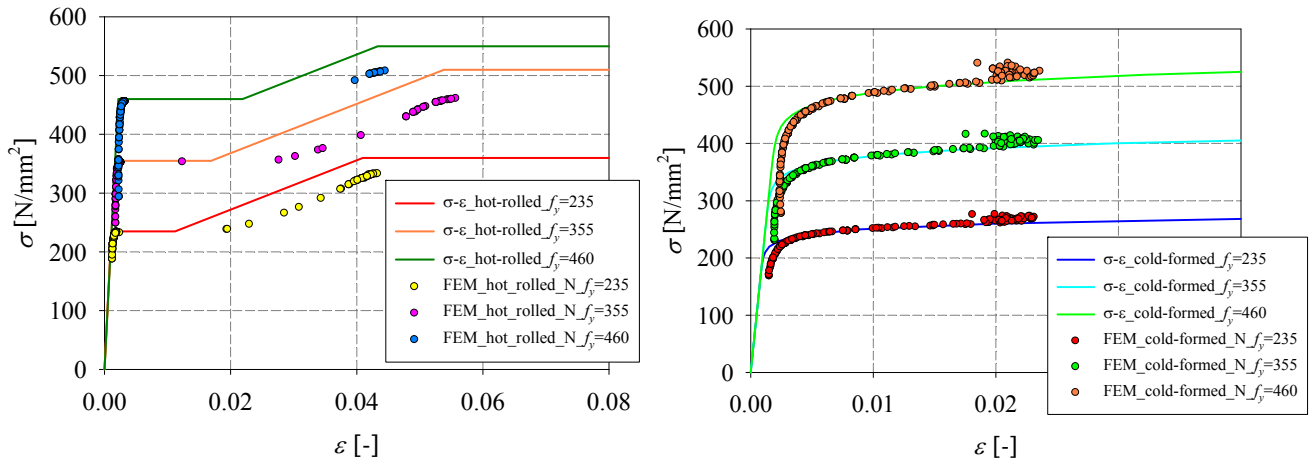


Figure 166 – Numerical stress-strain results reported with the hot-rolled and cold-formed material laws.

Zoomed graphs for small strains are presented in Figure 167 and Figure 168. The results are consistent with what has been discussed in the state of the art section 2.1.2. For slender sections, the post-buckling strengths can be greater than the buckling strengths and this increase might be quite considerable for such slender sections. Therefore, their post-buckling reserves would be significant. That is why the results with the lowest ultimate stresses reached higher strains with higher post-buckling reserves. When the sections become less slender, the post-buckling reserves become smaller and the critical buckling stress would be close to the yield stress. Therefore, the yielding would start almost immediately after buckling. Such tendency is clearly shown in Figure 167 and Figure 168 when the cross-sections become less and less slender, until they reach a certain level at which they become stocky enough to reach the yield plateau without local buckling occurrence and undergo further strains.

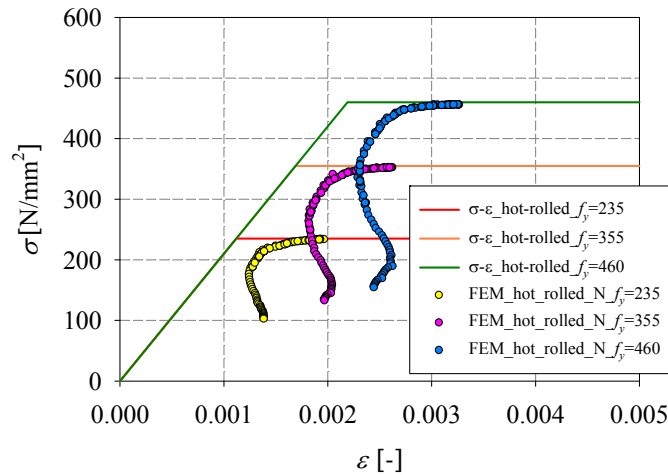


Figure 167 – Numerical stress-strain results reported with the hot-rolled material laws.

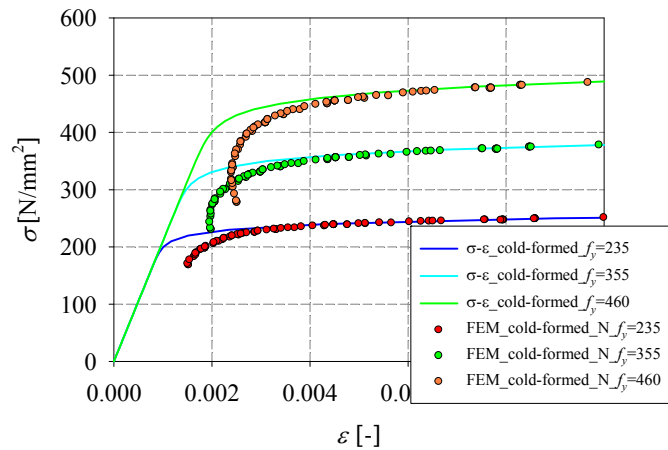


Figure 168 – Numerical stress-strain results reported with the cold-formed material laws.

5.1.3. Influence of cross-section shape and load case

The cross-section shapes and the load cases are one of the leading parameters in the derivation of the interaction formulae. An example of simple load cases such as compression or major-axis bending are used herein to show their important influence on the cross-section capacities of hollow sections with various aspect ratios h/b .

For the simple compression case represented in Figure 169, it is shown that rectangular hollow sections ($h/b > 1.0$) reach higher relative section resistance compared to square

hollow sections possessing the same relative slenderness, particularly in the slender range. The level of restraint offered by the narrow faces of the rectangular section to the wider ones is therefore shown to provide an increased cross-section resistance through stress redistributions once local buckling develops in the more buckling-prone plates. Consequently, the cross-section resistance is increased with the h/b ratio, and square sections consequently exhibit the lowest resistance to compression ($h/b=1.0$) owing to simultaneous buckling of the constitutive plates.

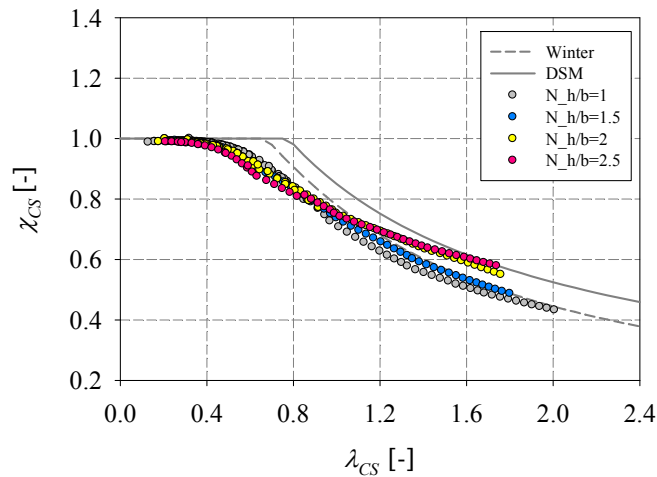


Figure 169 – FE results for square and rectangular sections under compression, various aspect ratios, S355.

For major-axis bending, the opposite is shown in Figure 170: the square hollow sections are seen to achieve higher relative resistances than the rectangular ones possessing the same cross-section slenderness, particularly in the slender range. The load case type plays a delicate role and decisive one for the structural behavior of elements. Contrarily to the compression case, the compressed flanges in the major-axis bending load cases find themselves in need for a greater restraint from the webs which in turn have higher slenderness in rectangular sections than square ones.

Consequently, the restraint provided by the webs to the flanges will be greater in the case of square sections, thus delaying the onset of local buckling. This is pronounced for slender sections, where failure occurs largely within the elastic range. For stocky sections, failure

will be achieved at higher strains, where plasticity leads the structural behavior, reducing the detrimental restraint brought to the flanges.

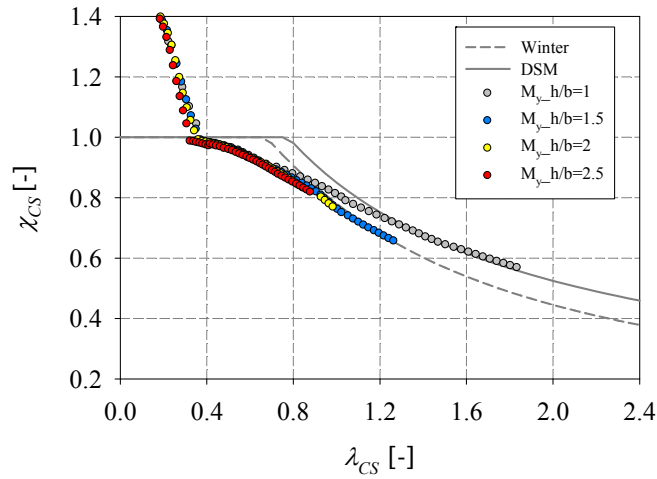


Figure 170 – FE results for square and rectangular sections under major axis bending moment, various aspect ratios, S355.

1.1.1. Influence of warping and second-order effects

Kettler [7] conducted a detailed study concerning the effect of warping and second-order effects. It showed that the full plastic capacity can only be reached when the warping moment M_w is present in the case of biaxial bending and a high level of axial forces.

Therefore, the warping moment that is needed to reach the full plastic capacity of the relevant cross-section needs a warping restraint to develop itself. This warping restraint can be brought either by an endplate or by adjacent parts of the profile. However, it is also demonstrated that the internal indeterminate torsional equilibrium between the primary and secondary torsional moment could be sufficient to resist the warping moment resulting from plasticity effects. The resulting deformations are very small for tubular profiles and the warping disturbances are locally restricted. Therefore, tubular profiles are always able to activate their full plastic cross-section capacity because of their very high torsional stiffness. (unlike open sections) and no warping problems are to be expected in this study.

This very high torsional stiffness also affects the second-order effects which will be minor compared to the one resulted in open sections. Kettler [7] showed that the differences arising from the data points $M_{end,u}$ (which can be interpreted as the applied stresses at the

end of the specimen) and the calculated $M_{mid,u}$ data points (which are the actual stresses at the middle cross-section) are due to global second-order effects. In case of tubular sections, these differences were seen to be very small and are anyway included in all the numerical results of this thesis.

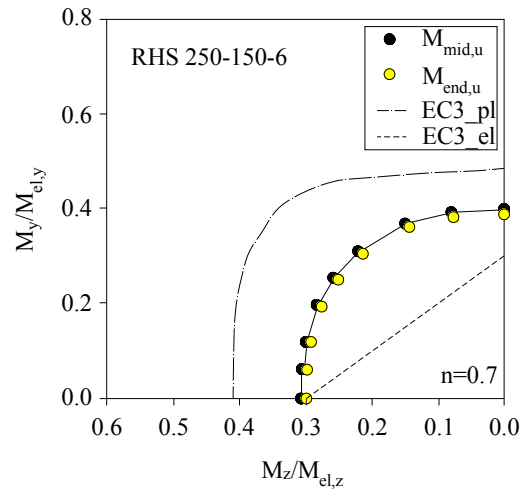


Figure 171 – Comparison of end moments and mid moments of a rectangular hollow section subjected to combined loading with a high level of axial force [7].

5.2. Towards a design proposal: Mechanical background

As previously stated in section 2.3, the ‘buckling curve’ approach will be adopted in this study, since it allows simple, fast and accurate calculation. Three analytical ways of formulating the design curve can be considered:

- (i) Mathematical formulations;
- (ii) Merchant-Rankine formulation;
- (iii) Ayrton-Perry format.

The three different ways will be briefly discussed in the following sub-sections, with the target of selecting the most appropriate formulation type, which will be adopted for the development of the design curves.

5.2.1. Empirical formulations

Several authors have proposed purely empirical relationships. For instance, for flexural member buckling, the most famous ones are the formulae of Baar [112], Young [113] and Bjorhovde [114].

It is clear that the following type of series can enable a rigorous representation of almost any curve, provided that the number n is sufficiently high, which will involve a large number of parameters a_i and make impractical the use of this kind of formulation:

$$\chi = \sum_{i=0}^n a_i \lambda^i \quad (108)$$

Baar [112], proposed buckling curves using this format and adopted 4 parameters per curve, and tested various mathematical series:

$$\chi = 1 + \sum_{i=1}^4 a_i \lambda^i \quad (109)$$

$$\chi = \frac{1}{1 + \sum_{i=1}^4 a_i \lambda^i} \quad (110)$$

$$\chi = \frac{1 + a_4 \lambda}{1 + \sum_{i=1}^3 a_i \lambda^i} \quad (111)$$

In 1972, Young [113] proposed an inverse mathematical equation for the derivation of slightly different member buckling curves compared to CECM equations [115]:

$$\lambda^2 = \sum_{i=1}^4 a_i \chi^{i-2} \quad (112)$$

This proposal presented a major inconvenient for practical applications, since the determination of χ required successive approximations.

Eventually, Bjorhovde [114] used polynomial equations for the determination of the member buckling curves of the Structural Stability Council (SSRC), however with a discontinuous description, i.e. 4 polynomial equations per curve. Also, his proposals presented many

inconvenients, since a large number of parameters were required and the discontinuities caused unnecessary complexity.

5.2.2. Merchant-Rankine formulation

The combination of the resistance limit $\chi = 1.0$ with the formula of a perfect plate with post-critical effects, i.e. the well-known Von Karman formula $\chi = 1/\lambda$, will lead to an upper bound of buckling curves through the Ayrton-Perry formula discussed in more details in the following section.

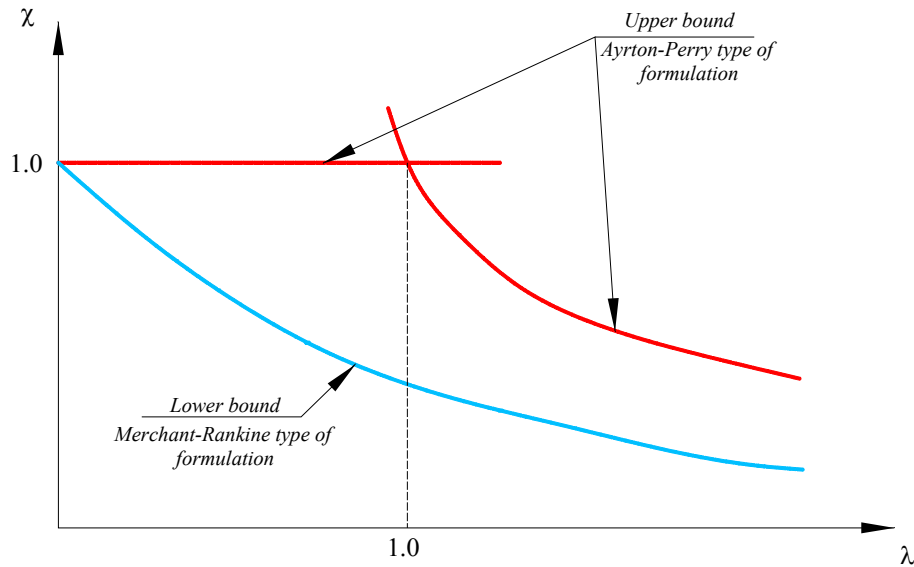


Figure 172 – Upper and lower bounds of buckling curves.

As for the lower bound of buckling curves, Merchant was the first to suggest a linear interaction formula for member buckling, hereafter referred to as the Rankine equation [116]:

$$\frac{\sigma_{ult}}{\sigma_{cr}} + \frac{\sigma_{ult}}{\sigma_y} = 1.0 \quad (113)$$

where σ_{ult} refers to the ultimate stress. For plates, the critical buckling stress σ_{cr} would be equal to $k \frac{\pi^2 E}{12(1-\nu^2)} \left(\frac{t}{b}\right)^2$ and for columns it would be relative to the Euler curve. σ_y is the corresponding yield stress.

In a non-dimensional form, Equation (113) could be written as follows:

$$\chi + \chi \cdot \lambda^2 = 1 \quad (114)$$

However, with member buckling curves, it turned out that the Merchant-Rankine is not truly respected since the member buckling curve d [20] happened to be situated below the Merchant-Rankine curve. More details can be found in Rondal [43].

Equation (114) can be rewritten as follows:

$$\chi = \frac{1}{1 + \lambda^2} \quad (115)$$

Lindner [117] and Unger [118] proposed a generalization of the Merchant-Rankine equation, with the use of the following equation:

$$\chi = \left(\frac{1}{1 + \lambda^{2n}} \right)^{1/n} \quad (116)$$

Lindner [117] and Unger [119] proposed various values of n corresponding to the different member curves (a_0 , a , b , c and d). The authors of the project revision of DIN 4114-Stabilitätsfälle im Stahlbau [120], adopted a polynomial equation for the determination of the n parameter:

$$n = \sum_{i=0}^4 a_i \lambda^i \quad (117)$$

with given a_i values (see [43]).

Possibilities for a ‘plastic plateau’ in the reduction curve ($\lambda \leq \lambda_0$) can be easily introduced in the Merchant-Rankine type of formula with the following equation:

$$\chi = \left(\frac{1}{1 + \lambda^{2n} - \lambda_0^{2n}} \right)^{1/n} \quad (118)$$

For the case of plate buckling, the Merchant-Rankine linear equation can be written as:

$$\chi = \frac{1}{1 + \lambda} \quad (119)$$

with the consideration of the Von Karman equation to replace the Euler formula.

The Lindner and Unger proposal with the consideration of the end-of-plateau would thus be:

$$\chi = \left(\frac{1}{1 + \lambda^n - \lambda_0^n} \right)^{1/n} \quad (120)$$

5.2.3. Ayrton-Perry format

The physical basis of the Ayrton-Perry formulation lies in the adoption of a failure criteria based on the attainment of the yield limit, with the following equation of a column subjected to a pure compression with an initial curvature amplitude e_0 :

$$\frac{N}{A} + \frac{M''}{W_{el}} = f_y \quad (121)$$

Equation (121) can be rearranged in terms of stresses, where σ_{ult} represents the ultimate stress and W_{el} the elastic modulus:

$$\sigma_{ult} + \frac{\sigma_{ult} \cdot e_0}{\left(1 - \frac{\sigma_{ult}}{\sigma_{cr}}\right)} \cdot \frac{A}{W_{el}} = f_y \quad (122)$$

which in turn can be represented in the following form:

$$\sigma_{ult} (\sigma_{cr} - \sigma_{ult}) + \sigma_{cr} \sigma_{ult} e_0 \frac{A}{W_{el}} = f_y (\sigma_{cr} - \sigma_{ult}) \quad (123)$$

$$f_y (\sigma_{cr} - \sigma_{ult}) - \sigma_{ult} (\sigma_{cr} - \sigma_{ult}) = \sigma_{ult} \sigma_{cr} e_0 \frac{A}{W_{el}} \quad (124)$$

$$(\sigma_{cr} - \sigma_{ult})(f_y - \sigma_{ult}) = \eta \sigma_{cr} \sigma_{ult} \quad (125)$$

$$\text{With } \eta = \frac{e_0 A}{W_{el}}$$

In a non-dimensional form, Equation (125) can be written as follows, by multiplying both sides of it by $1/f_y$:

$$(1 - \chi)(1 - \chi \lambda^2) = \eta \chi \quad (126)$$

where χ is the reduction factor, λ is the relative slenderness and η is the factor accounting for generalized imperfections.

In order to provide an appropriate representation of a buckling curve, the η parameter relative to imperfections should fulfil the following conditions:

- (i) Include the geometrical and mechanical imperfection effects;
- (ii) Represent appropriately the end-of-plateau limit, where $\chi = 1$ for $\lambda \leq \lambda_0$ (λ_0 being the end-of-plateau limit);
- (iii) Allow to retrace the Von Karman (in case of a perfect plate) or Euler curve (in case of a perfect column) crossed with the defined plastic plateau, for a value of η equal to zero.

Figure 172 shows in a clear way that the Ayrton-Perry formula reflects the two failure modes (instability limit from one hand and resistance limit from another hand), and highlights clearly the imperfections' effects, which act primary around $\lambda = \lambda_{rel} = 1.0$.

In case of plates, the Ayrton-Perry format will thus be rearranged as the following:

$$(1 - \chi_{plates})(1 - \chi_{plates} \lambda_{plates}) = \eta \chi_{plates} \quad (127)$$

with the consideration of the resistance plateau to be limited to $\chi_{plates} = 1$ and the instability limit defined with the Von Karman formula with $\chi_{plates} = 1 / \lambda_{plates}$

Concerning the η value, Dwight [121] proposed the following equation:

$$\eta = \alpha (\lambda - \lambda_0) \quad (128)$$

where α is an imperfection factor to be determined and λ_0 the end-of-plateau limit. Many propositions have been performed to define the values of α and λ_0 for the case of global buckling curves. This same equation will also be adopted in the derivation of local buckling curves.

The following sub-section will introduce the adopted type of formulation for the derivation of local buckling curves and the appropriate modifications to be considered so that the cross-section resistance of hollow plated steel members can be calculated.

5.2.4. Adopted formulation

The Ayrton-Perry (also sometimes denoted as Perry-Robertson) formula has been selected as the type to be adopted for the derivation of the corresponding OIC formulae. Embedded is a simple yet accurate way of considering both failure limits to be defined, with possible plateau and generalise-imperfection factor. In addition, both the resistance limit and the instability limit can be adapted to the trends observed in the numerical results. Accordingly, four parameters were combined in an extended Ayrton-Perry format. Therefore, the following four variables can be incorporated into the Ayrton-Perry formula and were locally calibrated through a best-fit procedure (see Figure 173 for graphical interpretations):

- (i) β , characterising the resistance limit: since stocky cross-sections usually gain from strain-hardening reserves, $\chi_{CS} > 1.0$ predictions may be appropriate. β values higher than 1.0 aim at accounting for these potential benefits;
- (ii) δ , relative to the instability limit: as some cross-sections are shown to exhibit post-buckling reserves higher than predicted by the Von Karman formula (relative to simple plates), an additional factor shall account for a possible variation of the instability limit;
- (iii) The end-of-plateau λ_0 value;
- (iv) The imperfection factor which will be called α_{CS} to avoid confusion with the α angle defining the degree of bi-axiality (see section 4.3.4).

The corresponding ‘extended’ Ayrton-Perry format then becomes the following:

$$(\beta - \chi_{CS})(1 - \chi \lambda_{CS}^{\delta}) = \eta \chi_{CS} \quad (129)$$

Equation (129) can be rearranged into the following form:

$$\lambda^{\delta} \chi_{CS}^2 - \chi_{CS} (\beta \lambda_{CS}^{\delta} + \eta + 1) + \beta = 0 \quad (130)$$

which will lead to:

$$\chi_{CS} = \frac{\beta \lambda_{CS}^{\delta} + \eta + 1 - \sqrt{(\beta \lambda_{CS}^{\delta} + \eta + 1)^2 - 4 \lambda_{CS}^{\delta} \beta}}{2 \lambda_{CS}^{\delta}} \quad (131)$$

Introducing $\phi = 0.5(1 + \eta + \lambda^{\delta} \beta)$, Equation (131) can be written as the following:

$$\chi_{CS} = \frac{\phi - \sqrt{\phi^2 - \lambda_{CS}^\delta \beta}}{\lambda_{CS}^\delta} \quad (132)$$

This equation can now be multiplied by the complement of $\phi - \sqrt{\phi^2 - \lambda_{CS}^\delta \beta}$:

$$\chi_{CS} = \frac{\phi - \sqrt{\phi^2 - \lambda_{CS}^\delta \beta}}{\lambda_{CS}^\delta} \left[\frac{\phi + \sqrt{\phi^2 - \lambda_{CS}^\delta \beta}}{\phi + \sqrt{\phi^2 - \lambda_{CS}^\delta \beta}} \right] \quad (133)$$

This finally leads to the extended form of Ayrton-Perry adapted for the cross-section buckling behavior:

$$\chi_{CS} = \frac{\beta}{\phi + \sqrt{\phi^2 - \lambda_{CS}^\delta \beta}} \quad (134)$$

with

$$\phi = 0.5(1 + \alpha_{CS}(\lambda_{CS} - \lambda_0) + \lambda^\delta \beta) \quad (135)$$

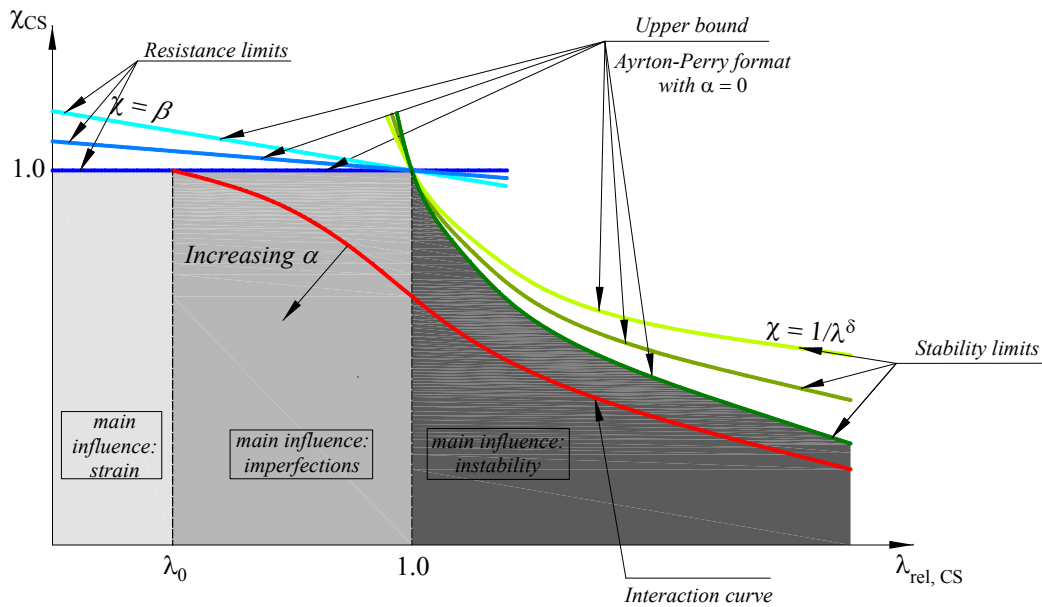


Figure 173 – Schematic representation of the adopted Ayrton-Perry approach.

In Eurocodes, the actual approach follows the Winter formula presented in section 2.1. It consists in the following equation:

$$\chi_{CS} = \frac{1}{\lambda_{CS}} - \frac{0.22}{\lambda_{CS}^2} \quad (136)$$

The first term $1/\lambda_{CS}$ of the equation is relative to Von Karman instability equation followed by a correction factor equal to $\frac{0.22}{\lambda_{CS}^2}$, function of λ_{CS} and taking into account a correction relative to imperfection effects.

The DSM, which was recently adopted in the North American and Australian standards for the design of cold-formed steel structural members, is based on the consideration of the same type of Winter formula but with a modification of its relative factors, and the adoption of a higher instability limit through the replacement of the Von Karman's exponent by 0.8 instead of 1.0. As already mentioned in section 2.5.1, the DSM formula for local buckling of thin-walled cold-formed sections is thus presented through the following equation:

$$\chi_{CS} = \frac{1}{\lambda_{CS}^{0.8}} - \frac{0.15}{\lambda_{CS}^{1.6}} \quad (137)$$

In the following sub-sections, the derived and calibrated proposed design formulae are presented in OIC-defined axes graphs, i.e. the horizontal axis relates to the generalized cross-section slenderness λ_{CS} while the vertical axis reports on the cross-section reduction factor χ_{CS} . The winter and DSM curves being considered as reference curves were also added in all presented graphs, with no intention of comparison since Winter was meant for plates subjected to compression and DSM's targets were mainly thin-walled – mostly open – cold-formed sections.

5.3. Determination of interaction curves

With the adoption of the previously-detailed Ayrton-Perry extended format, locally fitted factors were defined for simple load cases (including axial compression, major-axis bending and minor-axis bending) and combined load cases. The proposed design curves for simple load cases of hot-rolled and cold-formed cross-sections will be presented in this section, followed by proposed design curves relative to combined load cases.

5.3.1. Simple load cases

5.3.1.1. Axial compression

5.3.1.1.1. Hot-rolled sections

Numerical results relative to all treated hot-rolled cross-sections in compression were presented in Figure 174 and grouped based on the following aspect ratios: $h/b = 1, 1.5, 2$ and 2.5 .

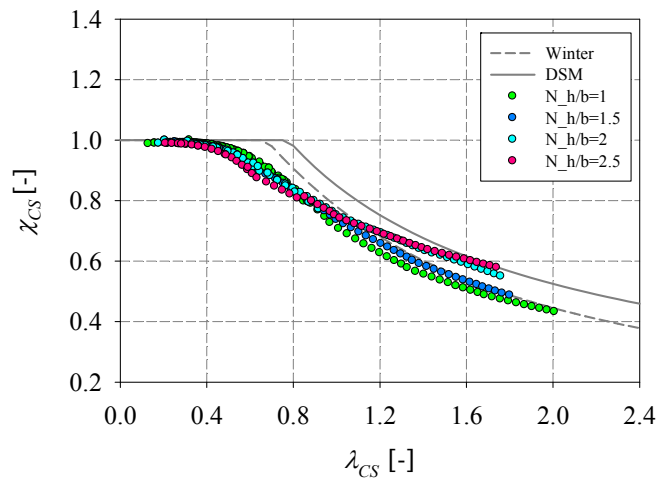


Figure 174 – FE results relative to various cross-section ratios in compression, S235 (both European and virtual sections are considered in this graph).

The following interpretations can be stated based on the obtained results:

- (i) Clear tendencies for large slenderness values can be seen. The Von Karman stability curve was clearly not suitable and new clear tendencies could be derived. Therefore a choice of a simple curve, function of the aspect ratio was proposed through a best-fit, leading to the δ value as follows:

$$\delta = -0.4 h/b + 1.45 \quad (138)$$

for h/b values comprised between 1.0 and 2.5.

It has to be noted that the cross-section reduction factor relative to aspect ratios situated in between the 4 cross-section aspect ratios used to define the proposed design curves,

can be found through a simple interpolation. Additional computations with cross-sections having respectively aspect ratios of $h/b = 1.1$ and 1.8 were made (see Figure 175) to show that the interpolation is possible in a continuous way with the proposed design curves.

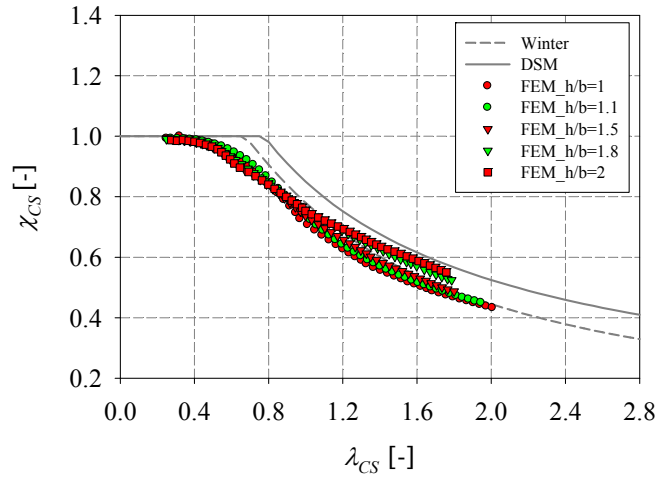


Figure 175 – Computations relative to hot-rolled sections with $h/b = 1.1$ and $h/b = 1.8$.

- (ii) The resistance limit was kept to $\chi_{CS,max} = 1.0$ (i.e. $\beta = 1.0$) since strain-hardening reserves for hot-rolled sections were only observed for unrealistic section shapes and deformation levels. In other words, the results in which the peak loads are in excess of the traditional plastic capacities due to strain-hardening were deemed unrealistic and were therefore disregarded (see Figure 176).

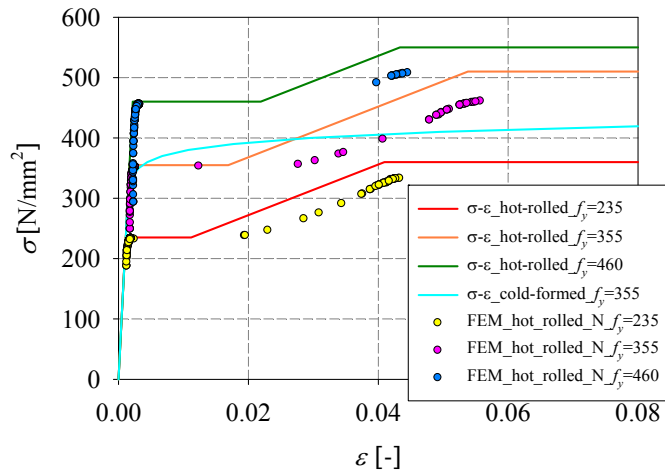


Figure 176 – Ultimate strains reached for all the numerical calculations relative to hot-rolled cross-sections.

- (iii) Based on the observations of Figure 174, λ_0 could be set to 0.35, since it represented a suitable value for the end of plateau at which numerical values reached a cross-section penalty χ_{CS} equal to 1.0.
- (iv) It can be seen that in the $\lambda_{CS} \in [\lambda_0; 1.0]$ range where the influence of imperfections rules the resistance, the square sections are seen to be less penalised by local instabilities. Oppositely, once buckling becomes predominant, the square sections find themselves with the worst penalty compared to rectangular sections, owing to higher restraints brought by adjacent plates. This is clearly shown in Figure 177. Accordingly, a value of $\alpha_{CS} = 0.15$ was proposed through a local fitting.

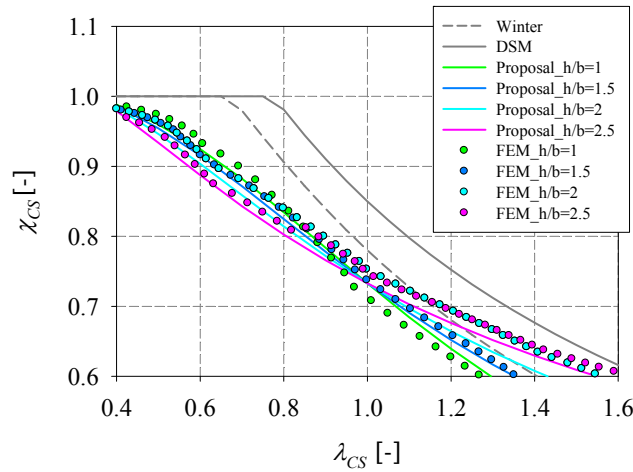


Figure 177 – Zoomed area of Figure 174.

A comparison of the proposed calibration expression $\eta_{proposal}$ to the values of η_{GMNIA} that describe the numerical values has been done. The results for square sections and the relative equations are shown in Figure 178, in which it can be clearly seen that the proposed equation is describing well enough the numerical results in the $\lambda_{CS} \in [0.4; 1.0]$ range which is the range mostly affected by geometrical imperfections.

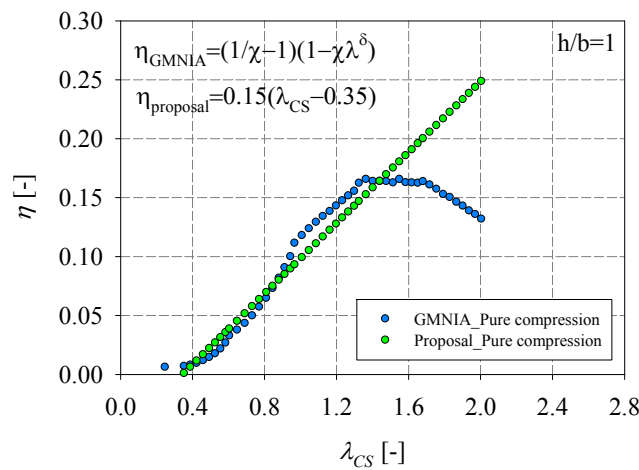


Figure 178 – Comparison of the factor $\eta_{proposal}$ with the numerical values η_{GMNIA} for square sections in compression.

The linear segment of η_{GMNA} in that range indicates that geometrical imperfections are dominant here, whereas for higher λ_{CS} cross-section slenderness, large deformations become more relevant.

- (v) All results relative to the three considered steel grades S235, S355 and S460 are presented in Figure 179. It is clearly seen that an increased yield stress shall lead to a higher design curve. However, all “proposal” curves were based on results relative to a yield stress of 235 MPa, since negligible differences were observed between cross-section capacities relative to different yield stresses (maximum of 4% difference).

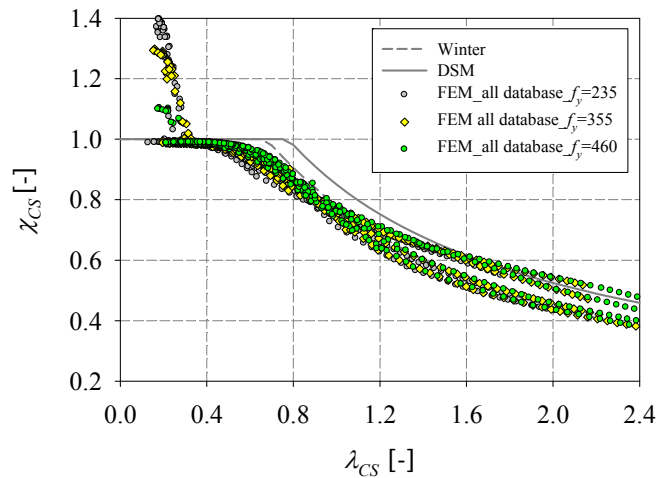


Figure 179 – All FE results of hot-rolled sections subjected to compression, represented in function of the yield stress.

Based on the previous interpretations, Figure 180 and Table 37 represent the design curves for the case of hot-rolled sections in pure compression. It is to be noted that Table 37 represents the proposed curves for the four aspect ratios studied in this work. In section 7, a general summary of the proposed curves relative to any h/b aspect ratio is presented.

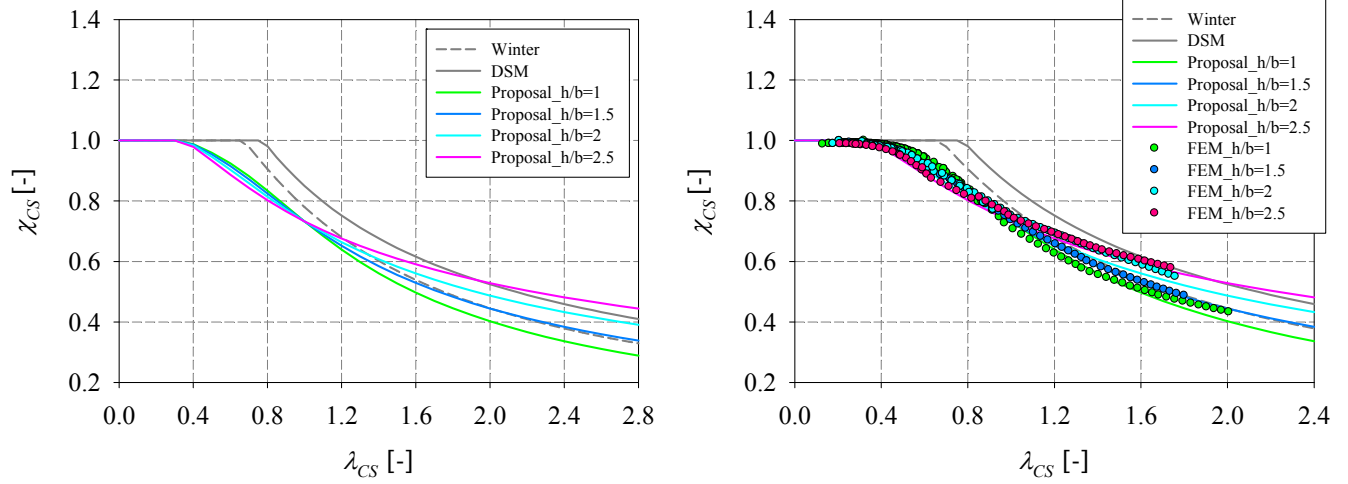
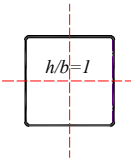
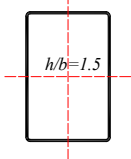
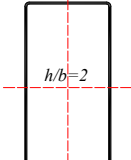
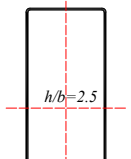


Figure 180 – Design curves proposals relative to hot-rolled sections in compression
a) without numerical results, b) with numerical results.

Table 37 – Design curves for the case of hot-rolled hollow sections in compression.

Cross-section	β	δ	λ_0	α_{CS}	χ_{CS}	ϕ
	1	1.05	0.35	0.15	$\chi_{CS} = \frac{1}{\phi + \sqrt{\phi^2 - \lambda_{CS}^{1.05}}}$ for $\lambda_{CS} > 0.35$ $\chi_{CS} = 1$ when for $\lambda_{CS} \leq 0.35$	$\phi = 0.5(1 + 0.15(\lambda_{CS} - 0.35) + \lambda_{CS}^{1.05})$
	1	0.85	0.35	0.15	$\chi_{CS} = \frac{1}{\phi + \sqrt{\phi^2 - \lambda_{CS}^{0.85}}}$ for $\lambda_{CS} > 0.35$ $\chi_{CS} = 1$ when for $\lambda_{CS} \leq 0.35$	$\phi = 0.5(1 + 0.15(\lambda_{CS} - 0.35) + \lambda_{CS}^{0.85})$
	1	0.65	0.35	0.15	$\chi_{CS} = \frac{1}{\phi + \sqrt{\phi^2 - \lambda_{CS}^{0.65}}}$ for $\lambda_{CS} > 0.35$ $\chi_{CS} = 1$ when for $\lambda_{CS} \leq 0.35$	$\phi = 0.5(1 + 0.15(\lambda_{CS} - 0.35) + \lambda_{CS}^{0.65})$
	1	0.45	0.35	0.15	$\chi_{CS} = \frac{1}{\phi + \sqrt{\phi^2 - \lambda_{CS}^{0.45}}}$ for $\lambda_{CS} > 0.35$ $\chi_{CS} = 1$ when for $\lambda_{CS} \leq 0.35$	$\phi = 0.5(1 + 0.15(\lambda_{CS} - 0.35) + \lambda_{CS}^{0.45})$

5.3.1.1.2. Cold-formed sections

The response of cold-formed sections differs from that of hot-rolled hollow sections mostly regarding strain-hardening effects. They can indeed be shown to be non-negligible for plastic and compact cross-section geometries and shall be accounted for. Accordingly, two design

approaches have been developed for cold-formed sections that specifically lead to $\chi_{CS} > 1.0$ beneficial factors at low λ_{CS} ranges.

Numerical results relative to all cold-formed cross-sections in compression were presented in Figure 181 and grouped based on the following aspect ratios: $h/b = 1, 1.5, 2$ and 2.5 .

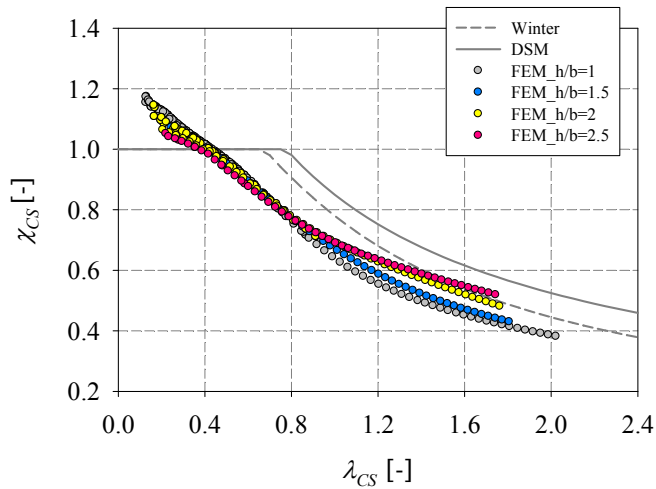


Figure 181 – FE results relative to various aspect ratios, S235.

Two approaches will be presented hereafter with a justification of each parameter based on observed results and tendencies of Figure 181.

1st approach

The first proposal strictly follows the principles and calibration procedure detailed before for hot-rolled sections, and therefore relies on a single, continuous interaction curve. The interpretations and aspects of the 1st approach are as follows:

- (i) Similarly to hot-rolled sections, clear tendencies for large slenderness values can be seen. Clear relations, function of the aspect ratio could be derived. Therefore a choice of a simple curve, function of the aspect ratio was proposed through a best-fit, leading to the key δ parameter defined as follows, for h/b values comprised between 1 and 2.5:

$$\delta = -0.4 h/b + 1.45 \tag{139}$$

- (ii) Within the first approach, the end of plateau λ_0 was set to 0. However, the ideal resistance limit was changed to allow for obvious strain-hardening. Therefore, a β factor was defined as follows:

$$\beta = -0.15 \lambda_{CS} + 1.15 \quad (140)$$

In other words, the (ideal) resistance limit is so that $\chi_{CS} = -0.15 \lambda_{CS} + 1.15$ (see red dashed line in Figure 185). This consequently leads to a potential 15% maximum benefit from strain-hardening reserves.

- (iii) In the intermediate slenderness range, the interaction curve is characterised by a α_{CS} factor, here defined as a function of δ (i.e. indirectly as a function of the h/b ratio):

$$\alpha_{CS} = 0.1 \delta + 3/40 \quad (141)$$

- (iv) In Figure 182, all results are represented in terms of the yield stress. Again, a unified curve (based on S235 results) for the three yield stresses has been adopted, for the sake of simplification since the results are showing inconsiderable differences (see Figure 183). However, these differences are seen to be higher and almost constant along the whole range of slenderness, unlike hot-rolled sections where the difference would occur, as expected, only in the range of slenderness belonging to the zone influenced by imperfections (due to residual stresses consideration). This could be explained with Figure 184 in which the material laws relative to both cold formed and hot-rolled sections are presented. The penalty factor χ_{CS} was relative to R_{RESIST} which is based on the attainment of the resistance limit corresponding to a plastic plateau. Therefore, it can be seen in Figure 184 that the areas highlighted in yellow increase with the increase of the yield stress. This is due to the choice of the Ramberg-Osgood adopted material law. Therefore the differences between observed tendencies in Figure 182 are justified through the previous explanation.

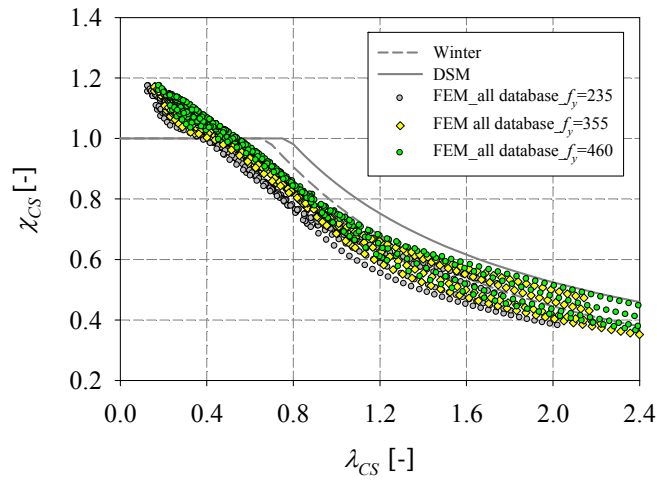


Figure 182 – All FE results of cold-formed sections subjected to compression, represented in function of the yield stress.

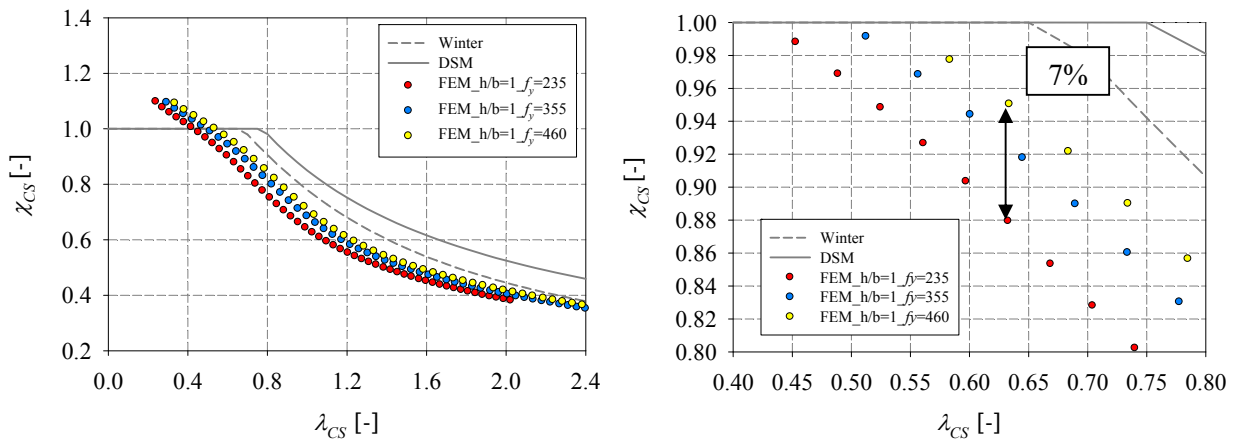


Figure 183 – FE results of square cross-sections represented in function of the yield stress (left); zoomed area of results situated between $\lambda_{CS} = 0.4$ and $\lambda_{CS} = 0.8$ (right).

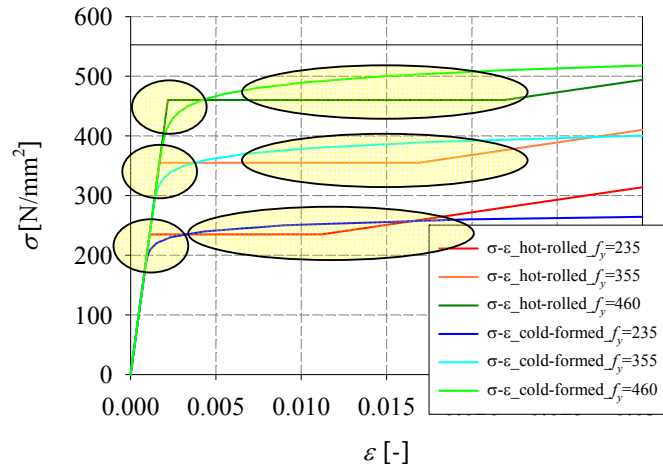


Figure 184 – Adopted material laws relative to hot-rolled and cold formed sections.

Figure 185 depicts the proposed design curves for cold-formed sections subjected to compression; a graphical comparison with the FE results is possible with Figure 185. As can be seen, the agreement with the proposed parametric $\lambda_{CS} - \chi_{CS}$ curves is excellent. One may also note the reversal in order of the curves between the intermediate λ_{CS} (0.4 to 0.8) and large χ_{CS} values. Table 38 summarizes the proposed design curves for the case of cold-formed sections in compression.

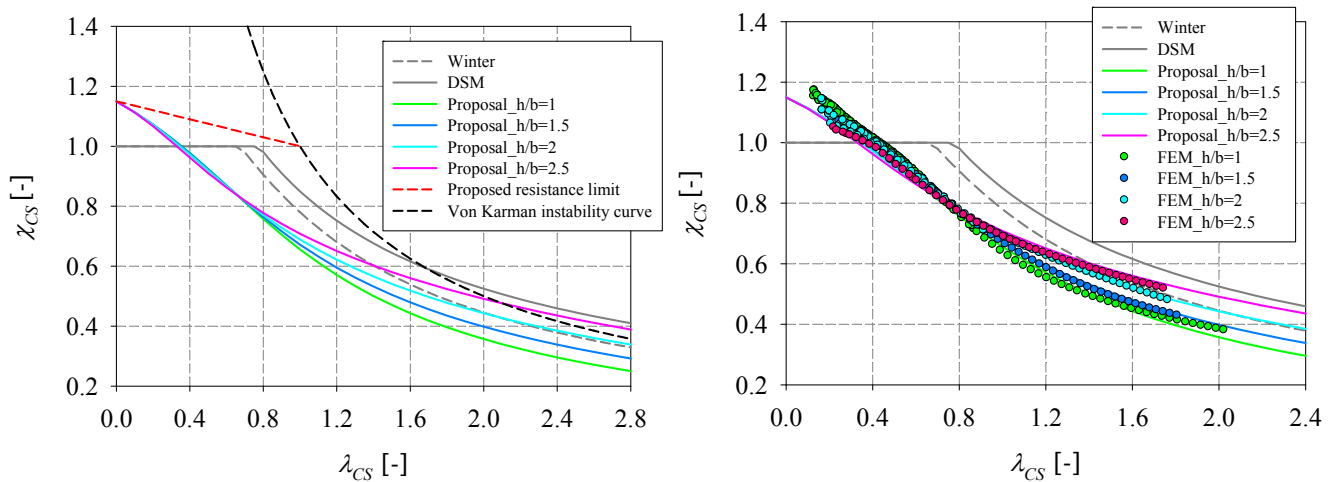
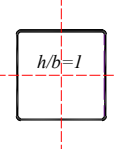
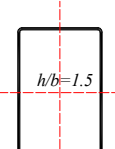
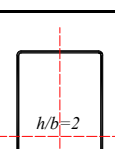
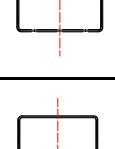


Figure 185 – Proposed design curves for cold-formed sections in compression, 1st approach
a) without numerical results, b) with numerical results.

Table 38 – Design curves for the case of cold-formed hollow sections in compression
(1st approach).

Cross-section	β	δ	λ_0	α_{CS}	χ_{CS}	ϕ
	$-0.15 \lambda_{CS} + 1.15$	1.05	0	0.18	$\chi_{CS} = \frac{\beta}{\phi + \sqrt{\phi^2 - \lambda_{CS}^{1.05} \beta}}$	$\phi = 0.5(1 + 0.18\lambda_{CS} + \lambda_{CS}^{1.05})$
	$-0.15 \lambda_{CS} + 1.15$	0.85	0	0.16	$\chi_{CS} = \frac{\beta}{\phi + \sqrt{\phi^2 - \lambda_{CS}^{0.85} \beta}}$	$\phi = 0.5(1 + 0.16\lambda_{CS} + \lambda_{CS}^{0.85})$
	$-0.15 \lambda_{CS} + 1.15$	0.65	0	0.14	$\chi_{CS} = \frac{\beta}{\phi + \sqrt{\phi^2 - \lambda_{CS}^{0.65} \beta}}$	$\phi = 0.5(1 + 0.14\lambda_{CS} + \lambda_{CS}^{0.65})$
	$-0.15 \lambda_{CS} + 1.15$	0.45	0	0.12	$\chi_{CS} = \frac{\beta}{\phi + \sqrt{\phi^2 - \lambda_{CS}^{0.45} \beta}}$	$\phi = 0.5(1 + 0.12\lambda_{CS} + \lambda_{CS}^{0.45})$

2nd approach

As an alternative to the 1st approach, a second one was derived, able to take the benefits of strain-hardening as well. In contrast, the 2nd proposal relies on a strain-based format at low slenderness. Accordingly:

- (i) A wider $\lambda_0 = 0.40$ plateau is adopted, and, for $\lambda_{CS} \leq \lambda_0$ cases, a relationship between the strain level and λ_{CS} is established as follows:

$$\frac{\varepsilon}{\varepsilon_y} = \left(\frac{0.4}{\lambda_{CS}} \right)^{1.5} \quad (142)$$

for $\lambda_{CS} \leq 0.4$

where ε_y corresponds to the strain level at first yield; coefficients in equation (142) were fitted according to the results plotted in Figure 186.

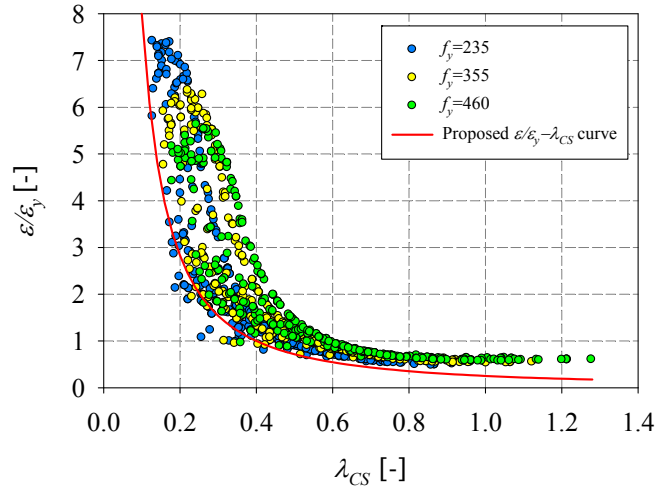


Figure 186 – Normalized strain demand in function of the relative slenderness.

The proposed equation, used in the design proposal for λ_{CS} values up to 0.40, is seen to propose a quite safe-sided lower bound approximation of the obtained results.

(ii) In a 2nd step, χ_{CS} is calculated as a function of $\varepsilon / \varepsilon_y$ as follows:

$$\chi_{CS} = 1.15 - \frac{0.15}{\left(\varepsilon / \varepsilon_y\right)^{0.6}} \quad (143)$$

Again, this equation has been proposed on the basis of FE results as plotted in Figure 187.

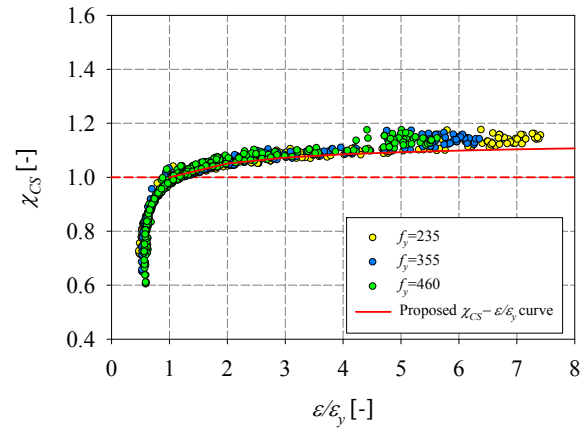


Figure 187 – Cross-section capacity as function of the strain demand.

(iii) Eventually, for $\lambda_{CS} > \lambda_0$ situations, this 2nd approach makes use of an identical format as for the 1st approach, however with the following δ and α_{CS} coefficients proposed based on a best-fit:

$$\delta = -0.4 h / b + 1.45 \quad (10)$$

$$\alpha_{CS} = 0.1 \delta + 7 / 40 \quad (11)$$

Similarly to the first approach, Figure 188 and Table 39 summarized the proposed second approach design curves relative to cold-formed cross-sections subjected to compression.

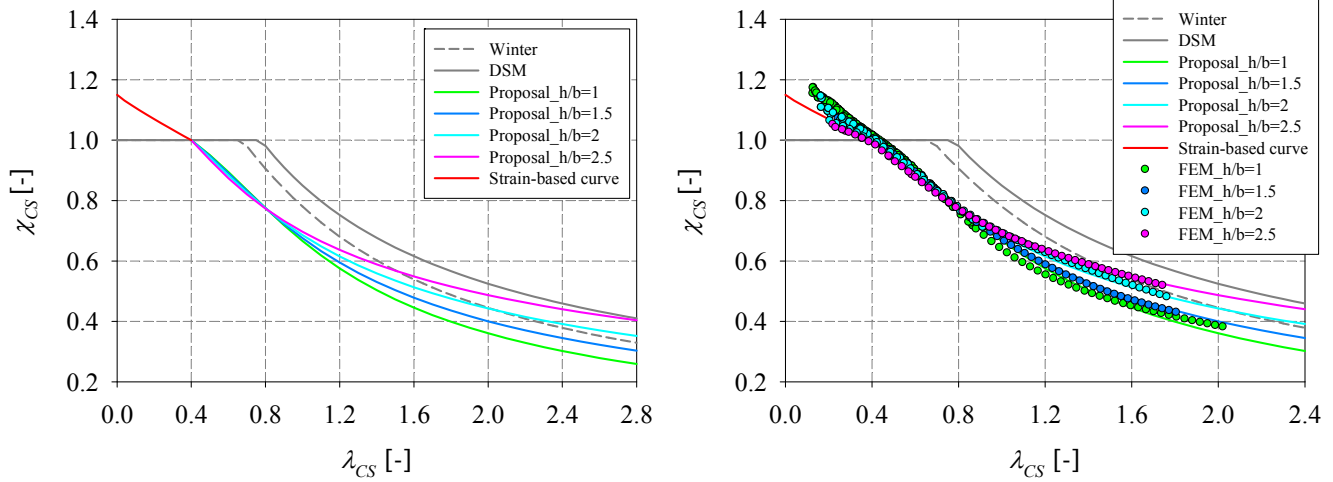
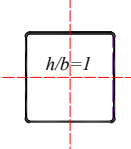
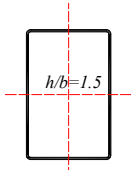
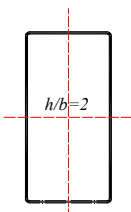
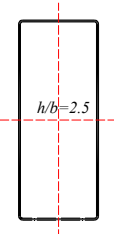


Figure 188 – Design curves proposals relative to cold-formed sections in compression, 2nd approach.
a) without numerical results, b) with numerical results.

Table 39 – Design curves for the case of cold-formed hollow sections in compression
(2nd approach for $\lambda_{CS} > \lambda_0$).

Cross-section	β	δ	λ_0	α_{CS}	χ_{CS}	ϕ
	1	1.05	0.4	0.28	$\chi_{CS} = \frac{1}{\phi + \sqrt{\phi^2 - \lambda_{CS}^{1.05}}}$ For $\lambda_0 > 0.4$	$\phi = 0.5(1 + 0.28(\lambda_{CS} - 0.4) + \lambda_{CS}^{1.05})$
	1	0.85	0.4	0.26	$\chi_{CS} = \frac{1}{\phi + \sqrt{\phi^2 - \lambda_{CS}^{0.85}}}$ For $\lambda_0 > 0.4$	$\phi = 0.5(1 + 0.26(\lambda_{CS} - 0.4) + \lambda_{CS}^{0.85})$
	1	0.65	0.4	0.24	$\chi_{CS} = \frac{1}{\phi + \sqrt{\phi^2 - \lambda_{CS}^{0.65}}}$ For $\lambda_0 > 0.4$	$\phi = 0.5(1 + 0.24(\lambda_{CS} - 0.4) + \lambda_{CS}^{0.65})$

	1	0.45	0.4	0.22	$\chi_{CS} = \frac{1}{\phi + \sqrt{\phi^2 - \lambda_{CS}^{0.45}}}$ <p>For $\lambda_0 > 0.4$</p>	$\phi = 0.5(1 + 0.22(\lambda_{CS} - 0.4) + \lambda_{CS}^{0.45})$
---	---	------	-----	------	---	--

5.3.1.2. Major-axis bending

5.3.1.2.1. Hot-rolled sections

For the case of hot-rolled cross-sections subjected to major-axis bending, design curves were also proposed with fitted factors through the adoption of the Ayrton-Perry formula. Numerical results are presented in Figure 189.

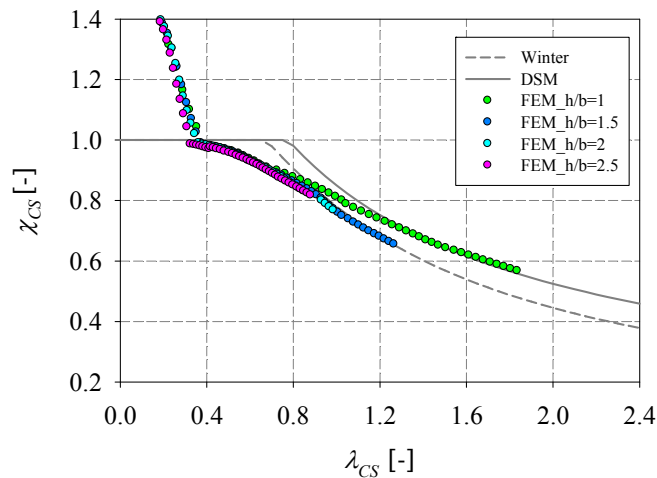


Figure 189 – FE results relative to various cross-section ratios in major-axis bending, S235.

The following interpretations can be stated based on the obtained results:

- (i) Three clear tendencies can be observed in Figure 189. For large h/b ratios (> 2.0), the results would hardly differ. To confirm this statement, additional numerical computations were conducted for higher h/b ratios, since for such cases the critical elastic buckling load multiplier increases considerably due to their increased major-axis inertia, leading to a considerable ‘shifting’ to the left of the relative slenderness values. Figure 190, in which the additional computed numerical results are presented, can

clearly show that results relative to aspect ratios higher than 2 hardly differ allowing thus a proposition of one curve applicable for such aspect ratio range (> 2.0).

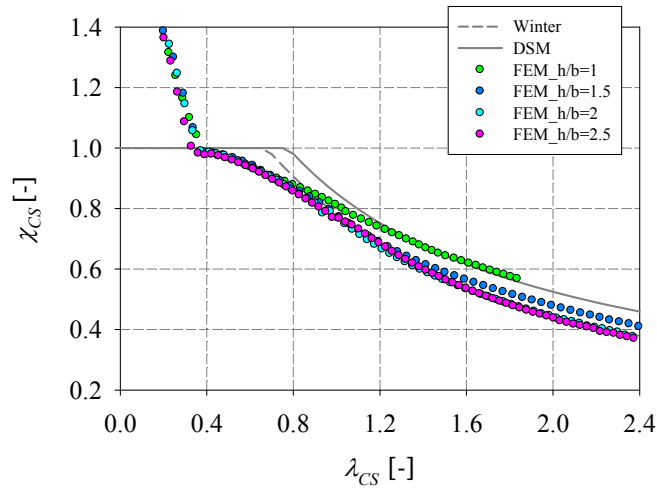


Figure 190 – Extension of numerical results for cross-sections having the following two aspect ratios: $h/b = 2$ and 2.5 .

Therefore, a choice of a simple curve function of the aspect ratio was proposed through a best fit. This curve would be applicable for h/b values comprised between 1.0 and 2.0. The proposed δ formula is as follows:

$$\delta = 0.4h/b + 0.25 \quad (144)$$

- (ii) The resistance limit was set to $\chi_{CS,max} = 1.0$ (i.e. $\beta = 1.0$) since no strain hardening reserve was deemed allowed to be considered for hot-rolled sections.
- (iii) Based on the observations of Figure 189, λ_0 could be set to 0.35, since it represented a suitable value for the end of plateau at which numerical values reached a cross-section penalty χ_{CS} equal to 1.0.
- (iv) Similarly to compression load cases of cold-formed sections, α_{CS} coefficient was determined through a simple equation function of δ as follows:

$$\alpha_{CS} = 1/10\delta + 3/200 \quad (145)$$

(v) The yield stress was not accounted for in the design formulae since their effect was again negligible (see Figure 191).

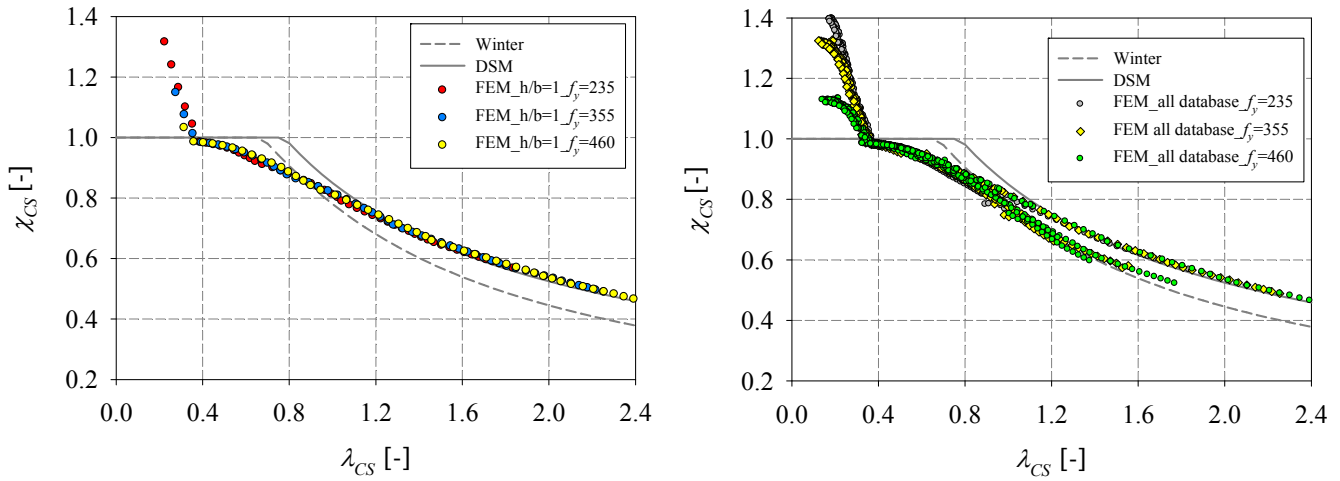


Figure 191 – a) FE results of square cross-sections represented in function of the yield stress,
b) All FE results of hot-rolled sections subjected to major-axis bending, represented in function of the yield stress.

Figure 192 and Table 40 depict the proposed design curves for hot-rolled sections subjected to major-axis bending. As can be seen in the graphical comparison with FE results, agreement with the proposed parametric $\lambda_{CS} - \chi_{CS}$ curves is excellent.

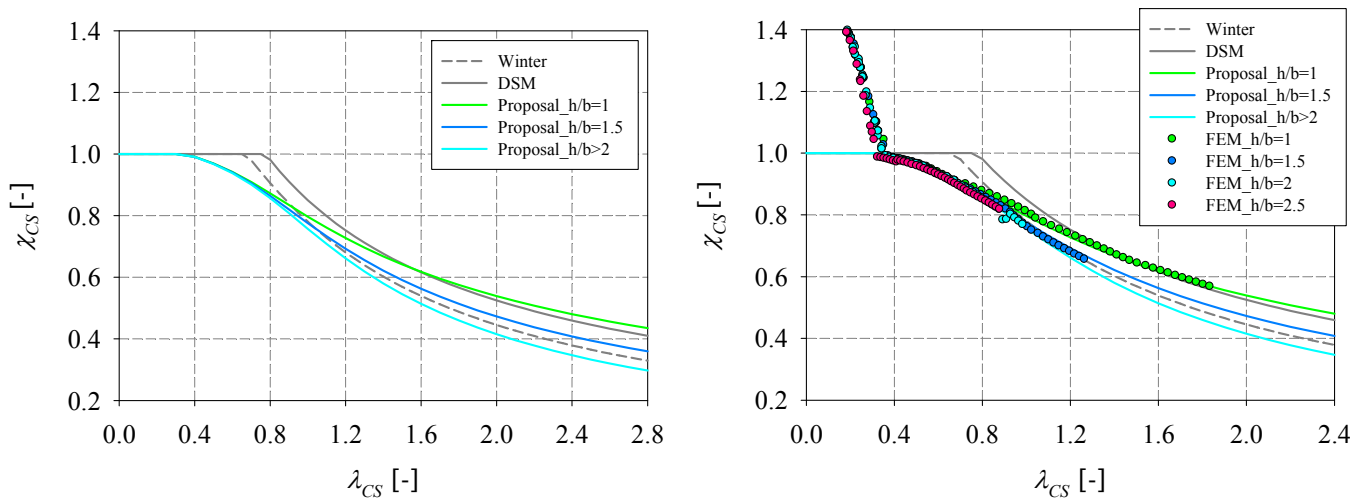
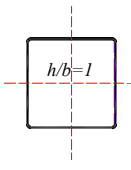
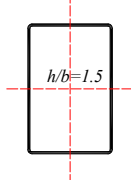
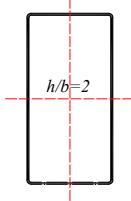


Figure 192 – Design curves proposals relative to hot-rolled sections subjected to major-axis bending
a) without numerical results, b) with numerical results.

Table 40 – Design curves for the case of hot-formed hollow sections subjected to a major-axis bending moment.

Cross-section	β	δ	λ_0	α_{CS}	χ_{CS}	ϕ
	1	0.65	0.35	0.08	$\chi_{CS} = \frac{1}{\phi + \sqrt{\phi^2 - \lambda_{CS}^{0.65}}}$ for $\lambda_{CS} > 0.35$ $\chi_{CS} = 1$ when $\lambda_{CS} \leq 0.35$	$\phi = 0.5(1 + 0.08(\lambda_{CS} - 0.35) + \lambda_{CS}^{0.65})$
	1	0.85	0.35	0.1	$\chi_{CS} = \frac{1}{\phi + \sqrt{\phi^2 - \lambda_{CS}^{0.85}}}$ for $\lambda_{CS} > 0.35$ $\chi_{CS} = 1$ when $\lambda_{CS} \leq 0.35$	$\phi = 0.5(1 + 0.1(\lambda_{CS} - 0.35) + \lambda_{CS}^{0.85})$
	1	1.05	0.35	0.12	$\chi_{CS} = \frac{1}{\phi + \sqrt{\phi^2 - \lambda_{CS}^{1.05}}}$ for $\lambda_{CS} > 0.35$ $\chi_{CS} = 1$ when $\lambda_{CS} \leq 0.35$	$\phi = 0.5(1 + 0.12(\lambda_{CS} - 0.35) + \lambda_{CS}^{1.05})$

5.3.1.2.2. Cold-formed sections

Similarly to the compression load case, two approaches are presented for cold-formed sections subjected to major-axis bending. Numerical results relative to all cold-formed cross-sections in major-axis bending are presented in the following figure:

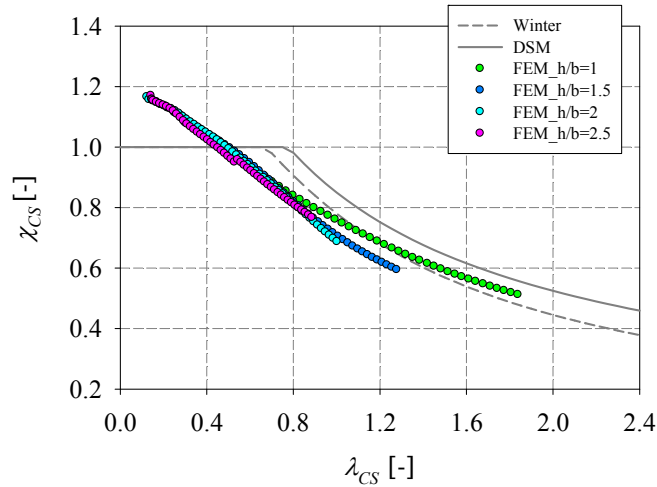


Figure 193 – FE results relative to various cross-section ratios subjected to a major-axis bending moment, S235 (the European and derived sections are considered in this graph).

The two approaches will be presented hereafter with a justification of each parameter based on observed results in Figure 193.

1st approach

In the first approach relying on a single continuous interaction curve, the following aspects were derived:

- (i) Additional numerical computations were conducted for high h/b ratios to cover a wider range of slenderness. Based on observations in Figure 194, three tendencies for high λ_{CS} slenderness values were expressed through the following δ proposed formula:

$$\delta = 0.4h/b + 0.25 \quad (146)$$

for h/b values comprised between 1.0 and 2.0. Based on Figure 194, the δ value relative to an aspect ratio of 2.0 is considered to be appropriate as well as for higher aspect ratio than 2.0.

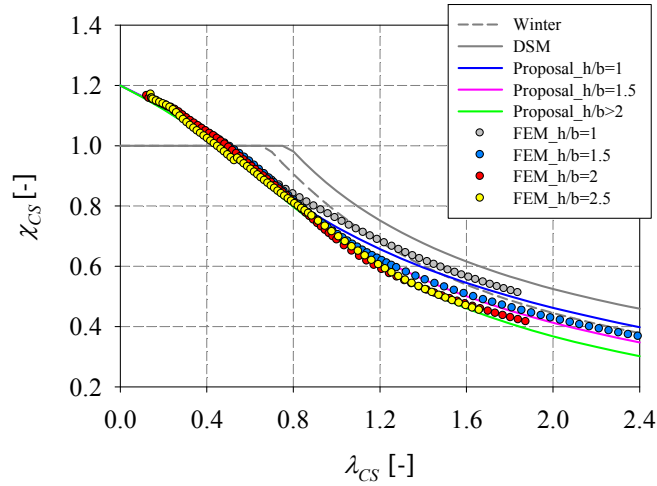


Figure 194 – Extension of numerical results for cross-sections having the following three aspect ratio $h/b = 1.5, 2$ and 2.5 .

- (ii) The end of plateau λ_0 was set to 0, since the ideal resistance limit ($\chi_{CS} = 1.0$) was changed through the consideration of the following β formula:

$$\beta = -0.20\lambda + 1.20 \quad (147)$$

The resistance plateau was set to $\chi_{CS} = -0.20\lambda + 1.20$ (see red dashed line in Figure 196) since a strain hardening reserve would be allowed to be considered for cold-formed sections. This consequently leads to a potential 20% maximum benefit from strain-hardening reserves.

- (iii) The α_{CS} factor was defined as a function of δ , through the following fitted expression:

$$\alpha_{CS} = 1/10\delta + 7/200 \quad (148)$$

Equation (148) is applicable for h/b values comprised between 1.0 and 2.0 (for values higher than 2.0, the δ value relative to an aspect ratio of 2.0 is considered to be appropriate).

- (iv) Similarly to previous studies mentioned before, the effect of the yield stress was seen to be negligible, and was not taken into account in the proposed design curves (see Figure 195).

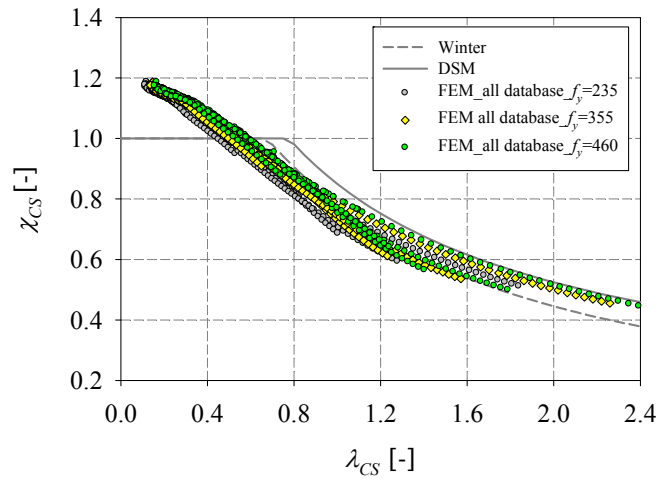
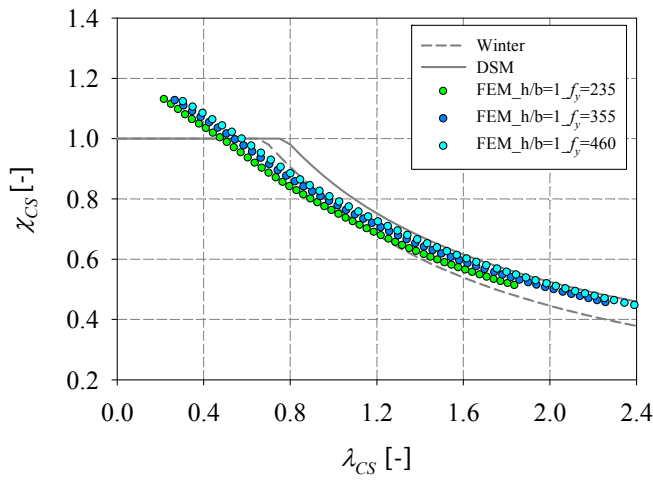


Figure 195 – a) FE results of square cross-sections represented in function of the yield stress
 b) All FE results of cold-formed sections subjected to a major-axis bending, represented in function of the yield stress.

Figure 196 and Table 41 depict the proposed 1st approach design curves for cold-formed sections subjected to major-axis bending.

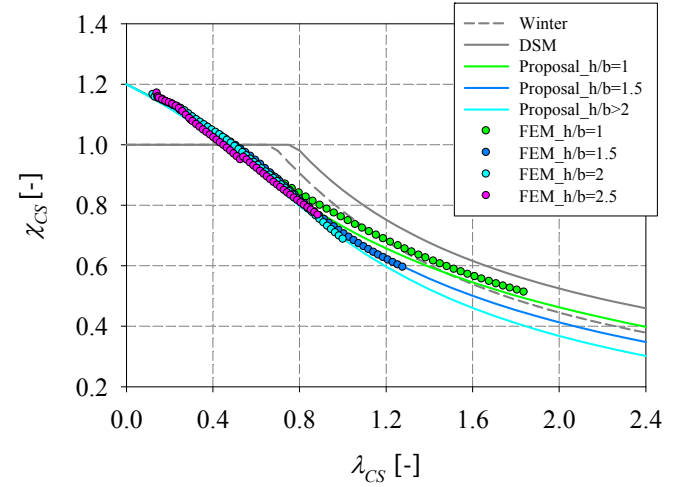
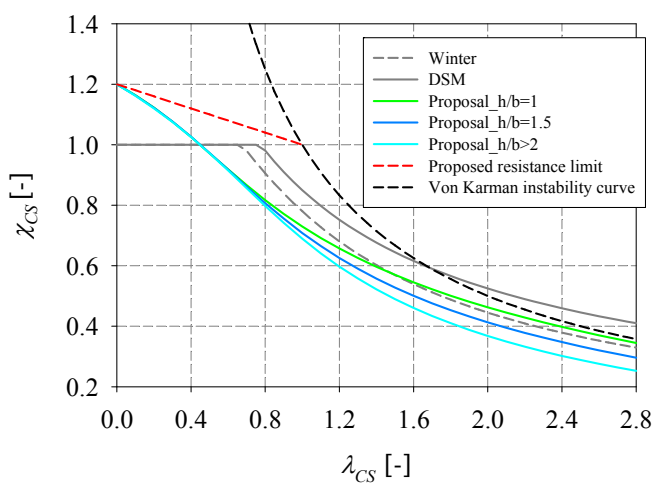
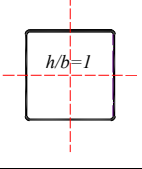
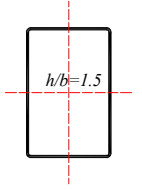
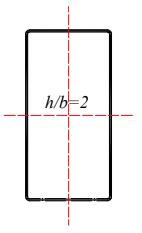


Figure 196 – Design curves proposals relative to cold-formed sections subjected to a pure major-axis bending moment, 1st approach.

Table 41 – Design curves for the case of cold-formed hollow sections subjected to a major-axis bending (1st approach).

Cross-section	β	δ	λ_0	α_{CS}	χ_{CS}	ϕ
	$-0.20\lambda + 1.20$	0.65	0	0.1	$\chi_{CS} = \frac{\beta}{\phi + \sqrt{\phi^2 - \lambda_{CS}^{0.65} \beta}}$	$\phi = 0.5(1 + 0.1\lambda_{CS} + \lambda_{CS}^{0.65})$
	$-0.20\lambda + 1.20$	0.85	0	0.12	$\chi_{CS} = \frac{\beta}{\phi + \sqrt{\phi^2 - \lambda_{CS}^{0.85} \beta}}$	$\phi = 0.5(1 + 0.12\lambda_{CS} + \lambda_{CS}^{0.85})$
	$-0.20\lambda + 1.20$	1.05	0	0.14	$\chi_{CS} = \frac{\beta}{\phi + \sqrt{\phi^2 - \lambda_{CS}^{1.05} \beta}}$	$\phi = 0.5(1 + 0.14\lambda_{CS} + \lambda_{CS}^{1.05})$

2nd approach

In the second approach relying on a strain-based format at low slenderness, the key parameters were defined as follows:

- (i) a wider $\lambda_0 = 0.40$ plateau is adopted, and, for $\lambda_{CS} \leq \lambda_0$ cases, a relationship between the strain level and λ_{CS} is established as follows:

$$\frac{\varepsilon}{\varepsilon_y} = \left(\frac{0.4}{\lambda_{CS}} \right)^{1.5} \quad (149)$$

for $\lambda_{CS} \leq 0.4$

where ε_y corresponds to the strain level at first yield; coefficients in Equation (149) were fitted according to the results plotted in Figure 197.

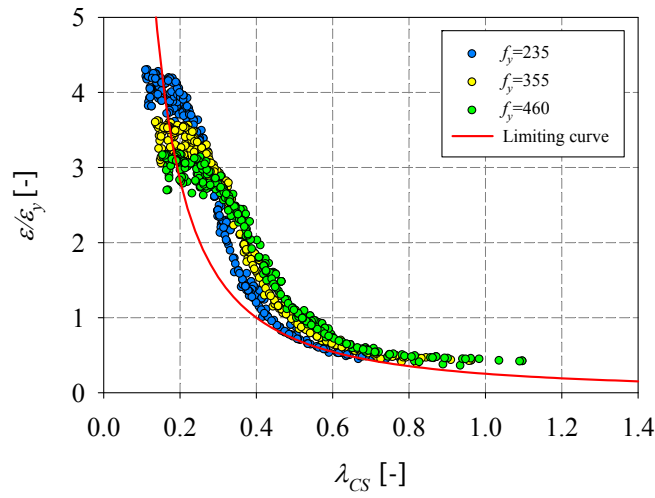


Figure 197 – Normalized strain demand in function of the relative slenderness.

(ii) Then, in a 2nd step, χ_{CS} is calculated as a function of $\varepsilon / \varepsilon_y$ as follows:

$$\chi_{CS} = 1.2 - \frac{0.2}{(\varepsilon / \varepsilon_y)^{0.6}} \quad (150)$$

Again, this equation has been proposed on the basis of FE results as plotted in Figure 198.

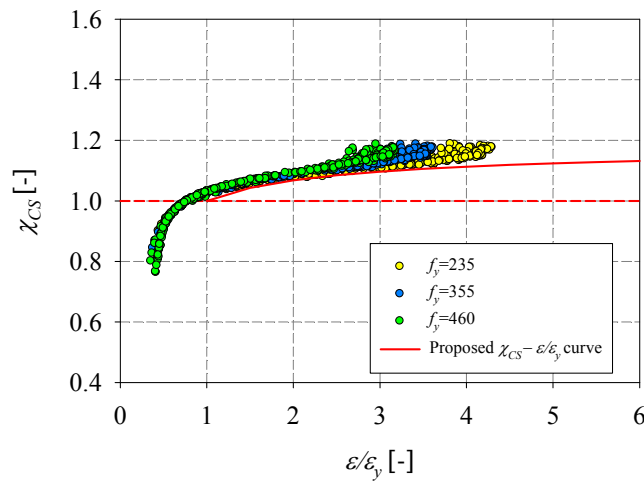


Figure 198 – Cross-section capacity as function of the strain demand.

(iii) for $\lambda_{CS} > \lambda_0$ situations, this 2nd approach makes use of an identical format as for the 1st approach, but with the following δ and α_{CS} coefficients:

$$\delta = 0.4h/b + 0.25 \tag{151}$$

$$\alpha_{CS} = 1/4\delta - 1/80 \tag{152}$$

for h/b values comprised between 1.0 and 2.0.

The resulting proposed design curves are presented in Figure 199 and Table 42.

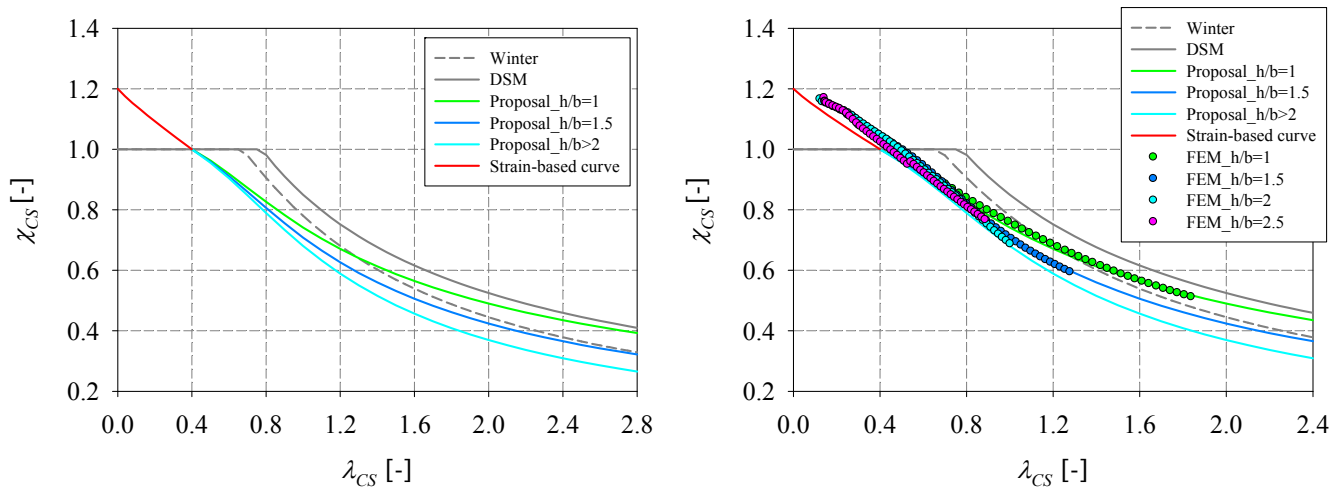
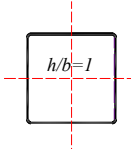
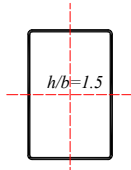
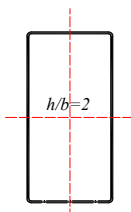


Figure 199 – Design curves proposals relative to cold-formed sections in major-axis bending, 2nd approach.

Table 42 – Design curves for the case of cold-formed hollow sections subjected to a major-axis bending, (2nd approach for $\lambda_{CS} > \lambda_0$)

Cross-section	β	δ	λ_0	α_{CS}	χ_{CS}	ϕ
	1	0.65	0.40	0.15	$\chi_{CS} = \frac{1}{\phi + \sqrt{\phi^2 - \lambda_{CS}^{0.65}}}$ for $\lambda_{CS} > 0.40$	$\phi = 0.5(1 + 0.15(\lambda_{CS} - 0.40) + \lambda_{CS}^{0.65})$
	1	0.85	0.40	0.2	$\chi_{CS} = \frac{1}{\phi + \sqrt{\phi^2 - \lambda_{CS}^{0.85}}}$ for $\lambda_{CS} > 0.40$	$\phi = 0.5(1 + 0.2(\lambda_{CS} - 0.40) + \lambda_{CS}^{0.85})$
	1	1.05	0.40	0.25	$\chi_{CS} = \frac{1}{\phi + \sqrt{\phi^2 - \lambda_{CS}^{1.05}}}$ for $\lambda_{CS} > 0.40$	$\phi = 0.5(1 + 0.25(\lambda_{CS} - 0.40) + \lambda_{CS}^{1.05})$

5.3.1.3. Minor-axis bending

5.3.1.3.1. Hot-rolled sections

For the case of cross-sections subjected to minor-axis bending, the curve corresponding to a major-axis bending relative to an aspect ratio of $h/b = 1.0$ was adopted as the only curve for all the cross-sections subjected to such load case. This is due to the fact that with rectangular sections subjected to a minor-axis bending, the moment of inertia relative to the weak axis I_z will not increase with an increased h/b ratio as much as the moment of inertia relative to the strong axis I_y would, in the case of a major-axis bending. Therefore, the relative slenderness would find itself almost stable with cross-sections subjected to a minor-axis bending, while it would decrease considerably in the case of a major-axis bending (due to an increase in the R_{STAB} factor) leading to a left shifting of the results in the $\chi_{CS} - \lambda_{CS}$ graph. This is clearly seen in Figure 200 in which three selected cross-sections (termed CS1, CS2 and CS3) with

varying h/b ratios were adopted and their corresponding relative slenderness was compared in function of their h/b ratios for both load cases of major and minor-axis bending.

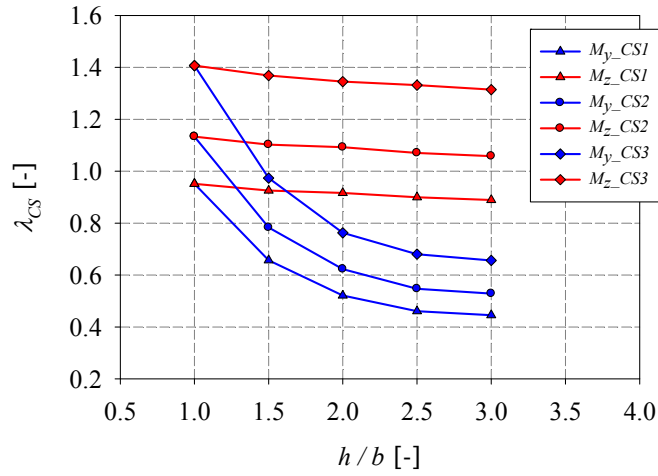


Figure 200 – Comparison of the relative slenderness of different cross-section with various aspect ratios subjected to a minor and a major-axis bending moment.

Similarly to other cases, the yield stress was not taken into account in the proposed derived formula due to its negligible effect. Figure 201 shows all the results represented in terms of the different yield stresses.

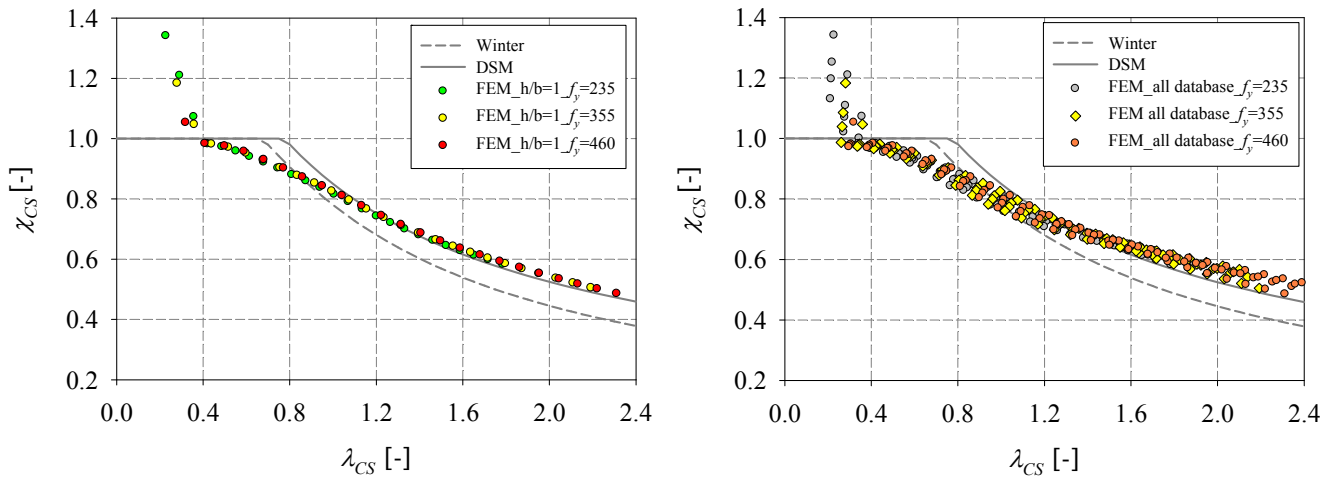


Figure 201 – a) FE results of square cross-sections represented in function of the yield stress,
b) All FE results of hot-rolled sections subjected to a minor-axis bending moment,
represented in function of the yield stress.

The resulting design curve is shown in Figure 202 with its parameters being defined in Table 43.

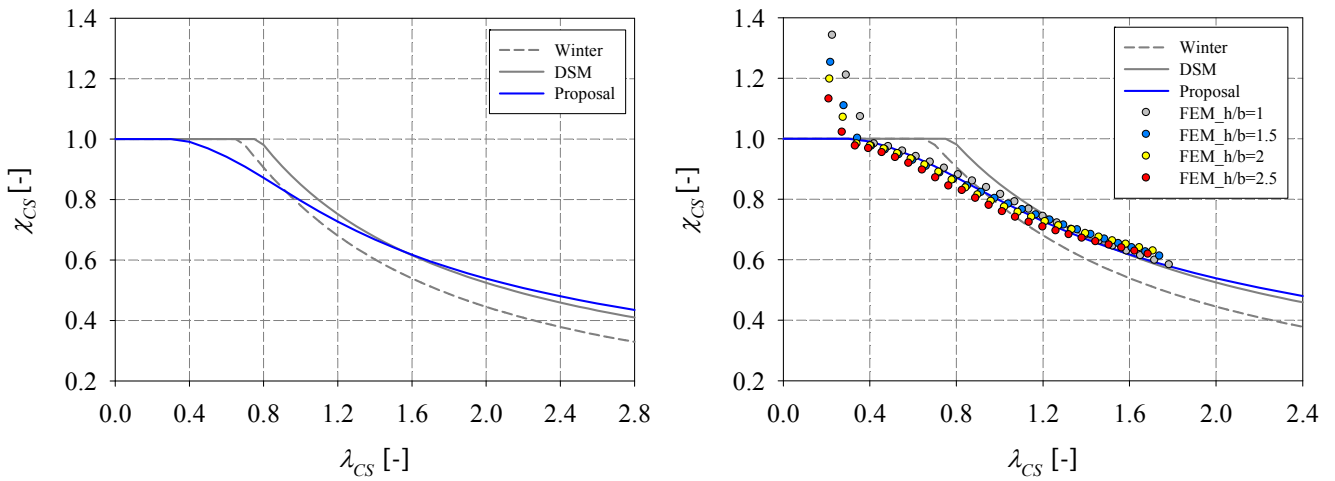
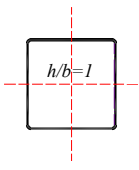


Figure 202 – Design curve proposal relative to hot-rolled sections subjected to a pure minor-axis bending

a) without numerical results, b) with numerical results.

Table 43 – Design curve for the case of hot-rolled hollow sections subjected to a minor-axis bending.

Cross-section	β	δ	λ_0	α_{CS}	χ_{CS}	ϕ
	1	0.65	0.35	0.08	$\chi_{CS} = \frac{1}{\phi + \sqrt{\phi^2 - \lambda_{CS}^{0.65}}}$ for $\lambda_{CS} > 0.35$ $\chi_{CS} = 1$ when for $\lambda_{CS} \leq 0.35$	$\phi = 0.5(1 + 0.08(\lambda_{CS} - 0.35) + \lambda_{CS}^{0.65})$

5.3.1.3.2. Cold-formed sections

Also for cold formed sections, and with both the first and second approach, one single curve was adopted for all hollow cross-sections subjected to minor-axis bending. The curve relative to a square section subjected to major-axis bending was selected as the relevant curve. For $\lambda_{CS} \leq 0.4$ with the second approach, the same strain-based formula adopted for the load case of major-axis bending was also considered for the case of minor-axis bending. Figure 203 to Figure 205, Table 44 and Table 45 show the corresponding numerical results with both proposed curves relative to both approaches.

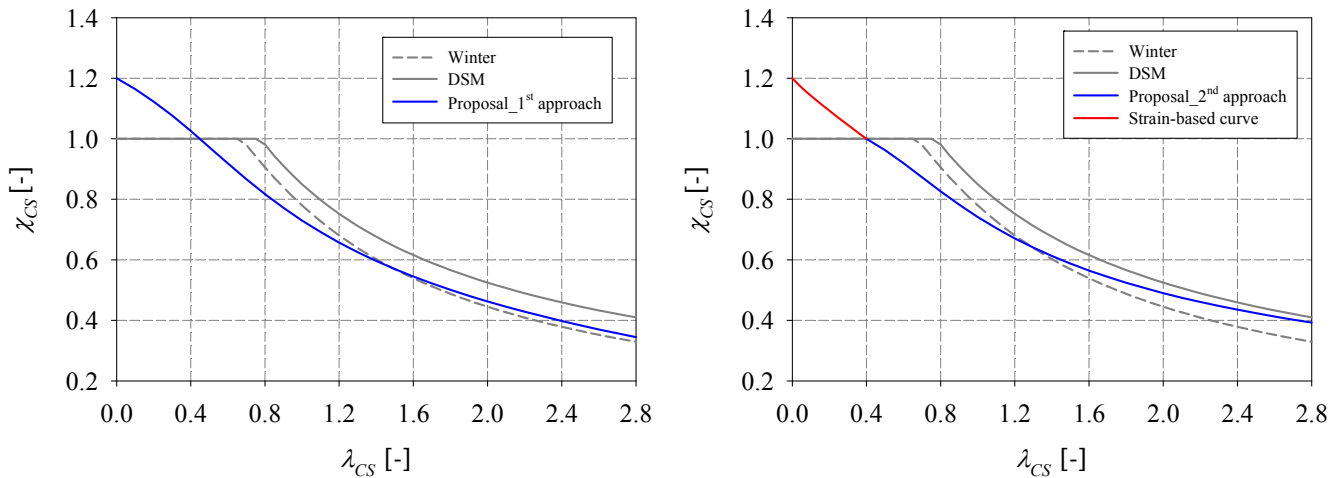


Figure 203 – Design curves proposals relative to cold-formed sections subjected to a minor-axis bending, 1st approach (left), 2nd approach (right).

Table 44 – Design curves for the case of cold-formed hollow sections subjected to a minor-axis bending, 1st approach.

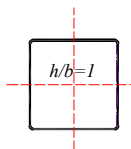
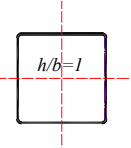
Cross-section	β	δ	λ_0	α_{CS}	χ_{CS}	ϕ
	$-0.20\lambda + 1.20$	0.65	0	0.1	$\chi_{CS} = \frac{1}{\phi + \sqrt{\phi^2 - \lambda_{CS}^{0.65}}}$	$\phi = 0.5(1 + 0.1\lambda_{CS} + \lambda_{CS}^{0.65})$

Table 45 – Design curves for the case of cold-formed hollow sections subjected to a minor-axis bending, (2nd approach for $\lambda_{CS} > \lambda_0$)

Cross-section	β	δ	λ_0	α_{CS}	χ_{CS}	ϕ
	1	0.65	0.40	0.15	$\chi_{CS} = \frac{\beta}{\phi + \sqrt{\phi^2 - \lambda_{CS}^{0.65} \beta}}$ for $\lambda_{CS} > 0.40$	$\phi = 0.5(1 + 0.15(\lambda_{CS} - 0.40) + \lambda_{CS}^{0.65})$

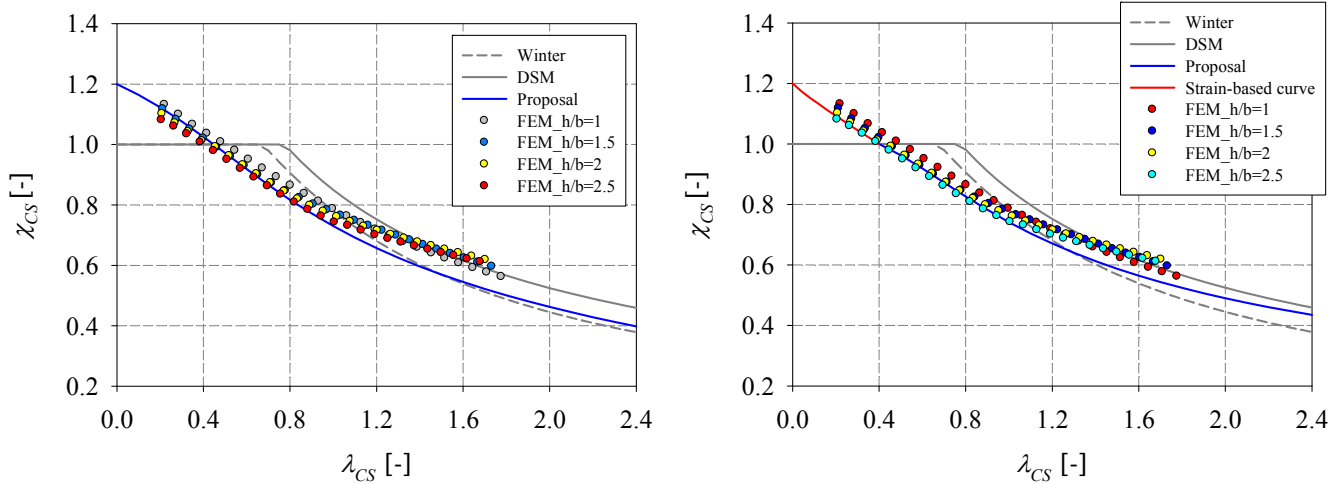


Figure 204 – Numerical results corresponding to cold - formed sections subjected to a minor-axis bending represented with the proposed approaches, 1st approach (left), 2nd approach (right).

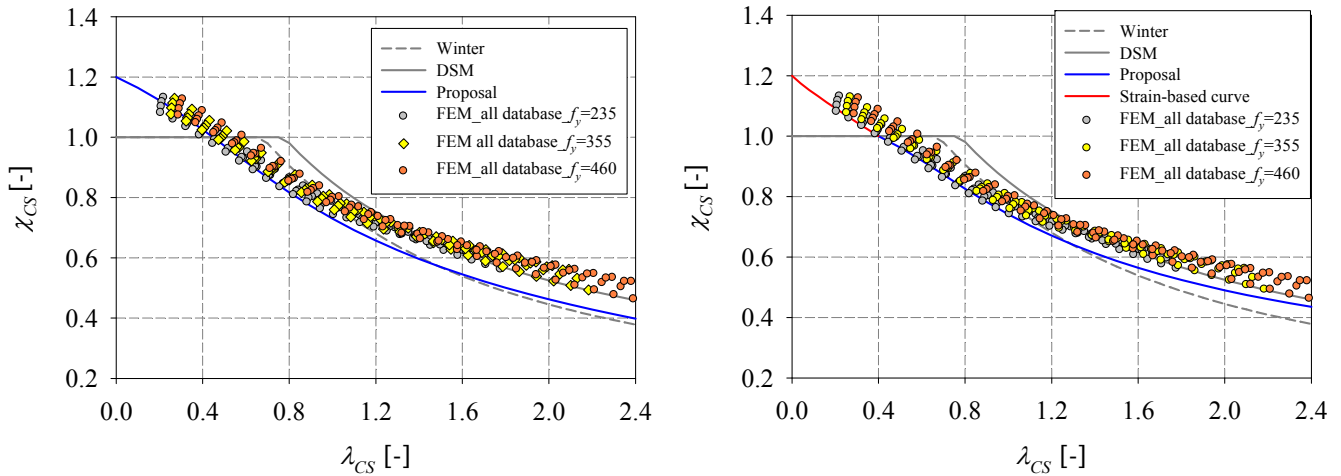


Figure 205 – Numerical results corresponding to cold - formed sections subjected to a minor-axis bending represented in function of the yield stresses, 1st approach (left), 2nd approach (right).

5.3.2. Combined load cases

5.3.2.1.1. Hot-rolled sections

For the combined cases, the previously-detailed Ayrton-Perry extended format was also adopted. The presence of axial forces (by means of parameter n^{16}) was seen to have the most important effect on the structural behaviour of a cross-section subjected to a combined loading in which axial forces are present. The influence of a minor-axis bending or/and a major-axis bending was seen to be insignificant with the presence of axial forces (especially for high axial forces) and was therefore not considered as a parameter in the derived formulae. Consequently, a continuity between proposed curves for simple and combined load cases must be provided and two limiting boundary curves for $n=1.0$ and $n=0$ should be relative to a curve of a simple load case; the Ayrton-Perry derived formula for cross-sections subjected to compression was taken as the reference limiting curve for which $n=1.0$, and the major-axis bending one was taken as the limiting curve in which $n=0$. When the level of axial forces was increased, the cross-section penalty was decreasing until a certain ‘turning point’ where the cross-section penalty was increasing to reach the curve relative to a pure compression for $n=1.0$. Since all calculations were based on the EC3 plastic interaction

¹⁶ n being the level of axial forces defined as $n=N/N_{pl}$.

curves, the turning point was occurring at a level of a targeted axial forces equal to $20\%N_{pl}$ ($n = 0.2$). For all cross-section aspect ratios, the turning point was similar and equal to 20% of N_{pl} . In Eurocode 3, an approximation is performed when using the plastic interaction equations. For example, in the case of major-axis bending with axial compression, the interaction can be ignored as long as the axial load can be fully taken by the half of the webs' area, since the webs in that case will contribute the least to the support of the applied bending moment. The EC3 formula allows for an axial loading equivalent to 25% of N_{pl} , without a reduction to the bending resistance. EC3 presumes this in the design model which can sometimes lead to unsafe results since reality is different than EC3 assumptions. This can be readily observed in Figure 206 and Figure 207, wherein the value of m_y ¹⁷ remains constant up to a maximum of $n = 0.25$.

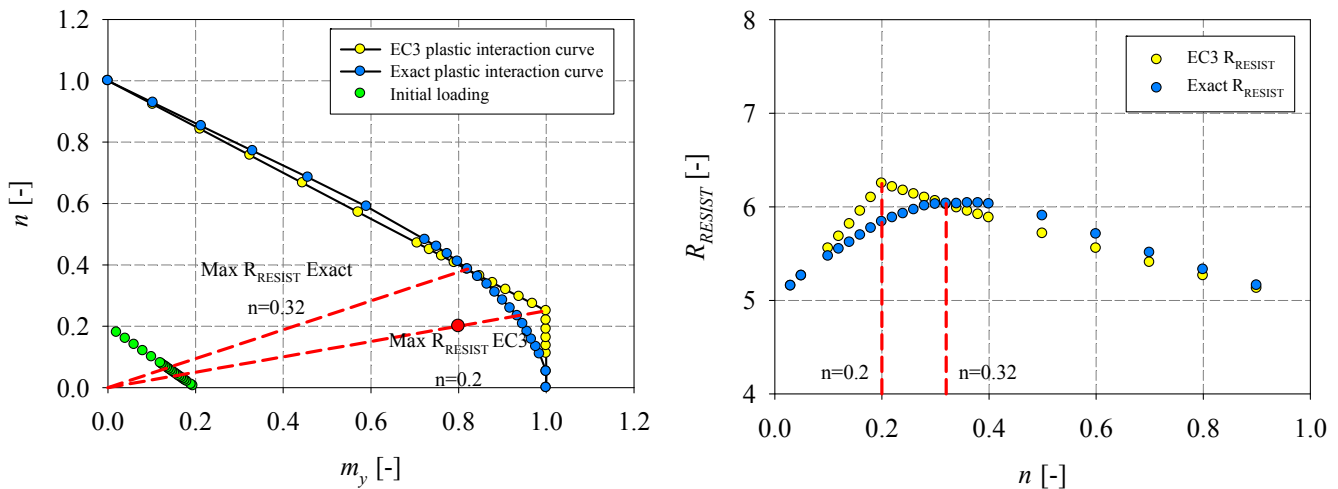


Figure 206 – R_{RESIST} calculation based on EC3 and exact formulation for a rectangular cross-section ($h/b = 1.5$)

a) n vs. m_y , b) R_{RESIST} vs. n

¹⁷ m_y being the level of major-axis bending, defined as $m_y = M/M_{pl}$.

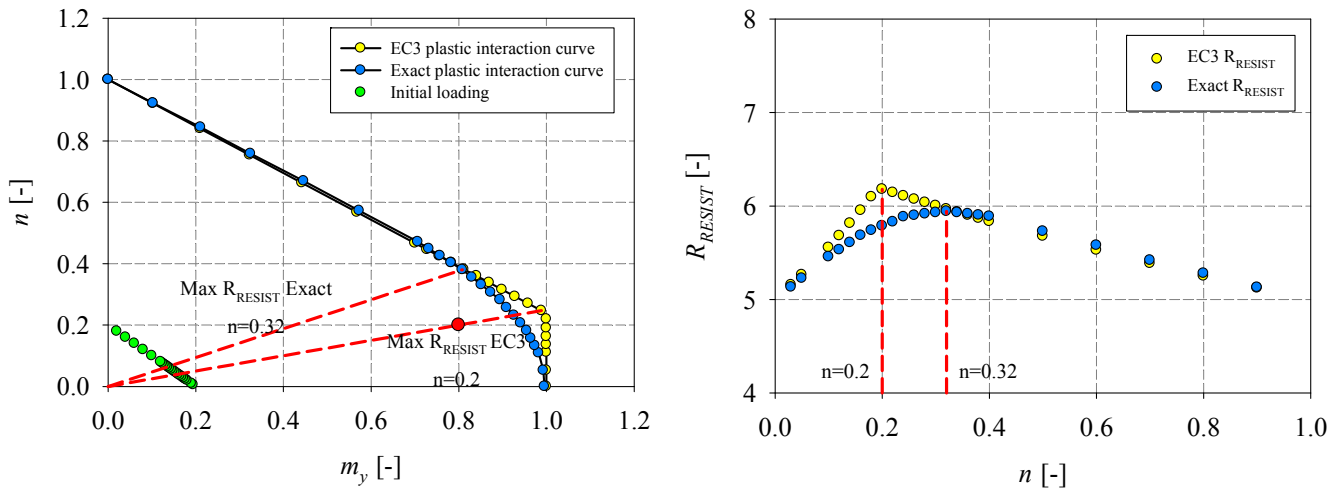


Figure 207 – R_{RESIST} calculation based on EC3 and exact formulation for a rectangular cross-section ($h/b = 1$)

a) n vs. m_y , b) R_{RESIST} vs. n

A recall to the EC3 interaction curves will further explain this fact; in the case of combined load case with compression and major or minor-axis bending, the EC3 interaction formula is as the following:

For $N + M_y$:

$$M_{N,y,Rd} = M_{pl,y,Rd} (1-n) / (1-0.5a_w) \quad (153)$$

$$\text{with } M_{N,y,Rd} \leq M_{pl,y,Rd}$$

where $a_w = (A - 2bt) / A$ but $a_w \leq 0.5$

For $N + M_z$:

$$M_{N,z,Rd} = M_{pl,z,Rd} (1-n) / (1-0.5a_f) \quad (154)$$

$$\text{with } M_{N,z,Rd} \leq M_{pl,z,Rd}$$

where $a_w = (A - 2ht) / A$ but $a_f \leq 0.5$

The bifurcation point for which the effect of the axial force becomes allowed to be taken into account in the derivation of the plastic moment resistance, can be found through the following equation:

$$\frac{(1-n)}{(1-0.5a_w)} = 1 \quad (155)$$

Therefore

$$n = 0.5a_w \quad (156)$$

For square sections, a_w would be almost equal to 0.5 (equal flanges and webs dimensions). For higher aspect ratios h/b , a_w would certainly increase, but with the limiting restriction of $a_w < 0.5$, the bifurcation point would be similar between all hollow sections and located at $n = 0.25$. Two examples are presented for a square cross-section ($h/b = 1$) and a rectangular cross-section ($h/b = 1.5$) subjected to a combined loading of compression and major-axis bending. On the left graphs of Figure 206 and Figure 207, R_{RESIST} results are reported in an $n - m_y$ plot, according to EC3 plastic equations and according to an exact calculation of the plastic capacity. On the right graphs, R_{RESIST} values are reported in function of the level of axial forces according to EC3 plastic interaction equations and to an exact calculation of the plastic capacity. It can be seen that the level of axial forces corresponding to the bifurcation point corresponds well to $n = 0.25$, as previously explained. However, the considered targeted loading corresponding to the bifurcation point was taken equal to $n = 0.2$ (red spot), which was then divided by 5 (as an initial loading) and increased in a iterative procedure in order to reach the value of $n = 0.25$. Therefore, for a targeted loading having a level of axial forces equal to 20% of N_{pl} , R_{RESIST} would reach its maximum, leading to the smallest value of the cross-section penalty χ_{CS} .

It should be mentioned that the bifurcation point would differ if the true interaction calculations were taken into account. This is clearly seen in Figure 206 and Figure 207 where the level of axial forces for which R_{RESIST} is the maximum would occur for a higher value of n compared to the approximated EC3 value. Actually, an exact calculation of R_{RESIST} (through the use of a dedicated Matlab software R_{RESIST} [111]) takes into account all the interactions,

for values of n as small as they are. The resulting approximations will only be the result of the software capacities and not technical interaction simplification as in the Eurocodes.

However, this difference between Eurocode interaction formulae and the exact R_{RESIST} calculation will not have a significant impact on the derived curves since the derived formula in itself will not change but only the condition of applicability would differ according to the true bifurcation calculated point (which will not be very far from the EC3 bifurcation point). For example, Figure 208 shows numerical results computed with both sources of R_{RESIST} (EC3 and the exact computation) for square cross-sections subjected to combined cases with various degrees of axial forces. It can be clearly seen that differences occur only in the proximity of the ‘bifurcation point’ which is equal to 20% of N_{pl} according to EC3 calculations, and 30% of N_{pl} according to an exact calculation of R_{RESIST} .

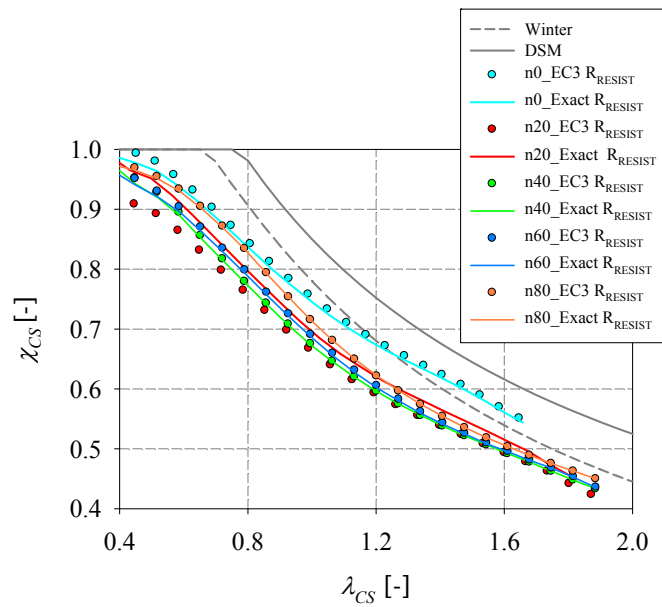


Figure 208 – Comparison of results computed with R_{RESIST_EC3} and $Exact_R_{RESIST}$ for square cross-sections subjected to combined load cases with various degrees of axial forces.

The n parameter was included in the η factor of the Ayrton-Perry formula. The original η formula for simple load cases is as follows:

$$\eta = \alpha(\lambda_{CS} - \lambda_0) \tag{157}$$

with α being the parameter taking into account the effect of imperfections and λ_0 being the considered limit of the plastic plateau.

With the inclusion of the n parameter, the proposed η formula would thus become as the following:

$$\eta = (\alpha + \alpha(1-n))(\lambda_{cs} - (\lambda_0 - \lambda_0(1-n))) \quad (158)$$

$$\text{for } 0.2 \leq n \leq 1$$

That way, for $n = 1$, Equation (157) would be restored with the limiting curve being relative to a pure compression load case.

For values of n smaller than 0.2, the proposed η formula would be as the following:

$$\eta = (\alpha + \alpha n)(\lambda_{cs} - (\lambda_0 - \lambda_0 n)) \quad (159)$$

$$\text{for } 0 \leq n < 0.2$$

That way, for $n = 0$, Equation (157) would be restored with the limiting curve being relative to a major-axis bending load case.

A brief summary of the proposed curves are presented in Table 46. Figure 209 to Figure 213 show the proposed design curves presented and classified in terms of the aspect ratios h/b , for the different levels of axial loads treated and analysed in this study.

The yield stress was not accounted for in the design formula since their negligible effect is obviously seen in Figure 214.

Table 46 – Design curves proposals relative to hot-rolled sections subjected to combined load cases.

Proposed Ayrton-Perry formula for $0.2 \leq n \leq 1$		
$\chi_{CS} = \frac{\beta}{\phi + \sqrt{\phi^2 - \lambda_{CS}^\delta \beta}}$ $\phi = 0.5 \left(1 + (\alpha_{CS} + \alpha_{CS}(1-n)) (\lambda_{CS} - (\lambda_0 - \lambda_0(1-n))) + \lambda_{CS}^\delta \beta \right)$ <p style="text-align: center;">For $\lambda > \lambda_0 - \lambda_0(1-n)$</p> $\chi_{CS} = 1 \text{ For } \lambda \leq \lambda_0 - \lambda_0(1-n)$		
Fabrication process	Parameters	
Hot-rolled	β	1
	λ_0	0.35
	α_{CS}	0.15
	δ	$-0.4h/b + 1.45$
Proposed Ayrton-Perry formula for $0 \leq n < 0.2$		
$\chi_{CS} = \frac{\beta}{\phi + \sqrt{\phi^2 - \lambda_{CS}^\delta \beta}}$ $\phi = 0.5 \left(1 + (\alpha_{CS} + n(1-n)) (\lambda_{CS} - (\lambda_0 - \lambda_0 n)) + \lambda_{CS}^\delta \beta \right)$ <p style="text-align: center;">For $\lambda_{CS} > \lambda_0 - \lambda_0 n$</p> $\chi_{CS} = 1 \text{ For } \lambda \leq \lambda_0 - \lambda_0 n$		
Fabrication process	Parameters	
Hot-rolled	β	1
	λ_0	0.35
	α_{CS}	$1/10\delta + 3/200$
	δ	$0.4h/b + 0.25$

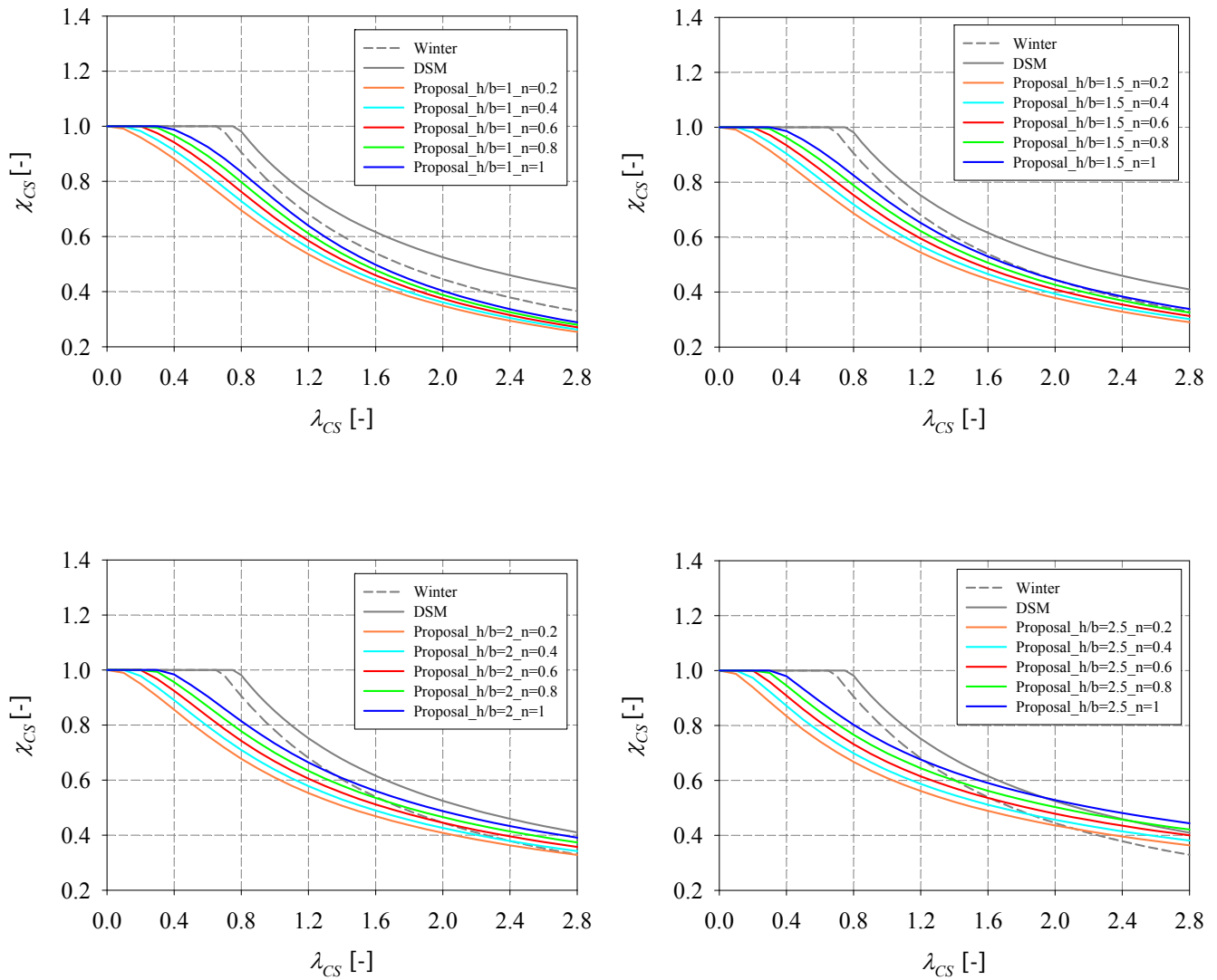


Figure 209 – Design curves proposals relative to hot-formed sections subjected to combined load cases.

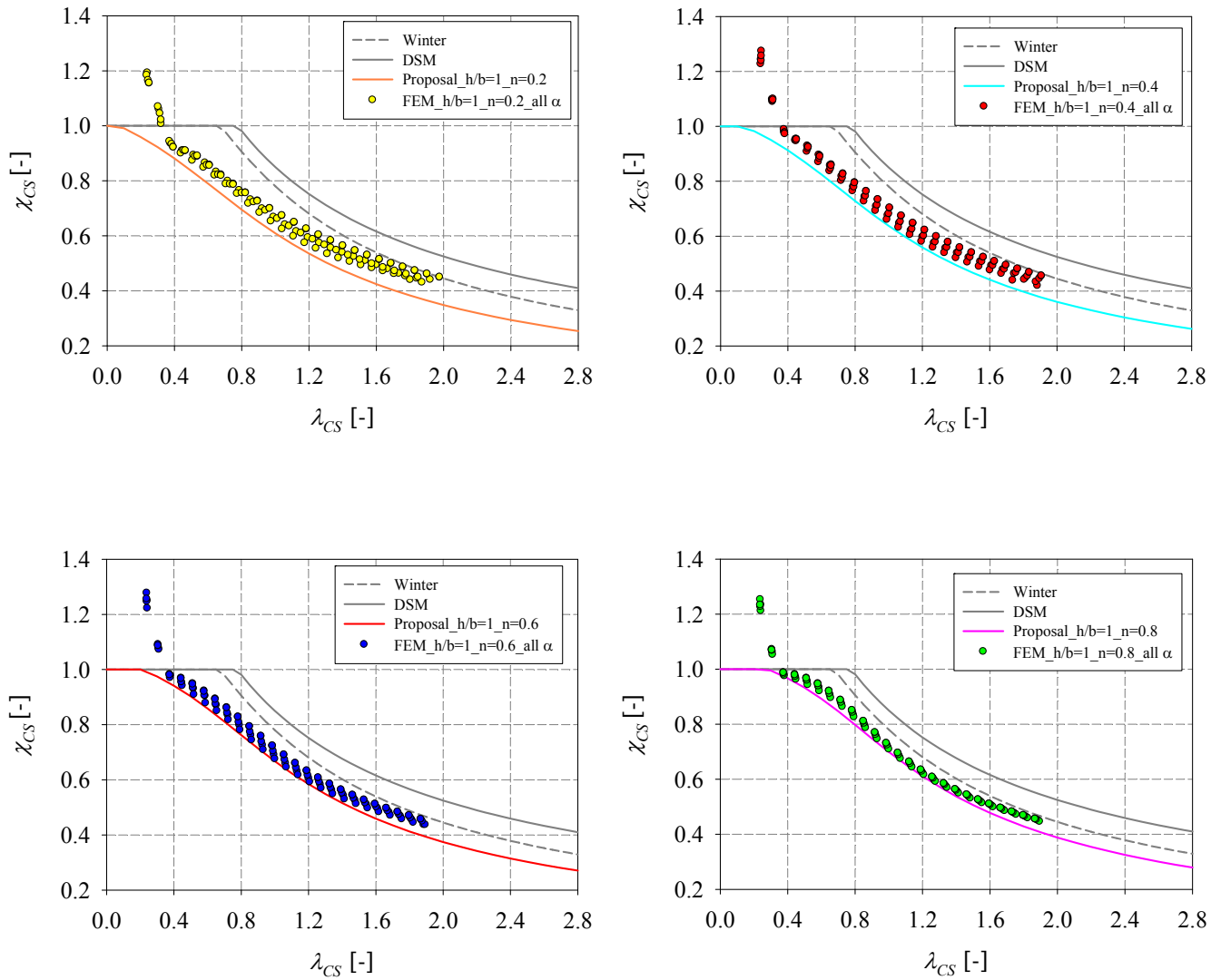


Figure 210 – FE results and design curves relative to square cross-sections ($h/b = 1.0$)
subjected to combined loading with various degrees of axial forces.

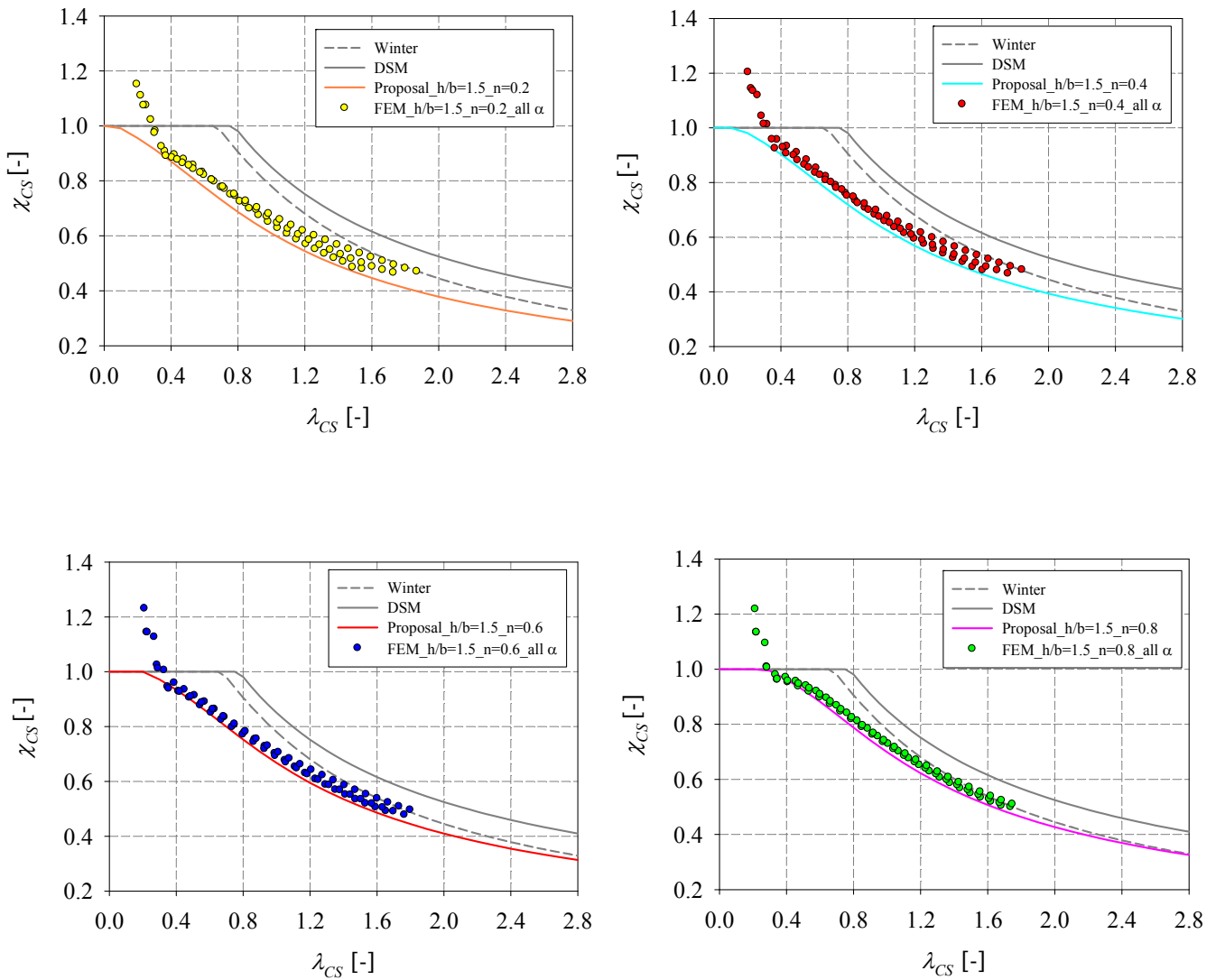


Figure 211 – FE results and design curves relative to rectangular cross-sections ($h/b = 1.5$)
subjected to combined loading with various degrees of axial forces.

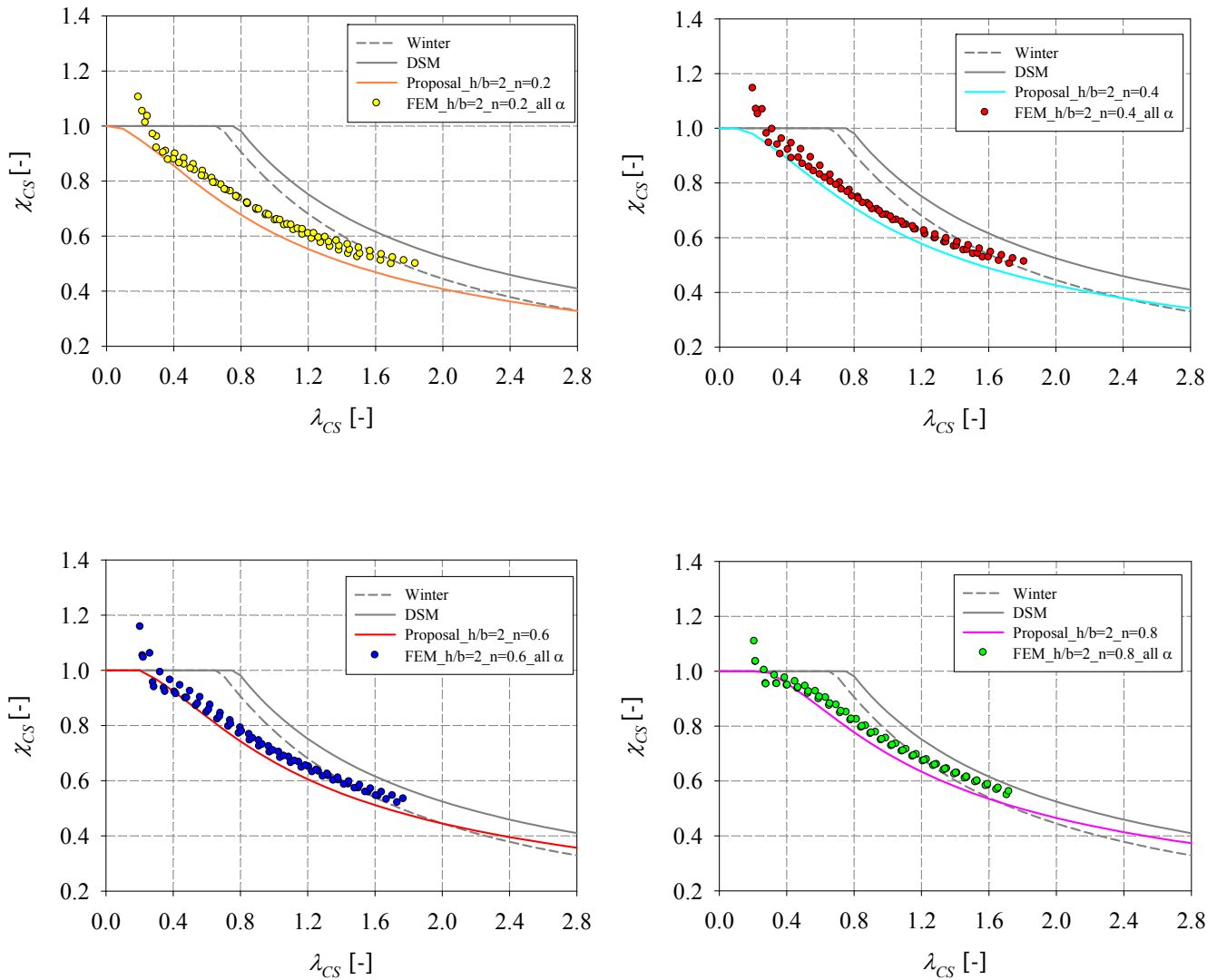


Figure 212 – FE results and design curves relative to rectangular cross-sections ($h/b = 2.0$)
subjected to combined loading with various degrees of axial forces.

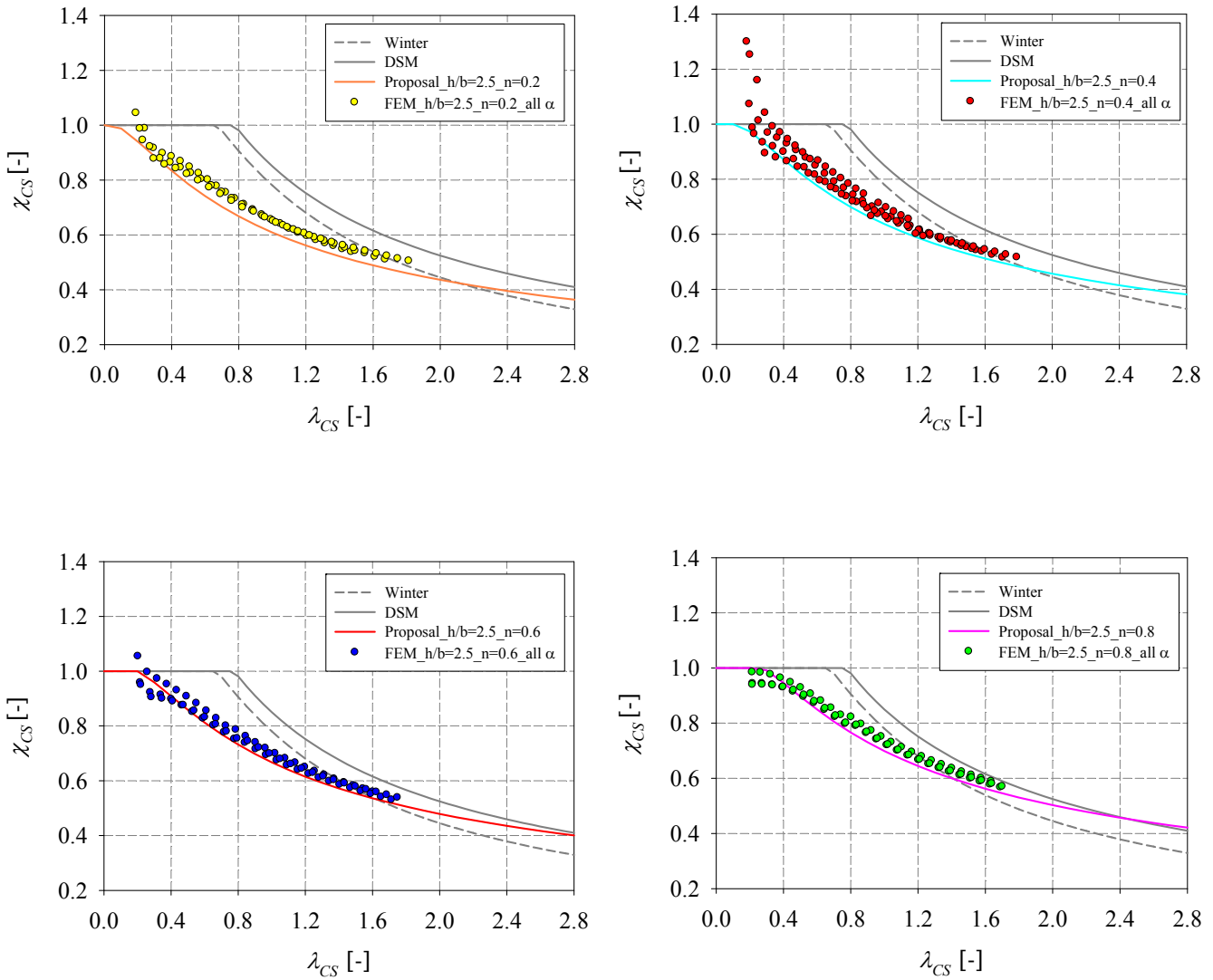


Figure 213 – FE results and design curves relative to rectangular cross-sections ($h/b = 2.5$)
subjected to combined loading with various degrees of axial forces.

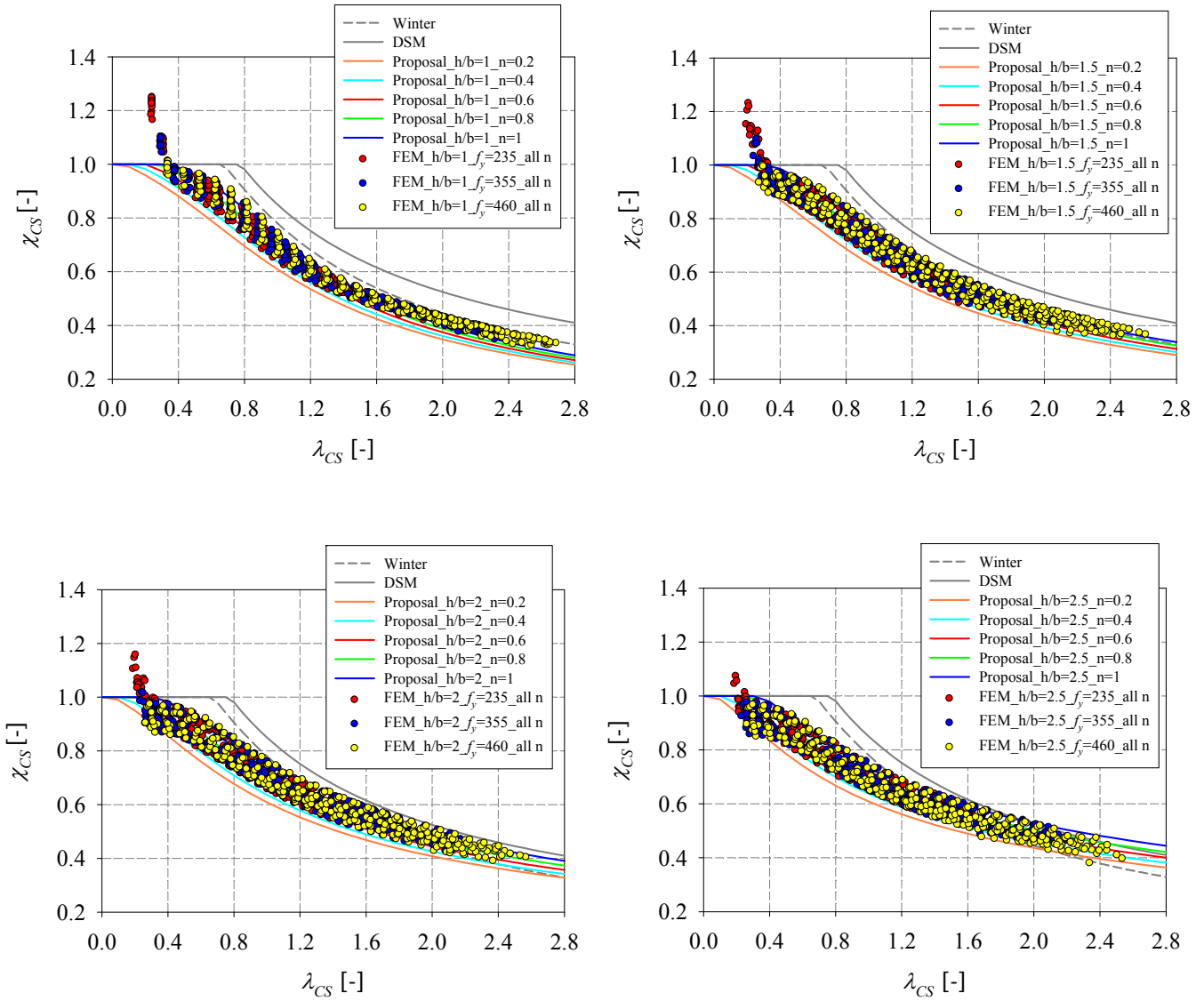


Figure 214 – FE results of cross-sections represented in function of the yield stress.

Additional numerical computations were conducted for low levels of axial forces ($n < 0.2$), since no available computations were made for such range and a confirmation of the accuracy of the proposed design curve is needed. Figure 215 presents the corresponding results of rectangular cross-sections having aspect ratios $h/b = 1.5$ with two levels of axial forces: $n = 0.15$ and $n = 0.10$. It is obviously seen that for small levels of axial forces, the effect of the minor and major-axis proportions will be more obvious. However, the scatter is still limited and the assumption of a curve based only on the n parameter would be sufficiently accurate. As a reminder, the curves relative to levels of axial forces smaller than $20\%N_{pl}$ would converge to the proposed design curve relative to major-axis bending load case. However, additional computations for other aspect ratios are needed to confirm the adequacy of the proposed curves.

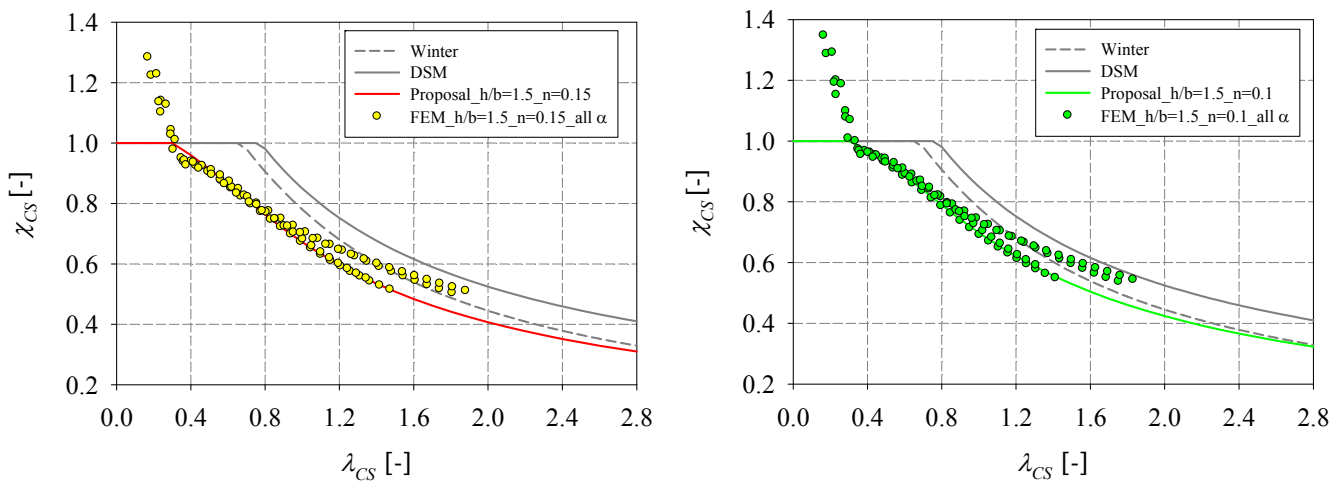


Figure 215 – FE results and design curves relative to rectangular cross-sections ($h/b = 1.5$) subjected to combined loading with various small degrees of axial forces.

5.3.2.1.2. Cold-formed sections

Again, two design approaches have been developed for cold-formed sections that specifically lead to $\chi_{CS} > 1.0$ beneficial factors at low λ_{CS} ranges.

1st approach

Similarly to the proposed design curves relative to hot-rolled sections, the n parameter was included in the η factor of the Ayrton-Perry formula. However, the main difference between hot-rolled and cold-formed sections subjected to a combined loading with different levels of axial forces is the minimized difference between the various curves relative to the different levels of axial forces n . This is mainly due to the adopted material laws. Different levels of axial forces would lead to different levels of ultimate reached strains which were in majority smaller than the yield strain relative to the hot-rolled material law. An example in Figure 216a is shown, where multiple combined load cases with different levels of axial forces are presented for square cold-formed cross-sections (S235). In the region of strains smaller than the yield strain of the hot-rolled material law (yellow area in Figure 216b), the non-linearity of the adopted simple Ramberg-Osgood material law for cold-formed sections will result in a smaller tangent modulus compared to the relative one in the hot-rolled material law. Therefore, the corresponding stress levels relative to the different strains reached in a cold-formed material law, will not differ as much as the stresses relative to a hot-rolled material law.

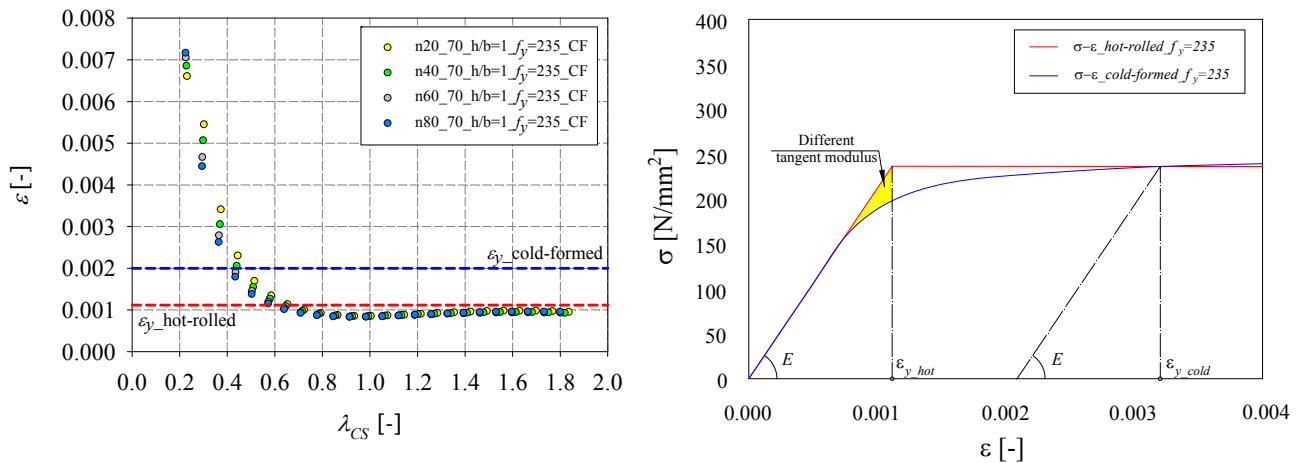


Figure 216 – a) Ultimate strains in function of the relative slenderness for combined load cases of square cross-sections b) Differences between hot-rolled and cold-formed material laws.

This effect was included in the proposed formula through an exponent to the n parameter, depending on the aspect ratio h/b , since it was seen that with increased h/b ratios, the difference between structural responses relative to various levels of axial forces would increase as well.

For simple load cases, η is equal to:

$$\eta = \alpha_{CS} (\lambda_{CS} - \lambda_0) \quad (160)$$

With the inclusion of the n parameter, the proposed η formula would thus become as the following:

$$\eta = (\alpha_{CS} + \alpha_{CS} (1 - n^\gamma)) (\lambda_{CS}) \quad (161)$$

$$\text{for } 0.2 \leq n \leq 1$$

$$\text{with } \gamma = \frac{h/b}{5} - 0.1$$

That way for $n = 1$, Equation (160) would be restored with the limiting curve being relative to a pure compression load case.

For values of n smaller than 0.2, the proposed η formula would be as the following:

$$\eta = (\alpha_{CS} + \alpha_{CS} n^\gamma) (\lambda_{CS}) \quad (162)$$

$$\text{for } 0 \leq n < 0.2$$

$$\text{with } \gamma = \frac{h/b}{5} - 0.1$$

That way for $n = 0$, Equation (160) would be restored with the limiting curve being relative to a major-axis bending load case.

It should be noted that the proposed curves relative to levels of axial forces smaller than 20% of N_{pl} need to be validated since no numerical results were available for such range.

A brief summary of the proposed curves are presented in Table 47. Figure 217 to Figure 221 show the proposed design curves presented and classified in terms of the aspect ratios h/b ,

for the different levels of axial loads treated and analysed in this study. Figure 222 shows the negligible effect of the yield stress.

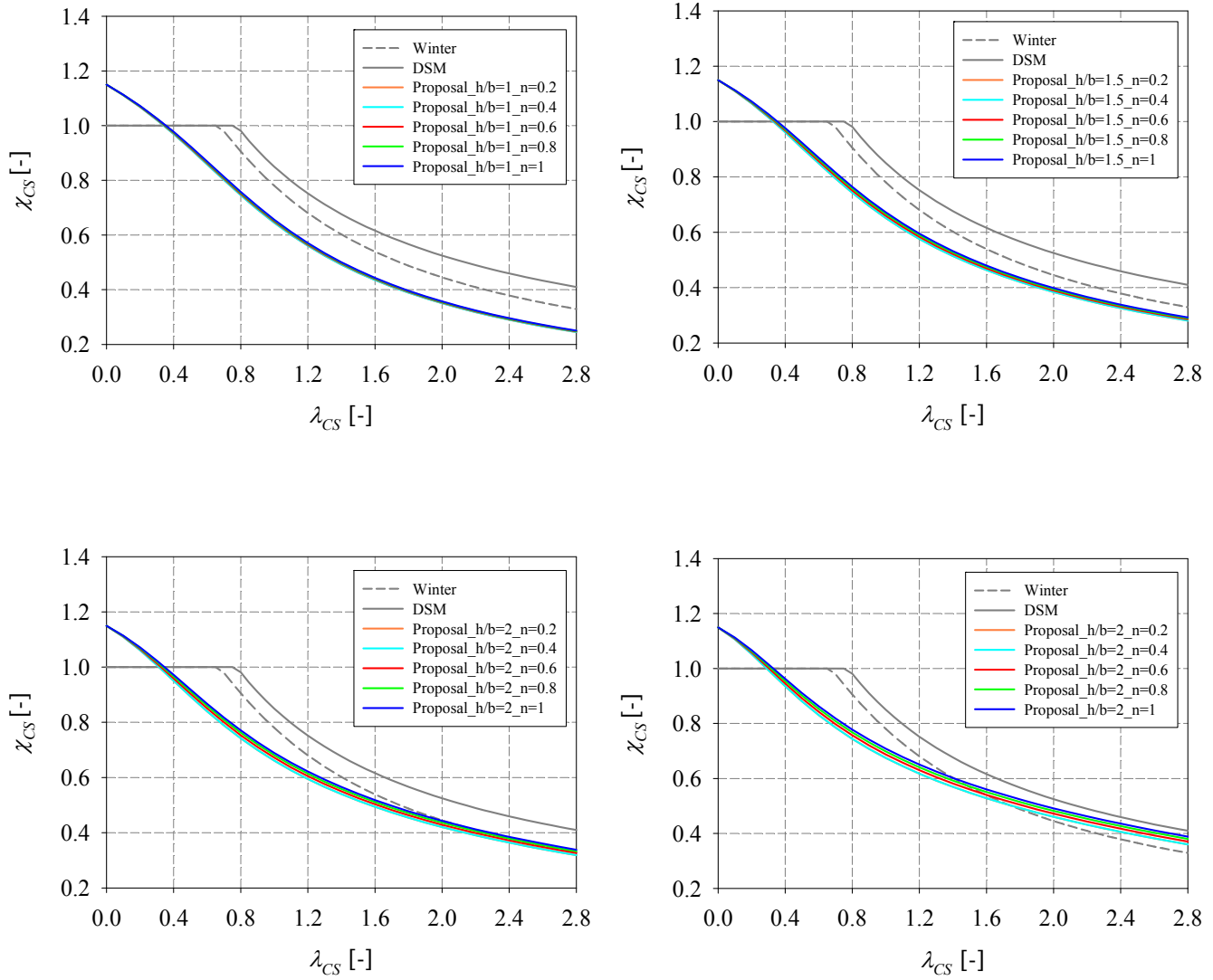


Figure 217 – Design curves proposals relative to cold-formed sections subjected to combined load cases (1st approach).

Table 47 – Design curves proposals relative to cold-formed sections subjected to combined load cases (1st approach).

Proposed Ayrton-Perry formula for $0.2 \leq n \leq 1$		
$\chi_{CS} = \frac{\beta}{\phi + \sqrt{\phi^2 - \lambda_{CS}^\delta \beta}}$ $\phi = 0.5 \left(1 + (\alpha_{CS} + \alpha_{CS} (1 - n^\gamma)) (\lambda_{CS} - (\lambda_0 - \lambda_0 (1 - n^\gamma))) + \lambda_{CS}^\delta \beta \right)$ <p>With $\gamma = (h/b)/5 - 1/10$</p>		
Fabrication process	Parameters	
Cold-formed First approach	β	$-0.15\lambda + 1.15$
	λ_0	0
	α_{CS}	$1/10\delta + 3/40$
	δ	$-0.4h/b + 1.45$
Proposed Ayrton-Perry formula for $0 \leq n < 0.2$		
$\chi_{CS} = \frac{\beta}{\phi + \sqrt{\phi^2 - \lambda_{CS}^\delta \beta}}$ $\phi = 0.5 \left(1 + (\alpha_{CS} + n(1 - n^\gamma)) (\lambda_{CS} - (\lambda_0 - \lambda_0 n^\gamma)) + \lambda_{CS}^\delta \beta \right)$ <p>With $\gamma = (h/b)/5 - 1/10$</p>		
Fabrication process	Parameters	
Cold-formed First approach	β	$-0.20\lambda + 1.20$
	λ_0	0
	α_{CS}	$1/10\delta + 7/200$
	δ	$0.4h/b + 0.25$

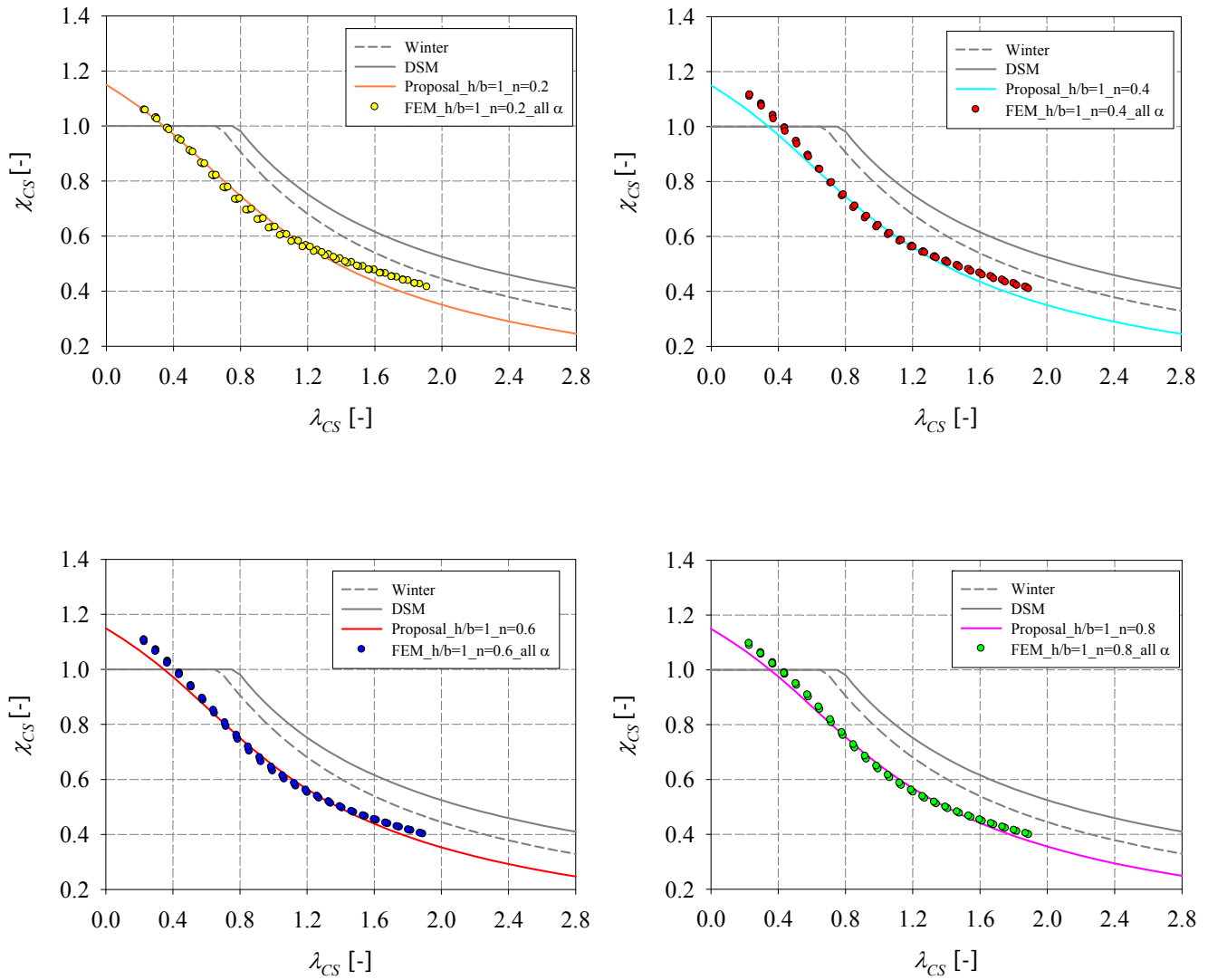


Figure 218 – FE results and design curves relative to square cross-sections ($h/b = 1.0$) subjected to combined loading with various degrees of axial forces (1st approach).

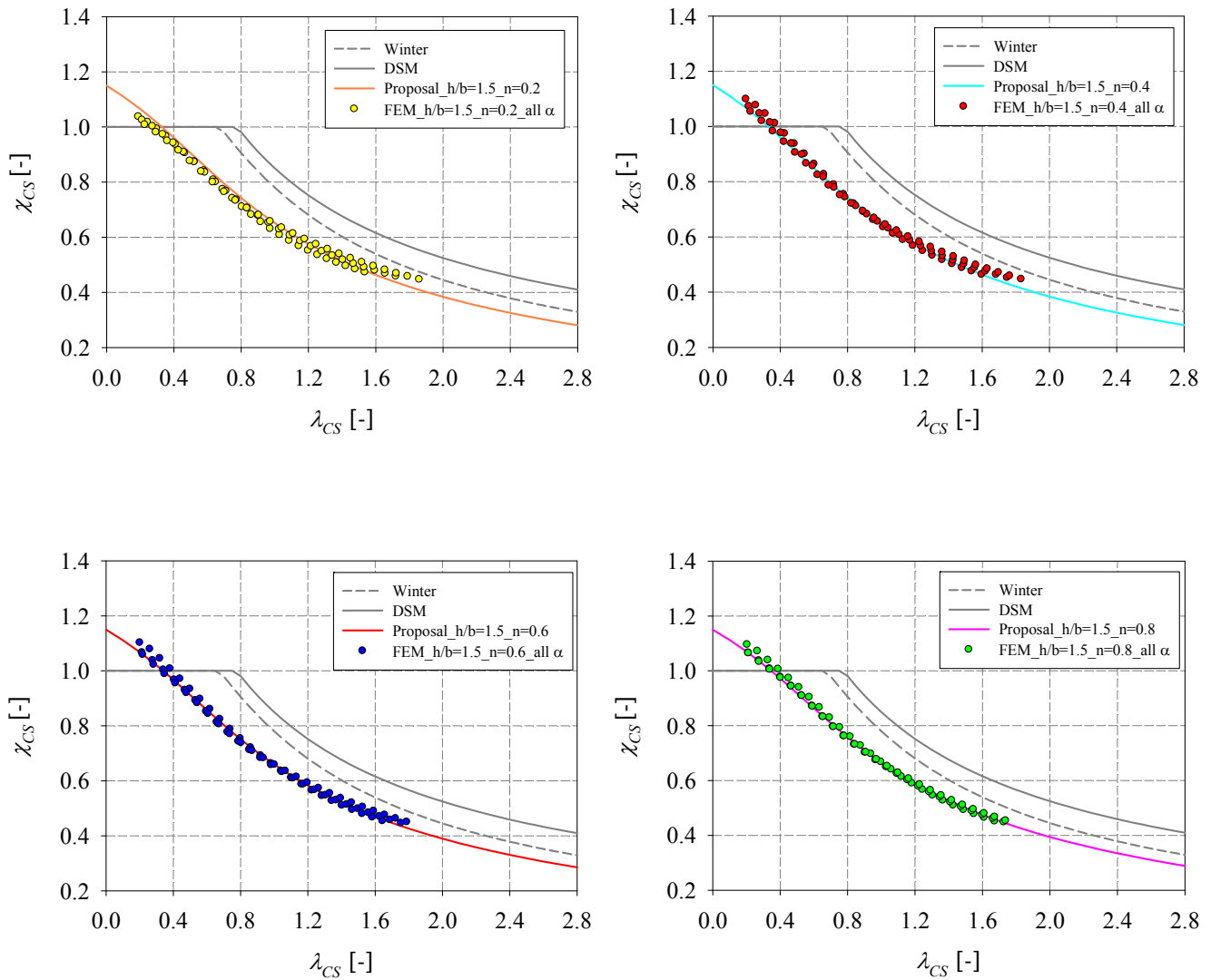


Figure 219 – FE results and design curves relative to square cross-sections ($h/b = 1.5$) subjected to combined loading with various degrees of axial forces (1st approach).

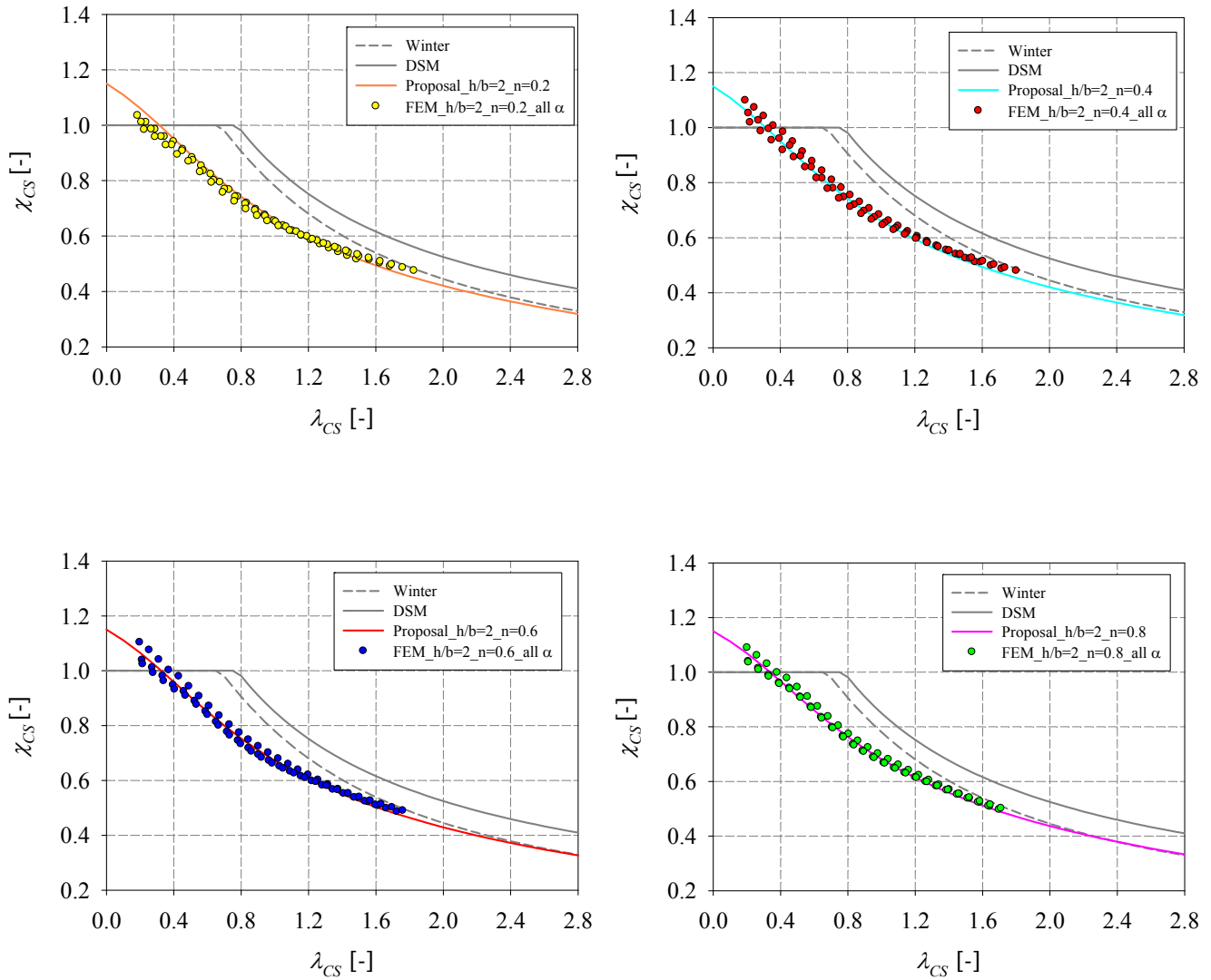


Figure 220 – FE results and design curves relative to square cross-sections ($h/b = 2.0$)
subjected to combined loading with various degrees of axial forces (1st approach).

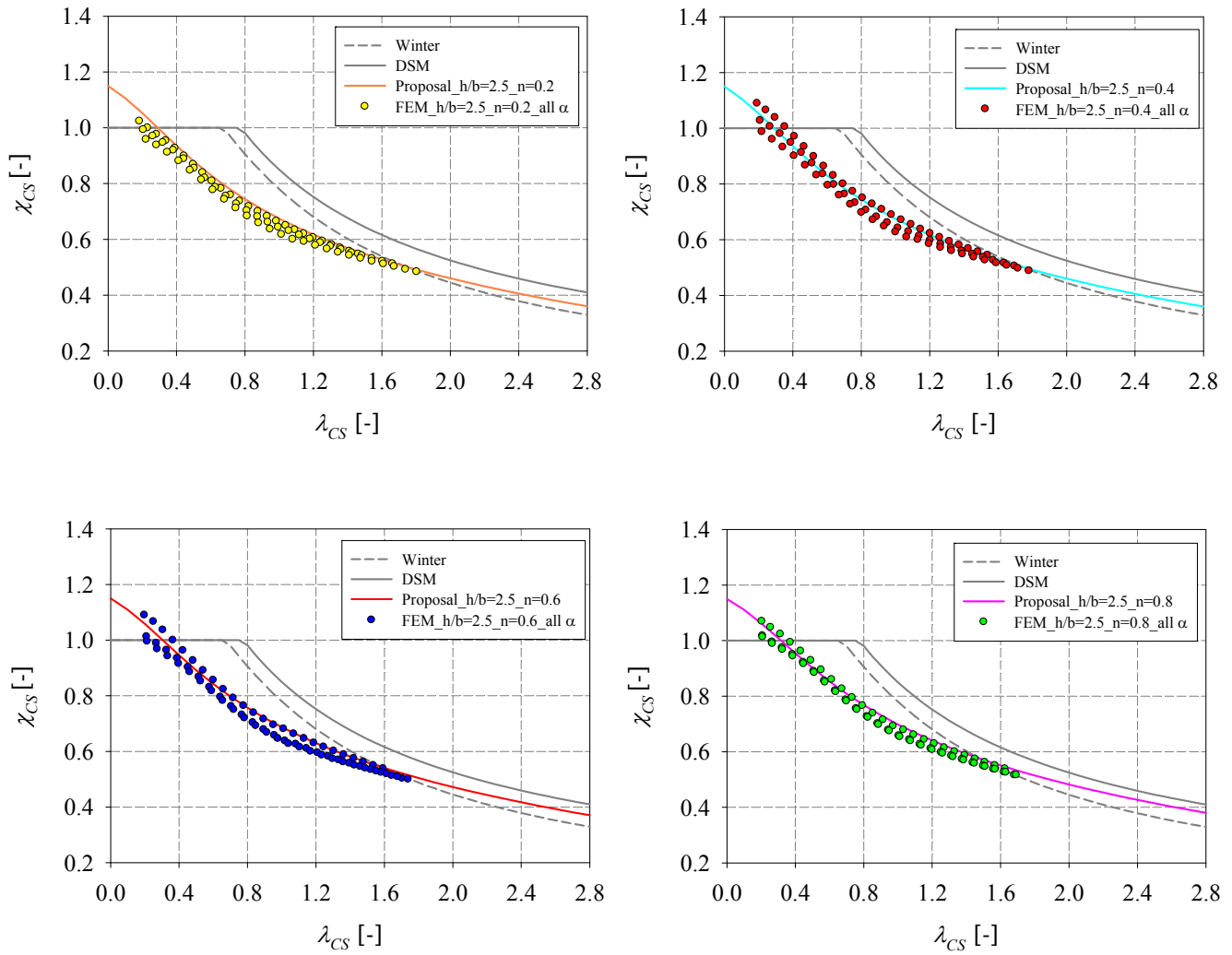


Figure 221 – FE results and design curves relative to square cross-sections ($h/b = 2.5$) subjected to combined loading with various degrees of axial forces (1st approach).

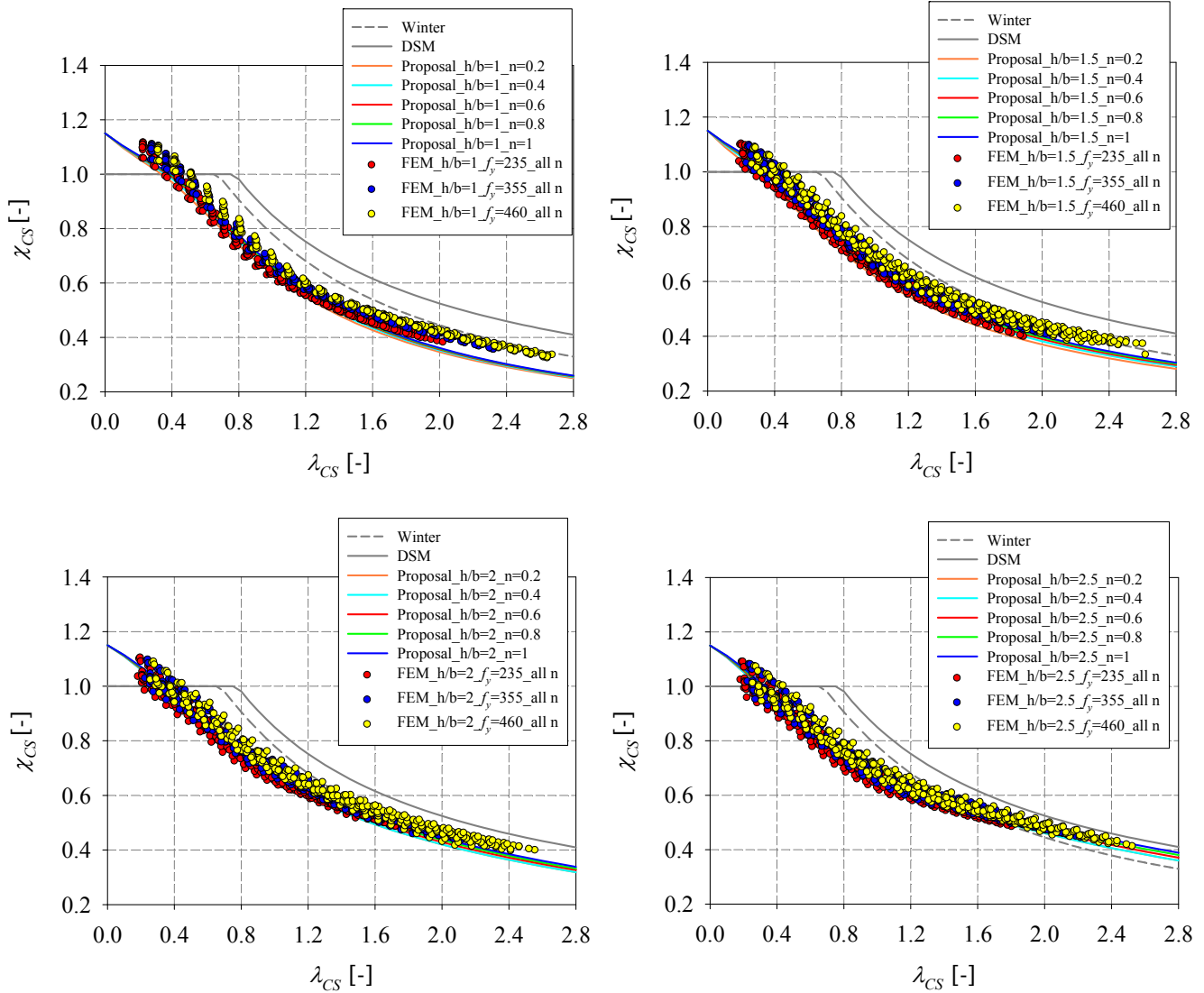


Figure 222 – FE results of cross-sections represented in function of the yield stress
(1st approach).

2nd approach

As previously mentioned, the 2nd approach relies on the consideration of a strain-based format at low slenderness.

The proposed η formula would be as the following,

$$\eta = (\alpha_{CS} + \alpha_{CS}(1-n^\gamma))(\lambda_{CS} - (\lambda_0 - \lambda_0(1-n^\gamma))) \quad (163)$$

$$\text{for } 0.2 \leq n \leq 1$$

$$\text{for } \lambda \geq \lambda_0 - \lambda_0(1-n^\gamma)$$

$$\text{with } \gamma = \frac{h/b}{5} - 0.1$$

For values of n smaller than 0.2, the proposed η formula would be as the following:

$$\eta = (\alpha_{CS} + \alpha_{CS}n^\gamma)(\lambda_{CS} - (\lambda_0 - \lambda_0n^\gamma)) \quad (164)$$

$$\text{for } 0 \leq n < 0.2$$

$$\text{for } \lambda \geq \lambda_0 - \lambda_0n^\gamma$$

$$\text{with } \gamma = \frac{h/b}{5} - 0.1$$

For the strain based region, i.e. for $\lambda < \lambda_0 - \lambda_0(1-n^\gamma)$ when $0.2 \leq n < 1$ and $\lambda < \lambda_0 - \lambda_0n^\gamma$ when $0 \leq n < 0.2$, the insertion of the deformation demand for the determination of the reduction factor was accounted for in a similar manner discussed previously and with the similar equations in which the accurate end of plateau formula is inserted.

Therefore the first step would thus consist in the following equations:

$$\frac{\varepsilon}{\varepsilon_y} = \left(\frac{\lambda_0 - \lambda_0(1-n^\gamma)}{\lambda_{CS}} \right)^{1.5} \quad (165)$$

$$\text{For } \lambda < \lambda_0 - \lambda_0(1-n^\gamma)$$

When $0.2 \leq n \leq 1$

And:

$$\frac{\varepsilon}{\varepsilon_y} = \left(\frac{\lambda_0 - \lambda_0 n^\gamma}{\lambda_{CS}} \right)^{1.5} \quad (166)$$

For $\lambda < \lambda_0 - \lambda_0 n^\gamma$

When $0 \leq n < 0.2$

The second step consisting of a relation between $\varepsilon / \varepsilon_y$ and the reduction factor χ_{CS} was unchanged and would thus be for the cases where level of axial forces are comprised between 0.2 and 1 (with the limiting curve being the one derived for the pure compression cases) as the following:

$$\chi_{CS} = 1.15 - \frac{0.15}{\left(\varepsilon / \varepsilon_y \right)^{0.6}} \quad (167)$$

And

$$\chi_{CS} = 1.2 - \frac{0.2}{\left(\varepsilon / \varepsilon_y \right)^{0.6}} \quad (168)$$

would thus be the equation for the case where level of axial forces are comprised between 0 and 0.2 (with the limiting curve being the one derived for the major-axis bending cases).

A brief summary of the proposed curves are presented in Table 48. Figure 223 to Figure 227 show the proposed design curves presented and classified in terms of the aspect ratios h/b , for the different levels of axial loads treated and analysed in this study. Figure 228 show the effect of yield stress on the cross-section resistance of all cross-sections with various aspect ratios h/b .

Table 48 – Design curves proposals relative to cold-formed sections subjected to combined load cases (2st approach).

Proposed Ayrton-Perry formula for $0.2 \leq n \leq 1$		
$\chi_{CS} = \frac{\beta}{\phi + \sqrt{\phi^2 - \lambda_{CS}^\delta \beta}}$ $\phi = 0.5 \left(1 + (\alpha_{CS} + \alpha_{CS} (1 - n^\gamma)) (\lambda_{CS} - (\lambda_0 - \lambda_0 (1 - n^\gamma))) + \lambda_{CS}^\delta \beta \right)$ <p>With $\gamma = (h/b)/5 - 1/10$</p>		
Fabrication process	Parameters	
Cold-formed Second approach	For $\lambda \leq \lambda_0 - \lambda_0 (1 - n^\gamma)$	
	$\chi_{CS} = 1.15 - \frac{0.15}{(\varepsilon / \varepsilon_y)^{0.6}}$	
	With $\frac{\varepsilon}{\varepsilon_y} = \left(\frac{\lambda_0 - \lambda_0 (1 - n^\gamma)}{\lambda_{CS}} \right)^{1.5}$	
	For $\lambda_{CS} > \lambda_0 - \lambda_0 (1 - n^\gamma)$	
	β	1
	λ_0	0.40
	α_{CS}	$1/10\delta + 7/40$
δ	$-0.4h/b + 1.45$	
Proposed Ayrton-Perry formula for $0 \leq n < 0.2$		
$\chi_{CS} = \frac{\beta}{\phi + \sqrt{\phi^2 - \lambda_{CS}^\delta \beta}}$ $\phi = 0.5 \left(1 + (\alpha + n(1 - n^\gamma)) (\lambda_{CS} - (\lambda_0 - \lambda_0 n^\gamma)) + \lambda_{CS}^\delta \beta \right)$ <p>With $\gamma = (h/b)/5 - 1/10$</p>		
Fabrication process	Parameters	
Cold-formed Second approach	For $\lambda_{CS} \leq \lambda_0 - \lambda_0 n^\gamma$	
	$\chi_{CS} = 1.20 - \frac{0.20}{(\varepsilon / \varepsilon_y)^{0.6}}$	
	With $\frac{\varepsilon}{\varepsilon_y} = \left(\frac{\lambda_0 - \lambda_0 n^\gamma}{\lambda_{CS}} \right)^{1.5}$	
	For $\lambda_{CS} > \lambda_0 - \lambda_0 n^\gamma$	
	β	1
	λ_0	0.40
	α_{CS}	$1/4\delta - 1/80$
δ	$0.4h/b + 0.25$	

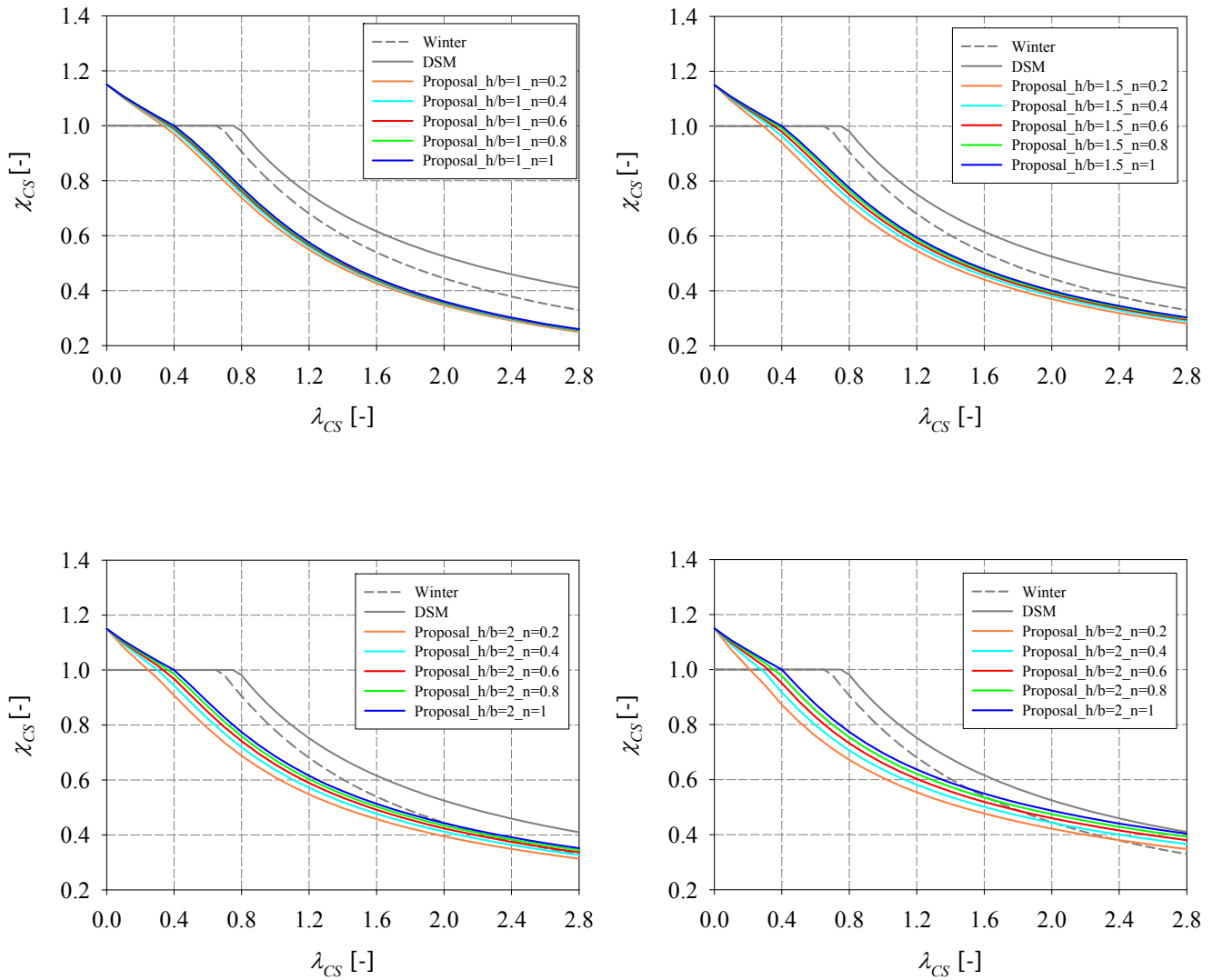


Figure 223 – Design curves proposals relative to cold-formed sections subjected to combined load cases (2nd approach).

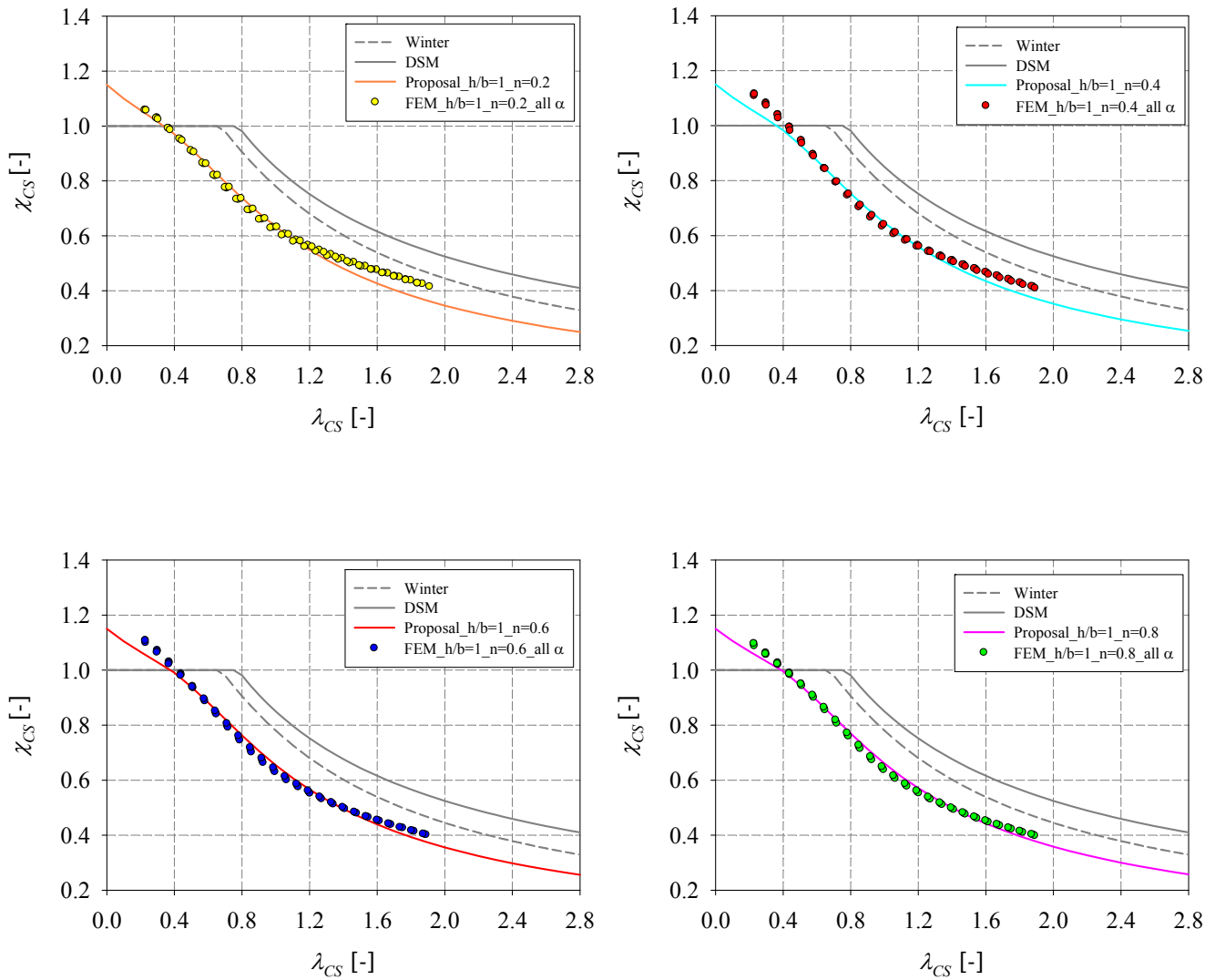


Figure 224 – FE results and design curves relative to square cross-sections ($h/b = 1.0$) subjected to combined loading with various degrees of axial forces (2nd approach).

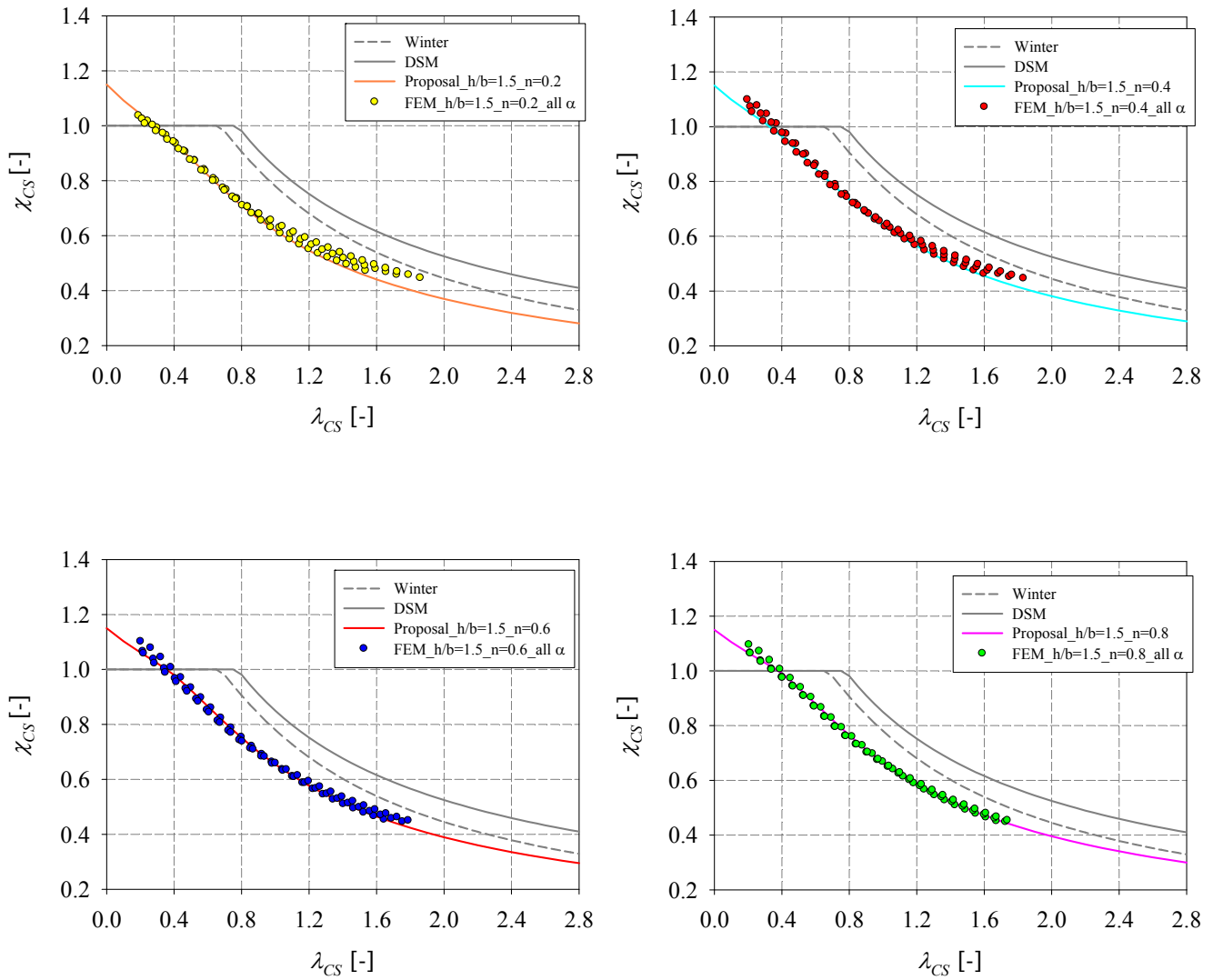


Figure 225 – FE results and design curves relative to square cross-sections ($h/b = 1.5$) subjected to combined loading with various degrees of axial forces (2nd approach).

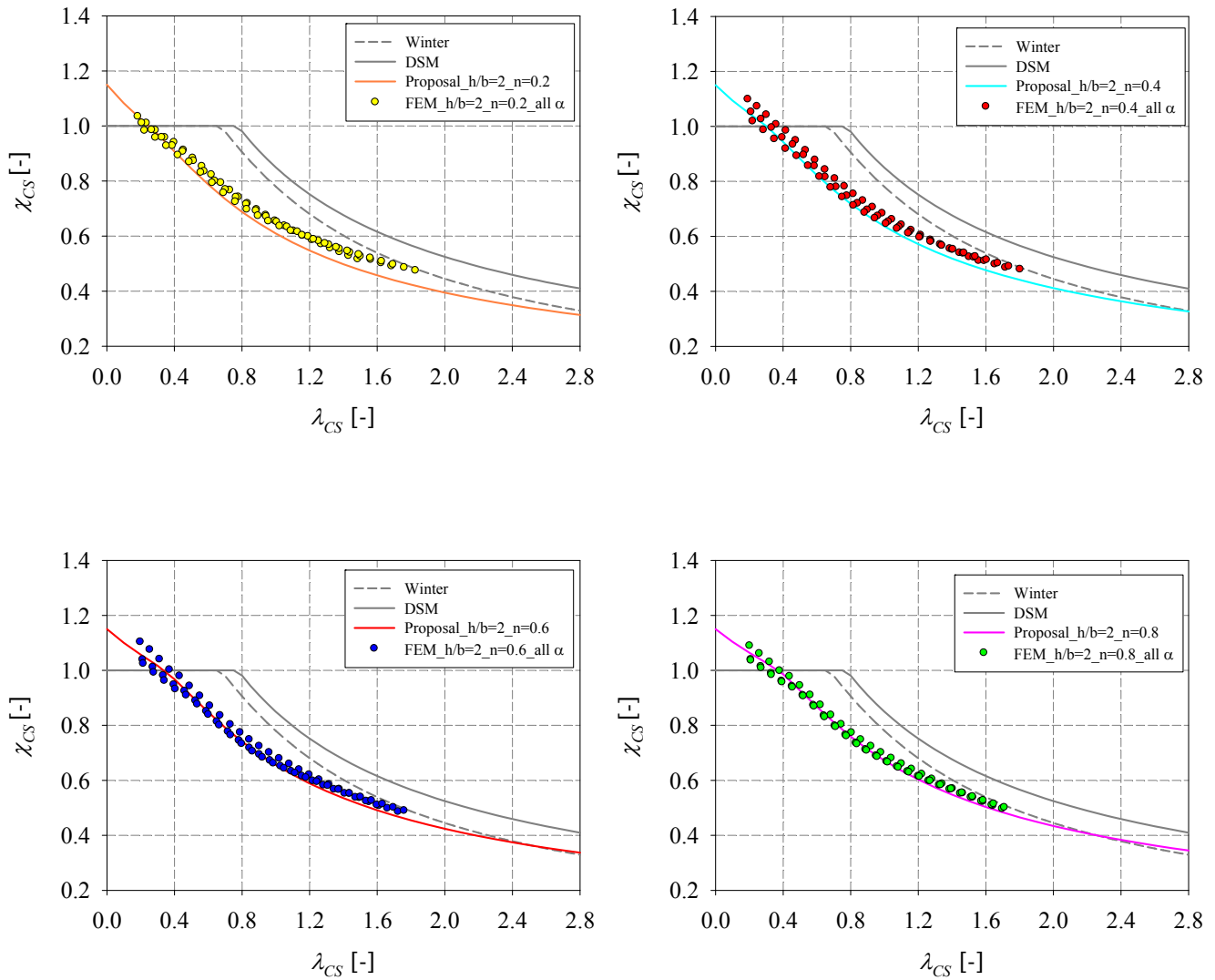


Figure 226 – FE results and design curves relative to square cross-sections ($h/b = 2.0$) subjected to combined loading with various degrees of axial forces (2nd approach).

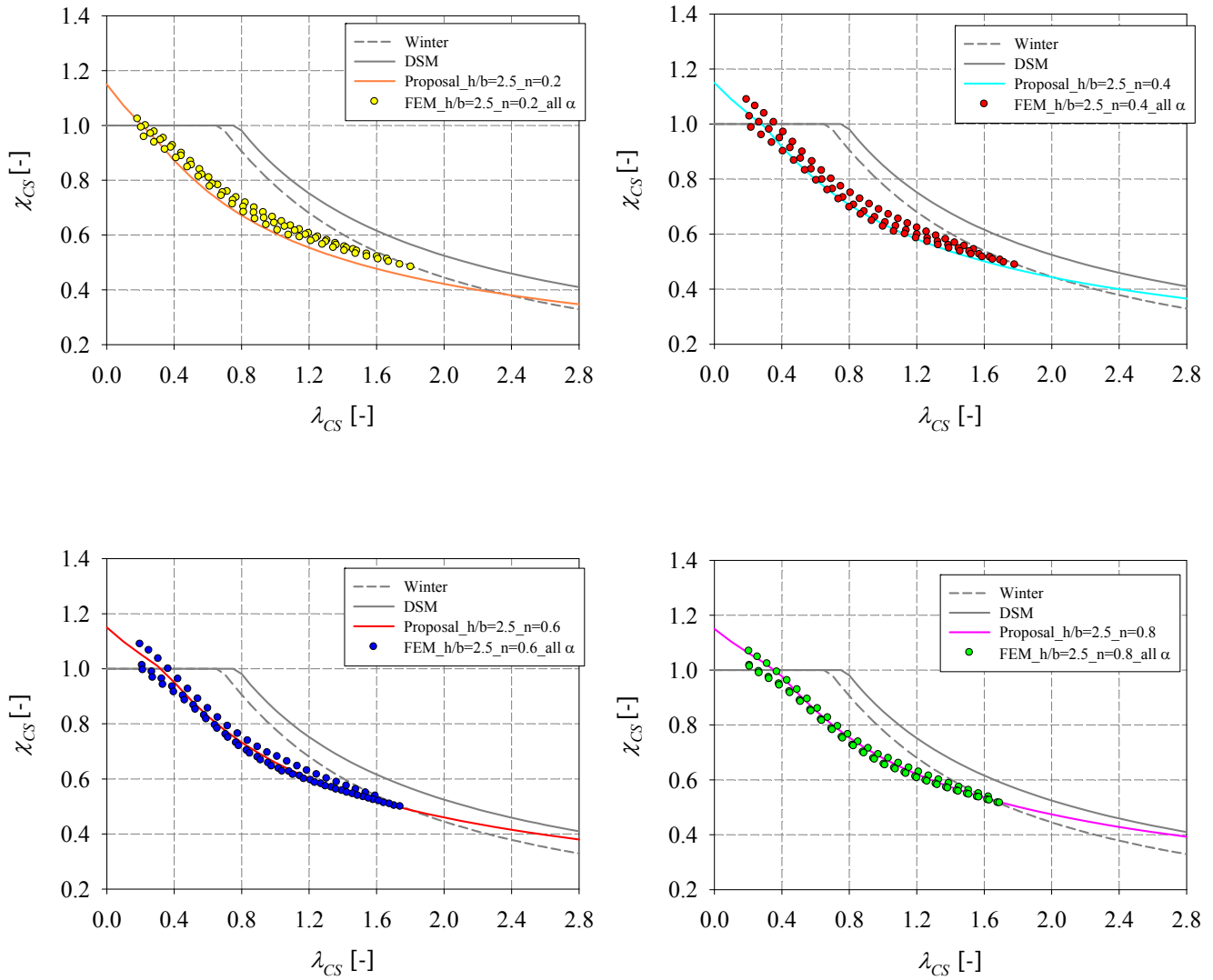


Figure 227 – FE results and design curves relative to square cross-sections ($h/b = 2.5$) subjected to combined loading with various degrees of axial forces (2nd approach).

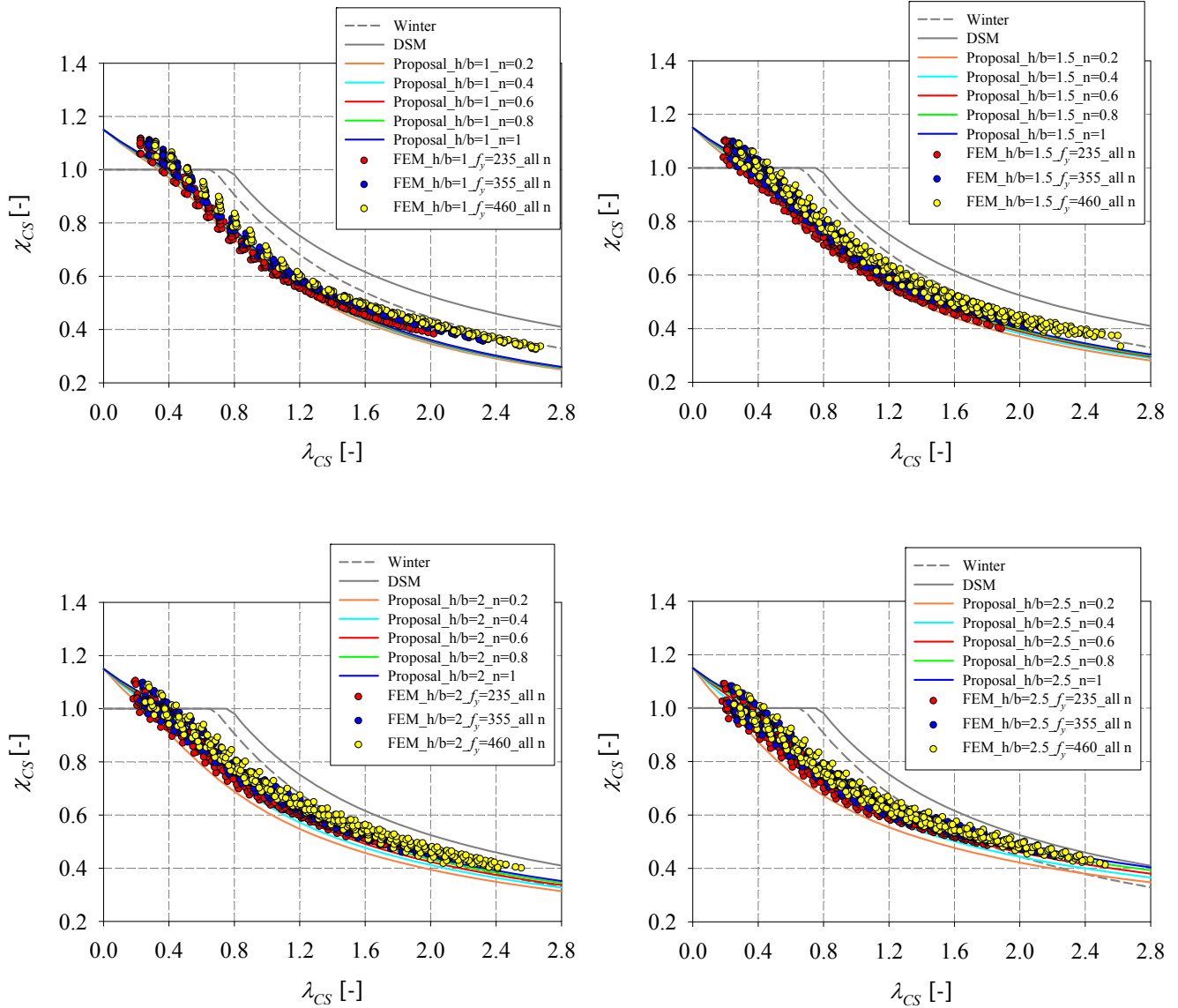


Figure 228 – FE results of cross-sections represented in function of the yield stress (2nd approach).

6. Accuracy of proposed models – Comparison with actual rules

Table 49 proposes statistical results of the comparison between FEM, EC3 and proposal calculations for all the computed results. As can be seen, the resistance estimates are significantly improved by the new proposal, and the mean and standard deviation values also indicate a better level of consistency compared to EC3 calculations. With the adoption of the EC3 procedure, the calculations can sometimes lead to unconservative results and sometimes to overly conservative results.

Table 49 – Comparison between FEM, EC3 and proposal results for all treated load cases.

Type of load case	Load case	Fabrication process	Approach	Number of results	$\chi_{FEM} / \chi_{proposal}$				χ_{FEM} / χ_{EC3}			
					Average	Min	Max	St.Dev	Average	Min	Max	St.Dev
Simple	N	Hot-rolled	-	1506	1.03	0.97	1.41	0.07	0.97	0.85	1.41	0.09
	M _y	Hot-rolled	-	1506	1.09	0.95	1.44	0.13	1.11	0.92	1.44	0.16
	M _z	Hot-rolled	-	300	1.01	0.95	1.34	0.04	1.03	0.91	1.34	0.05
Combined	n0	Hot-rolled	-	900	1.02	0.79	1.43	0.10	1.21	0.92	1.53	0.12
	n20	Hot-rolled	-	5076	1.10	0.83	1.35	0.06	1.11	0.70	1.59	0.16
	n40	Hot-rolled	-	1500	1.08	0.93	1.32	0.05	1.09	0.79	1.47	0.12
	n60	Hot-rolled	-	5076	1.06	0.92	1.49	0.05	1.05	0.82	1.45	0.09
	n80	Hot-rolled	-	1500	1.06	0.93	1.29	0.04	1.00	0.87	1.29	0.05
Simple	N	Cold-formed	First	1482	1.05	0.96	1.28	0.04	0.95	0.75	1.17	0.11
	M _y	Cold-formed	First	1482	1.04	0.99	1.12	0.02	1.08	0.82	1.43	0.10
	M _z	Cold-formed	First	300	1.07	0.96	1.26	0.06	1.00	0.83	1.13	0.06
Combined	n0	Cold-formed	First	900	1.09	0.94	1.61	0.12	1.20	0.90	1.61	0.12
	n20	Cold-formed	First	5850	1.03	0.89	1.34	0.05	1.06	0.71	1.72	0.16
	n40	Cold-formed	First	1500	1.04	0.89	1.29	0.06	1.05	0.75	1.50	0.13
	n60	Cold-formed	First	5850	1.04	0.91	1.25	0.05	1.00	0.78	1.29	0.09
	n80	Cold-formed	First	1500	1.04	0.94	1.24	0.05	0.94	0.80	1.13	0.06
Simple	N	Cold-formed	Second	1482	1.04	0.95	1.23	0.03	0.95	0.75	1.17	0.11
	M _y	Cold-formed	Second	1482	1.05	0.99	1.13	0.02	1.08	0.82	1.43	0.10
	M _z	Cold-formed	Second	300	1.05	0.96	1.16	0.04	1.00	0.83	1.13	0.06
Combined	n0	Cold-formed	Second	900	1.09	0.93	1.59	0.12	1.20	0.90	1.61	0.12
	n20	Cold-formed	Second	5850	1.06	0.93	1.30	0.04	1.06	0.71	1.71	0.16
	n40	Cold-formed	Second	1500	1.06	0.91	1.25	0.05	1.05	0.75	1.50	0.13
	n60	Cold-formed	Second	5850	1.05	0.92	1.22	0.03	1.03	0.78	1.36	0.09
	n80	Cold-formed	Second	1500	1.04	0.95	1.20	0.04	0.94	0.80	1.13	0.06

Figure 230 to Figure 232 show comparisons between FEM, EC3 and ‘proposal’ results for hot-rolled and cold-formed¹⁸ cross-sections subjected to compression. On the left column, plots illustrating comparisons between $\chi_{FEM} / \chi_{proposal}$ and χ_{FEM} / χ_{EC3} ratios are presented, while the right column shows these same results in the form of histograms in an attempt to better illustrate and translate the observations of the left column plots. The following remarks and analysis can be stated based on these figures:

- (i) Green circles in Figure 230 to Figure 232 mark the passage between class 3 and class 4 cross-sections i.e. between plastic capacities and effective ones. It can be clearly seen that unlike EC3, no discontinuity is noticed with the new design curves and a smooth conservative continuity is provided;
- (ii) It can be seen that Eurocode 3 predictions are even more unconservative in the case of cold-formed sections than hot-rolled sections. Hence, FE results relative to slender cold-formed cross-sections showed smaller cross-section capacities than hot-rolled sections since the adopted Ramberg-Osgood material law which is based on an exploitation of strain hardening, lies below the hot-rolled elastic plastic material law for a certain range of strains. Therefore, the EC3 calculations being developed on the basis of bilinear (elastic, perfectly-plastic) material behavior would show more unsafe results for slender cold-formed sections because of the position of the Ramberg-Osgood material law with respect to the hot-rolled material law (yellow area in Figure 229);

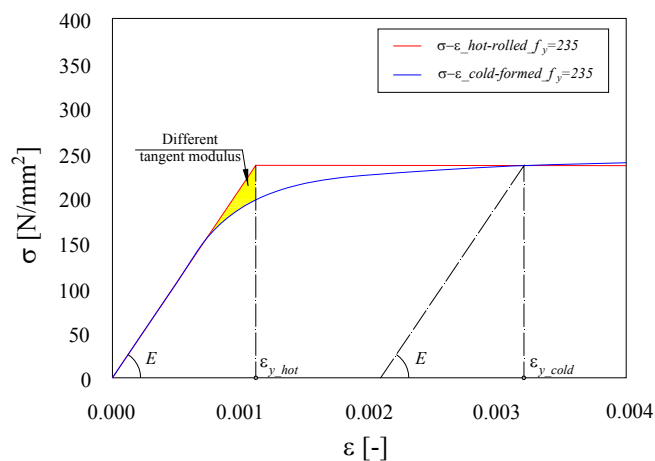


Figure 229 – Differences between hot-formed and cold-formed material laws.

¹⁸ Both proposed approaches relative to cold-formed cross-sections are presented.

- (iii) In the case of hot-rolled cross-sections, the strain-hardening was not accounted for in the proposed design curve, since it would occur for large unrealistic deformations. Therefore, both results, computed with EC3 specifications and the new design proposal, would lead to similar overlapped results illustrated at the small slenderness range (right plot of Figure 230). This would explain why overconservative results appear in the right histogram plot (see blue circles);
- (iv) For large slenderness ranges (i.e. $\lambda_{CS} > 2.0$) results computed with the proposed design curves are showing conservative tendencies. These results correspond to invented cross-sections and constitute a small proportion of the total number of conducted results;
- (v) With cold-formed cross-sections, and with EC3 calculations, histograms plots are illustrating somewhat equivalent conservative and unconservative results (see black and red circles), while the majority of the results seem unconservative on the left plot. This is due to stacked and piled results at small slenderness range and does not change the fact that for a very wide slenderness range, EC3 computations are showing unconservative results and the classification system is seen to be unsuitable for such types of cross-sections;
- (vi) For this particular load case, the second proposed approach for cold-formed sections is seen to present better results since a bigger number of $\chi_{FEM} / \chi_{proposal}$ ratios are close to 1.0.

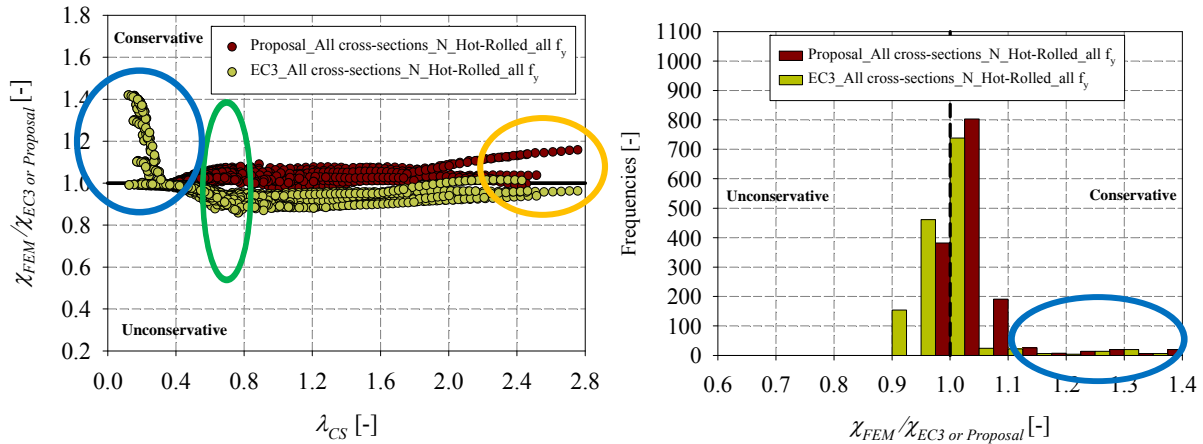


Figure 230 – All cross-sections, Hot-rolled, Pure compression a) Comparison of Proposal and EC3 results with FEM results b) Frequency distributions (total number of results: 1506).

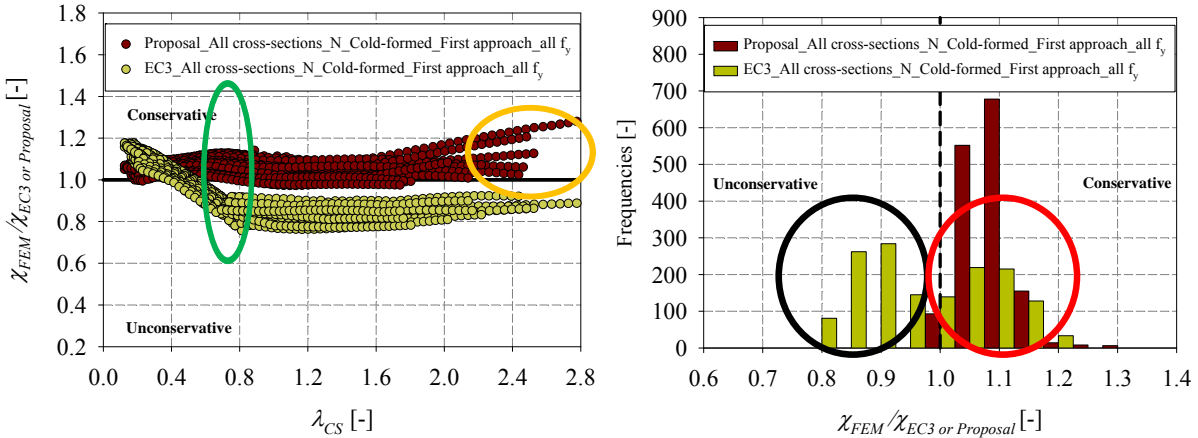


Figure 231 – All cross-sections, Cold-formed, First approach, Pure compression a) Comparison of Proposal and EC3 results with FEM results b) Frequency distributions (total number of results: 1482).

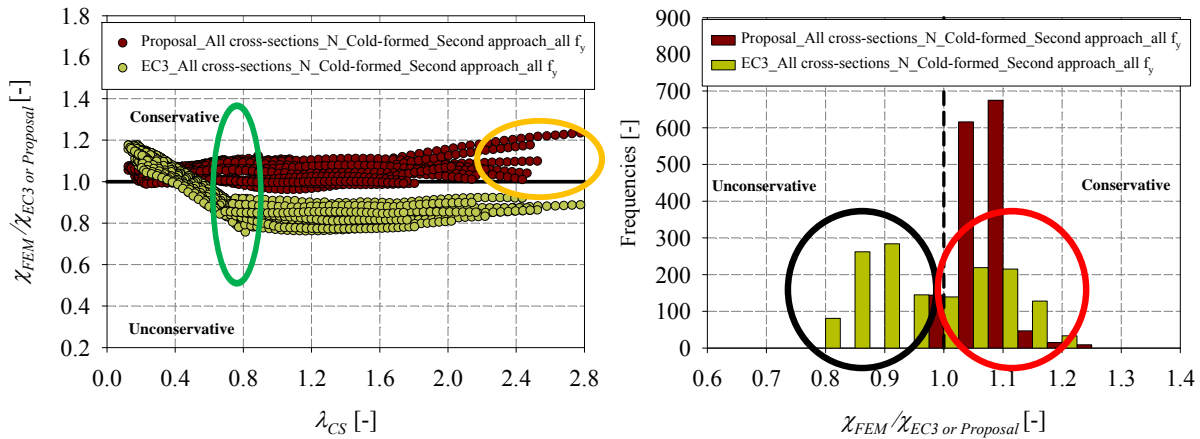


Figure 232 – All cross-sections, Cold-formed, Second approach, Pure compression a) Comparison of Proposal and EC3 results with FEM results b) Frequency distributions (total number of results: 1482).

Figure 234 to Figure 236 show comparisons between FEM, EC3 and ‘proposal’ results for all hot-rolled and cold-formed cross-sections subjected to major-axis bending with the three considered steel grades in this work. The following remarks and analysis can be made based on these figures:

- (i) The green circles in Figure 234 to Figure 236 highlight the sudden discontinuity due to the loss of resistance at the border between class 2 cross-sections and class 3 cross-sections. This discontinuity is leading to overconservative EC3 predictions due to the brutal passage from plastic to elastic capacities, while OIC predictions are showing continuous acceptable conservative results. In Figure 233, only square cross-sections subjected to major-axis bending were selected to show, in a clearer way, the discontinuous behavior of cross-sections assigned to plastic elastic or effective classes according to EC3 specifications;

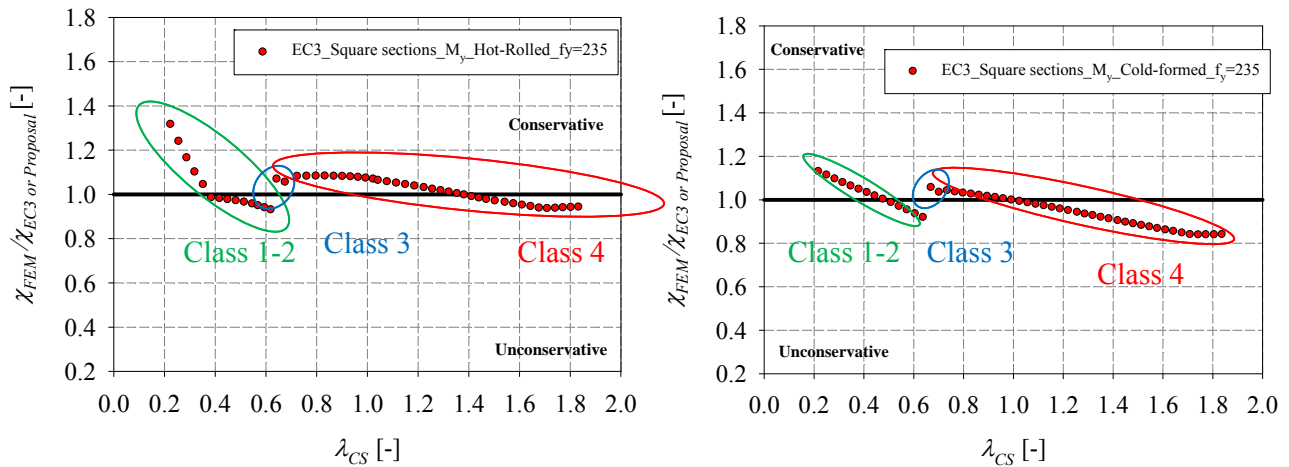


Figure 233 – Comparison of EC3 results with FEM results for square cross-sections subjected to major-axis bending
a) hot-rolled cross-sections, b) cold-formed cross-sections.

- (ii) Similarly to hot-rolled cross-sections in compression, strain hardening was not accounted for in the proposed design model. Therefore, for small slenderness ranges, EC3 and ‘proposal’ results give overconservative similar tendencies. This is further illustrated in the histogram of Figure 234 with a red circle;

- (iii) In the case of cold-formed sections, the results computed according to the proposed design curves (with the two approaches) are showing much better distributions, both in terms of mean and standard deviation;
- (iv) In contrast with the compression case, the first proposed approach for the design of cold-formed sections is showing slightly better results, since a bigger number of computed results is closer to a ratio $\chi_{FEM} / \chi_{proposal}$ equal to 1.0.

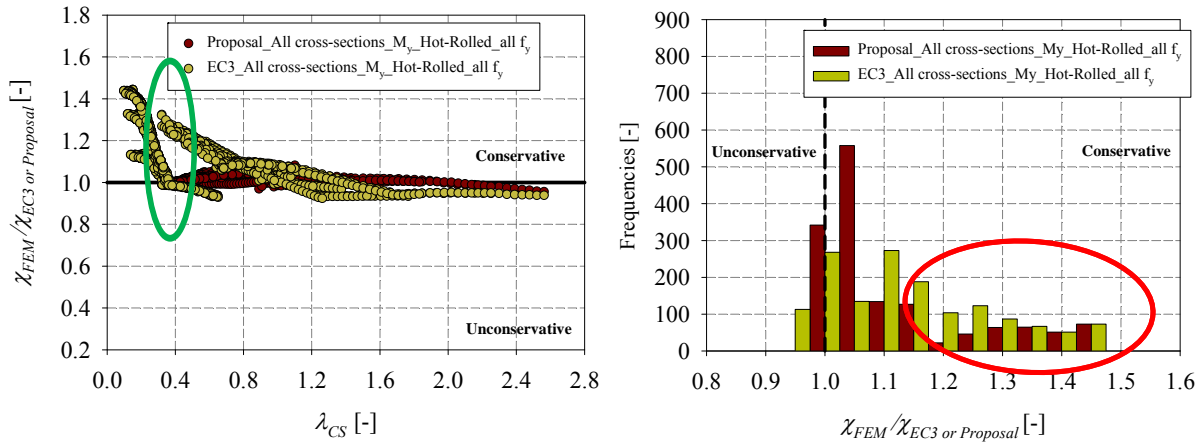


Figure 234 – All cross-sections, Hot-rolled, Major-axis bending a) Comparison of Proposal and EC3 results with FEM results b) Frequency distributions (total number of results: 1506).

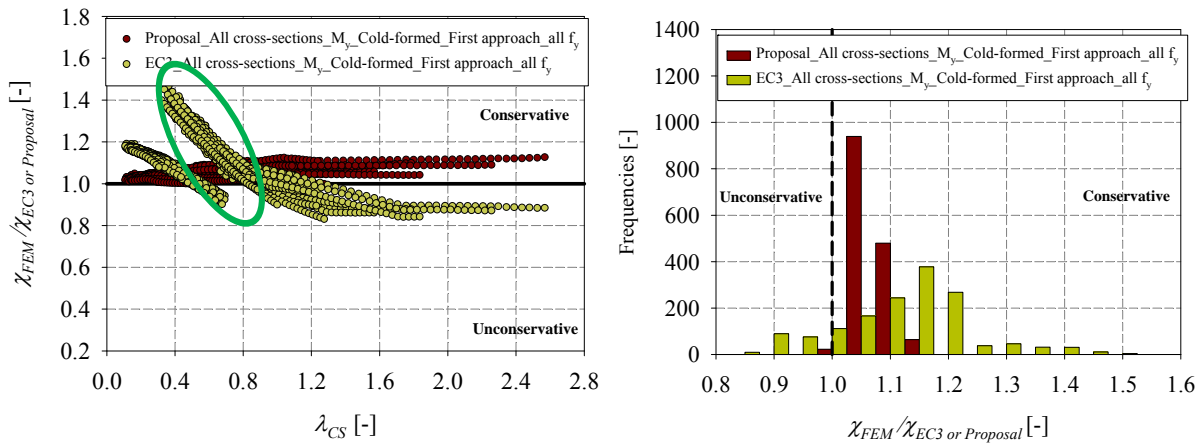


Figure 235 – All cross-sections, Cold-formed, First approach, Major-axis bending a) Comparison of Proposal and EC3 results with FEM results b) Frequency distributions (total number of results: 1482).

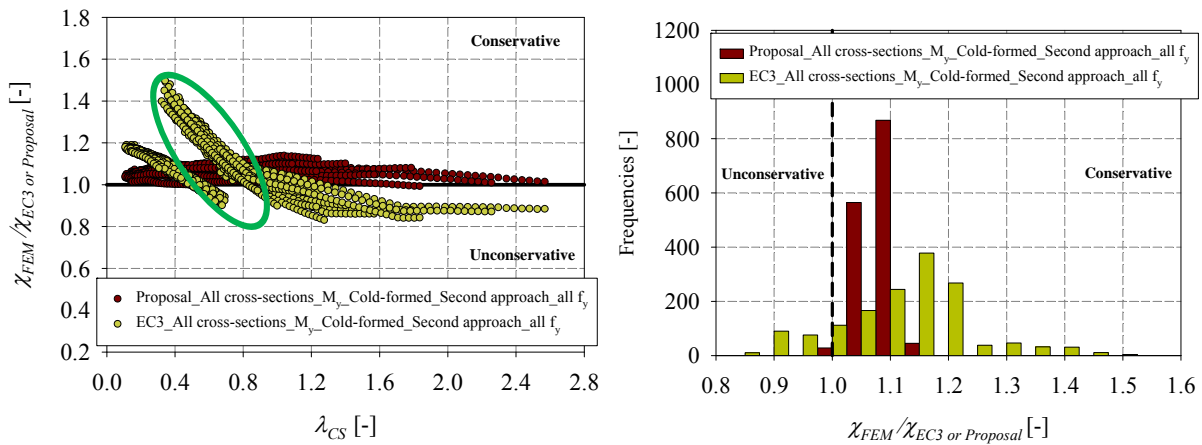


Figure 236 – All cross-sections, Cold-formed, Second approach, Major-axis bending a) Comparison of Proposal and EC3 results with FEM results b) Frequency distributions (total number of results: 1482).

Figure 238 to Figure 240 show comparisons between FEM, EC3 and ‘proposal’ results for hot-rolled and cold-formed cross-sections subjected to combined load cases with 20% of N_{pl} , while Figure 241 to Figure 243 present results relative to combined load cases with 60% of N_{pl} . These two cases were selected since results with $n = 0.2$ are supposed to represent the least satisfactory proposed outcome and results with $n = 0.6$ would represent one of the best proposed outcome. Moreover, EC3 predictions were dissociated from ‘proposal’ results, for the sake of clarity and better observations. The following remarks and analysis can be made stated on these figures:

- (i) Similarly to major-axis bending, EC3 results show significant discontinuities due to the different discrete behavioral classes based on plastic, elastic or effective capacities (see Figure 237). Only square cross-sections subjected to combined loading with 60% of N_{pl} were selected and represented in Figure 237 for a clearer visualization of the different behaviors of EC3 classes. OIC predictions are showing way better continuous results with smaller standard deviations compared to EC3 predictions.

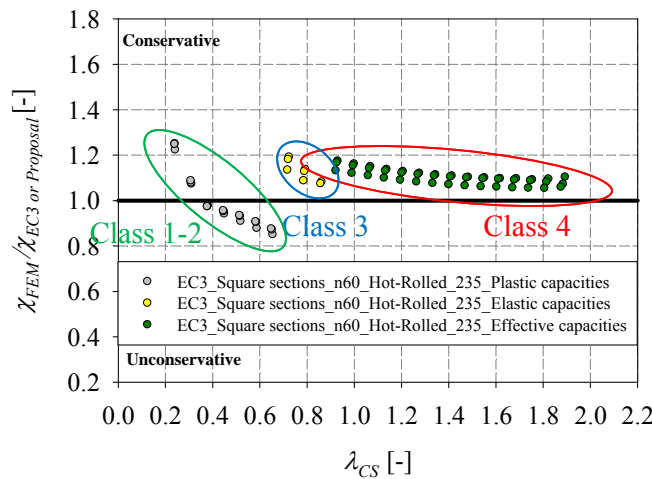


Figure 237 – Comparison of EC3 results with FEM results for square cross-sections subjected to combined loadings with level of axial load equal to 20% of N_{pl} .

- (ii) In hot-rolled cases (i.e. Figure 238 and Figure 241), both ratios relative to EC3 and ‘proposal’ results would lead to similar tendencies for compact sections, since no strain hardening was accounted for in the proposed design curves.

- (iii) For the case of combined loading with $n = 0.2$, two tendencies are observed with EC3 calculations (marked with red and black arrows). Red arrows are pointing to combined load cases with compression, major-axis bending and minor-axis bending, while black arrows are pointing towards compression with major or minor-axis bending.
- (iv) It is clearly seen that conservative tendencies are reached for the case of combined loading with $n = 0.2$ (see green circles). This would be expected since the proposed design curve relative to $n = 0.2$ (associated with the ‘turning point’) is the lowest proposed design curve with the most conservative results. However, even though this conservatism is supposed to be the worst case scenario, it is still acceptable since it is occurring for large slenderness corresponding to invented cross-sections which do not represent the majority of treated cross-sections. This is further illustrated in the histograms in which very acceptable distributions of ‘proposal’ results are seen with tolerable number of conservative results. For the case of combined loading with $n = 0.6$, this would be less obvious. Improved distributions, mean and standard deviation are seen with the proposal results compared to actual EC3 computations.

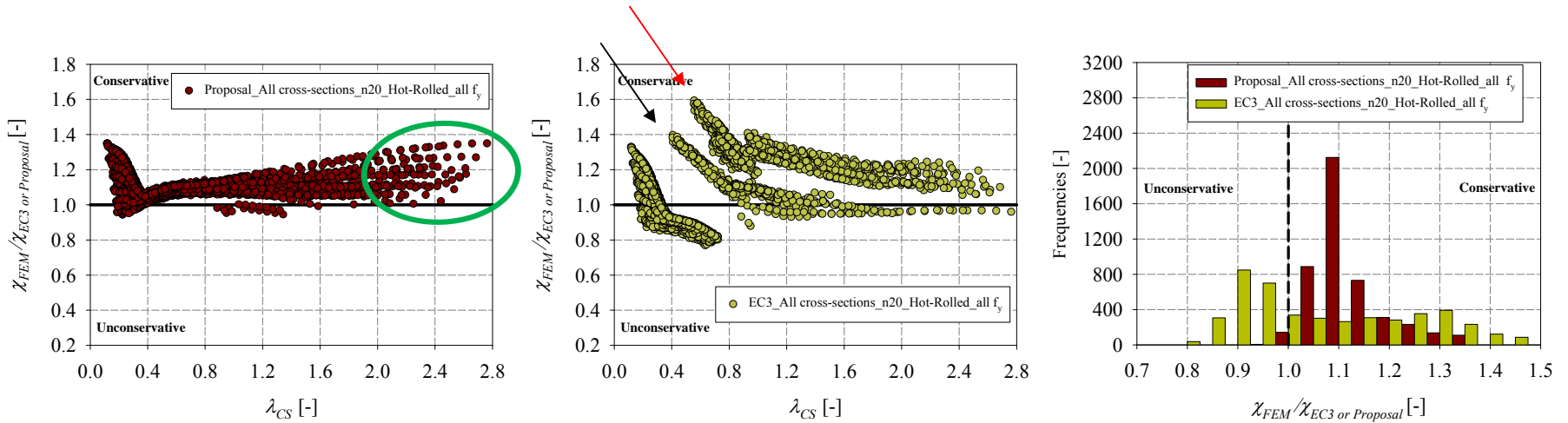


Figure 238 – All cross-sections, Hot-rolled, Combined loading with level of axial load equal to 20% of N_{pl} a) Comparison of Proposal and EC3 results with FEM results b) Frequency distributions (total number of results: 5076).

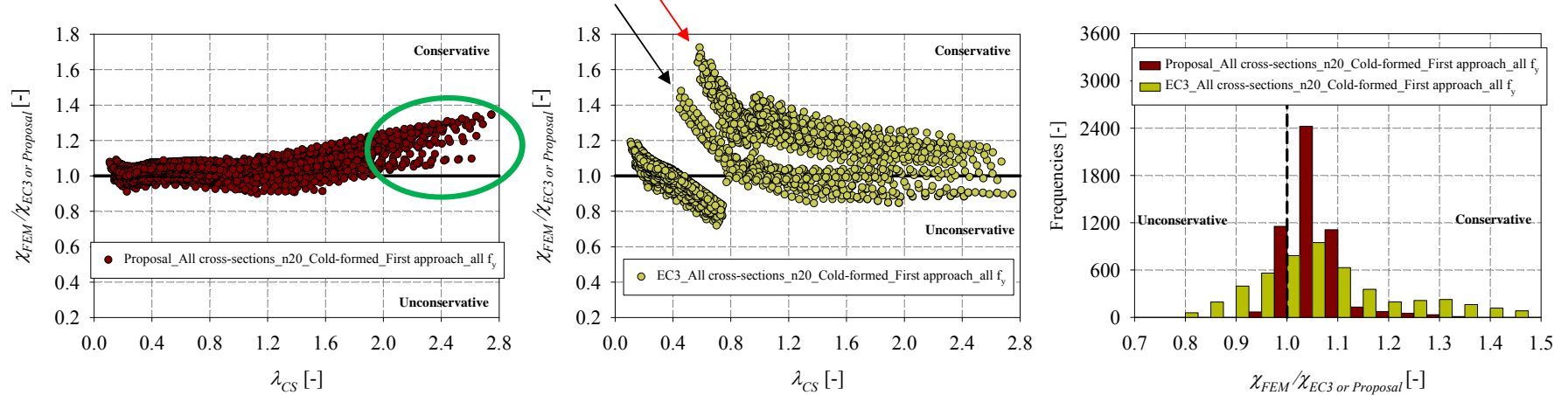


Figure 239 – All cross-sections, Cold-formed, First approach, Combined loading with level of axial load equal to 20% of N_{pl} a) Comparison of Proposal and EC3 results with FEM results b) Frequency distributions (total number of results: 5850).

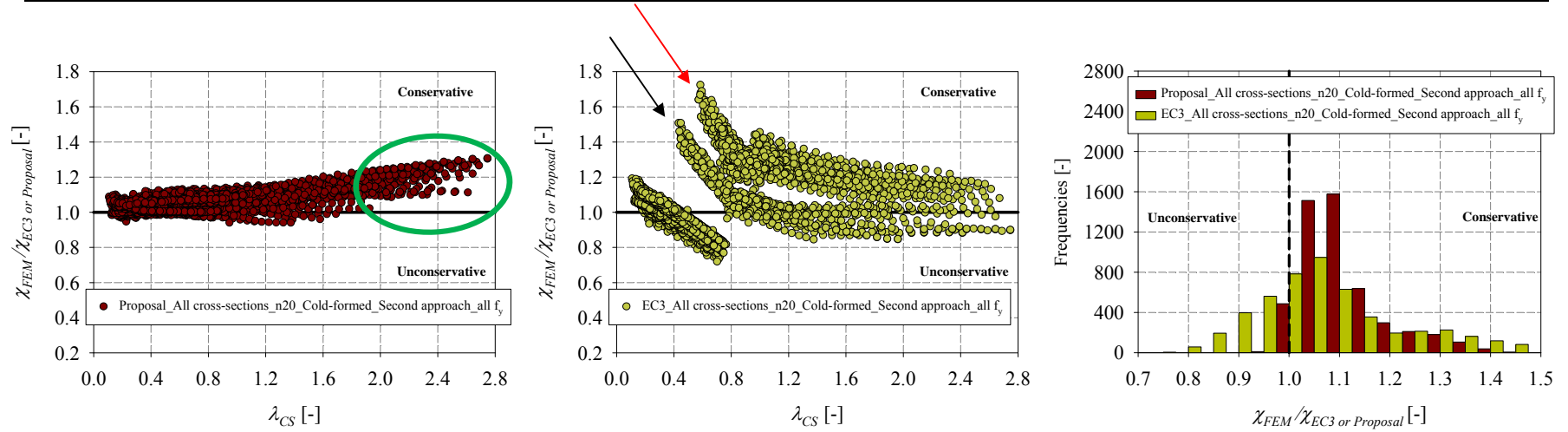


Figure 240 – All cross-sections, Cold-formed, First approach, Combined loading with level of axial load equal to 20% of N_{pl} a) Comparison of Proposal and EC3 results with FEM results b) Frequency distributions (total number of results: 5850).

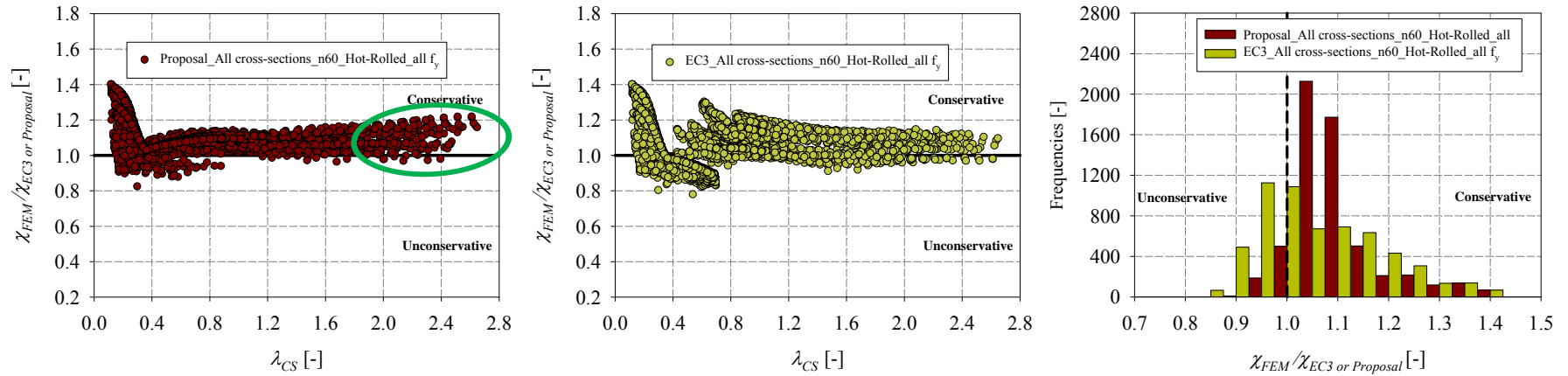


Figure 241 – All cross-sections, Hot-rolled, Combined loading with level of axial load equal to 60% of N_{pl} a) Comparison of Proposal and EC3 results with FEM results b) Frequency distributions (total number of results: 5076).

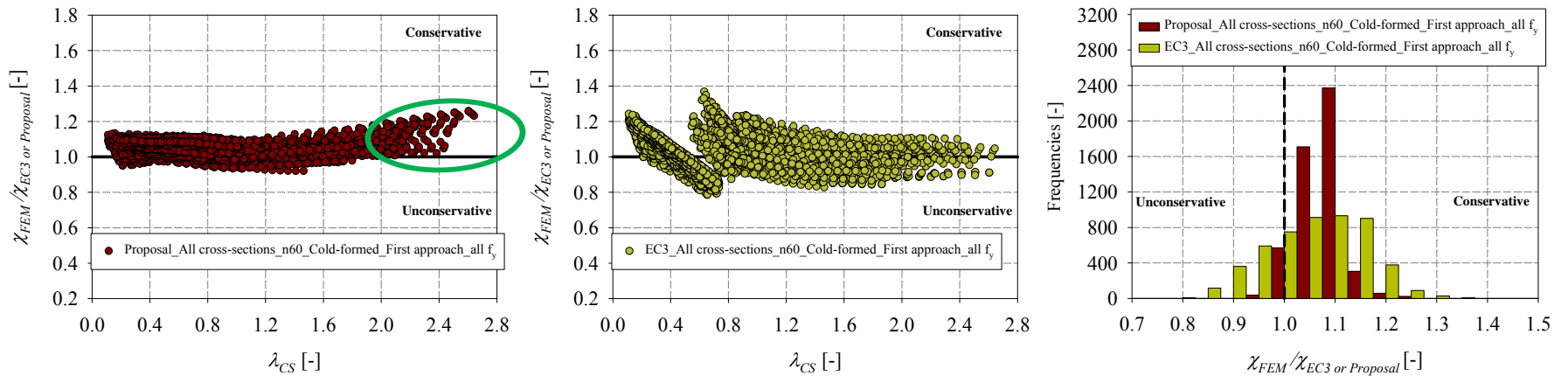


Figure 242 – All cross-sections, Cold-formed, First approach, Combined loading with level of axial load equal to 60% of N_{pl} a) Comparison of Proposal and EC3 results with FEM results b) Frequency distributions (total number of results: 5850).

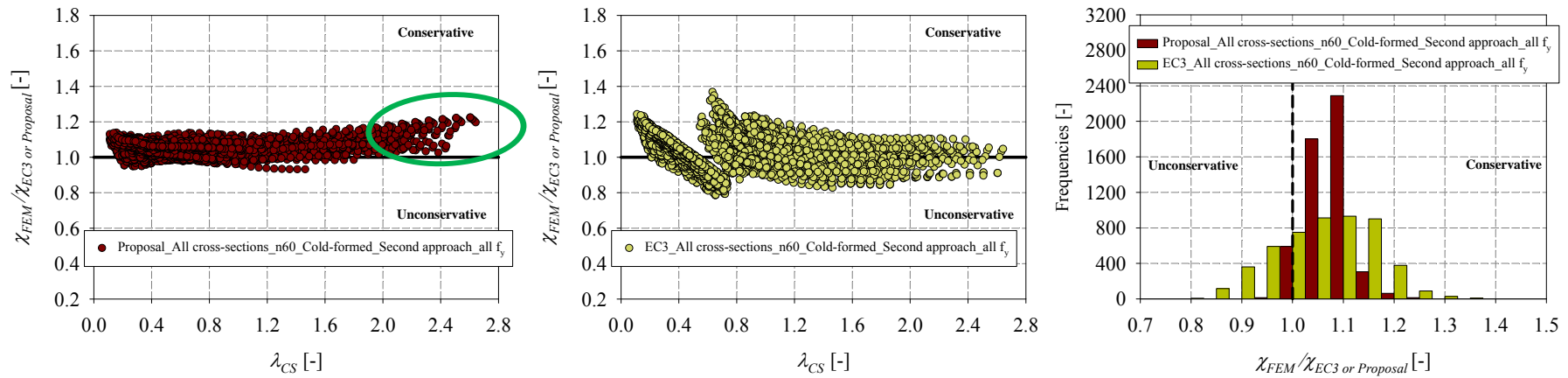


Figure 243 – All cross-sections, Cold-formed, Second approach, Combined loading with level of axial load equal to 60% of N_{pl} a) Comparison of Proposal and EC3 results with FEM results
b) Frequency distributions (total number of results: 5850).

In Figure 244 to Figure 255, only the European (catalogue) cross-sections are considered. The derived sections were excluded in order to better see the improvements brought by the new proposal with only existing manufactured cross-sections. This would particularly concern the combined load cases with $n = 0.2$, where conservatism was observed for large slenderness (>2.0). This conservatism would disappear if only European cross-sections are considered because the maximum slenderness reached with these sections is no more than $\lambda_{CS} = 1.4$. This is clearly shown in Figure 250 and Figure 254 against Figure 239 and Figure 240 for cold-formed sections. In the case of hot-rolled cross-sections, conservatism would still be observed for small slenderness since strain hardening was not accounted for.

The comparisons between histograms clearly demonstrate the improved accuracy features of the proposed new rules especially in terms of the standard deviation. The proposed simple design rules are then seen to be much more accurate than the actual ones. The accuracy of the proposed interaction curves is further illustrated through Figure 256 and Figure 257, in which results relative to selected cross-sections, are presented in $m_y - m_z$ graphs. The difference between FEM and the proposal results are seen to be very acceptable.

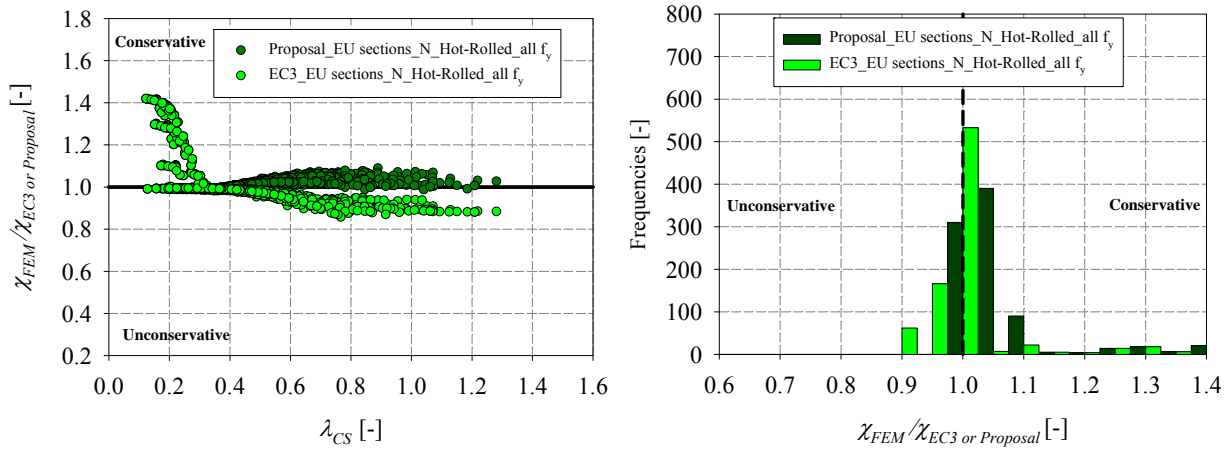


Figure 244 – European sections, Hot-rolled, Pure compression a) Comparison of Proposal and EC3 results with FEM results b) Frequency distributions (total number of results: 870).

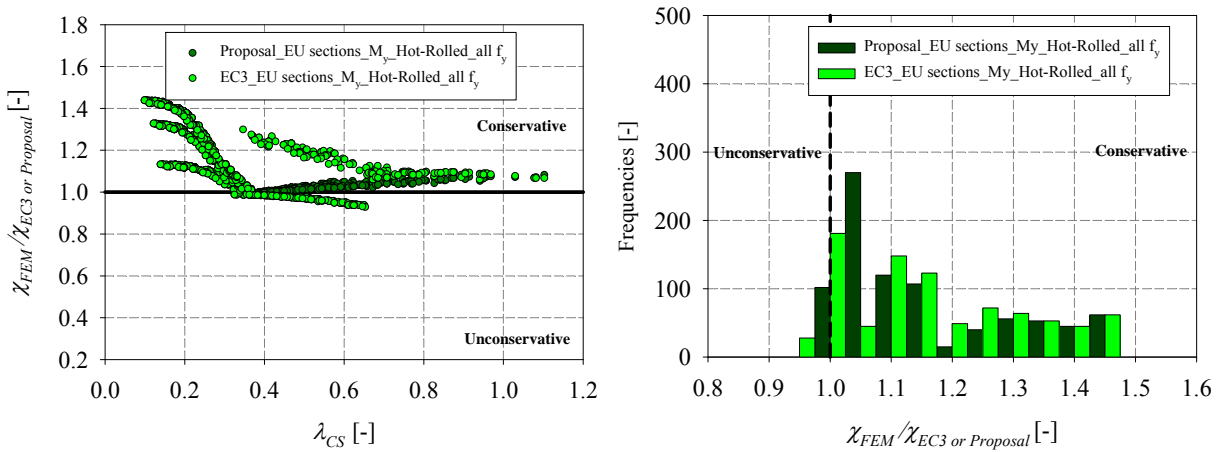


Figure 245 – European sections, Hot-rolled, Major-axis bending a) Comparison of Proposal and EC3 results with FEM results b) Frequency distributions (total number of results: 870).

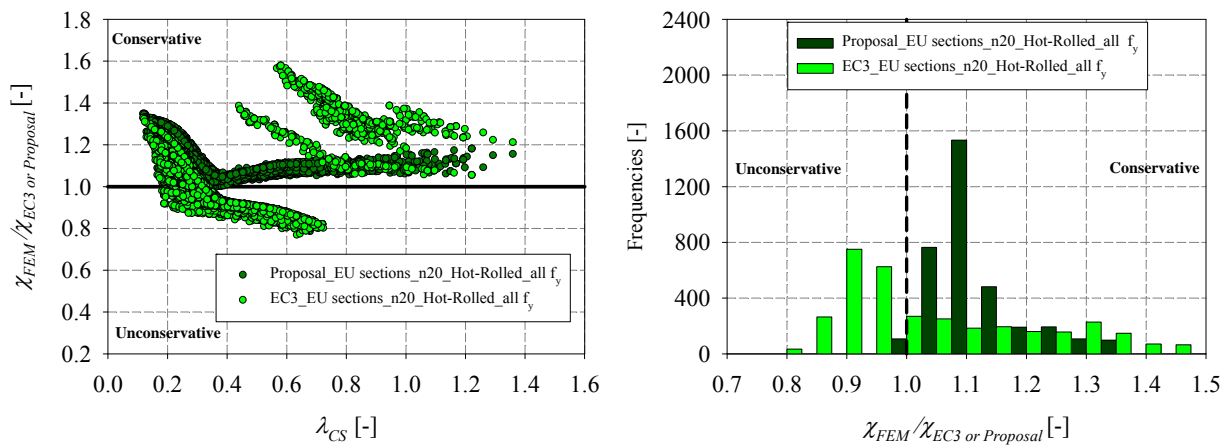


Figure 246 – European sections, Hot-rolled, Combined loading with level of axial load equal to 20% of N_{pl} a) Comparison of Proposal and EC3 results with FEM results b) Frequency distributions (total number of results: 4350).

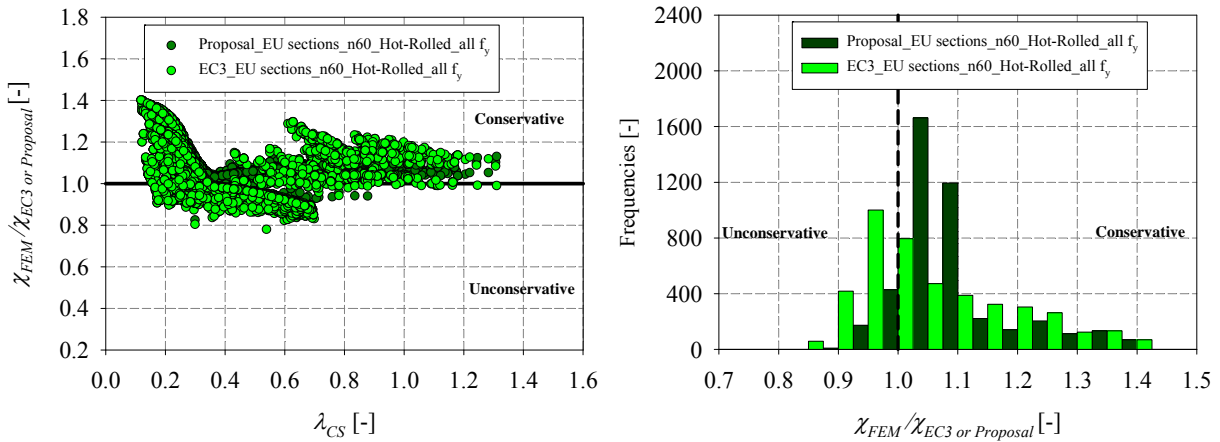


Figure 247 – European sections, Hot-rolled, Combined loading with level of axial load equal to 60% of N_{pl} a) Comparison of Proposal and EC3 results with FEM results b) Frequency distributions (total number of results: 4350).

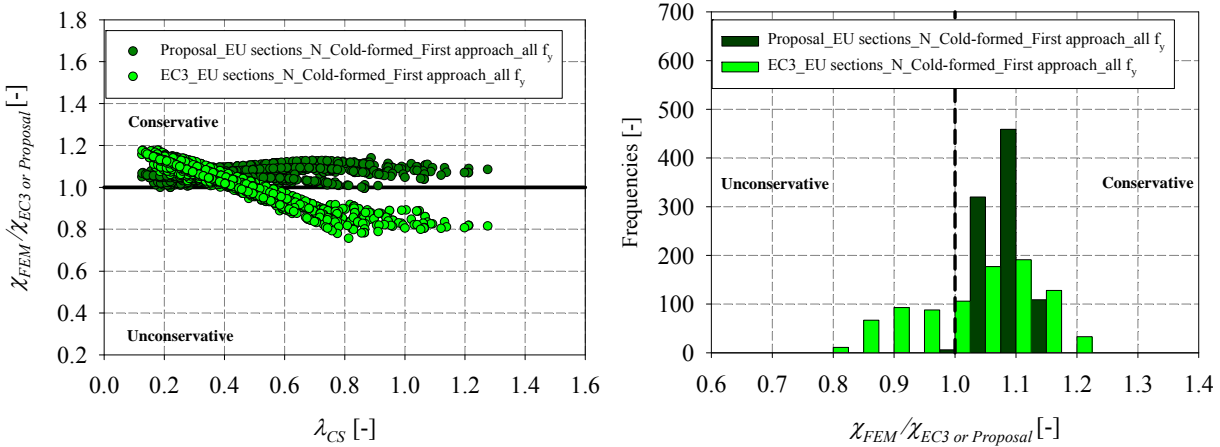


Figure 248 – European sections, Cold-formed, First approach, Pure compression a) Comparison of Proposal and EC3 results with FEM results b) Frequency distributions (total number of results: 894).

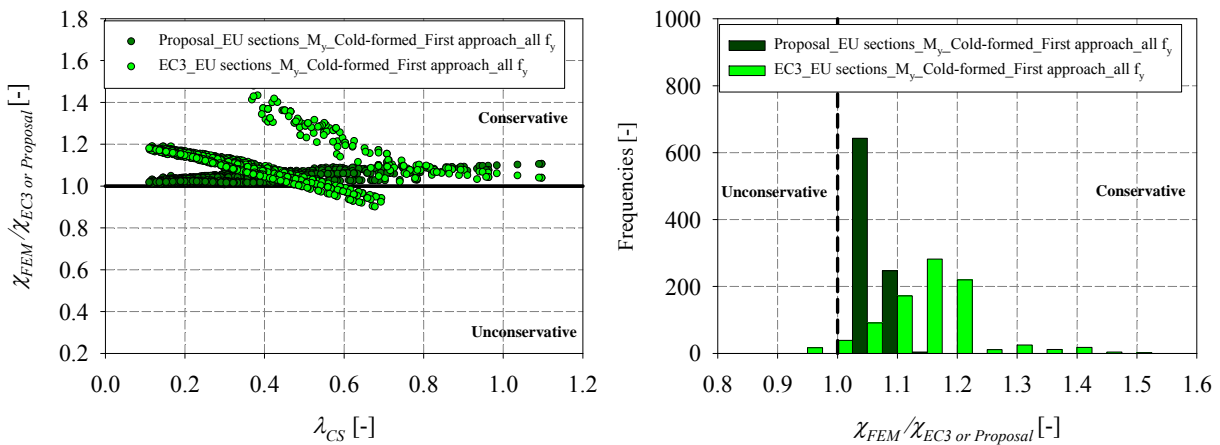


Figure 249 – European sections, Cold-formed, First approach, Major-axis bending a) Comparison of Proposal and EC3 results with FEM results b) Frequency distributions (total number of results: 894).

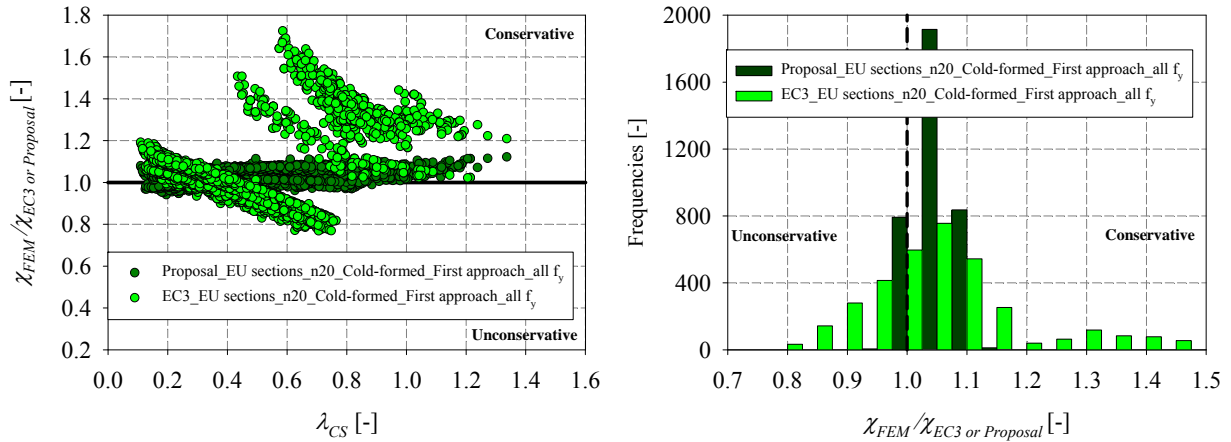


Figure 250 – European sections, Cold-formed, First approach, Combined loading with level of axial load equal to 20% of N_{p1} a) Comparison of Proposal and EC3 results with FEM results b) Frequency distributions (total number of results: 3576).

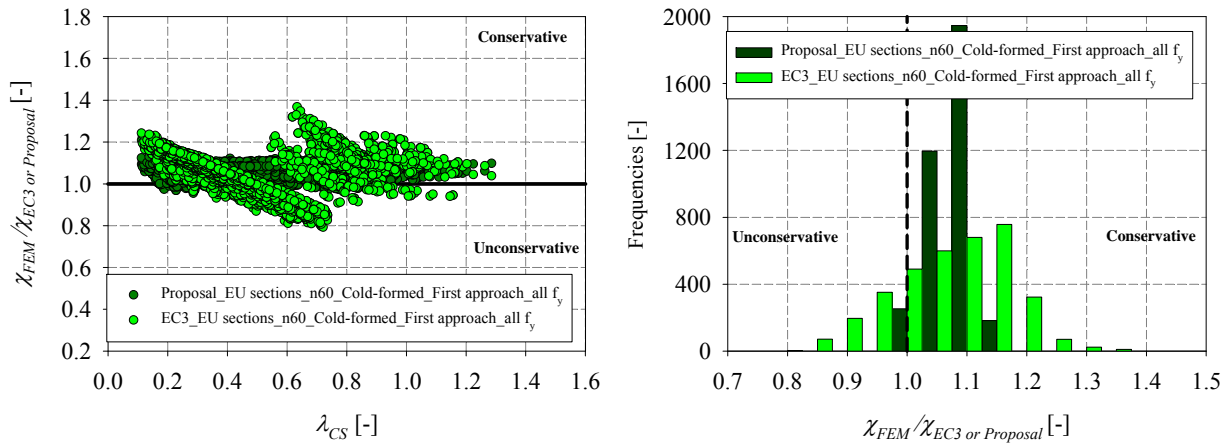


Figure 251 – European sections, Cold-formed, First approach, Combined loading with level of axial load equal to 60% of N_{p1} a) Comparison of Proposal and EC3 results with FEM results b) Frequency distributions (total number of results: 3576).

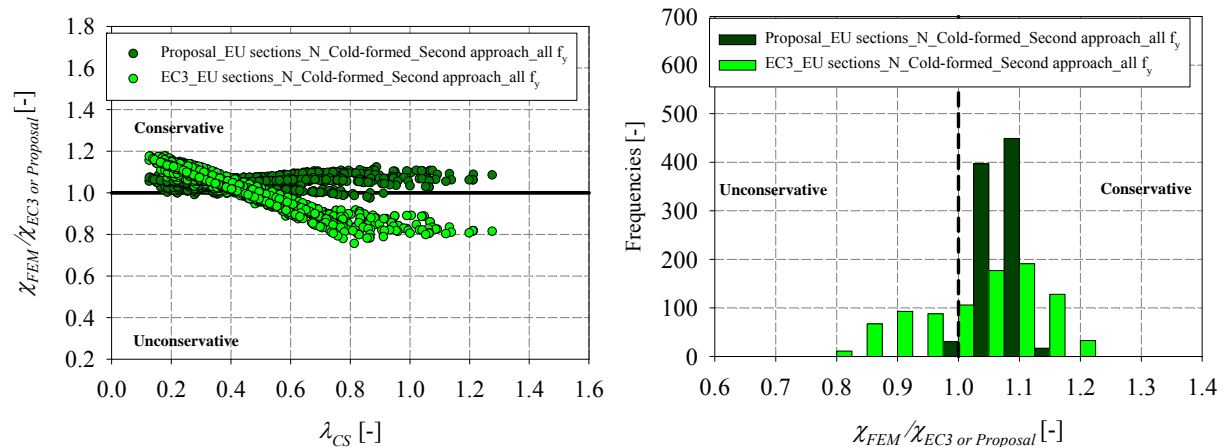


Figure 252 – European sections, Cold-formed, Second approach, Pure compression a) Comparison of Proposal and EC3 results with FEM results b) Frequency distributions (total number of results: 894).

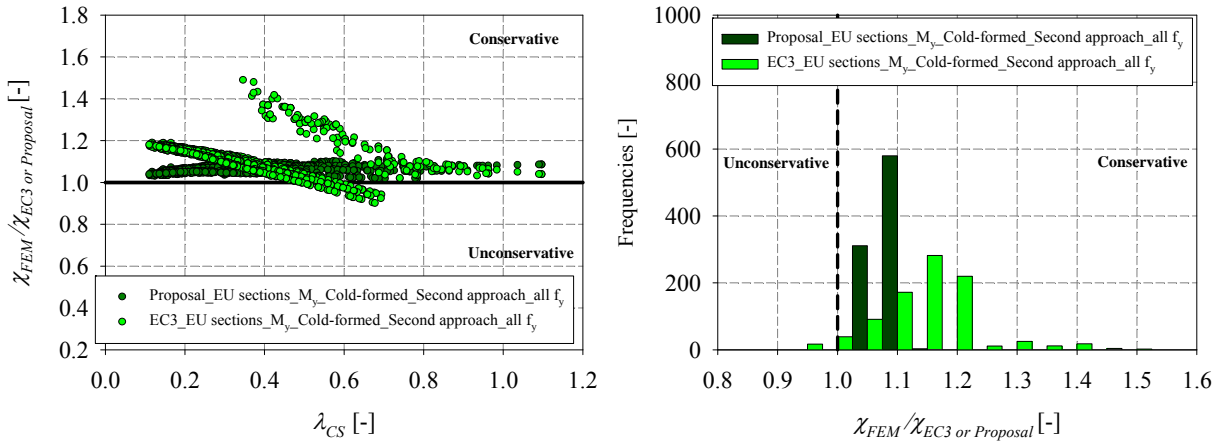


Figure 253 – European sections, Cold-formed, Second approach, Major-axis bending a) Comparison of Proposal and EC3 results with FEM results b) Frequency distributions (total number of results: 894).

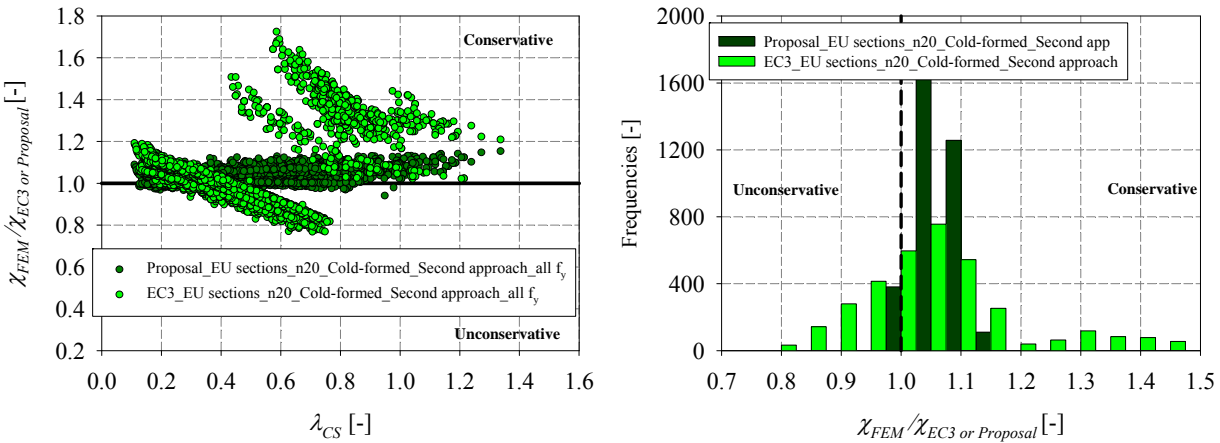


Figure 254 – European sections, Cold-formed, Second approach, Combined loading with level of axial load equal to 20% of N_{pl} a) Comparison of Proposal and EC3 results with FEM results b) Frequency distributions (total number of results: 3576)

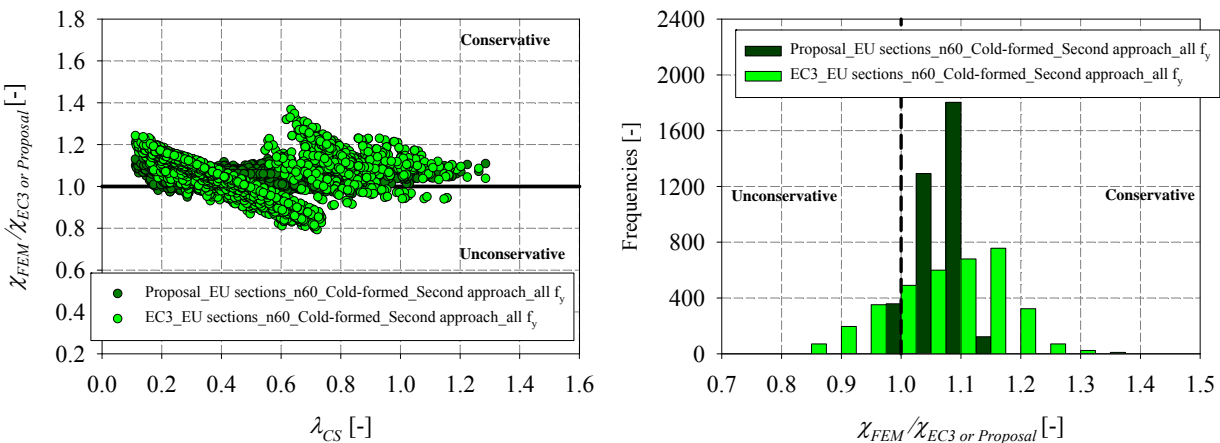


Figure 255 – European sections, Cold-formed, Second approach, Combined loading with level of axial load equal to 60% of N_{pl} a) Comparison of Proposal and EC3 results with FEM results b) Frequency distributions (total number of results: 3576).

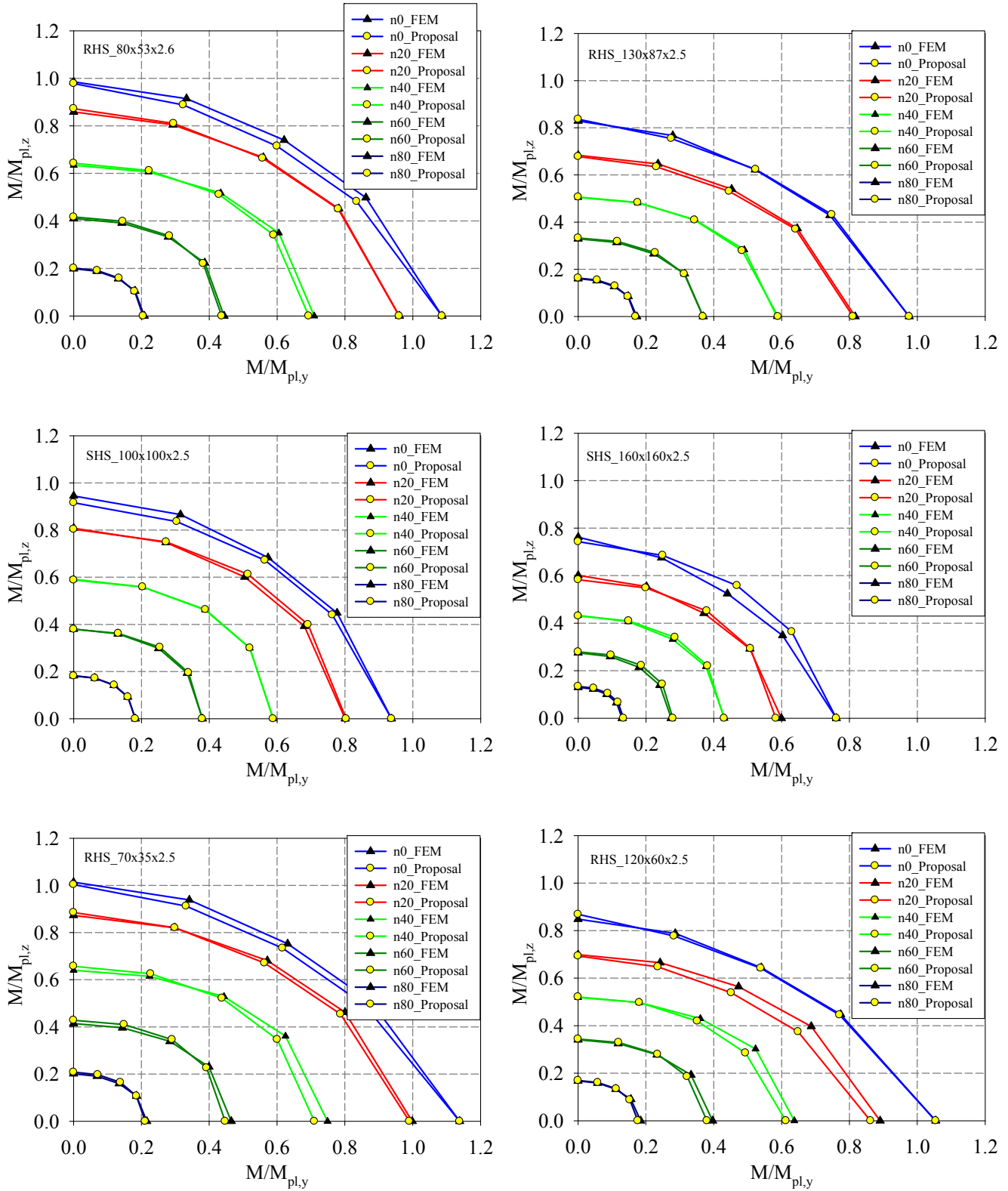


Figure 256 – FEM and proposal results relative to cold-formed sections subjected to combined loading (Second approach, S235).

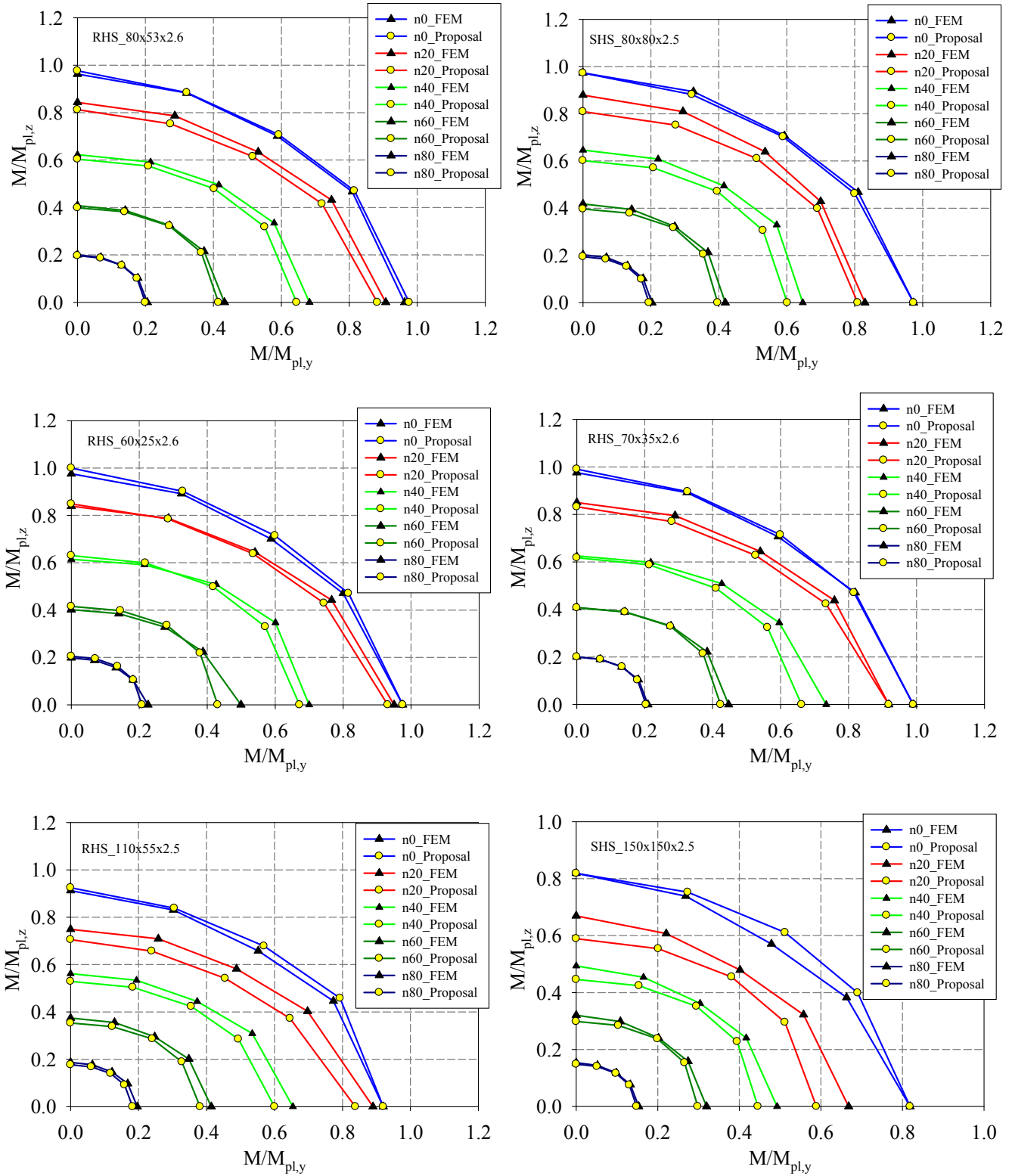


Figure 257 – FEM and proposal results relative to hot-rolled sections subjected to combined loading (S235).

7. Summary and recommendations

The proposed OIC interaction design curves for the cross-sectional behavior of plated tubular sections are summarized and presented in Table 50 and Table 51. The followings steps and remarks will be recommended for the design of steel hollow sections:

(i) The key information that the engineer must provide given a certain loading on a cross-section, are as follows:

(i1) The elastic buckling load multiplier R_{STAB} ;

(i2) The plastic load multiplier R_{RESIST} ;

(i3) Calculation of the cross-section slenderness $\lambda_{CS} = \sqrt{\frac{R_{RESIST}}{R_{STAB}}}$;

(i4) Choice of adequate parameters and curve corresponding to his case (fabrication process, cross-section dimensions, load type...) based on Table 50 and Table 51. For example, if the engineer has a combined loading including axial forces, the level of these axial forces must be determined to choose the adequate curve to use. If no axial forces are present, i.e. with a biaxial bending load case, the engineer should use the adequate curve relative to $n = 0$.

(i5) Calculation of the cross-section penalty χ_{CS} ;

(i6) Get $R_{ULT} = \chi_{CS} \cdot R_{RESIST}$.

(ii) For the case of cold-formed sections, the second approach is recommended in design, since it is grounded on a strain-based format at low slenderness and is therefore scientifically more acceptable and correct.

Figure 258 illustrates the previous mentioned steps in a clearer way. The green arrows include the steps relative to the 2nd approach for cold-formed sections and are therefore recommended.

Worked examples are presented in the following chapter to better illustrate the application of the method and its benefits in comparison to application of current EC3 rules.

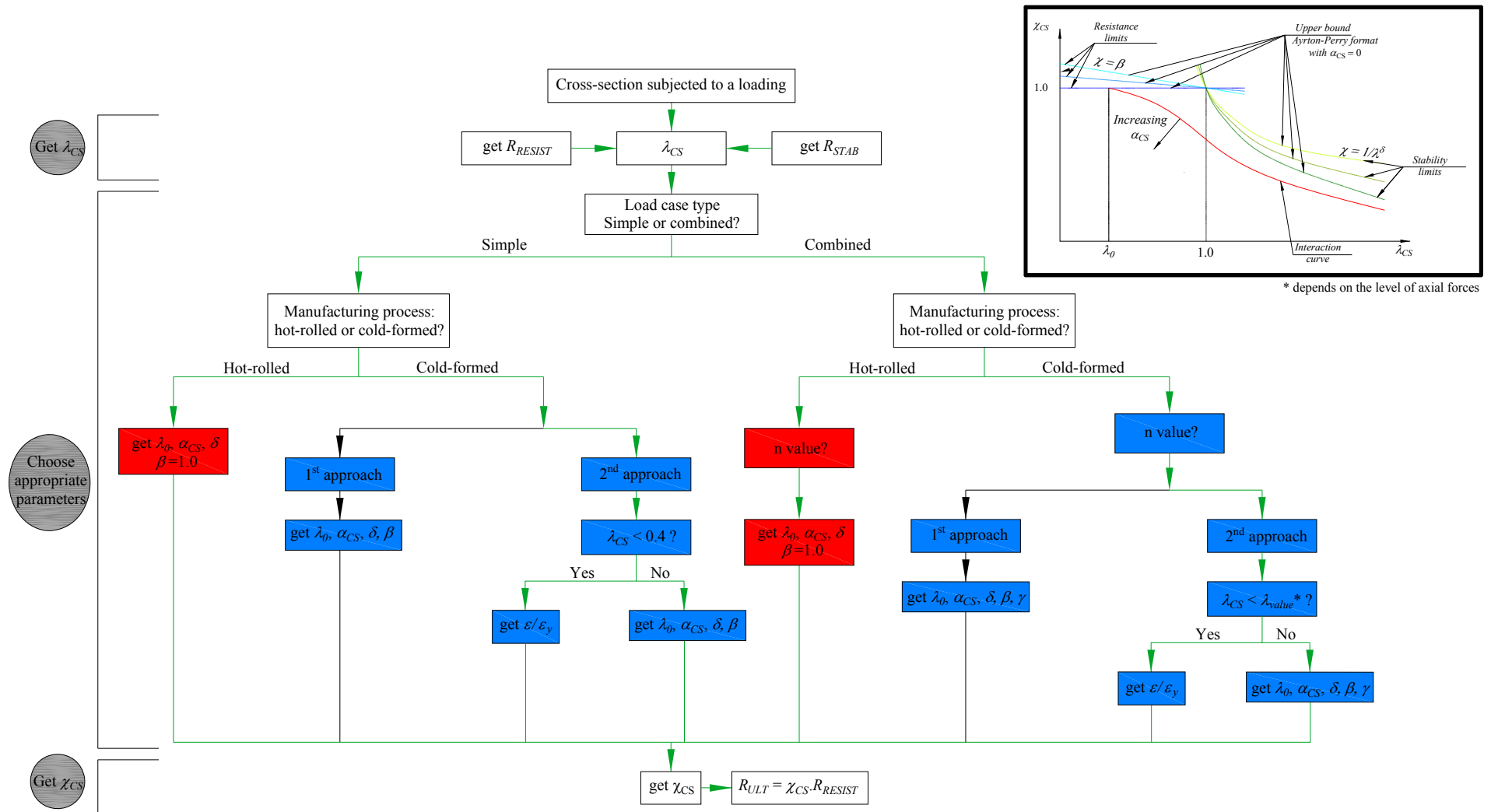


Figure 258 – Application steps of the proposed OIC design curves.

Table 50 – Proposed OIC design curves for simple load cases.

Simple load cases			
General format			
$\lambda_{CS} = \sqrt{\frac{R_{RESIST}}{R_{STAB,CS}}}$			
$\phi = 0.5(1 + \alpha_{CS}(\lambda_{CS} - \lambda_0) + \lambda_{CS}^\delta \beta)$			
$\chi_{CS} = \frac{\beta}{\phi + \sqrt{\phi^2 - \lambda_{CS}^\delta \beta}}$			
Hot-rolled hollow sections			
$\lambda_0 = 0.35$ and $\chi_{CS} \leq 1.0$ i.e. $\beta = 1.0$			
Parameters	α_{CS}	δ	
Compression	0.15	$-0.4 h/b + 1.45$	
Major-axis bending	$0.1 \delta + 3/200$	$0.4 h/b + 0.25$	
Minor-axis bending	0.08	0.65	
Cold-formed hollow sections – 1st approach			
$\lambda_0 = 0$			
Parameters	δ	α_{CS}	β
Compression	$-0.4 h/b + 1.45$	$0.1 \delta + 3/40$	$-0.15 \lambda_{CS} + 1.15$
Major-axis bending	$0.4 h/b + 0.25$	$0.1 \delta + 7/200$	$-0.2 \lambda_{CS} + 1.20$
Minor-axis bending	0.65	0.1	$-0.2 \lambda_{CS} + 1.20$
Cold-formed hollow sections – 2nd approach			
$\lambda_0 = 0.40$ and $\frac{\varepsilon}{\varepsilon_y} = \left(\frac{0.4}{\lambda_{CS}}\right)^{1.5}$			
Parameters	$\lambda_{CS} \leq \lambda_0$	$\lambda_{CS} > \lambda_0$ ($\beta = 1.0$)	
		δ	α_{CS}
Compression	$\chi_{CS} = 1.15 - \frac{0.15}{(\varepsilon/\varepsilon_y)^{0.6}}$	$-0.4 h/b + 1.45$	$0.1 \delta + 7/40$
Major-axis bending	$\chi_{CS} = 1.2 - \frac{0.2}{(\varepsilon/\varepsilon_y)^{0.6}}$	$0.4 h/b + 0.25$	$0.25 \delta - 1/80$
Minor-axis bending	$\chi_{CS} = 1.2 - \frac{0.2}{(\varepsilon/\varepsilon_y)^{0.6}}$	0.65	0.15

Table 51 – Proposed OIC design curves for combined load cases.

Combined load cases for hot-rolled cross-sections		
Proposed Ayrton-Perry formula for $0.2 \leq n \leq 1$		
General format		
$\lambda_{CS} = \sqrt{\frac{R_{RESIST}}{R_{STAB,CS}}}$		
$\phi = 0.5 \left(1 + (\alpha_{CS} + \alpha_{CS}(1-n)) (\lambda_{CS} - (\lambda_0 - \lambda_0(1-n))) + \lambda_{CS}^\delta \beta \right)$		
$\chi_{CS} = \frac{\beta}{\phi + \sqrt{\phi^2 - \lambda_{CS}^\delta \beta}} \text{ For } \lambda_{CS} > \lambda_0 - \lambda_0(1-n)$		
$\chi = 1 \text{ for } \lambda_{CS} \leq \lambda_0 - \lambda_0(1-n)$		
Parameters		
$\lambda_0 = 0.35$		
δ	α_{CS}	β
$-0.4 h/b + 1.45$	0.15	1
Proposed Ayrton-Perry formula for $0 \leq n < 0.2$		
General format		
$\lambda_{CS} = \sqrt{\frac{R_{RESIST}}{R_{STAB,CS}}}$		
$\phi = 0.5 \left(1 + (\alpha_{CS} + n(1-n)) (\lambda_{CS} - (\lambda_0 - \lambda_0 n)) + \lambda_{CS}^\delta \beta \right)$		
$\chi_{CS} = \frac{\beta}{\phi + \sqrt{\phi^2 - \lambda_{CS}^\delta \beta}} \text{ For } \lambda_{CS} > \lambda_0 - \lambda_0 n$		
$\chi = 1 \text{ For } \lambda_{CS} \leq \lambda_0 - \lambda_0(1-n)$		
Parameters		
$\lambda_0 = 0.35$		
δ	α_{CS}	β
$0.4h/b + 0.25$	$1/10\delta + 3/200$	1
Combined load cases for cold-formed cross-sections**		
Proposed Ayrton-Perry formula for $0.2 \leq n < 1$		
General format		
$\lambda_{CS} = \sqrt{\frac{R_{RESIST}}{R_{STAB,CS}}}$		
$\phi = 0.5 \left(1 + (\alpha_{CS} + \alpha_{CS}(1-n^\gamma)) (\lambda_{CS} - (\lambda_0 - \lambda_0(1-n^\gamma))) + \lambda_{CS}^\delta \beta \right)$		
With $\gamma = (h/b)/5 - 1/10$		
$\chi_{CS} = \frac{\beta}{\phi + \sqrt{\phi^2 - \lambda_{CS}^\delta \beta}}$		
1 st approach – Parameters		
$\lambda_0 = 0$		
δ	α_{CS}	β

$-0.4h/b+1.45$	$1/10\delta+3/40$	$-0.15\lambda+1.15$
2nd approach – Parameters		
$\lambda_0 = 0.40$		
For $\lambda_{CS} \leq \lambda_0 - \lambda_0(1-n^\gamma)$		
$\chi_{CS} = 1.15 - \frac{0.15}{(\varepsilon/\varepsilon_y)^{0.6}}$		
$\frac{\varepsilon}{\varepsilon_y} = \left(\frac{\lambda_0 - \lambda_0(1-n^\gamma)}{\lambda_{CS}} \right)^{1.5}$		
For $\lambda_{CS} > \lambda_0 - \lambda_0(1-n^\gamma)$		
δ	α_{CS}	β
$-0.4h/b+1.45$	$1/10\delta+7/40$	1
Proposed Ayrton-Perry formula for $0 \leq n < 0.2$		
General format		
$\lambda_{CS} = \sqrt{\frac{R_{RESIST}}{R_{STAB,CS}}}$		
$\phi = 0.5 \left(1 + (\alpha_{CS} + n(1-n^\gamma)) (\lambda_{CS} - (\lambda_0 - \lambda_0 n^\gamma)) + \lambda_{CS}^\delta \beta \right)$		
With $\gamma = (h/b)/5 - 1/10$		
$\chi_{CS} = \frac{\beta}{\phi + \sqrt{\phi^2 - \lambda_{CS}^\delta \beta}}$		
1st approach – Parameters		
$\lambda_0 = 0$		
δ	α_{CS}	β
$0.4h/b+0.25$	$1/10\delta+7/200$	$-0.2\lambda+1.20$
2nd approach – Parameters		
$\lambda_0 = 0.40$		
For $\lambda_{CS} \leq \lambda_0 - \lambda_0 n^\gamma$		
$\chi_{CS} = 1.20 - \frac{0.20}{(\varepsilon/\varepsilon_y)^{0.6}}$		
$\frac{\varepsilon}{\varepsilon_y} = \left(\frac{\lambda_0 - \lambda_0 n^\gamma}{\lambda_{CS}} \right)^{1.5}$		
For $\lambda_{CS} > \lambda_0 - \lambda_0(1-n^\gamma)$		
δ	α_{CS}	β
$0.4h/b+0.25$	$1/4\delta-1/80$	1

8. Worked examples

8.1. Introduction

Present set of case studies is relative to hollow section members. Square (SHS 250x5 – S355) and rectangular sections (200x100x5 – S355) are considered, both from a cross-sectional point of view. While the first example deals with a beam-column under compression and mono-axial bending, the second one considers both major and minor-axis bending and compression.

As a particular point, these examples illustrate the practical difficulty to determine the class of a tubular cross-section according to Eurocode 3 which appears to be disproportionate with respect to the information it provides.

8.2. Square hollow section: SHS 250x5

8.2.1. Cross-section and member properties

The considered hot-rolled square section is subjected to a compression force $N_{Ed} = 600$ kN, and a major bending moment $M_{y,Ed} = 50$ kN.m. (S355).

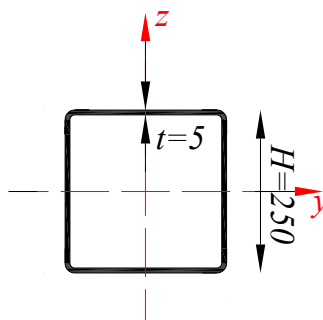


Figure 259 – Considered cross-section (SHS).

Table 52 – Cross-section properties (SHS).

Web and flange width (H)	250 mm
Thickness (t)	5 mm
Radius (r)	7.5 mm
Cross-section area (A)	4835.6 mm ²

Inertia (I_z, I_y)	$I_y = I_z = 47781763.65 \text{ mm}^4$
Section plastic modulus ($W_{pl,y}, W_{pl,z}$)	$W_{pl,y} = W_{pl,z} = 442262.9 \text{ mm}^3$
Section elastic modulus ($W_{el,y}, W_{el,z}$)	$W_{el,y} = W_{el,z} = 382254.1 \text{ mm}^3$

8.2.2. Cross-section resistance

8.2.2.1. Eurocode 3 approach

Cross section classification:

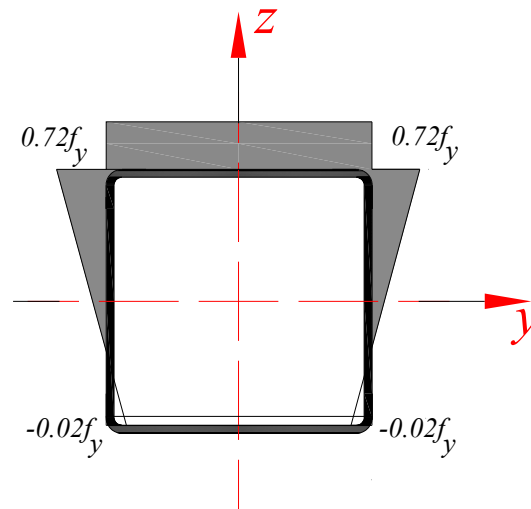


Figure 260 – Stress distribution (SHS).

Web class calculation:

The determination of the section class is done with the actual stress distribution:

$$\sigma_{\text{sup}} = \frac{N_{Ed}}{A} + \frac{M_{y,Ed} \cdot v}{I_y} = \frac{600 \cdot 10^3}{48.35 \cdot 10^2} + \frac{50 \cdot 10^6 \cdot \frac{250}{2}}{47.8 \cdot 10^6} = 254.84 \text{ MPa} \quad (0.169)$$

$$\sigma_{\text{inf}} = \frac{N_{Ed}}{A} - \frac{M_{y,Ed} \cdot v}{I_y} = \frac{600 \cdot 10^3}{48.35 \cdot 10^2} - \frac{50 \cdot 10^6 \cdot \frac{250}{2}}{47.8 \cdot 10^6} = -6.65 \text{ MPa} \quad (0.170)$$

Where v is the half flange or web width

The corresponding stresses at the plate extremities are calculated as follows:

$$\sigma_1 = \frac{254.84 \cdot (h - 2 \cdot r - t)}{h} = \frac{254.84 \cdot (250 - 2 \cdot 7.5 - 5)}{250} = 234.5 \text{ MPa} \quad (0.171)$$

$$\sigma_2 = \frac{-6.65 \cdot (h - 2 \cdot r - t)}{h} = \frac{-6.65 \cdot (250 - 2 \cdot 7.5 - 5)}{250} = -6.11 \text{ MPa} \quad (0.172)$$

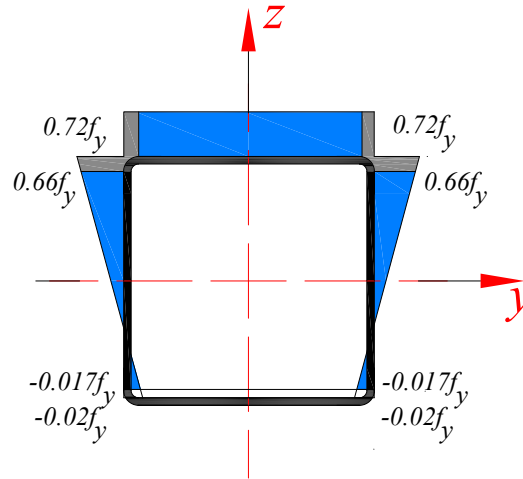


Figure 261 – Stress distribution at the plate extremities (SHS).

$$\frac{c_{web}}{t} = \frac{c_{flange}}{t} = \frac{h - t - 2r}{t} = \frac{230 \text{ mm}}{5 \text{ mm}} = 46 \quad (0.173)$$

$$\psi = \frac{\sigma_2}{\sigma_1} = \frac{-6.11}{234.5} = -0.026 \quad (0.174)$$

Web in compression and flexion:

Class 3 limit with $\psi > -1$:

$$\frac{42\varepsilon}{0.67 + 0.33\psi} = \frac{42 \cdot 0.81}{0.67 + 0.33(-0.026)} = 51.4 > \frac{c_{flange}}{t} = \frac{c_{web}}{t} = 46 \quad (0.175)$$

Class 2 limit:

Plastic neutral axis position:

$$z \cdot t_w \cdot f_y = \frac{N_{Ed}}{2} \quad (0.176)$$

$$z = 169 \text{ mm} \quad (0.177)$$

$$c = \frac{b-z}{2} = \frac{230-169}{2} = 30.5 \quad (0.178)$$

$$\alpha = \frac{b-c}{b} = \frac{230-30.5}{230} = 0.87 \quad (0.179)$$

$$\frac{456 \cdot \varepsilon}{13 \cdot \alpha - 1} = \frac{456 \cdot 0.81}{13 \cdot 0.87 - 1} = 36 < \frac{c_{flange}}{t} = \frac{c_{web}}{t} = 46 \quad (0.180)$$

The web is found to be in class 3.

Flange class calculation:

Class 3 limit:

$$42\varepsilon = 42 \cdot 0.81 = 34.02 < \frac{c_{flange}}{t} = \frac{c_{web}}{t} = 46 \quad (0.181)$$

The flange is found to be in class 4.

Thus, the cross-section is found to be in Class 4.

Effective cross section calculation:

$$k_\sigma = 4$$

$$\bar{b} = b - 2 \cdot r - t = 250 - 2 \cdot 7.5 - 5 = 230 \quad (0.182)$$

$$\bar{\lambda}_p = \sqrt{\frac{f_y}{\sigma_{cr}}} = \frac{\bar{b}/t}{28,4 \cdot \varepsilon \cdot \sqrt{k_\sigma}} = \frac{230/5}{28,4 \cdot 0.81 \cdot \sqrt{4}} = 0.99 > 0,673 \quad (0.183)$$

$$\rho_f = \frac{\bar{\lambda}_p - 0.055(3 + \psi)}{\bar{\lambda}_p^2} = \frac{0.99 - 0.055(3 + 1)}{0.99^2} = 0.78 \quad (0.184)$$

$$b_{eff} = \rho_f \cdot \bar{b} = 0.78 \cdot 230 = 179.4 \text{ mm} \quad (0.185)$$

$$b_{e1} = b_{e2} = 0.5 b_{eff} = 0.5 \cdot 179.4 = 89.7 \text{ mm} \quad (0.186)$$

With respect to Figure 262

Stress distribution (compression positive)		Effective ^p width b_{eff}				
		$\psi = 1:$ $b_{eff} = \rho \bar{b}$ $b_{e1} = 0,5 b_{eff} \quad b_{e2} = 0,5 b_{eff}$				
		$1 > \psi \geq 0:$ $b_{eff} = \rho \bar{b}$ $b_{e1} = \frac{2}{5 - \psi} b_{eff} \quad b_{e2} = b_{eff} - b_{e1}$				
		$\psi < 0:$ $b_{eff} = \rho b_c = \rho \bar{b} / (1 - \psi)$ $b_{e1} = 0,4 b_{eff} \quad b_{e2} = 0,6 b_{eff}$				
$\psi = \sigma_2 / \sigma_1$	1	$1 > \psi > 0$	0	$0 > \psi > -1$	-1	$-1 > \psi > -3$
Buckling factor k_{σ}	4,0	$8,2 / (1,05 + \psi)$	7,81	$7,81 - 6,29\psi + 9,78\psi^2$	23,9	$5,98 (1 - \psi)^2$

Figure 262 – Internal compressed elements.

The effective cross-section properties are thus calculated as follows,

$$A_{eff} = \pi (r + 0.5t)^2 - \pi (r - 0.5t)^2 + 2(h - 2r - t) + 2\rho_f (b - 2r - t) = 3837.27 \text{ mm}^2 \quad (0.187)$$

$$\begin{aligned}
 I_{y,eff} &= \frac{(b-2r-t) \cdot t^3}{12} + (b-2r-t)t \left(v' - \frac{t}{2}\right)^2 + 2 \cdot \left[\frac{(h-2 \cdot r-t)^3 t}{12} \right] + (h-2r-t) \cdot t \cdot \left(v - \frac{h}{2}\right)^2 \\
 &+ (b-2r-t) \cdot t \cdot \rho \cdot \left[\left(v - \frac{t}{2}\right)^2 (b-2r-t) \cdot t \cdot \rho \right] \\
 &+ 2 \left[\left(\frac{(r+t/2)^4}{16} + \frac{\pi (r+t/2)^2}{4} \left(v' - \frac{t}{2} - r\right)^2 \right) - \left(\frac{(r-t/2)^4}{16} + \frac{\pi (r-t/2)^2}{4} \left(v' - \frac{t}{2} - r\right)^2 \right) \right] \\
 &+ 2 \left[\left(\frac{(r+t/2)^4}{16} + \frac{\pi (r+t/2)^2}{4} \left(v - \frac{t}{2} - r\right)^2 \right) - \left(\frac{(r-t/2)^4}{16} + \frac{\pi (r-t/2)^2}{4} \left(v - \frac{t}{2} - r\right)^2 \right) \right] \\
 &= \frac{(250-2 \cdot 7.5-5) \cdot 5^3}{12} + (250-2 \cdot 7.5-5) \cdot 5 \cdot \left(116.95 - \frac{5}{2}\right)^2 + 2 \cdot \left[\frac{(250-2 \cdot 7.5-5)^3 \cdot 5}{12} \right] \\
 &+ (250-2 \cdot 7.5-5) \cdot 5 \cdot \left(133.05 - \frac{250}{2}\right)^2 + (250-2 \cdot 7.5-5) \cdot 5 \cdot 0.576 \cdot \left[\left(v - \frac{5}{2}\right)^2 (250-2 \cdot 7.5-5) \cdot 5 \cdot 0.576 \right] \\
 &+ 2 \left[\left(\frac{(7.5+5/2)^4}{16} + \frac{\pi (7.5+5/2)^2}{4} \left(116.95 - \frac{5}{2} - 7.5\right) 7.5^2 \right) - \left(\frac{(7.5-5/2)^4}{16} + \frac{\pi (7.5-5/2)^2}{4} \left(116.95 - \frac{5}{2} - 7.5\right)^2 \right) \right] \quad (0.188) \\
 &+ 2 \left[\left(\frac{(7.5+5/2)^4}{16} + \frac{\pi (7.5+5/2)^2}{4} \left(133.05 - \frac{5}{2} - 7.5\right) 7.5^2 \right) - \left(\frac{(7.5-5/2)^4}{16} + \frac{\pi (7.5-5/2)^2}{4} \left(133.05 - \frac{5}{2} - 7.5\right)^2 \right) \right] \\
 &= 44223750.33 \text{ mm}^4
 \end{aligned}$$

$$I_{z,eff} = I_z - \frac{(\bar{b} - \rho \bar{b})^3 t}{12} = 47781763.65 - \frac{(229 - 0.576 \cdot 229)^3 \cdot 5}{12} = 44223750.33 \text{ mm}^4 \quad (0.189)$$

Effective cross section properties:

$$N_{eff,Rd} = A_{eff} \cdot f_y = 3837.27 \cdot 355 \cdot 10^{-3} = 1362.23 \text{ kN} \quad (0.190)$$

$$W_{y,eff} = \frac{I_{y,eff}}{v} = \frac{44223750.4}{133.05} = 338752.4 \text{ mm}^3 \quad (0.191)$$

$$W_{z,eff} = \frac{I_{z,eff}}{v} = \frac{44223750.4}{175} = 338752.4 \text{ mm}^3 \quad (0.192)$$

$$M_{y,eff,Rd} = M_{z,eff,Rd} = W_{y,eff} \cdot f_y = 338752 \cdot 355 \cdot 10^{-6} = 120.3 \text{ kNm} \quad (0.193)$$

Cross-section verification:

$$\frac{N_{Ed}}{N_{eff,Rd}} + \frac{M_{y,Ed}}{M_{eff,y,Rd}} = \frac{600}{1362.2} + \frac{50}{120.3} = 0.86 \leq 1 \quad (0.194)$$

8.2.2.2. OIC approach

Step 1: $R_{RESIST} = 1.69$ – from Eurocode 3 plastic equations (shall be replaced by a dedicated software in the near future).

Step 2: $R_{STAB} = 1.62$ – from numerical tool (CUFSM in the present case – shall be replaced by a dedicated software in the near future).

Step 3: $\lambda_{CS} = \sqrt{\frac{1.69}{1.62}} = 1.02$

Step 4:

$$n = \frac{N_{Ed}}{N_{pl}} = 0.349$$

$$\delta = -0.4h / b + 1.45 = 1.05 ; \alpha_{CS} = 0.15 ; \beta = 1 ; \lambda_0 = 0.35$$

$$\begin{aligned} \phi &= 0.5 \left(1 + (\alpha_{CS} + \alpha_{CS} (1-n)) (\lambda_{CS} - (\lambda_0 - \lambda_0 (1-n))) + \lambda_{CS}^\delta \beta \right) \\ &= 0.5 \left(1 + (0.15 + 0.15(1-0.349)) (1.02 - (0.35 - 0.35(1-0.349))) + 1.02^{1.05} \right) = 1.12 \end{aligned}$$

$$\chi_{CS} = \frac{\beta}{\phi + \sqrt{\phi^2 - \lambda_{CS}^\delta \beta}} = \frac{1}{1.12 + \sqrt{1.12^2 - 1.02^{1.05}}} = 0.62$$

$$\chi_{CS} = \frac{1}{1.12 + \sqrt{1.12^2 - 1.02^{1.05}}} = 0.62$$

Step 5: $R_{ULT} = \chi_{CS} \cdot R_{RESIST} = 0.62 \times 1.69 = 1.05 > 1.0$

Satisfactory (value above 1.0 indicates that the actual loading needs to be increased to reach failure).

The criterion for cross-section resistance is fulfilled for the given profile according to the OIC approach, however $R_{ULT,EC3}$ is equal to 1.14 leading to overconservative EC3 results with a deviation of 9% ($1.14 / 1.05 = 9\%$).

8.3. Rectangular hollow section: RHS 200x100x5

8.3.1. Cross-section properties

The considered cold-formed rectangular section is subjected to a compression force $N_{Ed} = 360$ kN, a strong bending moment, $M_{y,Ed} = 17$ kN.m and a weak bending moment $M_{z,Ed} = 8.7$ kN.m

0 kN.m (S355).

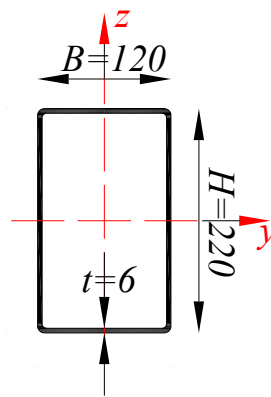


Figure 263 – Considered cross-section (RHS).

Table 53 – Cross-section properties (RHS).

Web width (H)	200 mm
Flange width (B)	100 mm
Thickness (t)	7.5 mm
Radius (r)	9 mm
Cross-section area (A)	2835 mm ²
Inertia (I_y)	$I_y = 14382547 \text{ mm}^4$
Inertia (I_z)	$I_z = 4876020 \text{ mm}^4$
Section plastic modulus ($W_{pl,y}$)	$W_{pl,y} = 181372 \text{ mm}^3$

Section plastic modulus ($W_{pl,z}$)	$W_{pl,z} = 112091 \text{ mm}^3$
Section elastic modulus ($W_{el,y}$)	$W_{el,y} = 143825 \text{ mm}^3$
Section elastic modulus ($W_{el,z}$)	$W_{el,y} = 97520 \text{ mm}^3$

1.1.2. Cross-section resistance

1.1.2.1. Eurocode 3 approach

Cross section classification:

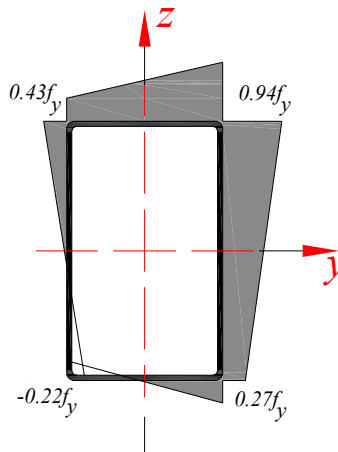


Figure 264 – Stress distribution (RHS).

The stress distribution in the web is:

$$\sigma_{\text{sup}} = \frac{N_{Ed}}{A} + \frac{M_{y,Ed} \cdot v}{I_y} + \frac{M_{z,Ed} \cdot v'}{I_z} = \frac{360 \cdot 10^3}{2835} + \frac{17 \cdot 10^6 \cdot \frac{200}{2}}{14382547} + \frac{8.7 \cdot 10^6 \cdot \frac{100}{2}}{4876020} = 334.4 \text{ MPa} \quad (0.195)$$

$$\sigma_{\text{inf}} = \frac{N_{Ed}}{A} - \frac{M_{y,Ed} \cdot v}{I_y} + \frac{M_{z,Ed} \cdot v'}{I_z} = \frac{360 \cdot 10^3}{2835} - \frac{17 \cdot 10^6 \cdot \frac{200}{2}}{14382547} + \frac{8.7 \cdot 10^6 \cdot \frac{100}{2}}{4876020} = 98 \text{ MPa} \quad (0.196)$$

At the plate extremities:

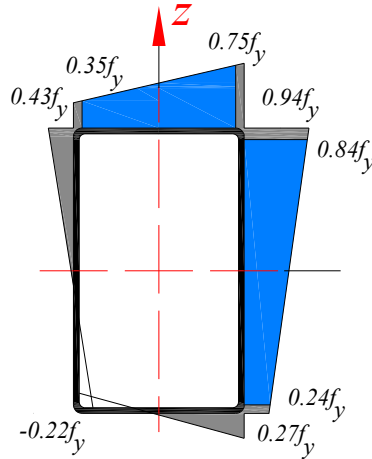


Figure 265 – Stress distribution at the plate extremities (RHS).

$$\sigma_1 = \frac{334 \cdot (h - 2 \cdot r - t)}{h} = \frac{334 \cdot (200 - 2 \cdot 7.5 - 5)}{200} = 300.6 \text{ MPa} \quad (0.197)$$

$$\sigma_2 = \frac{98 \cdot (h - 2 \cdot r - t)}{h} = \frac{98 \cdot (200 - 2 \cdot 7.5 - 5)}{200} = 88.2 \text{ MPa} \quad (0.198)$$

$$\frac{c_{web}}{t} = \frac{h - t - 2r}{t} = \frac{180}{5} = 36 \quad (0.199)$$

$$\psi = \frac{\sigma_2}{\sigma_1} = \frac{88.2}{300.6} = 0.29 \quad (0.200)$$

Web in compression and flexion:

Class 3 limit with $\psi > -1$:

$$\frac{42\varepsilon}{0.67 + 0.33\psi} = \frac{42 \cdot 0.81}{0.67 + 0.33(0.29)} = 44.4 > \frac{c_{web}}{t} = 36 \quad (0.201)$$

Class 2 limit:

$$38 \cdot \sqrt{\frac{235}{355}} = 30.9 < \frac{c_{web}}{t} = 36 \quad (0.202)$$

The web is found to be class 3.

The stress distribution at the flange is:

$$\sigma_{\text{sup}} = \frac{N_{Ed}}{A} + \frac{M_{y,Ed} \cdot v}{I_y} + \frac{M_{z,Ed} \cdot v'}{I_z} = \frac{360 \cdot 10^3}{2835} + \frac{17 \cdot 10^6 \cdot \frac{200}{2}}{14382547} + \frac{8.7 \cdot 10^6 \cdot \frac{100}{2}}{4876020} = 334.4 \text{ MPa} \quad (0.203)$$

$$\sigma_{\text{inf}} = \frac{N_{Ed}}{A} + \frac{M_{y,Ed} \cdot v}{I_y} - \frac{M_{z,Ed} \cdot v'}{I_z} = \frac{360 \cdot 10^3}{2835} + \frac{17 \cdot 10^6 \cdot \frac{200}{2}}{14382547} - \frac{8.7 \cdot 10^6 \cdot \frac{100}{2}}{4876020} = 156 \text{ MPa} \quad (0.204)$$

At the plate extremities:

$$\sigma_1 = \frac{334.4 \cdot (h - 2 \cdot r - t)}{h} = \frac{334.4 \cdot (100 - 2 \cdot 7.5 - 5)}{100} = 268 \text{ MPa} \quad (0.205)$$

$$\sigma_2 = \frac{156 \cdot (h - 2 \cdot r - t)}{h} = \frac{156 \cdot (100 - 2 \cdot 7.5 - 5)}{100} = 125 \text{ MPa} \quad (0.206)$$

$$\frac{c_{\text{flange}}}{t} = \frac{b - t - 2r}{t} = \frac{80}{5} = 16 \quad (0.207)$$

$$\psi = \frac{\sigma_2}{\sigma_1} = \frac{125}{268} = 0.47 \quad (0.208)$$

Web in compression and flexion:

Class 1 limit with

$$33 \cdot \sqrt{\frac{235}{355}} = 27 < \frac{c_{\text{flange}}}{t} = 16 \quad (0.209)$$

The flange is found to be class 1.

Thus, the cross-section is found to be class 3.

Cross section verification:

$$\frac{N_{Ed}}{N_{el,Rd}} + \frac{M_{y,Ed}}{M_{el,y,Rd}} + \frac{M_{z,Ed}}{M_{el,z,Rd}} = \frac{360 \cdot 10^3}{2835 \cdot 355} + \frac{17 \cdot 10^6}{143825 \cdot 355} + \frac{8.7 \cdot 10^6}{97520 \cdot 355} = 0.94 \leq 1 \quad (0.210)$$

8.3.1.1. OIC approach

Step 1: $R_{RESIST} = 1.69$ – from Eurocode 3 plastic equations (shall be replaced by a dedicated software in the near future).

Step 2: $R_{STAB} = 3.59$ – from numerical tool (CUFSM in the present case – shall be replaced by a dedicated software in the near future).

Step 3: $\lambda_{CS} = \sqrt{\frac{1.69}{3.59}} = 0.69$

Step 4:

1st approach:

$$n = \frac{N_{Ed}}{N_{pl}} = 0.357$$

$$\gamma = \left(\frac{h/b}{5}\right) - \frac{1}{10} = 0.3; \delta = -0.4h/b + 1.45 = 0.65; \alpha_{CS} = \frac{1}{10}\delta + \frac{3}{40} = 0.14; \beta = -0.15\lambda_{CS} + 1.15 = 1.04; \lambda_0 = 0$$

$$\begin{aligned} \phi &= 0.5 \left(1 + (\alpha_{CS} + \alpha_{CS}(1-n^\gamma)) (\lambda_{CS} - (\lambda_0 - \lambda_0(1-n^\gamma))) + \lambda_{CS}^\delta \beta \right) \\ &= 0.5 \left(1 + (0.14 + 0.14(1-0.357^{0.3})) (0.69 - (0 - 0(1-0.357^{0.3}))) + 0.69^{0.3} 1.04 \right) = 0.97 \end{aligned}$$

$$\chi_{CS} = \frac{\beta}{\phi + \sqrt{\phi^2 - \lambda_{CS}^\delta \beta}} = \frac{1.04}{0.97 + \sqrt{0.97^2 - 0.69^{0.65} 1.04}} = 0.79$$

2nd approach

$$n = \frac{N_{Ed}}{N_{pl}} = 0.357$$

$$\gamma = \left(\frac{h/b}{5}\right) - \frac{1}{10} = 0.3; \delta = -0.4h/b + 1.45 = 0.65; \alpha_{CS} = \frac{1}{10}\delta + \frac{7}{40} = 0.24; \beta = 1; \lambda_0 = 0.40$$

$$\begin{aligned} \phi &= 0.5 \left(1 + (\alpha_{CS} + \alpha_{CS}(1-n^\gamma)) (\lambda_{CS} - (\lambda_0 - \lambda_0(1-n^\gamma))) + \lambda_{CS}^\delta \beta \right) \\ &= 0.5 \left(1 + (0.24 + 0.24(1-0.357^{0.3})) (0.69 - (0.40 - 0.40(1-0.357^{0.3}))) + 0.69^{0.3} 1 \right) = 0.95 \end{aligned}$$

$$\chi_{CS} = \frac{\beta}{\phi + \sqrt{\phi^2 - \lambda_{CS}^{\delta} \beta}} = \frac{1}{0.95 + \sqrt{0.95^2 - 0.69^{0.65} 1}} = 0.77$$

Step 5:**1st approach**

$$R_{ULT} = \chi_{CS} \cdot R_{RESIST} = 0.79 \times 1.69 = 1.33 > 1.0 .$$

2nd approach

$$R_{ULT} = \chi_{CS} \cdot R_{RESIST} = 0.76 \times 1.69 = 1.30 > 1.0$$

Satisfactory (value above 1.0 indicates that the actual loading needs to be increased to reach failure).

The criterion for cross-section resistance is fulfilled for the given profile according to the O.I.C. approach, however $R_{ULT,EC3}$ is equal to 1.06 leading to overconservative EC3 results with a benefit brought by O.I.C. approach equal to 25% with the first approach ($1.33 / 1.06 = 1.25$) and 22% with the second approach ($1.30 / 1.06 = 1.22$).

8.4. Summary of results and conclusions

As was clearly demonstrated in the previous pages, the ease and efficiency of application of the OIC in comparison with the actual Eurocode 3 design rules bears no doubts.

In particular, the cross-section classification step has been shown to be disproportionate with respect to the information it provides.

In addition, the following higher resistances have been reached through the OIC approach, compared to Eurocode 3 predictions:

SHS, cross-section check: +3%;

RHS, cross-section check: +25%;

9. Conclusions

9.1. General

The main aim of this thesis is to investigate the behaviour of hollow cross-sections and propose suitable new design approach for the prediction of their cross-section capacities, through a new concept termed the Overall Interaction Concept OIC. This was deemed necessary since the effective width method and the cross-section classification which are adopted in actual standards have many shortcomings and inconsistencies. The following summary can be given of the topics treated in this thesis, listed in the order of appearance in the main body of the text:

- (i) In the 1st introductory chapter, inconsistencies and problems in current local buckling design rules were presented in a general form. The OIC approach was introduced and explained. The scope and limitations of the concerned subject treating only the local buckling behaviour of hollow sections were stated. The thesis organization was then introduced and explained.
- (ii) In chapter 2, a comprehensive survey concerning the field of the cross-section resistance was conducted. A detailed history of the local buckling handling and development was made, along with an actual description of the methods used in nowadays standards. The shortcomings of the classification system were pointed out, and the newly existing approaches were presented and commented (Direct Strength Method and the Continuous Strength Method).
- (iii) In chapter 3, an experimental study of the behaviour of cold-formed, hot-rolled and hot-finished square, rectangular and circular sections was presented. The cross-sections were subjected to different kind of loading including simple load cases and combined ones.
- (iv) In chapter 4, the behaviour of the tested elements was simulated via finite element analysis with the aim of using the calibrated model to conduct an extensive set of finite element calculations in order to multiply the available number of tests. Therefore, a parametric study has been undertaken and concerned cold-formed and hot-rolled sections with the consideration of adequate imperfections, material properties, geometrical dimensions, residual stresses and various load cases, leading to more than 40,000 simulations.

- (v) Chapter 5 consisted in targeting the leading parameters for the derivation of several adequate interaction curves, which were then proposed based on the numerical results with the use of an extended Ayrton-Perry approach covering simple and combined load cases for both hot-rolled and cold-formed sections.
- (vi) In chapter 6, the accuracy of the proposed design formulae was examined. Statistical results of the comparison between FEM, EC3 and proposal calculations for all the computed results were presented. The resistance estimates were significantly improved by the new proposal, with mean and standard deviation values indicating a far better level of accuracy and consistency.
- (vii) In chapter 7, a summary of all proposed formulae and recommendations for practical design were presented;
- (viii) In chapter 8, worked examples were presented to illustrate the effectiveness, the simplicity and the economic benefit of the newly developed design proposals.

Going back to the objective set at the beginning of this thesis, it can be seen that they were fulfilled and a totally new design proposal dealing with the local buckling behaviour of steel hollow sections was developed based on the conducted experimental and numerical tests of this study.

9.2. Personal contributions

The original contributions made in this thesis from a **theoretical** point of view include the following listed points:

- (i) The development of a new design formula capable of describing the buckling behaviour of hot-rolled cross-sections subjected to compression, major-axis bending and minor-axis bending; they were obtained by extending the well known 'Ayrton-Perry' formula to cross-sections. The following aspects were included in the proposed formula (Chapter 5 6 & 7):
- (i1) The cross-section shape was taken into account through the parameter h/b ;
 - (i2) Normal steel grades can follow one proposed curve;
 - (i3) The imperfections' influence was included through the parameter α_{CS} ;

- (i4) The ideal resistance limit was introduced through a β parameter equal to 1.0.
- (ii) The development of a new design formula capable of describing the buckling behaviour of cold-formed cross-sections subjected to compression, major-axis bending and minor-axis bending. Two design approaches have been developed for cold-formed sections that specifically lead to $\chi_{CS} > 1.0$ beneficial factors at low λ_{CS} ranges. (i1), (i2) and (i3) are also applicable for cold-formed sections along with these following aspects (Chapter 5 6 & 7) :
- (ii1) A first approach relying on a single continuous interaction curve. The ideal resistance limit ($\beta = 1.0$) was changed to allow for obvious strain-hardening leading to a potential 15% maximum benefit from strain hardening;
- (ii2) A second approach relying on a strain-based format at low slenderness. In a first step, a relationship between the strain level $\varepsilon / \varepsilon_y$ and λ_{CS} was established. Then, in a second step, χ_{CS} was calculated as a function of the strain level $\varepsilon / \varepsilon_y$.
- (iii) The development of a new design formula capable of describing the buckling behaviour of hot-rolled cross-sections subjected to combined loading ($N + M_y$ or $N + M_z$ or $N + M_y + M_z$); (i1), (i2), (i3) and (i4) were applicable for the combined load cases of hot-rolled cross-sections. However, the presence of axial forces (by means of the parameter n) was seen to have the most important effect on the structural behaviour and was included in the derived extended Ayrton-Perry formula (Chapter 5 6 & 7).
- (iv) The development of a new design formula capable of describing the buckling behaviour of cold-formed cross-sections subjected to combined loading ($N + M_y$ or $N + M_z$ or $N + M_y + M_z$); (i1), (i2), (i3), (i4), (ii1) and (ii2) were applicable for the combined load cases of cold-formed cross-sections. However, the presence of axial forces (by means of the parameter n) was seen to have a minor influence on the structural behaviour of cold-formed sections, due to the difference type of material law corresponding to such fabrication process. Therefore this effect was included in the proposed formula through an exponent γ to the n parameter, depending on the aspect ratio h/b (Chapter 5 6 & 7).

Contributions to the consolidation of existing engineering knowledge included the following points:

- (i) A comprehensive discussion of the origins of the plate buckling background, methods to get an adequate buckling curves and shortcomings of the existing classification system (Chapter 2 & 5).
- (ii) A wide experimental campaign consisting of 57 cross-section tests comprising 12 stub columns and 45 cross-sectional tests with various loading conditions, cross-section shapes and fabrication modes (Chapter 3);
- (iii) A sensitivity study on the influence of different shapes and amplitudes of initial local geometric imperfections on the cross-section capacity (Chapter 4);
- (iv) A Load-path sensitivity study to characterize the differences that arise in the structural response of sections if the load is applied in different sequences for a given combination (Chapter 4).

The original contributions made in this thesis from a **practical** point of view include the following listed points:

- (i) Straightforward derived formulae, requiring only an adequate choice of parameters for each design case (i.e. fabrication process, cross-section shape and load case);
- (ii) Strain hardening due to cold-work of forming was accounted for in the interaction curves;
- (iii) Derived formulae are applicable to any normal steel grade (<460 MPa);
- (iv) No effective width calculations, no iterations and gross cross-sectional properties are required within the new proposed derived formulae.

9.3. Suggestions for further studies

The investigations carried out in the scope of this thesis identified several areas where further research is required. They consisted in the following:

- (i) A deeper analysis of the load cases consisting in biaxial bending with no axial forces. As already discussed, the absence of an axial compression would lead to a distinction between the levels of biaxiality applied on the cross-section. The actual proposed approach considers a single curve for all the degrees of biaxiality, leading sometimes to

conservative results (with high h/b aspect ratios) and to slightly unconservative results (with low h/b aspect ratios). A first attempt to overcome this shortcoming has been made but need further improvements and developments. It consists in the following:

The behavior of a square and a rectangular section subjected to a bi-axial bending differ in a considerable way depending on the angle α characterizing the degree of bi-axiality. Figure 266 illustrates two graphs relative to a square (left) and ‘highly’ rectangular cross-section (i.e. high aspect ratio h/b). For a square cross-section, the behavior relative to loading cases in which α is comprised between 0 and 45 degrees would be equal to the behavior relative to loading cases in which α is comprised between 45 and 90 degrees (in Figure 266, cross-sections having the same color indicate equivalent loading cases). This won’t be applicable for rectangular sections and the behavior relative to a major-axis bending would differ from a minor-axis bending; these two loading cases would be equivalent for a square cross-section, but considered as the extreme loading cases for a rectangular cross-section. However, this passage of loading cases from being ‘equivalent’ to being ‘extreme’ doesn’t happen in a brutal way, but is rather a function of the h/b ratio and the ‘extreme’ stage would be reached for relatively high h/b ratios. This aspect should be examined with more details in the future. A proposal for high h/b ratios (i.e. corresponding to the ‘extreme’ stage) has been developed. A modification of the factor η accounting for imperfections has been made through the inclusion of the angle of biaxiality α . It consists in the following equations:

$$\eta_{\text{biaxial-bending}} = \left(\alpha_{CS,My} - \left(\alpha_{CS,My} - \alpha_{CS,Mz} \right) \frac{\alpha}{90} \right) \left(\lambda_{CS} - \left(\lambda_{0,My} - \left(\lambda_{0,My} - \lambda_{0,Mz} \right) \frac{\alpha}{90} \right) \right) \quad (211)$$

Or also

$$\eta_{\text{biaxial-bending}} = \left(\alpha_{CS,Mz} + \left(\alpha_{CS,My} - \alpha_{CS,Mz} \right) \frac{\alpha}{90} \right) \left(\lambda_{CS} - \left(\lambda_{0,Mz} + \left(\lambda_{0,My} - \lambda_{0,Mz} \right) \frac{\alpha}{90} \right) \right) \quad (212)$$

Equation (211) has been proposed in a way that if $\alpha = 0$ degrees, the interaction curve relative to a major-axis bending is obtained, and the one relative to a minor-axis bending would thus be obtained for $\alpha = 90$ degrees. The opposite is found in Equation (212), where the interaction curve relative to a major-axis bending is obtained for $\alpha = 90$ degrees, and the one relative to a pure minor-axis bending is obtained for $\alpha = 0$ degrees.

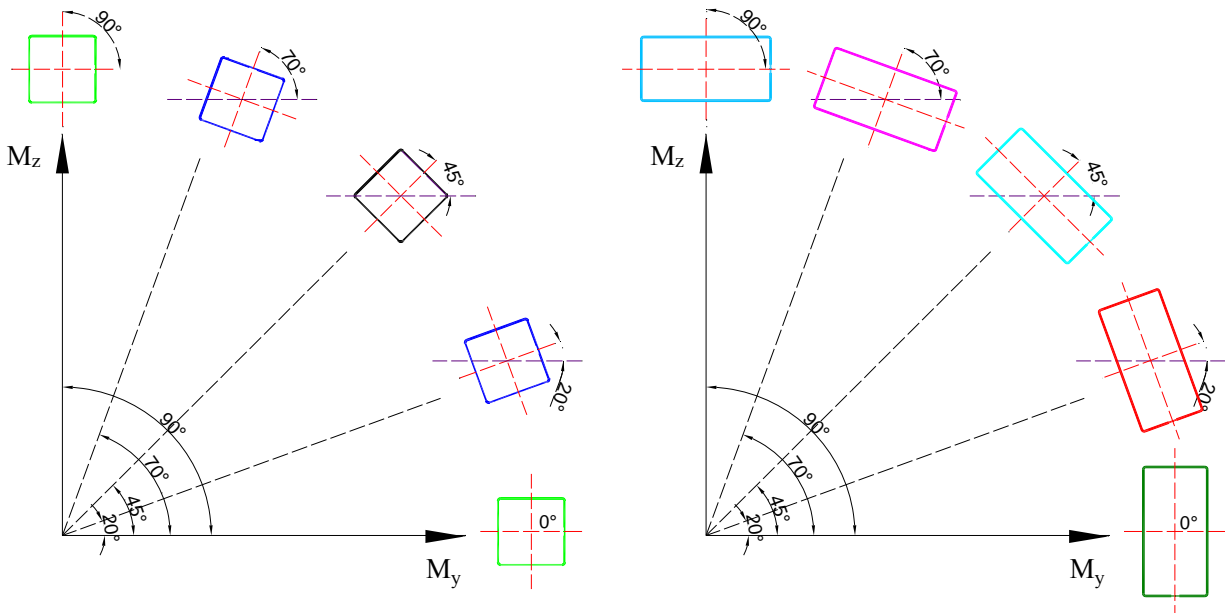


Figure 266 – Representation of various degrees of biaxiality for both a square cross-section and a rectangular cross-section.

- (ii) Further numerical results are needed to examine and validate the proposed approach for cold-formed and hot-rolled sections subjected to combined loading with levels of axial forces smaller than 20% of N_{pi} ;
- (iii) For now, the OIC proposed interaction formulae are calibrated only to work for cross-sections subjected the previously mentioned simple and combined loads. Many other contributions need to be developed to have a complete ‘package’, i.e. shear provisions, accurate determination of the rotational capacity for stocky sections etc...;
- (iv) The analysis of other buckling modes than local buckling is also required starting with the members behaviour (global buckling) and including the coupling of instabilities (Local and global instabilities). The incorporation of χ_{CS} should be accounted for and a first attempt in the case of members is made through the use of a modified member relative slenderness λ_{MB} in which R_{RESIST} is substituted by $\chi_{CS} \cdot R_{RESIST}$. Further developments and assertions are needed in this field.

10. REFERENCES

- [1] B. W. Schafer, "Designing cold-formed steel using the direct strength method", *18th International Specialty Conference on Cold-Formed Steel Structures*, 26-Oct-2006.
- [2] L. Gardner, "The continuous strength method", *ICE-Institution of Civil Engineers 127-133*, 2008.
- [3] R. Greiner, M. Kettler, A. Lechner, J.-P. Jaspart, N. Boissonnade, E. Bortolotti, K. Weynand, C. Ziller, and R. Order, "RFCS Semi-Comp: Plastic member capacity of semi-compact steel sections - a more economic design", Final report (01/01/06 - 30/06/07) - RFCS - Steel RTD (Contract RFS-CR-04044), 2007.
- [4] N. Boissonnade, "The concept of cross-section classes in Eurocode 3 into question", *ECCS TC8 Meet*, Lisbon, 2011.
- [5] L. Gardner, F. Wang, and A. Liew, "Influence of Strain Hardening on The Behaviour And Design of Steel Structures", *International Journal of Structural Stability and Dynamics Vol.5, No 5, 855-875*, 2010.
- [6] S.T.S.S., "Research project STSS-Simple Tools Sell Steel", 2012.
- [7] M. Kettler, "Elastic-Plastic Cross-Sectional Resistance Of Semi-Compact H- And Hollow Sections", PhD thesis, Technical University of Graz, 2008.
- [8] M. Bruneau, C. Uang, and R. Sabelli, "Ductile design of steel structures", *Second edition*, 2011.
- [9] S. Timoshenko and J. Gere, "Theory of Elastic Stability", *2nd edition*, McGraw-Hill, New York, USA. 1969.
- [10] H. N. Hill, "Chart for critical compressive stress of flat rectangular plates", *National Advisory Committee for Aeronautics*, Aug-1940.
- [11] E. Z. Stowel and E. Lundquist, "Local Instability of Columns With I, Z, Channel and Rectangular-Tube Sections", Dec-1939.
- [12] F. Bleich, "Buckling strength of metal structures" McGraw-Hill, New York, 1952.
- [13] M. Seif and B. W. Schafer, "Local buckling of structural steel shapes", *Journal of Constructional Steel Research*, 2010.
- [14] M. Seif and B. W. Schafer, "Elastic buckling finite strip analysis of the AISC sections database and proposed local plate buckling coefficients", *Structures ASCE*, 2009.
- [15] Z. Li and B. W. Schafer, "Buckling analysis of cold-formed steel members with general boundary conditions using CUFSM: conventional and constrained finite strip methods", *Proc. 20th Intl Spec Conf Cold-Form. Steel Struct. St Louis MO* Novemb. 2010.
- [16] R. Bebiano, "GBTUL - Buckling and Vibration Analysis of Thin-Walled Members", Technical University of Lisbon, 2008.

- [17] T. Von Karman, E. Sechler, and L. Donel, "Strength of Thin Plates in Compression", *Society of Mechanical Engineers - Transactions - Applied Mechanics*, 54(2): 53-56, 1932.
- [18] G. Winter, "Strength of Thin Steel Compression Flanges", *Bull. 353 Cornell Univ. Eng. Exp. Stn. Ithaca NY*, 1947.
- [19] W.-W. Yu and R. Laboube, "Cold-Formed Steel Design", John Wiley & Sons., vol. Forth edition.
- [20] EN 1993-1-1, "Eurocode 3: Design of steel structures, Part 1-1: General rules and rules for buildings", 2005.
- [21] N. Trahair, M. Bradford, D. Nethercot, and L. Gardner, "The Behaviour And Design Of Steel Structures To EC3", Fourth edition. Taylor & Francis, 2007.
- [22] I. Madsen, "Report on plate girder tests", *Iron Steel Eng.*, 18(11), Nov-1941.
- [23] J. B. Dwight and K. E. Moxham, "Welded steel plates in compression", *The structural engineer*, 47(2), Feb-1969.
- [24] Aluminium Company of America, "ALCOA Structural Handbook" Pittsburgh, 1958.
- [25] M. Lyse and H. J. Godfrey, "Investigation of Web Buckling in Steel Beams", *Transactions, American Society of Civil Engineers, paper No 1907, 1934, pp. 675-695*, 1934.
- [26] J. A. Ewing, "The Strength of Materials", Cambridge, 1899.
- [27] E. Meyer, "Die Berechnung der Durchbiegung von Staben deren Material dem Hook'schen Gesetze nicht folgt", *Zeitschrift des Vereines Deutscher Ingenieure*, 52(5), p.167, 1908.
- [28] G. Kazinczy, "Trials with fixed-end beams", *Betonszemle*, Issue 2, pp. 68-71, 83-87 & 101-104, 1914.
- [29] N. C. Kist, "Die Zahigkeit des Materials als Grundlage fur die Berechnung von Brucken, Hochbauten und ahnlichen konstruktionen aus Flubeisen", *Der Eisenbau* 11, No. 23, pp. 425-428, 1920.
- [30] H. Maier-Leibnitz, "Test results: Their Interpretation and Application", *International Association for Bridge and Structural Engineering*, 2nd Congress, Berlin, Germany, 1936.
- [31] H. Maier-Leibnitz, "Beitrag Zur Frage Der Tatsachlichen Tragfahigkeit Einfacher Und Durchlaufender Balkentrager aus Baustahl", *St 37 und Holz, Die Bautechnik* 6, pp. 11-14 & 27-31, 1928.
- [32] J. H. Schaim, "Der durchlaufende Trager unter Berucksichtigung der Plastizitat", *Stahlbau* 3, pp. 13-15, 1930.
- [33] K. Girkmann, "Uber die Auswirkung der, Selbsthilde' des Baustahls in rahmernartigen Stabweken", *Stahlbau* 5, pp. 121-127, 1932.

- [34] J. F. Baker and J. W. Roderick, "Further tests on Beams and Portals", *Second interim Report, Research Committee of the Institute of Welding, Transactions of the Institute of Welding*, Vol 3, No2, 1940.
- [35] J. F. Baker and J. W. Roderick, "An experimental Investigation of the Strength of Seven Portal Frames", *First interim Report, Research Committee of the Institute of Welding, Transactions of the Institute of Welding*, Vol 1, No4, 1938.
- [36] J. F. Baker, M. R. Horne, and J. Heyman, *The Steel Skeleton, "Plastic Behaviour and Design"*, Cambridge University Press, Cambridge, England, Volume 2, 1956.
- [37] C. Massonnet, "Die europaischen Empfehlungen (EKS) fur die plastische Bemessung von Stahltragwerken", *Acier-Stahl-Steel* 32, pp.146-156, 1976.
- [38] J. Kragerup, "Five notes on Plate Buckling", Tech. Univ. Den. Dpt Struct. Eng. Ser. R N143, 1982.
- [39] A. N. Sherbourne and R. M. Korol, "Post-buckling of axially compressed plates", *Journal of Structural Division ASCE*, Vol 98 2223-2234, 1972.
- [40] R. M. Korol and A. N. Sherbourne, "Strength Predictions of Plates in Uniaxial Compression", *Journal of Structural Division ASCE*, Vol 98 1965-1988, 1972.
- [41] J. B. Dwight and K. E. Moxham, "Welded steel plates in compression", *The structural engineer*, vol 47, pp.49-66, 1969.
- [42] K. E. Moxham, "Buckling tests on individual welded steel plates in compression", University of Cambridge, engineering department, report n CUED/C-Struct/TR.3, 1971.
- [43] J. Rondal, "Contribution à l'étude de la stabilité des profils creux à parois minces", PhD thesis, Université de Liège, 1984.
- [44] S. Bild and G. L. Kulak, "Local Buckling Rules for Structural Steel Members", *Journal of Constructional Steel Research* 20: 1-52, 1991.
- [45] T. Wilkinson, "The Plastic Behaviour of Cold-Formed Rectangular Hollow Sections", PhD thesis, The University of Sydney, 1999.
- [46] A. Lechner, "Plastic Capacity of Semi-Compact Cross-Sections", PhD thesis, Technical University of Graz, 2005.
- [47] AISC LRFD, "AISC - Load & Resistance Factor Design: Structural Members, Specifications & Codes", 1994.
- [48] AS 4100, "Australian Standard AS 4100 Steel Structures", 1998.
- [49] BS 5950-1:2000, "British Standard BS 5950-1 Structural use of steelwork in buildings, Part 1: Code of practice for design - Rolled and Welded Sections", Great Britain-2000.
- [50] DIN 18800, "DIN 18800_1 Stahlbauten Bemessung & Konstruktion 2", 1990.
- [51] M. Villette, "Paradoxes, contradictions et erreurs des prescriptions de l'EN 1993-1-1 pour la classification des section".

- [52] P. Maitre, “Nouvelles règles de construction métallique. Résistance des sections”, Socotec, 1995.
- [53] B. W. Schafer, “Review: the direct strength method of cold formed steel member design”, *Journal of Constructional Steel Research*, 2008.
- [54] AISC 2004, “North American Specification. Appendix 1: Design of cold-formed steel structural members using the Direct Strength Method: supplement to the North American specification for the design of cold-formed steel structures”, 2004.
- [55] G. Hancock, Y. Kwon, and E. Bernard, “Strength design curves for thin-walled sections undergoing distortional buckling”, *Journal of Constructional Steel Research*, 1994.
- [56] B. W. Schafer, “Local, Distortional, and Euler buckling in thin-walled columns”, *Journal of Constructional Steel Research*, 2002.
- [57] B. W. Schafer, “Distortional buckling of cold-formed steel columns. Final Report to the American Iron and Steel Institute: Washington (DC)”, 2000.
- [58] B. W. Schafer, “Review the direct strength method of cold formed steel member design”, *Stability and Ductility of Steel Structures*, 06-Sep-2006.
- [59] G. Hancock, C. Rogers, and R. Schuster, “Comparison of the distortional buckling method for flexural members with tests”, *Proc. Thirteen. Interanational Spec. Conf. Cold-Form. Steel Struct.*, 1996.
- [60] Y. Shifferaw and B. W. Schafer, “Towards a direct strength method for cold-formed steel beam-column”, *Annual SSRC Stability Conference*, 2010.
- [61] Y. Shifferaw and B. W. Schafer, “Inelastic bending capacity in cold-formed steel members”, *Annual SSRC Stability Conference*, 2007.
- [62] Y. Li, “Extension of The Direct Strength Method to Hot-Rolled and Welded H Profile Cross-Sections”, PhD thesis, Université de Liège, 2014.
- [63] S. Afshan and L. Gardner, “The continuous strength method for structural stainless steel design”, *Thin-Walled Structures* 68: 42-49, 2013.
- [64] EN 1993-1-5, “Eurocode 3: Design of Steel Structures, Part 1-5: Plated structural elements”, 2005.
- [65] A. Liew, “Design of Structural Steel Elements with the Continuous Strength Method”, PhD thesis, Imperial College, 2014.
- [66] A. Liew and L. Gardner, “Ultimate capacity of structural steel cross-sections under compression, bending and combined loading”, Struct. Press.
- [67] O. Zhao, B. Rossi, L. Gardner, and B. Young, “Behaviour of structural stainless steel cross-sections under combined loading-Part II: Numerical modelling and design approach”, *Eng. Struct.*, 2014.
- [68] EN 10210-2, “Hot finished structural hollow sections of non-alloy and fine grain steels”, 2006.

- [69] EN 10219-1, "Cold-formed welded structural hollow sections of non-alloy and fine grain steels", 2006.
- [70] J. Lu, handbook of measurement of residual stresses, Fairmont press, 1996.
- [71] E. Macherauch and V. Hauk, "Residual stresses in science and technology; Origin, measurement and evaluation of residual stresses"
- [72] L. Tong, G. Hou, Y. Chen, F. Zhou, kai Shen, and A. yang, "Experimental investigation on longitudinal residual stresses for cold formed thick walled square hollow sections", *Journal of Constructional Steel Research* 73, 105-116, 2012.
- [73] P. W. Key and G. J. Hancock, "A theoretical investigation of the column behaviour of cold-formed square hollow sections", *Thin-walled structures* 16, 31-64, 1993.
- [74] R. B. Cruise and L. Gardner, "Residual stress analysis of structural stainless steel sections", *Journal of Constructional Steel Research* 64, 352-366, 2008.
- [75] R. Cruise and L. Gardner, "Residual stress analysis of structural stainless steel sections", *Journal of Constructional Steel Research* 64: 352-366, 2008.
- [76] M. Jandera and J. Machacek, "Residual stress pattern of Stainless steel"
- [77] M. Jandera, L. Gardner, and J. Machacek, "Residual stresses in cold-formed stainless steel hollow sections", *Journal of Constructional Steel Research* 64, 1255-1263, 2008.
- [78] B. W. Schafer and T. Pekoz, "Computational modeling of cold-formed steel characterizing geometric imperfections and residual stresses", *Journal of Constructional Steel Research*, 1998.
- [79] R. Thiebaud and J. P. Lebet, "Experimental study of residual stresses in thick steel plates", *Proceedings of the annual stability conference, Structural Stability Research Council*, 2012.
- [80] P. J. Withers, M. Turski, L. Edwards, P. J. Bouchard, and D. J. Buttle, "Recent advances in residual measurement", *International journal of pressure vessels and piping* 85, 118-127, 2008.
- [81] S. P. Chiew and M. S. Zhao, "Comparative study on cold-formed, hot-formed and hot-finished structural hollow sections", *Tubular Structures XIV*, 2012.
- [82] N. Tebedge, G. Alpsten, and L. Tall, "Residual stress measurement by the sectioning method", *Experimental Mechanics*, 13, 1973.
- [83] G. A. Alpsten and L. Tall, "Residual stresses in heavy welded shapes", Fritz laboratory report: research L.U.I.O.(ed.), 1969.
- [84] T. Galambos, "Guide to stability design criteria for metal structures", Fifth ed. New York: John Wiley and Sons Inc, 1998.
- [85] D. Sherman, "Residual stress measurement in tubular members", *Journal of the structural division*, ASCE; 95(4): 635-48, 1969.
- [86] M. Jandera and J. Machacek, "Residual stress pattern of Stainless steel"

- [87] K. J. R. Rasmussen and Hancock, "Design of cold-formed stainless steel tubular members I:columns", *Journal of Structural Engineering, American Society of Civil Engineers*, Vol. 119, pp 2349-2367, 1993.
- [88] K. J. R. Rasmussen and Hancock, "Design of cold-formed stainless steel tubular members II:Beams", *Journal of Structural Engineering, ASCE*, Vol. 119, pp 2368-2386, 1993.
- [89] K. J. R. Rasmussen, "Recent research on stainless steel tubular structures", *Journal of structural engineering*, Vol 54, No. 1, pp. 75-88, 2000.
- [90] M. Jandera, L. Gardner, and J. Machacek, "Residual stresses in cold-formed stainless steel hollow sections", *Journal of Constructional Steel Research* 64:1255-1263, 2008.
- [91] N. Stranghoner, "Untersuchungen zum Rotationsverhalten von Tragern aus Hohlprofilen", PhD thesis, RWTH Aachen, Institute of Steel Construction, 1995.
- [92] G. Sedlacek and J. Rondal, "Buckling behaviour of hot-formed SHS in high strength steel grade E-460", Cidect report 2T-2/99, 1999.
- [93] S.-P. Chiew, S.-L. Lee, and N. E. Shanmugan, "Experimental study of thin-walled steel box columns", *Journal of Structural Engineering* 113.1987, Vol. 10, pp. 2208-220.
- [94] M. Clarin, "High strength steel-Local buckling and residual stresses", PhD thesis, Lulea University of Technology, Dept. of Civil and Environmental Engineering, 2004.
- [95] J. Salvarinas, J. Barber, and P. Birkemoe, "An experimental investigation of the column behavior of cold-formed stress-relieved hollow structural steel sections", 1978.
- [96] T. Usami and Y. Fukumoto, "Local and overall buckling of welded box columns", *Journal of the structural division* 108, Proc. ASCE, 1982, ST3, pp. 525-542.
- [97] T. Usami and Y. Fukumoto, "Welded box compression members", *Journal of Structural Engineering* 110, Vol. 10, pp. 2457-2471, 1984.
- [98] J. Grimault, A. Plumier, and J. Rondal, "Buckling of thin-walled rectangular profiles under eccentrically axial forces", Final report, 1983.
- [99] K. kloppel, R. Schmied, and J. Schubert, "Die traglast mittig und aubermittig gedruckter dunnwandiger stutzen mit kastenformigen querschnitt im uberkritischen bereich unter verwendung der nichtlinearen beultheorie, Teil II, Stahlbau 1", Issue 1&3, pp. 9-19 & 73-83, 1969.
- [100] L. Gardner, N. Saari, and F. Wang, "Comparative experimental study of hot-rolled and cold-formed rectangular hollow sections", *Thin-Walled Structures* 48: 495-507, 2010.
- [101] M. Kotelko, T. Lim, and J. Rhodes, "Post-failure behaviour of box section beams under pure bending (an experimental study)", *Thin-Walled Structures*, 38(2):179-194, 2000.
- [102] P. W. Key, S. W. Hasan, and G. J. Hancock, "Column behavior of cold-formed hollow sections", *Structural Engineering-ASCE*,114(2):390-407, 1988.
- [103] X. L. Zhao and G. J. Hancock, "Tests to determine plate slenderness limits for cold-formed rectangular hollow sections of grade C450", *Journal of the Australian Steel Institute* 25(4):2-16, 1991.

- [104] Greish and Ulg, Finelg, "Non linear finite element analysis software" University of Liege - The engineering office Greisch, 1999.
- [105] Hibbitt, Karlsson, and Sorensen, "Abaqus 6.4 User's Manual" pawtucket, RI, 2003.
- [106] R. G. Dawson and A. C. Walker, "Post-buckling of geometrically imperfect plates", *Journal of Structural division ASCE*; 98(1): 75-94, 1972.
- [107] R. B. Cruise and L. Gardner, "Measurement and prediction of geometric imperfections in structural stainless steel members", *Structural engineering and mechanics*; 24(1): 63-89, 2006.
- [108] DIN 18800, "DIN 18800_2 knicken" 1990.
- [109] ECCS, "Ultimate limit state calculation of sway frames with rigid joints", ECCS publications, n 33-1987.
- [110] M. Hayeck, J. Nseir, E. Saloumi, and N. Boissonnade, "Use of Ramberg-Osgood material laws in the finite element modeling cold-formed tubes", *Proc. 15th Int. Symp. Tubual Struct.*, p. May 2015.
- [111] V. Epiney, "Resistance et stabilité des éléments en acier fléchis et tendus", Master HES-SO Ingénierie du Territoire MIT, 2015.
- [112] S. Baar, "Courbes de flambement de la C.E.C.M-Recherche d'une equation simple représentant aux mieux les points donnés", Rapport à la comission 8 de la C.E.C.M., S.E.R.C.O.M., n SB/1W St 26, Liège, 1970.
- [113] B. W. Young, "Axially loaded steel columns", Cambridge University, engineering department, report n CUED/C-struct/TR.11, 1971.
- [114] R. Bjorhovde, "Deterministic and probabilistic approaches to the strength of steel columns", Ph.D. Dissertation, Lehigh University, 1972.
- [115] SSRC, Structural Stability Research Council, "S.S.R.C. guide to stability criteria for metal structures", Third edition, B.G. Johnson editor, Wiley, New-york, 1976.
- [116] W. Merchant, "The failure load or rigidly jointed frame works as influenced by stability", *The Structural Engineer* vol. 32, 1954.
- [117] J. Lindner, "Näherungen für die Europäischen Knickspannungskurven, Die bautechnik", heft 10, pp. 344-347, 1978.
- [118] "Ein Konzept zur Berechnung der traglast von biegedrillknickgefährdeten staben unter berücksichtigung des einflusses geometrischer und werkstofflicher imperfektionen", *Stahlbau Heft 11*, no. pp/ 329-338, Nov. 1977.
- [119] B. Unger, "Ein Konzept zur Berechnung der Traglast von Biegedrillknickgefährdeten staben unter Berücksichtigung des einflusses geometrischer und Werkstofflicher Imperfektionen", *Heft 11*, pp.329-338, 1977.
- [120] DIN 4114, Teil 1, "DIN. Stabilitätsfälle im stahlbau, knicken von Staben und Stabwerken", Deutsches Institut für normung, Berlin, Entwurf, 1978.

- [121] J. B. Dwight, "Use of Perry formula to represent the new european strut curves",
Cambridge University, engineering department, report n CUED/C-struct/TR.30, 1972.

11. Annexes

11.1. Annex 1 – Geometrical dimensions

Table 54 – Measured geometrical dimensions

Test #	Specimen	H or D [mm]	B [mm]	t [mm]
1	RHS_LC1_S355CF_200x100x4	200	100.7	3.78
2	RHS_LC1_S355CF_220x120x6	220.42	120.57	5.82
3	RHS_LC1_S355HF_250x150x5	250	150.25	5.22
4	RHS_LC1_S355HF_200x100x5	198.7	99.2	5.27
5	SHS_LC1_S355CF_200x200x5	200	198.8	4.68
6	SHS_LC1_S355CF_200x200x6	200.6	200.5	5.7
7	SHS_LC1_S355HF_200x200x5	200	198.8	5.17
8	SHS_LC1_S355HF_200x200x6.3	199.5	199	6.58
9	CHS_LC1_S355CF_159x6.3	159	-	6.5
10	CHS_LC1_S355HF_159x6.3	159	-	6.9
11	CHS_LC1_S355HF_159x5	159	-	5.48
12	CHS_LC1_S355HF_159x7.1	159	-	7.5
13	RHS_LC2_S355CF_200x100x4	200.1	100.7	3.96
14	RHS_LC2_S355CF_220x120x6	219	120.5	6.25
15	RHS_LC2_S355HF_250x150x5	249.5	149.5	5.25
16	RHS_LC2_S355HF_200x100x5	-	-	-
17	SHS_LC2_S355CF_200x200x5	200.44	200.94	4.92
18	SHS_LC2_S355CF_200x200x6	200.2	200.25	6.1
19	SHS_LC2_S355HF_200x200x5	200.4	200.94	5.21
20	SHS_LC2_S355HF_200x200x6.3	200.3	199.5	6.55
21	CHS_LC2_S355CF_159x6.3	159	-	6.9
22	CHS_LC2_S355HF_159x6.3	159	-	6.4
23	CHS_LC2_S355HF_159x5	159	-	5.5
24	CHS_LC2_S355HF_159x7.1	-	-	-
25	RHS_LC3_S355CF_200x100x4	200	100.7	4.07
26	RHS_LC3_S355CF_220x120x6	220	120.56	6.25
27	RHS_LC3_S355HF_250x150x5	250.1	149.5	4.87
28	RHS_LC3_S355HF_200x100x5	198.2	99.2	5.48
29	SHS_LC3_S355CF_200x200x5	200.44	200.94	4.98
30	SHS_LC3_S355CF_200x200x6	200.25	199.9	6.1
31	SHS_LC3_S355HF_200x200x5	199.4	198.8	5.23
32	SHS_LC3_S355HF_200x200x6.3	200.6	199.3	6.32
33	CHS_LC3_S355CF_159x6.3	159	-	6.9
34	CHS_LC3_S355HF_159x6.3	159	-	6.28
35	CHS_LC3_S355HF_159x5	159	-	5.49
36	CHS_LC3_S355HF_159x7.1	159	-	7.13
37	2_SHS_LC1_S355CF_200x200x6	200.4	199.4	5.9

38	2_SHS_LC2_S355CF_200x200x6	200.6	199.9	6.1
39	2_SHS_LC3_S355CF_200x200x6	200	200	6.2
40	RHS_LC4_S355CF_220x120x6	220	120.44	6.18
41	RHS_LC5_S355CF_220x120x6	220.5	120.57	6.2
42	RHS_LC6_S355CF_220x120x6	219.5	120.5	6.26
43	RHS_LC4_S355CF_200x100x4	200.44	100.64	4.06
44	RHS_LC5_S355CF_200x100x4	200.5	100.26	4.09
45	RHS_LC6_S355CF_200x100x4	200	100.51	3.9
46	RHS_Stub_S355CF_200x100x4	200.5	100.28	3.69
47	RHS_Stub_S355CF_220x120x6	220.6	120.02	5.85
48	RHS_Stub_S355HF_250x150x5	250	150	5.05
49	RHS_Stub_S355HF_200x100x5	199.2	100.01	5.3
50	SHS_Stub_S355CF_200x200x5	200	201.5	4.72
51	SHS_Stub_S355CF_200x200x6	200	199.7	5.9
52	SHS_Stub_S355HF_200x200x5	200.1	200.2	5.14
53	SHS_Stub_S355HF_200x200x6.3	199.9	199.9	6.42
54	CHS_Stub_S355CF_159x6.3	159	-	6.76
55	CHS_Stub_S355HF_159x6.3	159	-	6.92
56	CHS_Stub_S355HF_159x5	159	-	5.42
57	CHS_Stub_S355HF_159x7.1	159	-	7.45

11.2. Annex 2 – Detailed results of tensile tests

Table 55 – Measured material properties

Coupon	Cut from section	Position	E [N/mm ²]	f_y [N/mm ²]	ϵ_y [%]	f_u [N/mm ²]	ϵ_u [%]	ϵ_T^* [%]	f_u / f_y [-]	E_m [N/mm ²]	f_{ym}^{**} [N/mm ²]	ϵ_y [%]	f_{um} [N/mm ²]	ϵ_{um} [%]	ϵ_{Tm} [%]	$(f_u / f_y)_m$ [-]
1_1L	RHS 200x100x5 S355 Hot- finished	Flat a	217303	426	0.19	525	17.2	25.9	1.23	215000	420	0.19	520	17.5	26.4	1.23
1_2L		Flat b	214437	431	0.20	514	18	24.8	1.19							
1_1S		Flat c	215984	421	0.19	530	17.6	28	1.25							
1_2S		Flat d	215770	406	0.18	511	18.3	27	1.25							
1_1C		Corner a	202788	404	0.19	505	14.3	16.7	1.25	210394	411	0.19	512	14.7	16.65	1.24
1_2C		Corner b	218000	418	0.19	520	15.2	16.6	1.24							
2_1L	RHS 200x100x4 S355 Cold-formed	Flat a	215270	478	0.22	573	11	17.7	17.78	216630	494.6	0.22	611	11.9	19.65	1.23
2_2L		Flat b	219391	486	0.22	588	12.6	18.4	18.34							
2_1S		Flat c	212861	512	0.24	654	12.5	20.2	22.3							
2_2S		Flat d	219000	501	0.22	630	11.6	22.3	20.2							
2_1C		Corner a	215000	-	-	612	0.84	2.7	2.7	213000	-	-	601	1.2	2.9	-
2_2C		Corner b	211000	-	-	560	1.56	3.1	3.13							
3_1	SHS 200x200x6 S355 Cold-formed	Flat b	211230	492	0.23	590	13.4	24.5	1.19	217363	500.5	0.23	596	13.8	23.25	1.19
3_2		Flat a	221638	496.3	0.22	588	12.6	22.3	1.18							
3_3		Flat c	216959	481.4	0.22	597	13.1	19.6	1.24							
3_4		Flat d	219628	532	0.24	612	16.3	26.6	1.15							
3_1C		Corner a	205000	-	-	630.5	1.47	2.8	-	210500	-	-	617.8	1.1	1.9	-
3_2C		Corner b	216000	-	-	605.1	0.74	1.1	-							
4_1	SHS 200x200x5 S355 Hot- finished	Flat a	211579	477.7	0.22	525.1	15.02	23.7	1.09	211489	475	0.22	523	14.6	25.5	1.1
4_2		Flat b	212313	461	0.21	511.9	15.53	25.1	1.11							
4_3		Flat c	210343	469	0.22	518.18	14.96	25.7	1.1							
4_4		Flat d	211724	494	0.23	537.44	13.06	27.7	1.08							
4_1C		Corner a	203940	579.5	0.28	611.6	8.8	14.2	1.05	211023	544	0.25	578.2	8.93	12	1.06
4_2C		Corner b	218105	508.7	0.23	544.8	9.1	9.8	1.07							

5_1	SHS 200x200x5 S355 Cold-formed	Flat c	218000	488.2	0.22	593.8	14.73	23.4	1.21	214848	480.2	0.22	585	14.5	23.2	1.21
5_2		Flat b	220000	466.9	0.21	567.2	14.56	22.6	1.21							
5_3		Flat a	214000	495	0.23	580	14.57	21.5	1.17							
5_4		Flat d	207369	470.5	0.22	600	14.52	25.5	1.27							
5_1C		Corner a	213000	-	-	587.2	0.83	1.34	-	209500	-	-	573.35	1.2	2.5	-
5_2C		Corner b	206000	-	-	560	1.64	3.74	-							
6_1L	RHS 250x150x5 S355 Hot- finished	Flat a	213352	449.6	0.21	573	17	24.4	1.27	212190	447	0.21	576.6	17.7	26.1	1.28
6_2L		Flat b	214052	451.6	0.21	574.9	15.7	24.1	1.27							
6_1S		Flat c	215757	443.4	0.20	579.5	16.8	22.4	1.30							
6_2S		Flat d	205600	444.2	0.21	579.1	21.4	33.5	1.30							
6_1C		Corner a	211000	435	0.20	532	12.4	12.2	1.22	210750	435	0.20	535	11.7	11.6	1.23
6_2C		Corner b	210500	435	0.20	538	11.13	11.1	1.23							
7_1L	RHS 220x120x6 S355 Cold-formed	Flat a	203304	435.7	0.21	530.8	14.1	25.6	1.21	206597	454.7	0.22	563.6	15.5	25.6	1.23
7_2L		Flat b	219169	445.2	0.20	544.1	13.3	23.7	1.22							
7_1S		Flat c	207043	469.1	0.22	593.6	14.3	24.4	1.26							
7_2S		Flat d	196874	468.4	0.23	585.7	20.3	28.9	1.25							
7_1C		Corner a	203000	-	-	676.5	0.94	1.38	-	207000	-	-	644	1	1.6	-
7_2C		Corner b	211000	-	-	611.4	1.11	1.84	-							
8_1	SHS 200x200x6.3 S355 Hot- finished	Flat a	217132	452.8	0.20	494.2	15.4	22.62	1.09	215998	453	0.20	496	15.9	23.7	1.09
8_2		Flat b	215992	448.7	0.20	496	16.4	24.43	1.10							
8_1		Flat c	216535	449.2	0.20	503	15.8	24.2	1.11							
8_2		Flat d	214336	460	0.21	-	-	-	-							
8_1C		Corner a	209500	478	0.22	-	-	8.1	-	209750	482.6	0.23	523.4	7.6	7.73	1.08
8_2C		Corner b	210000	487.3	0.23	523.4	7.6	7.36	1.07							
10_1	CHS 159x5 S355 Hot-rolled	C_a	215000	455	0.21	573.5	7.02	8.4	1.26	215000	457.7	0.21	577.3	7.02	8.45	1.26
10_2		C_b	215000	460.5	0.21	581.2	7.02	8.5	1.26							
11_1	CHS 159x6.3 S355 Cold- formed	C_a	194654	607.3	0.31	628.2	1.1	1.92	1.03	194654	607.3	0.31	628.2	1.1	1.92	1.03
11_2		C_b	-	-	-	-	-	-	-							

New Design Method For The Cross-Section Resistance
Of Steel Hollow Sections

Annexes

12_1	CHS 159x7.1 S355 Hot-rolled	C_a	212000	442	0.20	557.1	12.7	15.2	1.26	212000	442	0.20	557.1	12.7	15.2	1.26
12_2		C_b	-	-	-	-	-	-	-							
13_1	CHS 159x6.3 S355 Hot-rolled	C_a	213000	458	0.21	673.6	13.3	16.7	1.47	213000	401.5	0.19	607.8	11.7	14.6	1.52
13_2		C_b	213500	345	0.18	542	10.1	12.5	1.57							

* ϵ_T Total strain at failure

** f_{ym} yield strength, upper yield strength for hot-finished and hot-rolled profiles and 0.2% proportional limit for cold-formed profiles

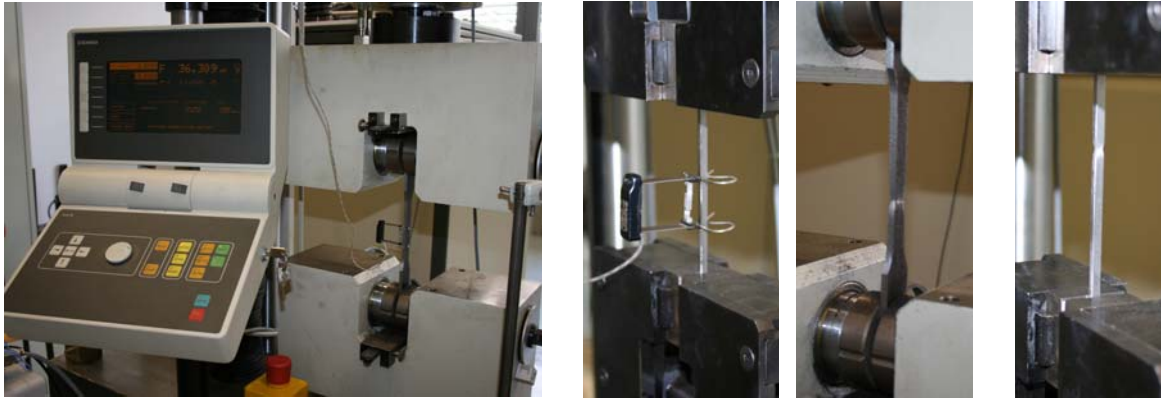


Figure 267 – Test setup and coupons before failure



Figure 268 – General view of the coupons before testing



Figure 269 – Curvature due to flexural stresses included in the cold formed profiles

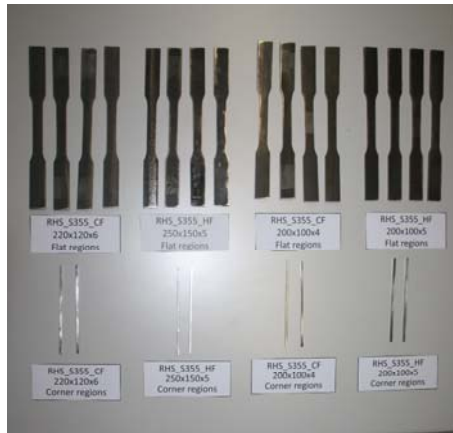


Figure 270 – Coupons extracted from square and rectangular sections before testing

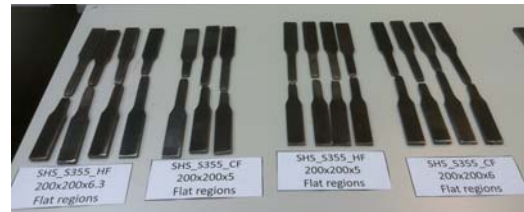


Figure 271 – Coupons extracted from square and rectangular sections after testing

11.3. Annex 3 – Detailed results of residual stresses determination

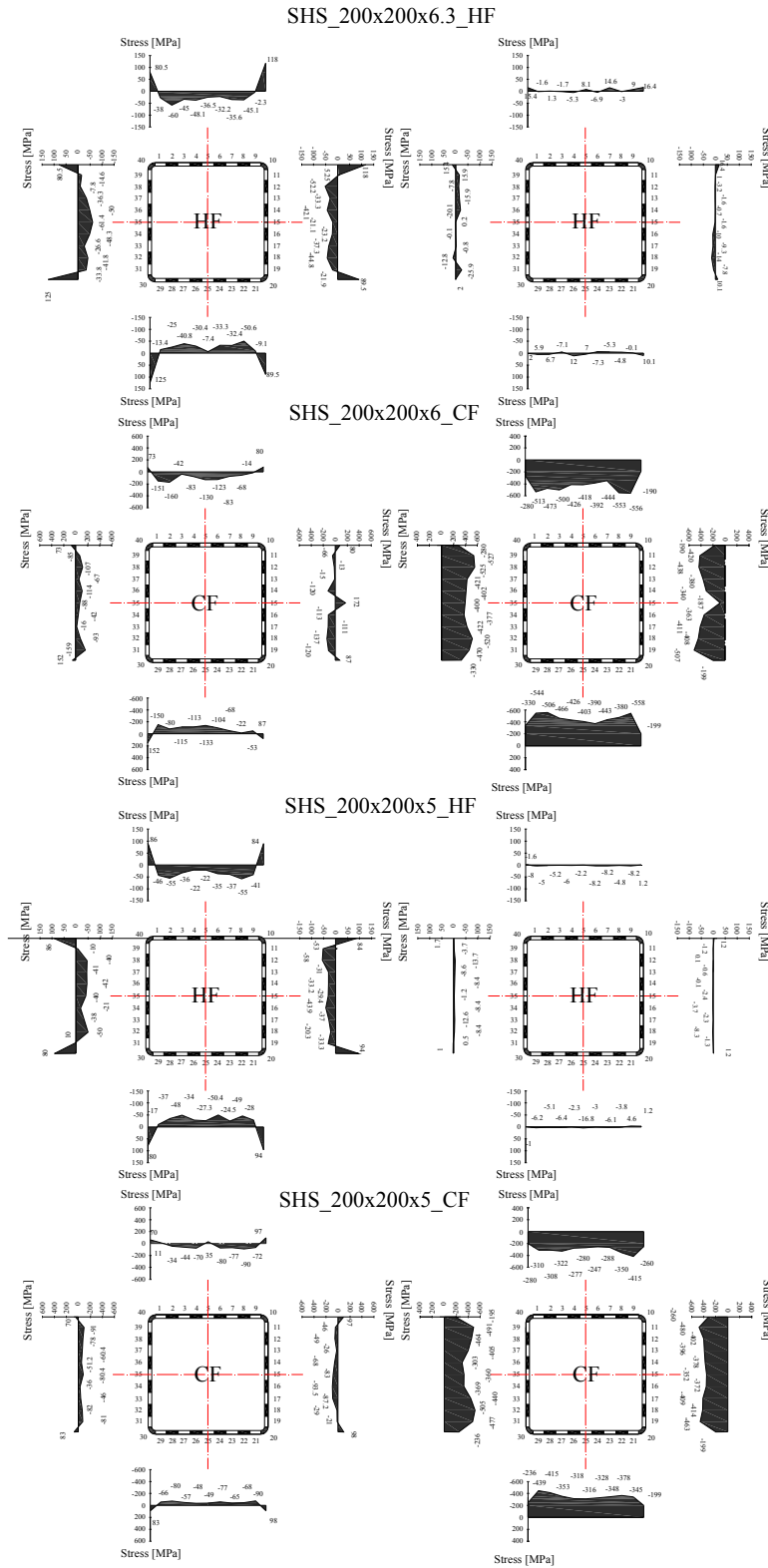


Figure 272 – Measured membrane (right column) and flexural (left column) residual stresses of square sections

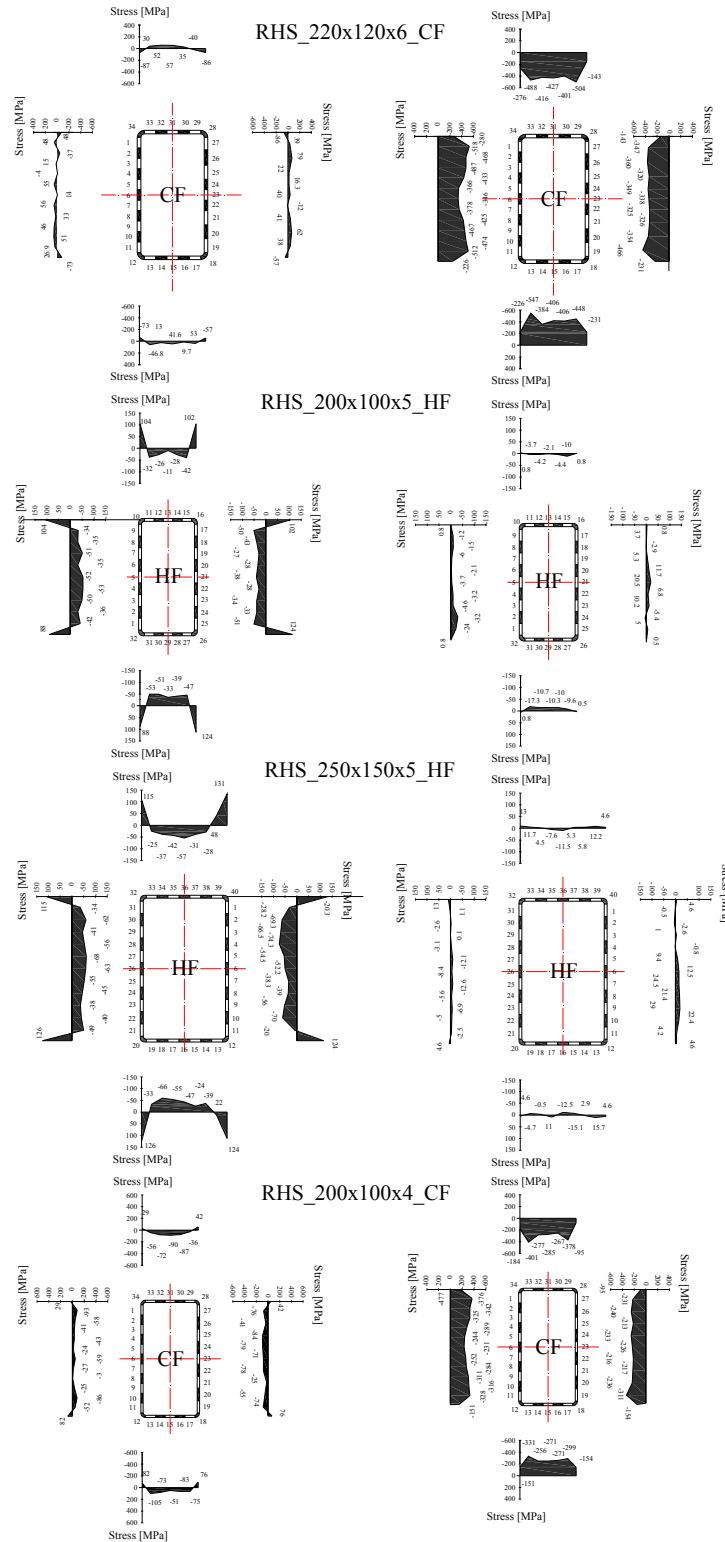


Figure 273 – Measured membrane (right column) and flexural (left column) residual stresses of rectangular sections

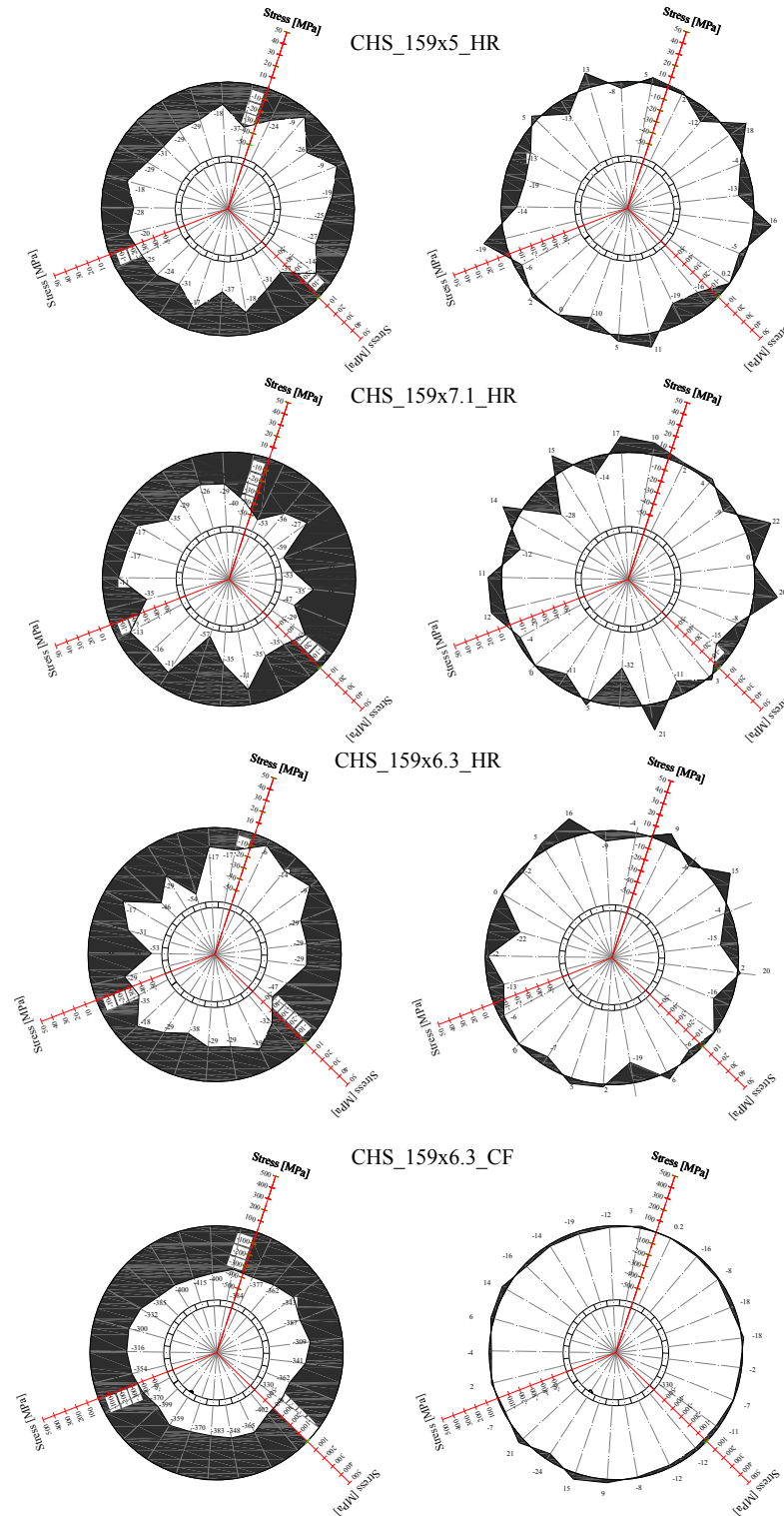


Figure 274 – Measured membrane (right column) and flexural (left column) residual stresses of circular sections

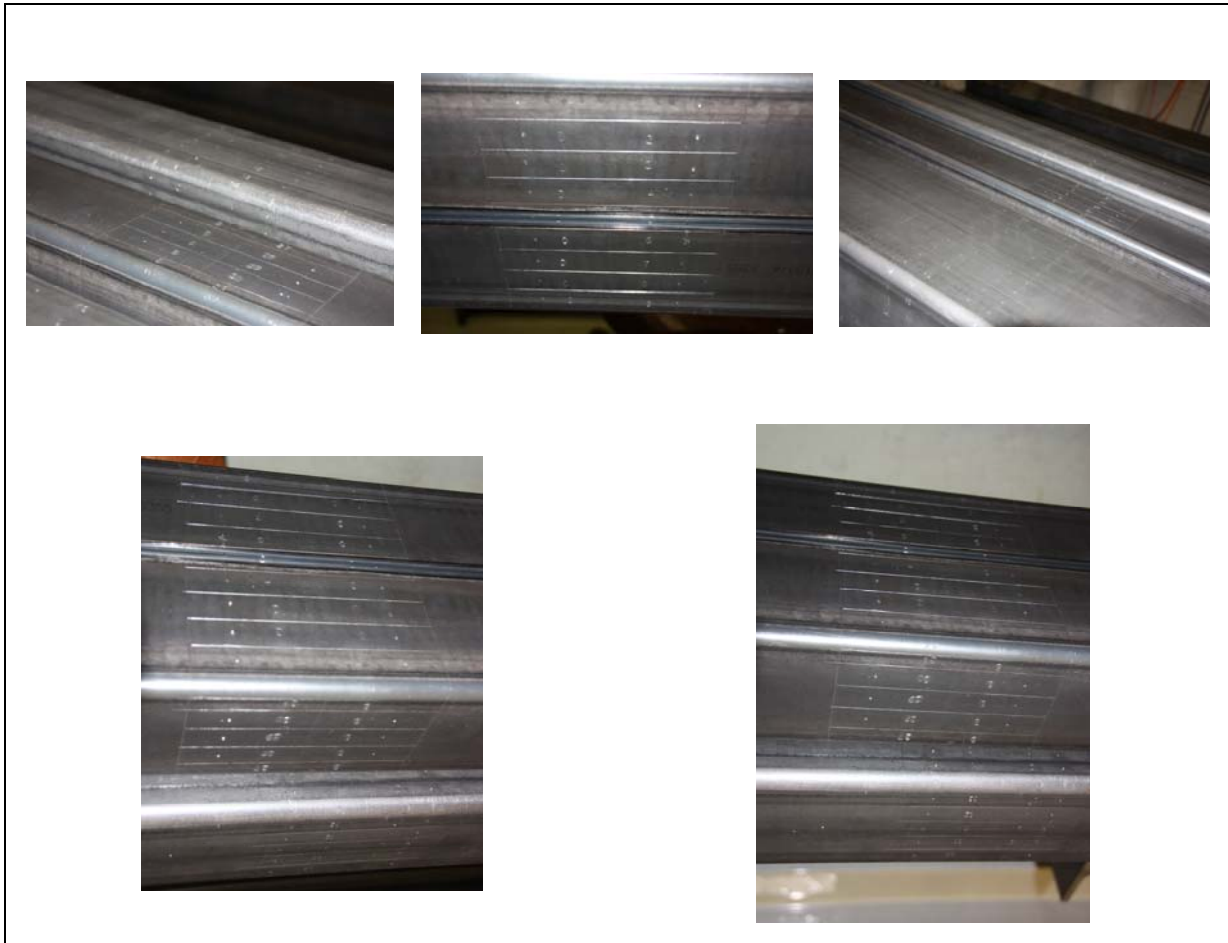


Figure 275 – Strip marking



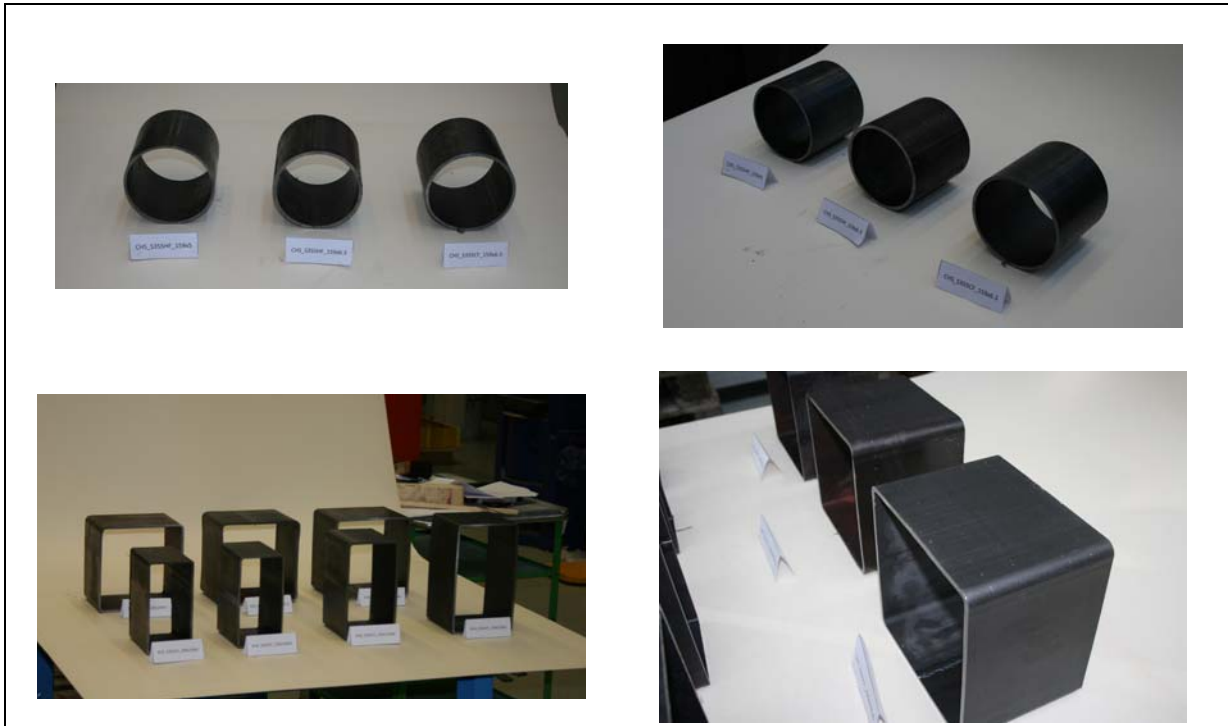


Figure 276 – Cutting the space reserved for residual stresses and containing the marked strips, after measuring initial lengths and curvatures of the corresponding strips

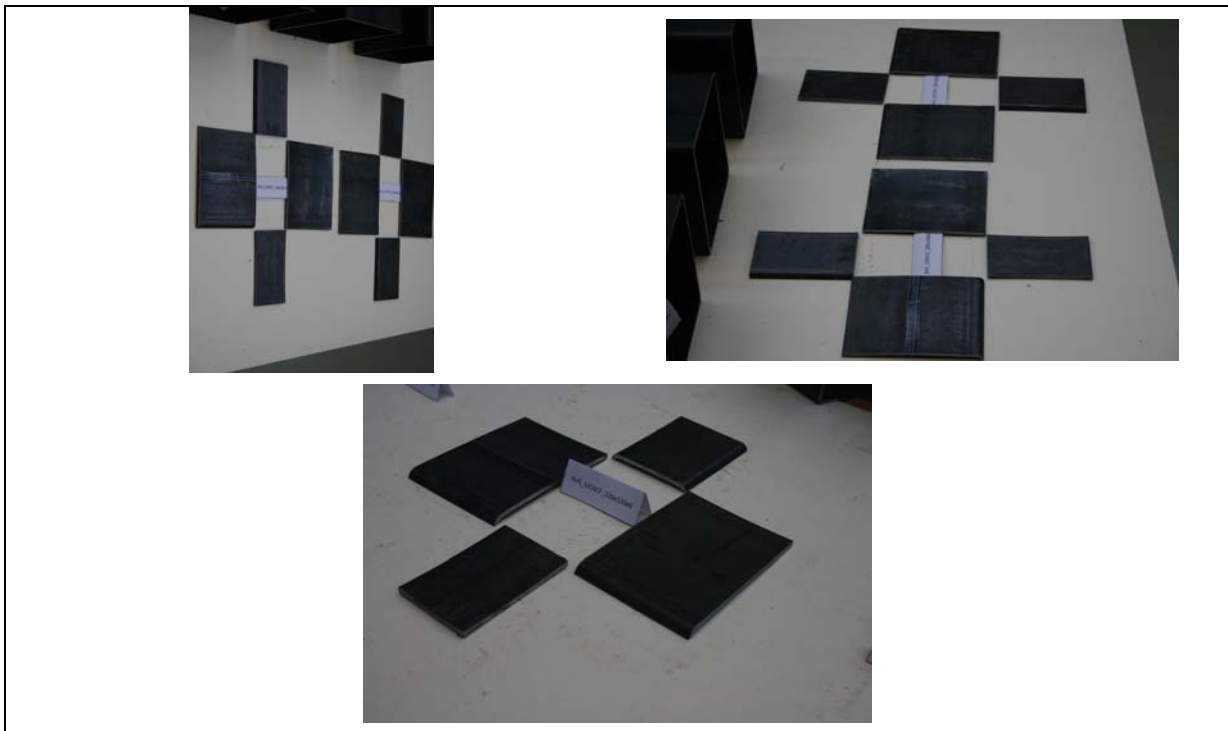


Figure 277 – Cutting of the constitutive plates (for circular profiles no need to pass through this phase because direct cutting of the strips is applied)



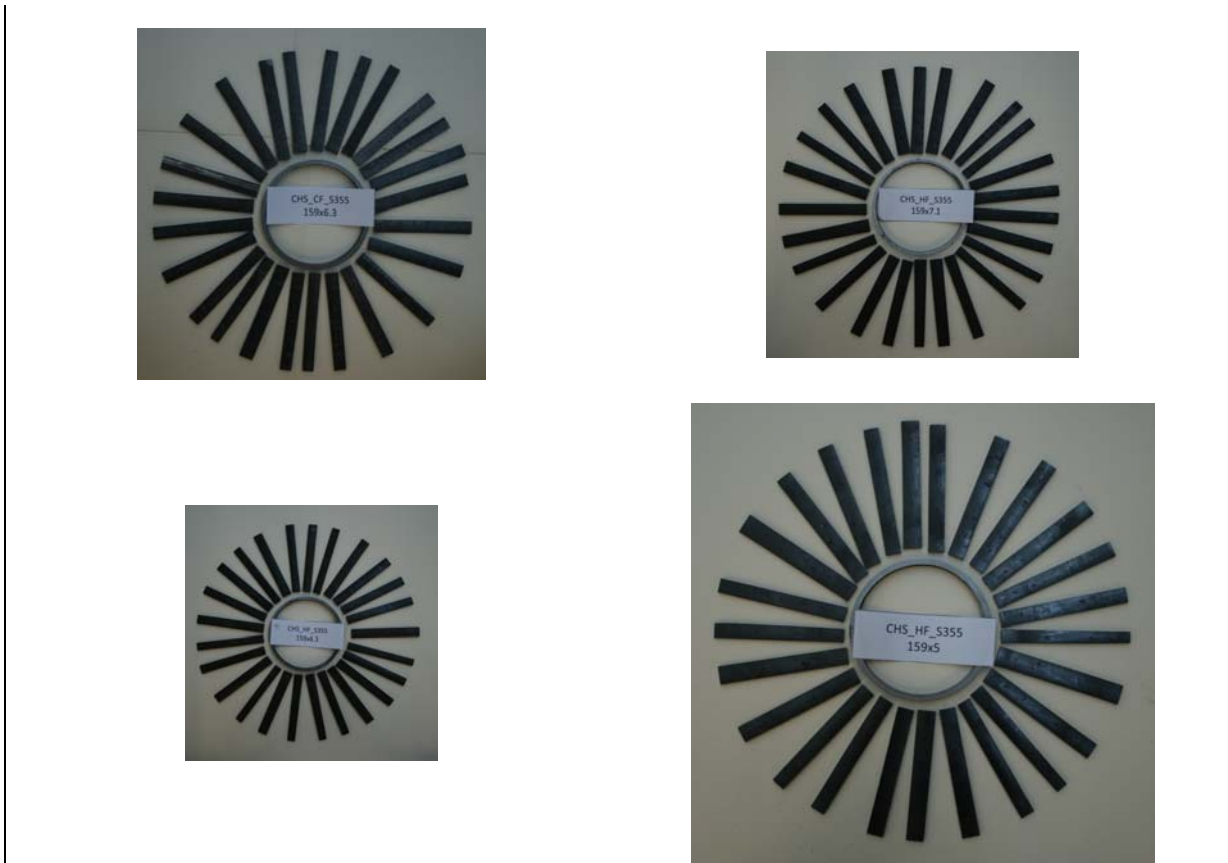


Figure 278 – Cutting of each strip corresponding to each section, and measurement of the final lengths and curvatures.

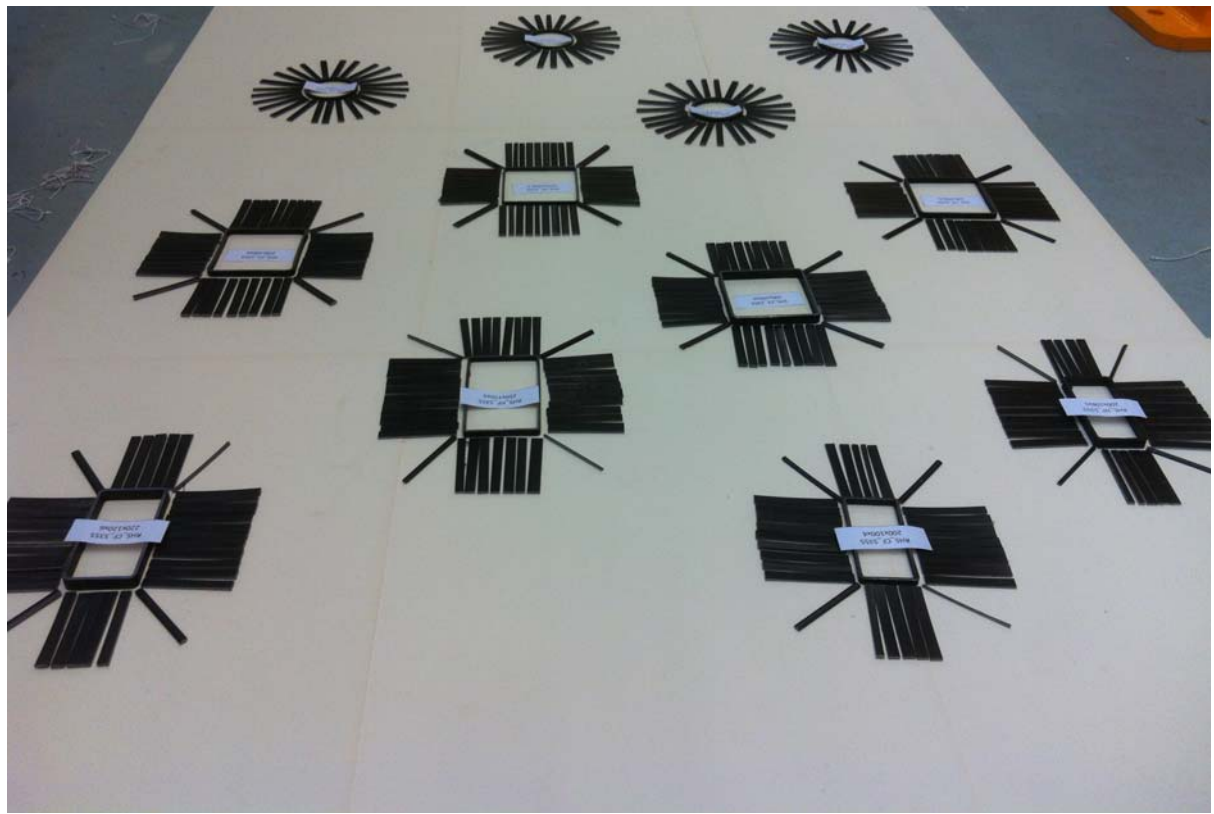
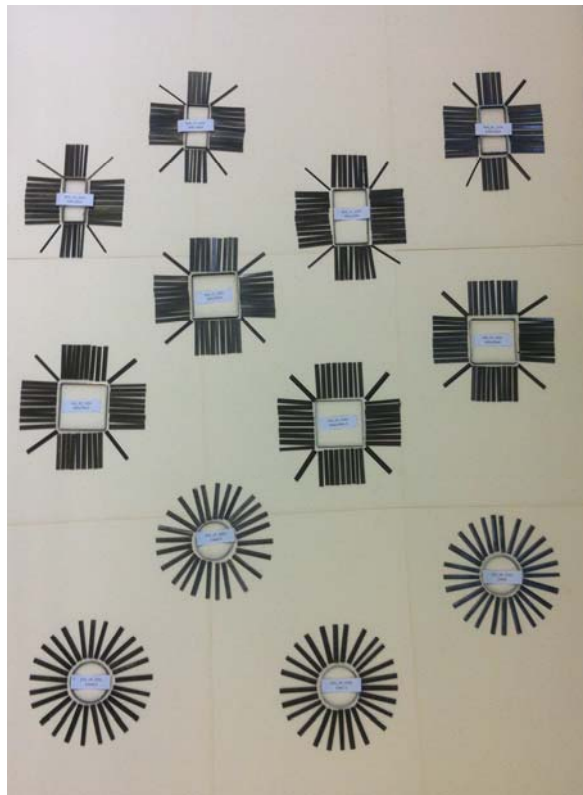




Figure 279 – General view of the sections' strips all together

11.4. Annex 4 – Detailed results of geometrical imperfection measurements

As already explained in section 2, the sections' geometrical imperfections were measured with respect to a set of linear variable transducers regularly spaced in a purposely-designed bar.

Several phases had to be followed before obtaining the final geometrical imperfections distributions:

- (i) **Phase 1:** LVDTs were initialized to zero reference values on a flat, perfectly horizontal thick marble, then placed upon the specimen;
- (ii) **Phase 2:** the values measured the 9 LVDTs were recorded, and extrapolation to the extremities of each specimen has been done based on the obtained data;
- (iii) **Phase 3:** a reference point at the beginning of each profile was selected, allowing setting this first value as a zero reference point, and all the other data were relative to this reference;
- (iv) **Phase 4:** a subtraction between the first and last value is done in this phase using the simple principle of Thales;
- (v) **Phase 5:** a final subtraction of each specimen's self-weight deflection is done;
- (vi) **Phase 6:** a double extrapolation is finally performed in order to fit the measured mesh into the numerical mesh of non-linear FE software FINELg; accordingly, the mesh used in the FE simulations contains the (measured) information on initial geometrical imperfections.

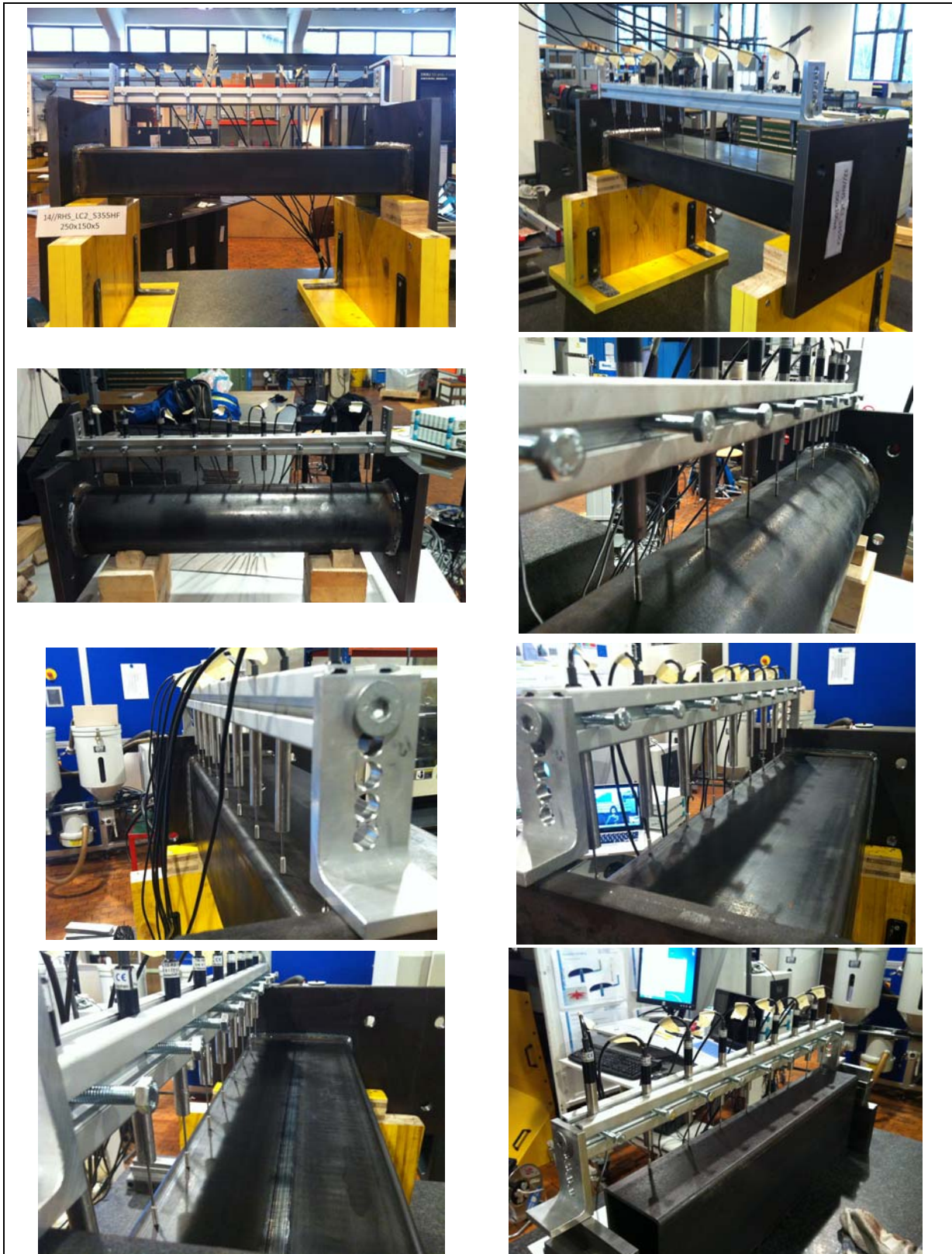


Figure 280 – General view of the set up with the bar containing the LVDTs for the imperfections measurements

11.5. Annex 5 – Detailed results of stub column tests

This annex presents the full set of results relative to stub column tests, and provides comparisons between experimental results and their numerical counterparts.

All measurements and results relative to a given test are summarized on a 3 pages standard format, as described in the following lines.

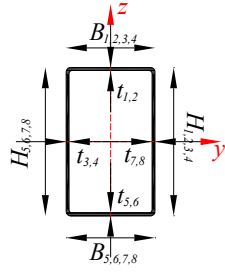
The first page provides:

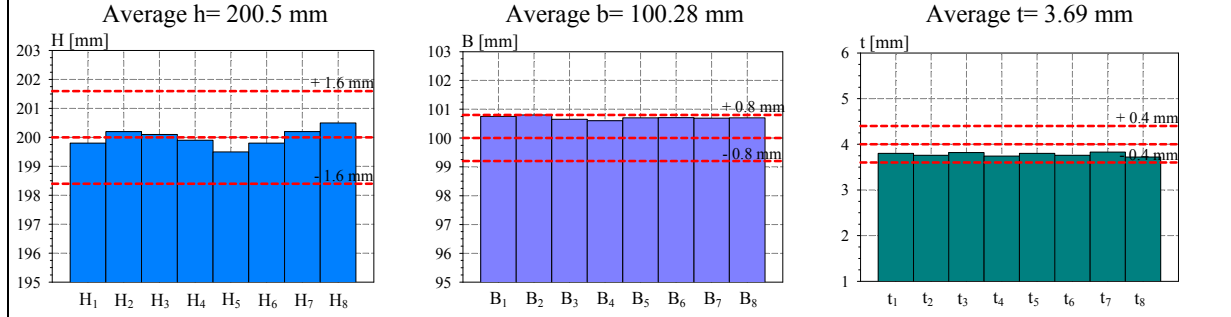
- (i) Specimen name, geometry and details;
- (ii) Geometrical measured dimensions with the correspondent tolerances;
- (iii) Measured material properties;
- (iv) Measured membrane and flexural stresses.

The second page provides measured geometrical imperfections, with contour plots of each plate's imperfections and two (amplified) 3D imperfect shapes with the measured mesh fitted in the non-linear finite element software.

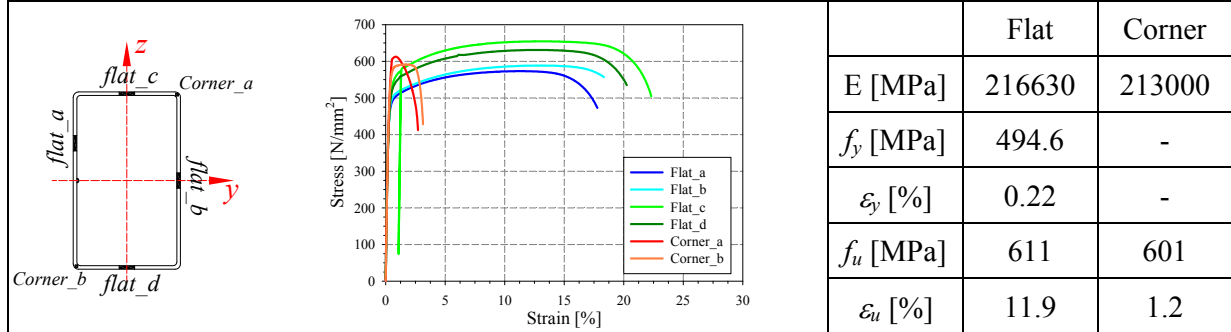
The third page provides:

- (i) Load-displacement curves from both experimental and numerical sources (at point load application);
- (ii) A diagram of strain gauges recordings;
- (iii) A comparison between material and stub column stress-strain curves;
- (iv) A qualitative comparison between experimental and FE buckling shape at failure.

<p>Specimen name</p> <p>RHS_S355_Stub 200x100x4 CF</p>	<p>Shape</p> 	<p>Details</p> <p>Shape: Rectangular Hollow Section</p> <p>Nominal yield limit: 355 MPa</p> <p>Load case: Stub, Pure compression</p> <p>H=200mm B=100mm t=4mm</p> <p>Fabrication process: Cold formed</p>
--	--	---



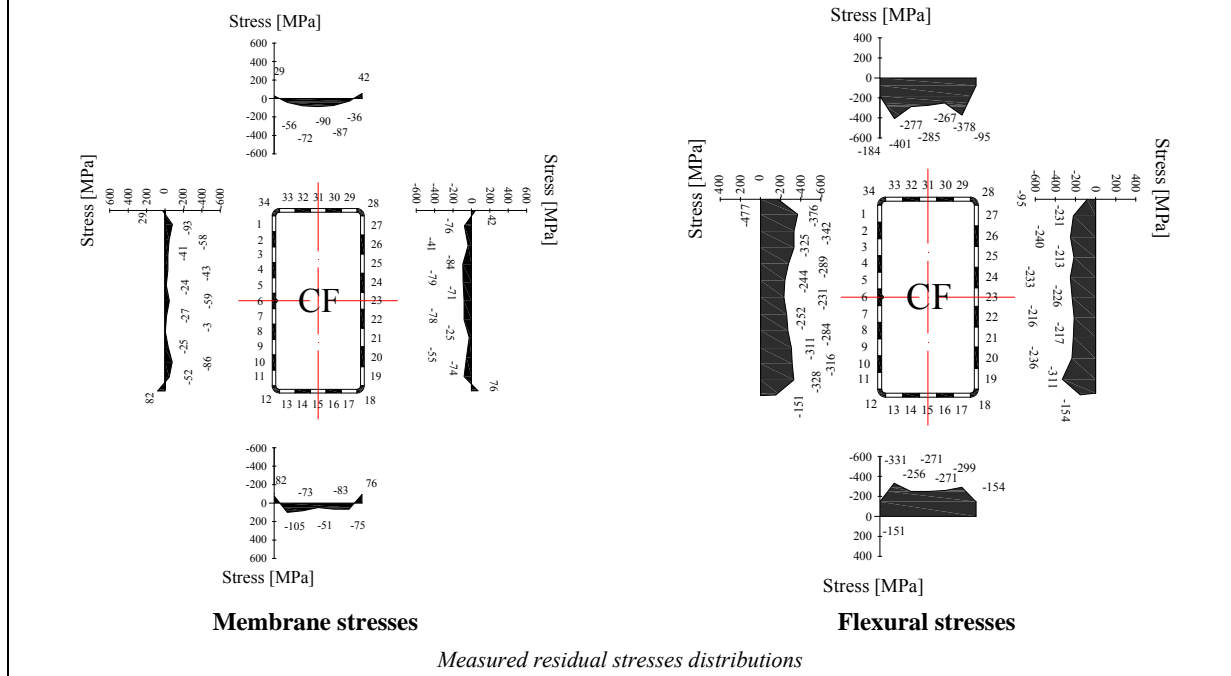
Cross-sectional measured dimensions and tolerances

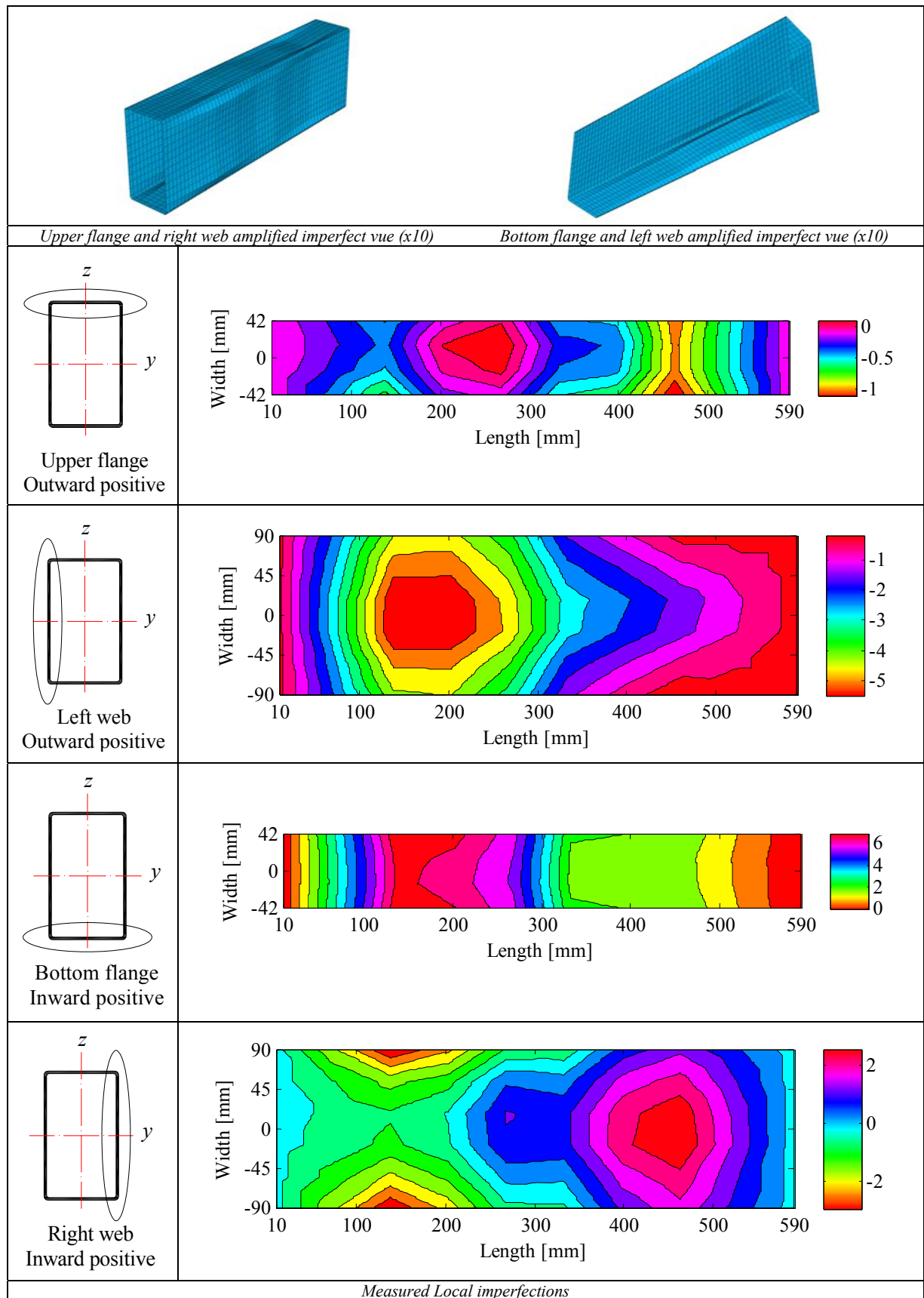


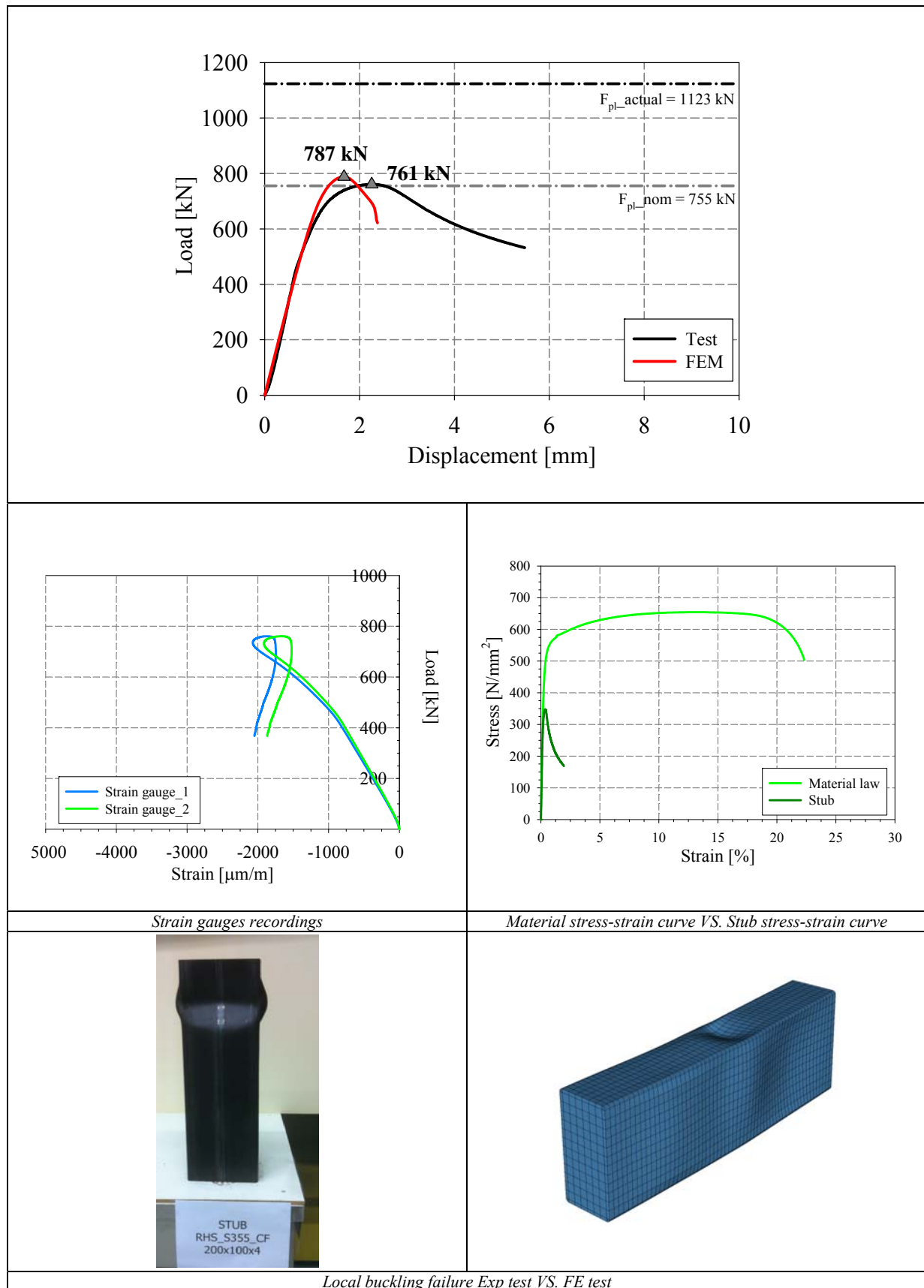
Tensile coupons location

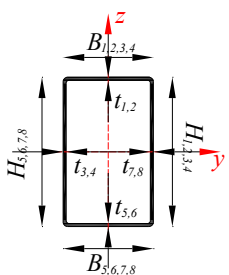
Material stress-strain curves

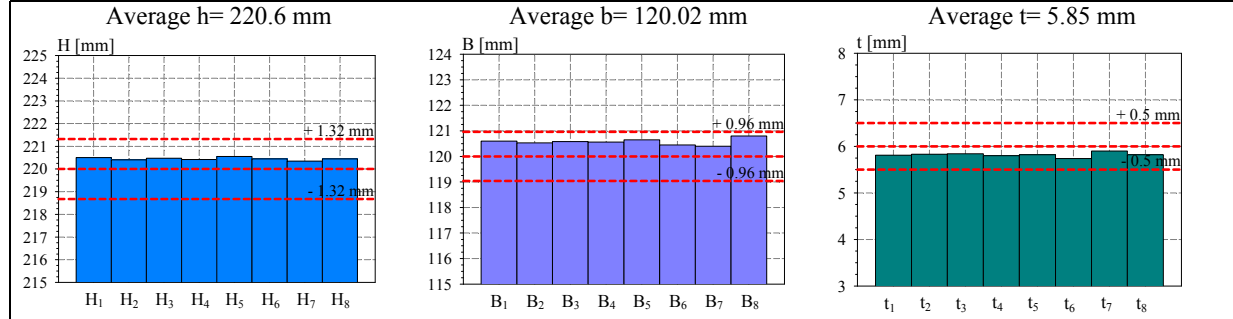
Material average properties



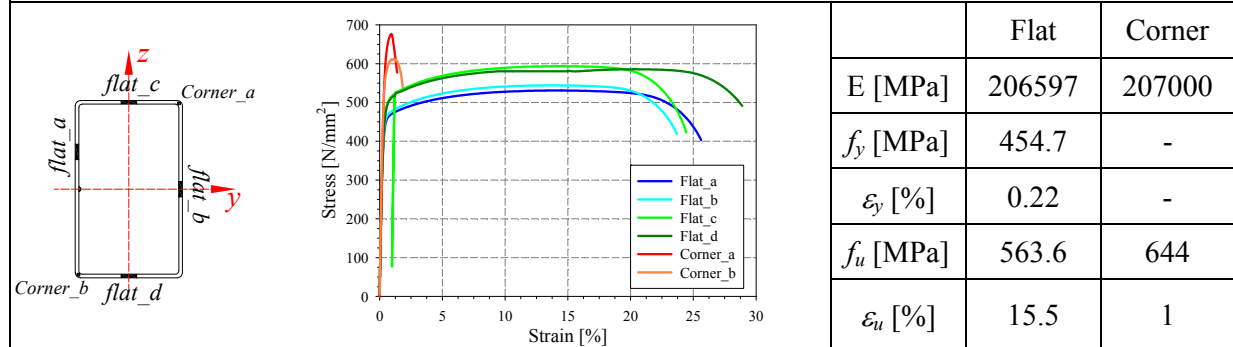




<p>Specimen name</p> <p>RHS_S355_Stub 220x120x6 CF</p>	<p>Shape</p> 	<p>Details</p> <p>Shape: Rectangular Hollow Section</p> <p>Nominal yield limit: 355 MPa</p> <p>Load case: Stub, Pure compression</p> <p>H=220mm B=120mm t=6mm</p> <p>Fabrication process: Cold formed</p>
--	--	---



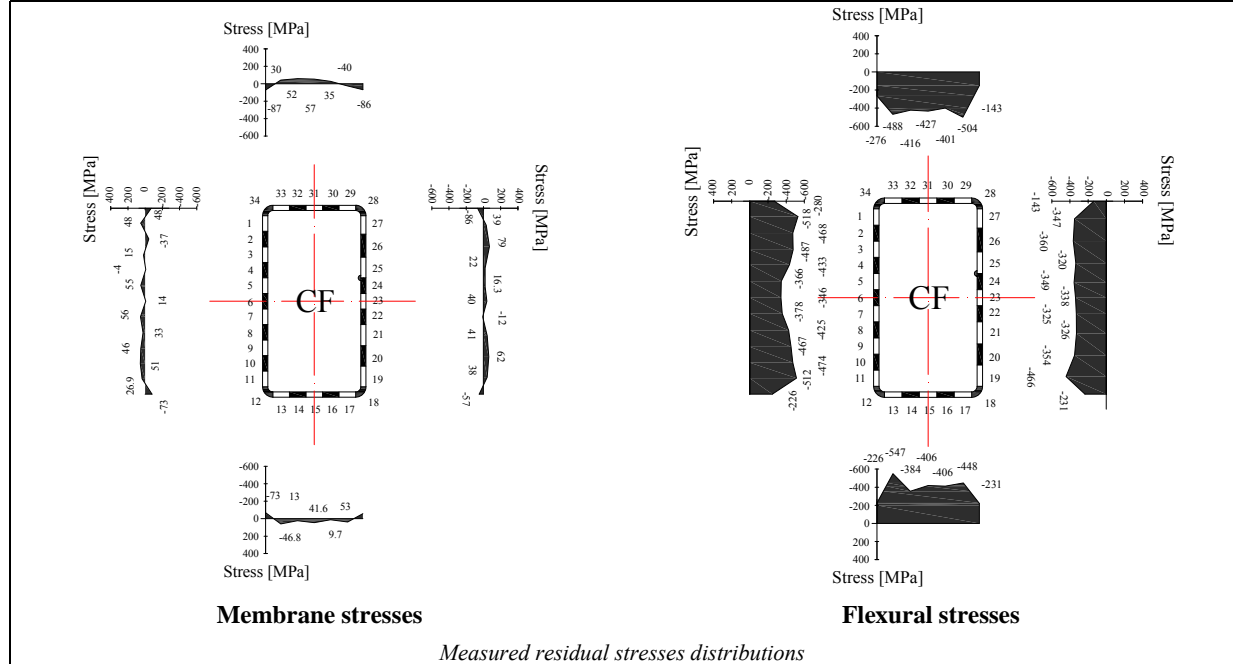
Cross-sectional measured dimensions and tolerances

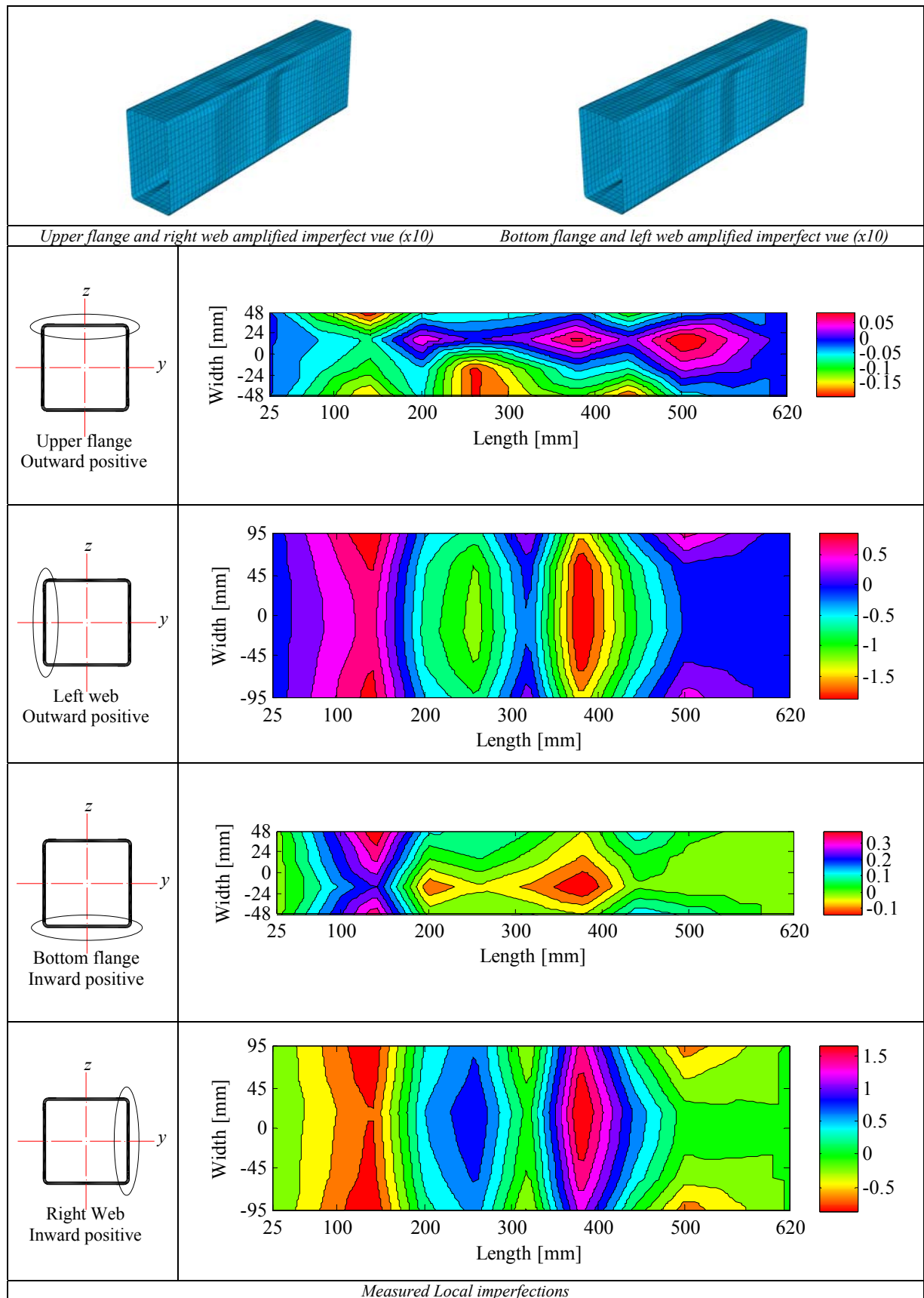


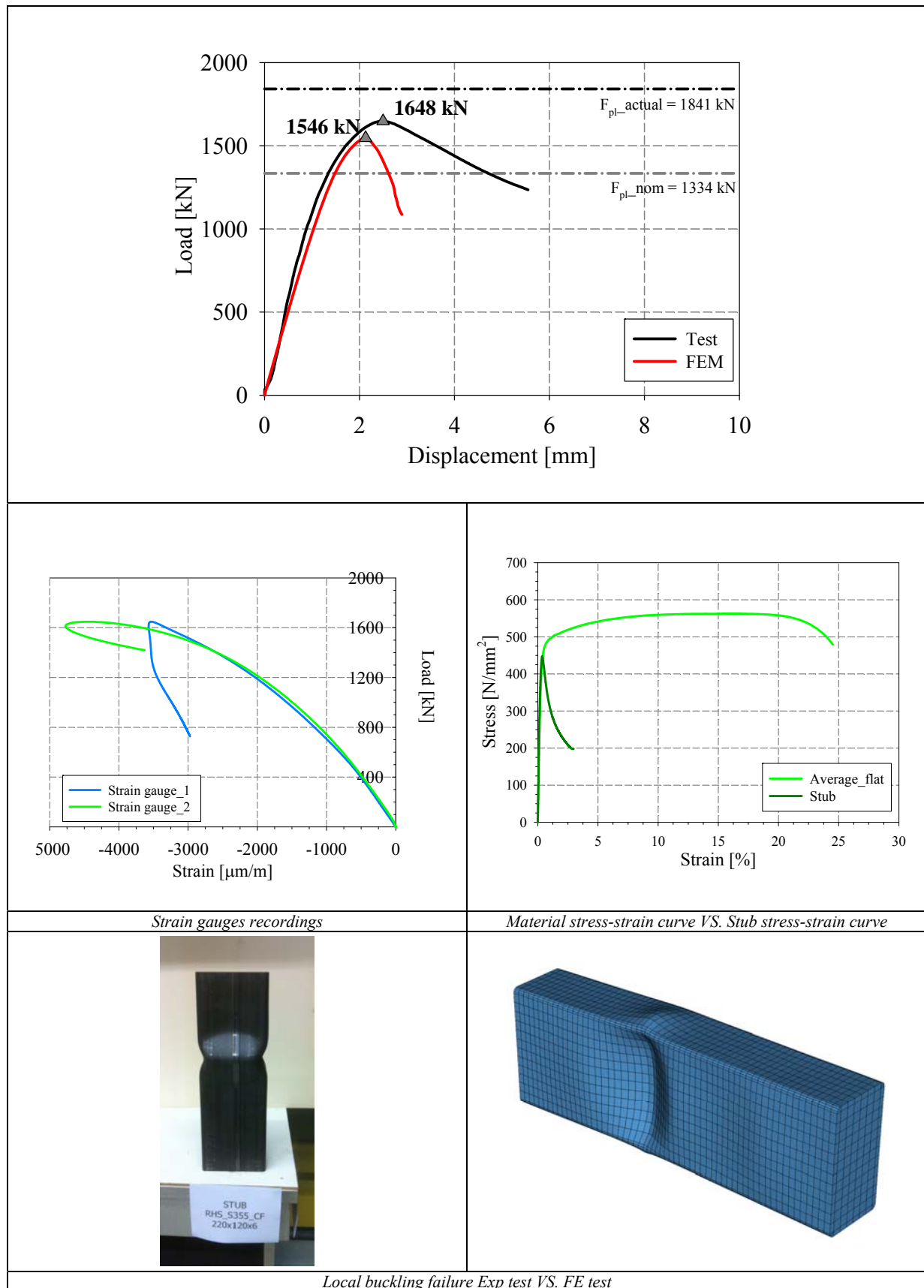
Tensile coupons location

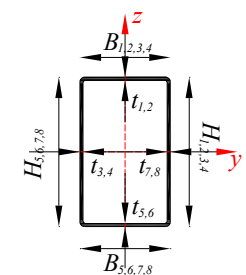
Material stress-strain curves

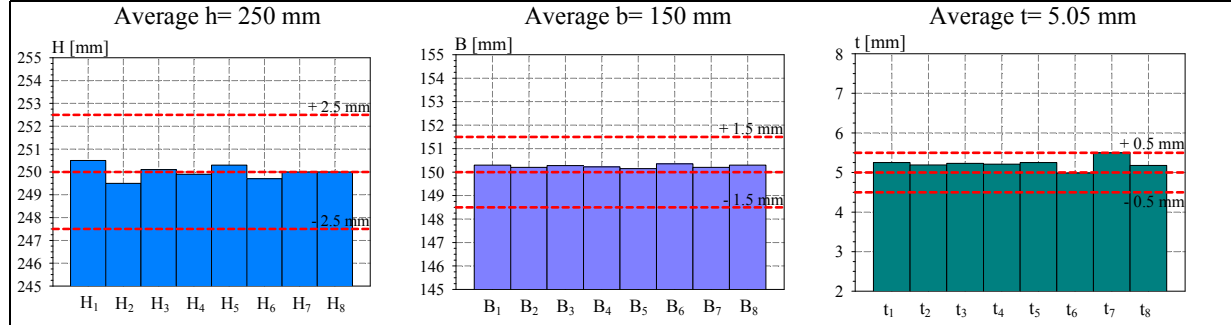
Material average properties



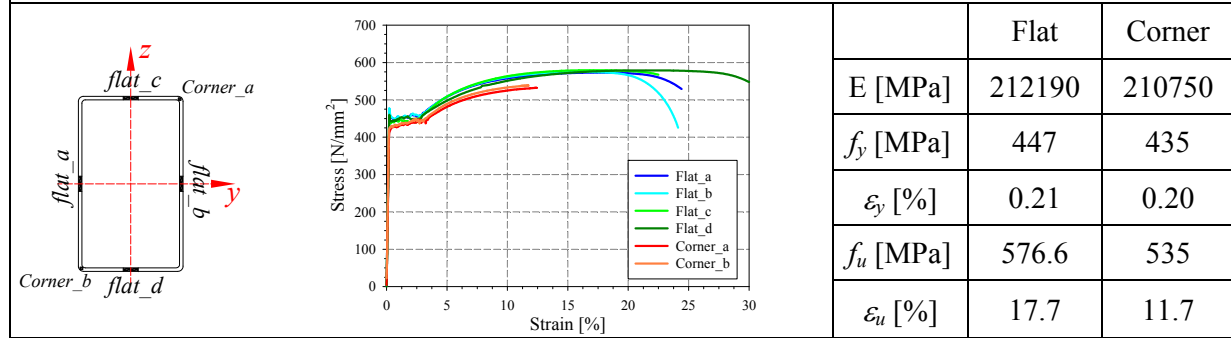




<p>Specimen name</p> <p>RHS_S355_Stub 250x150x5 HF</p>	<p>Shape</p> 	<p>Details</p> <p>Shape: Rectangular Hollow Section</p> <p>Nominal yield limit: 355 MPa</p> <p>Load case: Stub, Pure compression</p> <p>H=250mm B=150mm t=5mm</p> <p>Fabrication process: Hot formed</p>
--	--	--



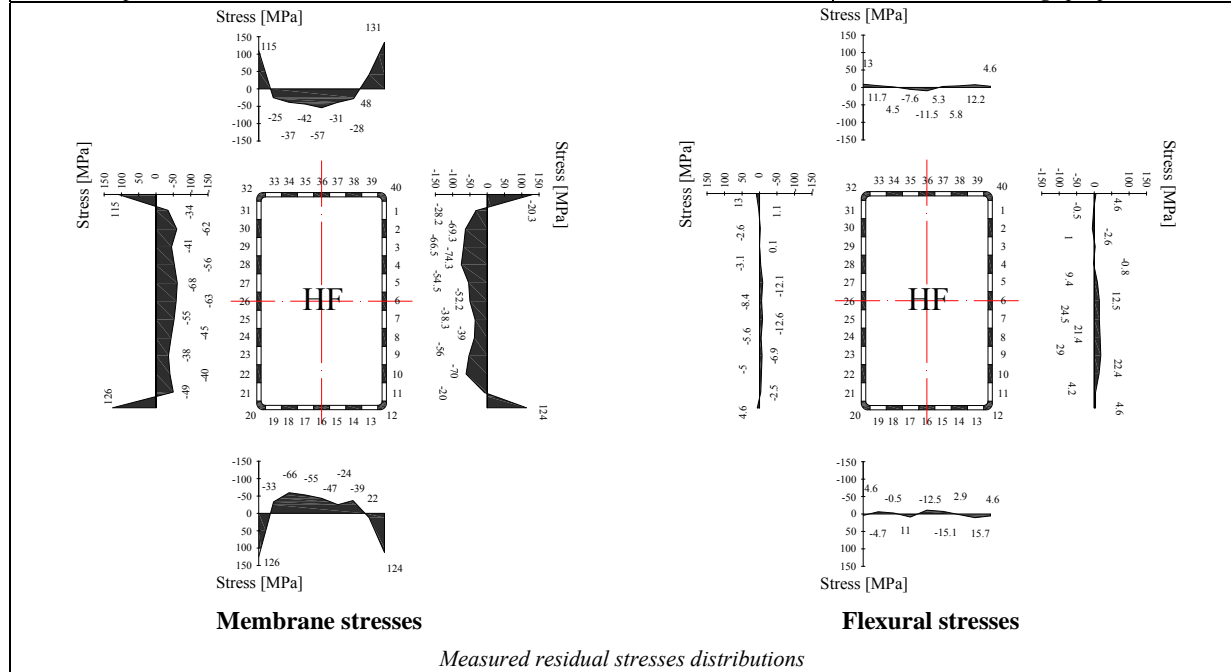
Cross-sectional measured dimensions and tolerances

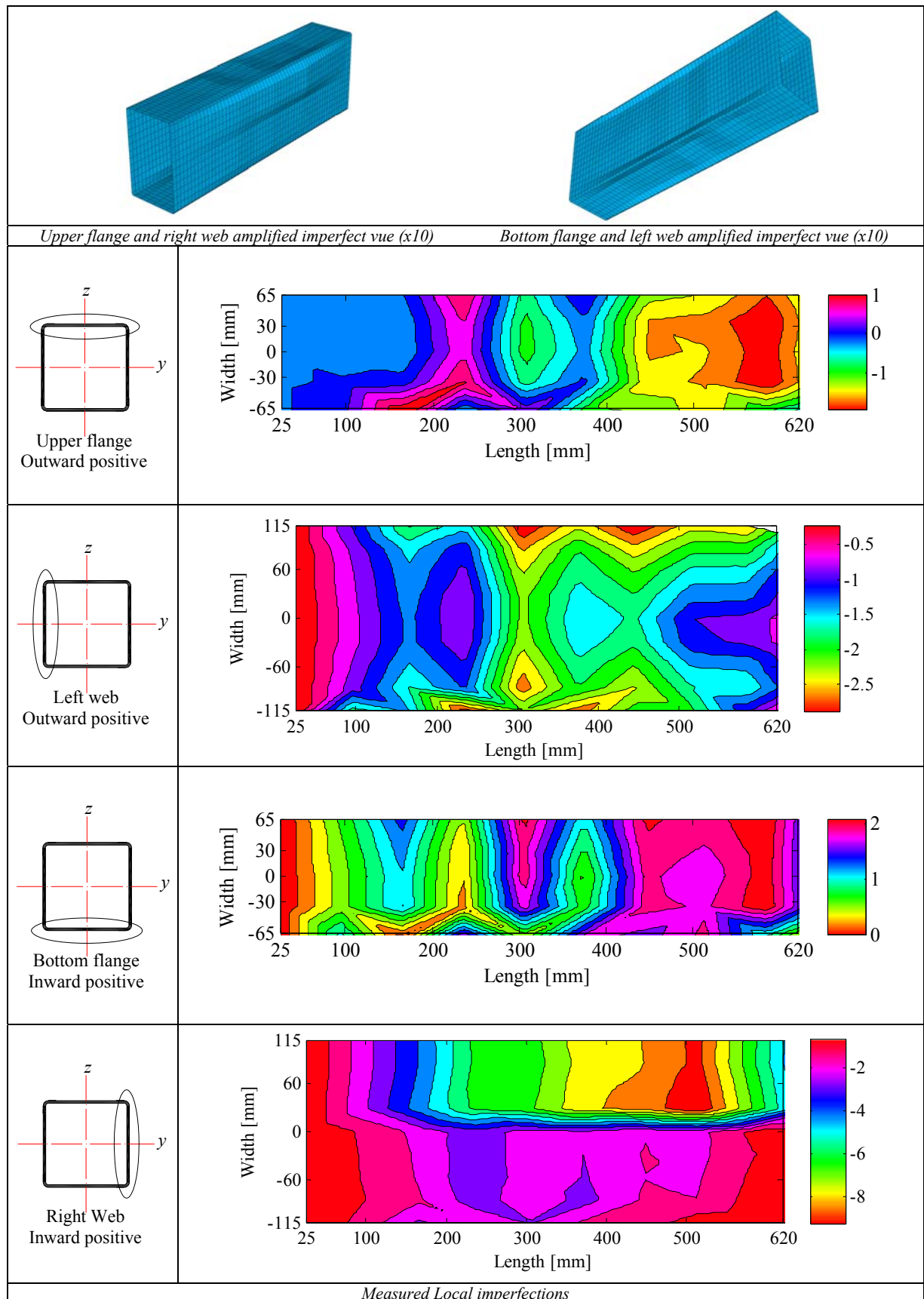


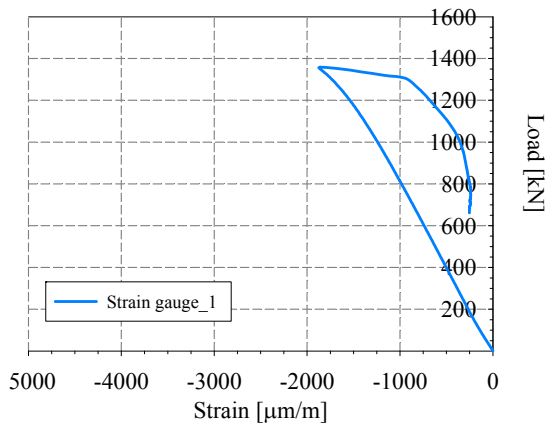
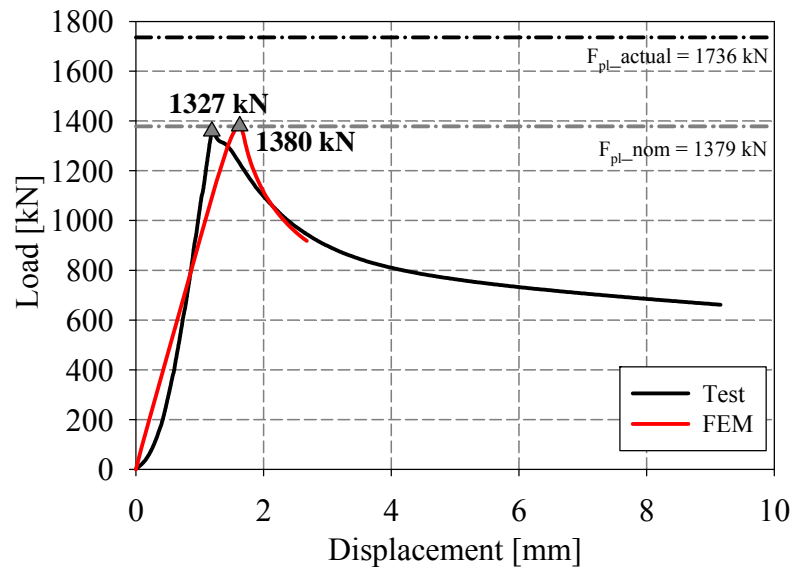
Tensile coupons location

Material stress-strain curves

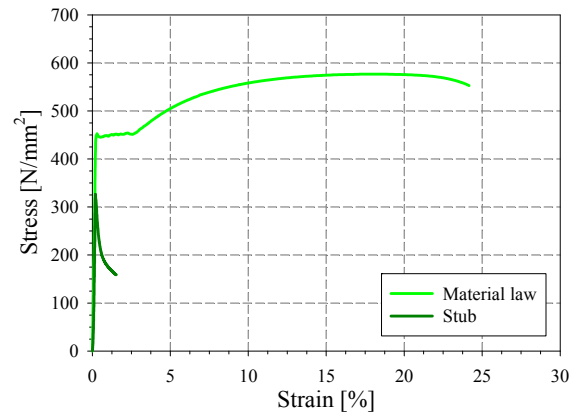
Material average properties



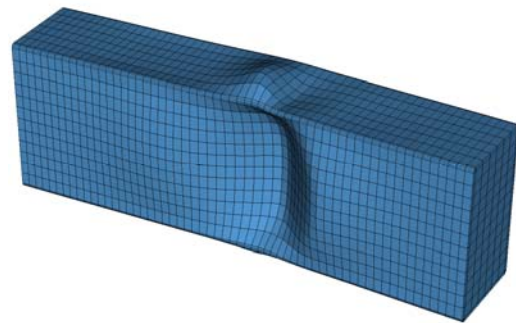




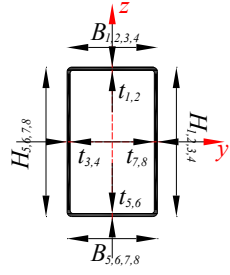
Strain gauges recordings

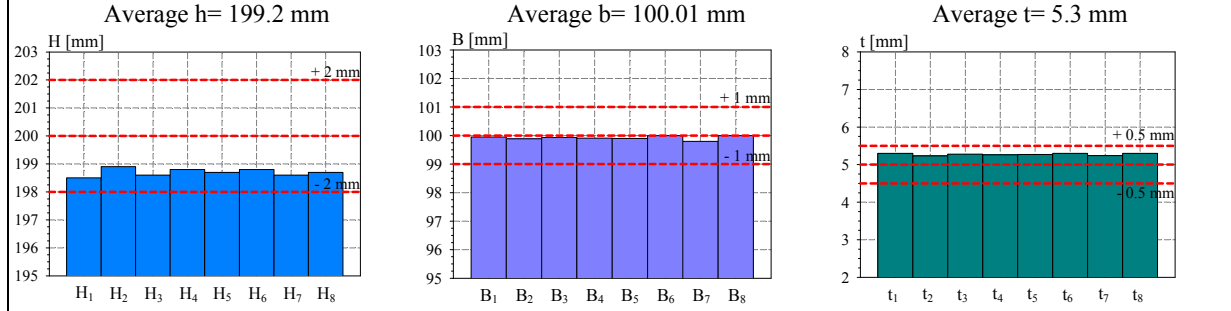


Material stress-strain curve VS. Stub stress-strain curve

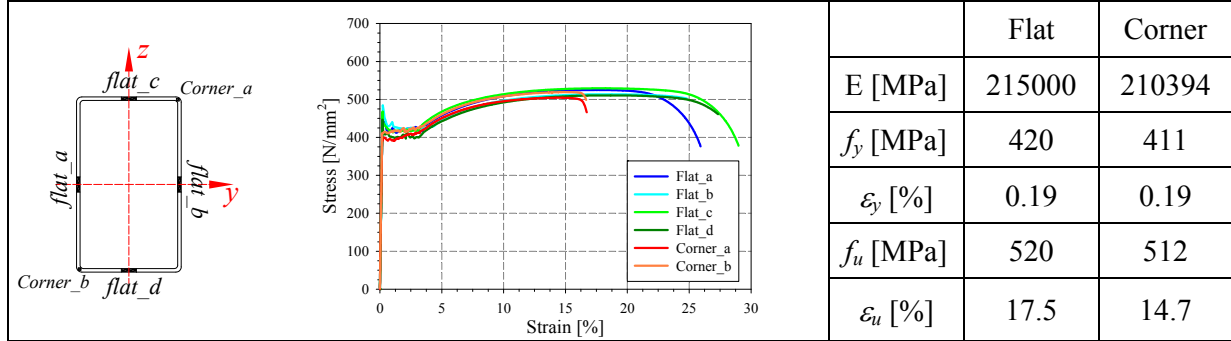


Local buckling failure Exp test VS. FE test

<p>Specimen name</p> <p>RHS_S355_Stub 200x100x5 HF</p>	<p>Shape</p> 	<p>Details</p> <p>Shape: Rectangular Hollow Section Nominal yield limit: 355 MPa Load case: Stub, Pure compression H=200mm B=100mm t=5mm Fabrication process: Hot formed</p>
--	--	--



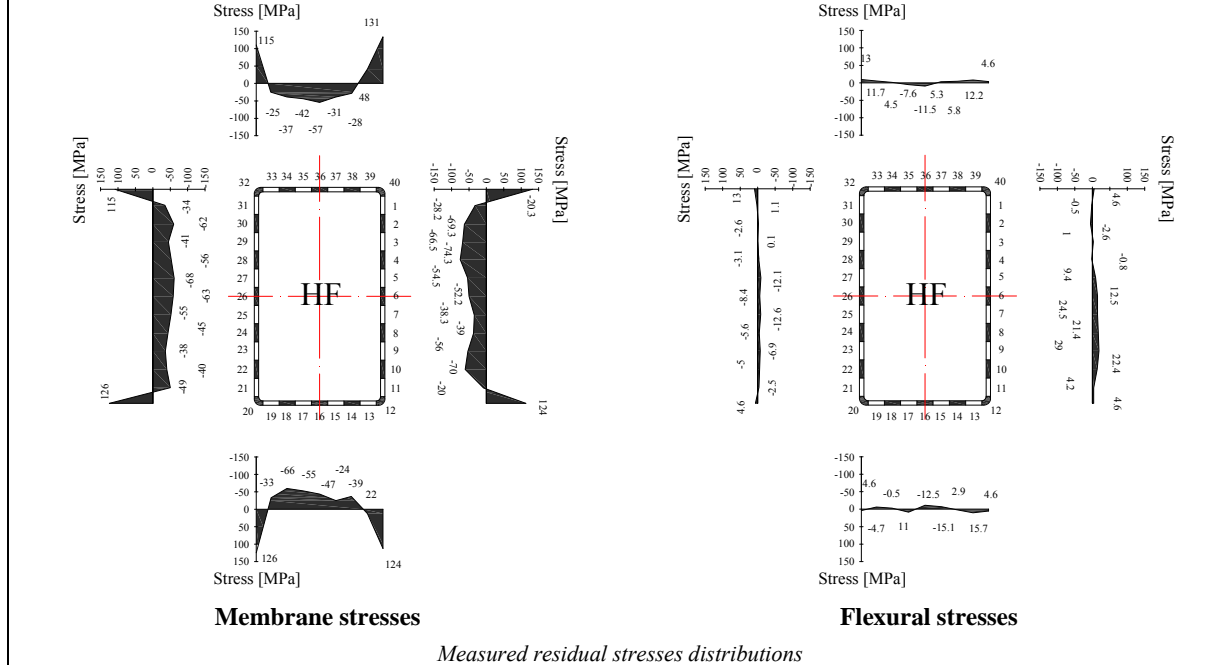
Cross-sectional measured dimensions and tolerances

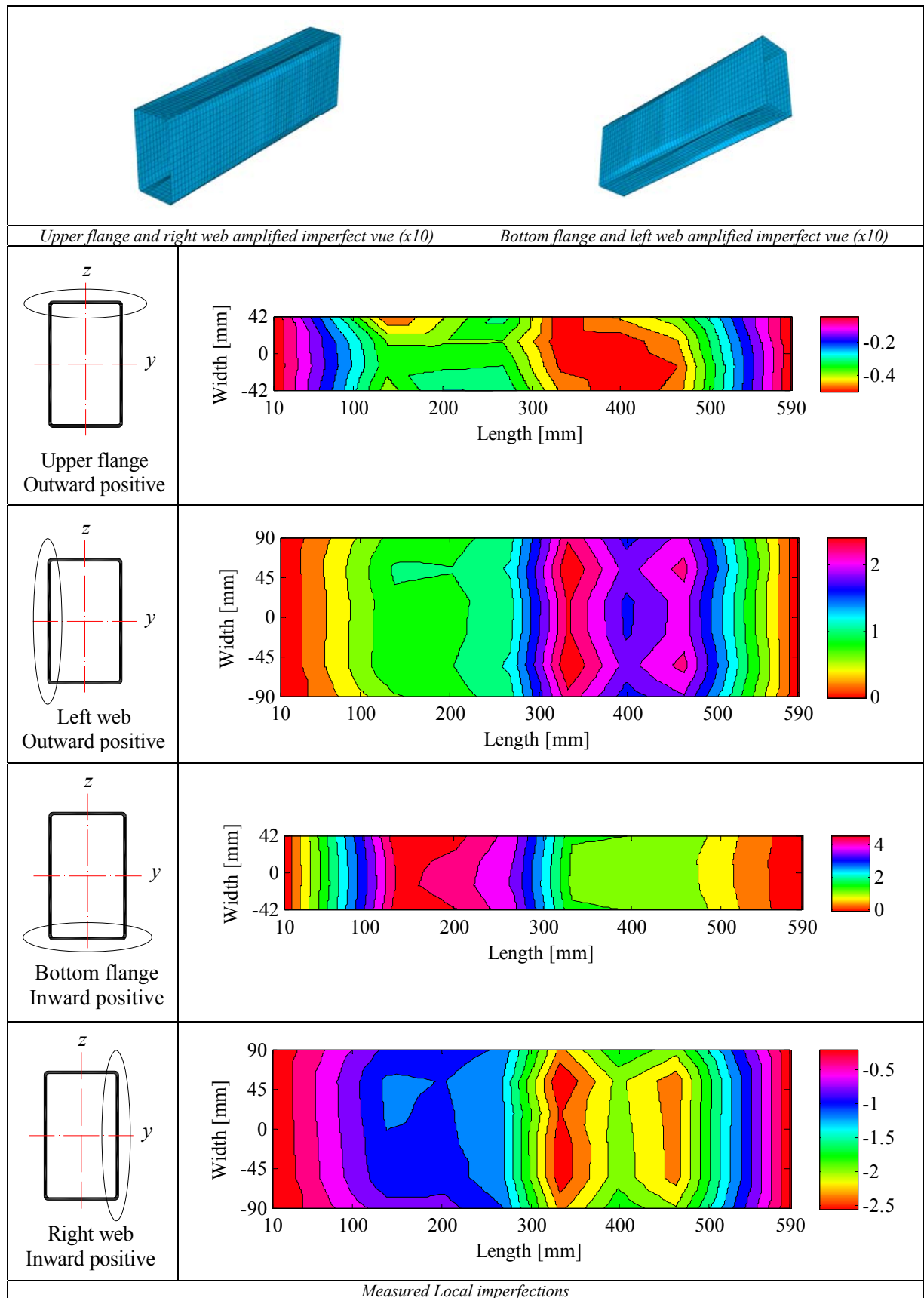


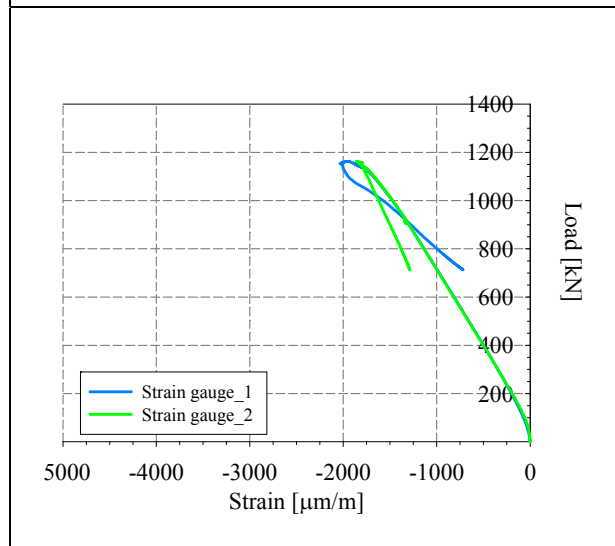
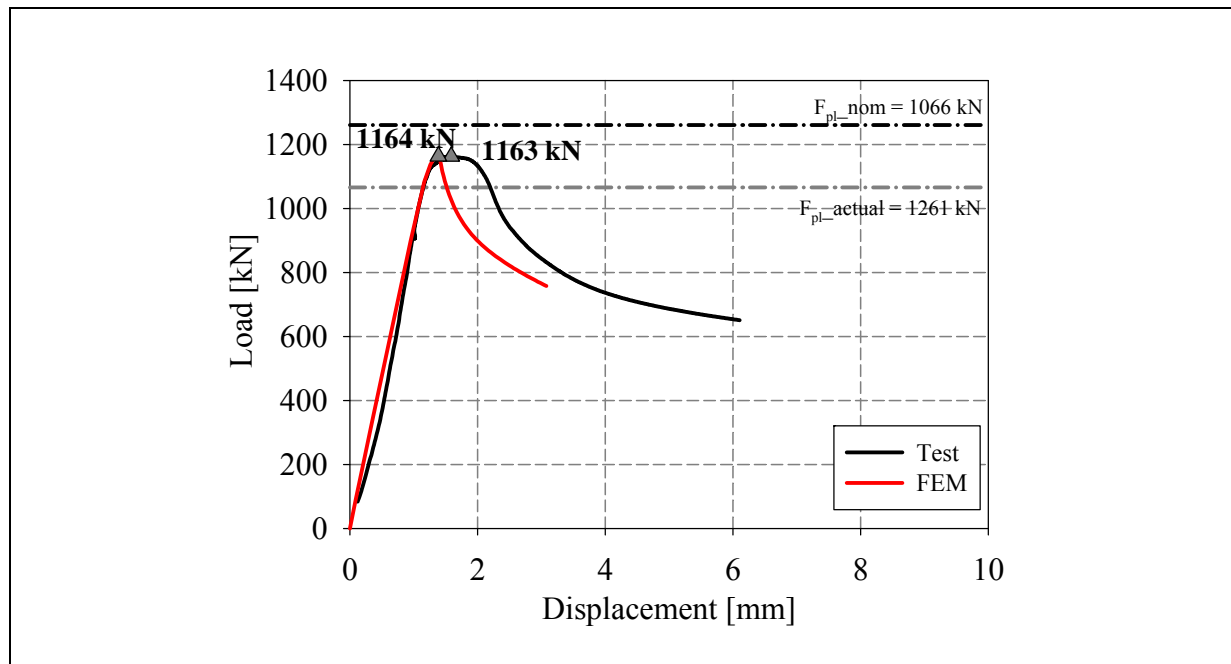
Tensile coupons location

Material stress-strain curves

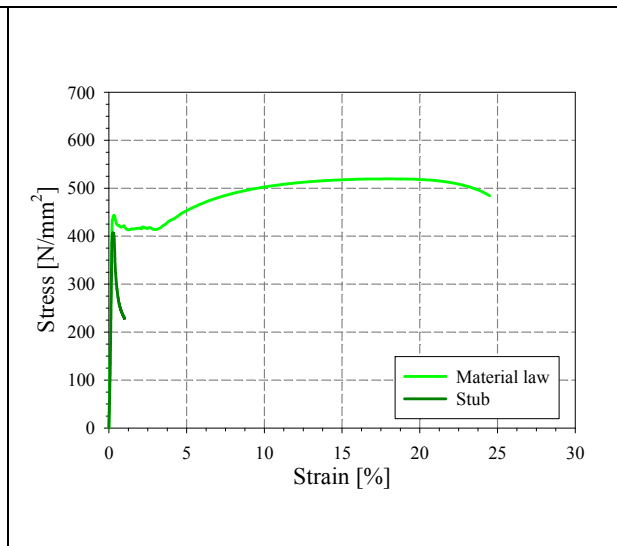
Material average properties



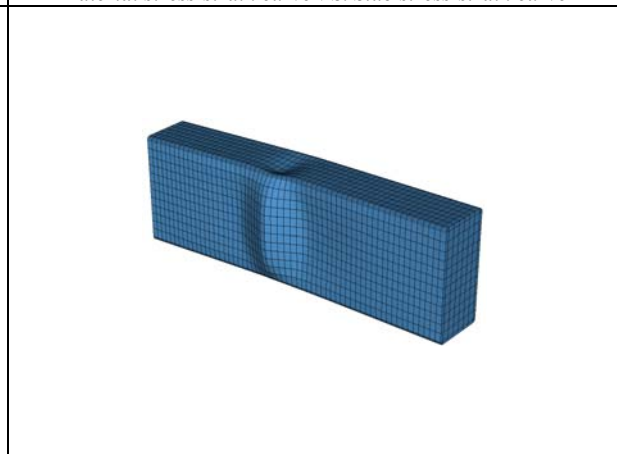




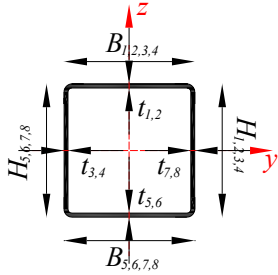
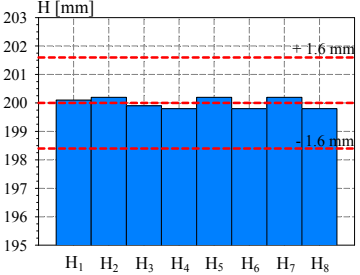
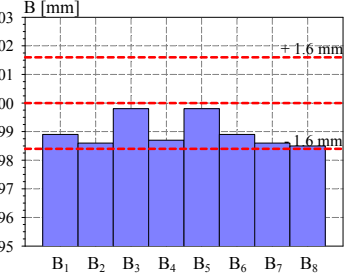
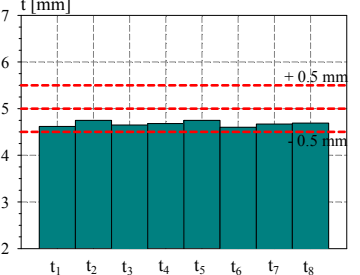
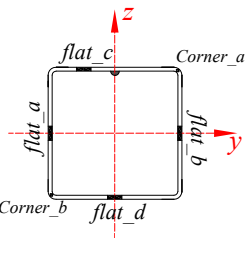
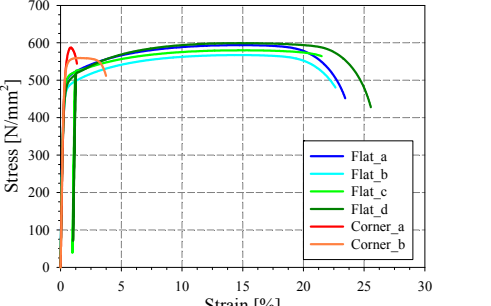
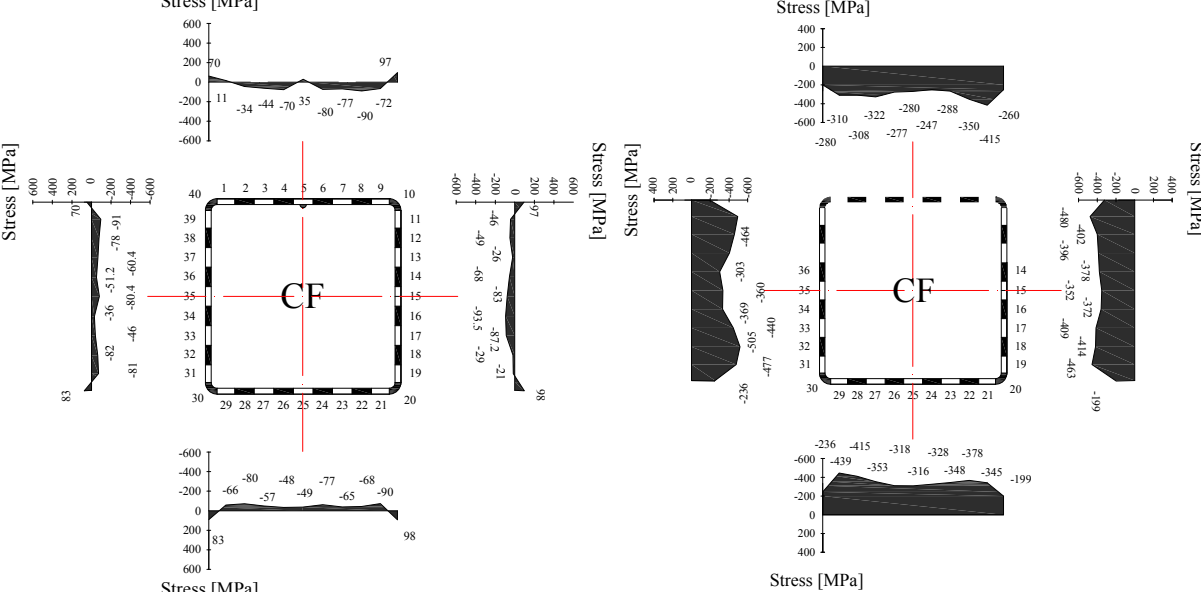
Strain gauges recordings

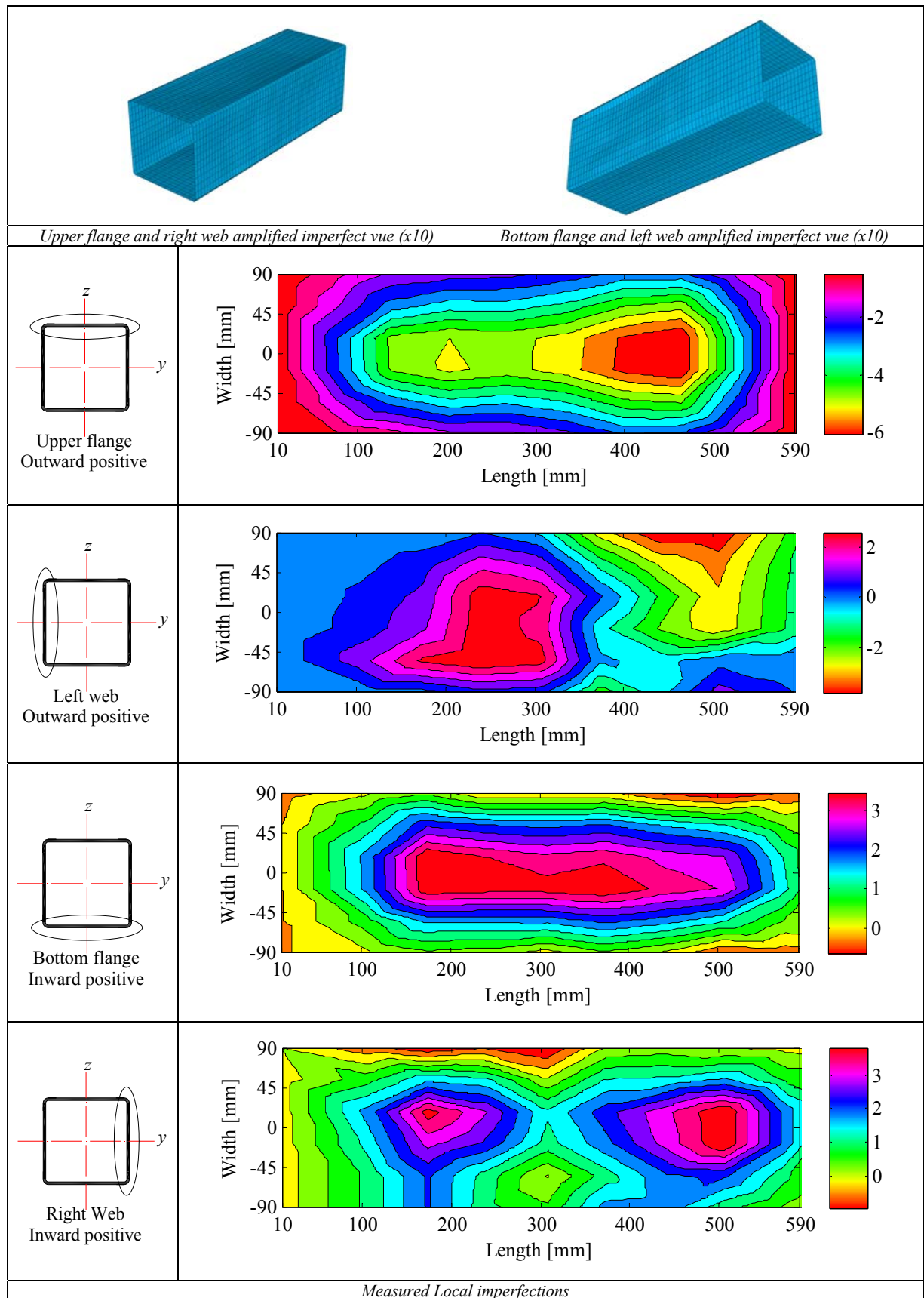


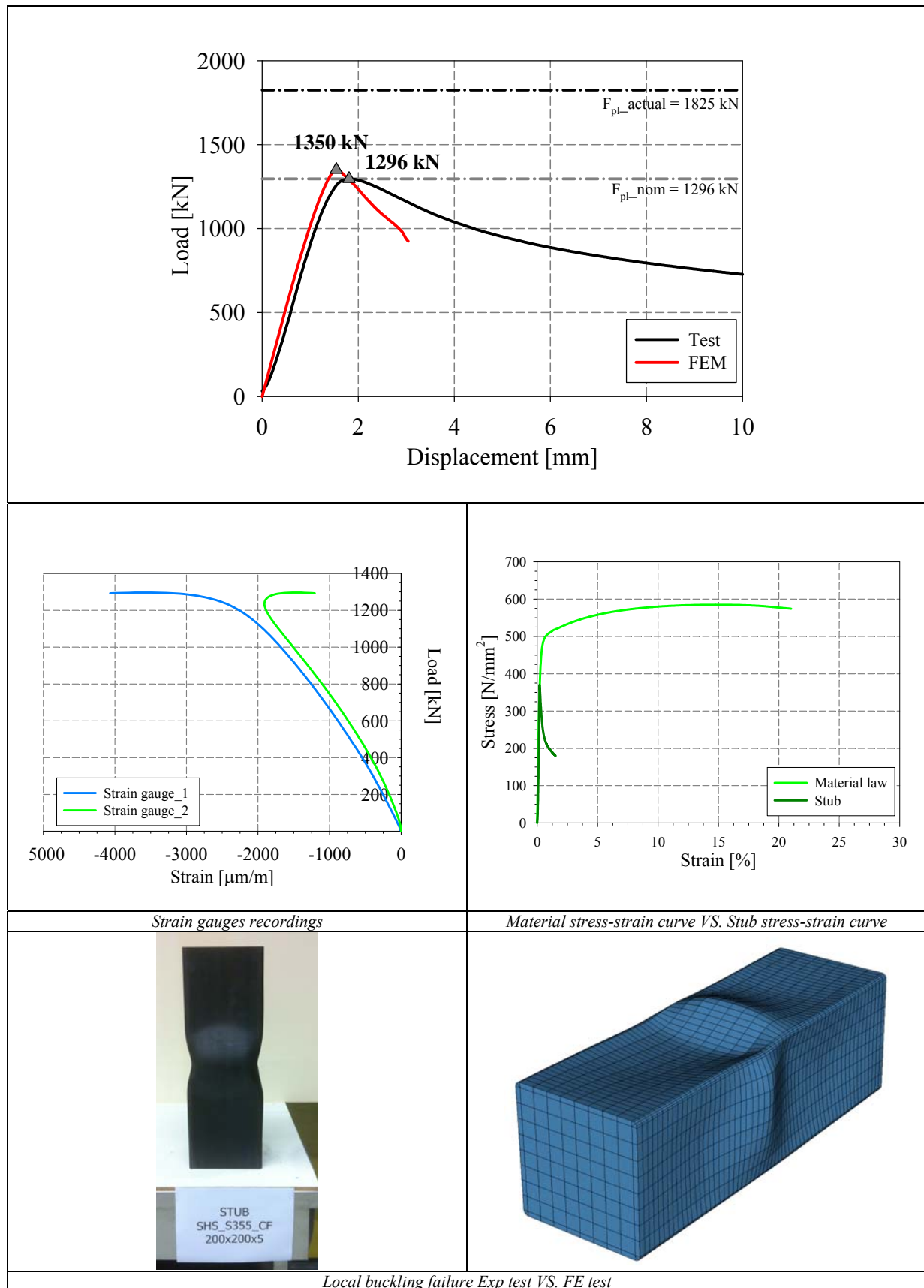
Material stress-strain curve VS. Stub stress-strain curve



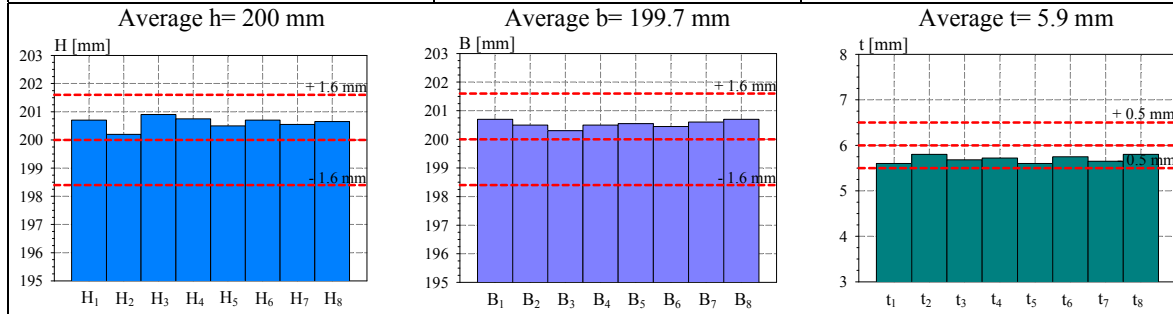
Local buckling failure Exp test VS. FE test

Specimen name	Shape	Details																				
<p>RHS_S355_Stub 200x200x5 CF</p>		<p>Shape: Square Hollow Section Nominal yield limit: 355 MPa Load case: Stub, Pure compression H=200mm B=200mm t=5mm Fabrication process: Cold formed</p>																				
Average h= 200 mm		Average b= 201.5 mm		Average t= 4.72 mm																		
																						
<i>Cross-sectional measured dimensions and tolerances</i>																						
			<table border="1"> <thead> <tr> <th></th> <th>Flat</th> <th>Corner</th> </tr> </thead> <tbody> <tr> <td>E [MPa]</td> <td>214848</td> <td>209500</td> </tr> <tr> <td>f_y [MPa]</td> <td>480.2</td> <td>-</td> </tr> <tr> <td>ϵ_y [%]</td> <td>0.22</td> <td>-</td> </tr> <tr> <td>f_u [MPa]</td> <td>585</td> <td>573.35</td> </tr> <tr> <td>ϵ_u [%]</td> <td>14.5</td> <td>1.2</td> </tr> </tbody> </table>			Flat	Corner	E [MPa]	214848	209500	f_y [MPa]	480.2	-	ϵ_y [%]	0.22	-	f_u [MPa]	585	573.35	ϵ_u [%]	14.5	1.2
	Flat	Corner																				
E [MPa]	214848	209500																				
f_y [MPa]	480.2	-																				
ϵ_y [%]	0.22	-																				
f_u [MPa]	585	573.35																				
ϵ_u [%]	14.5	1.2																				
<i>Tensile coupons location</i>		<i>Material stress-strain curves</i>		<i>Material average properties</i>																		
			<p style="text-align: center;">Membrane stresses Flexural stresses</p> <p style="text-align: center;"><i>Measured residual stresses distributions</i></p>																			





Specimen name	Shape	Details
RHS_S355_Stub 200x200x6 CF		Shape: Square Hollow Section Nominal yield limit: 355 MPa Load case: Stub Pure compression $H=200\text{mm}$ $B=200\text{mm}$ $t=6\text{mm}$ Fabrication process: Cold formed



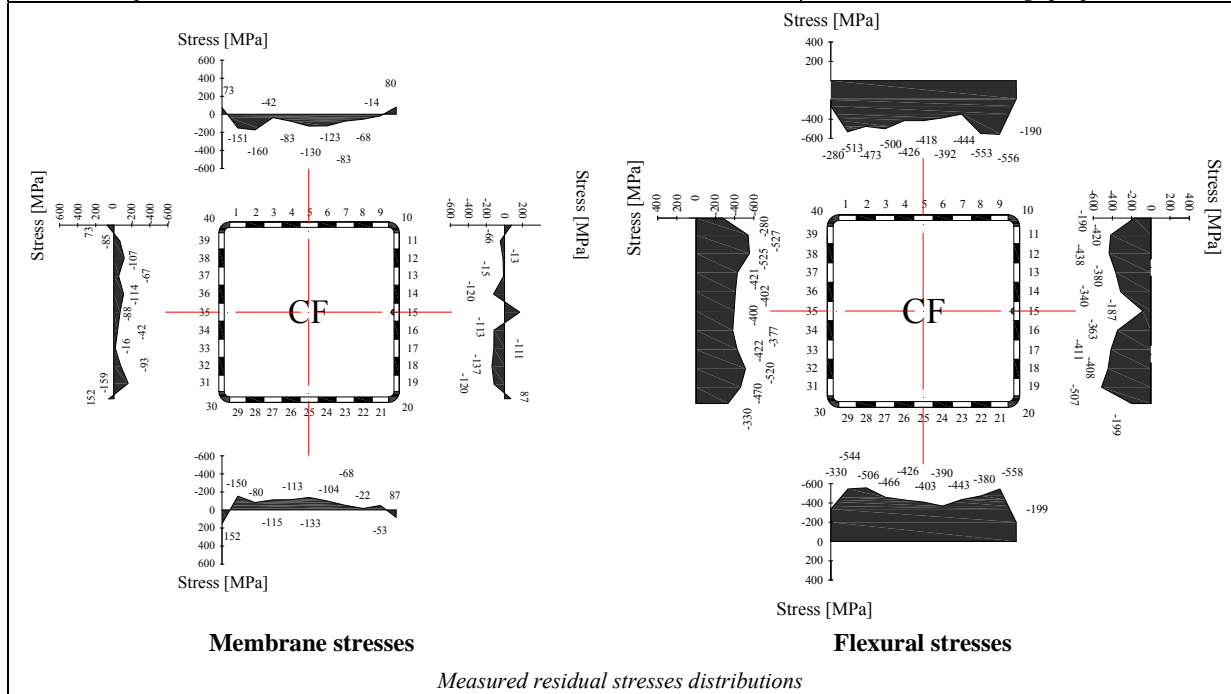
Cross-sectional measured dimensions and tolerances

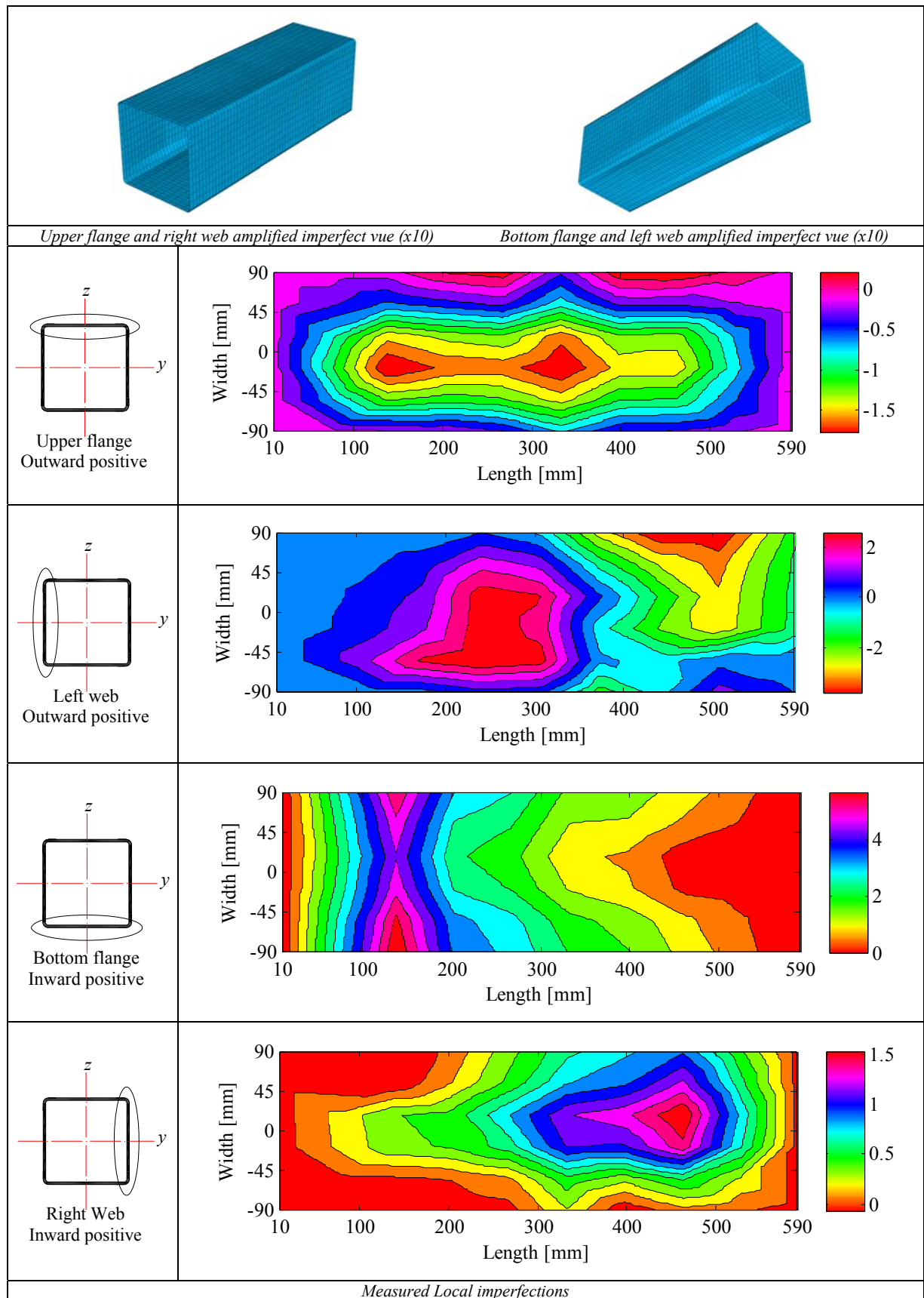
	Flat	Corner	
	E [MPa]	217363	210500
	f_y [MPa]	500.5	-
	ϵ_y [%]	0.23	-
	f_u [MPa]	596	617.8
ϵ_u [%]	13.8	1.1	

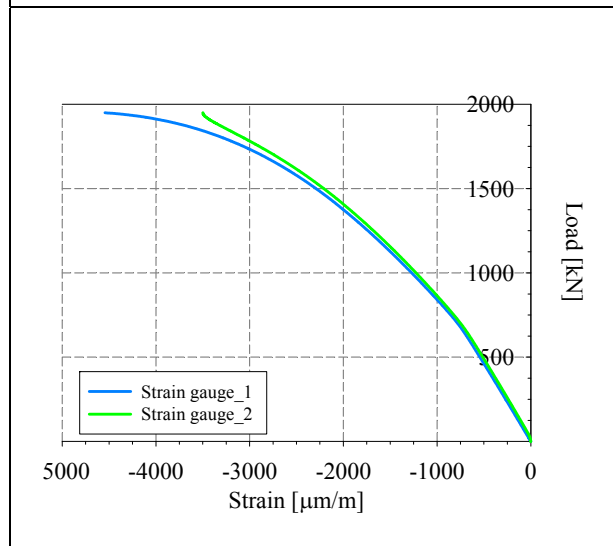
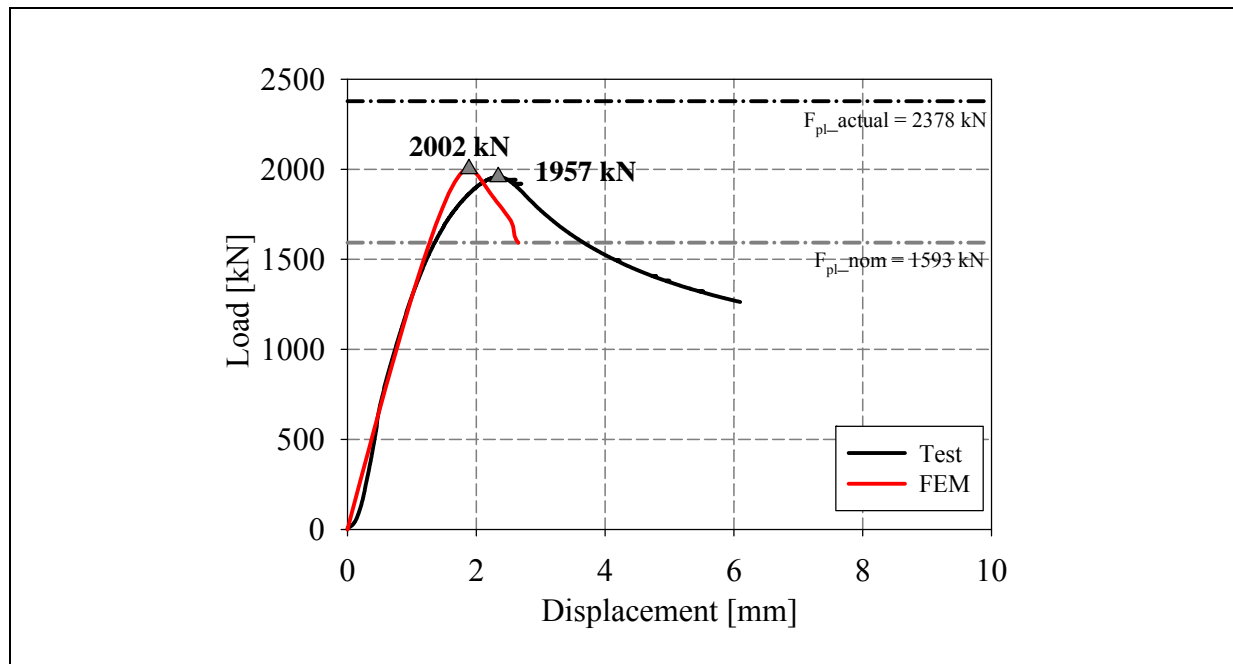
Tensile coupons location

Material stress-strain curves

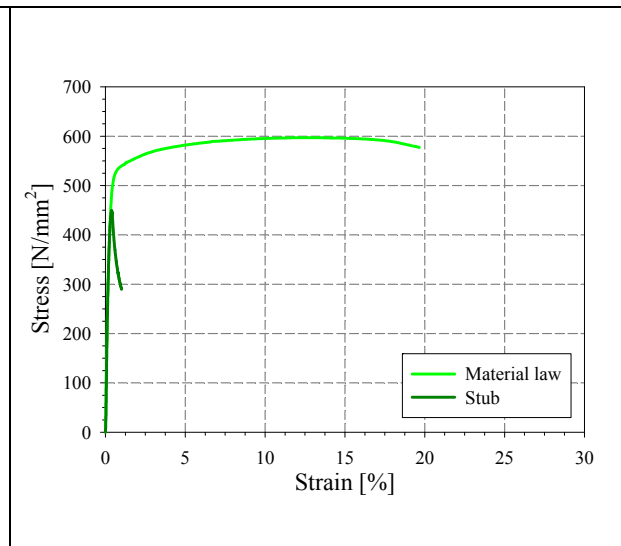
Material average properties



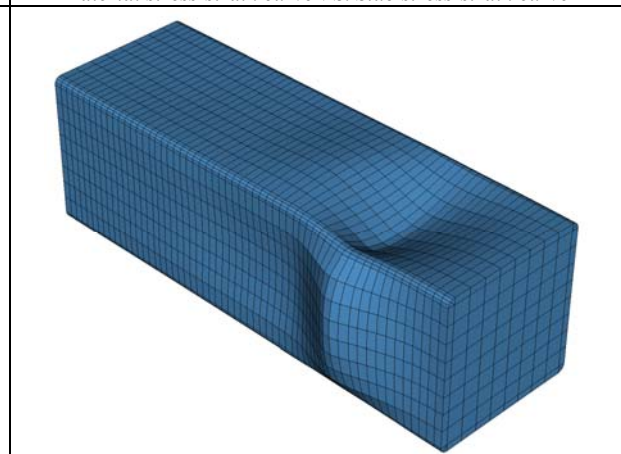




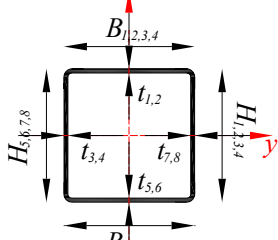
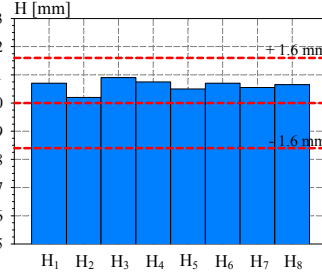
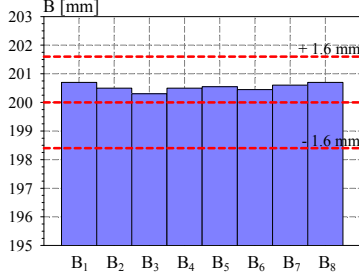
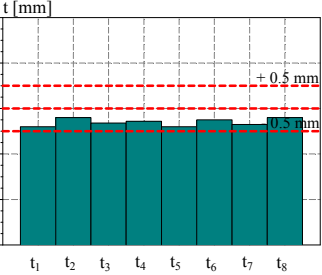
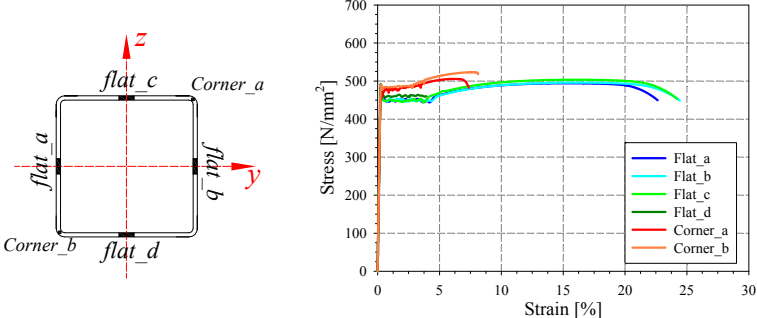
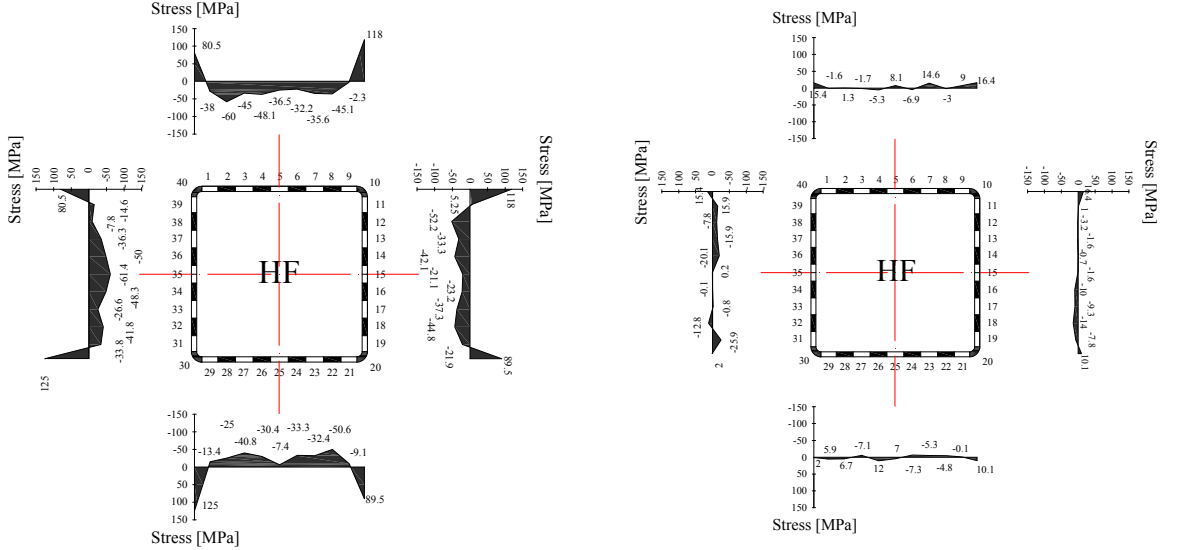
Strain gauges recordings

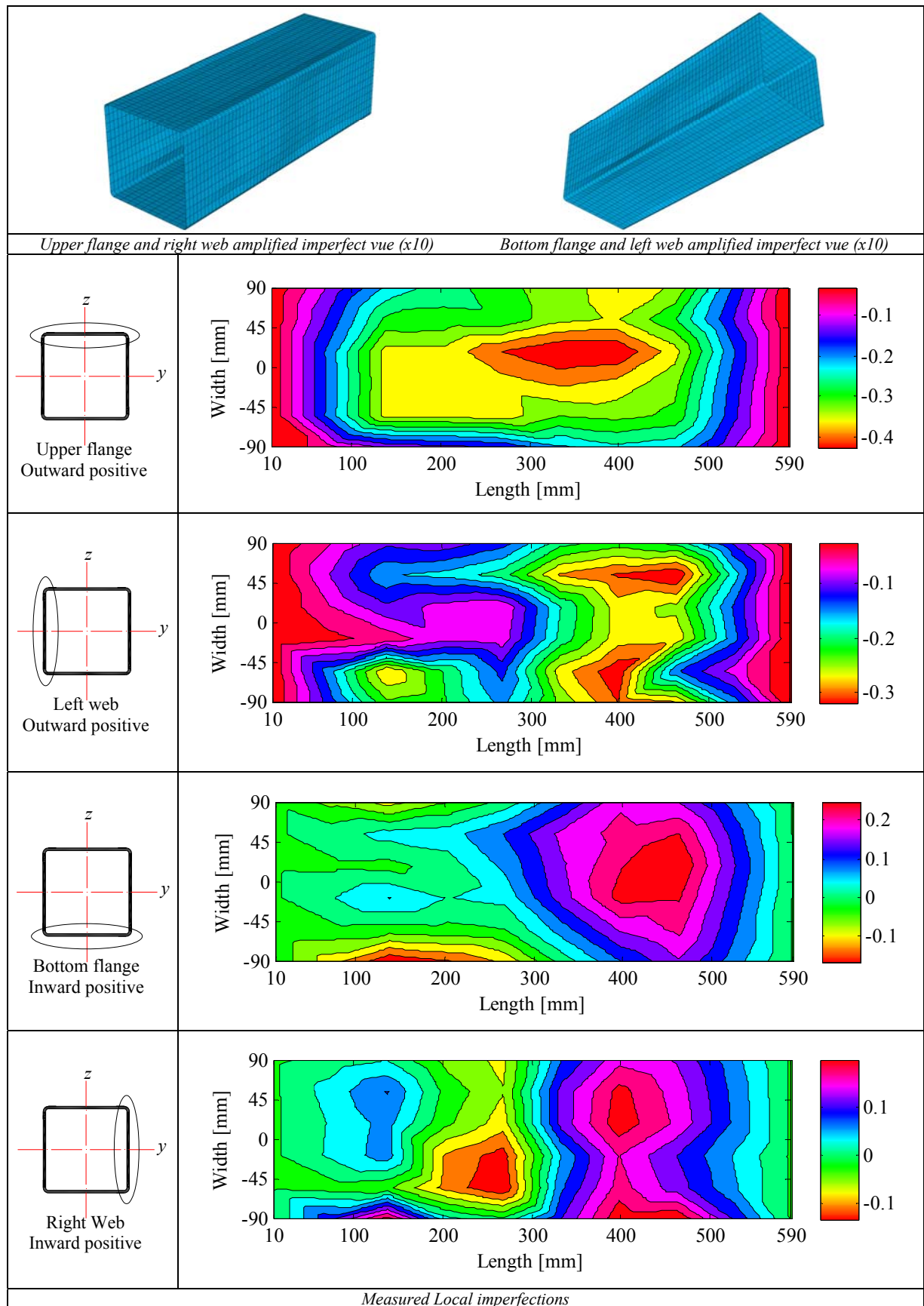


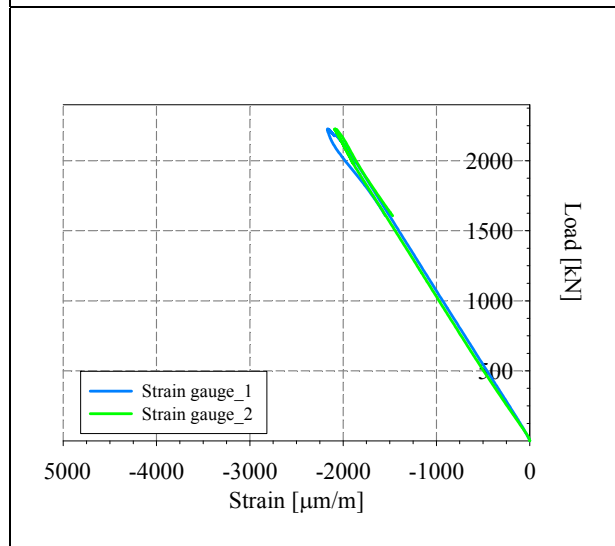
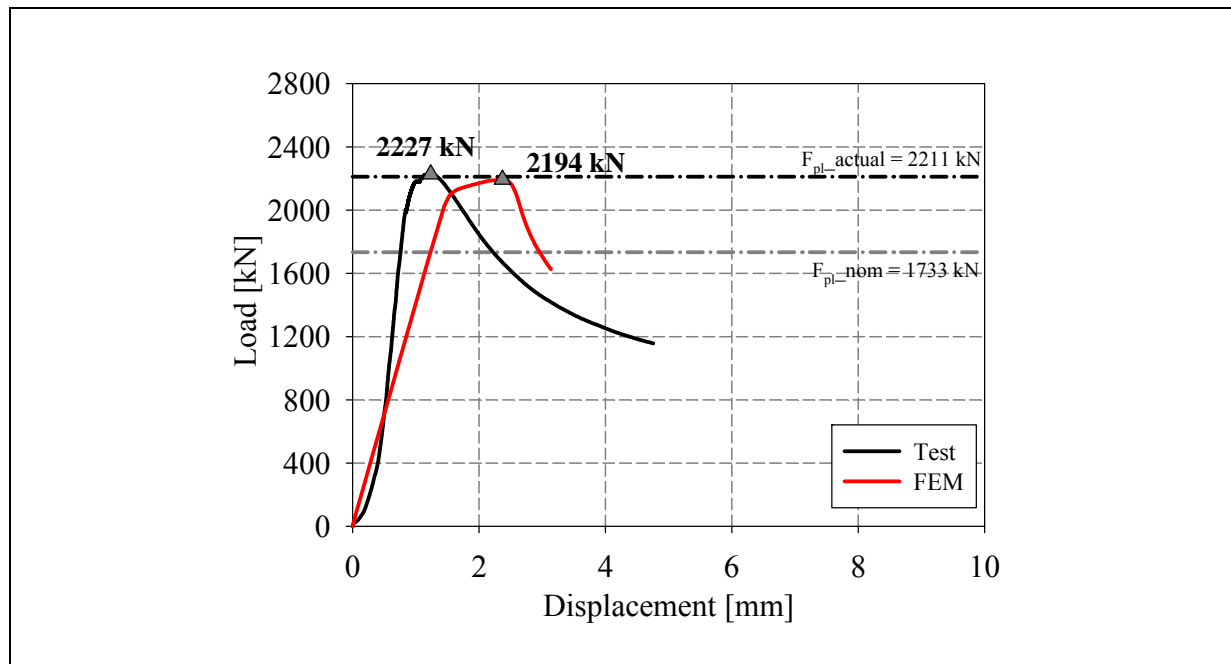
Material stress-strain curve VS. Stub stress-strain curve



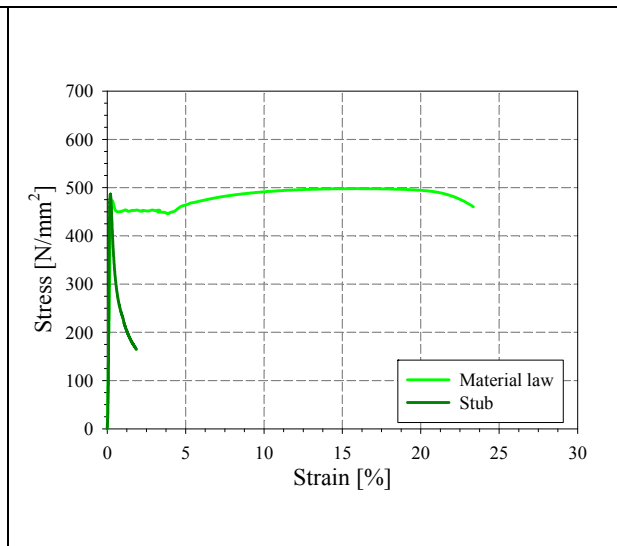
Local buckling failure Exp test VS. FE test

<p>Specimen name</p> <p>RHS_S355_Stub 200x200x6.3 HF</p>	<p>Shape</p> 	<p>Details</p> <p>Shape: Square Hollow Section Nominal yield limit: 355 MPa Load case: Stub Pure compression H=200mm B=200mm t=6mm Fabrication process: Hot formed</p>																		
<p>Average h= 199.9 mm</p> 	<p>Average b= 199.9 mm</p> 	<p>Average t= 6.42 mm</p> 																		
<p>Cross-sectional measured dimensions and tolerances</p>																				
	<table border="1"> <thead> <tr> <th></th> <th>Flat</th> <th>Corner</th> </tr> </thead> <tbody> <tr> <td>E [MPa]</td> <td>215998</td> <td>209750</td> </tr> <tr> <td>f_y [MPa]</td> <td>453</td> <td>482.6</td> </tr> <tr> <td>ϵ_y [%]</td> <td>0.20</td> <td>0.23</td> </tr> <tr> <td>f_u [MPa]</td> <td>496</td> <td>523.4</td> </tr> <tr> <td>ϵ_u [%]</td> <td>15.9</td> <td>7.6</td> </tr> </tbody> </table>			Flat	Corner	E [MPa]	215998	209750	f_y [MPa]	453	482.6	ϵ_y [%]	0.20	0.23	f_u [MPa]	496	523.4	ϵ_u [%]	15.9	7.6
	Flat	Corner																		
E [MPa]	215998	209750																		
f_y [MPa]	453	482.6																		
ϵ_y [%]	0.20	0.23																		
f_u [MPa]	496	523.4																		
ϵ_u [%]	15.9	7.6																		
<p>Tensile coupons location</p>	<p>Material stress-strain curves</p>	<p>Material average properties</p>																		
 <p style="text-align: center;">Membrane stresses Flexural stresses</p> <p style="text-align: center;"><i>Measured residual stresses distributions</i></p>																				

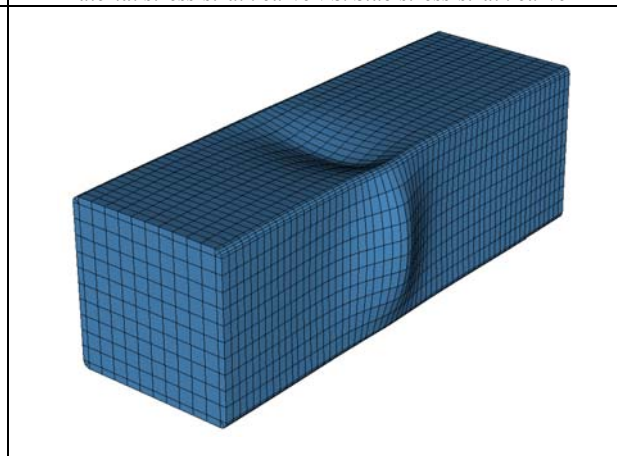




Strain gauges recordings

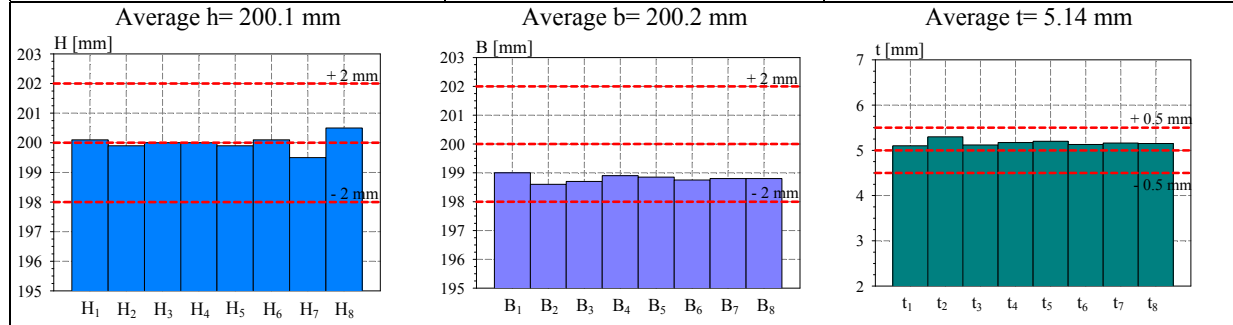


Material stress-strain curve VS. Stub stress-strain curve



Local buckling failure Exp test VS. FE test

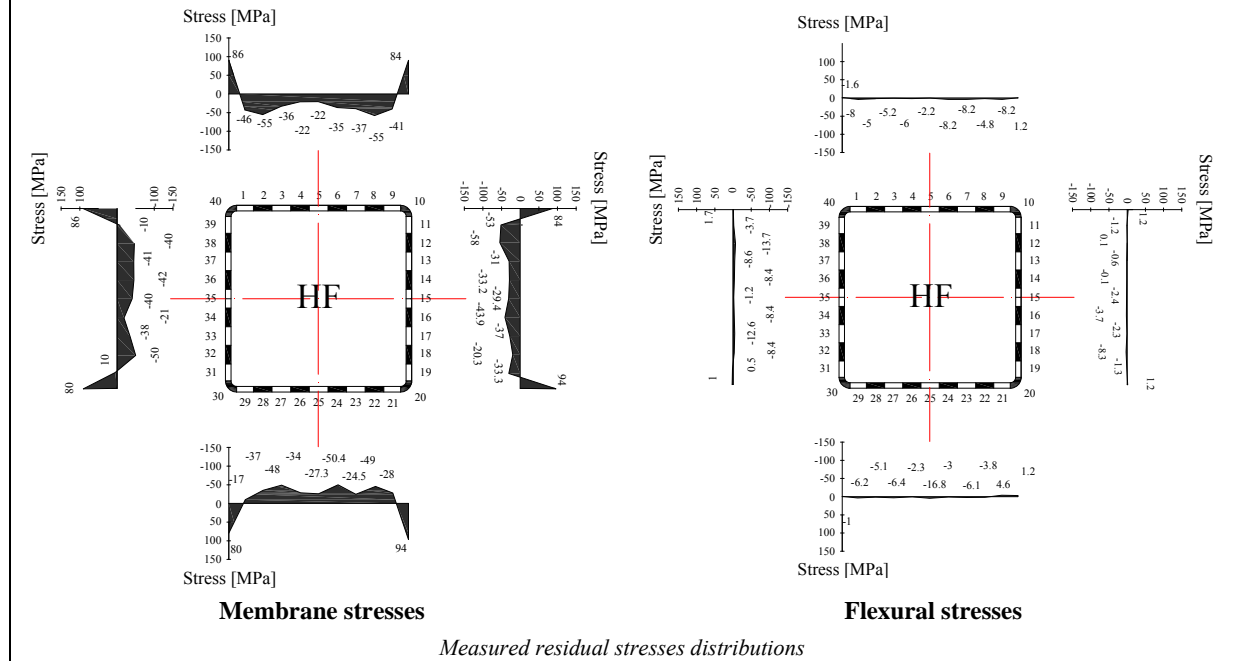
Specimen name	Shape	Details
RHS_S355_Stub 200x200x5 HF		Shape: Square Hollow Section Nominal yield limit: 355 MPa Load case: Stub, Pure compression H=200mm B=200mm t=5mm Fabrication process: Hot formed

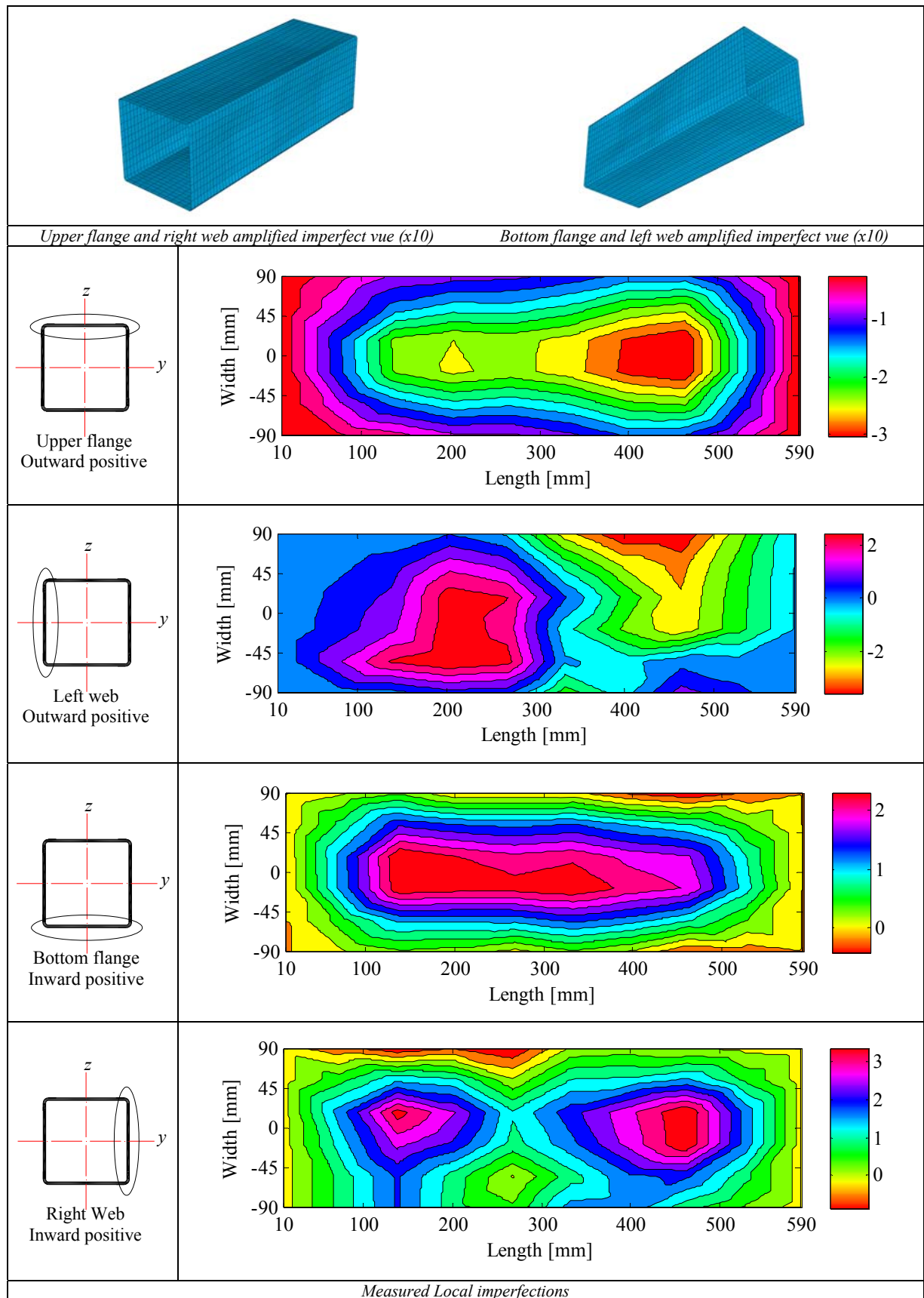


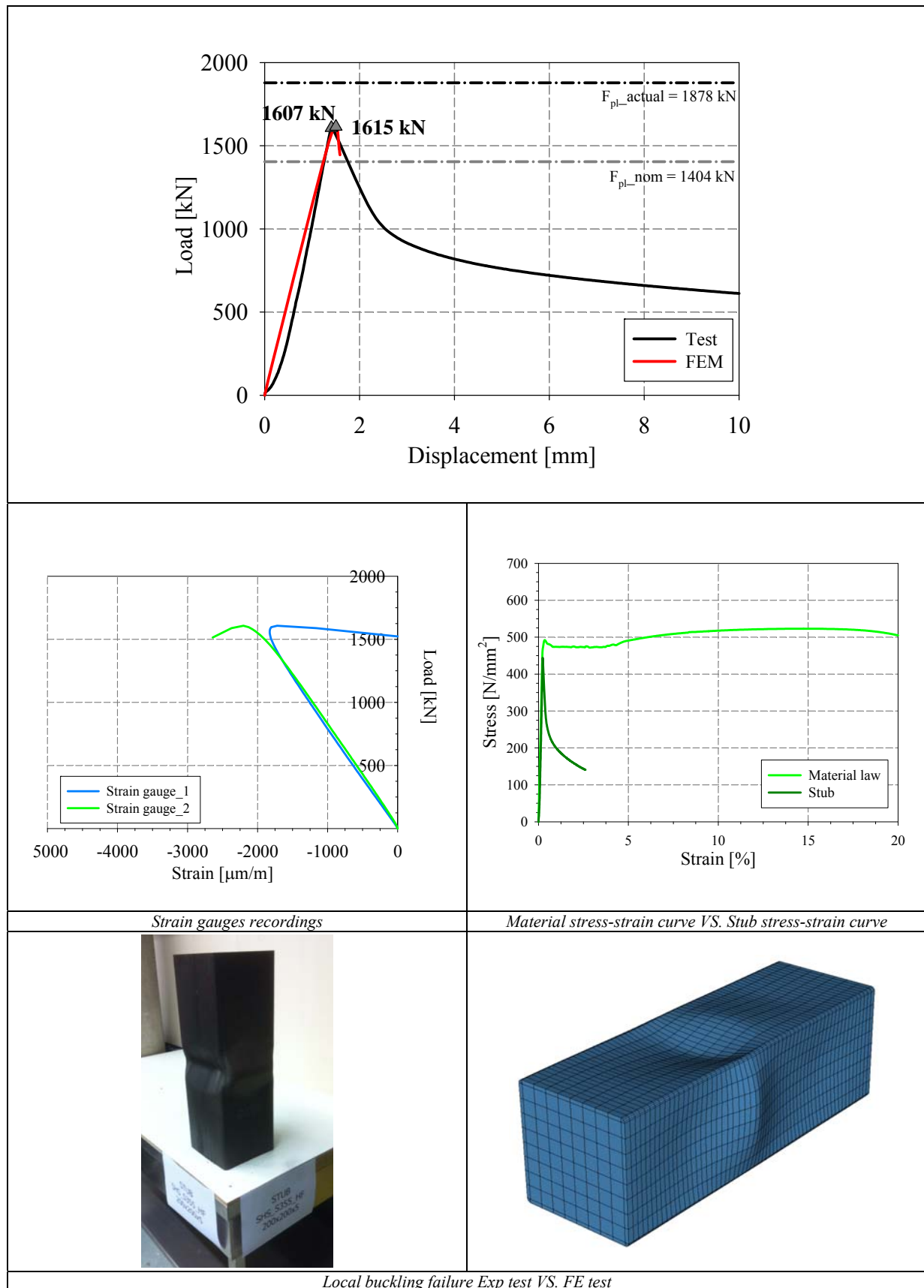
Cross-sectional measured dimensions and tolerances

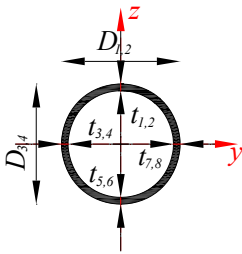
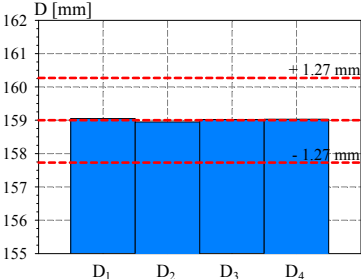
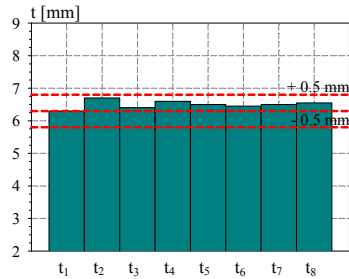
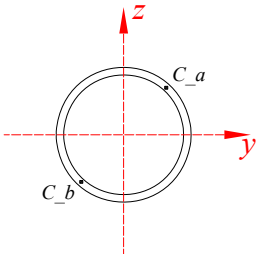
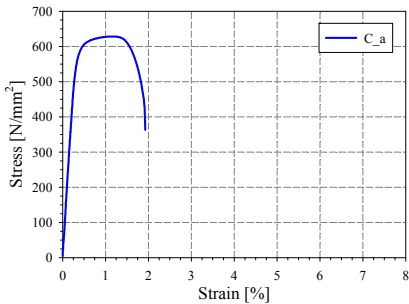
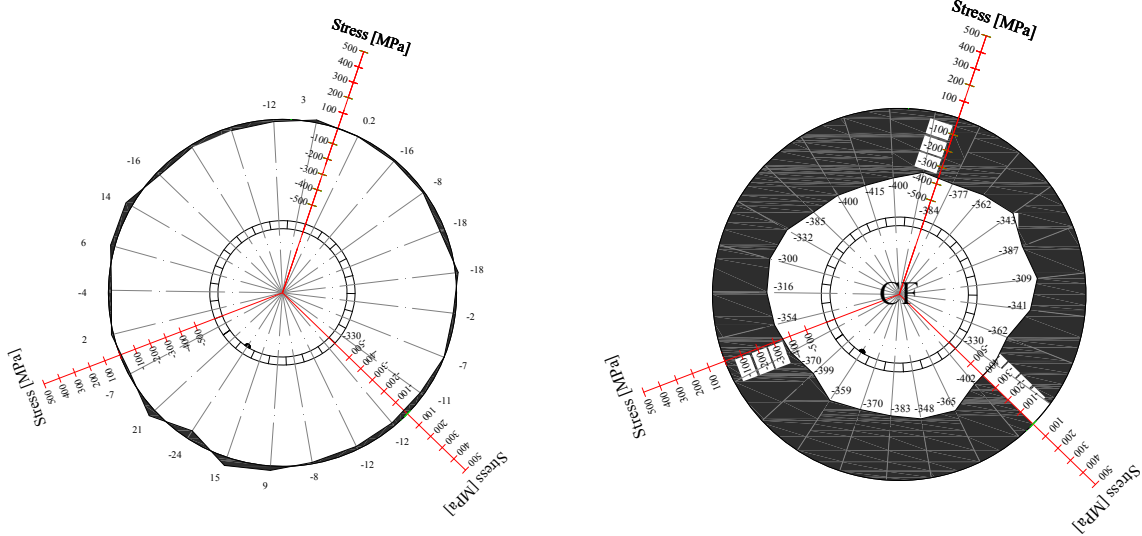
	Material stress-strain curves		Material average properties	
	Flat	Corner	E [MPa]	Corner
	211489	211023	f_y [MPa]	544
	475	544	ϵ_y [%]	0.25
	523	578.2	f_u [MPa]	8.93
	14.6	8.93	ϵ_u [%]	

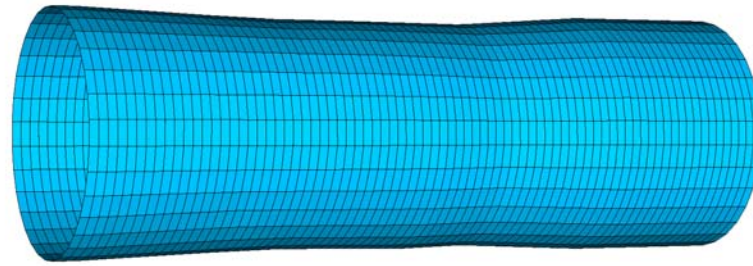
Tensile coupons location Material stress-strain curves Material average properties



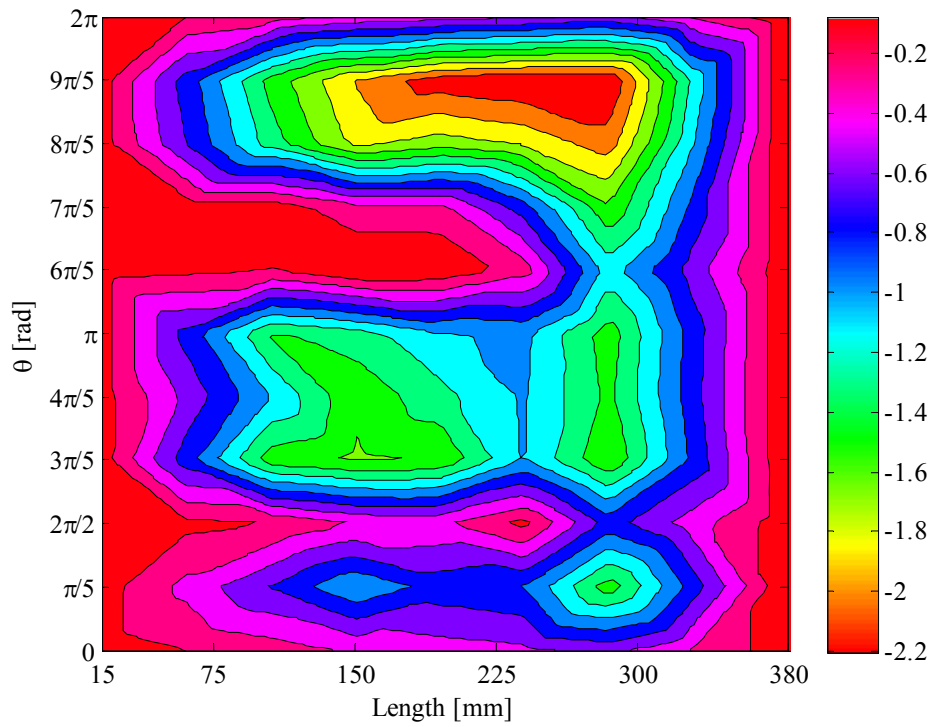
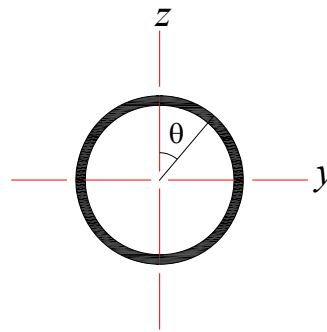




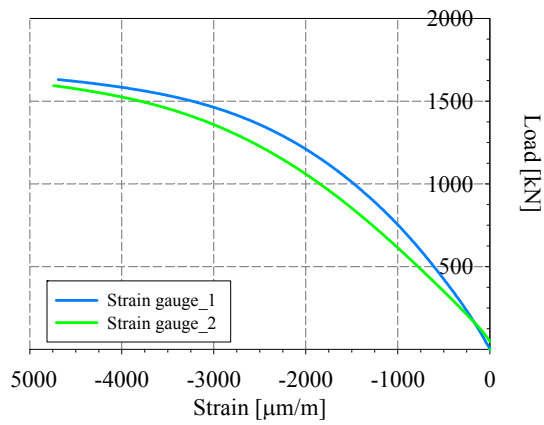
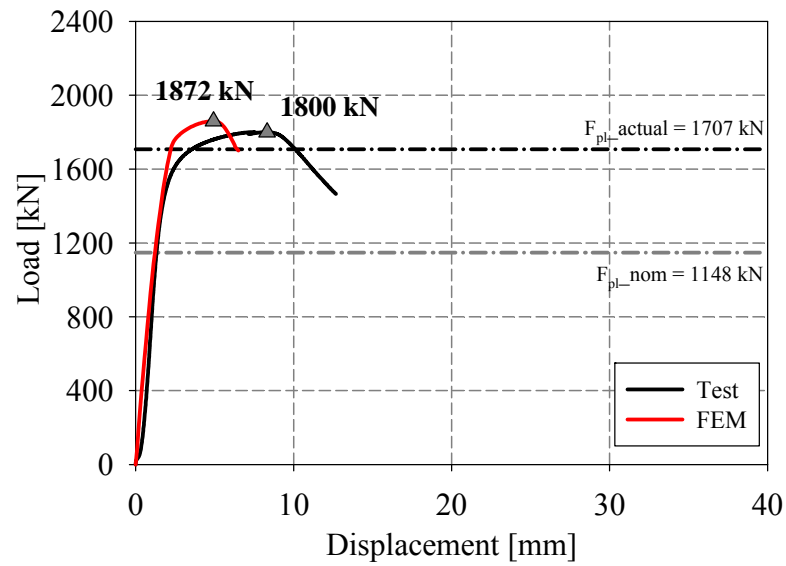
Specimen name	Shape	Details												
<p>CHS_S355_Stub 159x6.3 CF</p>		<p>Shape: Circular Hollow Section Nominal yield limit: 355 MPa Load case: Stub, Pure compression D=159mm t=6.3mm Fabrication process: Cold formed</p>												
<p>Average D= 159 mm</p> 		<p>Average t= 6.76 mm</p> 												
<p><i>Cross-sectional measured dimensions and tolerances</i></p>														
		<table border="1"> <thead> <tr> <th></th> <th>Average C a, C b</th> </tr> </thead> <tbody> <tr> <td>E [MPa]</td> <td>194654</td> </tr> <tr> <td>f_y [MPa]</td> <td>607.3</td> </tr> <tr> <td>ϵ_y [%]</td> <td>0.31</td> </tr> <tr> <td>f_u [MPa]</td> <td>628.2</td> </tr> <tr> <td>ϵ_u [%]</td> <td>1.1</td> </tr> </tbody> </table>		Average C a, C b	E [MPa]	194654	f_y [MPa]	607.3	ϵ_y [%]	0.31	f_u [MPa]	628.2	ϵ_u [%]	1.1
	Average C a, C b													
E [MPa]	194654													
f_y [MPa]	607.3													
ϵ_y [%]	0.31													
f_u [MPa]	628.2													
ϵ_u [%]	1.1													
<p><i>Tensile coupons location</i></p>	<p><i>Material stress-strain curves</i></p>	<p><i>Material average properties</i></p>												
 <div style="display: flex; justify-content: space-around; margin-top: 10px;"> <div data-bbox="440 1776 646 1803" style="text-align: center;"> <p>Membrane stresses</p> </div> <div data-bbox="1062 1776 1243 1803" style="text-align: center;"> <p>Flexural stresses</p> </div> </div> <p style="text-align: center; margin-top: 10px;"><i>Measured residual stresses distributions</i></p>														



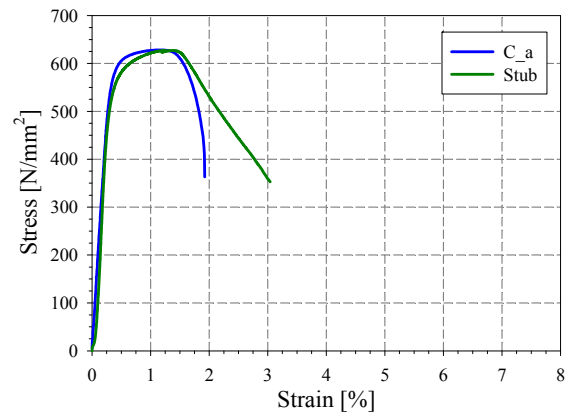
Amplified imperfect vue (x10)



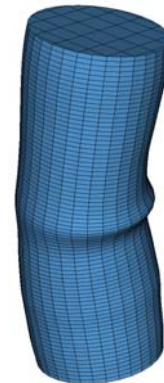
Measured Local imperfections



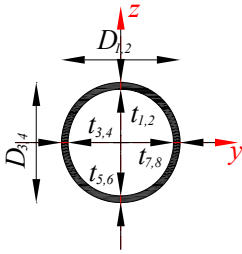
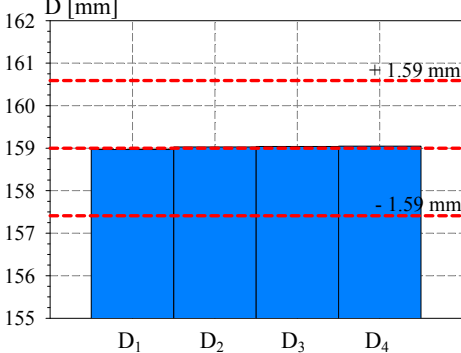
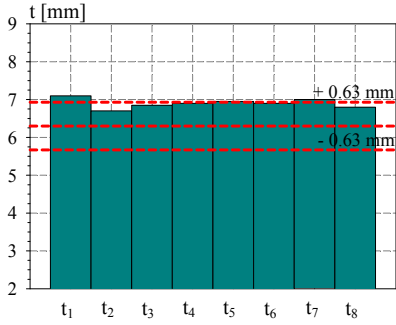
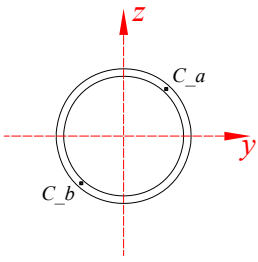
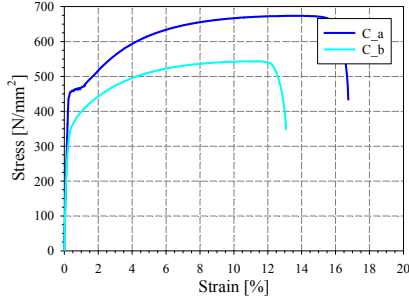
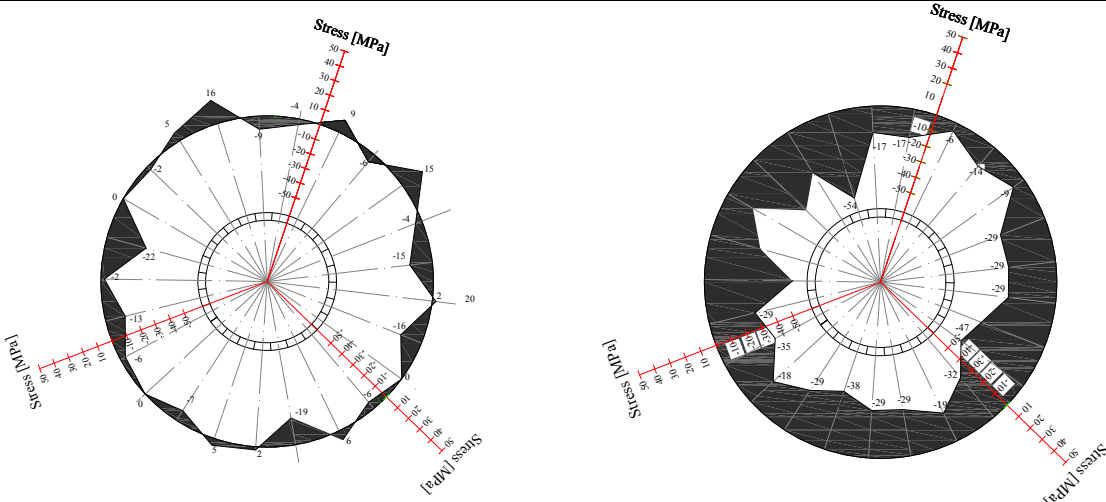
Strain gauges recordings

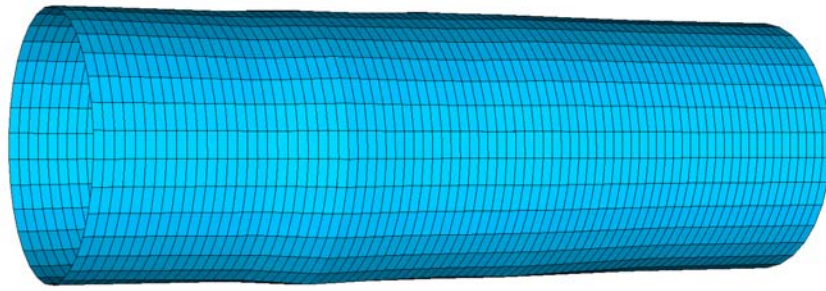


Material stress-strain curve VS. Stub stress-strain curve

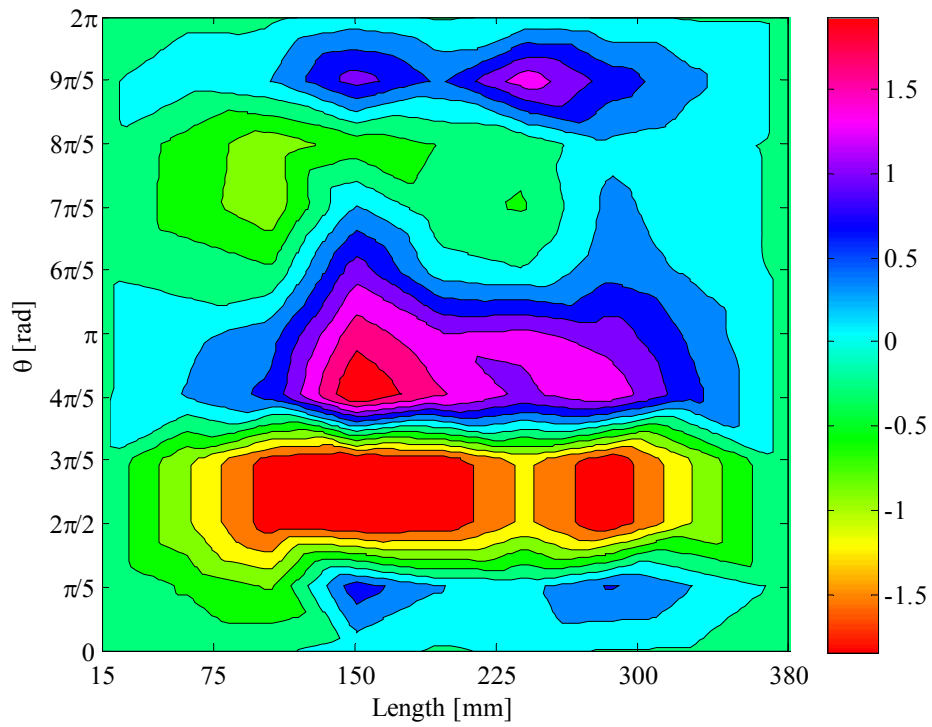
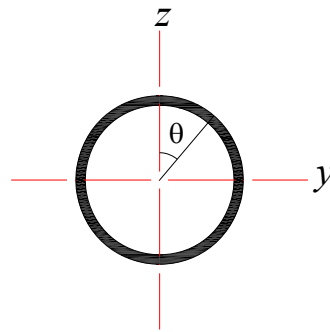


Local buckling failure Exp test VS. FE test

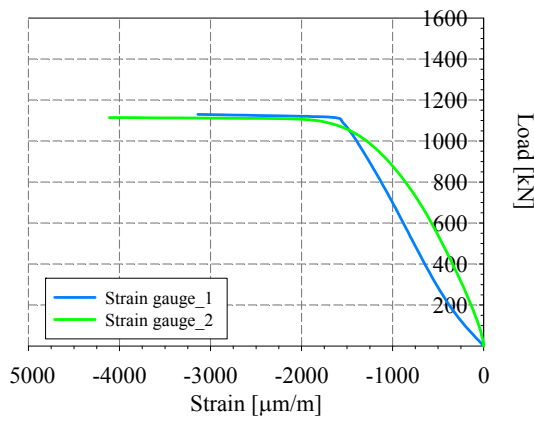
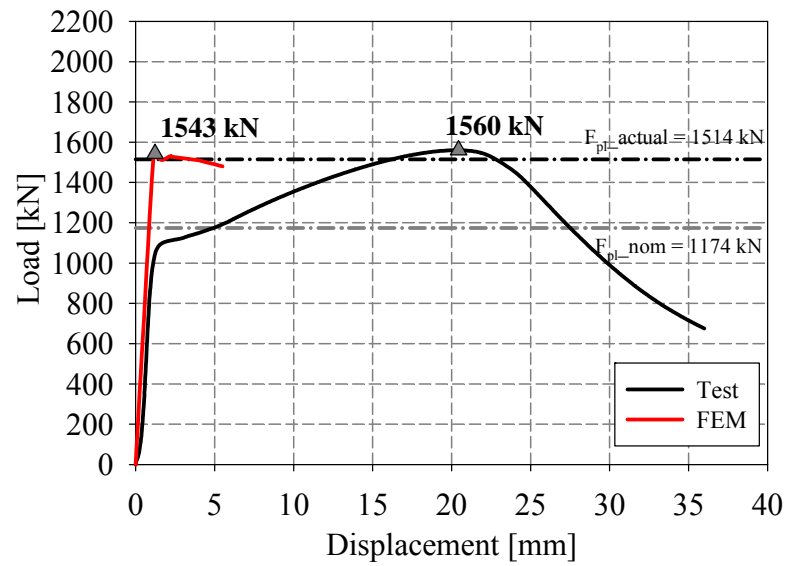
Specimen name	Shape	Details												
<p>CHS_S355_Stub 159x6.3 HR</p>		<p>Shape: Circular Hollow Section Nominal yield limit: 355 MPa Load case: LC1 Pure compression D=159mm t=6.3mm Fabrication process: Hot rolled</p>												
Average D= 159 mm		Average t= 6.92 mm												
														
<i>Cross-sectional measured dimensions and tolerances</i>														
		<table border="1"> <thead> <tr> <th></th> <th>Average C a, C b</th> </tr> </thead> <tbody> <tr> <td>E [MPa]</td> <td>213000</td> </tr> <tr> <td>f_y [MPa]</td> <td>401.5</td> </tr> <tr> <td>ϵ_y [%]</td> <td>0.19</td> </tr> <tr> <td>f_u [MPa]</td> <td>607.8</td> </tr> <tr> <td>ϵ_u [%]</td> <td>11.7</td> </tr> </tbody> </table>		Average C a, C b	E [MPa]	213000	f_y [MPa]	401.5	ϵ_y [%]	0.19	f_u [MPa]	607.8	ϵ_u [%]	11.7
	Average C a, C b													
E [MPa]	213000													
f_y [MPa]	401.5													
ϵ_y [%]	0.19													
f_u [MPa]	607.8													
ϵ_u [%]	11.7													
<i>Tensile coupons location</i>	<i>Material stress-strain curves</i>	<i>Material average properties</i>												
 <p style="text-align: center;">Membrane stresses Flexural stresses</p> <p style="text-align: center;"><i>Measured residual stresses distributions</i></p>														



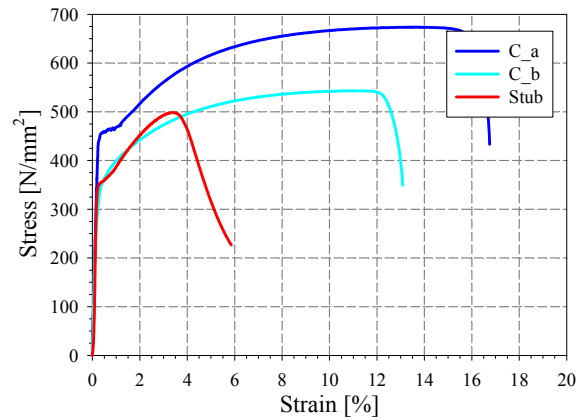
Amplified imperfect vue (x10)



Measured Local imperfections



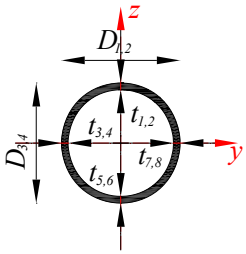
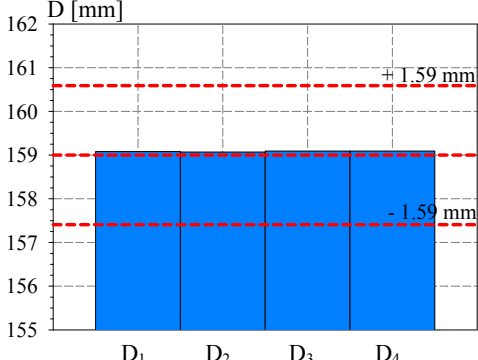
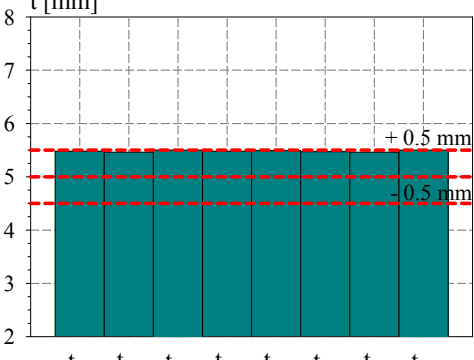
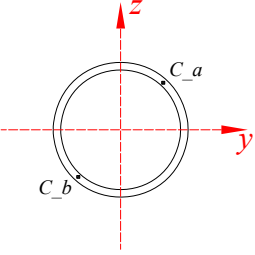
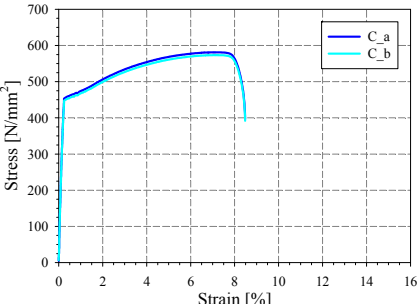
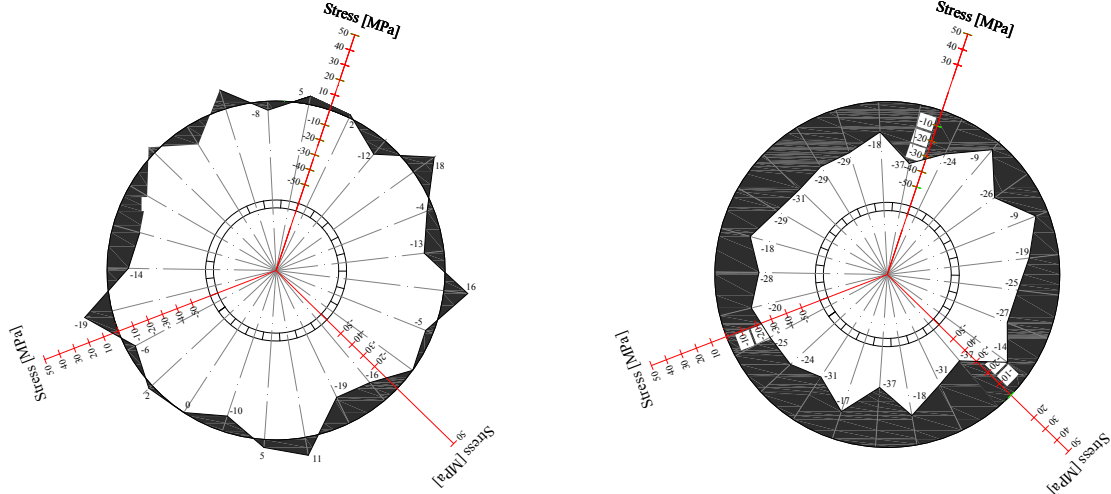
Strain gauges recordings

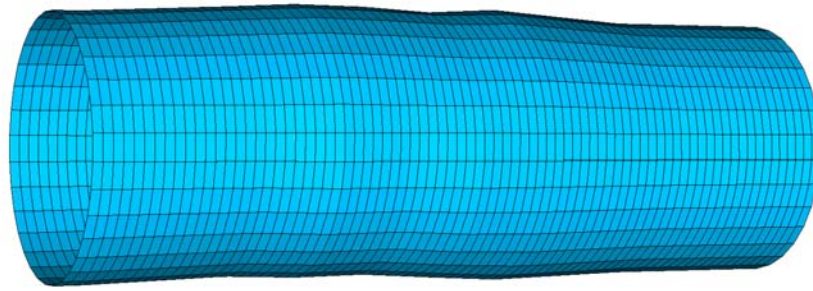


Material stress-strain curve VS. Stub stress-strain curve

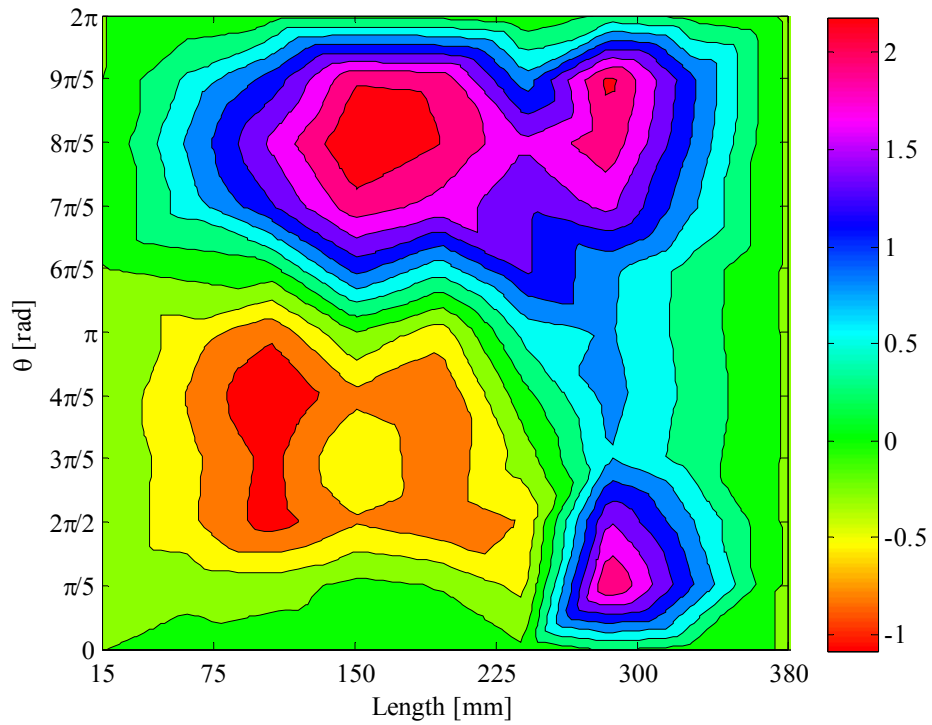
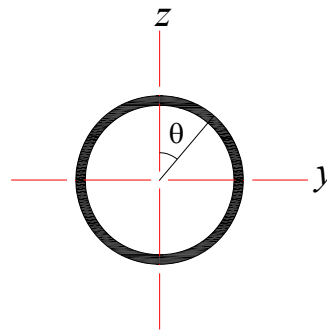


Local buckling failure Exp test VS. FE test

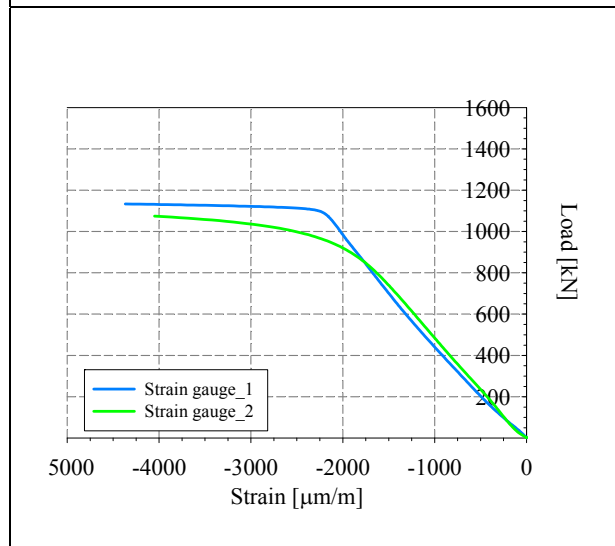
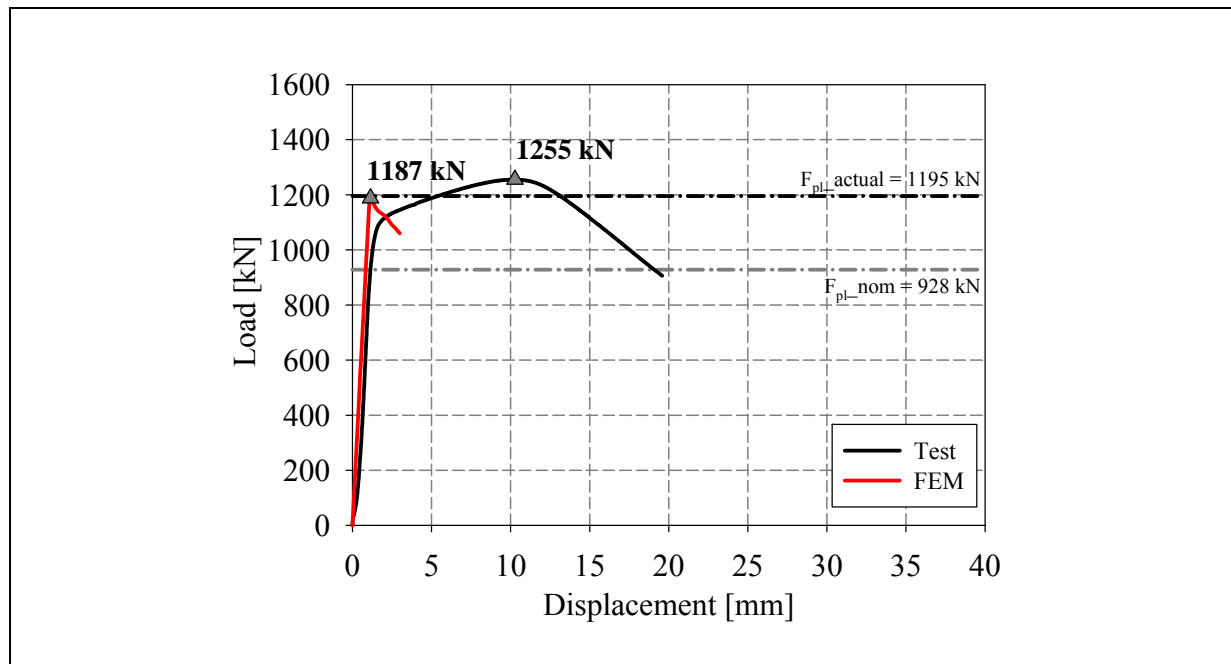
Specimen name	Shape	Details												
<p>CHS_S355_Stub 159x5 HR</p>		<p>Shape: Circular Hollow Section Nominal yield limit: 355 MPa Load case: Stub, Pure compression D=159mm t=5mm Fabrication process: Hot rolled</p>												
<p>Average D= 159 mm</p> 		<p>Average t= 5.42 mm</p> 												
<p><i>Cross-sectional measured dimensions and tolerances</i></p>														
		<table border="1"> <thead> <tr> <th></th> <th>Average C_a, C_b</th> </tr> </thead> <tbody> <tr> <td>E [MPa]</td> <td>215000</td> </tr> <tr> <td>f_y [MPa]</td> <td>457.7</td> </tr> <tr> <td>ϵ_y [%]</td> <td>0.21</td> </tr> <tr> <td>f_u [MPa]</td> <td>577.3</td> </tr> <tr> <td>ϵ_u [%]</td> <td>7.02</td> </tr> </tbody> </table>		Average C_a, C_b	E [MPa]	215000	f_y [MPa]	457.7	ϵ_y [%]	0.21	f_u [MPa]	577.3	ϵ_u [%]	7.02
	Average C_a, C_b													
E [MPa]	215000													
f_y [MPa]	457.7													
ϵ_y [%]	0.21													
f_u [MPa]	577.3													
ϵ_u [%]	7.02													
<p><i>Tensile coupons location</i></p>	<p><i>Material stress-strain curves</i></p>	<p><i>Material average properties</i></p>												
 <div style="display: flex; justify-content: space-around; margin-top: 10px;"> <div data-bbox="440 1843 651 1875" style="text-align: center;"> <p>Membrane stresses</p> </div> <div data-bbox="1057 1843 1243 1875" style="text-align: center;"> <p>Flexural stresses</p> </div> </div> <p style="text-align: center; margin-top: 10px;"><i>Measured residual stresses distributions</i></p>														



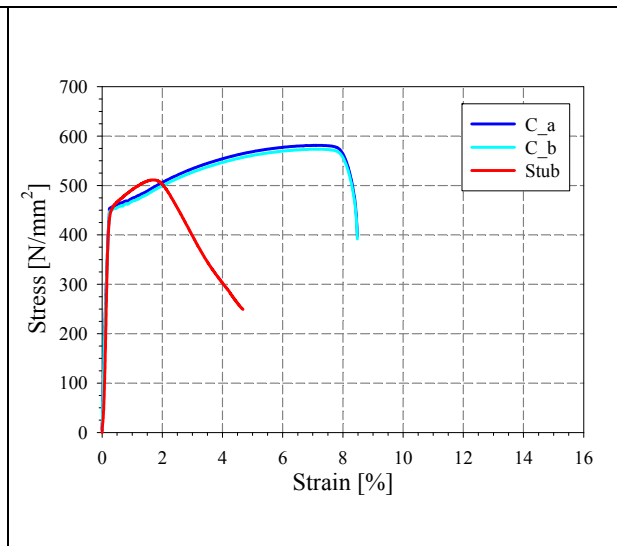
Amplified imperfect vue (x10)



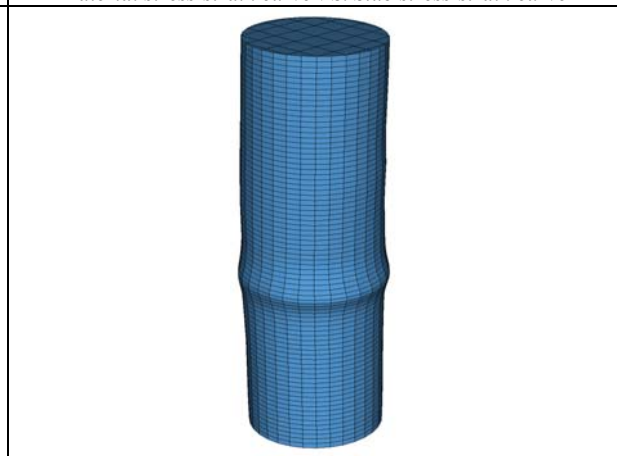
Measured Local imperfections



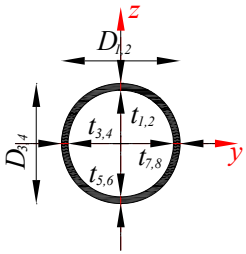
Strain gauges recordings

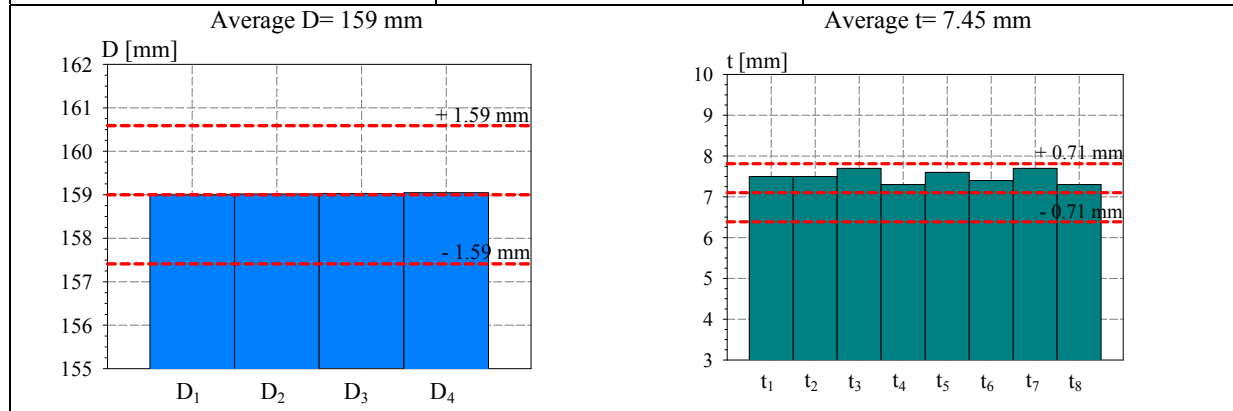


Material stress-strain curve VS. Stub stress-strain curve

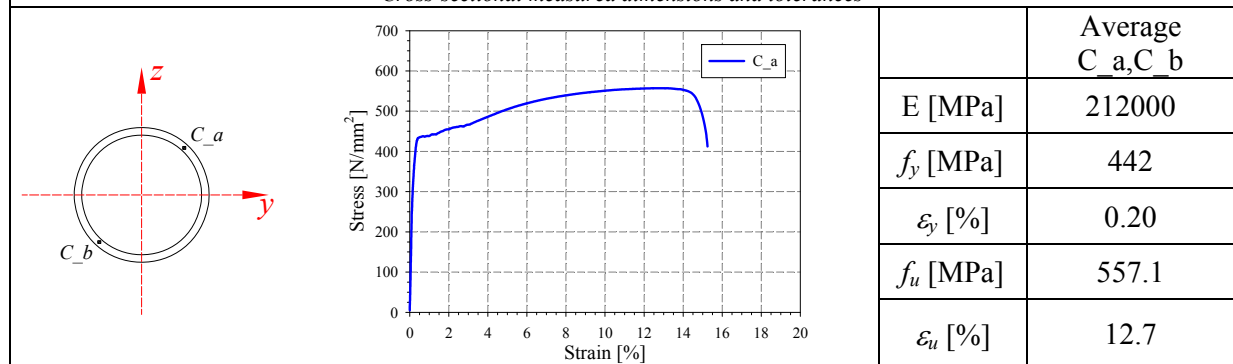


Local buckling failure Exp test VS. FE test

Specimen name	Shape	Details
CHS_S355_Stub 159x7.1 HR		Shape: Circular Hollow Section Nominal yield limit: 355 MPa Load case: Stub Pure compression D=159mm t=7.1mm Fabrication process: Hot rolled



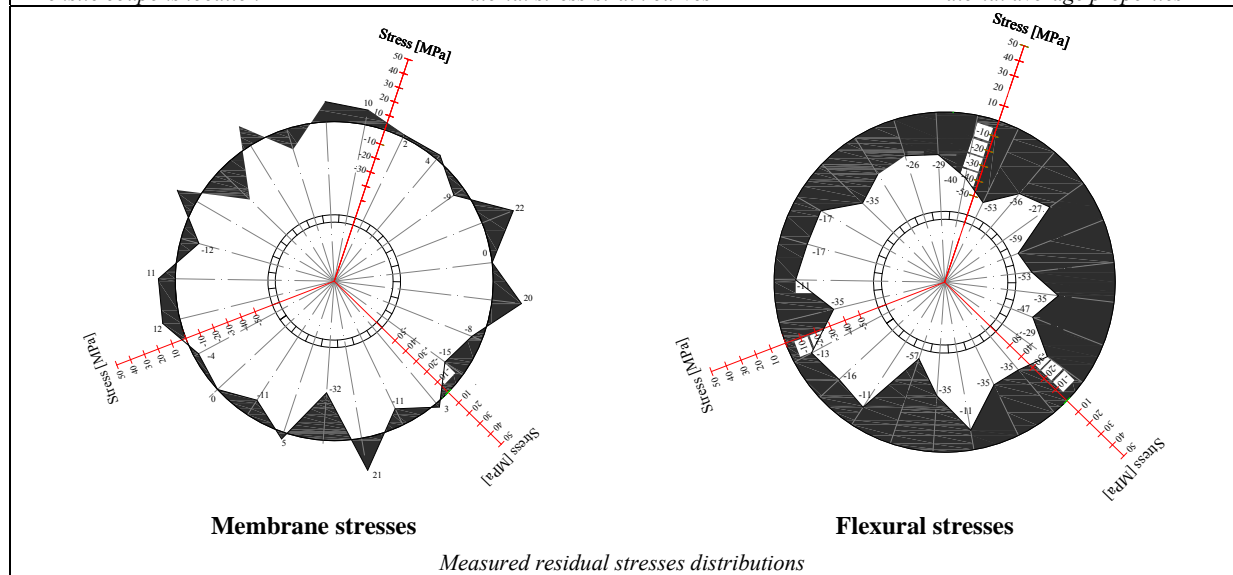
Cross-sectional measured dimensions and tolerances

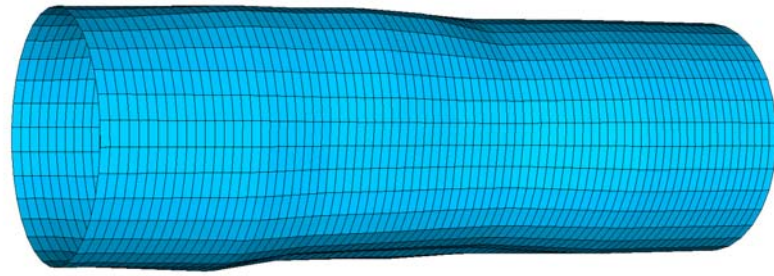


Tensile coupons location

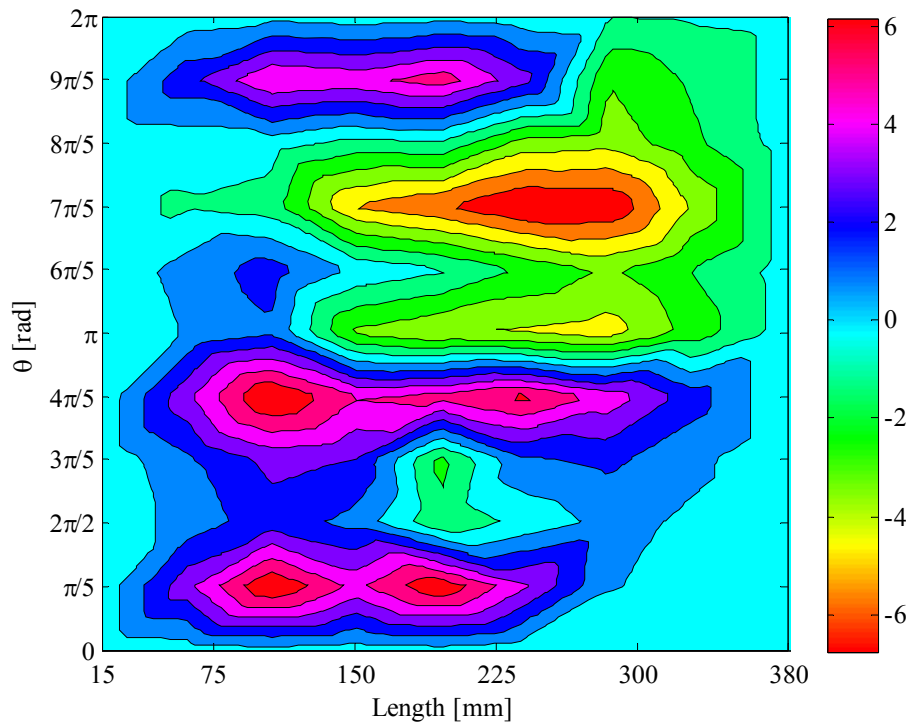
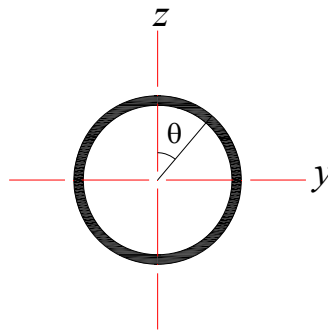
Material stress-strain curves

Material average properties

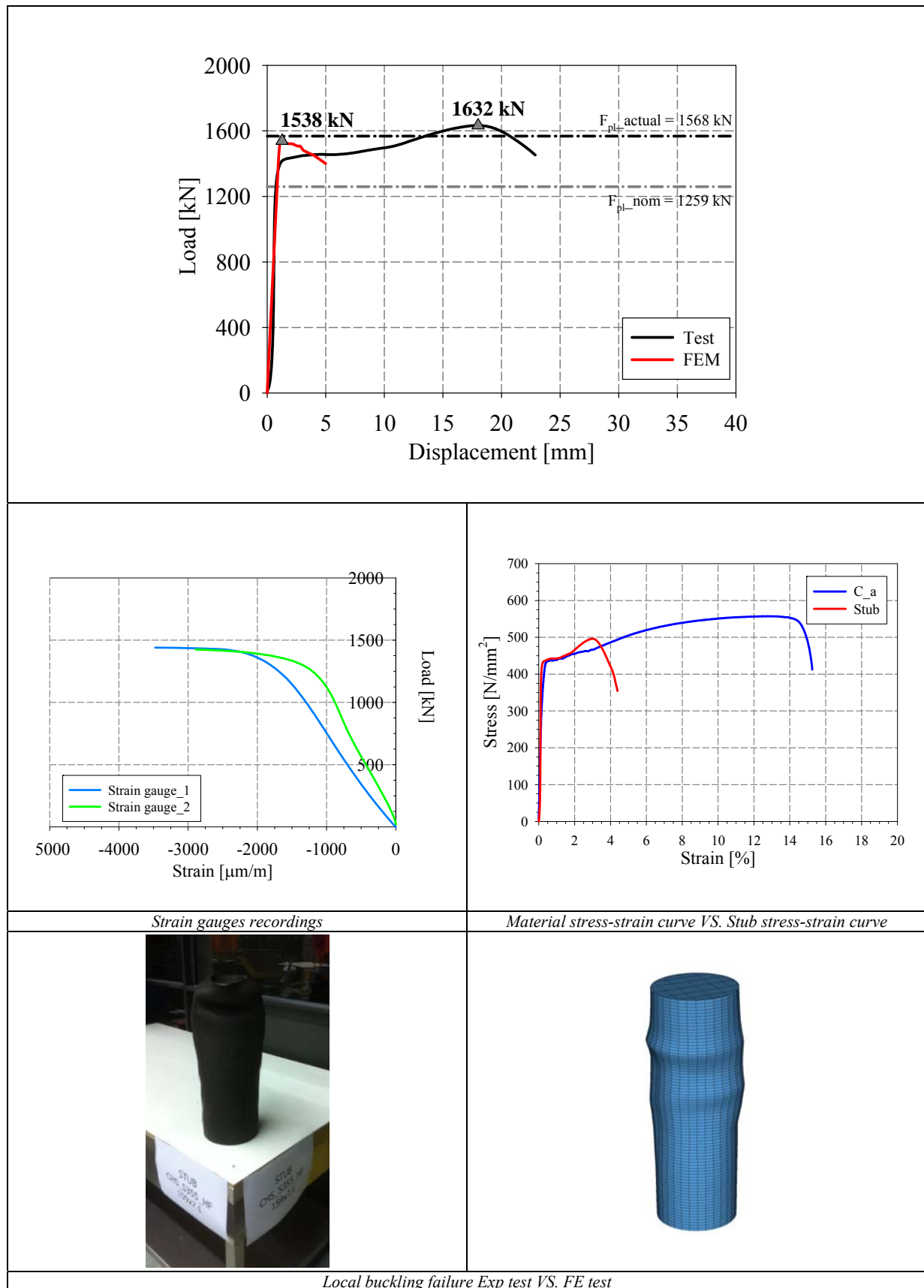




Amplified imperfect vue (x10)



Measured Local imperfections



11.6. Annex 6 – Detailed cross-section test results and comparison with FE results

This annex presents the complete set of results relative to the cross-section tests; it also provides a comparison of the experimental results with the results obtained from numerical simulations.

Results for each test are typically presented as a 4-pages summary, each of the 4 pages being organized as explained below.

Similarly to Annex 5 stub columns, the first page provides:

- (i) Specimen name, geometry and details;
- (ii) Geometrical measured dimensions with the correspondent tolerances;
- (iii) Measured material properties;
- (iv) Measured membrane and flexural stresses.

The second page provides measured geometrical imperfections, with contour plots of each plate's imperfections and two (amplified) 3D imperfect shape with the measured mesh fitted in the non-linear finite element software (similarly to stub column second page).

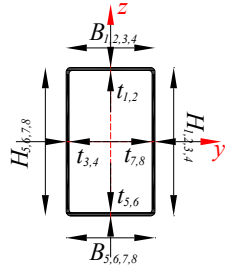
The third page provides:

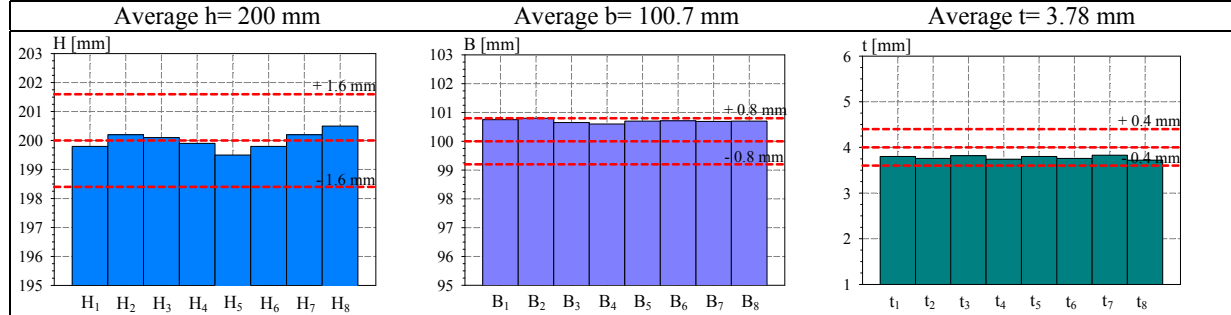
- (i) Upper and bottom LVDTs load-displacement curves relative to points of load application, with final average corrected curve (figures on the right are presented to provide information on the LVDTs' distributions and the specimen's position with its measured eccentricities);
- (ii) Diagrams showing strain and LVDTs recordings;
- (iii) Pictures of inelastic experimental local buckling failure.

The fourth page provides:

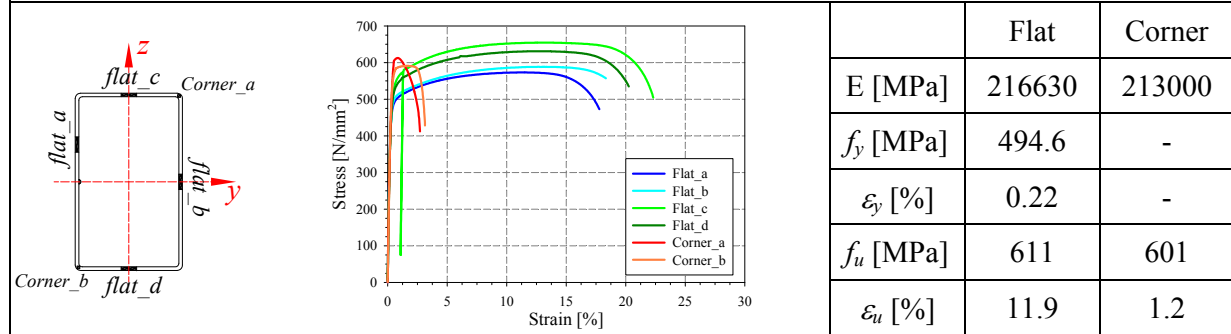
- (i) Load-displacement curves from both experimental and numerical sources (at point load application). Theoretical elastic and plastic load levels are also reported, for both the actual (measured) yield stress and for the nominal yield stress of 355 MPa;
- (ii) Non-dimensional cross-section capacity diagram;
- (iii) Non-dimensional M_y - M_z bending moment interaction diagram (obviously only for combined load cases);

(iv) Pictures of numerically-predicted failure modes.

<p>Specimen name</p> <p>RHS_S355_LC1 200x100x4 CF</p>	<p>Shape</p> 	<p>Details</p> <p>Shape: Rectangular Hollow Section</p> <p>Nominal yield limit: 355 MPa</p> <p>Load case: LC1 Pure compression</p> <p>H=200mm B=100mm t=4mm</p> <p>Fabrication process: Cold formed</p>
---	--	---



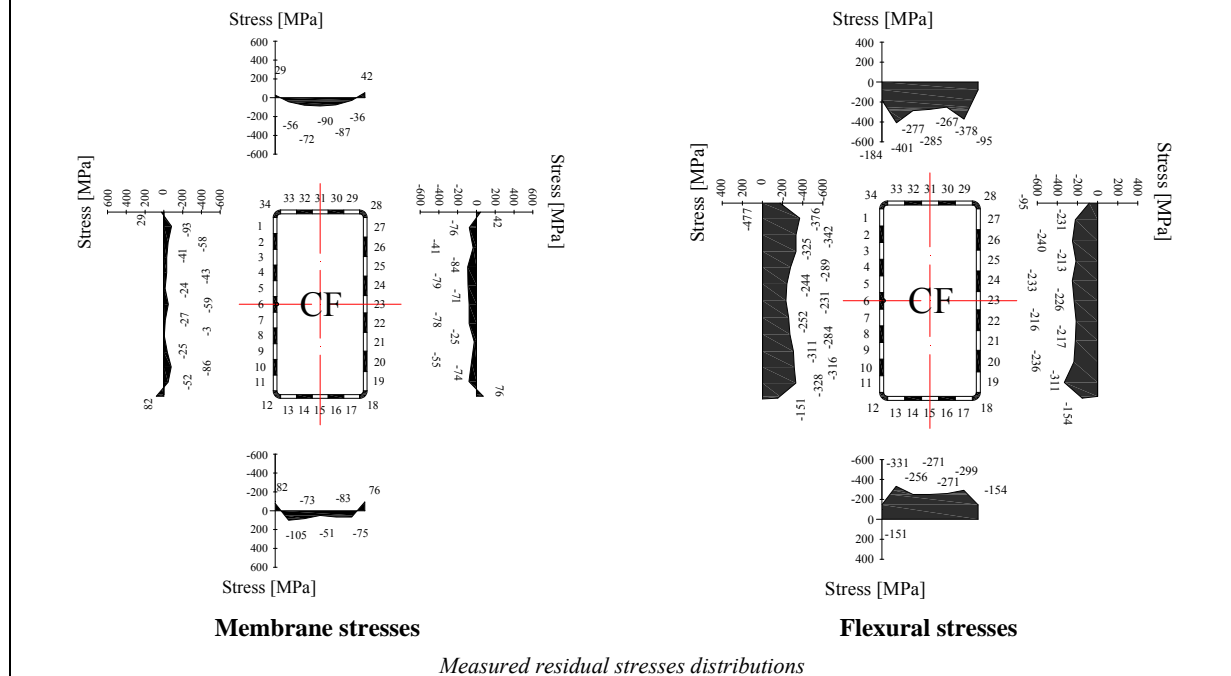
Cross-sectional measured dimensions and tolerances

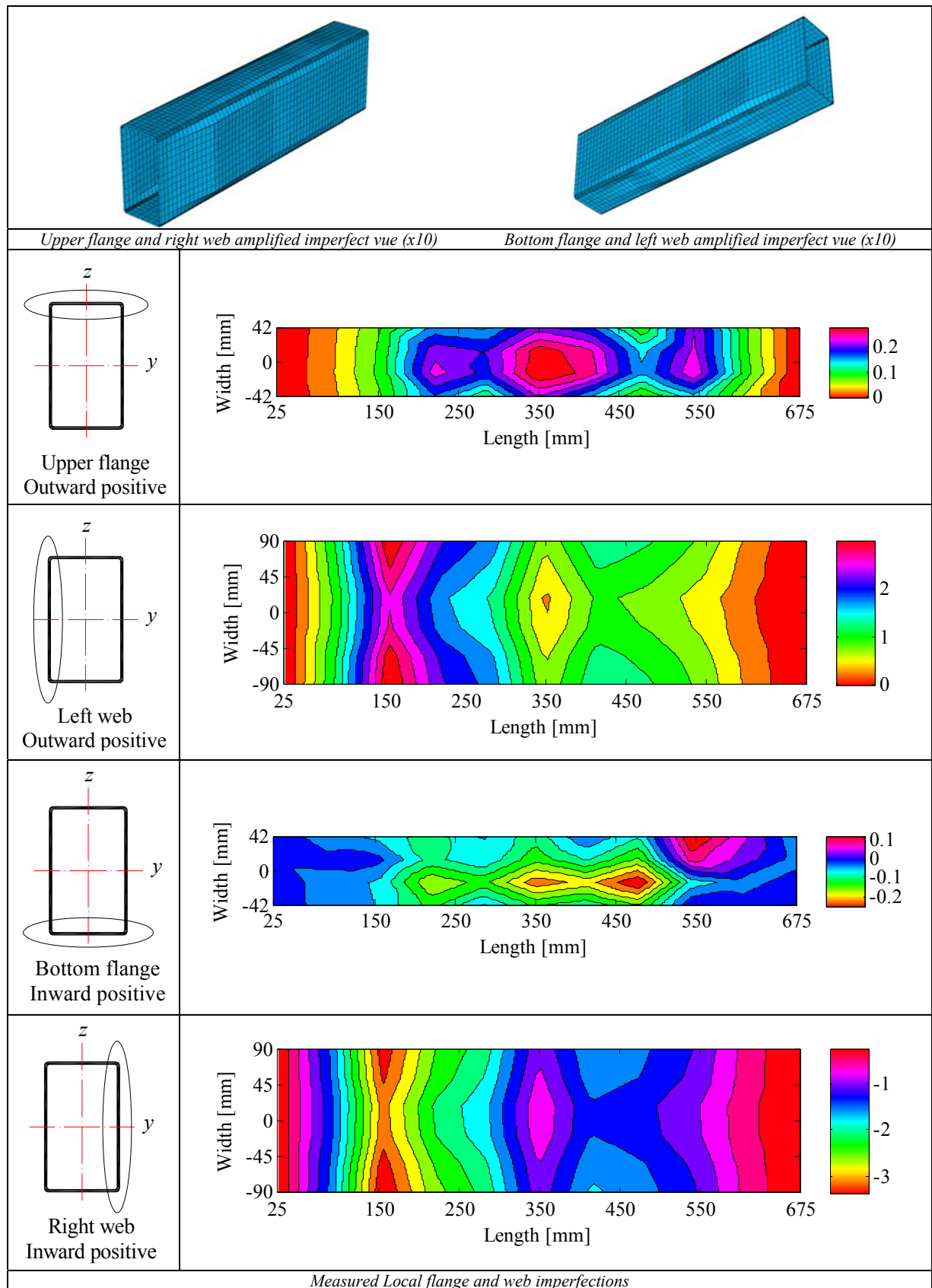


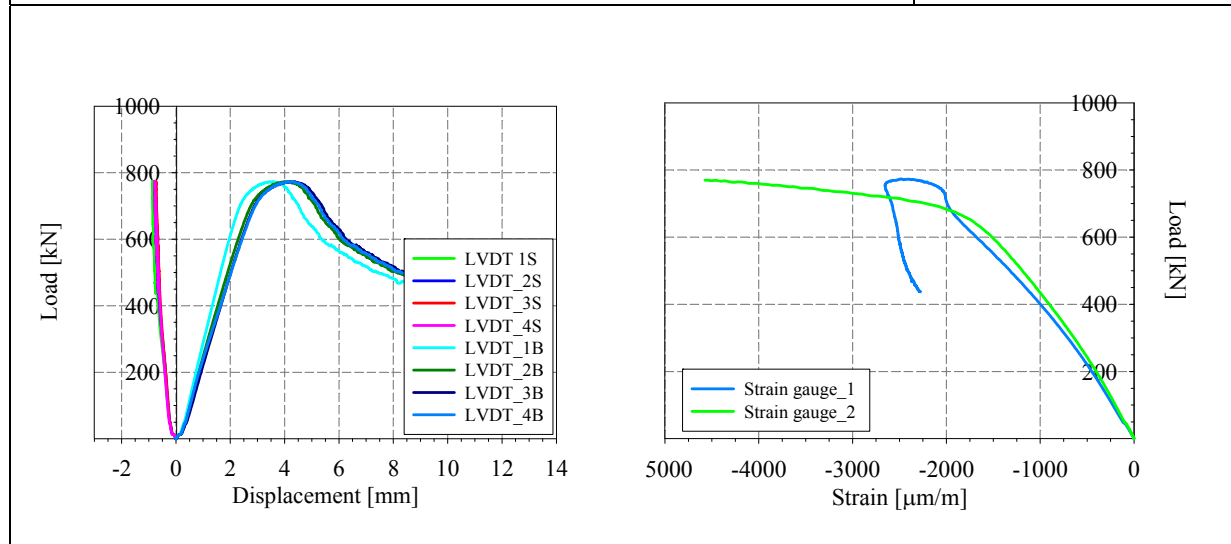
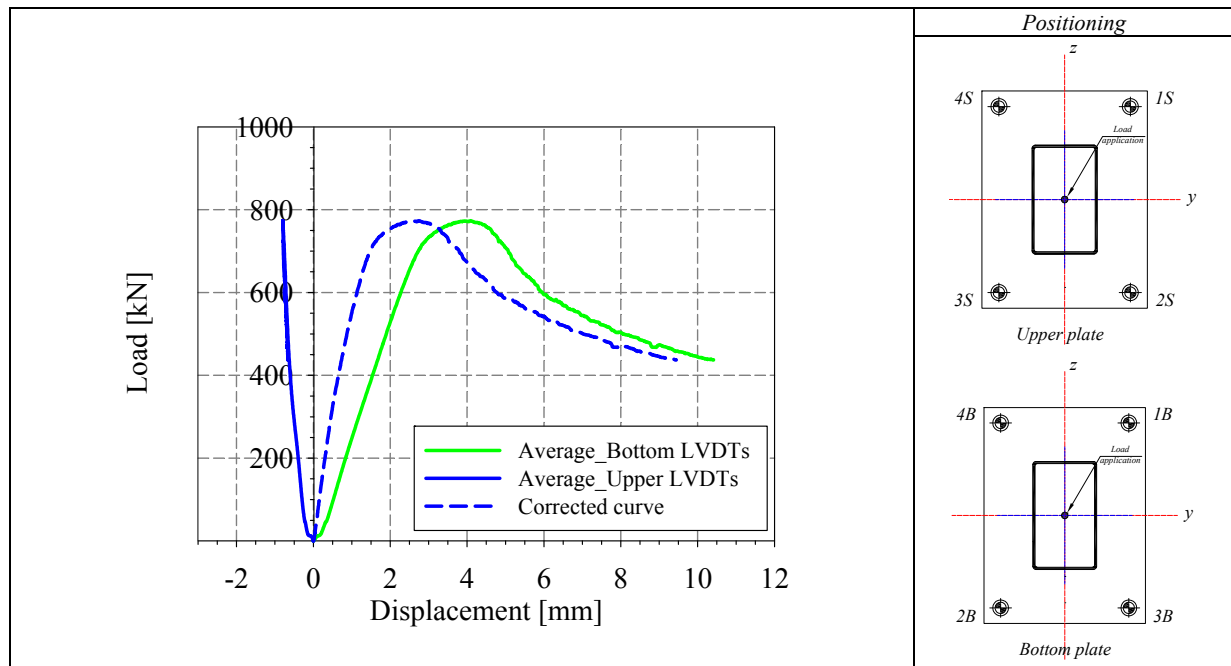
Tensile coupons location

Material stress-strain curves

Material average properties

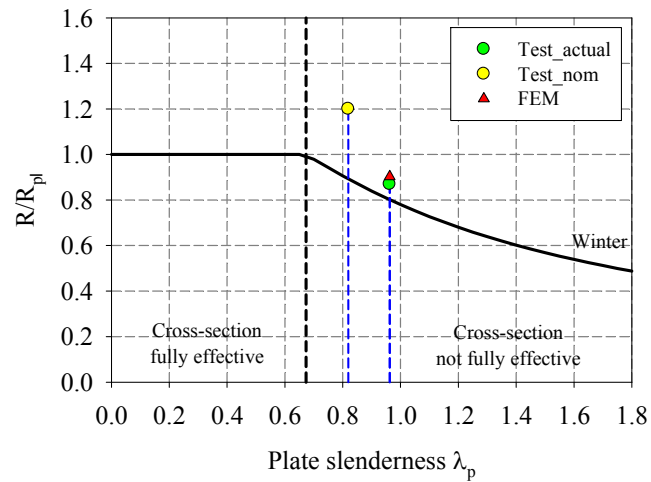
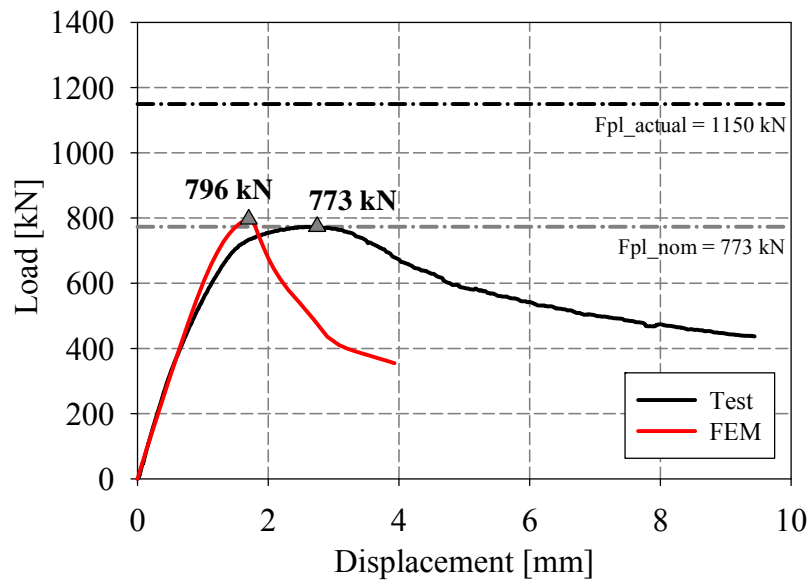




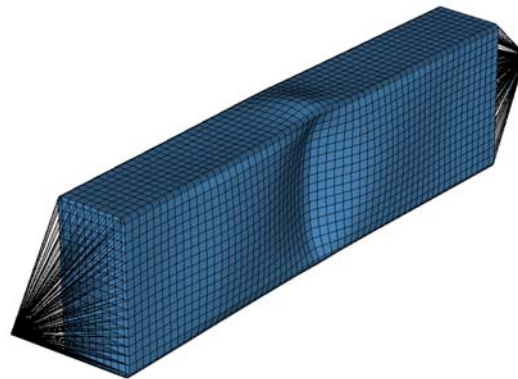


LVDT and strain gauges recordings

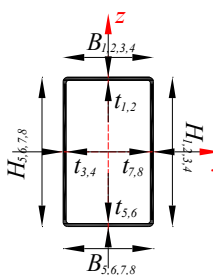


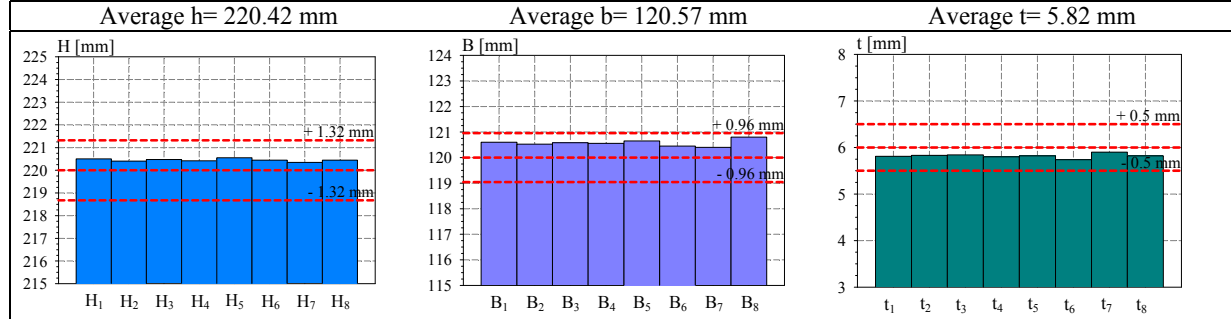


Non-dimensional cross section capacity in function of non-dimensional slenderness of decisive plate

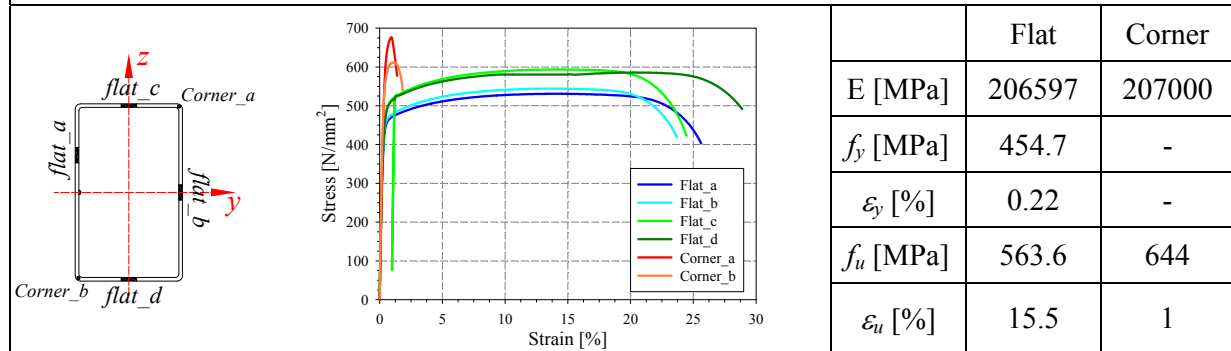


Numerical local buckling failure

<p>Specimen name</p> <p>RHS_S355_LC1 220x120x6 CF</p>	<p>Shape</p> 	<p>Details</p> <p>Shape: Rectangular Hollow Section</p> <p>Nominal yield limit: 355 MPa</p> <p>Load case: LC1 Pure compression</p> <p>H=220mm B=120mm t=6mm</p> <p>Fabrication process: Cold formed</p>
---	--	---



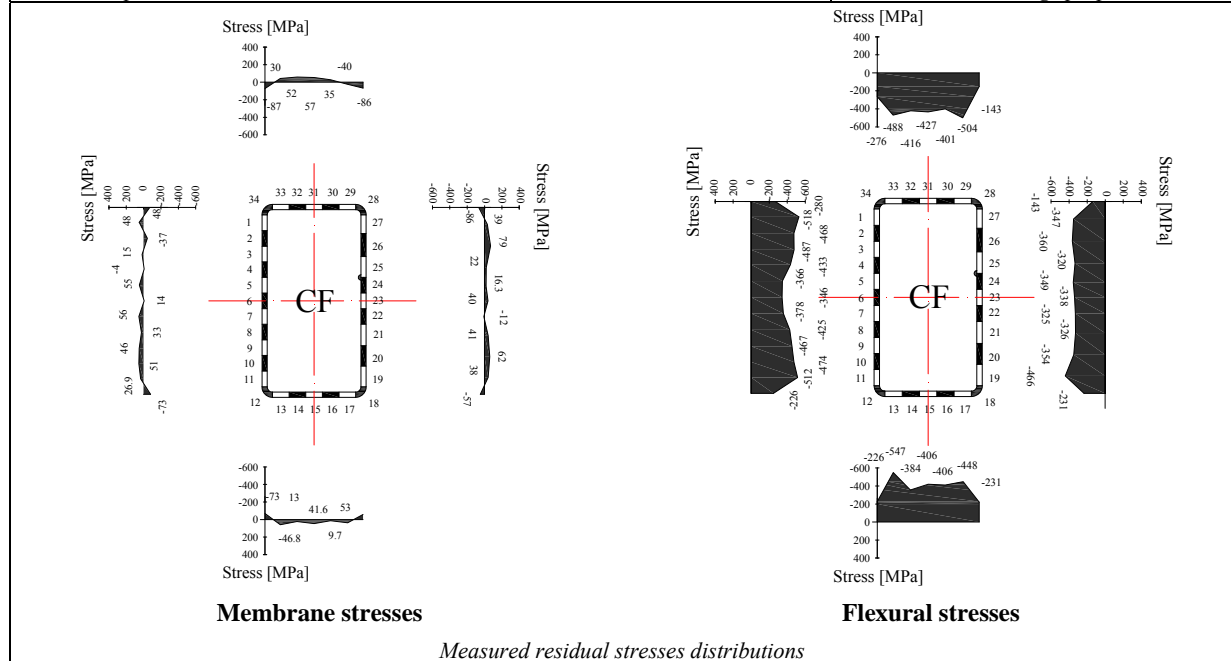
Cross-sectional measured dimensions and tolerances

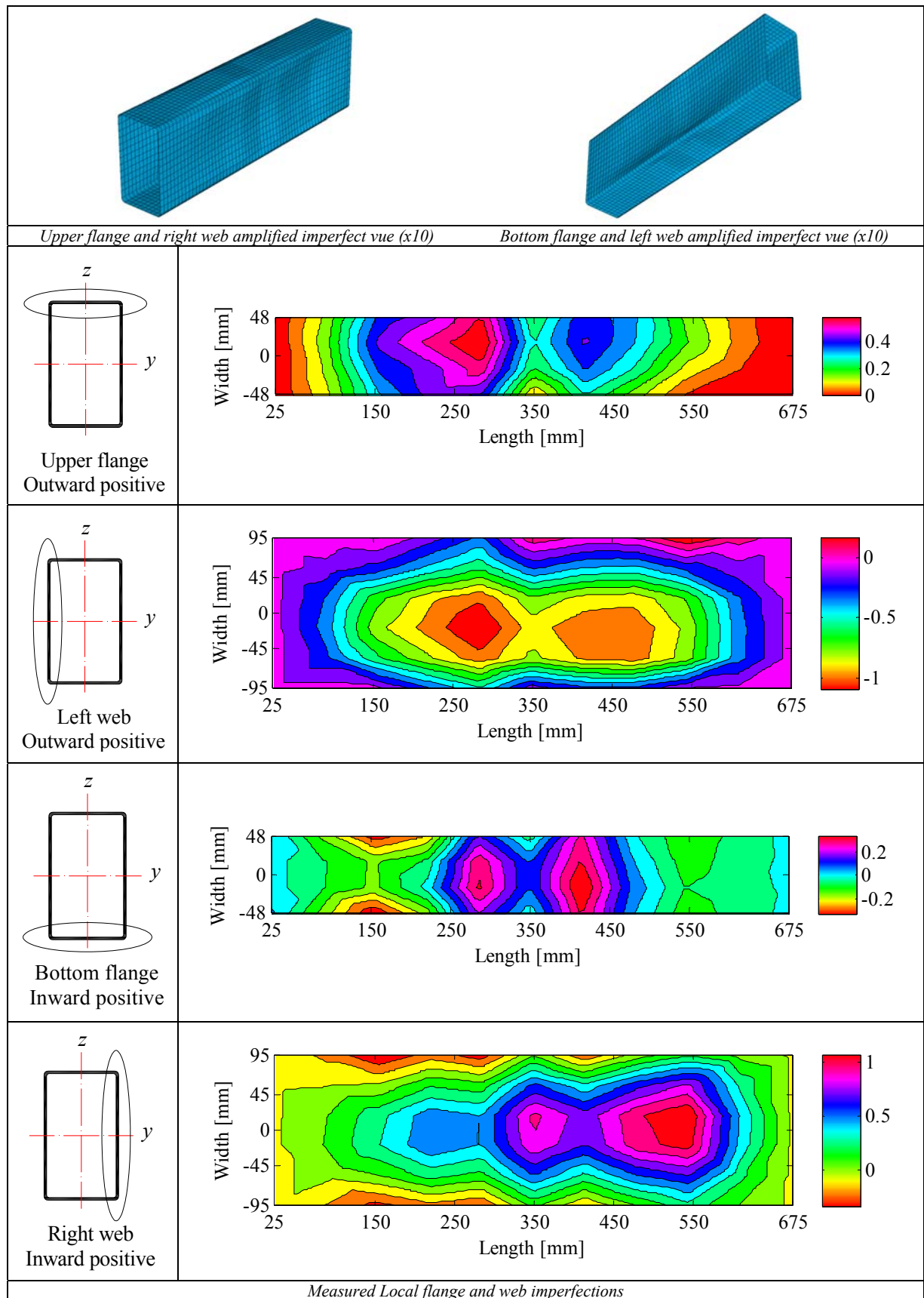


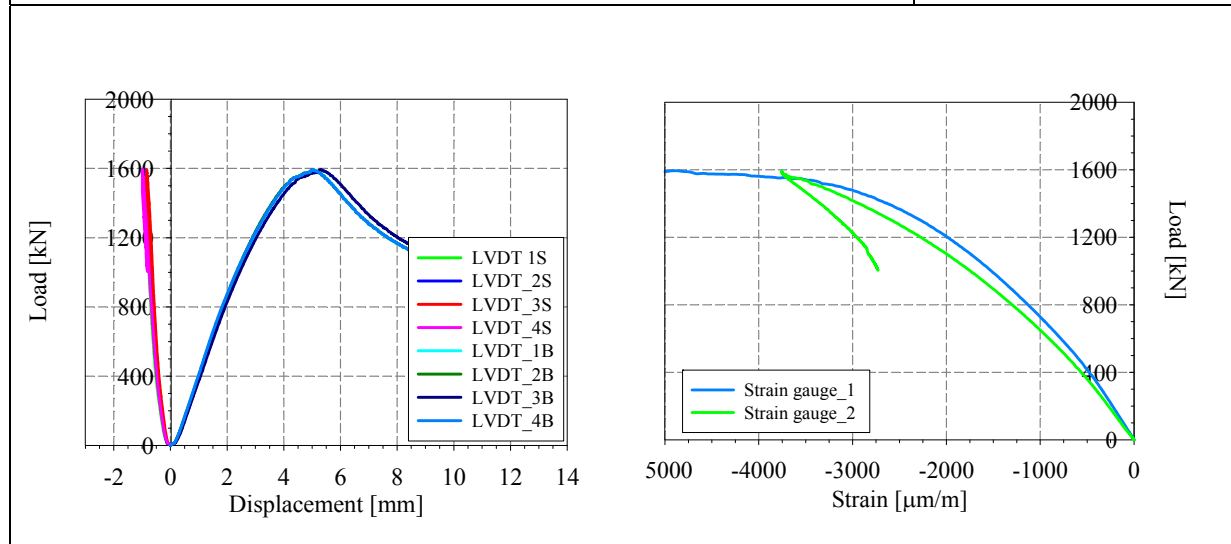
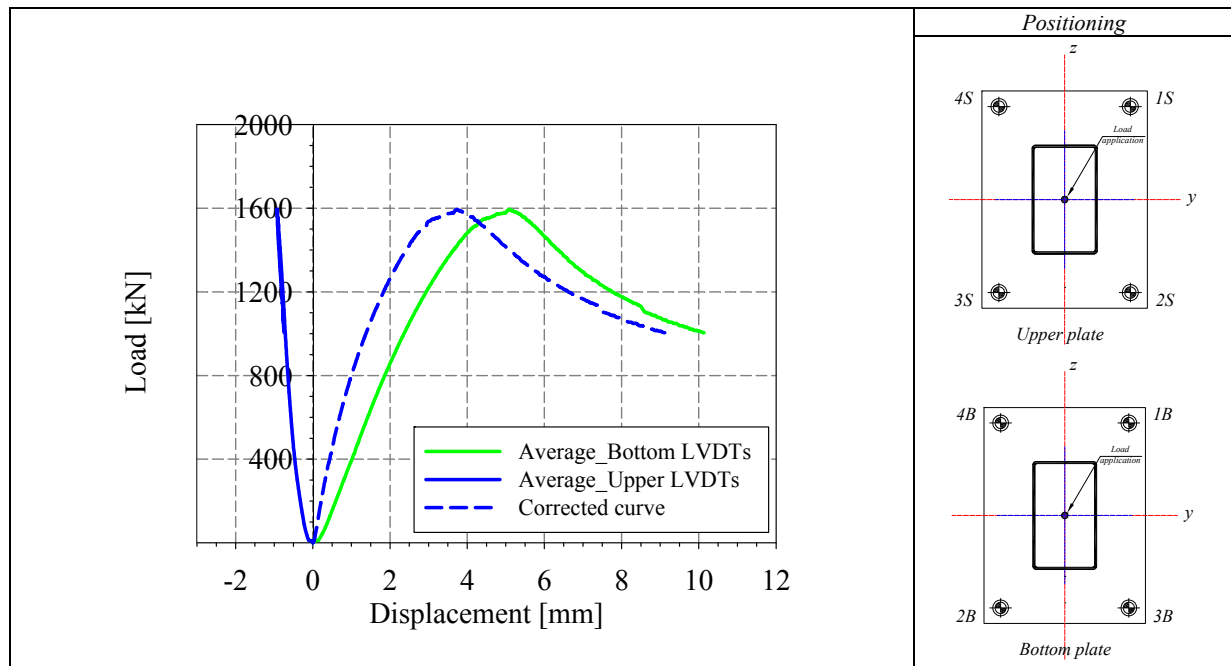
Tensile coupons location

Material stress-strain curves

Material average properties



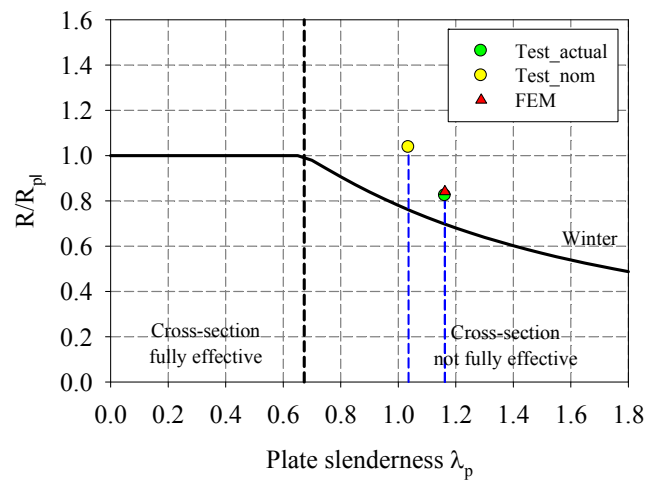
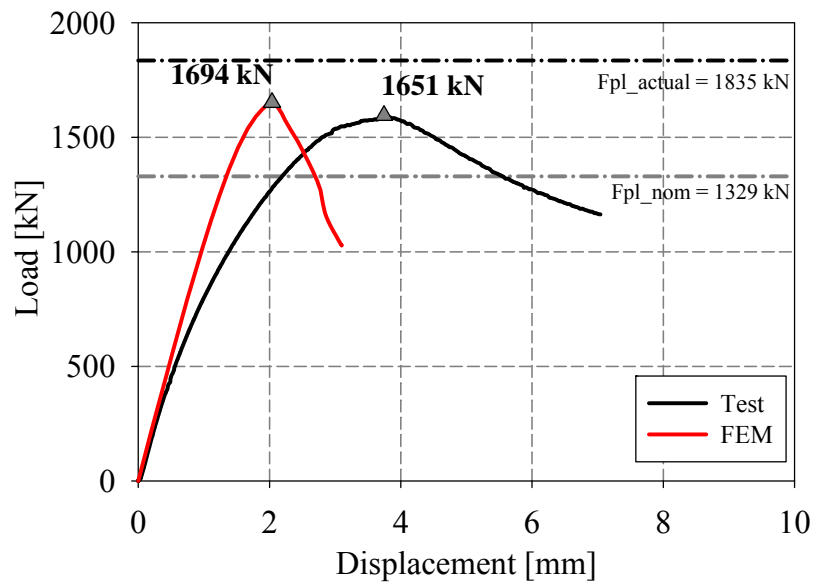




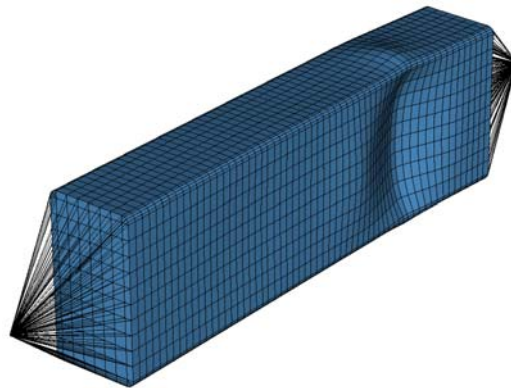
LVDT and strain gauges recordings



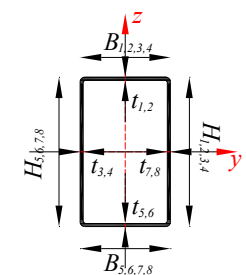
Local buckling failure

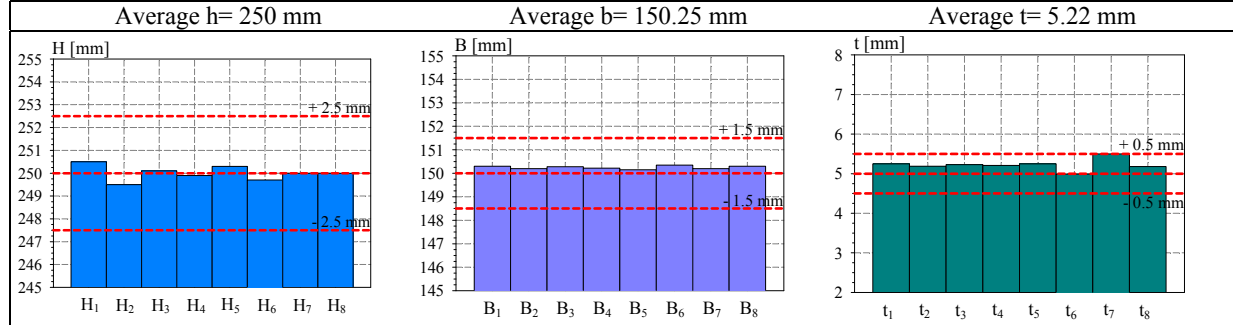


Non-dimensional cross section capacity in function of non-dimensional slenderness of decisive plate

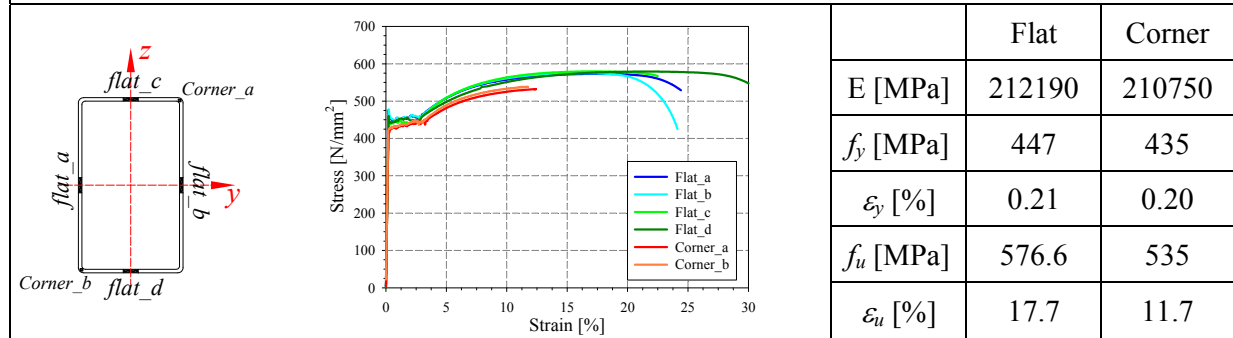


Numerical local buckling failure

<p>Specimen name</p> <p>RHS_S355_LC1 250x150x5 HF</p>	<p>Shape</p> 	<p>Details</p> <p>Shape: Rectangular Hollow Section</p> <p>Nominal yield limit: 355 MPa</p> <p>Load case: LC1 Pure compression</p> <p>H=250mm B=150mm t=5mm</p> <p>Fabrication process: Hot formed</p>
---	--	--



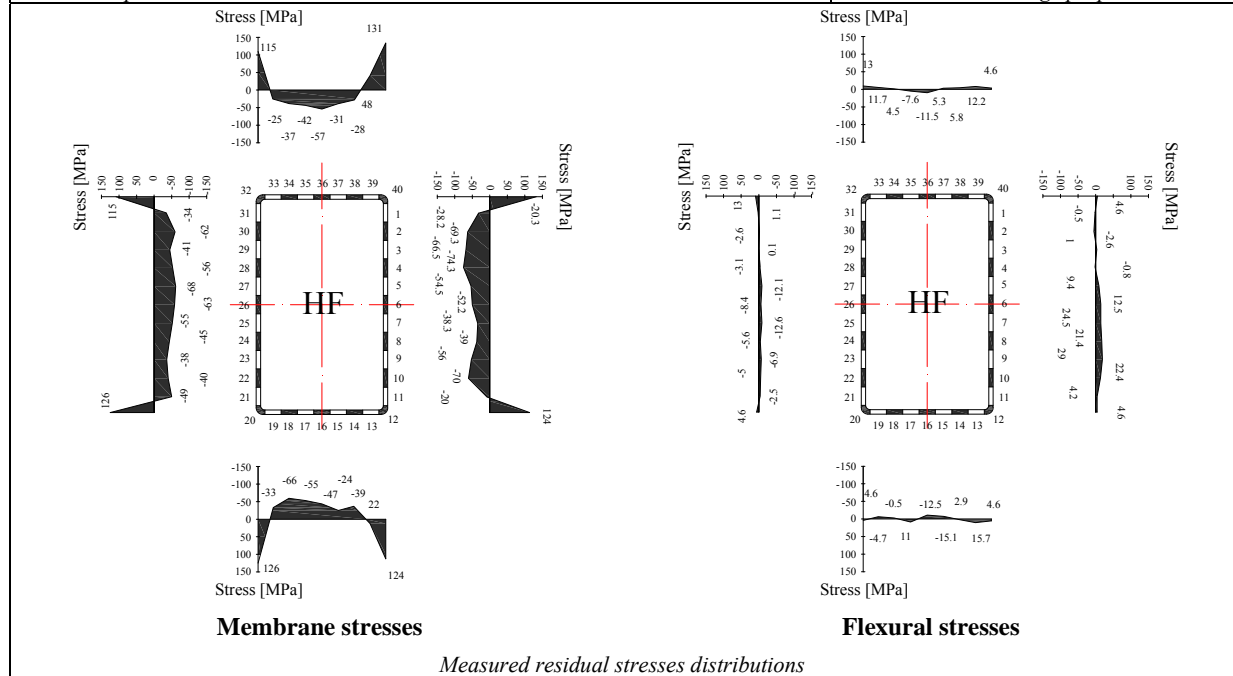
Cross-sectional measured dimensions and tolerances

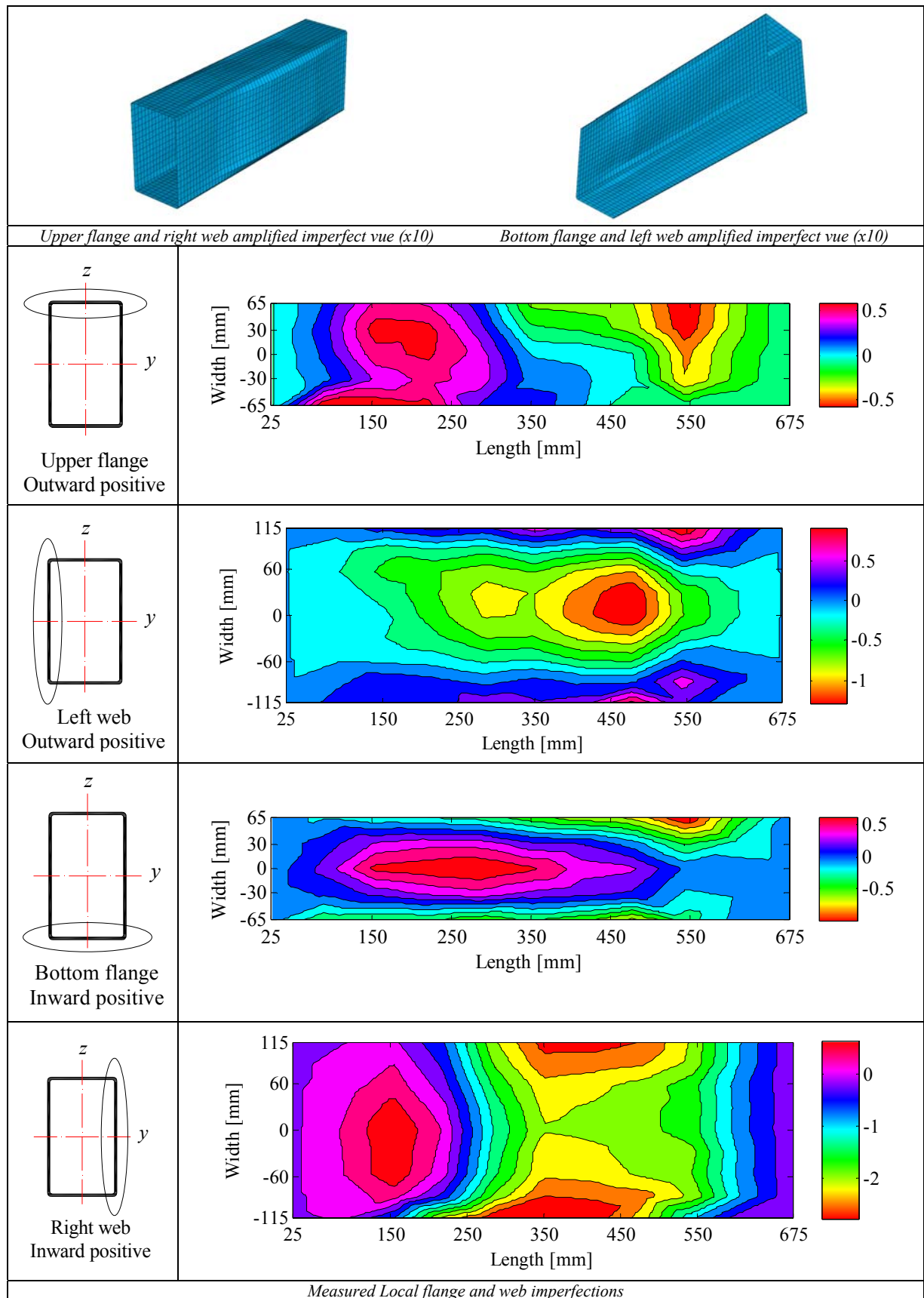


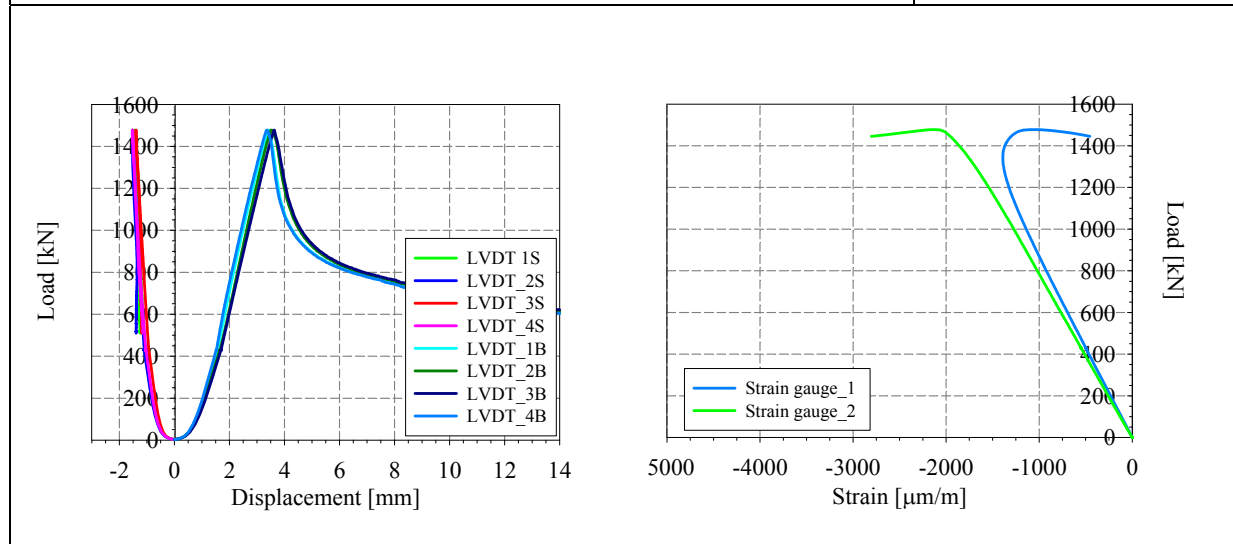
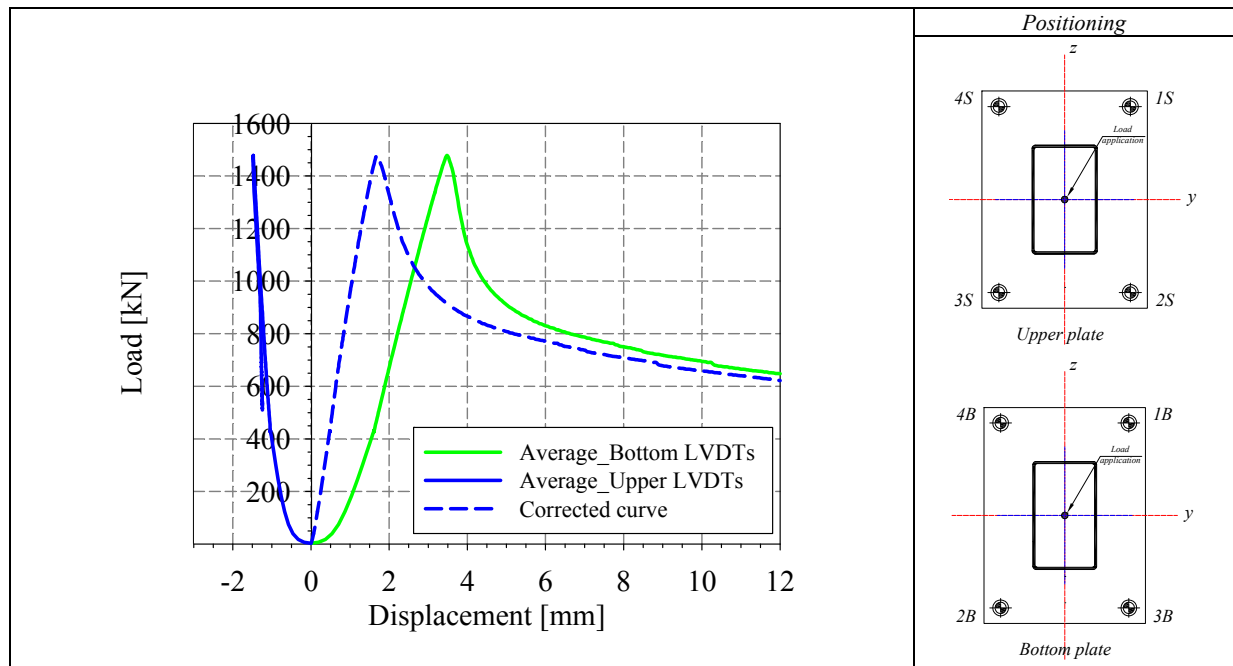
Tensile coupons location

Material stress-strain curves

Material average properties



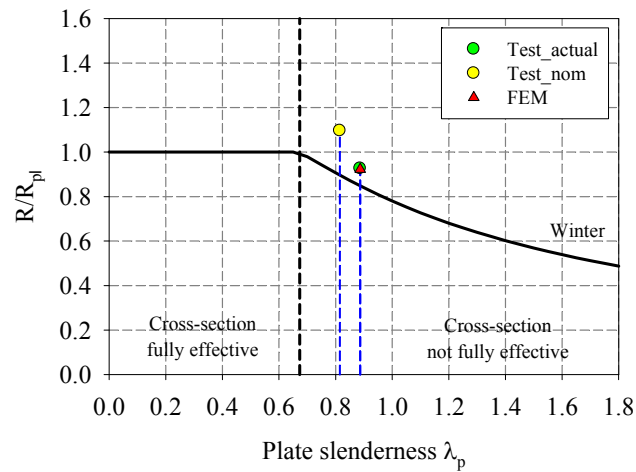
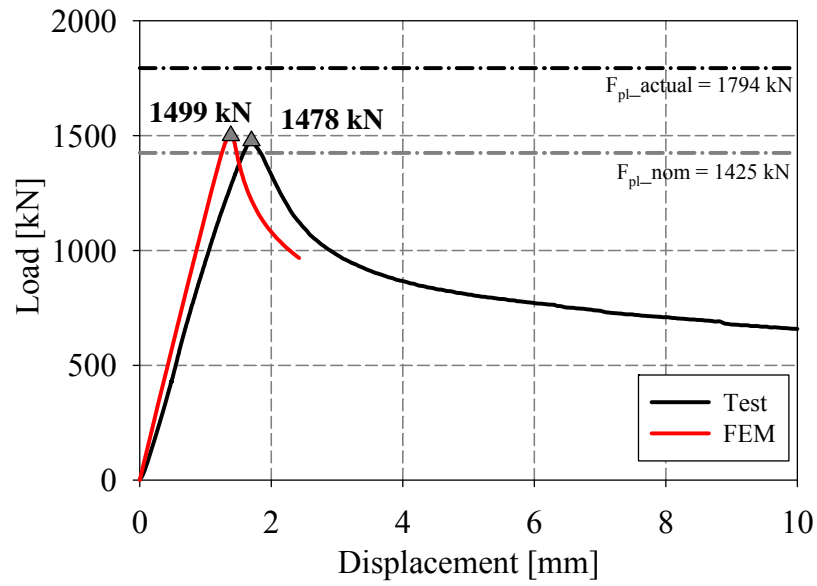




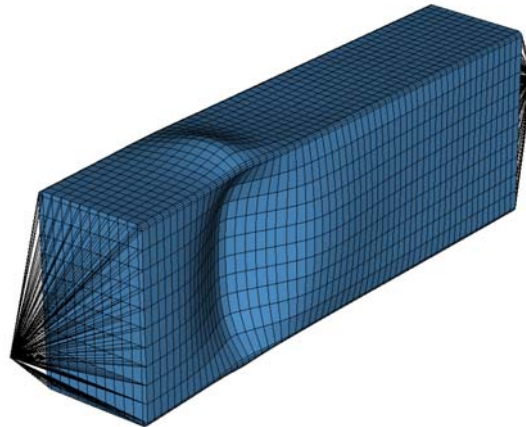
LVDT and strain gauges recordings



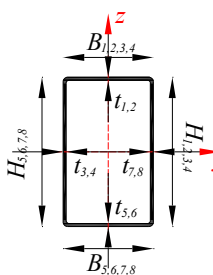
Local buckling failure

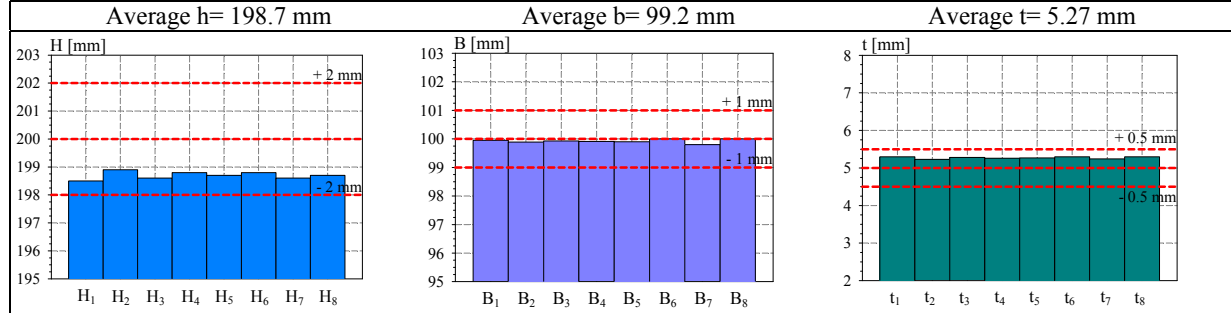


Non-dimensional cross section capacity in function of non-dimensional slenderness of decisive plate

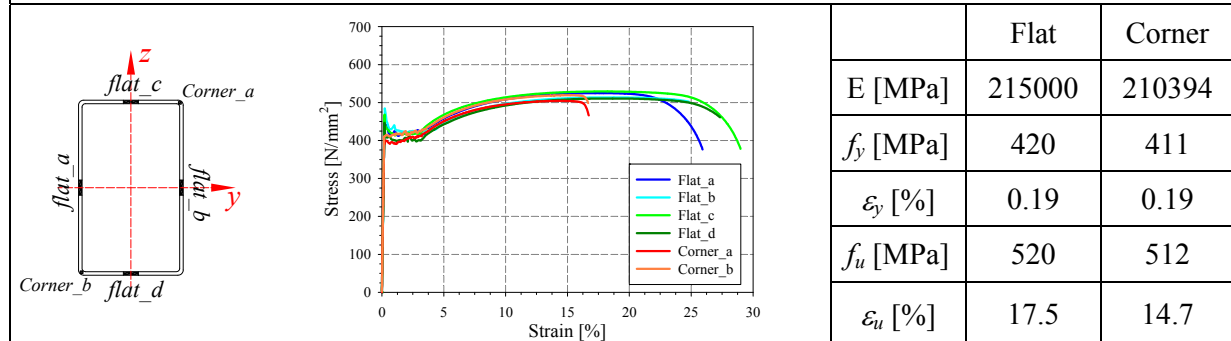


Numerical local buckling failure

<p>Specimen name</p> <p>RHS_S355_LC1 200x100x5 HF</p>	<p>Shape</p> 	<p>Details</p> <p>Shape: Rectangular Hollow Section Nominal yield limit: 355 MPa Load case: LC1 Pure compression H=200mm B=100mm t=5mm Fabrication process: Hot formed</p>
---	--	--



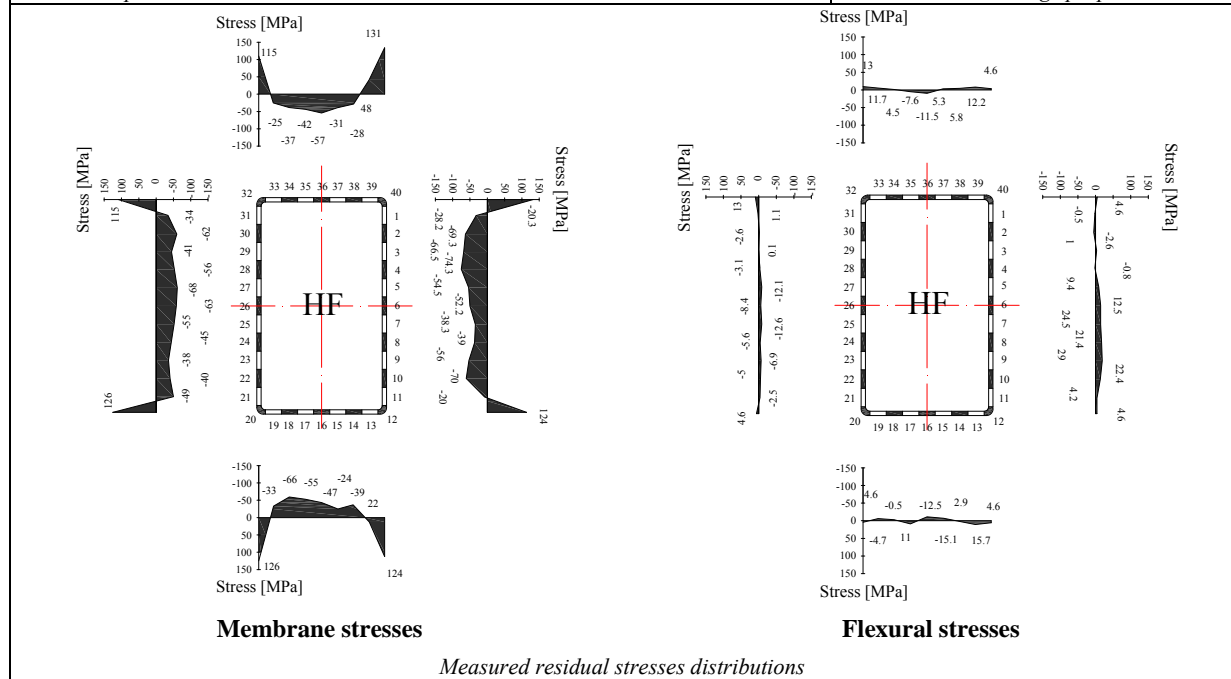
Cross-sectional measured dimensions and tolerances

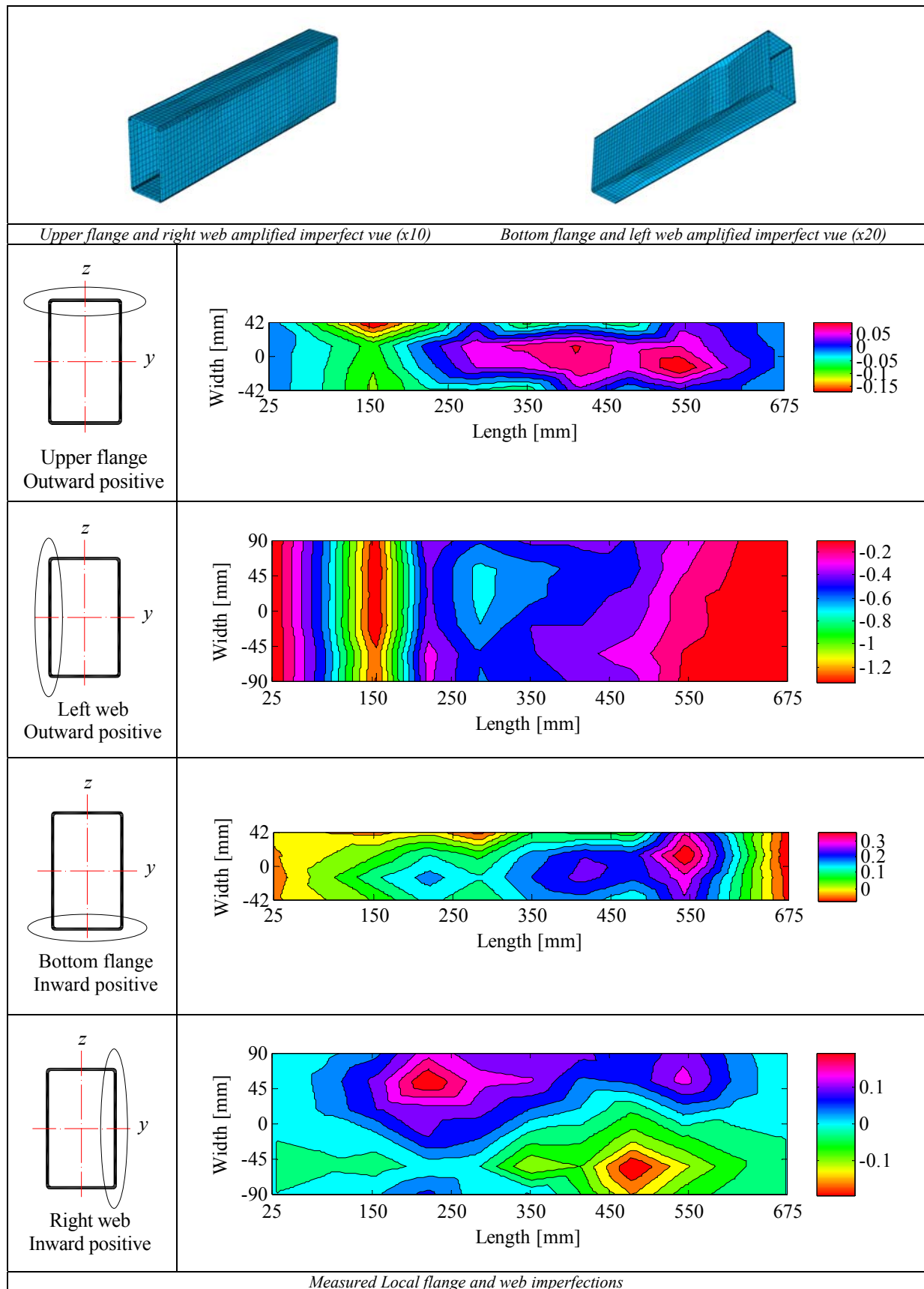


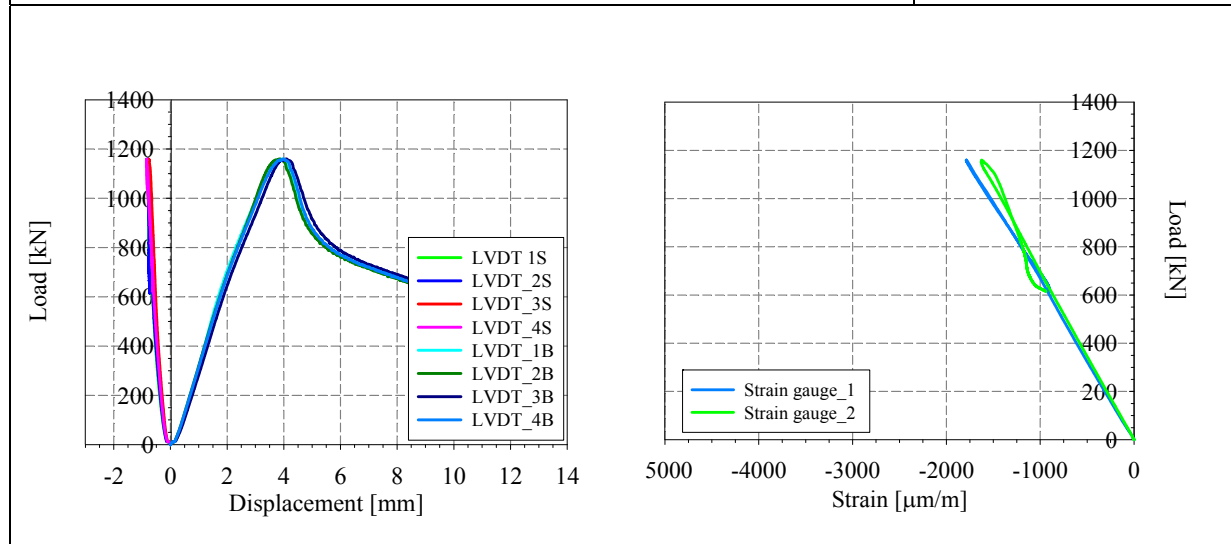
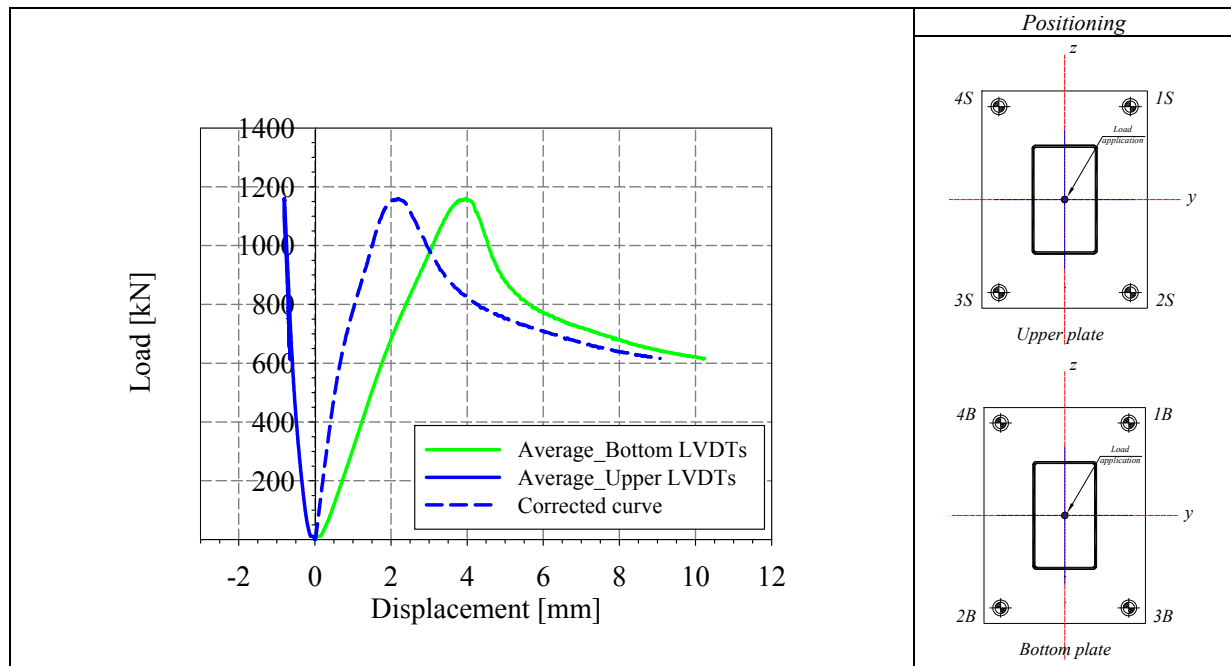
Tensile coupons location

Material stress-strain curves

Material average properties

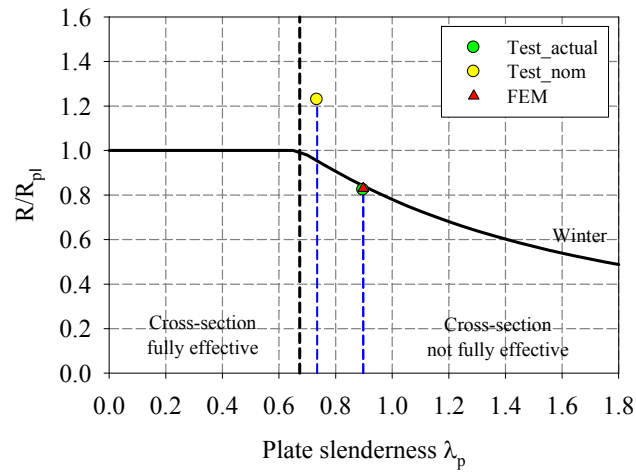
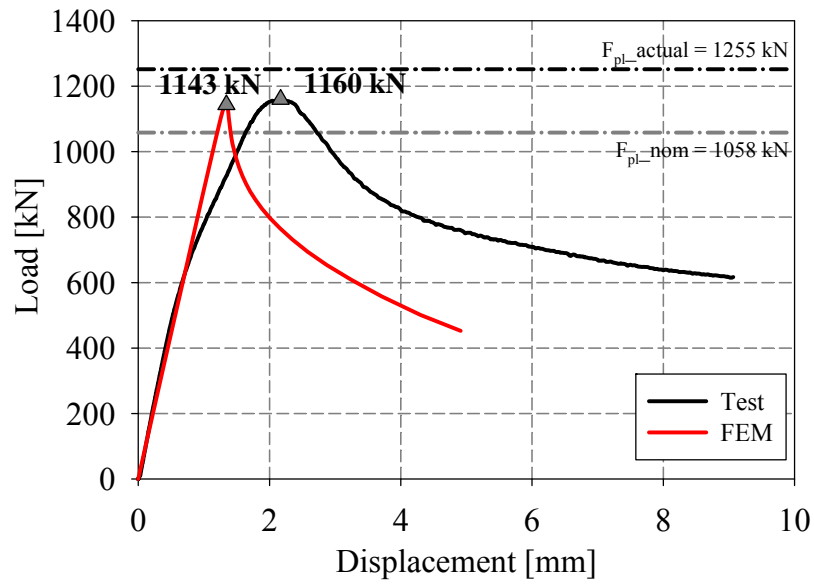




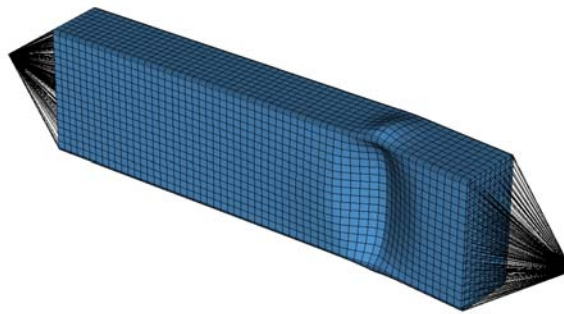


LVDT and strain gauges recordings



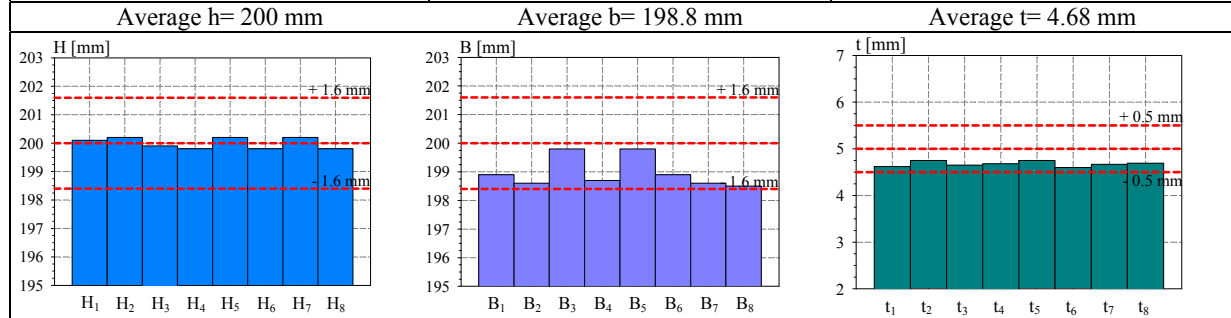


Non-dimensional cross section capacity in function of non-dimensional slenderness of decisive plate

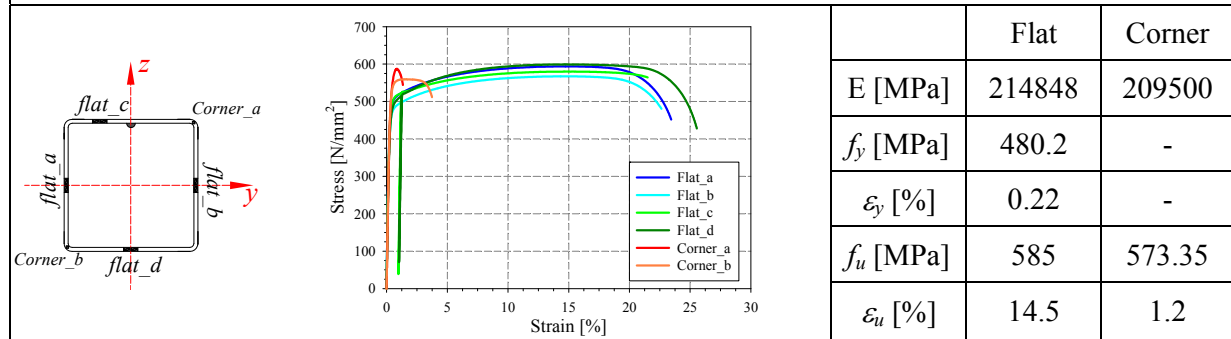


Numerical local buckling failure

<p>Specimen name</p> <p>RHS_S355_LC1 200x200x5 CF</p>	<p>Shape</p>	<p>Details</p> <p>Shape: Square Hollow Section Nominal yield limit: 355 MPa Load case: LC1 Pure compression H=200mm B=200mm t=5mm Fabrication process: Cold formed</p>
---	--------------	--



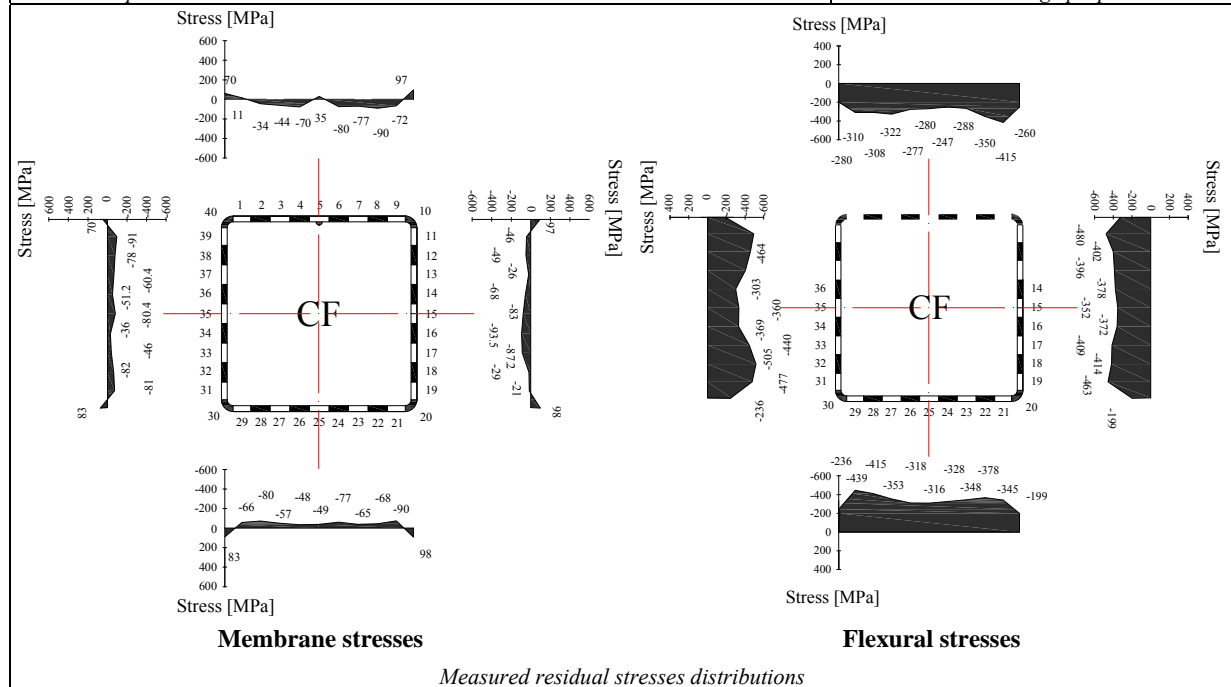
Cross-sectional measured dimensions and tolerances

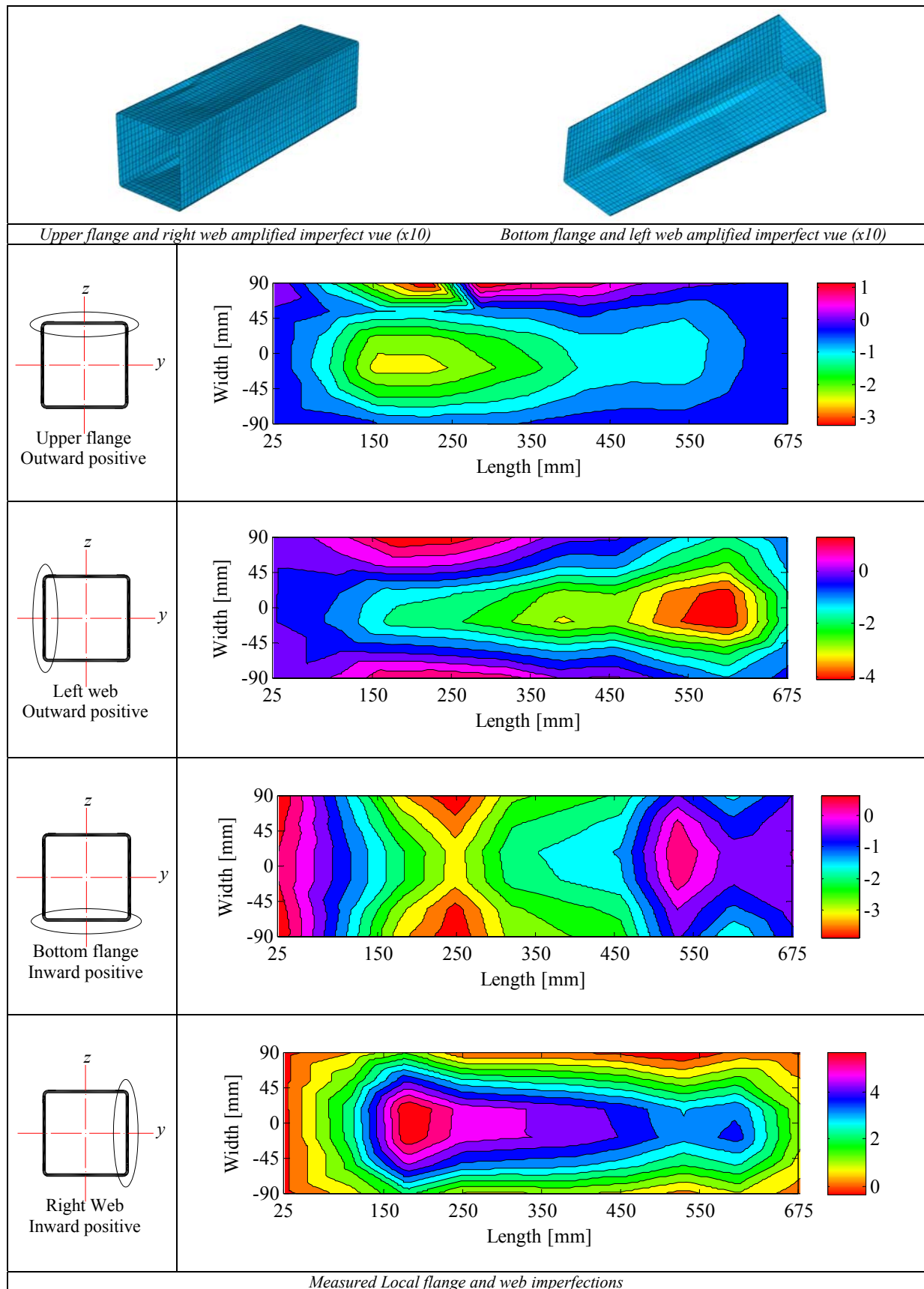


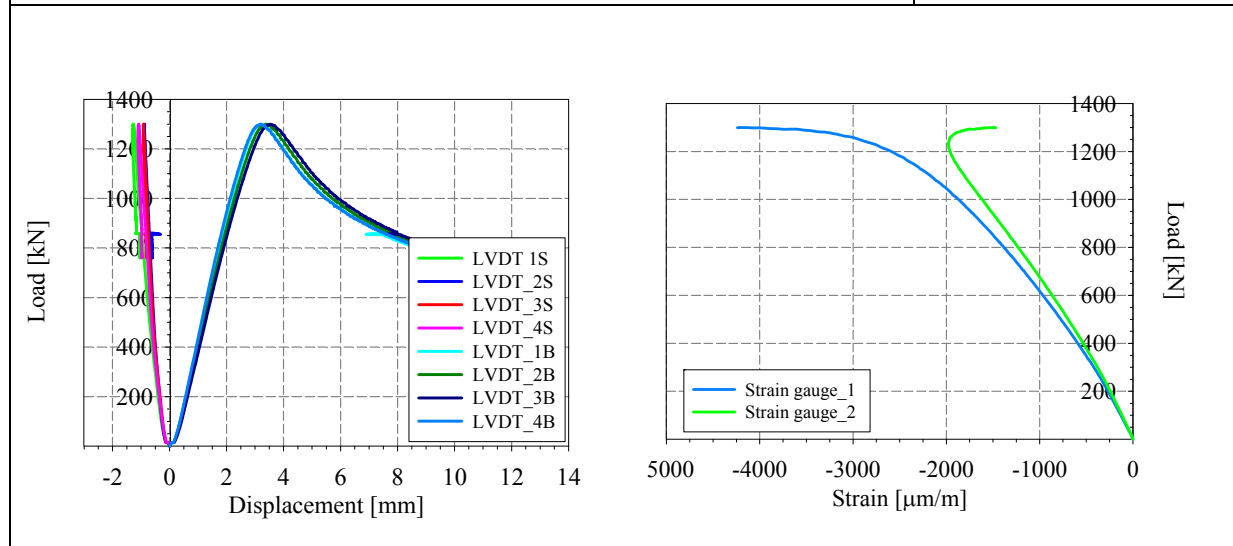
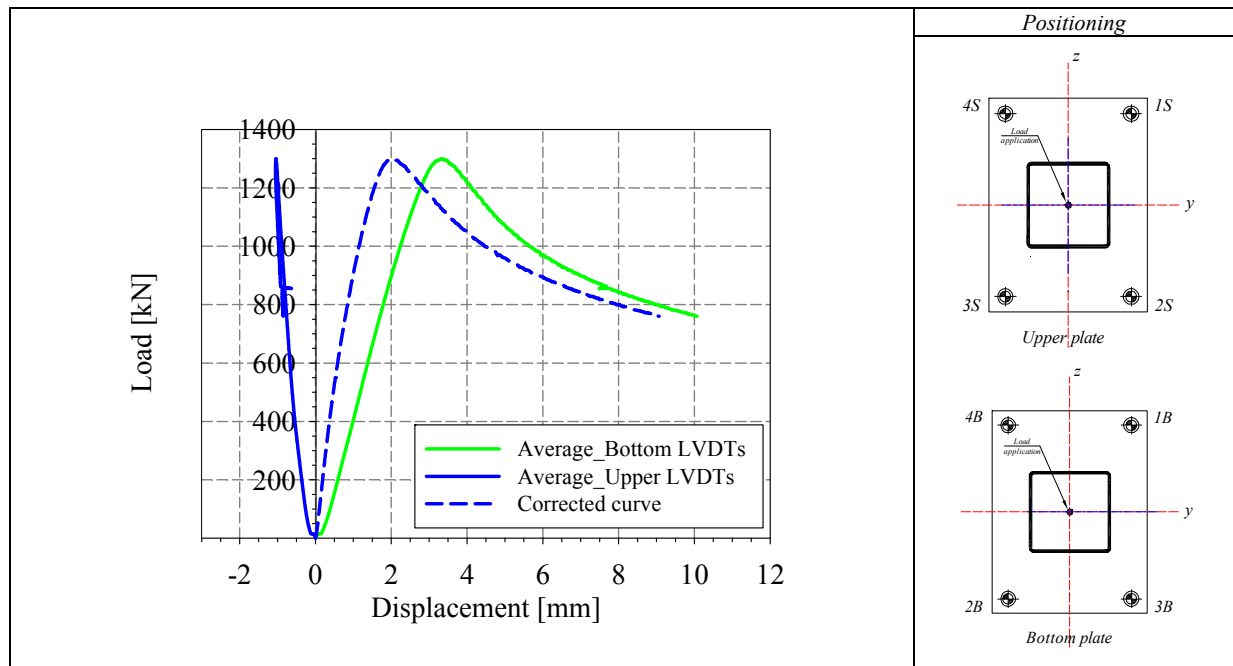
Tensile coupons location

Material stress-strain curves

Material average properties



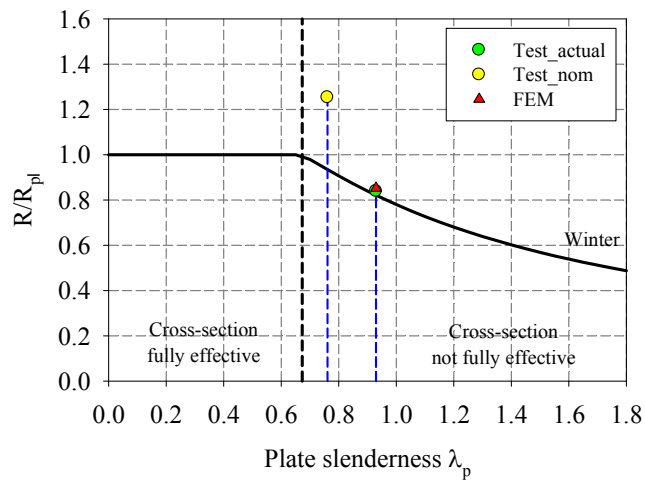
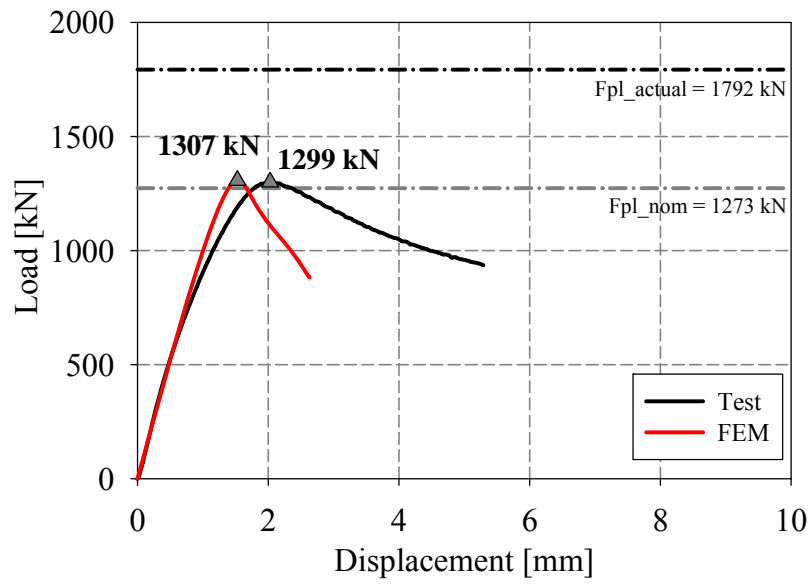




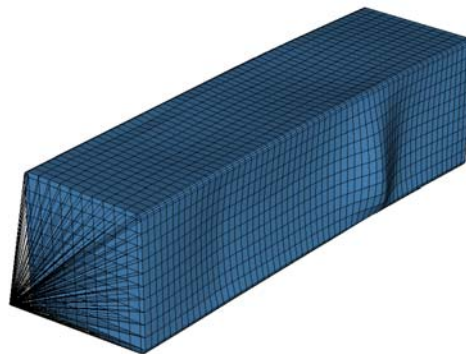
LVDT and strain gauges recordings



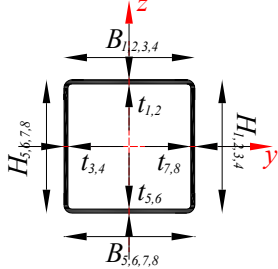
Local buckling failure

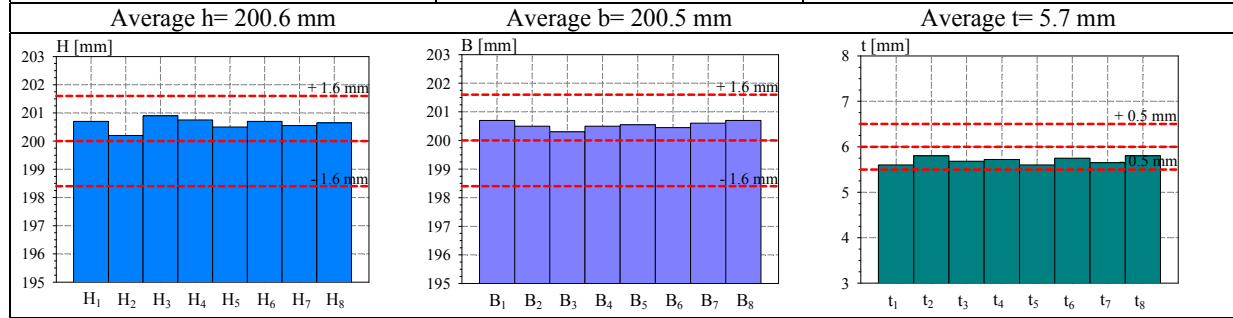


Non-dimensional cross section capacity in function of non-dimensional slenderness of decisive plate

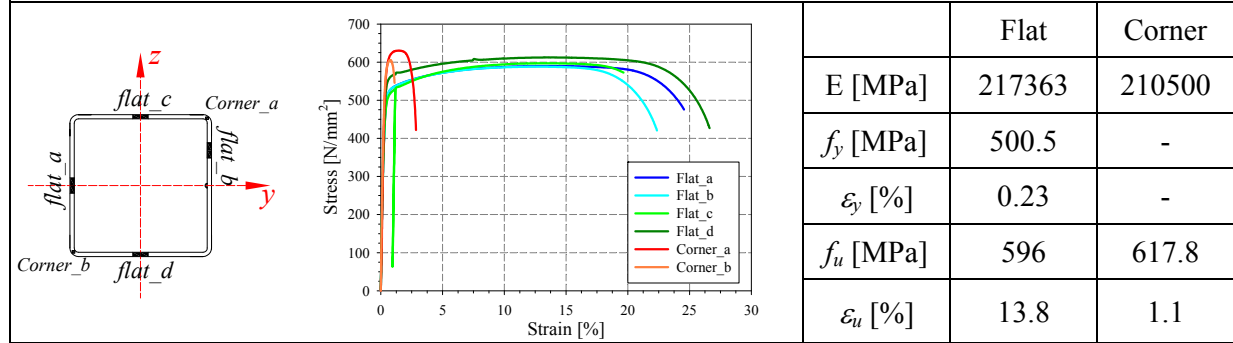


Numerical local buckling failure

Specimen name	Shape	Details
RHS_S355_LC1 200x200x6 CF		Shape: Square Hollow Section Nominal yield limit: 355 MPa Load case: LC1 Pure compression H=200mm B=200mm t=6mm Fabrication process: Cold formed



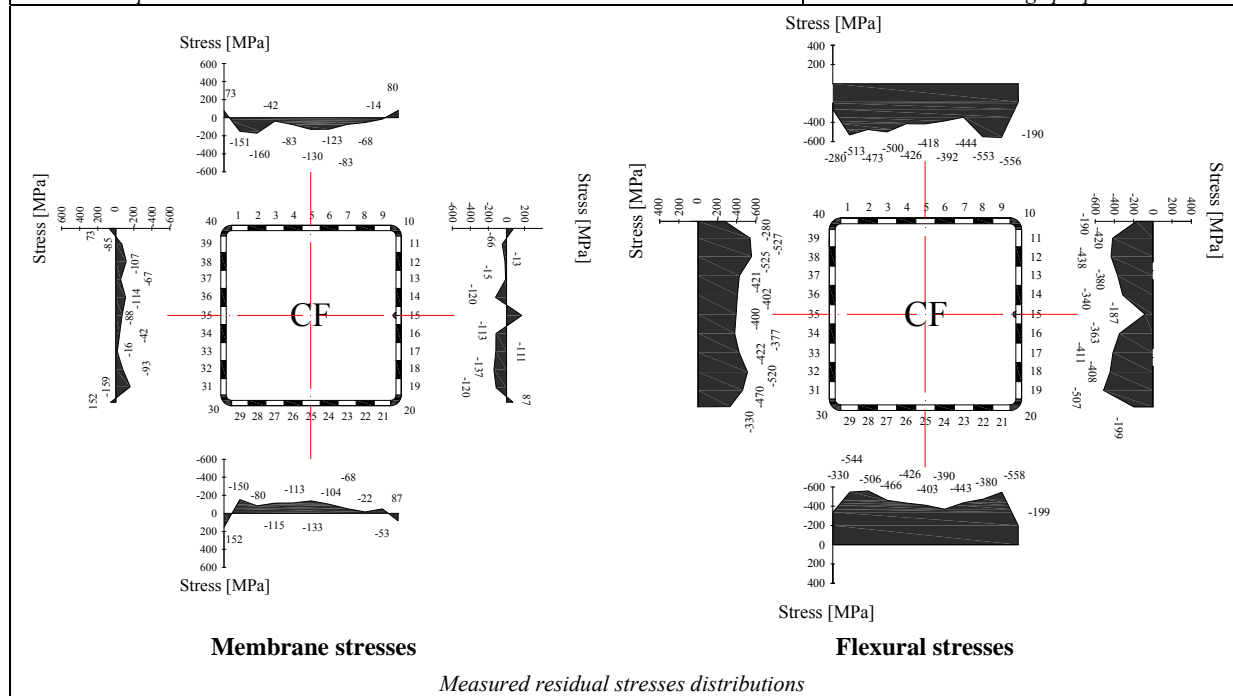
Cross-sectional measured dimensions and tolerances

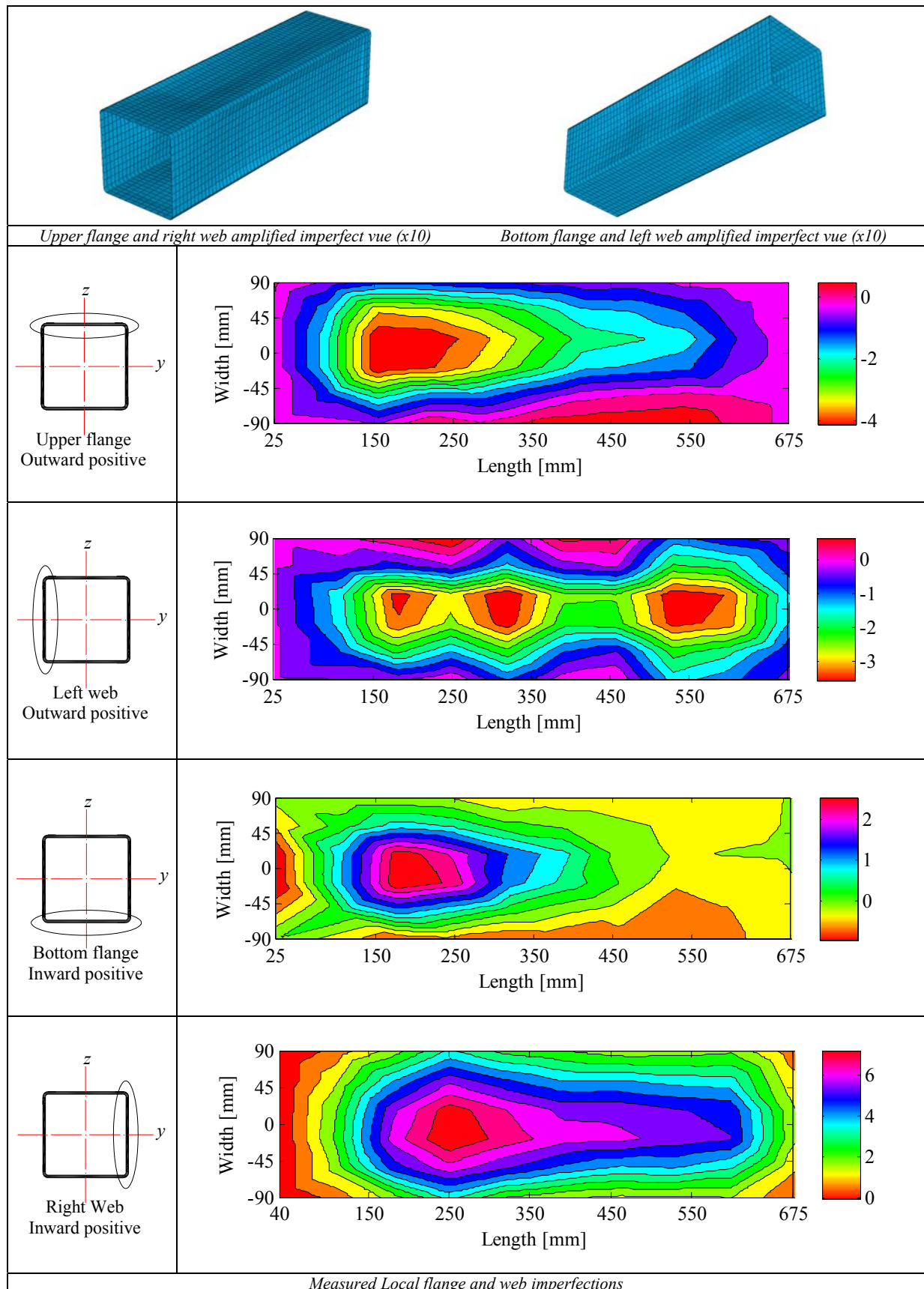


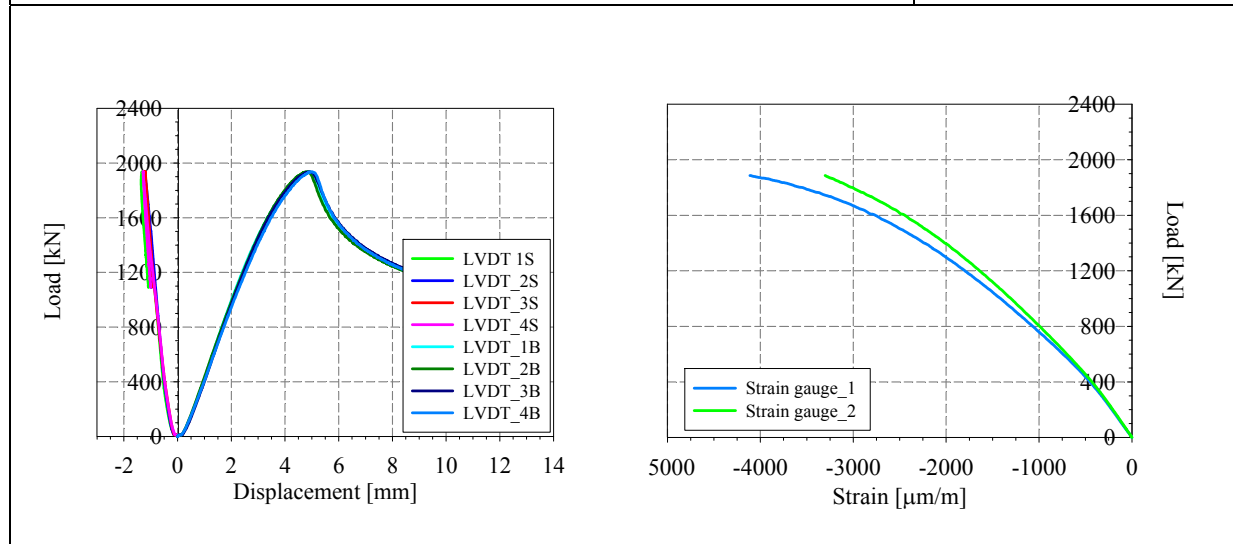
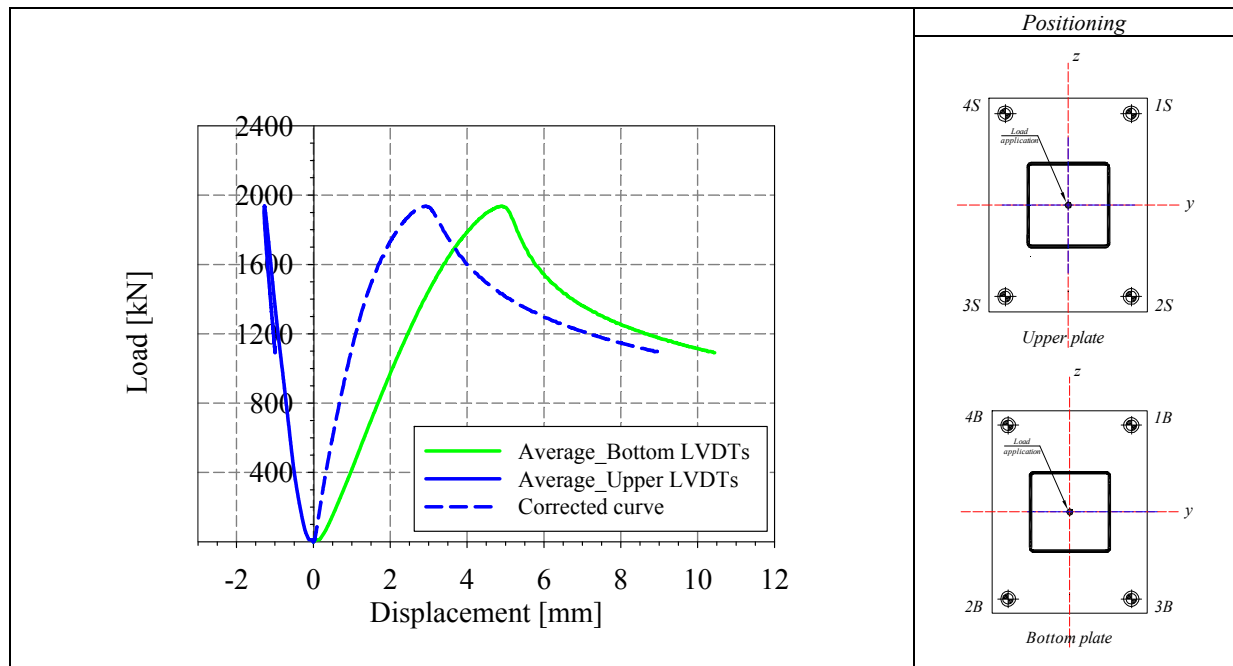
Tensile coupons location

Material stress-strain curves

Material average properties



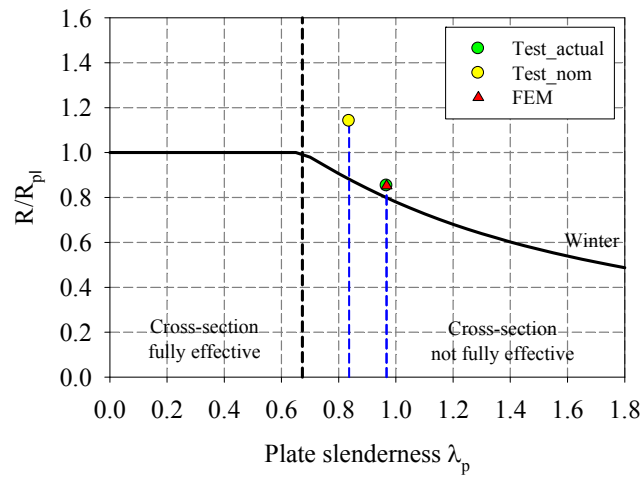
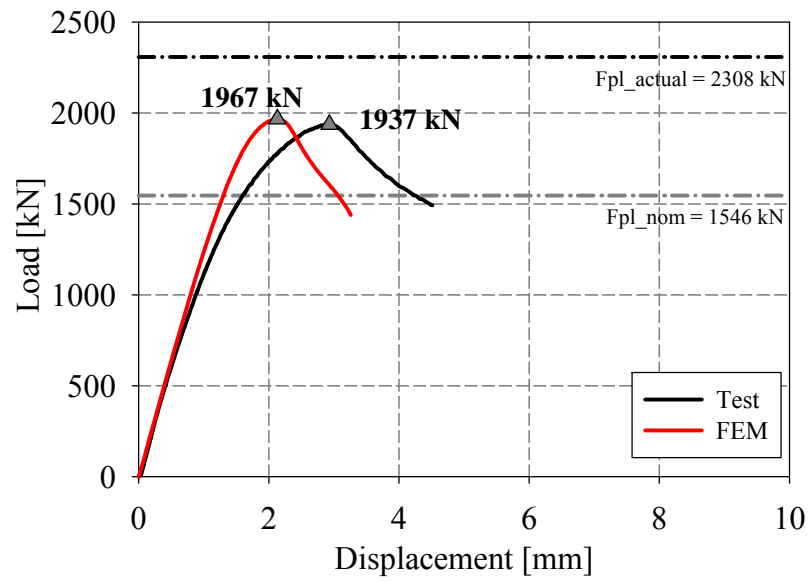




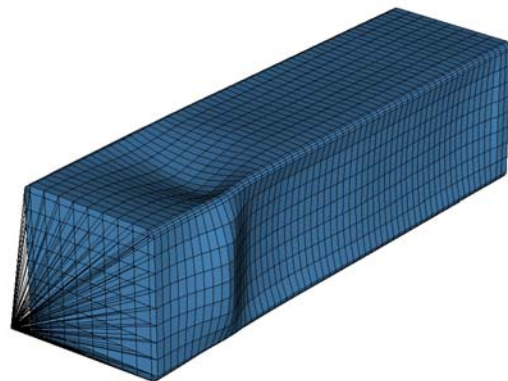
LVDT and strain gauges recordings



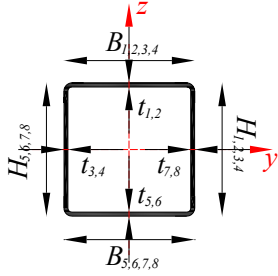
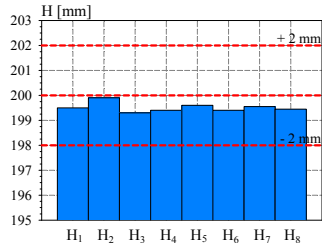
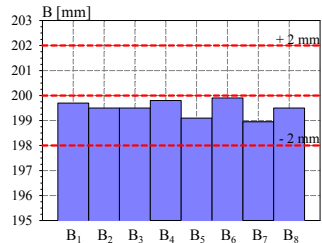
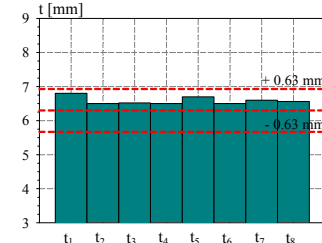
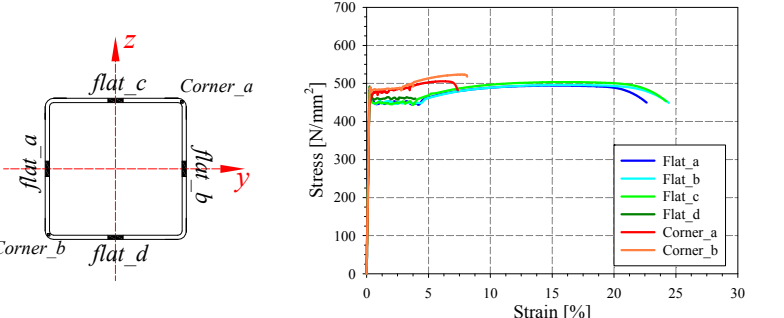
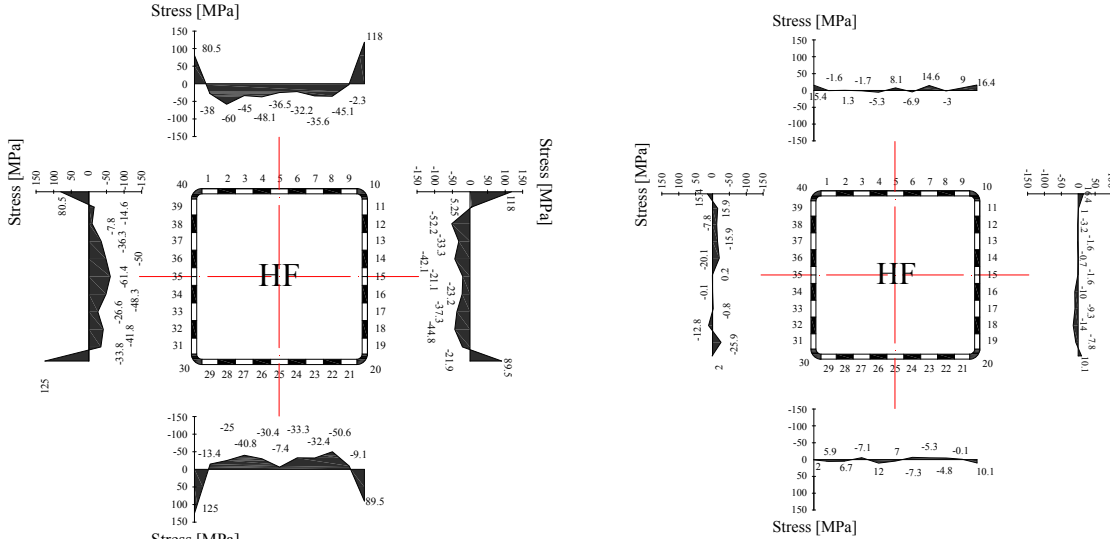
Local buckling failure

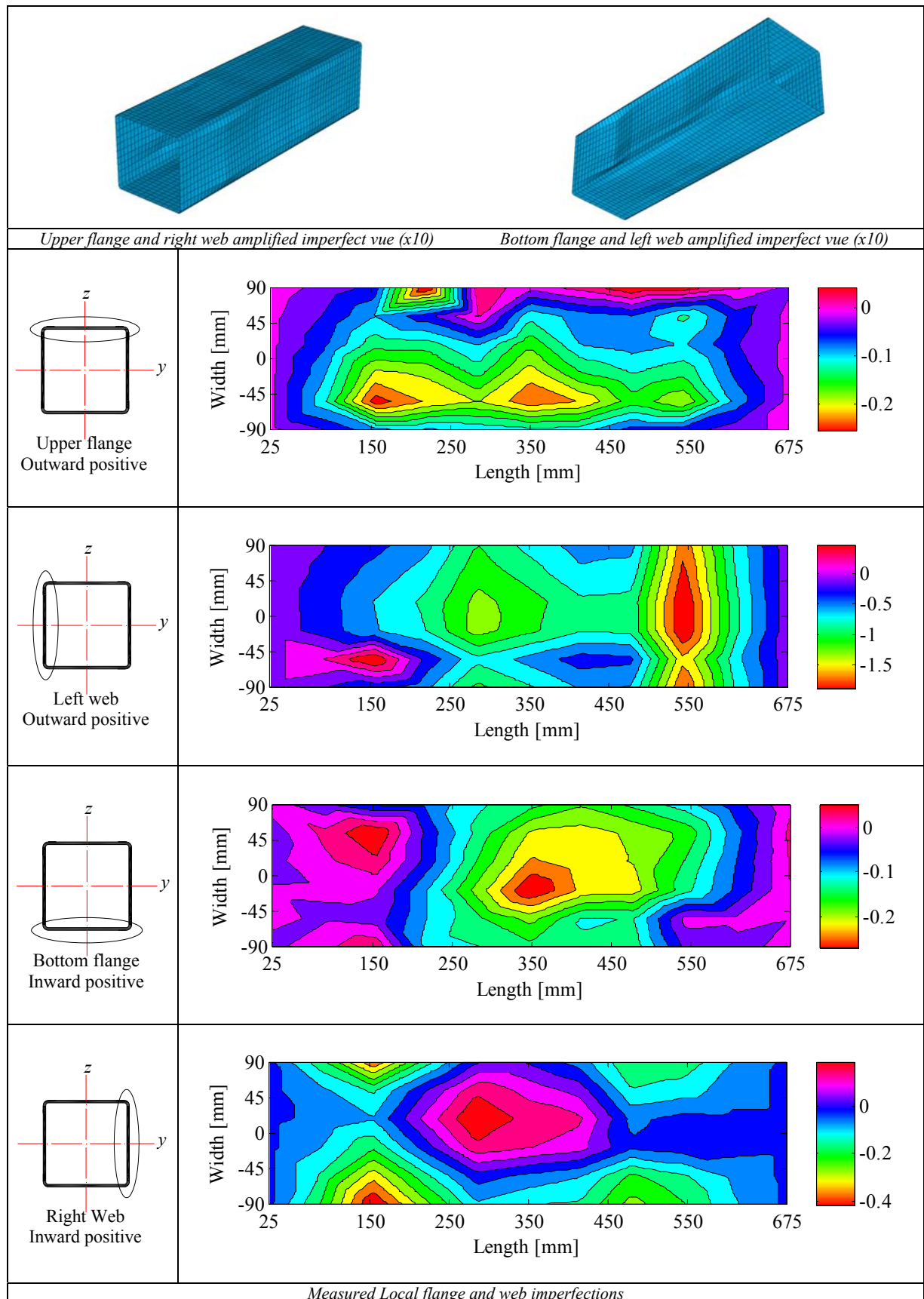


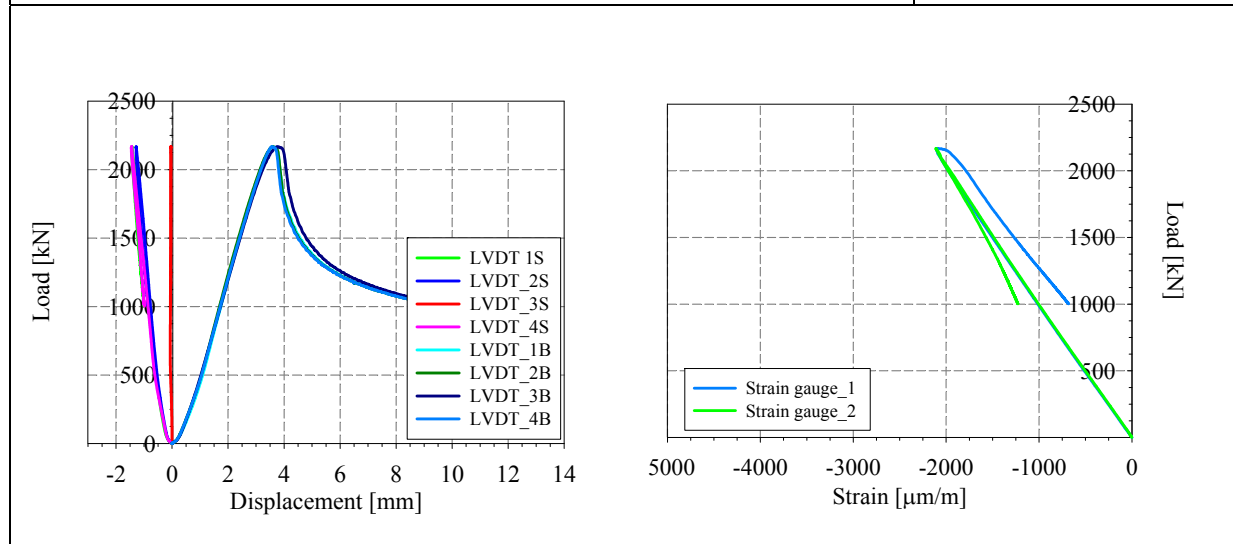
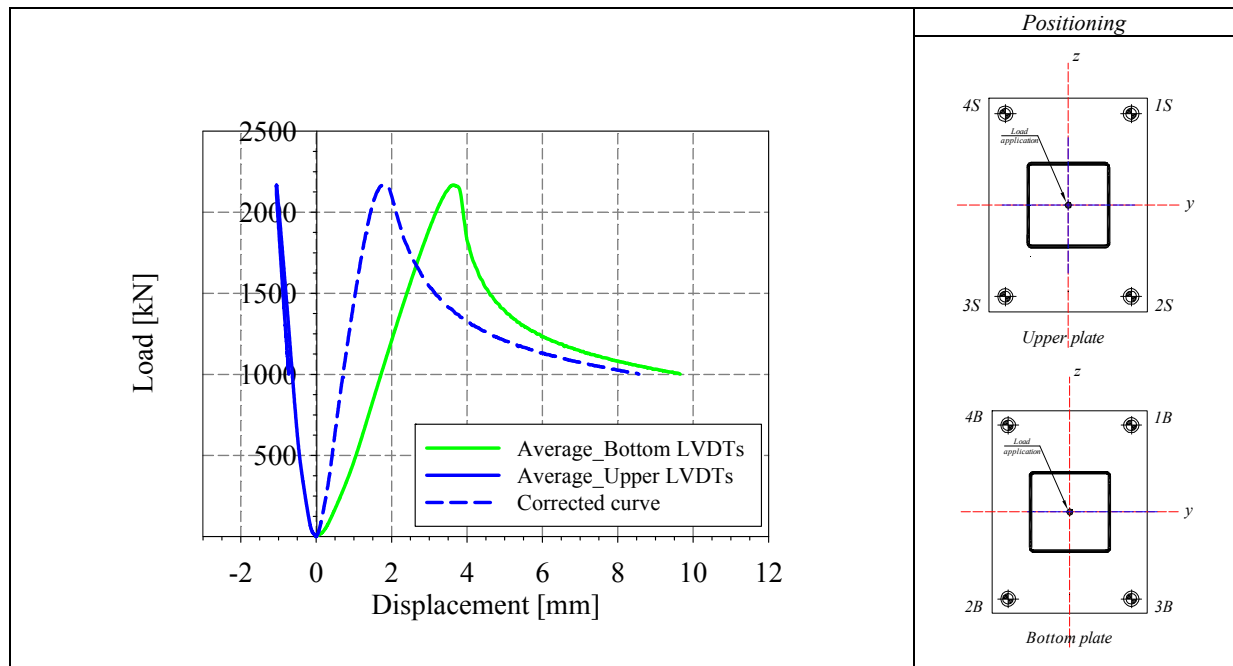
Non-dimensional cross section capacity in function of non-dimensional slenderness of decisive plate



Numerical local buckling failure

<p>Specimen name</p> <p>RHS_S355_LC1 200x200x6.3 HF</p>	<p>Shape</p> 	<p>Details</p> <p>Shape: Square Hollow Section Nominal yield limit: 355 MPa Load case: LC1 Pure compression H=200mm B=200mm t=6mm Fabrication process: Hot formed</p>																	
<p>Average h= 199.5 mm</p>	<p>Average b= 199 mm</p>	<p>Average t= 6.58 mm</p>																	
																			
<p>Cross-sectional measured dimensions and tolerances</p>																			
	<table border="1"> <thead> <tr> <th></th> <th>Flat</th> <th>Corner</th> </tr> </thead> <tbody> <tr> <td>E [MPa]</td> <td>215998</td> <td>209750</td> </tr> <tr> <td>f_y [MPa]</td> <td>453</td> <td>482.6</td> </tr> <tr> <td>ϵ_y [%]</td> <td>0.20</td> <td>0.23</td> </tr> <tr> <td>f_u [MPa]</td> <td>496</td> <td>523.4</td> </tr> <tr> <td>ϵ_u [%]</td> <td>15.9</td> <td>7.6</td> </tr> </tbody> </table>		Flat	Corner	E [MPa]	215998	209750	f_y [MPa]	453	482.6	ϵ_y [%]	0.20	0.23	f_u [MPa]	496	523.4	ϵ_u [%]	15.9	7.6
	Flat	Corner																	
E [MPa]	215998	209750																	
f_y [MPa]	453	482.6																	
ϵ_y [%]	0.20	0.23																	
f_u [MPa]	496	523.4																	
ϵ_u [%]	15.9	7.6																	
<p>Tensile coupons location</p>	<p>Material stress-strain curves</p>	<p>Material average properties</p>																	
	<p style="text-align: center;">Membrane stresses</p> <p style="text-align: center;">Flexural stresses</p>																		
<p>Measured residual stresses distributions</p>																			

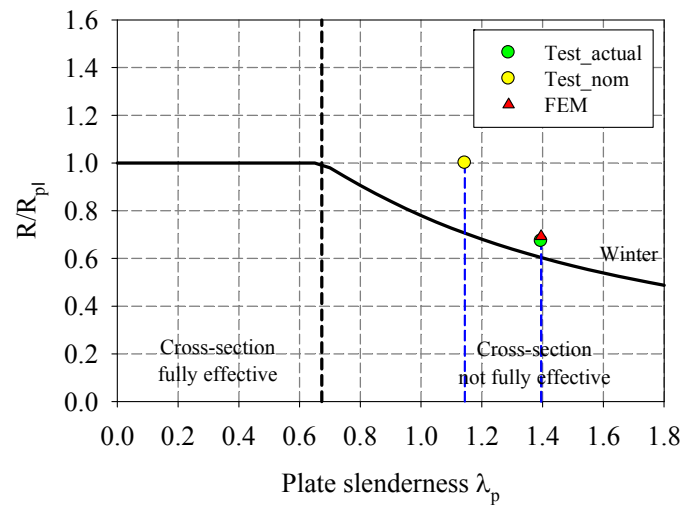
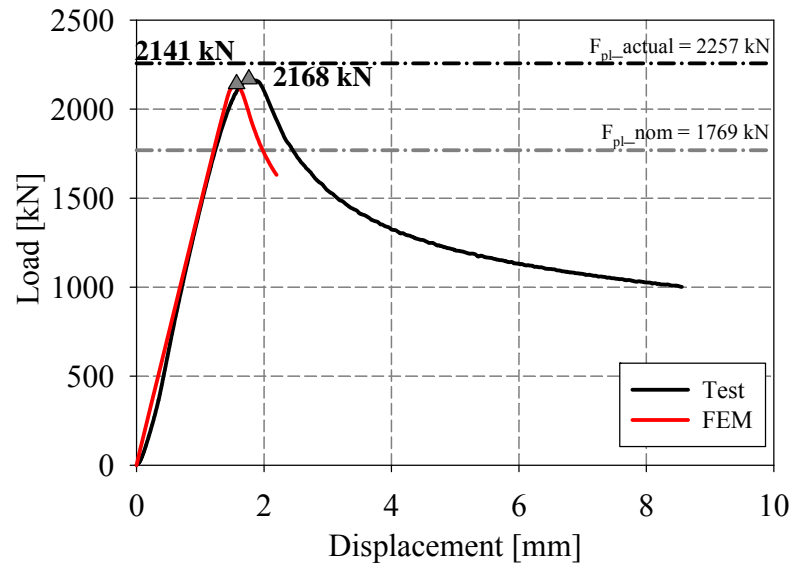




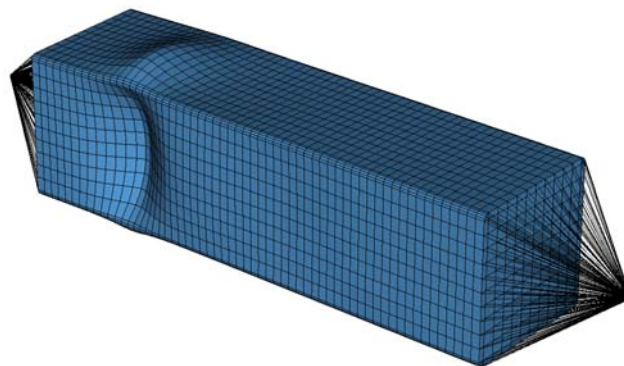
LVDT and strain gauges recordings



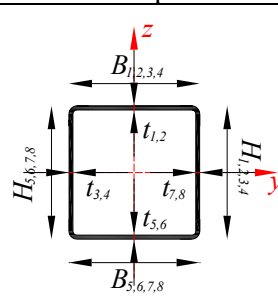
Local buckling failure

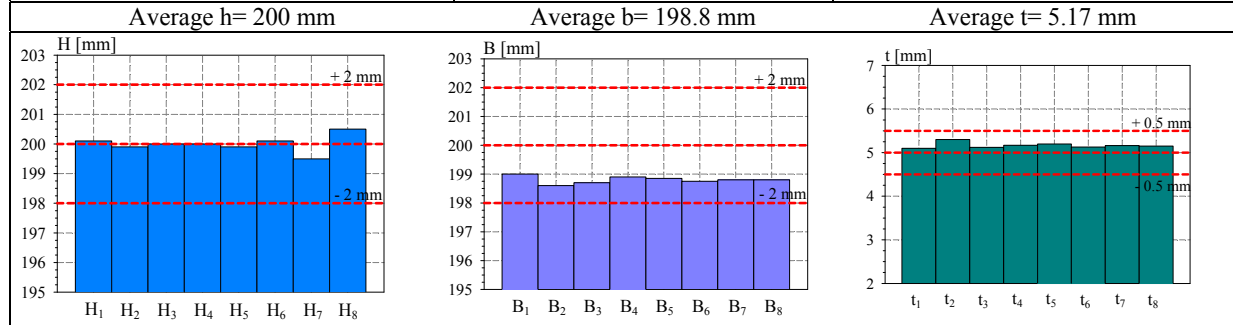


Non-dimensional cross section capacity in function of non-dimensional slenderness of decisive plate

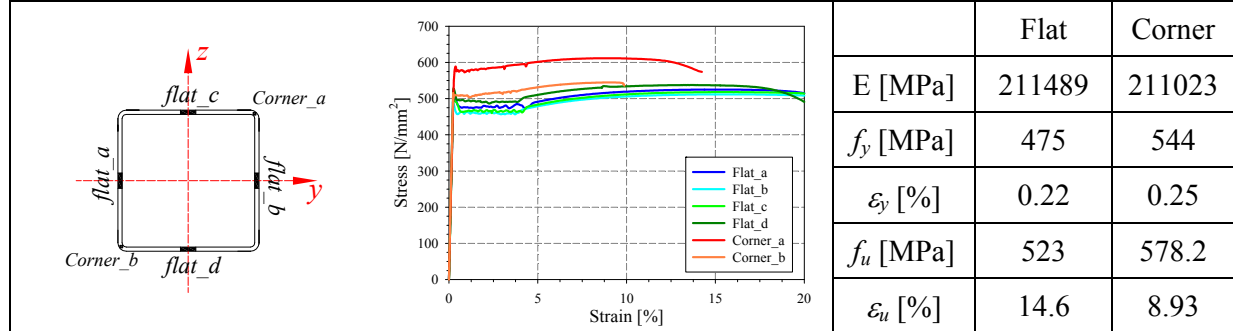


Numerical local buckling failure

<p>Specimen name</p> <p>RHS_S355_LC1 200x200x5 HF</p>	<p>Shape</p> 	<p>Details</p> <p>Shape: Square Hollow Section Nominal yield limit: 355 MPa Load case: LC1 Pure compression H=200mm B=200mm t=5mm Fabrication process: Hot formed</p>
---	---	---



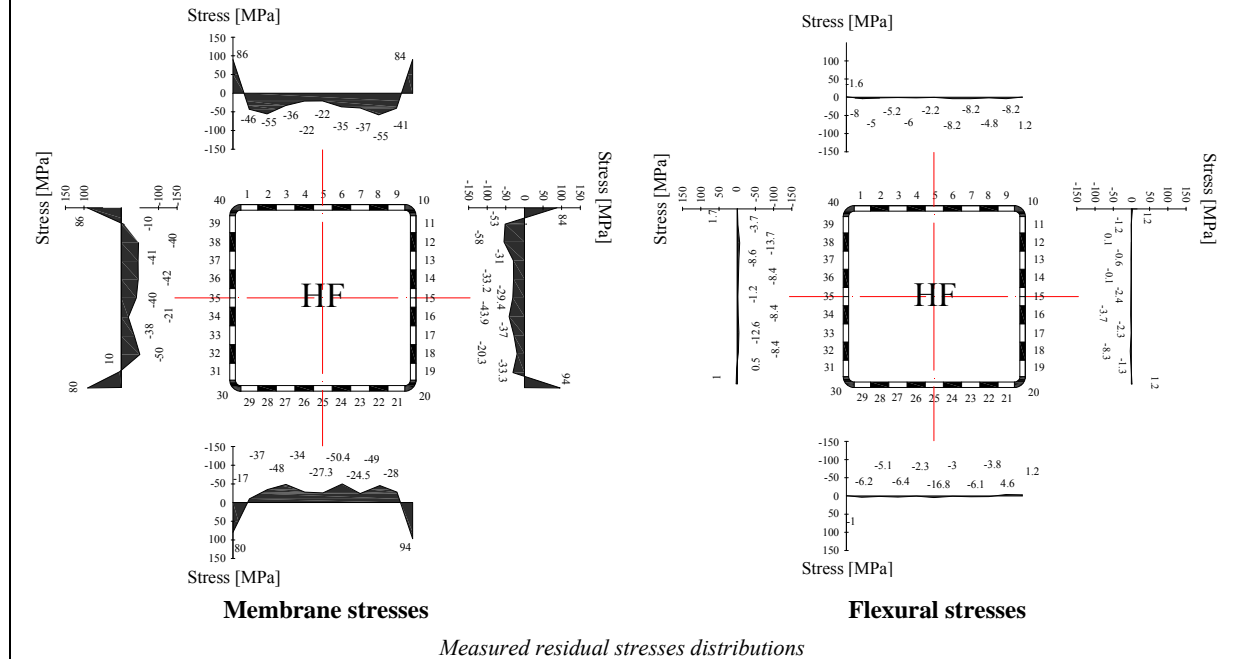
Cross-sectional measured dimensions and tolerances

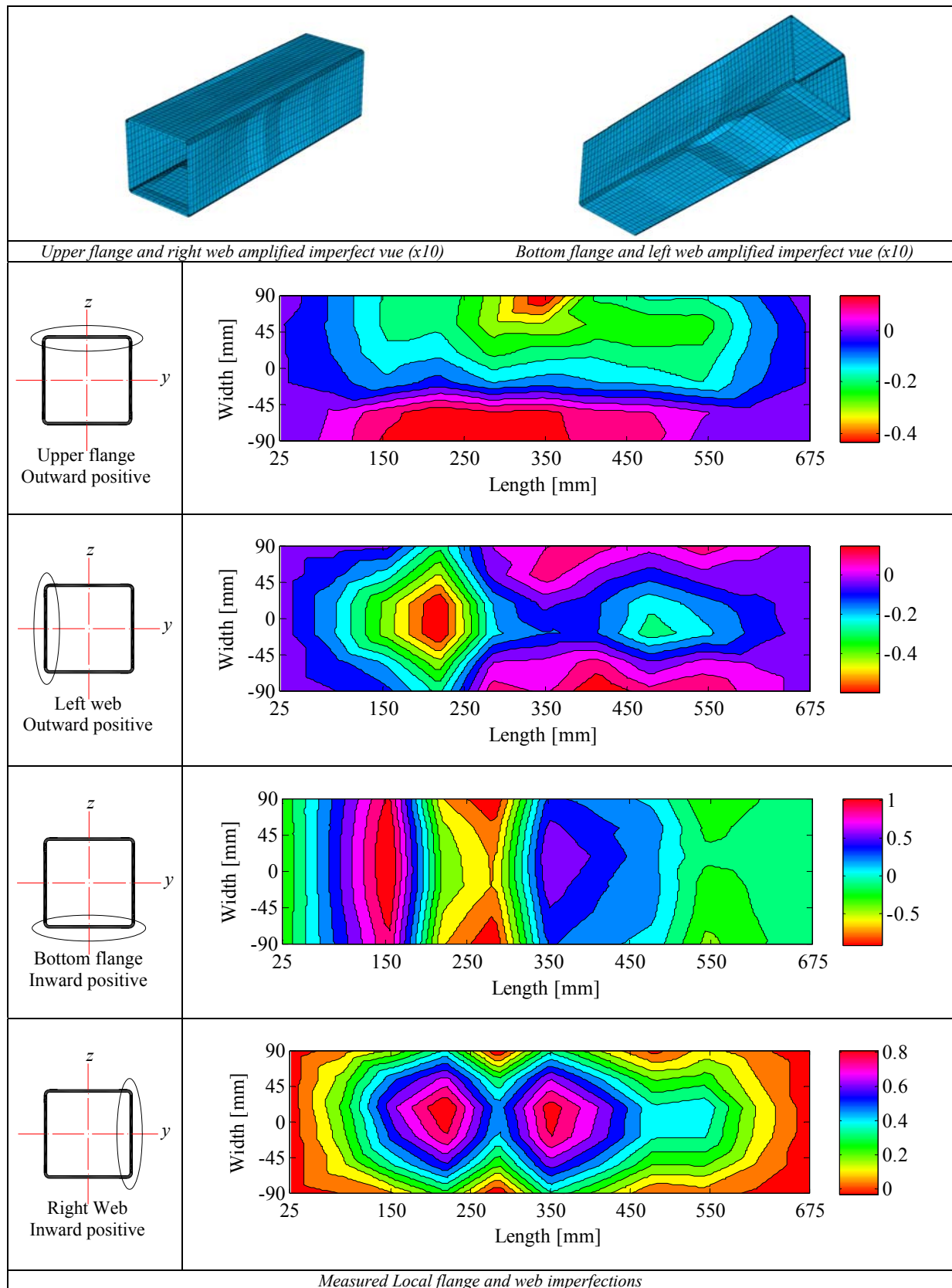


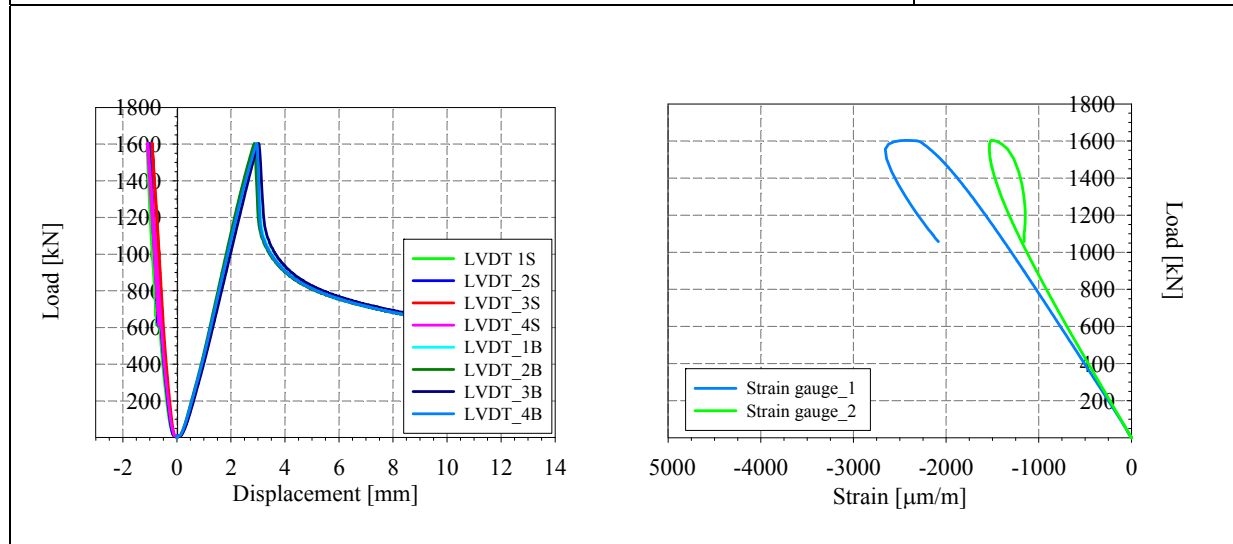
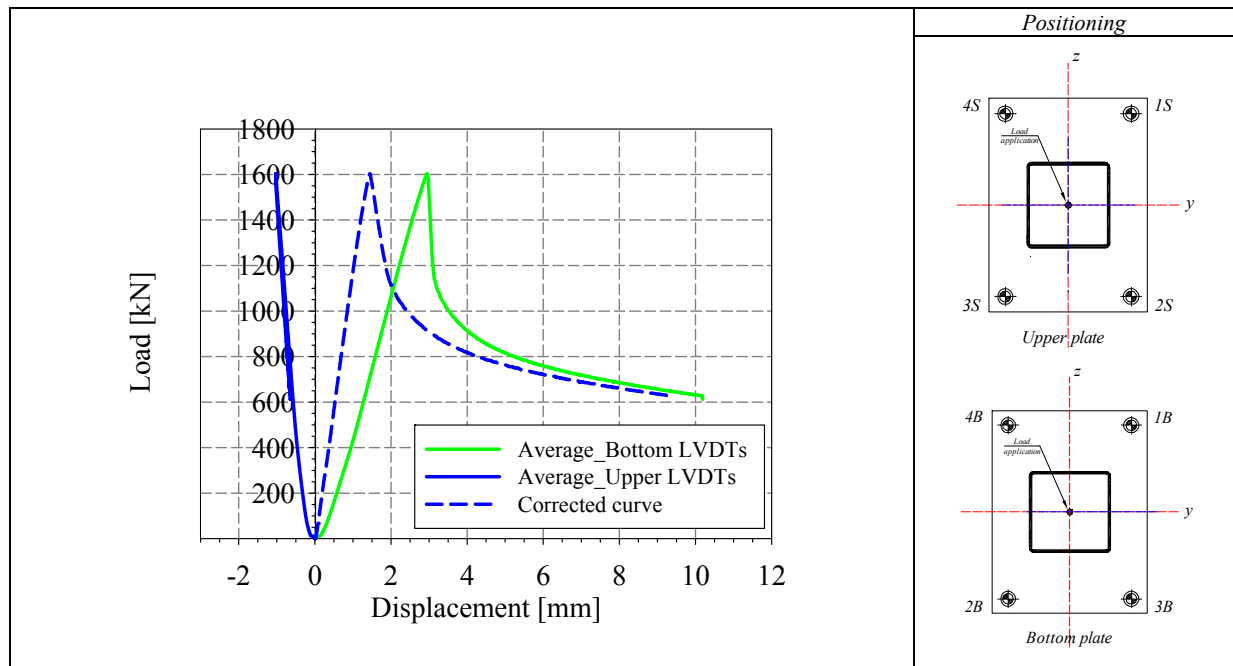
Tensile coupons location

Material stress-strain curves

Material average properties



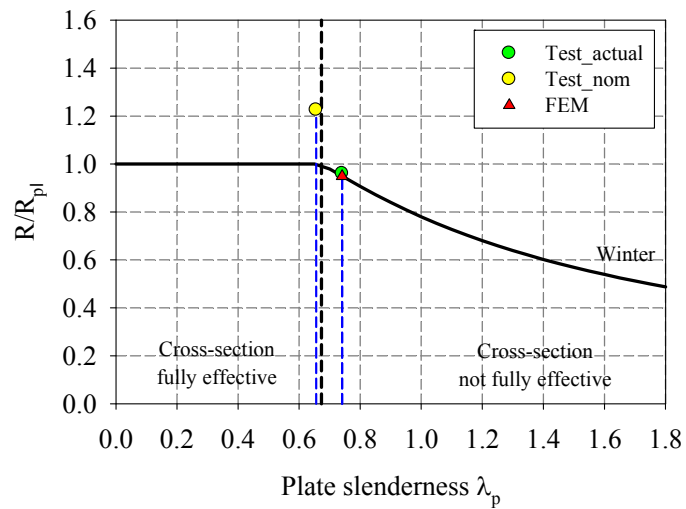
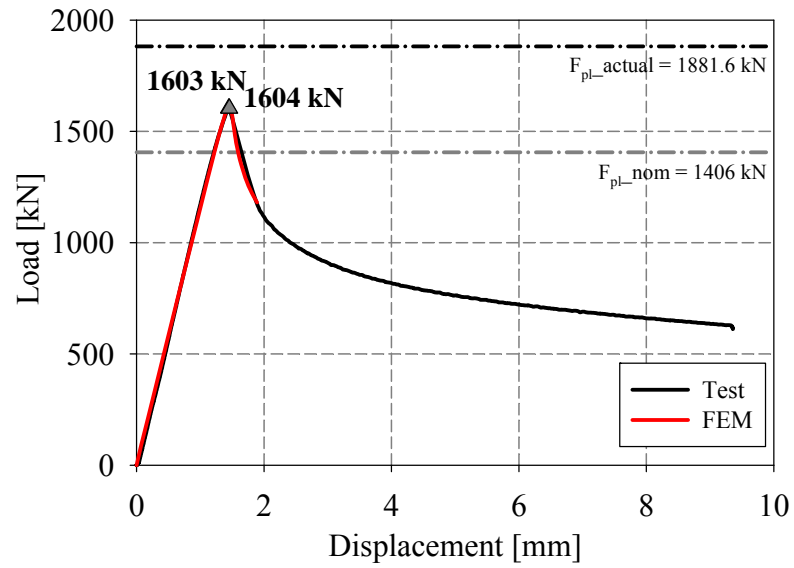




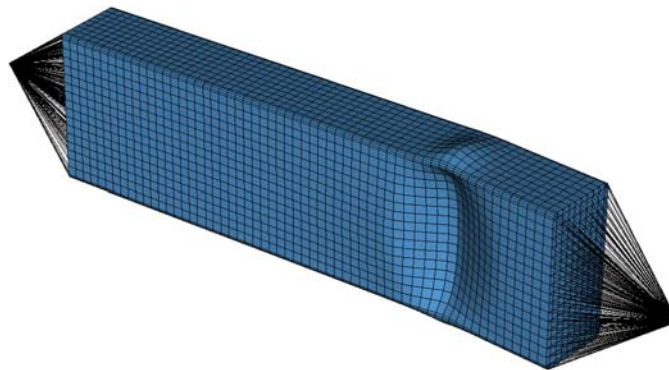
LVDT and strain gauges recordings



Local buckling failure

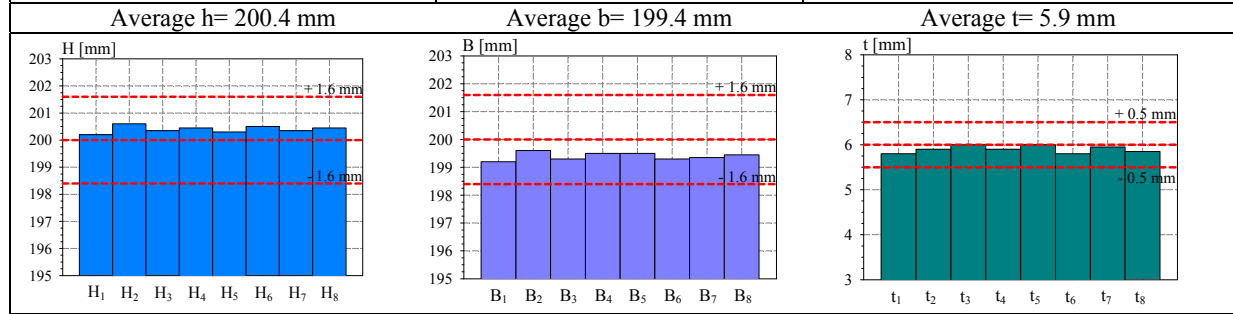


Non-dimensional cross section capacity in function of non-dimensional slenderness of decisive plate

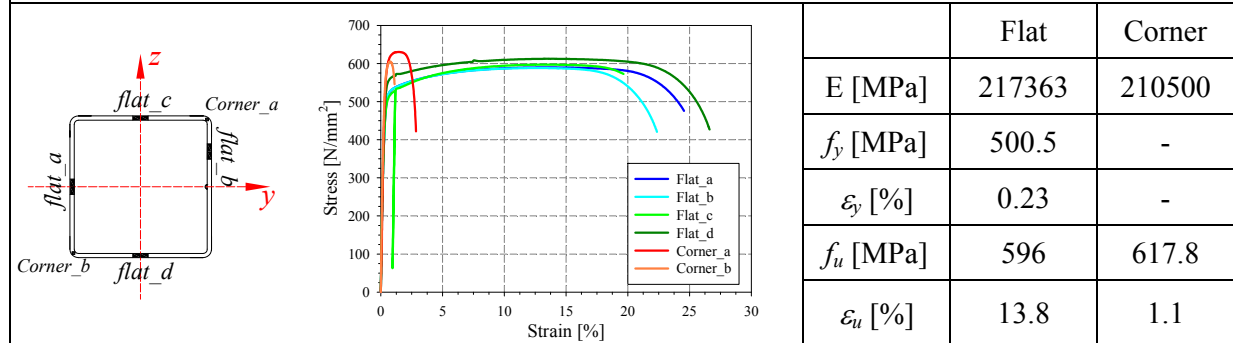


Numerical local buckling failure

<p>Specimen name</p> <p>RHS_S355_LC1 200x200x6 CF_2</p>	<p>Shape</p>	<p>Details</p> <p>Shape: Square Hollow Section Nominal yield limit: 355 MPa Load case: LC1 Pure compression H=200mm B=200mm t=6mm Fabrication process: Cold formed</p>
---	--------------	--



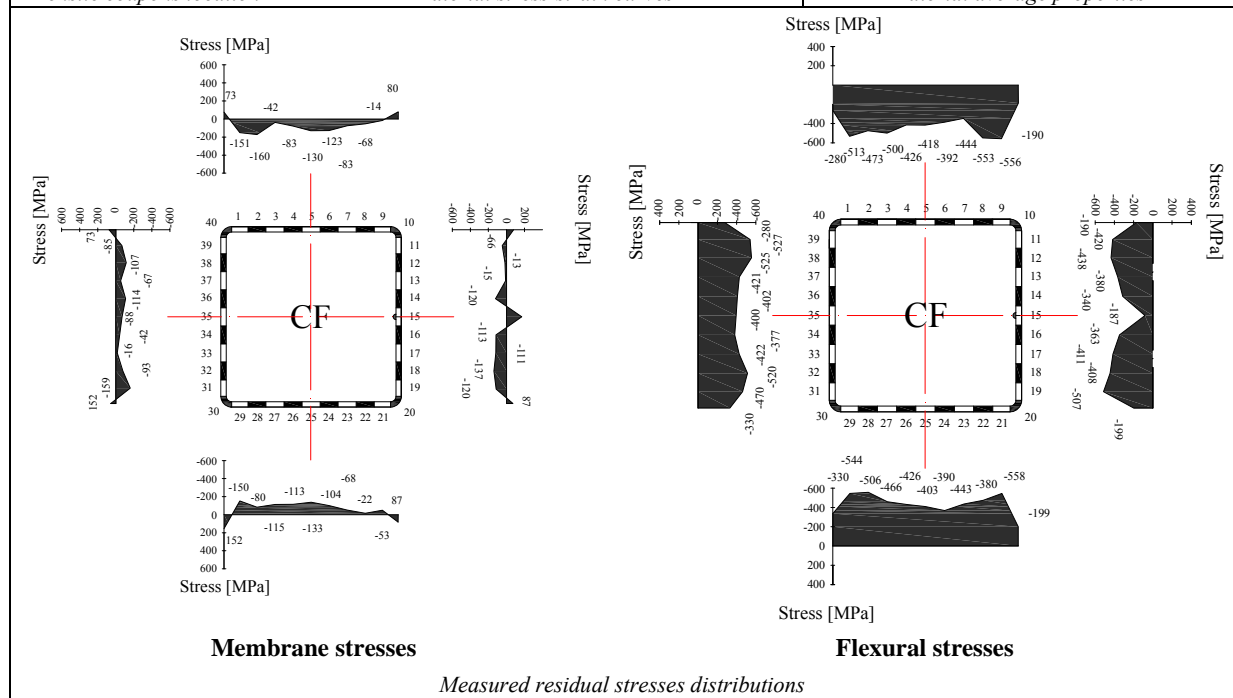
Cross-sectional measured dimensions and tolerances

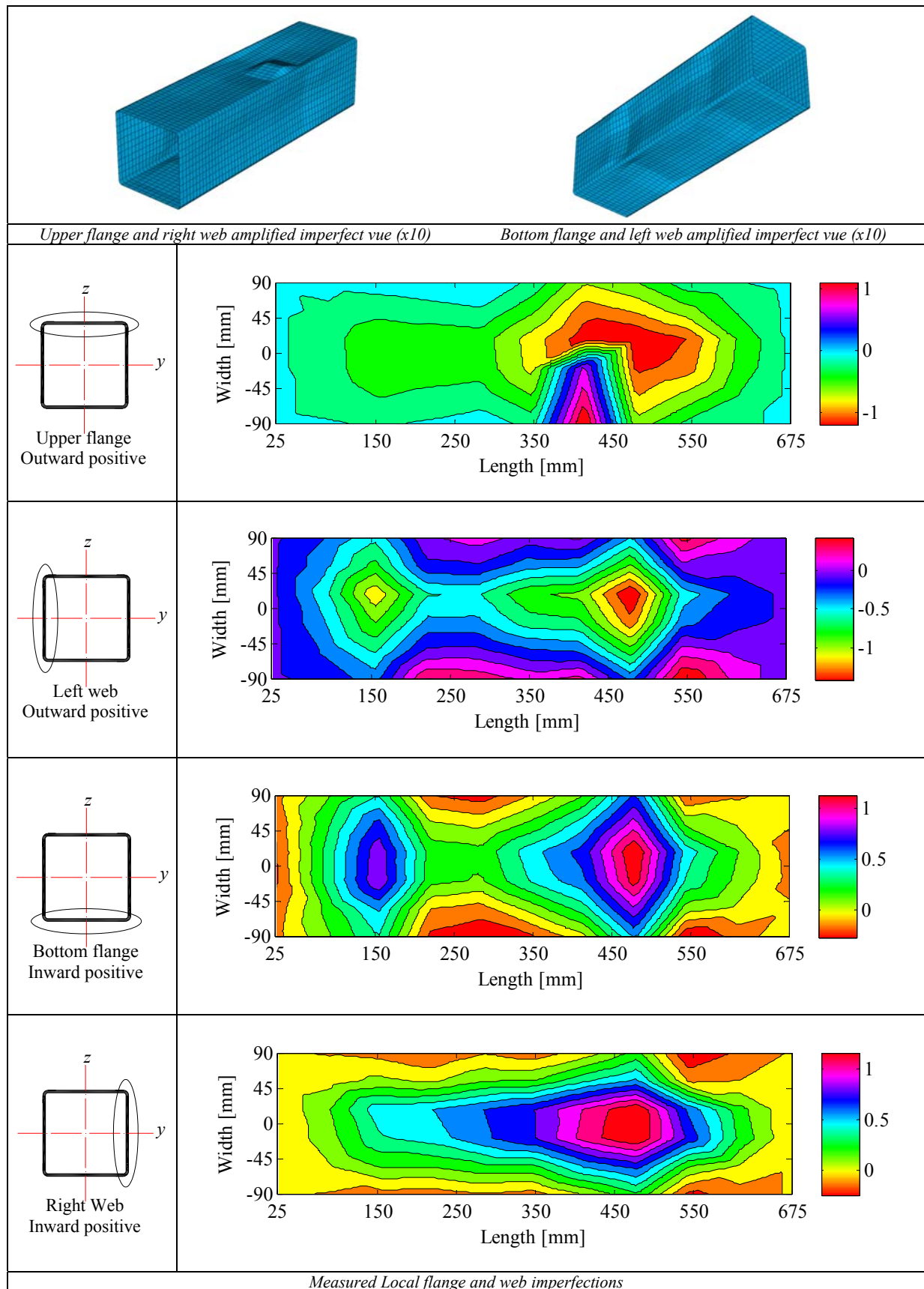


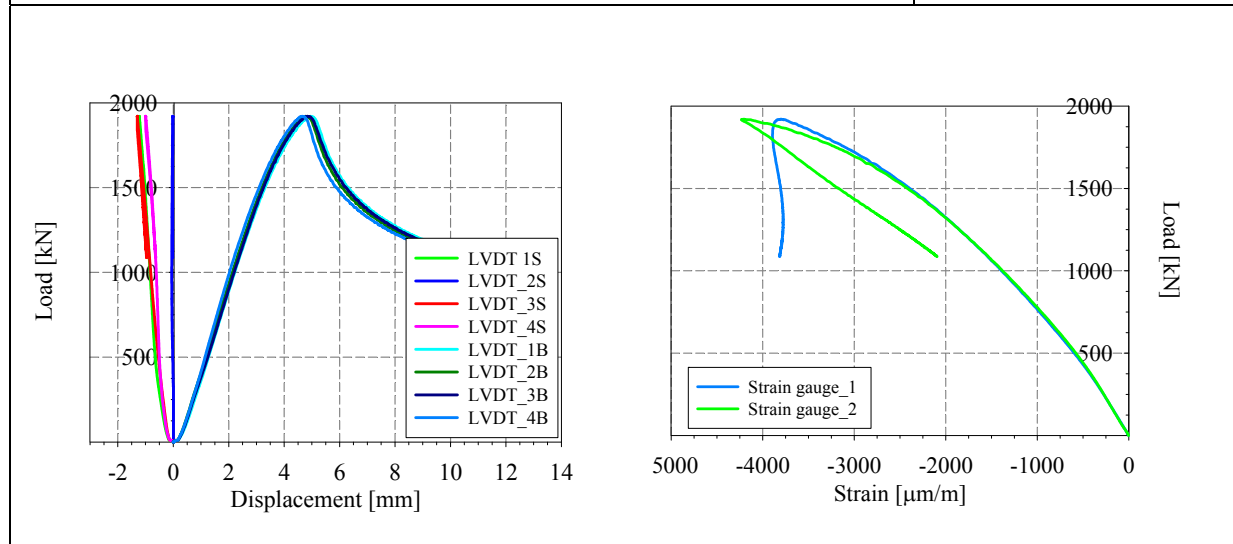
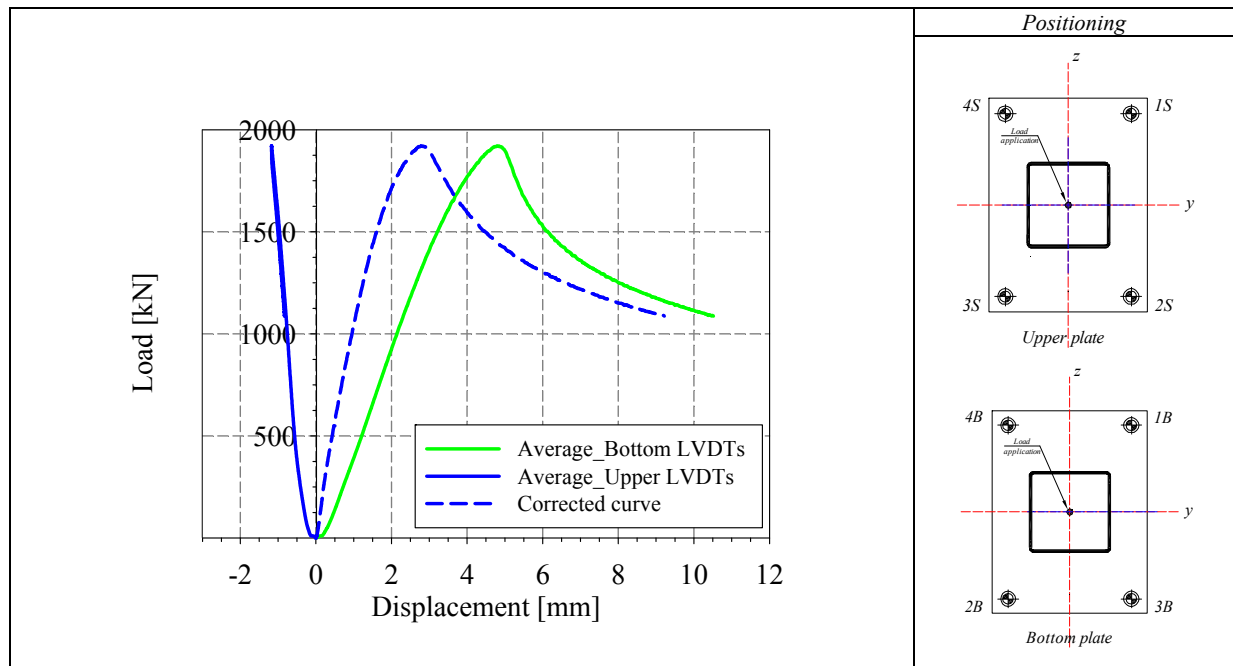
Tensile coupons location

Material stress-strain curves

Material average properties

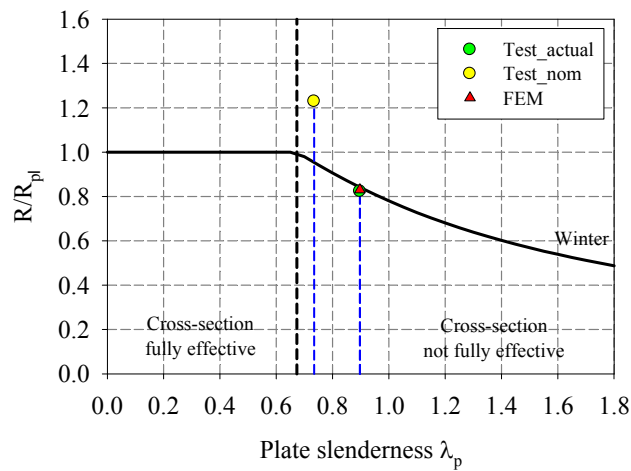
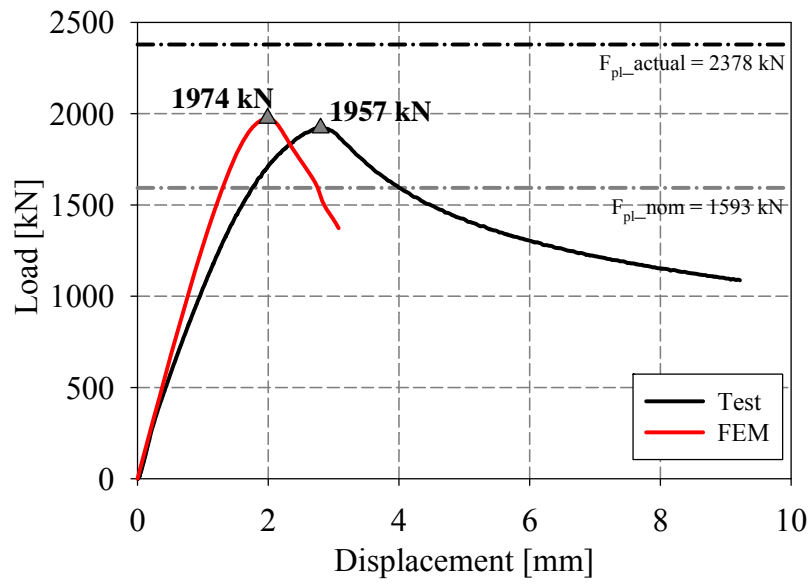




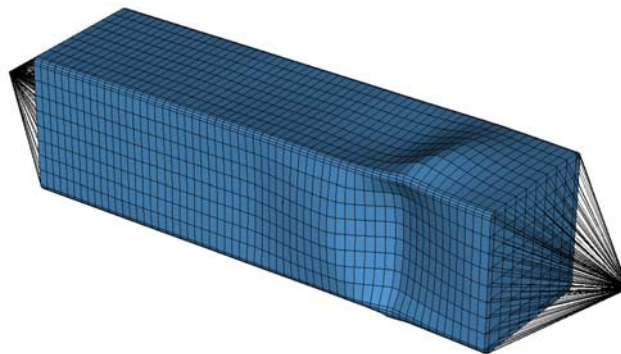


LVDT and strain gauges recordings

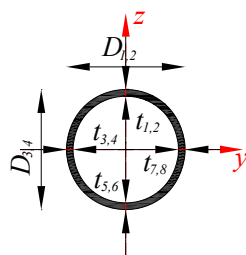


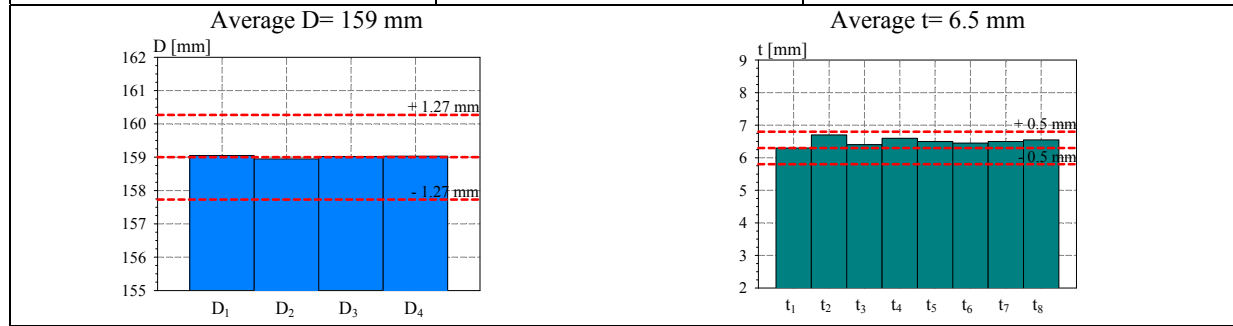


Non-dimensional cross section capacity in function of non-dimensional slenderness of decisive plate

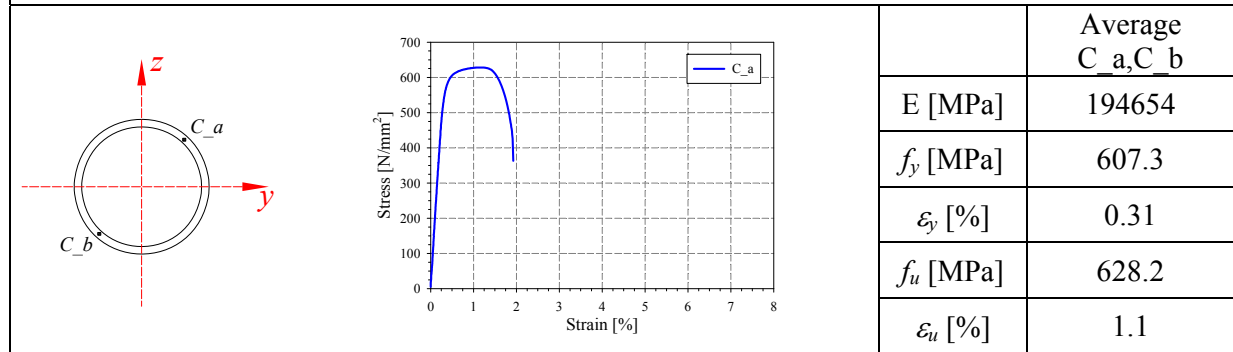


Numerical local buckling failure

<p>Specimen name</p> <p>CHS_S355_LC1 159x6.3 CF</p>	<p>Shape</p> 	<p>Details</p> <p>Shape: Circular Hollow Section Nominal yield limit: 355 MPa Load case: LC1 Pure compression D=159mm t=6.3mm Fabrication process: Cold formed</p>
---	--	--



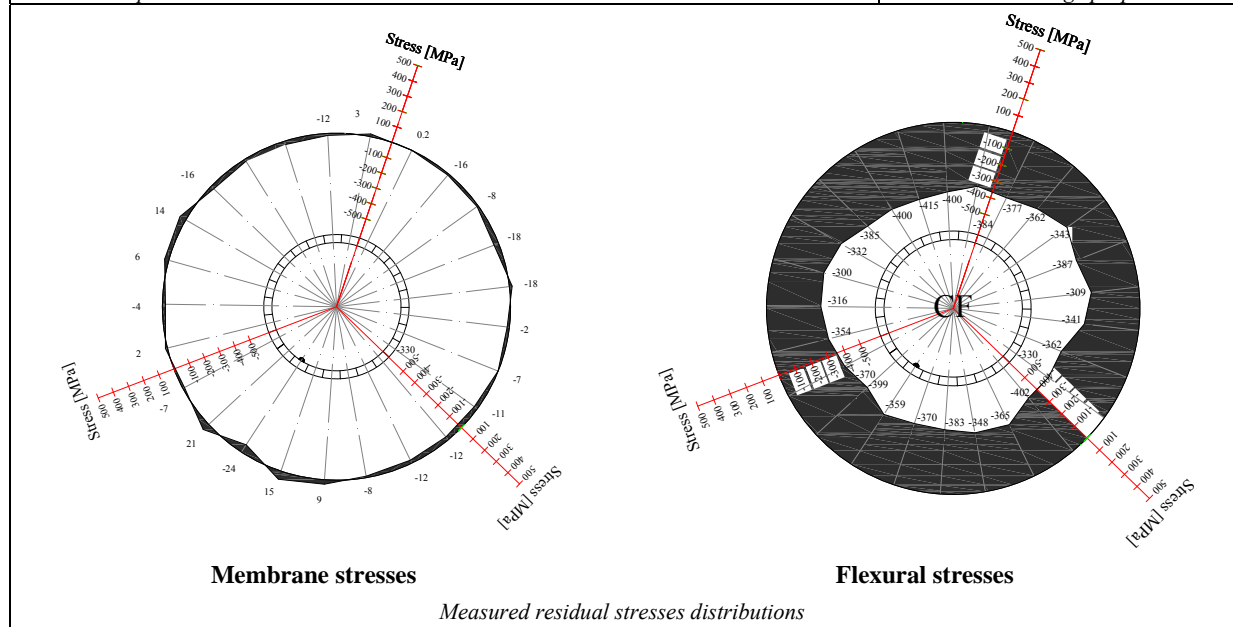
Cross-sectional measured dimensions and tolerances

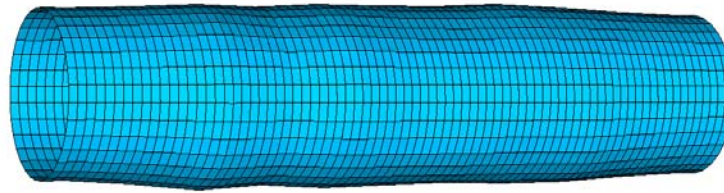


Tensile coupons location

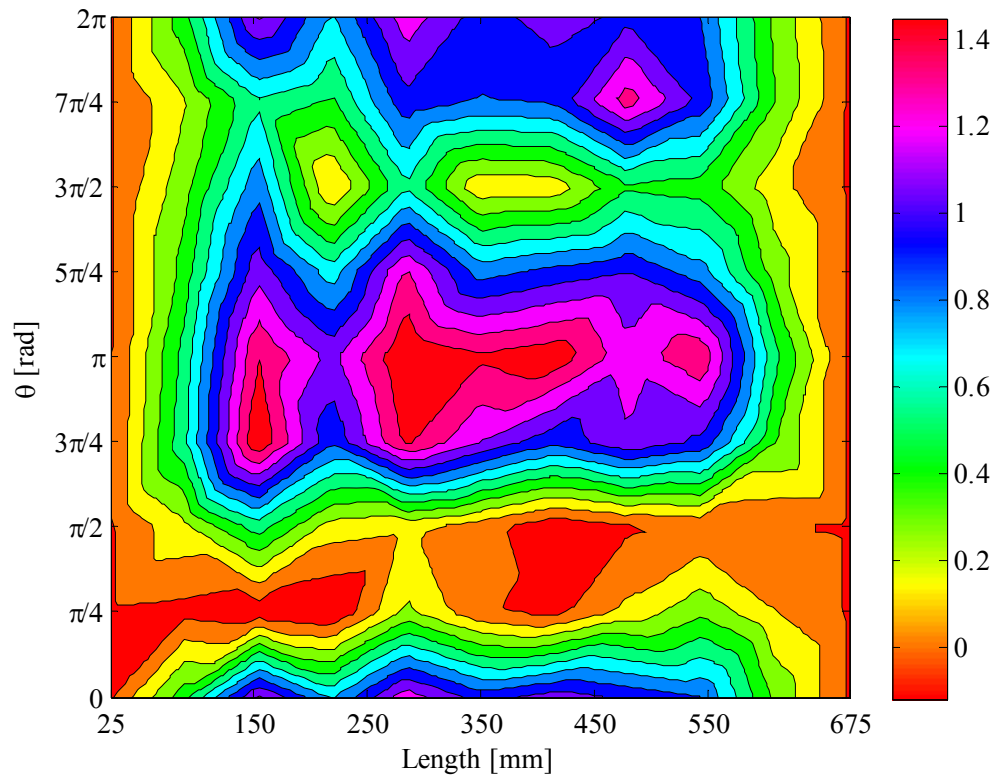
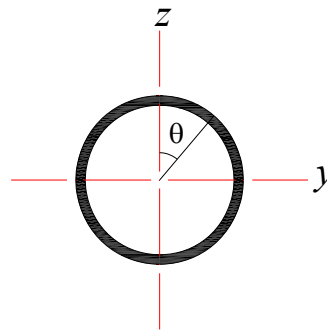
Material stress-strain curves

Material average properties

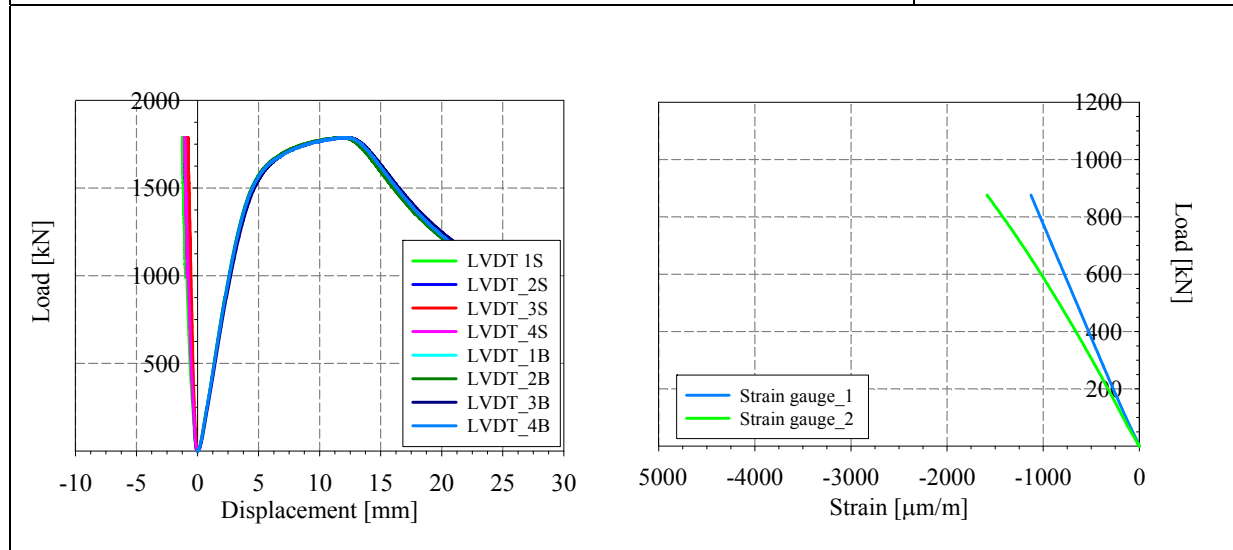
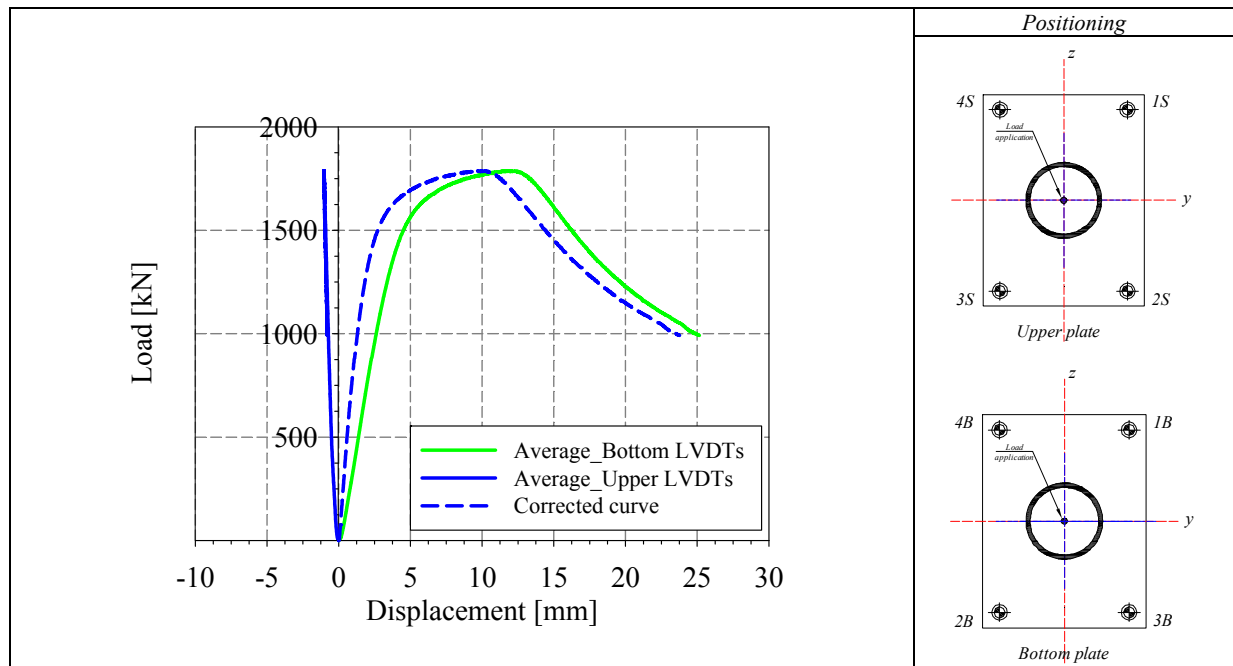




Amplified imperfect vue (x10)



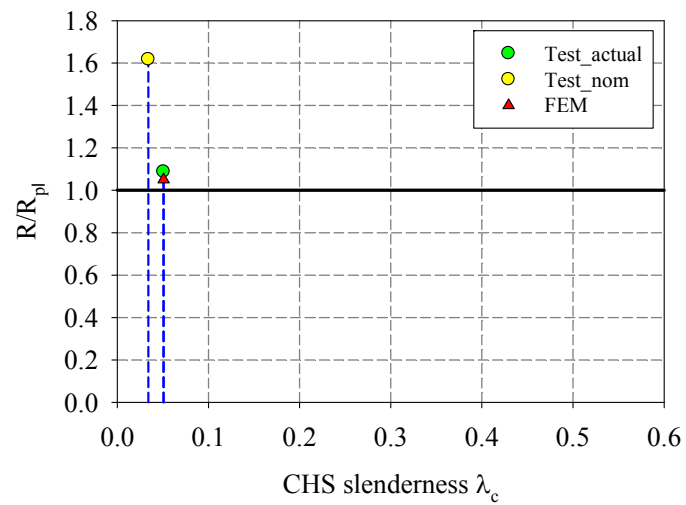
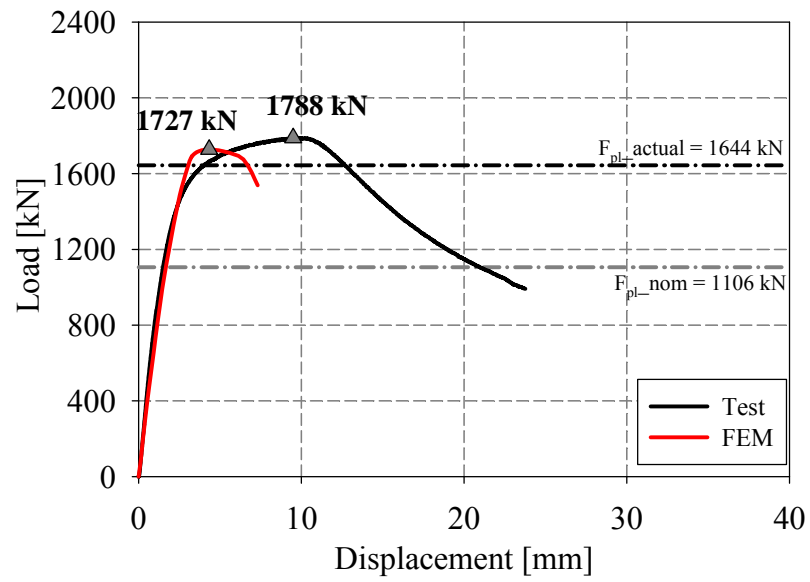
Measured Local imperfections



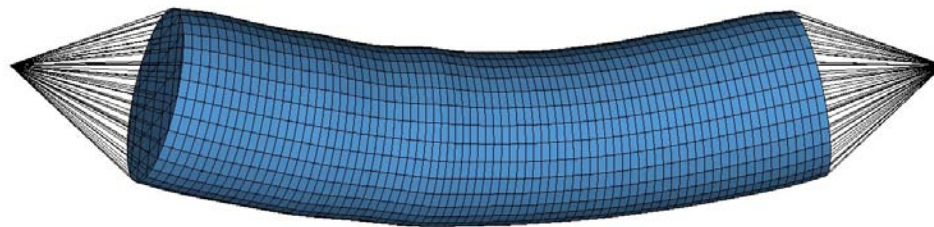
LVDT and strain gauges recordings



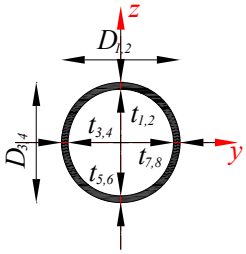
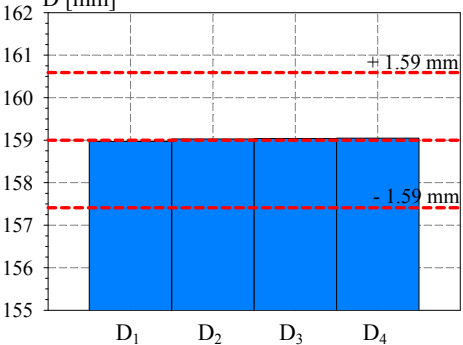
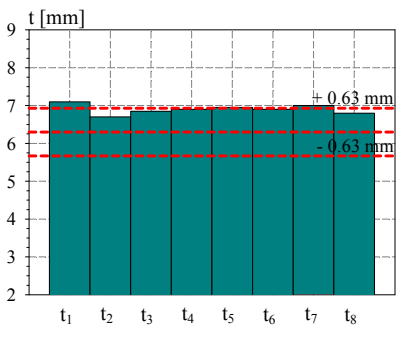
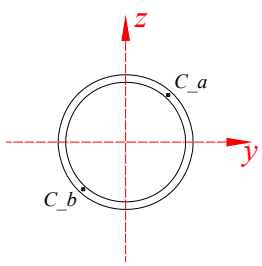
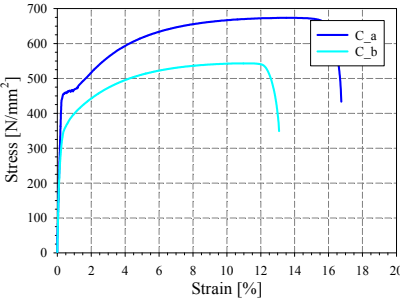
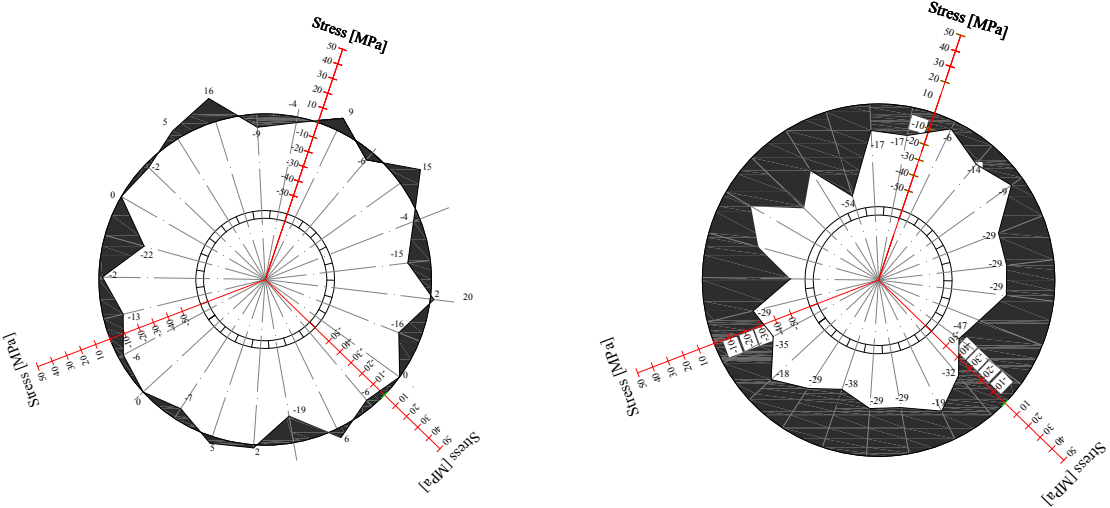
Local buckling failure

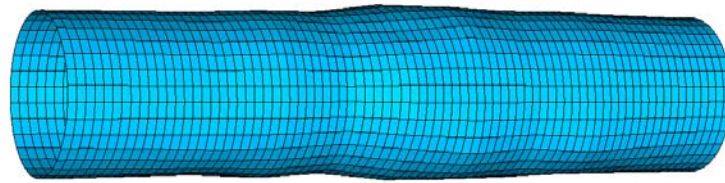


Non-dimensional cross section capacity in function of CHS slenderness

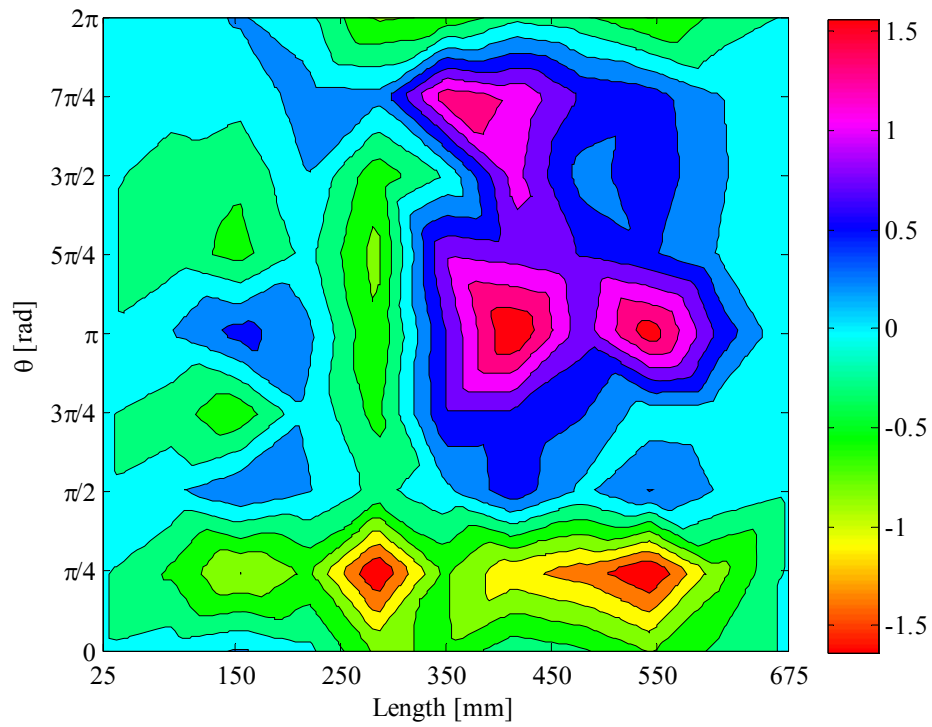
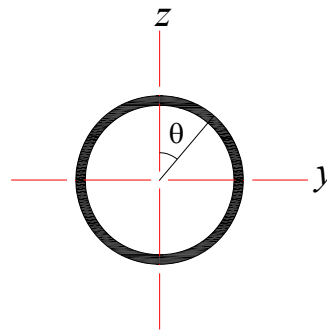


Numerical local buckling failure

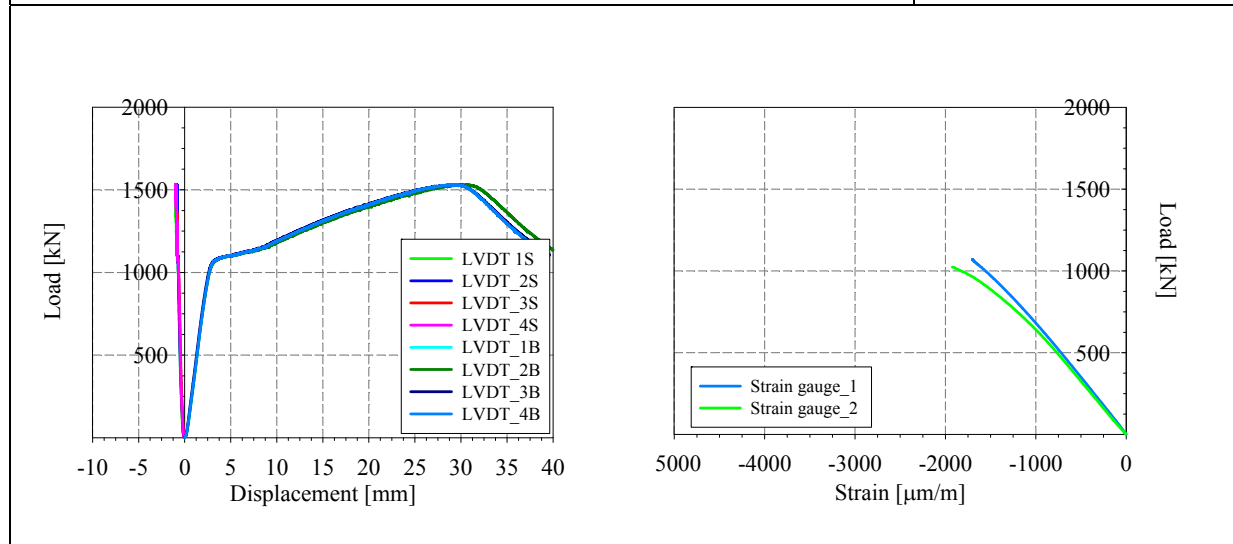
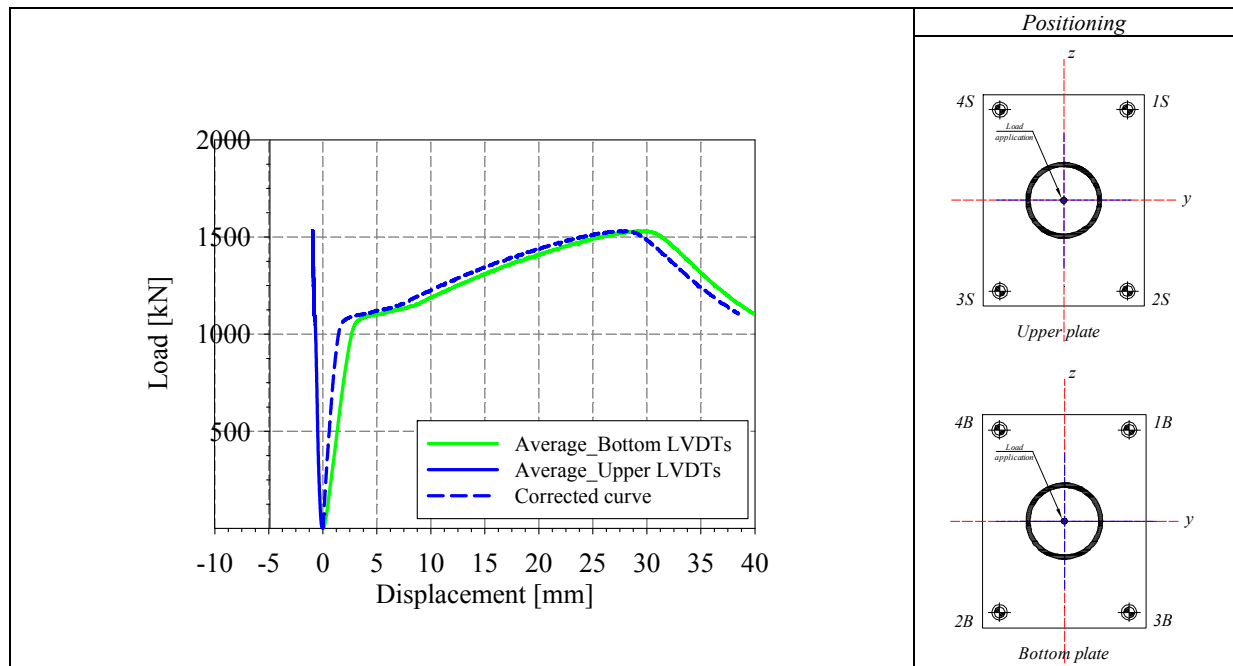
Specimen name	Shape	Details												
<p>CHS_S355_LC1 159x6.3 HR</p>		<p>Shape: Circular Hollow Section Nominal yield limit: 355 MPa Load case: LC1 Pure compression D=159mm t=6.3mm Fabrication process: Hot rolled</p>												
Average D= 159 mm		Average t= 6.9 mm												
														
<i>Cross-sectional measured dimensions and tolerances</i>														
		<table border="1"> <thead> <tr> <th></th> <th>Average C a, C b</th> </tr> </thead> <tbody> <tr> <td>E [MPa]</td> <td>213000</td> </tr> <tr> <td>f_y [MPa]</td> <td>401.5</td> </tr> <tr> <td>ϵ_y [%]</td> <td>0.19</td> </tr> <tr> <td>f_u [MPa]</td> <td>607.8</td> </tr> <tr> <td>ϵ_u [%]</td> <td>11.7</td> </tr> </tbody> </table>		Average C a, C b	E [MPa]	213000	f_y [MPa]	401.5	ϵ_y [%]	0.19	f_u [MPa]	607.8	ϵ_u [%]	11.7
	Average C a, C b													
E [MPa]	213000													
f_y [MPa]	401.5													
ϵ_y [%]	0.19													
f_u [MPa]	607.8													
ϵ_u [%]	11.7													
<i>Tensile coupons location</i>	<i>Material stress-strain curves</i>	<i>Material average properties</i>												
 <p style="text-align: center;">Membrane stresses Flexural stresses</p> <p style="text-align: center;"><i>Measured residual stresses distributions</i></p>														



Amplified imperfect vue (x10)



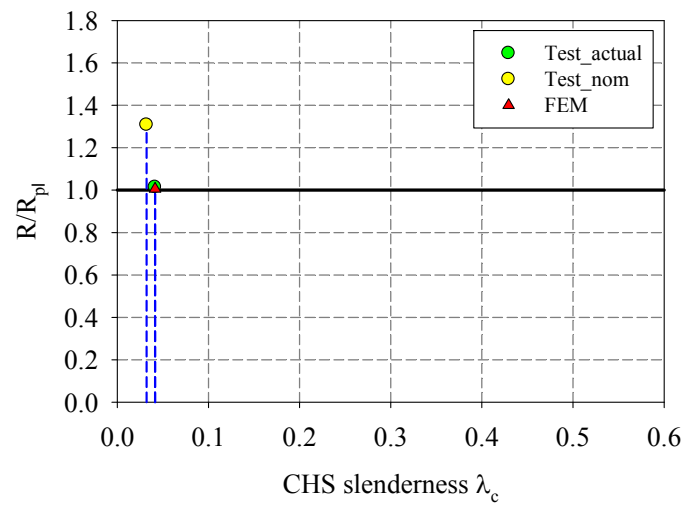
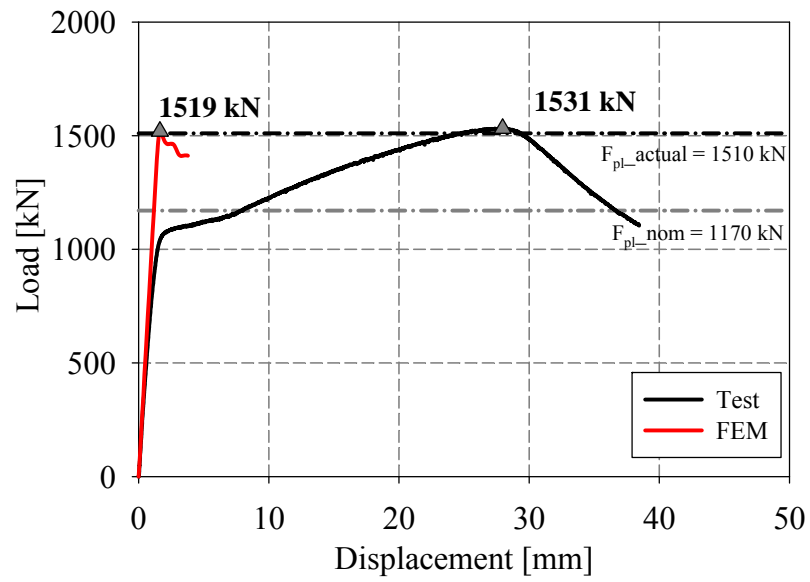
Measured Local imperfections



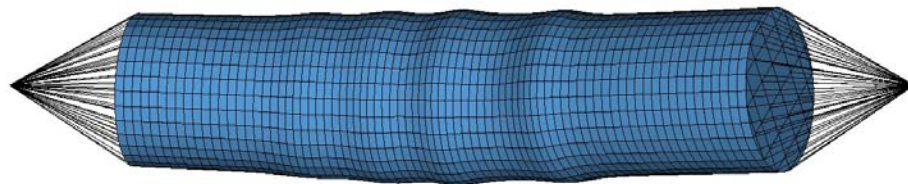
LVDT and strain gauges recordings



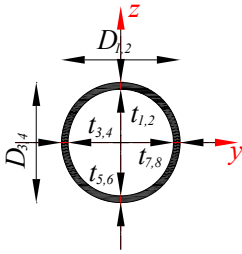
Local buckling failure

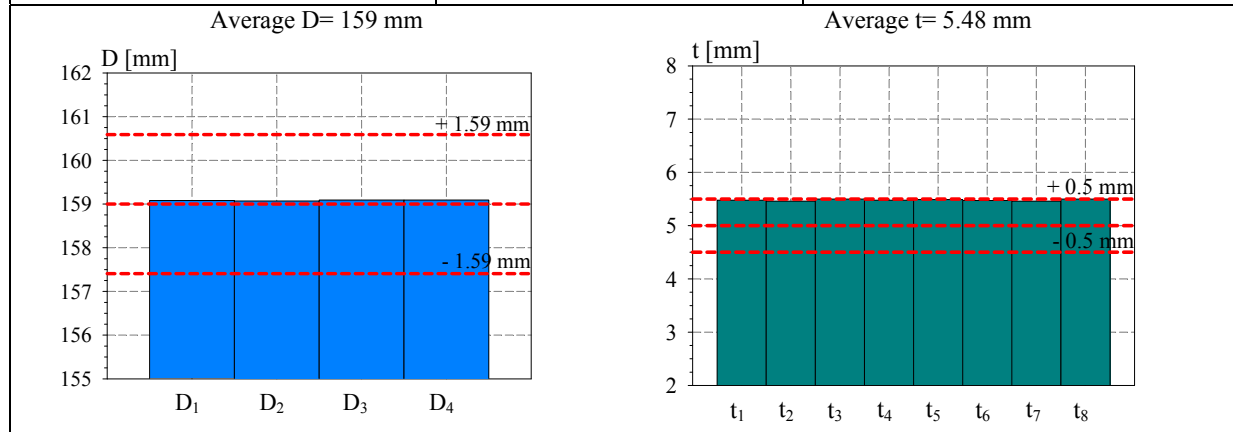


Non-dimensional cross section capacity in function of CHS slenderness

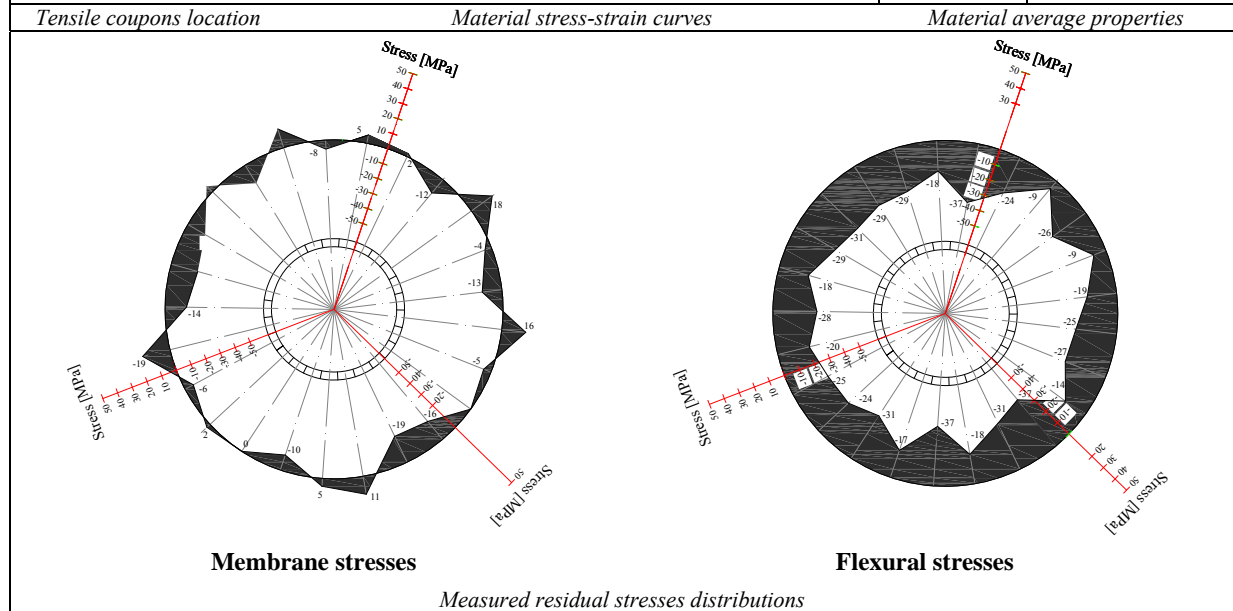
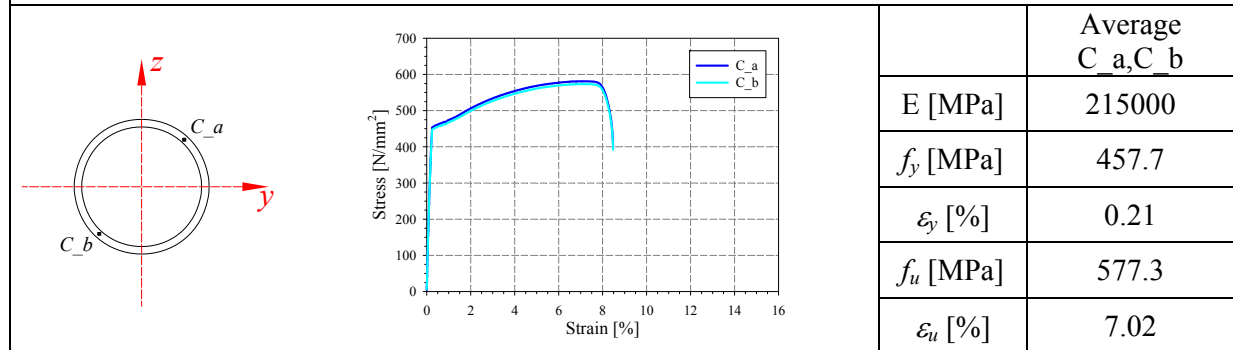


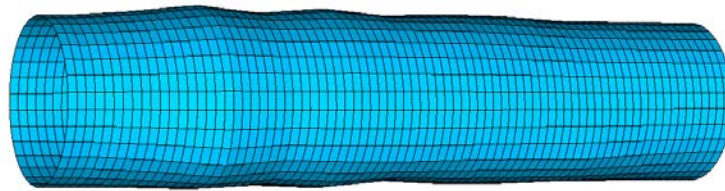
Numerical local buckling failure

Specimen name	Shape	Details
CHS_S355_LC1 159x5 HR		Shape: Circular Hollow Section Nominal yield limit: 355 MPa Load case: LC1 Pure compression D=159mm t=5mm Fabrication process: Hot rolled

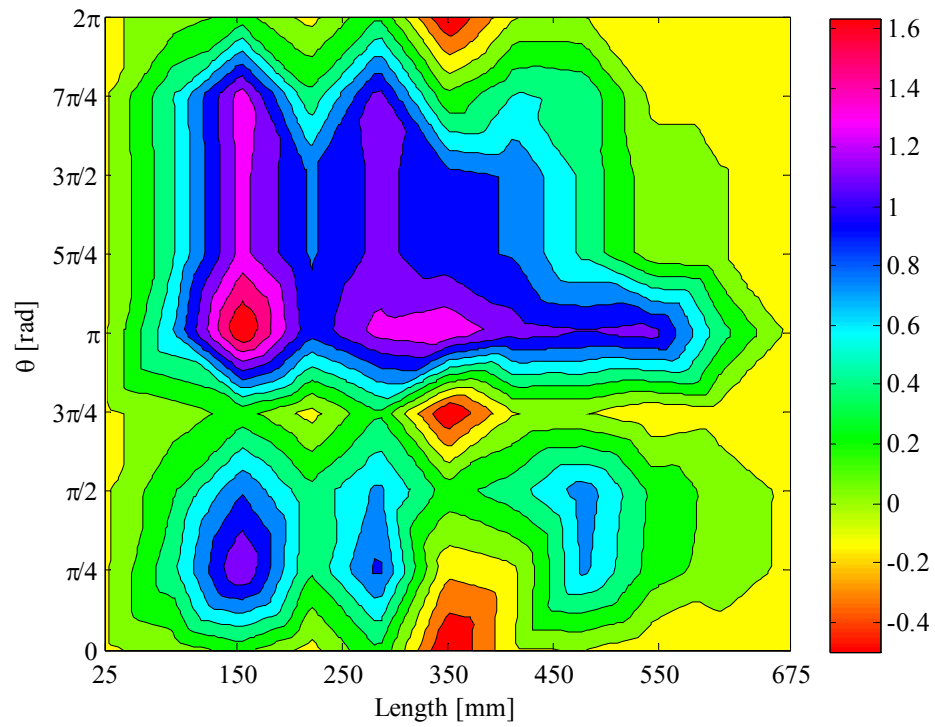
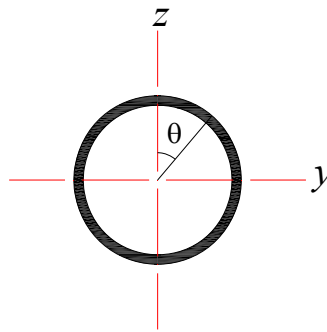


Cross-sectional measured dimensions and tolerances

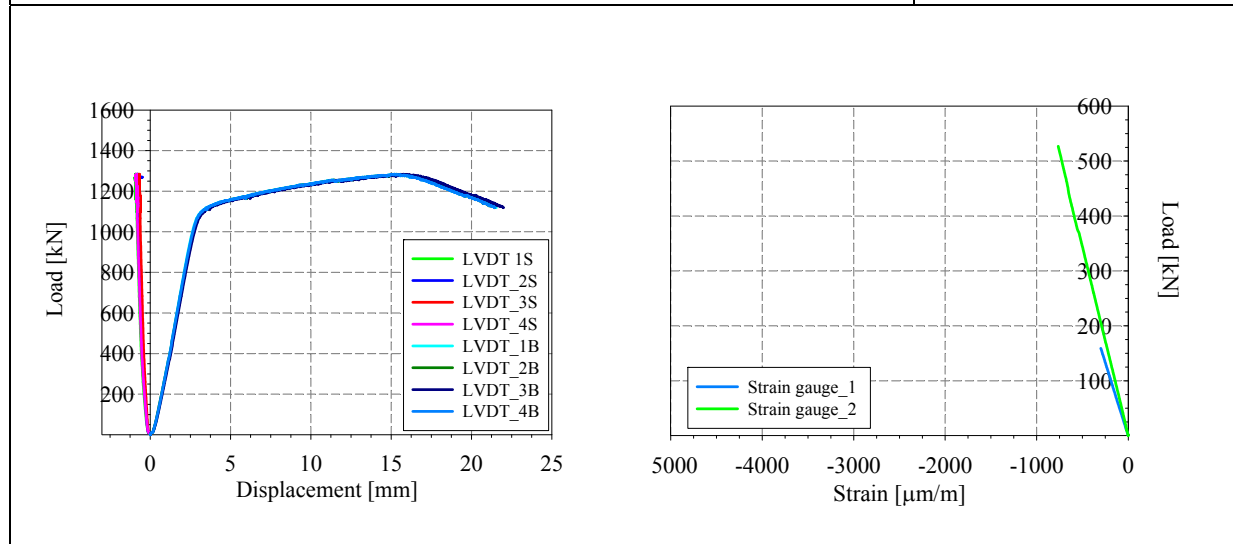
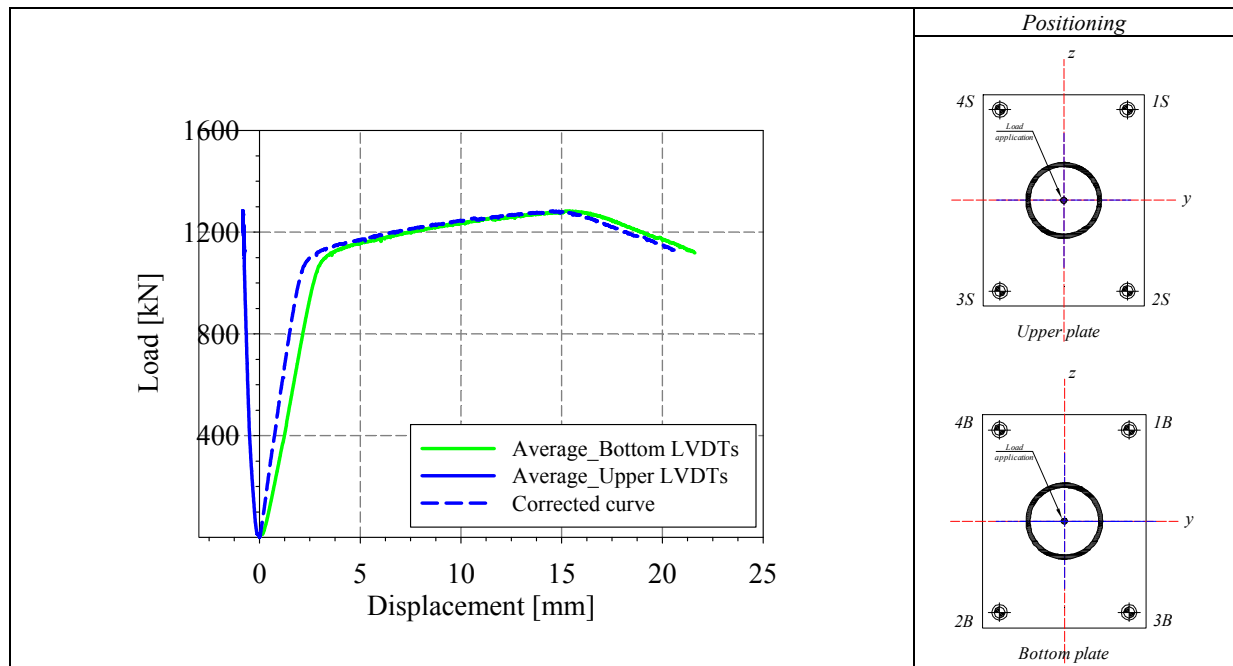




Amplified imperfect vue (x10)



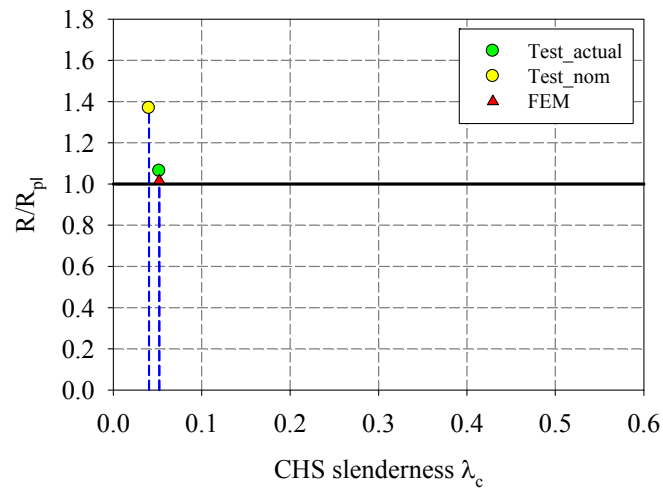
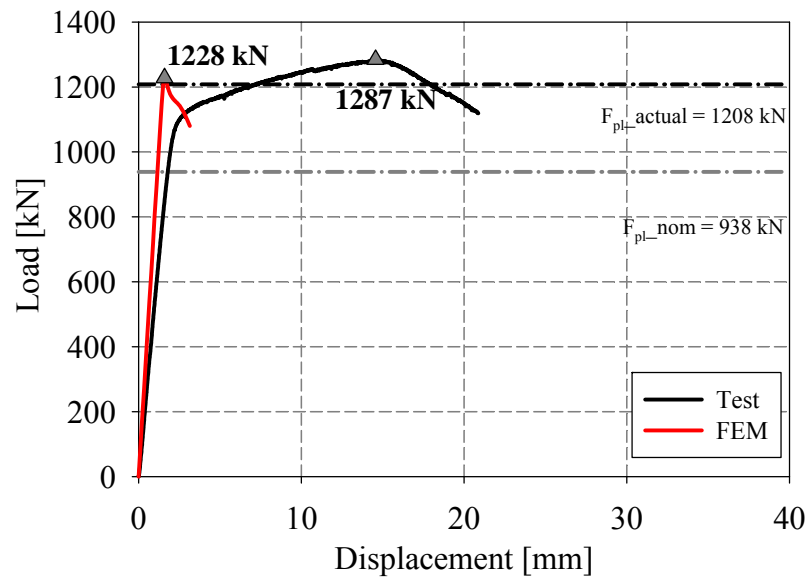
Measured Local imperfections



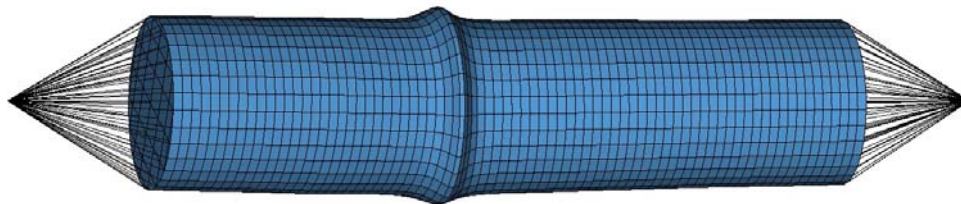
LVDT and strain gauges recordings



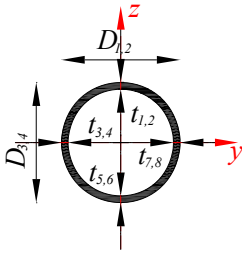
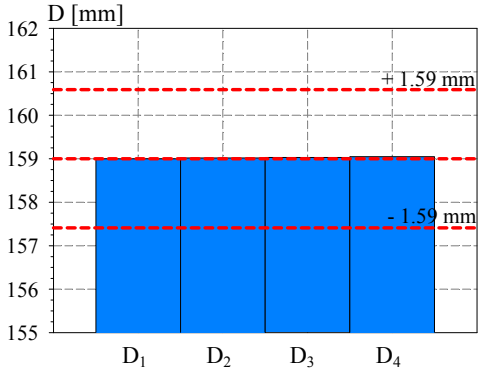
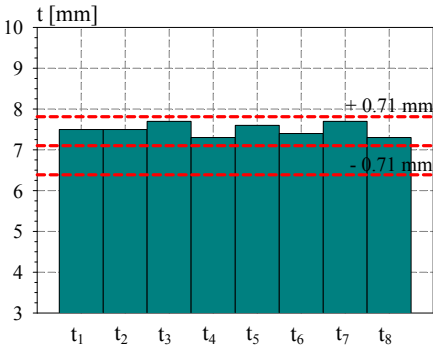
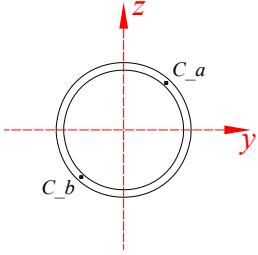
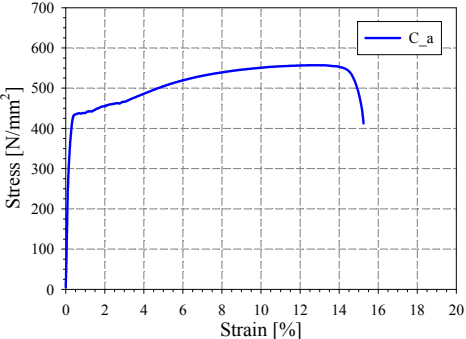
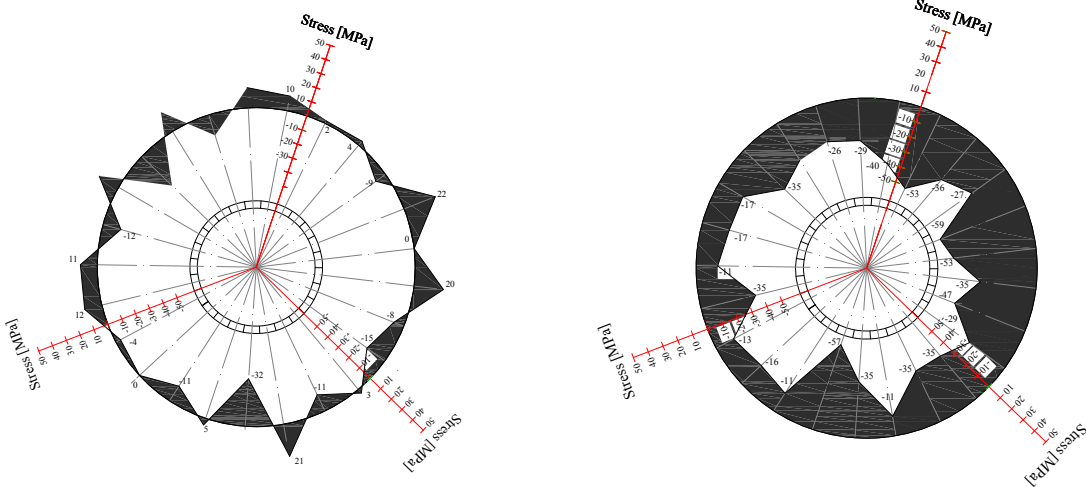
Local buckling failure

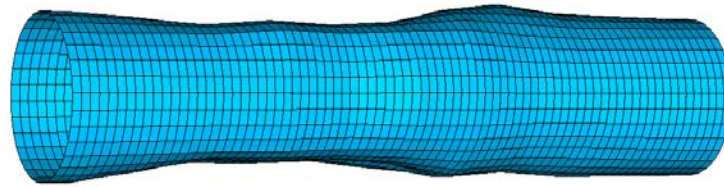


Non-dimensional cross section capacity in function of CHS slenderness

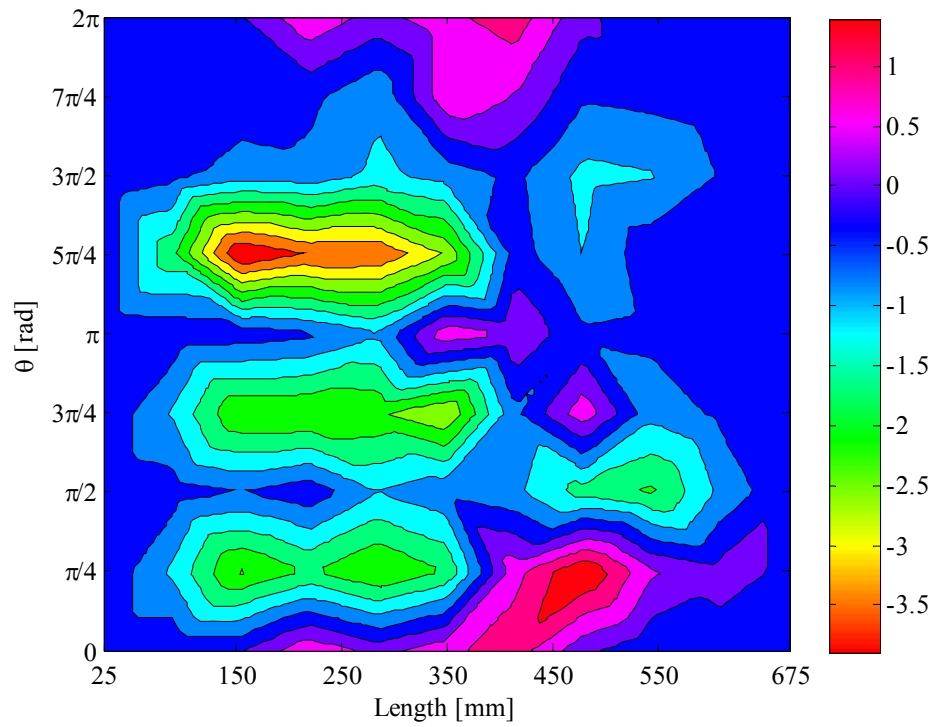
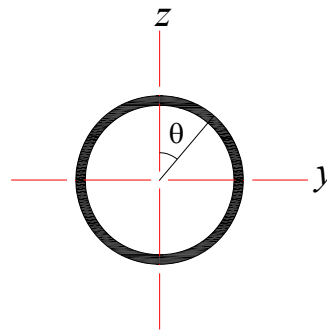


Numerical local buckling failure

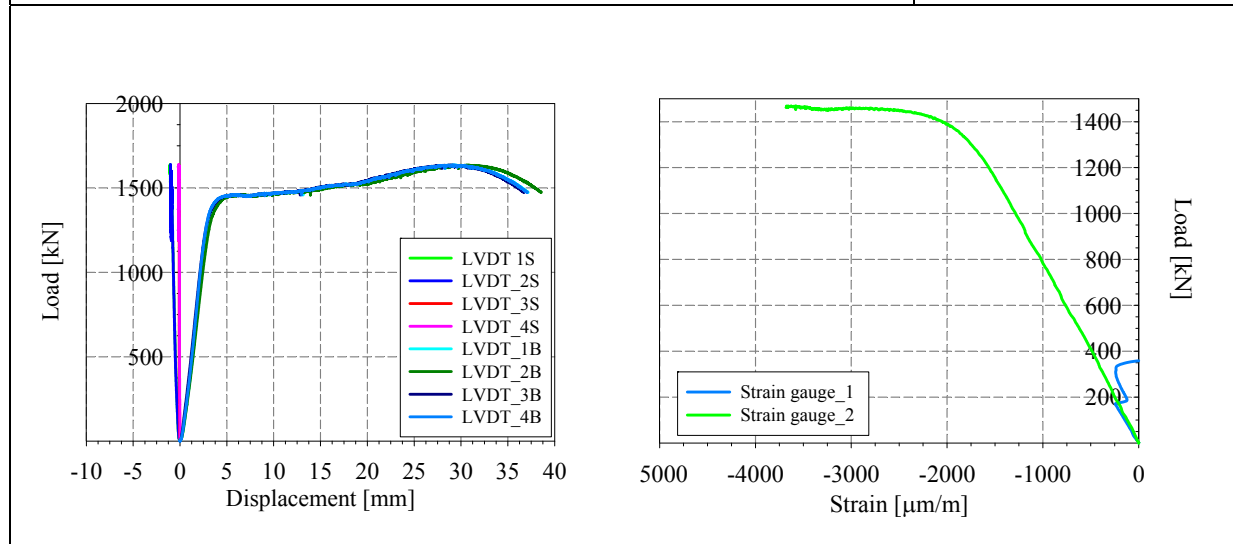
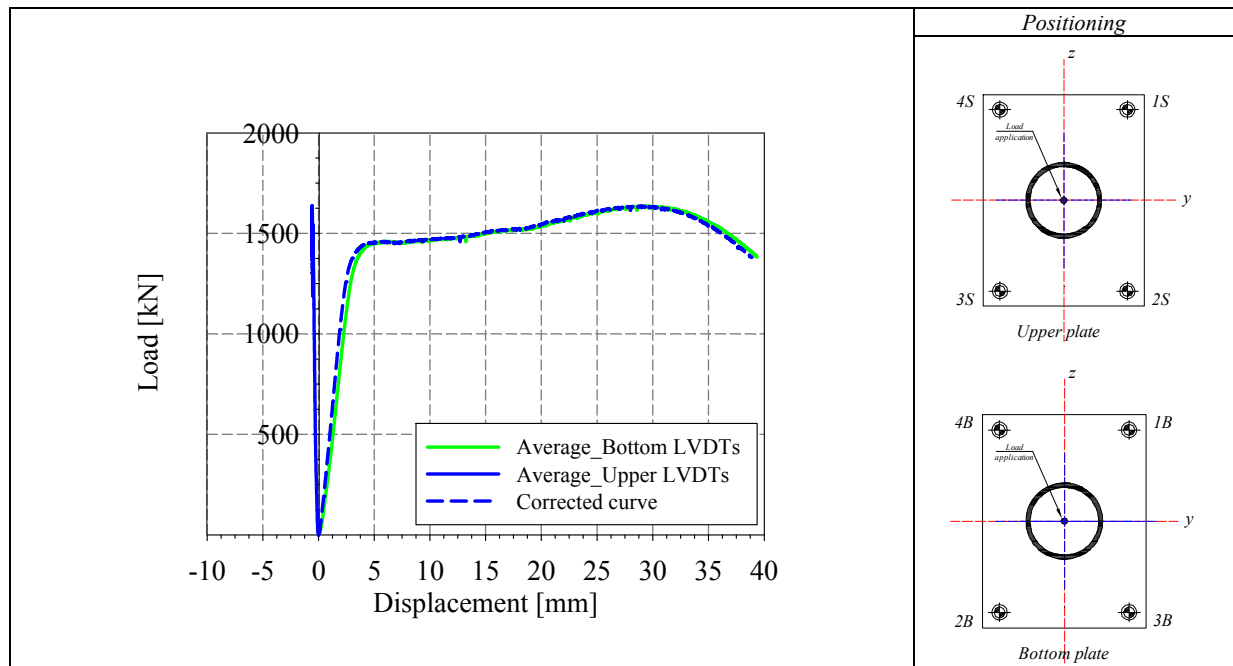
Specimen name	Shape	Details												
<p>CHS_S355_LC1 159x7.1 HR</p>		<p>Shape: Circular Hollow Section Nominal yield limit: 355 MPa Load case: LC1 Pure compression D=159mm t=7.1mm Fabrication process: Hot rolled</p>												
<p>Average D= 159 mm</p> 		<p>Average t= 7.5 mm</p> 												
<p><i>Cross-sectional measured dimensions and tolerances</i></p>														
		<table border="1"> <thead> <tr> <th colspan="2" data-bbox="1101 926 1255 993">Average C_a, C_b</th> </tr> </thead> <tbody> <tr> <td data-bbox="1101 993 1255 1050">E [MPa]</td> <td data-bbox="1255 993 1455 1050">212000</td> </tr> <tr> <td data-bbox="1101 1050 1255 1106">f_y [MPa]</td> <td data-bbox="1255 1050 1455 1106">442</td> </tr> <tr> <td data-bbox="1101 1106 1255 1163">ε_y [%]</td> <td data-bbox="1255 1106 1455 1163">0.20</td> </tr> <tr> <td data-bbox="1101 1163 1255 1220">f_u [MPa]</td> <td data-bbox="1255 1163 1455 1220">557.1</td> </tr> <tr> <td data-bbox="1101 1220 1255 1276">ε_u [%]</td> <td data-bbox="1255 1220 1455 1276">12.7</td> </tr> </tbody> </table>	Average C_a, C_b		E [MPa]	212000	f _y [MPa]	442	ε _y [%]	0.20	f _u [MPa]	557.1	ε _u [%]	12.7
Average C_a, C_b														
E [MPa]	212000													
f _y [MPa]	442													
ε _y [%]	0.20													
f _u [MPa]	557.1													
ε _u [%]	12.7													
<p><i>Tensile coupons location</i></p>	<p><i>Material stress-strain curves</i></p>	<p><i>Material average properties</i></p>												
 <div style="display: flex; justify-content: space-around; margin-top: 10px;"> <div data-bbox="443 1812 646 1839" style="text-align: center;">Membrane stresses</div> <div data-bbox="1065 1812 1243 1839" style="text-align: center;">Flexural stresses</div> </div> <p style="text-align: center; margin-top: 10px;"><i>Measured residual stresses distributions</i></p>														



Amplified imperfect vue (x10)



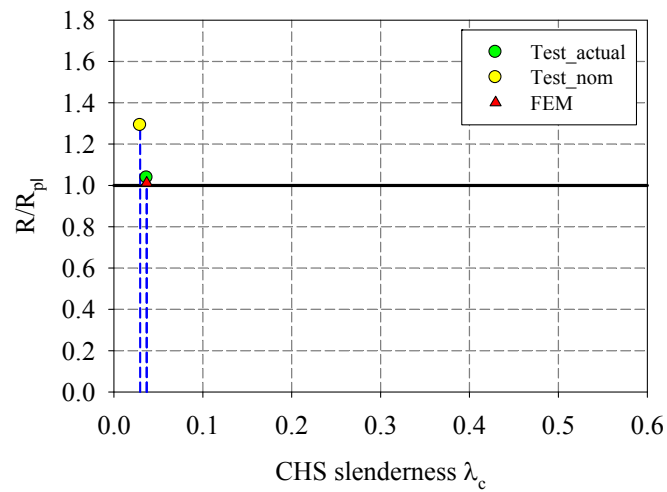
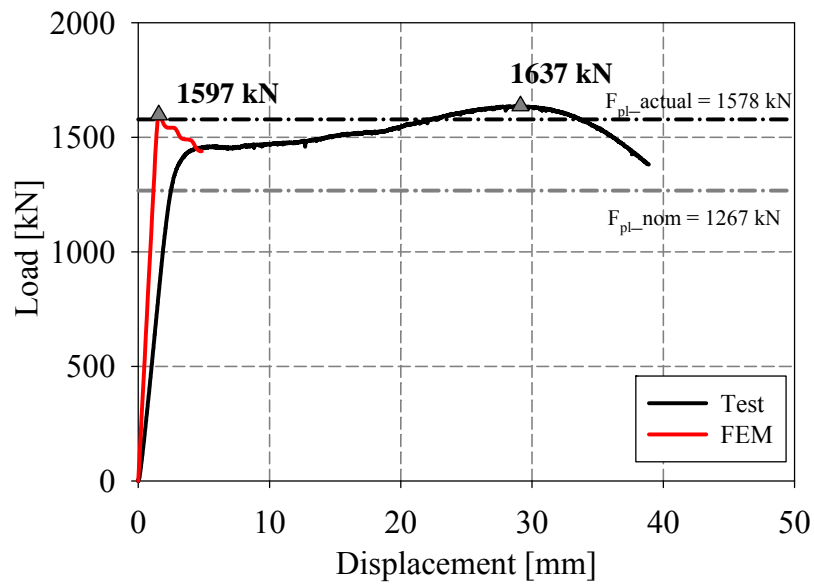
Measured Local imperfections



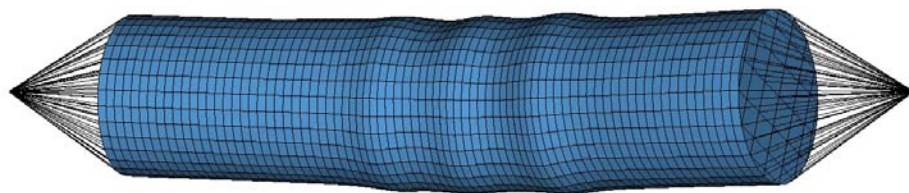
LVDT and strain gauges recordings



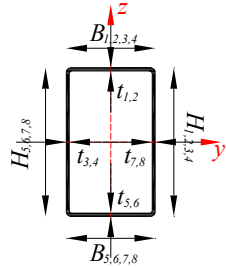
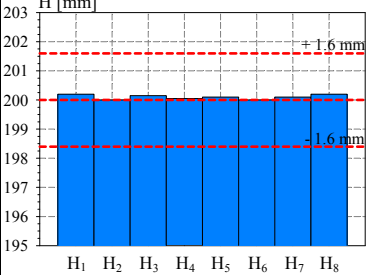
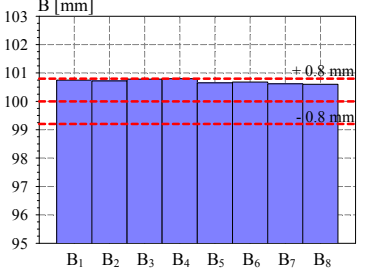
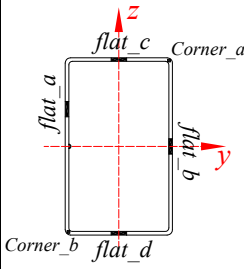
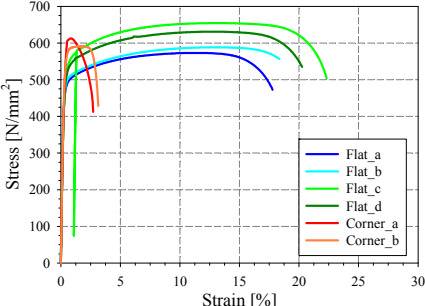
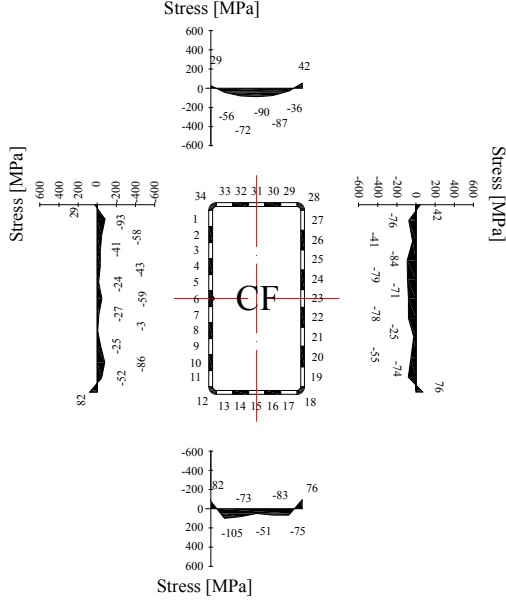
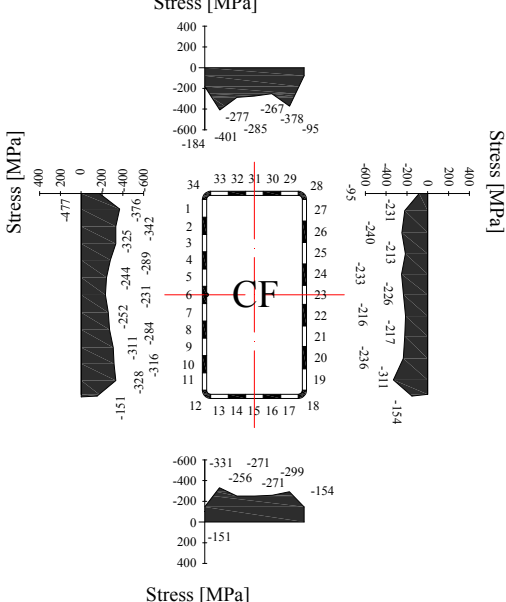
Local buckling failure

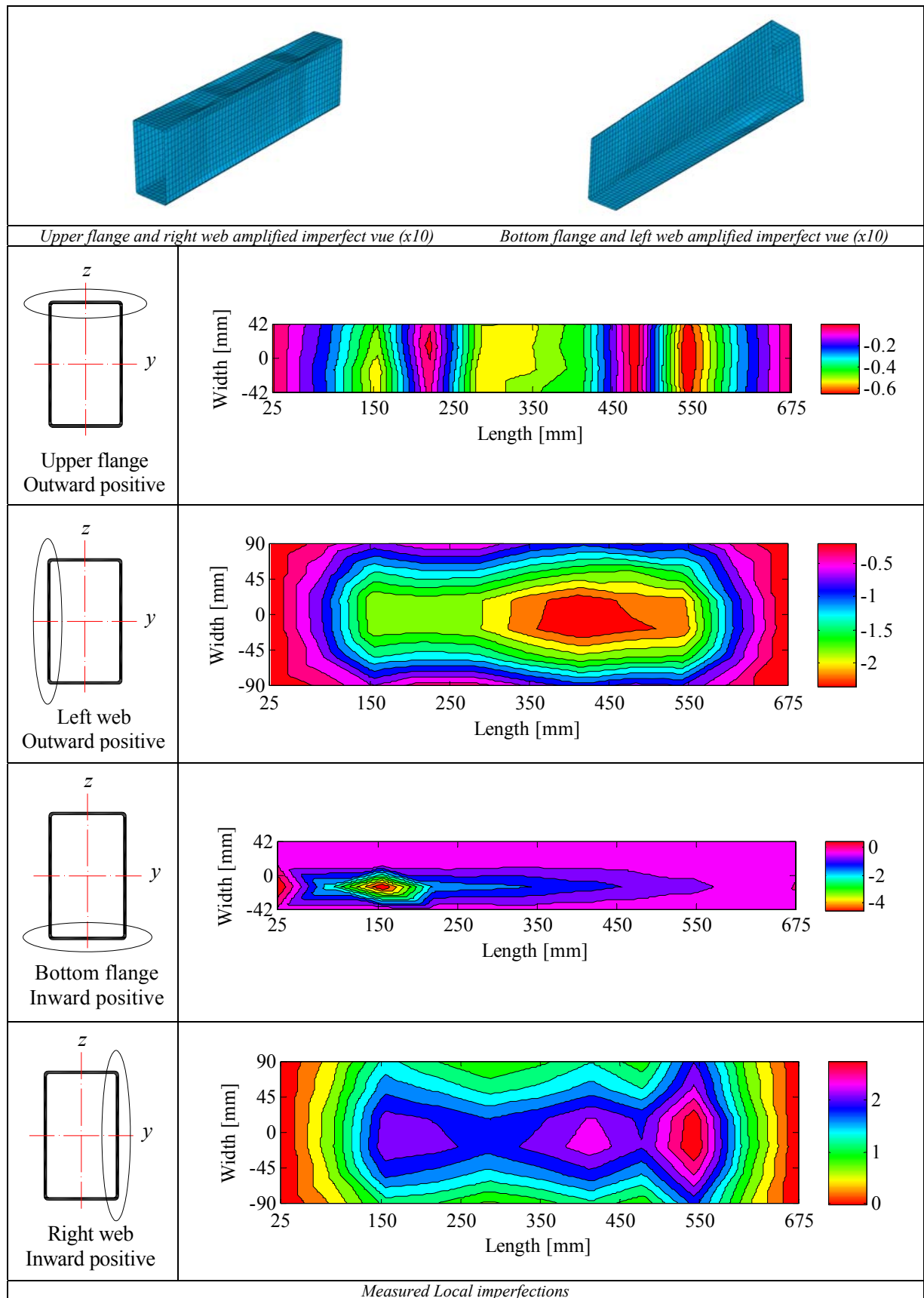


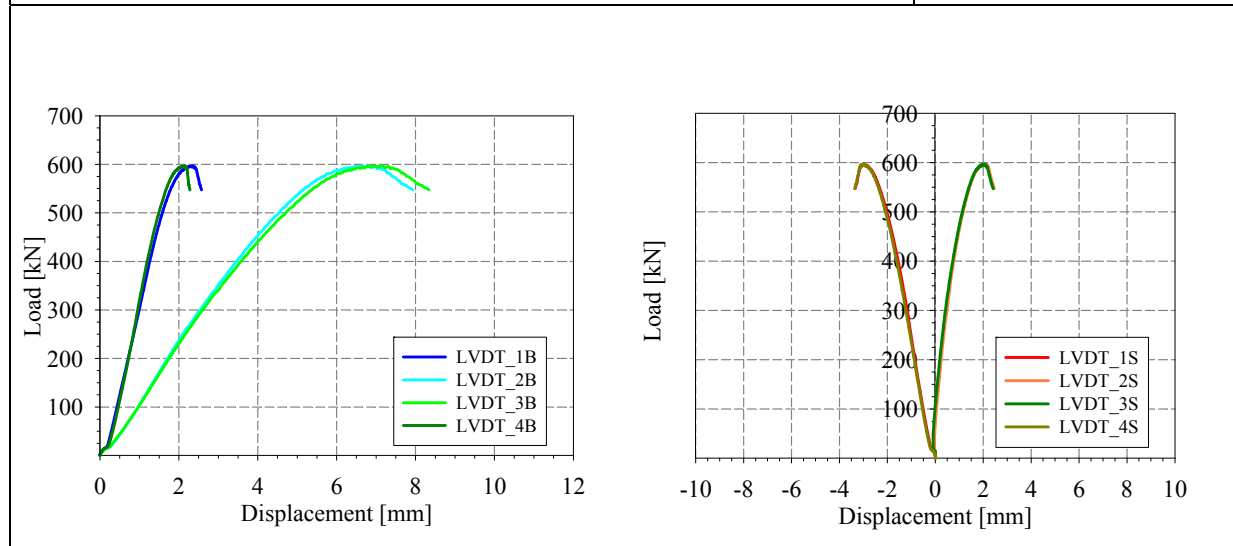
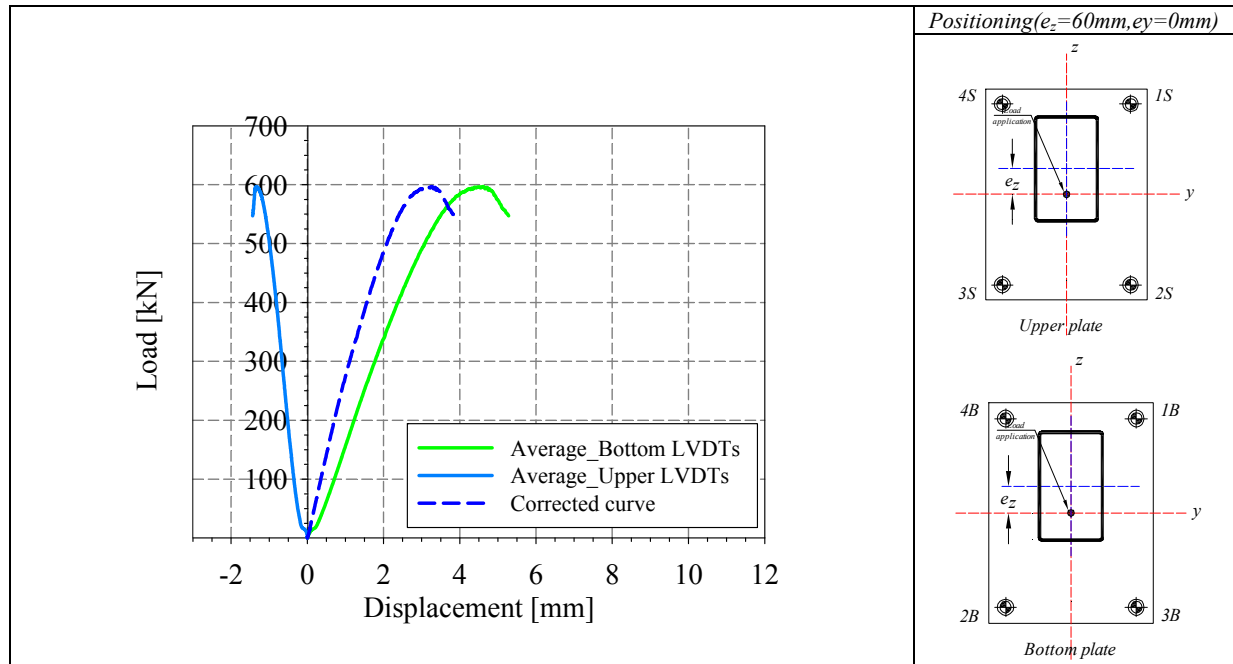
Non-dimensional cross section capacity in function of CHS slenderness



Numerical local buckling failure

Specimen name	Shape	Details																		
<p>RHS_S355_LC2 200x100x4 CF</p>		<p>Shape: Rectangular Hollow Section Nominal yield limit: 355 MPa Load case: N (50%) + M_y (50%) H=200mm B=100mm t=4mm Fabrication process: Cold formed</p>																		
<p>Average h= 200.1 mm</p>		<p>Average b= 100.7 mm</p>																		
																				
<p>Average t= 3.96 mm</p>																				
<p>Cross-sectional measured dimensions and tolerances</p>																				
 	<table border="1"> <thead> <tr> <th></th> <th>Flat</th> <th>Corner</th> </tr> </thead> <tbody> <tr> <td>E [MPa]</td> <td>216630</td> <td>213000</td> </tr> <tr> <td>f_y [MPa]</td> <td>494.6</td> <td>-</td> </tr> <tr> <td>ϵ_y [%]</td> <td>0.22</td> <td>-</td> </tr> <tr> <td>f_u [MPa]</td> <td>611</td> <td>601</td> </tr> <tr> <td>ϵ_u [%]</td> <td>11.9</td> <td>1.2</td> </tr> </tbody> </table>			Flat	Corner	E [MPa]	216630	213000	f_y [MPa]	494.6	-	ϵ_y [%]	0.22	-	f_u [MPa]	611	601	ϵ_u [%]	11.9	1.2
	Flat	Corner																		
E [MPa]	216630	213000																		
f_y [MPa]	494.6	-																		
ϵ_y [%]	0.22	-																		
f_u [MPa]	611	601																		
ϵ_u [%]	11.9	1.2																		
<p>Tensile coupons location</p>		<p>Material average properties</p>																		
 <p style="text-align: center;">Membrane stresses</p>		 <p style="text-align: center;">Flexural stresses</p>																		
<p>Measured residual stresses distributions</p>																				

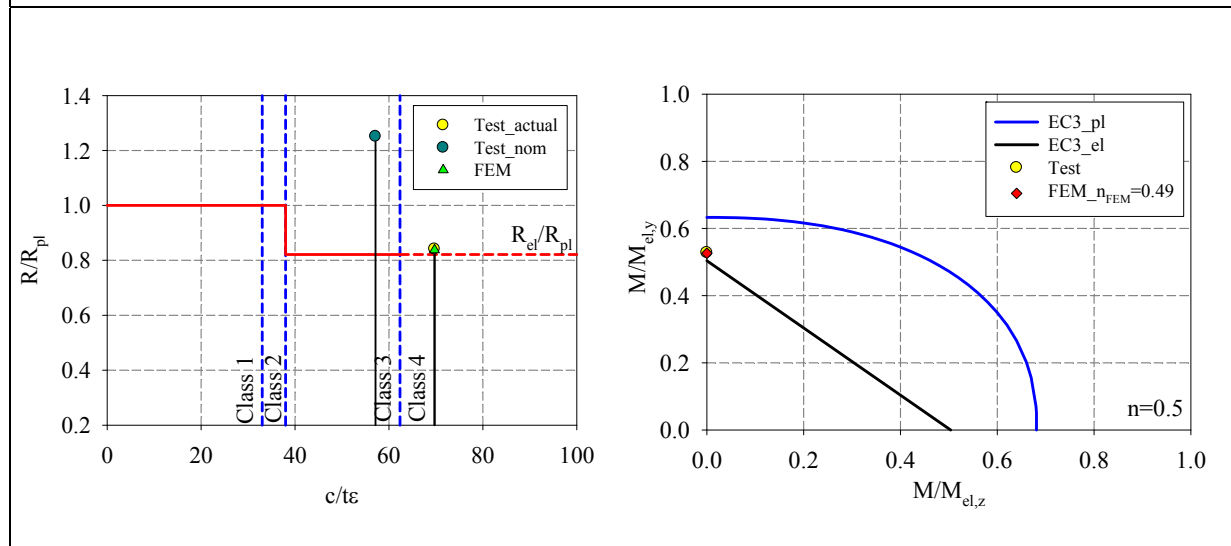
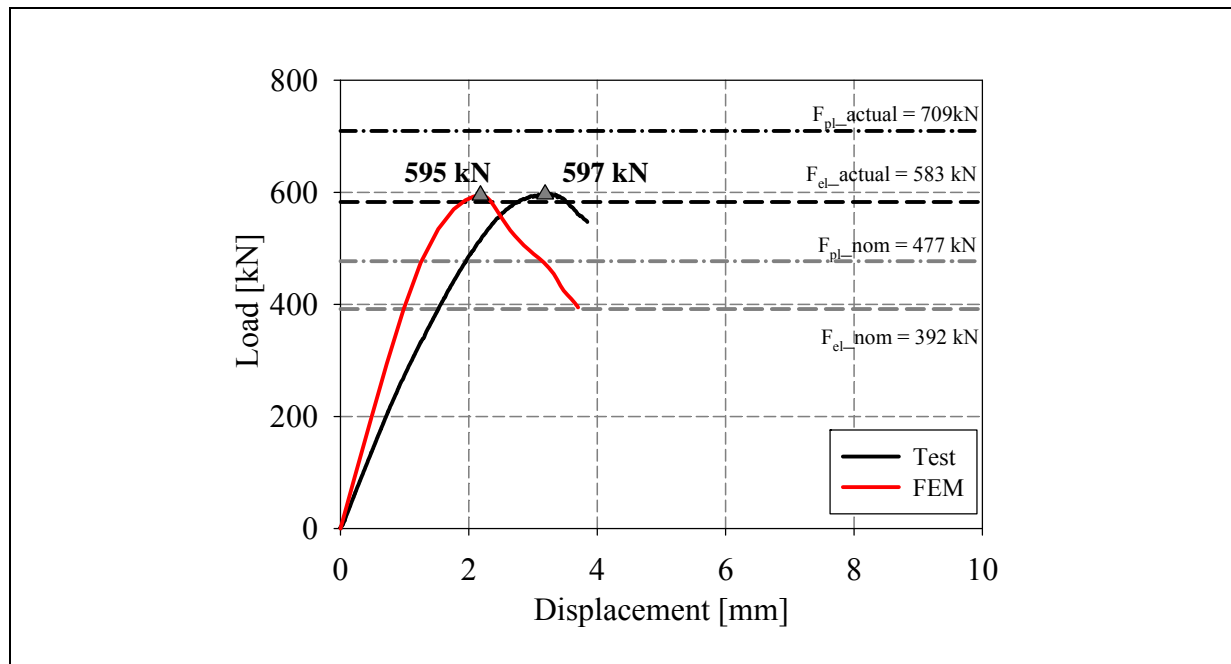




LVDT and strain gauges recordings

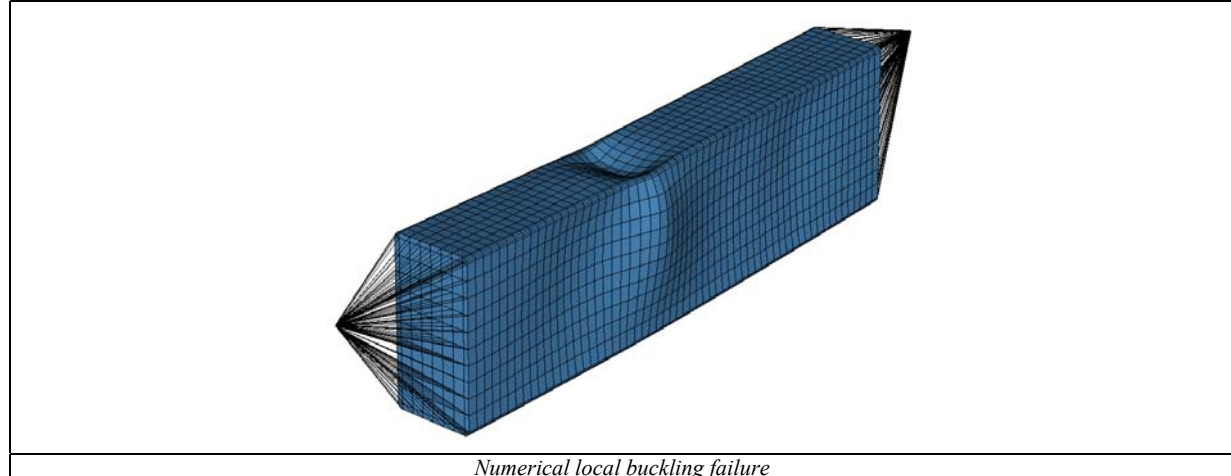


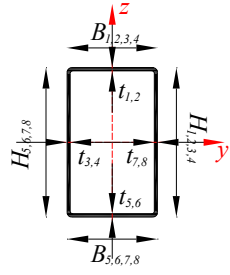
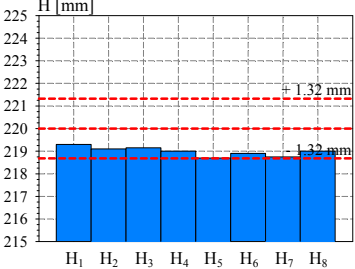
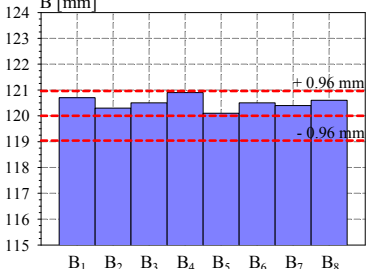
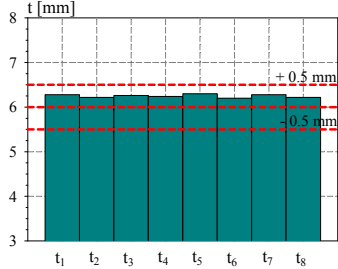
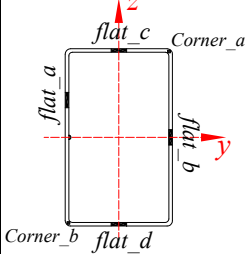
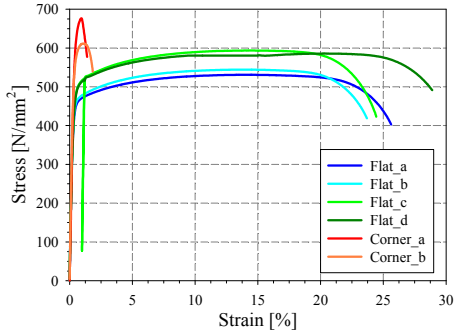
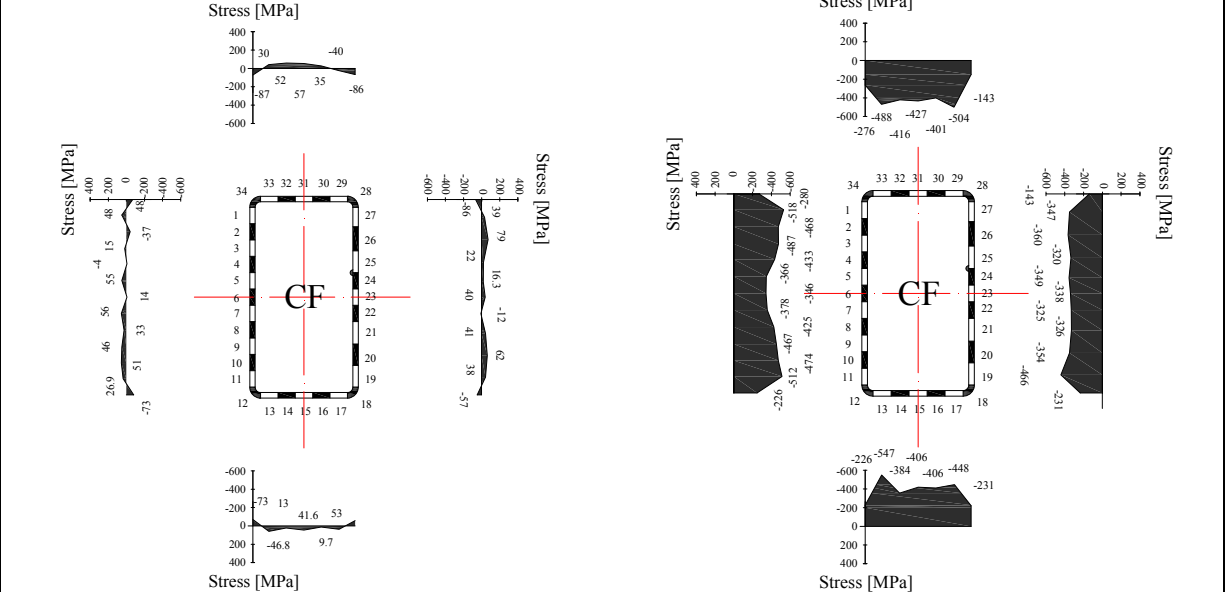
Local buckling failure

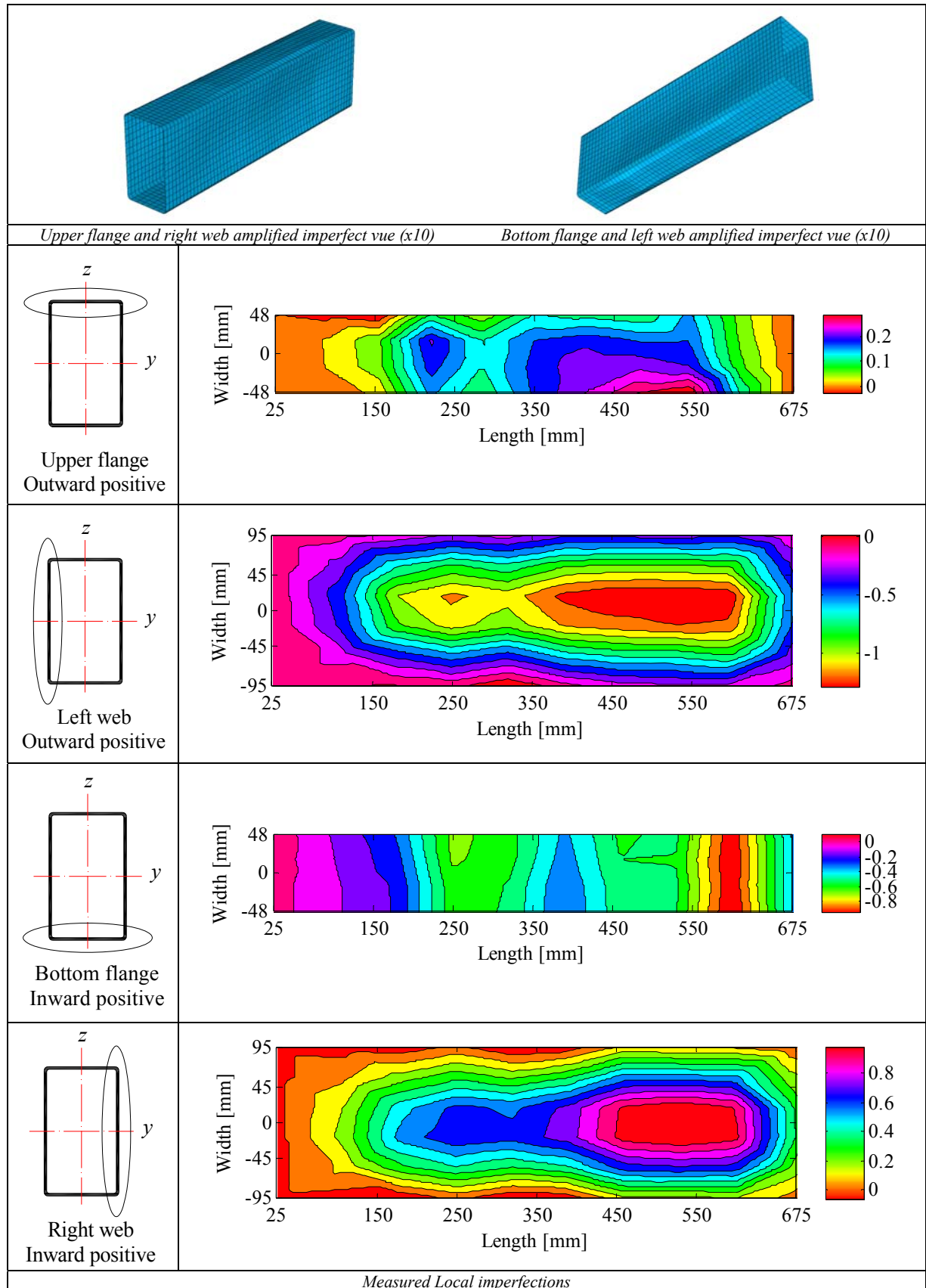


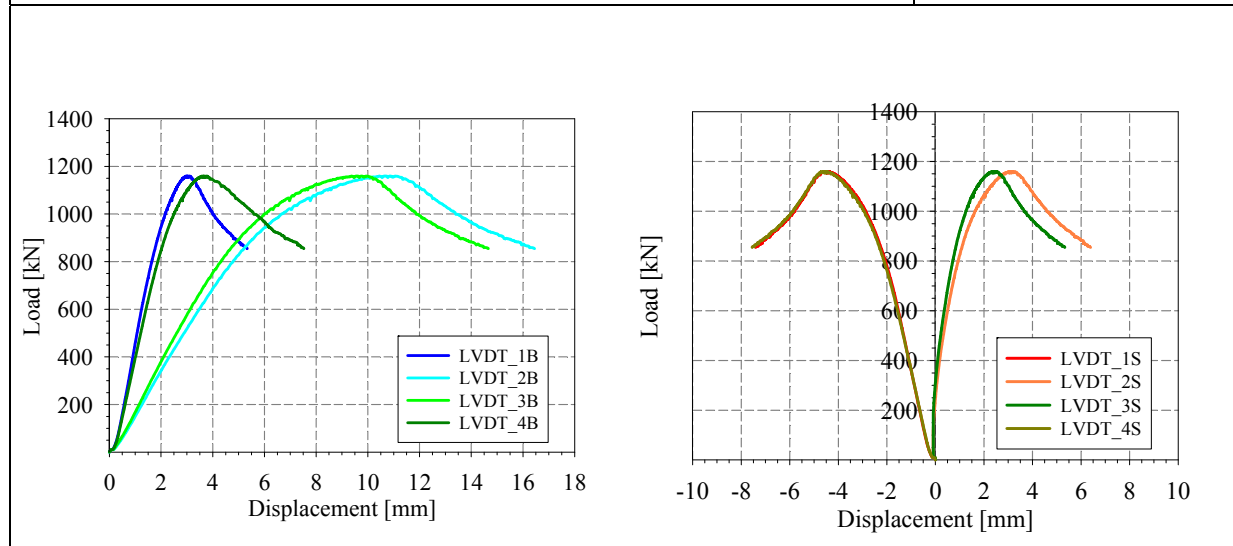
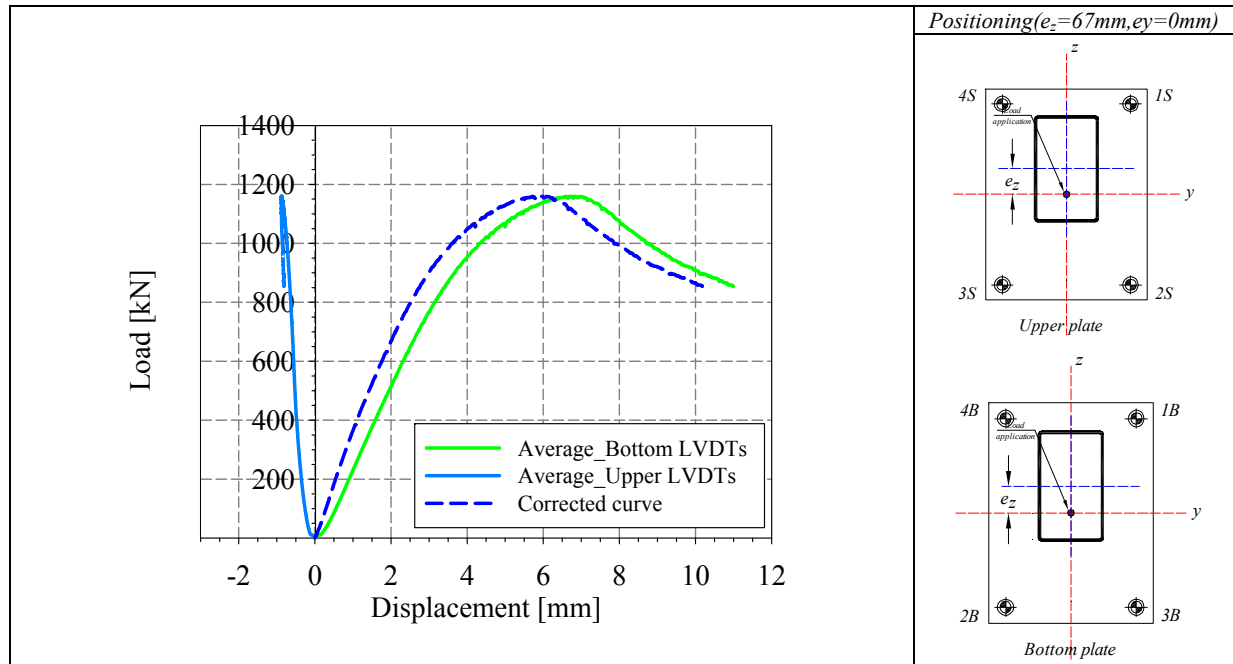
Cross-section resistance diagram

My-Mz bending moment interaction diagram



<p>Specimen name</p> <p>RHS_S355_LC2 220x120x6 CF</p>	<p>Shape</p> 	<p>Details</p> <p>Shape: Rectangular Hollow Section Nominal yield limit: 355 MPa Load case: N (50%) + M_y (50%) H=220mm B=120mm t=6mm Fabrication process: Cold formed</p>																		
<p>Average h= 219 mm</p> 	<p>Average b= 120.5 mm</p> 	<p>Average t= 6.25 mm</p> 																		
<p>Cross-sectional measured dimensions and tolerances</p>																				
		<table border="1"> <thead> <tr> <th></th> <th>Flat</th> <th>Corner</th> </tr> </thead> <tbody> <tr> <td>E [MPa]</td> <td>206597</td> <td>207000</td> </tr> <tr> <td>f_y [MPa]</td> <td>454.7</td> <td>-</td> </tr> <tr> <td>ε_y [%]</td> <td>0.22</td> <td>-</td> </tr> <tr> <td>f_u [MPa]</td> <td>563.6</td> <td>644</td> </tr> <tr> <td>ε_u [%]</td> <td>15.5</td> <td>1</td> </tr> </tbody> </table>		Flat	Corner	E [MPa]	206597	207000	f _y [MPa]	454.7	-	ε _y [%]	0.22	-	f _u [MPa]	563.6	644	ε _u [%]	15.5	1
	Flat	Corner																		
E [MPa]	206597	207000																		
f _y [MPa]	454.7	-																		
ε _y [%]	0.22	-																		
f _u [MPa]	563.6	644																		
ε _u [%]	15.5	1																		
<p>Tensile coupons location</p>	<p>Material stress-strain curves</p>	<p>Material average properties</p>																		
 <p style="text-align: center;">Membrane stresses Flexural stresses</p> <p style="text-align: center;"><i>Measured residual stresses distributions</i></p>																				

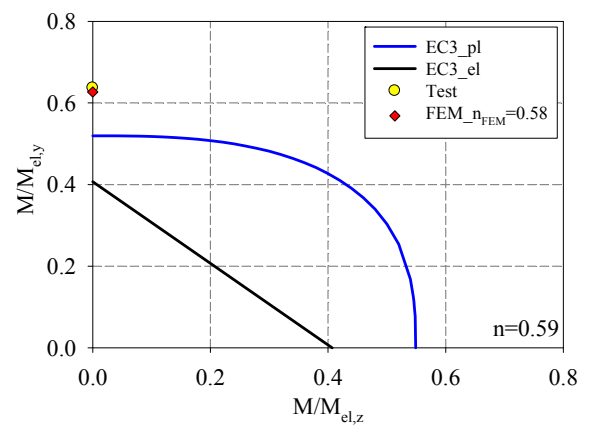
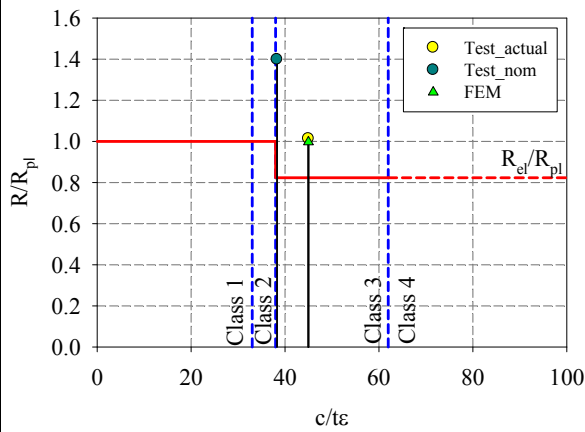
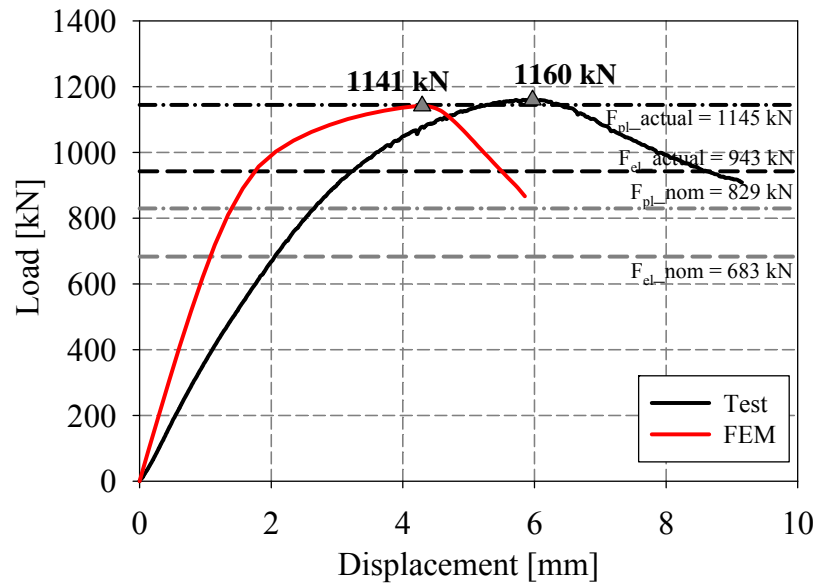




LVDT and strain gauges recordings

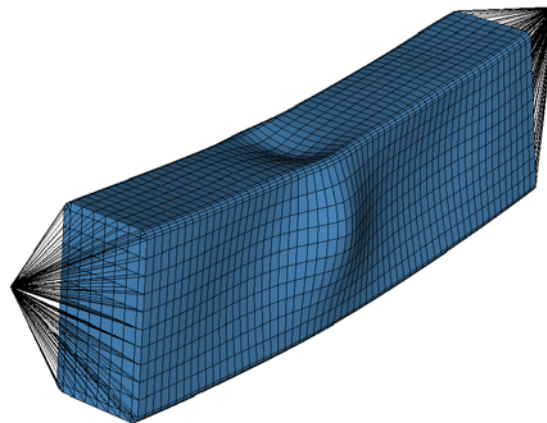


Local buckling failure

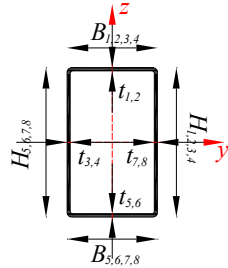
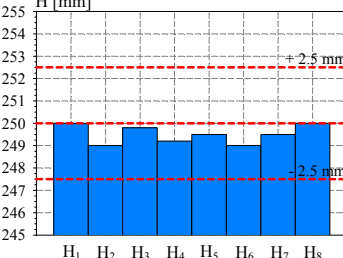
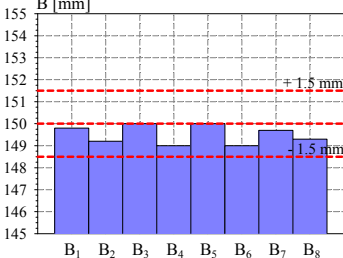
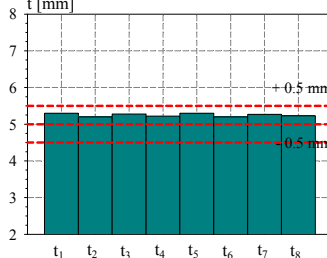
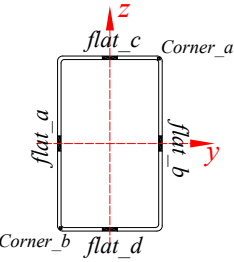
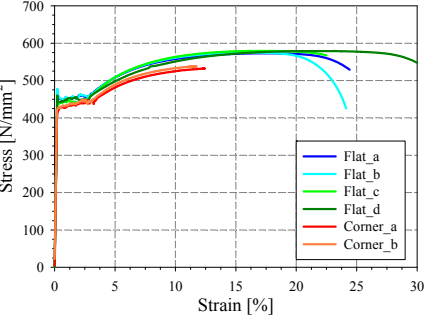
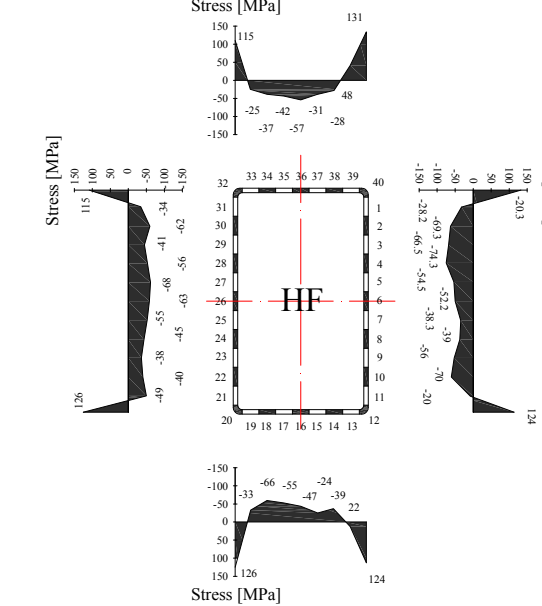
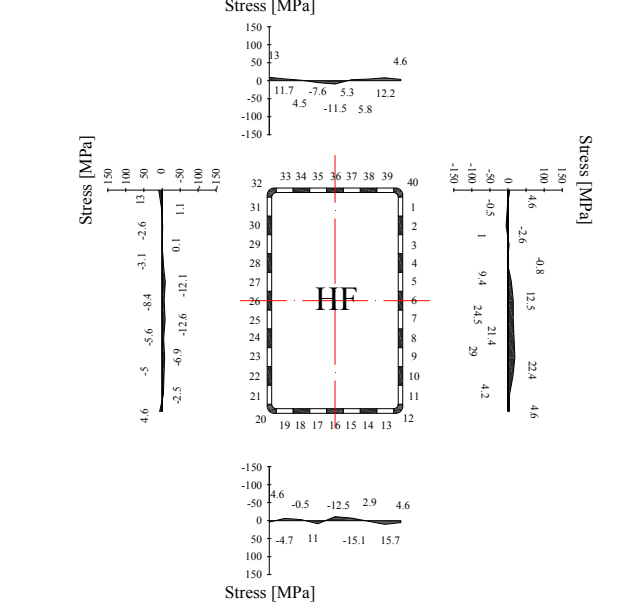


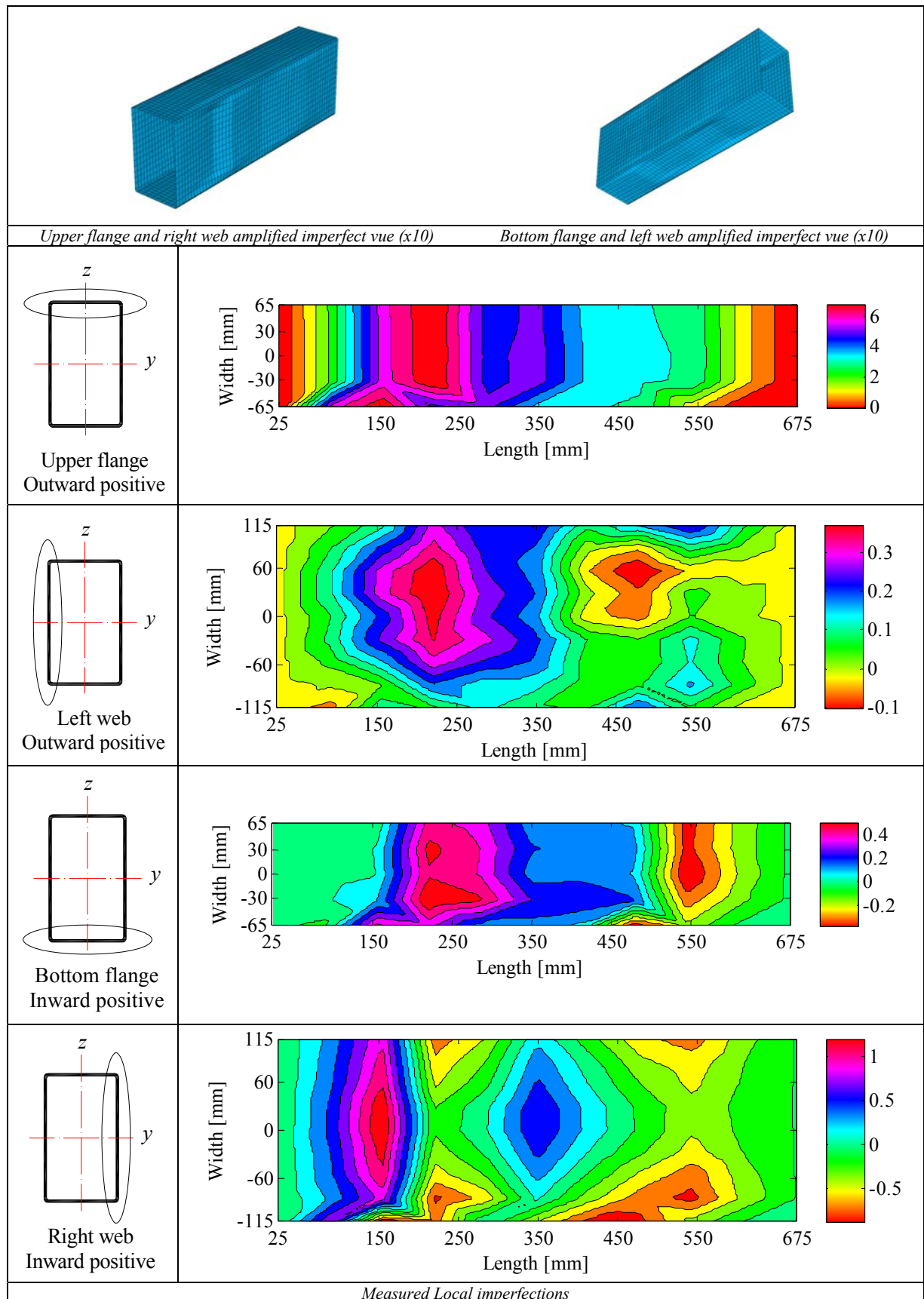
Cross-section resistance diagram

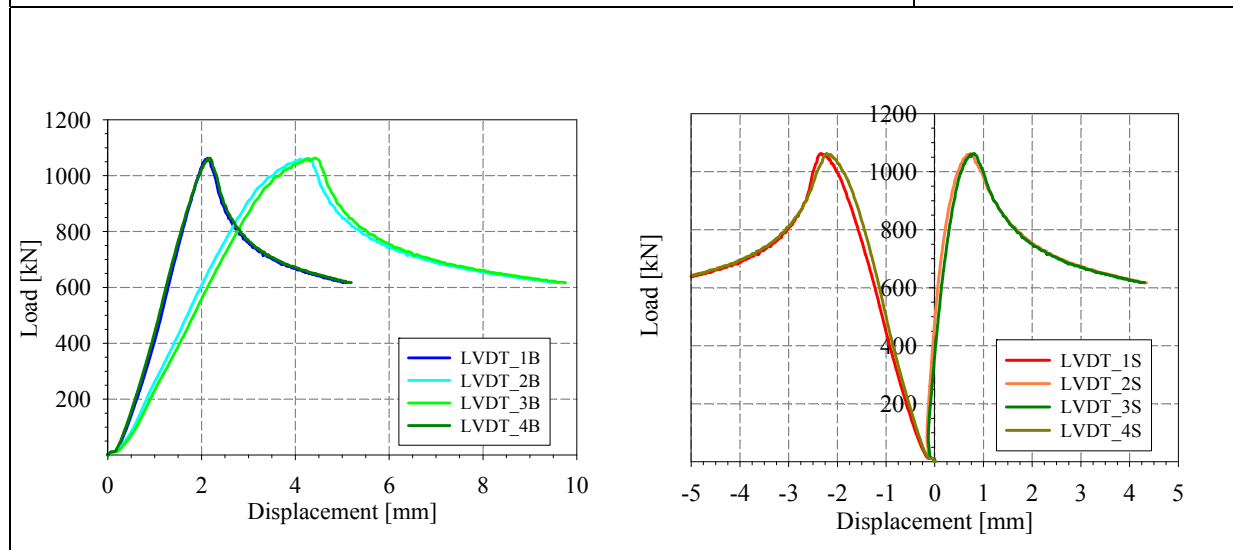
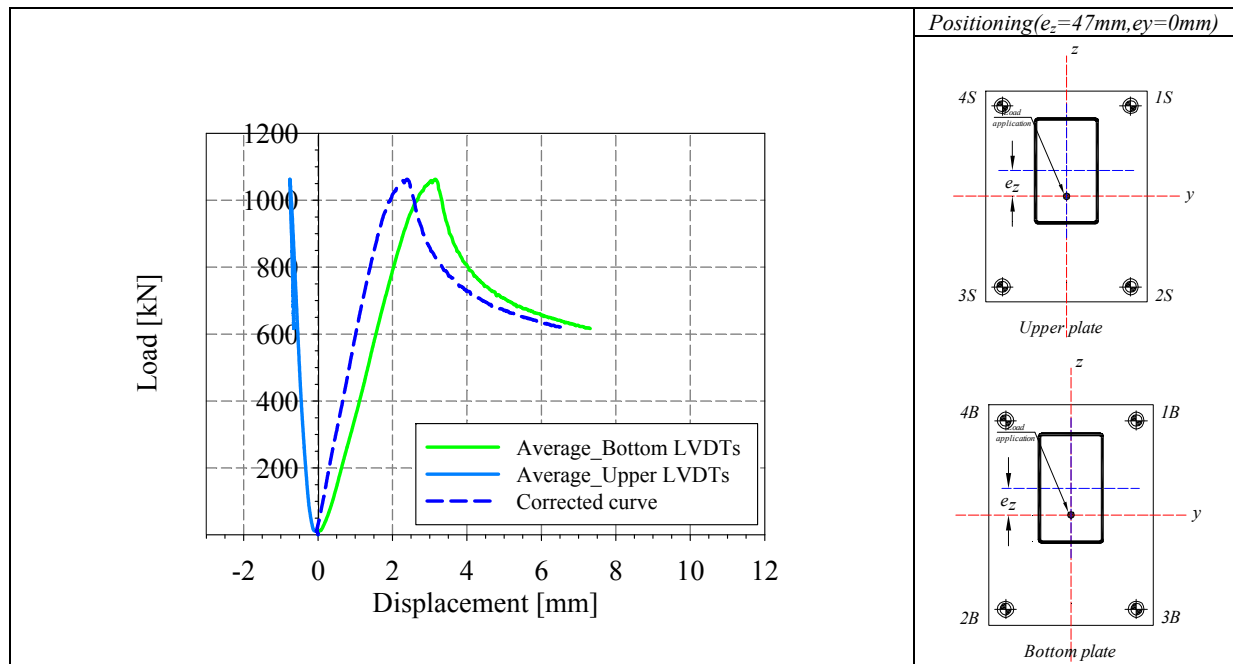
My-Mz bending moment interaction diagram



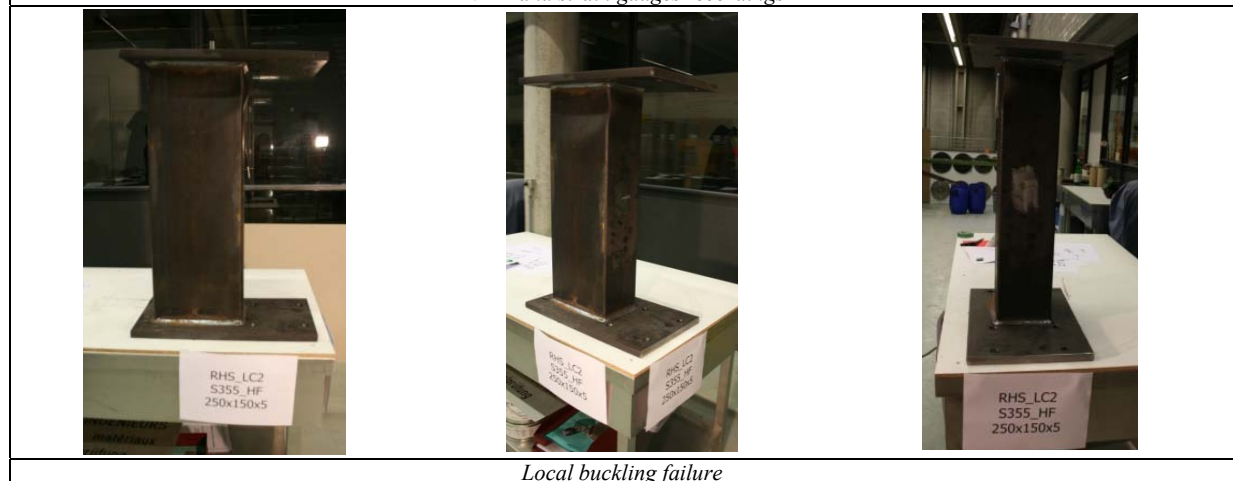
Numerical local buckling failure

Specimen name	Shape	Details																		
<p>RHS_S355_LC2 250x150x5 HF</p>		<p>Shape: Rectangular Hollow Section Nominal yield limit: 355 MPa Load case: N (50%) + M_y (50%) H=250mm B=150mm t=5mm Fabrication process: Hot formed</p>																		
<p>Average h= 249.5 mm</p> 	<p>Average b= 149.5 mm</p> 	<p>Average t= 5.25 mm</p> 																		
<i>Cross-sectional measured dimensions and tolerances</i>																				
		<table border="1"> <thead> <tr> <th></th> <th>Flat</th> <th>Corner</th> </tr> </thead> <tbody> <tr> <td>E [MPa]</td> <td>212190</td> <td>210750</td> </tr> <tr> <td>f_y [MPa]</td> <td>447</td> <td>435</td> </tr> <tr> <td>ε_y [%]</td> <td>0.21</td> <td>0.20</td> </tr> <tr> <td>f_u [MPa]</td> <td>576.6</td> <td>535</td> </tr> <tr> <td>ε_u [%]</td> <td>17.7</td> <td>11.7</td> </tr> </tbody> </table>		Flat	Corner	E [MPa]	212190	210750	f _y [MPa]	447	435	ε _y [%]	0.21	0.20	f _u [MPa]	576.6	535	ε _u [%]	17.7	11.7
	Flat	Corner																		
E [MPa]	212190	210750																		
f _y [MPa]	447	435																		
ε _y [%]	0.21	0.20																		
f _u [MPa]	576.6	535																		
ε _u [%]	17.7	11.7																		
<i>Tensile coupons location</i>	<i>Material stress-strain curves</i>	<i>Material average properties</i>																		
 <p style="text-align: center;">Membrane stresses</p>	 <p style="text-align: center;">Flexural stresses</p>																			
<i>Measured residual stresses distributions</i>																				

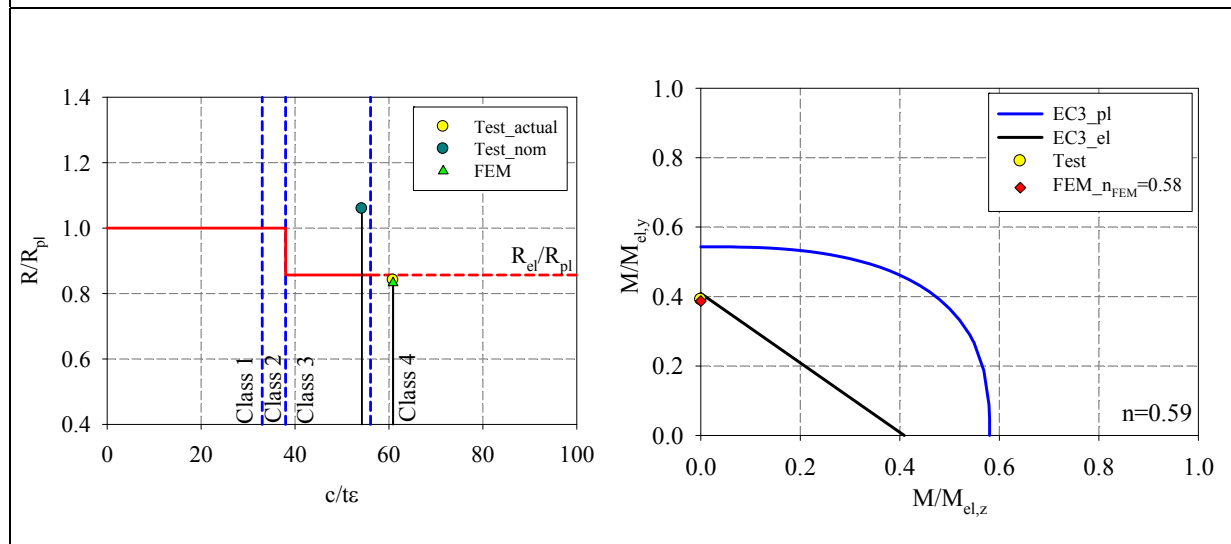
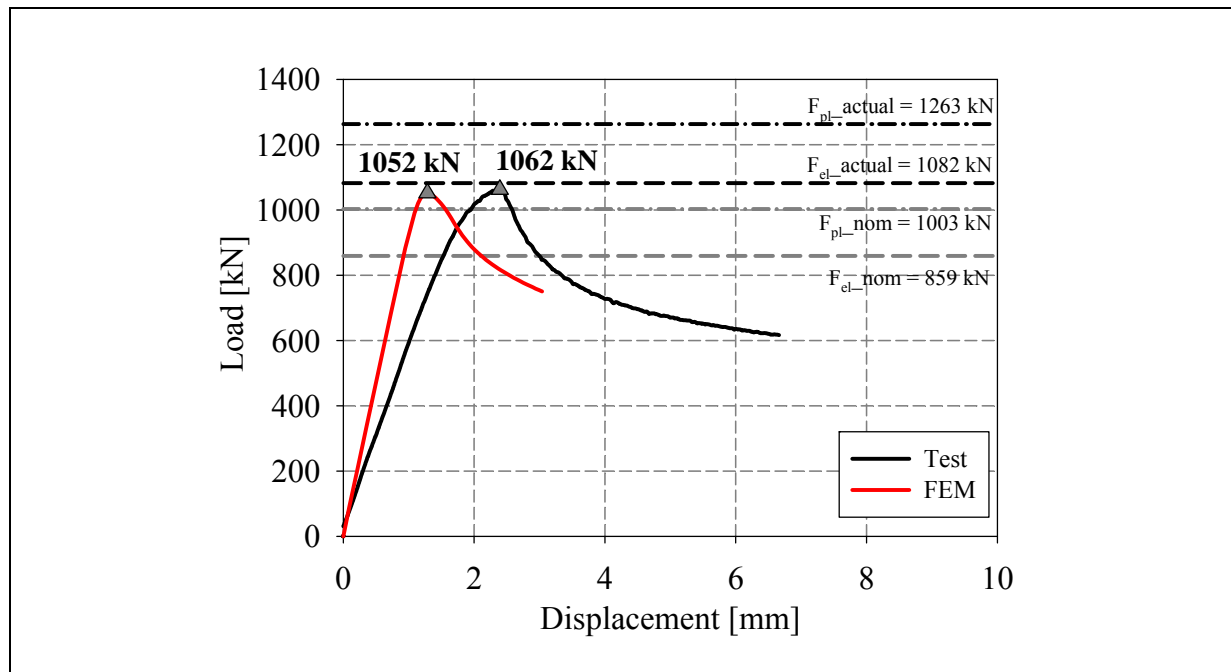




LVDT and strain gauges recordings

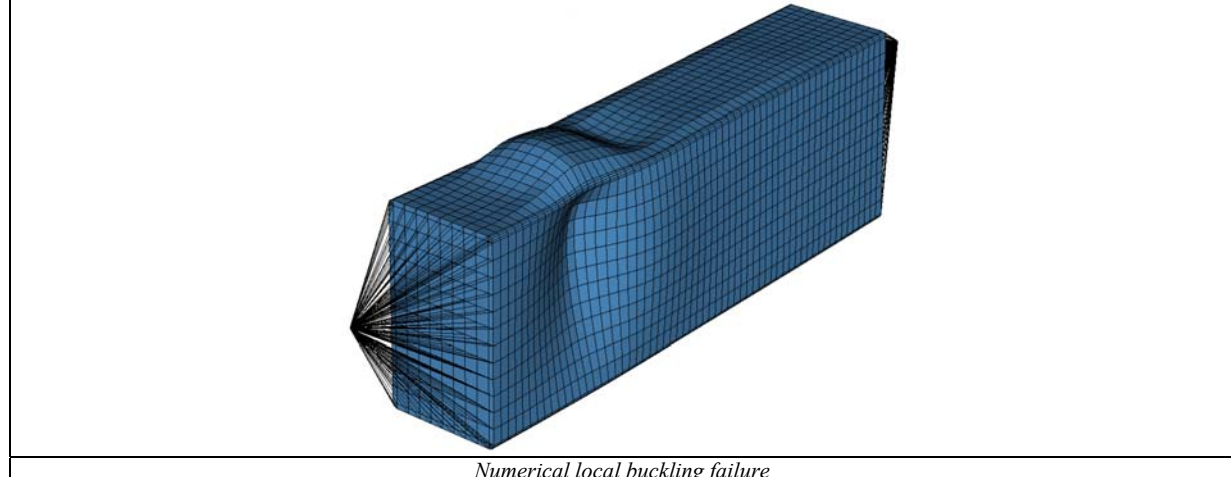


Local buckling failure

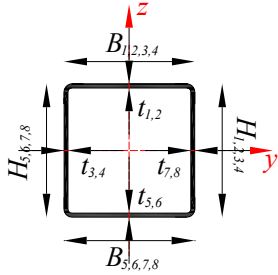
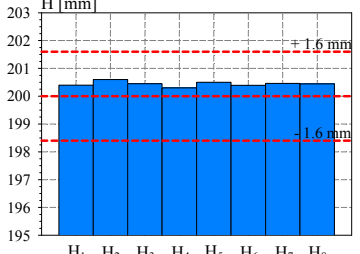
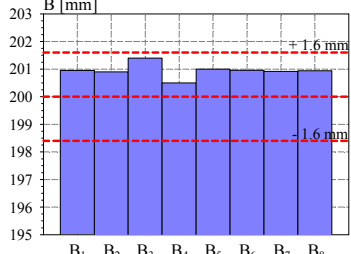
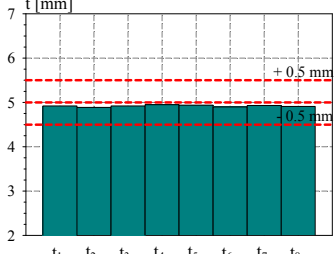
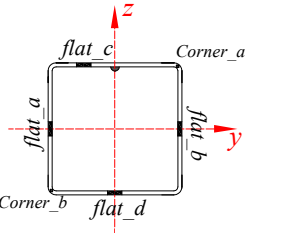
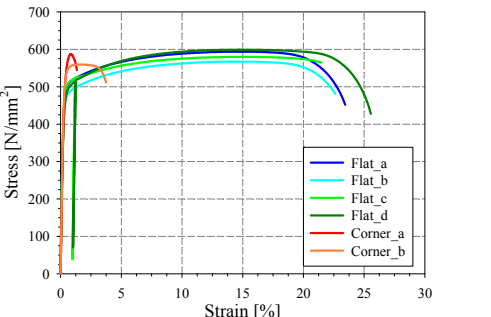
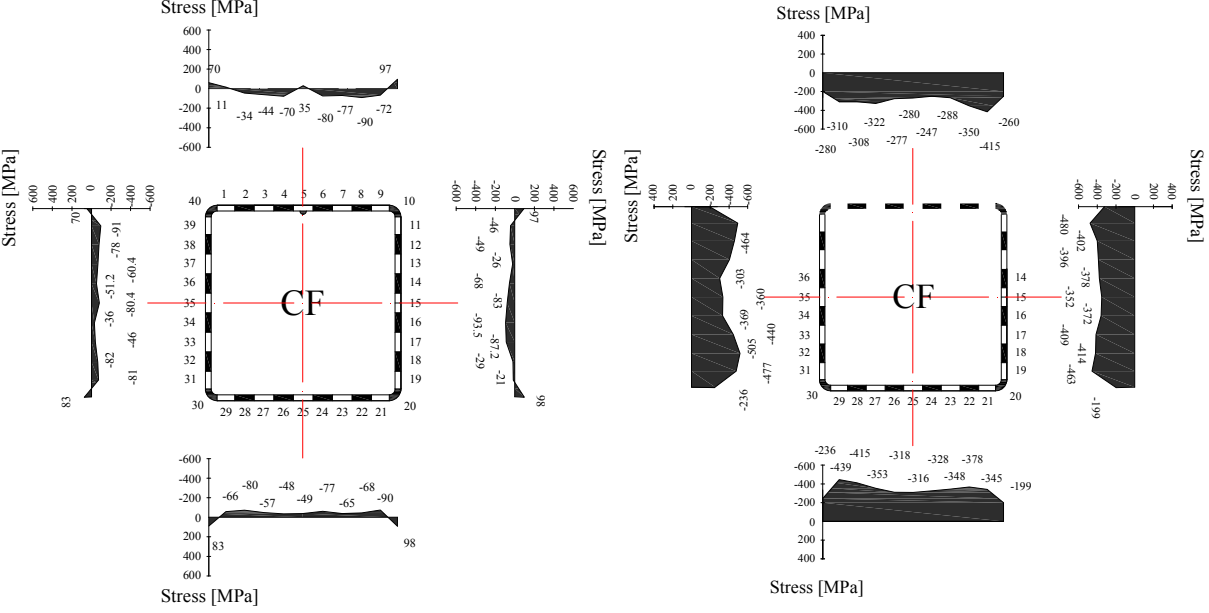


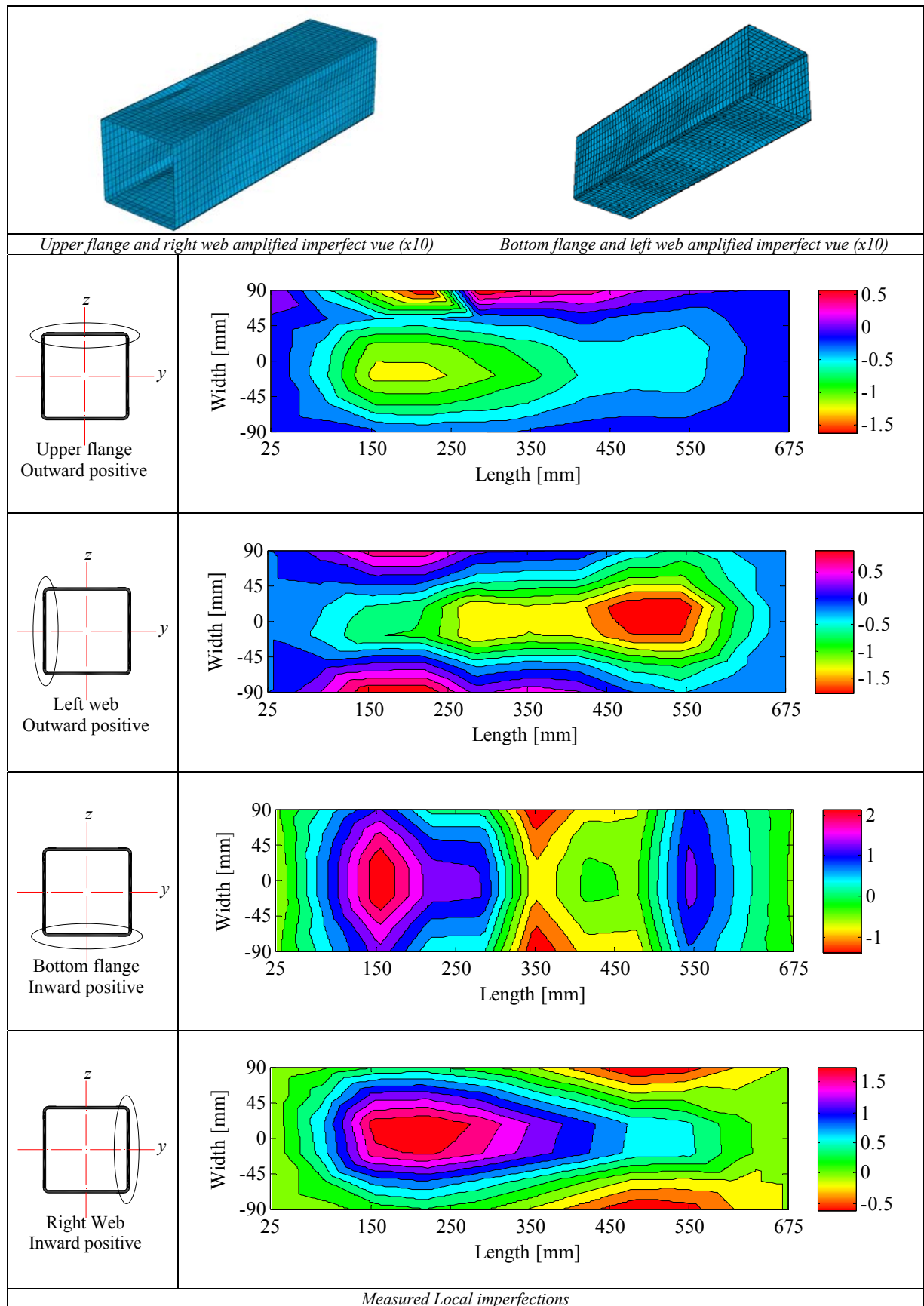
Cross-section resistance diagram

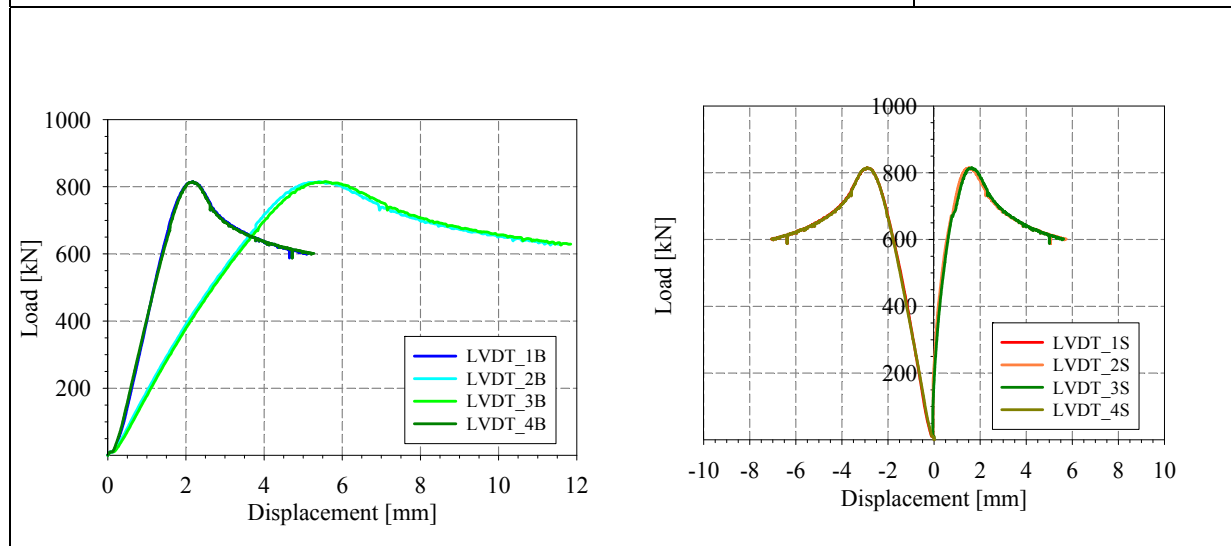
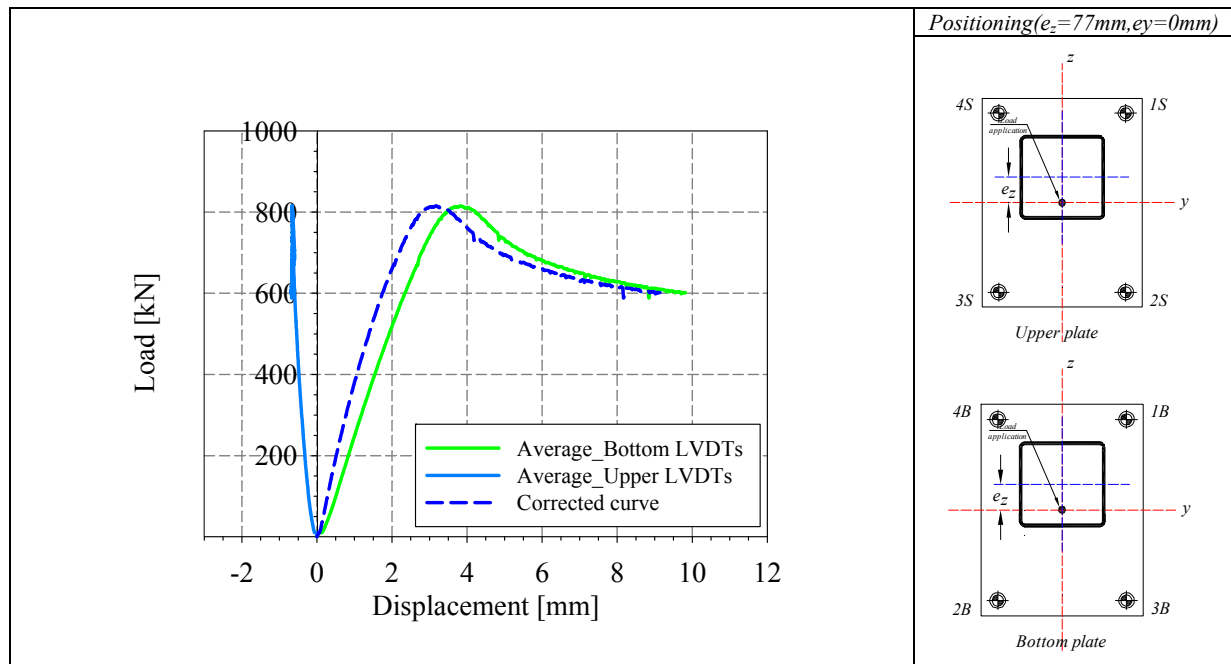
M_y - M_z bending moment interaction diagram



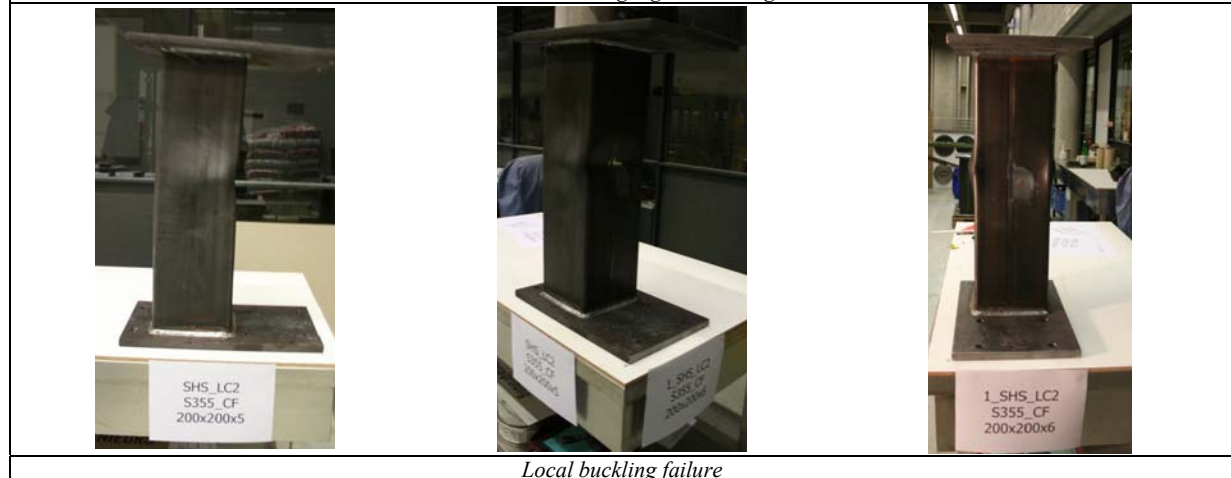
Numerical local buckling failure

<p>Specimen name</p> <p>RHS_S355_LC2 200x200x5 CF</p>	<p>Shape</p> 	<p>Details</p> <p>Shape: Square Hollow Section Nominal yield limit: 355 MPa Load case: N (50%) + My (50%) H=200mm B=200mm t=5mm Fabrication process: Cold formed</p>																		
<p>Average h= 200.44 mm</p> 	<p>Average b= 200.94 mm</p> 	<p>Average t= 4.92 mm</p> 																		
<p>Cross-sectional measured dimensions and tolerances</p>																				
		<table border="1"> <thead> <tr> <th></th> <th>Flat</th> <th>Corner</th> </tr> </thead> <tbody> <tr> <td>E [MPa]</td> <td>214848</td> <td>209500</td> </tr> <tr> <td>f_y [MPa]</td> <td>480.2</td> <td>-</td> </tr> <tr> <td>ϵ_y [%]</td> <td>0.22</td> <td>-</td> </tr> <tr> <td>f_u [MPa]</td> <td>585</td> <td>573.35</td> </tr> <tr> <td>ϵ_u [%]</td> <td>14.5</td> <td>1.2</td> </tr> </tbody> </table>		Flat	Corner	E [MPa]	214848	209500	f_y [MPa]	480.2	-	ϵ_y [%]	0.22	-	f_u [MPa]	585	573.35	ϵ_u [%]	14.5	1.2
	Flat	Corner																		
E [MPa]	214848	209500																		
f_y [MPa]	480.2	-																		
ϵ_y [%]	0.22	-																		
f_u [MPa]	585	573.35																		
ϵ_u [%]	14.5	1.2																		
<p>Tensile coupons location</p>	<p>Material stress-strain curves</p>	<p>Material average properties</p>																		
 <p style="text-align: center;">Measured residual stresses distributions</p>																				

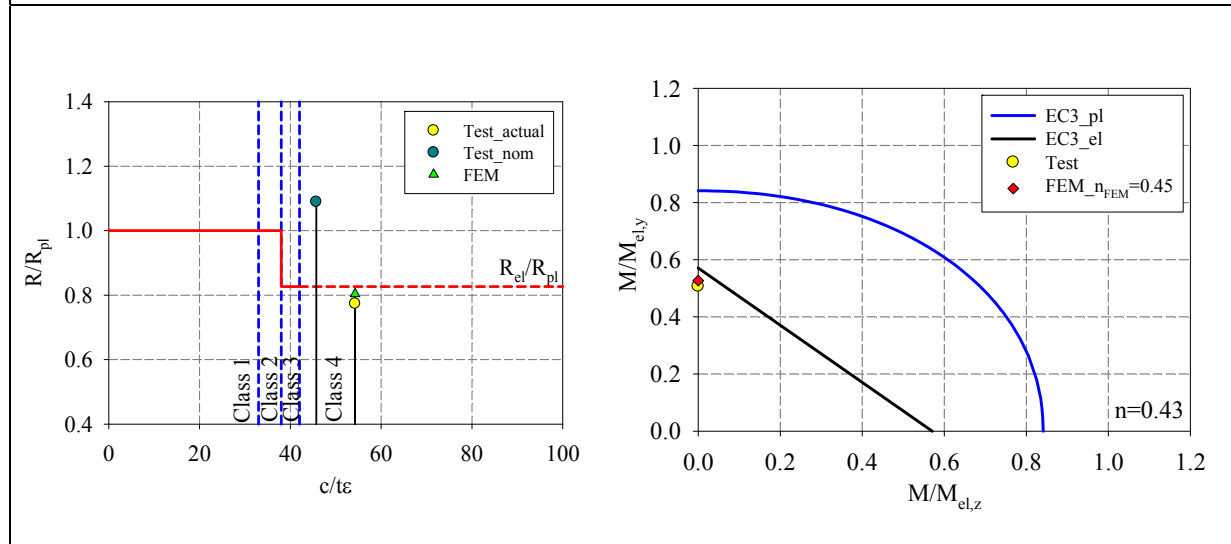
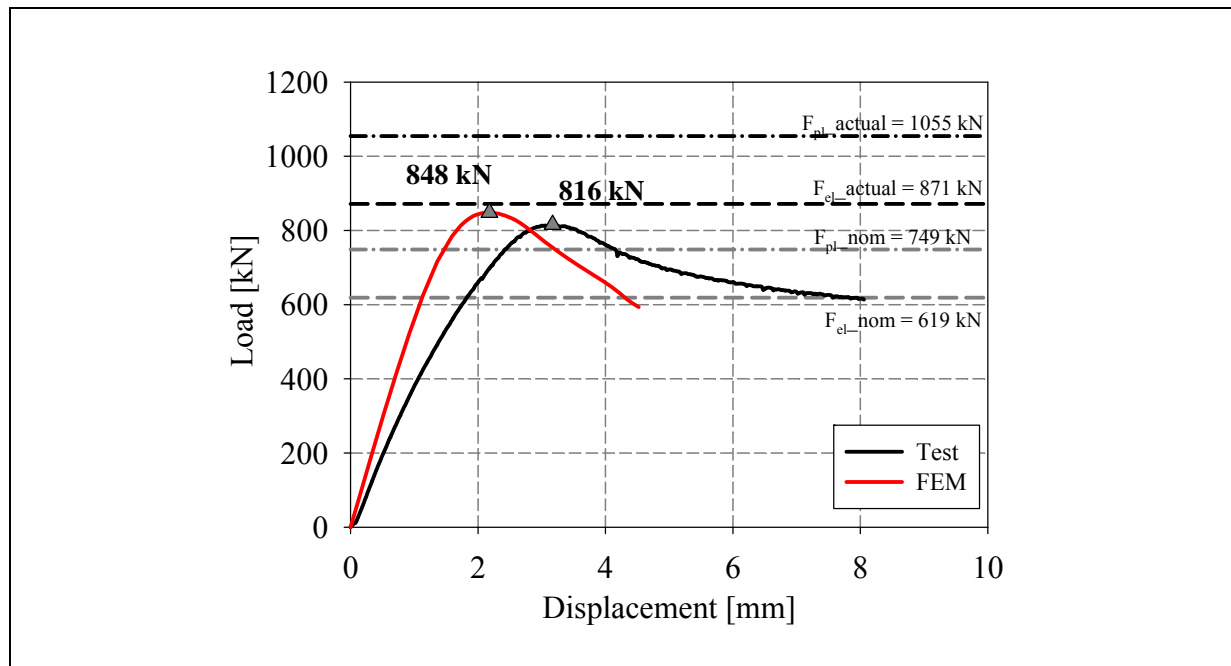




LVDT and strain gauges recordings

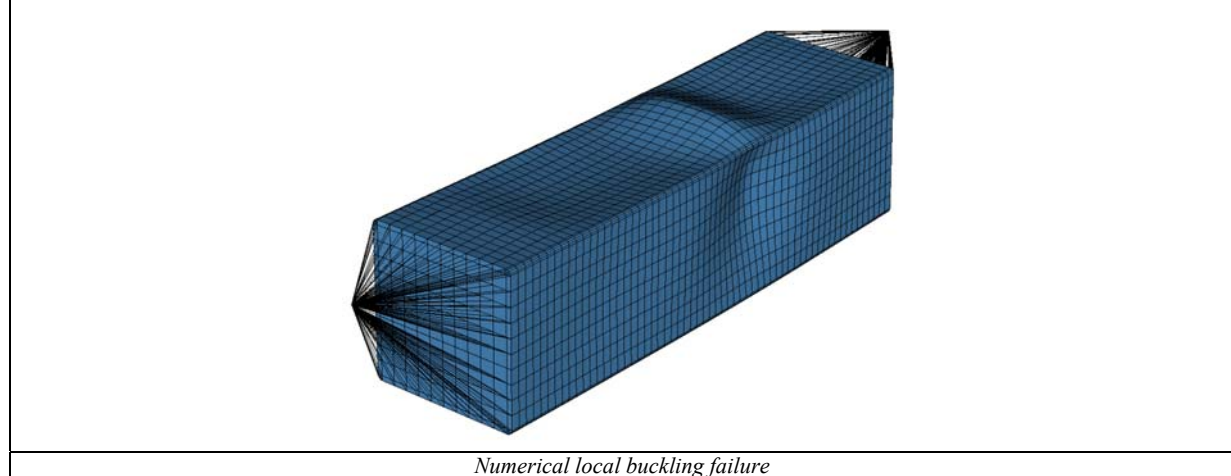


Local buckling failure

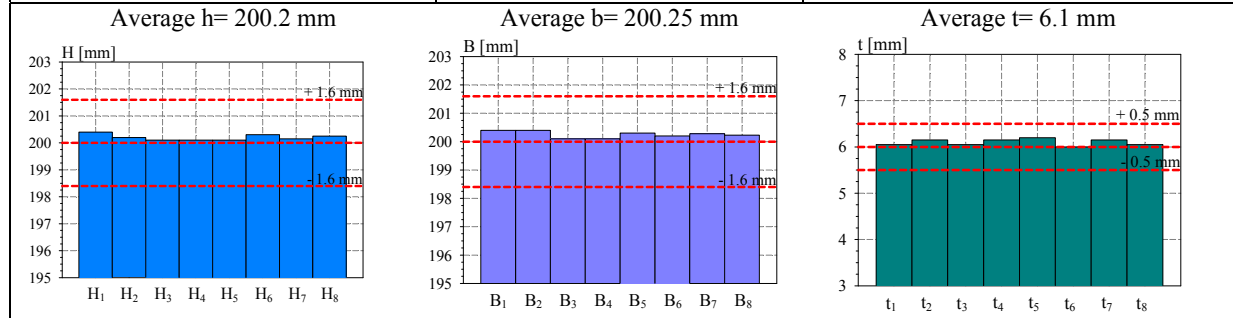


Cross-section resistance diagram

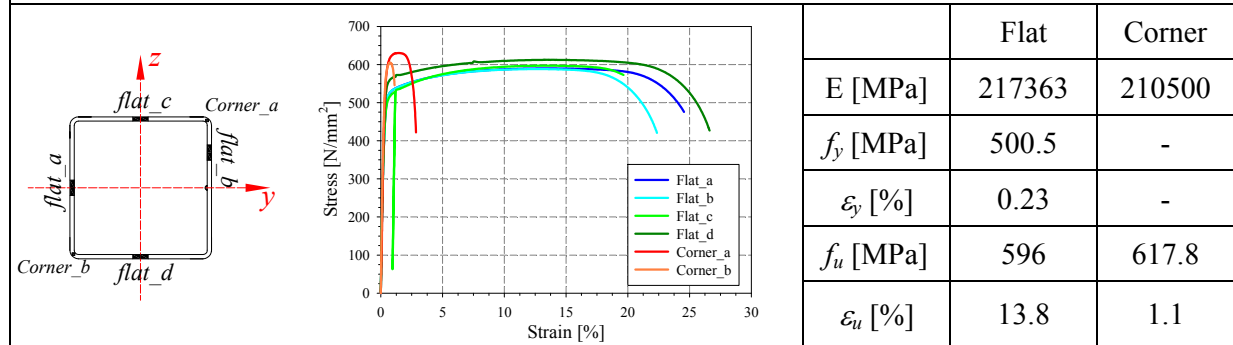
M_y - M_z bending moment interaction diagram



<p>Specimen name</p> <p>RHS_S355_LC2 200x200x6 CF</p>	<p>Shape</p>	<p>Details</p> <p>Shape: Square Hollow Section Nominal yield limit: 355 MPa Load case: N (50%) + M_y (50%) H=200mm B=200mm t=6mm Fabrication process: Cold formed</p>
---	--------------	---



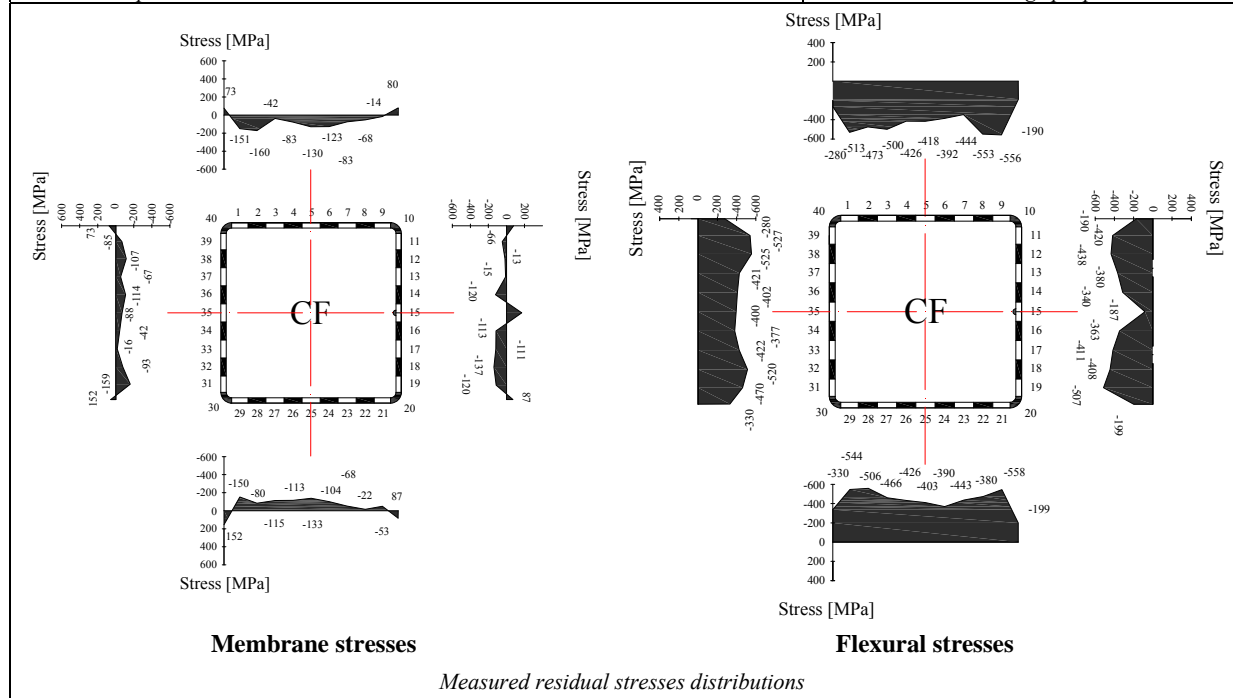
Cross-sectional measured dimensions and tolerances

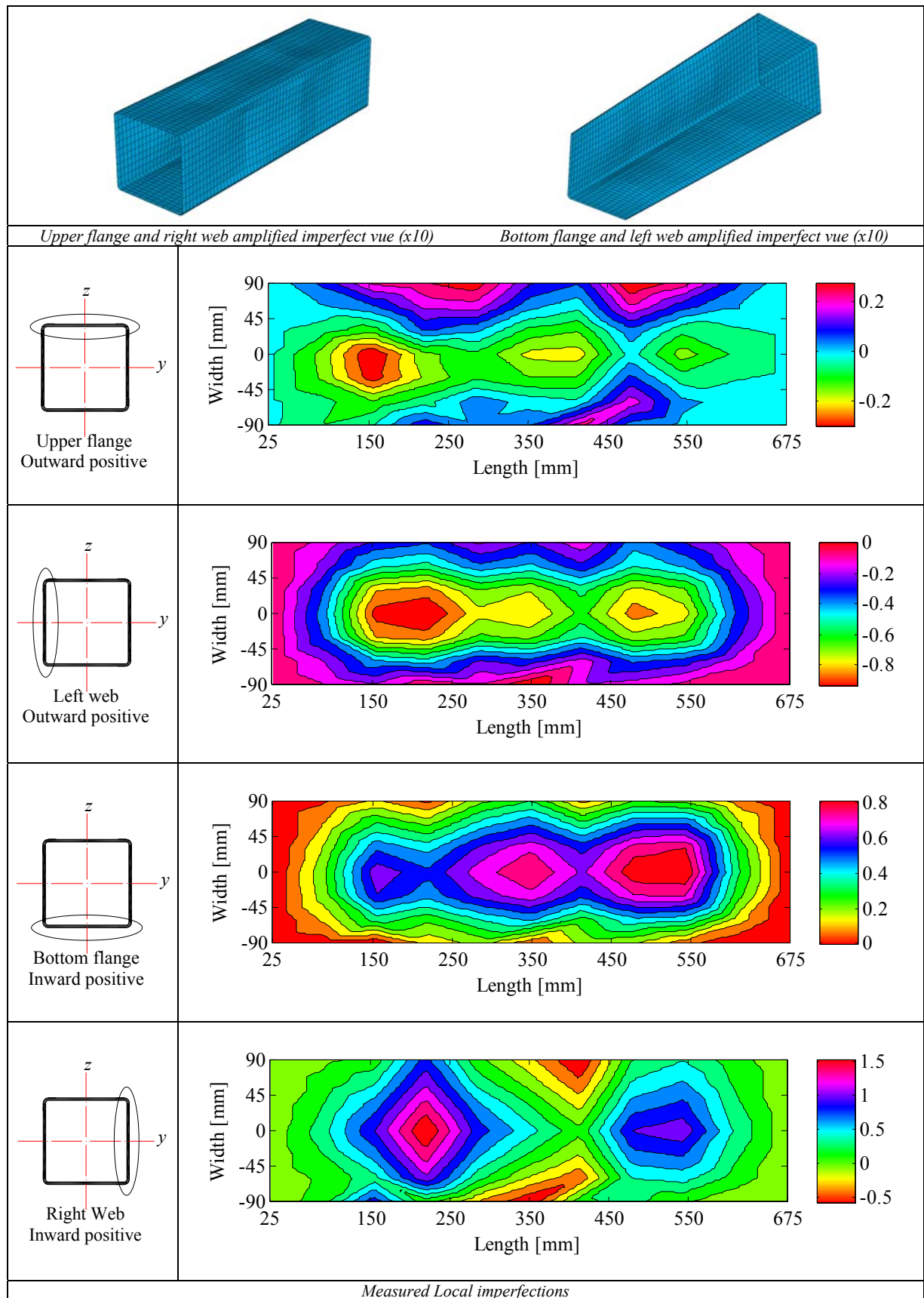


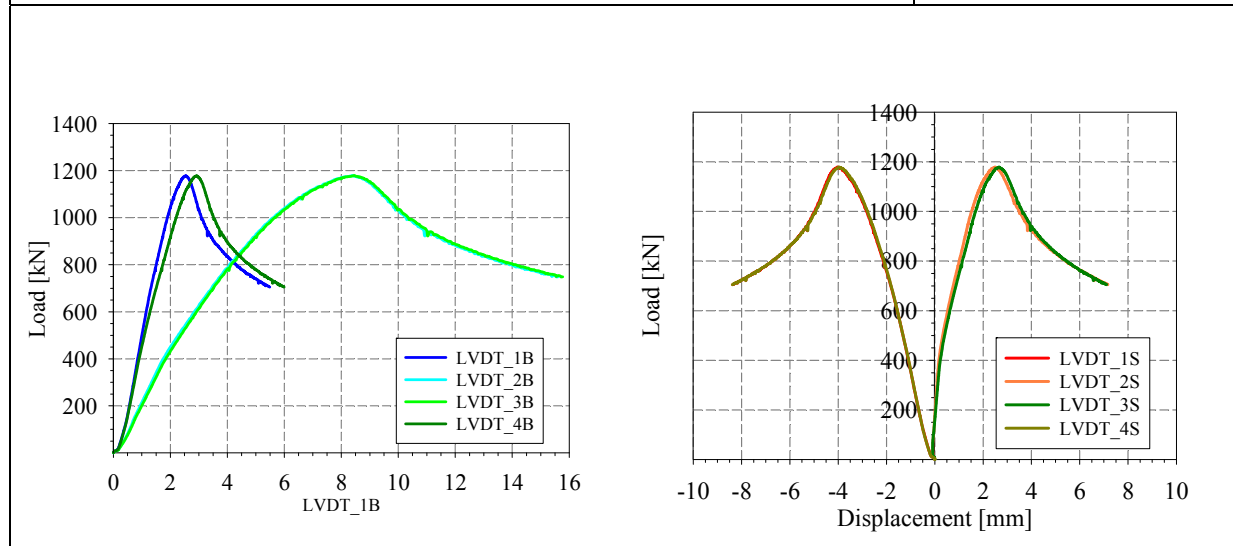
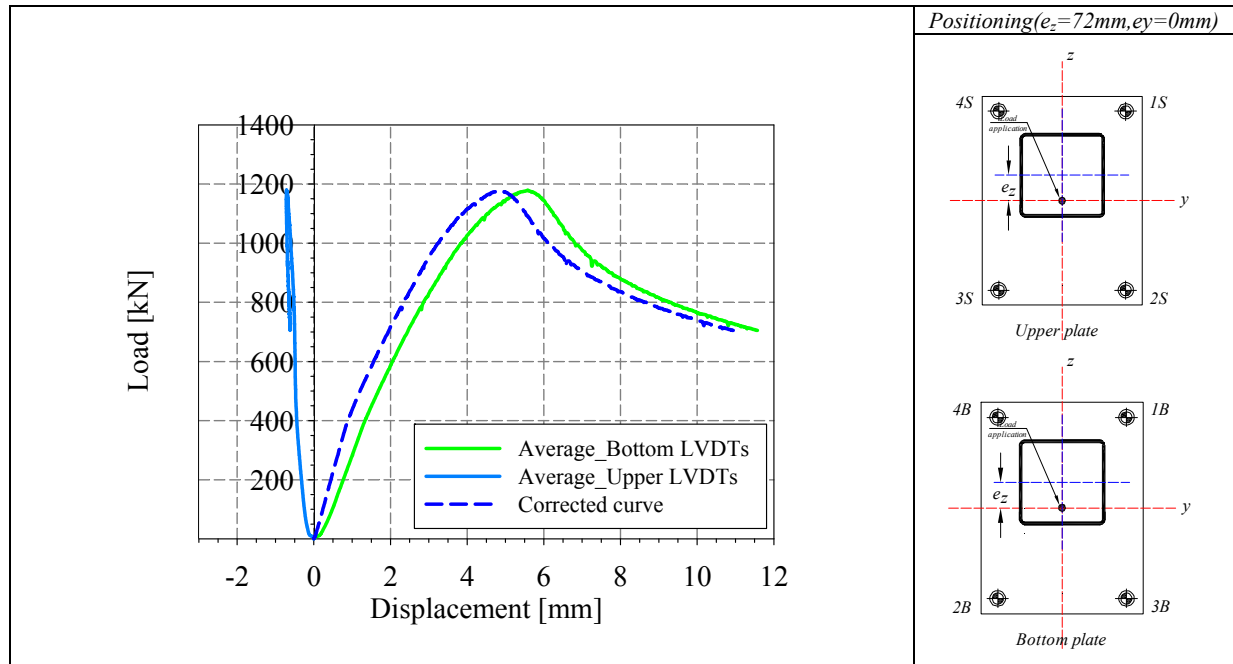
Tensile coupons location

Material stress-strain curves

Material average properties



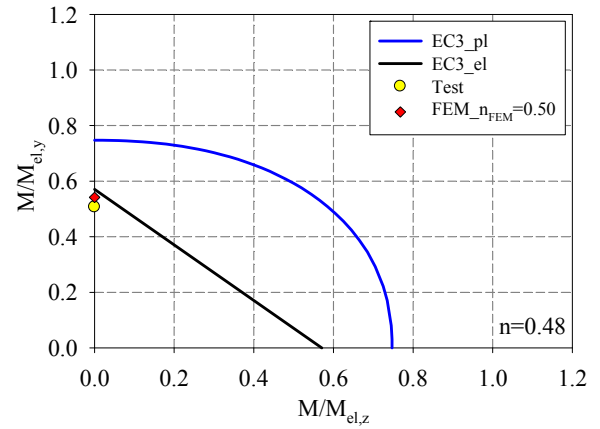
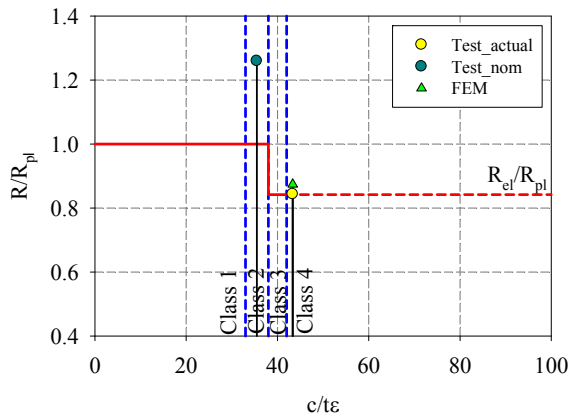
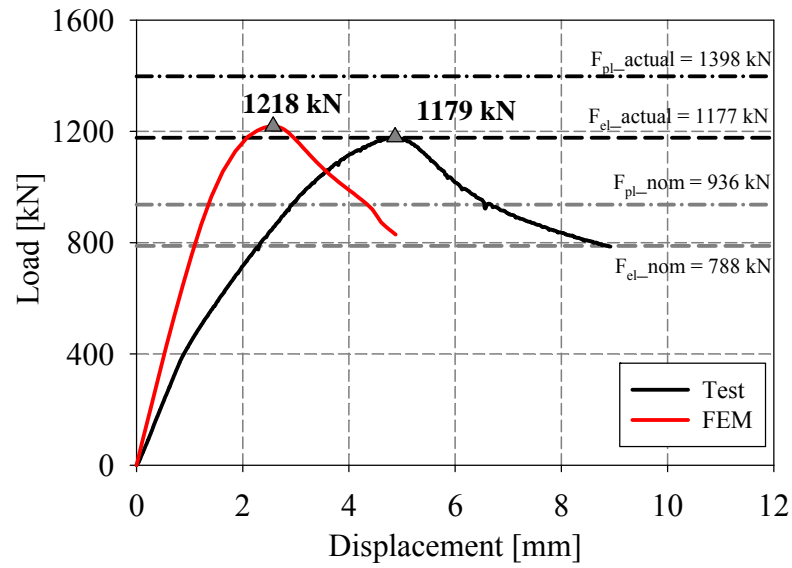




LVDT and strain gauges recordings

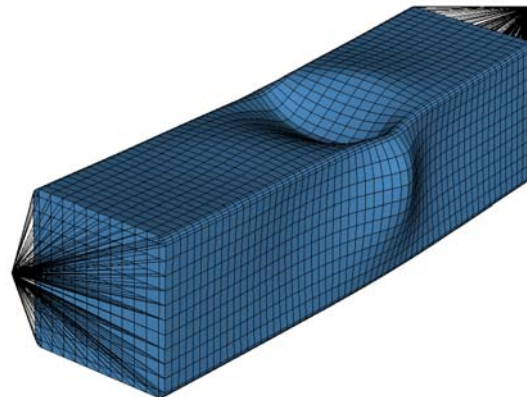


Local buckling failure

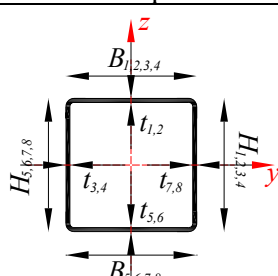


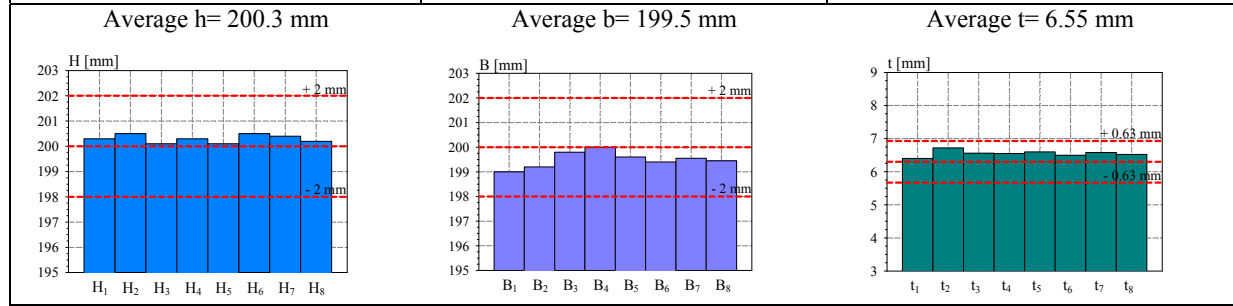
Cross-section resistance diagram

My-Mz bending moment interaction diagram

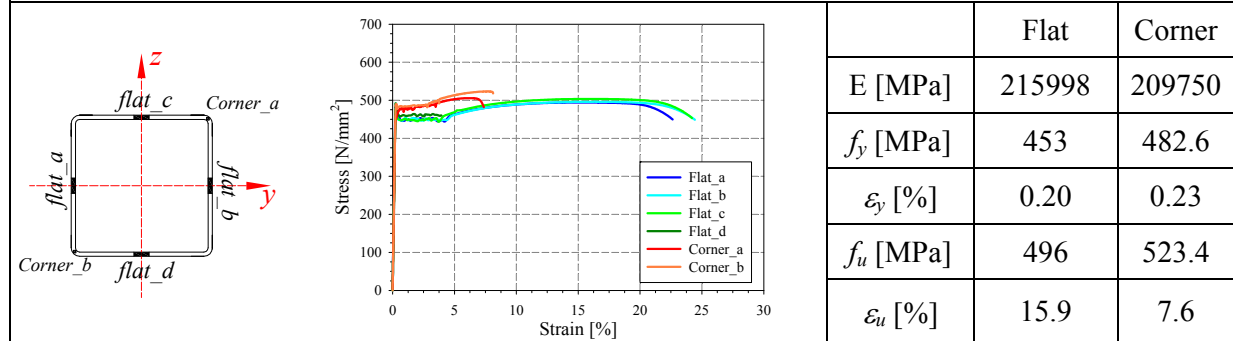


Numerical local buckling failure

<p>Specimen name</p> <p>RHS_S355_LC2 200x200x6.3 HF</p>	<p>Shape</p> 	<p>Details</p> <p>Shape: Square Hollow Section Nominal yield limit: 355 MPa Load case: N (50%) + M_y (50%) H=200mm B=200mm t=6mm Fabrication process: Hot formed</p>
---	--	---



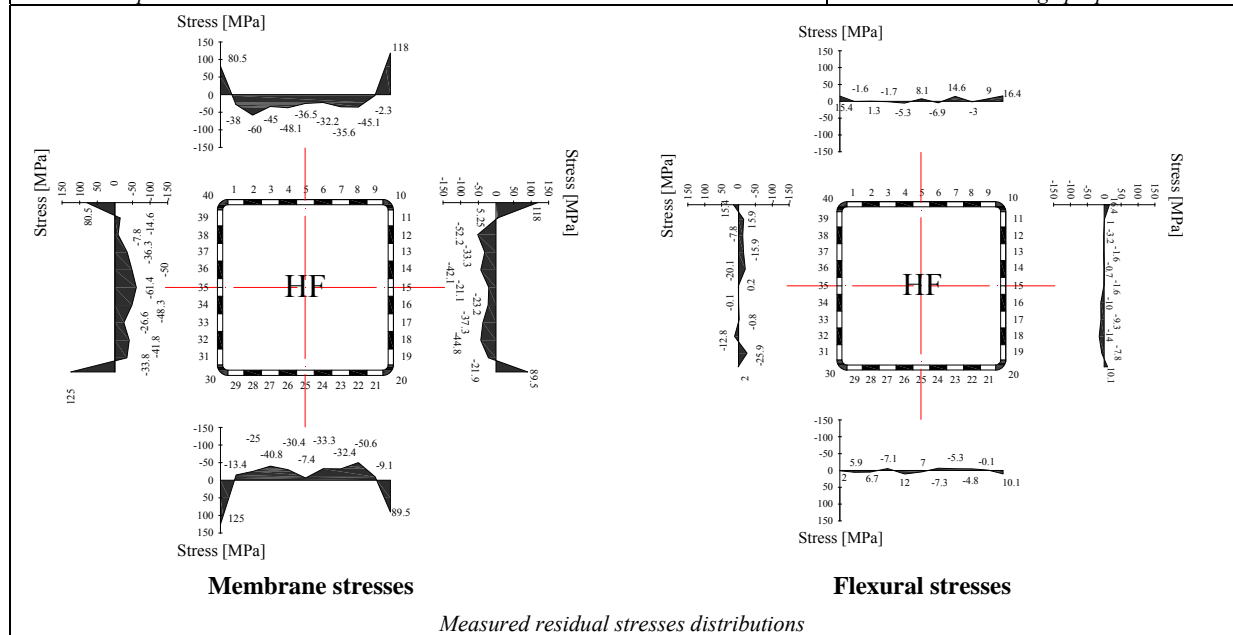
Cross-sectional measured dimensions and tolerances

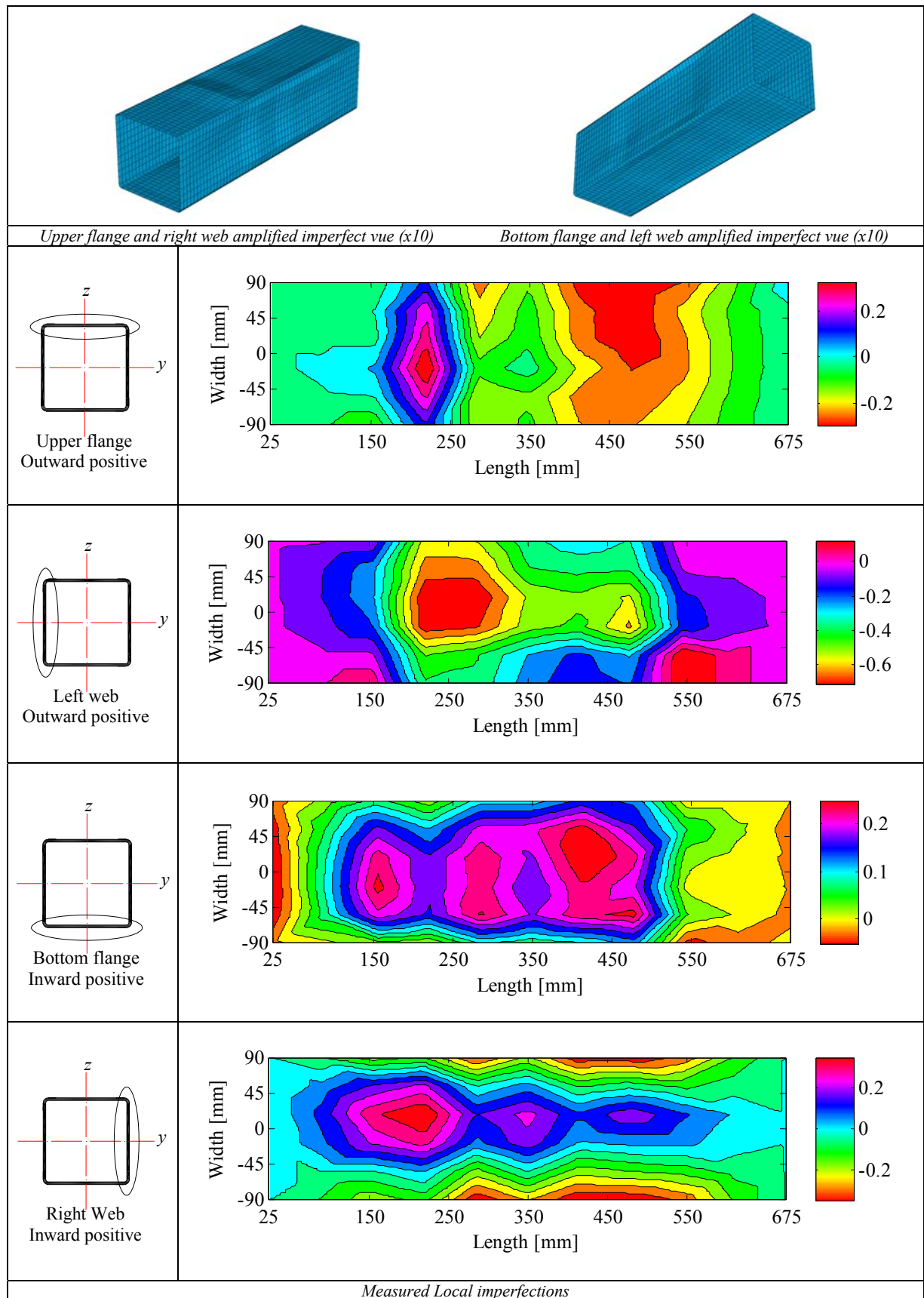


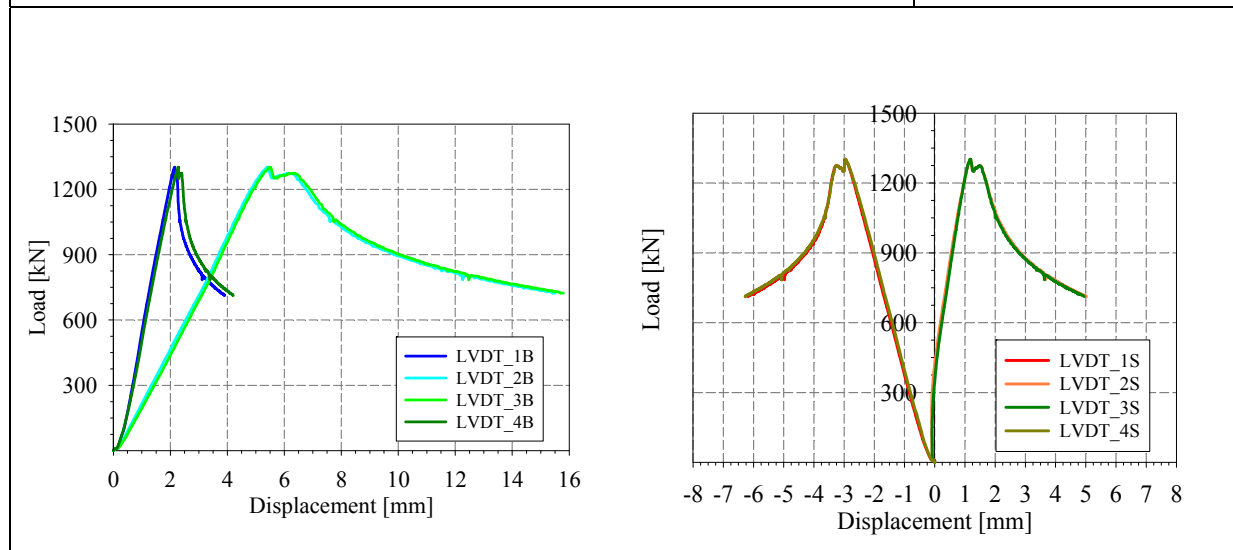
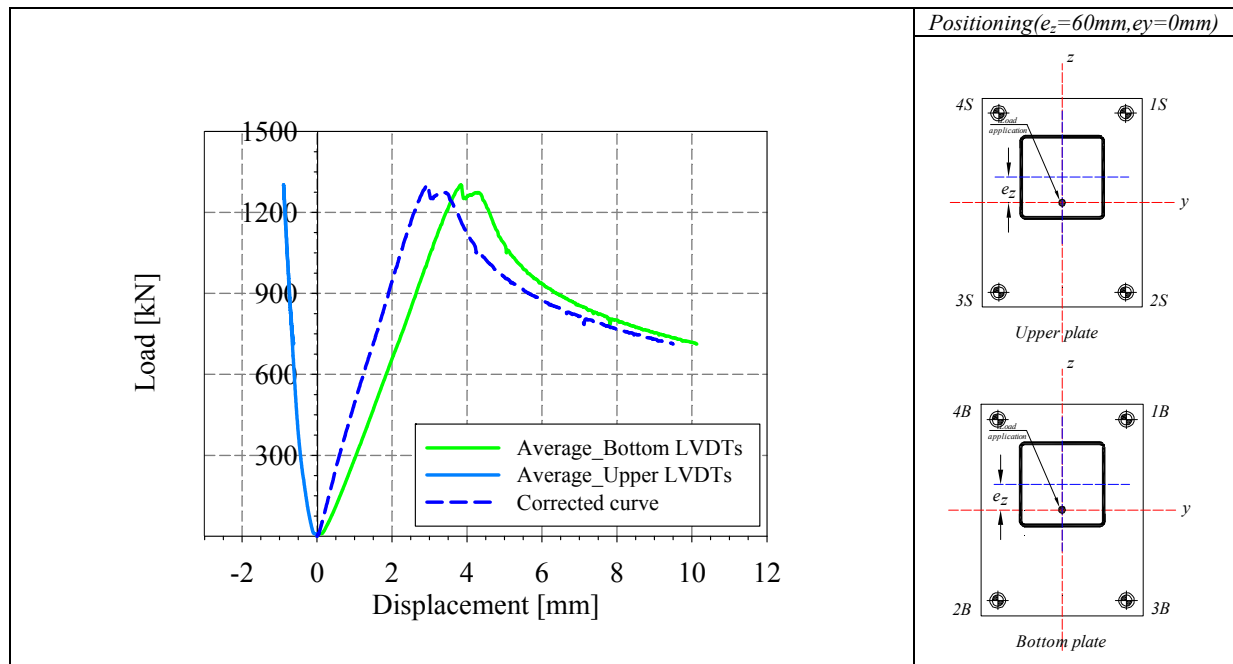
Tensile coupons location

Material stress-strain curves

Material average properties



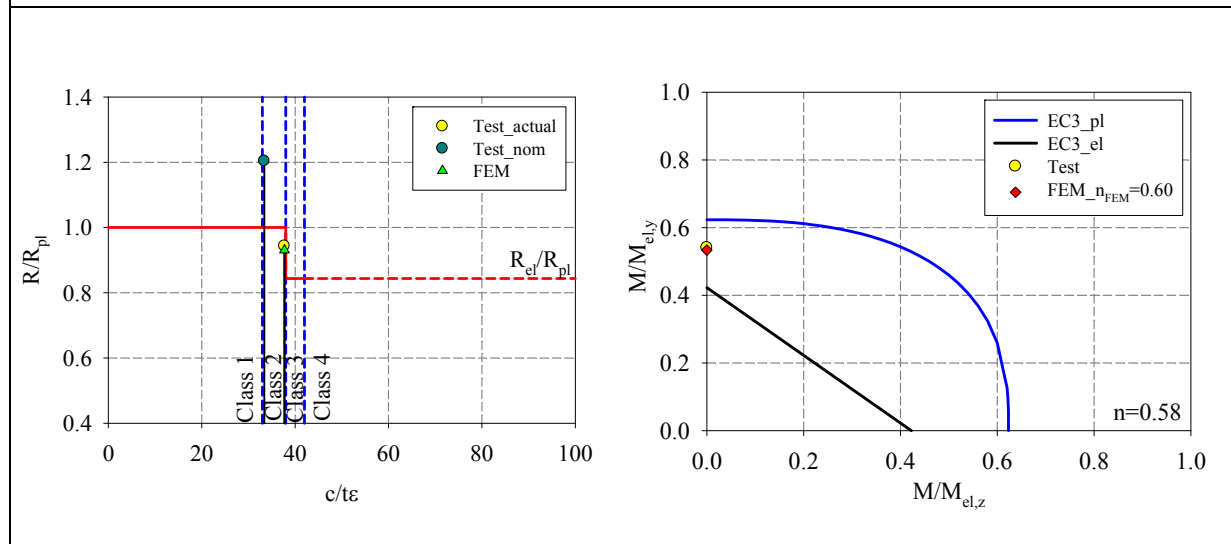
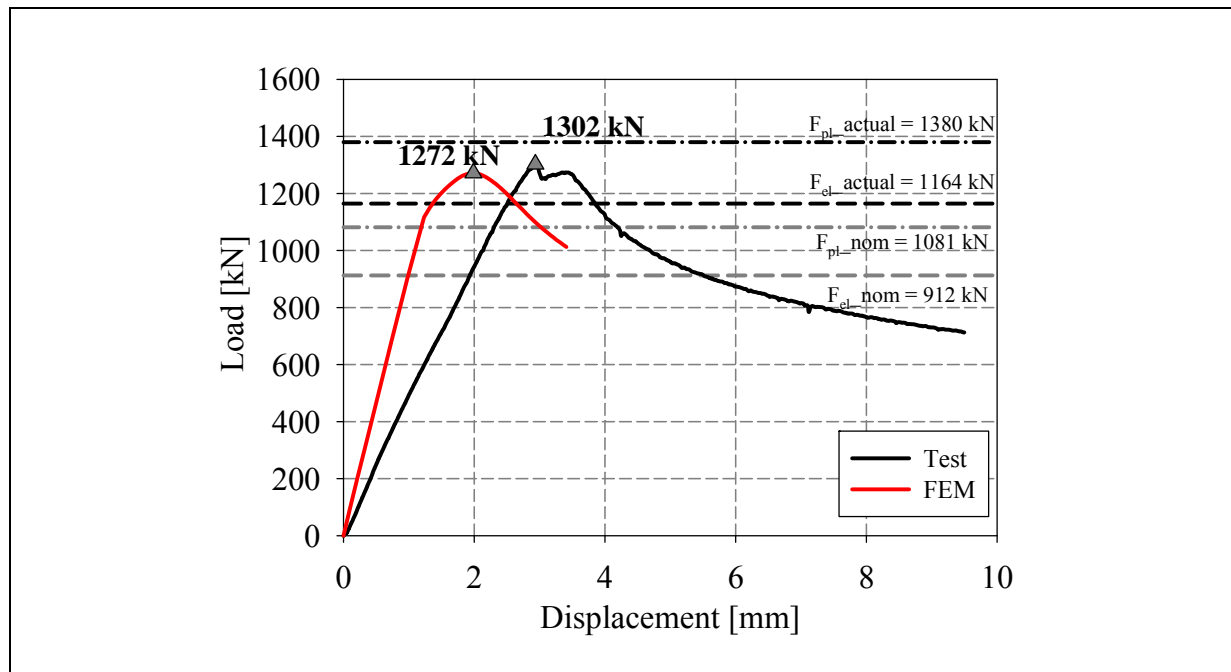




LVDT and strain gauges recordings

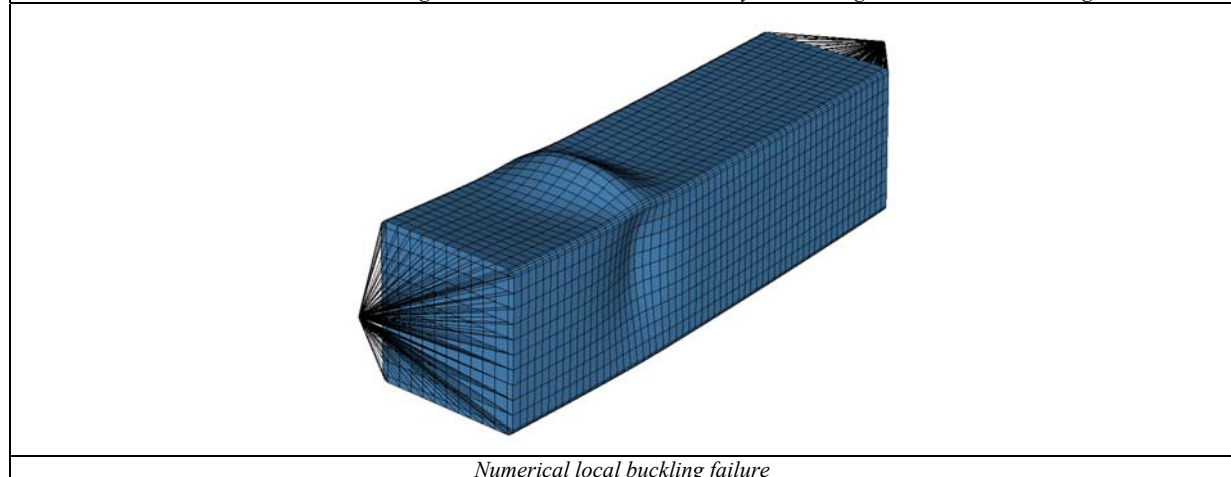


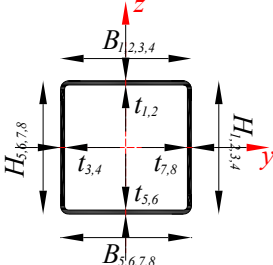
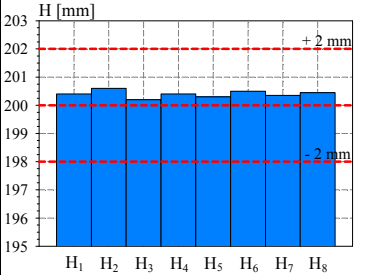
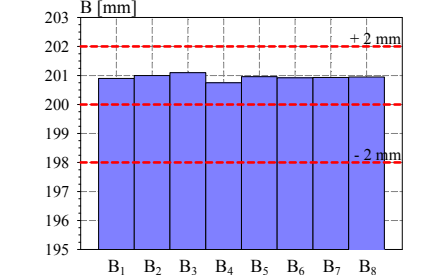
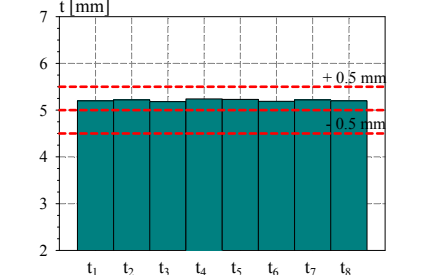
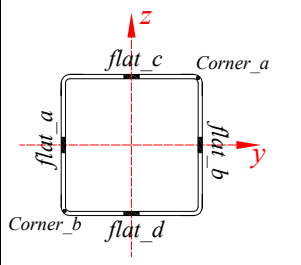
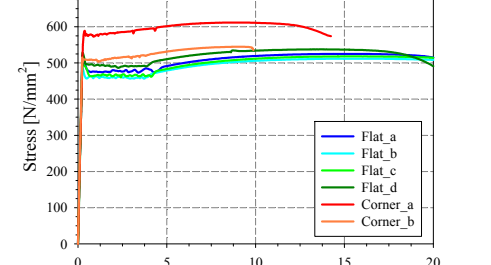
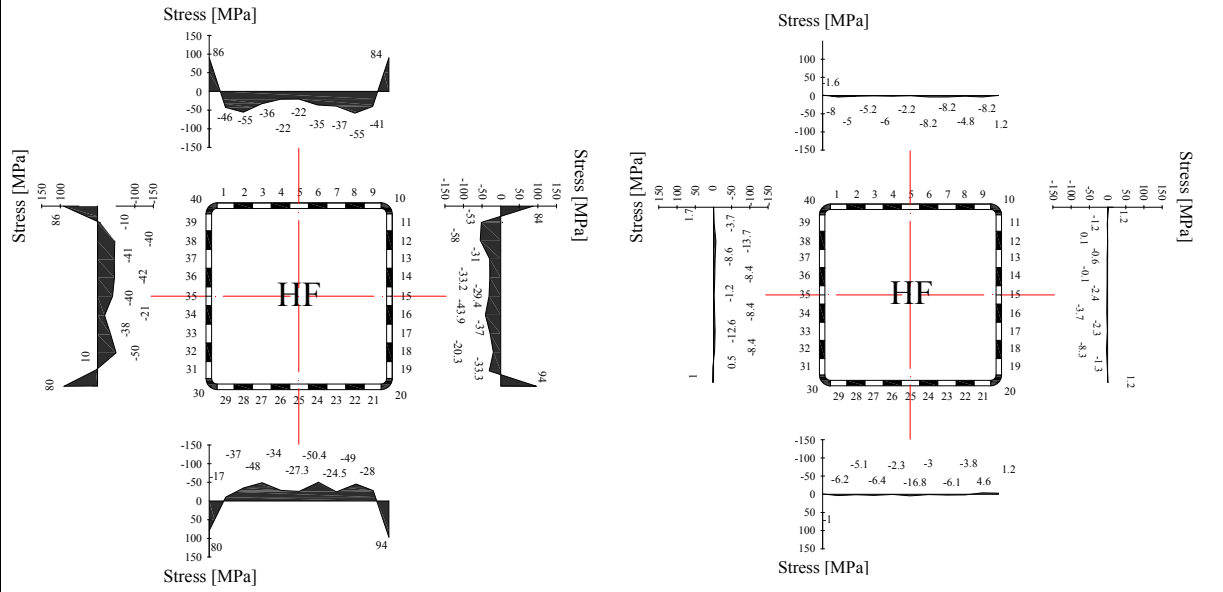
Local buckling failure

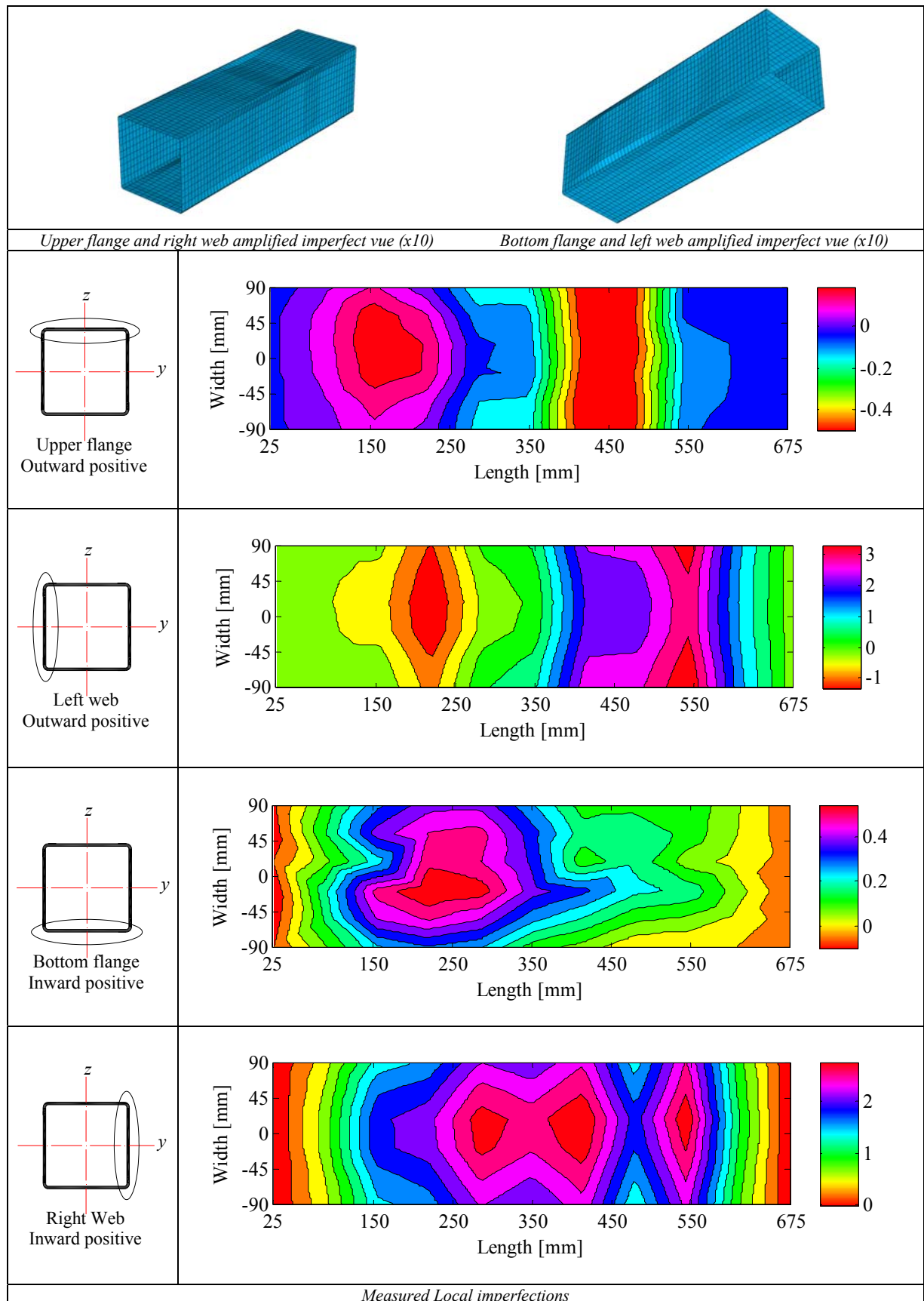


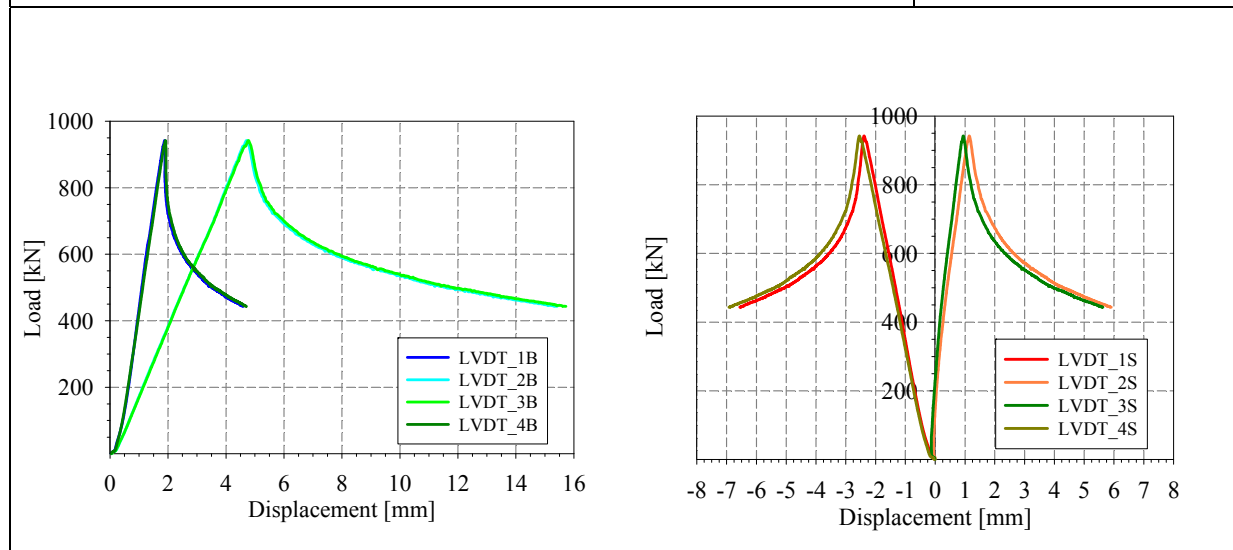
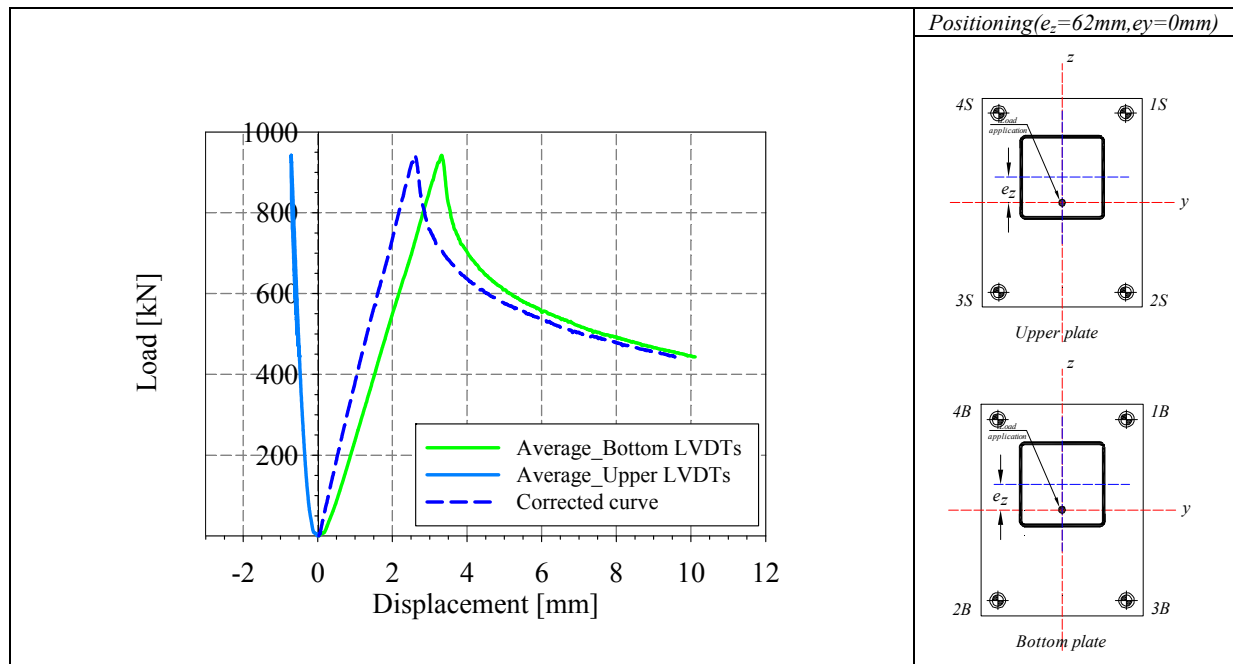
Cross-section resistance diagram

M_y - M_z bending moment interaction diagram



<p>Specimen name</p> <p>RHS_S355_LC2 200x200x5 HF</p>	<p>Shape</p> 	<p>Details</p> <p>Shape: Square Hollow Section Nominal yield limit: 355 MPa Load case: N (50%) + M_y (50%) H=200mm B=200mm t=5mm Fabrication process: Hot formed</p>																		
<p>Average h= 200.4 mm</p> 	<p>Average b= 200.94 mm</p> 	<p>Average t= 5.21 mm</p> 																		
<p><i>Cross-sectional measured dimensions and tolerances</i></p>																				
		<table border="1"> <thead> <tr> <th></th> <th>Flat</th> <th>Corner</th> </tr> </thead> <tbody> <tr> <td>E [MPa]</td> <td>211489</td> <td>211023</td> </tr> <tr> <td>f_y [MPa]</td> <td>475</td> <td>544</td> </tr> <tr> <td>ϵ_y [%]</td> <td>0.22</td> <td>0.25</td> </tr> <tr> <td>f_u [MPa]</td> <td>523</td> <td>578.2</td> </tr> <tr> <td>ϵ_u [%]</td> <td>14.6</td> <td>8.93</td> </tr> </tbody> </table>		Flat	Corner	E [MPa]	211489	211023	f_y [MPa]	475	544	ϵ_y [%]	0.22	0.25	f_u [MPa]	523	578.2	ϵ_u [%]	14.6	8.93
	Flat	Corner																		
E [MPa]	211489	211023																		
f_y [MPa]	475	544																		
ϵ_y [%]	0.22	0.25																		
f_u [MPa]	523	578.2																		
ϵ_u [%]	14.6	8.93																		
<p><i>Tensile coupons location</i></p>	<p><i>Material stress-strain curves</i></p>	<p><i>Material average properties</i></p>																		
 <p style="text-align: center;">Membrane stresses Flexural stresses</p> <p style="text-align: center;"><i>Measured residual stresses distributions</i></p>																				

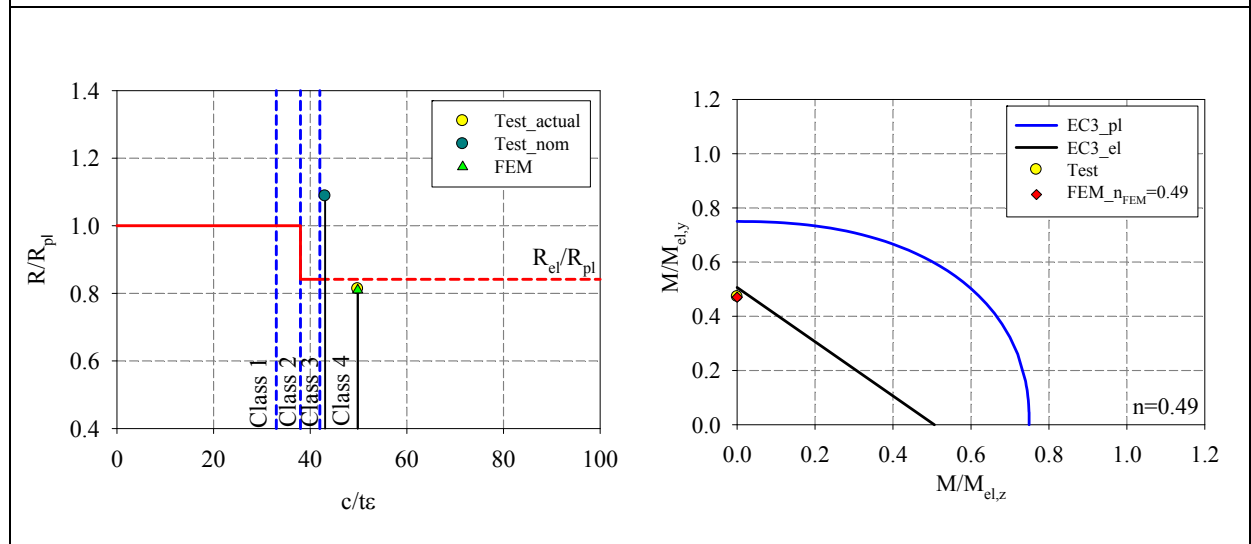
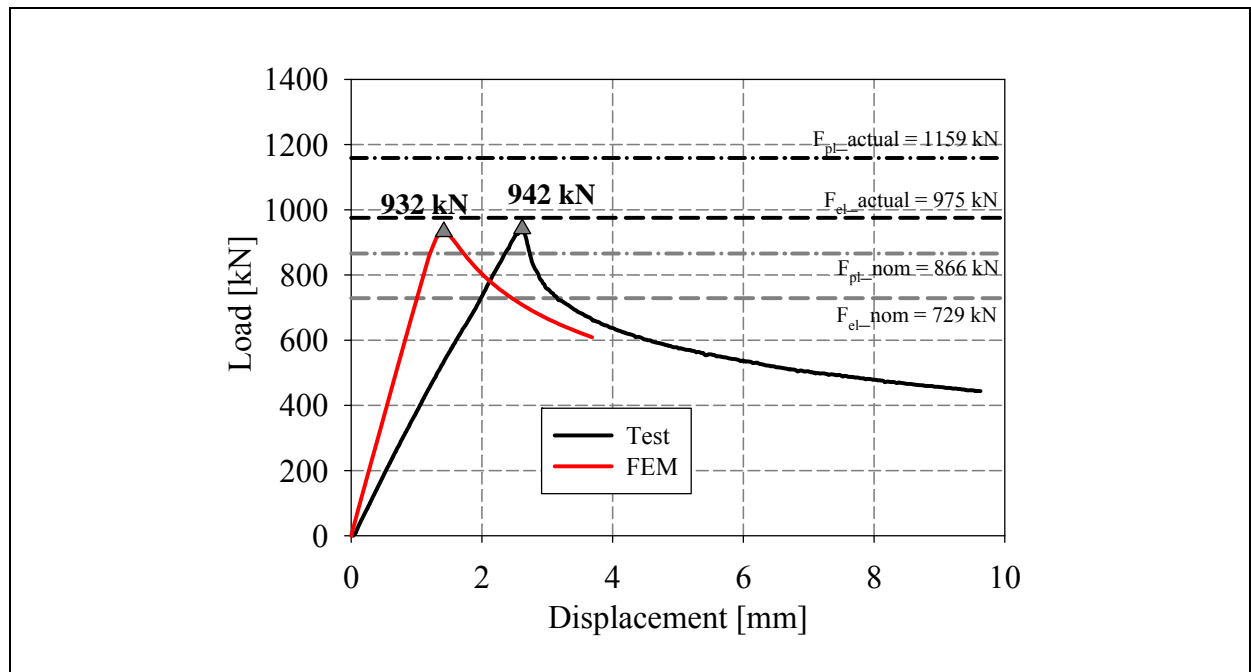




LVDT and strain gauges recordings

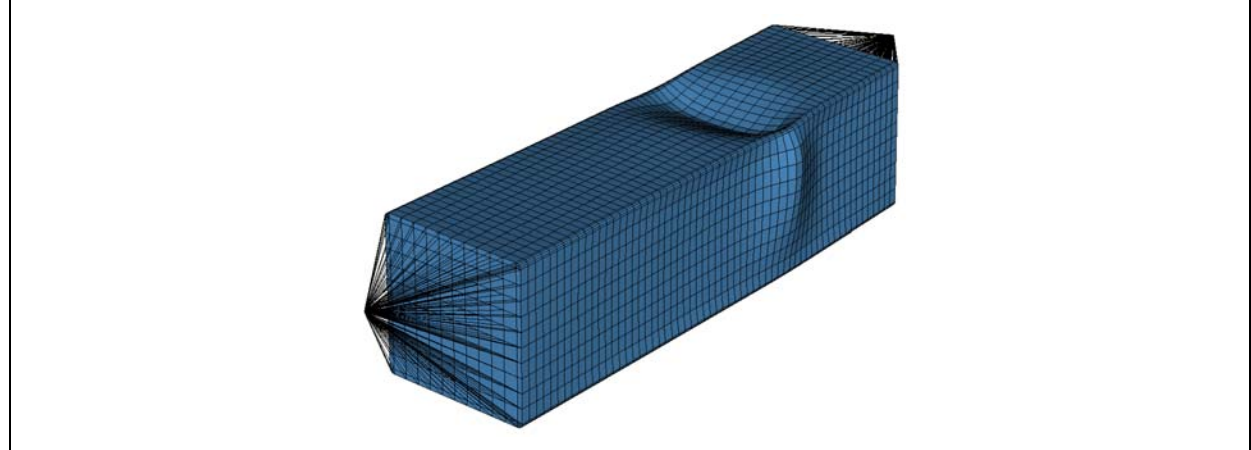


Local buckling failure

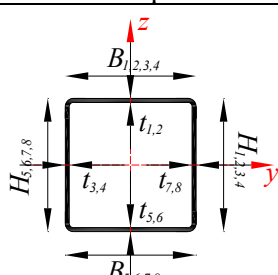


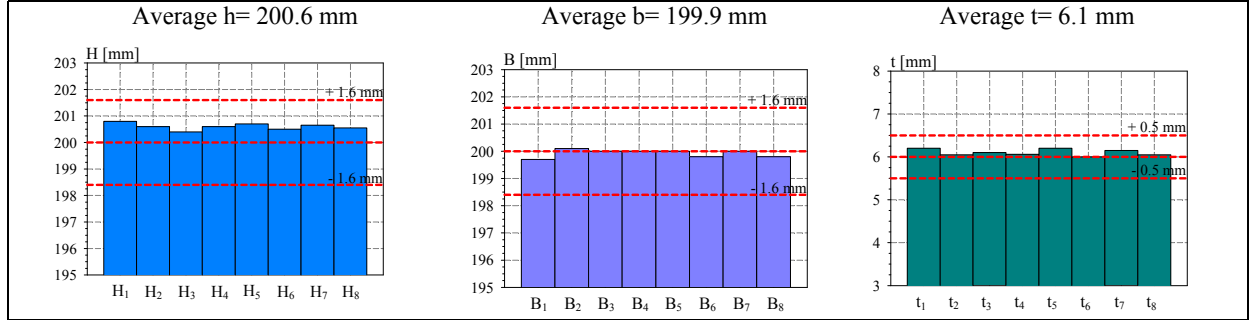
Cross-section resistance diagram

My-Mz bending moment interaction diagram

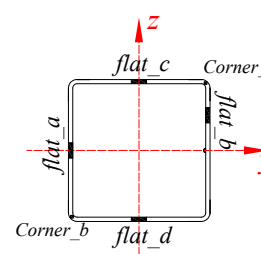
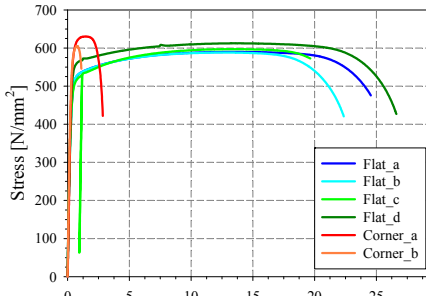


Numerical local buckling failure

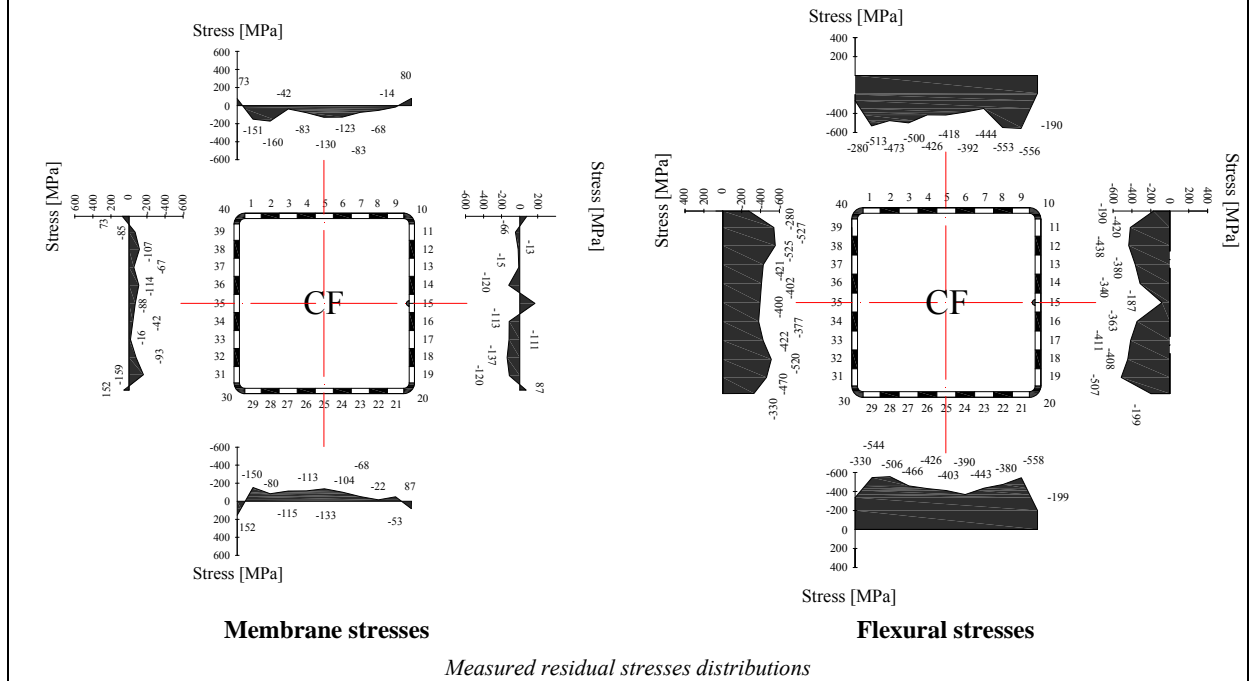
<p>Specimen name</p> <p>RHS_S355_LC2 200x200x6 CF_2</p>	<p>Shape</p> 	<p>Details</p> <p>Shape: Square Hollow Section Nominal yield limit: 355 MPa Load case: N (50%) + M_y (50%) H=200mm B=200mm t=6mm Fabrication process: Cold formed</p>
---	---	--

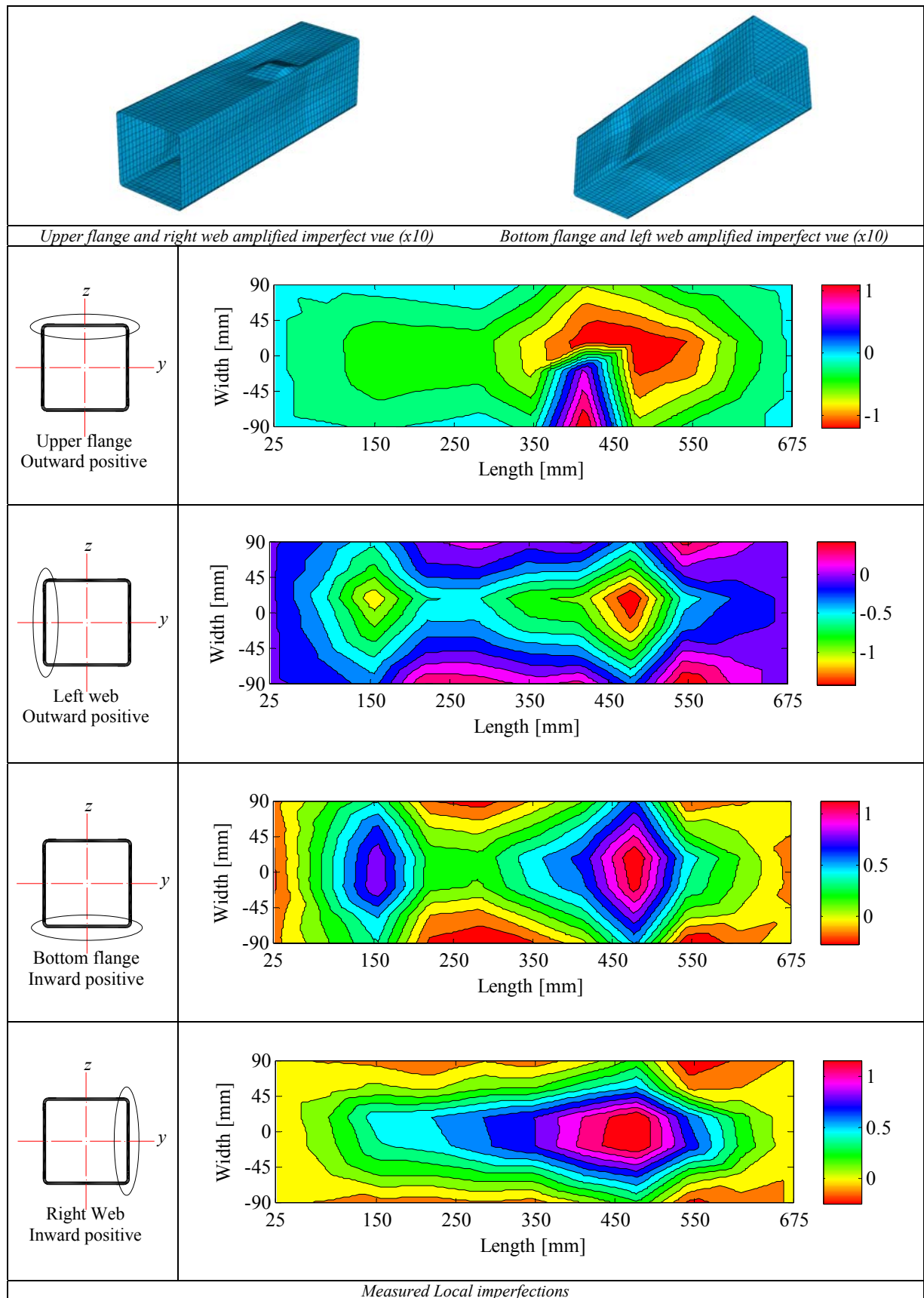


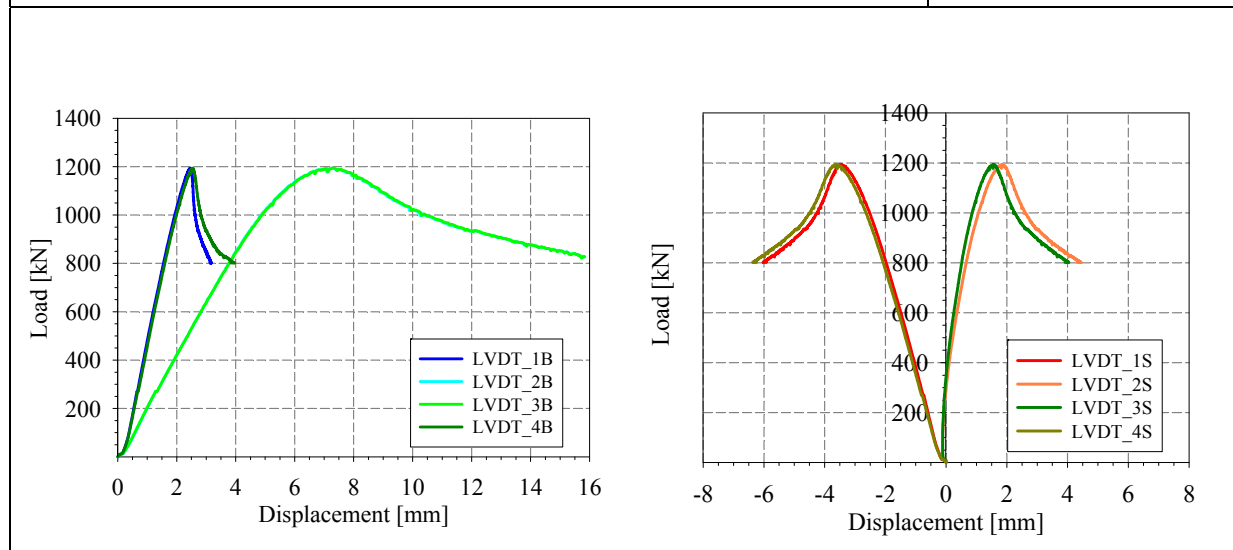
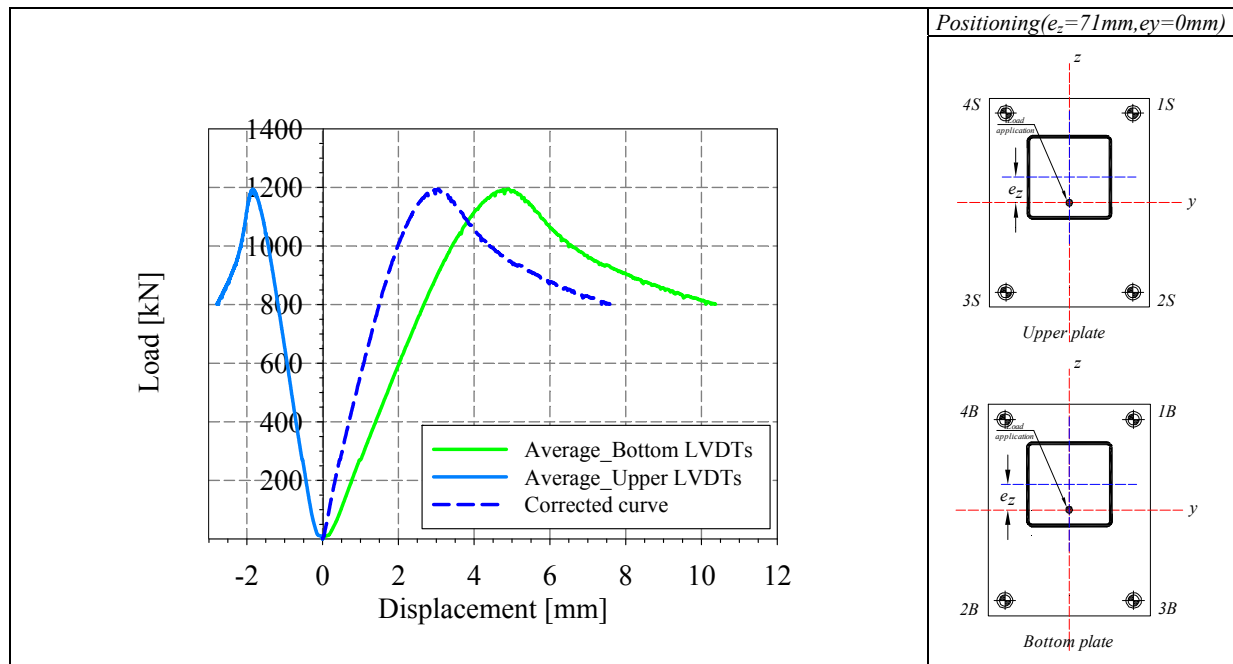
Cross-sectional measured dimensions and tolerances

		<table border="1"> <thead> <tr> <th></th> <th>Flat</th> <th>Corner</th> </tr> </thead> <tbody> <tr> <td>E [MPa]</td> <td>217363</td> <td>210500</td> </tr> <tr> <td>f_y [MPa]</td> <td>500.5</td> <td>-</td> </tr> <tr> <td>ϵ_y [%]</td> <td>0.23</td> <td>-</td> </tr> <tr> <td>f_u [MPa]</td> <td>596</td> <td>617.8</td> </tr> <tr> <td>ϵ_u [%]</td> <td>13.8</td> <td>1.1</td> </tr> </tbody> </table>		Flat	Corner	E [MPa]	217363	210500	f_y [MPa]	500.5	-	ϵ_y [%]	0.23	-	f_u [MPa]	596	617.8	ϵ_u [%]	13.8	1.1
	Flat	Corner																		
E [MPa]	217363	210500																		
f_y [MPa]	500.5	-																		
ϵ_y [%]	0.23	-																		
f_u [MPa]	596	617.8																		
ϵ_u [%]	13.8	1.1																		

Tensile coupons location Material stress-strain curves Material average properties



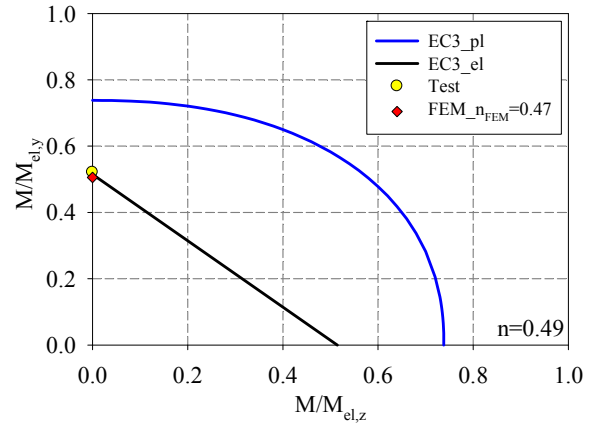
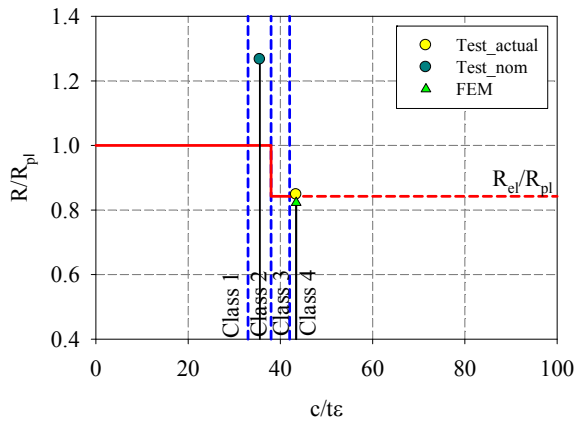
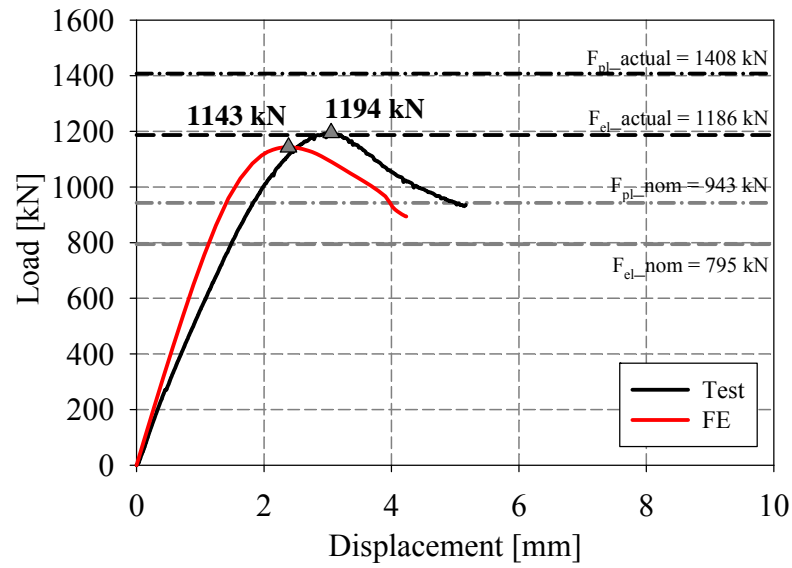




LVDT and strain gauges recordings

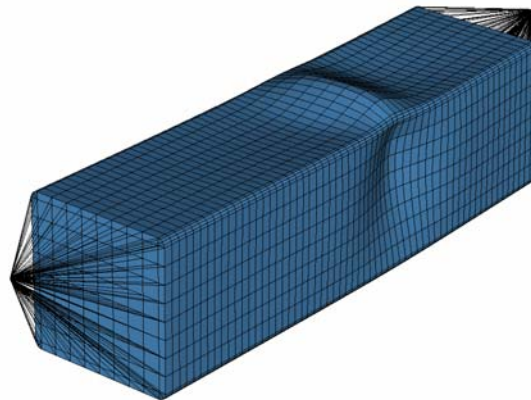


Local buckling failure

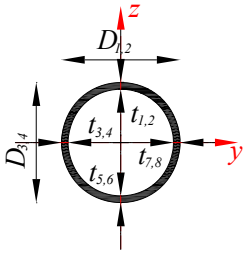
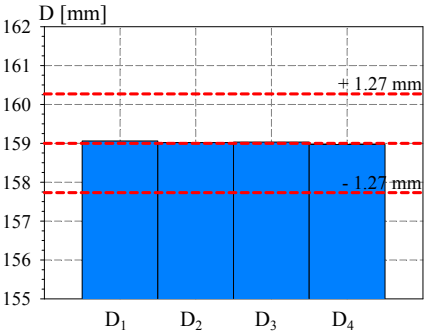
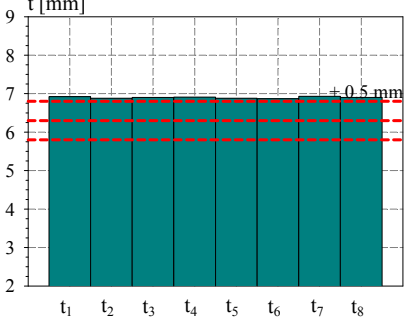
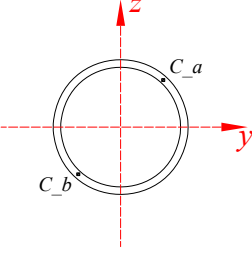
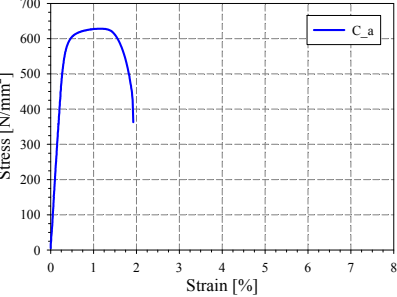
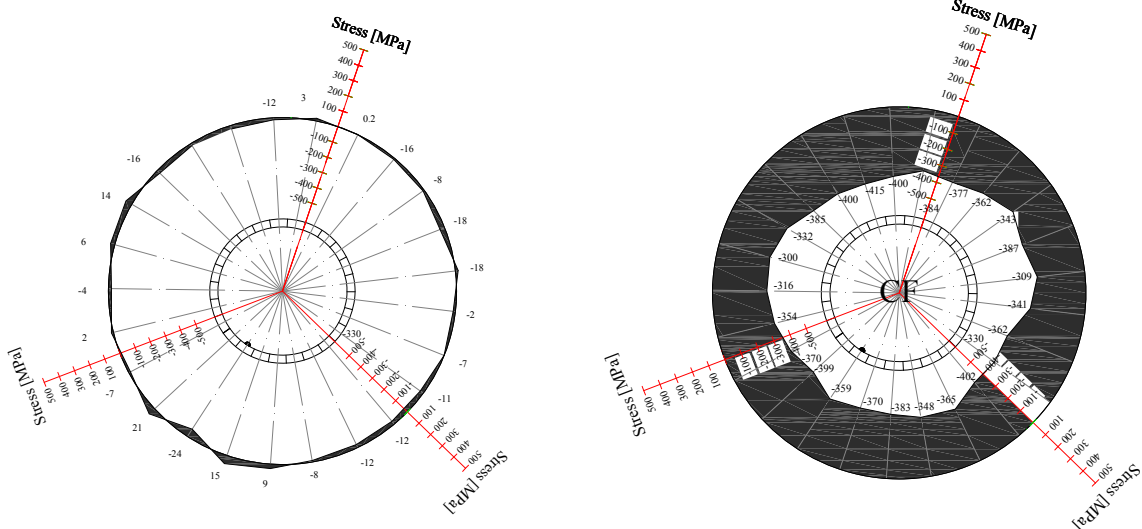


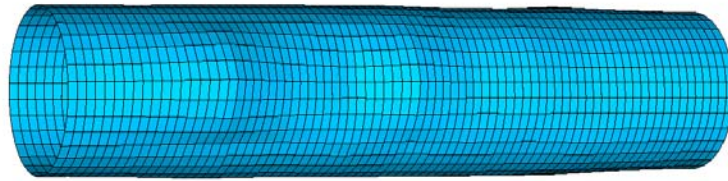
Cross-section resistance diagram

My-Mz bending moment interaction diagram

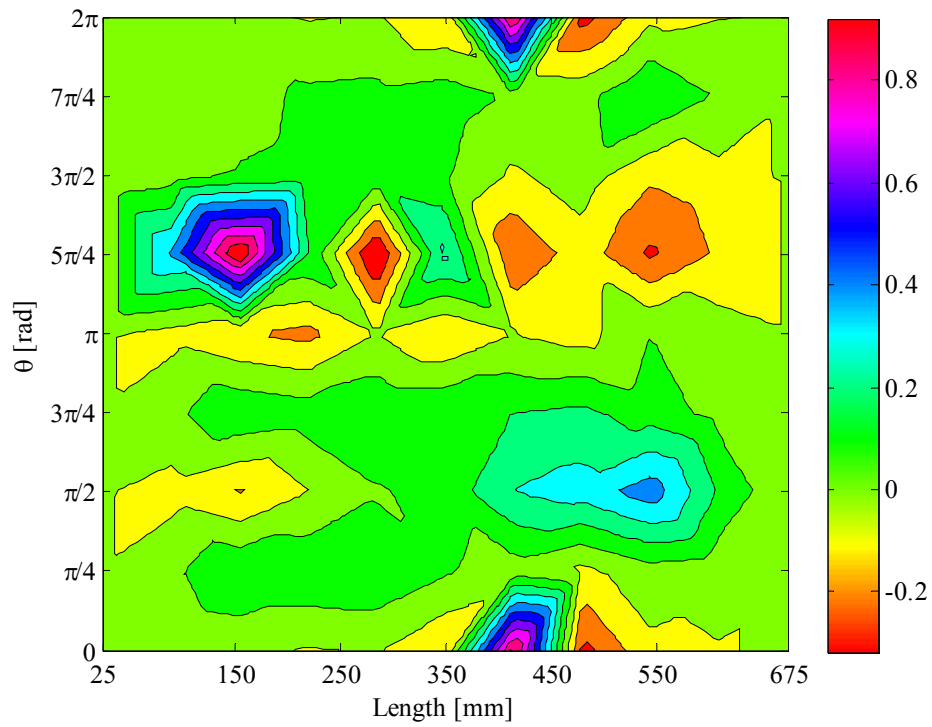
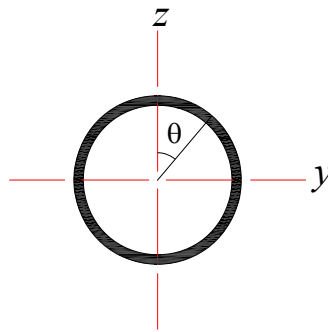


Numerical local buckling failure

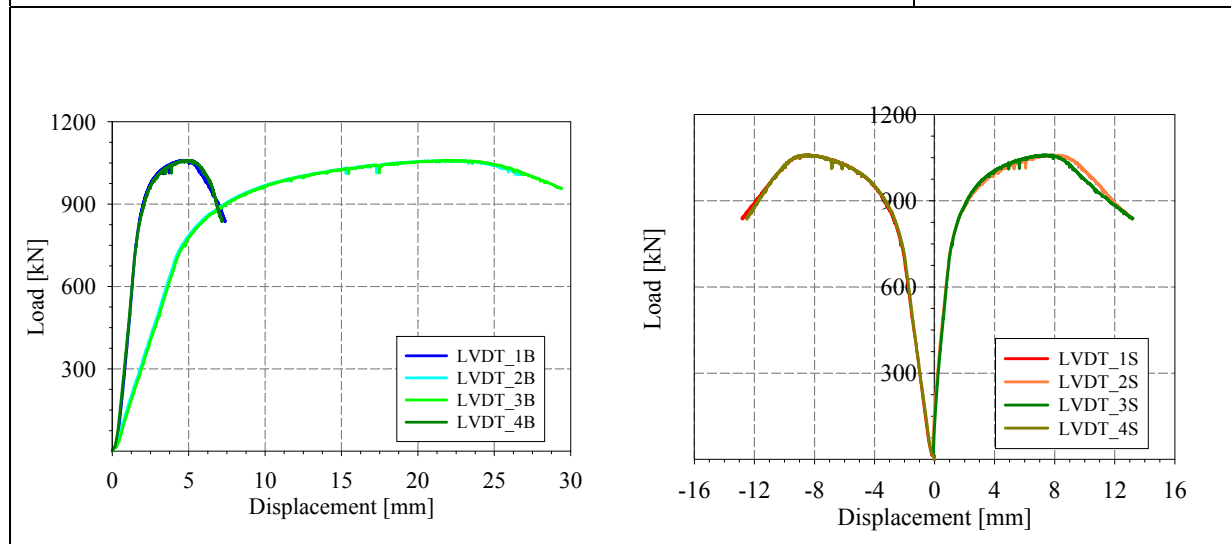
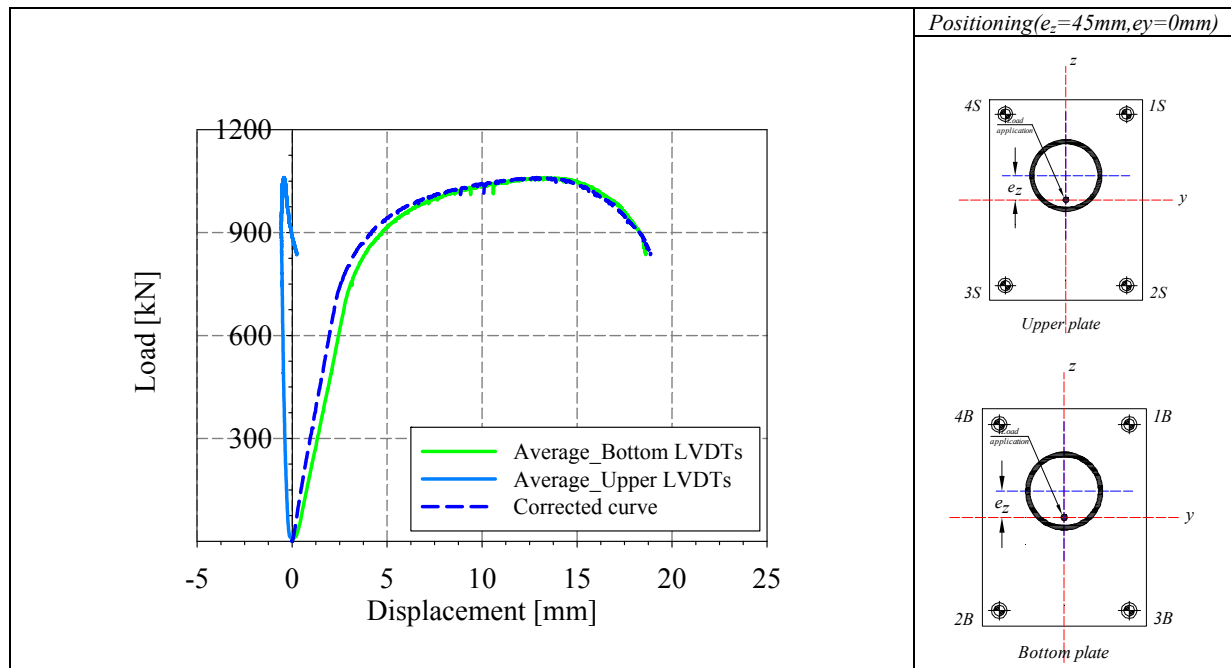
Specimen name	Shape	Details												
<p>CHS_S355_LC2 159x6.3 CF</p>		<p>Shape: Circular Hollow Section Nominal yield limit: 355 MPa Load case: N (50%) + M_y (50%) D=159mm t=6.3mm Fabrication process: Cold formed</p>												
Average D= 159 mm		Average t= 6.9 mm												
														
<i>Cross-sectional measured dimensions and tolerances</i>														
		<table border="1"> <thead> <tr> <th colspan="2" data-bbox="1105 907 1459 982">Average C_a, C_b</th> </tr> </thead> <tbody> <tr> <td data-bbox="1105 982 1255 1031">E [MPa]</td> <td data-bbox="1255 982 1459 1031">194654</td> </tr> <tr> <td data-bbox="1105 1031 1255 1079">f_y [MPa]</td> <td data-bbox="1255 1031 1459 1079">607.3</td> </tr> <tr> <td data-bbox="1105 1079 1255 1127">ε_y [%]</td> <td data-bbox="1255 1079 1459 1127">0.31</td> </tr> <tr> <td data-bbox="1105 1127 1255 1176">f_u [MPa]</td> <td data-bbox="1255 1127 1459 1176">628.2</td> </tr> <tr> <td data-bbox="1105 1176 1255 1251">ε_u [%]</td> <td data-bbox="1255 1176 1459 1251">1.1</td> </tr> </tbody> </table>	Average C _a , C _b		E [MPa]	194654	f _y [MPa]	607.3	ε _y [%]	0.31	f _u [MPa]	628.2	ε _u [%]	1.1
Average C _a , C _b														
E [MPa]	194654													
f _y [MPa]	607.3													
ε _y [%]	0.31													
f _u [MPa]	628.2													
ε _u [%]	1.1													
<i>Tensile coupons location</i>	<i>Material stress-strain curves</i>	<i>Material average properties</i>												
 <p style="text-align: center;">Membrane stresses Flexural stresses</p> <p style="text-align: center;"><i>Measured residual stresses distributions</i></p>														



Amplified imperfect vue (x10)



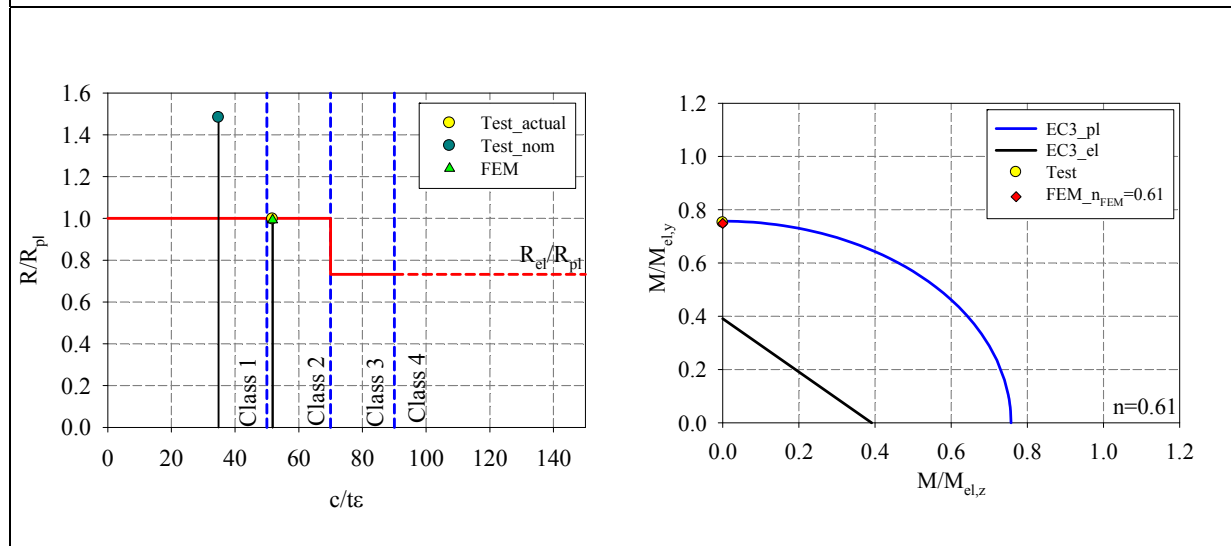
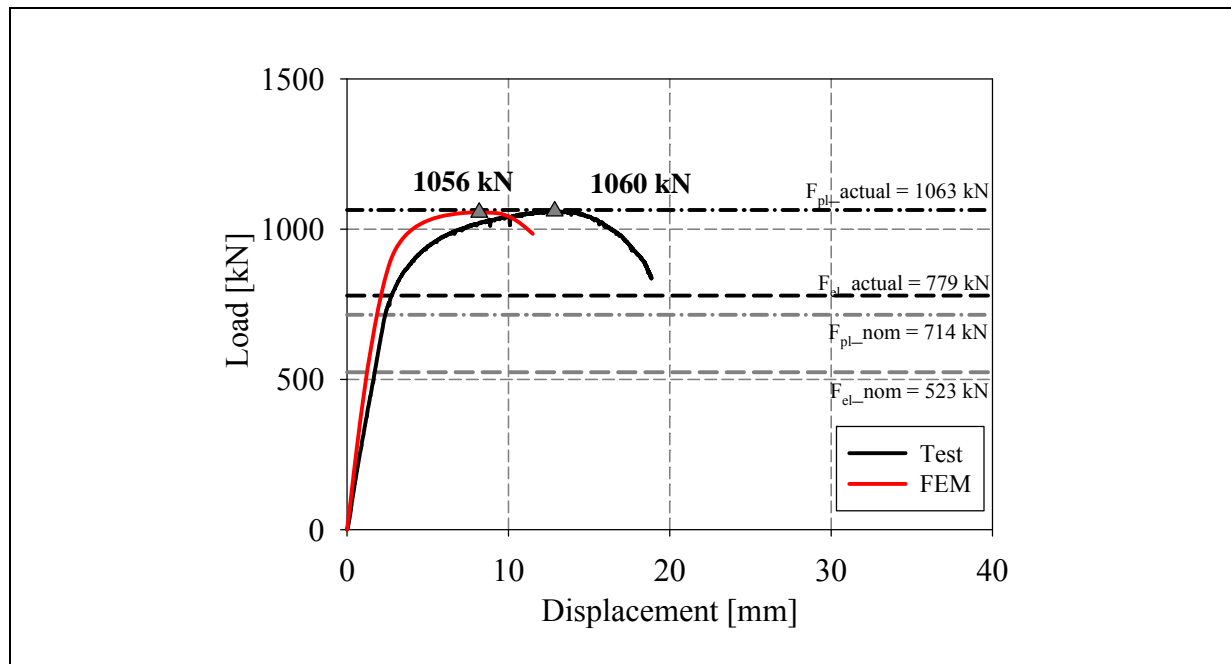
Measured Local imperfections



LVDT and strain gauges recordings

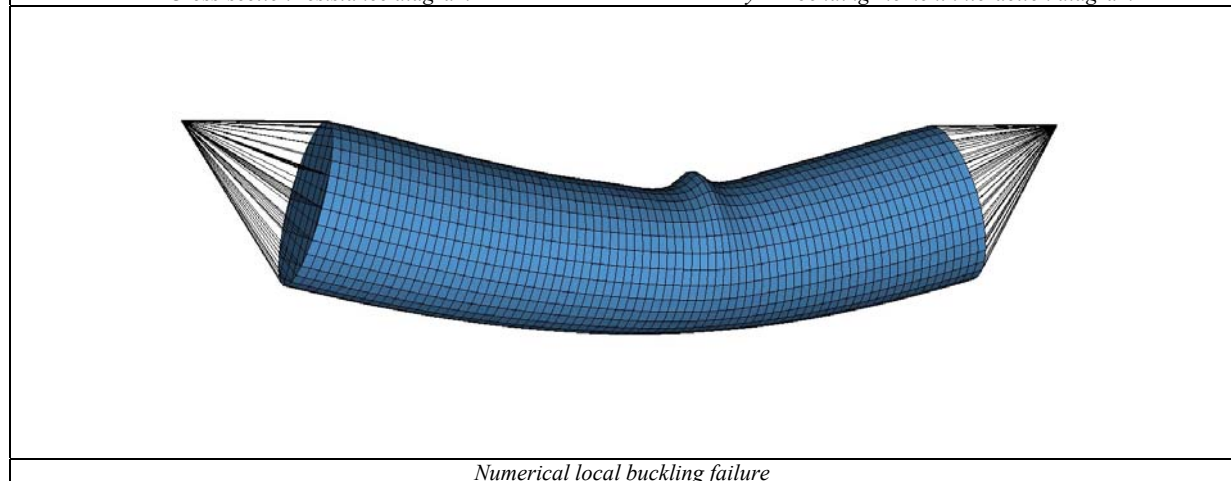


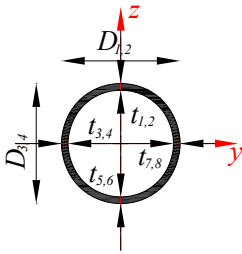
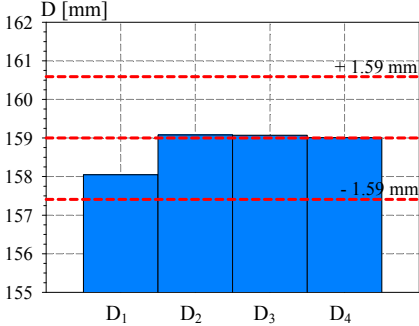
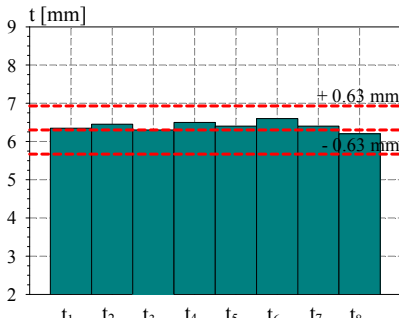
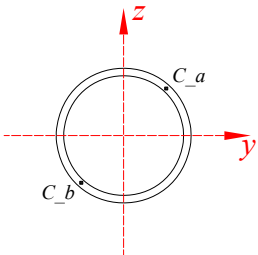
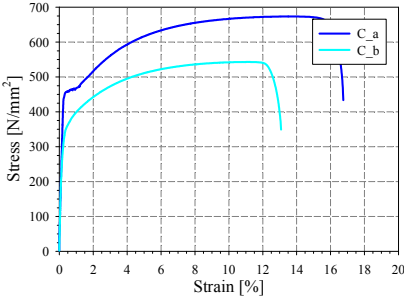
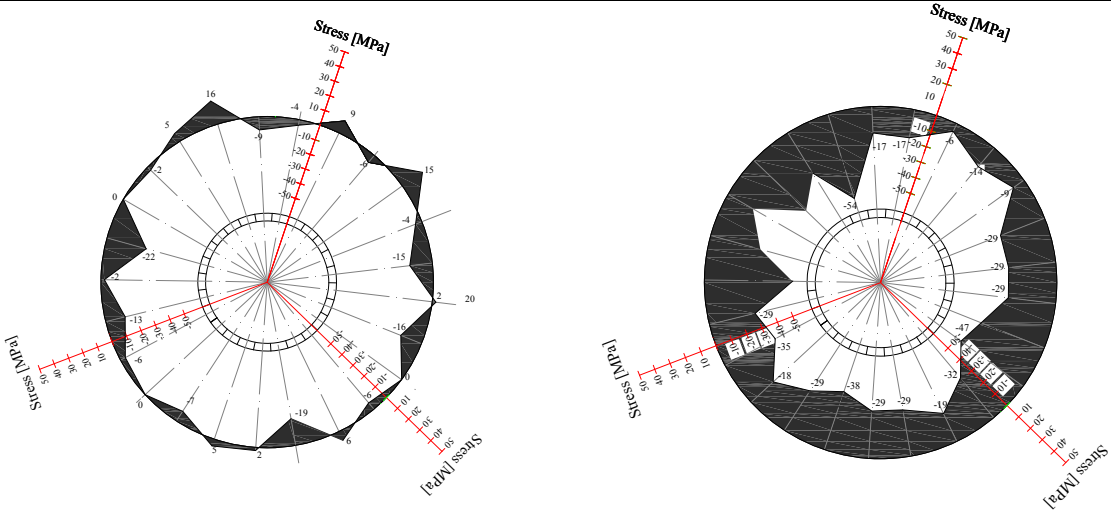
Local buckling failure

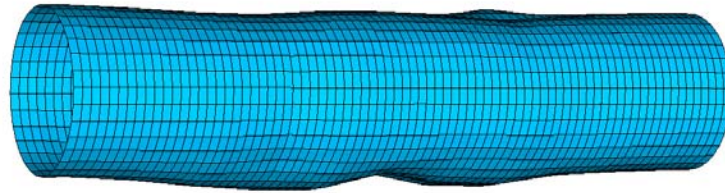


Cross-section resistance diagram

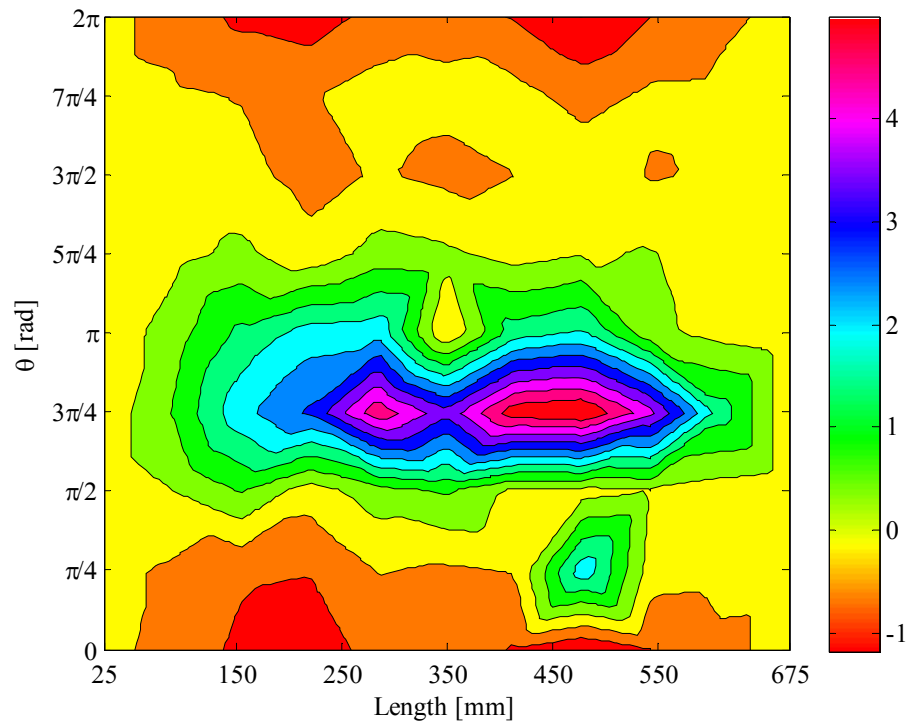
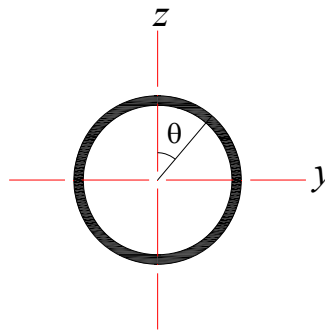
My-Mz bending moment interaction diagram



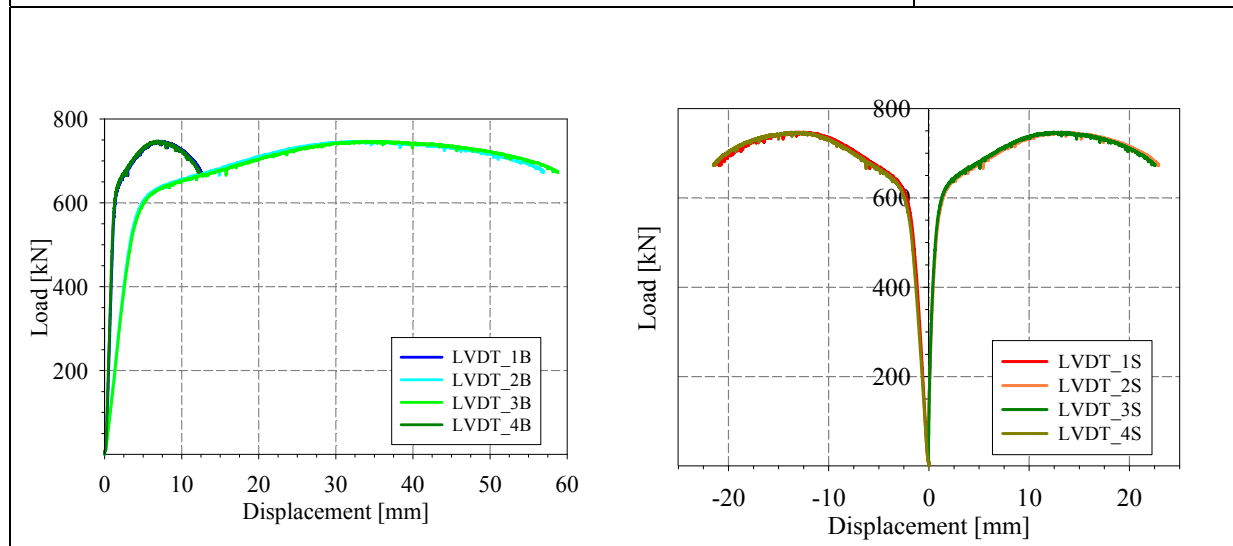
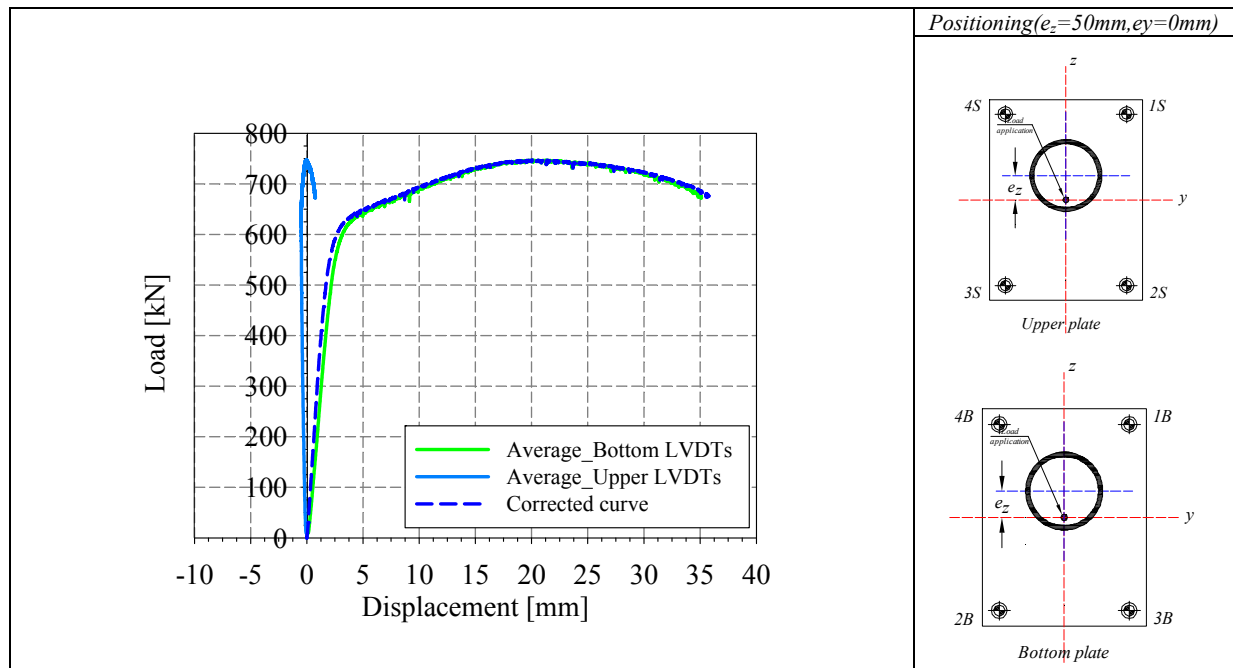
Specimen name	Shape	Details											
<p>CHS_S355_LC2 159x6.3 HR</p>		<p>Shape: Circular Hollow Section Nominal yield limit: 355 MPa Load case: N (50%) + M_y (50%) D=159mm t=6.3mm Fabrication process: Hot rolled</p>											
Average D= 159 mm		Average t= 6.4 mm											
													
<i>Cross-sectional measured dimensions and tolerances</i>													
	 <table border="1" data-bbox="1105 898 1459 1245"> <thead> <tr> <th></th> <th>Average C_a, C_b</th> </tr> </thead> <tbody> <tr> <td>E [MPa]</td> <td>213000</td> </tr> <tr> <td>f_y [MPa]</td> <td>401.5</td> </tr> <tr> <td>ϵ_y [%]</td> <td>0.19</td> </tr> <tr> <td>f_u [MPa]</td> <td>607.8</td> </tr> <tr> <td>ϵ_u [%]</td> <td>11.7</td> </tr> </tbody> </table>		Average C_a, C_b	E [MPa]	213000	f_y [MPa]	401.5	ϵ_y [%]	0.19	f_u [MPa]	607.8	ϵ_u [%]	11.7
	Average C_a, C_b												
E [MPa]	213000												
f_y [MPa]	401.5												
ϵ_y [%]	0.19												
f_u [MPa]	607.8												
ϵ_u [%]	11.7												
<i>Tensile coupons location</i>	<i>Material stress-strain curves</i>	<i>Material average properties</i>											
 <div style="display: flex; justify-content: space-around;"> <div data-bbox="444 1793 646 1822" style="text-align: center;">Membrane stresses</div> <div data-bbox="1062 1793 1247 1822" style="text-align: center;">Flexural stresses</div> </div> <p style="text-align: center;"><i>Measured residual stresses distributions</i></p>													



Amplified imperfect vue (x10)



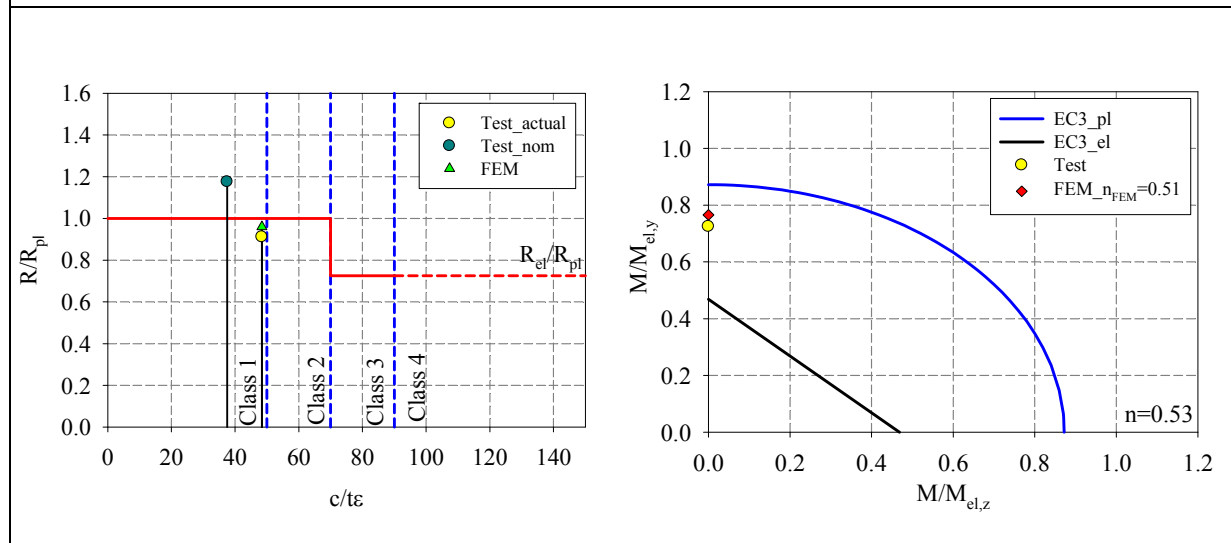
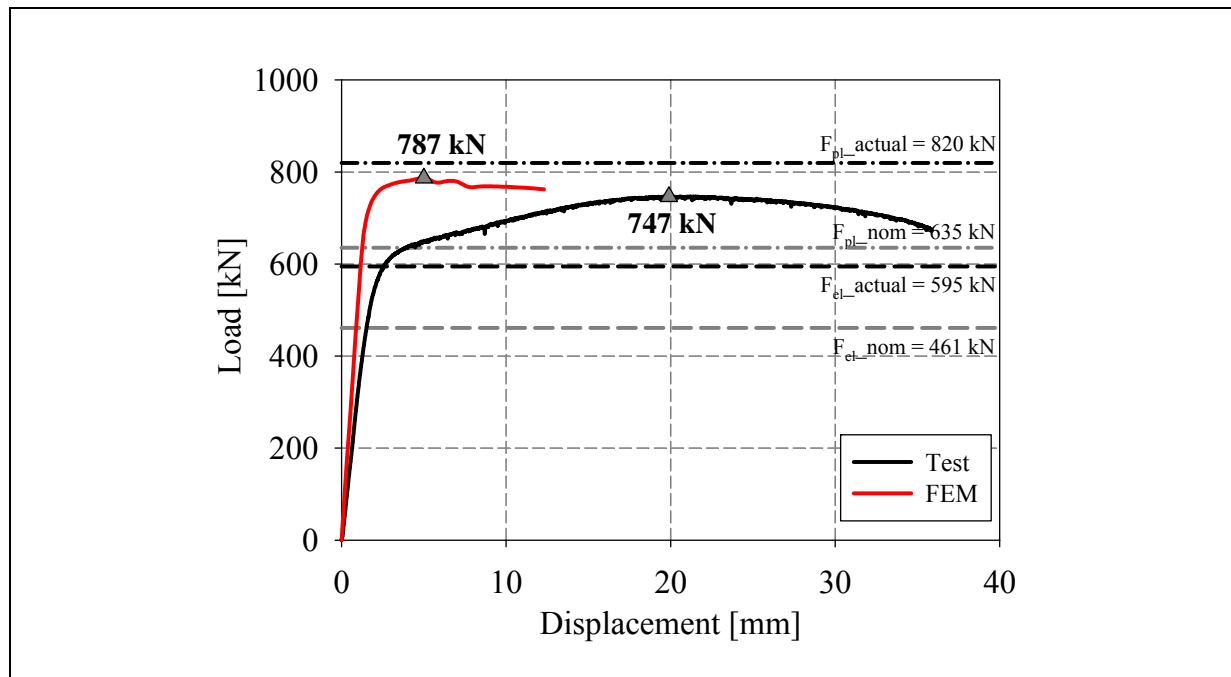
Measured Local imperfections



LVDT and strain gauges recordings

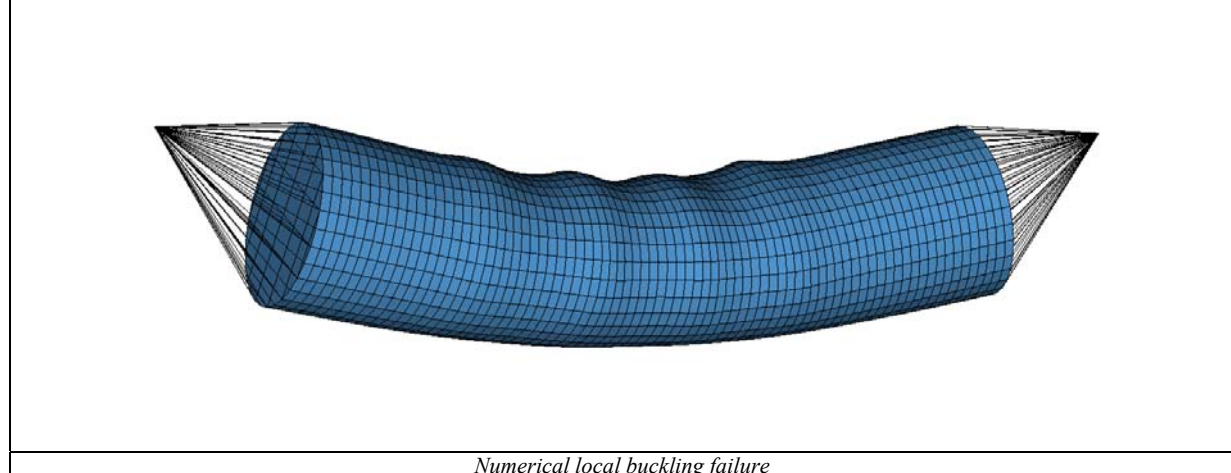


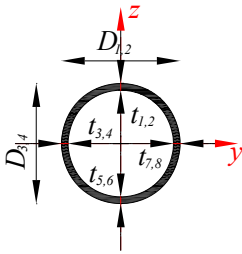
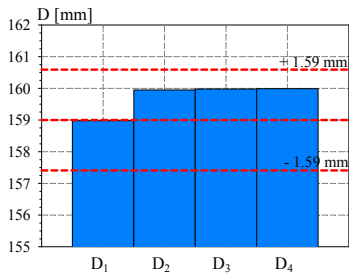
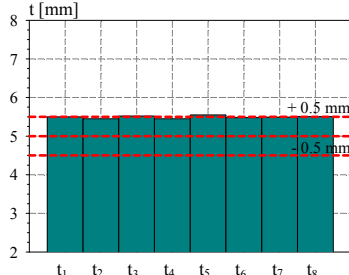
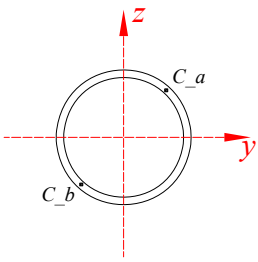
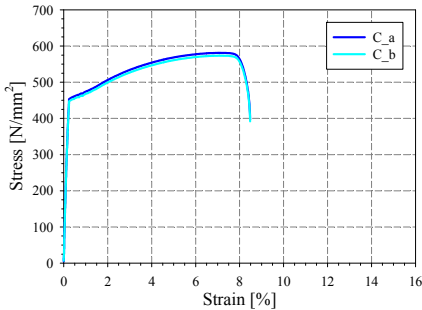
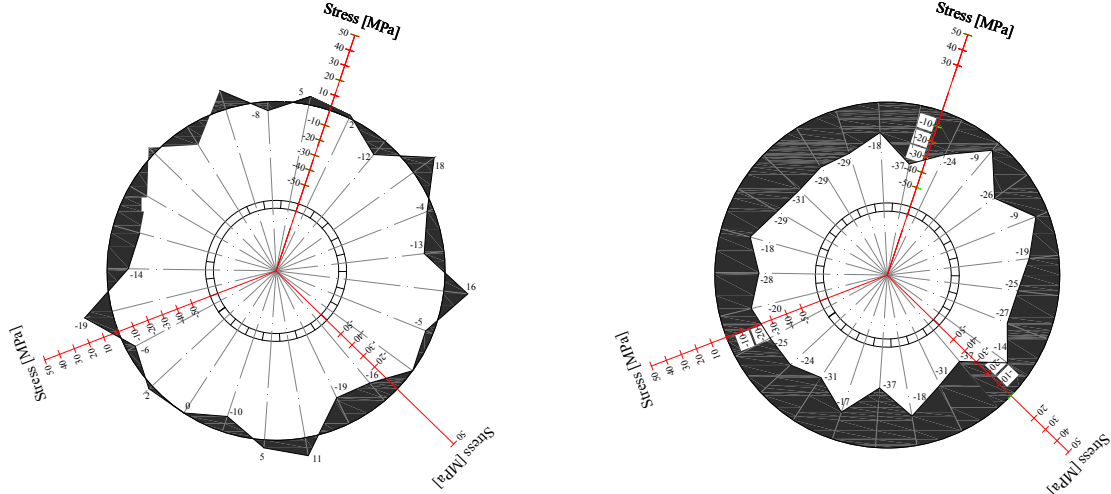
Local buckling failure

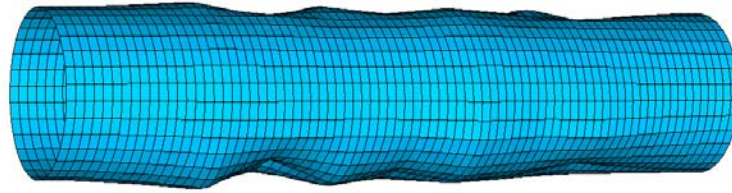


Cross-section resistance diagram

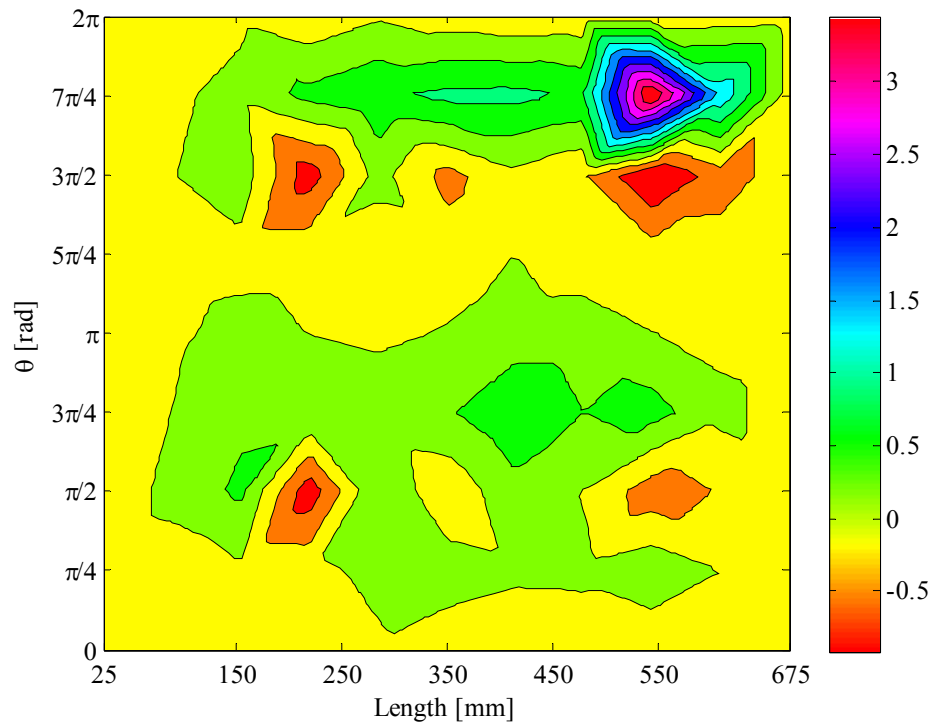
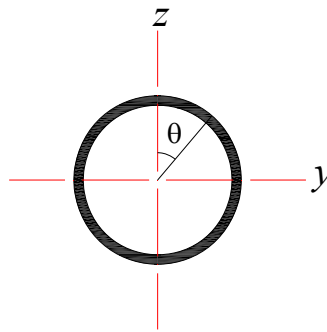
My-Mz bending moment interaction diagram



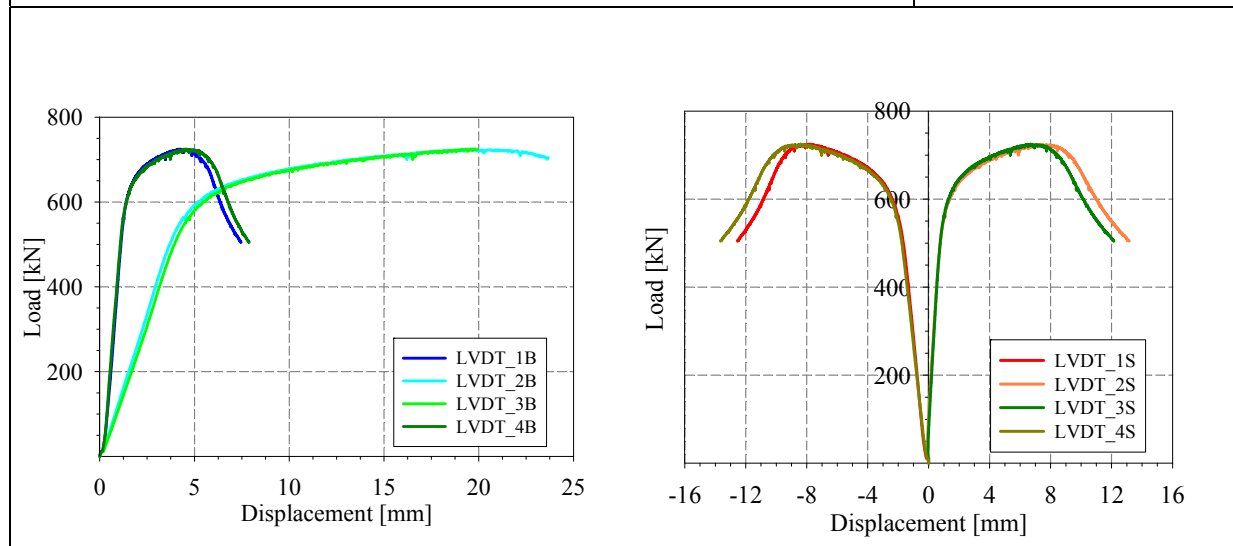
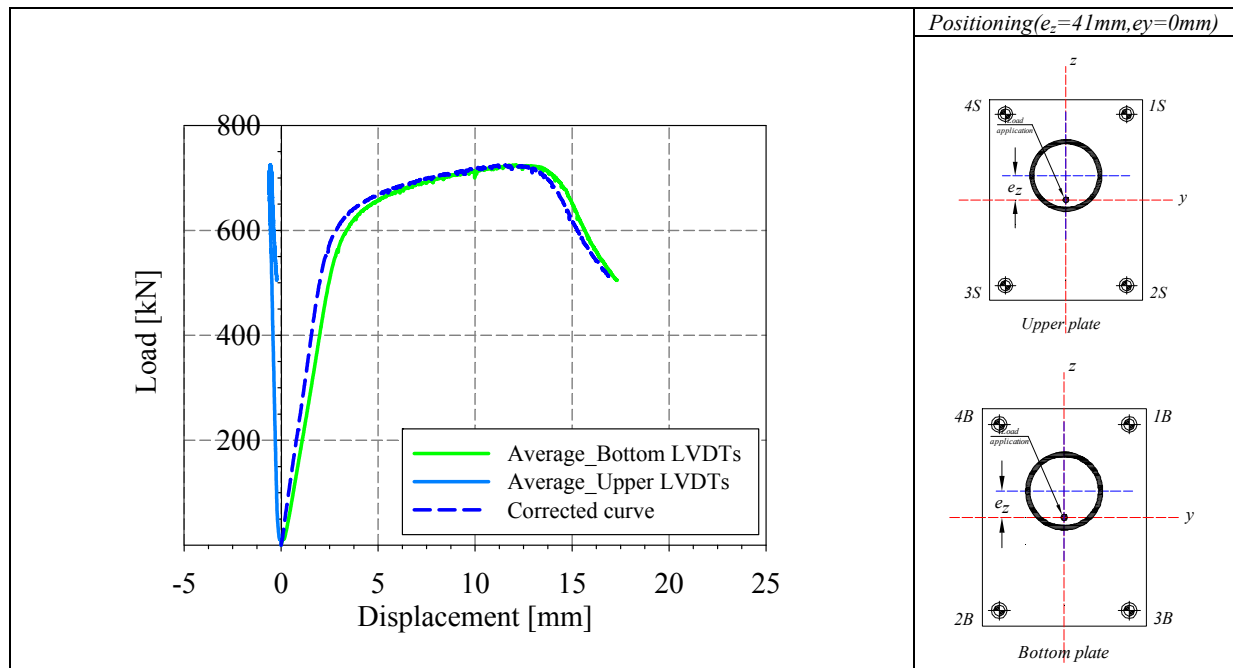
Specimen name	Shape	Details												
<p>CHS_S355_LC2 159x5 HR</p>		<p>Shape: Circular Hollow Section Nominal yield limit: 355 MPa Load case: N (50%) + M_y (50%) D=159mm t=5mm Fabrication process: Hot rolled</p>												
Average D= 159 mm		Average t= 5.5 mm												
														
<i>Cross-sectional measured dimensions and tolerances</i>														
		<table border="1"> <thead> <tr> <th></th> <th>Average C a,C b</th> </tr> </thead> <tbody> <tr> <td>E [MPa]</td> <td>215000</td> </tr> <tr> <td>f_y [MPa]</td> <td>457.7</td> </tr> <tr> <td>ϵ_y [%]</td> <td>0.21</td> </tr> <tr> <td>f_u [MPa]</td> <td>577.3</td> </tr> <tr> <td>ϵ_u [%]</td> <td>7.02</td> </tr> </tbody> </table>		Average C a,C b	E [MPa]	215000	f_y [MPa]	457.7	ϵ_y [%]	0.21	f_u [MPa]	577.3	ϵ_u [%]	7.02
	Average C a,C b													
E [MPa]	215000													
f_y [MPa]	457.7													
ϵ_y [%]	0.21													
f_u [MPa]	577.3													
ϵ_u [%]	7.02													
<i>Tensile coupons location</i>	<i>Material stress-strain curves</i>	<i>Material average properties</i>												
 <div style="display: flex; justify-content: space-around; margin-top: 10px;"> <div data-bbox="440 1738 646 1766" style="text-align: center;">Membrane stresses</div> <div data-bbox="1062 1738 1243 1766" style="text-align: center;">Flexural stresses</div> </div> <p style="text-align: center; margin-top: 10px;"><i>Measured residual stresses distributions</i></p>														



Amplified imperfect vue (x10)



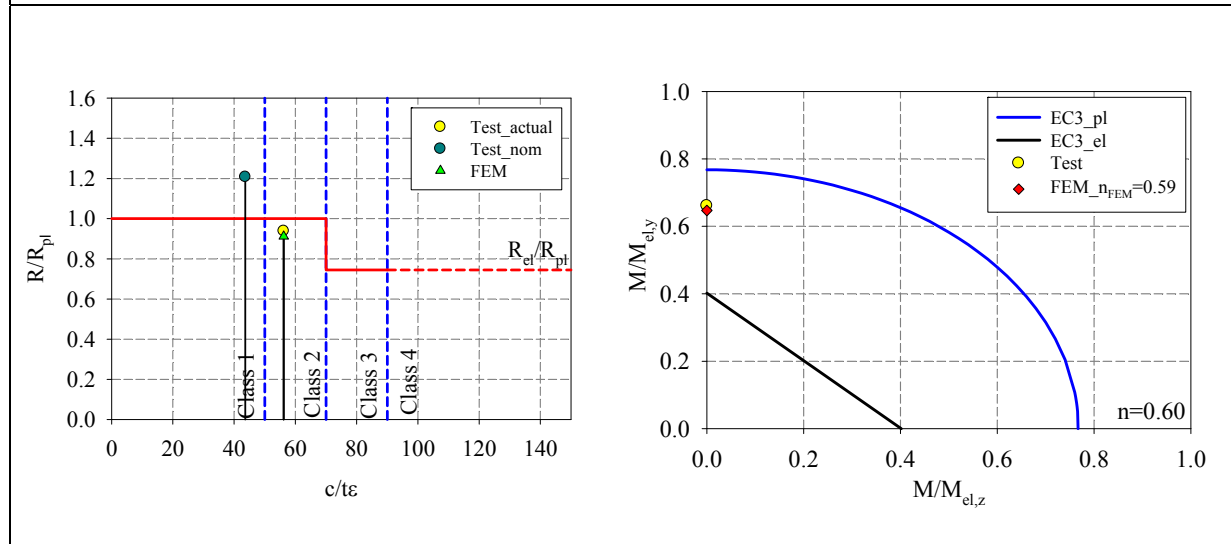
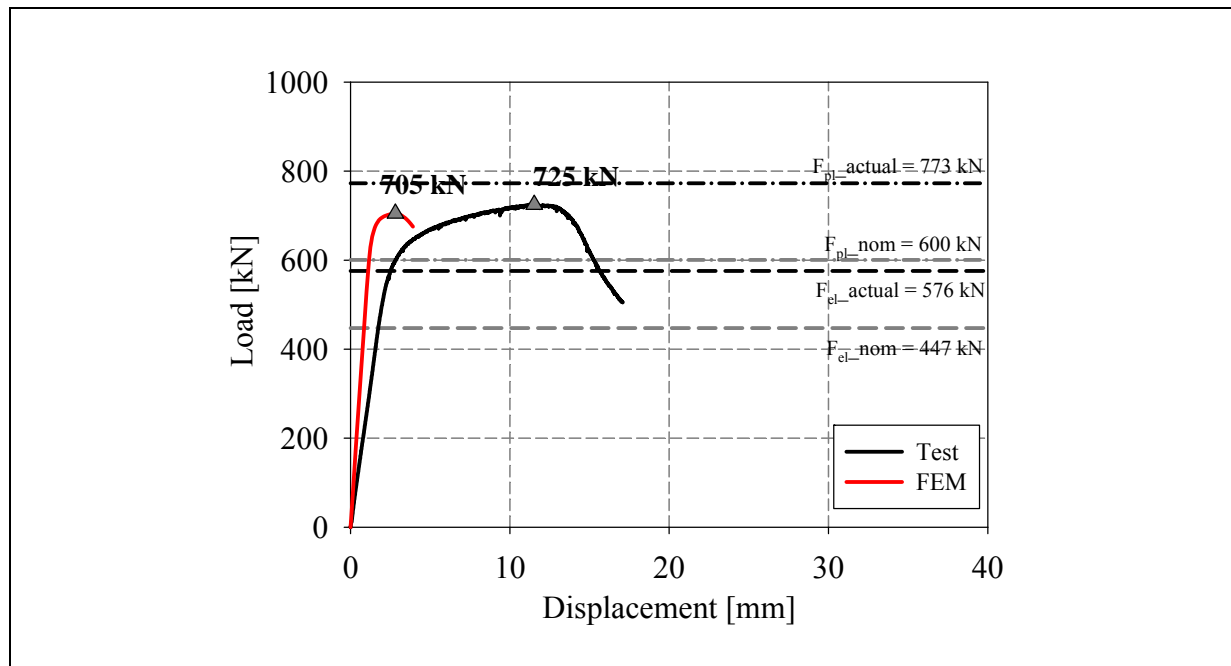
Measured Local imperfections



LVDT and strain gauges recordings

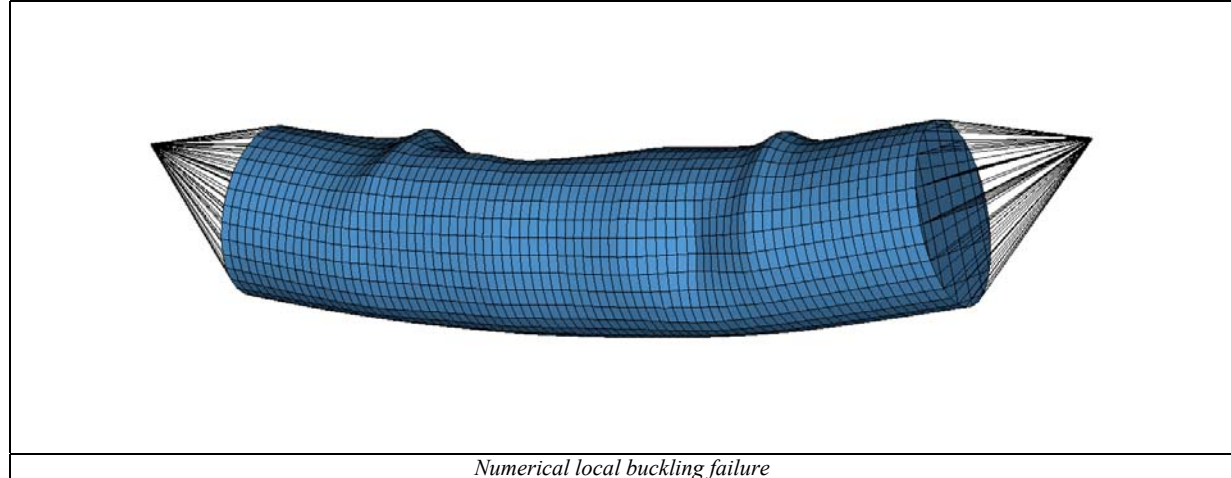


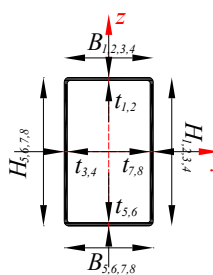
Local buckling failure

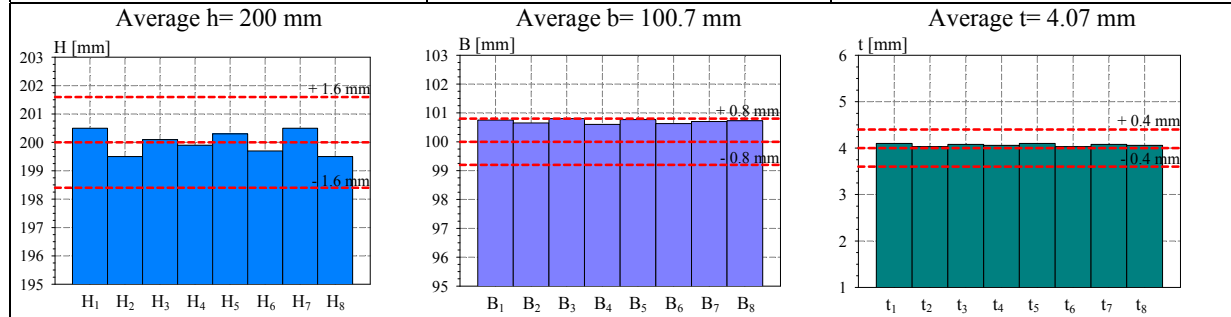


Cross-section resistance diagram

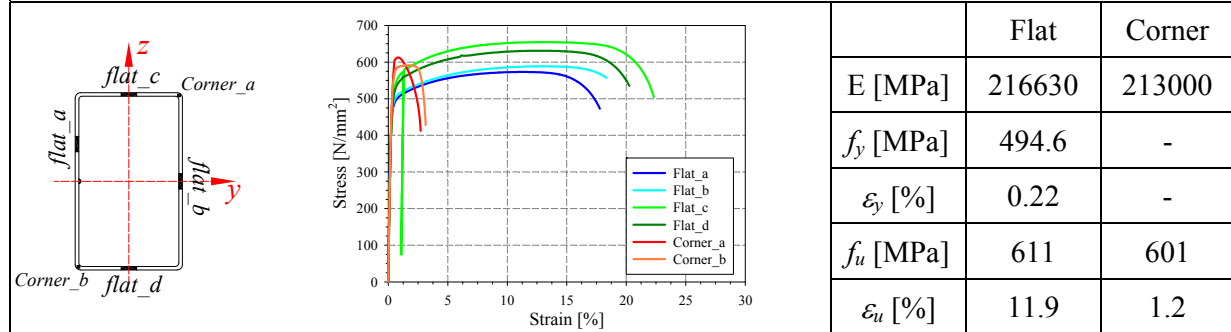
My-Mz bending moment interaction diagram



<p>Specimen name</p> <p>RHS_S355_LC3 200x100x4 CF</p>	<p>Shape</p> 	<p>Details</p> <p>Shape: Rectangular Hollow Section</p> <p>Nominal yield limit: 355 MPa</p> <p>Load case: N(33%)+M_y(33%)+M_y(33%)</p> <p>H=200mm B=100mm t=4mm</p> <p>Fabrication process: Cold formed</p>
---	--	---



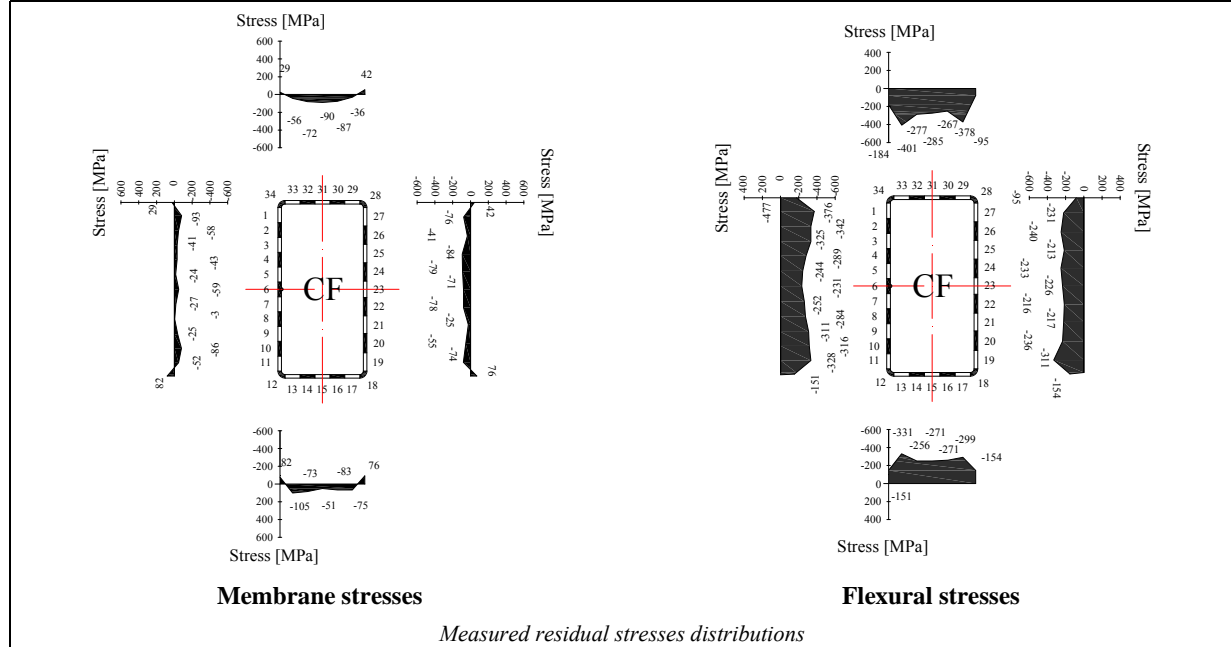
Cross-sectional measured dimensions and tolerances

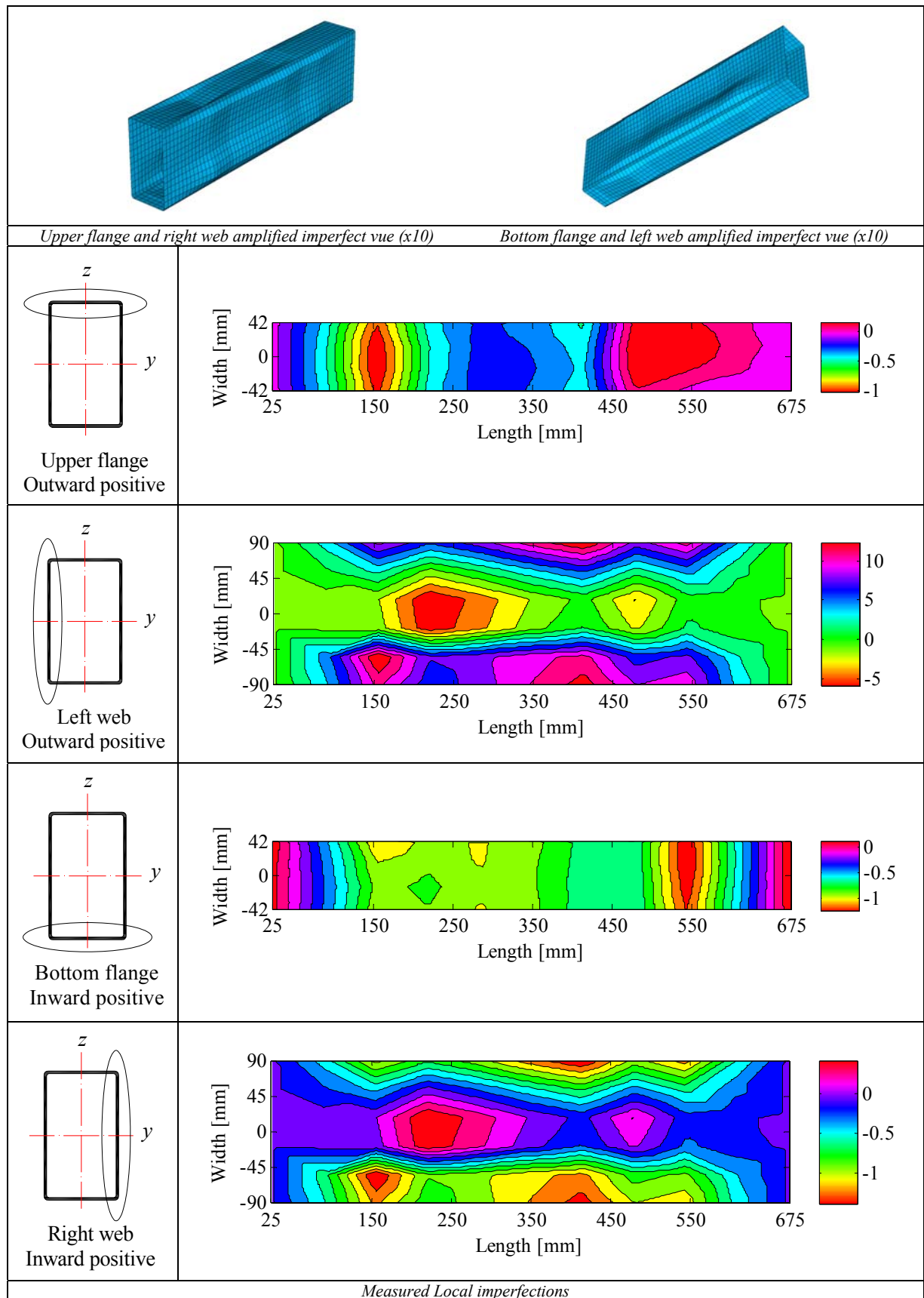


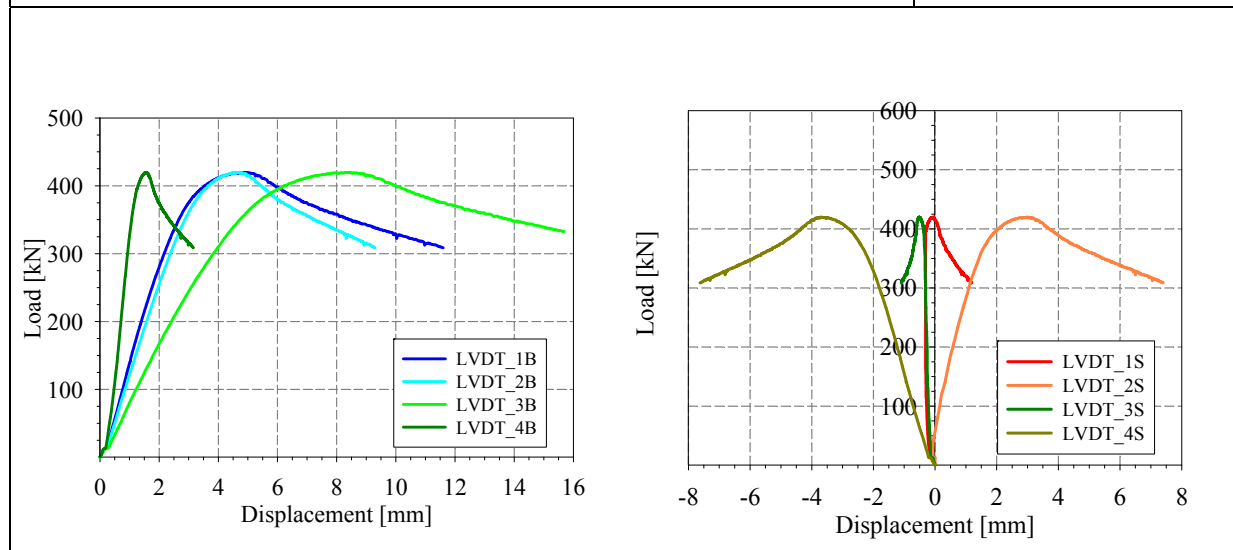
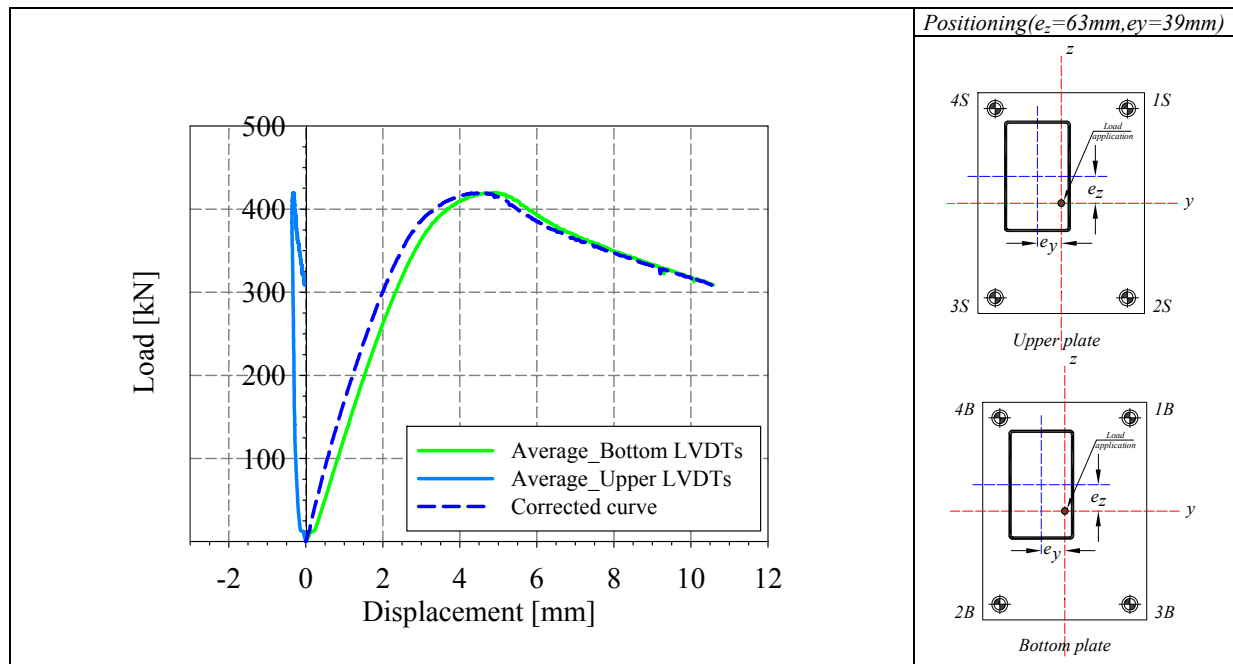
Tensile coupons location

Material stress-strain curves

Material average properties



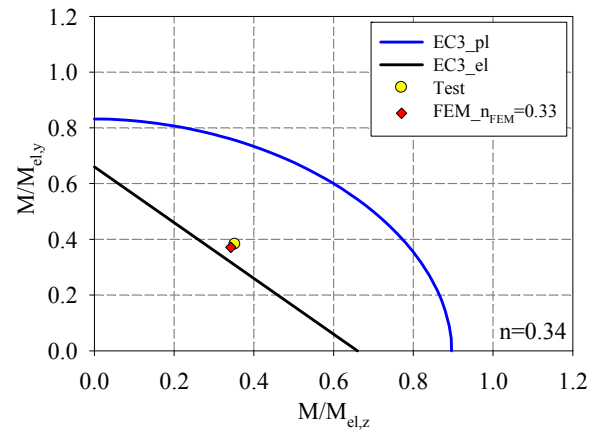
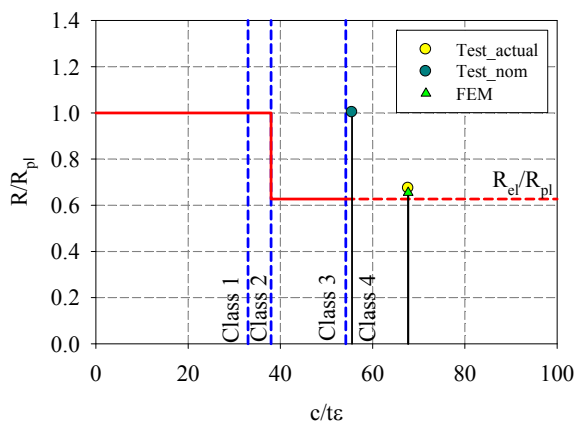
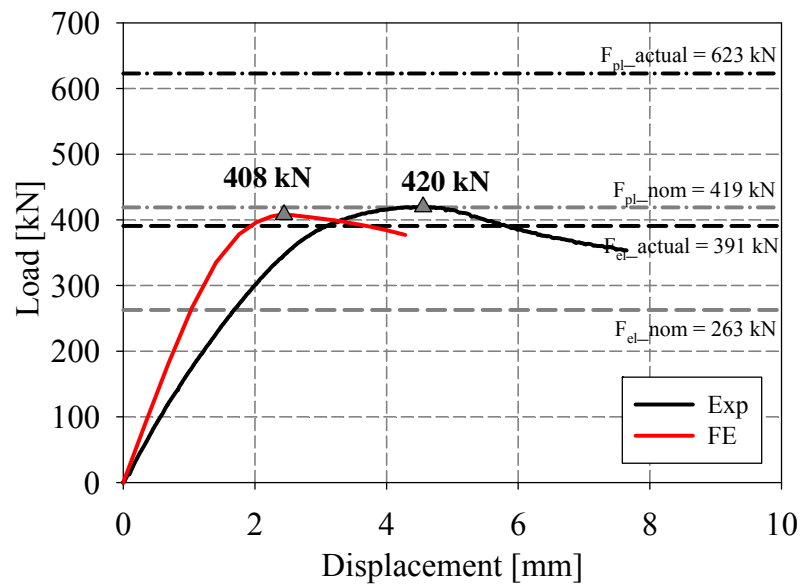




LVDT and strain gauges recordings

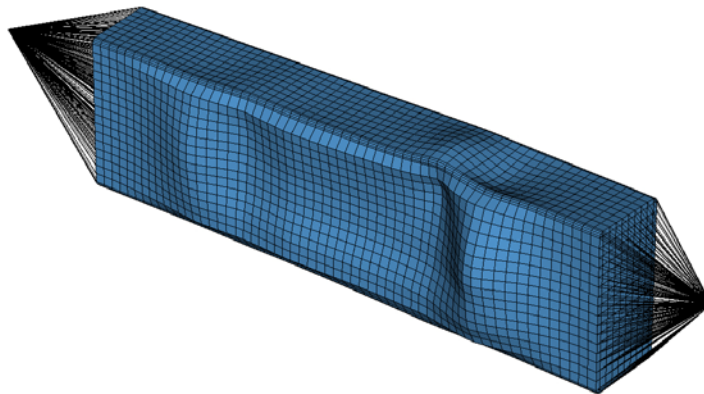


Local buckling failure

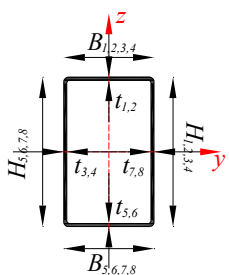


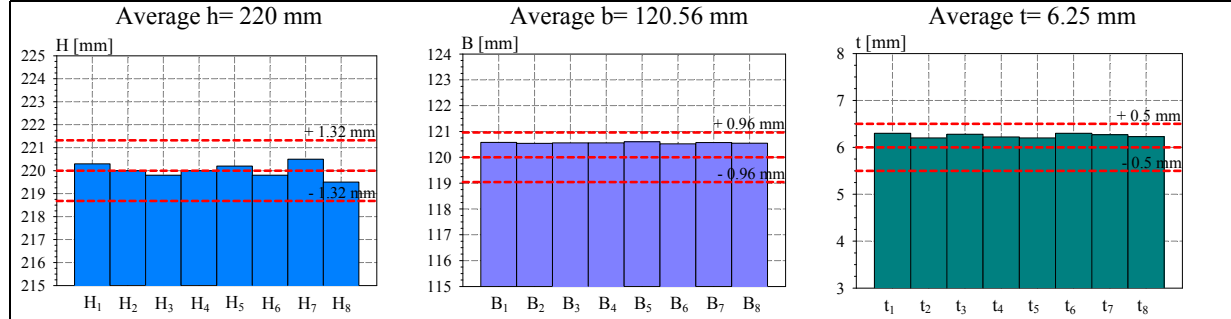
Cross-section resistance diagram

My-Mz bending moment interaction diagram

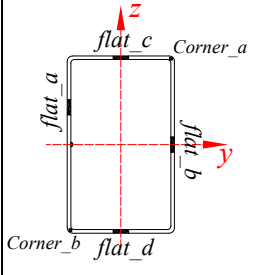
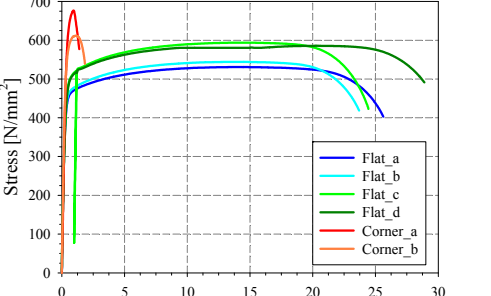


Numerical local buckling failure

<p>Specimen name</p> <p>RHS_S355_LC3 220x120x6 CF</p>	<p>Shape</p> 	<p>Details</p> <p>Shape: Rectangular Hollow Section</p> <p>Nominal yield limit: 355 MPa</p> <p>Load case: N(33%)+M_y(33%)+M_y(33%)</p> <p>H=220mm B=120mm t=6mm</p> <p>Fabrication process: Cold formed</p>
---	--	---



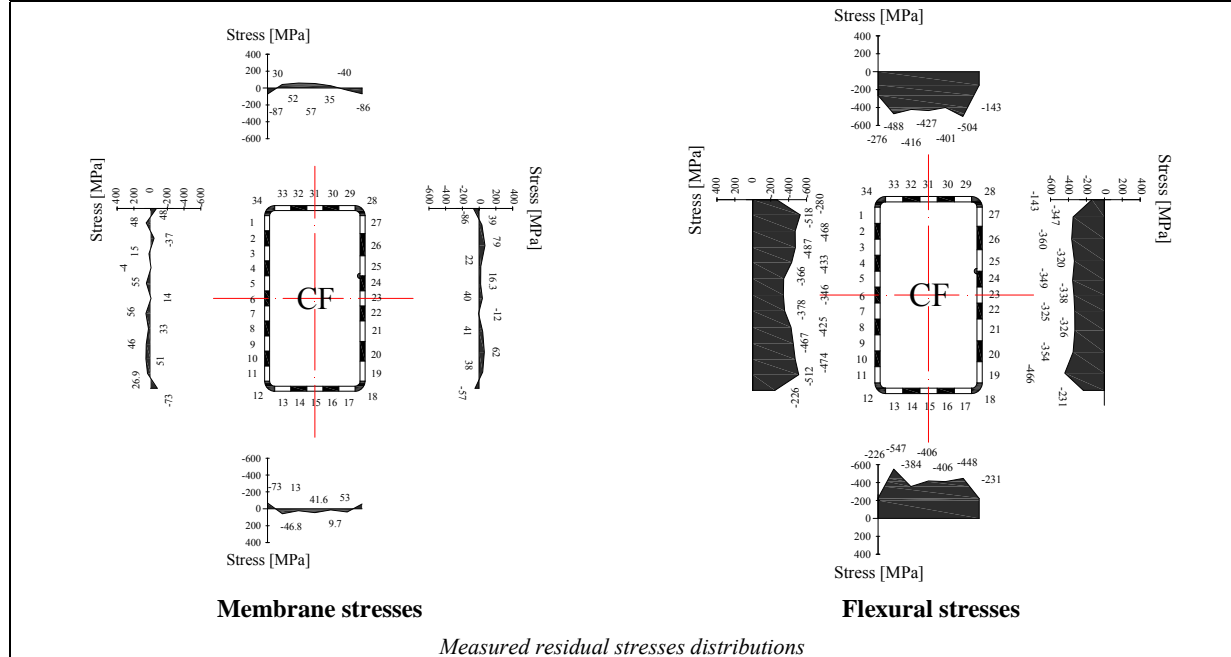
Cross-sectional measured dimensions and tolerances

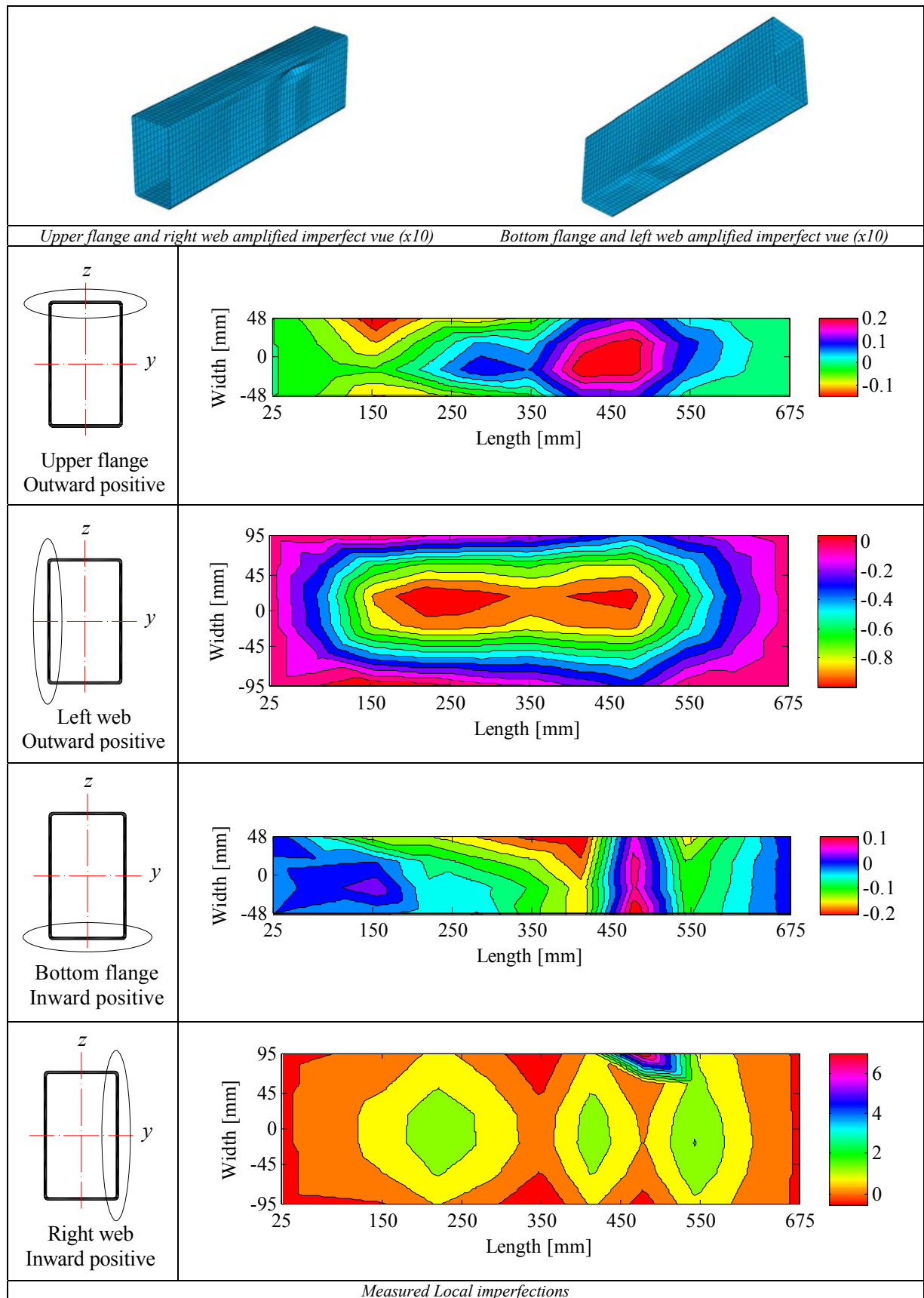
		<table border="1"> <thead> <tr> <th></th> <th>Flat</th> <th>Corner</th> </tr> </thead> <tbody> <tr> <td>E [MPa]</td> <td>206597</td> <td>207000</td> </tr> <tr> <td>f_y [MPa]</td> <td>454.7</td> <td>-</td> </tr> <tr> <td>ε_y [%]</td> <td>0.22</td> <td>-</td> </tr> <tr> <td>f_u [MPa]</td> <td>563.6</td> <td>644</td> </tr> <tr> <td>ε_u [%]</td> <td>15.5</td> <td>1</td> </tr> </tbody> </table>		Flat	Corner	E [MPa]	206597	207000	f _y [MPa]	454.7	-	ε _y [%]	0.22	-	f _u [MPa]	563.6	644	ε _u [%]	15.5	1
	Flat	Corner																		
E [MPa]	206597	207000																		
f _y [MPa]	454.7	-																		
ε _y [%]	0.22	-																		
f _u [MPa]	563.6	644																		
ε _u [%]	15.5	1																		

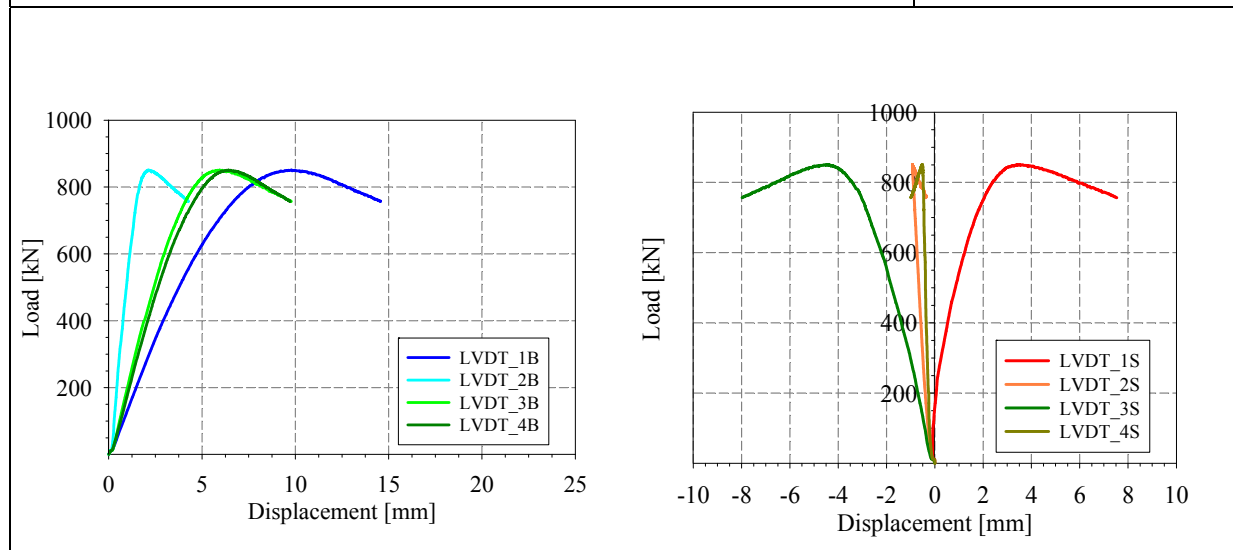
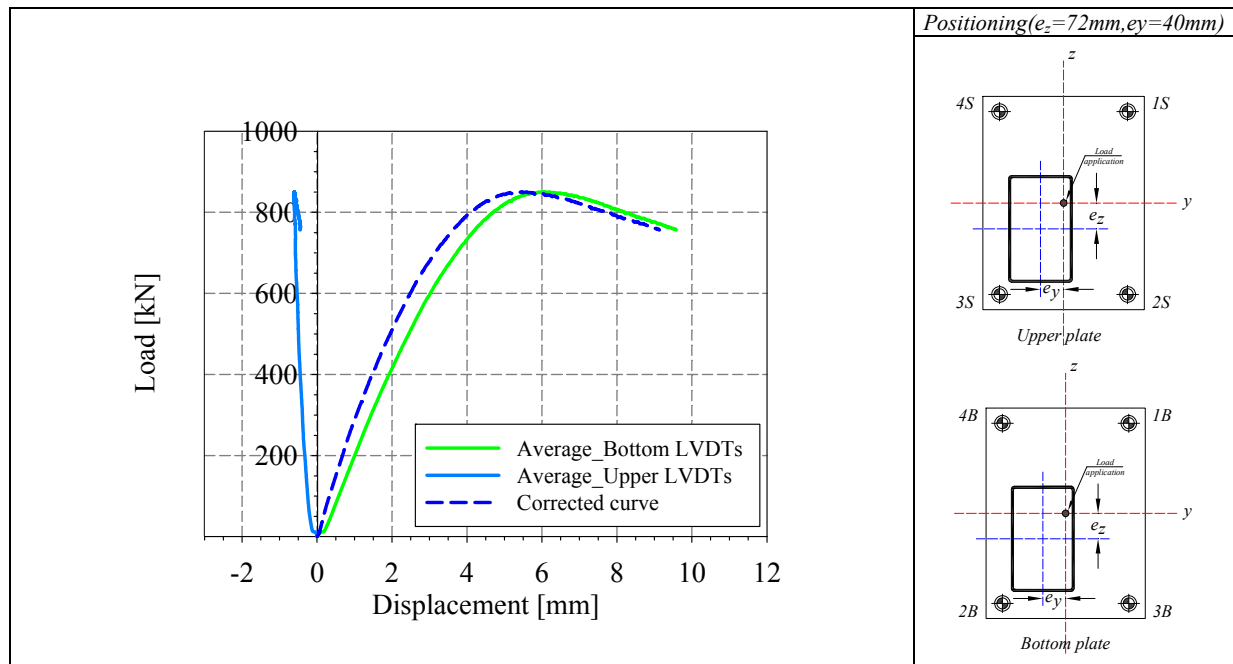
Tensile coupons location

Material stress-strain curves

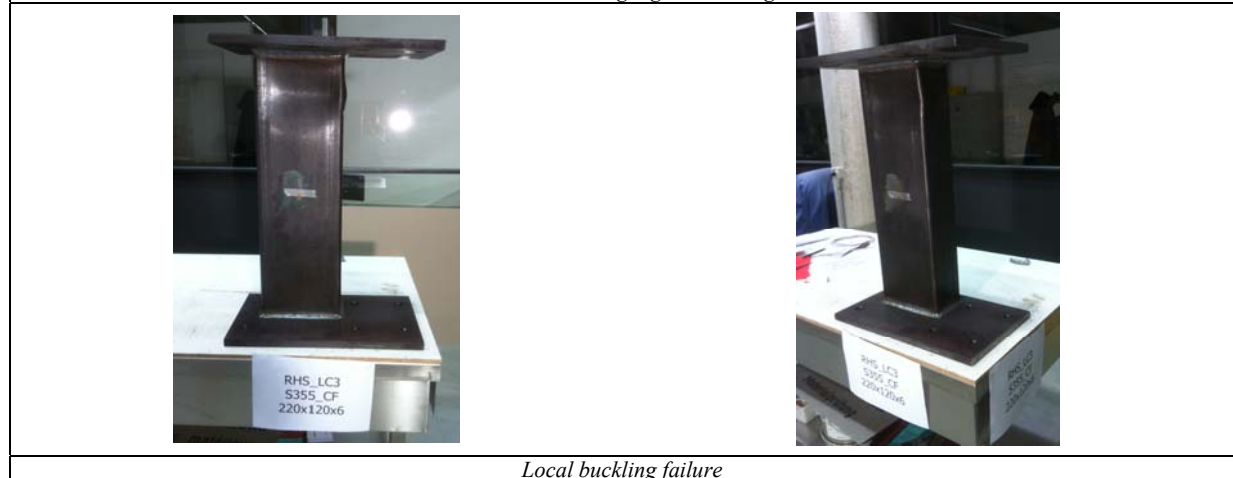
Material average properties



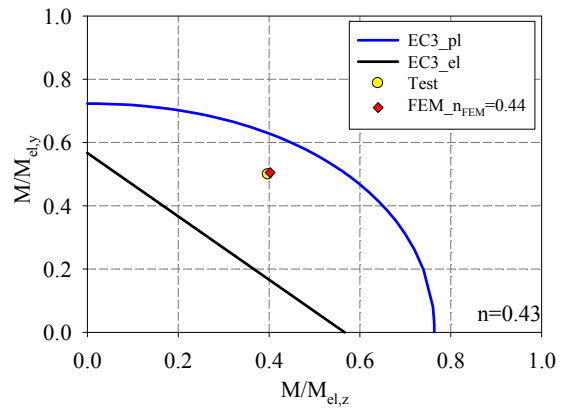
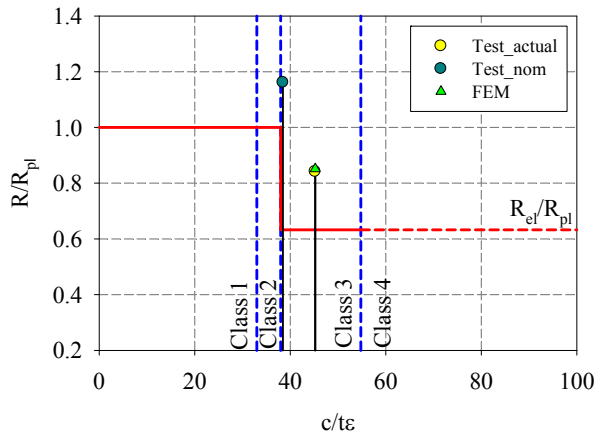
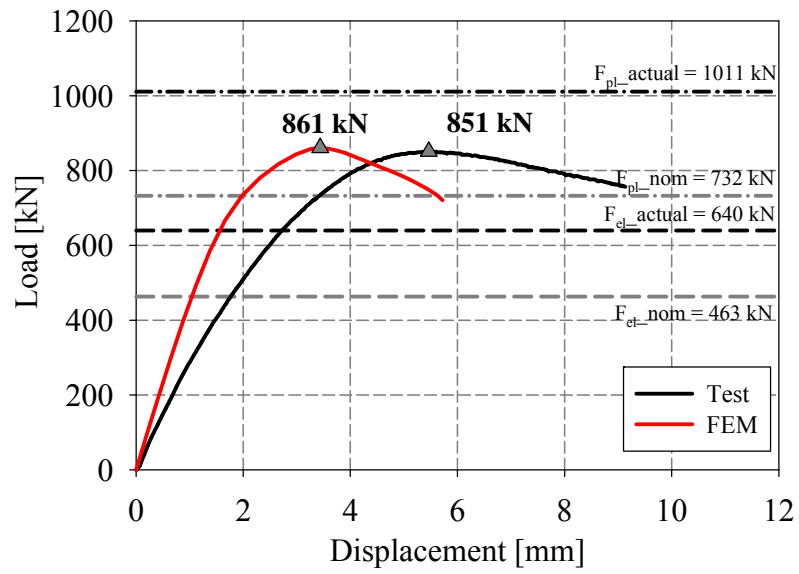




LVDT and strain gauges recordings

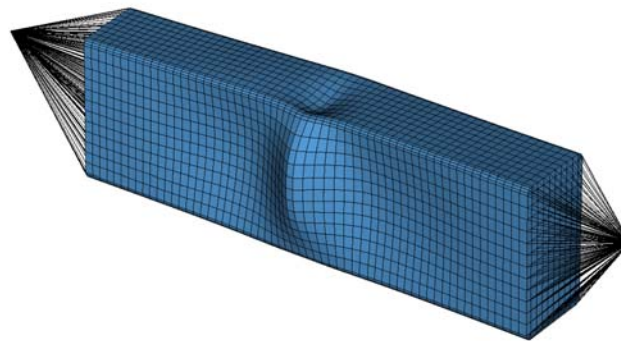


Local buckling failure

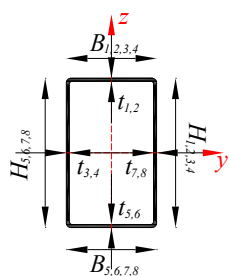


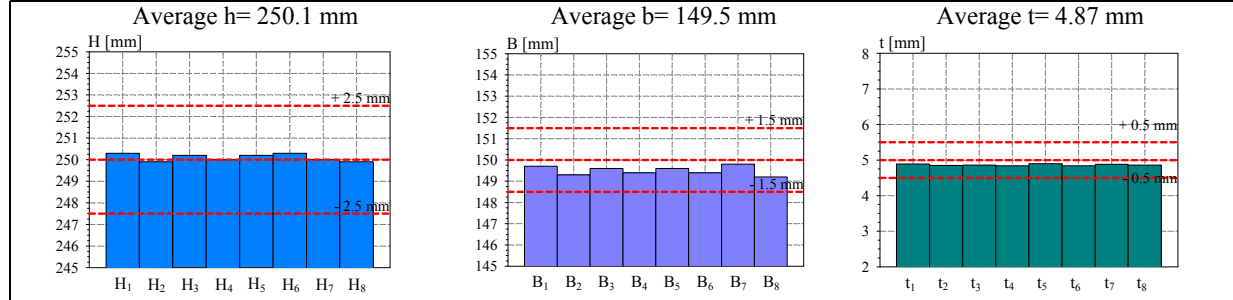
Cross-section resistance diagram

M_y - M_z bending moment interaction diagram

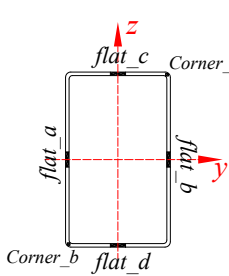
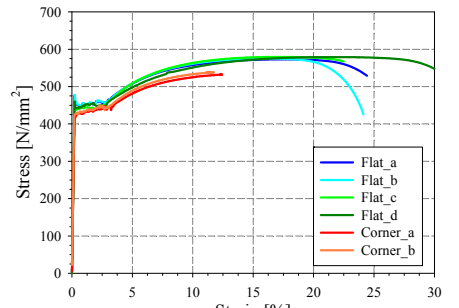


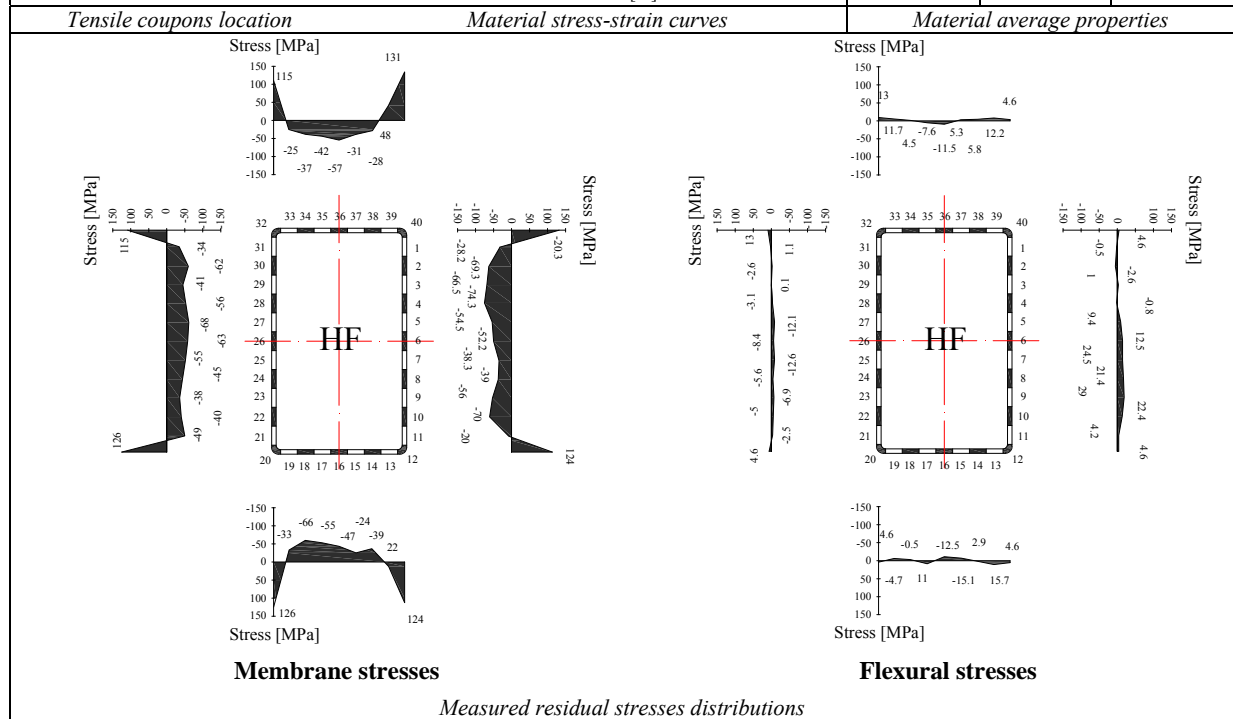
Numerical local buckling failure

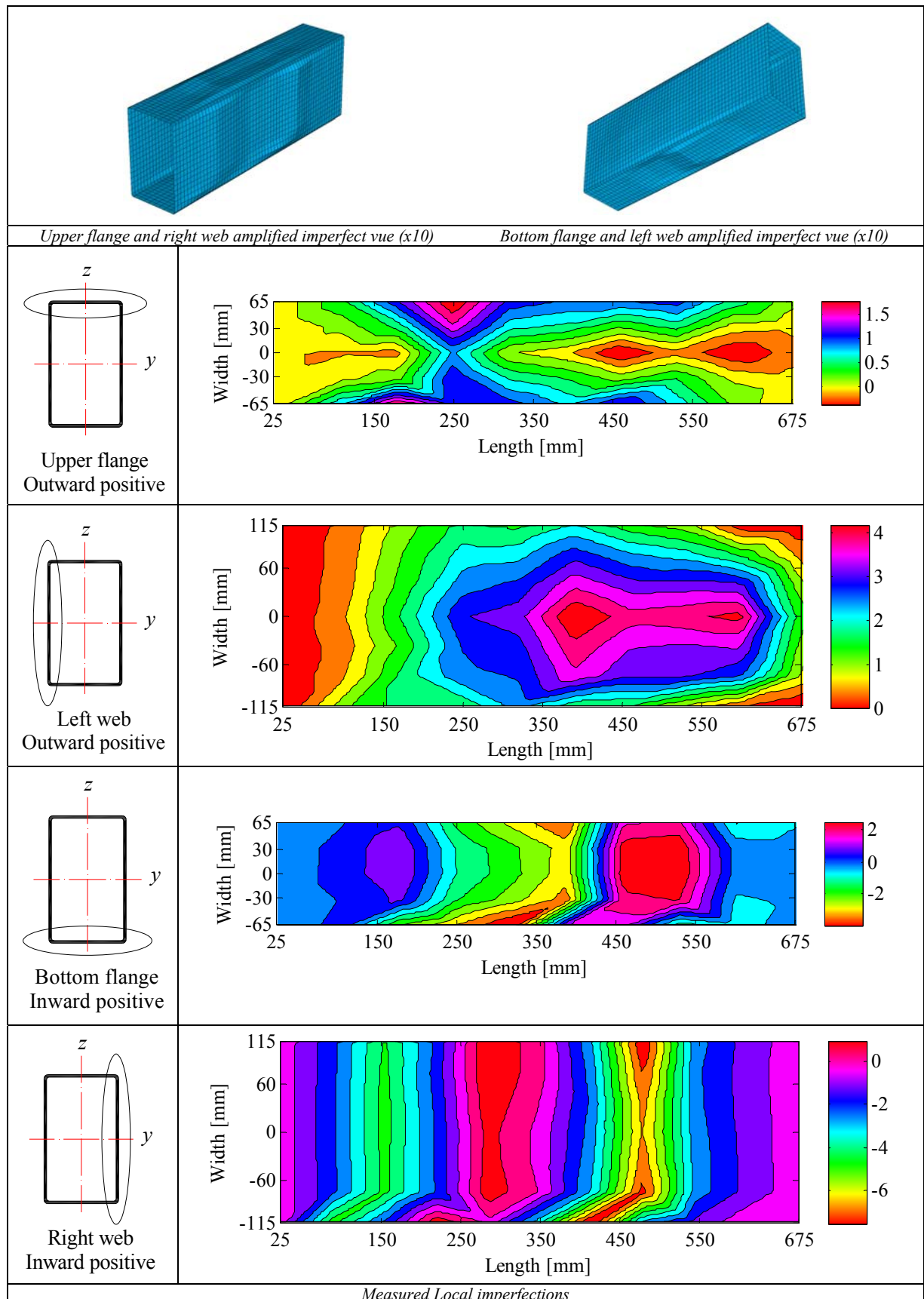
<p>Specimen name</p> <p>RHS_S355_LC3 250x150x5 HF</p>	<p>Shape</p> 	<p>Details</p> <p>Shape: Rectangular Hollow Section</p> <p>Nominal yield limit: 355 MPa</p> <p>Load case: N(33%)+My(33%)+My(33%)</p> <p>H=250mm B=150mm t=5mm</p> <p>Fabrication process: Hot formed</p>
---	---	--

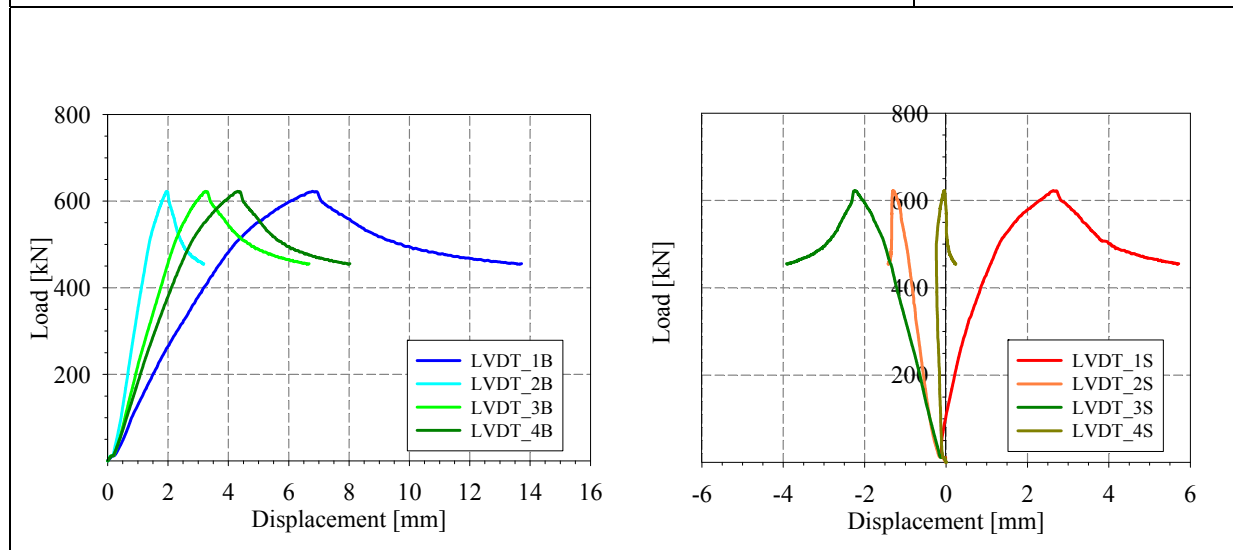
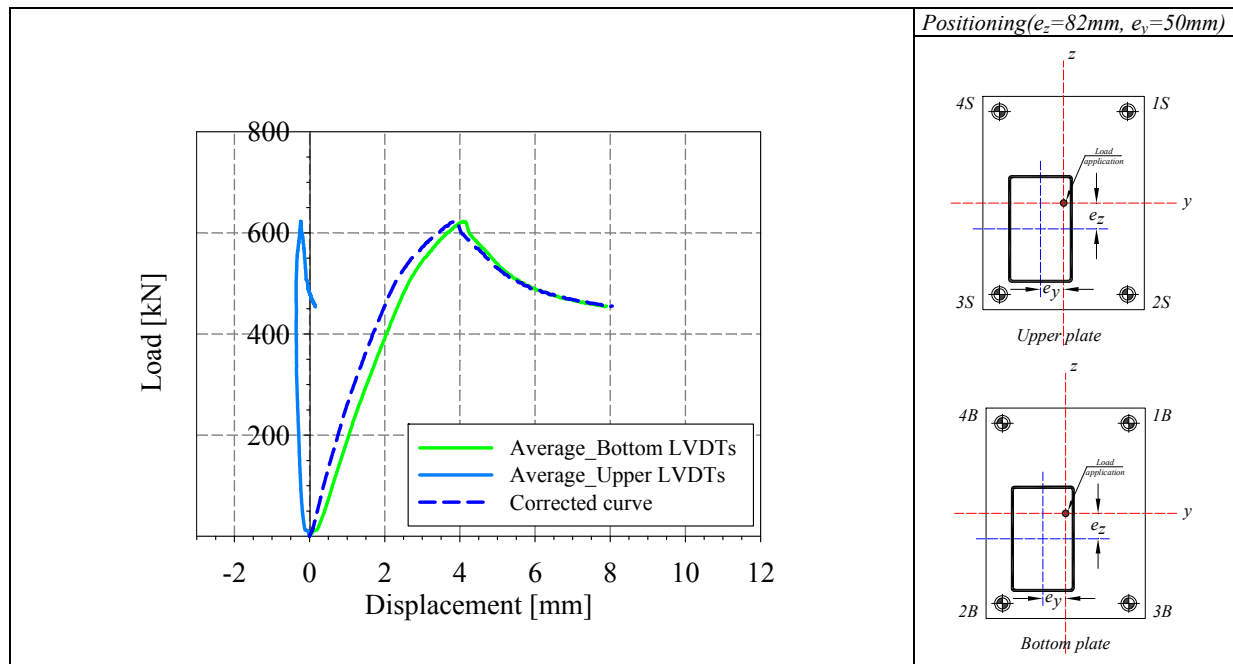


Cross-sectional measured dimensions and tolerances

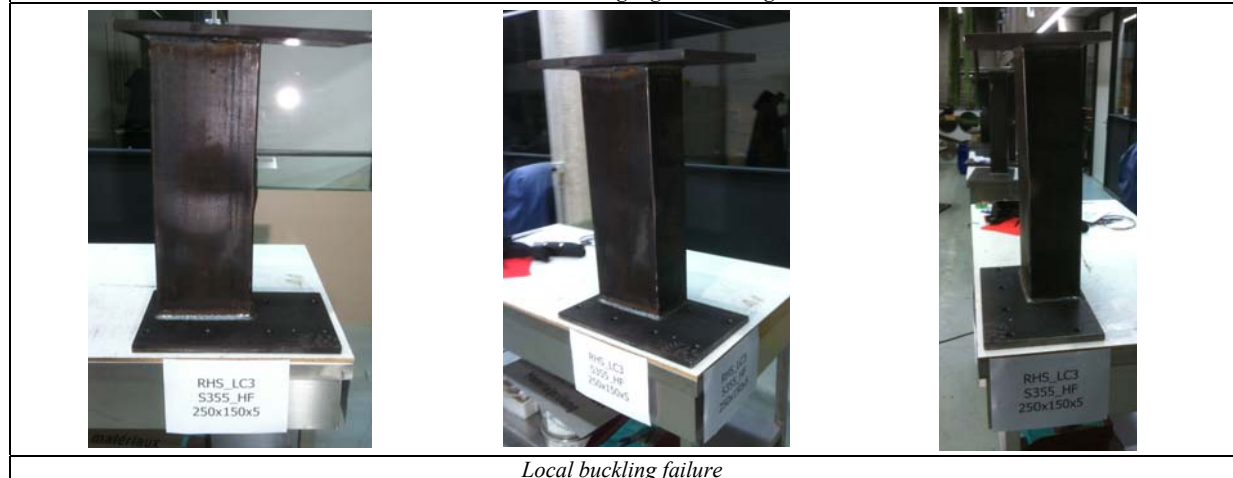
<p>Tensile coupons location</p> 	<p>Material stress-strain curves</p> 	<p>Material average properties</p> <table border="1"> <thead> <tr> <th></th> <th>Flat</th> <th>Corner</th> </tr> </thead> <tbody> <tr> <td>E [MPa]</td> <td>212190</td> <td>210750</td> </tr> <tr> <td>f_y [MPa]</td> <td>447</td> <td>435</td> </tr> <tr> <td>ϵ_y [%]</td> <td>0.21</td> <td>0.20</td> </tr> <tr> <td>f_u [MPa]</td> <td>576.6</td> <td>535</td> </tr> <tr> <td>ϵ_u [%]</td> <td>17.7</td> <td>11.7</td> </tr> </tbody> </table>		Flat	Corner	E [MPa]	212190	210750	f_y [MPa]	447	435	ϵ_y [%]	0.21	0.20	f_u [MPa]	576.6	535	ϵ_u [%]	17.7	11.7
	Flat	Corner																		
E [MPa]	212190	210750																		
f_y [MPa]	447	435																		
ϵ_y [%]	0.21	0.20																		
f_u [MPa]	576.6	535																		
ϵ_u [%]	17.7	11.7																		



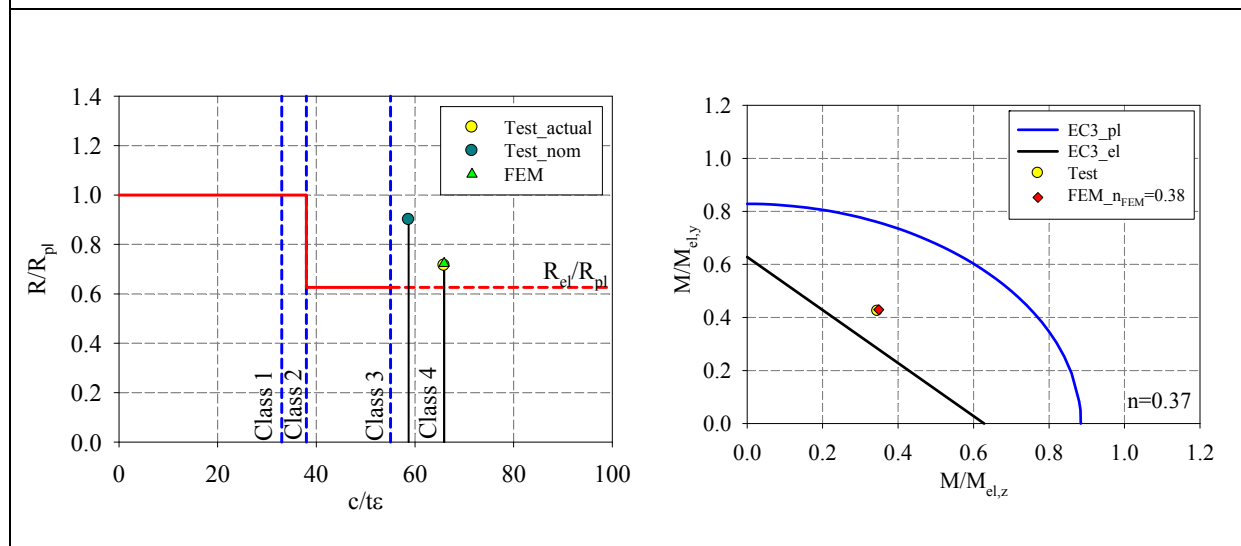
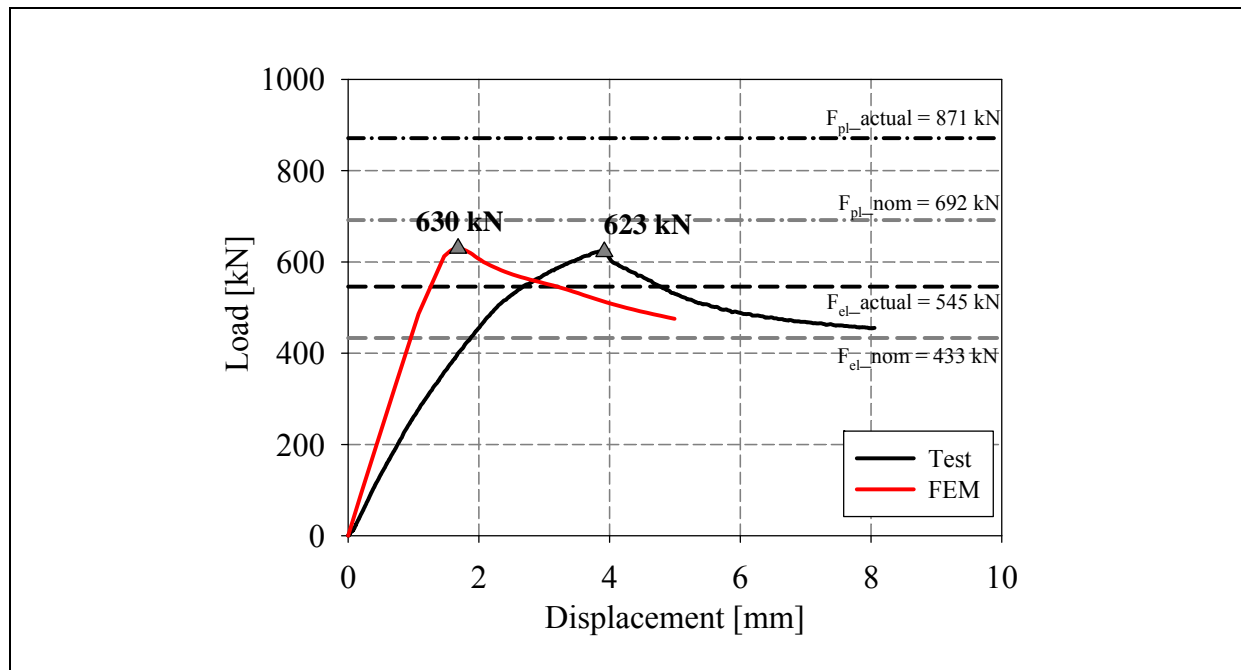




LVDT and strain gauges recordings

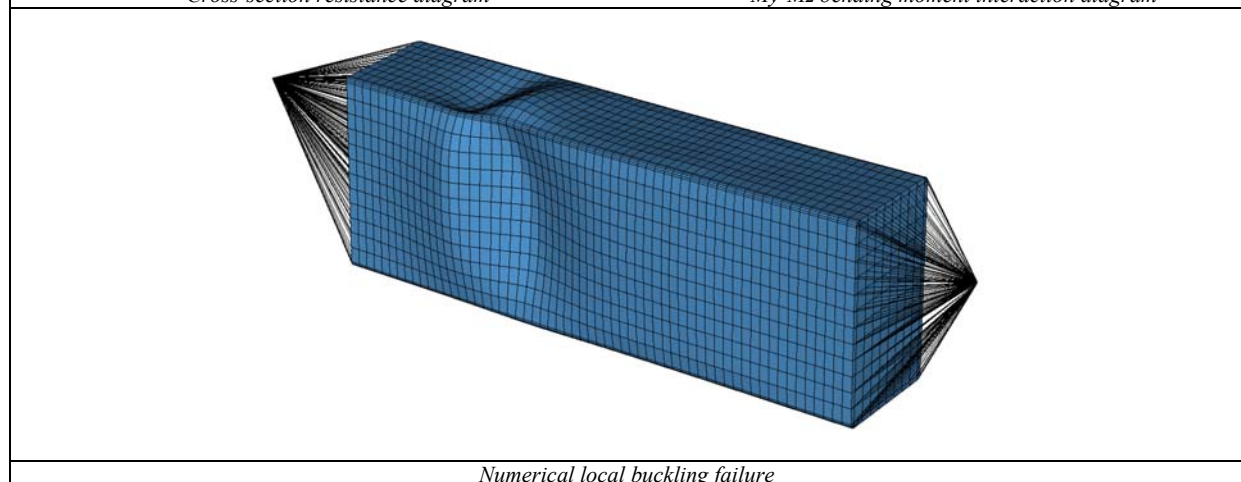


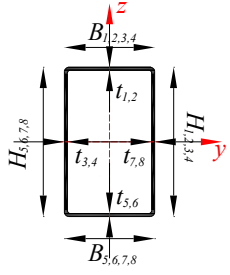
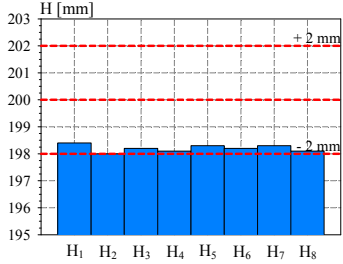
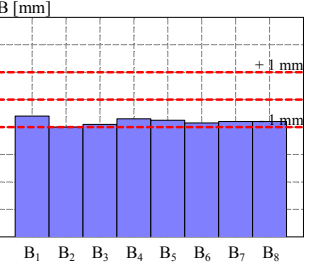
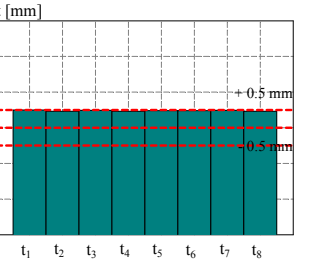
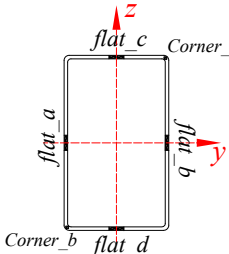
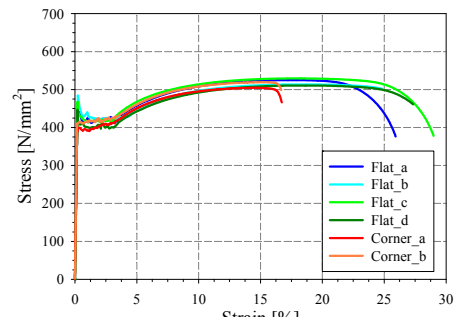
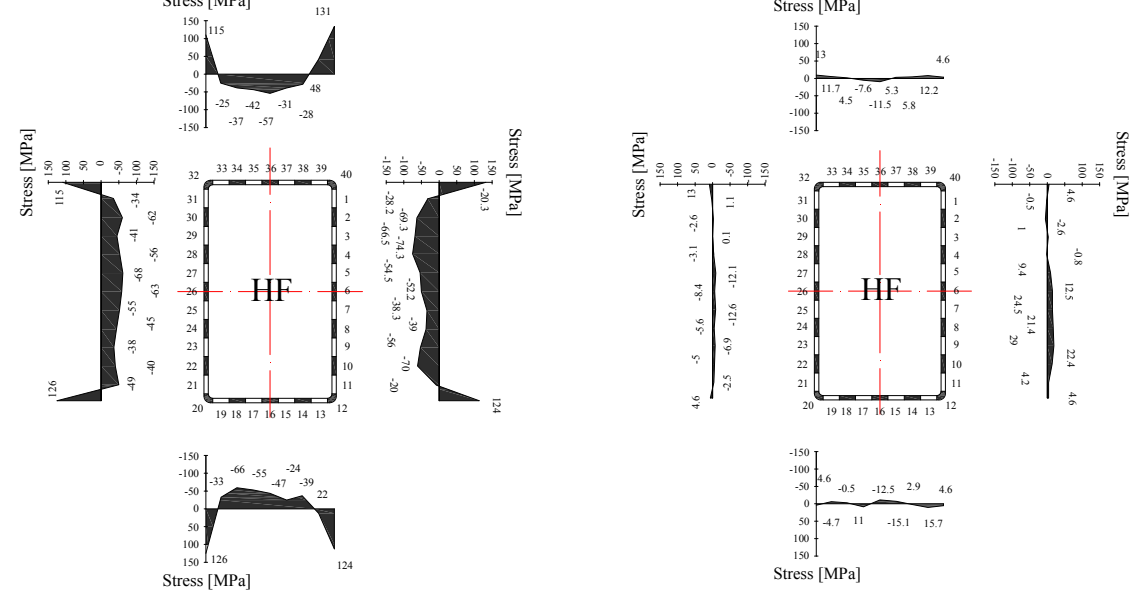
Local buckling failure

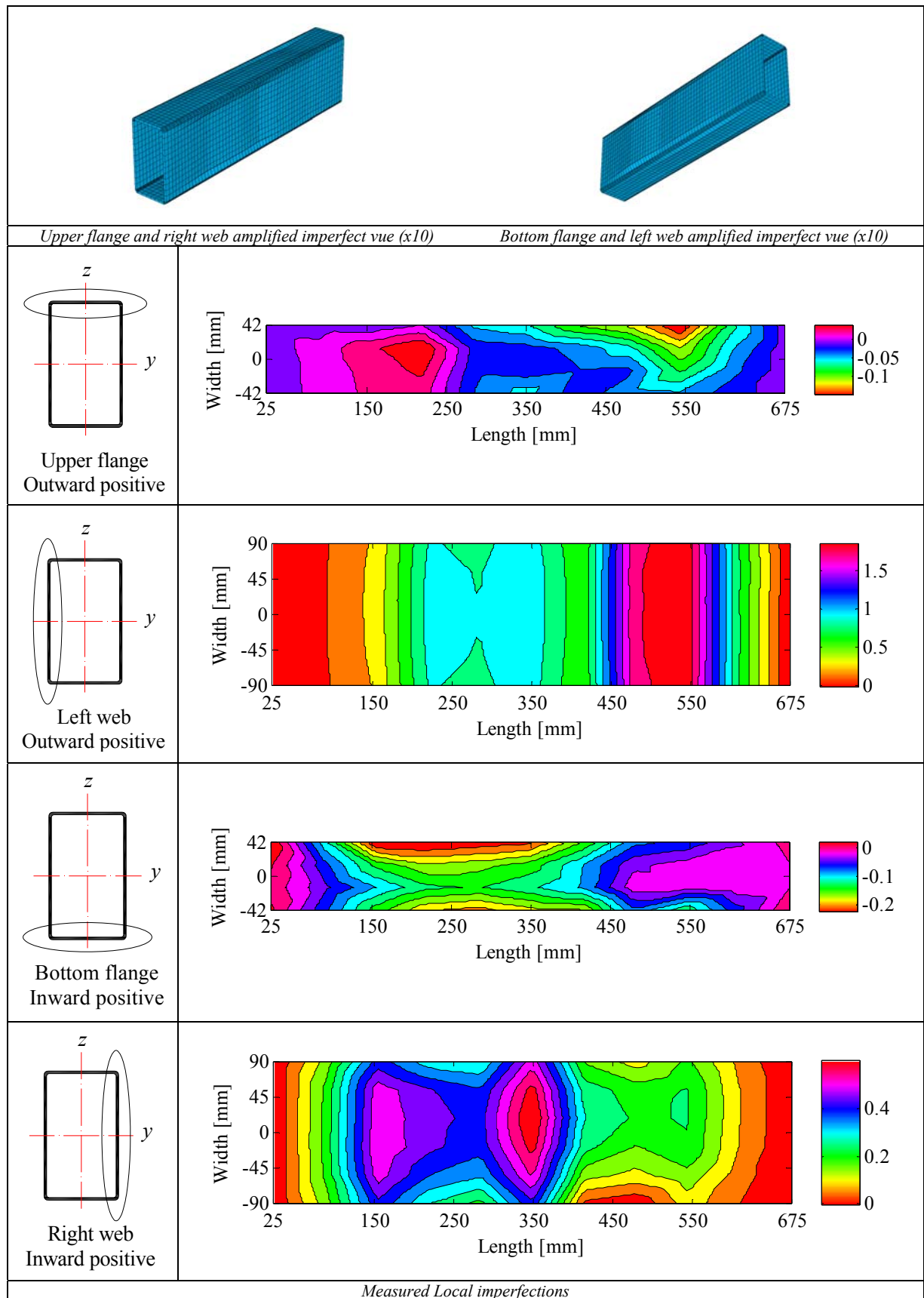


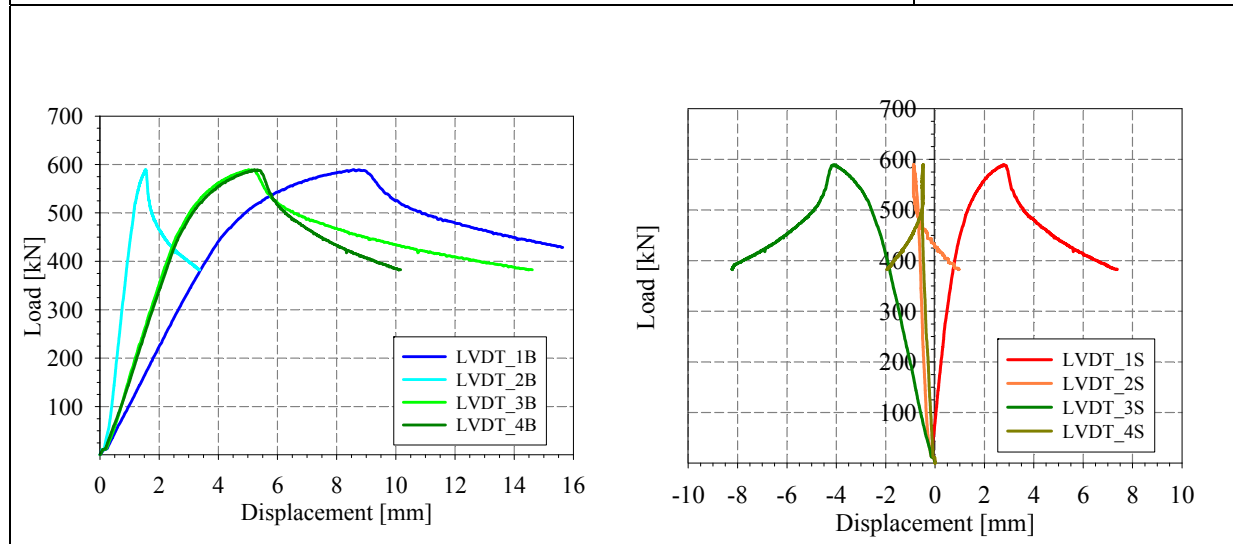
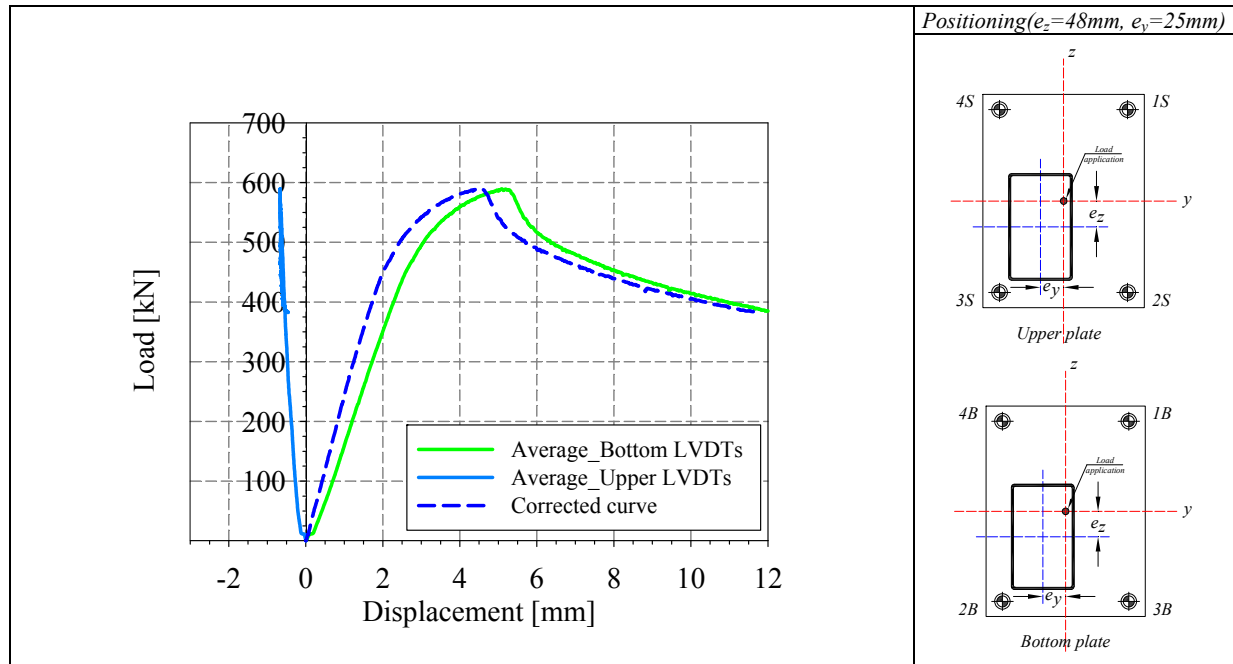
Cross-section resistance diagram

M_y - M_z bending moment interaction diagram



Specimen name	Shape	Details																		
<p>RHS_S355_LC3 200x100x5 HF</p>		<p>Shape: Rectangular Hollow Section Nominal yield limit: 355 MPa Load case: N(33%)+M_y(33%)+M_y(33%) H=200mm B=100mm t=5mm Fabrication process: Hot formed</p>																		
<p>Average h= 198.2 mm</p> 	<p>Average b= 99.2 mm</p> 	<p>Average t= 5.48 mm</p> 																		
<i>Cross-sectional measured dimensions and tolerances</i>																				
 	<table border="1"> <thead> <tr> <th></th> <th>Flat</th> <th>Corner</th> </tr> </thead> <tbody> <tr> <td>E [MPa]</td> <td>215000</td> <td>210394</td> </tr> <tr> <td>f_y [MPa]</td> <td>420</td> <td>411</td> </tr> <tr> <td>ε_y [%]</td> <td>0.19</td> <td>0.19</td> </tr> <tr> <td>f_u [MPa]</td> <td>520</td> <td>512</td> </tr> <tr> <td>ε_u [%]</td> <td>17.5</td> <td>14.7</td> </tr> </tbody> </table>			Flat	Corner	E [MPa]	215000	210394	f _y [MPa]	420	411	ε _y [%]	0.19	0.19	f _u [MPa]	520	512	ε _u [%]	17.5	14.7
	Flat	Corner																		
E [MPa]	215000	210394																		
f _y [MPa]	420	411																		
ε _y [%]	0.19	0.19																		
f _u [MPa]	520	512																		
ε _u [%]	17.5	14.7																		
<i>Tensile coupons location</i>	<i>Material stress-strain curves</i>	<i>Material average properties</i>																		
 <div style="display: flex; justify-content: space-around;"> <div data-bbox="308 1827 698 1900"> <p>Membrane stresses</p> </div> <div data-bbox="1088 1827 1461 1900"> <p>Flexural stresses</p> </div> </div> <p style="text-align: center;"><i>Measured residual stresses distributions</i></p>																				

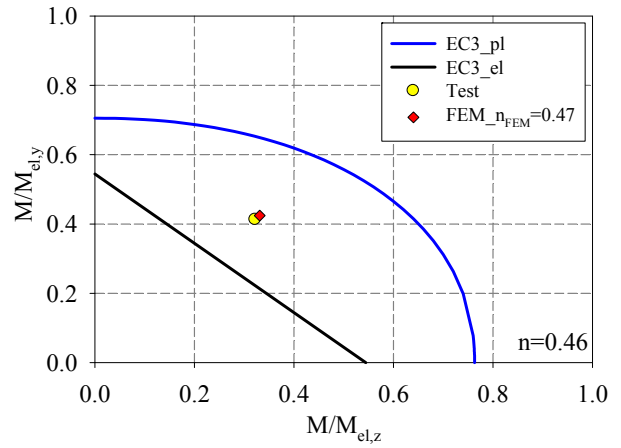
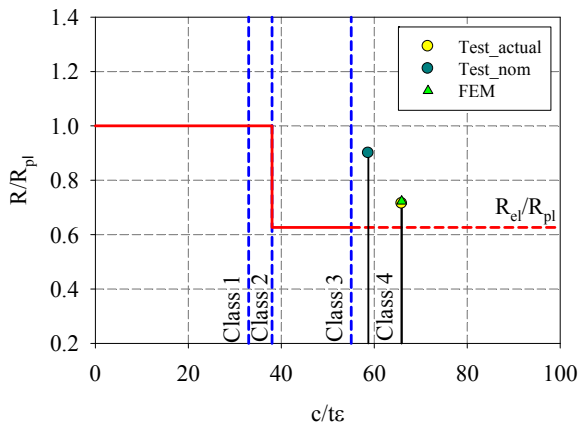
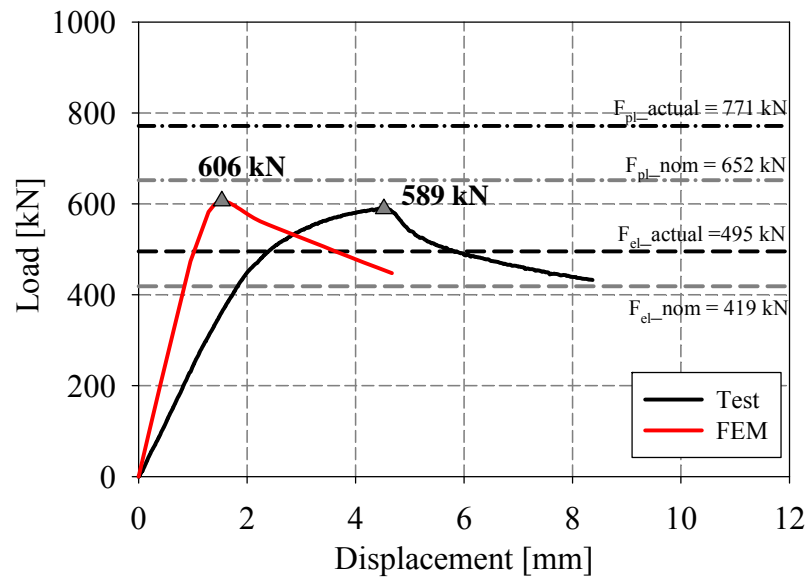




LVDT and strain gauges recordings

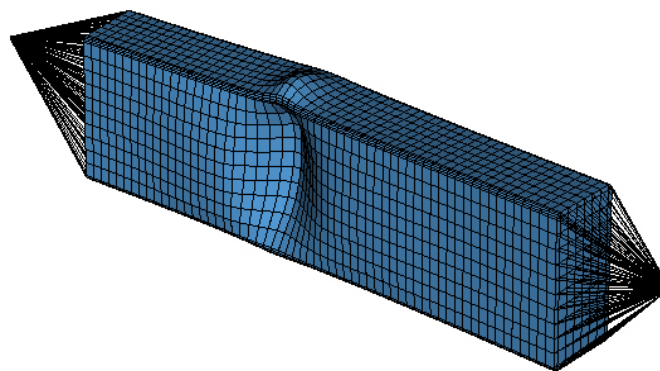


Local buckling failure

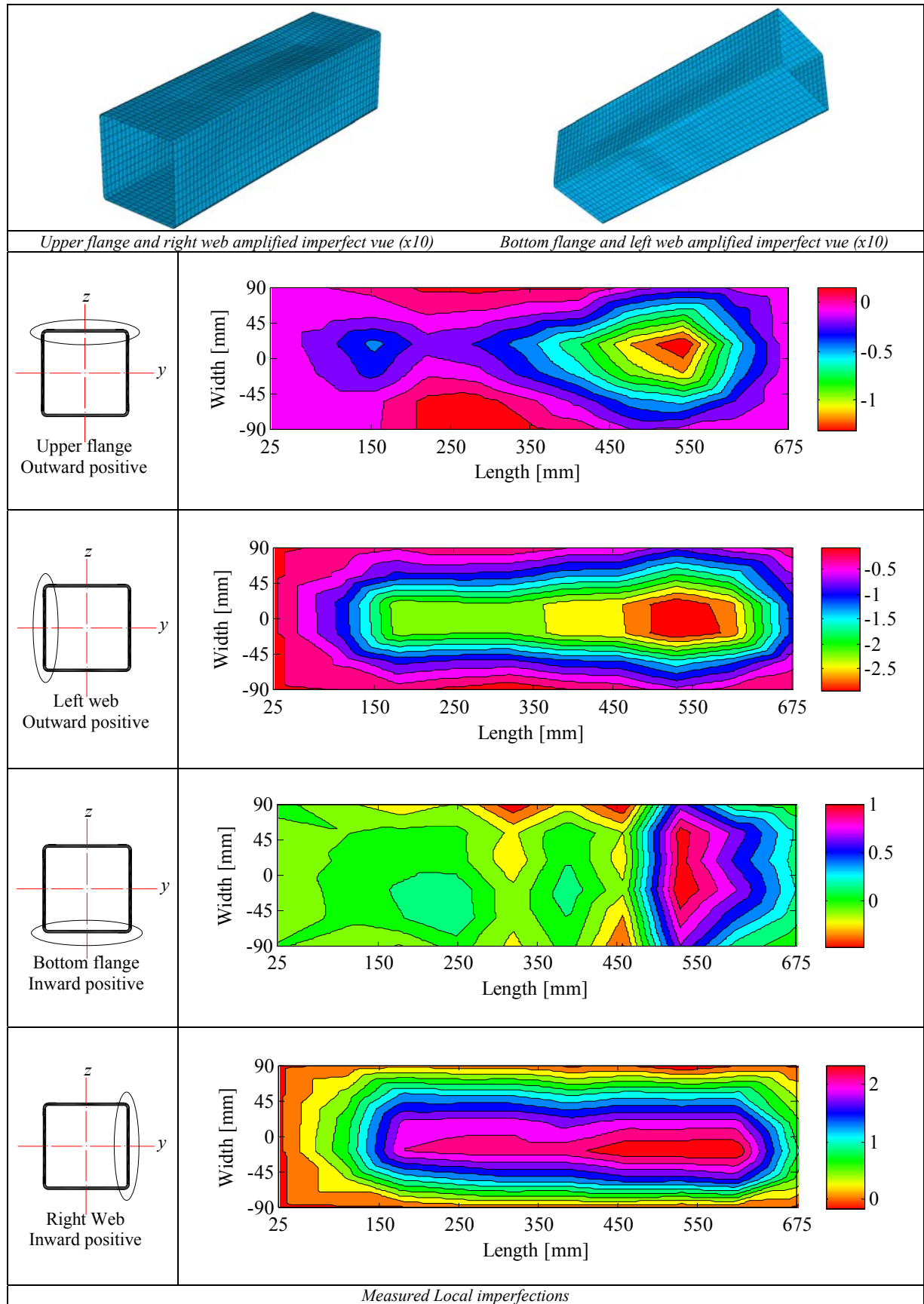


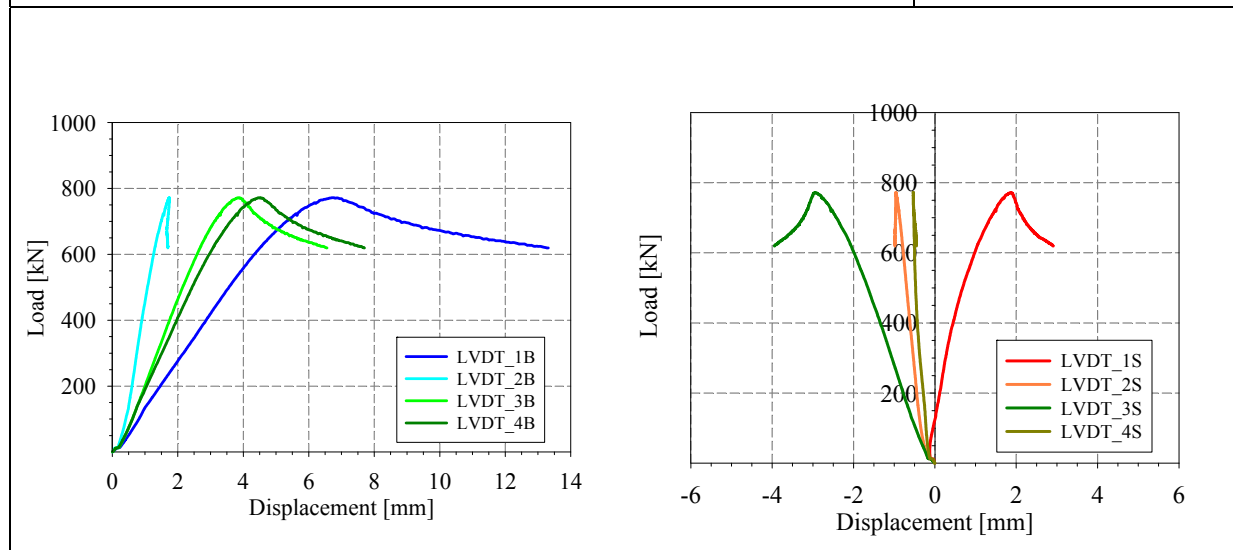
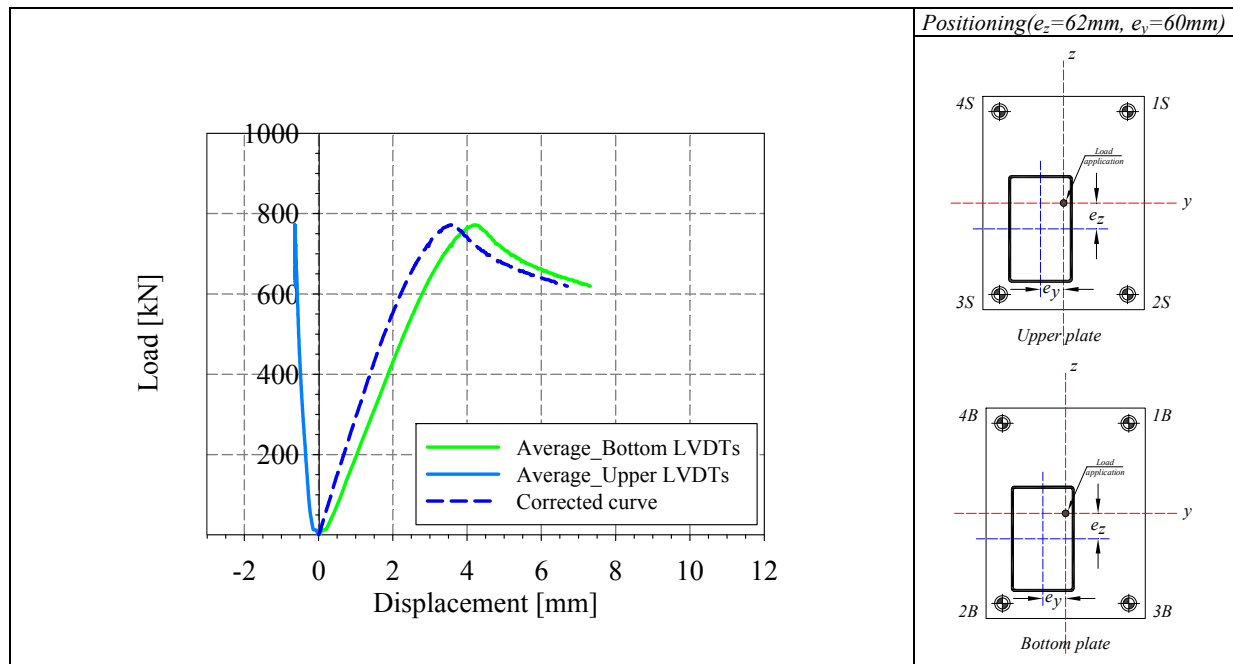
Cross-section resistance diagram

My-Mz bending moment interaction diagram

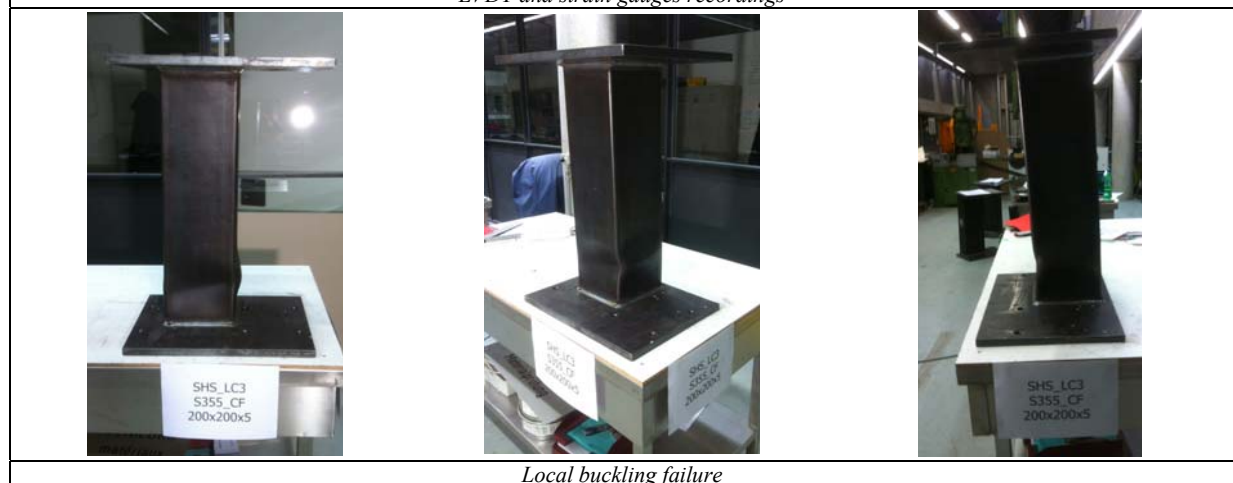


Numerical local buckling failure

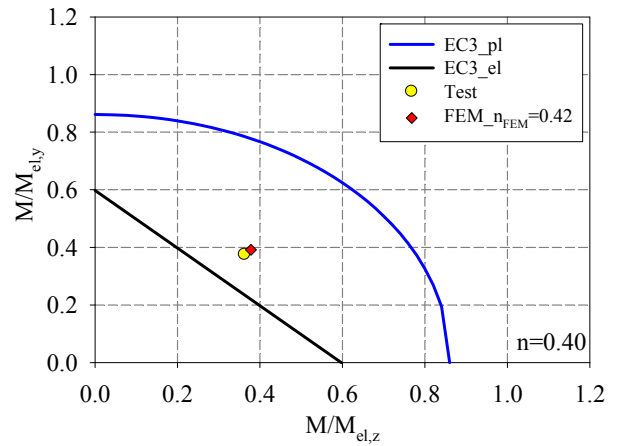
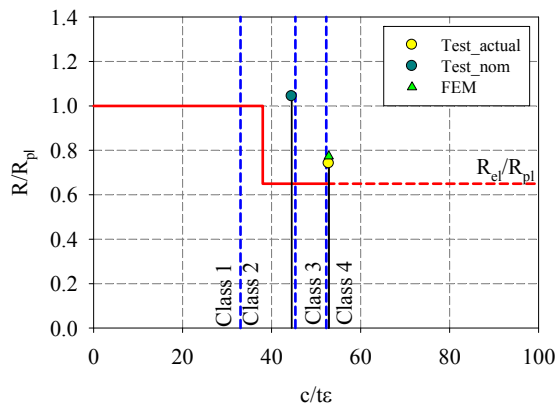
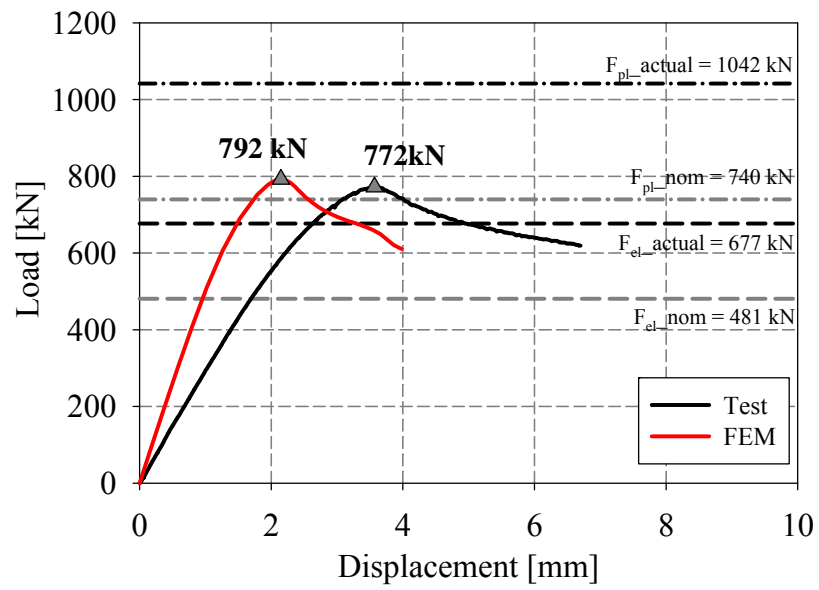




LVDT and strain gauges recordings

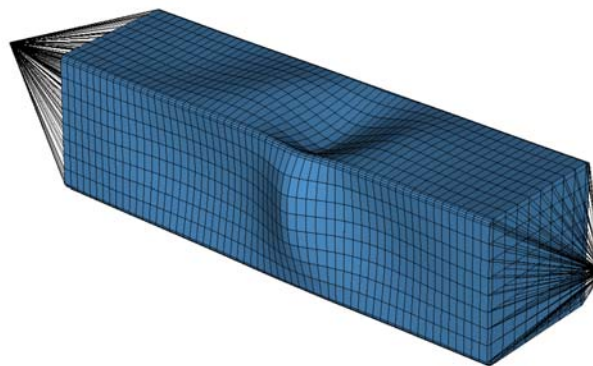


Local buckling failure



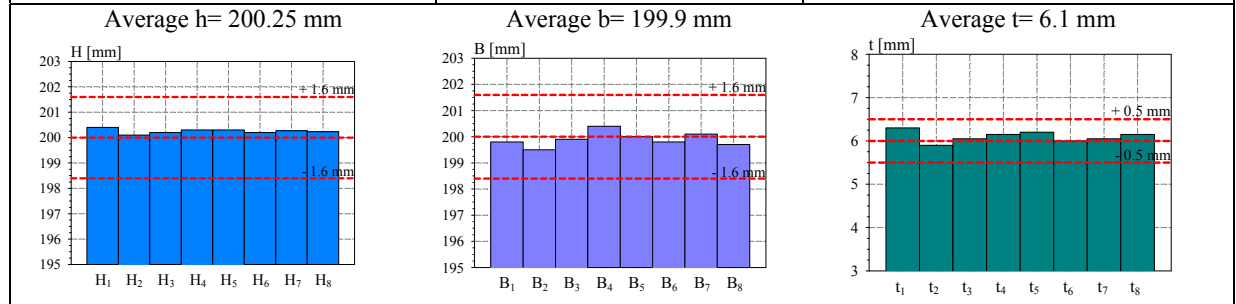
Cross-section resistance diagram

My-Mz bending moment interaction diagram



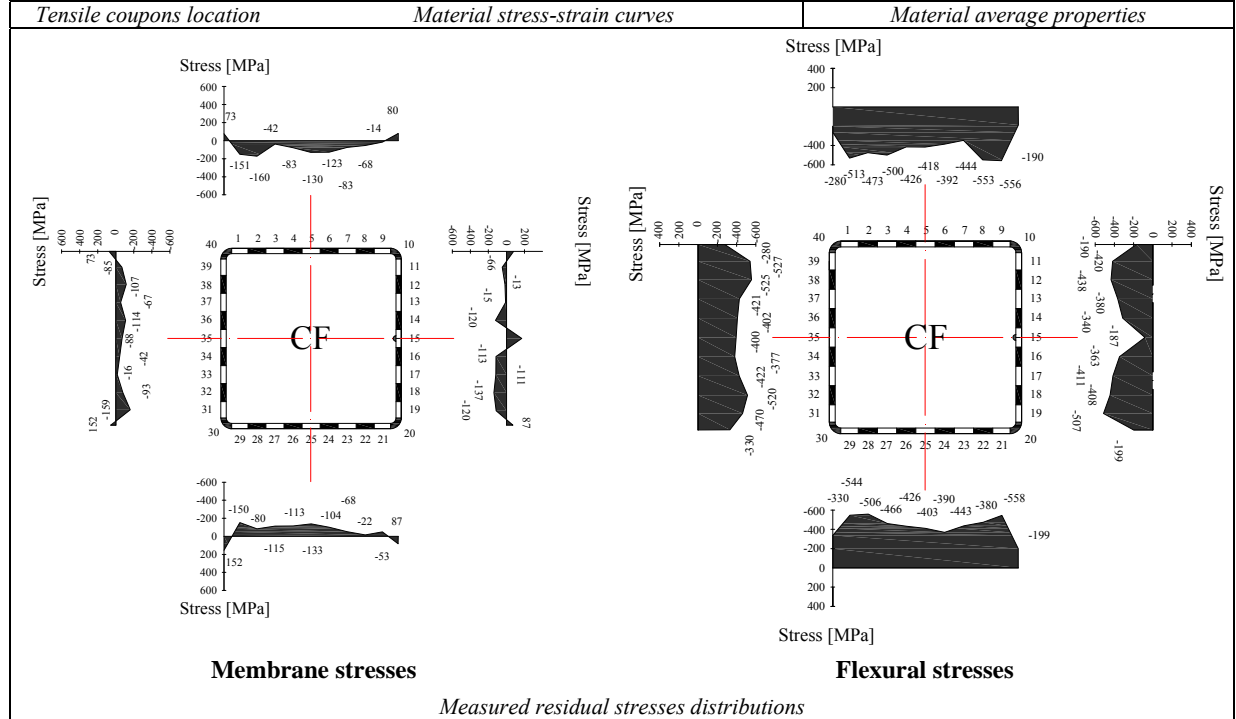
Numerical local buckling failure

Specimen name	Shape	Details
RHS_S355_LC3 200x200x6 CF		Shape: Square Hollow Section Nominal yield limit: 355 MPa Load case: N(33%)+M _y (33%)+M _z (33%) H=200mm B=200mm t=6mm Fabrication process: Cold formed



Cross-sectional measured dimensions and tolerances

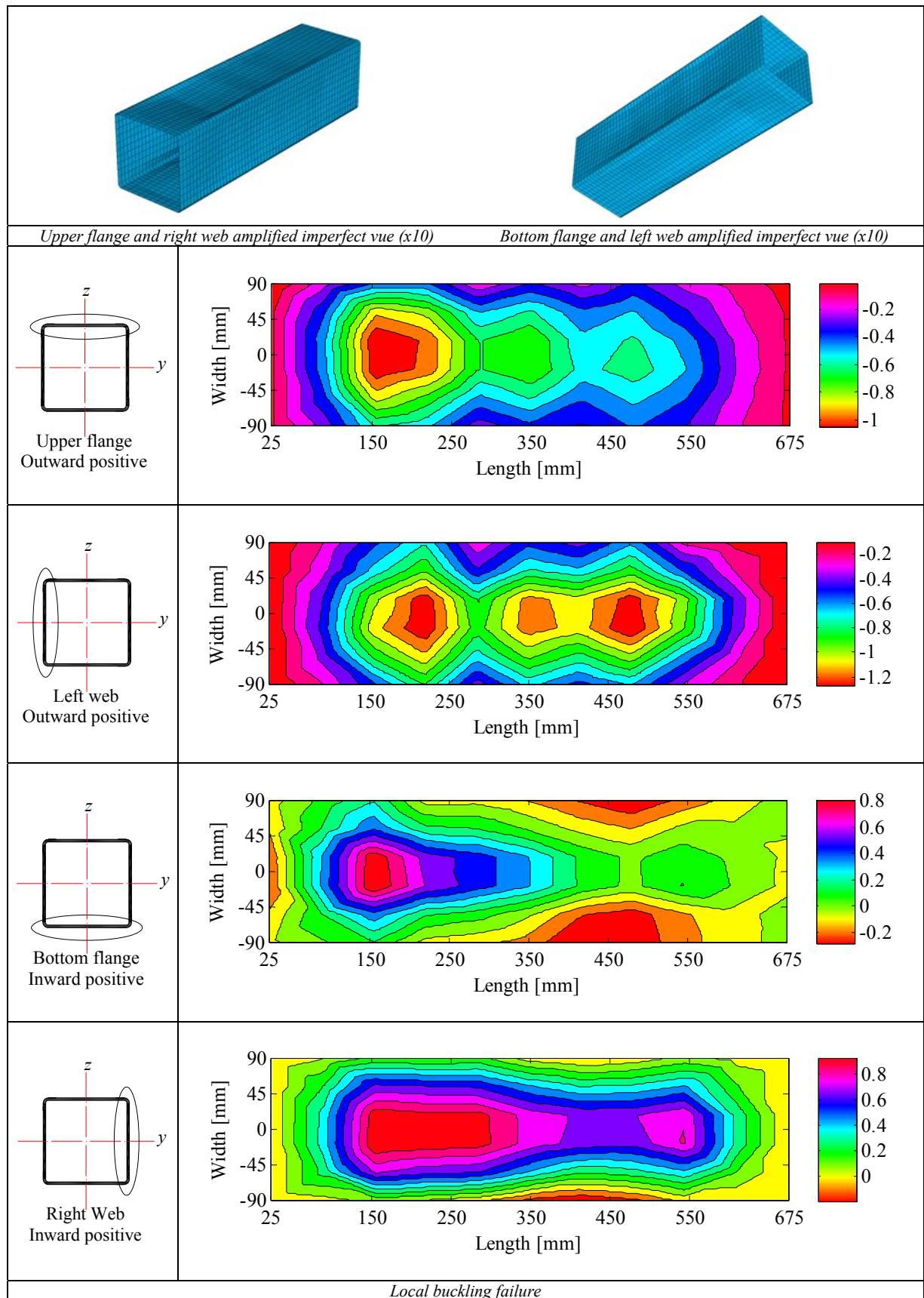
Tensile coupons location	Material stress-strain curves	Material average properties		
		Flat	Corner	
		E [MPa]	217363	210500
		f _y [MPa]	500.5	-
		ε _y [%]	0.23	-
		f _u [MPa]	596	617.8
		ε _u [%]	13.8	1.1

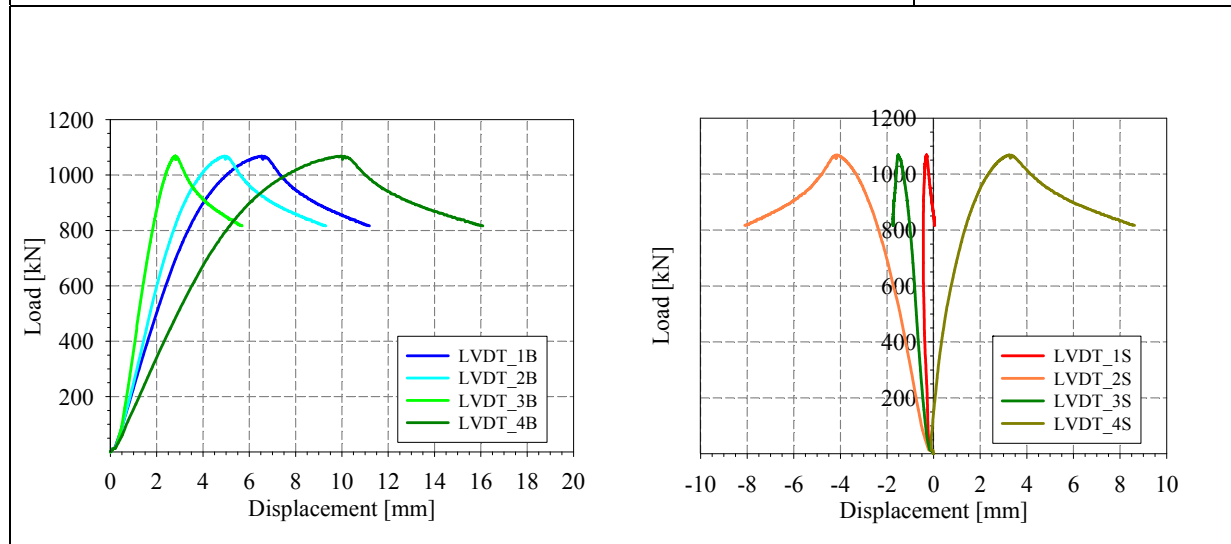
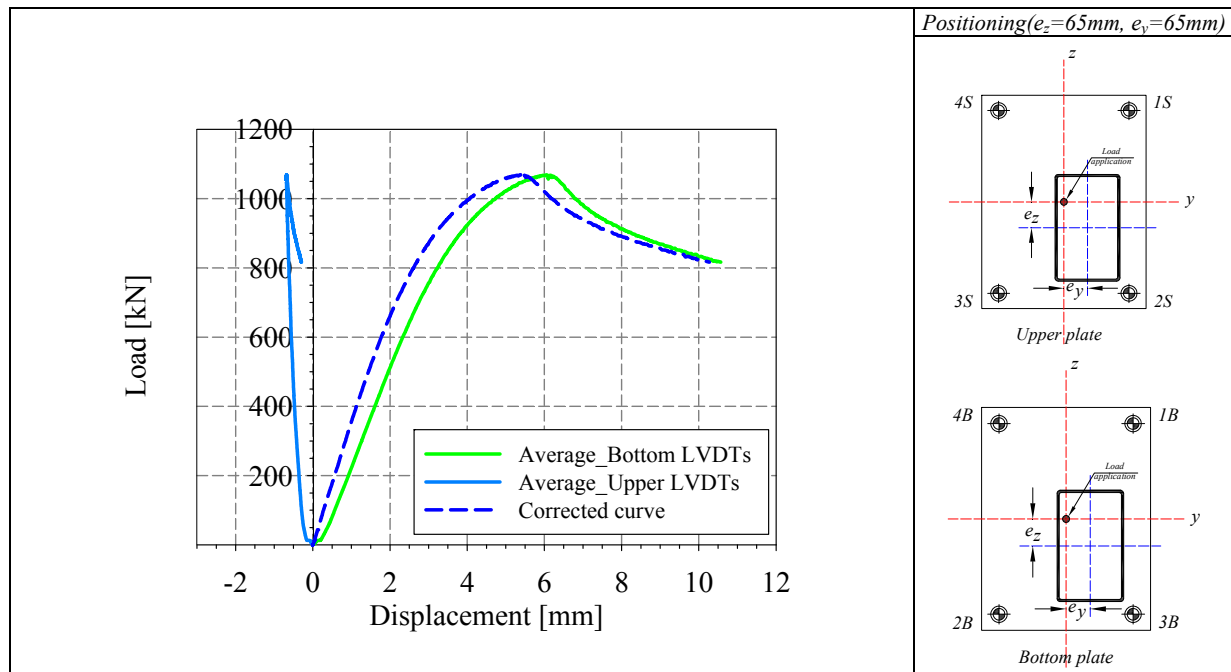


Membrane stresses

Flexural stresses

Measured residual stresses distributions

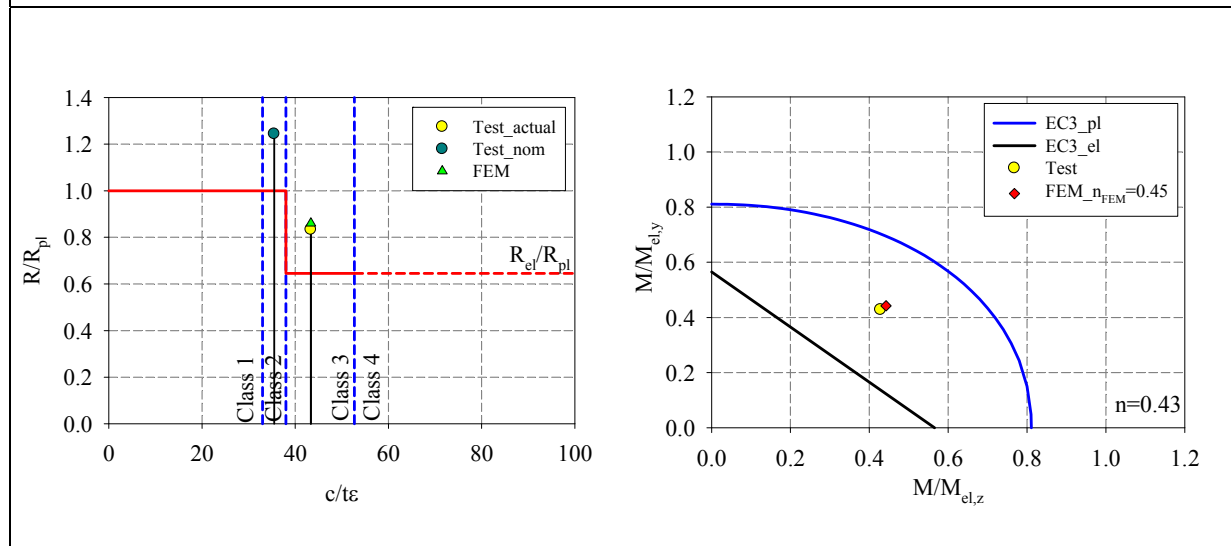
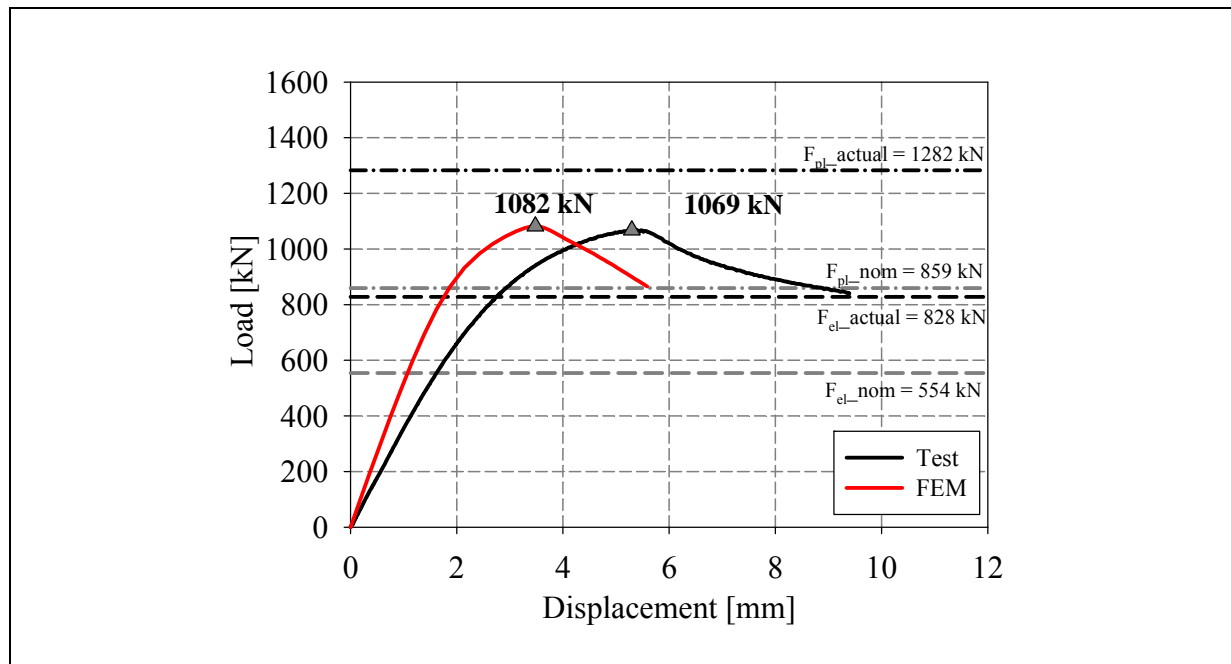




LVDT and strain gauges recordings

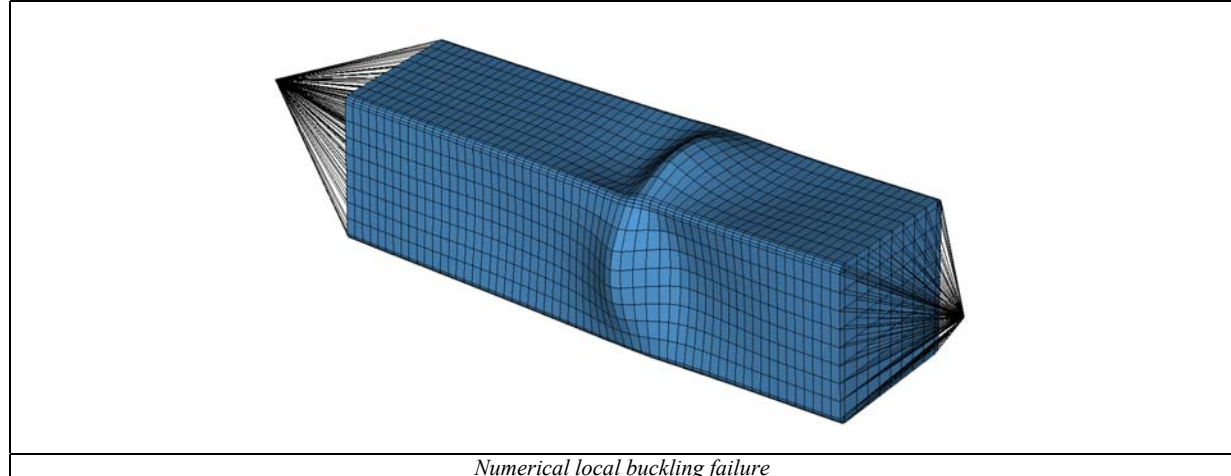


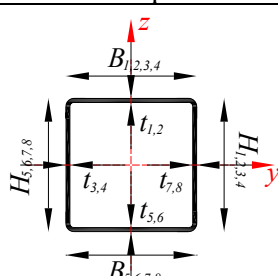
Local buckling failure

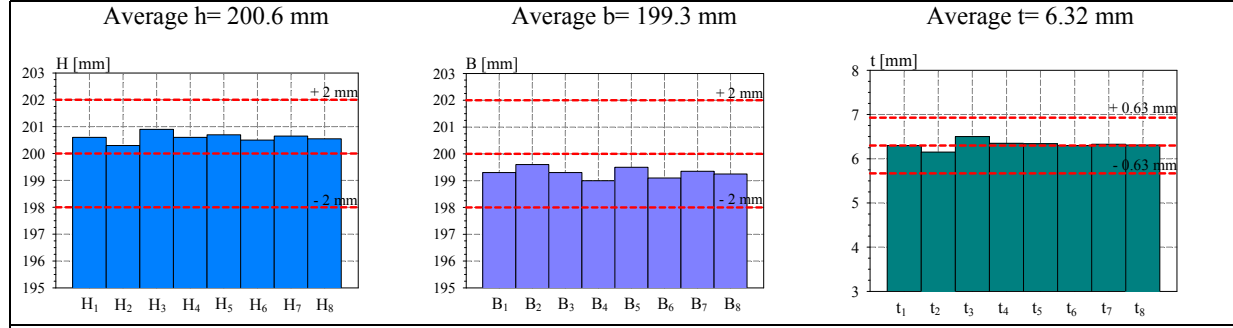


Cross-section resistance diagram

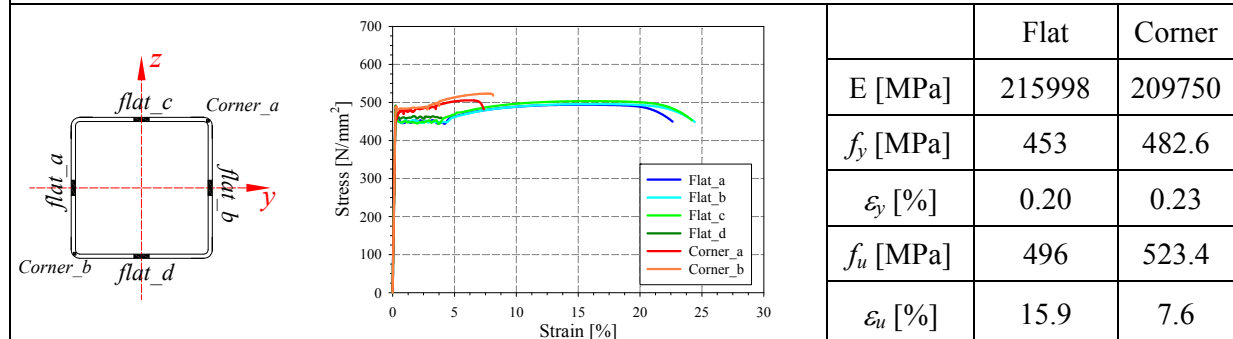
My-Mz bending moment interaction diagram



<p>Specimen name</p> <p>RHS_S355_LC3 200x200x6.3 HF</p>	<p>Shape</p> 	<p>Details</p> <p>Shape: Square Hollow Section Nominal yield limit: 355 MPa Load case: N (50%) + M_y (50%) H=200mm B=200mm t=6mm Fabrication process: Hot formed</p>
---	--	---



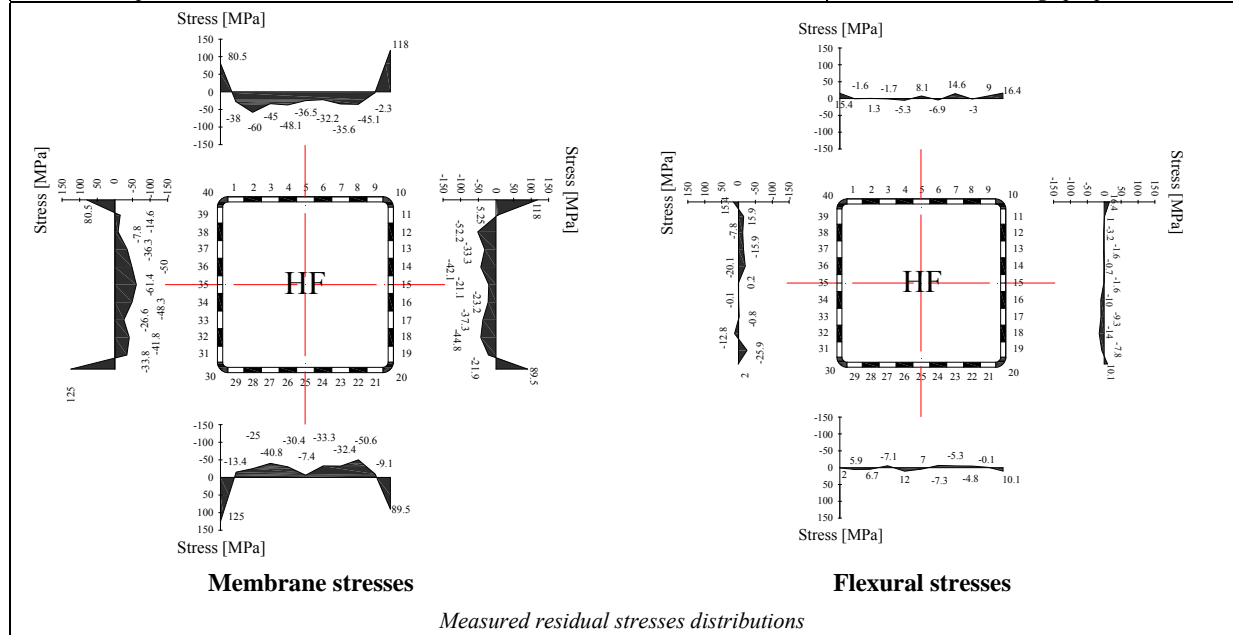
Cross-sectional measured dimensions and tolerances

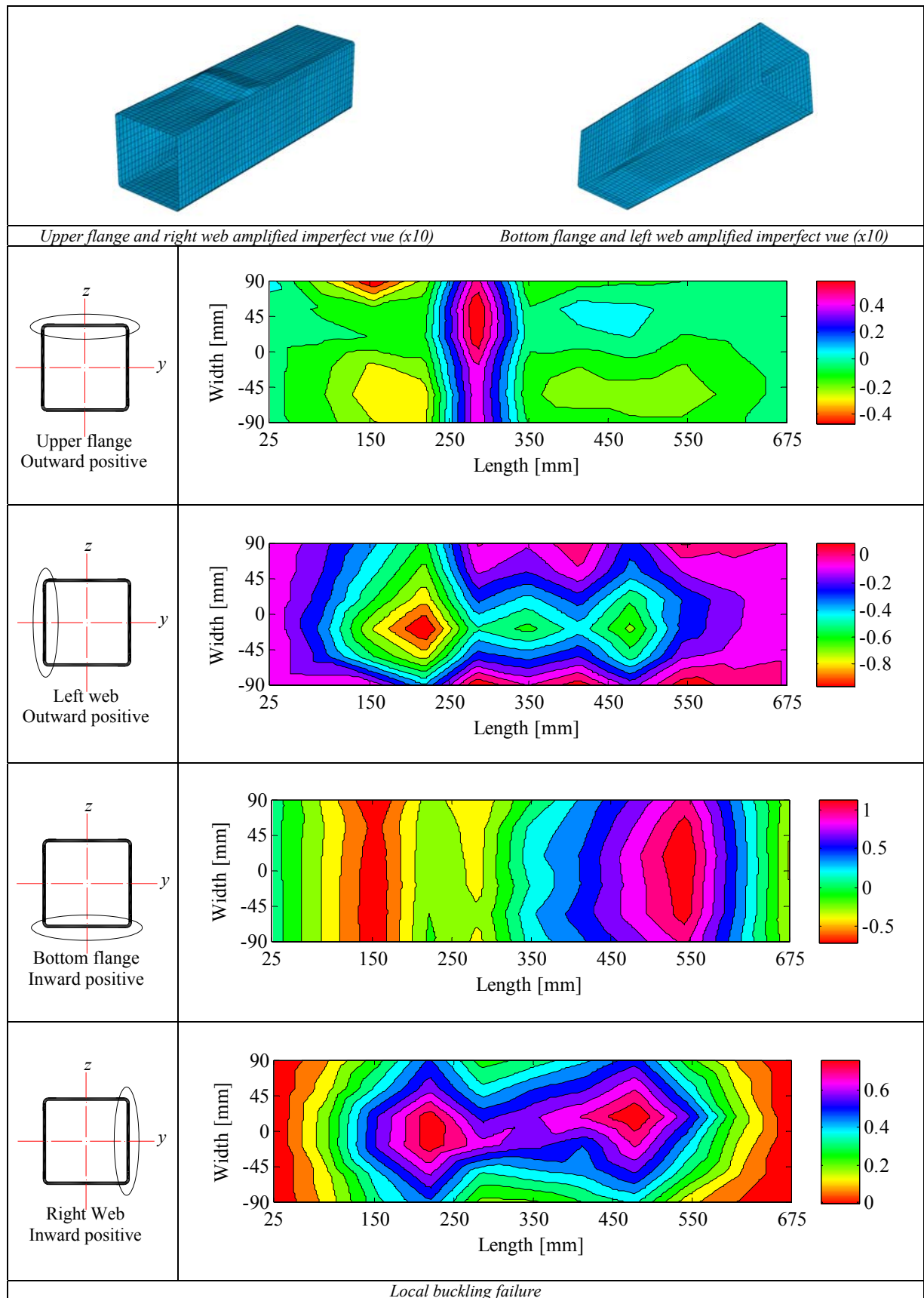


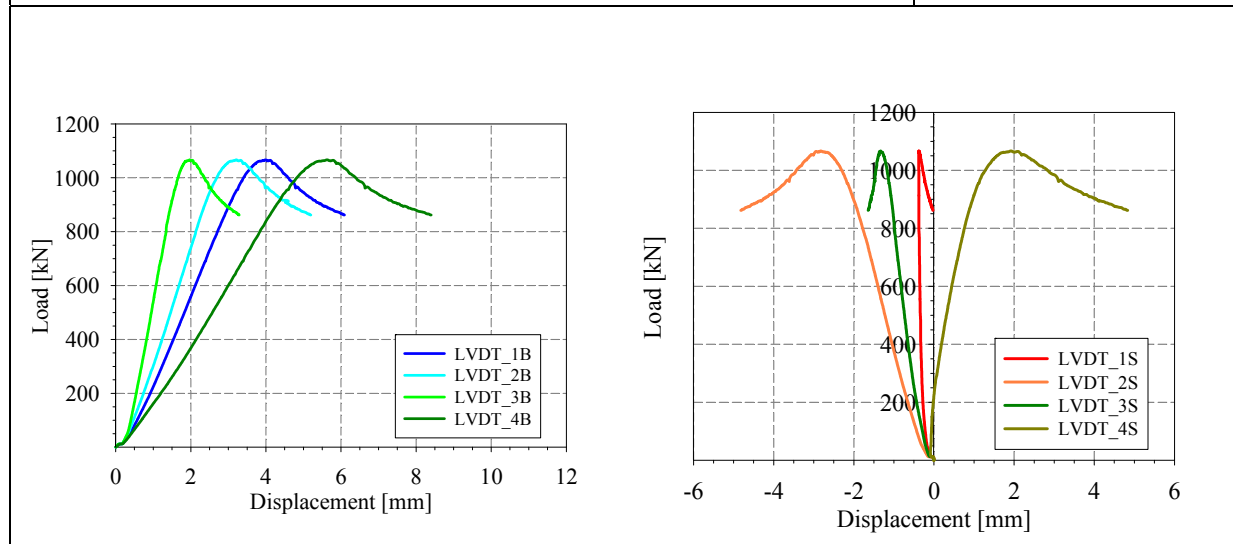
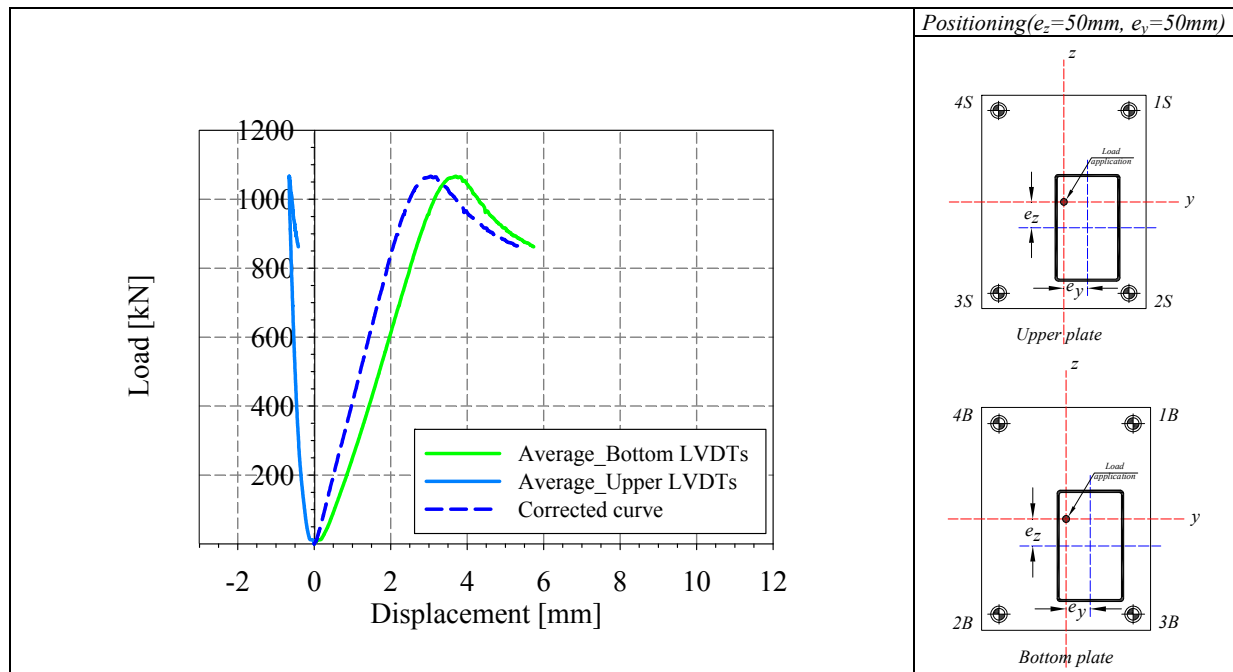
Tensile coupons location

Material stress-strain curves

Material average properties



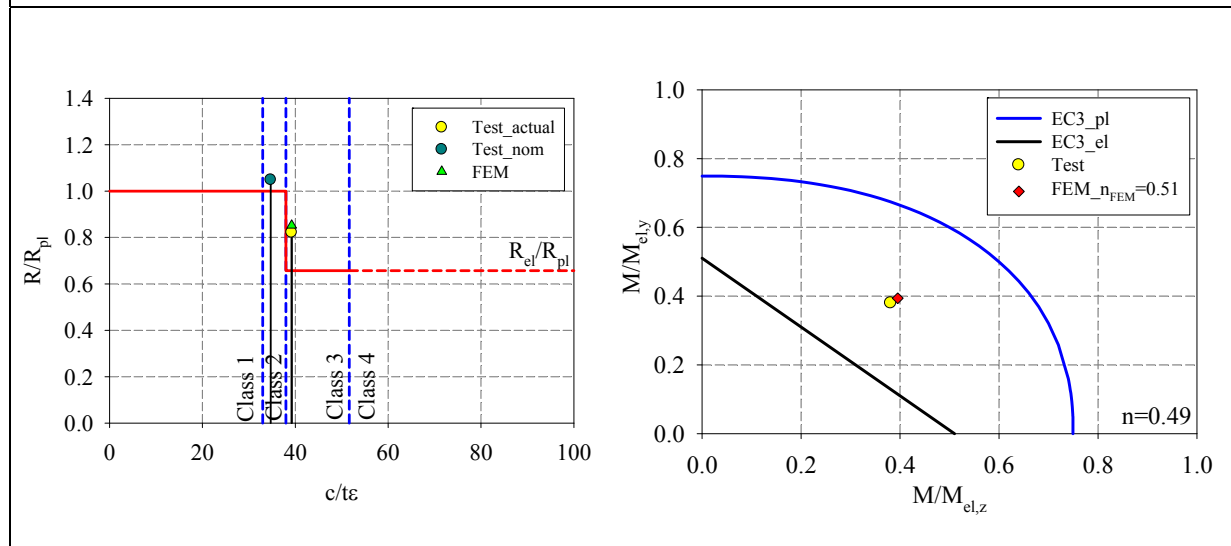
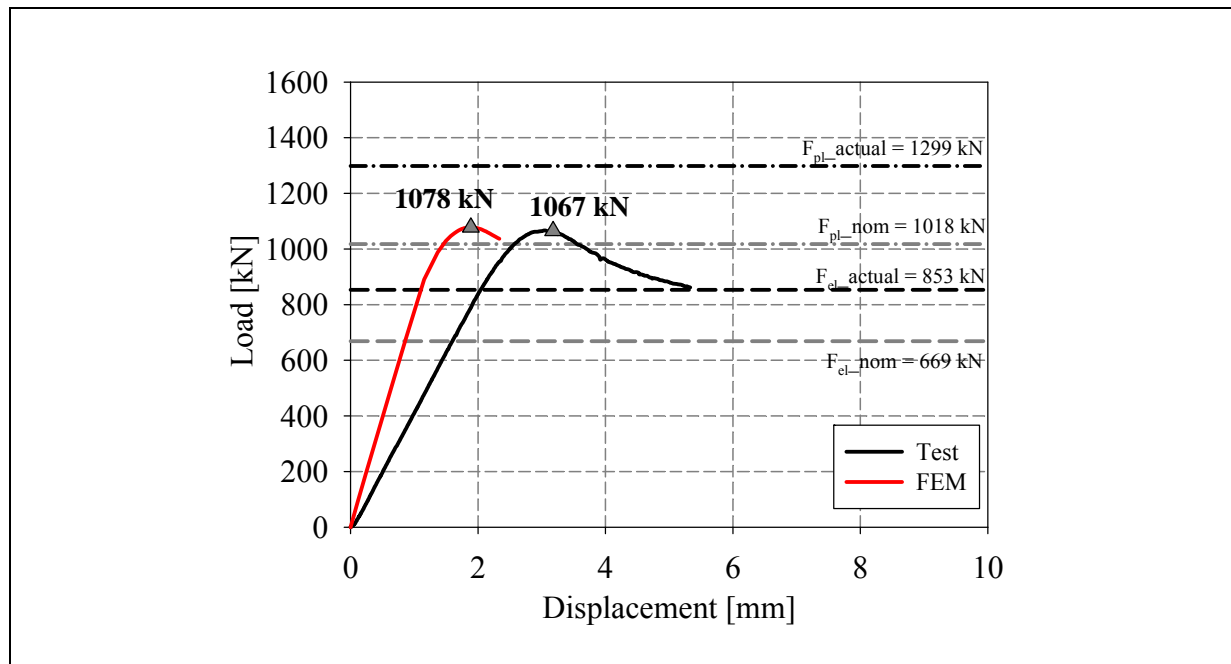




LVDT and strain gauges recordings

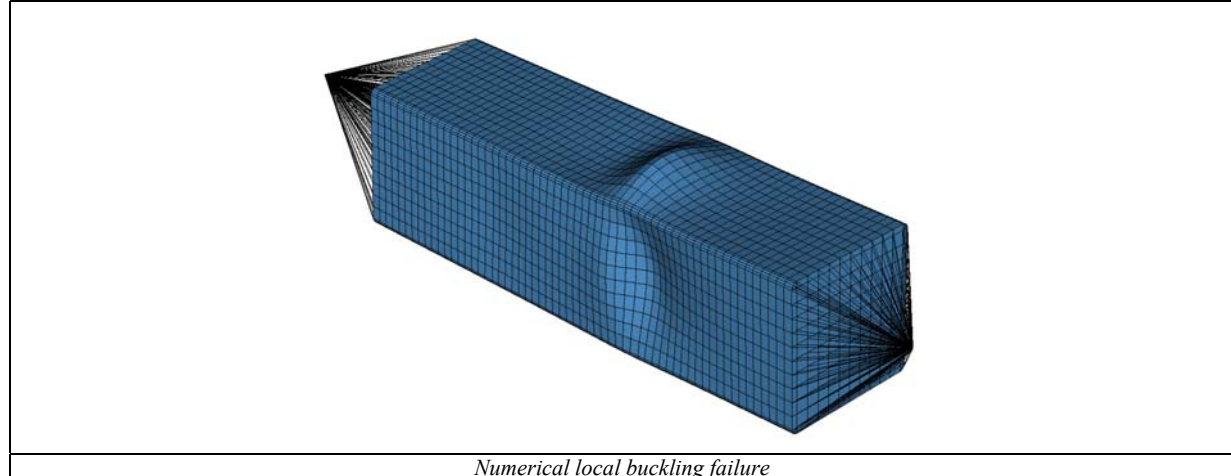


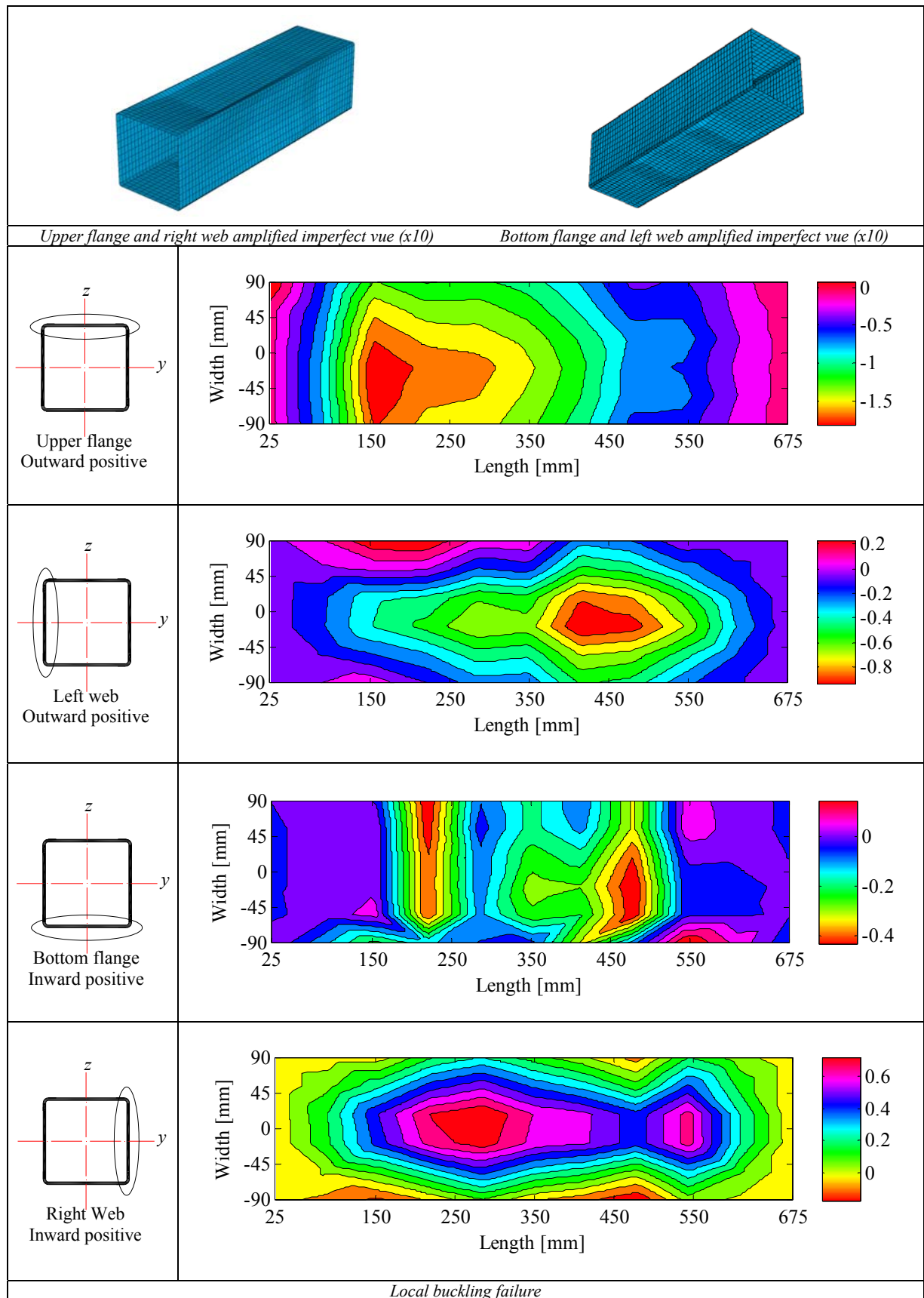
Local buckling failure

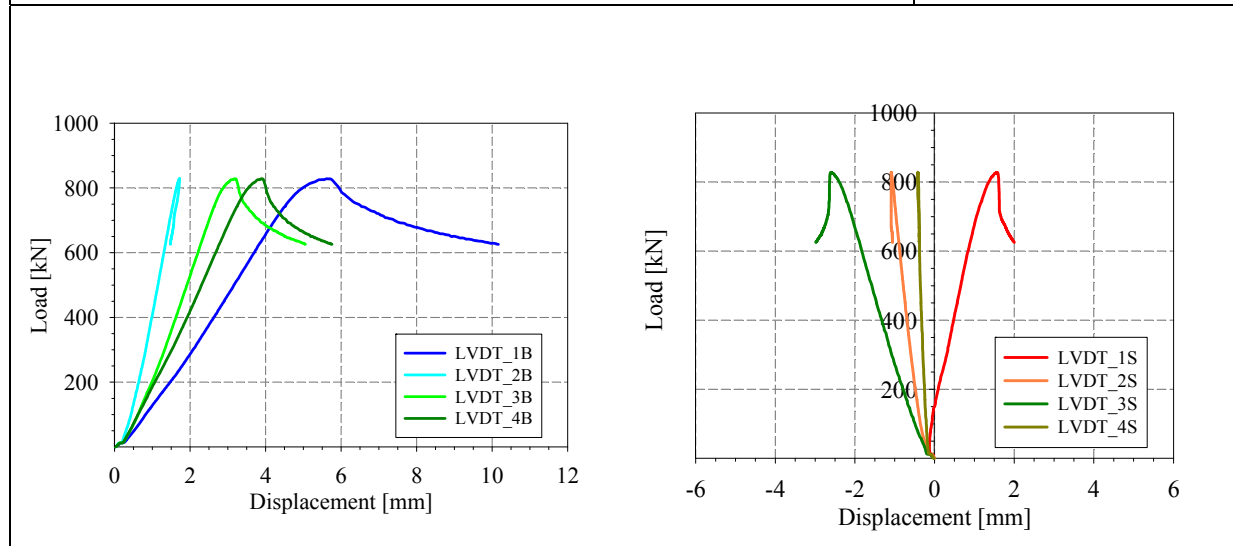
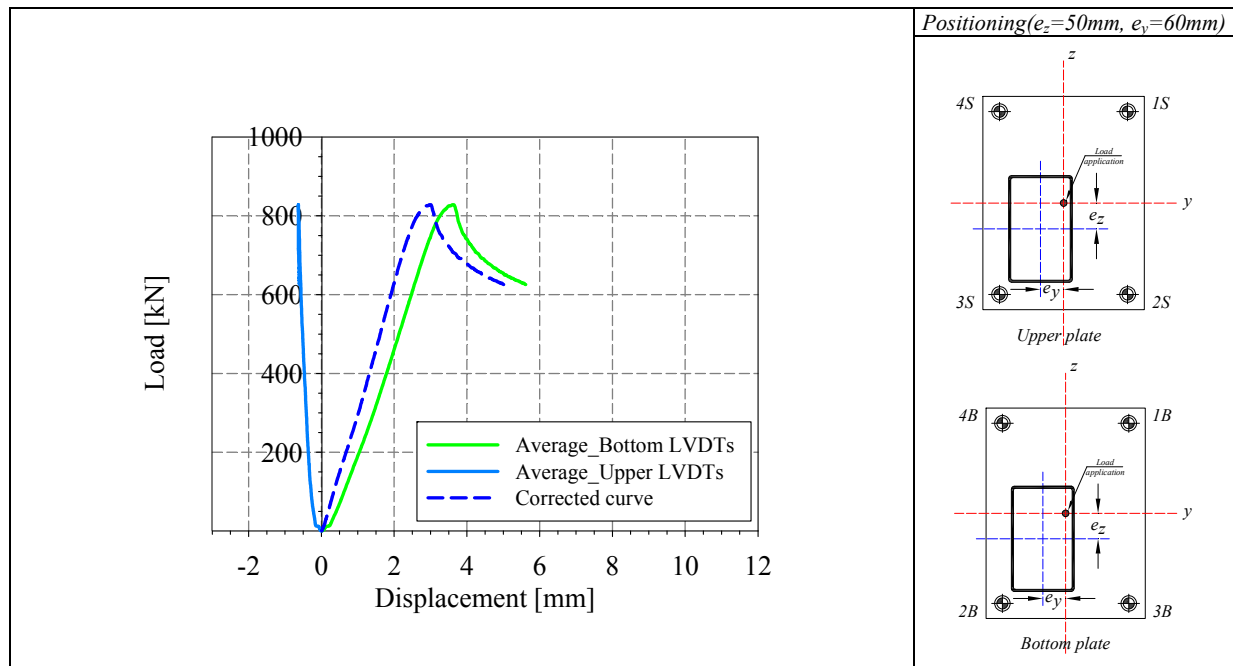


Cross-section resistance diagram

My-Mz bending moment interaction diagram



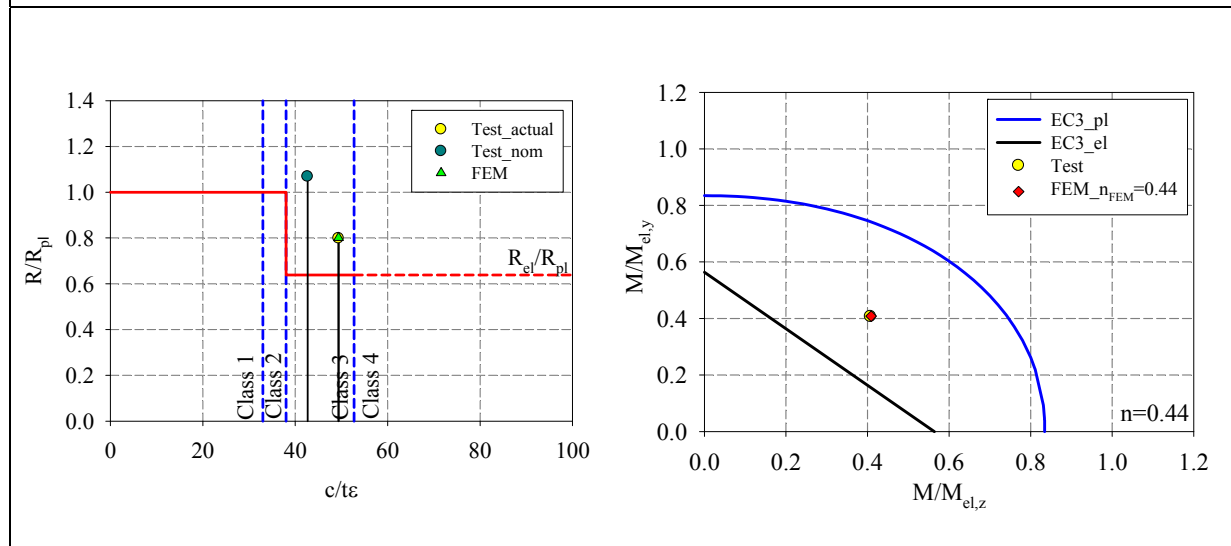
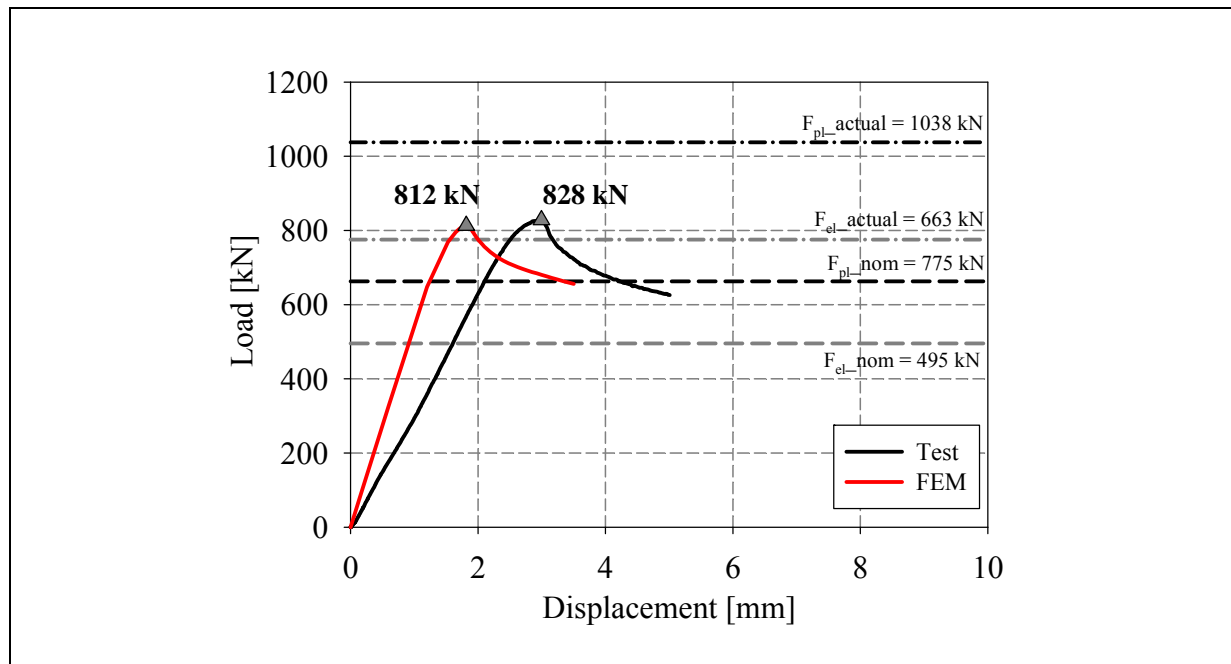




LVDT and strain gauges recordings

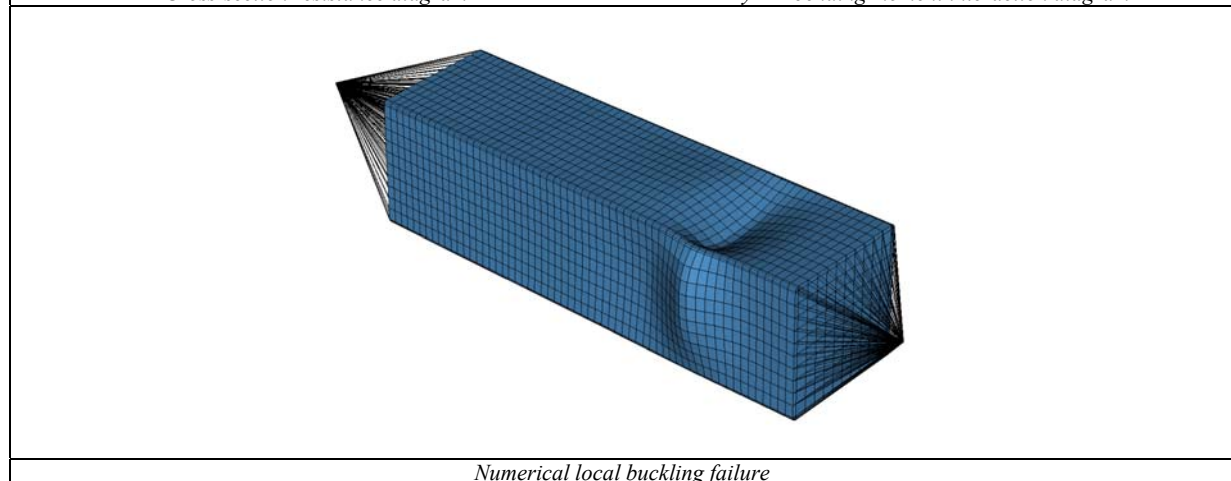


Local buckling failure

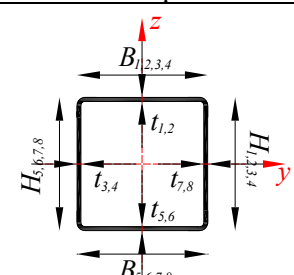


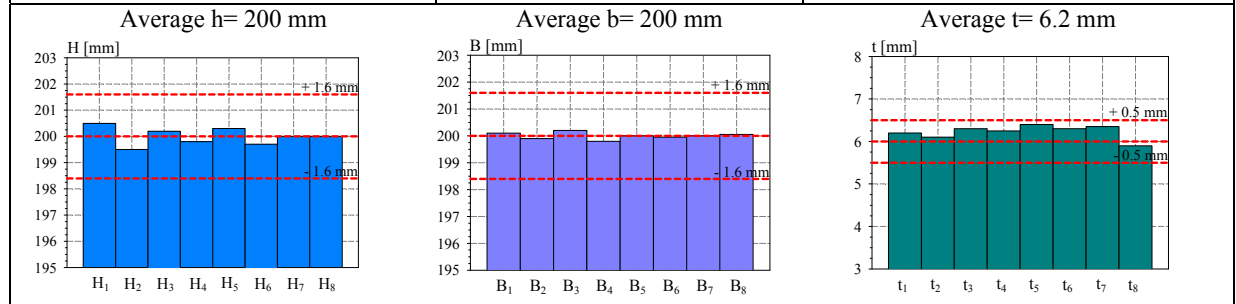
Cross-section resistance diagram

My-Mz bending moment interaction diagram

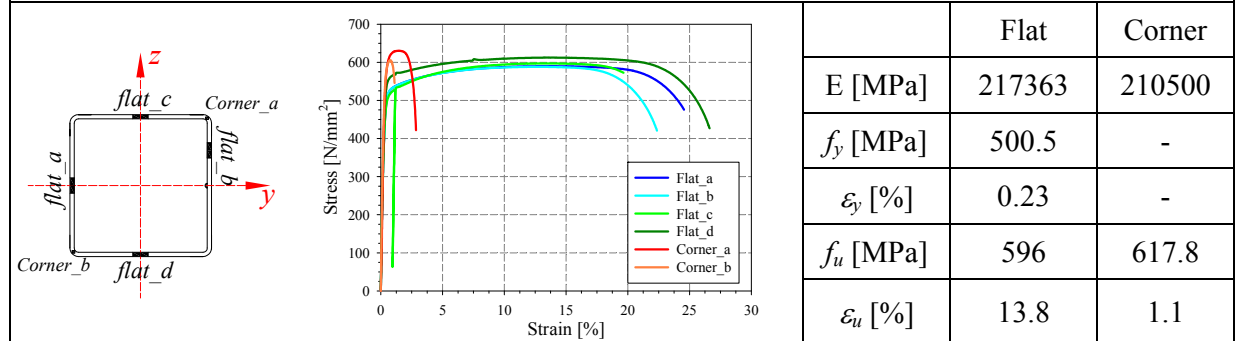


Numerical local buckling failure

<p>Specimen name</p> <p>RHS_S355_LC3 200x200x6 CF_2</p>	<p>Shape</p> 	<p>Details</p> <p>Shape: Square Hollow Section Nominal yield limit: 355 MPa Load case: N(33%)+M_y(33%)+M_z(33%) H=200mm B=200mm t=6mm Fabrication process: Cold formed</p>
---	--	--



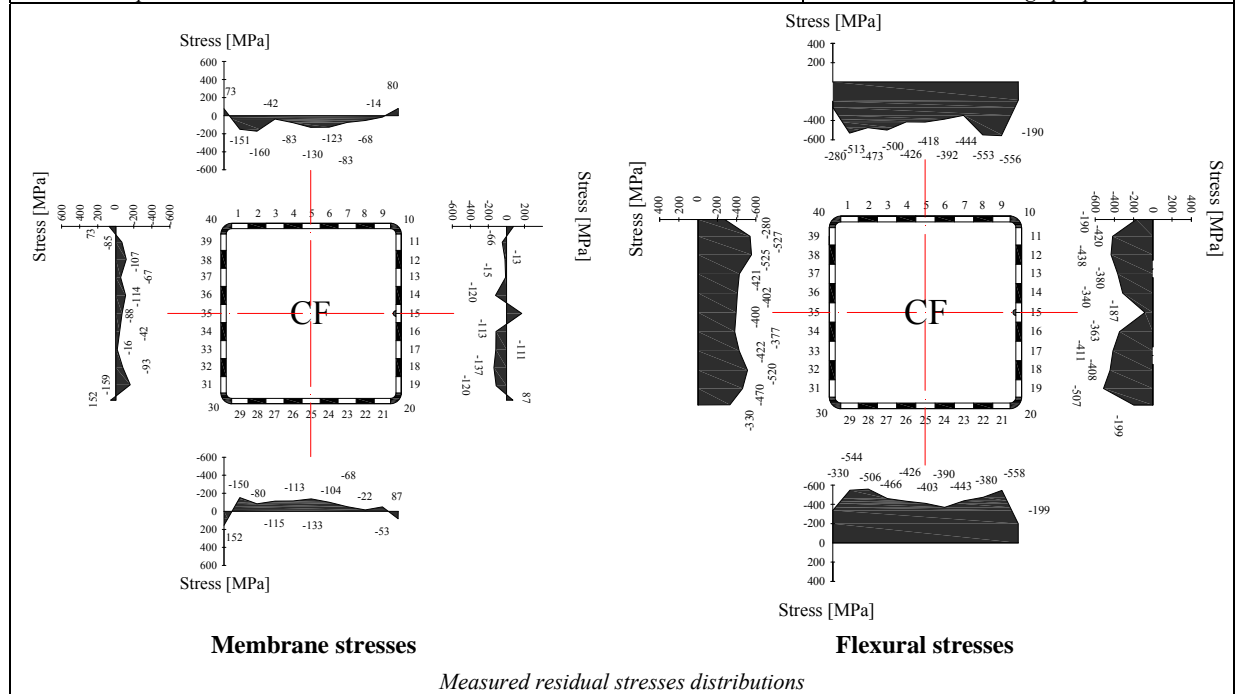
Cross-sectional measured dimensions and tolerances

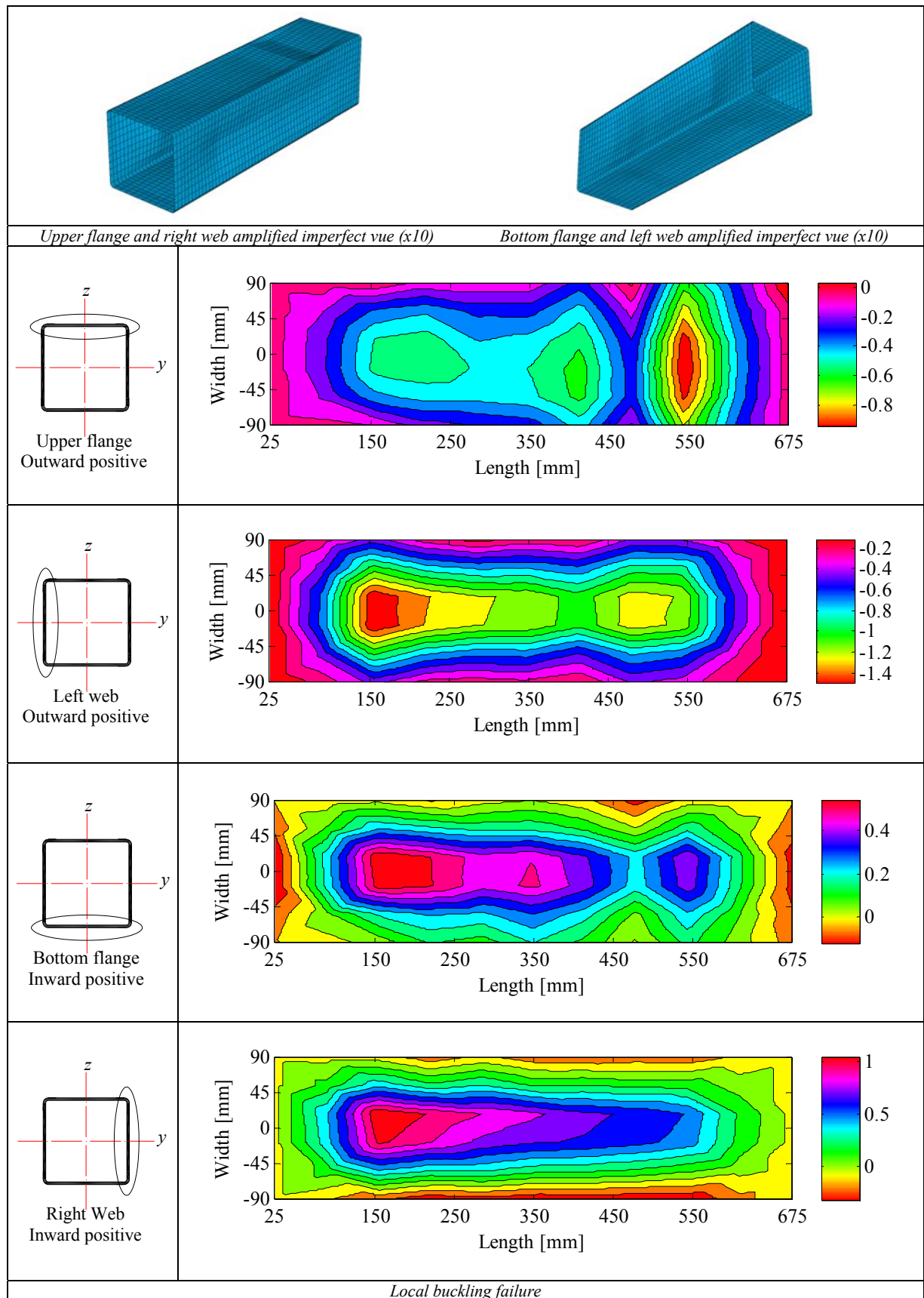


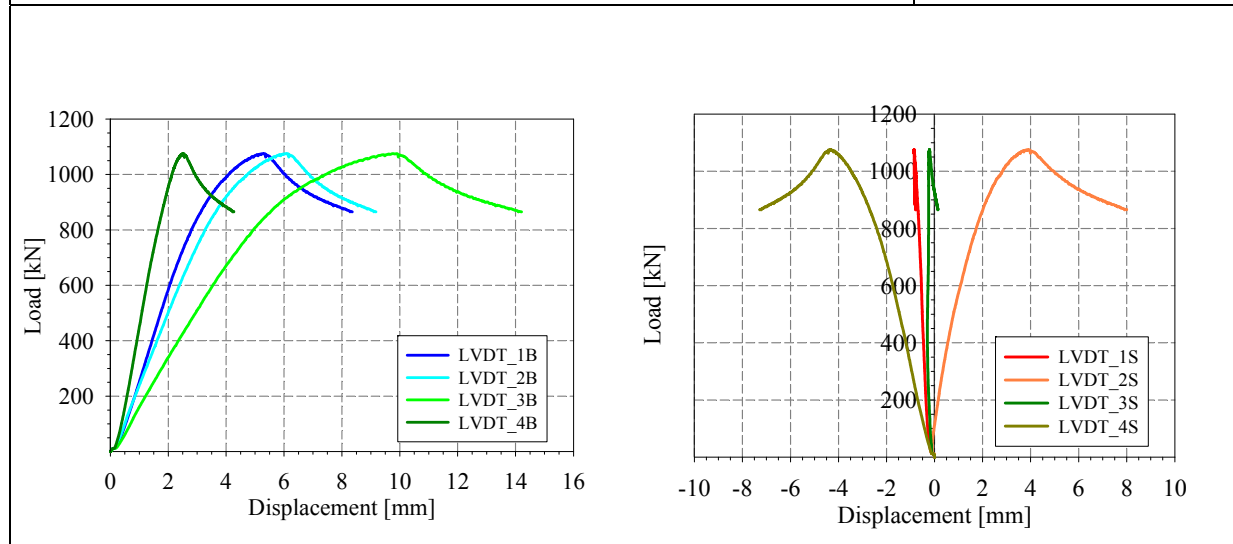
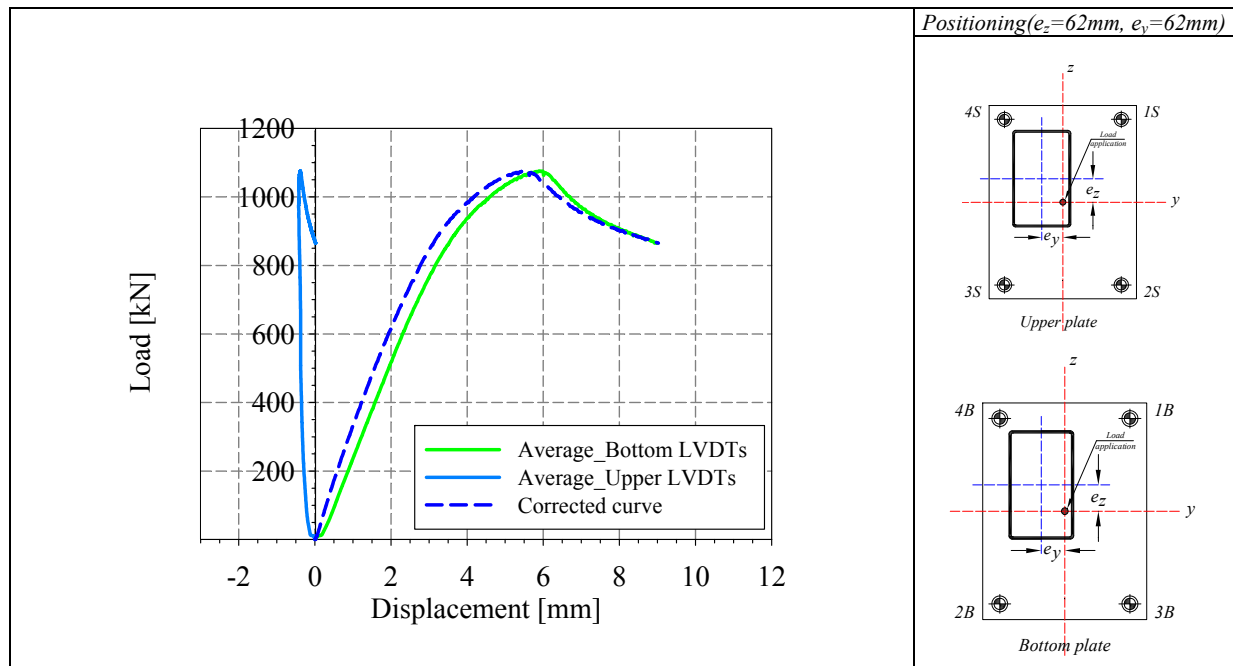
Tensile coupons location

Material stress-strain curves

Material average properties



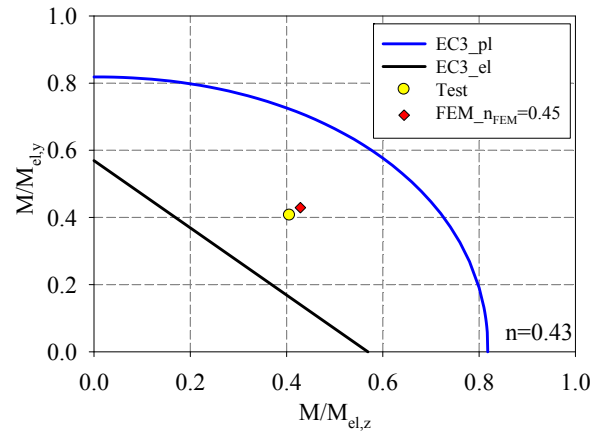
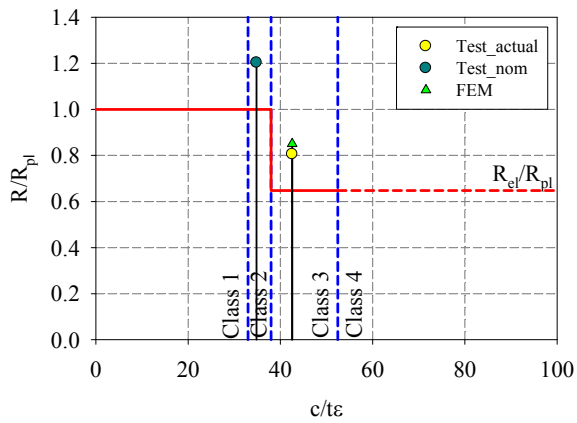
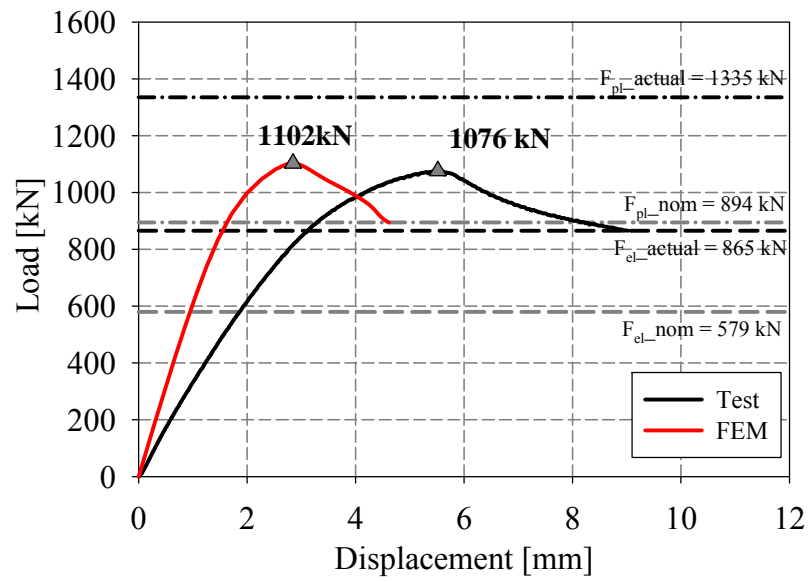




LVDT and strain gauges recordings

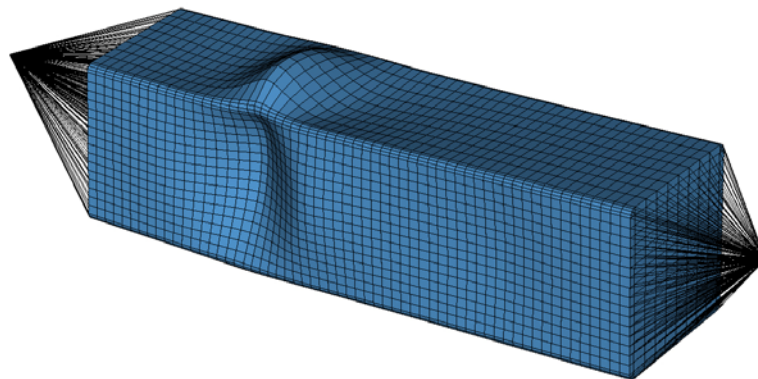


Local buckling failure

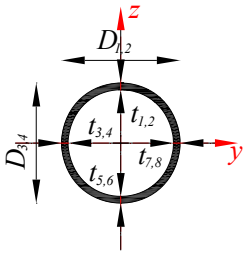


Cross-section resistance diagram

My-Mz bending moment interaction diagram

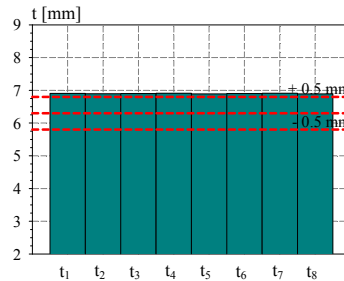
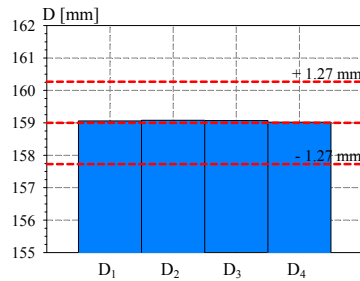


Numerical local buckling failure

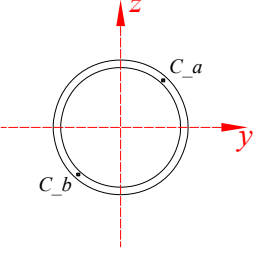
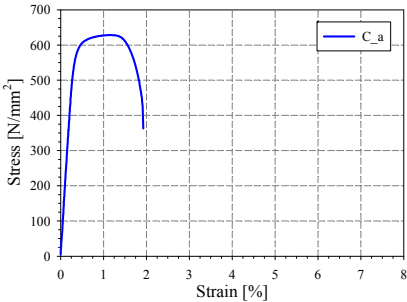
Specimen name	Shape	Details
<p>CHS_S355_LC3 159x6.3 CF</p>		<p>Shape: Circular Hollow Section Nominal yield limit: 355 MPa Load case: N(33%)+M_y(33%)+M_y(33%) D=159mm t=6.3mm Fabrication process: Cold formed</p>

Average D= 159 mm

Average t= 6.9 mm



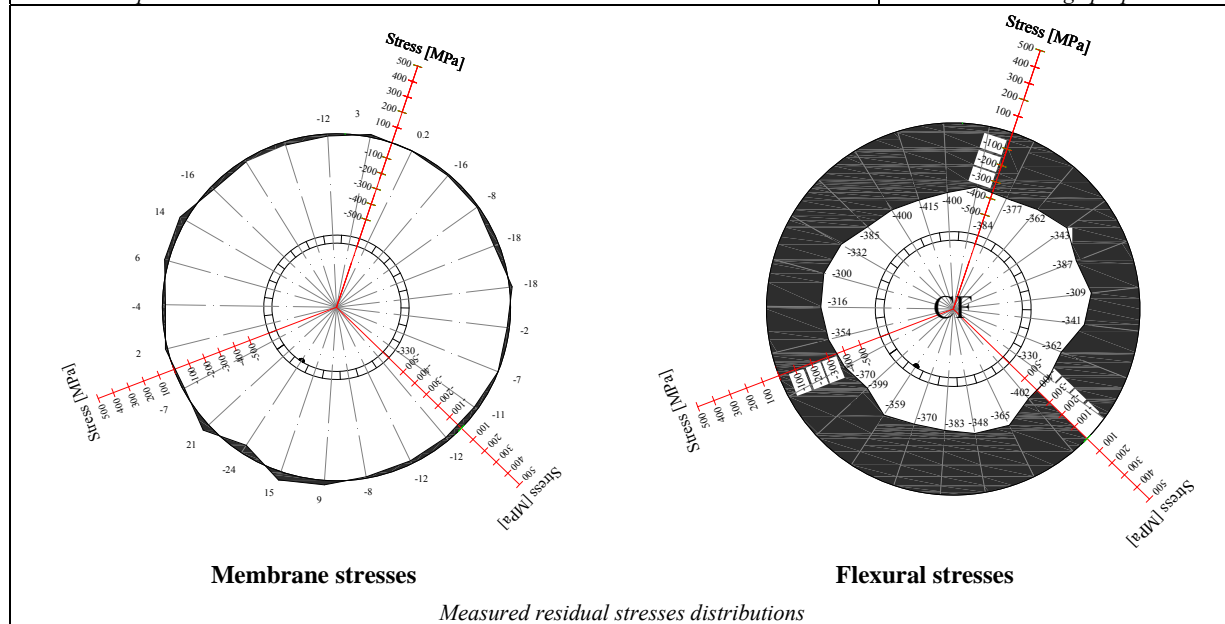
Cross-sectional measured dimensions and tolerances

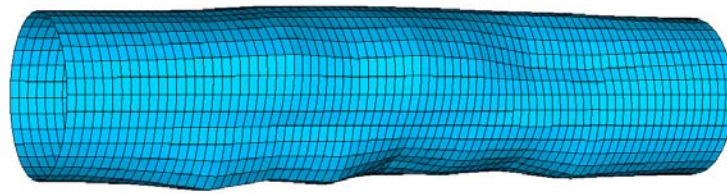
		<table border="1"> <thead> <tr> <th></th> <th>Average C_a, C_b</th> </tr> </thead> <tbody> <tr> <td>E [MPa]</td> <td>194654</td> </tr> <tr> <td>f_y [MPa]</td> <td>607.3</td> </tr> <tr> <td>ε_y [%]</td> <td>0.31</td> </tr> <tr> <td>f_u [MPa]</td> <td>628.2</td> </tr> <tr> <td>ε_u [%]</td> <td>1.1</td> </tr> </tbody> </table>		Average C _a , C _b	E [MPa]	194654	f _y [MPa]	607.3	ε _y [%]	0.31	f _u [MPa]	628.2	ε _u [%]	1.1
	Average C _a , C _b													
E [MPa]	194654													
f _y [MPa]	607.3													
ε _y [%]	0.31													
f _u [MPa]	628.2													
ε _u [%]	1.1													

Tensile coupons location

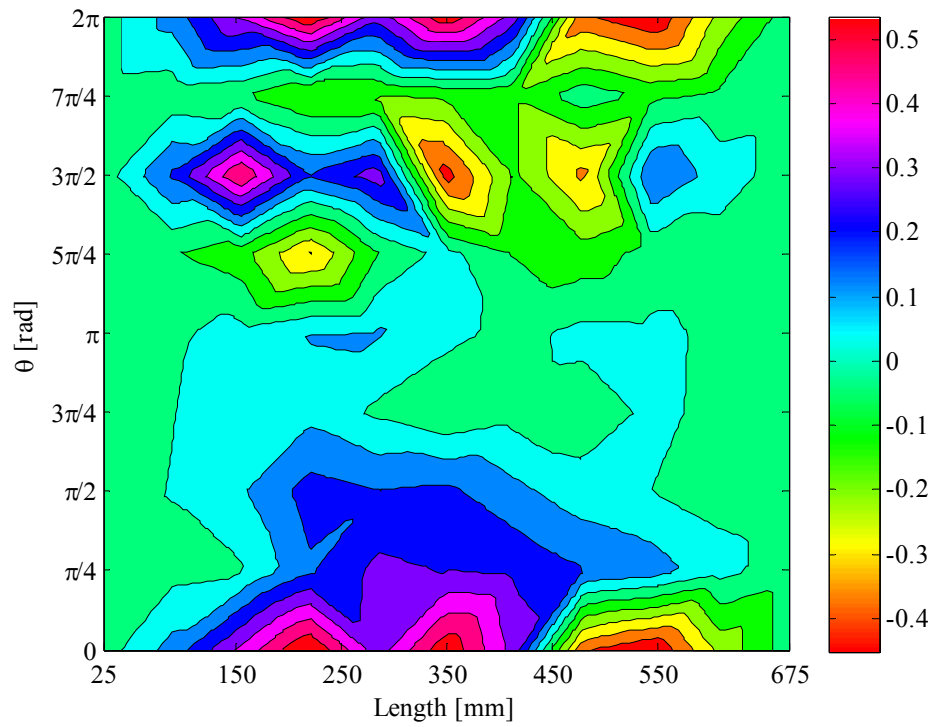
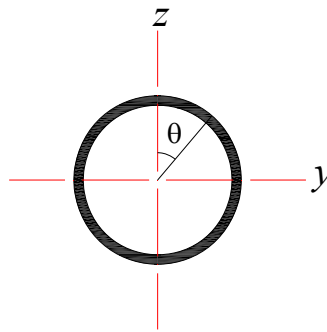
Material stress-strain curves

Material average properties

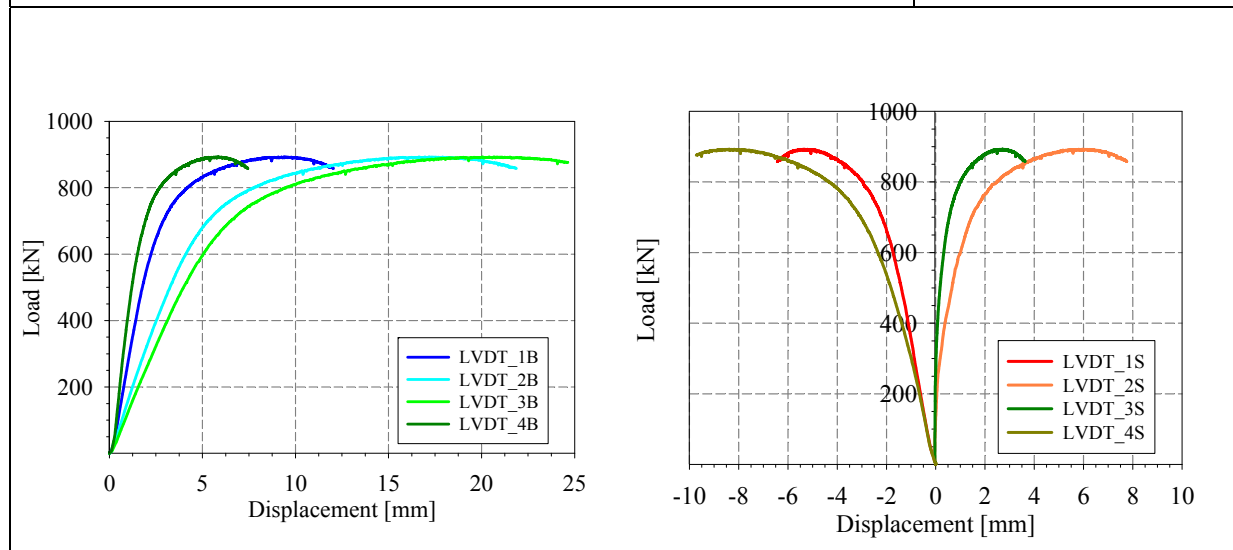
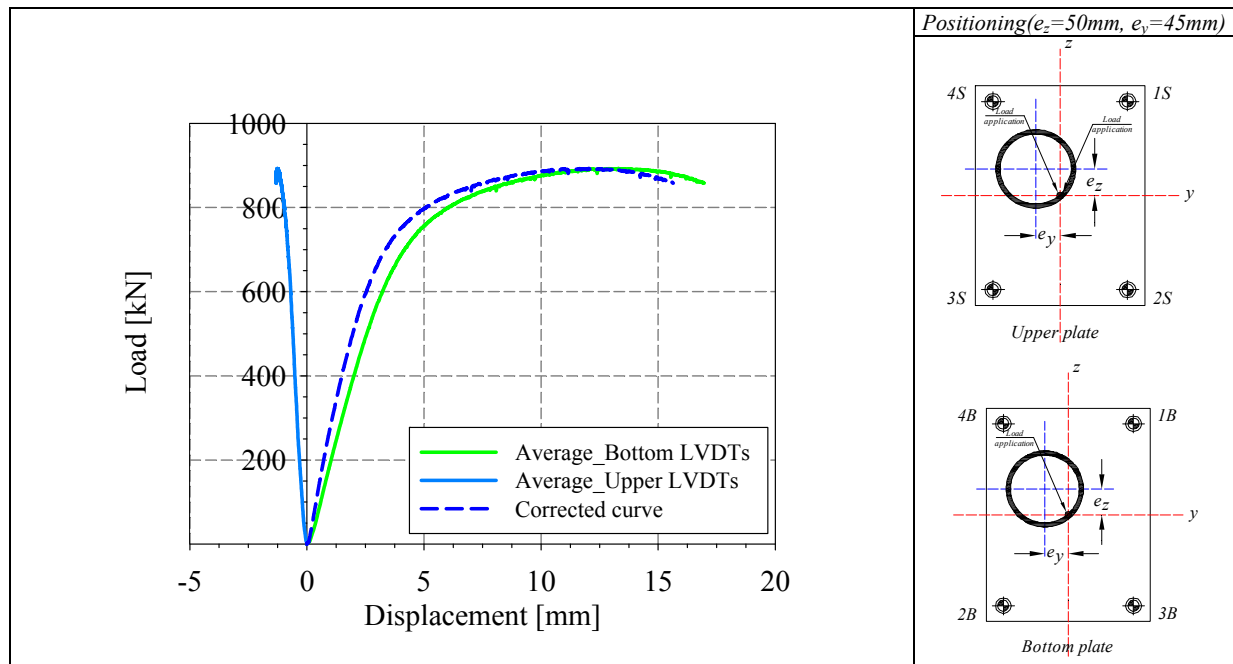




Amplified imperfect vue (x10)



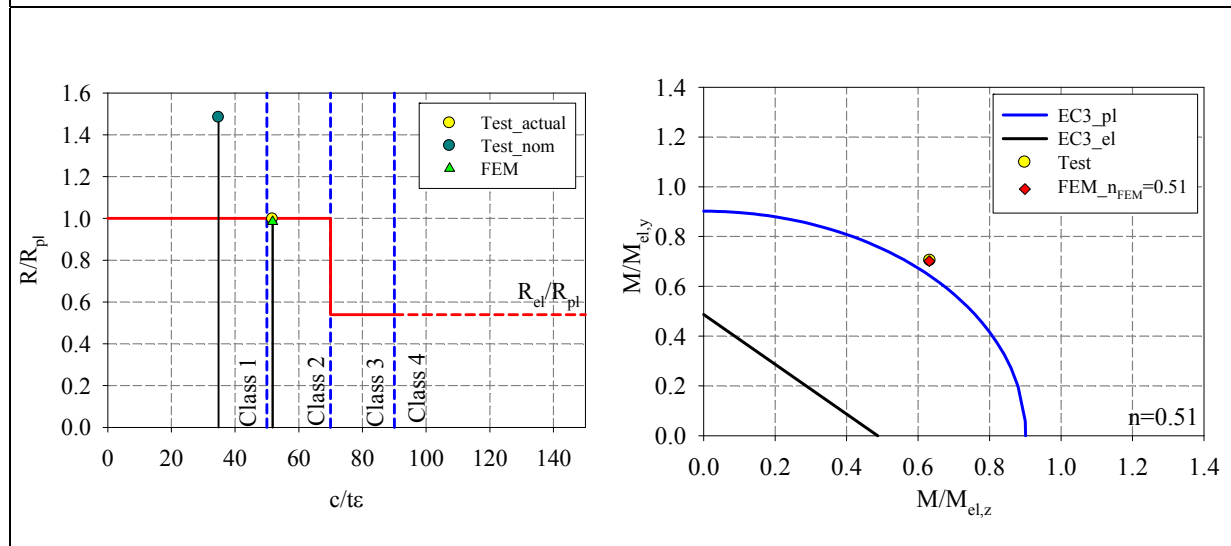
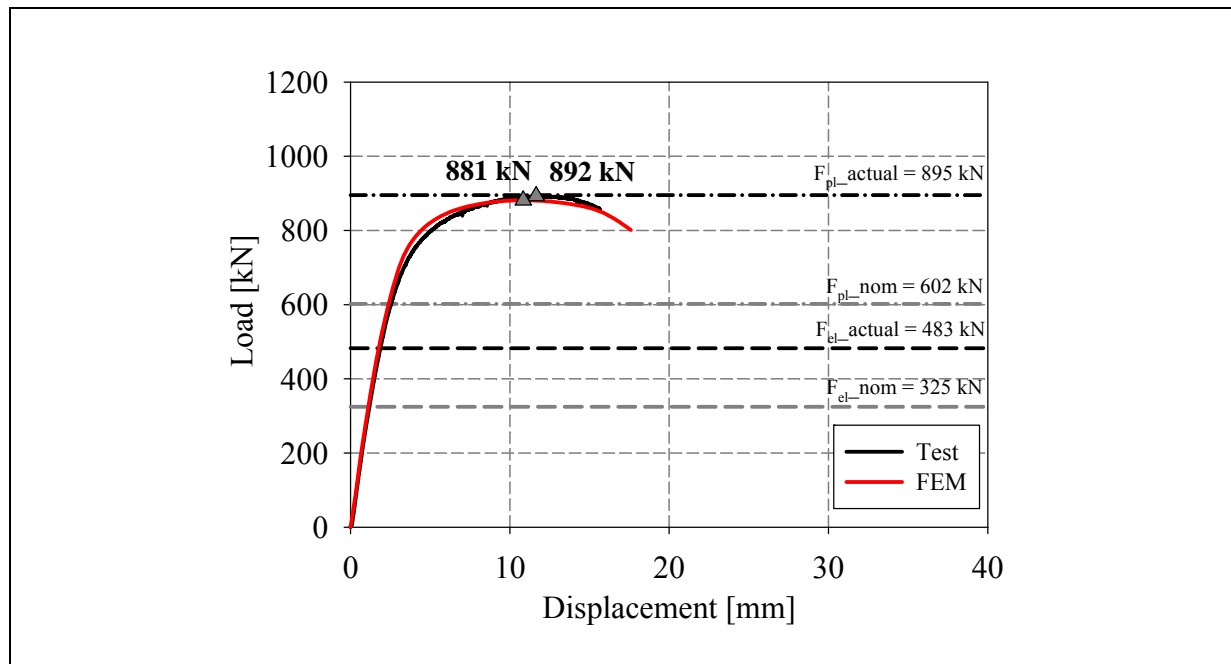
Measured Local imperfections



LVDT and strain gauges recordings

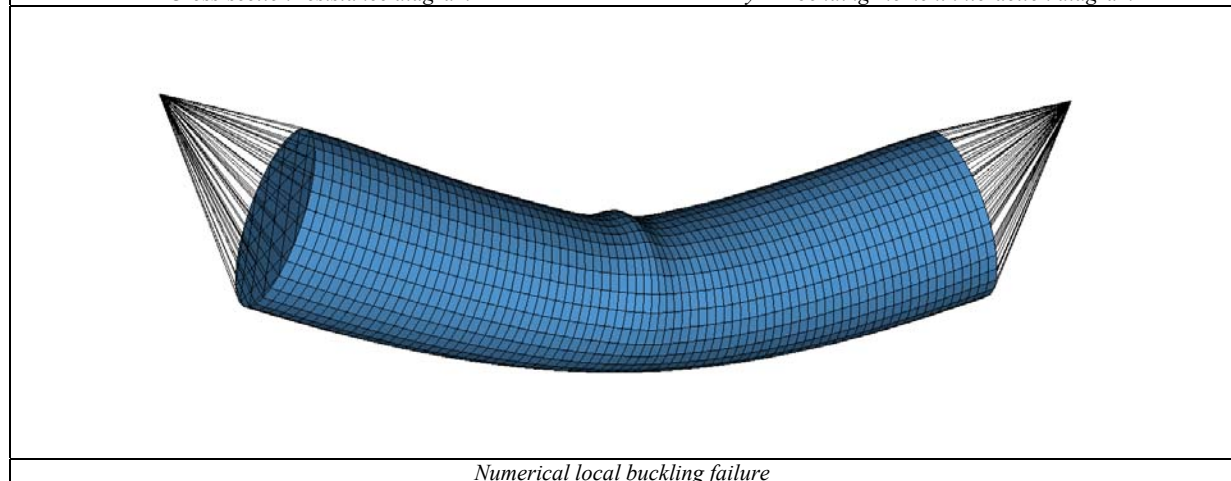


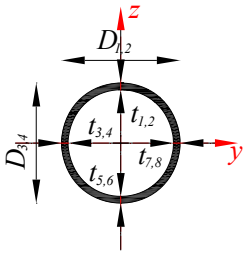
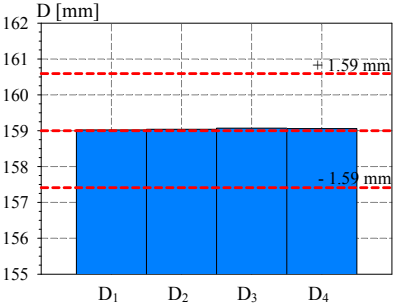
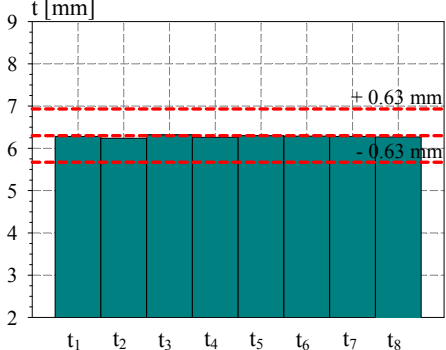
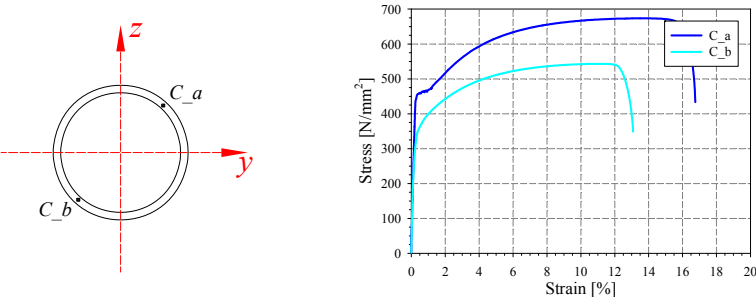
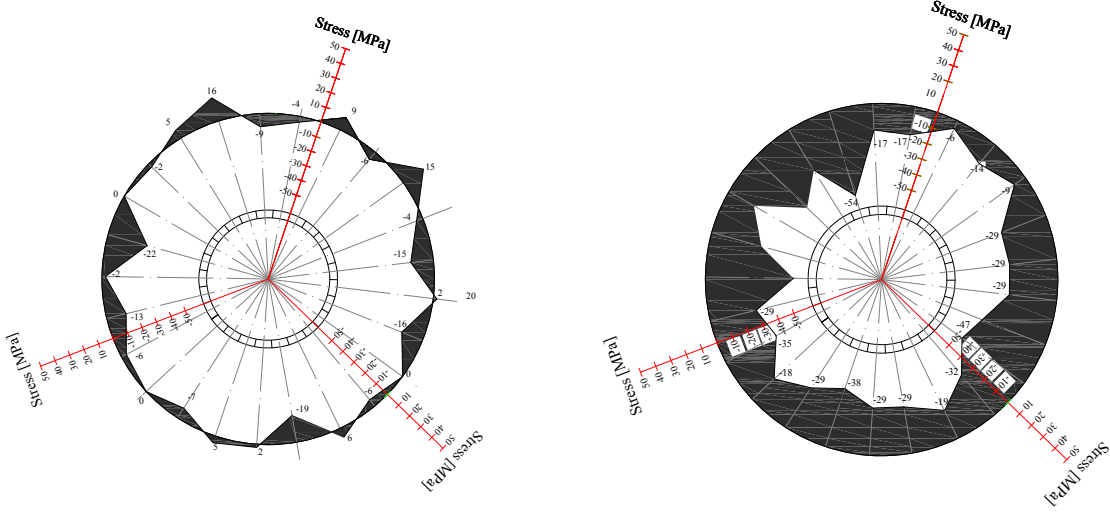
Local buckling failure

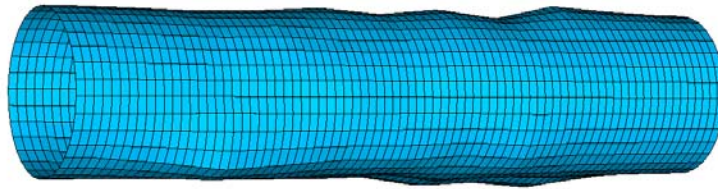


Cross-section resistance diagram

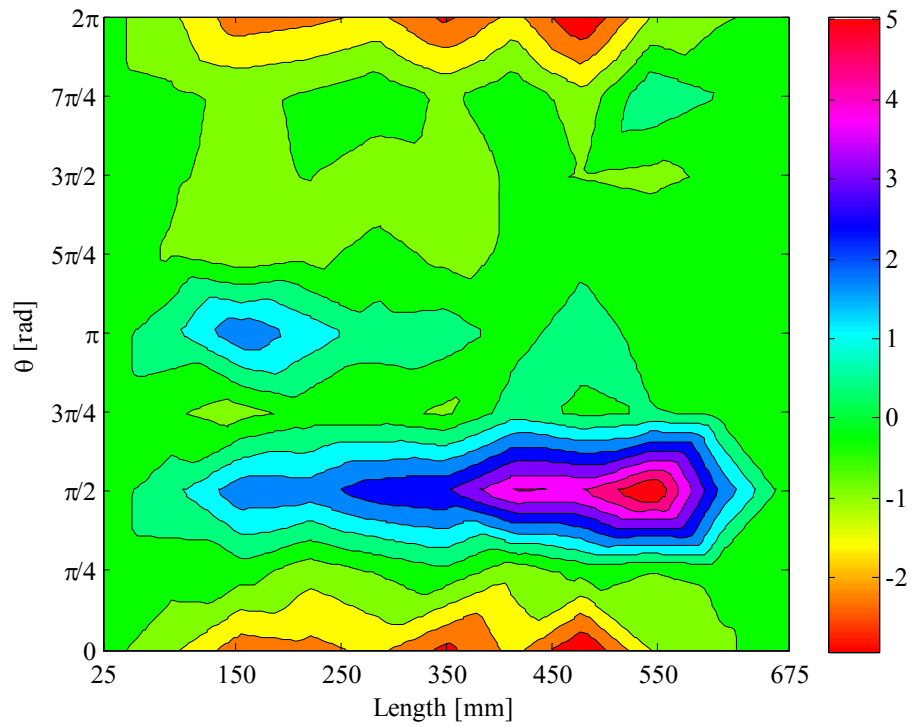
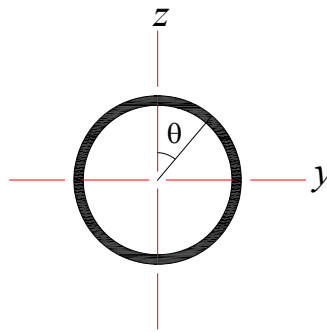
My-Mz bending moment interaction diagram



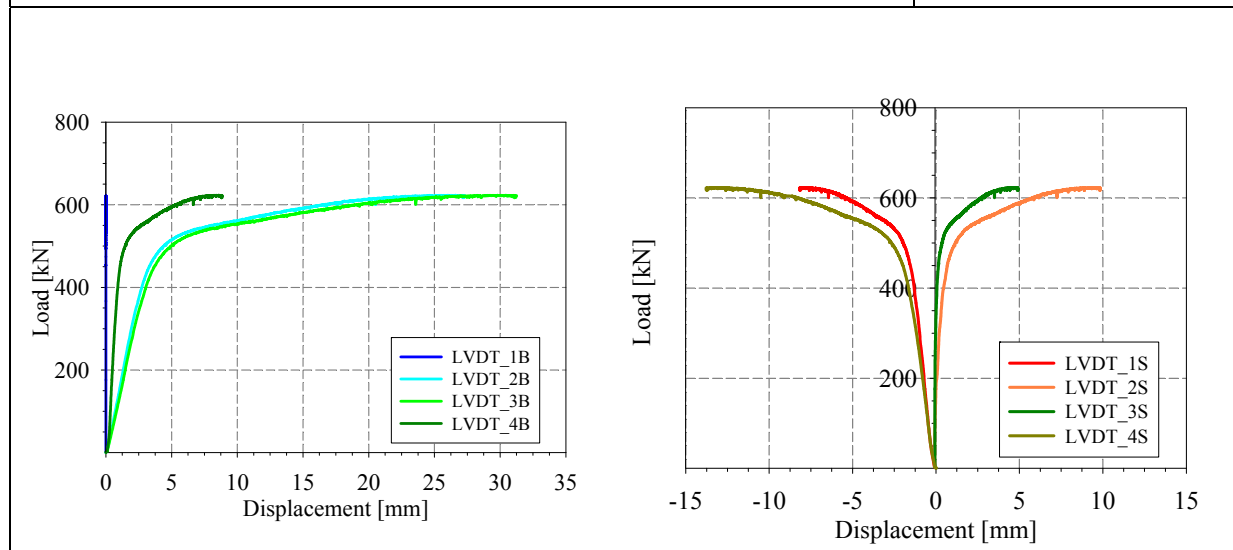
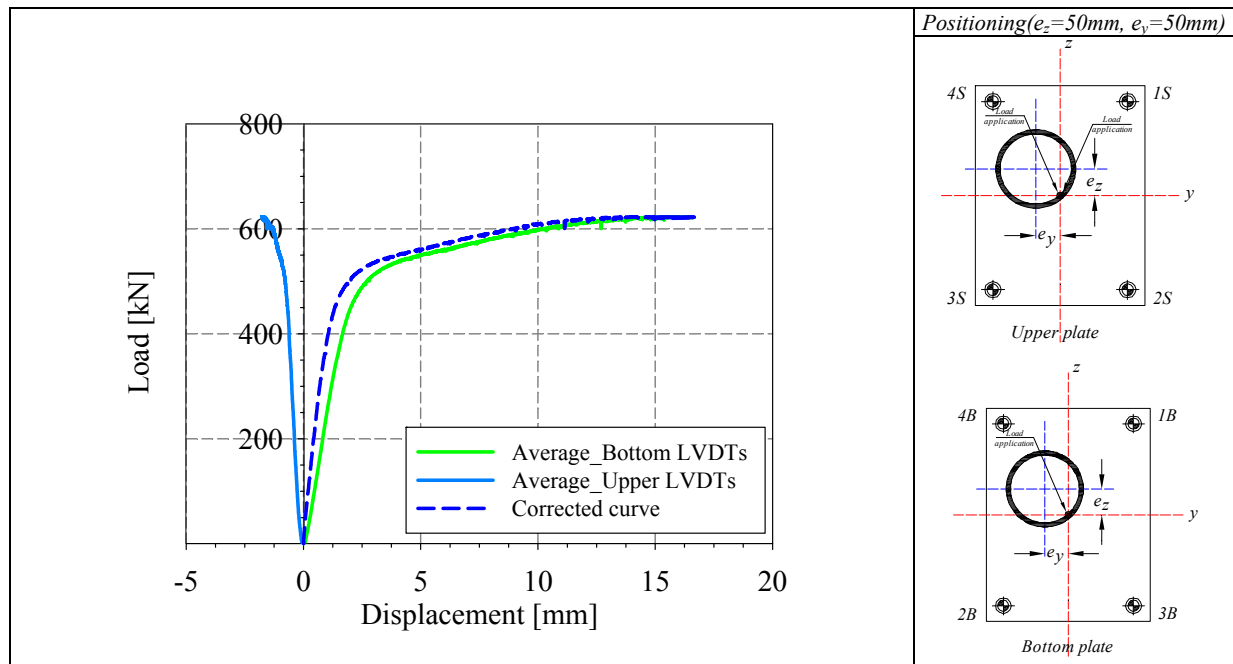
Specimen name	Shape	Details											
<p>CHS_S355_LC3 159x6.3 HR</p>		<p>Shape: Circular Hollow Section Nominal yield limit: 355 MPa Load case: N(33%)+M_y(33%)+M_y(33%) D=159mm t=6.3mm Fabrication process: Hot rolled</p>											
<p>Average D= 159 mm</p> 		<p>Average t= 628 mm</p> 											
<p><i>Cross-sectional measured dimensions and tolerances</i></p>													
	<table border="1"> <thead> <tr> <th></th> <th>Average C_a, C_b</th> </tr> </thead> <tbody> <tr> <td>E [MPa]</td> <td>213000</td> </tr> <tr> <td>f_y [MPa]</td> <td>401.5</td> </tr> <tr> <td>ε_y [%]</td> <td>0.19</td> </tr> <tr> <td>f_u [MPa]</td> <td>607.8</td> </tr> <tr> <td>ε_u [%]</td> <td>11.7</td> </tr> </tbody> </table>		Average C _a , C _b	E [MPa]	213000	f _y [MPa]	401.5	ε _y [%]	0.19	f _u [MPa]	607.8	ε _u [%]	11.7
	Average C _a , C _b												
E [MPa]	213000												
f _y [MPa]	401.5												
ε _y [%]	0.19												
f _u [MPa]	607.8												
ε _u [%]	11.7												
<p><i>Tensile coupons location</i></p>	<p><i>Material stress-strain curves</i></p>	<p><i>Material average properties</i></p>											
 <p style="text-align: center;">Membrane stresses Flexural stresses</p> <p style="text-align: center;"><i>Measured residual stresses distributions</i></p>													



Amplified imperfect vue (x10)



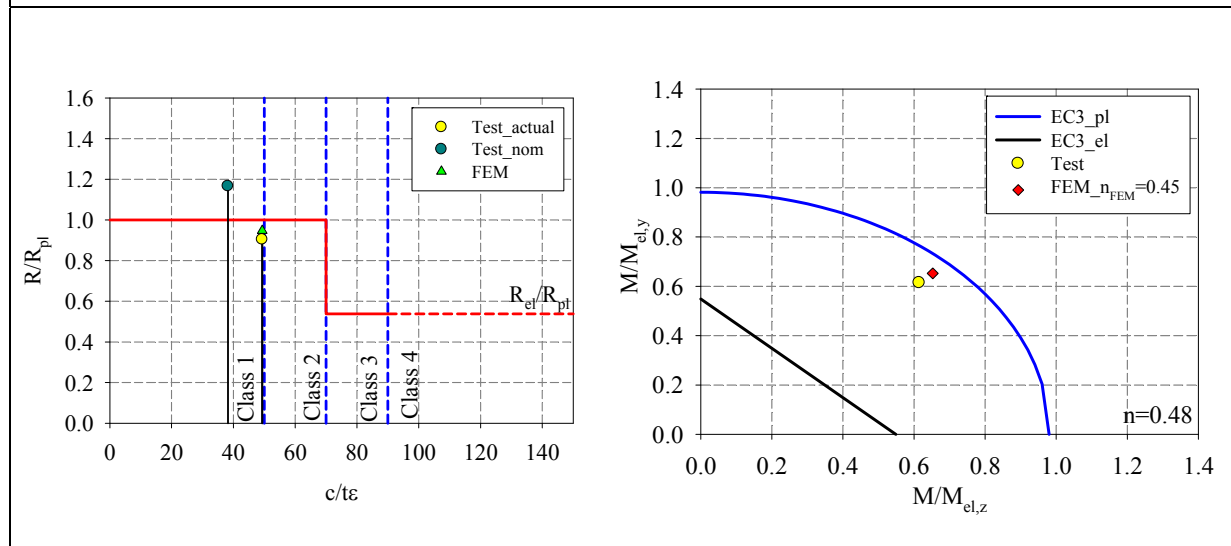
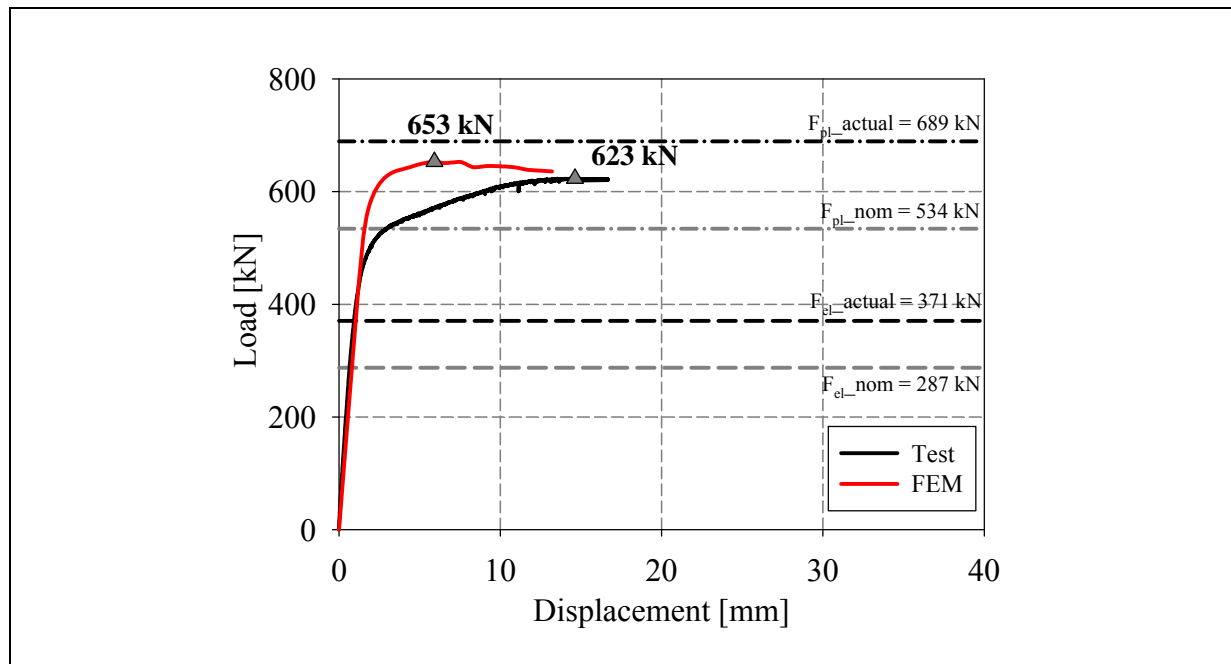
Measured Local imperfections



LVDT and strain gauges recordings

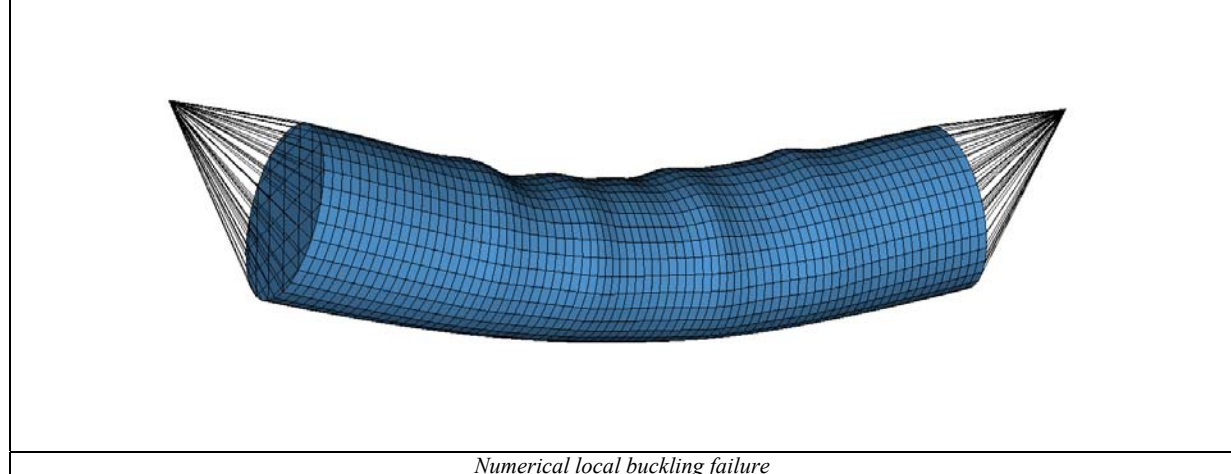


Local buckling failure

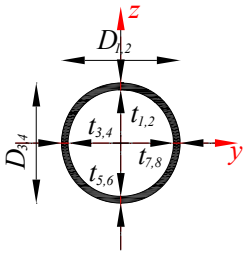
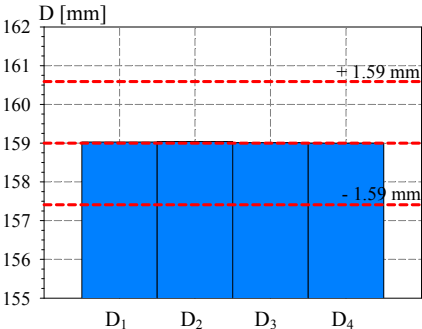
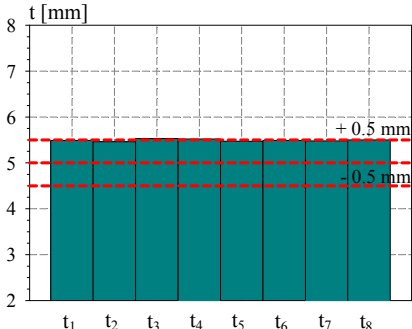
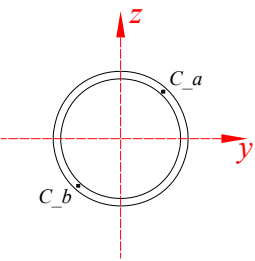
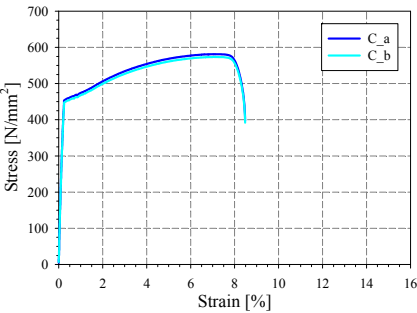
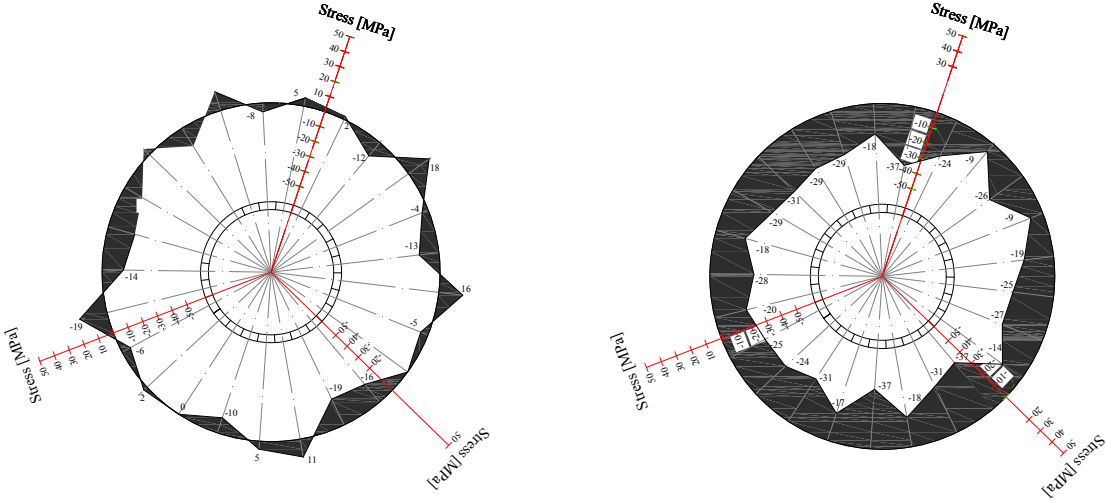


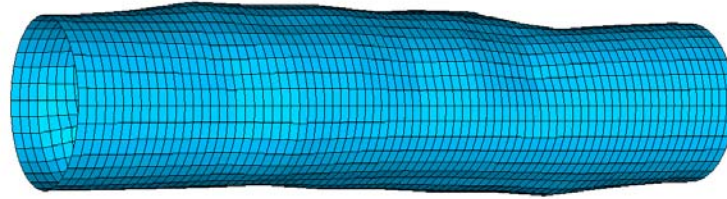
Cross-section resistance diagram

My-Mz bending moment interaction diagram

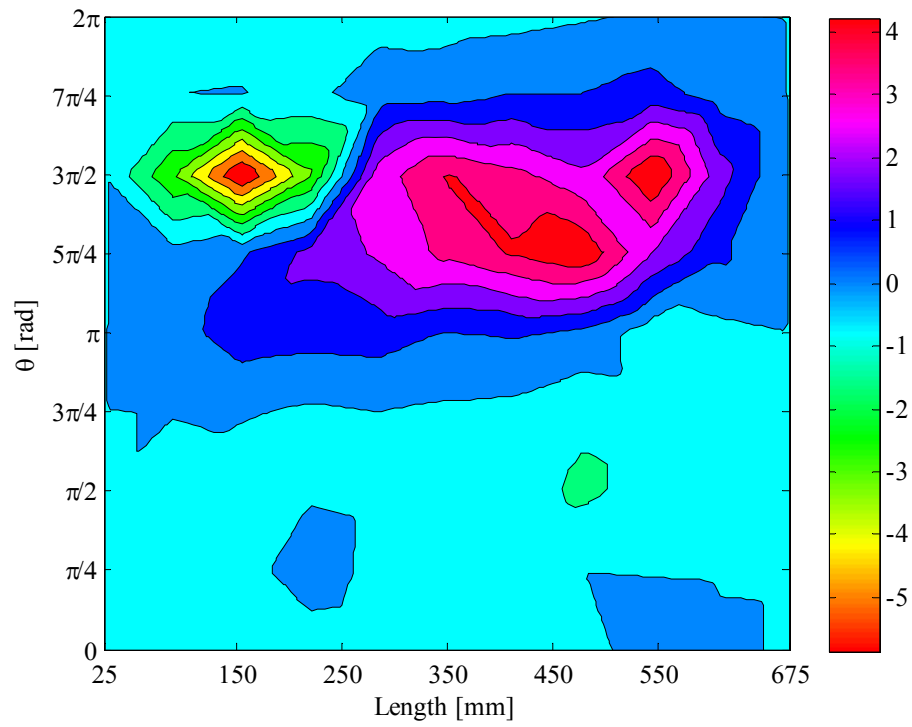
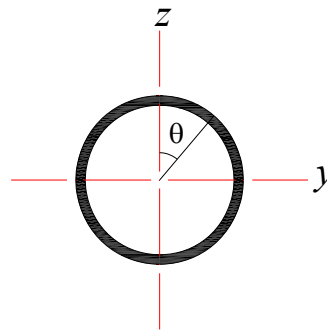


Numerical local buckling failure

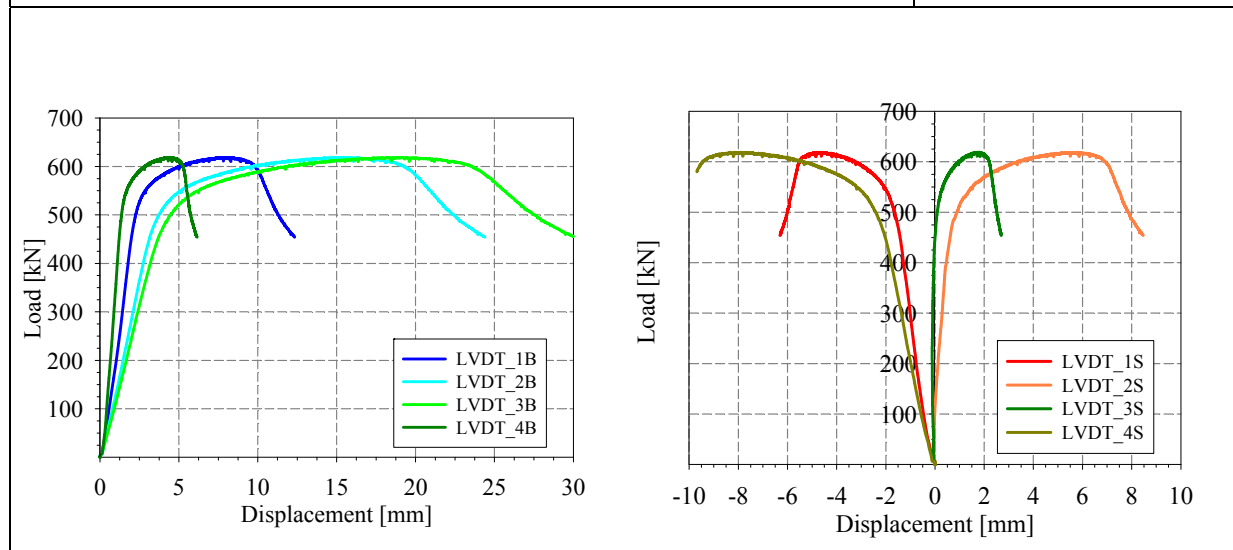
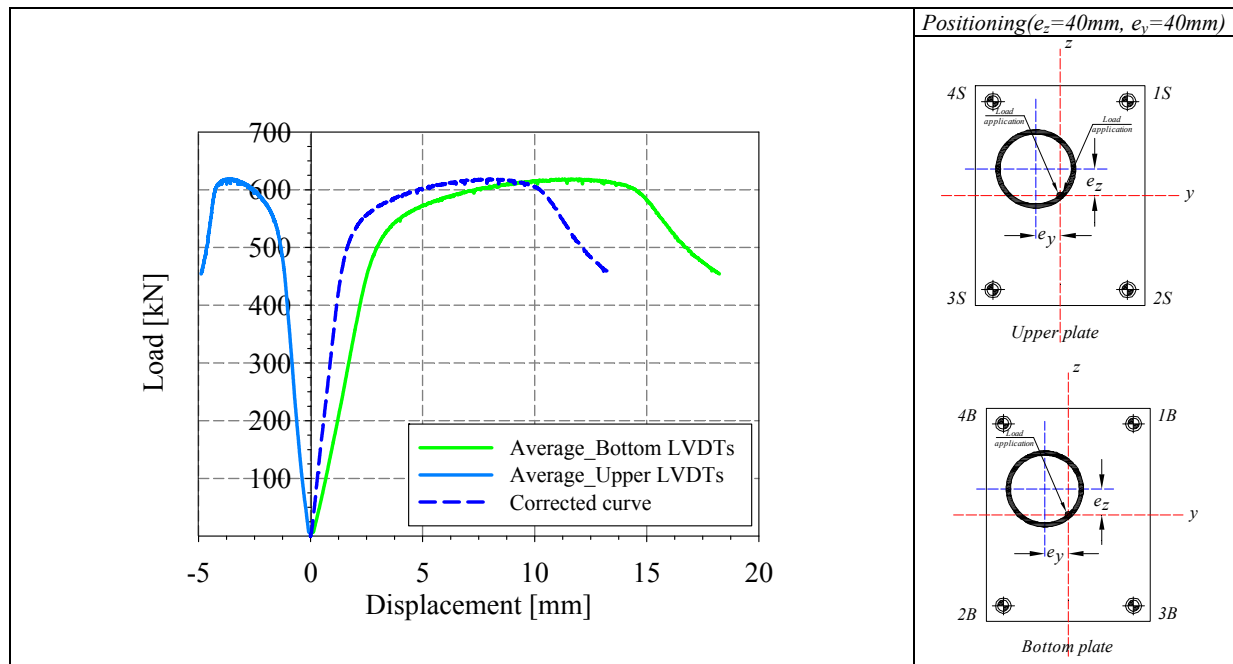
Specimen name	Shape	Details												
<p>CHS_S355_LC3 159x5 HR</p>		<p>Shape: Circular Hollow Section Nominal yield limit: 355 MPa Load case: N(33%)+M_y(33%)+M_y(33%) D=159mm t=5mm Fabrication process: Hot rolled</p>												
Average D= 159 mm		Average t= 5.49 mm												
														
<i>Cross-sectional measured dimensions and tolerances</i>														
		<table border="1"> <thead> <tr> <th></th> <th>Average C_a, C_b</th> </tr> </thead> <tbody> <tr> <td>E [MPa]</td> <td>215000</td> </tr> <tr> <td>f_y [MPa]</td> <td>457.7</td> </tr> <tr> <td>ε_y [%]</td> <td>0.21</td> </tr> <tr> <td>f_u [MPa]</td> <td>577.3</td> </tr> <tr> <td>ε_u [%]</td> <td>7.02</td> </tr> </tbody> </table>		Average C _a , C _b	E [MPa]	215000	f _y [MPa]	457.7	ε _y [%]	0.21	f _u [MPa]	577.3	ε _u [%]	7.02
	Average C _a , C _b													
E [MPa]	215000													
f _y [MPa]	457.7													
ε _y [%]	0.21													
f _u [MPa]	577.3													
ε _u [%]	7.02													
<i>Tensile coupons location</i>	<i>Material stress-strain curves</i>	<i>Material average properties</i>												
 <div style="display: flex; justify-content: space-around; margin-top: 10px;"> <div data-bbox="440 1808 651 1839">Membrane stresses</div> <div data-bbox="1062 1808 1243 1839">Flexural stresses</div> </div> <p style="text-align: center;"><i>Measured residual stresses distributions</i></p>														



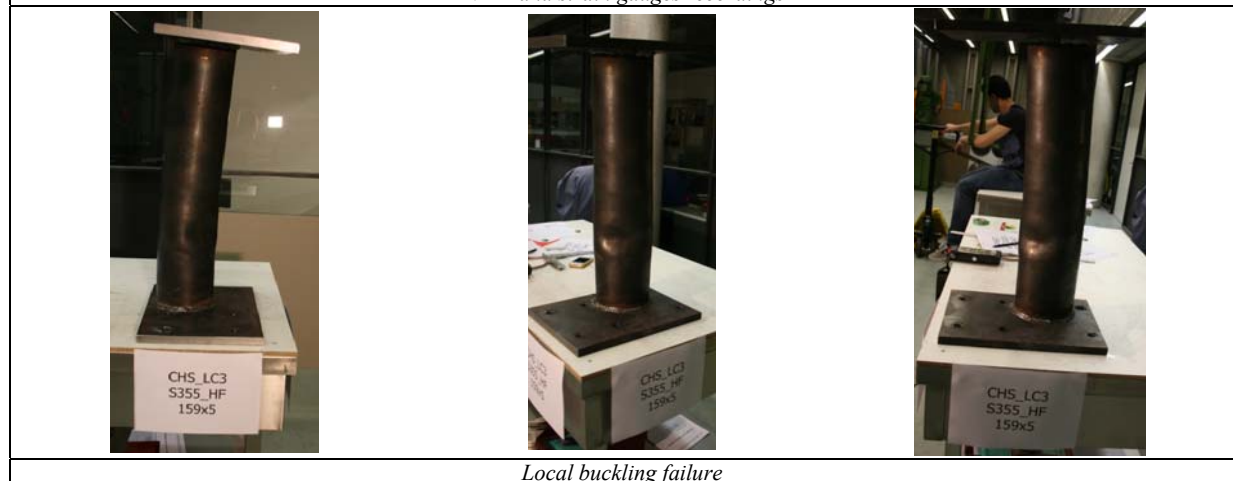
Amplified imperfect vue (x10)



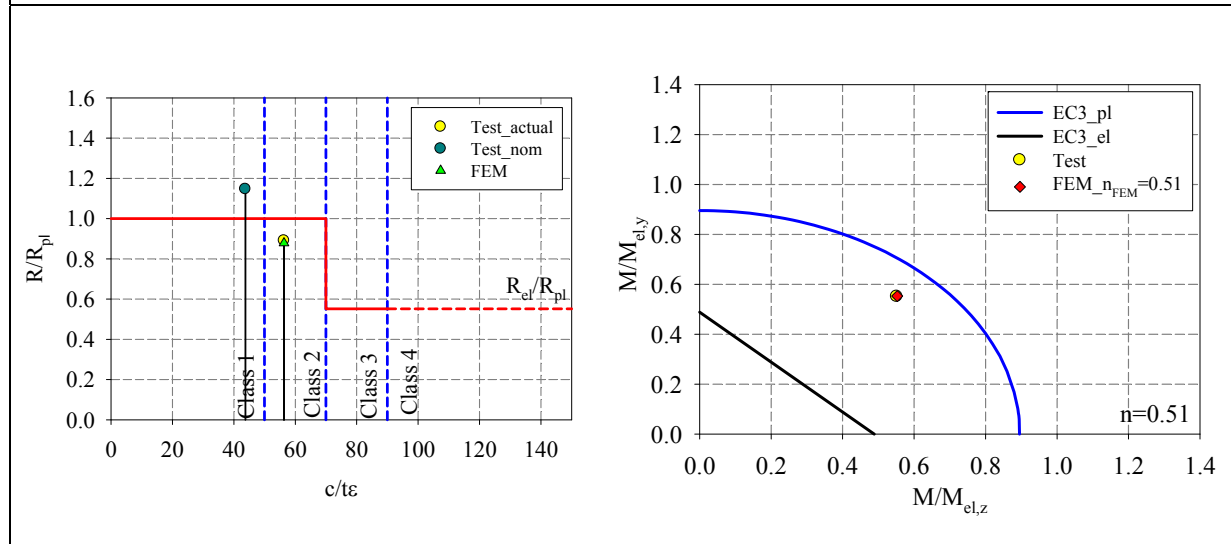
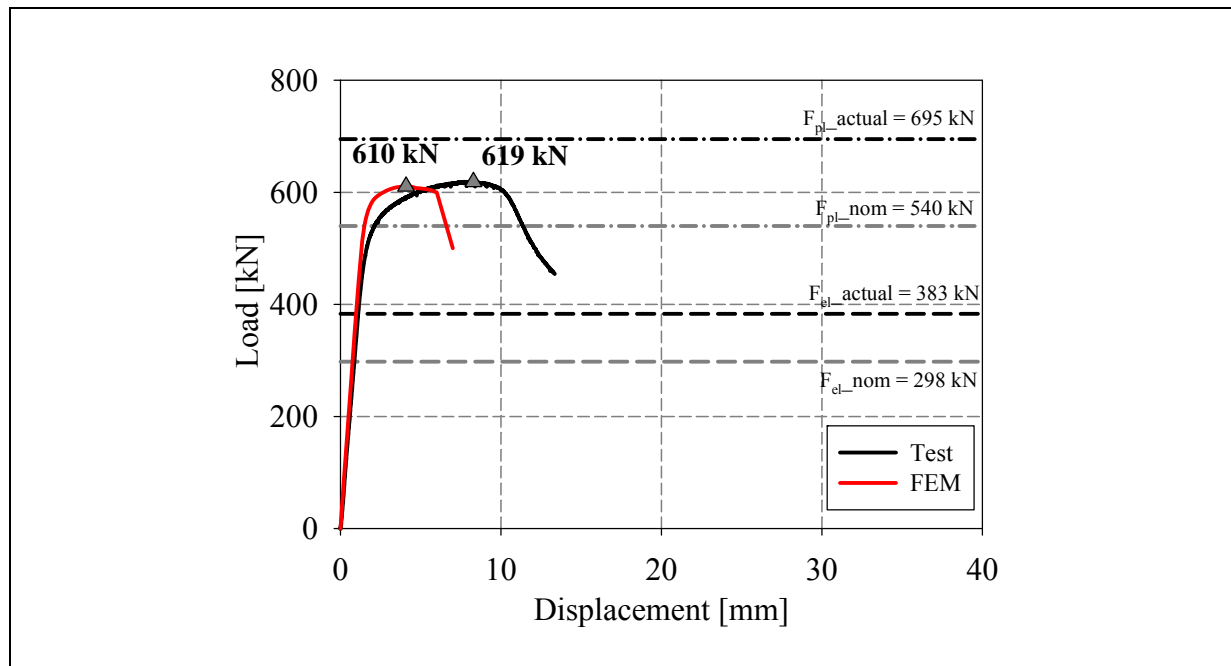
Measured Local imperfections



LVDT and strain gauges recordings

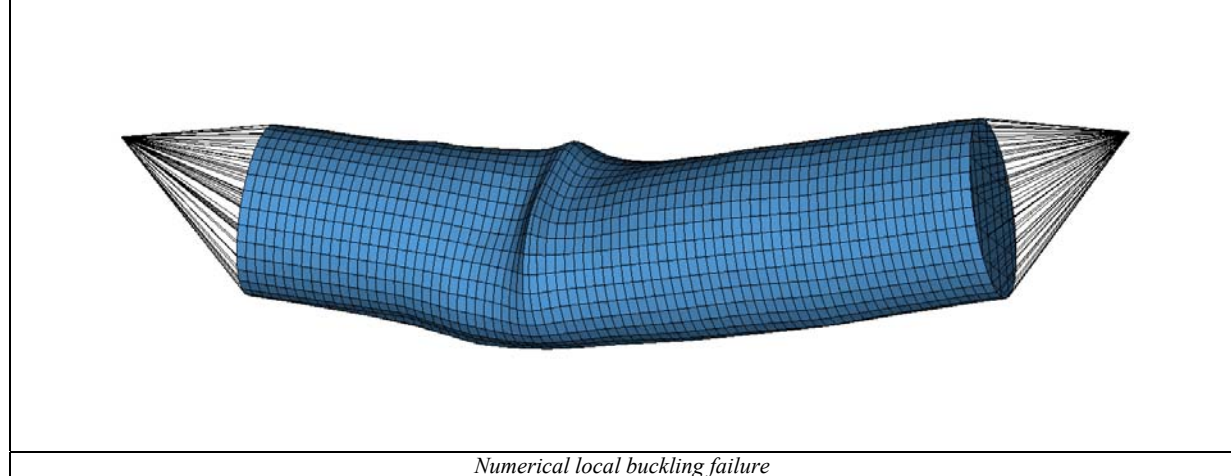


Local buckling failure

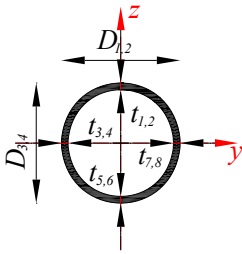
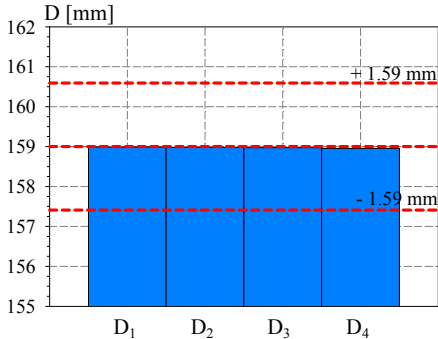
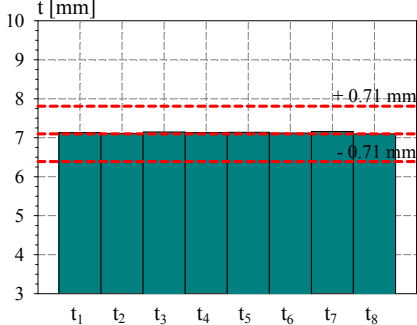
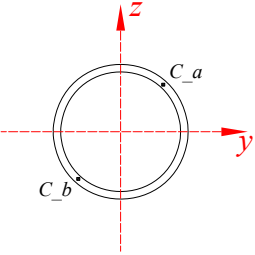
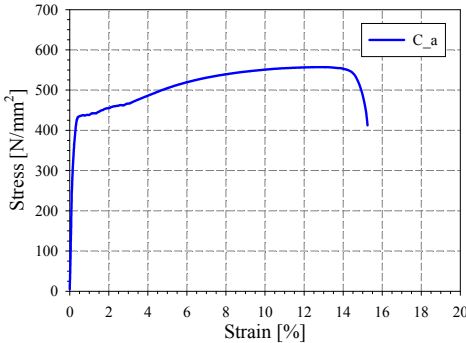
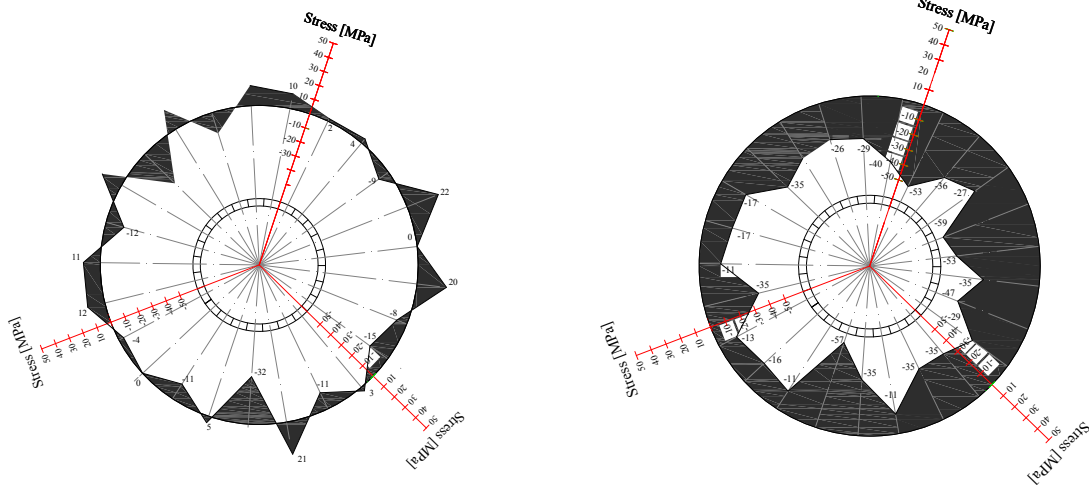


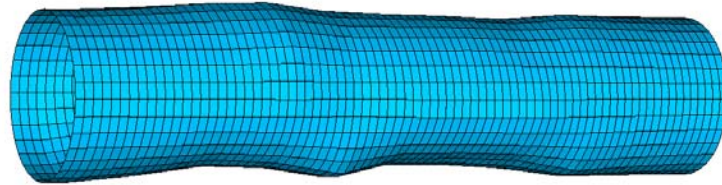
Cross-section resistance diagram

My-Mz bending moment interaction diagram

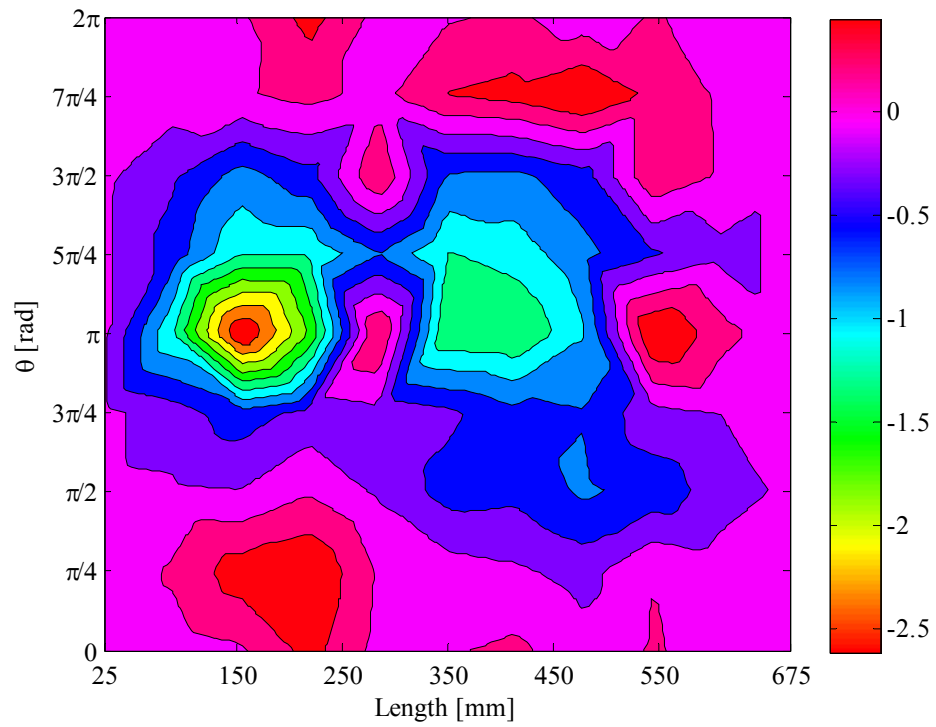
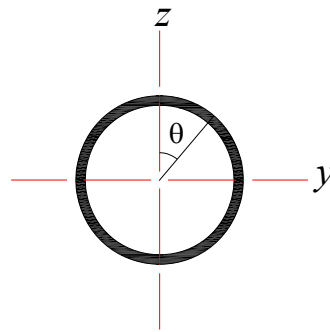


Numerical local buckling failure

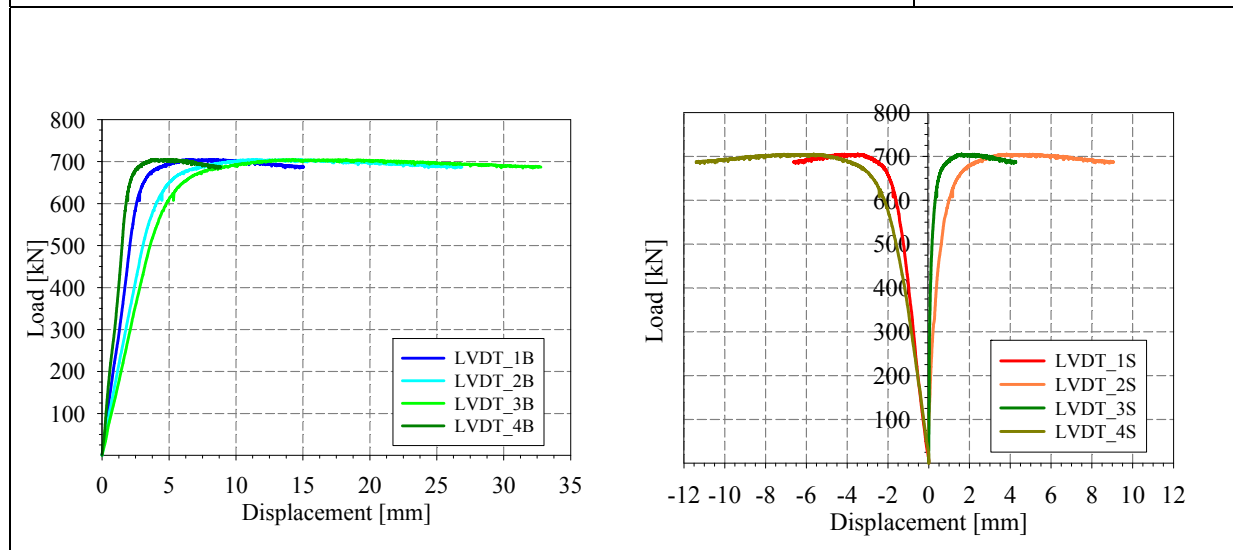
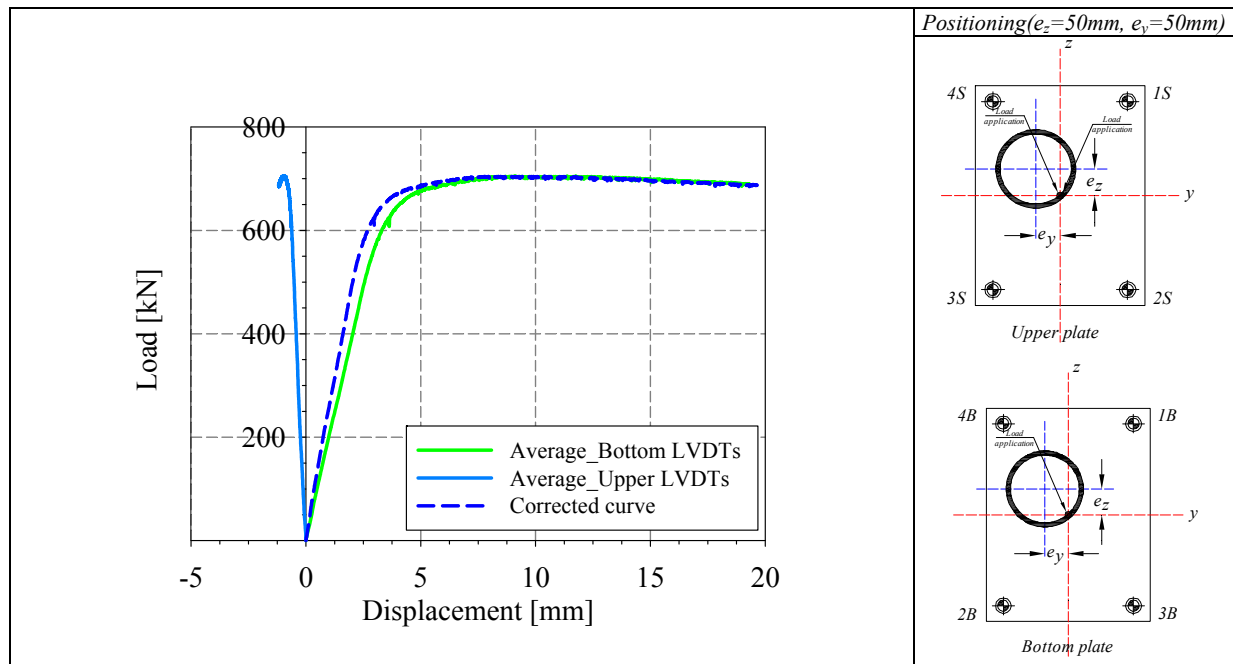
Specimen name	Shape	Details												
<p>CHS_S355_LC3 159x7.1 HR</p>		<p>Shape: Circular Hollow Section Nominal yield limit: 355 MPa Load case: N(33%)+M_y(33%)+M_z(33%) D=159mm t=7.1mm Fabrication process: Hot rolled</p>												
<p>Average D= 159 mm</p> 		<p>Average t= 7.13 mm</p> 												
<p><i>Cross-sectional measured dimensions and tolerances</i></p>														
		<table border="1"> <thead> <tr> <th colspan="2" data-bbox="1105 926 1255 993">Average C_a, C_b</th> </tr> </thead> <tbody> <tr> <td data-bbox="1105 993 1255 1050">E [MPa]</td> <td data-bbox="1255 993 1459 1050">212000</td> </tr> <tr> <td data-bbox="1105 1050 1255 1106">f_y [MPa]</td> <td data-bbox="1255 1050 1459 1106">442</td> </tr> <tr> <td data-bbox="1105 1106 1255 1163">ε_y [%]</td> <td data-bbox="1255 1106 1459 1163">0.20</td> </tr> <tr> <td data-bbox="1105 1163 1255 1220">f_u [MPa]</td> <td data-bbox="1255 1163 1459 1220">557.1</td> </tr> <tr> <td data-bbox="1105 1220 1255 1276">ε_u [%]</td> <td data-bbox="1255 1220 1459 1276">12.7</td> </tr> </tbody> </table>	Average C _a , C _b		E [MPa]	212000	f _y [MPa]	442	ε _y [%]	0.20	f _u [MPa]	557.1	ε _u [%]	12.7
Average C _a , C _b														
E [MPa]	212000													
f _y [MPa]	442													
ε _y [%]	0.20													
f _u [MPa]	557.1													
ε _u [%]	12.7													
<p><i>Tensile coupons location</i></p>	<p><i>Material stress-strain curves</i></p>	<p><i>Material average properties</i></p>												
 <div style="display: flex; justify-content: space-around; margin-top: 10px;"> <div data-bbox="440 1808 647 1839" style="text-align: center;"> <p>Membrane stresses</p> </div> <div data-bbox="1062 1808 1243 1839" style="text-align: center;"> <p>Flexural stresses</p> </div> </div> <p style="text-align: center; margin-top: 10px;"><i>Measured residual stresses distributions</i></p>														



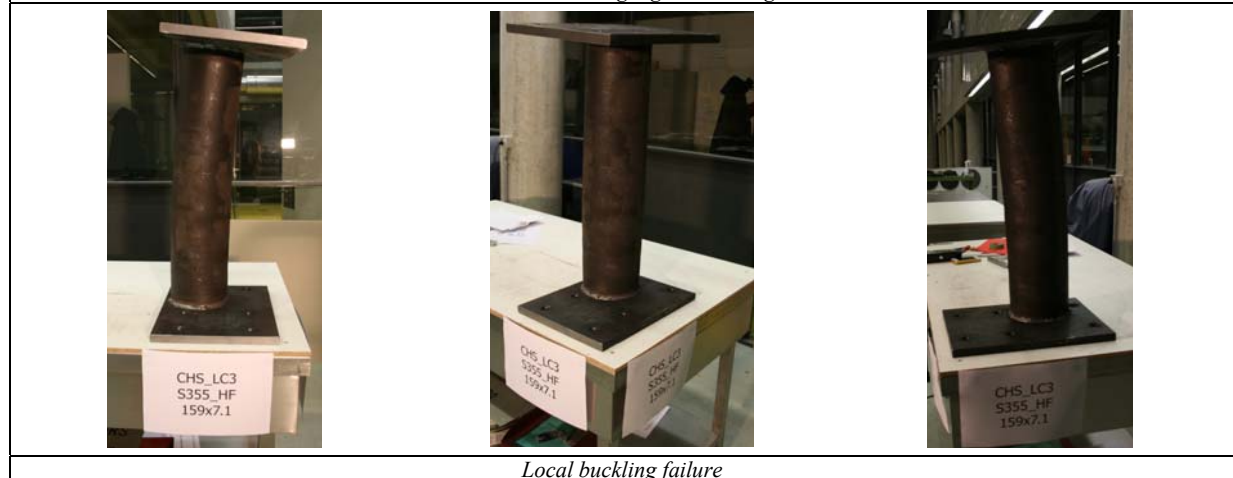
Amplified imperfect vue (x10)



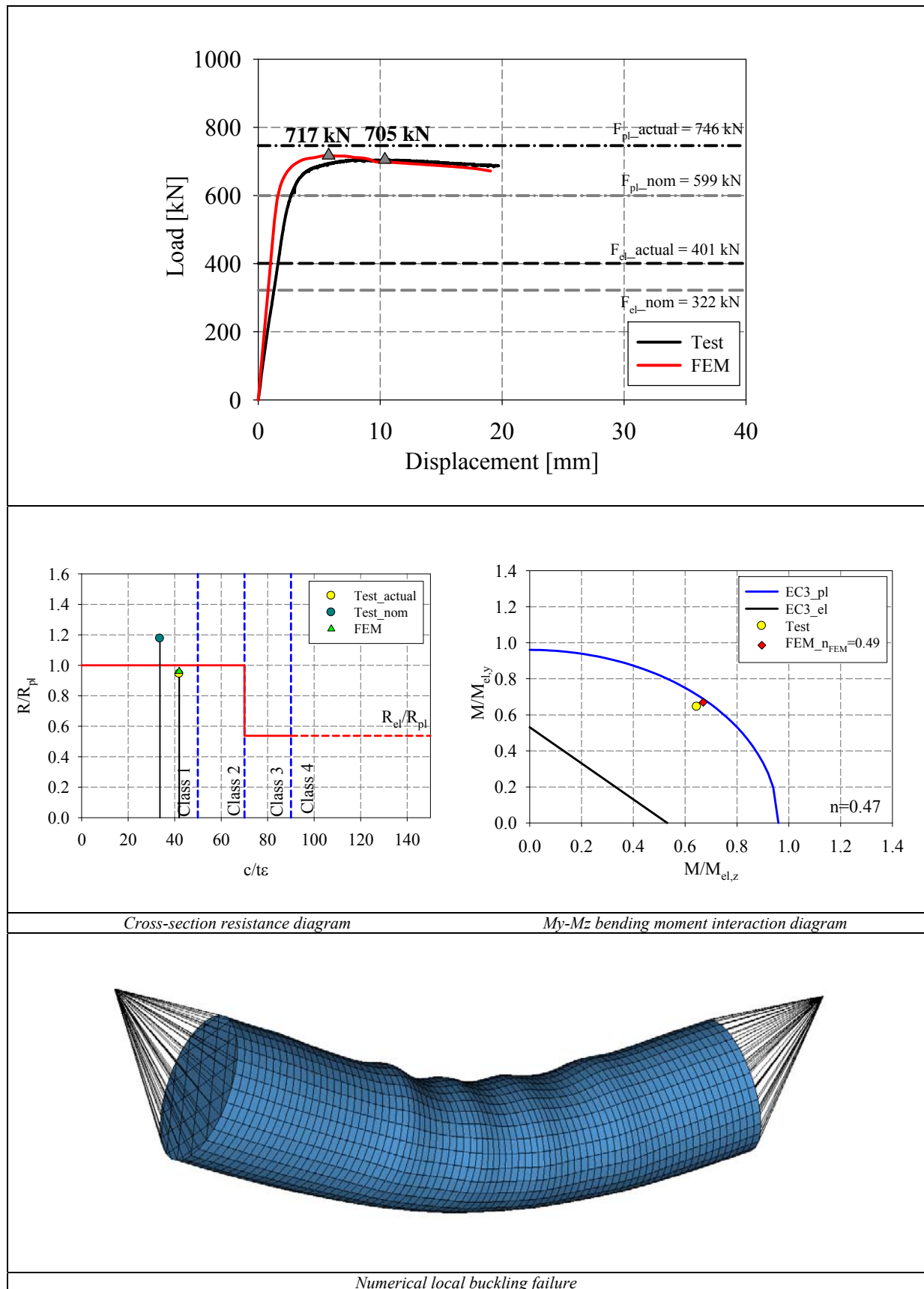
Measured Local imperfections

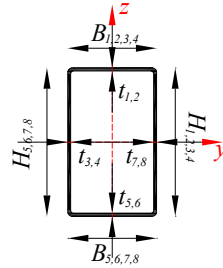
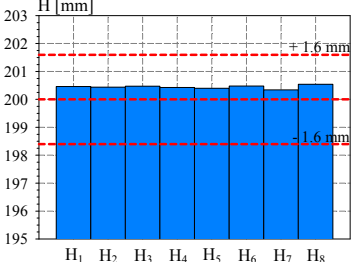
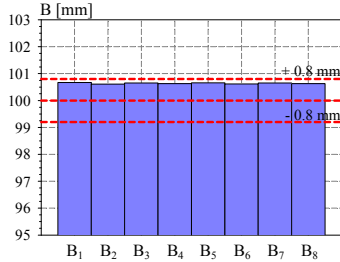
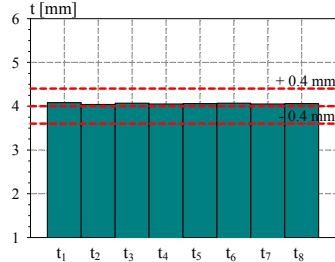
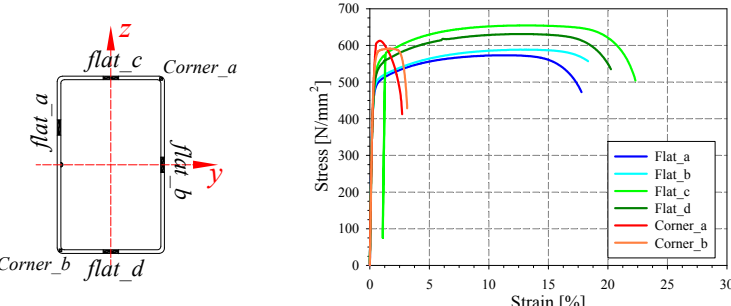
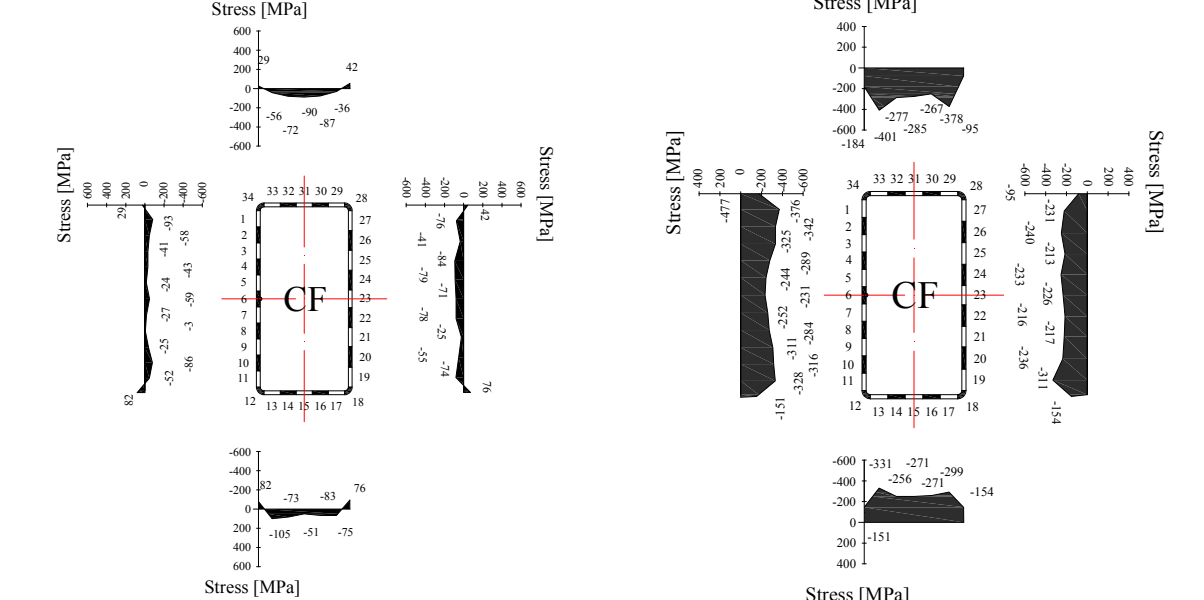


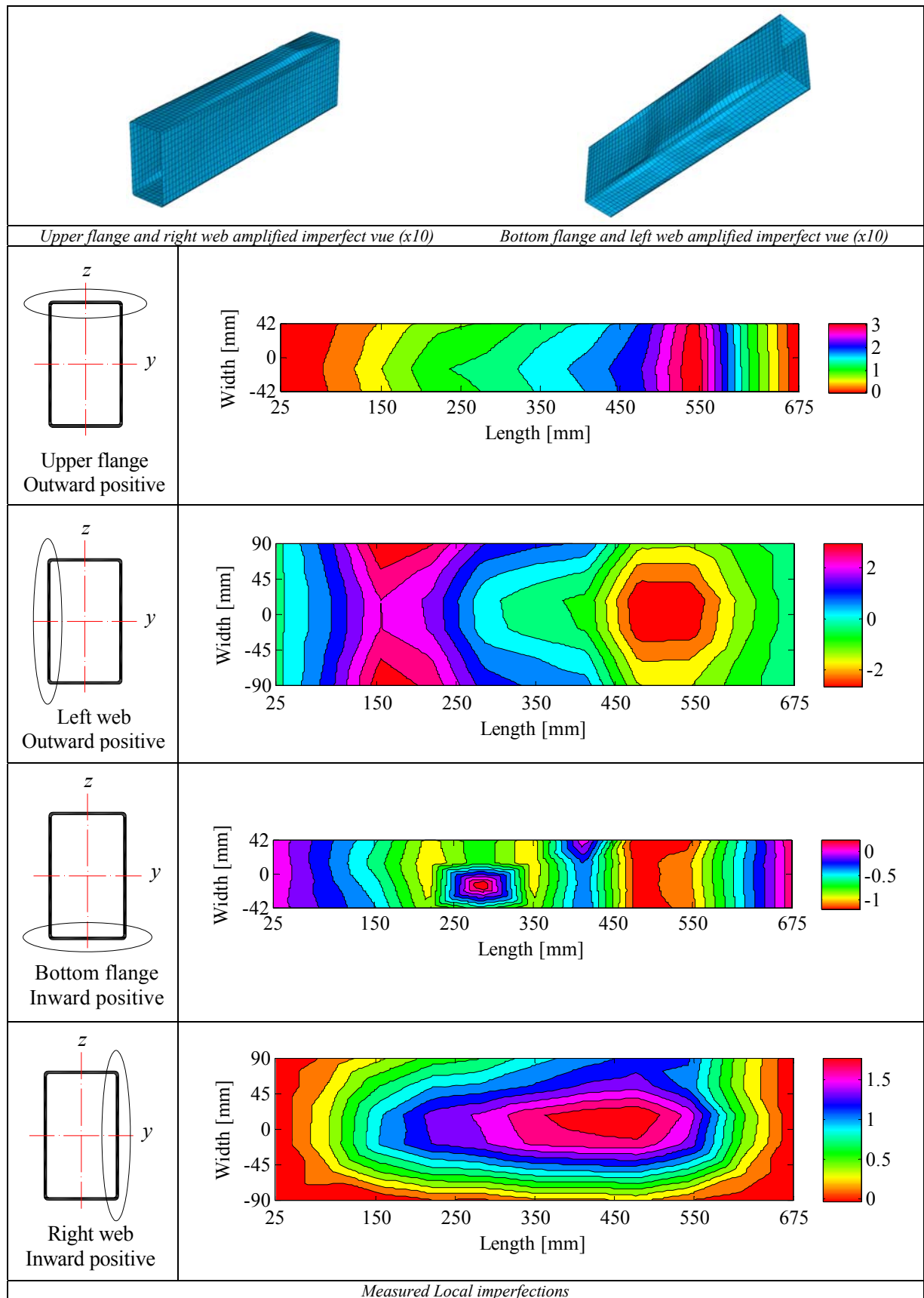
LVDT and strain gauges recordings

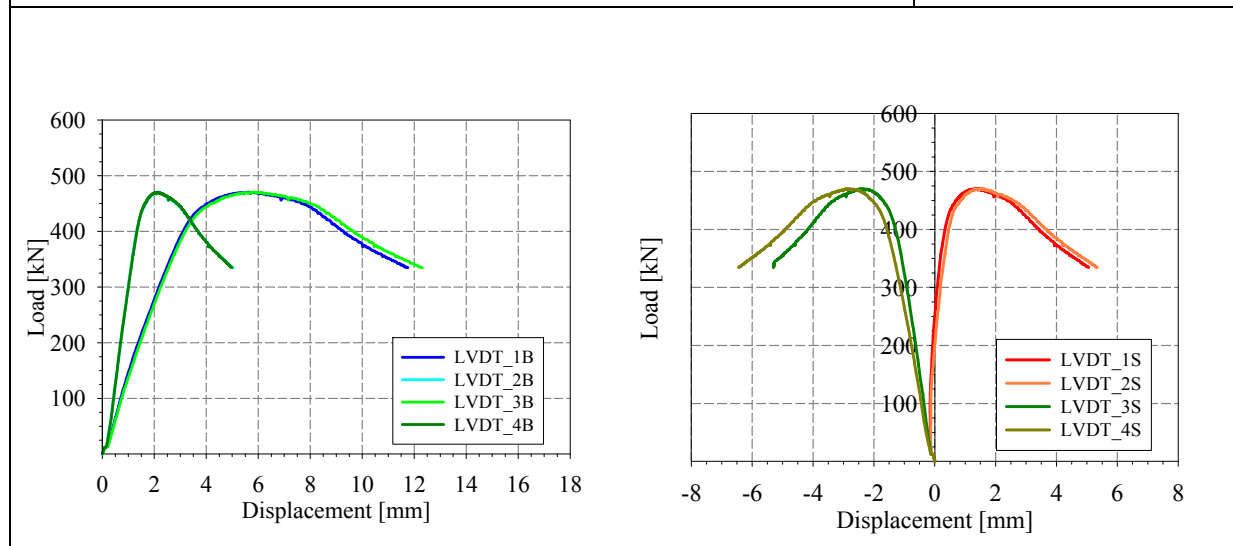
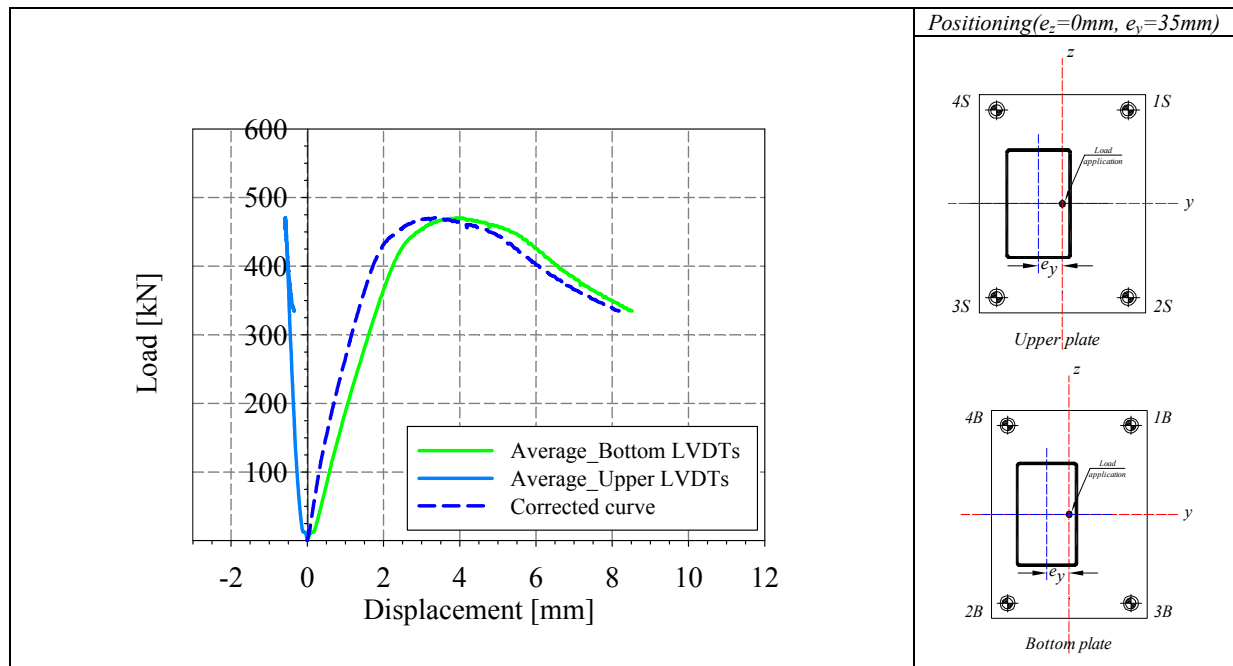


Local buckling failure

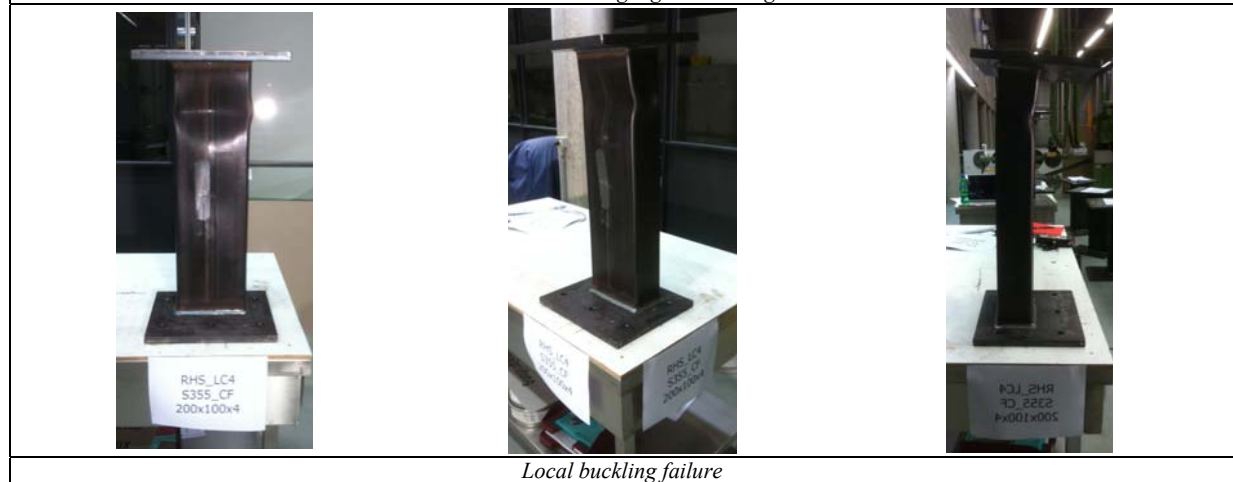


<p>Specimen name</p> <p>RHS_S355_LC4 200x100x4 CF</p>	<p>Shape</p> 	<p>Details</p> <p>Shape: Rectangular Hollow Section</p> <p>Nominal yield limit: 355 MPa</p> <p>Load case: N(50%)+M_z(%50)</p> <p>H=200mm B=100mm t=4mm</p> <p>Fabrication process: Cold formed</p>																		
<p>Average h= 200.44 mm</p> 	<p>Average b= 100.64 mm</p> 	<p>Average t= 4.06 mm</p> 																		
<p>Cross-sectional measured dimensions and tolerances</p>																				
	<table border="1"> <thead> <tr> <th></th> <th>Flat</th> <th>Corner</th> </tr> </thead> <tbody> <tr> <td>E [MPa]</td> <td>216630</td> <td>213000</td> </tr> <tr> <td>f_y [MPa]</td> <td>494.6</td> <td>-</td> </tr> <tr> <td>ε_y [%]</td> <td>0.22</td> <td>-</td> </tr> <tr> <td>f_u [MPa]</td> <td>611</td> <td>601</td> </tr> <tr> <td>ε_u [%]</td> <td>11.9</td> <td>1.2</td> </tr> </tbody> </table>			Flat	Corner	E [MPa]	216630	213000	f _y [MPa]	494.6	-	ε _y [%]	0.22	-	f _u [MPa]	611	601	ε _u [%]	11.9	1.2
	Flat	Corner																		
E [MPa]	216630	213000																		
f _y [MPa]	494.6	-																		
ε _y [%]	0.22	-																		
f _u [MPa]	611	601																		
ε _u [%]	11.9	1.2																		
<p>Tensile coupons location</p>	<p>Material stress-strain curves</p>	<p>Material average properties</p>																		
 <p style="text-align: center;">Membrane stresses Flexural stresses</p> <p style="text-align: center;"><i>Measured residual stresses distributions</i></p>																				

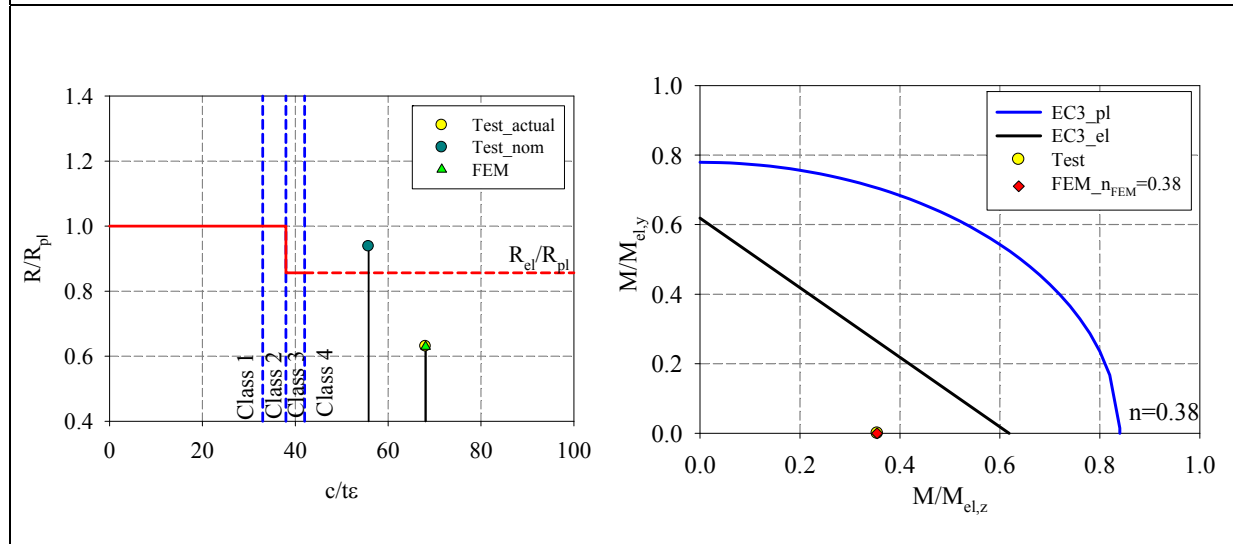
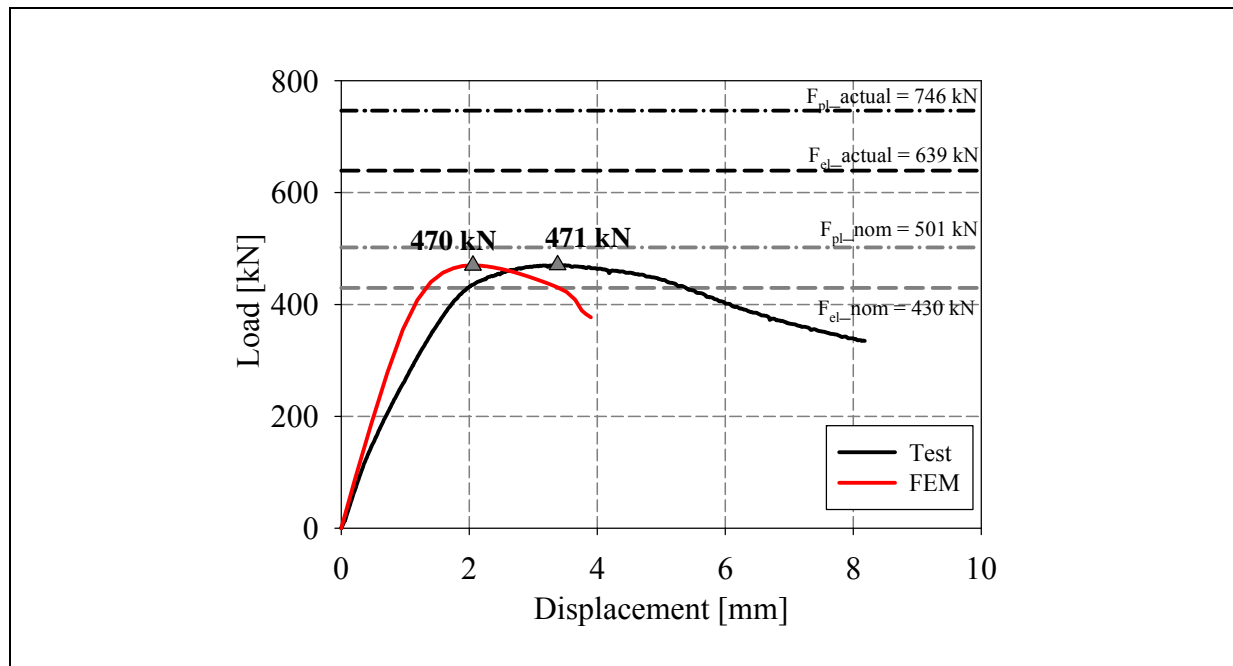




LVDT and strain gauges recordings

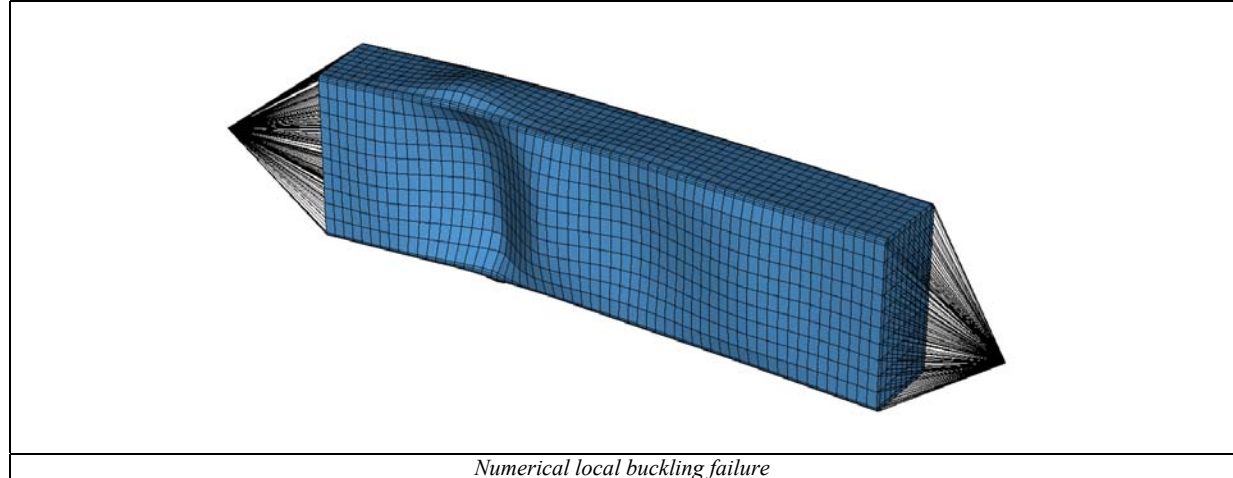


Local buckling failure

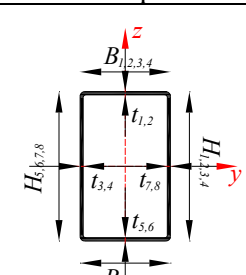


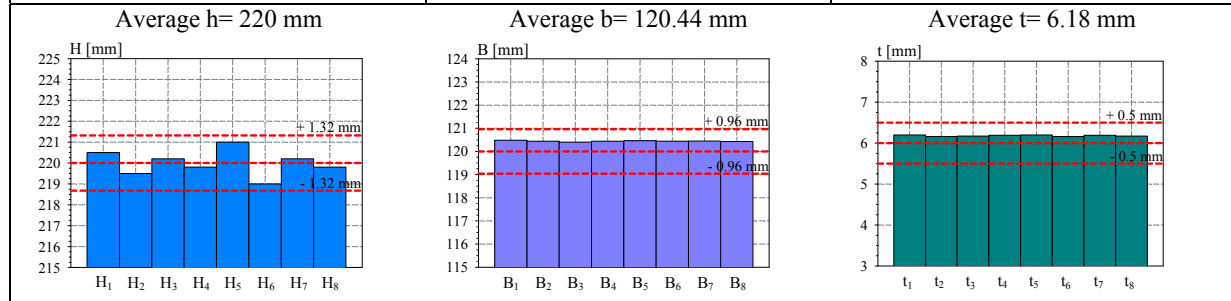
Cross-section resistance diagram

My-Mz bending moment interaction diagram

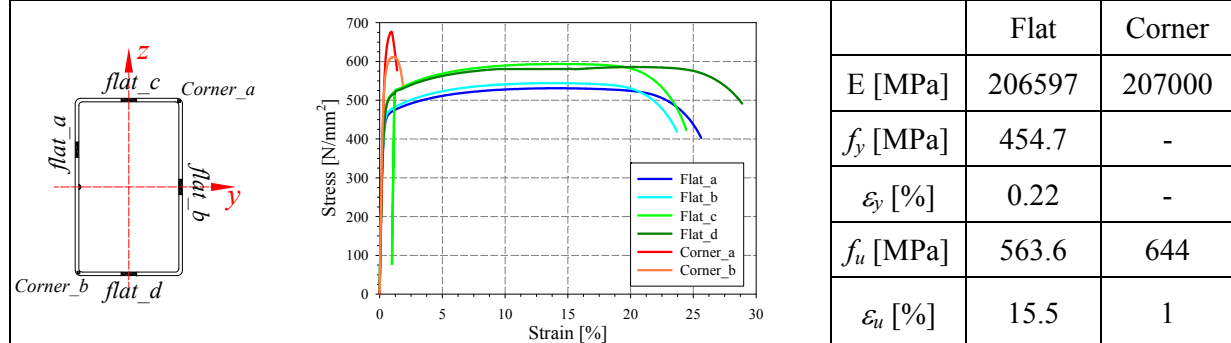


Numerical local buckling failure

<p>Specimen name</p> <p>RHS_S355_LC4 220x120x6 CF</p>	<p>Shape</p> 	<p>Details</p> <p>Shape: Rectangular Hollow Section Nominal yield limit: 355 MPa Load case: N(50%)+M_z(%50) H=220mm B=120mm t=6mm Fabrication process: Cold formed</p>
---	--	--



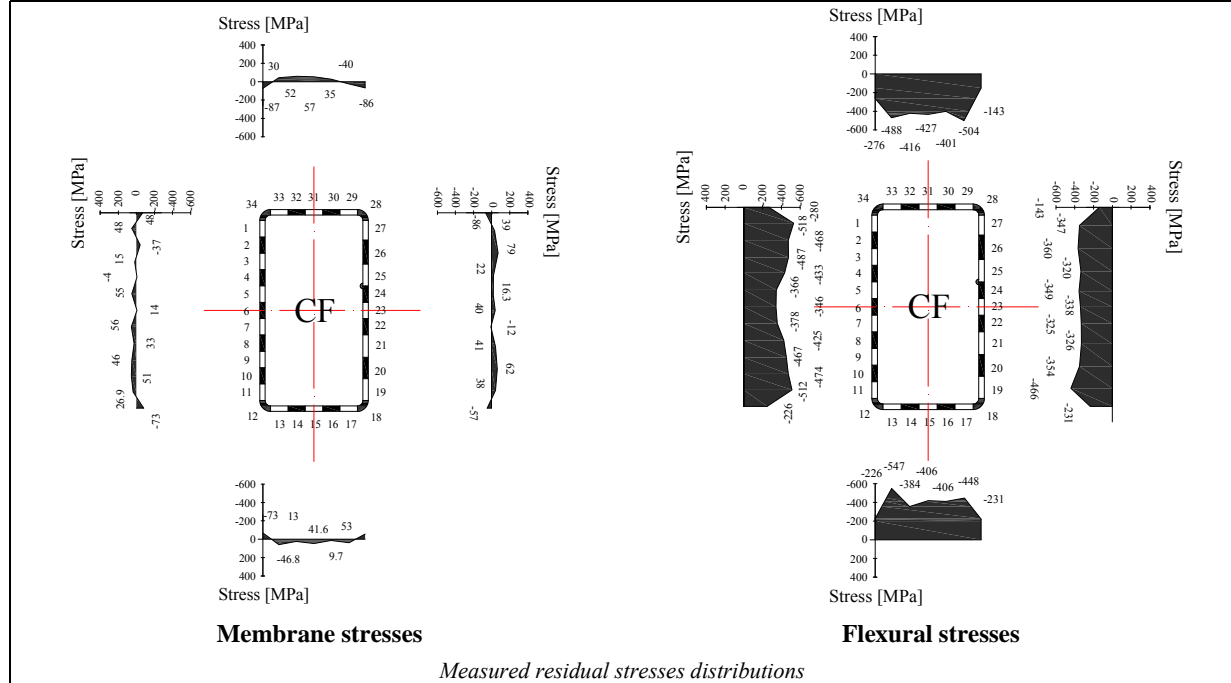
Cross-sectional measured dimensions and tolerances

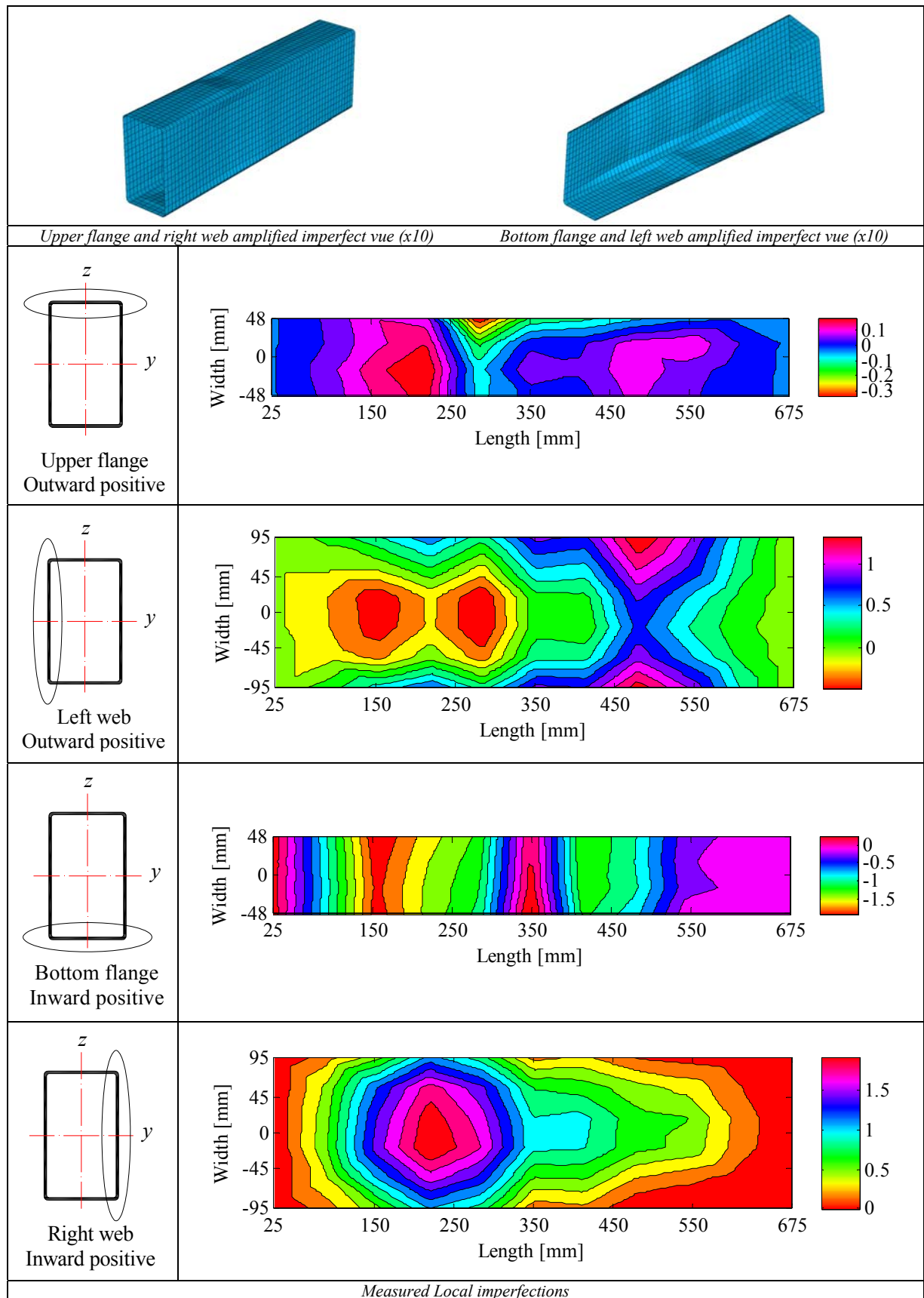


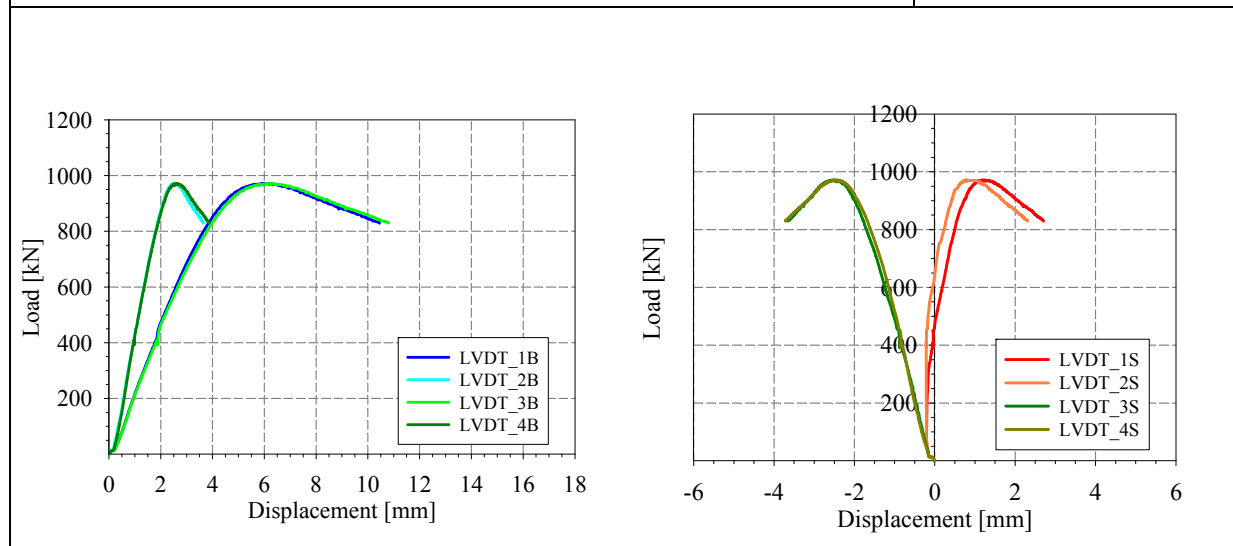
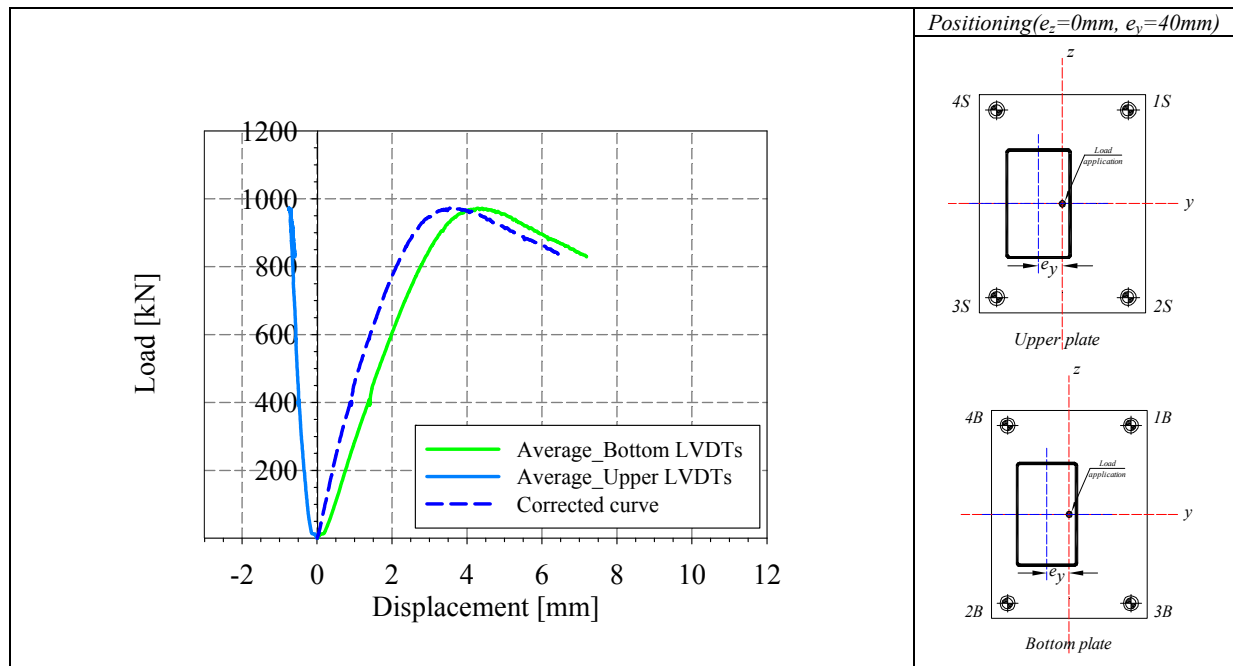
Tensile coupons location

Material stress-strain curves

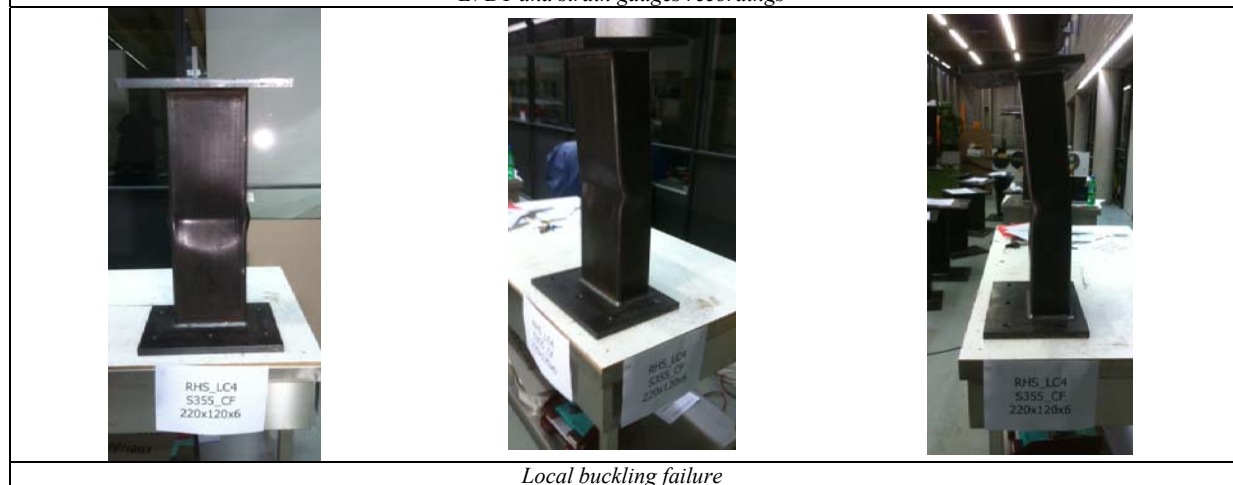
Material average properties



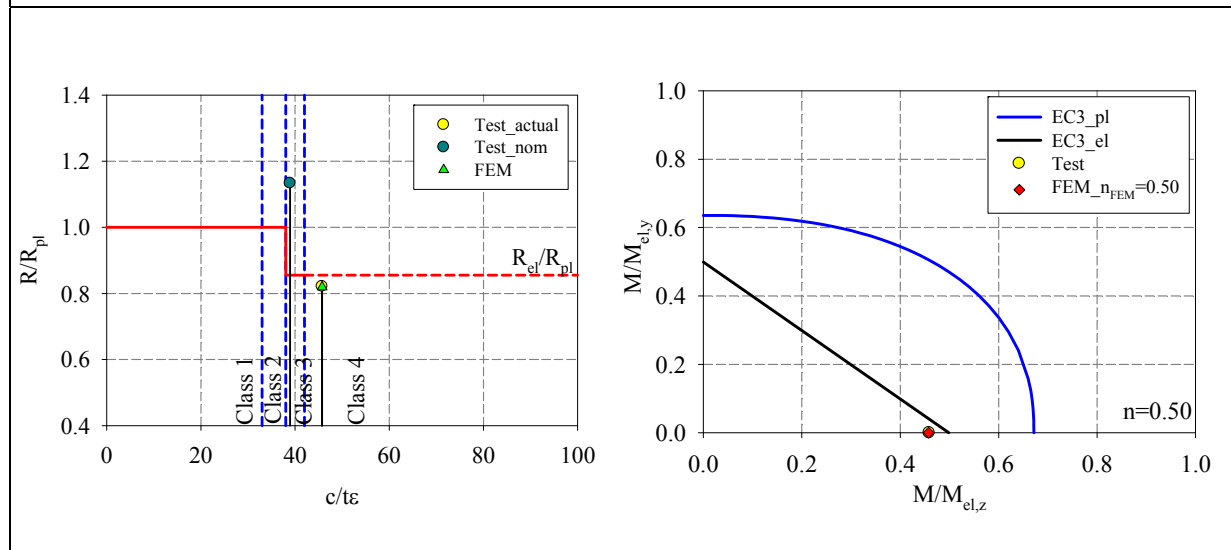
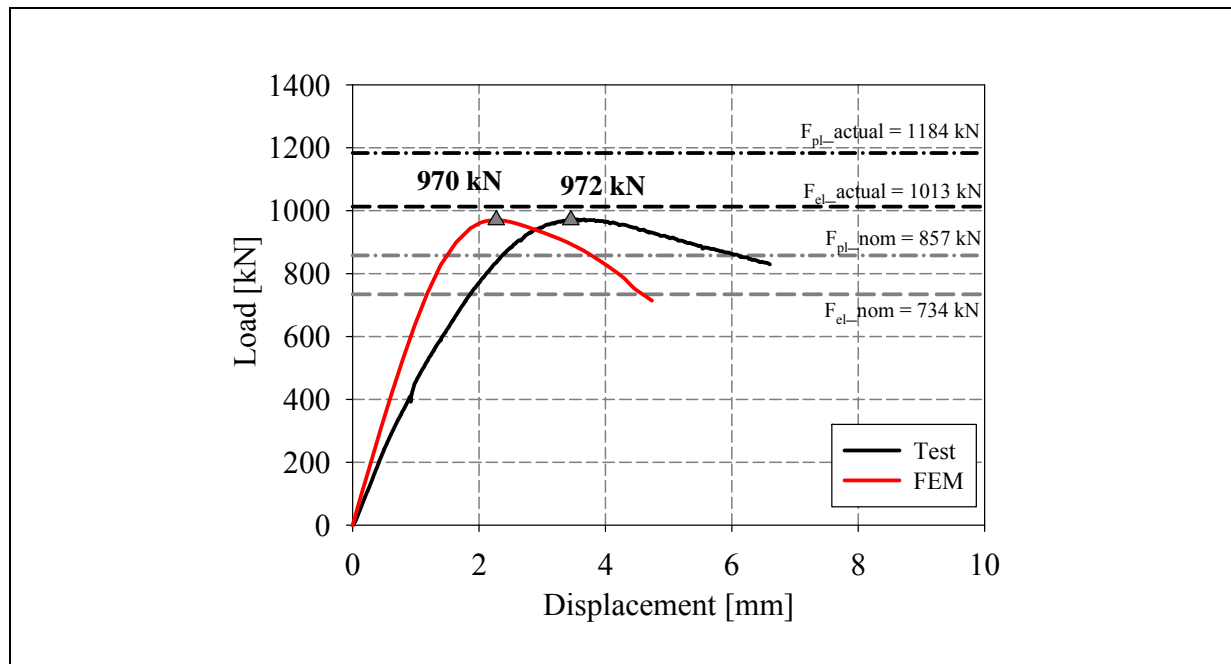




LVDT and strain gauges recordings

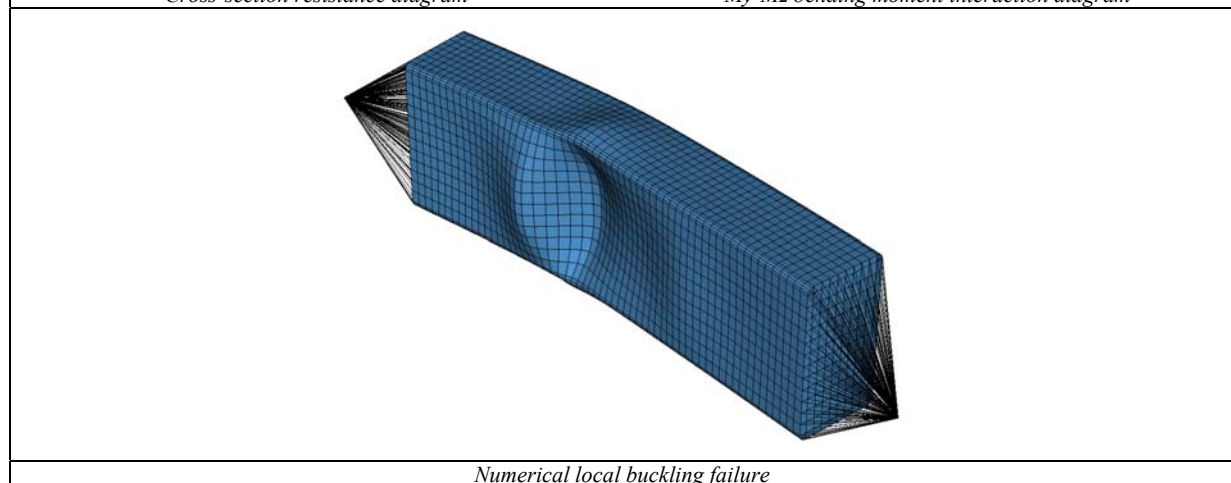


Local buckling failure

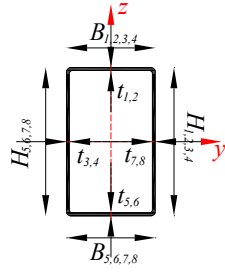
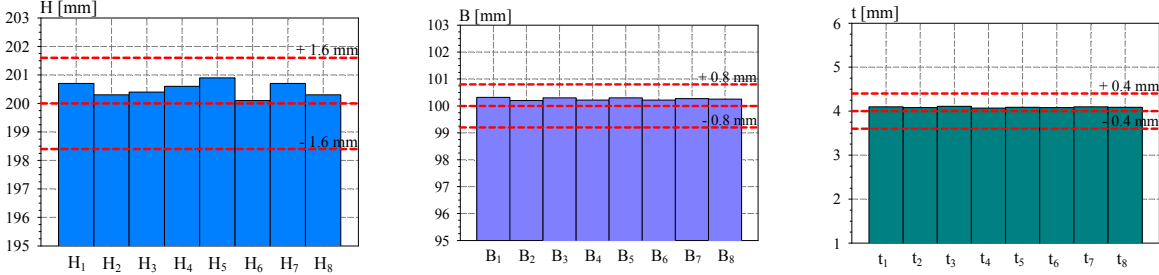
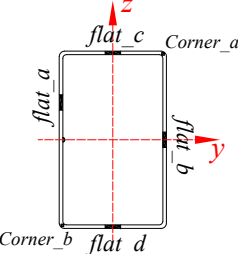
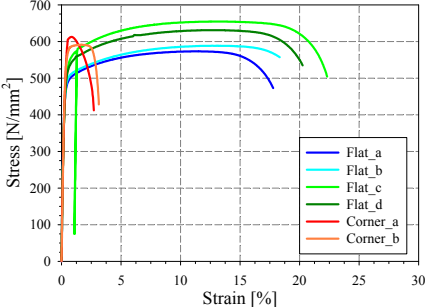
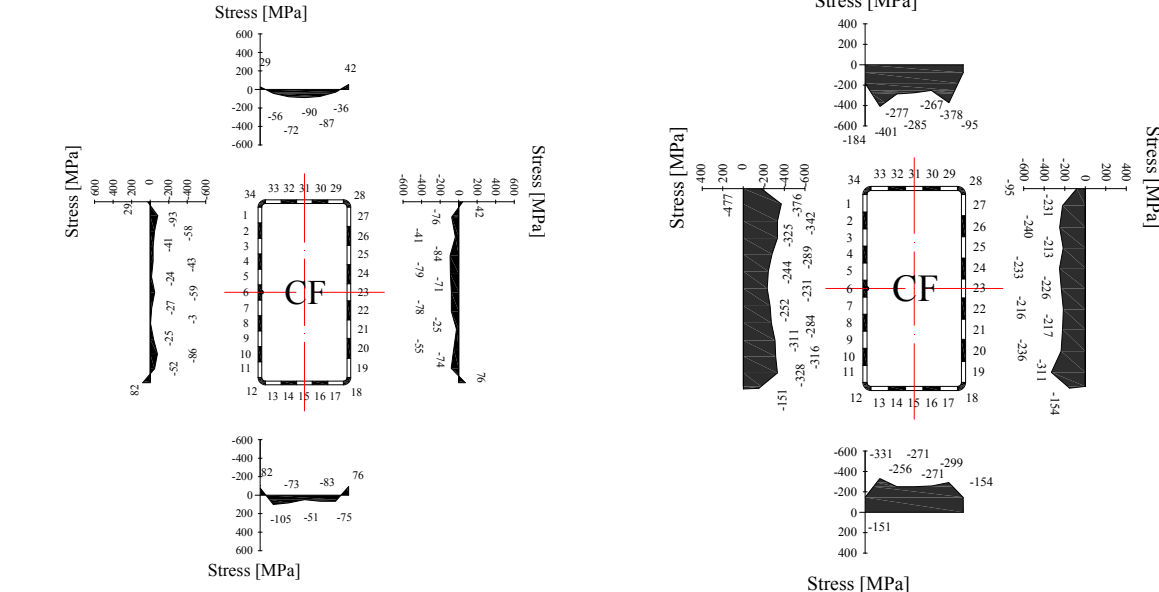


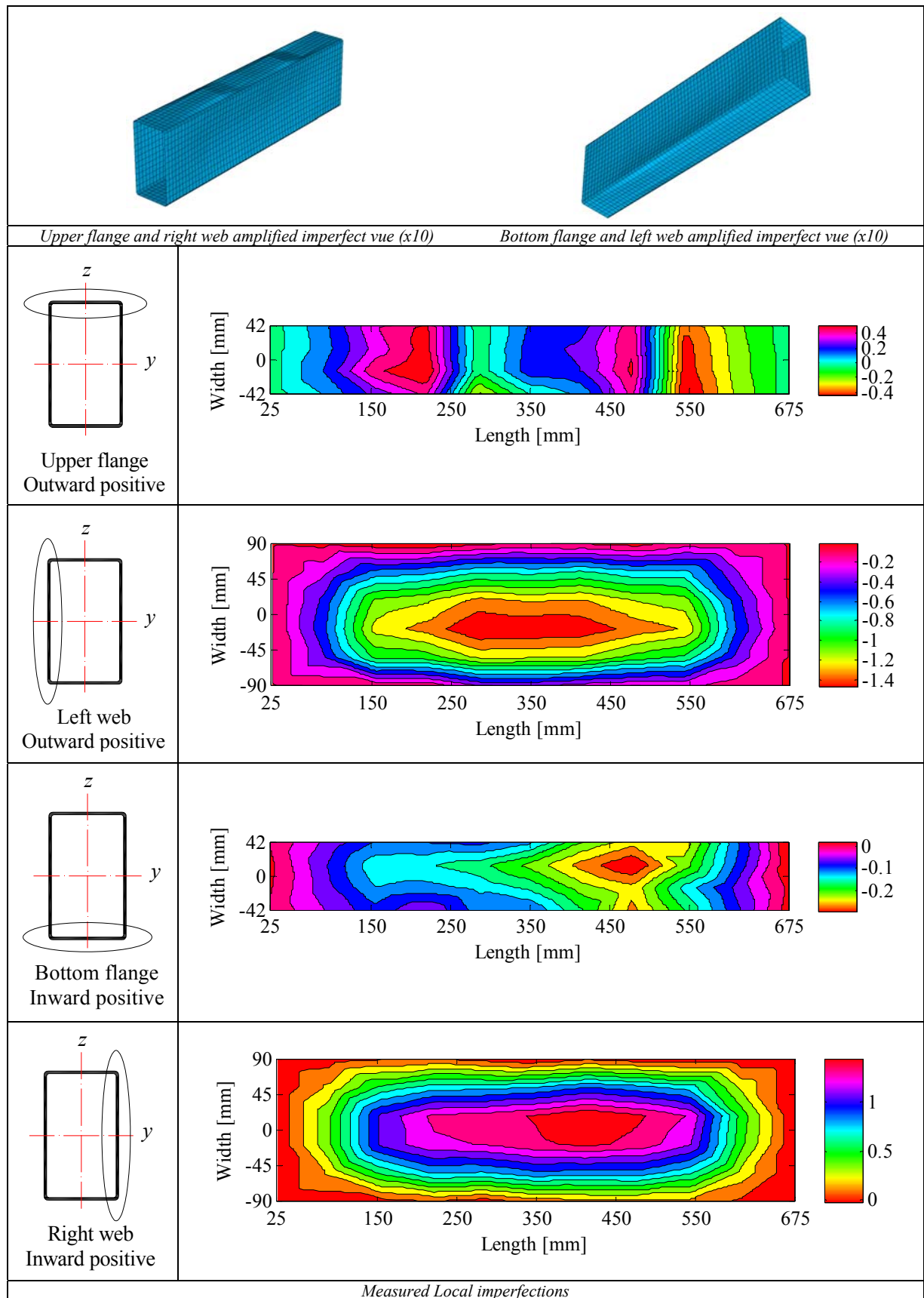
Cross-section resistance diagram

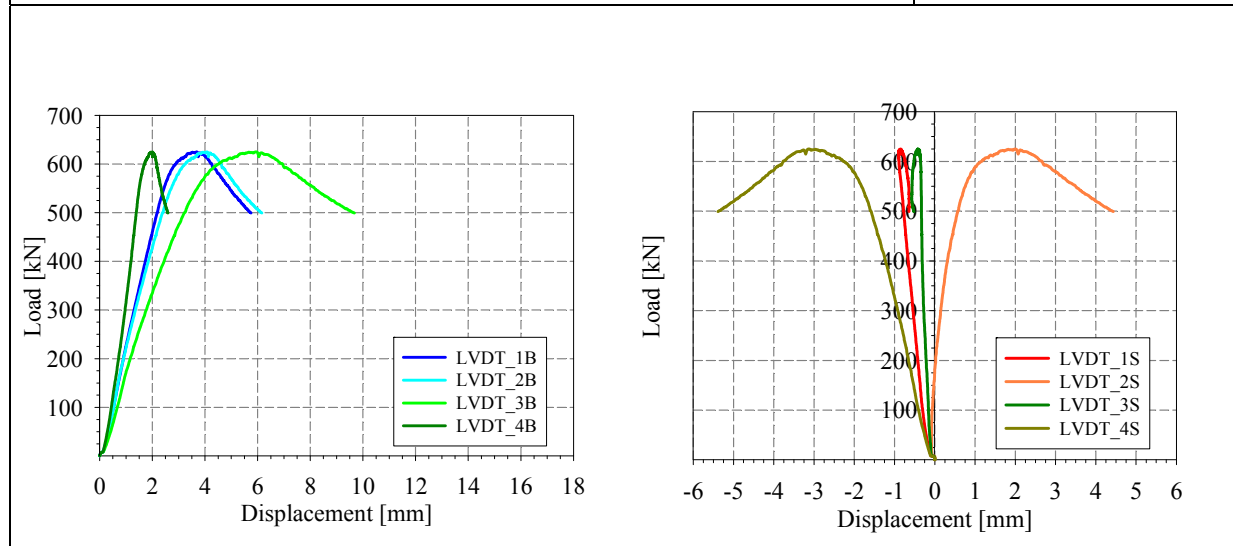
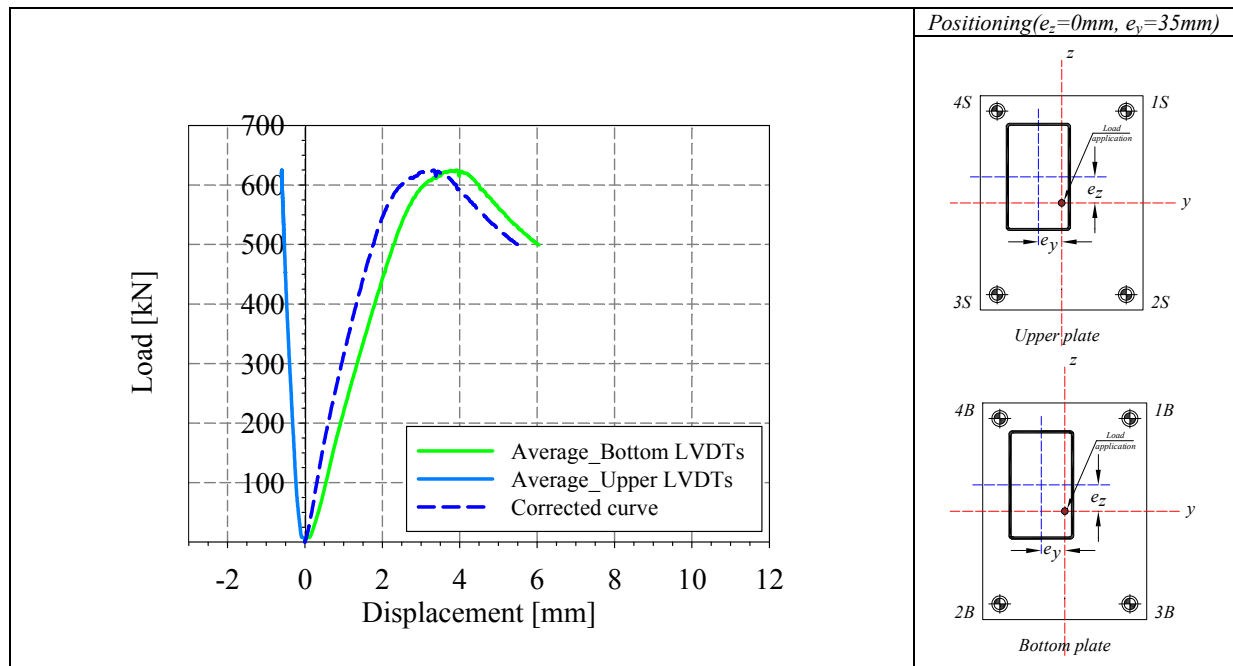
My-Mz bending moment interaction diagram



Numerical local buckling failure

<p>Specimen name</p> <p>RHS_S355_LC5 200x100x4 CF</p>	<p>Shape</p> 	<p>Details</p> <p>Shape: Rectangular Hollow Section</p> <p>Nominal yield limit: 355 MPa</p> <p>Load case: N(50%)+M_y(%25)+M_z(25%)</p> <p>H=200mm B=100mm t=4mm</p> <p>Fabrication process: Cold formed</p>																		
<p>Average h= 200.5 mm Average b= 100.26 mm Average t= 4.09 mm</p> 																				
<p><i>Cross-sectional measured dimensions and tolerances</i></p>																				
<p><i>Tensile coupons location</i></p>  <p><i>Material stress-strain curves</i></p> 	<table border="1"> <thead> <tr> <th></th> <th>Flat</th> <th>Corner</th> </tr> </thead> <tbody> <tr> <td>E [MPa]</td> <td>216630</td> <td>213000</td> </tr> <tr> <td>f_y [MPa]</td> <td>494.6</td> <td>-</td> </tr> <tr> <td>ε_y [%]</td> <td>0.22</td> <td>-</td> </tr> <tr> <td>f_u [MPa]</td> <td>611</td> <td>601</td> </tr> <tr> <td>ε_u [%]</td> <td>11.9</td> <td>1.2</td> </tr> </tbody> </table> <p><i>Material average properties</i></p>			Flat	Corner	E [MPa]	216630	213000	f _y [MPa]	494.6	-	ε _y [%]	0.22	-	f _u [MPa]	611	601	ε _u [%]	11.9	1.2
	Flat	Corner																		
E [MPa]	216630	213000																		
f _y [MPa]	494.6	-																		
ε _y [%]	0.22	-																		
f _u [MPa]	611	601																		
ε _u [%]	11.9	1.2																		
<p><i>Measured residual stresses distributions</i></p>  <p>Membrane stresses Flexural stresses</p>																				

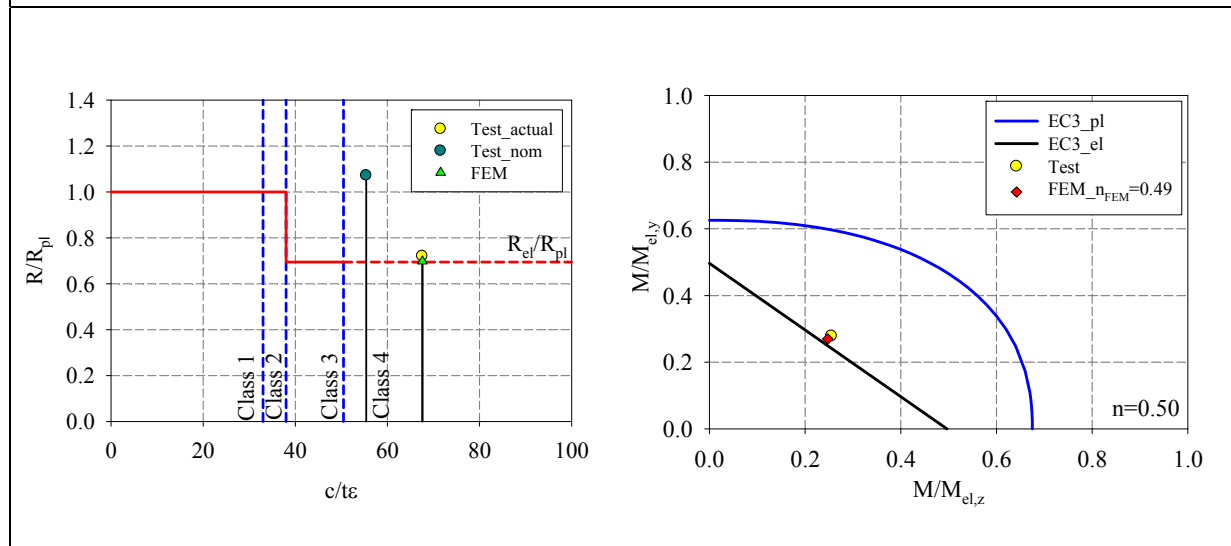
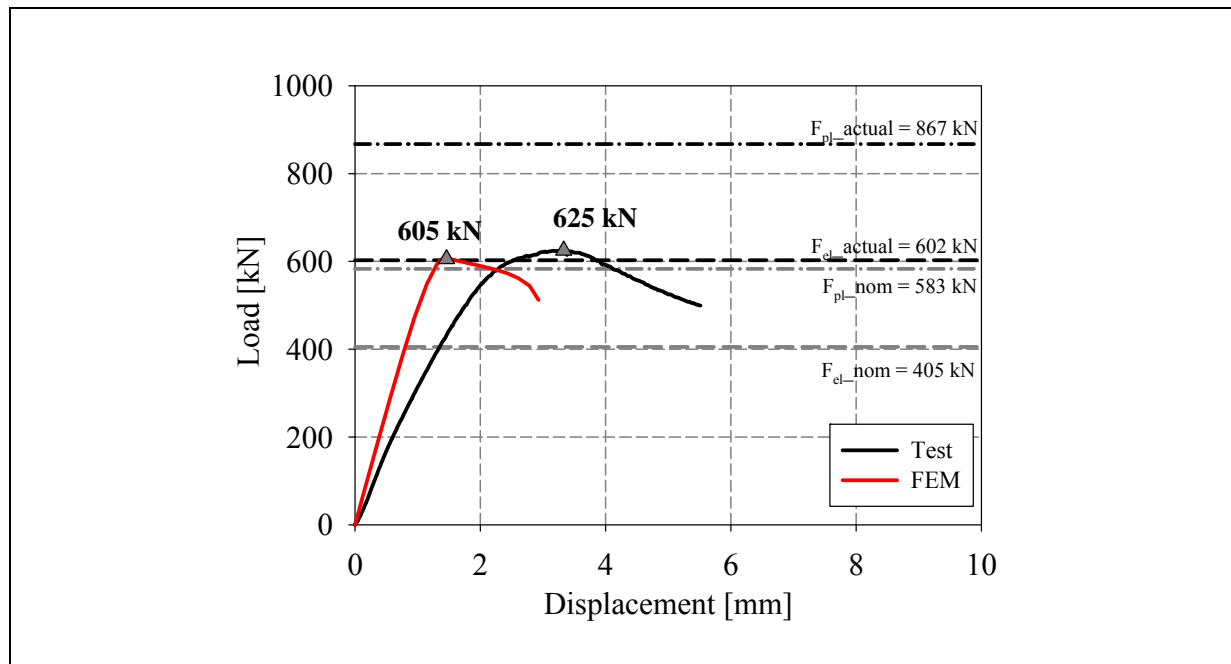




LVDT and strain gauges recordings

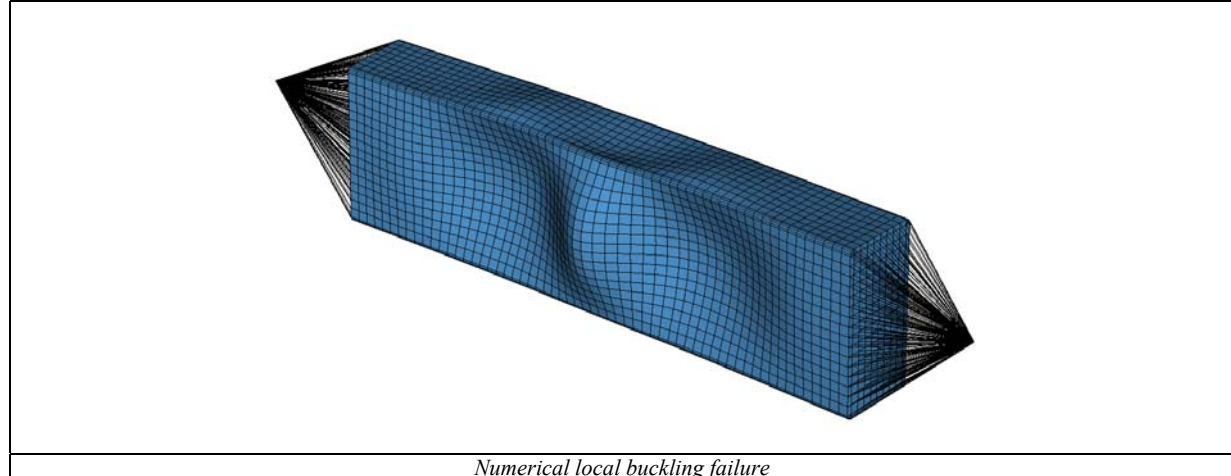


Local buckling failure

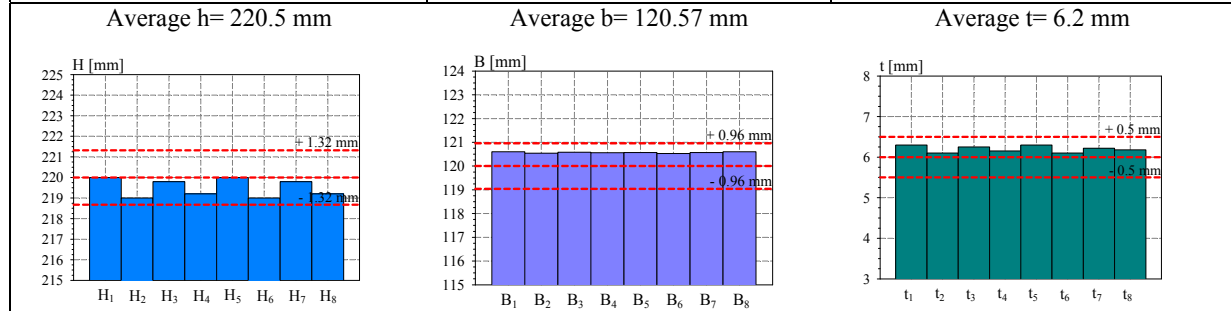


Cross-section resistance diagram

My-Mz bending moment interaction diagram



Specimen name	Shape	Details
RHS_S355_LC5 220x120x6 CF		Shape: Rectangular Hollow Section Nominal yield limit: 355 MPa Load case: N(50%)+M _y (%25)+M _z (25%) H=220mm B=120mm t=6mm Fabrication process: Cold formed



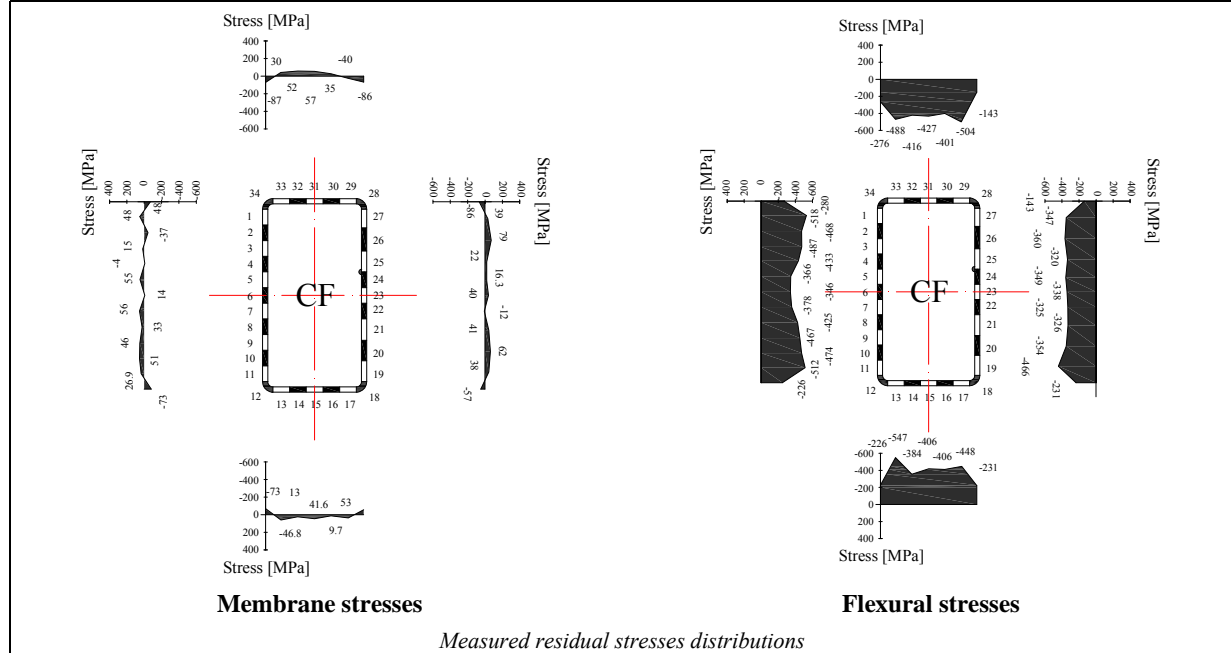
Cross-sectional measured dimensions and tolerances

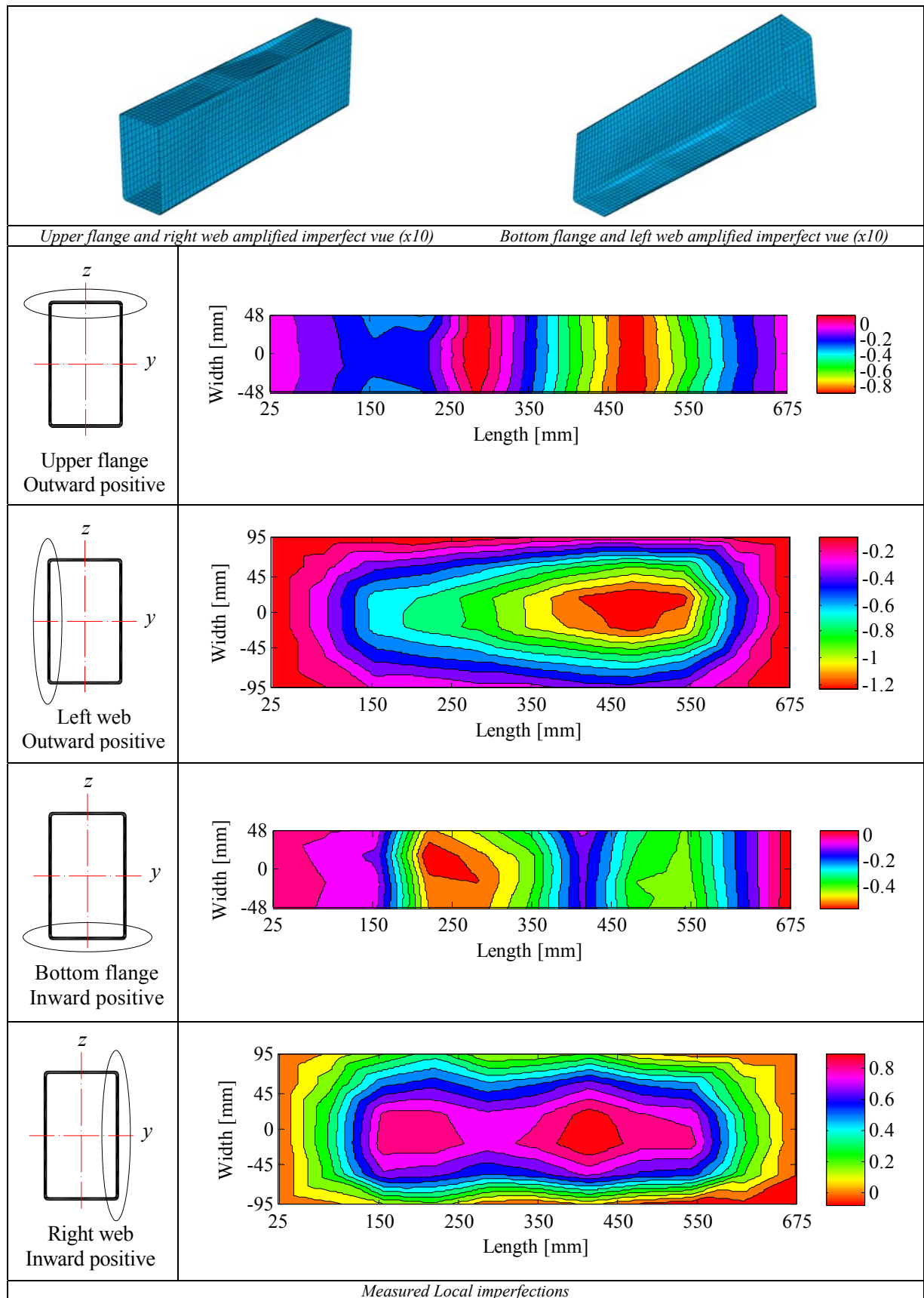
	Material stress-strain curves		Material average properties	
	Flat	Corner	E [MPa]	Corner
	E [MPa]	206597	207000	
	f_y [MPa]	454.7	-	
	ϵ_y [%]	0.22	-	
	f_u [MPa]	563.6	644	
	ϵ_u [%]	15.5	1	

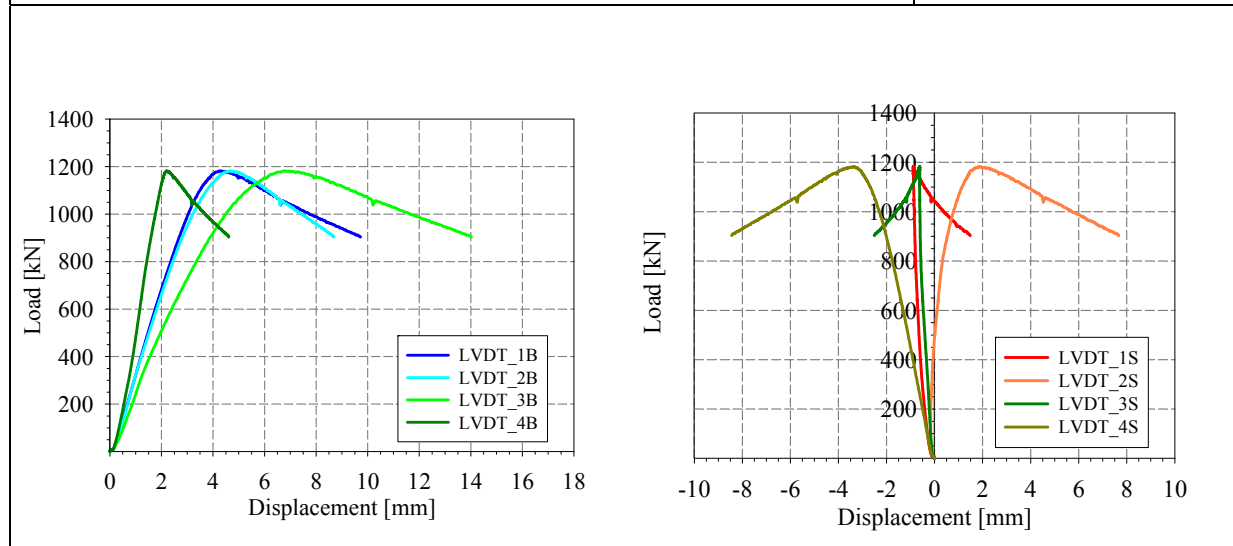
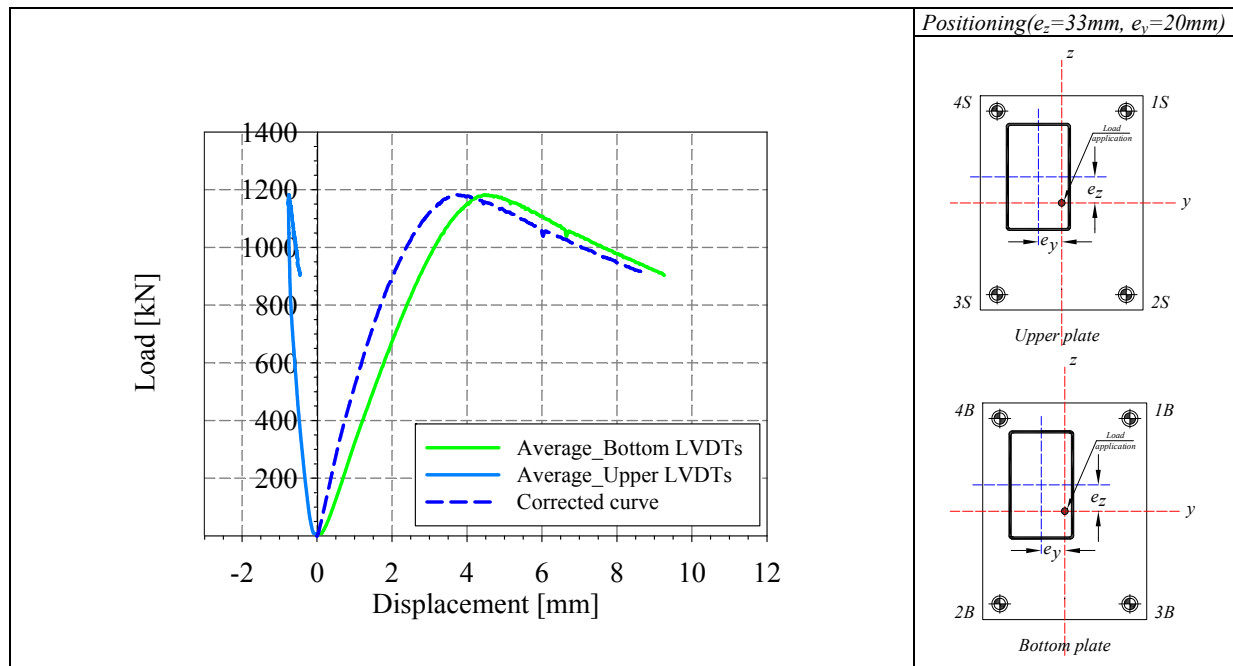
Tensile coupons location

Material stress-strain curves

Material average properties



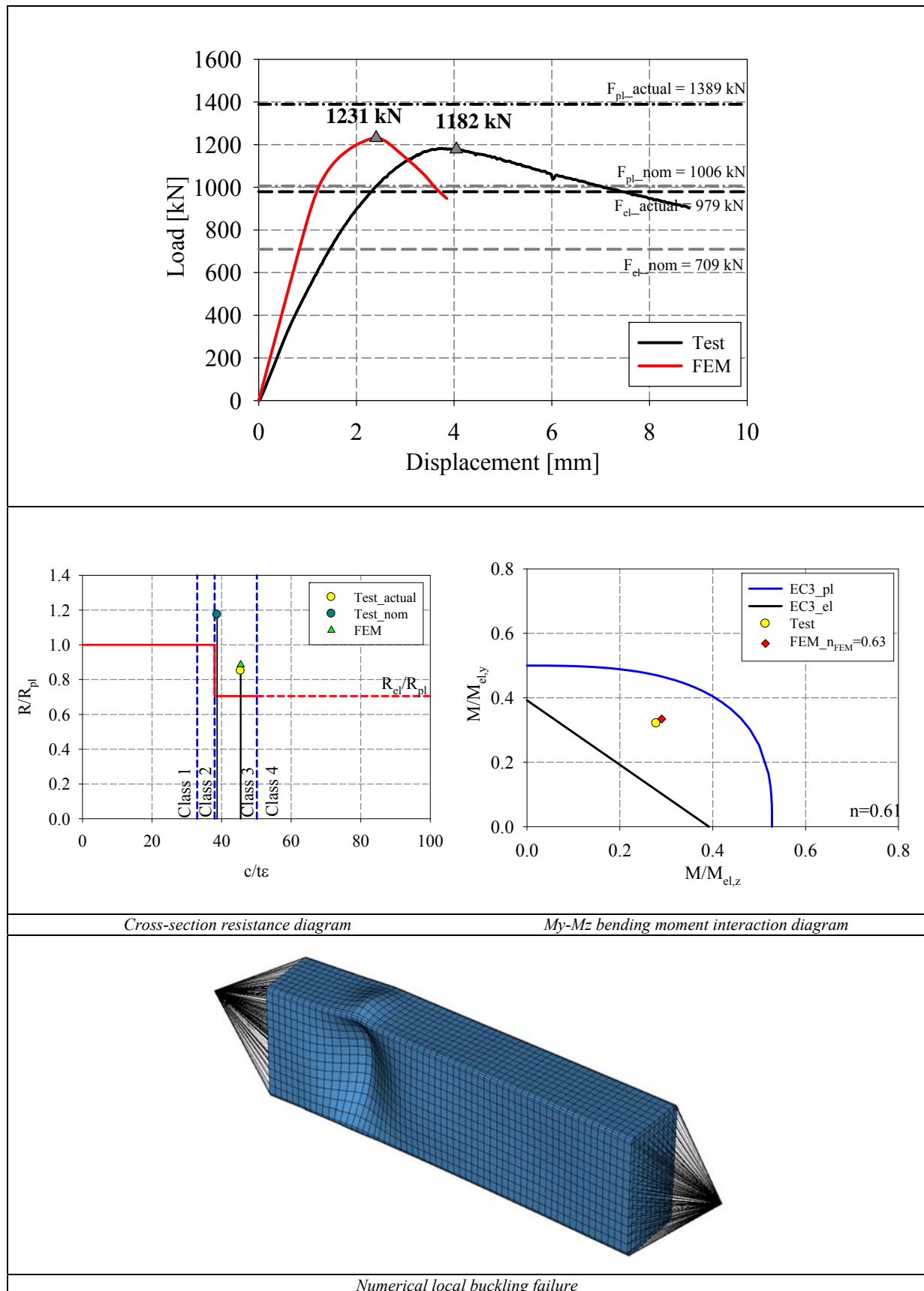


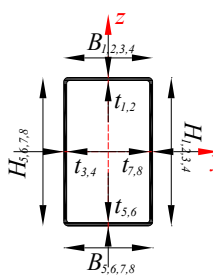


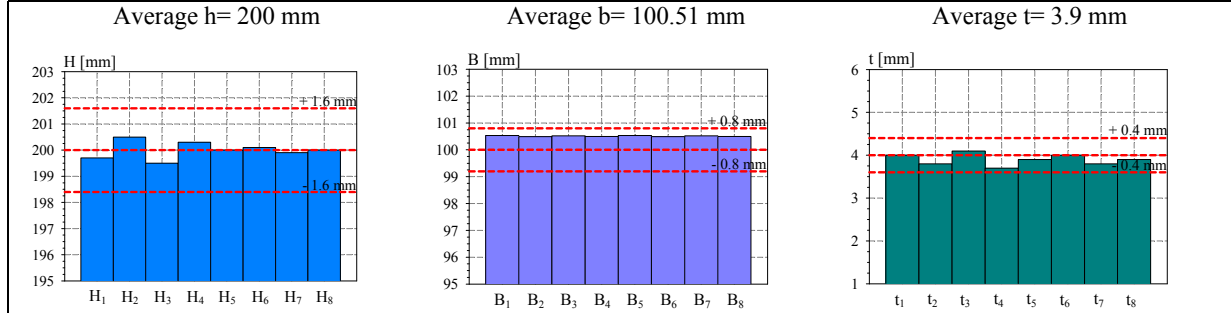
LVDT and strain gauges recordings



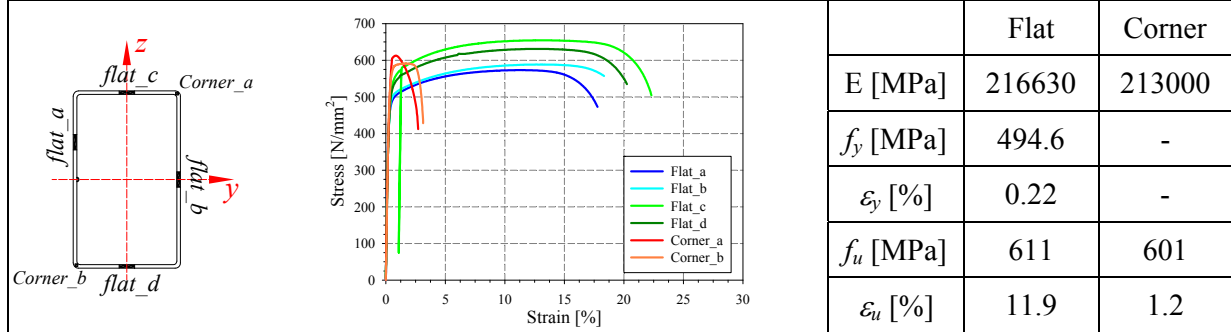
Local buckling failure



<p>Specimen name</p> <p>RHS_S355_LC6 200x100x4 CF</p>	<p>Shape</p> 	<p>Details</p> <p>Shape: Rectangular Hollow Section</p> <p>Nominal yield limit: 355 MPa</p> <p>Load case: N(80%)+M_y(%10)+M_z(10%)</p> <p>H=200mm B=100mm t=4mm</p> <p>Fabrication process: Cold formed</p>
---	--	---



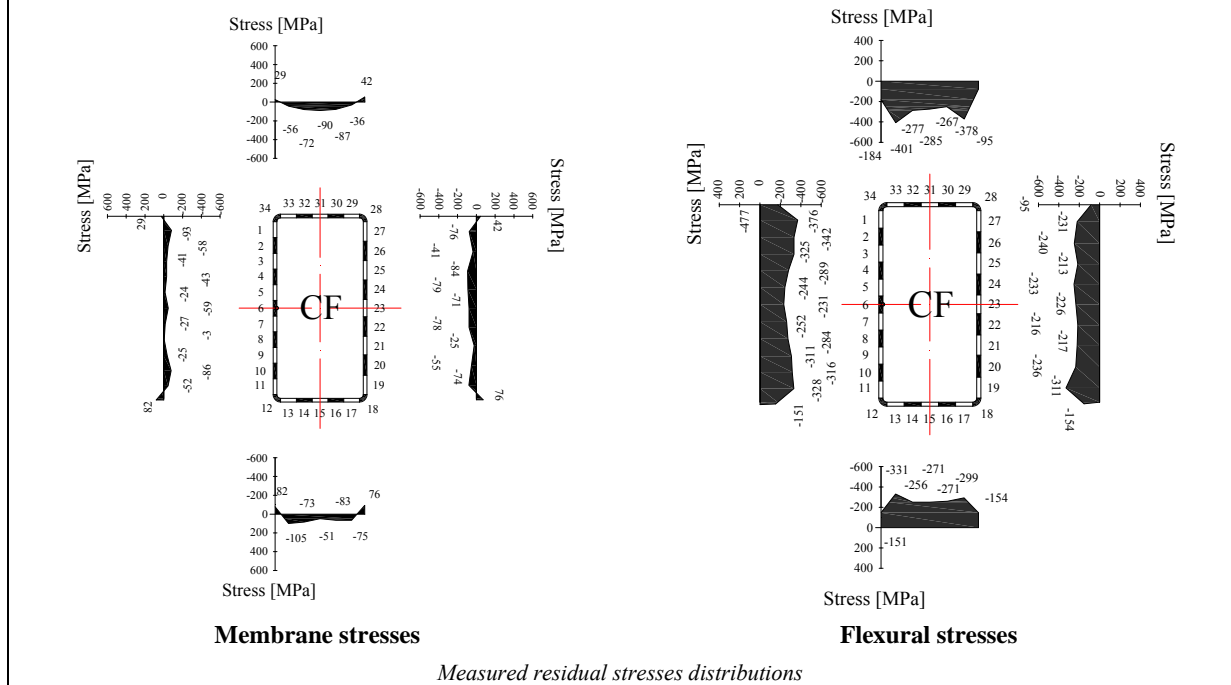
Cross-sectional measured dimensions and tolerances

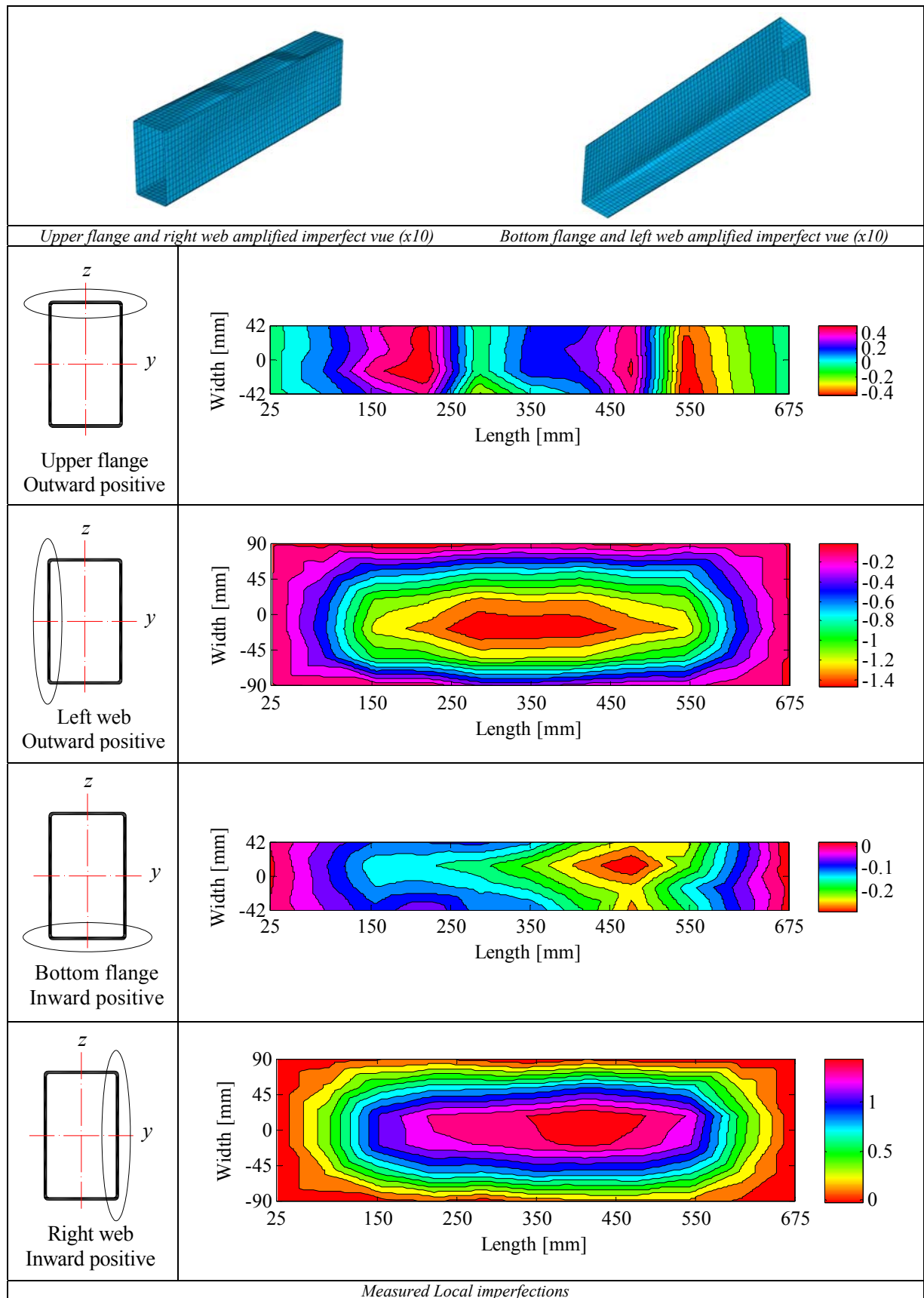


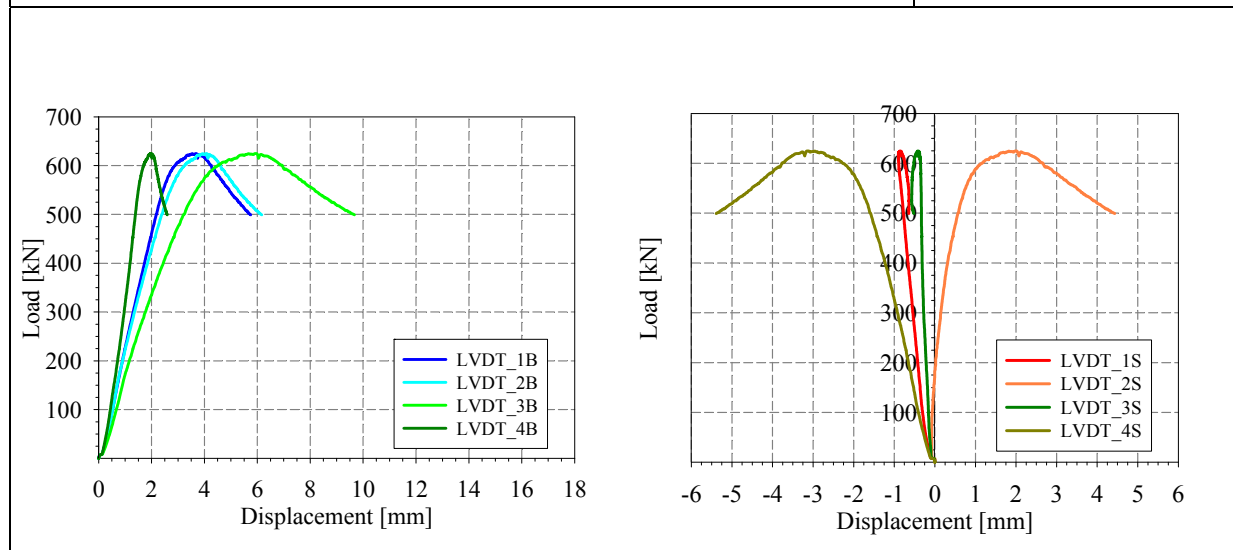
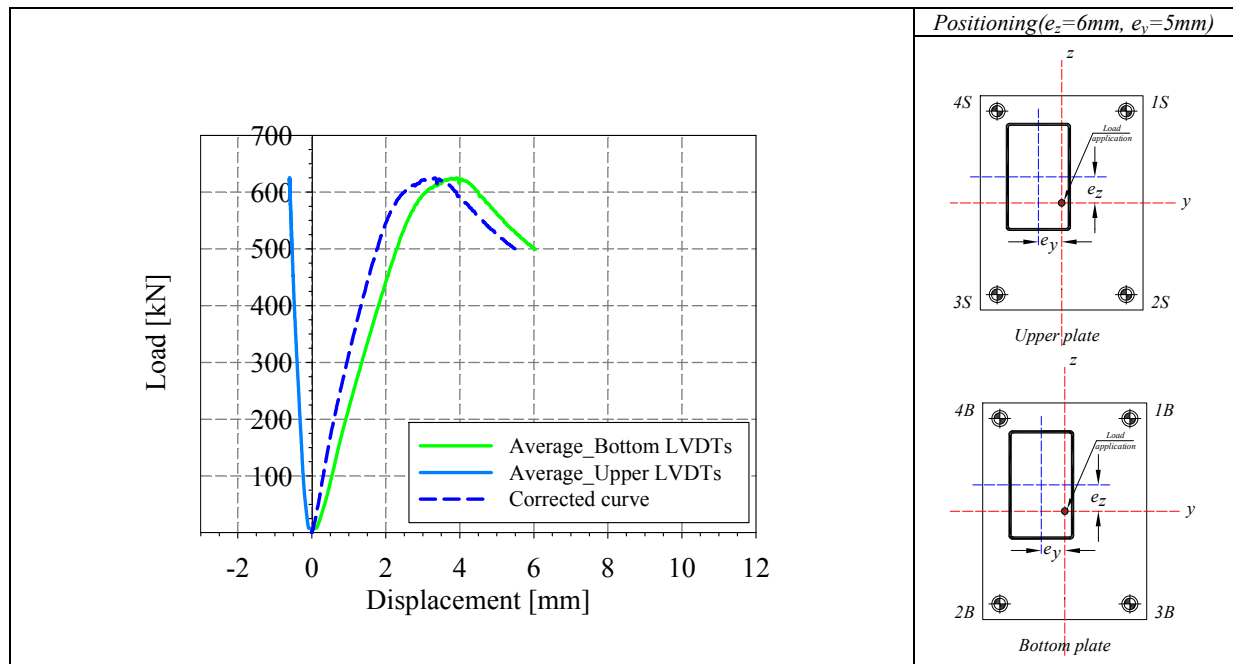
Tensile coupons location

Material stress-strain curves

Material average properties

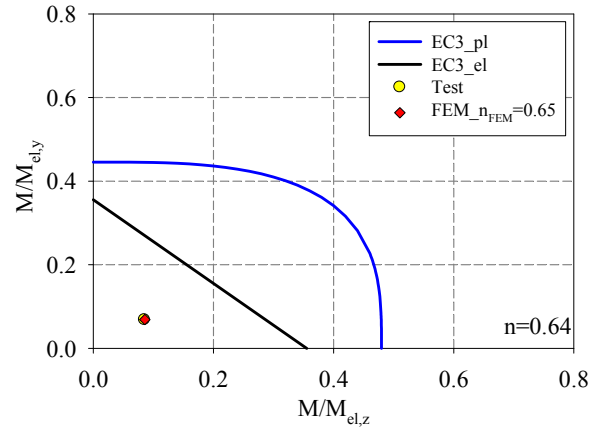
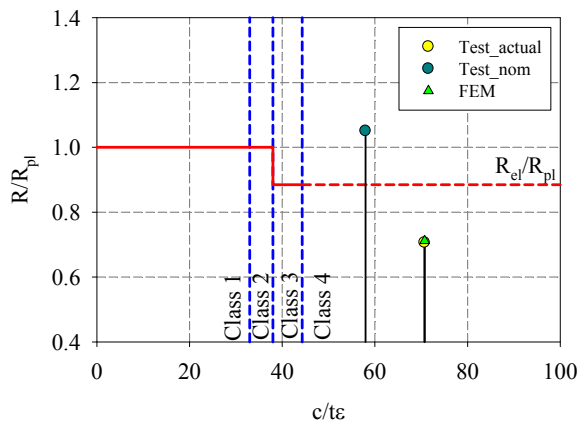
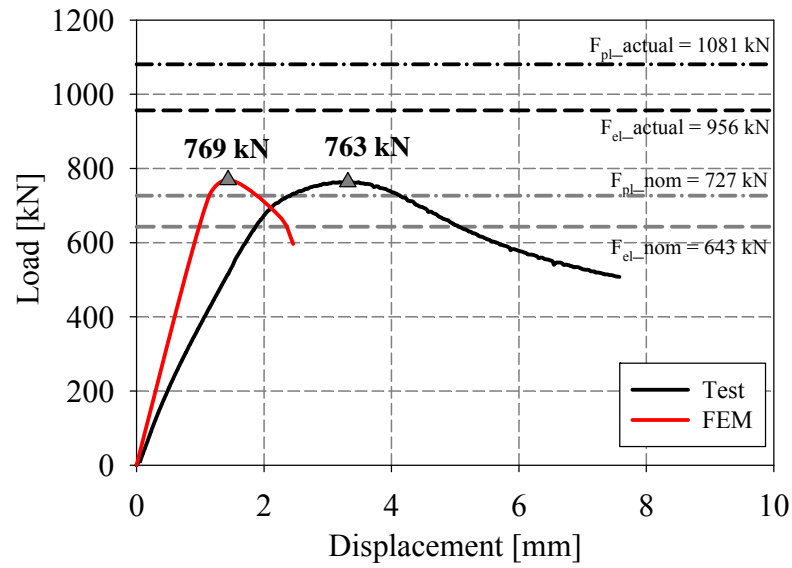






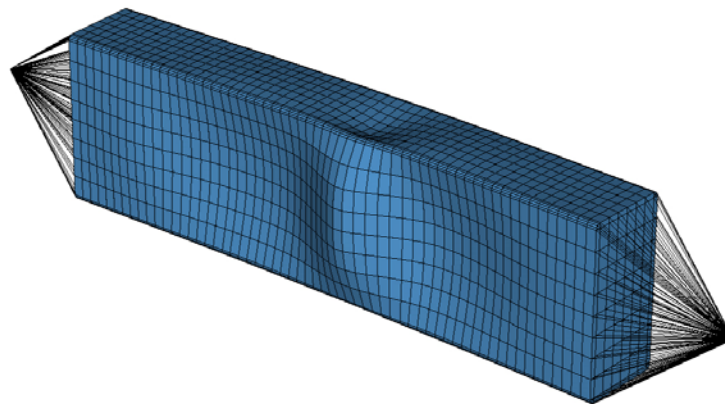
LVDT and strain gauges recordings



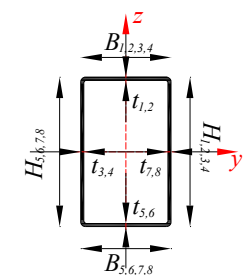


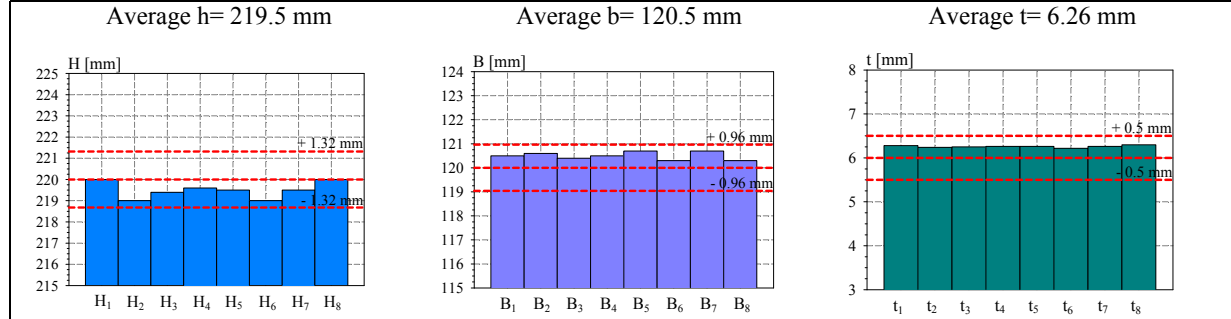
Cross-section resistance diagram

M_y - M_z bending moment interaction diagram

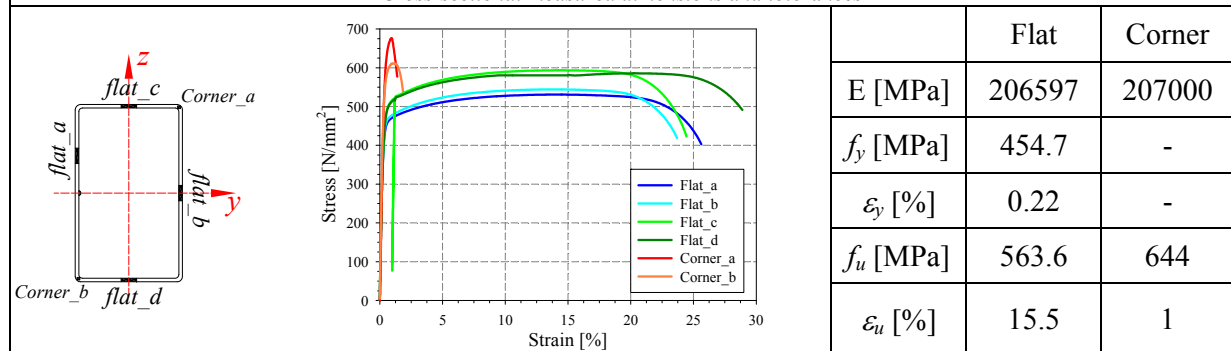


Numerical local buckling failure

<p>Specimen name</p> <p>RHS_S355_LC6 220x120x6 CF</p>	<p>Shape</p> 	<p>Details</p> <p>Shape: Rectangular Hollow Section</p> <p>Nominal yield limit: 355 MPa</p> <p>Load case: N(80%)+M_y(%10)+M_z(10%)</p> <p>H=220mm B=120mm t=6mm</p> <p>Fabrication process: Cold formed</p>
---	--	---



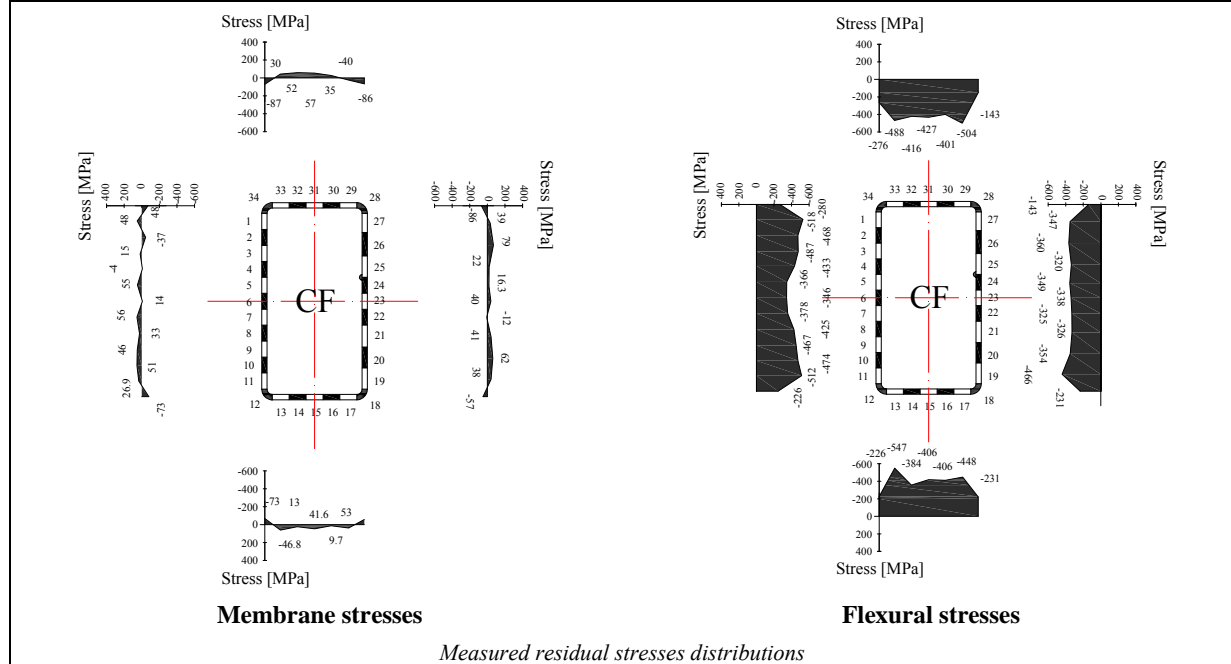
Cross-sectional measured dimensions and tolerances

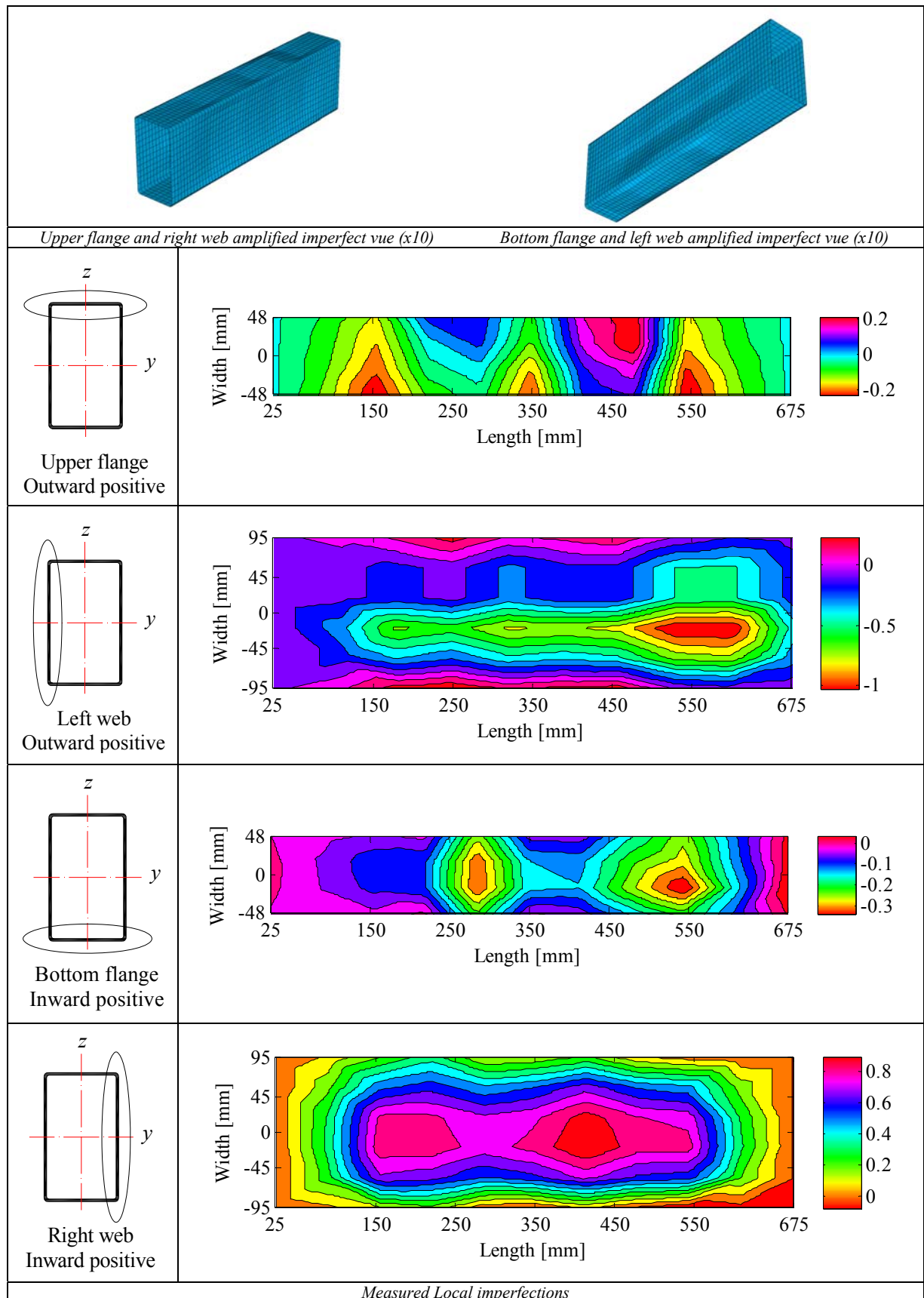


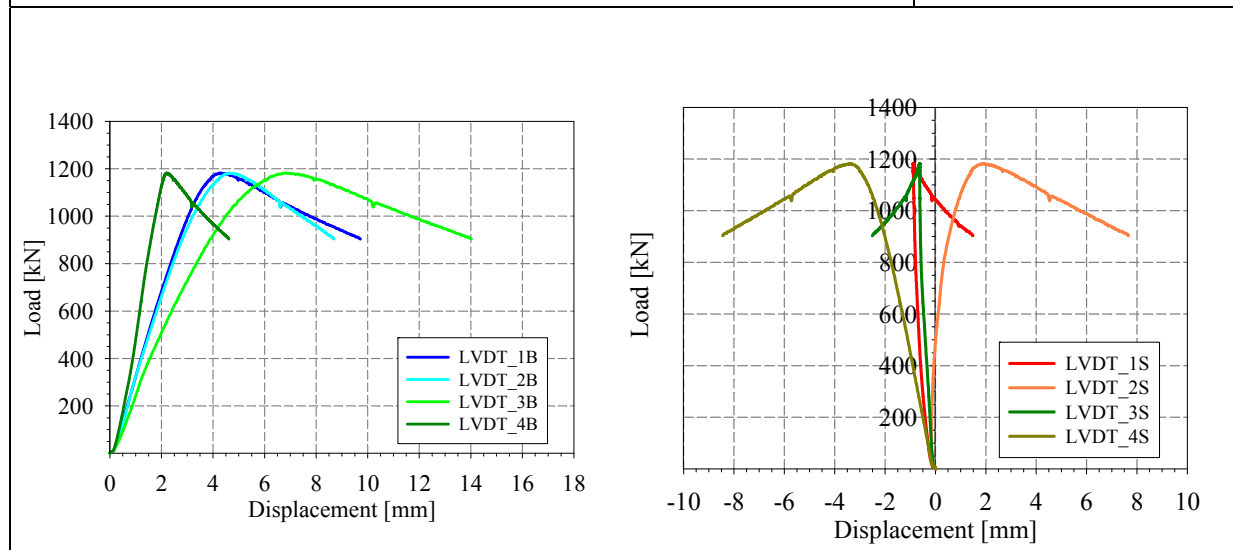
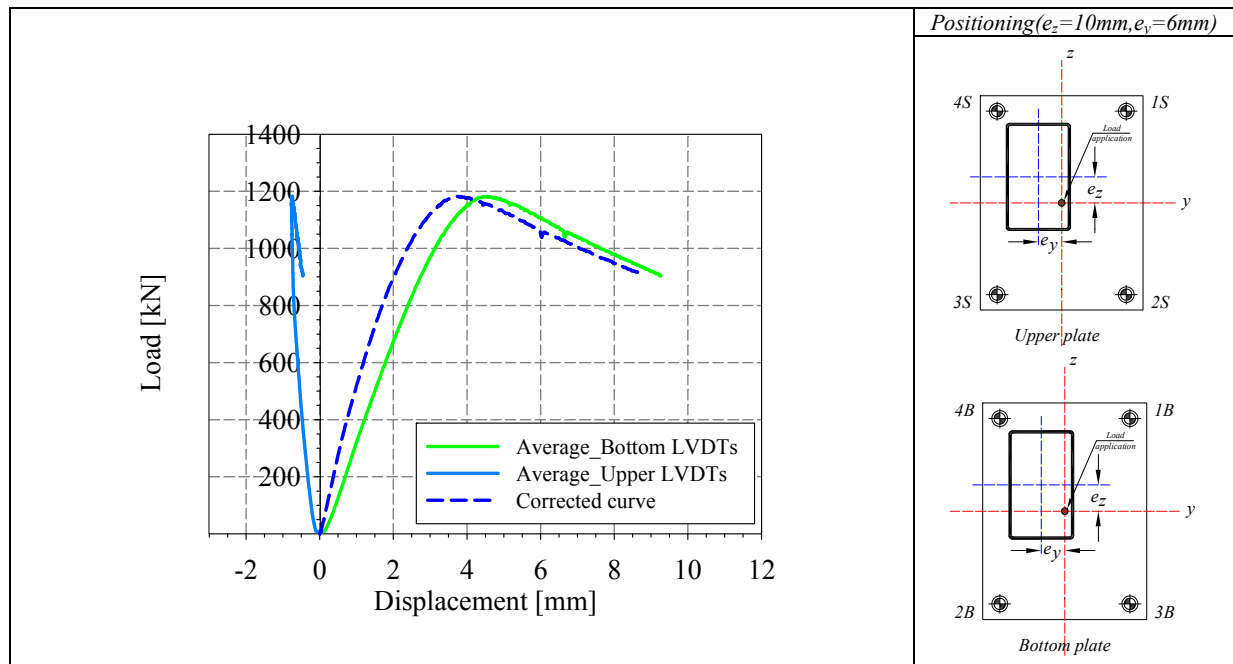
Tensile coupons location

Material stress-strain curves

Material average properties

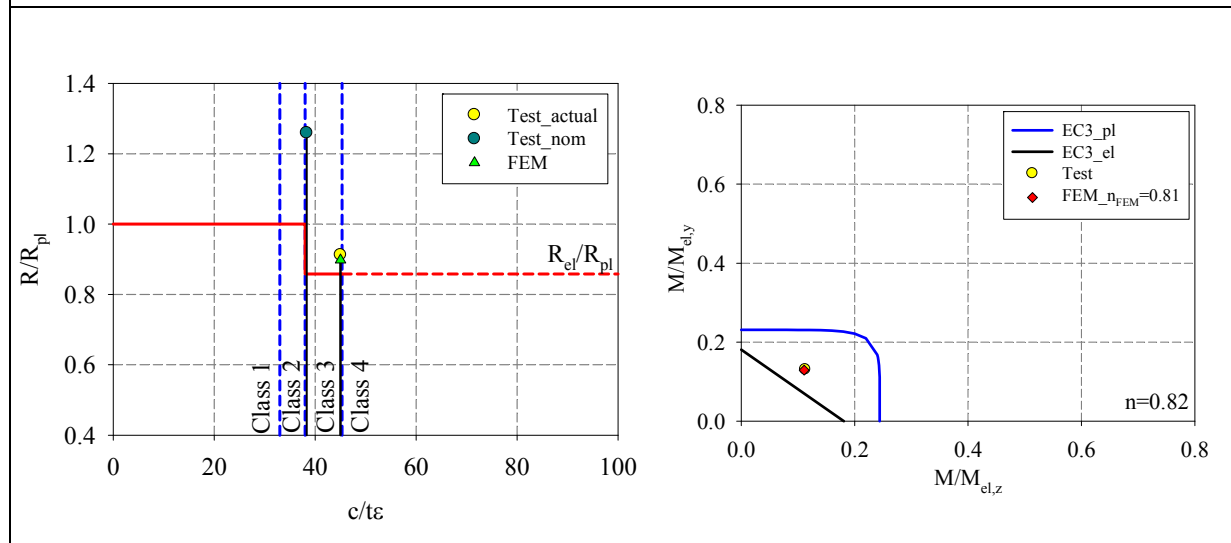
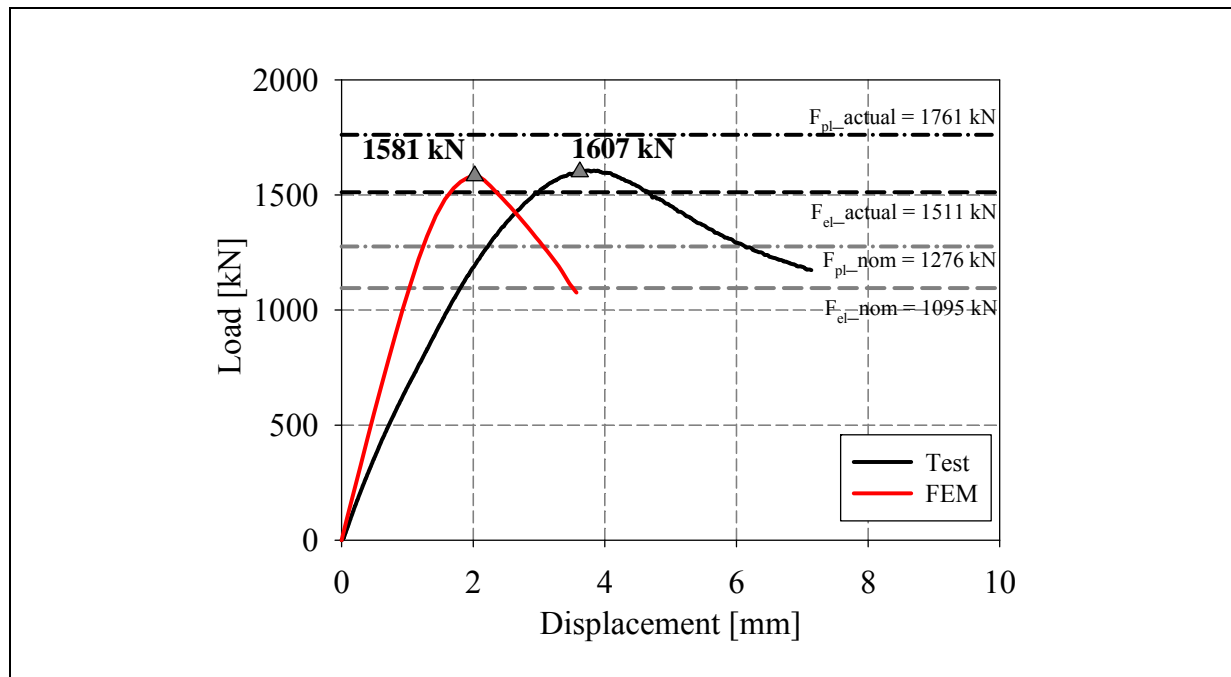






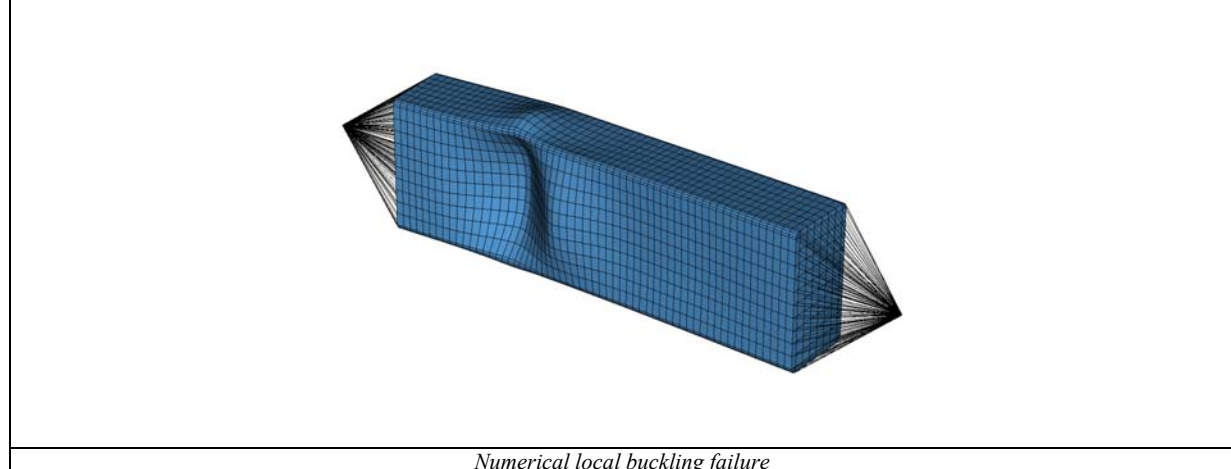
LVDT and strain gauges recordings





Cross-section resistance diagram

M_y - M_z bending moment interaction diagram



Liste of Figures

Figure 1– Australia stadium (Australia), the kelpies (Scotland), Liege Guillemins railway station (Belgium), Madrid Barajas international airport (Spain), London eye (Britain).....	22
Figure 2 – Principles and application steps of proposed “Overall Interaction Concept”.....	26
Figure 3 – Behavior of plates under edge compression.	32
Figure 4 – Behavior of rectangular plates under edge compression.	34
Figure 5 – Behavior of square plates under edge compression.....	34
Figure 6 – Lateral deflection of a buckled plate.....	34
Figure 7 – Buckling coefficient for rectangular plate.	36
Figure 8 – Load versus out-of-plane displacement curves.....	38
Figure 9 – k -curves.....	40
Figure 10 – Values of k for various boundary conditions.	41
Figure 11 – Local buckling coefficients for I-section (left) and box section (right) compression members.	42
Figure 12 – Values of k for centrally loaded columns of rectangular tube section from [11].	44
Figure 13 – Cross-section geometry for use in Equations (19) (20) and (21).....	46
Figure 14 – Buckling of a plate under uni-axial compression.	49
Figure 15 – Stress distribution and effective widths b_e (points A, B and C are to be referred to in Figure 3).	49
Figure 16 – Experimental determination of effective width [18].....	51
Figure 17 – Correlation between test data on stiffened compression and design criteria [19].	53
Figure 18 – Effective section of a member with residual stresses [21].....	54
Figure 19 – Effect of residual stresses and initial imperfections on plate buckling.....	55
Figure 20 – Stress-deflection curve for a plate subjected to mono-axial compression.....	59

Figure 21 – Plastic mechanism.....	60
Figure 22 – Plate local buckling curves.	61
Figure 23 – Definition of plate widths.	66
Figure 24 – Ratio of flange widths definitions-flat width (EN,DIN) over mid-thickness width(BS)-I-sections,b-ratio of flange width definitions; flat width (EN,DIN)over clear-width (AS 4100),I-section [7].	67
Figure 25 – Ratio of the web widths definitions; flat width over clear-width ; I-sections [7].	67
Figure 26 – a) Ratio of widths definitions; flat-width over clear-width,hot-finished RHS, b) Ratio of widths definitions; flat width over clear-width; cold-formed RHS [7].	68
Figure 27 – Numerical comparison of local buckling rules, a) case 4 β -format_all classes, b) case 4 δ -format_all classes.	70
Figure 28 – Numerical comparison of local buckling rules, a) case 4 γ -format_all classes, b) case 4 μ -format_all classes.....	71
Figure 29 – Numerical comparison of local buckling rules_case 4 β -format_class 1(left), class 2 (middle), class 3 (right).	73
Figure 30 – Comparison of local buckling rules_case 4 δ -format_class 1(left), class 2 (middle), class 3 (right).	73
Figure 31 – Numerical comparison of local buckling rules_case 4 γ -format_class 1(left), class 2 (middle), class 3 (right).	74
Figure 32 – Numerical comparison of local buckling rules_case 4 μ -format_class 1(left), class 2 (middle), class 3 (right).	74
Figure 33 – Eurocode 3 cross-section classes.	75
Figure 34 – Plate buckling coefficient (of the web) from the AISC and from the finite strip analysis for the rectangular hollow sections subjected to a strong bending moment [13].	77
Figure 35 – k_{min} values for two types of stress distributions on a simply supported plate.	78

Figure 36 – Comparison of class 3 cross-section resistances according to various standards for a hot finished RHS under major-axis bending – a) flange decisive – b) web decisive [7].	82
Figure 37 – Comparison of class 3 cross-section resistances according to various standards for a hot finished RHS under major-axis bending – Flange decisive [7].....	82
Figure 38 – Comparison of class 3 cross-section resistances according to various standards for a hot finished RHS under major-axis bending – Web decisive [7].....	83
Figure 39 – Design proposal for cross-section resistance of tubular sections [7].....	83
Figure 40 – Verification of class 1 criteria for two dissymmetric cross-sections differing in their web thicknesses, and subjected to a major-axis bending moment.....	85
Figure 41 – Verification of class 2 criteria for three dissymmetric cross-sections differing in their web thicknesses, and subjected to a pure major-axis bending moment.....	86
Figure 42 – Plate slenderness limits for class 4 categories, based on the EN 1993-1-5, Table 4.1-4.2 and the EN 1993-1-1, table 5.3.1.....	91
Figure 43 – Comparison of the Direct Strength Method predictor curves with test data for columns.....	95
Figure 44 – Comparison of the DSM predictor curves with test data for beams.....	96
Figure 45 – P-M-M space.....	98
Figure 46 – Test-to-predicted ratio for the Effective Width Method (left) and the Direct Strength Method (right) for all lipped columns [1].....	100
Figure 47 – Comparison of stub columns test with Eurocodes [2] & [63].	103
Figure 48 – Comparison of beam test results with Eurocodes [2] & [63].	103
Figure 49 – CSM elastic, linear hardening material model.....	104
Figure 50 – Stub column load end-shortening response ($N_u > N_y$) (left), beam moment-curvature response ($M_u > M_{el}$) (right).....	105
Figure 51 – Base curve-relationship between strain ratio and slenderness.....	107
Figure 52 – Partition of a 3500 m beam.....	113

Figure 53 – Measured dimensions.	117
Figure 54 – Measured cross-sectional dimensions and tolerances – RHS_200x100x5_HF..	117
Figure 55 – Geometrical imperfections measurement – LVDTs detail.	118
Figure 56 – Measured local flange and web geometrical imperfections of specimen SHS_LC2_200x200x6_CF.....	119
Figure 57 – Cold-rolled (left bottom) and hot rolled fabrication process.	122
Figure 58 – Analytical models for through-thickness residual stresses; (a) analytical model for panel removal residual stress, (b) analytical model for layering residual stresses.....	123
Figure 59 – Strip length and curvature measurements.	127
Figure 60 – Strip-cutting process.	129
Figure 61 – Cross-section released strips after cutting.	130
Figure 62 – Measured membrane (right column) and flexural (left column) stresses of square sections (part 1).	132
Figure 63 – Measured membrane (right column) and flexural (left column) stresses of square sections (part 2).	133
Figure 64 – Measured membrane (right column) and flexural (left column) stresses of rectangular sections (part 1).	134
Figure 65 – Measured membrane (right column) and flexural (left column) stresses of rectangular sections (part 2).	135
Figure 66 – Measured membrane (right column) and flexural (left column) stresses of circular sections (part 1).	136
Figure 67 – Measured membrane (right column) and flexural (left column) stresses of circular sections (part 2).	137
Figure 68 – Geometrical deformation due to residual stresses.	139
Figure 69 – Adopted block representation for the calculation of the non-equilibrated stresses (Profile SHS_HF_200x200x6.3).	141

Figure 70 – Locations of the tensile coupons were cut from different faces.	143
Figure 71 – Necked and straight tensile coupons.....	144
Figure 72 – Tensile coupons testing.....	145
Figure 73 – Stress-strain curves from flat and corner regions of a cold formed profile – SHS_200x200x6_CF.....	145
Figure 74 – Stress-strain curves from flat and corner regions of a hot-finished profile – RHS_250x150x5_HF.....	146
Figure 75 – General test setup and failure shapes of the stub columns.	148
Figure 76 – Load-displacement corrected curves.	150
Figure 77 – Material vs. stub stress-strain curves - RHS_200x100x4_CF.	151
Figure 78 – Material vs. stub stress-strain curves – CHS_159_6.3_CF.	151
Figure 79 – Material vs. stub stress-strain curves – CHS_159_7.1_HF.	152
Figure 80 – General test configuration – Front and side views.	154
Figure 81 – Hinge detail.....	155
Figure 82 – Endplate fixed to bottom hinge plate with bolts.....	155
Figure 83 – LVDTs and specimen positions on upper and bottom endplates.....	156
Figure 84 – General test setup of cross-section tests.	158
Figure 85 – Failure shapes of all cross-section tests.	159
Figure 86 – Comparison of cross-section capacity of RHS and SHS experimental results with EC3- resistances – nominal f_y value – combined load cases.....	163
Figure 87 – Comparison of cross-section capacity of RHS and SHS experimental results with EC3- resistances – actual f_y value – combined load cases.	163
Figure 88 – Comparison of cross-section capacity of RHS and SHS experimental results with EC3- resistances – nominal f_y value – simple load cases.....	164

Figure 89 – Comparison of cross-section capacity of RHS and SHS experimental results with EC3- resistances – actual f_y value – simple load cases. 164

Figure 90 – Comparison of cross-section capacity of CHS experimental results with EC3- resistances – nominal f_y value – combined load cases. 165

Figure 91 – Comparison of cross-section capacity of CHS experimental results with EC3- resistances – actual f_y value – combined load cases..... 165

Figure 92 – Comparison of cross-section capacity of CHS experimental results with EC3- resistances – nominal f_y value – simple load cases. 166

Figure 93 – Comparison of cross-section capacity of CHS experimental results with EC3- resistances – actual f_y value – simple load cases..... 166

Figure 94 – Gathered results and comparison with DSM curve. 167

Figure 95 – Experimental results relative to pure compression load cases, a) cold-formed cross-sections, b) hot-rolled and hot-formed cross-sections. 168

Figure 96 – Experimental results relative to major-axis bending load cases. 168

Figure 97 – Experimental results relative to combined load cases, a) cold-formed cross-sections, b) hot-rolled and hot-formed cross-sections..... 169

Figure 98– Mesh configurations. 174

Figure 99 – LBA (left) and GMNIA (right) results for SHS and RHS sections. 175

Figure 100 – Finite element model assumptions..... 176

Figure 101 – Applied load with shifted truss center corresponding to different load cases. . 177

Figure 102 – Detail view of the corner modeling. 177

Figure 103 – Adopted measured membrane stresses for section SHS_HF_200_200_6.3..... 178

Figure 104 – Material stress strain laws adopted in FE calculations for specimens RHS_220x120x6_CF. 179

Figure 105 – Material stress strain laws adopted in FE calculations for specimens RHS_200x100x4_CF.	180
Figure 106 – FE peak loads vs. experimental loads.	181
Figure 107 – Numerical vs. experimental load displacement curves of specimens, a) LC2_RHS_250x150x5_HF, b) LC1_RHS_250x150x5_HF.	185
Figure 108 – Numerical vs. experimental load displacement curves of specimens, a) LC3_SHS_200x200x6_CF, b) LC1_SHS_200x200x5_CF.	185
Figure 109 – Testing rig and torsional restraints of loading points of the specimen [7].	187
Figure 110 – Stress-strain curve for specimen sc_A17-1-SHS 180/5 – S355.	189
Figure 111 – Residual stress patterns for a) square hollow sections, b) rectangular hollow sections [50].	190
Figure 112 – FE results vs experimental results.	191
Figure 113 – Support conditions and external load application.	193
Figure 114 – Local imperfection according to Eurocode 1993 part 1-5.	194
Figure 115 – Adopted imperfections for the 45 plated tests.	197
Figure 116 – Initial imperfections introduced by hand for the RHS 200x100x4 specimen... ..	198
Figure 117 – Different imperfections of specimen RHS 200x100x4 introduced through the first buckling mode.	199
Figure 118 – Ultimate results of cold-formed sections according to the different adopted imperfections.	202
Figure 119 – Ultimate results of hot-finished sections according to the different imperfections adopted.	203
Figure 120 – Ultimate results of hot-finished stub columns according to the different imperfections adopted.	204
Figure 121 – Ultimate results of hot-finished stub columns according to the different imperfections adopted.	204

Figure 122 – Ultimate results of hot-formed stub columns according to the different imperfections adopted. 206

Figure 123 – Ultimate results of hot-rolled stub columns according to the different imperfections adopted. 208

Figure 124 – Ultimate results of hot-rolled stub columns according to the different imperfections adopted. 208

Figure 125 – RHS cross-section capacities subjected to pure compression under different imperfections’ amplitude..... 210

Figure 126 – RHS cross-section capacities subjected to major-axis bending under different imperfections’ amplitude..... 210

Figure 127 – Local geometrical imperfections adopted for both square and rectangular hollow sections..... 211

Figure 128 – Half sine wave in a rectangular cross-section..... 212

Figure 129 – Load-path representation. 213

Figure 130 – Comparison of GMNIA results for the SHS 60x60x2.6 – a) $M / M_{el,y}$ vs. $M / M_{el,z}$ diagram – b) N / N_{pl} vs. $M / M_{el,y}$ diagram. 217

Figure 131 – Comparison of GMNIA results for the SHS 80x80x2.58 – a) $M / M_{el,y}$ vs. $M / M_{el,z}$ diagram – b) N / N_{pl} vs. $M / M_{el,y}$ diagram..... 217

Figure 132 – Comparison of GMNIA results for the SHS 100x100x2.56 – a) $M / M_{el,y}$ vs. $M / M_{el,z}$ diagram – b) N / N_{pl} vs. $M / M_{el,y}$ diagram..... 217

Figure 133 – Comparison of GMNIA results for the SHS 150x150x2.54 – a) $M / M_{el,y}$ vs. $M / M_{el,z}$ diagram – b) N / N_{pl} vs. $M / M_{el,y}$ diagram..... 218

Figure 134 – Comparison of GMNIA results for the SHS 200x200x2.53 – a) $M / M_{el,y}$ vs. $M / M_{el,z}$ diagram – b) N / N_{pl} vs. $M / M_{el,y}$ diagram..... 218

Figure 135 – Comparison of GMNIA results for the SHS 250x250x2.52 – a) $M / M_{el,y}$ vs. $M / M_{el,z}$ diagram – b) N / N_{pl} vs. $M / M_{el,y}$ diagram..... 218

Figure 136 – Comparison of GMNIA results for the RHS 60x30x2.6 – a) $M / M_{el,y}$ vs. $M / M_{el,z}$ diagram – b) N / N_{pl} vs. $M / M_{el,y}$ diagram.	219
Figure 137 – Comparison of GMNIA results for the RHS 80x40x2.58 – a) $M / M_{el,y}$ vs. $M / M_{el,z}$ diagram – b) N / N_{pl} vs. $M / M_{el,y}$ diagram.	219
Figure 138 – Comparison of GMNIA results for the RHS 100x50x2.56 – a) $M / M_{el,y}$ vs. $M / M_{el,z}$ diagram – b) N / N_{pl} vs. $M / M_{el,y}$ diagram.	219
Figure 139 – Comparison of GMNIA results for the RHS 150x75x2.54 – a) $M / M_{el,y}$ vs. $M / M_{el,z}$ diagram – b) N / N_{pl} vs. $M / M_{el,y}$ diagram.	220
Figure 140 – Comparison of GMNIA results for the RHS 200x100x2.53 – a) $M / M_{el,y}$ vs. $M / M_{el,z}$ diagram – b) N / N_{pl} vs. $M / M_{el,y}$ diagram.	220
Figure 141 – Comparison of GMNIA results for the RHS 250x125x2.52 – a) $M / M_{el,y}$ vs. $M / M_{el,z}$ diagram – b) N / N_{pl} vs. $M / M_{el,y}$ diagram.	220
Figure 142 – GMNIA results for the load case n30_50 – a) Square hollow sections – b) Rectangular hollow sections.	221
Figure 143 – GMNIA results for the load case n30_70 – a) Square hollow sections – b) Rectangular hollow sections.	221
Figure 144 – GMNIA results for the load case n70_50 – a) Square hollow sections – b) Rectangular hollow sections.	221
Figure 145 – Elastic-perfectly plastic with 2% strain hardening adopted material law.	222
Figure 146 – Assumptions for material behavior.	223
Figure 147 – DIN recommendations for residual stresses.	223
Figure 148 – Numerical residual stress assumptions (with 2 elements at the corners).	224
Figure 149 – Selection of load cases for $N + M_y + M_z$ combined situations.	226
Figure 150 – Strength surface of a rectangular hollow section.	226
Figure 151– Adopted simple Ramberg-Osgood material law for flat regions.	228
Figure 152– Adopted multi-linear material law for corner regions.	229

Figure 153 – Comparison of R_{RESIST} calculations with MNA, EC3 and Matlab tool for the combined load case: n40_70. 231

Figure 154 – Comparison of R_{RESIST} calculations with MNA, EC3 and Matlab software for the combined load case: n60_70. 232

Figure 155 – Comparison of R_{RESIST} calculations with MNA, EC3 and Matlab software for the combined load case: n80_70. 232

Figure 156 – Highest disparities likely to occur between the EC3 plastic equations and Matlab software – Example for RHS 200x100x4 section. 236

Figure 157 – Comparison of R_{RESIST} calculations with EC3 and Matlab tool for the combined load case: a) n0_45, b) n40_45..... 237

Figure 158 – Comparison of R_{RESIST} calculations with EC3 and Matlab software for the combined load case: n80_45. 237

Figure 159 – Comparison of R_{RESIST} calculations with, EC3 and Matlab software for the combined load case: n20_45. 239

Figure 160 – $R_{STAB_FINELg} / R_{STAB_CUFSM}$ graphical representation as a function of sections' slenderness (class). 241

Figure 161 – Experimental and numerical test results relative to pure compression load cases, a) cold-formed cross-sections, b) hot-rolled and hot-formed cross-sections. 244

Figure 162 – Experimental and numerical test results relative to major-axis bending load cases. 244

Figure 163 – Experimental and numerical test results relative to combined load cases, a) cold-formed cross-sections, b) hot-rolled and hot-formed cross-sections. 245

Figure 164 – Hot-rolled and cold-formed material laws adopted in numerical computations. 246

Figure 165 – Numerical results relative to hot-rolled and cold-formed cross-sections subjected to compression..... 248

Figure 166 – Numerical stress-strain results reported with the hot-rolled and cold-formed material laws.	249
Figure 167 – Numerical stress-strain results reported with the hot-rolled material laws.	250
Figure 168 – Numerical stress-strain results reported with the cold-formed material laws...	250
Figure 169 – FE results for square and rectangular sections under compression, various aspect ratios, S355.....	251
Figure 170 – FE results for square and rectangular sections under major axis bending moment, various aspect ratios, S355.....	252
Figure 171 – Comparison of end moments and mid moments of a rectangular hollow section subjected to combined loading with a high level of axial force [7].	253
Figure 172 – Upper and lower bounds of buckling curves.	255
Figure 173 – Schematic representation of the adopted Ayrton-Perry approach.	260
Figure 174 – FE results relative to various cross-section ratios in compression, S235 (both European and virtual sections are considered in this graph).....	262
Figure 175 – Computations relative to hot-rolled sections with $h/b = 1.1$ and $h/b = 1.8$...	263
Figure 176 – Ultimate strains reached for all the numerical calculations relative to hot-rolled cross-sections.	264
Figure 177 – Zoomed area of Figure 174.....	265
Figure 178 – Comparison of the factor $\eta_{proposal}$ with the numerical values η_{GMNIA} for square sections in compression.....	265
Figure 179 – All FE results of hot-rolled sections subjected to compression, represented in function of the yield stress.	266
Figure 180 – Design curves proposals relative to hot-rolled sections in compression a) without numerical results, b) with numerical results.	267
Figure 181 – FE results relative to various aspect ratios, S235.	269

Figure 182 – All FE results of cold-formed sections subjected to compression, represented in function of the yield stress. 271

Figure 183 – FE results of square cross-sections represented in function of the yield stress (left); zoomed area of results situated between $\lambda_{CS} = 0.4$ and $\lambda_{CS} = 0.8$ (right). 271

Figure 184 – Adopted material laws relative to hot-rolled and cold formed sections. 272

Figure 185 – Proposed design curves for cold-formed sections in compression, 1st approach a) without numerical results, b) with numerical results. 272

Figure 186 – Normalized strain demand in function of the relative slenderness. 274

Figure 187 – Cross-section capacity as function of the strain demand. 275

Figure 188 – Design curves proposals relative to cold-formed sections in compression, 2nd approach. a) without numerical results, b) with numerical results. 276

Figure 189 – FE results relative to various cross-section ratios in major-axis bending, S235. 277

Figure 190 – Extension of numerical results for cross-sections having the following two aspect ratios: $h/b = 2$ and 2.5 278

Figure 191 – a) FE results of square cross-sections represented in function of the yield stress, b) All FE results of hot-rolled sections subjected to major-axis bending, represented in function of the yield stress. 279

Figure 192 – Design curves proposals relative to hot-rolled sections subjected to major-axis bending a) without numerical results, b) with numerical results. 279

Figure 193 – FE results relative to various cross-section ratios subjected to a major-axis bending moment, S235 (the European and derived sections are considered in this graph). ... 281

Figure 194 – Extension of numerical results for cross-sections having the following three aspect ratio $h/b = 1.5, 2$ and 2.5 282

Figure 195 – a) FE results of square cross-sections represented in function of the yield stress b) All FE results of cold-formed sections subjected to a major-axis bending, represented in function of the yield stress. 283

Figure 196 – Design curves proposals relative to cold-formed sections subjected to a pure major-axis bending moment, 1st approach. 283

Figure 197 – Normalized strain demand in function of the relative slenderness. 285

Figure 198 – Cross-section capacity as function of the strain demand. 285

Figure 199 – Design curves proposals relative to cold-formed sections in major-axis bending, 2nd approach. 286

Figure 200 – Comparison of the relative slenderness of different cross-section with various aspect ratios subjected to a minor and a major-axis bending moment. 288

Figure 201 – a) FE results of square cross-sections represented in function of the yield stress, b) All FE results of hot-rolled sections subjected to a minor-axis bending moment, represented in function of the yield stress. 289

Figure 202 – Design curve proposal relative to hot-rolled sections subjected to a pure minor-axis bending a) without numerical results, b) with numerical results. 289

Figure 203 – Design curves proposals relative to cold-formed sections subjected to a minor-axis bending, 1st approach (left), 2nd approach (right). 290

Figure 204 – Numerical results corresponding to cold - formed sections subjected to a minor-axis bending represented with the proposed approaches, 1st approach (left), 2nd approach (right). 291

Figure 205 – Numerical results corresponding to cold - formed sections subjected to a minor-axis bending represented in function of the yield stresses, 1st approach (left), 2nd approach (right). 292

Figure 206 – R_{RESIST} calculation based on EC3 and exact formulation for a rectangular cross-section ($h/b = 1.5$) a) n vs. m_y , b) R_{RESIST} vs. n 293

Figure 207 – R_{RESIST} calculation based on EC3 and exact formulation for a rectangular cross-section ($h/b = 1$) a) n vs. m_y , b) R_{RESIST} vs. n 294

Figure 208 – Comparison of results computed with R_{RESIST_EC3} and $Exact_R_{RESIST}$ for square cross-sections subjected to combined load cases with various degrees of axial forces. 296

Figure 209 – Design curves proposals relative to hot-formed sections subjected to combined load cases.....	299
Figure 210 – FE results and design curves relative to square cross-sections ($h/b = 1.0$) subjected to combined loading with various degrees of axial forces.....	300
Figure 211 – FE results and design curves relative to rectangular cross-sections ($h/b = 1.5$) subjected to combined loading with various degrees of axial forces.....	301
Figure 212 – FE results and design curves relative to rectangular cross-sections ($h/b = 2.0$) subjected to combined loading with various degrees of axial forces.....	302
Figure 213 – FE results and design curves relative to rectangular cross-sections ($h/b = 2.5$) subjected to combined loading with various degrees of axial forces.....	303
Figure 214 – FE results of cross-sections represented in function of the yield stress.....	304
Figure 215 – FE results and design curves relative to rectangular cross-sections ($h/b = 1.5$) subjected to combined loading with various small degrees of axial forces.....	305
Figure 216 – a) Ultimate strains in function of the relative slenderness for combined load cases of square cross-sections b) Differences between hot-rolled and cold-formed material laws.....	306
Figure 217 – Design curves proposals relative to cold-formed sections subjected to combined load cases (1 st approach).....	308
Figure 218 – FE results and design curves relative to square cross-sections ($h/b = 1.0$) subjected to combined loading with various degrees of axial forces (1 st approach).....	310
Figure 219 – FE results and design curves relative to square cross-sections ($h/b = 1.5$) subjected to combined loading with various degrees of axial forces (1 st approach).....	311
Figure 220 – FE results and design curves relative to square cross-sections ($h/b = 2.0$) subjected to combined loading with various degrees of axial forces (1 st approach).....	312

Figure 221 – FE results and design curves relative to square cross-sections ($h/b = 2.5$) subjected to combined loading with various degrees of axial forces (1st approach)..... 313

Figure 222 – FE results of cross-sections represented in function of the yield stress (1st approach)..... 314

Figure 223 – Design curves proposals relative to cold-formed sections subjected to combined load cases (2nd approach)..... 318

Figure 224 – FE results and design curves relative to square cross-sections ($h/b = 1.0$) subjected to combined loading with various degrees of axial forces (2nd approach)..... 319

Figure 225 – FE results and design curves relative to square cross-sections ($h/b = 1.5$) subjected to combined loading with various degrees of axial forces (2nd approach)..... 320

Figure 226 – FE results and design curves relative to square cross-sections ($h/b = 2.0$) subjected to combined loading with various degrees of axial forces (2nd approach)..... 321

Figure 227 – FE results and design curves relative to square cross-sections ($h/b = 2.5$) subjected to combined loading with various degrees of axial forces (2nd approach)..... 322

Figure 228 – FE results of cross-sections represented in function of the yield stress (2nd approach)..... 323

Figure 229 – Differences between hot-formed and cold-formed material laws..... 325

Figure 230 – All cross-sections, Hot-rolled, Pure compression a) Comparison of Proposal and EC3 results with FEM results b) Frequency distributions (total number of results: 1506). .. 327

Figure 231 – All cross-sections, Cold-formed, First approach, Pure compression a) Comparison of Proposal and EC3 results with FEM results b) Frequency distributions(total number of results: 1482). 327

Figure 232 – All cross-sections, Cold-formed, Second approach, Pure compression a) Comparison of Proposal and EC3 results with FEM results b) Frequency distributions(total number of results: 1482). 327

Figure 233 – Comparison of EC3 results with FEM results for square cross-sections subjected to major-axis bending a) hot-rolled cross-sections, b) cold-formed cross-sections. 328

Figure 234 – All cross-sections, Hot-rolled, Major-axis bending a) Comparison of Proposal and EC3 results with FEM results b) Frequency distributions (total number of results: 1506). 330

Figure 235 – All cross-sections, Cold-formed, First approach, Major-axis bending a) Comparison of Proposal and EC3 results with FEM results b) Frequency distributions(total number of results: 1482). 330

Figure 236 – All cross-sections, Cold-formed, Second approach, Major-axis bending a) Comparison of Proposal and EC3 results with FEM results b) Frequency distributions(total number of results: 1482). 330

Figure 237 – Comparison of EC3 results with FEM results for square cross-sections subjected to combined loadings with level of axial load equal to 20% of N_{pl} 331

Figure 238 – All cross-sections, Hot-rolled, Combined loading with level of axial load equal to 20% of N_{pl} a) Comparison of Proposal and EC3 results with FEM results b) Frequency distributions(total number of results: 5076). 333

Figure 239 – All cross-sections, Cold-formed, First approach, Combined loading with level of axial load equal to 20% of N_{pl} a) Comparison of Proposal and EC3 results with FEM results b) Frequency distributions(total number of results: 5850). 333

Figure 240 – All cross-sections, Cold-formed, First approach, Combined loading with level of axial load equal to 20% of N_{pl} a) Comparison of Proposal and EC3 results with FEM results b) Frequency distributions(total number of results: 5850). 334

Figure 241 – All cross-sections, Hot-rolled, Combined loading with level of axial load equal to 60% of N_{pl} a) Comparison of Proposal and EC3 results with FEM results b) Frequency distributions(total number of results: 5076). 335

Figure 242 – All cross-sections, Cold-formed, First approach, Combined loading with level of axial load equal to 60% of N_{pl} a) Comparison of Proposal and EC3 results with FEM results b) Frequency distributions(total number of results: 5850). 335

Figure 243 – All cross-sections, Cold-formed, Second approach, Combined loading with level of axial load equal to 60% of N_{pl} a) Comparison of Proposal and EC3 results with FEM results b) Frequency distributions(total number of results: 5850). 336

Figure 244 – European sections, Hot-rolled, Pure compression a) Comparison of Proposal and EC3 results with FEM results b) Frequency distributions (total number of results: 870). 338

Figure 245 – European sections, Hot-rolled, Major-axis bending a) Comparison of Proposal and EC3 results with FEM results b) Frequency distributions (total number of results: 870). 338

Figure 246 – European sections, Hot-rolled, Combined loading with level of axial load equal to 20% of N_{pl} a) Comparison of Proposal and EC3 results with FEM results b) Frequency distributions (total number of results: 4350). 338

Figure 247 – European sections, Hot-rolled, Combined loading with level of axial load equal to 60% of N_{pl} a) Comparison of Proposal and EC3 results with FEM results b) Frequency distributions (total number of results: 4350). 339

Figure 248 – European sections, Cold-formed, First approach, Pure compression a) Comparison of Proposal and EC3 results with FEM results b) Frequency distributions (total number of results: 894). 339

Figure 249 – European sections, Cold-formed, First approach, Major-axis bending a) Comparison of Proposal and EC3 results with FEM results b) Frequency distributions (total number of results: 894). 339

Figure 250 – European sections, Cold-formed, First approach, Combined loading with level of axial load equal to 20% of N_{pl} a) Comparison of Proposal and EC3 results with FEM results b) Frequency distributions(total number of results: 3576). 340

Figure 251 – European sections, Cold-formed, First approach, Combined loading with level of axial load equal to 60% of N_{pl} a) Comparison of Proposal and EC3 results with FEM results b) Frequency distributions (total number of results: 3576). 340

Figure 252 – European sections, Cold-formed, Second approach, Pure compression a) Comparison of Proposal and EC3 results with FEM results b) Frequency distributions (total number of results: 894). 340

Figure 253 – European sections, Cold-formed, Second approach, Major-axis bending a) Comparison of Proposal and EC3 results with FEM results b) Frequency distributions (total number of results: 894).	341
Figure 254 – European sections, Cold-formed, Second approach, Combined loading with level of axial load equal to 20% of N_{pl} a) Comparison of Proposal and EC3 results with FEM results b) Frequency distributions (total number of results: 3576)	341
Figure 255 – European sections, Cold-formed, Second approach, Combined loading with level of axial load equal to 60% of N_{pl} a) Comparison of Proposal and EC3 results with FEM results b) Frequency distributions (total number of results: 3576).	341
Figure 256 – FEM and proposal results relative to cold-formed sections subjected to combined loading (Second approach, S235).	342
Figure 257 – FEM and proposal results relative to hot-rolled sections subjected to combined loading (S235).	343
Figure 258 – Application steps of the proposed OIC design curves.	345
Figure 259 – Considered cross-section.	349
Figure 260 – Stress distribution.	350
Figure 261 – Stress distribution at the plate extremities.	351
Figure 262 – Internal compressed elements.	353
Figure 263 – Considered cross-section.	356
Figure 264 – Stress distribution.	357
Figure 265 – Stress distribution at the plate extremities.	358
Figure 266 – Representation of various degrees of biaxiality for both a square cross-section and a rectangular cross-section.	367
Figure 267 – Test setup and coupons before failure	382
Figure 268 – General view of the coupons before testing	382
Figure 269 – Curvature due to flexural stresses included in the cold formed profiles	383

Figure 270 – Coupons extracted from square and rectangular sections before testing.....	383
Figure 271 – Coupons extracted from square and rectangular sections after testing.....	383
Figure 272 – Measured membrane (right column) and flexural (left column) residual stresses of square sections	385
Figure 273 – Measured membrane (right column) and flexural (left column) residual stresses of rectangular sections.....	386
Figure 274 – Measured membrane (right column) and flexural (left column) residual stresses of circular sections	387
Figure 275 – Strip marking	388
Figure 276 – Cutting the space reserved for residual stresses and containing the marked strips, after measuring initial lengths and curvatures of the corresponding strips.....	389
Figure 277 – Cutting of the constitutive plates (for circular profiles no need to pass through this phase because direct cutting of the strips is applied)	389
Figure 278 – Cutting of each strip corresponding to each section, and measurement of the final lengths and curvatures.....	391
Figure 279 – General view of the sections’ strips all together.....	393
Figure 280 – General view of the set up with the bar containing the LVDTs for the imperfections measurements	395

Liste of Tables

Table 1 – Source of k values plotted in Figure 9.	39
Table 2 – Studied elements and load conditions.	63
Table 3 – Format of local buckling rules.	64
Table 4 – Conversion factors.	65
Table 5 – Definition of width of plate elements in selected design specifications.	65
Table 6 – Denomination of cross-section classes in each specification.	68
Table 7 – Numerical comparison of local buckling rules (case 1, 2, 3, and 5).	72
Table 8 – Determination of the plate buckling coefficient for particular cases.	78
Table 9 – λ_p values relative to the class 3-4 border.	79
Table 10 – Comparison of b/t ratios with relative plate slenderness values λ_p	80
Table 11 – Application of table 5.2 of EN 1933-1-1 for two dissymmetric sections subjected to a major-axis bending with different web thicknesses (highlighted in red).	84
Table 12 – Application of table 5.2 of EN 1933-1-1 for three dissymmetric sections subjected to a major-axis bending.	86
Table 13 – Application of table 5.2 of EN 1933-1-1 for 5 dissymmetric sections subjected to a major-axis bending.	88
Table 14 – Test program for cross-sectional tests.	115
Table 15 – Main and sub-sources of Type I residual stresses.	122
Table 16 – Residual stresses measuring techniques.	125
Table 17 – Percentage of non-equilibrated stresses.	142
Table 18 – Measured properties and ultimate loads of stub columns.	149
Table 19 – Comparison of numerical and experimental ultimate loads.	160

Table 20 – Summary of the gathered test data.....	169
Table 21 – Comparison of numerical and experimental ultimate loads.....	183
Table 22 – Test program for cross-section tests [7].....	186
Table 23 – Measured cross-sectional dimensions [7].	188
Table 24 – Measured material properties [7].	189
Table 25 – Comparison of experimental and numerical ultimate loads.....	190
Table 26 – Comparison of experimental ultimate load factor with ultimate load factors of cold-formed sections according to the different imperfections adopted.	201
Table 27 – Comparison of experimental ultimate load factor with ultimate load factors of hot-finished sections according to the different imperfections adopted.	202
Table 28 – Comparison of experimental ultimate load factor with ultimate load factors of cold-formed stub columns according to the different imperfections adopted.....	203
Table 29 – Comparison of experimental ultimate load factor with ultimate load factors of hot-finished stub columns according to the different imperfections adopted.....	203
Table 30 – Adopted combined load cases for European sections.....	227
Table 31 – Adopted combined load cases for invented sections.....	227
Table 32 – Comparisons of R_{RESIST_EC3} and R_{RESIST_MNA} with R_{RESIST_Matlab} , load cases: n40_70, n60_70, n80_70.....	233
Table 33 – Illustrated errors with area consideration in the Eurocode 3.....	234
Table 34 – Comparisons of R_{RESIST_EC3} with R_{RESIST_Matlab} , load cases: n0_45, n40_45 and n80_45.....	238
Table 35 – Comparisons of R_{RESIST_EC3} with R_{RESIST_Matlab} , load case: n20_45.....	239
Table 36 – R_{STAB_FINELg} vs. R_{STAB_CUFSM} tabulated values for calculated sections under combined load case.	241

Table 37 – Design curves for the case of hot-rolled hollow sections in compression.	268
Table 38 – Design curves for the case of cold-formed hollow sections in compression (1 st approach).....	273
Table 39 – Design curves for the case of cold-formed hollow sections in compression (2 nd approach for $\lambda_{CS} > \lambda_0$).	276
Table 40 – Design curves for the case of hot-formed hollow sections subjected to a major-axis bending moment.	280
Table 41 – Design curves for the case of cold-formed hollow sections subjected to a major-axis bending (1 st approach).	284
Table 42 – Design curves for the case of cold-formed hollow sections subjected to a major-axis bending, (2 nd approach for $\lambda_{CS} > \lambda_0$).	287
Table 43 – Design curve for the case of hot-rolled hollow sections subjected to a minor-axis bending.	290
Table 44 – Design curves for the case of cold-formed hollow sections subjected to a minor-axis bending, 1 st approach.	291
Table 45 – Design curves for the case of cold-formed hollow sections subjected to a minor-axis bending, (2 nd approach for $\lambda_{CS} > \lambda_0$).	291
Table 46 – Design curves proposals relative to hot-rolled sections subjected to combined load cases.	298
Table 47 – Design curves proposals relative to cold-formed sections subjected to combined load cases (1 st approach).	309
Table 48 – Design curves proposals relative to cold-formed sections subjected to combined load cases (2 st approach).	317
Table 49 – Comparison between FEM, EC3 and proposal results for all treated load cases.	324
Table 50 – Proposed OIC design curves for simple load cases.	346
Table 51 – Proposed OIC design curves for combined load cases.	347

Table 52 – Cross-section properties (SHS).....	349
Table 53 – Cross-section properties (RHS).....	356
Table 54 – Measured geometrical dimensions.....	377
Table 55 – Measured material properties.....	379